Biological Magnetic Resonance
Volume 8

Spin Labeling

Theory and Applications

A Continuation Order Plan is available for this series. A continuation order will bring delivery of each new volume immediately upon publication. Volumes are billed only upon actual shipment. For further information please contact the publisher.

Biological Magnetic Resonance
Volume 8

Spin Labeling
Theory and Applications

Edited by

Lawrence J. Berliner
Ohio State University
Columbus, Ohio

and

Jacques Reuben
Hercules Incorporated
Research Center
Wilmington, Delaware

PLENUM PRESS • NEW YORK AND LONDON

The Library of Congress has cataloged the first volume of this series as follows:

Library of Congress Cataloging in Publication Data

Main entry under title:

Biological magnetic resonance:

Includes bibliographies and indexes.
1. Magnetic resonance. 2. Biology—Technique. I. Berliner, Lawrence, J. II. Reuben, Jacques.
QH324.9.M28B56 574.19'285 78-16035
AACR1

Personal computer software intended to supplement Chapter 1 of this volume (Schneider and Freed) will be found on a diskette mounted inside the back cover.

If your diskette is defective in manufacture or has been damaged in transit, it will be replaced at no charge if returned within 30 days of receipt to Managing Editor, Plenum Press, 233 Spring Street, New York, NY 10013.

The publisher makes no warranty of any kind, expressed or implied, with regard to the software reproduced on the diskette or the accompanying documentation. The publisher shall not be liable in any event for incidental or consequential damages or loss in connection with, or arising out of, the furnishing, performance, or use of the software.

ISBN-13:978-1-4612-8060-6 e-ISBN-13:978-1-4613-0743-3
DOI:10.1007/978-1-4613-0743-3

© 1989 Plenum Press, New York
Softcover reprint of the hardcover 1st edition 1989

A Division of Plenum Publishing Corporation
233 Spring Street, New York, N.Y. 10013

All rights reserved

No part of this book may be reproduced, stored in a retrieval system, or transmitted in any form or by any means, electronic, mechanical, photocopying, microfilming, recording, or otherwise, without written permission from the Publisher

Contributors

Jacob Anglister • Department of Polymer Research, Weizmann Institute of Science, Rehovot 76100, Israel

Barney L. Bales • Department of Physics and Astronomy, California State University, Northridge, California 91330

Albert H. Beth • Department of Molecular Physiology and Biophysics, Vanderbilt University, Nashville, Tennessee 37232

P. A. de Jager • Department of Molecular Physics, Agricultural University, 6703 BC Wageningen, The Netherlands

Gareth R. Eaton • University of Denver, Denver, Colorado 80208

Sandra S. Eaton • University of Colorado at Denver, Denver, Colorado 80204

Jim B. Feix • National Biomedical ESR Center, Department of Radiology, Medical College of Wisconsin, Milwaukee, Wisconsin 53226

Jack H. Freed • Baker Laboratory of Chemistry, Cornell University, Ithaca, New York 14853-1301

Olga H. Hankovszky • Central Laboratory, Chemistry, University of Pécs, H-7643 Pécs, Hungary

M. A. Hemminga • Department of Molecular Physics, Agricultural University, 6703 BC Wageningen, The Netherlands

Kálmán Hideg • Central Laboratory, Chemistry, University of Pécs, H-7643 Pécs, Hungary

James S. Hyde • National Biomedical ESR Center, Department of Radiology, Medical College of Wisconsin, Milwaukee, Wisconsin 53226

Derek Marsh • Department of Spectroscopy, Max Planck Institute for Biophysical Chemistry, D-3400 Göttingen, Federal Republic of Germany

Ronald P. Mason • Laboratory of Molecular Biophysics, National Institute of Environmental Health Sciences, Research Triangle Park, North Carolina 27709

Carolyn Mottley • Department of Chemistry, Luther College, Decorah, Indiana 52101

Jane H. Park • Department of Molecular Physiology and Biophysics, Vanderbilt University School of Medicine, Nashville, Tennessee 37232

Bruce H. Robinson • Department of Chemistry, University of Washington, Seattle, Washington 98195

David J. Schneider • Baker Laboratory of Chemistry, Cornell University, Ithaca, New York 14853-1301. *Present address:* IBM Corporation, Kingston, New York 12401.

Witold K. Subczynski • Department of Biophysics, Institute of Molecular Biology, Jagiellonian University, Crakow, Poland

Wolfgang E. Trommer • Department of Chemistry, University of Kaiserslautern, Kaiserslautern, Federal Republic of Germany

Preface

We present this special topics volume on an area which has not received thorough coverage for over 12 years. *Spin Labeling: Theory and Applications* represents a complete update on new theoretical aspects and applications of the spin-label method. In the "line-shape theory" sections, we are especially pleased to include an IBM-compatible diskette supplied by David Schneider and Jack Freed which contains fast, accurate, ready-to-use software for slow-motion simulations. Barney Bales discusses inhomogeneous broadening phenomena in detail. Several developments in techniques and interpretation in saturation transfer spectroscopy have appeared since the publication of *Spin Labeling II: Theory and Applications* (L. J. Berliner, ed., Academic Press, 1979). We have included an up-to-date chapter on spin-label applications by M. A. Hemminga and P. A. de Jager. By incorporating ^{15}N and deuterium into nitroxide spin labels, several unique advantages are derived in line-shape analysis. Albert Beth and Bruce Robinson have contributed a detailed chapter on the analysis of these labels in the slow-motion regime while Jane Park and Wolfgang Trommer present the advantages for specific biochemical examples in our "applications" section. Derek Marsh's contribution on spin-label spectral analysis may be regarded as a summary chapter which touches on several of the detailed spectral analysis methods described in the earlier chapters.

New and specialized applications which focus on electron-electron spin interactions with spin labels are featured in chapters by Jim Hyde and Jim Feix on ELDOR, by Gareth and Sandra Eaton on metal ion-electron spin-spin splittings, and by Jim Hyde and Witold Subczynski on spin-label oximetry. Newer aspects of nitroxide synthesis are discussed in a quite thorough chapter by Kalman Hideg and Olga Hankovsky. Ronald Mason and Carolyn Mottley have provided us with a detailed chapter on the techniques, advantages, and pitfalls of spin trap chemistry. An appendix to this volume contains a comprehensive chapter on the detailed synthesis of ^{15}N perdeuterated spin labels by Jane Park and Wolfgang Trommer. We have retained the recipe format so that the reader can duplicate the syntheses from this book without resorting to the original literature. The marriage of proton NMR, site-specific isotopic labeling, and spin-label paramagnetic relaxation has been eloquently delineated in a problem-oriented chapter on antibody structure by Jacob Anglister.

We are extremely proud of this much-awaited volume. As always, we strive to provide the highest quality volumes for our readers that meet state-of-the-art standards

in both coverage and pedagogical approach. It is always our intention not only to review the literature, but also to teach the principles and criticize the approaches in an unbiased fashion. We sincerely hope to maintain our high standards and to cover new, promising methods as they mature. To this end, comments from our readers would be greatly appreciated.

Lawrence J. Berliner
Jacques Reuben

Contents

Chapter 1

Calculating Slow Motional Magnetic Resonance Spectra: A User's Guide

David J. Schneider and Jack H. Freed

1. Introduction 1
2. General Theoretical Considerations 3
   - 2.1. Terms Included in the Liouville and Diffusion Superoperators 4
   - 2.2. Definitions of Coordinate Systems 5
   - 2.3. Basis Vectors and Scalar Product in Operator Space 7
   - 2.4. Construction of the Spin Hamiltonian 10
   - 2.5. Matrix Elements of the Liouville Superoperator 14
   - 2.6. Construction and Matrix Elements of the Diffusion Superoperator 15
   - 2.7. Components of the Starting Vector 18
   - 2.8. The High-Field Approximation 20
3. Magnetic Resonance Line Shapes and the Complex Symmetric Lanczos Algorithm 21
   - 3.1. The Real Symmetric Lanczos Algorithm 22
   - 3.2. The Complex Symmetric Lanczos Algorithm 25
   - 3.3. The Real Symmetric Conjugate Gradients Algorithm 27
   - 3.4. The Complex Symmetric Conjugate Gradients Algorithm 30
   - 3.5. The Continued-Fraction Representation of the Spectral Function 32
   - 3.6. Convergence of the Sequence of Approximate Spectral Functions 36
4. Computational Considerations 42
   - 4.1. Naming Conventions for Files 44
   - 4.2. Array Dimensions and Common Blocks 44
   - 4.3. The Parameter Input Program: LBLL 45

4.4. Spectral Calculations: EPRLL and EPRCGL 48
4.5. Calculation of the Spectral Function: TDLL 54
4.6. "Field Sweep" Conjugate-Gradients Calculations: EPRBL and TNLL 55
4.7. Auxiliary Programs: D200, STVT, MATLST, and VECLST 56
4.8. Porting Programs to Other Machines 57
5. Example Calculations 59
5.1. Model Calculations and General Strategy 60
5.2. Examples from the Literature 65
Appendix: Parameters for Example Calculations 68
References 73

Chapter 2

Inhomogeneously Broadened Spin-Label Spectra

Barney L. Bales

1. Introduction 77
2. Experimental Determination of Hyperfine Coupling Constants ... 80
2.1. NMR and ENDOR 80
2.2. ESR Simulation 81
2.3. Solvent Dependence of Hyperfine Coupling Constants 88
3. Gaussian Contributions to Spin-Label Line Shapes 88
Example 1 93
4. The Voight Approximation and a One-Parameter Description of Line Shapes 93
Example 2 96
5. Line-Shape Comparisons 97
5.1. Unresolved Hyperfine Multiplets 97
5.2. A Universal Nitroxide 98
5.3. Gaussian–Lorentzian Sum Approximations 101
6. Correcting the Linewidth of an Inhomogeneously Broadened Line 103
6.1. Known Hyperfine Coupling Constants 103
Example 3. Solvent Dependence of ΔH_{pp}^{G} 103
Example 4. Dependence of ΔH_{pp}^{G} on Spin-Label Alignment in an Ordered Fluid 104
6.2. Unknown Hyperfine Coupling Constants 105
Example 5 106
6.3. Additional Broadening Method 108
7. The Relationship of Linewidth Ratios to Measured Line-Height Ratios 108
7.1. Rotational Correlation Times 108
Example 6 112

7.2. Linewidth Ratios Over a Broader Range 112
Example 7. Measuring Oxygen Concentrations Using Unresolved Spin-Label Spectra 112
8. Accurate Estimate of Relative Doubly-Integrated Spectral Intensities 113
Example 8. A Hypothetical Spin-Label Partitioning Experiment 114
9. Determining Spin-Exchange Frequencies of Spin Labels in Liquids of Low Viscosity 115
10. Deuterated Spin Labels 121
10.1. Gaussian Linewidth of Deuterated Spin Labels 121
10.2. Proton Contamination of a Deuterated Spin Label 122
Example 9 123
Example 10 124
11. Conclusions 124
Appendix 125
References 126

Chapter 3

Saturation Transfer Spectroscopy of Spin Labels: Techniques and Interpretation of Spectra

M. A. Hemminga and P. A. de Jager

1. Introduction 131
2. Basic Principles of Saturation Transfer ESR 132
2.1. The Spin Hamiltonian 132
2.2. ESR Spectra of Immobilized Spin Labels 133
2.3. The Bloch Equations 136
2.4. Qualitative Explanation of ST-ESR 140
2.5. Spectral Displays of ST-ESR 143
2.6. Analysis of ST-ESR Spectra 145
3. Measurements of Saturation Transfer ESR Spectra 148
3.1. The Resonant Cavity 148
3.2. Effect of Sample on Cavity Properties 150
3.3. Phase-Sensitive Detection 152
3.4. Calibration Procedures 154
3.5. Standard Conditions for ST-ESR Spectroscopy 156
4. Analysis of Saturation Transfer ESR Spectra 158
4.1. Isotropic Motion 159
4.2. Anisotropic Motion 166
5. Future Developments 173
References 174

Chapter 4

Nitrogen-15 and Deuterium Substituted Spin Labels for Studies of Very Slow Rotational Motion

Albert H. Beth and Bruce H. Robinson

1. Introduction 179
2. Overview of Rotational Diffusion Models 181
   - 2.1. Definition of Rotational Correlation Times 182
   - 2.2. Isotropic Rotational Diffusion 184
   - 2.3. Anisotropic Rotational Diffusion in an Isotropic Medium 184
   - 2.4. Uniaxial Rotational Diffusion in an Anisotropic Medium 187
3. Sensitivity of cw-ST-EPR Signals to Rotational Motion 188
   - 3.1. Choice of Signal 188
   - 3.2. Sensitivity to Motion 189
   - 3.3. The Case of Isotropic Motion and Anisotropic Magnetic Tensors 195
   - 3.4. Effects of Anisotropic Motion and Anisotropic Tensors 197
   - 3.5. Geometric Considerations for Analyzing Anisotropic Motion 198
4. Analysis of cw-ST-EPR Data 199
   - 4.1. Isotropic Model Systems 199
   - 4.2. Anisotropic Model Systems 200
   - 4.3. Anisotropic Motional Modeling by Computer Simulations 201
   - 4.4. Overview of Theory for Computation of ST-EPR Spectra 202
5. Studies of Isotropic Motion with Nitrogen-15 Spin Labels 202
   - 5.1. V_1 EPR Signals as a Function of τ_r 202
   - 5.2. Dependence of the V_2' Signal on τ_r 204
6. Effects of Anisotropic Rotational Diffusion on V_2' Spectra..... 207
   - 6.1. Sensitivity of V_2' to Uniaxial Rotation 208
   - 6.2. Effects of Labeling Geometry 210
   - 6.3. Sensitivity of V_2' to Anisotropic Rotational Diffusion of Axially Symmetric Ellipsoids in an Isotropic Medium 212
   - 6.4. Relationship between Effective Correlation Times and Anisotropic Motion 213
7. Optimization of Sensitivity of V_2' to Motion 217
   - 7.1. Altering Sensitivity to Motion by Selection of ν_0 217
   - 7.2. Altering Sensitivity to Motion by Selection of ν_m 223
8. Analysis of Overlapping Motional Species 224
   - 8.1. One Fast and One Slow Motional Component 224
   - 8.2. Two or More Slow Motional Components 226
9. Computer Modeling of Nitrogen-14 V_2' Signals 230
   - 9.1. Isotropic Motion Simulations 230
   - 9.2. Anisotropic Motion Simulations 232
   - 9.3. Signal-to-Noise Ratio and Motional Sensitivity of Nitrogen-15 versus Nitrogen-14 Spin Labels 233

10. Saturation Recovery EPR Studies with Nitrogen-15 Spin Labels 234
10.1. Overview of the Experiment 234
10.2. Spectrometer Variables 235
10.3. Strategies for Extraction of Motional Information 236
10.4. Theory of Saturation Recovery 236
10.5. Pseudosecular Terms 238
10.6. Isotropic Brownian Motion—Secular Terms Only 239
10.7. Results of Calculations of SR Curves for Isotropic Motion 240
10.8. Results of Calculations of SR Curves for Nonaxial Tensors 240
10.9. Effects of Pseudosecular Terms 240
10.10. Pseudosecular Terms using Nitrogen-14 244
10.11. Population Analysis: An Estimate of Amplitudes 245
11. Conclusions 247
References 249

Chapter 5

Experimental Methods in Spin-Label Spectral Analysis

Derek Marsh

1. Introduction 255
2. Inhomogeneous Broadening 256
3. Fast Rotational Motion 259
4. Slow Rotational Motion 262
5. Anisotropic Rotation: Lipids/Membranes 265
6. Spin-Spin Interactions and Lateral Diffusion 269
6.1. Spin-Spin Exchange 270
6.2. Translational Diffusion and Bimolecular Collision Rate 273
6.3. Dipolar Spin-Spin Broadening 274
6.4. Separation of Exchange and Dipole-Dipole Interactions ... 275
7. Lipid-Protein Interactions 277
7.1. Spectral Subtraction/Addition 278
7.2. Measurements at 35 GHz 280
7.3. Analysis of Lipid-Protein Association 281
7.4. Two-Site Exchange Simulations 286
8. Saturation Transfer ESR 291
8.1. Power and Modulation Calibration and the Effects of Sample Shape, Size, and Dielectric Absorption 291
8.2. Anisotropic Rotation 294
8.3. Integral Method: Multicomponent Spectra 297
8.4. Dispersion Spectra: Difference Spectroscopy 298
References 300

Chapter 6

Electron–Electron Double Resonance

James S. Hyde and Jim B. Feix

1. Introduction 305
   1.1. Definitions and Background 305
   1.2. Historical Overview 307
2. Rate Equations 310
3. Spin-Label Relaximetry 314
4. Apparatus 317
5. Applications 320
   5.1. Lateral Diffusion in Membranes 320
   5.2. Studies Utilizing ^{14}N:^{15}N Spin-Label Pairs 321
   5.3. ELDOR in Cells 330
   5.4. Comparison with Spin-Exchange Line Broadening 331
   5.5. Further Application of ^{14}N:^{15}N Methodology 331
6. Future Opportunities 333
   References 334

Chapter 7

Resolved Electron–Electron Spin–Spin Splittings in EPR Spectra

Gareth R. Eaton and Sandra S. Eaton

1. The Scope of Electron Spin-Spin Interactions 340
2. The Nature of Electron Spin-Spin Interactions 341
   2.1. Dipolar Interaction 341
   2.2. Exchange Interaction 343
   2.3. Hamiltonian for Spin-Spin Interaction 346
   2.4. Computational Approaches 348
3. Analogies between Nuclear-Nuclear, Electron-Nuclear, and Electron-Electron Spin-Spin Interactions and Long-Range Electron Transfer 349
4. Spin-$\frac{1}{2}$-Spin-$\frac{1}{2}$ Interaction 351
   4.1. Spin-Spin Splitting 351
   4.2. Half-Field Transitions 357
   4.3. Geometrical Information 360
5. Spin 1-Spin $\frac{1}{2}$ 364
6. Spin $\frac{3}{2}$-Spin $\frac{1}{2}$ 365
7. Spin $\frac{5}{2}$-Spin $\frac{1}{2}$ 366
   7.1. Mn(II) Interacting with $S = \frac{1}{2}$ 366
   7.2. High-Spin Fe(III) Interacting with $S = \frac{1}{2}$ 369

8. Spin $\frac{7}{2}$-Spin $\frac{1}{2}$ 371
9. Chemical Properties Revealed via Spin-Spin Interactions 373
9.1. Kinetics of Ligand Exchange for Cu(II) 373
9.2. Coordination Equilibria 373
9.3. Weak Orbital Overlaps 374
10. Spin-Spin Interactions in Biological Systems 376
10.1. Cobalt(II)-Radical Interaction 376
10.2. Mo(V) Interaction with Fe/S Cluster 377
10.3. Iron-Nitroxyl Interaction 378
10.4. Nitroxyl-Nitroxyl Interaction 382
11. Exchange Interaction through Multiatom Linkages 384
12. Quantitative EPR Measurements 389
13. Summary and Prognosis 390
References 391

Chapter 8

Spin-Label Oximetry

James S. Hyde and Witold K. Subczynski

1. Introduction 399
2. Physics 401
2.1. Bimolecular Collisions 401
2.2. Magnetic Interactions 402
2.3. The Absolute T_1 Method 406
2.4. The Absolute T_2 Method 407
3. Experimental Methods 408
3.1. TPX Gas-Exchange Sample Cell 408
3.2. T_1-Sensitive Methods 413
3.3. T_2 (Linewidth-Sensitive) Methods 416
4. Applications 421
5. Future Opportunities 422
References 422

Chapter 9

Chemistry of Spin-Labeled Amino Acids and Peptides: Some New Mono- and Bifunctionalized Nitroxide Free Radicals

Kálmán Hideg and Olga H. Hankovszky

1. Introduction 427

2. Spin Labeling of Amino Acids and Peptides 429
2.1. Reagents for Labeling at the Amino Terminal 429
2.2. C-Terminal Spin-Labeled Amino Acids and Peptides 440
2.3. Amino Acids and Peptides Labeled in the Side Chain 442
3. Nitroxide Amino Acids 447
3.1. Imidazolinyl Nitroxide Amino Acids 447
3.2. Pyrrolidine Nitroxide Amino Acids 448
3.3. Pyrrolinyl Nitroxide Amino Acids 448
3.4. Piperidinyl Nitroxide Amino Acids 448
4. New Mono- and Bifunctionalized Spin Labels 450
4.1. Reactions with 3-Functionalized-3-Pyrroline-1-Oxyl Derivatives 450
4.2. Cross-Linking Spin-Label Reagents 454
4.3. Spin-Labeled Pyrrolidine-1-Oxyl Fatty Acids 463
5. Experimental Procedures for Preparation of Some Pyrroline and Pyrrolidine Nitroxide Spin Labels 466
References 481

Chapter 10

Nitroxide Radical Adducts in Biology: Chemistry, Applications, and Pitfalls

Carolyn Mottley and Ronald P. Mason

1. Introduction 489
2. Halogenated Compounds 491
2.1. Carbon Tetrachloride 491
2.2. Halothane 493
2.3. Others 494
3. Lipid Peroxidation 494
3.1. Linoleic Acid 494
3.2. Methyl Linoleate 495
3.3. Arachidonic Acid 495
3.4. Lipid Peroxyl and Alkoxy Radicals 497
4. Hemoprotein-Organic Hydroperoxides 498
5. Sulfur-Centered Radicals 502
5.1. Sulfur Dioxide, Bisulfite, Sulfite, and Sulfate 502
5.2. Thiols 504
6. Pyridinyl Radicals 507
7. Hydrazines 507
8. Oxygen-Centered Radicals 513
9. Aldehydes 514
9.1. Glyceraldehyde and Other Monosaccharides 514
9.2. Malonaldehyde and Acetylacetone 516

10. Lignin Model Dimers 517
11. 3-Methylindole 519
12. Indole Acetic Acid 519
13. Ethanol 520
14. Tryptophan 521
15. Nitrobenzyl Chlorides 521
16. Azide and Cyanide 522
17. Styrene 522
18. Spin Traps as Enzyme Inhibitors 523
19. Spin Traps as Enzyme Substrates 524
20. *In Vivo* Spin Trapping and Spin Trapping in Cells 525
    20.1. Spin Trapping in Cells 525
    20.2. Site-Directed Spin Traps 527
    20.3. *In Vivo* Spin Trapping 528
21. Spin Adduct Identification 529
    21.1. Isotope Methods 530
    21.2. Isolation and Identification by HPLC, GC, and MS 530
22. Spin Adduct Imposters 531
23. Summary 532
    References 532

Chapter 11

Advantages of ^{15}N and Deuterium Spin Probes for Biomedical Electron Paramagnetic Resonance Investigations

Jane H. Park and Wolfgang E. Trommer

1. Introduction 547
2. Maleimide Spin Label (DMSL or ^{15}N,DMSL): A Covalent Ligand for Sulfhydryl Groups of Proteins 549
    2.1. Advantages of Deuterated Maleimide Spin Label (DMSL) for Studies of Proteins 549
    2.2. Advantages of Doubly Substituted ^{15}N,Deuterated Maleimide Spin Label (^{15}N,DMSL) 552
    2.3. Advantages of ^{15}N,Deuterated Maleimide Spin Label (^{15}N,DMSL) for Studies of Soluble and Membrane-Bound Enzymes 552
    2.4. Future Applications 563
3. Coenzyme Spin Labels: Studies on Coenzyme Binding to Enzymes and Catalytic Mechanisms 563
    3.1. Comparison of Spin-Labeled Maleimide Inhibitors (DMSL and ^{15}N,DMSL) and Coenzyme Analogs (SL-NAD^+) for EPR Studies of Enzymes 563

3.2. The Evaluation of Binding of Isotopically Substituted N^6-SL-NAD^+ or C8-SL-NAD^+ Using Lactic Dehydrogenase 564
3.3. Glyceraldehyde-3-phosphate Dehydrogenase (GAPDH) and SL-NAD^+ Binding with Unusual Electron–Electron Dipolar Interactions (Splitting of Peaks) 566
3.4. Interactions of N^6-(D_{17})SL-NAD^+ with GAPDH Bound to Band-3 Protein of Erythrocyte Membranes 579
3.5. Binding of Deuterated and ^{15}N,Deuterated-SL-NADH Analogs to β-Hydroxybutyrate Dehydrogenase (BDH) 580
3.6. Binding of Spin-Labeled Adenine Nucleotides to Dehydrogenases and F_1ATPase..... 581
3.7. Future Applications 582
4. Advantages of ^{15}N, and ^{15}N,Deuterated Stearic Acid and Cholestane Spin Labels for Evaluation of Motion of Lipids in Membranes 582
4.1. Improved Spectral Sensitivity of Rapidly Tumbling ^{15}N and ^{15}N,Deuterium Substituted Stearic Acid and Cholestane Analogs 583
4.2. Advantages of ^{15}N and ^{15}N,Deuterated Stearic Acid Spin Labels for Studies on Binding to Proteins..... 583
4.3. Improved Spectral Analysis of Lipid Motion in Erythrocyte (RBC) Membranes with ^{15}N-5-NS and (^{15}N,D_{12})-5-NS 587
4.4. Investigation of Erythrocyte Abnormalities Using ^{15}N-5-NS 588
4.5. Studies of Collision Frequency and Vertical Fluctuations of ^{14}N and ^{15}N Spin-Labeled Pairs of Fatty Acids in Membranes Using ELDOR Spectroscopy 589
4.6. Future Applications 591
References 592

Chapter 12

Magnetic Resonance Study of the Combining Site Structure of a Monoclonal Anti-Spin-Label Antibody

Jacob Anglister

1. Introduction 597
2. Amino Acid Composition of the Antibody Combining Site 599
3. Distance Determination 604
4. Contributions of Heavy and Light Chains to the Combining Site 607
5. Determination of Short Distances 608
6. Conclusion..... 612
References 612

Appendix

Approaches to the Chemical Synthesis of ^{15}N and Deuterium Substituted Spin Labels

Jane H. Park and Wolfgang E. Trommer

1. Introduction 615
2. Synthesis of Deuterated and ^{15}N,Deuterated Maleimide Spin Labels (DMSL and ^{15}N-DMSL) 616
3. Synthesis of Deuterated and ^{15}N,Deuterated Adenine Nucleotide Derivatives 619
   3.1. Synthesis of N^6-(D_{17})SL-AMP (10a) or N^6-(^{15}N,D_{17})SL-AMP (10b) 619
   3.2. Synthesis of C8-(D_{17})SL-AMP (12a) or C8(^{15}N,D_{17})SL-AMP (12b) 620
   3.3. Synthesis of N^6-SL-ATP (14) 621
   3.4. Synthesis of C8-(^{15}N,D_{17})SL-ATP 623
   3.5. Synthesis of N^6- or C8-SL-Analogs of AMPPCP or AMPPNP 624
   3.6. Synthesis of a Mixture of 2′- and 3′-(^{15}N,D_{13})SL-ATP (17) 625
   3.7. Synthesis of N^6-SL-ADP and C8-SL-ADP 626
   3.8. Synthesis of N^6-(D_{17})SL-NAD^+ (18a) and N^6-(^{15}N,D_{17})SL-NAD^+ (18b) 626
   3.9. Synthesis of C8-(D_{17})SL-NAD^+ and C8-(^{15}N,D_{17})SL-NAD^+ 627
4. Synthesis of ^{15}N and ^{15}N,Deuterated Stearic Acid Spin Labels ... 628
   4.1. Synthesis of ^{15}N-5-Doxylstearic Acid Spin Label (26) 628
   4.2. Synthesis of ^{15}N-12-Doxylstearic Acid-d_{41} (27) 631
5. Conclusions 632
   References 632

Contents of Previous Volumes 635

Index 641

1

Calculating Slow Motional Magnetic Resonance Spectra

A User's Guide

David J. Schneider and Jack H. Freed

1. INTRODUCTION

In the first volume of *Spin Labeling: Theory and Applications* a chapter was written by one of us (J.H.F.) in which a detailed theory for the interpretation of ESR spectra of spin labels in the slow motional regime (Freed, 1976) was presented. The specific emphasis of that review was on the interpretation of nitroxide spin label spectra and contained many such examples. In the ensuing 13 years, there have been a number of important developments. First and foremost has been the development and implementation of powerful computational algorithms that have been specifically tailored for the solution of these types of problems (Moro and Freed, 1981; Vasavada *et al.*, 1987). The use of these algorithms often leads to more than an order-of-magnitude reduction in computer time for the calculation of any given spectrum as well as a dramatic reduction in computer memory requirements. Concomitant with these improvements in computational methodology has been the revolution in the power and availability of computer hardware. Taken together, these improvements in hardware and software have made it possible to quickly and conveniently perform spectral calculations on small laboratory computers which formerly required the resources of a large mainframe computer. The increase in the available computing power has also made it feasible to incorporate more sophisticated models of molecular structure and dynamics into the line-shape calculation programs.

In this chapter, we wish to make the results of the above-mentioned developments conveniently available to a wider audience. To this end, a diskette containing a set of programs for ESR line-shape programs has been included with this book (see inside

David J. Schneider and Jack H. Freed • Baker Laboratory of Chemistry, Cornell University, Ithaca, New York 14853-1301. David J. Schneider's present address is IBM Corporation, Kingston, New York 12401.

back cover). These programs incorporate those features of the general theory that have been found to be most useful for the calculation of conventional cw ESR spectra of nitroxide spin labels in isotropic liquids, liquid crystals, and covalently labeled polymers. Our desire to supply a set of programs that are relatively compact and simple to use has necessarily involved some compromises in versatility and generality. Nevertheless, we feel that the compromises are not severe and that the programs supplied here will likely satisfy the needs of most of the readers. We will clearly state below the range of validity and limitations of the programs presented here. More general programs are, of course, available from the authors.

Unfortunately, time and space do not permit us to cover all of the applications of these programs that already exist in the literature, but a brief survey is provided in Section 5.2, along with appropriate references. The programs provided here should enable the reader to redo many of these calculations in order to gain familiarity with their use and to actually begin to compare the output with experimental spectra.

Once one begins to compare experimental and computed spectra in earnest, another basic problem emerges: the procedure of varying input parameters in a trial-and-error fashion to obtain a good fit to experimental data can be quite tedious and time-consuming for complicated systems, even with more efficient programs and faster computers. The manual fitting of spectra in this manner is as much an art as a science. However, since spectra can now be so quickly and reliably computed, it is no longer unreasonable to attempt the analysis of experimental spectra in a completely automated fashion using a general nonlinear least-squares fitting procedure to optimize the parameters characterizing the system (Crepeau *et al.*, 1987). Significant progress toward this goal has recently been made in our laboratory. Such a computation frequently requires the calculation of more than 100 spectra as the nonlinear least-squares procedure is iterated toward an optimal parameter set. Not many years ago this herculean task would have been unthinkable for complex slow motional spectra. In addition, much progress has recently been made toward the solution of the general problem of an automated determination of optimal basis sets (Vasavada *et al.*, 1987). It is important to realize that these developments have been made possible, in large part, by the more efficient algorithms on which the programs supplied with this book are based.

The set of programs described in this guide are designed for the efficient and accurate calculation of cw ESR spectra of doublet radicals ($S = \frac{1}{2}$), possibly coupled to one nuclear spin (e.g., typical nitroxide spin labels), in the limit of high static magnetic fields, slow molecular motions, and weak microwave fields. In its present form, it can also be used on a variety of NMR problems in the analogous case of an $I = \frac{1}{2}$ nucleus coupled to one other nuclear spin (Campbell *et al.*, 1979) and, for an $I = 1$ nucleus, by a simple modification (Meirovitch and Freed, 1979). However, these programs should not be used for the calculation of spectra in the low field or very fast motional limits, since the nonsecular terms that are omitted from the spin Hamiltonian in these programs give rise to significant effects in either of these cases. In particular, these programs should not be used for accurate calculations of X-band spectra of transition metal ions such as Cu^{2+} and VO^{2+}. Fast motional spectra can easily be calculated using a motional narrowing theory and a far simpler program, while low field spectra can be calculated by methods similar to those in these programs (Moro, 1980a; Meirovitch *et al.*, 1982; Gorcester, 1985).

These programs are an outgrowth of a set of programs written by G. Moro in 1980 (Moro, 1980a, 1980b; Moro and Freed, 1981; Meirovitch *et al.*, 1982). The older

programs were quite complicated as they were written in FORTRAN IV and highly optimized for use on a small computer with a very limited amount of physical memory. The present set of programs are written in a more modular, easily portable fashion in FORTRAN 77. As supplied, these programs should compile and run without error on IBM PCs[1] or compatibles under MS-DOS[2] (ver. 2.11 or higher) and Microsoft[2] Fortran (ver. 3.0 or higher). Because of the wide availability of this type of hardware and software, users of these programs can use the results of small calculations with the PC version as a reference point in porting these programs to a more powerful machine to be used for routine calculations. In addition, the faster PCs equipped with floating point coprocessors can themselves be used for many calculations.

Since this chapter is devoted primarily to a description of the programs and their implementation and use, it will be assumed that the reader is already familiar with the basic aspects of the theory as presented in the chapters by Nordio (1976) and Freed (1976) in the first volume of this series. References to equations in the article by Freed, denoted here as I, will be given whenever appropriate.

The body of this work is broken up into four main sections. First, in Section 2 a qualitative overview of the theory behind these programs, along with the necessary definitions and a summary of the types of terms which are included in the calculations, are presented. Next, Section 3 is devoted to a description of the algorithms used in the spectral calculations and related topics such as the continued fraction representation of the spectral line shape function. The implementation of the programs is discussed in Section 4, as well as suggestions on modifying them to run on other machines. Finally, in Section 5 a general strategy for fitting experimental data to these programs is presented as well as several model calculations and a survey of published results.

This organization was adopted so that the work could be utilized in two very different ways, depending on the interests and inclinations of the reader. One approach would be to simply find a PC, insert the diskette, and use Sections 4.3, 4.5, and 5 as a user's manual for the programs, referring to the definitions in Section 2 only when necessary. This pragmatic approach has the distinct advantage of quickly acquainting the user with the art of fitting theoretical models to experimental data. A second, more cautious, approach would be to begin by carefully studying the material in Section 2 before attempting to use the programs. The reader who adopts this approach will probably make fewer serious errors in choosing appropriate parameters and interpreting the results. Regardless of the initial approach, there is no substitute for experience in using the programs and developing a feel for the effects of varying different input parameters on the calculated spectrum. Likewise, it is difficult to properly interpret the final results without being familiar with the theory behind the parameters and how they enter into the calculations. In addition, Section 3 should provide valuable insight into the workings, both in theory and in practice, of the algorithms on which the spectral calculations are based.

2. GENERAL THEORETICAL CONSIDERATIONS

The stochastic Liouville equation (SLE) is used here to describe the time evolution of the orientation-dependent density operator, and thereby the time evolution of the

[1] IBM is a registered trademark of International Business Machines Corp.

[2] MS-DOS and Microsoft are registered trademarks of Microsoft Corporation.

magnetization operator of the individual spins. Averaging this result over the ensemble of spins in the sample leads to an equation describing the time evolution of the macroscopic magnetization. The Fourier–Laplace transform of the time autocorrelation function of the x component of the macroscopic magnetization in the laboratory-fixed frame can be identified with the frequency-swept cw ESR spectrum in the limit of very weak microwave fields (i.e., in the linear response regime). However, in most experiments it is the field-swept rather than the frequency-swept cw ESR spectrum that is obtained. This restricts the direct application of the present method to the high-field limit where the results from the two types of experiments are essentially indistinguishable.

For the present purposes, the stochastic Liouville equation amounts to treating the spin degrees of freedom of the system in a quantum-mechanical fashion, while the orientation of the molecule is determined by a classical stochastic process. The quantum-mechanical spin degrees of freedom are coupled to the classical orientational degrees of freedom through the anisotropic part of the orientation-dependent spin Hamiltonian, so that the tumbling of the molecule drives time-dependent fluctuations in the energy levels of the spin system. The choice of stochastic process used to model the reorientation of the molecules affects the time evolution of the spin system and therefore the resulting ESR spectrum. More detailed explanations and derivations of the ideas presented here are available in several places in the literature (Freed, 1976; Schneider and Freed, 1989).

The central result of the stochastic Liouville theory (Freed, 1976; Schneider and Freed, 1989) as applied to the magnetic resonance line-shape problem is that the unsaturated, high-field, frequency-swept cw ESR spectrum, $I(\omega - \omega_0)$, is given in compact "matrix element" notation (cf. equation I-7) as

$$I(\omega - \omega_0) = \left(\frac{1}{\pi}\right)\langle\langle v|[(\tilde{\mathbf{\Gamma}} - i\mathcal{L}) + i(\omega - \omega_0)I]^{-1}|v\rangle\rangle \tag{1}$$

In this equation, ω is the sweep frequency and $\omega_0 = g_0\beta_e B_0/\hbar$ where B_0 is the static magnetic field, $g_0 = \frac{1}{3}(g_{xx} + g_{yy} + g_{zz})$, β_e is the Bohr magneton, and $\hbar$ is Planck's constant divided by 2π. Also, $\mathcal{L}$ is the Liouville superoperator associated with the orientation-dependent spin Hamiltonian, $\tilde{\mathbf{\Gamma}}$ is the "symmetrized" diffusion superoperator used to model the classical reorientational motion, and I is the identity operator. The starting vector, $|v\rangle\rangle$, includes both the spin operator for the allowed ESR transitions and the equilibrium probability distribution function for the orientation of the radicals. The quantity $(\tilde{\mathbf{\Gamma}} - i\mathcal{L})$ is commonly referred to as the stochastic Liouville superoperator.

2.1. Terms Included in the Liouville and Diffusion Superoperators

The types of terms allowed in the Liouville and diffusion superoperators limit the types of systems which can be modeled. The Liouville superoperator used here is for doublet radicals ($S = \frac{1}{2}$) interacting with a single nucleus of arbitrary spin, such as a nitroxide. In particular, the secular and pseudosecular terms in the spin Hamiltonian arising from electron Zeeman and hyperfine interactions are included in the calculation. The nuclear quadrupole, nuclear Zeeman, and the nonsecular portions of the electron

Zeeman and hyperfine tensors are completely neglected. These terms can be included in a more complete treatment (Moro, 1980a; Meirovitch *et al.*, 1982; Gorcester, 1985), but are usually not necessary for nitroxide radicals in the slow motional and high-field limits.

The reorientational dynamics of the spin label (assumed to be rigid) is modeled by a symmetrized rotational diffusion superoperator with a restoring potential of the form (cf. equation I-55)

$$U(\Omega) = -k_B T\left\{ \sum_{L=2,4} \lambda_0^L \mathcal{D}_{00}^L(\Omega) + \lambda_2^L[\mathcal{D}_{02}^L(\Omega) + \mathcal{D}_{0-2}^2(\Omega)] \right\} \tag{2}$$

where $\Omega = (\alpha, \beta, \gamma)$ represents a set of Euler angles describing the orientation of the radical relative to a laboratory-fixed frame (cf. Section 2.2). The functions $\mathcal{D}_{MK}^L(\Omega)$ are the generalized spherical harmonics or Wigner rotation matrix elements. We note that for $M = 0$,

$$\mathcal{D}_{0K}^L(\Omega) = \left(\frac{4\pi}{2L+1}\right)^{1/2} Y_{LK}(\beta, \gamma) \tag{3}$$

where the $Y_{LK}(\beta, \gamma)$ are the well-known spherical harmonics (Rose, 1957; Messiah, 1962; Biedenharn and Louck, 1981). A restoring potential of this type is appropriate for modeling the rotational dynamics of spin probes in uniaxial liquid-crystalline media. In addition to the diffusive type terms one may model jump processes between an arbitrary number of equivalent sites, and Heisenberg spin exchange interactions are included and can be utilized when appropriate. The overall "diffusion" operator is assumed to be the simple superposition of these terms. The user can choose between the three canonical models of Brownian, jump, and free diffusion (cf. equations I-34 to I-44) to describe the dynamics of radicals in isotropic media (Freed, 1976; Korst and Antsiferova, 1979).

2.2. Definitions of Coordinate Systems

Before discussing the types of terms which are included in the Liouville and diffusion superoperators in these calculations, several coordinate systems must be defined (cf. Figures 1 and 2 below). First, $(\hat{x}_L, \hat{y}_L, \hat{z}_L)$ is the laboratory-fixed reference frame, where the $\hat{z}_L$ axis is along the static magnetic field, the $\hat{y}_L$ axis is along the axis of polarization of the (linearly polarized) oscillating magnetic field of the microwave radiation, and the $\hat{x}_L$ axis is chosen to make a right-handed coordinate system.

The second frame of interest is the director frame, $(\hat{x}_d, \hat{y}_d, \hat{z}_d)$. The $\hat{z}_d$ axis of the director frame is taken to be along the symmetry axis of the restoring potential while the $\hat{x}_d$ and $\hat{y}_d$ axes are taken to be coincident with the $\hat{x}_L$ and $\hat{y}_L$ laboratory axes, respectively, when $\hat{z}_L \parallel \hat{z}_d$. With this choice of axes, the director tilt is defined by rotation through an angle ψ about the $\hat{y}_L$ axis which takes the $\hat{z}_L$ axis into the $\hat{z}_d$ axis. If there is no restoring potential present, the director frame is taken to be coincident with the laboratory frame. This generalization of distinct director and laboratory frames was

not included in the programs given in I, but is included here, as it is important for the analysis of many experiments on model membranes and other liquid-crystalline samples.

The director and laboratory frames will be referred to as space-fixed frames, since they are defined to appear to the experimenter as being fixed in space and are related to one another by a simple (time-independent) coordinate transformation. The orientation of the laboratory and director frames for a simplified experiment involving spin probes dissolved in an oriented uniaxial liquid-crystal sample sandwiched between two glass plates is given in Figure 1. In this figure ψ would be positive, since this rotation would advance a right-handed screw along the positive $\hat{y}_L = \hat{y}_d$ axis. Note that in I the laboratory frame is denoted (x, y, z) and the director frame (x'', y'', z''). Also, both of the Euler angles used in I to relate laboratory and director frames are not needed for uniaxial liquid crystals.

The third coordinate system is defined by the principal axis system of the magnetic tensors, $(\hat{x}_m, \hat{y}_m, \hat{z}_m)$. Here it is assumed that the principal axis systems of the A and g tensors are coincident and rigidly fixed in the molecular framework. The final coordinate system is the principal axis system of the rotational diffusion tensor, $(\hat{x}_R, \hat{y}_R, \hat{z}_R)$. The diffusion tensor, $\mathbf{R}$, is assumed to be axially symmetric, and the $\hat{z}_R$ axis is defined to be parallel to the unique axis of the diffusion tensor. Because of the assumed axial symmetry of the diffusion tensor, the $\hat{x}_R$ and $\hat{y}_R$ axes are arbitrary and can be chosen to simplify the calculation of the matrix elements. As in the case of the laboratory and diffusion frames, it is assumed that the diffusion frame can be rotated into the magnetic frame by a rotation through an angle ϕ about the $\hat{y}_R$ axis. The angle ϕ is called the diffusion tilt angle. In general, a second Euler angle is required to specify an arbitrary tilt between the diffusion and magnetic frames. This second angle, as well as a general tilt between the principal axis systems of the g and A tensors (Meirovitch *et al.*, 1982), have not been included in the present set of programs for simplicity. In practice, the quality of the rigid limit spectra for nitroxide spin labels rarely justifies the inclusion of these features in dynamical calculations.

The magnetic and diffusion frames are rigidly fixed with respect to the molecular framework and are therefore referred to as molecular or body-fixed frames. The relationship between the magnetic and diffusion frames for an idealized spin labeled

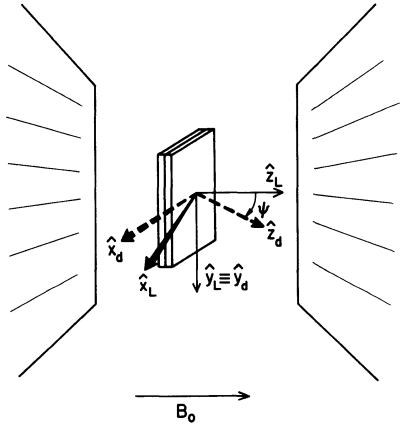

Figure 1. Diagram of laboratory and director frames for an experiment involving spin probes dissolved in an oriented liquid crystal sandwiched between two glass plates. Note that $\hat{z}_L \| \mathbf{B}_0$ and that $\hat{x}_L$, $\hat{x}_d$, $\hat{z}_L$, and $\hat{z}_d$ all lie in the same plane. For most conventional experimental setups, where TE_{102} cavities are used, the $\hat{y}_L \equiv \hat{y}_d$ axis is vertical when viewed by the experimenter in the laboratory while $\hat{z}_L$ is horizontal.

polymer is given in Figure 2. For simplicity, it is assumed here that the six-membered piperidine ring is planar and that the N—O bond lies in the symmetry plane defined by the ring. These simplistic assumptions are made only to simplify the diagram and the related discussion and are not required in general. In this idealized situation, symmetry restrictions constrain the principal axis systems of the g and A tensors to be coincident. In addition, symmetry arguments also require that one of the principal axes of the magnetic tensors lie along the N—O bond, one be perpendicular to the plane defined by the piperidine ring, and one be parallel to the line connecting C_2 and C_6. The established convention for labeling the magnetic axes is to take $\hat{z}_m$ as the axis which is perpendicular to the ring, the $\hat{x}_m$ axis along N—O bond, and the $\hat{y}_m$ axis parallel to the line connecting C_2 and C_6 (Freed, 1976; Lajzerowicz-Bonneteau, 1976) to give a right-handed coordinate system. A consequence of this convention is that A_{zz} is numerically the largest of the three principal components of the hyperfine interaction tensor for nitroxide spin labels based on the 2,2,6,6-tetramethylpiperidine-1-oxyl moiety (e.g., TEMPONE, TEMPOL, TEMPAMINE, etc.). It should be recognized that this choice is a matter of convention and that there are many situations when a different choice is very advantageous. It should be noted that in I the diffusion frame is denoted (x', y', z') and the magnetic frame (x''', y''', z''').

2.3. Basis Vectors and Scalar Product in Operator Space

The role of the SLE is to determine the time evolution of the orientation-dependent density operator. Hence the stochastic Liouville operator is a superoperator in the sense that it maps operators into operators rather that wave functions into wave functions. To use this formalism, a basis set of orientation-dependent spin operators must be introduced. The orientation-dependent density operator acts as both a classical probability distribution function for the orientation of the molecule relative to a space-fixed frame and a quantum-mechanical density operator for the spin system. As such, it can be expanded in the direct product space spanned by a complete orthonormal set of

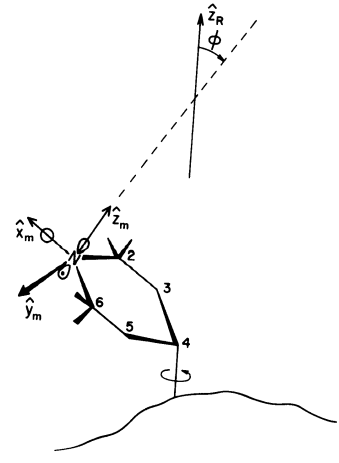

Figure 2. Diagram of the magnetic and diffusion frames for an experiment involving an idealized spin-labeled polymer. It is assumed that $\hat{z}_R$ is parallel to the covalent bond between C_4 and the polymer and that there is rapid rotation about this bond modulated by the slow overall tumbling of the polymer backbone. In accordance with the standard convention, $\hat{x}_m$ is taken along the N—O bond, $\hat{y}_m$ is parallel to the line connecting C_2 and C_4, and $\hat{z}_m$ is normal to the plane defined by the idealized flat piperidine ring.

spatial functions of the Euler angles specifying the orientation of the radical in space and a set of electron and nuclear spin projectors. The general properties of super-operators and bases in operator space have been treated by many authors (Fano, 1957; Jeener, 1982; Löwdin, 1982, 1985).

A convenient and advantageous choice of spatial functions for rotational diffusion problems such as this are the normalized Wigner rotation matrix elements (Freed, 1976). Using Dirac notation, the basis functions are

$$\langle \Omega | L, M, K \rangle = \sqrt{\frac{2L+1}{8\pi^2}}\, \mathcal{D}^L_{MK}(\Omega) \tag{4}$$

where the indices L, M, and K are integral, $0 \leq L$, and $|M|, |K| \leq L$. These functions form an orthonormal set in the sense that

$$\begin{aligned} \langle L_1, M_1, K_1 | L_2, M_2, K_2 \rangle &= \int d\Omega \langle L_1, M_1, K_1 | \Omega \rangle \langle \Omega | L_2, M_2, K_2 \rangle \\ &= N_L(L_1, L_2) \left(\frac{1}{8\pi^2} \right) \int d\Omega\, \mathcal{D}^{L_1 *}_{M_1 K_1}(\Omega) \mathcal{D}^{L_2}_{M_2, K_2}(\Omega) \\ &= \delta_{L_1, L_2} \delta_{M_1, M_2} \delta_{K_1, K_2} \end{aligned} \tag{5}$$

where the normalization factor $N_L(L_1, L_2)$ is defined as

$$N_L(L_1, L_2) = \sqrt{(2L_1 + 1)(2L_2 + 1)} \tag{6}$$

This choice of basis enables one to easily apply group theoretical arguments in evaluating matrix elements.

The most convenient basis for the spin part of the basis vector for ESR problems is a direct product of projectors for the electronic spins (with quantum numbers S and m_S) and nuclear spins (with quantum numbers I and m_I):

$$|p^S, q^S; p^I, q^I \rangle\!\rangle = (|S, m_S\rangle\langle S, m'_S|) \otimes (|I, m_I\rangle\langle I, m'_I|) \tag{7}$$

where $p^S = m_S - m'_S$ and $q^S = m_S + m'_S$, and similarly for p^I and q^I. In the following discussions the principal spin quantum numbers S and I will be suppressed. These direct product projectors are complete and orthonormal with respect to the trace metric defined as

$$\langle\!\langle \rho | \sigma \rangle\!\rangle = \mathrm{tr}\{\rho^\dagger \sigma\} \tag{8}$$

where ρ and σ are arbitrary spin operators, the symbol † implies Hermitian conjunction, and the trace is taken over both the electronic and nuclear spin quantum numbers, i.e.,

$$\begin{aligned} \langle\!\langle p_1^S, q_1^S; p_1^I, q_1^I | p_2^S, q_2^S; p_2^I, q_2^I \rangle\!\rangle &= \langle m_S | m''_S \rangle \langle m_I | m''_I \rangle \,\mathrm{tr}_S\{|m'_S\rangle\langle m''_S|\}\, \mathrm{tr}_I\{|m'_I\rangle\langle m''_I|\} \\ &= \delta_{p_1^S, p_2^S} \delta_{q_1^S, q_2^S} \delta_{p_1^I, p_2^I} \delta_{q_1^I, q_2^I} \end{aligned} \tag{9}$$

This is the conventional scalar product of two operators.

It is quite useful to give the following physical interpretation of the spin indices of the basis vectors. First, consider a g-tensor-only problem ($I = 0$). Since the p^S index labels the difference in electron spin projection numbers, a state with $p^S = 0$ corresponds to a diagonal spin density matrix element, i.e., it represents the population of the spin state with projection quantum number $m_S = q^S/2$. In the same manner, the states with $p^S = \pm 1$ represent off-diagonal density matrix elements which are connected to the diagonal density matrix elements by the microwave radiation field, i.e., they represent magnetic-dipole allowed electron spin transitions. The q_S index distinguishes between the (possibly degenerate) transitions with the same value of p^S. The interpretation is only slightly more complicated when the electron spin is coupled to a nuclear spin via the hyperfine interaction. Here, the $p^S = p^I = 0$ states correspond to diagonal density matrix elements, the $p^S = \pm 1$, $p^I = 0$ states correspond to allowed ESR transitions, and the states with $p^S = 0$ and $p^I = \pm 1$ represent allowed NMR transitions. The rest of the states represent forbidden transitions of various types. For example, the states with $p^S = \pm 1$ and $p^I = \pm 1$ represent singly forbidden ESR transitions, since both the electron and nuclear spin projection quantum numbers are different. Similarly, the states with $p^S = \pm 1$ and $p^I = \pm 2$ represent doubly forbidden ESR transitions. Analogous interpretations are possible for the remainder of the states in terms of forbidden ESR and/or NMR transitions. This interpretation is very useful to keep in mind when trying to understand the physical meaning of the sometimes overwhelming equations which arise in these problems.

The direct product of the spin and spatial parts gives the total basis vector

$$|L, M, K; p^S, q^S; p^I, q^I\rangle\!\rangle = |L, M, K\rangle \otimes |p^S, q^S; p^I, q^I\rangle\!\rangle \tag{10}$$

which, by equations (5) and (9), must satisfy the following orthonormality conditions:

$$\begin{aligned}\langle\!\langle L_1, M_1, K_1; p_1^S, q_1^S; p_1^I, q_1^I | L_2, M_2, K_2; p_2^S, q_2^S; p_2^I, q_2^I\rangle\!\rangle \\ = \delta_{L_1, L_2}\delta_{M_1, M_2}\delta_{K_1, K_2}\delta_{p_1^S, p_2^S}\delta_{q_1^S, q_2^S}\delta_{p_1^I, p_2^I}\delta_{q_1^I, q_2^I}\end{aligned} \tag{11}$$

The basis set which consists of all basis vectors with $L \leq L_{\max}$ will be denoted $\{\mathcal{B}(L_{\max})\}$. This basis has been constructed in a manner which makes no use of any symmetries related to the stochastic Liouville superoperator or starting vector. However, it has the distinct advantage over the symmetry-adapted basis set constructed in Section 2.8 in that the matrix elements of the Liouville and diffusion superoperators are more convenient to calculate in this basis.

The large number of indices needed to completely specify the states makes the expressions for the matrix elements of the Liouville and diffusion superoperators rather unwieldy. To partially alleviate these difficulties, the shorthand notation

$$|\sigma_n\rangle\!\rangle \equiv |L_n, M_n, K_n; p_n^S, q_n^S; p_n^I, q_n^I\rangle\!\rangle \tag{12}$$

for the basis vectors will often be used in the following.

A vector in the direct product space can be associated with an arbitrary orientation-dependent spin operator in an unique manner. This vector can be defined in terms of its components in the basis $\{\mathcal{B}(L_{\max})\}$,

$$\sigma \leftrightarrow |\sigma\rangle\!\rangle = \sum c_{L,M,K,p^S,q^S,p^I,q^I} |L, M, K, p^S, q^S, p^I, q^I\rangle\!\rangle \tag{13}$$

2.4. Construction of the Spin Hamiltonian

One of the most tedious aspects of calculating matrix elements of the Liouville and diffusion superoperators is keeping track of the coordinate frames in which the various quantities are defined. For instance, components of the magnetic tensors are time-independent in a body-fixed frame such as the magnetic or diffusion frames introduced above. In contrast, the static magnetic field, B_0, is only static in a reference frame which is fixed in space. The confusion is compounded by the fact that the spectrum is given in terms of the autocorrelation function of the component of the magnetization along the $\hat{x}_L$ axis, but the magnetic tensors which determine magnetization are most conveniently studied in a frame fixed in the molecule. To unravel these complications in a general manner it is extremely useful to introduce the concept of an irreducible spherical tensor operator (ISTO).

There are several alternative ways to define an ISTO (Biedenharn and Louck, 1981). Because of the present interest in the behavior of various quantities under rotation, it seems appropriate to use the definition that an operator T^J is an ISTO of rank J if it can be written as a sum of components which transform as

$$T_i^{(J,M)} \rightarrow T_f^{(J,M)} = \sum_{M'=-J}^{J} T_i^{(J,M')} \mathscr{D}^J_{M'M}(\Xi_{i\rightarrow f}) \tag{14}$$

where $\Xi_{i\rightarrow f}$ represent the set of Euler angles which take the initial frame into the final frame and the functions $\mathscr{D}^J_{M'M}(\Xi)$ are again the Wigner rotation matrix elements (Messiah, 1962; Biedenharn and Louck, 1981). These functions will play a central role in the following discussion. For this problem, only tensor operators of rank zero, one, and two are important. A list of the important tensorial quantities, their ranks, and the most "natural" type of frame of reference for defining them are given in Table 1.

We note here that the spin Hamiltonian is a rank-zero tensor. This must be so, since it is necessary that the energy of the spin system is independent of the coordinate system used to describe the orientation of the molecule in space and the quantization axes of the spin and magnetic field operators (Kivelson, 1972; Biedenharn and Louck, 1981). Since the Hamiltonian must be a scalar (i.e., a rank-zero tensor), it can be written as a contraction of tensors (cf. equation I-17),

$$H(\Omega) = \sum_{\mu,m,l} F^{(l,m)}_{\mu,\eta} * A^{(l,m)}_{\mu,\eta} = \sum_{\mu,m,l} (-1)^m F^{(l,-m)}_{\mu,\eta} A^{(l,m)}_{\mu,\eta} \tag{15}$$

TABLE 1
Important Tensorial Quantities

Tensor	Rank	Frame of definition
Spin Hamiltonian	0	
Electron spin	1	Space
Nuclear spin	1	Space
Magnetic field	1	Space
g tensor	2	Molecular
A tensor	2	Molecular

where the $F_{\mu,\eta}^{(l,m)}$ are proportional to the standard ISTO components of the magnetic tensor of type μ in the reference frame η. The quantities $A^{(l,m)}$ are the ISTO components of the tensors which arise from the coupling of spin and/or magnetic field operators. For reasons which will become clearer in Section 2.7, it is convenient to parameterize the orientation of the molecule by specifying the orientation of the diffusion frame (body-fixed) with respect to the director frame (space-fixed) by a set of Euler angles (Rose, 1957; Messiah, 1962; Biedenharn and Louck, 1981),

$$\Omega \equiv \Omega_{d\to R} = (\alpha, \beta, \gamma) \tag{16}$$

Since the simple product of two distinct ISTOs does not necessarily transform as an ISTO [cf. equation (14)], it is useful to introduce the decomposition of a product of two ISTOs into a new set of ISTOs. This coupling relies on well-known results, presented below, from the quantum theory of angular momentum (Messiah, 1962; Biedenharn and Louck, 1981). If $T^{j_1}(1)$ and $T^{j_2}(2)$ are two distinct ISTOs of rank j_1 and j_2, respectively, then the product $[T^{j_1}(1) \times T^{j_2}(2)]$ in general decomposes into a sum of ISTO operators, $T_m^j(1,2)$.

$$T_m^j(1,2) \equiv [T^{j_1}(1) \times T^{j_2}(2)]_m^j = \sum_{m_1,m_2} \langle j_1, m_1, j_2, m_2 | j_1, j_2, j, m\rangle T_{m_1}^{j_1}(1) T_{m_2}^{j_2}(2) \tag{17}$$

where $\langle j_1, m_1, j_2, m_2 | j_1, j_2, j, m\rangle$ is a Clebsch–Gordon coefficient. This same scheme of coupling ISTOs can be used to form the $A_{\mu,\eta}^{(l,m)}$ in equation (15) and to construct a rotationally invariant quantity from the product of $F_{\mu,\eta}^{(l,m)*}$ and $A_{\mu,\eta}^{(l,m)}$. Actually, the spin Hamiltonian is usually defined as a sum of dot products of ISTOs rather than a contraction of ISTOs. These two definitions differ by a factor of $\sqrt{2l+1}$. The spin Hamiltonian as defined in equation (15) is consistent with the usual definition in terms of dot products.

To illustrate these concepts, consider the g-tensor contribution to the spin Hamiltonian, $H = \beta_e \mathbf{B}_0 \cdot g \cdot \mathbf{S}$. The g tensor is a real symmetric Cartesian tensor which, by definition, is diagonal in the magnetic frame (cf. Section 2.2). As such, it must decompose into a sum of a rank-zero tensor (Nordio, 1976),

$$g^{(0,0)} = -\frac{1}{\sqrt{3}}(g_{xx} + g_{yy} + g_{zz}) \tag{18}$$

and the five components of a second-rank tensor, $g^{(2,m)}$,

$$g^{(2,\pm 2)} = \tfrac{1}{2}(g_{xx} - g_{yy}), \qquad g^{(2,\pm 1)} = 0, \qquad g^{(2,0)} = \sqrt{\tfrac{2}{3}}[g_{zz} - \tfrac{1}{2}(g_{zz} + g_{yy})] \tag{19}$$

The constant of proportionality between the $F_{g,m}^{(l,m)}$ and the $g^{(l,m)}$ is just the Bohr magneton, β_e, which would give the Hamiltonian the proper units of energy. In practice, however, it is desirable to convert the Hamiltonian into angular frequency units since

a frequency-swept spectrum is desired.[3] Hence the $F_{g,m}^{(l,m)}$ are given by

$$F_{g,m}^{(0,0)} = -\frac{1}{\sqrt{3}}\left(\frac{\beta_e}{\hbar}\right)(g_{xx} + g_{yy} + g_{zz}) \tag{20}$$

and

$$F_{g,m}^{(2,\pm 2)} = \frac{1}{2}\left(\frac{\beta_e}{\hbar}\right)(g_{xx} - g_{yy}), \qquad F_{g,m}^{(2,\pm 1)} = 0, \qquad F_{g,m}^{(2,0)} = \sqrt{\frac{2}{3}}\left(\frac{\beta_e}{\hbar}\right)[g_{zz} - \tfrac{1}{2}(g_{xx} + g_{yy})] \tag{21}$$

The next step is to construct the ISTO components of the tensor product of $\mathbf{B}_0$ and $\mathbf{S}$. This is most conveniently done in the laboratory frame, since $\mathbf{B}_0 \| \hat{z}_L$ and the autocorrelation function of the component of the magnetization along the $\hat{x}_L$ axis is (hopefully!) related to the observed experimental spectrum. In the laboratory frame, the coupling of the rank-one operators associated with $\mathbf{B}_0$ and $\mathbf{S}$ also gives rise to a zero- and a second-rank tensor,

$$A_{g,L}^{(0,0)} = -\left(\frac{1}{\sqrt{3}}\right) B_0 S_z \tag{22}$$

$$A_{g,L}^{(2,\pm 2)} = 0, \qquad A_{g,L}^{(2,\pm 1)} = \mp(\tfrac{1}{2}) B_0 S_{\pm}, \qquad A_{g,L}^{(2,0)} = (\sqrt{\tfrac{2}{3}}) B_0 S_z \tag{23}$$

The arguments for construction of the hyperfine portion of the spin Hamiltonian follow the same lines. The results are

$$A_{A,L}^{(0,0)} = -\left(\frac{1}{\sqrt{3}}\right)[S_z I_z + \tfrac{1}{2}(S_+ I_- + S_- I_+)] \tag{24}$$

$$A_{A,L}^{(2,\pm 2)} = \tfrac{1}{2} S_{\pm} I_{\pm}, \qquad A_{A,L}^{(2,\pm 1)} = \mp\tfrac{1}{2}(S_{\pm} I_z + S_z I_{\pm}), \qquad A_{A,L}^{(2,0)} = \sqrt{\tfrac{2}{3}}[S_z I_z - \tfrac{1}{4}(S_+ I_- + S_- I_+)] \tag{25}$$

and

$$F_{A,m}^{(0,0)} = -\frac{1}{\sqrt{3}}\left(\frac{g_e \beta_e}{\hbar}\right)(A_{xx} + A_{yy} + A_{zz}) \tag{26}$$

$$F_{A,m}^{(2,\pm 2)} = \frac{1}{2}\left(\frac{g_e \beta_e}{\hbar}\right)(A_{xx} - A_{yy}), \qquad F_{A,m}^{(2,\pm 1)} = 0,$$

$$F_{A,m}^{(2,0)} = \sqrt{\frac{2}{3}}\left(\frac{g_e \beta_e}{\hbar}\right)[A_{zz} - \tfrac{1}{2}(A_{xx} + A_{yy})] \tag{27}$$

This completes the construction of the ISTO components of the $F_{\mu,m}$ and $A_{\mu,L}$ tensors.

Once the ISTO components $F_{\mu,m}^{(l,m)}$ and $A_{\mu,L}^{(l,m)}$ have been constructed, they must be transformed into a common coordinate frame, so that the spin Hamiltonian can be written in the form given in equation (15). To accomplish this, the transformation law used to define an ISTO can be used. Since the quantity of interest is the autocorrelation function of the projection of the magnetization along the $\hat{x}_L$ axis, it makes sense to leave the spin and magnetic field operators alone and transform the $F_{\mu,m}$ tensor into the laboratory frame. The complete transformation from the magnetic frame into the

[3] This is somewhat misleading in the sense that the Hamiltonian as used in the computation of the matrix elements of the Liouville superoperator is converted into units of gauss rather than angular frequency. This is done so that the resulting spectrum can easily be compared to experimental ESR spectra obtained in the field-swept mode.

laboratory frame can be broken up into three successive transformations which can be schematically represented as $m \rightarrow R \rightarrow d \rightarrow L$. This can be stated more precisely as

$$F_{\mu,L}^{(0,0)} = F_{\mu,m}^{(0,0)} \tag{28}$$

$$F_{\mu,L}^{(2,m)} = \sum_{m',m'',m'''=-2}^{2} F_{\mu,m}^{(2,m''')} \mathscr{D}_{m'''m''}^{2}(\Phi_{m\rightarrow R}) \mathscr{D}_{m''m'}^{2}(\Omega_{R\rightarrow d}) \mathscr{D}_{m'm}^{2}(\Psi_{d\rightarrow L}) \tag{29}$$

However, the rotation angles defined in Section 2.2 are for the opposite sense of rotation, $\Omega \equiv \Omega_{d\rightarrow R} \neq \Omega_{R\rightarrow d}$ [cf. equation (16)]. Put another way, in terms of the sense of rotations used to define the angles of rotation in Section 2.2, the components of the F_μ tensors have been constructed in the final (L) frame rather than the initial (d) frame (Nordio, 1976) given definitions of the coordinate systems and Euler angles. This confusion always arises in the problems involving both space- and body-fixed frames (Biedenharn and Louck, 1981).

One way to resolve this problem is to use the properties of the Wigner rotation matrix elements (Messiah, 1962; Biedenharn and Louck, 1981),

$$\mathscr{D}_{M'M}^{J}(\Xi_{f\rightarrow i}) = \mathscr{D}_{MM'}^{J*}(\Xi_{i\rightarrow f}) \tag{30}$$

which follows from the unitary nature of the rotation operator. Using equations (29) and (30), the components of the F_μ tensor in the laboratory frame can be written as

$$F_{\mu,L}^{(0,0)} = F_{\mu,m}^{(0,0)} \tag{31}$$

$$F_{\mu,L}^{(2,m)} = \sum_{m',m'',m'''=-2}^{2} \mathscr{D}_{mm'}^{2*}(\Psi_{L\rightarrow d}) \mathscr{D}_{m'm''}^{2*}(\Omega_{d\rightarrow R}) \mathscr{D}_{m''m'''}^{2*}(\Phi_{R\rightarrow m}) F_{\mu,m}^{(2,m''')} \tag{32}$$

where the senses of the rotations are now consistent with the definitions in Section 2.2, i.e., $\Psi_{L\rightarrow d} = (0, \psi, 0)$, $\Omega_{d\rightarrow R} = (\alpha, \beta, \gamma)$, and $\Phi_{R\rightarrow m} = (0, \phi, 0)$. Finally, it is actually the complex conjugate of the tensor F_μ which appears in equation (15), so

$$F_{\mu,L}^{(0,0)*} = F_{\mu,m}^{(0,0)*} \tag{33}$$

$$F_{\mu,L}^{(2,m)*} = \sum_{m',m'',m'''=-2}^{2} d_{mm'}^{2}(\psi) \mathscr{D}_{m'm''}^{2}(\Omega) d_{m''m'''}^{2}(\phi) F_{\mu,m}^{(2,m''')} \tag{34}$$

where use has been made of the fact that general Wigner rotation matrix elements take on a simpler form when the rotation depends only on the second of the three Euler angles (Messiah, 1962; Biedenharn and Louck, 1981) and that the elements of the $F_{\mu,m}$ tensors are real.

Now, putting the pieces together, the spin Hamiltonian is a sum of two parts, the sum of contractions of zero-rank tensors

$$H_0 = \sum_{\mu} F_{\mu,L}^{(0,0)} A_{\mu,L}^{(0,0)} \tag{35}$$

and a sum of contractions of second-rank tensors

$$H_1(\Omega) = \sum_{\mu,m',m'',m'''} d_{mm'}^{2}(\psi) \mathscr{D}_{m'm''}^{2}(\Omega) d_{m''m'''}^{2}(\phi) F_{\mu,m}^{(2,m''')} A_{\mu,L}^{(2,m)} \tag{36}$$

It is noteworthy that the only portion of the spin Hamiltonian which is dependent on the angles Ω arises from the contraction of second-rank tensors. The interested reader is encouraged to independently verify equation (36) by transforming the A_μ tensor from the laboratory frame into the magnetic frame. This construction is more straightforward, since the A_μ tensor transforms in the manner stated in equation (14) with the sense of rotations given in Section 2.2.

The construction given here is consistent with the results given by Nordio (1976) and Meirovitch *et al.* (1982). For more details on these matters, the reader is urged to consult the review chapters written by Kivelson (1972) and Nordio (1976) and the more comprehensive treatments given in standard texts (Rose, 1957; Messiah, 1962; Biedenharn and Louck, 1981). A different convention has been used in I [compare equation (14) and equation I-46], but the final results are equivalent.

2.5. Matrix Elements of the Liouville Superoperator

Using the definition of the scalar product in operator space [cf. equations (5), (9), and (11)] and the definition of the Liouville superoperator as the commutator with the spin Hamiltonian [cf. equation (15)],

$$\mathscr{L}|\sigma\rangle\!\rangle = |H\sigma - \sigma H\rangle\!\rangle \tag{37}$$

the matrix elements of the Liouville superoperator in the basis $\{\mathscr{B}(L_{\max})\}$ are

$$\begin{aligned}\langle\!\langle\sigma_1|\mathscr{L}|\sigma_2\rangle\!\rangle = &\sum_{\mu,l,m,m',m'',m'''} d^l_{mm'}(\psi)d^l_{m''m'''}(\phi)F^{(l,m''')}_{\mu,m}N_L(L_1,L_2)\\ &\times\left(\frac{1}{8\pi^2}\right)\int d\Omega\,\mathscr{D}^{L_1*}_{M_1K_1}(\Omega)\mathscr{D}^{l}_{m'm''}(\Omega)\mathscr{D}^{L_2}_{M_2K_2}(\Omega)\\ &\times\langle p_1^S, q_1^S; p_1^I, q_1^I|[A^{(l,m)}_{\mu,L}]^\times|p_2^S, q_2^S; p_2^I, q_2^I\rangle\end{aligned} \tag{38}$$

The integral over Ω can easily be expressed in terms of Wigner 3-J symbols as (Edmonds, 1957)

$$\left(\frac{1}{8\pi^2}\right)\int d\Omega\,\mathscr{D}^{L_1*}_{M_1K_1}(\Omega)\mathscr{D}^{l}_{m'm''}(\Omega)\mathscr{D}^{L_2}_{M_2K_2}(\Omega) = \begin{pmatrix}L_1 & l & L_2\\ M_1 & m' & M_2\end{pmatrix}\begin{pmatrix}L_1 & l & L_2\\ K_1 & m'' & K_2\end{pmatrix} \tag{39}$$

Since $l = 0$ or 2 in equations (38) and (39), the so-called "triangle" conditions on the 3-J symbols restrict the nonzero matrix elements of the Liouville superoperator to lie within a band about the diagonal determined by $|L_1 - L_2| \leq 2$.

To evaluate the spin part of the matrix elements, it is first necessary to examine the action of the spin commutator superoperators on the standard basis of spin projectors. We note that these basis vectors are eigenvectors of the $J_z^\times$ operator. This fact will be used later in the discussion of the symmetry-adapted basis set (cf. Section 2.8). The matrix elements of the $[A_{\mu,L}]^\times$ superoperators can also be evaluated in this manner using equations (22)–(25). The complete expressions for the matrix elements of the Liouville superoperator are quite tedious and will not be presented here (but see Meirovitch *et al.* 1982). The results presented so far are sufficient to give the reader a feeling for the symmetry arguments presented in Section 2.8.

2.6. Construction and Matrix Elements of the Diffusion Superoperator

The symmetrized diffusion operator, $\tilde{\mathbf{\Gamma}}$, is assumed to be a sum of five independent terms corresponding to the processes:

1. $\tilde{\mathbf{\Gamma}}_{\text{iso}}$: potential-independent part of rotational motion,
2. $\tilde{\mathbf{\Gamma}}_{\text{ex}}$: Heisenberg spin exchange,
3. $\tilde{\mathbf{\Gamma}}_{U}$: potential-dependent part of rotational motion,
4. $\tilde{\mathbf{\Gamma}}_{\text{av}}$: effects of anisotropic viscosity,
5. $\tilde{\mathbf{\Gamma}}_{\text{dj}}$: jumping between equivalent sites,

so that the total symmetrized diffusion superoperator can be written as

$$\tilde{\mathbf{\Gamma}} = \tilde{\mathbf{\Gamma}}_{\text{iso}} + \tilde{\mathbf{\Gamma}}_{\text{ex}} + \tilde{\mathbf{\Gamma}}_{U} + \tilde{\mathbf{\Gamma}}_{\text{av}} + \tilde{\mathbf{\Gamma}}_{\text{dj}} \tag{40}$$

The first two processes are independent of the existence of a restoring potential and are thus appropriate for modeling the motion of radicals in isotropic liquids. In contrast, the last three processes require the local environment of the radical to have lower than spherical symmetry. These contributions will be discussed separately below.

The general forms of some of the contributions to the diffusion superoperator are somewhat awkward. In these cases, the matrix elements of the corresponding operator will be presented rather than the operator itself.

2.6.1. Contributions to the Diffusion Superoperator in Isotropic Media

The matrix elements of $\tilde{\mathbf{\Gamma}}_{\text{iso}}$ in the basis $\{\mathcal{B}(L_{\max})\}$ are (Freed, 1976; Moro, 1980a; Moro and Freed, 1981; Meirovitch *et al.*, 1982)

$$\begin{aligned}\langle\langle\sigma_1|\tilde{\mathbf{\Gamma}}_{\text{iso}}|\sigma_2\rangle\rangle = {} & \delta_{L_1,L_2}\delta_{M_1,M_2}\delta_{K_1,K_2}\delta_{p_1^s,p_2^s}\delta_{q_1^s,q_2^s}\delta_{p_1^I,p_2^I}\delta_{q_1^I,q_2^I} \\ & \times\left\{\frac{R_\perp L_1(L_1+1)}{[1+\tau_\perp R_\perp L_1(L_1+1)]^{E_\perp}} + \frac{R_\parallel K_1^2}{[1+\tau_\parallel R_\parallel K_1^2)]^{E_\parallel}}\right. \\ & \left. - \frac{R_\perp K_1^2}{[1+\tau'_\perp R_\perp L_1(L_1+1)]^{E'_\perp}}\right\}\end{aligned} \tag{41}$$

Here, $R_\parallel$ and $R_\perp$ are the parallel and perpendicular components of the rotational diffusion tensor, $\mathbf{R}$. That is, $R_\parallel$ is related to the correlation time for the motion of the spin probe about the symmetry axis, $\hat{z}_R$, of the diffusion tensor, while $R_\perp$ is related to motion perpendicular to this symmetry axis. The parameters characterizing the three canonical rotational diffusion models are

- Brownian: $\tau_j = 0$, $E_j = 0$,
- free: $\tau_j \neq 0$, $E_j = \frac{1}{2}$,
- jump: $\tau_j \neq 0$, $E_j = 1$,

where $j = \parallel, \perp$ and the nonzero values of the τ_j parameters for jump and free diffusion are to be interpreted as mean residence times at each site, between jumps (cf. equations I-34 to I-44). The matrix of $\tilde{\mathbf{\Gamma}}_{\text{iso}}$ is seen to be both real and diagonal in this basis.

The use of different models for the parallel and perpendicular rotational motions (with subscripts $\|$ and $\perp$) is justifiable only if there exists a clear time-scale separation characterizing these two processes (Mason *et al.*, 1974; Freed, 1976; Meirovitch and Freed, 1979; Campbell *et al.*, 1979; Meirovitch *et al.*, 1984) (e.g., when $R_\|$ is dominated by a relatively more rapid *internal* motion, see Campbell *et al.*, 1979).

The form of the Heisenberg spin exchange contribution to the diffusion superoperator is based on two approximations:

- The lifetime of the radical-pair interaction is short compared both to the effective exchange time and the rotational correlation times.
- The exchange rate does not depend on the relative orientation of the two members of the radical-pair (see also Zientara and Freed, 1979).

The validity of these approximations for the system under study should be carefully scrutinized before including this term in a calculation. The matrix elements of $\tilde{\mathbf{\Gamma}}_{ex}$ in these limits are

$$\langle\langle\sigma_1|\tilde{\mathbf{\Gamma}}_{ex}|\sigma_2\rangle\rangle = \delta_{L_1,L_2}\delta_{M_1,M_2}\delta_{K_1,K_2}\delta_{p_1^S,p_2^S}\delta_{p_1^I,p_2^I} \times \omega_{HE}[\delta_{q_1^S,q_2^S}\delta_{q_1^I,q_2^I} - \tfrac{1}{2}\delta_{p_{1,0}^S}\delta_{q_1^I,q_2^I} - (2I+1)^{-1}\delta_{p_{1,0}^I}\delta_{q_1^S,q_2^S}] \tag{42}$$

2.6.2. Contributions to the Diffusion Superoperator in Anisotropic Media

The Fokker–Planck equation for the stochastic motion of a particle in an external potential is conveniently soluble only for the Brownian model, so attention will be restricted to this special case. The symmetrized diffusion (Smoluchowski) superoperator in this case is

$$\tilde{\mathbf{\Gamma}}_O \equiv \tilde{\mathbf{\Gamma}}_{iso} + \tilde{\mathbf{\Gamma}}_U = [\hat{L} - (\hat{L}U)/2k_BT]\mathbf{R}[\hat{L} + (\hat{L}U)/2k_BT] \tag{43}$$

where $\hat{L}$ is the generator of infinitesimal rotations of the diffusion frame relative to the director frame, $\mathbf{R}$ is the rotational diffusion tensor, and $U \equiv U(\Omega)$ is given in equation (2). A simple decomposition of $\tilde{\mathbf{\Gamma}}_U$ exists due to the particular form of the restoring potential. This becomes more obvious if equation (43) is cast into the form

$$\tilde{\mathbf{\Gamma}}_O = R_\perp\hat{L}^2 + (R_\| - R_\perp)\hat{L}_z^2 + \left(\frac{1}{2k_BT}\right)[R_\perp(\hat{L}U)^2 + (R_\| - R_\perp)(\hat{L}_zU)^2] - \left(\frac{1}{2k_BT}\right)^2[R_\perp(\hat{L}_+U)(\hat{L}_-U) + R_\|(\hat{L}_zU)^2] \tag{44}$$

The matrix elements of the sum of the first two terms in equation (44) coincide with those of the Brownian diffusion superoperator in isotropic media (cf. Section 2.6.1). We note that in equation (44), the action of each of the operators $\hat{L}^2$, $\hat{L}_z^2$, and $\hat{L}_\pm$ on members of the basis set $\{\mathcal{B}(L_{max})\}$ is

$$\hat{L}^2|L, M, K; p^S, q^S; p^I, q^I\rangle\rangle = L(L+1)|L, M, K; p^S, q^S; p^I, q^I\rangle\rangle \tag{45}$$

$$\hat{L}_z|L, M, K; p^S, q^S; p^I, q^I\rangle\rangle = K|L, M, K; p^S, q^S; p^I, q^I\rangle\rangle \tag{46}$$

$$\hat{L}_\pm|L, M, K; p^S, q^S; p^I, q^I\rangle\rangle = \sqrt{L(L+1) - K(K\pm1)}|L, M, K\pm1; p^S, q^S; p^I, q^I\rangle\rangle \tag{47}$$

If these three equations are used to further simplify the form of equation (44), we obtain

$$\tilde{\mathbf{\Gamma}}_U = \sum_{L=2}^{8} \sum_{K=-L}^{L} X_K^L \mathscr{D}_{0K}^L(\Omega) \tag{48}$$

The X_K^L parameters in equation (48) for $L \neq 0$ are numerical coefficients which depend on the potential parameters (Meirovitch *et al.*, 1982).[4] These coefficients satisfy

$$X_K^L = X_{-K}^L \tag{49}$$

and $X_K^L = 0$ if either L or K is odd.

The matrix elements of $\tilde{\mathbf{\Gamma}}_U$ can now be written as

$$\begin{aligned} \langle\langle \sigma_1 | \tilde{\mathbf{\Gamma}}_U | \sigma_2 \rangle\rangle = {} & \delta_{M_1,M_2} \delta_{p_1^s,p_2^s} \delta_{q_1^s,q_2^s} \delta_{p_1^I,p_2^I} \delta_{q_1^I,q_2^I} \\ & \times \sum_{L=2}^{8} (-1)^{M_1-K_1} X_{K_1-K_2}^L N_L(L_1, L_2) \\ & \times \begin{pmatrix} L_1 & L & L_2 \\ M_1 & 0 & -M_1 \end{pmatrix} \begin{pmatrix} L_1 & L & L_2 \\ K_1 & K_2 - K_1 & -K_2 \end{pmatrix} \end{aligned} \tag{50}$$

The matrix of $\tilde{\mathbf{\Gamma}}_U$ is seen to be real and symmetric in this basis, but is not diagonal.

Before proceeding, it is useful to make a few remarks about the implications of the form of $\tilde{\mathbf{\Gamma}}_U$. Since the restoring potential is a linear combination of the Wigner rotation matrix elements for which $M = 0$, it is clear that the restoring potential is independent of the Euler angle α. Therefore, the restoring potential is axially symmetric in the director frame, hence the term is uniaxial. Indeed, this requirement is used to define the director frame in uniaxial liquid crystals. The main point, however, is that this symmetry implies that all spin probe molecules whose orientations in space are related by a simple rotation about the $\hat{z}_d$ axis experience similar forces and thus will reorient in a similar manner. In contrast, the restoring potential can depend on the Euler angle γ if the $K = 2$ terms are included in the expansion. If the potential does depend on γ, then spin probes whose orientations in space are related by a nontrivial rotation about the $\hat{z}_R$ axis at a given time will experience different forces and thus will reorient dissimilarly, so long as they continue to experience different forces. However, it has been assumed for convenience that the diffusion tensor, which is related to the geometry of the spin probe molecules, is axially symmetric about $\hat{z}_R$. This symmetry of the diffusion tensor implies that the reorientational dynamics of spin probes related by rotations about $\hat{z}_R$ should be similar, not dissimilar as suggested by the preceding argument. The resolution of this apparent conflict is simply that the axial symmetry of the spin probe is usually only approximate. In essence, the effect of the diffusional terms which depend only on the deviation of the diffusion tensor from axial symmetry are usually quite small and have been neglected. However, even if the assumption of an axially symmetric diffusion tensor for a given radical is valid for studies involving isotropic media, the terms which involve the effect of the asymmetric portion of the restoring potential on the reorientational dynamics can still be quite large for the same

[4] A factor of 1/4 is missing in front of the double summation in equation A23 in this reference.

radical in liquid crystalline media. Therefore, these terms may be included in the calculation if necessary. In summary, the effects of molecular asymmetry are usually more pronounced in asymmetric environments than in symmetric environments.

It is also possible to have discrete-jump-type motions between equivalent sites. This type of motion can be incorporated into the model for the reorientational dynamics of the probe molecules by the inclusion of a term of the form

$$\langle\langle \sigma_1 | \tilde{\Gamma}_{\mathrm{dj}} | \sigma_2 \rangle\rangle = \delta_{L_1 L_2} \delta_{M_1 M_2} \delta_{K_1 K_2} \delta_{p_1^S p_2^S} \delta_{q_1^S q_2^S} \delta_{p_1^I p_2^I} \delta_{q_1^I q_2^S} \tau_{\mathrm{dj}}^{-1} [1 - \delta_{0,(K_1 \bmod n_s)}] \tag{51}$$

where n_s is the number of equivalent sites and τ_{dj}^{-1} is the discrete jump frequency.

In the presence of an orienting potential, the viscosity can be a tensorial quantity. This effect can also be included by adding a term $\tilde{\Gamma}_{\mathrm{av}}$. The correction term to $\tilde{\Gamma}_{\mathrm{iso}}$ can be written as

$$\begin{aligned} \langle\langle \sigma_1 | \tilde{\Gamma}_{\mathrm{av}} | \sigma_2 \rangle\rangle_{\mathrm{iso}} = {} & \delta_{L_1, L_2} \delta_{M_1, M_2} \delta_{K_1, K_2} \delta_{p_1^S, p_2^S} \delta_{q_1^S, q_2^S} \delta_{p_1^I, p_2^I} \delta_{q_1^I, q_2^I} \\ & \times [\hat{R}_\perp L_1 (L_1 + 1) + (\hat{R}_\parallel - \hat{R}_\perp) M_1^2] \end{aligned} \tag{52}$$

where $\hat{R}_\parallel$ is the parallel diffusion coefficient in the director frame. The correction terms to $\tilde{\Gamma}_U$ can be found in Polnaszek and Freed (1975).

2.7. Components of the Starting Vector

Since a symmetrized diffusion operator is being used, and the spectral function associated with the $\hat{x}_L$ component of the electronic magnetization is desired, the appropriate starting vector is

$$\begin{aligned} |v\rangle\rangle &= (2I + 1)^{-1/2} |S_x \otimes I_I \otimes P_0^{1/2}\rangle\rangle \\ &= (1/\sqrt{2})[|v_1\rangle\rangle + |v_{-1}\rangle\rangle] \end{aligned} \tag{53}$$

where $P_0(\Omega)$ is the equilibrium probability distribution for the spin probes and is given by

$$P_0(\Omega) = \frac{\exp[-U(\Omega)/k_B T]}{\int d\Omega \exp[-U(\Omega)/k_B T]} \tag{54}$$

In addition, I_I is the unit operator in the nuclear spin space, and

$$|v_{\pm 1}\rangle\rangle = (2I + 1)^{-1/2} |S_\pm \otimes I_I \otimes P_0^{1/2}\rangle\rangle \tag{55}$$

In the basis $\{\mathcal{B}(L_{\max})\}$ [cf. equations (10) and (11)] the elements of the vectors $|v_{\pm 1}\rangle\rangle$ making up the starting vector are

$$\begin{aligned} \langle L, M, K; p^S, q^S; p^I, q^I | v_{\pm 1} \rangle = {} & \left[\frac{2L + 1}{8\pi^2 (2I + 1)} \right]^{1/2} \left[\int d\Omega \exp[-U(\Omega)/k_B T] \right]^{-1/2} \\ & \times \langle p^S, q^S; p^I, q^I | S_\pm \otimes I_I \rangle\rangle \\ & \times \int d\Omega \, \mathcal{D}_{MK}^{L*}(\Omega) \exp[-U(\Omega)/2k_B T] \end{aligned} \tag{56}$$

Some simple symmetry arguments can greatly simplify this expression. First, the restoring potential has only $M = 0$ terms in its expansion [cf. equation (2)] and thus does not depend on the first Euler angle. This implies that only the basis vectors with $M = 0$ can have a nonzero projection on the starting vector. Second, all terms in the expansion of the restoring potential have even K quantum numbers, therefore only basis vectors with even K quantum numbers can have nonzero projections on the starting vector. Finally, since the Wigner rotation matrix elements with $M = 0$ are proportional to the usual spherical harmonics (Messiah, 1962; Biedenharn and Louck, 1981) and only the states with even values of K are important, one can further verify that only states with even L quantum numbers can have nonzero projections on the starting vector using a simple parity argument. Using these three observations and evaluating the spin part of equation (56) gives

$$\langle L, M, K; p^S, q^S; p^I, q^I \mid v_{\pm 1}\rangle = \delta_{p^S,\pm 1}\delta_{q^S,0}\delta_{p^I,0}\delta_{M,0}\delta_{(K \bmod 2),0}N_I\left[\frac{(2L+1)(L-K)!}{(L+K)!}\right]^{1/2}$$

$$\times \int_{-1}^{1} dz\, P_L^K(z)\exp[A(z)]\int_0^{2\pi} d\gamma \exp[iK\gamma + \cos(2\gamma)B(z)] \quad (57)$$

where $z = \cos\beta$, $P_L^K(z)$ is an associated Legendre function of the first kind, and

$$N_I = \left[8\pi^2(2I+1)\int d\Omega \exp[-U(\Omega)/k_B T]\right]^{-1/2} \quad (58)$$

$$A(z) = (\lambda_0^2/2)P_2^0(z) + (\lambda_0^4/2)P_4^2(z) \quad (59)$$

$$B(z) = (\lambda_2^2/2\sqrt{6})P_2^2(z) + (\lambda_2^4/6\sqrt{10})P_4^2(z) \quad (60)$$

The normalization factor N_I and similar factors which are independent of the basis-set quantum numbers will be ignored in the following. In the calculation of the starting vector, the unnormalized vector resulting from the neglect of trivial normalization factors is normalized numerically.

The integral over the angle γ can be expressed in terms of the modified Bessel functions of the first kind $I_n(y)$ (McLachlan, 1961) of strictly real argument as

$$\int_0^{2\pi} d\gamma \cos(K\gamma)\exp[\cos(2\gamma)B(z)] = 2\pi(2-\delta_{K,0})I_{K/2}(B(z)) \quad (61)$$

It is also possible to simply evaluate the double integral in equation (57) numerically, though this method becomes unstable for large L and/or K where the integrand is highly oscillatory.

2.8. The High-Field Approximation

Considerable simplifications in the above discussion are possible if one is able to take advantage of the approximations valid in the unsaturated, high-field, and slow motional limits. More precisely, if the follow statements are true:

- The anisotropic part of the spin Hamiltonian (the part arising from the contraction of second-rank tensors) is small compared to the isotropic part of the Zeeman interaction.
- The rotational motion is slow enough that $\omega_0 \tau_R \gg 1$, where τ_R is the rotational correlation time on the order of unity.
- The microwave radiation field is sufficiently weak that the spin system is not being saturated (i.e., the absorption mode signal is directly proportional to the incident microwave field).

then one can neglect all terms in the spin Hamiltonian which do not commute with S_z (i.e., the nonsecular terms) and also make the rotating wave approximation. When these approximations are valid, one can neglect the coupling of the basis vectors with different values of the p^S quantum number. Therefore, the subspaces labeled by different values of the p^S index evolve independently, and one can calculate the spectrum by knowing only the time evolution of the states with $p^S = 1$, since these are the ones which couple to the microwave radiation field in the rotating wave approximation.

With these simplifications in mind, it is possible to reformulate the problem by neglecting the nonsecular terms in the spin Hamiltonian and developing a new basis set which takes advantage of the fact that only the $p^S = 1$, $q^S = 0$ states need be considered, since these are the only states connected to the starting vector by the simplified stochastic Liouville superoperator. A careful analysis of this stochastic Liouville superoperator shows that the matrix of the stochastic Liouville superoperator is reduced to a complex symmetric form in the subspace spanned by the basis vectors (Meirovitch *et al.*, 1982; Schneider, 1989),

$$|L, M, K'; 1, 0; p^I, q^I\rangle\rangle = [2(1 + \delta_{K,0})]^{-1/2} \times (|L, M, K; 1, 0; p^I, q^I\rangle\rangle + (-1)^{L+K}|L, M, -K; 1, 0; p^I, q^I\rangle\rangle) \tag{62}$$

where the K' index is now constrained to be positive. Furthermore, the starting vector can have nonzero projections only on vectors within this subspace.

A further reduction in the size of the basis is possible by taking advantage of the symmetry of the matrix elements of the Liouville superoperator under the simultaneous reversal in sign of the M and p^I indices. The result of this analysis is that it is possible to further restrict one's attention to the subspace spanned by the basis vectors

$$|L, M', K'; 1, 0; p^I, q^I\rangle\rangle = [2(1 + \delta_{M,0}\delta_{p',0})]^{-1/2} \times (|L, M, K'; 1, 0; p^I, q^I\rangle\rangle + (-1)^{L+M}|L, -M, K'; 1, 0; -p^I, q^I\rangle\rangle) \tag{63}$$

and the new M' index is also positive. This is true only if the nonsecular terms in the spin Hamiltonian are omitted. Although the expressions for the matrix elements of the approximate high-field stochastic Liouville superoperator are somewhat awkward in

this basis, it does have the very significant advantage of reducing the dimension of the resulting matrix to a minimal size (Meirovitch *et al.*, 1982).

By symmetry arguments, it can also be shown that in special cases only small subsets of these basis vectors are needed (Meirovitch *et al.*, 1982). For instance, in the absence of director tilt, only the states with $M' = p^I$ are needed. Similarly, if there is no diffusion tilt, then $F^{2,\pm 1}_{\mu,R} = 0$, so that only basis vectors with even values of K' are important. Finally, if the magnetic tensors are axially symmetric in the diffusion frame so that $F^{2,m}_{\mu,R} = \delta_{m,0}$, then only the states with even values of L and $K' = 0$ are needed.

The programs in this package use all of these approximations and take advantage of the resulting reduction in the size of the basis set which must be considered. In the following, this high-field basis set will be used exclusively, therefore the primes on the M and K subscripts will be dropped to simplify the notation.

3. MAGNETIC RESONANCE LINE SHAPES AND THE COMPLEX SYMMETRIC LANCZOS ALGORITHM

In 1950, the Hungarian physicist and mathematician Cornelius Lanczos developed a very powerful algorithm for tridiagonalizing arbitrary square matrices (Lanczos, 1950), which now carries his name. The algorithm attracted quite a bit of interest shortly after its development, but fell into disrepute when it was found that it was prone to certain instabilities in practical numerical applications (Wilkinson, 1965). Interest in the Lanczos algorithm was renewed when the source of these instabilities was uncovered by Paige (Paige, 1976, 1980; Golub and Van Loan, 1983; Cullum and Willoughby, 1985).

The basic scheme behind the Lanczos algorithm is quite simple. For simplicity, the attention will be restricted here to real, symmetric, positive definite (RSPD) matrices with nondegenerate eigenvalues. Given an $N \times N$ RSPD matrix $\mathbf{A}$ and an arbitrary nonzero, real N-vector $\mathbf{v}$, we form the sequence of vectors $\mathbf{k}_j$, $j = 1, 2, \ldots, N$ using the formula

$$\mathbf{k}_n = \mathbf{A}^{(n-1)}\mathbf{v} \tag{64}$$

The elements of the set of vectors $\{\mathbf{k}_n\}$ generated in this manner are referred to as Krylov vectors. The application of the Gram-Schmidt orthonormalization procedure to the sequence of Krylov vectors, in order of appearance, gives a new orthornomal basis, denoted $\{\mathbf{q}_j\}$. Let $\mathbf{Q}$ be the $N \times N$ matrix composed of the vectors $\mathbf{q}_j$. In exact arithmetic, the matrix $\mathbf{T} = \mathbf{QAQ}^{tr}$ is tridiagonal and has the same eigenvalues as the original matrix $\mathbf{A}$.

In practice, the Lanczos algorithm does not actually generate the vectors $\mathbf{k}_n$. Instead, it forms the vectors $\mathbf{q}_j$, which will be referred to as Lanczos vectors, in a direct manner using a stepwise orthogonalization procedure that will be discussed in detail in Section 3.1. This procedure has the tremendous advantage that it requires only two, not N, intermediate vectors of dimension N. The instabilities observed in the computer implementation of the Lanczos algorithm are due to the fact that in finite precision

arithmetic the overall, or global, orthogonality of the sequence of Lanczos vectors generated by the simple stepwise orthogonalization procedure cannot be maintained.

Several methods, all essentially based on the results of Paige's error analysis, have been proposed to circumvent this difficulty in order to enable one to reliably determine the entire set of eigenvalues of large, sparse matrices (Parlett, 1980; Golub and Van Loan, 1983; Cullum and Willoughby, 1985). One set of methods is based on trying to maintain global orthogonality in an efficient manner (Parlett, 1980; Golub and Van Loan, 1983). The computer implementation of these methods has the drawback of requiring relatively large amounts of memory to hold intermediate vectors and the associated CPU time to perform the reorthogonalization steps. Alternatively, one can simply allow the instabilities to arise and run their course, giving rise to spurious or "ghost" eigenvalues. These spurious eigenvalues can be identified after the fact and discarded (Cullum and Willoughby, 1985). This method also requires the storage or recalculation of large numbers of intermediate results. It also may require the execution of far more than N Lanczos steps on an $N \times N$ matrix.

The loss of global orthogonality is a severe problem if one tries to use the Lanczos algorithm to calculate the entire eigenvalue spectrum of large matrices. Fortunately, it poses little or no problem if one uses the Lanczos algorithm to calculate spectral functions in the manner discussed below. These assertions will be justified in the following sections.

Not long after Lanczos made his contribution, Hestenes and Stiefel (1952) developed a related algorithm to solve linear systems of algebraic equations known as the conjugate gradients algorithm. The relationship between these two algorithms is very close, but not necessarily obvious at first glance. Given an $N \times N$ RSPD matrix $\mathbf{A}$ and a real N-vector $\mathbf{v}$, the conjugate gradients algorithm attempts to solve the system of linear algebraic equation $\mathbf{Ax} = \mathbf{v}$ for the unknown vector $\mathbf{x}$. The conjugate gradients algorithm can be thought of as a Lanczos algorithm where the tridiagonal matrix $\mathbf{T}$ is constructed in a factored form (Golub and Van Loan, 1983; Cullum and Willoughby, 1985). This factored form of $\mathbf{T}$ can then be used to generate a sequence of approximate solution vectors $\mathbf{x}_j$ where $\mathbf{x}_0 = \mathbf{v}$. In exact arithmetic this sequence terminates after at most N steps giving the exact solution vector.

As with the Lanczos algorithm, the conjugate gradients method is prone to the loss of orthogonality of the sequence of Lanczos vectors. This is manifested in the fact that the computer implementations of the conjugate gradients algorithm do not converge to the exact solution vector in at most N steps.

Again, this loss of orthogonality does not pose serious difficulties in the use of the conjugate gradients algorithm for the calculation of spectral functions. In addition, it can be used as a very effective means of determining a minimal truncation scheme (MTS) for a given problem (cf. Section 3.4).

3.1. The Real Symmetric Lanczos Algorithm

A short derivation of the Lanczos algorithm for real symmetric matrices will be given here as a reference for readers who are unfamiliar with the algorithm. The derivation given here is based on simple linear algebra and is slanted toward the generalizations needed for complex symmetric matrices. First, the Gram-Schmidt orthonormalization procedure will be used to derive the general three-term recursion

formula for the Lanczos vectors. These results will then be collected into a single matrix equation for the Lanczos tridiagonal matrix. The majority of this section is devoted to the study of the algorithm in infinite precision arithmetic. The impact of finite precision computer arithmetic on the algorithm is briefly summarized at the end.

As stated previously, the Lanczos algorithm amounts to the application of the Gram-Schmidt orthogonalization procedure to a sequence of vectors defined by the matrix in question and a starting vector. This starting vector is determined by the form of the desired spectral function.

To start the process of generating the set of Lanczos vectors, assume $\mathbf{A}$ is an $N \times N$ real symmetric matrix and that $\mathbf{v}$ is a given real N-vector. The vector $\mathbf{v}$ will serve as the starting vector. The first member in the orthonormal set of Lanczos vectors, $\mathbf{q}_1$, is taken to be parallel to the starting vector $\mathbf{v}$, i.e.,

$$\beta_0 \mathbf{q}_1 = \mathbf{k}_1 = \mathbf{v} \tag{65}$$

The requirement that the new set of vectors be normalized ($\mathbf{q}_i^{\mathrm{tr}} \mathbf{q}_i = 1$) implies $\beta_0 = \|\mathbf{v}\|$.

In the following steps, the vector $\mathbf{q}_{j+1}$ being added to the existing set of Lanczos vectors is written as a linear combination of the previous vectors and the vector $\mathbf{A}\mathbf{q}_j$, i.e.,

$$\mathbf{q}_{j+1} \equiv c_{j+1}^{(j+1)} \mathbf{A}\mathbf{q}_j + \sum_{k=1}^{j} c_k^{(j+1)} \mathbf{q}_k \tag{66}$$

The expansion coefficients, $c_k^{(j+1)}$, are determined by requiring that $\mathbf{q}_{j+1}$ be normalized and orthogonal to all previous Lanczos vectors. The relationship between the sets of Krylov and Lanczos vectors becomes evident if the relations defining the previous Lanczos vectors are inserted into equation (66) and terms of the form $\mathbf{A}^k \mathbf{v}$ are collected. The advantage of using the Lanczos vectors rather than the Krylov vectors is demonstrated below.

Now, one can proceed with the construction of the second Lanczos vector using equation (66) in the form

$$\beta_1 \mathbf{q}_2 = (\mathbf{A} - \alpha_1 \mathbf{I}) \mathbf{q}_1 \tag{67}$$

To determine the coefficient α_1, equation (67) is multiplied on the left by $\mathbf{q}_1^{\mathrm{tr}}$. If $\mathbf{q}_2$ is to be orthogonal to $\mathbf{q}_1$, it is clear that

$$\alpha_1 = \mathbf{q}_1^{\mathrm{tr}} \mathbf{A} \mathbf{q}_1 \tag{68}$$

In contrast, the coefficient β_1 is chosen to normalize the second Lanczos vector, $\mathbf{q}_2$, giving

$$\beta_1 = \|(\mathbf{A} - \alpha_1 \mathbf{I}) \mathbf{q}_1\| \tag{69}$$

In a similar fashion, the third vector is

$$\beta_2 \mathbf{q}_3 = (\mathbf{A} - \alpha_2 \mathbf{I}) \mathbf{q}_2 - \gamma_1 \mathbf{q}_1 \tag{70}$$

Again, γ_1 and α_2 are determined from the orthogonality requirements,

$$\gamma_1 = \mathbf{q}_1^{\mathrm{tr}}\mathbf{A}\mathbf{q}_2 = \beta_1 \tag{71}$$

$$\alpha_2 = \mathbf{q}_2^{\mathrm{tr}}\mathbf{A}\mathbf{q}_2 \tag{72}$$

These coefficients can now be used in equation (70) to give the general form of the three-term recursion relation on which the Lanczos algorithm is based,

$$\beta_2\mathbf{q}_3 = (\mathbf{A} - \alpha_2\mathbf{I})\mathbf{q}_2 - \beta_1\mathbf{q}_1 \tag{73}$$

Again, β_2 is chosen such that $\mathbf{q}_3$ is normalized, as done previously.

The explicit calculation of the fourth vector demonstrates the validity of the general form of the Lanczos recursion relation given in equation (73). In general, $\mathbf{q}_4$ must be expressible as a linear combination of $\mathbf{A}\mathbf{q}_3$, $\mathbf{q}_3$, $\mathbf{q}_2$, and $\mathbf{q}_1$,

$$\beta_3\mathbf{q}_4 = (\mathbf{A} - \alpha_3\mathbf{I})\mathbf{q}_3 - \gamma_2\mathbf{q}_2 - \delta_1\mathbf{q}_1 \tag{74}$$

To verify that equation (73) is indeed a prototype of a three-term recursion relation, it must be shown that $\delta_1 = 0$ and $\gamma_2 = \beta_2$. It is easy to see that $\delta_1 = 0$ by premultiplying equation (74) by $\mathbf{q}_1^{\mathrm{tr}}$,

$$\delta_1 = \mathbf{q}_1^{\mathrm{tr}}\mathbf{A}\mathbf{q}_3 \tag{75}$$

Using equation (67) this can be rewritten as

$$\delta_1 = (\beta_1\mathbf{q}_2 + \alpha_1\mathbf{q}_1)^{\mathrm{tr}}\mathbf{q}_3 \tag{76}$$

which vanishes by the orthogonality of the Lanczos vectors. In addition, premultiplying equations (73) and (74) by $\mathbf{q}_3^{\mathrm{tr}}$ gives $\beta_2 = \gamma_2$.

The same behavior is observed for all further vectors. Therefore, the general Lanczos recurrence relation

$$\beta_m\mathbf{q}_{m+1} = (\mathbf{A} - \alpha_m\mathbf{I})\mathbf{q}_m - \beta_{m-1}\mathbf{q}_{m-1} \tag{77}$$

can be used to generate all successive vectors $\mathbf{q}$ so long as the quantities β are nonzero. If $\beta_m = 0$ for $m < N$ then the procedure terminates. This occurrence is a manifestation of the fact that the starting vector does not have a projection on all eigenvectors of $\mathbf{A}$. In this case, the eigenvalues of the matrix $\mathbf{T}_m$ correspond to the subset of the eigenvalues of $\mathbf{A}$ whose associated eigenvectors have a nonzero projection on the starting vector (Parlett, 1980; Golub and Van Loan, 1983; Cullum and Willoughby, 1985).

We note that, from equation (77), it is clear that only the last two Lanczos vectors are required for the construction of the next member of the set. This surprising fact is one of the major reasons why the Lanczos algorithm is such an efficient means of computing spectral functions. The other major reason is that the matrix $\mathbf{A}$ is not modified, so full advantage can be taken of any special structure of the matrix elements of $\mathbf{A}$ to simplify the computation (e.g., sparsity or bandedness).

It is informative to summarize these results in a matrix form. The transformation matrix, $\mathbf{Q}_N$, whose jth row is given by the elements of $\mathbf{q}_j$ for $1 \leq j \leq N$, transforms the original $N \times N$ matrix $\mathbf{A}$ into a $N \times N$ real symmetric tridiagonal matrix, $\mathbf{T}_N$,

$$\mathbf{T}_N = \mathbf{Q}_N\mathbf{A}\mathbf{Q}_N^{\mathrm{tr}} \tag{78}$$

Using the Lanczos recursion relation derived above [see equation (77)], it is straightforward to verify that the matrix $\mathbf{T}_N$ is indeed symmetric and tridiagonal. The diagonal and off-diagonal matrix elements of $\mathbf{T}_N$ are just the coefficients appearing in equation (77),

$$(T_N)_{i,i} = \alpha_i \tag{79}$$

$$(T_N)_{i,i+1} = \beta_i \tag{80}$$

It can be shown that the matrix $\mathbf{T}_N$ can have only distinct eigenvalues, and that if $\beta_{m+1} = 0$ then the eigenvalues of $\mathbf{T}_m$ are identical to those eigenvalues of $\mathbf{A}$ whose corresponding eigenvectors have a nonzero projection on the starting vector [30, 31, 32] (Parlett, 1980; Golub and Van Loan, 1983; Cullum and Willoughby, 1985).

In addition, it is easy to verify that for each $m \leq N$,

$$\mathbf{Q}_m \mathbf{A} \mathbf{Q}_m^{\mathrm{tr}} = \mathbf{T}_m \tag{81}$$

where $\mathbf{Q}_m$ is the $m \times N$ matrix constructed from the first m Lanczos vectors, and $\mathbf{T}_m$ is identical to the $m \times m$ submatrix in the upper left-hand corner of $\mathbf{T}_N$. Furthermore, from the orthonormality of the Lanczos vectors, it follows that

$$\mathbf{Q}\mathbf{Q}^{\mathrm{tr}} = \mathbf{I}_m \tag{82}$$

where $\mathbf{I}_m$ is the $m \times m$ identity matrix.

The effect of the finite precision arithmetic on the Lanczos algorithm is the subject of Paige's analysis (Paige, 1976, 1980; Parlett, 1980; Golub and Van Loan, 1983; Cullum and Willoughby, 1985). The basic result of this analysis is quite simple, though the analysis itself is rather sophisticated and will not be presented here. The finite precision error analysis is based on the fact that as the matrices $\mathbf{T}_m$ in equation (81) increase in size as m is increased, the eigenvalues and eigenvectors of $\mathbf{T}_m$ become better and better approximations to the eigenvalues and eigenvectors of $\mathbf{A}$, but the convergence rate is not the same for all eigenvalue-eigenvector pairs. Assume for a moment that at step $m = M$ one of the eigenvalues of $\mathbf{T}_M$ is identical to one of the eigenvalues of the original matrix $\mathbf{A}$ to the working precision of the computer. The basic result of the finite precision error analysis is that all further Lanczos vectors $\mathbf{q}_m$ for $m > M$ tend to have a spurious projection along the eigenvector associated with the numerically converged eigenvalue. This phenomenon leads to a lack of orthogonality of these Lanczos vectors and the appearance of spurious eigenvalues.

However, this loss of orthogonality does not adversely affect spectral calculations performed in the manner advocated here. This subject is treated in Section 3.5.

3.2. The Complex Symmetric Lanczos Algorithm

The formal extension of the real symmetric Lanczos algorithm to handle non-Hermitian, complex symmetric matrices of the type which occur in magnetic resonance line-shape problems is relatively simple. In his original paper Lanczos (1950) showed

how certain classes of complex nonsymmetric matrices could be reduced to a complex tridiagonal form using a pair of closely related three-term recurrence relations. A starting vector is also needed for each recurrence relation. These relations are used to generate a biorthogonal set of vectors (Householder, 1964; Wilkinson, 1965; Golub and Van Loan, 1983; Cullum and Willoughby, 1985). The matrices constructed from these sets of biorthogonal vectors then define a general similarity transformation which reduces the matrix to tridiagonal form. These very general Lanczos recursion relations are sometimes used in the study of physical problems (Wassam, 1985a, 1985b).

However, if one is interested in studying complex symmetric matrices, a more definitive statement can be made. A classical result in linear algebra states that if two complex symmetric matrices are similar, then they are related to one another by a complex orthogonal transformation (Gantmacher, 1959; Horn and Johnson, 1985). Thus, if an $N \times N$ complex symmetric matrix $\mathbf{A}$ can be reduced to a complex symmetric tridiagonal matrix $\mathbf{T}_N$ by the Lanczos algorithm, the transformation matrix must be complex and orthogonal. A reexamination of the biorthogonal Lanczos relations for nonsymmetric matrices in this light shows that the pair of recursion relations degenerates to a single three-term recursion relation identical in form to equation (77) if the two starting vectors are chosen properly (Moro and Freed, 1986; Vasavada *et al.*, 1987). In the original Moro and Freed work (1981) the complex-symmetric form was introduced at the outset.

Though the form of the Lanczos recursion relation is identical for real symmetric and complex symmetric matrices, the elements of the resulting tridiagonal matrix and Lanczos vectors for the complex symmetric case require more explanation. In particular, the fact that the Lanczos vectors form a complex orthogonal matrix in the original basis means that they are not orthonormal in the usual sense. The canonical scalar product of two vectors $\mathbf{x}$ and $\mathbf{y}$ in an N-dimensional complex vector space is

$$\langle \mathbf{x}, \mathbf{y} \rangle \equiv \mathbf{x}^\dagger \mathbf{y} = \sum_{i=1}^{N} \xi_i^* \eta_i \tag{83}$$

A complete orthonormal set of basis vectors $\{\hat{e}_j, j = 1, 2, \ldots, N\}$, where $\langle \hat{e}_i, \hat{e}_j \rangle \langle \hat{e}'_i \hat{e}_j \rangle = \delta_{ij}$, has been introduced to obtain the final form (Gantmacher, 1959; Horn and Johnson, 1985), so that $\xi_i = \langle \hat{e}_i, \mathbf{x} \rangle$ and $\eta_i = \langle \hat{e}_i, \mathbf{y} \rangle$. The canonical vector norm in the same space is simply the positive square root of the canonical scalar product of a vector with itself,

$$\|\mathbf{x}\| \equiv \sqrt{\mathbf{x}^\dagger \mathbf{x}} = \left(\sum_{i=1}^{N} \|x_i\|^2 \right)^{1/2} \tag{84}$$

It should be noted that this norm is positive for all nonzero vectors, as it is a sum of nonnegative terms.

A complex vector space equipped with such a norm and scalar product is called a unitary space. This norm and scalar product endows the complex vector space with a geometrical structure very similar to a real Euclidean space (Schneider and Freed, in press).

The Lanczos vectors generated by the complex symmetric Lanczos algorithm, however, are not orthonormal with respect to this canonical scalar product. Instead,

to form a complex orthogonal matrix the Lanczos vectors must satisfy (Gantmacher, 1959; Horn and Johnson, 1985)

$$(\mathbf{q}_i, \mathbf{q}_j) \equiv \mathbf{q}_i^{\mathrm{tr}}\mathbf{q}_j = \sum_{k=1}^{N} q_i^{(k)} q_j^{(k)} = \delta_{ij} \tag{85}$$

where $q_m^{(k)} = (\hat{e}_k, \mathbf{q}_m)$. A set of vectors which satisfies equation (85) is called rectanormal (Choudhury and Horn, 1986; Schneider, 1989; Schneider and Freed, 1989) rather than orthonormal. We note that summands in equation (85) are not necessarily nonnegative, therefore it cannot be used to define a vector norm in the strict sense. However, one is free to define a "pseudonorm" or rectanorm of a vector as

$$\|\mathbf{x}\|_{\mathrm{ps}} \equiv \left(\sum_{i=1}^{N} \xi_i^2 \right)^{1/2} \tag{86}$$

Complex vector spaces equipped with a generalized norm and scalar product of this type [cf. equations (85) and (86)] are called complex orthogonal spaces. Since the rectanorm of a vector can be negative or even imaginary, the geometry of these spaces is much different from the more familiar unitary and Euclidean spaces (Schneider and Freed, 1989).

The calculation of the spectral function from the Lanczos tridiagonal matrix is discussed in Section 3.5.

3.3. The Real Symmetric Conjugate Gradients Algorithm

The conjugate gradients method of Hestenes and Stiefel (1952) amounts to a clever adaptation of the Lanczos algorithm for solving systems of linear algebraic equations. An exposition of the conjugate gradients algorithm as applied to RSPD matrices and its connection with the Lanczos algorithm (cf. Section 3.1) is presented here.

In the conjugate gradients algorithm, a sequence of approximate solution vectors, $\mathbf{x}_j$, for the problem

$$\mathbf{A}\mathbf{x} = \mathbf{v} \tag{87}$$

is desired. Associated with each approximate solution vector is a residual vector,

$$\mathbf{r}_j = \mathbf{v} - \mathbf{A}\mathbf{x}_j \tag{88}$$

Clearly, the norm of these residual vectors can be used as a measure of the deviation of the approximate solution vectors from the true solution vector, $\mathbf{x}$.

This algorithm can be used in several ways in magnetic resonance problems. First, the spectral function at a particular field position can be calculated directly, since equation (1) is equivalent to

$$I(\omega - \omega_0) = \left(\frac{1}{\pi}\right) \langle\langle x(\omega - \omega_0) | v \rangle\rangle \tag{89}$$

where $|x(\omega - \omega_0)\rangle\rangle$ is the solution to

$$[\tilde{\mathbf{\Gamma}} - i(\omega - \omega_0)\mathbf{I} - i\mathscr{L}]|x(\omega - \omega_0)\rangle\rangle = |v\rangle\rangle \tag{90}$$

Second, it can be used as an alternative means of generating the Lanczos tridiagonal matrix [cf. equation (106) below] in the calculation of the entire spectral function. In fact, the conjugate gradients algorithm often has a significant advantage over the usual Lanczos tridiagonalization procedure as described in Section 3.2. The third major application of the conjugate gradients algorithm is in the determination of a minimal truncation scheme for a given problem. Here, equation (90) is solved for a set of field positions; during this "field sweep," the maximum value of the modulus of each of the components of the solution vector divided by the amplitude of the spectral function [cf. equation (89)] is monitored. This quantity,

$$s_j = \max_{\omega - \omega_0} \frac{\|\hat{e}_j^{\mathrm{tr}} \mathbf{x}(\omega - \omega_0)\|}{\|\mathbf{v}^{\mathrm{tr}} \mathbf{x}(\omega - \omega_0)\|} \tag{91}$$

where $\hat{e}_j$ is the jth member of the original basis set, can then be used to assess the significance of the contribution of each basis vector in the overall solution of the problem. This application is discussed in more detail in Section 3.4.

In the conjugate gradients algorithm, the residual vectors are taken to be colinear with the Lanczos vectors,

$$\mathbf{q}_{j+1} = \pm \frac{1}{\rho_j} \mathbf{r}_j \tag{92}$$

This choice ensures that the sequence of the residual vectors, and therefore the sequence of approximate solution vectors, terminates after at most N steps (in exact arithmetic).

If this scheme of defining a residual vector and determining the approximate solution vector is to be successful, then one must be able to solve equation (88), or its equivalent, for the associated approximate solution vectors without actually inverting the matrix. This difficulty is most easily overcome by reformulating the conjugate gradients algorithm as a minimization problem of a special type. This discussion follows Golub and Van Loan (1983) quite closely. We consider the functional

$$F[\mathbf{y}] \equiv (\tfrac{1}{2})\mathbf{y}^{\mathrm{tr}} \mathbf{A} \mathbf{y} - \mathbf{y}^{\mathrm{tr}} \mathbf{v} \tag{93}$$

and note that, if $\mathbf{y} = \mathbf{x}$ where $\mathbf{x}$ is the solution to equation (87), then

$$\begin{aligned} F[\mathbf{x}] &= (\tfrac{1}{2})\mathbf{x}^{\mathrm{tr}} \mathbf{A} \mathbf{x} - \mathbf{x}^{\mathrm{tr}} \mathbf{v} \\ &= (\tfrac{1}{2})\mathbf{x}^{\mathrm{tr}} \mathbf{A}(\mathbf{x} - \mathbf{v}) - (\tfrac{1}{2})\mathbf{x}^{\mathrm{tr}} \mathbf{v} \\ &= (\tfrac{1}{2})\mathbf{v}^{\mathrm{tr}} \mathbf{A}^{-1} \mathbf{v} \end{aligned} \tag{94}$$

It is easy to see that this is actually a unique minimum point by examining $F[\mathbf{x} + \mathbf{y}]$ where $\mathbf{y}$ is an arbitrary vector,

$$\begin{aligned} F[\mathbf{x} + \mathbf{y}] &= (\tfrac{1}{2})(\mathbf{x} + \mathbf{y})^{\mathrm{tr}} \mathbf{A}(\mathbf{x} + \mathbf{y}) - (\mathbf{x} + \mathbf{y})_j^{\mathrm{tr}} \mathbf{v} \\ &= F[\mathbf{x}] + (\tfrac{1}{2})\mathbf{y}^{\mathrm{tr}} \mathbf{A} \mathbf{y} \end{aligned} \tag{95}$$

Since **A** has been assumed to be RSPD, the solution vector **x** must be unique and

$$F[\mathbf{x}+\mathbf{y}] - F[\mathbf{x}] > 0 \tag{96}$$

for all vectors $\mathbf{y} \neq 0$. Thus, the problem of solving the system of linear algebraic equations in equation (87) can be reformulated as a minimization problem involving the functional $F[\mathbf{y}]$ defined by equation (93).

One is now left with the problem of developing a systematic scheme for the minimization of $F[\mathbf{y}]$ subject to the constraint that the residual vectors are collinear with the Lanczos vectors [cf. equation (92)]. To begin, it is clear from equation (88) that the difference between two successive residual vectors can be written as

$$\begin{aligned} \mathbf{r}_j - \mathbf{r}_{j-1} &= -\mathbf{A}(\mathbf{x}_j - \mathbf{x}_{j-1}) \\ &\equiv -a_j \mathbf{A}\mathbf{p}_j \end{aligned} \tag{97}$$

This defines a new sequence of vectors, $\mathbf{p}_j$, which are known as conjugate direction vectors. The relationships between successive members of the sets of residual and approximate solution vectors can be reexpressed using the conjugate direction vectors:

$$\mathbf{r}_j = \mathbf{r}_{j-1} - a_j \mathbf{A}\mathbf{p}_j \qquad \text{and} \qquad \mathbf{x}_j = \mathbf{x}_{j-1} + a_j \mathbf{p}_j \tag{98}$$

Now, $F[\mathbf{x}_j]$ is just

$$\begin{aligned} F[\mathbf{x}_j] &= F[\mathbf{x}_{j-1} + a_j \mathbf{p}_j] \\ &= F[\mathbf{x}_{j-1}] + \left(\frac{a_j^2}{2}\right) \mathbf{p}_j^{\mathrm{tr}} \mathbf{A}\mathbf{p}_j - a_j \mathbf{p}_j^{\mathrm{tr}} \mathbf{v} \end{aligned} \tag{99}$$

By setting the derivative of equation (99) with respect to a_j equal to zero, it is easy to show that the minimum value

$$F[\mathbf{x}_j] = F[\mathbf{x}_{j-1}] - \left(\frac{1}{2}\right) \frac{(\mathbf{p}_j^{\mathrm{tr}} \mathbf{r}_{j-1})^2}{\mathbf{p}_j^{\mathrm{tr}} \mathbf{A}\mathbf{p}_j} \tag{100}$$

is attained when

$$a_j = \mathbf{p}_j^{\mathrm{tr}} \mathbf{r}_{j-1} / \mathbf{p}_j^{\mathrm{tr}} \mathbf{A}\mathbf{p}_j \tag{101}$$

It follows from this result and equation (98) that $\mathbf{p}_j$ and $\mathbf{r}_j$ are orthogonal,

$$\begin{aligned} \mathbf{A}\mathbf{p}_j &= -a_j^{-1}(\mathbf{r}_j - \mathbf{r}_{j-1}) \\ -a_j \mathbf{p}_j^{\mathrm{tr}} \mathbf{A}\mathbf{p}_j &= \mathbf{p}_j^{\mathrm{tr}}(\mathbf{r}_j - \mathbf{r}_{j-1}) \\ 0 &= \mathbf{p}_j^{\mathrm{tr}} \mathbf{r}_j \end{aligned} \tag{102}$$

A more detailed treatment (Golub and Van Loan, 1983; Cullum and Willoughby, 1985) shows that the conjugate direction vectors can also be obtained by

$$\mathbf{p}_j = \mathbf{r}_{j-1} + b_j \mathbf{p}_{j-1} \tag{103}$$

where

$$b_j = \rho_{j-1}^2 / \rho_{j-2}^2 \tag{104}$$

Now, equations (101)-(103) can be used to derive a more symmetrical formula for a_j,

$$a_j = \frac{(\mathbf{r}_{j-1} + \beta_j \mathbf{p}_{j-1})^{\mathrm{tr}} \mathbf{r}_{j-1}}{\mathbf{p}_j^{\mathrm{tr}} \mathbf{A} \mathbf{p}_j} = \frac{\rho_{j-1}^2}{\mathbf{p}_j^{\mathrm{tr}} \mathbf{A} \mathbf{p}_j} \tag{105}$$

This completes the exposition of the basic equations used in the conjugate gradients algorithm [cf. equations (98), (103)-(105)]. Using these equations, the problem of minimizing the functional $F[\mathbf{y}]$ over the entire N-dimensional space, and therefore the solution of the original set of linear algebraic equations, has been reduced to a sequence of simple one-dimensional minimizations.

The connection between the residual and Lanczos vectors in equation (92) can be exploited to derive the following equation for the Lanczos tridiagonal matrix from the quantities a_j and ρ_j as calculated by the conjugate gradients algorithm (Golub and Van Loan, 1983; Cullum and Willoughby, 1985):

$$\mathbf{T}_N = \mathbf{L}\mathbf{D}\mathbf{L}^{\mathrm{tr}} \tag{106}$$

where $\mathbf{D}$ is a diagonal matrix with elements

$$D_{ij} = a_j^{-1} \delta_{ij} \tag{107}$$

and $\mathbf{L}$ is a lower bidiagonal matrix with elements

$$L_{ij} = \delta_{ij} - \left(\frac{\rho_{j-1}}{\rho_{j-2}} \right) \delta_{i-1,j} \tag{108}$$

The sign ambiguity noted in equation (92) is a result of the fact that it is only ρ_j^2 that is actually calculated within the conjugate gradients algorithm. This same sign ambiguity can also lead to sign differences in the off-diagonal matrix elements of the tridiagonal matrices generated by the Lanczos and conjugate gradients algorithms. These sign differences do not affect the calculated spectrum, since only the squares of the off-diagonal matrix elements occur in the continued-fraction expansion of the spectral function [cf. equation (124)].

3.4. The Complex Symmetric Conjugate Gradients Algorithm

The generalization of the conjugate gradients algorithm to handle complex symmetric matrices is analogous to the generalization of the Lanczos algorithm treated in Section 3.2. In particular, the rectanorm [cf. equation (86)] and associated scalar product [cf. equation (85)] should be used everywhere instead of the usual unitary space norm and scalar product [cf. equations (83) and (84)].

However, there is one significant difficulty which can arise. Since the matrix **A** is now complex and symmetric, it cannot be assured that $\mathbf{p}_j^{tr}\mathbf{A}\mathbf{p}_j$ does not vanish for some index j, thereby disrupting the algorithm. In fact, the way that the matrix elements of the stochastic Liouville superoperator are calculated, this problem always arises on the very first step for calculations involving isotropic liquids. Fortunately, there is a very simple solution to this problem in that one can always choose an offset δ such that $\mathbf{p}_j^{tr}(\mathbf{A} + \delta\mathbf{I})\mathbf{p}_j \neq 0$ for all j. In practice, δ is usually chosen to be a small positive number on the order of the expected inhomogeneous linewidth of the experimental spectrum under consideration. Alternatively, one could simply use the Lanczos algorithm for the calculation. The presence of such an offset does not affect the results of either the Lanczos or conjugate gradients algorithms.

Using the connection between the Lanczos and conjugate gradients algorithms [as defined in equation (106)], one can calculate the entire spectral function while taking advantage of the modulus of the rectanorm of the residual vector to determine when to terminate the algorithm. The use of the error estimate provided by the residual vector can lead to substantial savings in computer time, despite the fact that each conjugate gradients step involves a little more computation than the corresponding Lanczos step. The offset δ which is required to avoid spurious divisions by zero is simply subtracted from the diagonal matrix elements of the tridiagonal matrix to give, within sign changes in the off-diagonal matrix elements, the same tridiagonal matrix as generated by the complex symmetric Lanczos algorithm in the absence of the offset.

Finally, the utility of the complex symmetric conjugate gradients algorithm in the determination of the MTS warrants further discussion. In this application, one is interested only in obtaining the quantities s_j, as defined in equation (91), which are used to assess the overall significance of the contribution of the jth basis vector to the spectral function. Therefore, it is not necessary to obtain the Lanczos tridiagonal matrix, but rapid convergence becomes very important since equation (90) must be solved at 10 to 100 different values of the sweep variable. Various methods of accelerating the convergence of the real symmetric conjugate gradients algorithm are known (Golub and Van Loan, 1983). Of these methods, the simplest one is known as the diagonal preconditioning scheme, which works well in cases where the diagonal matrix elements are much larger in amplitude than the off-diagonal elements. This is precisely the case for the matrix of the stochastic Liouville superoperator where the diagonal elements of the diffusion superoperator tend to increase in amplitude like L^2 while the magnitude of the elements of the Liouville superoperator tend to decrease as L increases. The diagonal preconditioning scheme amounts to solving the modified set of equations,

$$\mathbf{M}^{-1}(\mathbf{A} + \delta\mathbf{I})\mathbf{x} = \mathbf{M}^{-1}\mathbf{v} \tag{109}$$

where **M** is the diagonal matrix whose elements are just the positive square roots of the real parts of the diagonal matrix elements of $\mathbf{A} + \delta\mathbf{I}$. Thus, the real parts of the diagonal matrix elements of the scaled matrix

$$\tilde{\mathbf{A}} = \mathbf{M}^{-1}(\mathbf{A} + \delta\mathbf{I})\mathbf{M}^{-1} \tag{110}$$

are unity. This scaling improves both the numerical stability and rate of convergence of the algorithm. It is important to observe that the transformation defined in equation

(110) is not a similarity transformation. Using equation (110), it is straightforward to rewrite equation (109) in the form

$$\tilde{\mathbf{A}}\mathbf{y} = \mathbf{w} \tag{111}$$

where $\mathbf{w} = \mathbf{M}^{-1}\mathbf{v}$, and the solution to the original set of equations can be obtained from the relation

$$\mathbf{x} = \mathbf{M}\mathbf{y} \tag{112}$$

Thus, it is clear that a minor variant of the standard conjugate gradients algorithm may be used to solve the set of diagonally preconditioned equations and obtain the desired quantities. However, since this scheme involves a transformation which is not a similarity transformation [cf. equation (110)], one cannot reconstruct the Lanczos tridiagonal matrix in any simple manner.

3.5. The Continued-Fraction Representation of the Spectral Function

The continued-fraction representation of the spectral function holds a central position in both the theoretical and practical aspects of the methodology presented here. From a theoretical point of view, it allows one to view the Lanczos and conjugate gradients algorithms as a natural translation of the very powerful but abstract projection operator techniques of nonequilibrium statistical mechanics into a concrete computational framework. From a practical point of view, it represents an efficient means of obtaining an entire sequence of approximations to the spectral functions directly from the tridiagonal matrix. The emphasis here will be on the practical side. The interested reader is encouraged to consult the literature for surveys of the theoretical aspects (Moro and Freed, 1981; Wassam, 1985a; Dammers, 1985; Moro and Freed, 1986; Schneider and Freed, 1989).

The sequence of continued-fraction approximants to the spectral function is defined in terms of the elements of the tridiagonal matrix. The derivation of these approximants is quite straightforward in that it relies only on some basic linear algebra. To begin, the spectral function can be written in the form

$$J^{(N)}(z) = \mathbf{v}^{\dagger}[z\mathbf{I}_N + \mathbf{A}]^{-1}\mathbf{v} \tag{113}$$

The superscript and subscript N refer to the dimension of the matrix $\mathbf{A}$. The sequence of approximants to be constructed is actually a sequence of approximations to $J^{(N)}(z)$. The extent to which $J^{(N)}(z)$ is a good approximation to the experimental spectrum depends on the values chosen for the parameters on which the matrix $\mathbf{A}$ depends as well as on the basis set (cf. Section 2).

The transformation matrix $\mathbf{Q}_N$ defined by the Lanczos vectors allows one to rewrite equation (113) in terms of the tridiagonal matrix $\mathbf{T}_N$,

$$J^{(N)}(z) = \mathbf{v}^{\mathrm{tr}}\mathbf{Q}_N^{\mathrm{tr}}\mathbf{Q}_N[z\mathbf{I}_N + \mathbf{A}]^{-1}\mathbf{Q}_N^{\mathrm{tr}}\mathbf{Q}_N\mathbf{v} \tag{114}$$

$$= (\mathbf{Q}_N\mathbf{v})^{\mathrm{tr}}[z\mathbf{I}_n + \mathbf{T}_n]^{-1}(\mathbf{Q}_N\mathbf{v}) \tag{115}$$

Since the matrix $\mathbf{Q}_N$ is orthogonal, it must satisfy $\mathbf{Q}_N^{tr}\mathbf{Q}_N = \mathbf{I}_N$. In addition, the matrix elements in the first row of $\mathbf{Q}_N$ are just the components of $\mathbf{v}$. Using these two facts to simplify the right-hand side of equation (115) yields the particularly simple result that $J^{(N)}(z)$ is just the (1, 1) matrix element of the inverse of $[z\mathbf{I}_N + \mathbf{T}_N]$, i.e.,

$$J^{(N)}(z) = [z\mathbf{I}_N + \mathbf{T}_N]^{-1}_{1,1} \tag{116}$$

The entire sequence of continued-fraction approximants is obtained directly from equation (116). This is accomplished by using the determinant-cofactor formulas for the elements of the inverse matrix and by using Laplace's method to expand the determinants and cofactors. Using this approach, it is convenient to introduce the determinants $D^N_{l,m}$ of the diagonal blocks of $[z\mathbf{I}_N + \mathbf{T}_N]$,

$$D^N_{l,m}(z) = \det \begin{pmatrix} z+\alpha_l & \beta_l & & & \\ \beta_l & z+\alpha_{l+1} & \beta_{l+1} & & \\ & \beta_{l+1} & z+\alpha_{l+2} & \ddots & \\ & & \ddots & \ddots & \beta_{m-1} \\ & & & \beta_{m-1} & z+\alpha_m \end{pmatrix} \tag{117}$$

where it is assumed that $N \geq m \geq l$. The spectral function can then be written as the ratio of two of these determinants,

$$J^{(N)}(z) = D^N_{2,N}(z)/D^N_{1,N}(z) \tag{118}$$

It is noteworthy that the determinants appearing in the numerator and denominator of equation (118) are simply polynomials in z of order $N-1$ and N, respectively. The continued-fraction representation of $J^{(N)}(z)$ follows from equation (118) by using Laplace's method to derive a recurrence relation for the determinants. The expansion of $D^N_{1,N}(z)$ about its first row or column gives the result

$$D^N_{1,N}(z) = (z+\alpha_1)D^N_{2,N}(z) - \beta_1^2 D^N_{3,N}(z) \tag{119}$$

This expansion can then be inserted into the denominator of equation (118). Dividing both numerator and denominator by $D^N_{2,N}(z)$ gives

$$J^{(N)}(z) = \frac{D^N_{2,N}(z)}{(z+\alpha_1)D^N_{2,N} - \beta_1^2 D^N_{3,N}(z)} \tag{120}$$

$$= \frac{1}{z+\alpha_1 - \beta_1^2 D^N_{3,N}(z)/D^N_{2,N}(z)} \tag{121}$$

The reapplication of this technique for the ratio of determinants occurring in the denominator of equation (121) gives

$$J^{(N)}(z) = \cfrac{1}{z+\alpha_1 - \cfrac{\beta_1^2}{z+\alpha_2 - \beta_2^2 D^n_{4,N}(z)/D^N_{3,N}(z)}} \tag{122}$$

The recursive nature of the expansion into a continued fraction is now obvious. Using the standard notation for continued fractions, the complete expansion of $J^{(N)}(z)$ can be written as

$$J^{(N)}(z) = \frac{1}{z+\alpha_1-}\,\frac{\beta_1^2}{z+\alpha_2-}\,\frac{\beta_2^2}{z+\alpha_3-}\cdots\frac{\beta_{N-2}^2}{z+\alpha_{N-1}-}\,\frac{\beta_{N-1}^2}{z+\alpha_N} \tag{123}$$

The sequence of continued-fraction approximants, $J_m^{(N)}(z)$, is obtained simply by truncating the continued-fraction expansion appearing in equation (123),

$$J_m^{(N)}(z) = \frac{1}{z+\alpha_1-}\,\frac{\beta_1^2}{z+\alpha_2-}\,\frac{\beta_2^2}{z+\alpha_3-}\cdots\frac{\beta_{m-2}^2}{z+\alpha_{m-1}-}\,\frac{\beta_{m-1}^2}{z+\alpha_m} \tag{124}$$

This amounts to assuming that $\beta_m = 0$ for $m = 2, 3, \ldots, N$.

The line-shape function, $S_m^{(N)}(\Delta\omega)$, associated with a particular continued-fraction approximant is (in angular frequency units)

$$S_m^{(N)}(\Delta\omega) = \frac{1}{\pi}\,\mathrm{Re}\{J_m^{(N)}(1/T_2^0 + i\Delta\omega)\} \tag{125}$$

where $1/T_2^0$ is a real constant used to model line-broadening effects which are not explicitly included in the computation. However, following established practice, all calculated line-shape functions presented here will be plotted as a function of applied magnetic field rather than angular frequency. As stated earlier in Section 2, this conversion is only valid in the high-field approximation. In addition, the usual ESR signal obtained using field modulation and a lock-in amplifier is related to the derivative of $J_n^{(N)}(z)$,

$$S_m'^{(N)}(\omega - \omega_0) = \frac{1}{\pi}\,\mathrm{Re}\left\{\frac{dJ_m^{(N)}(1/T_2^0 + i(\omega - \omega_0))}{d\omega}\right\} \tag{126}$$

It is very important to note that since the previous elements of the Lanczos tridiagonal matrix are not modified by the execution of further steps, the continued-fraction approximant $J_m^{(N)}(z)$ can actually be evaluated after only m Lanczos steps. In other words, each member of the set of continued-fraction approximants to $J^{(N)}(z)$ can be evaluated after the corresponding number of Lanczos steps has been completed. The behavior of the family of continued-fraction approximants for a model problem is demonstrated in Section 3.6.

Since the determinant in the denominator of equation (118) is just the characteristic polynomial of $\mathbf{T}_N$, it is clear that there must be a close relationship between the eigenvalues and weight factors of $\mathbf{T}_m$ and the associated continued-fraction approximant. It is useful to explore this point in some detail, as these ideas are used frequently in the discussion of the convergence of the sequence of continued-fraction approximants in Section 3.6.

First, we note that the mth approximate spectral function $J_m^{(N)}(z)$, just like the true spectral function $J^{(N)}(z)$, may be written as the ratio of two determinants, where the order of the determinant in the denominator is one greater than the order of the determinant in the numerator,

$$J_m^{(N)}(z) = D_{2,m}^N(z)/D_{1,m}^N(z) \tag{127}$$

The denominator of equation (127) is just the characteristic polynomial of the truncated tridiagonal matrix $\mathbf{T}_m$. Assuming that the polynomial in the denominator of equation (127) can always be factored into the product of m distinct linear factors

$$D_{1,m}^N(z) = \prod_{j=1}^{m} (z + \Lambda_j) \tag{128}$$

one may decompose the ratio of polynomials in equation (127) into a sum of m distinct partial fractions (Gantmacher, 1959),

$$J_m^{(N)}(z) = \sum_{j=1}^{m} \frac{w_j^2}{z + \Lambda_j} \tag{129}$$

The coefficients w_j^2 are called weight factors. This procedure of expanding ratios of polynomials into partial fractions is commonly used in the indefinite integration of rational functions.

The connection between the eigenvalue-weight factor and continued-fraction representations can also be derived by writing equation (127) as the (1, 1) element of the inverse of the tridiagonal matrix $[z\mathbf{I}_m + \mathbf{T}_m]^{-1}$,

$$J_m^{(N)}(z) = \hat{e}_1^{\mathrm{tr}}[z\mathbf{I}_m + \mathbf{T}_m]^{-1}\hat{e}_1 \tag{130}$$

where $\hat{e}_1^{\mathrm{tr}} = (1, 0, 0, \ldots, 0)$. Assuming that the eigenvalues of $\mathbf{T}_m$ are distinct (Schneider, 1988), $\mathbf{T}_m$ can always be diagonalized by a complex orthogonal transformation (Gantmacher, 1959; Horn and Johnson, 1985),

$$\mathbf{O}\mathbf{T}_m\mathbf{O}^{\mathrm{tr}} = \mathbf{\Lambda}^{(m)} \tag{131}$$

This result can now be used to simplify equation (130),

$$\begin{aligned} J_m^{(N)}(z) &= \hat{e}_1^{\mathrm{tr}}\mathbf{O}^{\mathrm{tr}}\mathbf{O}[z\mathbf{I}_m + \mathbf{T}_m]^{-1}\mathbf{O}^{\mathrm{tr}}\mathbf{O}\hat{e}_1 \\ &= (\mathbf{O}\hat{e}_1)^{\mathrm{tr}}[z\mathbf{I}_m + \mathbf{\Lambda}_m]^{-1}(\mathbf{O}\hat{e}_1) \\ &= \sum_{j=1}^{m} \frac{O_{j1}^2}{z + \Lambda_j^{(m)}} \end{aligned} \tag{132}$$

A comparison of equations (129) and (132) shows that the weight factors w_j^2 are just the squares of the elements of the first row of the transformation matrix $\mathbf{O}$ which diagonalizes $\mathbf{T}_m$. In contrast to the elements of $\mathbf{T}_m$, which are not altered by the execution of more Lanczos steps, the eigenvalues and weight factors of $\mathbf{T}_m$ and $\mathbf{T}_{m+1}$ can be dramatically different. This point is explored in Section 3.6.

3.6. Convergence of the Sequence of Approximate Spectral Functions

There are two different types of convergence which must be considered in the application of the Lanczos algorithm to calculating magnetic resonance spectra. First, there is the question of how well $J^{(N)}(z)$ approximates the "true" spectral function defined by equation (1). The difference between equations (1) and (123) is due to the truncation of the basis set to a finite dimension. This is just the MTS problem discussed in Section 3.4. The second type of convergence is the central topic in this section, namely, the convergence of the sequence of approximants to the spectral function. For simplicity, this discussion will be presented in terms of the eigenvalue-weight factor representation of the approximate spectral functions rather than the continued-fraction representation and will be heuristic in nature with little attention paid to the mathematical details. The discussion of the convergence of the spectral functions in terms of the continued-fraction representation is more pleasing from a theoretical point of view, but it also involves more complicated and unfamiliar mathematical techniques (Schneider, 1989; Schneider and Freed, 1989).

To orient the reader, the values of the line-shape function $S_m^{(N)}(\omega - \omega_0)$ associated with a sequence of continued-fraction approximants for a particular calculation are presented in Figure 3 as a function of both the number of Lanczos steps and the applied magnetic field. The final line-shape function in the absorption [cf. equation (125)] and derivative modes is presented in Figures 4 and 5, respectively. This calculation was performed using TEMPONE-like magnetic parameters and moderately slow isotropic Brownian diffusion ($R_\parallel = R_\perp = 10^6\,\mathrm{s}^{-1}$). The MTS used here was taken from the appropriate entry in Table 2. These values were determined (Vasavada *et al.*, 1987) using the field-sweep conjugate gradients method (cf. Section 3.4). These plots all include a residual linewidth of 0.3 G, which is fairly typical for TEMPONE radicals in this motional regime.

The general features of the derivative spectrum given in Figure 5 are probably quite familiar to most readers. The large overall spectral width ($60\,\mathrm{G} \approx 2A_{zz}$), the narrowness of features of the high- and low-field extrema, and the splitting observed in the central region are all indications of slow rotational motion. This spectrum was calculated using 62 Lanczos steps giving a conjugate gradients residual of $\|r\|_{\mathrm{ps}} \approx 10^{-2}$ (cf. Section 3.4) indicating the convergence of the cw ESR spectrum. The corresponding absorption spectrum given in Figure 4 is probably not so familiar. It is presented here to help the reader in understanding the two-dimensional plot in Figure 3.

This particular calculation was chosen because it demonstrates the most common convergence behavior of the approximants as a function of the number of Lanczos steps. In Figure 3 the absorption-mode line-shape function is plotted as a function of the number of Lanczos steps and the difference between the applied magnetic field and the field at the center of the spectrum (3200 G). According to convention, each line-shape function is normalized to unit area.

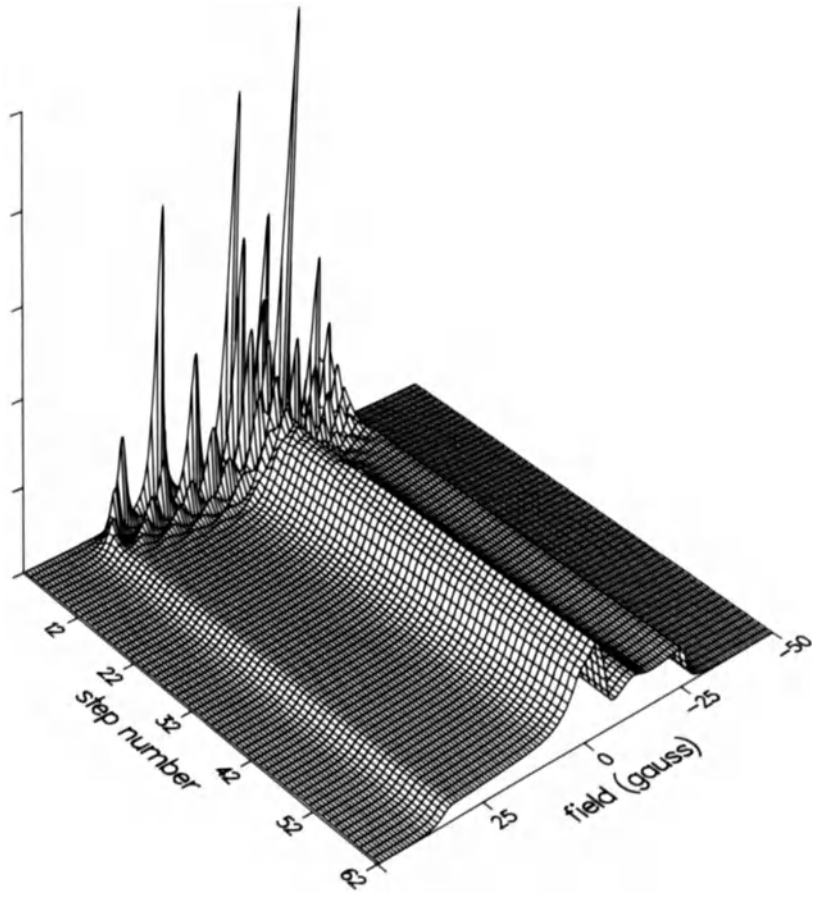

Figure 3. Two-dimensional plot of the convergence of the absorption-mode spectral function [cf. equation (125)] as a function of magnetic field and the number of Lanczos steps for TEMPONE spin probe undergoing slow isotropic Brownian diffusion. The diffusion and basis-set parameters were taken from line 2 of Table 2 and the magnetic parameters are given at the bottom of that table. The spectral functions for Lanczos steps 2 to 62 are plotted here. Note that the magnetic field increases to the left.

The final trace along the field axis in the immediate foregound of Figure 3 represents the fully converged absorption mode cw ESR spectrum determined by these input parameters. This trace is identical to the trace in Figure 4, except that Figure 3 is plotted so that the field decreases from left to right. The initial trace in the extreme background in Figure 3 corresponds to only two Lanczos steps.

The most striking aspect of Figure 3 is how quickly, as a function of the number of Lanczos steps, the approximate line-shape function begins to look like a reasonable cw ESR spectrum. An examination of the traces in the background of Figure 3 shows that the gross features of the final spectrum are well represented after only 10 to 15

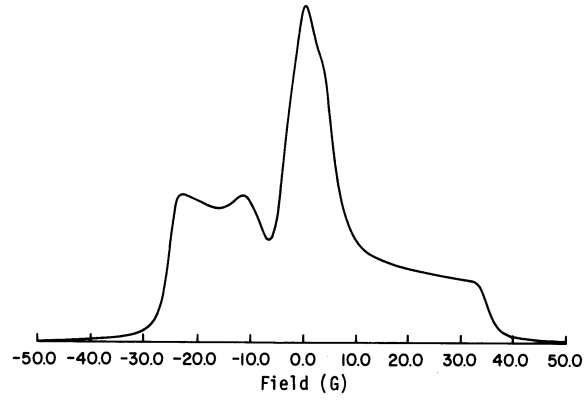

Figure 4. Fully converged (62 Lanczos steps) cw ESR absorption spectrum for the same magnetic, diffusion, and basis-set parameters as for Figure 3. This plot corresponds to the trace in the immediate foreground of Figure 3. Note that the magnetic field increases toward the right.

Lanczos steps. It is most convenient to discuss this phenomenon in terms of an eigenvalue-weight factor decomposition of the line-shape functions [cf. equations (129) and (132)] rather than in terms of continued fractions. These representations are, however, equivalent as was shown in Section 3.5. From this point of view, the spikes in the line-shape functions corresponding to the individual eigenvalues of the smaller tridiagonal matrices appear to decrease in amplitude and move out toward the wings to the spectrum as the dimension of the tridiagonal matrix is increased (cf. Figure 3). The regions between the spikes are gradually filled in by the new eigenvalues which must appear as the dimension of the tridiagonal matrix is increased. This extremely rapid convergence of the gross features of the spectrum is observed in essentially all calculations.

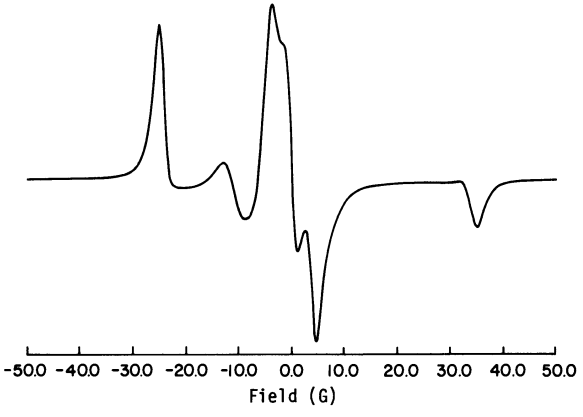

Figure 5. Fully converged (62 Lanczos steps) cw ESR derivative spectrum [cf. equation (126)] for the same magnetic, diffusion, and basis-set parameters as for Figures 3 and 4. Note that the magnetic field increases toward the right.

TABLE 2
Truncation Parameters and MTS for cw ESR Spectra

No.	Spin probe[a]	R^b	λ^c	$L^e_{max}{}^d$	$L^o_{max}{}^d$	$K_{max}{}^d$	$M_{max}{}^d$	N^e	$N_{min}{}^f$
1	TEMPONE	10^7	0	6	3	2	2	42	33
2	TEMPONE	10^6	0	14	7	6	2	171	100
3	TEMPONE	10^5	0	30	13	10	2	543	256
4	TEMPONE	10^4	0	54	15	10	2	990	447
5	TEMPONE	10^7	10	10	None	2	2	63	26
6	TEMPONE	10^6	5	12	3	2	2	78	42
7	TEMPONE	10^6	10	10	None	0	2	33	29
8	TEMPONE (90° tilt)	10^7	1	6	3	2	6	288	74
9	TEMPONE (90° tilt)	10^7	10	10	9	4	4	822	69
10	TEMPONE (90° tilt)	10^6	10	12	11	6	6	1779	245
11	CSL	10^6	0	14	7	14	2	231	162
12	CSL	10^5	0	30	13	30	2	762	474

[a] Values of g and A tensors for TEMPONE: $g_{xx} = 2.0088$, $g_{yy} = 2.0061$, $g_{zz} = 2.0027$, $A_{xx} = 5.8$ G, $A_{yy} = 5.8$ G, $A_{zz} = 30.8$ G. Values of g and A tensors for CSL: $g_{xx} = 2.0021$, $g_{yy} = 2.0089$, $g_{zz} = 2.0058$, $A_{xx} = 33.44$ G, $A_{yy} = 5.27$ G, $A_{zz} = 5.27$ G. Static magnetic field $B_0 = 3300$ G, $(\gamma_e T_2')^{-1} = 1.0$ G.
[b] Rotational diffusion constant (units of s^{-1}).
[c] Coefficient of first term in the expansion of the scaled restoring potential, $-U(\Omega)/k_B T$.
[d] L^e_{max} and L^o_{max} are the largest even value of L and odd value of L, respectively, for which there exist basis vectors with $s_j > 0.03$. Similarly, K_{max} and M_{max} are the largest values of K and M for which this occurs.
[e] N is the dimension of the matrix if all the basis vectors whose indices are less than or equal to L^e_{max}, L^o_{max}, K_{max}, and M_{max} are included.
[f] N_{min} is the dimension of the MTS (the number of basis vectors for which $s_j > 0.03$).

The convergence of the fine details of the line-shape function is emphasized in the difference plot presented in Figure 6. This plot was generated by subtracting the final converged line-shape trace from all the previous traces in Figure 3. There are three major points illustrated in Figure 6. The most obvious point is again the rapid convergence of the gross spectral features. The second point is that the wings of the spectrum converge far more rapidly than the central region. This phenomenon can be rationalized in terms of the close spacing of the eigenvalues in this area. It is well known in the real symmetric case that eigenvalues of the tridiagonal matrix corresponding to eigenvalues of the original matrix which are widely separated from their neighbors converge most quickly (Parlett, 1980; Golub and Van Loan, 1983; Cullum and Willoughby, 1985). This general trend also seems to hold true for complex symmetric matrices, where it has previously been noted that the line-shape function converges to within experimental accuracy well before closely spaced eigenvalues of the original matrix are resolved (Moro and Freed, 1981). Finally, it should be noted that it can happen that there is little change in the approximate line shape for a reasonably large number (10–15) of Lanczos steps followed by a sudden change where significant features can appear or disappear. Again, this phenomenon is well known in the real symmetric case where it is referred to as misconvergence (Parlett and Nour-Omid, 1985).

Until now, this discussion has been focused on interpreting the convergence of the approximate line shape in terms of the eigenvalues and weights of the sequence of tridiagonal matrices generated by the Lanczos algorithm. However, to understand the effects of finite precision computer arithmetic on the approximate line shapes, the

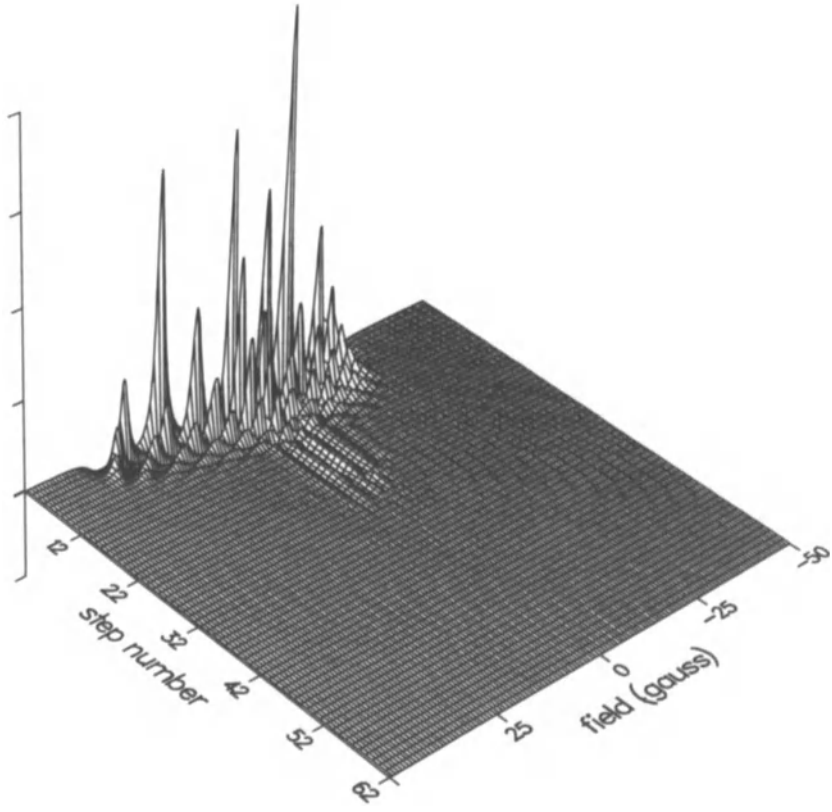

Figure 6. Two-dimensional difference plot of the convergence of the absorption-mode spectral function [cf. equation (125)] emphasizing the rapid convergence of the wings of the spectrum but slower convergence of the central region. This plot was generated by subtracting the fully converged absorption spectrum (shown in Figure 4) from all of the traces in Figure 3. Note that the magnetic field increases to the left as in Figure 3.

behavior of the eigenvalues and weights themselves must be examined more closely. Unfortunately, since both the eigenvalues and weights are complex numbers, it is nearly impossible to plot all of these quantities, as a function of the dimension of the associated matrices, in a meaningful way. However, it is possible to plot the imaginary parts of the eigenvalues of the tridiagonal matrices (i.e., the magnetic field positions of the individual complex Lorentzians) used to generate Figure 3. This is done in Figure 7 to further illustrate the spreading of the eigenvalues toward the wings of the spectrum as the dimension of the tridiagonal matrix increases. This is, however, just a small part of the story.

An examination of the lists of eigenvalues and weights reveals that, for the matrices of dimension 2 to 16, the real parts of the eigenvalues (i.e., the widths of the complex Lorentzians) are relatively small ($\mathrm{Re}\{\Lambda_j\} \leq 7.1$ G) and all eigenvalues have relatively large weights ($\|w_j^2\| \geq 10^{-3}$). In addition, the real parts and weights for the eigenvalues

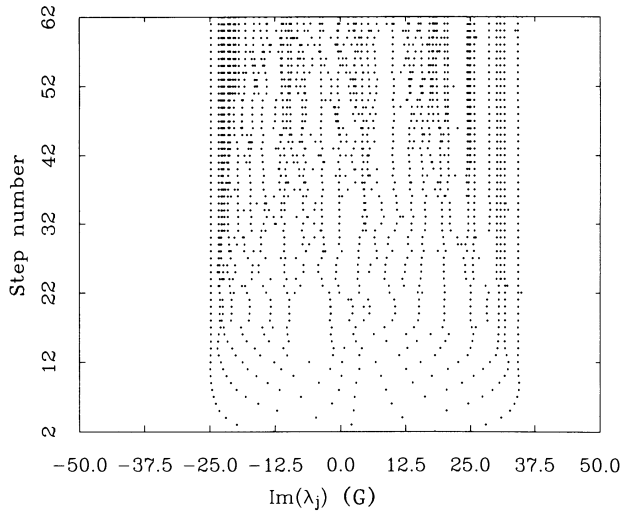

Figure 7. The imaginary parts of the eigenvalues of the sequence of Lanczos tridiagonal matrices used to generate Figure 3 as a function of the number of Lanczos steps. Note the rapid convergence of the eigenvalues near the high- and low-field extrema. In contrast, the central region shows considerable variation in the positions of the eigenvalues as the number of Lanczos steps increases.

in any given region in the spectrum vary substantially from step to step. Note that the gross features of the full converged spectrum have essentially been defined by step 15 (cf. Figure 3).

Now, after 17 steps a qualitatively different type of eigenvalue appears—one with a large real part (13.7 G) and a small weight ($\|w^2\| = 1.75 \times 10^{-6}$). The imaginary part of this eigenvalue is −13.0 G. This eigenvalue "disappears" at step 18. The eigenvalues and weights display bizarre behavior for the next several steps. In particular, some eigenvalues develop negative real parts corresponding to negative linewidths! Though these eigenvalues usually have negligible weight factors, occasionally they do not. However, if the eigenvalues with negative real parts have nonnegligible weight factors, the real part of these weight factors is also negative. In addition, these eigenvalues appear as part of a "pair." The imaginary parts of eigenvalues of the two members of the pair are nearly the same, while the real parts of the eigenvalues are nearly equal in magnitude, but opposite in sign. The weight factor associated with the member whose eigenvalue has a positive real part is usually quite small. The net contribution of this pair to the spectrum is quite small. As the dimension of the tridiagonal matrix increases still further, the frequency and relative importance of these physically unrealistic eigenvalues diminish rapidly which is indicative of their "spurious" nature.

In addition, near the end of this calculation, duplicate or "ghost" eigenvalues also begin to appear. However, the weight factor for all but one of the numerically multiple eigenvalues is on the order of the machine precision used in the calculation. In general, this remains valid until one performs far more than N Lanczos/conjugate gradients steps on an $N \times N$ matrix. Therefore, these unwanted duplicates of converged eigenvalues cannot corrupt the calculated spectrum using the computational strategy advocated here.

These observations suggest that it is not necessarily sufficient to calculate the line-shape function after every Lanczos step and terminate the procedure when no significant change is observed. This was the original suggestion by Moro and Freed (1981) on how to monitor convergence in practical problems. Indeed, this procedure works well on simple problems but sometimes can be misleading in problems involving potentials or very anisotropic reorientation.

Extensive experience (Vasavada *et al.*, 1987; Schneider, 1989; Crepeau, private communication) now suggests that the rectanorm of the residual occurring in the complex symmetric conjugate gradients algorithm can be used as a more reliable means of monitoring the convergence of the line-shape function (cf. Section 3.4).

More information on the qualitative and quantitative aspects of the convergence of the complex symmetric Lanczos algorithm for the calculation of ESR line-shape functions can be found in the references (Moro and Freed, 1981; Dammers, 1985; Vasavada *et al.*, 1987; Schneider, 1989; Schneider and Freed, 1989).

4. COMPUTATIONAL CONSIDERATIONS

Until about 1980, almost all slow motional magnetic resonance spectral calculations were either based on the solution of a system of linear equations by the *LU* algorithm (Freed *et al.*, 1971a, 1971b) or the complete diagonalization of the stochastic Liouville matrix (Gordon and Messenger, 1972; Goldman *et al.*, 1972; Freed, 1976). At that time, Moro and Freed (1981) introduced a modification of the Lanczos algorithm for real symmetric matrices (Lanczos, 1950; Parlett, 1980; Golub and Van Loan, 1983; Cullum and Willoughby, 1985) which is capable of handling complex symmetric matrices and which leads to at least an order of magnitude reduction in computer time over the traditional methods. The reader is referred to the literature for more information on the application of the complex symmetric Lanczos algorithm (Moro, 1980b; Moro and Freed, 1981; Cullum and Willoughby, 1985; Dammers, 1985; Moro and Freed, 1986; Schneider, 1988; Schneider and Freed, in press) and the related conjugate gradients algorithm (Vasavada *et al.*, 1987; Schneider, 1989; Schneider and Freed, 1989) to spectral calculations of various types.

In this section, the names of variables used in the computer programs will be printed in lower case teletype-style typeface (e.g., `ndim`, `zmat`) while the names of the programs, subroutines, and disk files will be printed in the corresponding upper case teletype-style typeface (e.g., LBLL, EPRLL).

The general organization of the program is as follows:

LBLL This program will prompt the user for the magnetic tensor parameters, diffusional model and associated parameters, basis-set truncation values, etc. This must be the first program of the set run, since all the other programs require the parameter file generated by LBLL as input. The parameters required by LBLL are defined in Section 2. This program also determines whether or not the dimension of the matrix is too large for the associated arrays in the main calculation programs, EPRLL, EPRCGL, and EPRBL.

EPRLL This program constructs the stochastic Liouville matrix, then tridiagonalizes it using the complex symmetric Lanczos algorithm.

EPRCGL This program is quite similar to EPRLL, but uses the complex symmetric conjugate gradients algorithm to tridiagonalize the stochastic Liouville matrix. The ouput of this program is compatible with the output of EPRLL.

EPRBL This program constructs the stochastic Liouville matrix in the same manner as done in EPRLL and EPRCGL. Rather than constructing the Lanczos tridiagonal matrix, the main calculation performed in EPRBL is the solution of the system of linear algebraic equations defining the spectral function by means of a preconditioned complex symmetric conjugate gradients procedure as outlined in Section 3.4. This calculation is performed at a sequence of magnetic fields to determine the contribution of each basis vector to the overall spectral function. This information can then be used to truncate the basis set for future calculations involving similar input parameters.

TDLL This program reads in the parameter file written by LBLL and the Lanczos tridiagonal matrix generated and stored by EPRLL or EPRCGL. The user is presented with several options:

1. List the elements of the tridiagonal matrix on the screen.
2. Write the elements of the tridiagonal matrix into a formatted file.
3. Diagonalize the tridiagonal matrix using the complex symmetric *QL* algorithm to obtain the eigenvalues and associated weighting factors.
4. Calculate the approximate cw ESR spectrum by evaluating the continued fraction representation of the spectral function.

The first three options are employed by more experienced users to analyze the behavior of the Lanczos algorithm as explained in Section 3.6. The last option is the preferred method of obtaining the approximate cw ESR spectrum for comparison with experimental data.

TNLL This is an auxiliary program which is used to process and print the output file generated by EPRBL.

MATLST This is an auxiliary program included here to aid users in porting these programs to new systems. It reads an optional matrix file generated by EPRLL or EPRCGL and prints it out in an intelligible manner.

VECLST This program plays a role analogous to MATLST for the starting vector.

D200 This program will calculate the order parameter for a radical subjected to a certain restoring potential. The order parameter is defined to be the canonically weighted average value of the $L = 2$ Legendre polynomial,

$$\langle \mathscr{D}^2_{00}(\Omega) \rangle = \langle P_2(\cos\beta) \rangle = \frac{\int d\Omega \, P_2(\cos\beta) \exp[-U(\Omega)/k_B T]}{\int d\Omega \exp[-U(\Omega)/k_B T]} \tag{133}$$

This program treats only the special case where $-U(\Omega)/k_B T = \lambda_0^2 P_2(\cos\beta)$, since in this case the integral above can easily be evaluated. This program can be used

in conjunction with LBLL to find the proper potential coefficient to give a desired order parameter.

4.1. Naming Conventions for Files

To simplify the problem of keeping track of the FORTRAN source files for these programs, as well as the output files generated by them, certain naming conventions have been adopted.

First, all of the FORTRAN source files contain only one program or subroutine. The file names for these source files are constructed from the name of the program or subroutine followed by the suffix ".F." For example, the source code for the program EPRCGL can be found in the file EPRCGL.F.

The common block and parameter definitions that are needed in many programs and subroutines are defined in so-called include files. These include files have been given names which reflect the usage of their contents and carry the suffix ".INC." For example, the value of the unit roundoff error is defined in the include file RNDOFF.INC and the arrays to hold the matrix elements of the stochastic Liouville superoperator are defined in EPRMAT.INC.

A consistent naming convention has also been used for the output files generated by these programs. This convention is similar to the one used by Moro (1980a). In particular, all files associated with a given set of input parameters are referred to using a two-character file identifier. This two-character file identifier is specified by the user when LBLL is executed to create the input parameter file for the calculation. The actual file names are constructed from a two-character prefix which indicates the nature of the contents of file, the two-character file identifier which was assigned in LBLL, and a three-character suffix which specifies whether the file is formatted or unformatted. The names of all formatted output files carry the suffix ".FMT," while the file names of unformatted files use the ".DAT" suffix.

To illustrate this convention, suppose that a given input parameter set was assigned the identifier "XY" by the user when running LBLL. The output file written by LBLL which contains the desired input parameters is given the name LBXY.DAT. The prefix "LB" indicates that this particular file was created by LBLL, while the suffix reflects the fact that this file was written in an unformatted manner. The names of the output files generated by the various programs will be outlined below when the programs are discussed in detail. In those discussions, the two-character file identifiers will be referred to simply as "??" to indicate any two characters that can be used to construct a valid file name.

4.2. Array Dimensions and Common Blocks

The declarations of parameters used to define the dimensions of important arrays that are used by several programs or subroutines are given in the include files STDDIM.INC and MAXL.INC. The user can easily change the dimensions of all the arrays whose dimensions are determined by the parameters in these two files in all the programs in a consistent manner by simply changing the value assigned to these parameters and recompiling all of the programs.

The file MAXL.INC defines an integer parameter (mxlval) which is used in LBLL to determine whether or not the maximum L value requested by the user is too large for a particular array (array nrb) in the subroutine MATRLL. This array is used to hold the starting/ending column number for each L value. This information is used to skip over the calculation of matrix elements which must be zero on symmetry grounds.

The file STDDIM.INC declares the integer parameters defining the maximum allowable number of Lanczos or conjugate gradients steps (mxstep) which may be requested in LBLL. It also declares the maximum allowable values for the dimension of the matrix of the stochastic Liouville operator (mxdim), as well as the number of matrix elements (mxel). Finally, it defines the maximum number of input parameter sets (mxcalc). All of these parameters are used to define dimensions of arrays in many programs and subroutines. They are also used to make sure that array subscripts remain within bounds.

The common block used to hold the data read in from the input parameter files generated by LBLL is defined in the file EPRDAT.INC. This file is included in all main programs except D200. The data stored in this common block is read in by the subroutine RDDAT and written by the subroutine WRDAT. The contents of this common block are defined in Section 4.3.

The arrays to hold the matrix elements of the stochastic Liouville superoperator (arrays zmat and zdiag) and associated column pointer array (array izmat) are defined in EPRMAT.INC. The dimension of these arrays is determined by the values stored in STDDIM.INC. The function of these arrays is discussed in Section 4.4.2.

The logical unit numbers for reading from the user's keyboard (luttyi), writing to the user's display device (luttyo), and reading and writing disk files (ludisk) are defined in the include file STDIO.INC. All I/O is done to one or another of these logical units. Only one logical file unit is required for reading and writing to the disk, since these programs were all written in a manner which requires at most only one disk file open at a time.

Finally, the files PIDEF.INC and RNDOFF.INC define the values of π (pi) and the unit roundoff error (rndoff), respectively. A short program to determine the unit roundoff error for any given computer is also given in the header of the file RNDOFF.INC.

4.3. The Parameter Input Program: LBLL

This program is the starting point for all spectral and basis-set calculations. The definitions of the various input parameters have been presented in Section 2.

At the beginning of the program the user is prompted for a two-character file identifier. This file identifier must consist of two nonnull ASCII characters and is used to construct a file name for the input parameter file. These characters are read in and an inquiry is made as to whether or not an old parameter file with the same name already exists on the disk. If such a file exists, it is read in, and its contents are displayed on the screen. Otherwise, a new file will be created at the end of the program. If an old file exists, its contents will be overwritten with the new input parameters.

Several sample input parameter files are included in the program distribution. The contents of these files are displayed in the Appendix. The actual input parameter files are stored in unformatted files on the disk. This scheme was adopted to discourage the direct manipulation of the contents of the parameter files. This ensures that the input parameter file is internally consistent.

The process of entering or altering parameters is quite straightforward. For each different type of parameter, the old or default values are displayed on the screen, and the user is prompted to decide whether he/she wants to change these values. The prompt string which is used is

```
Do you want to change these values? [Y/N]:
```

to which the user can respond affirmatively by entering a Y, y, or 1 followed by a carriage return. Alternatively, negative responses can be indicated by entering N, n, or 0 followed by a carriage return. All other responses are ignored and the prompt string is redisplayed.

The first group of parameters requested by the program comprises the rigid limit magnetic parameters used in the definition of the Liouville superoperator. These parameters are the principal components of the g tensor (gxx, gyy, and gzz), two times the nuclear spin (in2), the principal components of the A tensor (axx, ayy, and azz), and the static magnetic field corresponding to the center of the spectrum (b0). The program assumes that the values of the principal components of the A tensor and static field are given in units of gauss. The properly scaled $F_{\mu,m}$ tensors are constructed from this information (arrays fgm and fam).

The members of the second group of parameters are all related to the definition of the diffusion superoperator. The first parameter in this second group is the diffusion parameter index (ipdf) which selects the rotational diffusion model used in the calculation. The options for ipdf are

- ipdf = 0: Brownian diffusion (isotropic or anisotropic media),
- ipdf = 1: Free or jump diffusion (isotropic media),
- ipdf = 2: Brownian diffusion with anisotropic viscosity (anistropic media).

We note that not all options are valid if a restoring potential is present. When starting a series of calculations, it is usually recommended to start with the Brownian diffusion model unless other experimental data clearly indicate that the jump or free diffusion models are more appropriate. In general, this choice leads to the smallest basis sets and therefore the fastest computations. In addition, the Brownian model often leads to the best agreement with experiment—at least for nitroxide radicals in viscous liquids.

The next set of parameters requested by the program are the perpendicular (dxy) and parallel (dzz) principal components of the rotational diffusion tensor, $R_\perp$ and $R_\parallel$, respectively, in units of s^{-1}. If a nonzero value of ipdf has been selected, then the user is prompted to input the residence times $\tau_\perp$, $\tau'_\perp$, and $\tau_\parallel$ from equation (41) in units of s (tl, tkxy, and tkzz) and the corresponding model exponents (mpl, mpkxy, and mpkzz). Values for these parameters are not requested if Brownian motion has been selected (ipdf = 0). Note that it is possible to use different models for the perpendicular and parallel rotational motions. As stated previously, choosing a mixed diffusion model can be justified only when the diffusion tensor is very anisotropic. It is important to bear in mind the fact that the components of the rotational diffusion tensor are closely related to the molecular structure of the spin-bearing molecule (Freed, 1976).

Next, the user is prompted for the parameters related to the contribution to the diffusion superoperator due to jump-type motions of the radical between equivalent sites as defined in equation (51). The relevant parameters are the number of sites (`ist`) and jump frequency (`djf`). Also, a value for the Heisenberg spin exchange rate (`oss`) is requested. These contributions are rarely used in calculations involving nitroxide radicals in viscous media. The units of the discrete jump and Heisenberg spin exchange frequencies are s^{-1}.

The third major group of parameters is related to the restoring potential. First, the user is prompted to input the number of nonzero values of λ_K^L in the expansion of the resoring potential (`ipt`) in equation (2). For isotropic liquids, `ipt` = 0. If a nonzero value of `ipt` is entered, then the user is requested to enter the associated values of L and K (array `ixp`) and λ_K^L (array `cxp`). These terms can be input in any order, since they are immediately rearranged into a standard order (array `cpot`). It is often helpful to consult Figure 9 (see Section 5.1) or run the program `D200` (cf. Section 4.7) to determine a reasonable starting value for λ_0^2.

If a nonzero value of `ipt` has been requested, the user is also prompted for the angle, in degrees, between the static magnetic field and the unique symmetry axis of the restoring potential (`psi`). In isotropic liquids this angle is chosen to be zero. This completes the specification of the parameters used in the definition of the diffusion superoperator.

The specification of the Liouville superoperator is then completed by defining the diffusion tilt angle (`bed`) in units of degrees. Using this parameter, the scaled components of the $F_{\mu,R}$ tensors are calculated and stored (arrays `fgd` and `fad`). This completes the specification of the parameters defining the Liouville superoperator.

The last major group of parameters is related to defining the basis set and calculation type. First, the user must define the largest even value of L (`lemx`), odd value of L (`lomx`), and the maximum allowable values of the K, M, and p^I indices (`kmx`, `mmx`, and `ipnmx`) allowed in the basis. Suggested basis sets for a variety of problems can be found in Tables 2 and 3. We note that in these tables it has been assumed that the maximum value of the p^I index is two [cf. equation (7)]. The basis set defined in this manner is then checked for internal consistency and the appropriate symmetry restrictions are applied to make sure that no unnecessary basis vectors are included in the calculation. All basis vectors which satisfy the limits set by the user and can couple to the starting vector are included in the calculation. Second, the user is asked to set the maximum number of Lanczos/conjugate gradients steps allowed (nstep). Third, the user is asked to select the type of computation to be done (`itype`). The options are

- `itype` = 0: Lanczos spectral calculation,
- `itype` = 1: conjugate gradients spectral calculation,
- `itype` = 2: field swept conjugate gradients calculation for the determination of the MTS.

If a Lanczos calculation is selected, then no further questions are asked. Otherwise, the user must specify the maximum allowable modulus of the rectanorm of the conjugate gradients residual vector (`cgtol`) which is used as a termination criterion in the

conjugate gradients iterations as well as the real and imaginary parts of the origin shift (`shiftr` and `shifti`). This origin shift is required to avoid spurious divisions by zero during the conjugate gradients iterations. Finally, if a field-sweep conjugate-gradients calculation has been requested, the user must supply the initial and final fields (`fieldi` and `fieldf`) as well as the number of field positions at which the conjugate-gradients iteration is to be performed (`npt`). This completes the specification of the basis set and calculation options.

At this point, the new parameters are displayed on the screen for review. Since most internal limits and symmetry restrictions are silently enforced, the final values of the parameters displayed may not agree with the parameters specified by the user. This phenomenon may occur if the maximum values of the indices defining the basis set are not consistent with the appropriate symmetry restrictions. The program uses a very conservative strategy in modifying parameters given by the user. The user is strongly encouraged to determine the source of any discrepancies between the final parameter values and those that he or she gave in response to the program prompts before proceeding with a spectral calculation.

The last question presented to the user is whether or not a complete listing of the basis set should be displayed on the screen. If this is desired, the indices for the entire basis set will be listed on the screen in order of appearance in the stochastic Liouville superoperator matrix element calculation subroutine. Whether or not this final display option is selected, the program checks to make sure that the basis set is not too large for the arrays currently dimensioned in the main calculation programs. A warning message is issued if the matrix is too large. The program will then write out the parameter file, overwriting the old file if present, and exit. This is the only output file generated by LBLL and is assigned the name LB??.DAT. This parameter file is required to run all programs except D200.

4.4. Spectral Calculations: EPRLL and EPRCGL

The main spectral calculation programs are EPRLL and EPRCGL. These two programs are very similar and will be treated together whenever possible. The programs proceed in two stages.

In the first stage, the user is prompted to input a sequence of two-character file identifiers. This sequence is terminated by simply entering a carriage return at the prompt for another file identifier.

The second stage is the main body of the program involving the sequential execution of the following steps for each input file:

- construct a set of file names using the file identifier supplied by the user,
- read in the input parameter file created by LBLL and verify that the calculation type is correct,
- calculate the matrix elements of the stochastic Liouville operator,
- calculate the elements of the starting vector,
- tridiagonalize the matrix of the stochastic Liouville operator by the desired method (complex symmetric Lanczos or conjugate-gradients algorithms),
- update the input parameter file and save it,

- create or overwrite the output file containing the matrix elements of the Lanczos tridiagonal matrix.

If problems arise for a given input file, the remainder of that calculation is bypassed, and the next file is read in and processed.

Typically, there is only one new output file created by these programs. This file, TD??.DAT, contains the elements of the Lanczos tridiagonal matrix. This file is processed by TDLL (cf. Section 4.5). The input parameter file LB??.DAT, originally created by LBLL, is also modified. In addition, there are several sections of code that will produce files containing the elements of the stochastic Liouville matrix and starting vector, MT??.DAT and VT??.DAT, respectively (cf. Section 4.7). These files are needed only for debugging purposes, thus the sections of code that generate them are commented out in the programs supplied on the diskette.

The parameter file LB??.DAT is read into the common block defined in the include file EPRDAT.INC by the subroutine RDDAT. This common block is then used to pass these parameters to the matrix element calculation subroutine MATRLL and the starting vector calculation subroutine STVECT.

The dimensions of the various arrays are defined in the include file STDDIM.INC. The vector arrays are, for the most part, defined in dimension statements and passed to subroutines as arguments rather than through common blocks.

In contrast to the vector arrays, the matrix element and matrix element index arrays are defined in a common block in the include file EPRMAT.INC. The dimensions of these arrays are also controlled by parameters defined in the include file STDDIM.INC. The matrix elements and associated indices are calculated in MATRLL and directly stored in this common block. The matrix element and index arrays are passed to the tridiagonalization subroutines via this common block.

4.4.1. The Starting Vector Calculation Subroutine: STVECT

The structure of the subroutine STVECT, which calculates the elements of the starting vector, is quite simple. It consists of five nested loops over the L, K, M, p', and q' indices (lr, kr, mr, ipnr, and iqnr). The selection rules described in Section 2.7 are used to reduce the number of numerical integrations of equation (57) to a minimum. The calculation of the modified Bessel functions and associated Legendre functions in the integrand of equation (57) is discussed below. Since this integral depends only on the L and K indices, it is evaluated within the loop over K, but before the loop over M. Within the innermost loop, the unnormalized elements of the starting vector are stored (array v) and the norm of the unnormalized starting vector is evaluated. Following the completion of this set of five loops, the starting vector is normalized, the number of nonnegligible elements of the starting vector is determined (nelv), and the imaginary part of the starting vector is zeroed out.

The numerical evaluation of the elements of the starting vector becomes increasingly more difficult as the maximum L and K values in the basis set become larger. This is due to the highly oscillatory nature of the integrand in the definition of the starting vector elements [cf. equation (57)].

In part, these difficulties can be overcome by doing the integral over the Euler angle γ in equation (57) analytically in terms of the modified Bessel functions [cf.

equation (61)]. The modified Bessel functions can then be evaluated in a stable fashion. However, this evaluation is not trivial. The method employed in the subroutine BESSI is based on the following recurrence relation,

$$f_{n-1}(x) = (2n/x)f_n(x) + f_{n+1}(x) \tag{134}$$

This equation is satisfied by the modified Bessel functions themselves (McLachlan, 1961; Abramowitz and Stegun, 1964), but is used in the actual calculation to evaluate the ratio of two of these functions. It is known (Sookne, 1973a, 1973b; Cody, 1983; Press *et al.*, 1986) that this recurrence relation is numerically unstable in the direction of increasing n, but stable for decreasing n. Let us assume that one wishes to compute $I_m(x)$. In this scheme one chooses a sufficiently large M, where $M \gg m$, at which to begin the computation. The recurrence relation is then seeded with the values

$$f_{M+1}(x) = I_{M+1}(x)/I_M(x) \approx 0 \tag{135}$$

$$f_M(x) = I_M(x)/I_M(x) \equiv 1 \tag{136}$$

and equation (134) is evaluated for decreasing values of n all the way down to $n = 1$. While equation (136) is exact by definition, equation (135) is only approximately valid. However, for the same reason that the forward recurrence is unstable, the error introduced by this approximation is inconsequential if M is chosen properly (Press *et al.*, 1986). Finally, the desired result is given by

$$I_m(x) = f_m(x)I_0(x)/f_0(x) \tag{137}$$

The value of $I_0(x)$ is computed by using the Taylor series expansion for small values of x, or by an asymptotic approximation for large values by the subroutine BESSI0. The function $I_1(x)$ is also evaluated in this manner in the subroutine BESSI1. All three of these subroutines are modifications of routines with similar functionality in the book by Press *et al.* (1986).

The values of the associated Legendre functions are also calculated using a well-known recurrence relation,

$$(L - M)P_L^M(x) = (2L - 1)xP_{L-1}^M(x) - (L + m - 1)P_{L-2}^M(x) \tag{138}$$

However, this relation is evaluated in the direction of increasing values of L starting with the (exact) initial conditions

$$P_M^M(x) = (-1)^M(2M - 1)!!(1 - x^2)^{M/2} \qquad \text{and} \qquad P_{M+1}^M(x) = (2M + 1)xP_M^M(x)$$

Again, the subroutine PLGNDR used to evaluate the associated Legendre functions is a slight modification of a routine given by Press *et al.* (1986).

The subroutines BESSI and PLGNDR are called by the subroutine FZ to evaluate the integrand of equation (57). The numerical integration itself is performed using a Romberg integration scheme with cautious extrapolation (Press *et al.*, 1986) using the subroutine CCRINT taken from Bruno's thesis (1973).

4.4.2. The Matrix Element Calculation Subroutine: MATRLL

The matrix elements of both the upper and lower halves of the matrix are calculated and sorted in MATRLL, even though the matrix is complex and symmetric. This is done for several reasons. Unfortunately, the most important reason for adopting this approach is not obvious, since it has to do with how most multitasking computer operating systems manage users' programs and data.

Most multiuser operating systems limit the amount of physical memory that can be allocated to any one user. If the matrix is too large to fit in the physical memory allocated to the user by the operating system, the remainder of the data must reside on a disk and be swapped in and out of the limited amount of physical memory allocated to the program. The entire data set is divided up into smaller sections, called pages or segments. Typically, each page contains several thousand floating point numbers.

Now, consider the matrix-vector multiplication operation occurring in both the Lanczos and conjugate gradients algorithms. In most instances, the majority of the computer time used in a spectral calculation is spent doing matrix-vector multiplications. As the computation proceeds, if a matrix element or index which is needed does not currently reside in the physical memory, the page containing that element or index is read-off the disk and overwrites one of the least recently accessed pages allocated to the user. This operation is called paging. Unfortunately, paging is a very expensive operation—typically hundreds or thousands of floating point operations can be executed in the time it takes to read a page in from the disk. Therefore, it is prudent to store the matrix elements in the order that they are accessed. This enables one to minimize these costly paging operations.

When these programs were written, the existence of a scheme for storing only half of the matrix elements, but wording excessive paging overhead, was not known to the authors; therefore, the full matrix store scheme was adopted. Since that time, it was pointed out to us by Dr. Vijay Sonnad that there is a scheme that is widely used in mechanical engineering calculations which does enable one to take advantage of the symmetry of the matrix, but not incur any paging overhead. Unfortunately, there was not enough time to incorporate and fully test this scheme in the present set of programs.

The matrix elements are calculated inside a group of ten nested loops. The outer set of five loops run over the L, K, M, p', and q' indices for the row (lr, kr, mr, ipnr, and iqnr), while the inner set of five run over the related indices for the column (lc, kc, mc, ipnc, and iqnc). The number of the current row (nrow) and column (ncol) is monitored for use as indices for the matrix elements. The matrix elements of the stochastic Liouville superoperator are assembled inside the innermost loop. In addition, the row index corresponding to the beginning of each block of matrix elements with a given value of L is stored (array nrb). These indices are used later to determine in which column to start looking for nonzero matrix elements.

In all cases, the matrix elements of the diffusion superoperator are purely real, while the matrix elements of the Liouville superoperator are purely imaginary. Since the vast majority of off-diagonal matrix elements is purely imaginary, a special storage strategy for the matrix elements has been adopted. This strategy involves storing the real and imaginary parts of the nonzero matrix elements separately, and then only if they are nonzero. In particular, if a nonzero Liouville superoperator matrix element is found, the matrix element counter (`neltot`) is incremented, the matrix element is stored in the matrix element array (`zmat`), and the associated column number is stored in the matrix element index array (`izmat`). Next, if a nonzero diffusion superoperator matrix element for the same row and column is found, the matrix element counter is incremented, the matrix element is stored in the matrix element array, and -1 times the column number is stored in the index array. In addition, the diagonal matrix elements are also stored in a separate array (`zdiag`). This array is used only in the field-sweep conjugate-gradients calculation. The end of a row is signaled by incrementing the matrix element counter and inserting a zero value into both the matrix element and index arrays. In this way, the sign of the index element is used as a flag for whether the associated matrix element is real or imaginary, the absolute value of a nonzero index refers to the column number, and a zero index tags the end of a row. In addition, the end of the matrix is flagged by inserting another zero value into the matrix element and index arrays. This index information can be very efficiently decoded in the matrix-vector multiplication step coded in subroutine SCMVM.

If the number of matrix elements ever exceeds the dimensions of the arrays, the return error code (`ierr`) is set to one and control is passed back to the calling program. If this does not happen, the return code is set to zero indicating successful execution.

One of the major difficulties encountered in the calculation of matrix elements is the efficient and accurate evaluation of the Wigner 3-J symbols. Very slow motional calculations often require L truncation values of 80 or more. However, due to overflow problems, the function subroutine used by Moro is not usable for $L > 48$. This problem has been circumvented for the 3-J symbols of the type

$$\begin{pmatrix} L_1 & L_2 & L_3 \\ M_1 & M_2 & M_3 \end{pmatrix}$$

where $|L_2| \leq 2$, by using the algebraic formulas for these quantities. These formulas are given in an appendix in Edmonds's book (1957). These are the only type of 3-J symbols required in the calculation of matrix elements of the stochastic Liouville operator in the absence of a restoring potential. These formulas can safely by used for $L \gg 100$ without overflow. One is still restricted to $L \leq 48$ in the presence of a potential. This difficulty could be overcome by using an asymptotic approximation for the 3-J symbols for $L > 48$ (Edmonds, 1957).

4.4.3. The Lanczos and Conjugate-Gradients Subroutines: CSLNZS and CSCG

The complex symmetric Lanczos and conjugate-gradients algorithms used here are very straightforward. The more theoretical aspects of these algorithms have already been treated in Section 3.

The Lanczos subroutine (CSLNZS) is a simple translation of a single vector Lanczos tridiagonalization algorithm for real symmetric matrices given in algorithm 9.1-1 in the book by Golub and Van Loan (1983). The required numerical linear algebra operations are performed by calls to appropriate subroutines. The diagonal (array alpha) and off-diagonal (array beta) elements of the Lanczos tridiagonal matrix are stored and returned to the calling program.

Many of these subroutines are also called by the conjugate gradients subroutine (CSCG). This subroutine is also a simple translation of a single vector algorithm for real matrices given in algorithm 10.2-4 in the book by Golub and Van Loan (1983). The quantities generated by the conjugate-gradients algorithm that are needed for the construction of the Lanczos tridiagonal matrix (al and bl) are stored. The conjugate-gradients iteration is terminated when the modulus of the rectanorm of the residual vector becomes less than the tolerance specified by the user or if the maximum number of steps has been exceeded. When the conjugate-gradients iteration has finished, the required arrays are passed to the subroutine which actually constructs the Lanczos tridiagonal matrix (CGLTRI). This subroutine constructs the tridiagonal matrix using the scheme outlined by Golub and Van Loan (1983) and overwrites the input arrays with the elements of the tridiagonal matrix. If the calculation converges within the allotted number of steps, the number of conjugate-gradients steps actually executed (nstep) is returned to the calling program EPRCGL. If the calculation does not converge, -1 times the number of steps is returned as an error signal.

As stated previously, the most time-consuming operation in most spectral calculations is the matrix-vector multiplication step required in both the Lanczos and conjugate-gradients algorithms. Since this is such an important part of the calculation, and the implementation used here requires the decoding of the index array "on the fly," it seems worthwhile to discuss this procedure in detail.

The matrix-vector multiplication subroutine is SCMVM. The actual matrix-vector multiplication is carried out as a sequence of sparse vector dot products in which the rows of the matrix are successively dotted with the input vector (x) to give the elements of the output vector (y). Both the input and output vectors are indexed as two-dimensional arrays of double precision floating point numbers and are passed to this subroutine through the argument list.

The sparsity of the matrix is taken advantage of by doing only those matrix element-vector element multiplications which can give rise to nonzero results. Initially, the accumulators for the real and imaginary parts of the output vector elements (accr and acci) as well as the matrix element (iel) and row counters (ir) are set to zero. Now, the list of matrix elements is processed sequentially by incrementing the matrix element counter and examining the contents of the matrix element index array. If the value of that particular index element is nonzero, the absolute value of the index, which represents the column number of the associated matrix element, is used to pick out the correct element of the input vector. The matrix element is then multiplied by the input vector element in the manner indicated by the sign of the index element, and the accumulators are updated. This process is then repeated with the next matrix element and index until a zero index value is found. Since a zero index value indicates the end of a row, the row counter is incremented, the contents of the accumulators are stored in the positions of the output vector array specified by the updated row counter, and the accumulators are then zeroed out. In this manner, the matrix is processed row

by row. When the processing of the last row of the matrix is completed, the algorithm encounters the final zero index element labeling the end of the matrix. When this happens, the row counter is incremented to a value one greater than the dimension of the matrix. This event is used to detect the end of the matrix element and index lists and the completion of the matrix-vector multiplication step.

4.5. Calculation of the Spectral Function: TDLL

The program TDLL processes the Lanczos tridiagonal matrix generated by EPRLL or EPRCGL. Like the rest of the programs described here, the action that the program undertakes is to prompt the user to supply the two-character file identifier for the file to be processed. After accepting the two-character file identifier and constructing the file names, the program reads in the parameter file LB??.DAT written by LBLL and the Lanczos tridiagonal matrix file TD??.DAT which was generated by EPRLL or EPRCGL. The user is then presented with several options:

1. List the elements of the tridiagonal matrix on the screen.
2. Write the elements of the tridiagonal matrix into a formatted file.
3. Diagonalize the tridiagonal matrix.
4. Calculate the cw ESR spectrum.

The first option is self-explanatory. If the second option is selected, a file TD??.FMT is created. This file is just a list of the row number and the real and imaginary parts of the diagonal and superdiagonal elements of the Lanczos tridiagonal matrix.

The third option is to diagonalize the Lanczos tridiagonal matrix to obtain the eigenvalues and associated weighting factors. Though one can calculate the cw ESR spectrum from this information, this is not done here. If the cw ESR spectrum is desired, it can be calculated directly from the tridiagonal matrix by selecting the fourth option. The third option is most often used in the calculation of 2D-ESE spectra (Millhauser and Freed, 1984) and in the study of the convergence of the Lanczos and/or conjugate-gradients algorithms. The diagonalization algorithm used here is a simple variant of the complex symmetric *QL* algorithm of Cullum and Willoughby (1985). The major difference here is that the projections of the eigenvectors of the tridiagonal matrix on the starting vector are needed. The squares of these overlaps are the weighting factors [cf. equation (132)]. If this option is selected, a file EG??.FMT is written which contains the eigenvalue number, and the real and imaginary parts of the eigenvalues and associated weight factors. The eigenvalues are sorted in order of increasing imaginary parts (field positions) and are numbered accordingly. The *QL* and closely related *QR* algorithms are thoroughly treated in many reference works (Parlett, 1980; Golub and Van Loan, 1983; Cullum and Willoughby, 1985).

The most commonly used of the several options is the last one—the calculation of the approximate cw ESR spectrum. This is done by evaluating the continued-fraction representation of the spectral function. The elements of this continued fraction are defined by the matrix elements of the Lanczos tridiagonal matrix. If this option is selected, several more parameters must be supplied by the user. First, the magnetic field corresponding to the center of the spectrum is displayed, then the user is prompted for the beginning and ending fields (bi and bf), in units of gauss, relative to the center

of the spectrum. The default values for these parameters are −50 G and 50 G, respectively. Next, the user must supply two parameters defining the intrinsic linewidth for the spectrum (wint0 and wint2). The total intrinsic linewidth (wint), which is effectively a constant real positive term added to each diagonal element of the Lanczos tridiagonal matrix during the evaluation of the continued fraction [cf. equation (125)], is defined by

$$w^{\text{int}}(\psi) = w_0^{\text{int}} + w_2^{\text{int}} \cos^2 \psi \tag{139}$$

It is left to the user to verify that this quantity is positive. These parameters can be used to mimic the effects of dynamical processes which have not explicitly been included in the calculation and/or inhomogeneous broadening. The continued fraction itself is evaluated "from the bottom up" at a number of equally spaced points (mxpt) between the desired beginning and ending field values, inclusive. The selection of this option generates an output file SP??.FMT, which contains the field values and associated real and imaginary parts of the spectral function. To obtain the usual derivative mode spectrum, the real part of the spectral function must be numerically differentiated. Since many data plotting and analysis packages supply this function, it is not duplicated here.

4.6. "Field Sweep" Conjugate-Gradients Calculations: EPRBL and TNLL

These programs are used only for the determination of the MTS (cf. Section 3.4). The program EPRBL has a structure similar to EPRLL and EPRCGL, but uses the diagonally preconditioned complex symmetric conjugate-gradients algorithm to solve equations (111) and (112) at a set of equally spaced field positions. The range and number of points in the field sweep are determined by parameters entered into LBLL as described in Section 4.3.

For every desired set of input parameters, the matrix and starting vector are generated exactly as in EPRLL and EPRCGL. Within the loop over the input parameter sets, the field sweep is accomplished by varying the imaginary part of the origin shift and using the diagonally preconditioned complex symmetric conjugate-gradients algorithm to solve equations (111) and (112) at each point in the subroutine CSPCCG. This subroutine is based on the diagonally preconditioned version of the general preconditioned conjugate-gradients algorithm for real symmetric matrices given in algorithm 10.3-3 in the book by Golub and Van Loan (1983). However, we recall that only the real parts of the diagonal matrix elements are used as the preconditioning matrix (cf. Section 3.4). The subroutine CSPCCG is supplied with the starting vector (array b), dimension of the matrix (ndim), maximum number of conjugate-gradients steps allowed (cftol), and origin shift (temp). When it completes the calculation it returns the approximate solution vector (array x), the number of conjugate-gradient steps actually executed (ndone), and the estimated error based on the modulus of the rectanorm of the residual vector. Immediately after control is returned to EPRBL from CSPCCG, the exact residual is calculated and its unitary space norm is computed to give an improved error estimate (terror). The number of conjugate-gradients steps actually executed is also used as a flag to indicate whether or not the calculation in CSPCCG converged. After a short message is printed, the significance factors as defined in

equation (91) (array basis) and spectral function for that field position as given by equation (89) (array spect) are calculated. The field positions at which the current maximum values of the individual significance factors have been detected are also monitored (array basis). When the field sweep has been completed, the significance factors along with their associated field-values and the spectral function are written to the disk file BS??.DAT.

The basis-set truncation information contained in the output file BS??.DAT generated by EPRBL is further processed by the program TNLL. In this program, the significance factors and field values are read in and the significance factors are normalized so that the largest factor is unity. This step is necessitated by the fact that the largest significance factor, as defined by equation (91), can vary widely in amplitude. After this scaling has been completed, the s_j are printed along with their associated field values and basis-set quantum numbers. This list can then be scrutinized to determine the MTS (Vasavada *et al.*, 1987).

4.7. Auxiliary Programs: D200, STVT, MATLST, and VECLST

The program D200 can be quite useful in deciding upon a reasonable choice of λ_0^2 if the order parameter is known. The form of the equation for the order parameter actually used in this program can be derived by starting from equation (133) and letting $z = \cos\beta$ to get

$$\langle P_2(z)\rangle = \frac{3}{2}\left\{\frac{\int_0^1 dz\, z^2 \exp[3\lambda_0^2 z^2/2]}{\int_0^1 dz \exp[3\lambda_0^2 z^2/2]}\right\} - \frac{1}{2} \tag{140}$$

Now, the changes of variable $\varepsilon = \sqrt{3\lambda_0^2/2}$ and $y = \varepsilon z$ followed by integration by parts gives

$$\langle P_2(y/s)\rangle = \frac{3}{4\varepsilon^2}\left\{\frac{\varepsilon}{\exp[-\varepsilon^2]\int_0^\varepsilon dy \exp[y^2]} - 1\right\} - \frac{1}{2} \tag{141}$$

The remaining integral in the denominator of equation (141) is known as Dawson's integral (Abramowitz and Stegun, 1964). This integral is evaluated numerically by evaluating a continued-fraction expansion (Dijkstra, 1977). For more information about the numerical and analytical properties of Dawson's integral, see the literature (Fried and Conte, 1961; Abramowitz and Stegun, 1964; Dijkstra, 1977; Bender and Orszag, 1978). This program does not generate any output files.

The program STVECT is also useful during the initial stages of calculations involving restoring potentials. This program is little more than a stand-alone version of the subroutine STVECT. It is used to calculate the elements of the starting vector without doing the entire spectral calculation. In this manner it is possible to determine if a sufficiently large value of L^e_{max} has been chosen and examine the overall structure of the starting vector. The determination of L^e_{max} is simply based on making sure that the

average magnitude of the elements of the starting vector with $L = L^{e}_{max}$ is much less than the magnitude of the $L = 0$ terms. A reasonable value for the ratio of the $L = L^{e}_{max}$ to the $L = 0$ terms is 10^{-2} to 10^{-4}. This program does not produce any output files.

The last two programs are most useful in the process of porting these programs to other machines. The program MATLST is used to list out the matrix elements calculated by the subroutine MATRLL which is called by EPRBL, EPRCGL, and EPRBL. There exist some lines in the programs EPRLL and EPRCGL just after the calls to MATRLL which, if uncommented, will store the matrix elements of the stochastic Liouville operator in a file on the disk. This program will read in those files and generate an intelligible listing of the matrix elements on the screen. This is useful in verifying that the matrix elements generated on the target machine are correct. The program VECLST performs the analogous function for the starting vector. Again, there are commented lines in EPRLL and EPRCGL right after the call to the subroutine STVECT which, if uncommented, will store the elements of the starting vector in a file on the disk in the form that can be read in by VECLST. Neither of these programs generates output files.

4.8. Porting Programs to Other Machines

These programs are based on a set of programs written by G. Moro in 1980 (Moro, 1980a, 1980b; Moro and Freed, 1981; Meirovitch *et al.*, 1982). The older programs were very general, quite complicated, and written in FORTRAN IV for use on a computer with a very limited amount of physical memory. The present set of programs are written in a modular, more easily portable fashion in FORTRAN 77 and make use of the more advanced hardware that is available today. As supplied, these programs should compile and run without error on IBM PCs or compatibles under MS-DOS (ver. 2.11 or higher) and Microsoft Fortran (ver. 3.0 or higher). The PC version of these programs, as supplied here, is intended mainly as a reference point in porting these programs to a larger machine to be used for routine calculations. However, some users may find it sufficient to increase the matrix and vector dimensioning parameters in STDDIM.INC to the limits allowed by their compiler and use a PC for most calculations. The main limitation on this practice is that the segmented addressing used in these machines is not well suited to handling large arrays. Indeed, many FORTRAN 77 compilers for PCs limit the maximum size of single arrays or common blocks to 64 kbytes.

A serious attempt has been made to use only standard FORTRAN 77 features. The major exceptions to this rule are discussed below. This section is quite technical in nature, where it is assumed that the reader is a fluent FORTRAN programmer and has some knowledge of computer hardware.

The modular way in which these programs have been written makes it easier for the user to substitute more accurate or faster library subroutines for many of the function subroutines supplied here. In fact, most commonly available scientific library packages such as IMSL[5] and SLATEC[6] have many routines for calculating special functions and doing basic linear algebraic operations which are superior to those supplied here. Users are encouraged to use these library routines whenever possible.

[5] IMSL is a trademark of IMSL Corporation.

[6] Available from National Energy Software Center, Argonne National Laboratory.

4.8.1. Data Types and Explicit Declarations of Variables

In these programs, the following statements are true:

- All variables and parameters are explicitly declared. This has been done to make it easier to detect spelling errors with compilers which have the capability of flagging undeclared quantities.
- All integer variables and parameters are declared to be of type `integer`, not `integer*2` or `integer*4`.
- All floating point numbers are declared of type `double precision`, not `real*4` or `real*8`.
- Common blocks and parameters defining the dimensions of important arrays used in several programs or subroutines are defined in include files.

Unfortunately, include statements are not part of the FORTRAN 77 standard and their implementation varies widely.

It has been assumed throughout that long (4 byte) integers are the default integer length. If this is not the case, the use of long integers should be enabled or care taken to ensure that integer overflows do not occur at execution time.

The use of double precision (8 byte) floating point numbers throughout is somewhat excessive. However, most machines with enough computing power to handle serious calculations of this type also have enough physical memory where space is not a major issue. The use of double precision numbers throughout is actually required on some machines with small mantissas and large exponents.

The logical variables used here can be any length, but one cannot go wrong in sticking to the FORTRAN 77 default size of 4 bytes.

Extensive use has been made, especialty in EPRLL, of the fact that most compilers store complex numbers as two consecutive real quantities with the real part being first. When this is true, an N-dimensional `complex*16` array is compatible with an array dimensioned $2 \times N$ (not $N \times 2$!) of type `real*8`. If, for some reason, complex numbers are not stored in this manner, or if complex arithmetic and data types are not supported at all, the easiest solution would be to change all arrays and variables of type `complex*16` to $2 \times N$ dimensioned arrays of type `real*8` and do all complex arithmetic explicitly. This would also require function subroutines of type `complex*16` to be changed into conventional subroutines which return the real and imaginary part of the result through the argument list.

4.8.2. I/O Issues

One of the major sources of difficulty in porting FORTRAN 77 programs is the lack of uniformity of I/O features among compilers. As a rule, the required I/O functions in these programs are confined to specific subroutines and functions to make the programs easier to port to other machines.

A few of the more important sources of difficulty associated with doing I/O are listed below. Unfortunately, this list is not exhaustive.

- The logical units for writing to and reading from the screen and for opening disk files are defined in the include file STDIO.INC. All programs have been written such that at most one disk file is open at any given time.

- The status keyword "UNKNOWN" has been used in disk file open statements. Some compilers do not recognize this keyword. If this is the case, the keywords "OLD" or "NEW" could be substituted in appropriate places or the defaults status could be assumed and the status definition removed entirely.
- Not all compilers supply an inquire function as used in LBLL. If such a function is not supplied, it is relatively straightforward to write one by trying to open the file using the "NEW" and "OLD" status keywords with the I/O error handling mechanism provided by the ERR keyword.
- The $ edit descriptor to suppress the carriage return after writing to the screen is used when prompting the user for input. Some compilers do not recognize this edit descriptor. It can easily be omitted if necessary.
- A logical record length of 1024 bytes is used for the unformatted direct access files containing the input parameters which are written by the subroutine WRDAT and read in by RDDAT.

4.8.3. Vector and Parallel Computation

The modularity of these programs and the exclusion of screen and disk I/O from the subroutines where the majority of the heavy numerical work is done should make it easier to adapt these programs for use on array processors. We note that the word adapt rather than port has been used here. The work involved in getting programs running on array processors is often considerably more difficult than on conventional computers, because the unique features of the hardware often influence the extent to which the machine is programmable in standard FORTRAN. The added difficulty in adapting a program for use on an array processor must always be weighed against the expected decrease in execution time. In practice, only the serious user who is confronted with a large body of very slow motional spectra to analyze should consider this undertaking.

With this caveat in mind, the only programs which are serious candidates for adaptation to array processors are EPRLL, EPRCGL, and EPRBL. Even here, it may pay to adapt the code only for the Lanczos and/or conjugate-gradients algorithms, while doing the matrix element calculation on the host computer.

This story might be somewhat different on machines that have several array processors. Because of the structure of the arrays used in EPRLL to hold the entries of the stochastic Liouville matrix and the associated integer indices, it should not be too difficult to have different array processors generate the matrix elements for different sections of the matrix once a matrix element calculation subroutine is working at all. In addition, these same structures would allow one to break up the matrix-vector multiplication step of the Lanczos algorithm into several pieces, each of which could be independently executed by a separate array processor. This would not be so easy if only the upper or lower half of the matrix is stored, as was previously done (Moro,1980b; Gorcester, 1985), since each processor would need access to the entire matrix.

5. EXAMPLE CALCULATIONS

To aid the reader in using these programs, several model calculations are discussed in detail in Section 5.1. In addition, a short survey of actual applications of these

programs to the analysis of experimental data is given in Section 5.2. The presentation of these examples is intended to demonstrate how to choose reasonable input parameters as well as the wide variety of spectra that can be quickly and easily generated.

5.1. Model Calculations and General Strategy

The purpose of this section is to discuss in some detail a set of example calculations that can be run on a PC. In addition, some hints are given for doing careful, accurate calculations on a new system to extract out dynamical information. The calculations actually presented here are relatively simple but they do model the dynamics of "real" radicals.

The first issue that must be dealt with is the proper choice of g- and A-tensor values. These quantities should be determined for the particular system under study by a separate experiment to obtain the rigid-limit values of the magnetic tensors (Freed, 1976). The validity of the dynamical and structural information obtained from the slow-motional spectral calculation programs depends crucially on the use of accurate magnetic tensors. A rigid-limit spectral calculation program is not included in this set of programs, but several reliable programs can be easily obtained. In the following it will be assumed that the proper rigid-limit magnetic tensors are known. Finally, if the field sweep required to obtain the rigid-limit absorption spectrum is not much smaller than the field at the center of the sweep range, the programs discussed here should not be used to analyze the dynamics of the system since the nonsecular terms in the spin Hamiltonian have been omitted. Systems of this type should be analyzed with a program which includes the nonsecular terms (Moro, 1980a; Meirovitch *et al.*, 1982; Gorcester, 1985).

The next thing to consider is the structure of the radical and the orientation of the principal axes of the magnetic tensors in relation to the principal axes of the diffusion tensor. In many cases, constructing a molecular model is very helpful in determining a proper choice of axes and the associated diffusion tilt angle, ϕ (cf. Figure 2). In many cases, such as for the TEMPONE class of nitroxide spin probes, one can assume a spherically symmetric diffusion tensor. In this case, it is useful to assume that $\hat{z}_R$ coincides with that principal axis of the magnetic frame whose principal value differs the most from the other two. For X-band experiments on nitroxide radicals, the magnetic axis which is most different is the one with the largest A-tensor component. The labels of the magnetic frame axes can also be permuted to make this the $\hat{z}_m$ axis. This choice implies $\phi = 0$ and leads to the stochastic Liouville matrix of smallest dimension. The use of nonzero diffusion tilt angles in conjunction with a spherically symmetric diffusion tensor can lead to much larger matrices, but must finally give the same spectrum as the $\phi = 0$ case. For axially symmetric diffusion tensors, the calculated spectra can depend greatly on the diffusion tilt angle, especially if the diffusion tensor is very anisotropic (Mason *et al.*, 1974; Meirovitch and Freed, 1979; Campbell *et al.*, 1979; Meirovitch *et al.*, 1984). Typically, spin probes bound to polymers and large, rigid radicals such as cholestane require the use of axially symmetric diffusion tensors.

The structure of the thermodynamic phase of the solution must also be known. If the solution under investigation is isotropic (i.e., does not form a liquid crystalline phase at the particular temperature and pressure at which the experiment was conducted), then no restoring potential should be included in the calculation ($\lambda_K^L = 0$ for

all L and K), since one cannot exist in isotropic fluids. For radicals in liquid crystalline phases however, the restoring potential models the interaction of the radical with the surrounding solvent molecules and must be included in the calculation. If the sample is ordered on both the macroscopic and microscopic levels, then the director tilt angle, ψ, is determined by the angle between the static magnetic field and the preferred axis of alignment of the solvent molecules. A diagram showing this director tilt angle is given in Figure 1. On the other hand, if the sample is microscopically ordered but macroscopically disordered (MOMD), then it is possible to do a sequence of calculations at different director tilt angles and model the spectrum of the composite as the appropriately weighted integral of the spectra calculated as a function of the director tilt angle (Meirovitch *et al.*, 1984). These calculations are quite time-consuming, and it is more difficult to extract reliable information from such spectra, because they involve the superposition of many overlapping spectra. They should be avoided if possible by using macroscopically ordered samples. It also should be kept in mind that the diffusion tensor, at least to a first approximation, is independent of the value chosen for the coefficients of the restoring potential. It is strongly suggested that one start with a λ_0^2 term alone in the restoring potential and introduce the higher-order terms only if necessary. Often it is simpler to think in terms of the order parameter $\langle \mathscr{D}^2_{00}(\Omega) \rangle = \langle P_2(\cos\beta) \rangle$, rather than in terms of the potential expansion parameters, λ_K^L. To simplify this transitition, Figure 8 and the program D200 (cf. Section 4.7) have been provided.

Except when intentionally studying radical-radical interactions, it is very important to work with radical concentrations low enough to avoid Heisenberg spin exchange effects (as well as effects of dipole-dipole interactions) which broaden the spectra and obscure information about rotational reorientation. The radical concentration at which Heisenberg spin exchange begins to affect the spectrum varies widely and should be

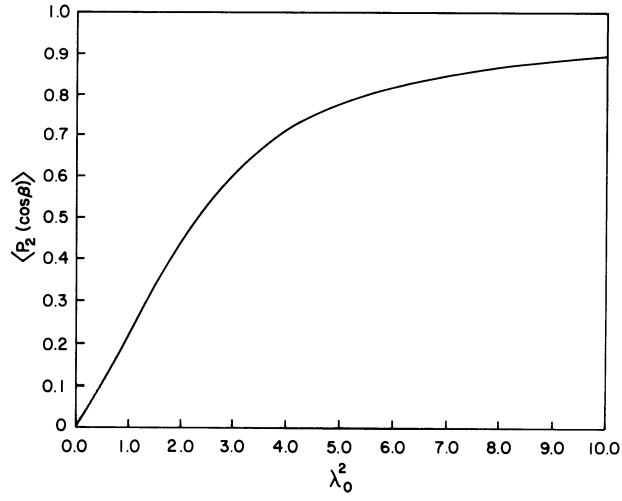

Figure 8. Plot of the order parameter as a function of λ_0^2 for $0 \leq \lambda_0^2 \leq 10$. For larger values of λ_0^2, the order parameter slowly approaches its asymptotic limit of unity. This plot was generated using the subroutine DAWSON which is described in Section 4.7.

determined by experiment. Care should also be taken to purge the solution under investigation of any oxygen for the same reason. These considerations are especially important for relatively fast motional spectra where the intrinsic broadening of the spectral features is largely due to the rotational motion.

These considerations usually give sufficient information to begin the process of calculating spectra to model experimental results. The general procedure in fitting experimental spectra is as follows:

1. Obtain accurate values for the rigid-limit magnetic tensors from fitting a rigid-limit spectrum.
2. Decide on a rotational diffusion model.
3. Using a molecular model, define an approximate diffusion asymmetry parameter and diffusion tilt angle.
4. Guess at a starting value for the coefficients of the restoring potential if present.
5. Guess at a starting value for the rotational correlation time.
6. Determine the proper basis set for the parameters chosen.
7. Calculate a spectrum and compare with the experimental result.
8. If a satisfactory fit has not been obtained, refine the estimate of $\bar{R}$ and go back to step 5, otherwise refine estimates of previous parameters and go back to step 4, 3, or 2.

Obviously, the time it takes to reach a satisfactory fit is drastically reduced if one can start with good estimates of the final parameters. There are several ways to accomplish this. First, and most important, is to have a thorough understanding of the definitions of the parameters that go into the calculation and the physically reasonable values they could have for the system under study before attempting any calculations. This knowledge will help to avoid spending time doing calculations with physically unreasonable parameters. Second, previous spectral calculations done on similar systems can be very instructive. A survey of previously published experimental spectra and the input parameters used to fit them is given in Section 5.2. And third, other experimental data, such as NMR, neutron, or X-ray scattering, etc., on the same or a closely related system may prove useful in obtaining good estimates of order parameters and other structural information.

Once a reasonable set of input parameters has been decided upon, the proper basis set should be determined. This is most reliably and conveniently accomplished by using the programs EPRBL and TNLL to determine the MTS. The data in Tables 2 and 3 were obtained using the diagonally preconditioned conjugate-gradients algorithm (Vasavada *et al.*, 1987). These truncation parameters can be used as they stand, or they can be used to aid in deciding on input basis-set truncation parameters for EPRBL. We note that the input basis-set truncation parameters for EPRBL must always be larger than the expected MTS basis-set truncation parameters for the problem.

Several of the calculations outlined in Table 2 can be executed on the PC version of the programs supplied with this book. The calculation corresponding to the second line of Table 2 has already been extensively studied in Section 3.6 and will not be treated further. The remaining calculations (lines one and five through seven in Table 2) will be discussed here, although in less detail.

TABLE 3
Table of Truncation Parameters and MTS for 2D-ESE Spectra[a]

No.	Spin probe	R	λ	L^{e}_{max}	L^{o}_{max}	K_{max}	M_{max}	N	N_{min}
1	TEMPONE	10^7	0	10	7	6	2	123	92
2	TEMPONE	10^6	0	22	17	10	2	429	307
3	TEMPONE	10^5	0	44	37	18	2	1485	971
4	TEMPONE	10^4	0	88	71	28	2	4614	2506
5	TEMPONE	10^7	10	16	7	2	2	108	76
6	TEMPONE	10^6	5	20	15	8	2	333	209
7	TEMPONE	10^6	10	16	11	4	2	168	120
8	TEMPONE (90° tilt)	10^7	1	10	7	6	10	1440	586
9	TEMPONE (90° tilt)	10^7	10	16	15	6	6	2601	607
10	TEMPONE (90° tilt)	10^6	10	20	19	10	12	8196	2835
11	CSL	10^6	0	22	19	22	2	600	485
12	CSL	10^5	0	46	37	46	2	2310	1815

[a] All parameters have the same meaning as in Table 2, except for s_j which is taken to be 0.0003.

The first line in Table 2 corresponds to moderately slow isotropic Brownian diffusion of the TEMPONE spin probe dissolved in an isotropic liquid ($R_{\|} = R_{\perp} = 10^7\ s^{-1}$). The smoothness of the prominent spectral features (cf. Figure 9), together with the reduced overall width of the spectrum compared to Figure 5, are indicative of faster motion. The large breadth of the high- and low-field extrema also indicates that this spectrum is in the vicinity of the minimum of the T_2 curve.

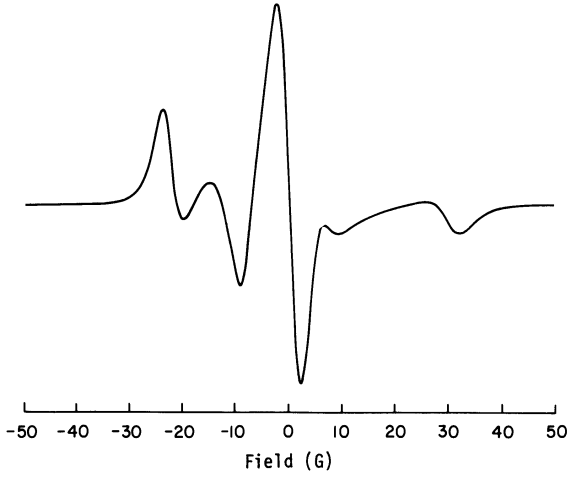

Figure 9. Plot of spectrum generated by input parameter file LBL1.DAT in the Appendix. The input parameters used to generate this plot correspond to line 1 of Table 2.

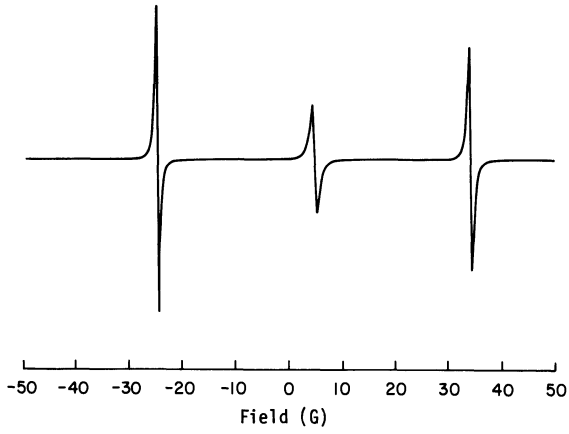

Figure 10. Plot of spectrum generated by input parameter file LBL5.DAT in the Appendix. The input parameters used to generate this plot correspond to line 5 of Table 2.

The calculation defined by the parameters on the fifth line of Table 2 is presented in Figure 10. This plot could be imagined to correspond to an experiment on the TEMPONE spin probe dissolved in a well-aligned smectic liquid crystal. The order parameter in this case is about 0.9 (cf. Figure 8). Note the unusual ratio of the heights of the three hyperfine lines. In addition, the hyperfine lines are well separated, despite the fact that the diffusion tensor is the same as in Figure 5. Both of these features are due to the fact that the probe is highly aligned by the restoring potential.

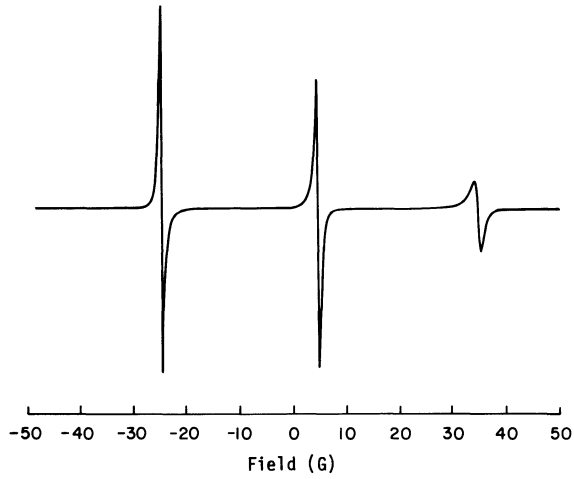

Figure 11. Plot of spectrum generated by input parameter file LBL6.DAT in the Appendix. The input parameters used to generate this plot correspond to line 6 of Table 2.

The plot in Figure 11 corresponds to line six of Table 2. When compared to Figure 10, this plot demonstrates the effects of lowering the order parameter to 0.8 and slowing down the motion by an order of magnitude. Note the widely separated hyperfine lines and shift in the ratio of peak heights.

The final plot in this set, Figure 12, corresponds to line seven of Table 2. This plot, when compared with Figure 11, shows the effect of increasing the order parameter from 0.8 to 0.9. The major changes are in the linewidths rather than the line positions. These last two plots emphasize the fact that not all "three line" nitroxide spectra are due to fast isotropic motion!

5.2. Examples from the Literature

In I, a number of examples of calculated spectra of nitroxide spin probes in isotropic and liquid crystalline media are given. A summary of a number of more recent applications, where the present package of programs can be effectively employed, is given here.

An important test of the theory behind these programs is to properly interpret the spectra of nitroxide spin probes in oriented liquid crystalline media as a function of the director tilt angle. This was done for thermotropic liquid crystals by Meirovitch *et al.* (1982). The appendices to that work also present a slightly more general theory for slow-motional line shapes than is given in the present chapter. Further studies along these lines may be found in Meirovitch and Freed (1984) and Meirovitch (1983) in which a variety of nitroxide spin probes were utilized.

The application of these ideas to oriented model membranes, as well as dispersions, is discussed in detail by Tanaka and Freed (1984, 1985) and Kar *et al.* (1985). In these studies, various chain-labeled lipids and cholestane spin labels were utilized to deter-

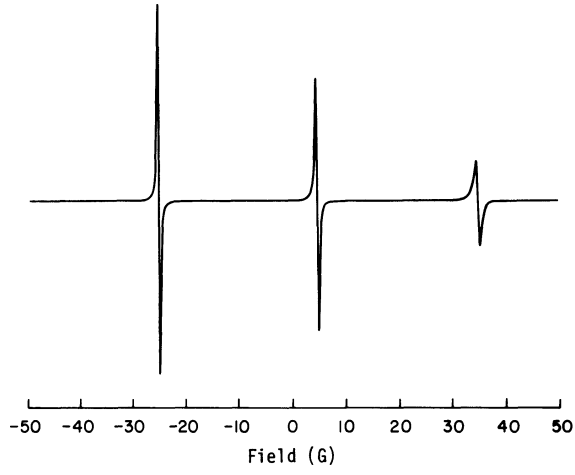

Figure 12. Plot of spectrum generated by input parameter file LBL7.DAT in the Appendix. The input parameters used to generate this plot correspond to line 7 of Table 2.

mine the ordering and dynamics in the various lipid phases as well as the effects of such additives as cholesterol and the small polypeptide gramicidin A. These applications have recently been reviewed by Freed (1987).

In dealing with dispersion samples of model membrane preparations, and macroscopic misalignment in general, it is necessary to obtain an average spectrum by properly weighting the spectra calculated for a range of different director tilt angles. This is just the MOMD model which was briefly mentioned in Section 5.1. Calculations based on this model are thoroughly described in a paper by Meirovitch *et al.* (1984). It is also employed in other recent work (Tanaka and Freed, 1984, 1985; Kar *et al.*, 1985).

An important development in the process of comparing calculated spectra to experimental data is the recent use of very general nonlinear least-squares fitting methods in conjunction with the powerful Lanczos and conjugate-gradients algorithms already described here. In this method, one simply allows the nonlinear least-squares algorithm to systematically vary the input parameters for the line-shape calculation program to minimize the deviations between the calculated and experimental spectra. This procedure can require 100 to 150 separate line-shape calculations, yet the overall running time is not inordinate owing to the efficiency of the algorithms chosen. Nevertheless, because of the extensive computations involved, these calculations are currently limited to large mainframe computers. In general, this appears to be a more unbiased, reliable, and accurate way to fit experimental data to theoretical models than the trial-and-error approach (Crepeau *et al.*, 1987).

In the past few years there have also been significant new developments which enhance the resolution and scope of studies of molecular dynamics by ESR spectrscopy. These are time-domain experiments based on electron-spin-echo (ESE) (Millhauser and Freed, 1984) (Millhauser *et al.*, 1987; Freed, 1987) or Fourier transform (FT) methods (Gorcester and Freed, 1986; 1988a; 1988b). The application of ESE techniques to the study of slow motions is discussed from a theoretical point of view by Schwartz *et al.* (1982) and examples of the interpretation of experimental data are given in papers by Millhauser and Freed (1984) and by Kar *et al.* (1984). The basic ESE technique has given rise to a new two-dimensional (2D) ESE technique wherein the homogeneous linewidth at each point in the spectrum is obtained as a function of the magnetic field. It shows a remarkable sensitivity to the details of the reorientational dynamics (Millhauser and Freed, 1984; Millhauser *et al.*, 1987; Freed, 1987) and has been successfully employed in the study of spin probe motion in model membranes (Kar *et al.*, 1984) and in the study of spin labeled proteins (Kar *et al.*, 1987). The present set of programs can be adapted to calculate this type of 2D-ESE spectra as discussed elsewhere (Millhauser and Freed, 1984; Vasavada *et al.*, 1987; Schneider and Freed, in press).

Other kinds of time-domain ESR spectroscopies exist, which cannot be treated by the present set of programs such as spin-echo ELDOR (Hornak and Freed, 1983; Dzuba *et al.*, 1984) and 2D-magnetization transfer ESE (Schwartz *et al.*, 1986). In general, the analysis of these experiments requires the more complete theory involving the slow-motional relaxation of both the longitudinal and transverse components of the magnetization. However, the Lanczos and conjugate-gradients algorithms can still be used to analyze these experiments—once the matrix elements are calculated (Schneider and Freed, 1989). This class of experiments is especially sensitive to very slow molecular motions.

A major breakthrough in ESR techniques has been the development of 2D-FT ESR spectroscopy. At the time of writing, its effectiveness in studying dynamics in the fast-motional regime has been demonstrated for nitroxides (Gorcester and Freed, 1986, 1988a, 1988b). These methods are expected, in the future, to be effectively employed for slow-motional spectroscopy providing valuable new information on the underlying dynamical processes. Such 2D spectra can also be described by a generalization of the methods described here.

Last of all, we wish to point out that these programs can be applied to experiments on slow-motional NMR spectroscopy (Meirovitch and Freed, 1979; Campbell *et al.*, 1979) and in more general form (Meirovitch *et al.*, 1982) to inorganic radicals such as the vanadyl (Campbell and Freed, 1980) and cupric (Subczynski *et al.*, 1987) ions which are often used in biophysical studies.

ACKNOWLEDGMENTS. We wish to thank Dr. R. H. Crepeau and Ms. Nancy Schneider for their extensive help in preparing and critically reading this manuscript. We also thank Mr. J. Gorcester and Dr. S. Rananavare for helpful discussions. This work was supported by NIH grant #GM25862 and NSF grants #DMR86-04200 and #CHE87-03014.

APPENDIX: PARAMETERS FOR EXAMPLE CALCULATIONS

```
########################   file : lbl1.dat   ########################



g-tensor [gxx,gyy,gzz] :   2.00880        2.00610        2.00270

twice the nuclear spin [in2] :  2

A-tensor [axx,ayy,azz] (gauss) :   5.80000        5.80000        30.8000

static field [B0] (gauss) :   3200.00

diffusion parameter [ipdf] = 0

diffusion tensor [dxy,dzz] (1/sec) =  .100000E+08    .100000E+08

discrete jumps parameters [ist,djf] :  0    .000000

Heisenberg spin exchange frequency [oss] =   .000000

number of terms in the potential [ipt] = 0

angle between B0 and local director [psi] (degrees) :   .000000

diffusion tilt index [itd] = 0

truncation values  [lemx,lomx,kmx,mmx,ipnmx] :   6    3    2    2    2

number of Lanczos/CG steps [nstep] :  33

calculation type (0=Lanczos,1=CG) [itype] : 0



##########################################################################
```

```
#########################   file : lbl2.dat   #########################

g-tensor [gxx,gyy,gzz] :   2.00880        2.00610        2.00270

twice the nuclear spin [in2] :  2

A-tensor [axx,ayy,azz] (gauss) :   5.80000        5.80000        30.8000

static field [B0] (gauss) :   3200.00

diffusion parameter [ipdf] = 0

diffusion tensor [dxy,dzz] (1/sec) =  .100000E+07    .100000E+07

discrete jumps parameters [ist,djf] :  0    .000000

Heisenberg spin exchange frequency [oss] =   .000000

number of terms in the potential [ipt] = 0

angle between B0 and local director [psi] (degrees) :   .000000

diffusion tilt index [itd] = 0

truncation values  [lemx,lomx,kmx,mmx,ipnmx] :  14   7   6   2   2

number of Lanczos/CG steps [nstep] : 100

calculation type (0=Lanczos,1=CG) [itype] : 0

#############################################################################
```

```
#########################   file : lbl5.dat   #########################


g-tensor [gxx,gyy,gzz] :   2.00880        2.00610        2.00270
twice the nuclear spin [in2] :  2
A-tensor [axx,ayy,azz] (gauss) :   5.80000        5.80000        30.8000
static field [B0] (gauss) :   3200.00
diffusion parameter [ipdf] = 0
diffusion tensor [dxy,dzz] (1/sec) =  .100000E+08    .100000E+08
discrete jumps parameters [ist,djf] :  0    .000000
Heisenberg spin exchange frequency [oss] =   .000000
number of terms in the potential [ipt] = 1
coefficients of the potential :
        ipt = 1  [l,k,coef.] = 2  0    10.0000
angle between B0 and local director [psi] (degrees) :   .000000
diffusion tilt index [itd] = 0
truncation values  [lemx,lomx,kmx,mmx,ipnmx] :  10    1    2    2    2
number of Lanczos/CG steps [nstep] :  63
calculation type (0=Lanczos,1=CG) [itype] : 0


#########################################################################
```

```
#########################   file : lbl6.dat   ########################

g-tensor [gxx,gyy,gzz] :   2.00880        2.00610        2.00270

twice the nuclear spin [in2] :  2

A-tensor [axx,ayy,azz] (gauss) :   5.80000        5.80000        30.8000

static field [B0] (gauss) :   3200.00

diffusion parameter [ipdf] = 0

diffusion tensor [dxy,dzz] (1/sec) =  .100000E+07    .100000E+07

discrete jumps parameters [ist,djf] :  0    .000000

Heisenberg spin exchange frequency [oss] =   .000000

number of terms in the potential [ipt] = 1

coefficients of the potential :

        ipt = 1  [l,k,coef.] = 2  0    5.00000

angle between B0 and local director [psi] (degrees) :   .000000

diffusion tilt index [itd] = 0

truncation values  [lemx,lomx,kmx,mmx,ipnmx] :  12    3    2    2    2

number of Lanczos/CG steps [nstep] :  78

calculation type (0=Lanczos,1=CG) [itype] : 0

#########################################################################
```

```
#########################   file : lbl7.dat   ########################


g-tensor [gxx,gyy,gzz] :   2.00880        2.00610        2.00270
twice the nuclear spin [in2] :  2
A-tensor [axx,ayy,azz] (gauss) :   5.80000        5.80000        30.8000
static field [B0] (gauss) :   3200.00
diffusion parameter [ipdf] = 0
diffusion tensor [dxy,dzz] (1/sec) =  .100000E+07    .100000E+07
discrete jumps parameters [ist,djf] :  0    .000000
Heisenberg spin exchange frequency [oss] =   .000000
number of terms in the potential [ipt] = 1
coefficients of the potential :
        ipt = 1  [l,k,coef.] = 2  0    10.0000
angle between B0 and local director [psi] (degrees) :   .000000
diffusion tilt index [itd] = 0
truncation values  [lemx,lomx,kmx,mmx,ipnmx] :  10    1    0    2    2
number of Lanczos/CG steps [nstep] :  33
calculation type (0=Lanczos,1=CG) [itype] : 0


#########################################################################
```

REFERENCES

Abramowitz, M. and Stegun, I. (eds.), 1964, *Handbook of Mathematical Functions*, Natl. Bur. Stand., Appl. Math. Ser., no. 55, U.S. Government Printing Office, Washington, D.C.

Bender, C. M., and Orszag, S. A., 1978, *Advanced Mathematical Methods for Scientists and Engineers*, McGraw-Hill, New York.

Biedenharn, L. C., and Louck, J. D., 1981, *Angular Momentum in Quantum Physics*, Addison-Wesley, Reading, Massachusetts.

Bruno, G. V., 1973, Application of the Stochastic Liouville Method in Calculating ESR Line Shapes in the Slow Tumbling Region and an ESR-ELDOR Study of Exchange, Ph.D. Thesis, Cornell University, Ithaca, New York.

Campbell, R. F., Meirovitch, E., and Freed, J. H., 1979, Slow-motional NMR line shapes for very anisotropic rotational diffusion, Phosphorus-31 NMR of phospholipids, *J. Phys. Chem.* **83**:525-533.

Campbell, R. F., and Freed, J. H., 1980, Slow-motional ESR spectra for vanadyl complexes and their model dependence, *J. Phys. Chem.* **84**:2668-2680.

Choudhury, D., and Horn, R. A., 1986, The Analog of the Gram-Schmidt Algorithm for Complex Bilinear Forms and Diagonalization of Complex Symmetric Matrices, Technical Report No. 454, Department of Mathematical Sciences, Johns Hopkins University, Baltimore, Maryland.

Cody, W. J., 1983, Algorithm 597: Sequence of modified Bessel function of the first kind, *ACM Trans. Math. Soft.* **9**:242-245.

Crepeau, R. H., Rananavare, S., and Freed, J. H., 1987, Automated Least-Squares Fitting of Slow Motional ESR Spectra, Abstracts of the 10th International EPR Symposium, Rocky Mountain Conference, Denver, CO.

Cullum, J. K., and Willoughby, R. A., 1985, *Lanczos Algorithms for Large Sparse Eigenvalue Computations*, Vols. I and II, Birkhäuser, Basel.

Dammers, A. J., 1985, Numerical Simulation of Electron Spin Resonance Spectra in the Slow Motion Regime, Ph.D. Thesis, Utrecht, The Netherlands.

Dijkstra, D., 1977, A continued fraction expansion for a generalization of Dawson's integral, *Math. Comp.*, **31**:503-510.

Dzuba, S. A., Maryaso, A. G., Salikhov, K. M., and Tsvetkov, Yu. D., 1984, Superslow rotations of nitroxide radicals studied by pulse EPR spectroscopy, *J. Magn. Reson.* **58**:95-117.

Edmonds, A. R., 1957, *Angular Momentum in Quantum Mechanics*, Princeton University Press, Princeton, New Jersey.

Fano, U., 1957, Description of states in quantum mechanics by density matrix and operator techniques, *Rev. Mod. Phys.* **29**:74-93.

Freed, J. H., Bruno, G. V., and Polnaszek, C. F., 1971a, Electron spin resonance lineshapes and saturation in the slow motional regime, *J. Phys. Chem.* **75**:3385-3399.

Freed, J. H., Bruno, G. V., and Polnaszek, C. F., 1971b, ESR line shapes for triplets undergoing slow rotational reorientation, *J. Chem. Phys.* **55**:5270-5281.

Freed, J. H., 1976, Ch. 3, Theory of Slow Tumbling ESR Spectra for Nitroxides, in *Spin Labeling: Theory and Applications* (L. Berliner, ed.), Vol. I, pp. 53-132, Academic Press, New York.

Freed, J. H., 1987, Molecular Rotational Dynamics in Isotropic and Oriented Fluids Studied by ESR, in *Rotational Dynamics of Small and Macromolecules in Liquids*, Lecture Notes in Physics, Vol. 293 (T. Dorfmüller and R. Pecora, eds.), pp. 89-142, Springer-Verlag, Berlin.

Fried, B. D., and Conte, S. D., 1961, *The Plasma Dispersion Function*, Academic Press, New York.

Gantmacher, F. R., 1959, *The Theory of Matrices*, Chelsea, New York.

Goldman, S. A., Bruno, G. V., Polnaszek, C. F., and Freed, J. H., 1972, An ESR study of anisotropic rotational reorientation and slow tumbling in liquid and frozen media, *J. Chem. Phys.* **56**:716-735.

Golub, G. H., and Van Loan, C., 1983, *Matrix Computations*, Johns Hopkins University Press, Baltimore, Maryland.

Gorcester, J., 1985, unpublished report, Cornell University, Ithaca, New York.

Gorcester, J., and Freed, J. H., 1986, Two-dimensional Fourier transform ESR spectroscopy, *J. Chem. Phys.* **85**:5375-5377.

Gorcester, J., and Freed, J. H., 1988a, Two-dimensional Fourier transform ESR correlation spectroscopy, *J. Chem. Phys.* **85**:4673-4693.

Gorcester, J., and Freed, J. H., 1988b, Linear prediction and projection of pure absorption line shapes in two-dimensional FTESR correlation spectroscopy, *J. Magn. Reson.* **78**:291-301.

Gordon, R. G., and Messenger, T., 1972, Ch. 13, Magnetic Resonance Line Shapes in Slowly Tumbling Molecules, in *Electron-Spin Relaxation in Liquids* (L. T. Muus and P. W. Atkins, eds.), pp. 341-381, Plenum Press, New York.

Hestenes, M. R., and Stiefel, E., 1952, Methods of conjugate gradients for solving linear systems, *J. Natl. Bur. Stand.* **49**:409-436.

Horn, R. A., and Johnson, C. A., 1985, *Matrix Analysis*, Cambridge University Press.

Hornak, J. P., and Freed, J. H., 1983, ELDOR spin echoes and slow motions, *Chem. Phys. Lett.* **101**:115-119.

Householder, A. S., 1964, *The Theory of Matrices in Numerical Analysis*, Blaisdell Publ. Co., New York (reprinted by Dover Publ., Inc. 1975).

Jeener, J., 1982, On operators, superoperators, Hamiltonians and Liouvillians, *Int. J. Quantum. Chem.*, Symp. 16, 485-560.

Kar, L., Millhauser, G. L., and Freed, J. H., 1984, Detection of slow motions in oriented lipid multilayers by two-dimensional electron-spin-echo spectroscopy, *J. Phys. Chem.* **88**:3951-3956.

Kar, L., Ney-Igner, E., and Freed, J. H., 1985, Electron spin resonance and electron-spin-echo study of oriented multilayers of $L\alpha$-dipalmitoylphosphatidylcholine water systems, *Biophys. J.* **48**:569-595.

Kar, L., Johnson, M. E., and Bowman, M. K., 1987, Electron spin-echo techniques for the study of protein motion, *J. Magn. Reson.* **75**:397-413.

Kivelson, D., 1972, Ch. 10, Electron Spin Resonance in Liquids. Selected Topics, in *Electron-Spin Relaxation in Liquids* (L. T. Muus and P. W. Atkins, eds.), pp. 213-277, Plenum Press, New York.

Korst, N. N., and Antsiferova, L. I., 1979, Study of slow molecular motions by stable-radical EPR, *Sov. Phys. Usp.* **21**:761-778.

Lajzerowicz-Bonneteau, J., 1976, Ch. 6, Molecular Structure of Nitroxides, in *Spin Labeling: Theory and Applications* (L. Berliner, ed.), Vol. I, pp. 239-249, Academic Press, New York.

Lanczos, C., 1950, An iteration method for the solution of the eigenvalue problem of linear differential and integral operators, *J. Natl. Bur. Stand.* **45**:255-282.

Löwdin, P. O., 1982, On operators, superoperators, Hamiltonians and Liouvillians, *Int. J. Quantum Chem.*, Symp. **16**:485-560.

Löwdin, P. O., 1985, Some aspects on the Hamiltonian and Liouvillian formalism, the special propagator methods, and the equation of motion approach, *Adv. Quantum Chem.* **17**:285-334.

Mason, R. P., Polnaszek, C. F., and Freed, J. H., 1974, Comments on the interpretation of electron spin resonance spectra of spin labels undergoing very anisotropic reorientation, *J. Phys. Chem.* **78**: 1324-1329.

McLachlan, N. W., 1961, *Bessel Functions for Engineers*, 2nd edn., Oxford University Press, New York.

Meirovitch, E., and Freed, J. H., 1979, Slow motional NMR lineshapes for very anisotropic diffusion: $I = 1$ nuclei, *Chem. Phys. Lett.* **64**:311-316.

Meirovitch, E., Igner, D., Igner, E., Moro, G., and Freed, J. H., 1982, Electron-spin relaxation and ordering in smectic and supercooled nematic liquid crystals, *J. Chem. Phys.* **77**:3915-3938.

Meirovitch, E., 1983, Electron spin resonance observations on the annealing process of low-water-content dipalmitoylphosphatidylcholine bilayers, *J. Phys. Chem.* **87**:845-850.

Meirovitch, E., and Freed, J. H., 1984, Analysis of slow-motional electron spin resonance spectra in smectic phases in terms of molecular configuration, intermolecular interactions, and dynamics, *J. Phys. Chem.* **88**:4995-5004.

Meirovitch, E., Nayeem, A., and Freed, J. H., 1984, Analysis of protein-lipid interactions based on model simulations of electron spin resonance spectra, *J. Phys. Chem.* **88**:3454-3465.

Messiah, A., 1962, *Quantum Mechanics*, Wiley, New York.

Millhauser, G. L., and Freed, J. H., 1984, Two-dimensional electron spin echo spectroscopy and slow motions, *J. Chem. Phys.* **81**:37-48.

Millhauser, G. L., Gorcester, J., and Freed, J. H., 1987, New Time-Domain ESR Methods for the Study of Slow Motions on Surfaces, in *Electron Magnetic Resonance of the Solid State* (J. A. Weil, ed.) pp. 571-597, Canadian Chemical Society, Ottowa, Canada.

Moro, G., 1980, EPRLF and EPRLP Routines, unpublished report, Cornell University, Ithaca, New York.

Moro, G., 1980, Implementation of the Lanczos Algorithm in the Calculation of Spectral Functions, unpublished report, Cornell University, Ithaca, New York.

Moro, G., and Freed, J. H., 1981, Calculation of ESR spectra and related Fokker-Planck forms by the use of the Lanczos algorithm, *J. Chem. Phys.* **74**:3757-3773.

Moro, G., and Freed, J. H., 1986, The Lanczos Algorithm in Molecular Dynamics: Calculation of Spectral Densities, in *Large-Scale Eigenvalue Problems, Mathematical Studies Ser.*, Vol 127 (J. Cullum and R. Willoughby, eds.), North-Holland, Amsterdam.

Nordio, P. L., 1976, Ch. 2, General Magnetic Resonance Theory, in *Spin Labeling: Theory and Applications* (L. J. Berliner, ed.), Vol. I, pp. 5-52, Academic Press, New York.

Paige, C. C., 1976, Error analysis of the Lanczos algorithm for tridiagonalizing a symmetric matrix, *J. Inst. Math. Appl.* **18**:341-349.

Paige, C. C., 1980, Accuracy and effectiveness of the Lanczos algorithm for the symmetric eigenproblem, *Linear Algebra & Appl.* **34**:235-258.

Parlett, B. N., 1980, *The Symmetric Eigenvalue Problem*, Prentice-Hall, Englewood Cliffs, N.J.

Parlett, B. N., and Nour-Omid, B., 1985, The use of a refined error bound when updating eigenvalues of tridiagonals, *Linear Algebra & Appl.* **68**:179-219.

Press, W. H., Flannery, B. P., Teukolsky, S. A., and Vetterling, W. T., 1986, *Numerical Recipes*, Cambridge University Press, New York.

Rose, M. E., 1957, *Elementary Theory of Angular Momentum*, Wiley, New York.

Schneider, D. J., 1989, Molecular Dynamics and Spin Relaxation: Theory, Computational Methodologies and Experimental Applications, Ph.D. Thesis, Cornell University, Ithaca, New York.

Schneider, D. J., and Freed, J. H., 1989, Spin relaxation and motional dynamics, *Adv. Chem. Phys.* **73**:387-527.

Schwartz, L. J., Stillman, A. E., and Freed, J. H., 1982, Analysis of electron spin echoes by spectral representation of the stochastic Liouville equation, *J. Chem. Phys.* **77**:5410-5425.

Schwartz, L. J., Millhauser, G. L., and Freed, J. H., 1986, Two-dimensional electron spin echoes: Magnetization transfer and molecular dynamics, *Chem. Phys. Lett.* **127**:60-66.

Sookne, D. J., 1973a, Bessel functions *I* and *J* of complex argument and integer order, *J. Res. Natl. Bur. Stand.* **77B**:111-124.

Sookne, D. J., 1973b, Bessel functions of real argument and integer order, *J. Res. Natl. Bur. Stand.* **77B**:125-132.

Subczynski, W. K., Antholine, W. E., Hyde, J. S., and Petering, D. H., 1987, Orientation and mobility of a copper square-planar complex in a lipid bilayer, *J. Am. Chem. Soc.* **109**:46-52.

Tanaka, H., and Freed, J. H., 1984, Electron spin resonance studies on ordering and rotational diffusion in oriented phosphatydlcholine multilayers: Evidence for a new chain-ordering transition, *J. Phys. Chem.* **88**:6633-6644.

Tanaka, H., and Freed, J. H., 1985, Electron spin resonance studies of lipid-gramicidin interactions utilizing oriented multilayers, *J. Phys. Chem.* **89**:350-360.

Vasavada, K. V., Schneider, D. J., and Freed, J. H., 1987, Calculation of ESR spectra and related Fokker-Planck forms by the use of the Lanczos Algorithm. II. Criteria for truncation of basis sets and recursive steps utilizing conjugate gradients, *J. Chem. Phys.* **86**:647-661.

Wassam, W. A. Jr., 1985a, Dual Lanczos vector space. I. A formal and numerical framework for the theoretical investigation of relaxation processes, *J. Chem. Phys.* **82**:3371-3385.

Wassam, W. A. Jr., 1985b, Dual Lanczos vector space. II. Lanczos transformations and contracted descriptions of relaxation processes, *J. Chem. Phys.* **82**:3386-3399.

Wilkinson, J. H., 1965, *The Algebraic Eigenvalue Problem*, Clarendon Press, Oxford.

Zientara, G. P. and Freed, J. H., 1979, Theory of Chemically-Induced Dynamic Spin Polarization. 5. Orientation-Dependent Effects, *J. Phys. Chem.* **83**:3333-3344.

2

Inhomogeneously Broadened Spin-Label Spectra

Barney L. Bales

1. INTRODUCTION

Inhomogeneous broadening of the ESR lines of nitroxide spin labels due to hyperfine structure is a pest that has complicated the work of spin labelers since shortly after the beginning of the spin-label era (Plachy and Kivelson, 1967; Poggi and Johnson, 1970) continually until the present (for example, Jolicoeur and Friedman, 1971; Kovarskii *et al.*, 1972; Bullock *et al.*, 1975; Ahn, 1976; Freed, 1976; Lim *et al.*, 1976; Jones and Schwartz, 1981; Ottaviani *et al.*, 1983; More *et al.*, 1984; Lee and Shetty, 1985). It is a problem that can and has been solved rigorously for a number of spin labels by combining NMR, ESR, and chemical substitution techniques (Kreilick, 1967; Brière *et al.*, 1967, 1970; Michon and Rassat, 1971; Chiarelli and Rassat, 1973; Lim *et al.*, 1976; Barbarin *et al.*, 1978a, 1978b; Labsky *et al.*, 1980; Windle, 1981; Ottaviani, 1987). These techniques taken together establish the hyperfine *pattern* of a given spin label and ESR simulation fine tunes the hyperfine coupling constants in a given set of experimental conditions. To proceed with rigor, this fine tuning must be done continually because the coupling constants vary with temperature (Kreilick, 1967; Brière *et al.*, 1967, 1970; Jolicoeur and Friedman, 1971; Atherton, 1975; Ottaviani, 1987) and solvent (Brière *et al.*, 1970; Freed, 1976; Lim *et al.*, 1976; Eaton *et al.*, 1980; Windle, 1981; Ottaviani, 1987). Also, the *effective* spacing of the hyperfine lines varies with spin-label concentration—a variation that depends strongly on temperature (Plachy and Kivelson, 1967). The effective spacing varies with spin-label alignment in an ordered fluid (Polnaszek and Freed, 1975; Bales *et al.*, 1984) and one can imagine that it might vary with other experimental parameters as well. Thus, the problem can be complicated but it can be solved with remarkable precision in some cases, notably with spin labels

Barney L. Bales • Department of Physics and Astronomy, California State University, Northridge, California 91330.

having particularly simple patterns or ones that give partially resolved ESR spectra. It is a tedious procedure, unavoidable if high precision is required in an experiment involving partially resolved ESR spectra. In most of the spin-label literature, the spectra are *unresolved*, either intrinsically by nature of the spin label and the experiment, or artificially, because of broadening due to oxygen or some other paramagnetic species. In unresolved spectra the procedures to correct for inhomogeneity become quite simple and remarkably accurate.

Inhomogeneous broadening due to *unresolved* hyperfine structure is spin labeling's version of a problem that keeps recurring (for example, Zemansky, 1930; Portis, 1953; Farach and Teitelbaum, 1967; Wertheim *et al.*, 1974) in which the information of interest, contained in a Lorentzian line, is obscured by perturbations that, in many cases, are Gaussian. Since nitroxide spin labels normally have twelve or more protons, the number of hyperfine lines is large, ranging from 13 in TEMPONE (Poggi and Johnson, 1970; Jolicoeur and Friedman, 1971; Windle, 1981) to an incredible 2646 in TEMPAMINE (Windle, 1981). Fortunately, when the hyperfine structure is *unresolved*, this same complexity insures that the profile of the hyperfine structure is nearly Gaussian, tremendously simplifying the problem. Thus each spin label in a given solvent at given concentration and temperature is characterized by the second moment, or alternatively the width, of the Gaussian profile.

Correcting for inhomogeneous broadening in unresolved lines proceeds in two steps: (1) one determines the Gaussian content of the line and (2) one determines the corrected quantity of interest, be it the linewidth, linewidth ratios calculated from intensity ratios, the spin exchange frequency, or the doubly integrated intensity of the first-derivative line.

The first step may be accomplished to first order if the hyperfine coupling constants have been determined by NMR, because the Gaussian content is given to within a constant of order unity by a simple function of the coupling constants [see equation (2) in Section 3]. Gaussian content may also be determined from ESR simulations. If these simulations are based on NMR measurements, then the fine tuning gives better coupling constants which give a more precise value of the Gaussian content. However, an experimental inhomogeneously broadened line may be simulated successfully with *many* sets of coupling constants that are *incorrect.* By "incorrect," we mean not only minor changes in the magnitude of the individual coupling constants but also completely different hyperfine patterns. The crucial point is that all of these incorrect patterns give the correct Gaussian content to high accuracy under conditions met by most spin labels. Thus, to accomplish step 1—determine the Gaussian content of a line—it is sufficient but not necessary to determine the coupling constants.

Since one may focus on the shape of the line instead of the underlying pattern, we suggested (Bales, 1982) that the shape be determined directly from the ESR line itself by measuring four points on the spectrum—the two normally measured to determine the linewidth and two more in the wings. This works extremely well for every case except one; if there is hyperfine coupling to a single proton that is very much larger than the average coupling to all of the others, the four-point method does not work well. Fortunately, it is simple to detect this situation from the ESR itself and involves very few spin labels.

Step 2—correcting the quantities of interest once the Gaussian content or the hyperfine coupling constants are determined—has been carried out by considering the

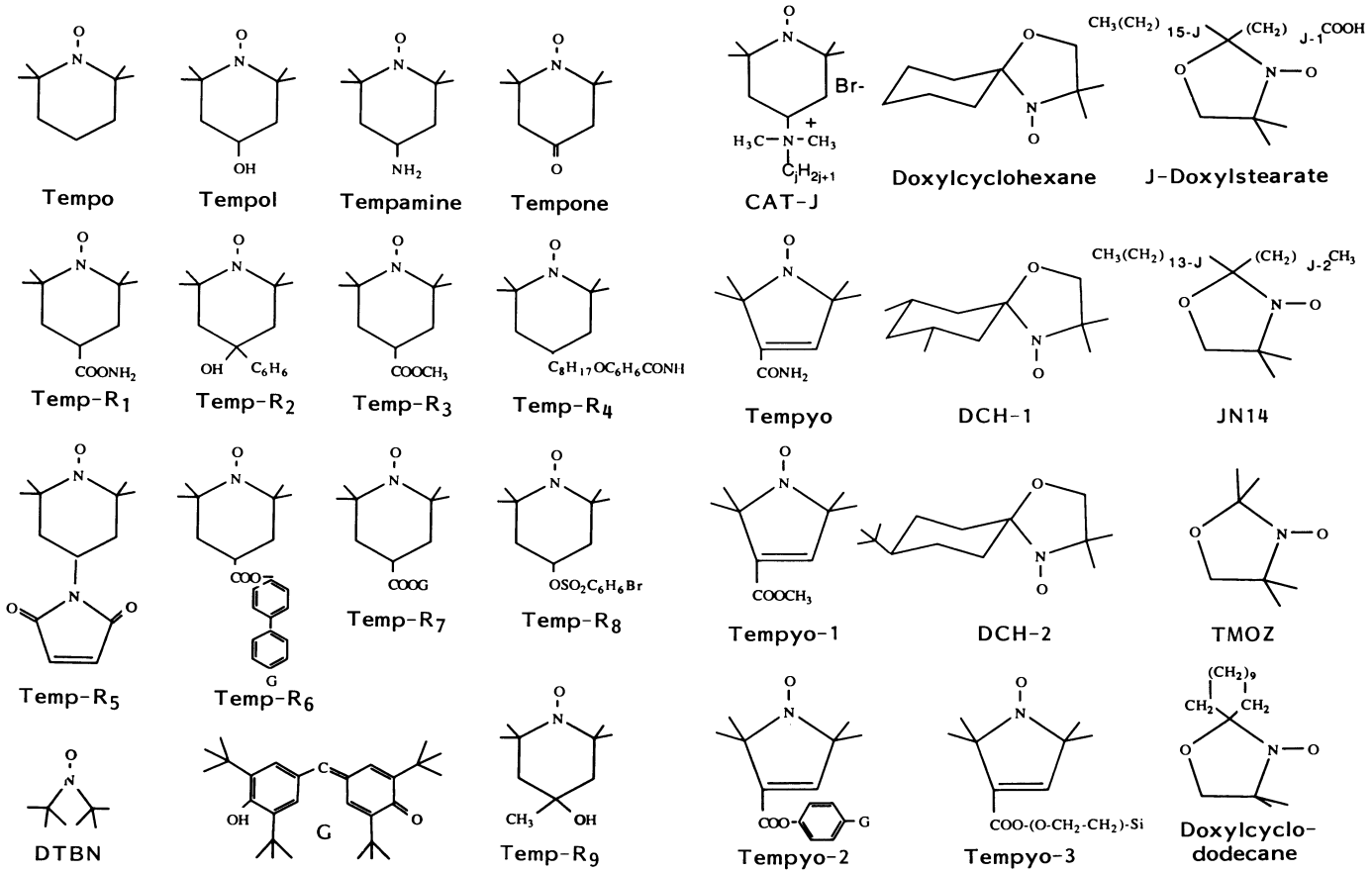

Figure 1. Spin labels discussed in this chapter and their acronyms.

line to be a Gaussian-Lorentzian convolution (Dobryakov and Lebedev, 1969; Lee and Shetty, 1985) or by constructing calibration curves of the intrinsic width as a function of the measured width (Poggi and Johnson, 1970; Chiarelli and Rassat, 1973; Bullock *et al.*, 1975; Ahn, 1976; Lim *et al.*, 1976; Jones and Schwartz, 1981). Unfortunately, since the Gaussian content depends on experimental parameters, one needs a *library* of calibration curves for each label and, if spin exchange occurs, the calibration curves depend on temperature as well. Fortunately, a remarkable mathematical accident discovered by Dobryakov and Lebedev (1969) makes the calibration curves unnecessary. They found a simple relationship between the linewidths of the Gaussian and Lorentzian components and the linewidth of the convolution.

The purpose of this chapter is to provide a practical guide to correct inhomogeneously broadened spin-label spectra. The highest goal would be to present a set of universally applicable correction techniques—i.e., applicable to all spin labels under all conditions based on the four-point method. That goal is unachievable, of course, but we can come surprisingly close. We give detailed estimates of errors and show how to check if the inhomogenous broadening is Gaussian. For a number of spin labels, more precise correction procedures are given in case more accuracy is required.

We treat the situation in which a spin label tumbles in the motional narrowing region either in an isotopic liquid or in a perfectly aligned uniaxial liquid crystal. In this case, in the absence of inhomogeneous broadening, the ESR spectrum consists of three Lorentzian-shaped lines corresponding to the nitrogen quantum numbers $M_I = \pm 1, 0$ if the concentration of spin label is low enough that spin exchange interactions between the labels broaden the individual hyperfine lines less than about $0.3a_N$ where a_N is the isotopic nitrogen hyperfine interaction (Plachy and Kivelson, 1967). We have in mind normal ^{14}N-based spin labels, although almost everything applies to ^{15}N-substituted spin labels. The discussion applies to first-derivative presentation of the ESR spectra. Figure 1 shows the spin labels discussed in this chapter with their acronyms.

2. EXPERIMENTAL DETERMINATION OF HYPERFINE COUPLING CONSTANTS

2.1. NMR and ENDOR

Unresolved hyperfine structure usually dominates the inhomogeneous broadening of spin-labeling spectra, so the relatively high resolution of nuclear resonance methods, NMR and ENDOR, is required to measure the hyperfine coupling constants. The NMR experiment must be carried out at high concentrations (Brière *et al.*, 1967; Kreilick, 1967) and perhaps at high temperature (Windle, 1981) in order to shorten the electron spin-relaxation time. Thus the dependence of the coupling constants on solvent and temperature has been investigated very little by NMR (Brière *et al.*, 1965, 1970). The ENDOR experiment does not have the disadvantage of requiring work at high concentrations, but it is severely limited in temperature range. Finding the number of nuclei with a given coupling constant is not easy in some cases in NMR and is even more difficult in ENDOR, so assignments sometimes have to be made by use of isotopic or chemical substitution (Brière *et al.*, 1967, 1970; Michon and Rassat, 1971; Chiarelli

and Rassat, 1973; Eaton *et al.*, 1980) and/or corroborated by ESR data (Michon and Rassat, 1971; Whisnant *et al.*, 1976; Marriott *et al.*, 1976; Barbarin *et al.*, 1978a, 1978b; Eaton *et al.*, 1980; Labsky *et al.*, 1980; Windle, 1981). Table 1 gives firmly established hyperfine coupling constants measured by NMR and ENDOR for eighteen spin labels. We have used the notation $a(N\mathrm{n})$ to mean the hyperfine coupling constant a, in gauss, due to N equivalent nuclei n and have not indicated the detailed assignments, since this is irrelevant for our purpose. We have taken the liberty to adjust N in some cases where subsequent work has shown that an adjustment is required. The symmetries of DTBN, TEMPONE, and the TEMPYO lead to simple, unambiguous NMR and ENDOR spectra. The NMR spectrum of TEMPO is easily interpreted as well, while the spectra of other piperidine-1-oxyl derivatives are more complex. In the case of TEMPOL, selective deuteration (Brière *et al.*, 1967) has led to a rigorous assignment of the coupling constants based on the NMR alone. The interpretation of the NMR of the other piperidine-1-oxyl derivatives then follows, since the results vary only slightly from label to label (More *et al.*, 1984). It is clear from the limited data in Table 1 that the coupling constants vary with temperature and solvent. In fact, since the coupling constant variations due to temperature and solvent are of the same order as the variations from label to label in the piperidine-1-oxyl family, when we refer to the inhomogeneous broadening of TEMPOL we are referring to quite a large collection of spin labels such as labeled polymers (Miller, 1979; Tsay *et al.*, 1982) and liquid crystal analogs (Jones and Schwartz, 1981), acylating spin label reagents (Morrisett, 1976), etc. The same remark applies to the pyrroline-1-oxyl derivatives, TEMPYO, etc. Thus, even though Table 1 is short, a sizable number of spin labels are, in effect, included.

Doxylcyclohexane is an example of a number of spin labels based on the 1-oxyl-2,2-dimethyloxazolidine moiety in which long-range, relatively large hyperfine couplings are observed. Such labels are the steroid analogs (Michon and Rassat, 1974; Marriott *et al.*, 1976) and doxylcyclododecane (Eaton *et al.*, 1980).

Notably absent from Table 1 are members of the doxyl labeled n-alkyl chains and 2,2,5,5-tetramethylpyrrolidin-1-oxyl-3-carboxylic acid (PCA).

2.2. ESR Simulation

It is important to establish that results from NMR and ESR are in agreement, not only to gain confidence in the interpretation of the data in both methods, but also to establish that simple (secular terms only) first-order fast motion ESR simulations are in agreement with the data. Operationally, such an ESR spectrum may be viewed as a superposition of Lorentzian lines imposed on a regularly spaced map of sticks, the structure of the map being dictated by the coupling constants. Even though one expects differing Lorentzian linewidths due to anisotopic proton hyperfine coupling tensors, this effect seems to be small enough to justify the use of the same Lorentzian linewidth for all of the lines (Poggi and Johnson, 1970; Jolicoeur and Friedman, 1971; More *et al.*, 1984; Ottaviani, 1987).

Figure 2 shows examples of ESR spectra simulated strictly from coupling constants measured by NMR measurements (Figures 2d, f, and g) and with a small additional nitrogen splitting (Figure 2a). In each case the ESR simulation is a simple map of Lorentzians of the same width. Table 2 gives results from a number of other experiments interpreted by ESR simulation. Rigorous comparison between NMR and ESR is not

TABLE 1
Proton Hyperfine Coupling Constants (gauss) for Nitroxide Spin Labels from NMR and ENDOR

Spin label	Solvent	Temp (K)	Coupling constants					Method	Reference
TEMPOL	Toluene	185	−0.464 (6H)	−0.304 (2H)	−0.571 (2H)			ENDOR[a]	Kirste *et al.* (1982)
	DTBN	297	−0.36 (6H)	−0.31 (2H)	−0.48 (2H)	−0.02 (6H)	+0.07 (1H)	NMR	Kopf and Kreilick (1969)
	Benzene	RT	−0.45 (6H)	−0.31 (2H)	−0.48 (2H)	−0.02 (6H)	+0.07 (1H)	NMR	Brière *et al.* (1967)
	Acetone	RT	−0.45 (6H)	−0.21 (2H)	−0.48 (2H)	−0.02 (6H)	+0.07 (1H)	NMR	Brière *et al.* (1970)
TEMPAMINE	Water	363	−0.463 (6H)	−0.315 (2H)	−0.450 (2H)	−0.038 (6H)	+0.088 (1H)	NMR[b]	Windle (1981)
	Neat	333	−0.462 (6H)[b]	−0.30 (2H)[c]	−0.49 (2H)[c]	−0.038 (6H)[b]	+0.093 (1H)[b]	NMR	Labsky *et al.* (1980)
TEMP-R_3	Toluene	185	−0.468 (6H)	−0.037 (2H)	−0.571 (2H)			ENDOR[a]	Kriste *et al.* (1982)
	Benzene	RT	−0.43 (6H)	−0.31 (2H)			+0.08 (1H)	NMR	Brière *et al.* (1967)
TEMP-R_6	Toluene	225	−0.464 (6H)	−0.289 (2H)	−0.550 (2H)			ENDOR[a]	Kirste *et al.* (1982)
TEMP-R_4	EBBA[d]	328	−0.410 (6H)	−0.310 (2H)	−0.490 (2H)			NMR	Barbarin *et al.* (1978b)
	EBBA	363	−0.43 (6H)	−0.310 (2H)	−0.490 (2H)			NMR	Barbarin *et al.* (1978a)
TEMP-R_9	Benzene	RT	−0.40 (6H)	−0.27 (2H)				NMR	Brière *et al.* (1967)
CAT-12	Water	370	−0.425 (6H)	−0.30 (2H)				NMR	Fox (1976)
TEMP-R_2	Acetone	RT	−0.44 (6H)	−0.31 (2H)	−0.50 (2H)	−0.08 (6H)		NMR	Brière *et al.* (1970)
TEMP-R_8	Acetone	RT	−0.41 (6H)	−0.32 (2H)		−0.04 (6H)		NMR	Brière *et al.* (1967)
TEMPO	CCl_4	RT	−0.23 (12H)	−0.39 (4H)	+0.180 (2H)			NMR	Brière *et al.* (1967)
	Methanol	RT	−0.21 (12H)	−0.40 (4H)	+0.200 (2H)			NMR	Brière *et al.* (1967)
	Benzene	318	−0.22 (12H)	−0.39 (4H)	+0.18 (2H)			NMR	Kreilick (1967)
TEMPONE	Toluene	195	−0.107 (12H)					ENDOR[a]	Kirste *et al.* (1982)
	Benzene	318	−0.11 (12H)	−0.01 (4H)				NMR	Kreilick (1967)
	Benzene	RT	−0.12 (12H)	−0.02 (4H)				NMR	Brière *et al.* (1967)
TEMPYO-1	Toluene	185	−0.236 (12H)	−0.521 (1H)				ENDOR[a]	Kirste *et al.* (1982)

TEMPOYO-2	Toluene	225	−0.239 (12H)	−0.493 (1H)			ENDOR[a]	Kirste *et al.* (1982)
DTBN	Methanol		−0.09 (18H)				NMR	Lim *et al.* (1976)
	Neat		−0.107 (18H)				NMR	Hauser *et al.* (1966)
TMOZ	Cl_3CD	RT	−0.12 (6H)	−0.05 (2H)			NMR	Michon and Rassat (1971)
Doxyl-cyclo-hexane	Cl_3CD	RT	−0.12 (6H)	−0.06 (2H)			NMR	Michon and Rassat (1971)
			−0.58 (2H)	−0.68 (2H)	+1.01 (2H)	+0.21 (2H)		
DCH-1	Cl_3CD	RT	−0.13 (6H)	−0.06 (2H)			NMR	Michon and Rassat (1971)
			−0.61 (2H)	−0.70 (2H)		+0.13 (2H)		
DCH-2	Cl_3CD	RT	−0.13 (6H)	−0.05 (2H)			NMR	Michon and Rassat (1971)
			−0.65 (2H)	−0.70 (2H)	1.06 (2H)	+0.17 (2H)		

[a] Error ± 0.004 G.
[b] Error ± 0.001 G.
[c] Error ± 0.01.
[d] Isotropic phase of the nematic liquid crystal *N*-(*p*-ethoxybenzylidene)-*p*-butylaniline.

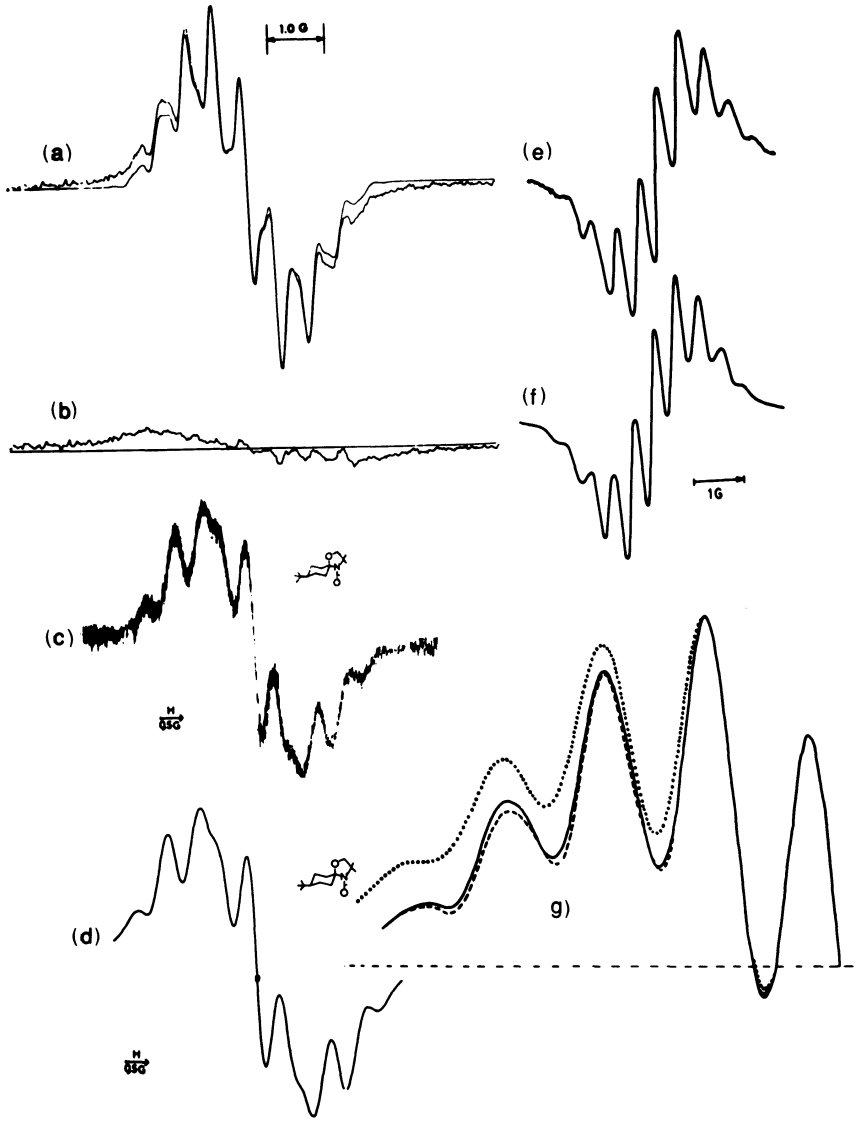

Figure 2. Examples of ESR spectra and their simulations using hyperfine coupling constants derived from NMR data. In each case, the same workers measured both the NMR and ESR which is the $M_I = 0$ multiplet. (a) Simulated and experimental spectra of TEMPAMINE in CCl_4 at 253 K and (b) the difference in the two spectra from (a) (Windle, 1981); (c) experimental and (d) simulated spectra of DCH-1 in chloroform (Michon and Rassat, 1971); (e) experimental and (f) simulated spectra of TEMPAMINE in methanol (Labsky *et al.* 1980), and (g) experimental, simulation · · · 0.446 (12H), and simulation --- 0.410 (6H), 0.310 (2H), 0.490 (2H) spectra of TEMP-R_4 in *N*-(*p*-ethoxybenzylidene)-*p*-butylaniline in the isotropic phase, $T = 363$ K (Barbarin *et al.*, 1978a, b). The ratio $\Delta H^{G}_{pp}/\Delta H^{L}_{pp} \equiv \chi$ is $\chi = 5.6$ in (d) and $\chi = 6.6$ in (f). Reproduced with permission.

possible even when care is taken to use the same solvent and temperature for the two measurements, because the concentration requirements are at two opposite extremes. The same spin exchange that makes the NMR experiment possible tends to collapse the hyperfine structure (Plachy and Kivelson, 1967) in the ESR experiment and this happens at surprisingly small concentrations (Bales and Willett, 1984). Nevertheless, comparison of coupling constants deduced from ESR simulations, given in Table 2, with those in Table 1 firmly establishes that the results are consistent. Resolution enhancement techniques, either in the data-taking process (Mossoba *et al.*, 1984) or by post-experimental techniques (Trousson and Lion, 1985) have further confirmed and refined the coupling constants in some cases. As an example, consider TEMPOL. The hyperfine coupling constants deduced from NMR are not easily assigned from the NMR spectrum alone, but ESR simulation easily distinguished the correct assignment (Table 1) from a plausible but incorrect assignment (Whisnant *et al.*, 1974), the correct assignment being confirmed by selective deuteration (Brière *et al.*, 1967). The examples

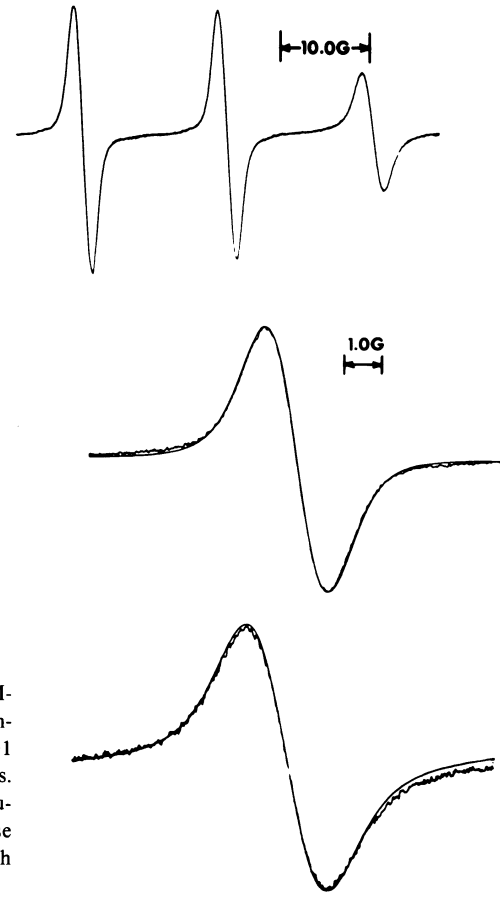

Figure 3. ESR spectra of (a) TEMPAMINE in 1,3-propanediol at room temperature, (b) $M_I = 0$, and (c) $M_I = -1$ experimental spectra and simulations. Hyperfine coupling constants were calculated from those in CCl_4 and water by use of equation (1). (From Windle, 1981, with permission.)

TABLE 2
Hyperfine Coupling Constants (gauss) for Nitroxide Spin Labels from ESR Spectral Simulation

Spin label	Solvent	Temp (K)	Coupling constants							Reference
TEMPOL	Benzene	RT	0.45 (6H)	0.31 (2H)	0.48 (2H)	0.07 (1H)	0.02 (6H)			Whisnant *et al.* (1974)
	CCl_4	295	0.460 (6H)	0.290 (2H)	0.430 (2H)	0.070 (1H)	0.030 (6H)		15.44 (1N)	Windle (1981)
	Water	295	0.440 (6H)	0.360 (2H)	0.450 (2H)	0.150 (1H)	0.060 (6H)		17.13 (1N)	Windle (1981)
	Ethanol	298	0.452 (6H)	0.320 (2H)	0.478 (2H)	0.070 (1H)	0.020 (6H)		16.09 (1N)	Ottaviani (1987)
		278	0.460 (6H)	0.325 (2H)	0.480 (2H)	0.070 (1H)	0.020 (6H)		16.13 (1N)	Ottaviani (1987)
		258	0.470 (6H)	0.333 (2H)	0.480 (2H)	0.080 (1H)	0.020 (6H)		16.15 (1N)	Ottaviani (1987)
	Pyridine	298	0.443 (6H)	0.312 (2H)	0.469 (2H)	0.070 (1H)	0.020 (6H)		15.56 (1N)	Ottaviani (1987)
		278	0.454 (6H)	0.318 (2H)	0.470 (2H)	0.080 (1H)	0.020 (6H)		15.58 (1N)	Ottaviani (1987)
		258	0.460 (6H)	0.322 (2H)	0.473 (2H)	0.080 (1H)	0.020 (6H)		15.60 (1N)	Ottaviani (1987)
TEMPAMINE	CCl_4	295	0.510 (6H)	0.290 (2H)	0.420 (2H)	0.040 (1H)	0.040 (6H)	0.050 (1N)	15.83 (1N)	Windle (1981)
	Methanol	253	0.462 (6H)	0.30 (2H)	0.49 (2H)	0.093 (1H)	0.047 (6H)		16.0 (1N)	Labsky *et al.* (1980)
	1,3-Propanediol	RT	0.467 (6H)	0.304 (2H)	0.436 (2H)	0.068 (1H)	0.040 (6H)	0.088 (1N)	16.33 (1N)	Windle (1981)
	Water	295	0.436 (6H)	0.315 (2H)	0.450 (2H)	0.090 (1H)	0.038 (6H)	0.120 (1N)	16.89 (1N)	Windle (1981)
TEMP-R_5	Sodium phosphate buffer	296	0.434 (6H)	0.182 (2H)	0.528 (2H)					Beth *et al.* (1980)
TEMP-R_4	EBBA	363	0.410 (6H)	0.310 (2H)	0.490 (2H)					Barbarin *et al.* (1978a, b)
TEMP-PROPHYRIN	Toluene		0.455 (6H)	0.295 (2H)	0.48 (2H)	0.08 (1H)	0.02 (6H)			More *et al.* (1984)
TEMPO	Benzene	281	0.23 (12H)	0.39 (4H)	0.18 (2H)					Whisnant *et al.* (1974)
	CCl_4	295	0.230 (12H)	0.390 (4H)	0.180 (2H)				15.63 (1N)	Windle (1981)
	Water	295	0.175 (12H)	0.400 (4H)	0.160 (2H)				17.32 (1N)	Windle (1981)
TEMPONE	CCl_4	295	0.115 (12H)						14.53 (1N)	Windle (1981)
	CCl_4	298	0.10 (12H)							Jolicoeur and Friedman (1971)

	n-butyl alcohol		0.1 (12H)						16.0 (1N)	Poggi and Johnson (1970)
	Water	295	0.060 (12H)						16.13 (1N)	Windle (1981)
	Water	273	0.06 (12H)							Jolicoeur and Friedman (1971)
	Water	373	0.08 (12H)							Jolicoeur and Friedman (1971)
DTBN	Water	258	0.091 (18H)						17.3 (1N)	Ahn (1976)
	Water	290	0.060 (18H)						17.21 (1N)	Windle (1981)
	Water	295	0.060 (18H)						17.14 (1N)	Lim *et al.* (1976)
	Ethylene glycol	253–273	0.08 (18H)						16.28 (1N)	Poggi and Johnson (1970)
	Methanol		0.08 (18H)						16.2 (1N)	Lim *et al.* (1976)
	Isopropyl alcohol	253–273	0.095 (18H)						15.87 (1N)	Poggi and Johnson (1970)
	n-pentane alcohol	189	0.11 (18H)						15.4 (1N)	Plachy and Kivelson (1967)
	n-pentane	189	0.11 (18H)						15.4 (1N)	Plachy and Kivelson (1967)
	Benzene	RT	0.12 (18H)						15.36 (1N)	Faber *et al.* (1967)
	CCl_4	295	0.110 (18H)						15.36 (1N)	Windle (1981)
TEMPYO	CCl_4	295	0.240 (12H)	0.440 (1H)					14.21 (1N)	Windle (1981)
	Water	295	0.200 (12H)	0.350 (1H)					16.07 (1N)	Windle (1981)
	Ethanol	298	0.232 (12H)	0.473 (1H)					15.01 (1N)	Ottaviani (1987)
		278	0.234 (12H)	0.480 (1H)					14.94 (1N)	Ottaviani (1987)
		258	0.235 (12H)	0.490 (1H)					14.91 (1N)	Ottaviani (1987)
	Pyridine	298	0.234 (12H)	0.485 (1H)					14.55 (1N)	Ottaviani (1987)
		278	0.235 (12H)	0.492 (1H)					14.52 (1N)	Ottaviani (1987)
		285	0.235 (12H)	0.508 (1N)					14.49 (1N)	Ottaviani (1987)
DOXYLCYC-LOHEXANE	Cl_3CD	RT	0.12 (6H)	0.07 (2H)	0.58 (2H)	0.68 (2H)	1.01 (2H)	0.21 (2H)		Michon and Rassat (1971)

of Figure 2 include the more complex hyperfine patterns. Fits to simpler labels like DTBN (Poggi and Johnson, 1970; Lim *et al.*, 1976) and TEMPONE (Jolicoeur and Friedman, 1971; Zager and Freed, 1982a, b) are excellent, although slight adjustments of the NMR data are sometimes required, as expected.

2.3. Solvent Dependence of Hyperfine Coupling Constants

Based upon a limited amount of work on the solvent dependence of the proton hyperfine coupling constants (Brière *et al.*, 1967; Lim *et al.*, 1976; Windle, 1981; Ottaviani, 1987), it has been suggested that proton coupling constants are proportional to the nitrogen coupling constant a_N (Windle, 1981).

We may write

$$a_j = \gamma_j a_N + \delta_j \tag{1}$$

for each proton coupling constant a_j and evaluate the constants δ_j and γ_j from measurements carried out in two solvents in which a_N varies significantly. Further work will be required to determine the role that various solvent parameters play (Knauer and Napier, 1976; Reddock and Konishi, 1979; Kamlet and Taft, 1979; Janzen *et al.*, 1982; Mukerjee *et al.*, 1982; Ottaviani, 1987). If equation (1) proves to be true generally, then one may predict the values of the a_j without measuring the polarity of the environment of the spin label.

Windle (1981) shows that equation (1) holds well in some cases for DTBN, and Figure 3 shows an impressive confirmation of the procedure for TEMPAMINE in 1,3-propanediol at room temperature. Windle (1981) calculated the coupling constants from a measurement of a_N using equation (1) and simulated the ESR spectrum in Figure 3 by fixing the a_j and adjusting the intrinsic linewidth. Despite the slight experimental asymmetries, the fit is excellent.

3. GAUSSIAN CONTRIBUTIONS TO SPIN-LABEL LINE SHAPES

First-order ESR simulations using the correct hyperfine coupling constants fit experimental spectra even in the wings of an unresolved spectrum. Is the converse true? Does a simulated ESR spectrum that agrees with experiment give the proper hyperfine coupling constants? As an example let us take the $M_I = 0$ line for TEMPAMINE in 1,3-propanediol at room temperature. Since the simulated spectrum fits well (Figure 3) we will use it as the "correct" spectrum which we plot with a solid line in Figure 4. Figure 4 also shows (dotted lines) a series of ESR spectra computed with incorrect hyperfine patterns, whose parameters are given in Table 3. The correct spectrum looks simple, but it is not, requiring 2646 lines and overnight on a PC to simulate. The number of lines required to simulate the incorrect spectra in Figure 4 is as follows: (a) 882, (b) 45, (c) 315, (d) 105, (e) 1, and (f) 2. (e) is the Voight shape (Section 4), and (f) is a sum of a Lorentzian and a Gaussian line shape. The latter takes a few seconds to compute on a personal computer. Figures 4(a)–(c) are simulated from natural simplifications of the correct hyperfine pattern. The pattern yielding Figure 4(b) is an extreme simplification and that of Figure 4(d) has almost nothing to do with

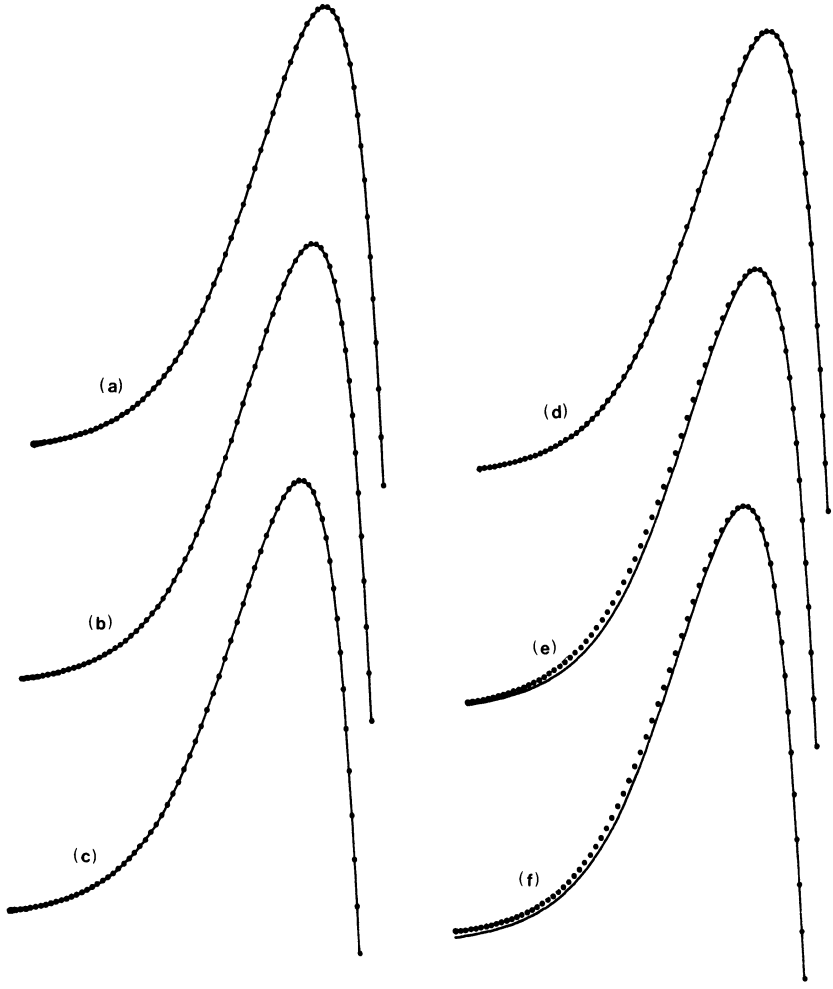

Figure 4. Spectra simulated from the correct (——) and various incorrect parameters (· · ·) for the $M_I = 0$ line of TEMPAMINE in 1,3-propanediol. Simulation parameters are given in Table 3. Spectrum (a) is simulated omitting a small nitrogen hyperfine coupling, placing the residual inhomogeneous broadening into the six small proton couplings. (b) is a severe simplification lumping all the large couplings into eight equivalent protons and all of the rest into four more. (c) maintains the three largest couplings and condenses the rest of the couplings into four equivalent protons. (d) is a fabrication called the "universal nitroxide" that is unrelated, as a pattern, to the correct pattern. (e) is the Voight and (f) is a Gaussian-Lorentzian line shape. Note that (e) and (f) are too high in the wings; they ought to be more Gaussian. In (a)-(f) and in the correct spectrum, $\Delta H_{pp}^{G}/\Delta H_{pp}^{L} \equiv \chi = 1.88$. Despite the wide variety of patterns in (a)-(d) at this value of χ has to look very carefully to distinguish the solid and dotted lines. The Voight (e) and the Gaussian-Lorentzian (f) can be made to fit almost perfectly as well by increasing χ.

TABLE 3
Parameters for the Simulation of the ESR Spectra in Figures 4 and 5[a]

Correct Hyperfine Coupling Constants.[b] Solid Lines in Figures 4 and 5					
0.467 (6H)	0.436 (2H)	0.304 (2H)	0.068 (1H)	0.040 (6H)	0.088 (1N)
Incorrect Hyperfine Coupling Constants. Dotted Lines in Figures 4 and 5					
a	0.467 (6H)	0.436 (2H)	0.304 (2H)	0.068 (1H)	0.071 (6H)
b	0.459 (8H)		0.234 (4H)		
c	0.467 (6H)	0.436 (2H)	0.304 (2H)	0.093 (4H)	
d	0.517 (6H)	0.259 (4H)	0.129 (2H)		
e	Voight Shape[c]				
f	Gaussian-Lorentzian Sum[d]				

[a] All coupling constants and ΔH_{pp}^{G} in gauss. $\Delta H_{pp}^{L} = 0.780$ G (Figure 4) or 0.431 G (Figure 5) in all cases except (f). In all cases except (e) and (f), equation (2) with $\alpha = 1.12$ gives $\Delta H_{pp}^{G} = 1.464$ G.
[b] Correct parameters taken from Table 3 of Windle (1981) appropriate for TEMPAMINE in 1,3-propanediol at room temperature.
[c] Equation (4) or (5) with $\Delta H_{pp}^{G} = 1.464$ G.
[d] Equation (13). The mixing parameter η_A calculated from equation (17) is $\eta_A = 0.663$ (Figure 4) and $\eta_A = 0.500$ (Figure 5).

the correct pattern while Figures 4(e) and 4(f) are even more extreme. Yet, they all fit pretty well. Furthermore, all of them except the last are simulated with the same Lorentzian linewidth ΔH_{pp}^{L} so a simulation of the experimental spectrum by any of them would have led to the correct ΔH_{pp}^{L}. The last simulation Figure 4(f) is a special case treated in Section 5.3 that also gives the same ΔH_{pp}^{L} if the analysis developed in Section 5.3 is applied. The patterns (a)-(d) also have the following in common: the second moments of the hyperfine patterns are the same; the patterns are all fairly complicated, the least number of lines being 45; and none of them has a large coupling to a single proton. Patterns (e) and (f) do not fit as well as (a) through (d) because we have insisted that they have the same Gaussian content as the others. If we *increase* the Gaussian content in (e) and (f) a bit, they fit about as well as the others.

Figure 5 is identical to Figure 4, except the intrinsic width ΔH_{pp}^{L} is decreased until a hint of resolution begins to appear. Figure 5 shows an obvious point, that incorrect patterns do not fit well if ΔH_{pp}^{L} is small enough that resolution begins to appear.

Operationally, a manifold may be thought of as a map of "sticks" upon which a Lorentzian line shape is imposed. The easiest maps to discuss are those produced by N equivalent protons because these are familiar patterns of binomial intensity. Figure 6 shows schematically the pattern due to six equivalent protons and superimposed is a Gaussian curve, illustrating a well-known property of the binomial distribution—that it becomes approximately Gaussian as N gets large (Reif, 1965). Interestingly, N does not have to be so large; already with $N = 6$ the approximation is pretty good. The full width of the Gaussian curve at the point of maximum slope, that is, the peak-to-peak width in a first-derivative curve, is just twice the square root of the second moment of the pattern (Reif, 1965). One could calculate the second moment of the pattern in Figure 6 directly or borrow the result from the one-dimensional random walk (Reif, 1965) to get the second moment $\sigma^2 = N(a/2)^2 = 3a^2/2$. Thus the Gaussian approximation to the pattern has a line width $\Delta H_{pp}^{G} = \sqrt{N}\,a$.

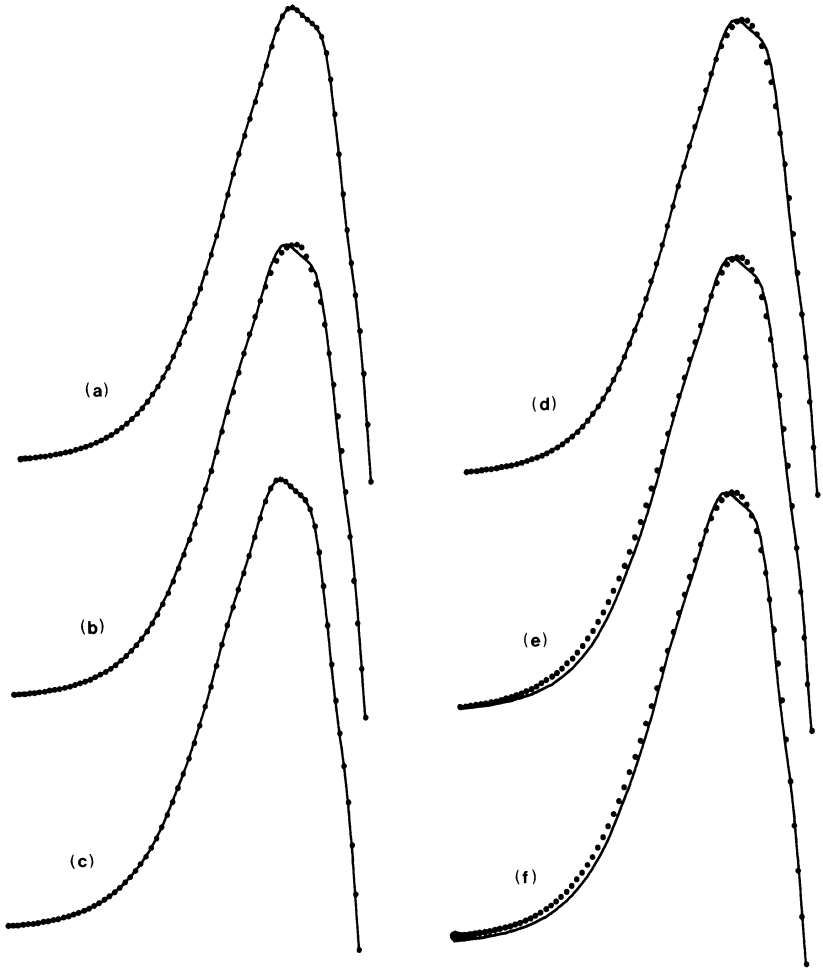

Figure 5. Spectra simulated from the correct (——) and various incorrect parameters (· · ·) for the $M_I = 0$ line of TEMPAMINE in 1,3-propanediol. Spectral simulations correspond to those in Figure 4 except that $\Delta H_{pp}^{G}/\Delta H_{pp}^{L} = \chi = 3.4$. The correct spectrum is not smooth near its peak indicating incipient resolution, thus $\chi = 3.4$ is defined to be χ_{incip} for TEMPAMINE. At values of $\chi > 2$ the severe approximations no longer faithfully reproduce the line but (c) shows that for $\chi \geq \chi_{incip}$ the details of the small couplings are unimportant.

Increasing the number of interacting, equivalent protons makes the Gaussian approximation better, so it is clear that for spin labels like DTBN ($N = 18$) and TEMPONE ($N = 12$) the Gaussian approximation is extremely good.

The more general case involves several sets of equivalent magnetic nuclei. Label each set by $j = 1, 2, \ldots$ and the hyperfine coupling constant of the nuclei in that set by a_j. The EPR spectrum consists of three inhomogeneously broadened nitrogen lines labeled by the nuclear quantum number M_I. One of these lines, which we refer to as a manifold, is a multiplet of $\prod (2N_jI_j + 1)$ lines, where N_j is the number of nuclei and

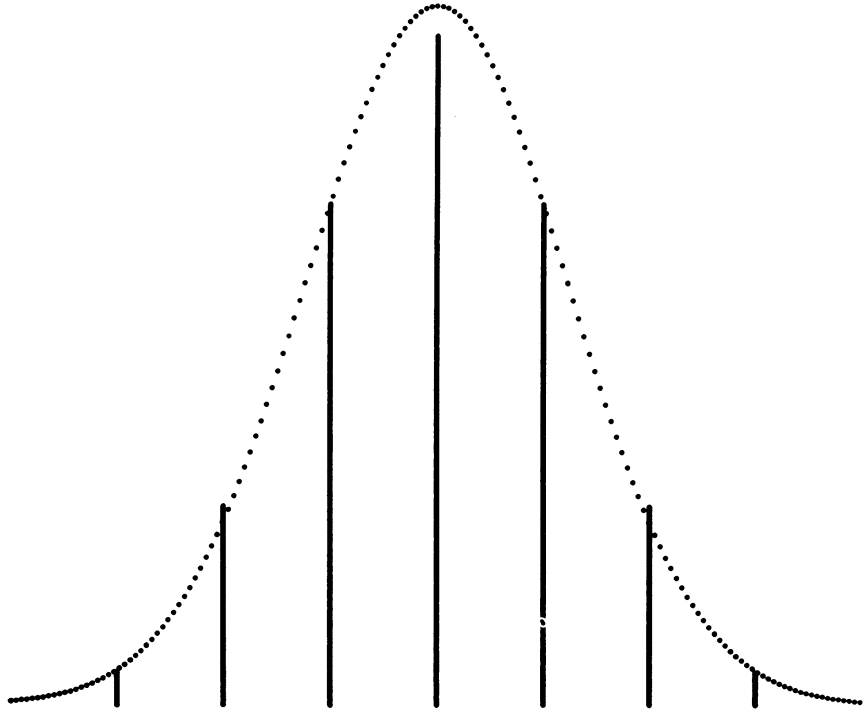

Figure 6. Binomial "stick" pattern for $N = 6$ and a Gaussian curve. Line spacing = a.

I_j the spin of the nuclei in the set j. The second moment of the hyperfine pattern of one manifold is given by $\sum N_j I_j(I_j + 1)a_j^2/3$. If the pattern is nearly Gaussian, then

$$\Delta H_{pp}^{G} = 2[\alpha \sum I_j(I_j + 1)N_j a_j^2/3]^{1/2} \tag{2}$$

• Gaussian Linewidths Add as Sums of Squares •

where the "fudge factor" α takes into account the small difference in the pattern width and the Gaussian width and is near unity. For the spectra in Figure 3, calculation using $\alpha = 1.12$ (Table 4 below) and data in Table 3 gives $\Delta H_{pp}^{G} = 1.46$ G in each case.

One may estimate α for a case in which the spin label contains N equivalent protons. For example, in Figure 6 the lines have relative intensity of 1:6:15:20:15:6:1. The full width at half maximum of the pattern cannot be determined because there is no stick of relative intensity 10, but linear interpolation between the sticks of relative intensities 15 and 6 would place such a stick at $14a/9$ distant from the center so $\Delta H_{1/2}(\text{pattern}) = 28a/9$ while

$$\Delta H_{1/2}(\text{curve}) = \sqrt{2 \ln 2}\Delta H_{pp} = \sqrt{2 \ln 2} \cdot \sqrt{6}a$$

Thus $\alpha \cdot 2 \ln 2 \cdot 6a^2 = (28a/9)^2$, so $\alpha = 1.16$. Similarly it can be shown that the same reasoning gives $\alpha = 1.06$ for DTBN and $\alpha = 1.08$ for TEMPONE. This simple estimate makes no sense if all of the protons are not equivalent and we choose to adjust α to a best fit value for each label. See equation (8) below.

In general, we define the effective hyperfine spacing as

$$a_e = \Delta H_{pp}^G / \sqrt{\alpha N} \tag{3}$$

where $N = \sum N_j$.

Example 1. Dalton *et al.* (1974) proposed that ESR of spin labels in the TEMPOL family could be simulated with $N_1 = 6$, $N_2 = 2$, and $N_3 = 2$ protons with coupling constants of relative magnitude 1 : 1.22 : 0.63. Let us calculate the parameters that would yield a spectrum in good agreement with those in Figure 4. If we call the coupling to the six protons a_1, then the pattern would be a_1 (6H), $1.22a_1$ (2H), and $0.63a_1$ (2H).

$$\Delta H_{pp}^G = \sqrt{\alpha}[6a_1^2 + 2(1.22a_1)^2 + 2(0.63a_1)^2]^{1/2} = 3.31a_1$$

using $\alpha = 1.12$ (Table 4). Setting $\Delta H_{pp}^G = 1.46$ G we calculate $a_1 = 0.441$ G so the pattern would be 0.441 (6H), 0.538 (2H), and 0.278 (2H)—not much different than the pattern in Figure 4(b) and one that fits just as well.

Universal treatment of inhomogeneously broadened spin-label ESR lines depends on the validity of the Gaussian approximation. It is clear, in turn, that the validity depends on the intrinsic width as well as the hyperfine pattern. A natural parameter that describes the relationship between the intrinsic width and the pattern is defined as follows:

$$\chi = \Delta H_{pp}^G / \Delta H_{pp}^L \tag{4}$$

At small values of χ, the Lorentzian width dominates and the pattern is less important. At large values of χ, the line tends to be resolved and the pattern may be important.

The spectra in Figure 4 are at $\chi = 1.88$ and those in Figure 5 at $\chi = 3.4$.

4. THE VOIGHT APPROXIMATION AND A ONE-PARAMETER DESCRIPTION OF LINE SHAPES

If the lines in a pattern are closely spaced and follow a Gaussian profile, then we may approximate the intensities of the Lorentzians with a continuous Gaussian function and, instead of adding the $\Pi(2N_jI_j + 1)$ lines, we integrate (see Figure 7). The intensity at H is found by adding the infinitely-closely spaced Lorentzians at positions H', one of which we indicate in Figure 7. The height of each Lorentzian goes like

$$I(H') \sim \exp(-[H_0 - H']^2/2\sigma^2)$$

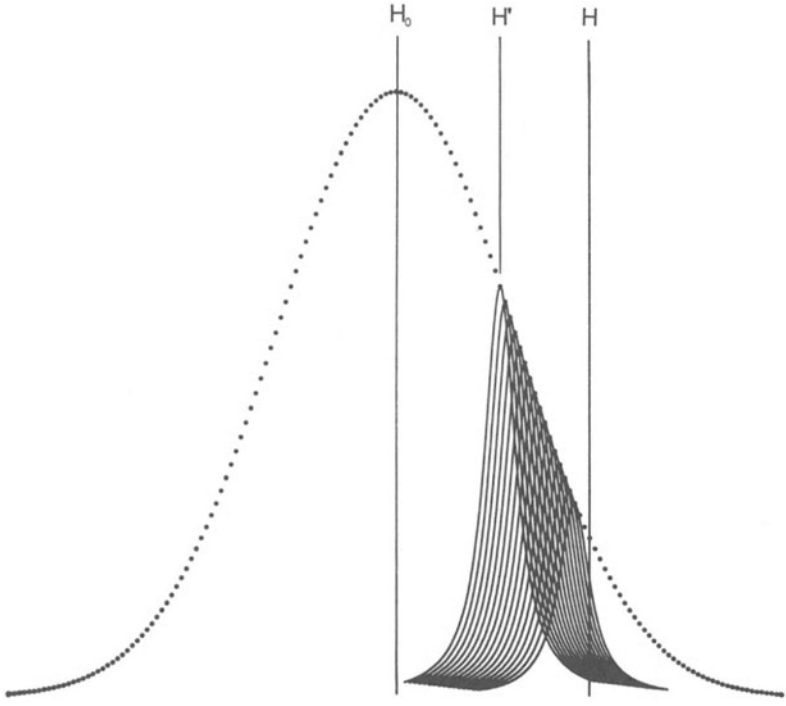

Figure 7. A schematic representation of construction of the Voight shape. Infinitely-closely spaced Lorenzian lines —— at various positions H' have intensities given by the Gaussian envelope · · · . The intensity at H of the Voight line is the sum of the intensities of all of the Lorentzians.

and the intensity of each Lorentzian at point H goes like $I(H')\{1 + [2(H - H')/\Delta H^{L}_{1/2}]^2\}^{-1}$. So the intensity is proportional to

$$^{v}Y(H)\alpha \int \frac{\exp[-(H' - H_0)^2/2\sigma^2]}{1 + \left(\dfrac{H - H'}{\Delta H^{L}_{1/2}/2}\right)^2} dH'$$

with $\sigma = \Delta H^{G}_{pp}/2$ and $\Delta H^{L}_{1/2} = \sqrt{3}\Delta H^{L}_{pp}$. Requiring that $\int_{-\infty}^{\infty} {}^{v}Y(H)dH = A$ where A, the area, is proportional to the number of spins and utilizing the definitions

$$v = \sqrt{2}(H - H_0)/\Delta H^{G}_{pp}, \qquad x = \sqrt{2}(H' - H_0)/\Delta H^{G}_{pp} \qquad \text{and} \qquad \chi = \Delta H^{G}_{pp}/\Delta H^{L}_{pp}$$

we arrive at the normalized Voight function

$$^{v}Y(v) = \frac{2\chi A}{\sqrt{3}\pi^{3/2}\Delta H^{G}_{pp}} \int_{-\infty}^{\infty} \frac{e^{-x^2}\,dx}{1 + \frac{2}{3}\chi^2(v - x)^2}$$

We are interested in the derivative of the absorption, so

$$
\begin{aligned}
{}^{v}Y' &= \frac{d}{dH}\,{}^{v}Y = \frac{\sqrt{2}}{\Delta H_{pp}^{G}}\frac{d}{dv}\,{}^{v}Y(v) \\
&= \frac{2\sqrt{2}\chi A}{\sqrt{3}\pi^{3/2}(\Delta H_{pp}^{G})^2}\int_{-\infty}^{\infty} e^{-x^2}\frac{d}{dv}\frac{1}{1+\frac{2}{3}\chi^2(v-x)^2}\,dx
\end{aligned}
$$

Taking the indicated derivative gives

$$
{}^{v}Y'(v) = [2(2/3\pi)^{3/2}\chi^3 A/(\Delta H_{pp}^{G})^2]\int_{-\infty}^{\infty}\frac{-2(v-x)\,e^{-x^2}\,dx}{[1+2\chi^2(v-x)^2/3]^2} \tag{5}
$$

Recognizing that d/dv may be replaced by $-d/dx$ in the integrand and then integrating by parts gives an alternative expression

$$
{}^{v}Y'(v) = [3(2/3\pi)^{3/2}\chi A/(\Delta H_{pp}^{G})^2]\int_{-\infty}^{\infty}\frac{-2x\,e^{-x^2}\,dx}{1+2\chi^2(v-x)^2/3} \tag{6}
$$

The two alternative expressions for ${}^{v}Y'$ in equations (5) and (6) are presented because equation (5) is more suitable for numerical evaluation at small χ while the other, equation (6), is better at large χ. The reason may be seen by realizing that the integrand of equation (5) is the product of a Gaussian with the first derivative of a Lorentzian while the reverse is true in equation (6). Numerically, it is sounder to have the narrower of the two lines in absorption form and to fix the grid relative to the narrower.

The line shape is determined by the integral in equation (5) or (6) and depends only on χ.

• The Shape of the Voight Depends Only on $\Delta H_{pp}^{G}/\Delta H_{pp}^{L}$ •

The Voight is a simple shape that varies from a Lorentzian at $\chi = 0$ to a Gaussian at $\chi = \infty$. To test if a given hyperfine pattern at a given value of χ is approximately Gaussian is straightforward but tedious, requiring the calculation of an integral for each point in the spectrum. One would calculate ΔH_{pp}^{G} from equation (2), generate a Voight with the proper ΔH_{pp}^{G}, and vary ΔH_{pp}^{L} until the manifold width of the Voight ΔH_{pp}^{0} matched that of the unresolved line. After matching V_{pp} of the two spectra, one would then judge the overall fit by some means. Fortunately, this tedious procedure is unnecessary for three reasons. First, one may take advantage of the simple, accidental relationship discovered by Dobryakov and Lebedev (1969),

$$
(\Delta H_{pp}^{G}/\Delta H_{pp}^{0})^2 + (\Delta H_{pp}^{L}/\Delta H_{pp}^{0}) = 1 \tag{7}
$$

to calculate the proper ΔH_{pp}^{L} eliminating the need to vary this quantity in the search for the correct ΔH_{pp}^{0}. Second, the discovery that a Gaussian–Lorentzian sum approximates a Voight well (Wertheim *et al.*, 1974) reduces tremendously the computation time (Section 5.3). Third, since the Voight is such a simple shape, it is possible to define a line-shape parameter, ψ, that is easy to measure and is a monotonic, sensitive

function of χ. The important line-shape changes occur in the wings of a Voight. We capitalize on the fact that the intensities of first-derivative Gaussian and Lorentzian lines of equal linewidth and height show a variation of almost 15% of V_{pp} at a magnetic field that is $\pm 1.34\,\Delta H^0_{pp}$ distant from the resonance field (Bales, 1982). See Figure 8. We note that the definition of ψ compensates somewhat for a slightly asymmetric spectrum: the contribution to V_w is smaller on one side and larger on the other. For a Gaussian, $\psi^G = 0.067$ and for a Lorentzian, $\psi^L = 0.213$. It is straightforward to compute a series of Voight shapes at different values of χ and measure ψ. The fit of the results to an empirical equation is presented in the next section.

Example 2. Hommel *et al.* (1978) noted that the empirical formula

$$\Delta H^L_{pp} = \Delta H^0_{pp} - 0.68/\Delta H^0_{pp}$$

fits the results of their simulations well for the spin-label TEMPYO-3 in poly(ethylene oxide). Their empirical formula is the same as equation (7) with $\Delta H^G_{pp} = \sqrt{0.68} = 0.82$ G which compares fairly well with $\Delta H^G_{pp} = 0.80$–0.97 G calculated from Windle's (1981) data for TEMPYO in water and CCl_4 (Table 4 below).

It is fortunate that equation (7) is so simple because one may easily algebraically change from one dependent variable to another. Stoneham (1972) has given an accurate relationship between the component linewidths and the convolution linewidth, but it is not as simple as equation (7). It is interesting that the simplicity of equation (7) is a peculiarity of the first-derivative spectrum: more complicated approximate expressions are appropriate for absorption spectra (Lee, 1977). Some useful variations of equation (7) are as follows:

$$\Delta H^0_{pp} = \Delta H^L_{pp}(1 + \sqrt{1 + 4\chi^2})/2 \tag{7a}$$

$$\Delta H^L_{pp} = \Delta H^0_{pp}(-1 + \sqrt{1 + 4\chi^2})/2\chi^2 \equiv Q(\chi)\Delta H^0_{pp} \tag{7b}$$

$$\Delta H^G_{pp} = \Delta H^0_{pp}(-1 + \sqrt{1 + 4\chi^2})/2\chi \tag{7c}$$

$$\chi = (\Delta H^0_{pp}/\Delta H^G_{pp} - \Delta H^G_{pp}/\Delta H^0_{pp})^{-1} \tag{7d}$$

$$\Delta H^L_{pp} = \Delta H^0_{pp}[1 - (\Delta H^G_{pp}/\Delta H^0_{pp})^2] \tag{7e}$$

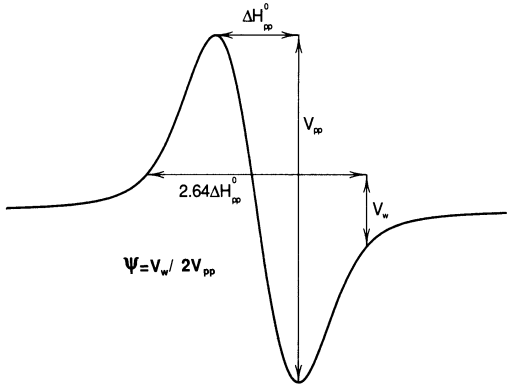

Figure 8. Definition of the line-shape parameter ψ. Note that for slight spectral asymmetries the value of V_W is compensated somewhat, being larger on one side and smaller on the other.

In effect, we now describe a Voight line by the experimentally accessible parameters: ΔH^0_{pp}, ψ, and V_{pp} instead of χ, ΔH^L_{pp}, and A. We refer to a line as "being a good Voight" if the unresolved hyperfine structure gives an approximately Gaussian profile.

5. LINE-SHAPE COMPARISONS

5.1. Unresolved Hyperfine Multiplets

Having adopted ψ as the line-shape parameter for the Voight, we now do the same for unresolved hyperfine multiplets. We sum the Lorentzian lines imposed on the hyperfine pattern map and ask the computer to find ΔH^0_{pp}, ψ, and V_{pp} vs. the input hyperfine constants ΔH^G_{pp}, ΔH^L_{pp}, and doubly integrated intensity A which is fixed at unity. For each pattern, at a certain value of $\chi = \chi_{incip}$ and higher, incipient structure begins to appear. The value of χ_{incip} is judged by eye from plots. For example, the simulated TEMPAMINE spectrum in Figure 5 is at $\chi_{incip} = 3.4$. Table 4 gives values for χ_{incip} and the parameter α of equation (2). This latter parameter was adjusted to give the best fit to equation (8) over the range $\chi = 0$ to $\chi = \chi_{incip}$,

$$\alpha = \frac{(\Delta H^0_{pp})^2 - \Delta H^L_{pp}\Delta H^0_{pp}}{4\sum I_j(I_j+1)N_j a_j^2/3} \tag{8}$$

where ΔH^0_{pp} is the simulated manifold width, and all other quantities are input parameters. If equations (2) and (7) were perfect, α would be of order unity and constant for all values of χ. The errors quoted in Table 4 are the standard deviations from the mean value of α in each case and show how remarkably well equations (2) and (7) represent the hyperfine multiplets of the spin labels of Table 4.

Is ψ a sensitive, monotonic function of χ for hyperfine multiplets as it was for a Voight? To what extent is ψ vs. χ the same for all spin labels? Figure 9 gives the answers. Plotted in Figure 9 is ψ vs. χ for the spin labels of Table 4, which effectively

TABLE 4
Gaussian Linewidths and the Parameters $\sqrt{\alpha}$ and χ_{incip}[a]

Spin label	ΔH^G_{pp} water	ΔH^G_{pp} CCl_4	$\sqrt{\alpha}$	χ_{incip}
TEMPO	1.07	1.19	1.04 ± 0.02	3.5[b]
TEMPONE	0.215	0.412	1.03 ± 0.04	2.3[c]
TEMPAMINE	1.41	1.53	1.06 ± 0.07	3.4[b]
DTBN	0.260	0.476	1.02 ± 0.01	2.4[c]
TEMPYO	0.802	0.973	1.03 ± 0.02	2.5[c]
TEMPOL	1.42	1.40	1.04 ± 0.03	2.6[c]

[a] ΔH^G_{pp} in gauss computed from equation (2) using data from Windle (1981).
[b] ±10% depending on solvent.
[c] ±5%.

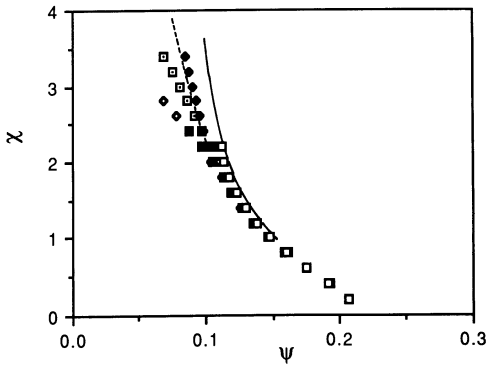

Figure 9. $\chi = \Delta H^G_{pp}/\Delta H^L_{pp}$ vs. ψ for DTBN, □; TEMPONE, ■; TEMPOL, ◇; TEMPYO, ◘; TEMPO, ◆; and TEMPAMINE, ⊡ in water at 295 K. The Voight (solid line) and universal (dashed line) shapes are shown.

covers all of the spin labels of Table 2 except for the doxyl labels. The Voight shape is represented by the solid line, and a model pattern that we call the "universal nitroxide," described below, by the dashed line. In every case except DTBN, χ is plotted up to χ_{incip} where an obvious onset of resolution begins to occur. Figure 9 encapsulates why one can handle inhomogeneous broadening of spin labels as a general problem by measuring only four points on the ESR line—all of the labels give a similar value of χ for a given value of ψ up to $\chi \sim 2.0$. TEMPAMINE and TEMPOL deviate to low χ with respect to TEMPO and the universal nitroxide. The Voight shape, for a given value of χ, gives a higher ψ (higher wings), a property evident in Figure 4. Thus all nitroxides, considered (and hundreds more not shown in Figure 9) real and contrived, behave the same until χ is large. At large χ, small errors in ψ give large errors in χ because the slope of the curves in Figure 9 become large.

5.2. A Universal Nitroxide

The results of Figure 9 motivate the development of a "universal nitroxide" that can be studied in detail and used to correct all inhomogeneously broadened spin-label spectra. One could select one of the known patterns, say that for TEMPO or TEMPAMINE, to fulfill that role except that unresolved spectra with line shapes of relatively high χ—well beyond χ_{incip} for the known labels—are observed for doxyl-labeled normal alkyl chains (Bales *et al.*, 1987a). One strategy to "fabricate" hyperfine patterns that are unresolved at high χ is to use coupling constants a_1, $0.5a_1$, $0.25a_1$, etc. because the next successive group of sticks in the hyperfine pattern map "fills the holes." There are as many ways to simulate a spectrum of a given ΔH^G_{pp} as there are solutions to equation (2)—that is, limitless—and we have calculated more than 100 of these. Table 5 gives a sample of such patterns. Patterns 1 and 4 are variations involving different multiples of the fundamental coupling constant than the "hole filling" scheme. All of the patterns produce spectra that remain unresolved to χ_{incip} larger than 4, and patterns 2, 3, and 7 remain so to $\chi_{incip} \sim 6$. One certainly expects that at high χ the simulated spectra would be sensitive to the pattern, and this is so, but much less so than we had anticipated: a plot of ψ vs. χ (not shown) is very similar to Figure 9. We choose pattern 7 to be the universal nitroxide. It gives values of χ for a given ψ about

TABLE 5
Hyperfine Coupling Constants (gauss) giving Hyperfine Patterns Designed to be Unresolved at High χ

Pattern number	Coupling constants				Number of lines[a]	ΔH_{pp}^{G}
1	a_1 (3H)	$0.67a_1$ (3H)	$0.33a_1$ (3H)	$0.22a_1$ (3H)	256	$2.35a_1$
2	a_1 (12H)	$0.50a_1$ (4H)	$0.25a_1$ (2H)		195	$3.88a_1$
3	a_1 (6H)	$0.50a_1$ (2H)	$0.33a_1$ (6H)		147	$2.86a_1$
4	a_1 (4H)	$0.50a_1$ (6H)	$0.25a_1$ (2H)		105	$2.54a_1$
5	a_1 (2H)	$0.50a_1$ (4H)	$0.25a_1$ (6H)		105	$1.97a_1$
6	a_1 (2H)	$0.50a_1$ (6H)	$0.25a_1$ (4H)		105	$2.07a_1$
7[b]	a_1 (6H)	$0.50a_1$ (4H)	$0.25a_1$ (2H)		105	$2.86a_1$
8	a_1 (3H)	$0.50a_1$ (3H)	$0.25a_1$ (3H)		64	$2.12a_1$

[a] Number of lines in one nitrogen manifold.
[b] Designated as the "Universal Nitroxide."

midway between the extremes of patterns 1-8 and is unresolved until $\chi = 6$. The number of protons corresponds to the probable number interacting with the unpaired electron in doxyl-labeled *n*-alkyl chains, the only case in which unresolved spectra of high χ are observed, as far as we know.

The solid line, derived from the Voight shape, is given by the empirical equation

$$\chi_{\text{Voight}} = \frac{-0.3336\psi^2 + 0.2526\psi - 0.0392}{\psi^2 - 0.3185\psi + 0.0168} \tag{9}$$

and the dashed line, derived from the universal shape, is given by

$$\chi_{\text{universal}} = \frac{-0.7624\psi^2 + 0.4091\psi - 0.0527}{\psi^2 - 0.2591\psi + 0.0075} \tag{10}$$

Equations (9) and (10) are approximately universally applicable, as is evident from Figure 9. To test their fidelity, we turn to simulated spectra of spin labels of known hyperfine structure. The computer measures ΔH_{pp}^{0} and ψ. Equations (9) and (10) give approximate values of χ which are used together with ΔH_{pp}^{0} in equations (7b) and (7c) to yield approximations to ΔH_{pp}^{L} and ΔH_{pp}^{G}. Both equations (9) and (10) are very accurate at small χ, which one expects since they are very similarly constructed at small χ (Figures 6 and 7), but the universal shape is superior at large χ. For example, the results from equations (9) and (10) are compared at $\chi = 2.0$ in Table 6. The universal shape is much better and accurate enough for most work up to $\chi = 2$. It is important to keep in mind that using no corrections at $\chi = 2$ gives an error in ΔH_{pp}^{L} of about 160%, so using the Voight is a lot better than doing nothing. At higher values of χ the universal shape is even better than the Voight. This is not to say that one can fit a spectrum better with a universal shape than a Voight shape. That is not so. The point is that the values of ΔH_{pp}^{L} and ΔH_{pp}^{G} are much better predicted with the former.

TABLE 6
Errors in Linewidth Determinations Based on the Voight [Equation (9)] and Universal Nitroxide [Equation (10)] Shapes ($\chi = 2.0$)

Spin label (solvent)	Error[a] in ΔH_{pp}^{L} (%)		Error[a] in ΔH_{pp}^{G} (%)	
	Voight	Universal	Voight	Universal
TEMPAMINE (H_2O)	+25	−1	−5	+1
TEMPAMINE (CCl_4)	+27	0	−6	0
TEMPO (H_2O)	+26	−1	−7	−1
TEMPO (CCl_4)	+18	−5	−4	+2
TEMPYO (H_2O or CCl_4)	+19	−4	−6	0
TEMPOL (H_2O or CCl_4)	+32	+2	−9	−3
TEMPONE (solvent independent)	+29	0	−9	−2
DTBN (solvent independent)	+11	−8	−4	+2

[a] Error = 100 × (calculated value − true value)/true value, where the calculated value is from equations (7b) and (7c) using χ calculated from equation (9) or equation (10).

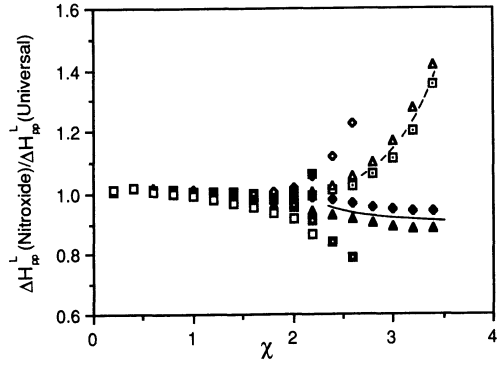

Figure 10. The ratio of the true intrinsic linewidth, ΔH_{pp}^{L} (Nitroxide), to the approximate intrinsic linewidth calculated from equation (10), ΔH_{pp}^{L} (Universal), vs. χ. The symbols have the same meaning as in Figure 9 with the addition here of TEMPO, ▲ and TEMPAMINE, △ in CCl_4 at 295 K. The variation of the positions of the points for the other spin labels from water to CCl_4 is less than the size of the symbols, so only the values in water are plotted. The solid line is a plot of equation (11) for TEMPO and the dashed line for TEMPAMINE. Plots of equation (11) for the other labels pass through the points with high precision and are not shown.

The results of corrections based on equation (10) for six spin labels from $\chi = 0$ to $\chi = \chi_{incip}$ are given in Figure 10. The results for DTBN and TEMPONE are solvent-independent, since changing solvents is just a matter of scaling ΔH^L_{pp} to arrive at the same χ and the same shape. For other labels one expects to be able to scale only if the ratios between the various a_j are constant. This is only approximately so for TEMPYO and not so for TEMPOL; nevertheless, the results for these two labels are virtually identical in water and carbon tetrachloride. The solvent dependence for TEMPO and TEMPAMINE is also small, as shown in Figure 10. Thus one may formulate more precise correction procedures at high χ for spin labels of known hyperfine structure that are approximately solvent-independent. We write precise corrected intrinsic linewidths as follows:

$$\frac{\Delta H^L_{pp}(\text{Nitroxide})}{\Delta H^L_{pp}(\text{Universal})} = A_0 + A_1\chi + A_2\chi^2 + A_3\chi^3 \tag{11}$$

where the coefficients are given in Table 7 and χ is first evaluated from equation (10). The accuracy of equation (11) is limited by the resolution in the computer simulations, which was $\Delta H^0_{pp}/2000$, i.e., much better than is experimentally achievable for spin labels DTBN, TEMPONE, TEMPOL, and TEMPYO, and is limited by the solvent dependence in TEMPO (±3% for $\chi = 2$ to 3.4) and TEMPAMINE (±4% for $\chi = 2$ to 3.4). Except for DTBN, the limit of applicability for equation (11) is evident without measuring ψ—one can immediately recognize that the line is not smooth in the regions of the peaks. The solid line in Figure 5 is such a case; however, one may still use equation (11) to high precision. The use of equation (11) does not require constancy of the a_j. The only requirement is that the pattern not alter more than the change involved in changing the solvent from CCl_4 to water.

Whether equation (11) is worth the extra work depends on the label used, the precision in the measurements, and the range of χ. Below $\chi = 2.0$ it is probably not justified except, perhaps, for DTBN. For TEMPO in water, equation (10) is better than equation (11).

5.3. Gaussian–Lorentzian Sum Approximations

Wertheim *et al.* (1974) found that the sum of a Gaussian and a Lorentzian closely approximated a Voight line shape. By finding a least-squares fit of the sum function

TABLE 7
Coefficients in Equation (11)

Spin label	A_0	A_1	A_2	A_3	Maximum χ
TEMPO	1.01	0.026	−0.031	0.0043	3.4
TEMPONE	0.98	0.175	−0.232	0.0762	2.2
TEMPAMINE	0.96	0.202	−0.197	0.0506	3.4
TEMPOL	0.97	0.211	−0.249	0.0785	2.6
DTBN	1.02	−0.032	0.022	−0.0170	2.2
TEMPYO	1.03	−0.084	0.113	−0.0450	2.6

to the Voight function, they were able to generate curves that related the mixing coefficient to the physically significant Voight parameter χ. The fact that a Voight may be so approximated (even though the sum does not make sense—one sums two lines each having widths equal to one another and equal to the envelope width) is important, because the sum may be computed a factor of 100–1000 times faster for a typical line depending on the number of points required. Moreover, the literature is filled with spectra simulated with the sum function. Our task is to relate the mixing coefficient in the sum function to the physically meaningful parameter χ.

Actually, there are two differences between what we present and the presentation of Wertheim *et al.* (1974). First, we are interested in first-derivative spectra so we add Gaussians and Lorentzians of equal peak-to-peak derivative linewidths, which is different than adding absorption spectra of equal half-widths. Second, we match the sum function and the Voight at the magic four points; that is, we set $\psi_{\text{voight}} = \psi_{\text{sum}}$ rather than find the least-squares fit—a procedure that gives about the same discrepancy as that between the sum and Voight intrinsically, and certainly much less than the discrepancy between a Voight and any real experimental spectrum.

There is one complicating issue. What does one mean by η percent Lorentzian in the sum function? The two most reasonable interpretations would be that η would refer to (1) doubly integrated intensities or (2) peak heights. Other interpretations are possible as well. Unfortunately authors do not always specify what is meant, so we work out both cases (1) and (2).

Using η_H to refer to the line-height interpretation and η_A the doubly integrated intensity (area) interpretation, the sum functions may be written in the form

$$ {}^{S}Y'_{H} = \eta_H \frac{8V_{pp}\xi}{[3+\xi^2]^2} + (1-\eta_H)\frac{\sqrt{e}}{2} V_{pp}\xi e^{-\xi^2/2} \tag{12} $$

and

$$ {}^{S}Y'_{A} = \eta_A \frac{8\sqrt{3}}{\pi(\Delta H^0_{pp})^2} \frac{\xi}{[3+\xi^2]^2} + (1-\eta_A)\frac{4}{\sqrt{2\pi}(\Delta H^0_{pp})^2} \xi e^{-\xi^2/2} \tag{13} $$

where $\xi = 2(H - H_0)/\Delta H^0_{pp}$. The doubly integrated intensity of ${}^{S}Y'_{A}$ is unity and of ${}^{S}Y'_{H}$ is proportional to $(\Delta H^0_{pp})^2 V_{pp}$, the proportionality depending on the line shape. We may find ψ for the function ${}^{S}Y'_{H}$ by setting $H - H_0 = 1.32\Delta H^0_{pp}$ (i.e., $\xi = 2.64$) in order to evaluate V_w and calculate $\psi = V_w/2V_{pp}$. For ${}^{S}Y'_{A}$, one must first find the peak height V_{pp} by setting $\xi = 1$. Then we find V_w by setting $\xi = 2.64$ and calculate $\psi = V_w/2V_{pp}$. These computations give

$$ \psi_A = \frac{0.129 - 0.012\eta_A}{1.936 - 1.384\eta_A} \tag{14} $$

and

$$ \psi_H = 0.146\eta_H + 0.066 \tag{15} $$

6. CORRECTING THE LINEWIDTH OF AN INHOMOGENEOUSLY BROADENED LINE

6.1. Known Hyperfine Coupling Constants

If one is sure that there is no label-label spin exchange and one knows the coupling constants, correcting inhomogeneously broadened lines to first order is trivial. One measures ΔH^0_{pp} and uses equation (7e) to obtain ΔH^L_{pp} (see Figure 11). Nevertheless, we recommend that all linewidths be measured using four points as if the coupling constants were not known, according to the scheme given in Figure 11. It is not much more work and one has an internal consistency check that would uncover unsuspected spin exchange, coupling constant temperature-dependence, partial spin-label orientation, etc. There are cases in which the four-point method is not applicable. Examples are: (a) linewidth data previously reported but not corrected, (b) ESR spectra of spin labels partitioned between aqueous and lipid phases in which the linewidths of the two high-field lines corresponding to the two phases are accessible but the wings are not, (c) spectra which suffer overlap with other spectra.

Example 3. Solvent Dependence of ΔH^G_{pp}. Assuming that equation (1) proves to be generally true for spin labels, in cases in which ψ may not be measured, one may estimate ΔH^G_{pp} from a measurement of a_N which normally is easy to measure. Thanks to Windle's work, we may evaluate the constants δ_j and γ_j for six important spin-label types. Substitution of equation (1) into equation (2) gives an expression for $(\Delta H^G_{pp})^2$ that is quadratic in a_N and whose coefficients are the functions of the γ_j and δ_j. For

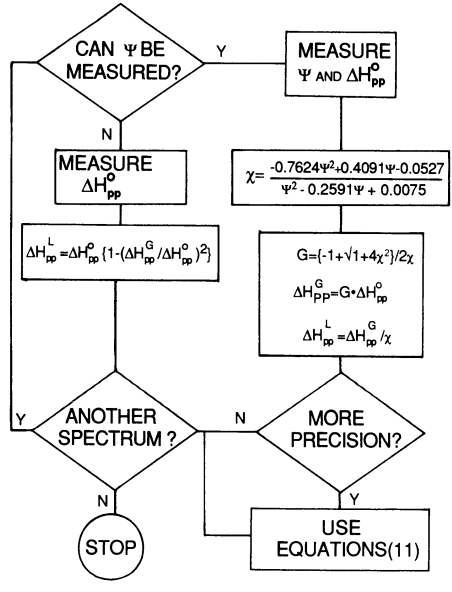

Figure 11. Scheme to correct the linewidths if the hyperfine patttern is known. If ψ can be measured, we recommend doing so, treating the data as if the pattern were unknown in order to detect unsuspected variations in ΔH^G_{pp}. The option to use equation (11) for more precision is available if the experimental results justify their use.

the six spin labels measured by Windle (1981), with only a slight loss in precision, ΔH_{pp}^{G} may be written in the simpler form

$$\Delta H_{pp}^{G} = Da_N + E \tag{16}$$

The discrepancy between equation (16) and the more rigorous quadratic equation is 1% for TEMPO, $\frac{1}{2}$% for TEMPYO, TEMPAMINE, and TEMPOL, and is exactly equivalent to the quadratic for any spin label of fully equivalent protons, such as DTBN and TEMPONE. The coefficients in equation (16) evaluated from Windle's (1981) data are given in Table 8.

Ottaviani (1987) has investigated the solvent dependence of the proton hyperfine coupling constants for TEMPOL and TEMPYO in ethanol and pyridine (Table 2). For TEMPOL, the detailed dependence of a_j on a_N is different than that of Windle (1981) but the dependence of ΔH_{pp}^{G} agrees well. Perhaps the differences in the individual coupling constants are a matter of the lack of uniqueness of these parameters in a successful fit. For TEMPYO, Ottaviani's (1987) results differ significantly from those of Windle (1981), even for ΔH_{pp}^{G}, so caution is in order when employing Table 8 in the case of TEMPYO.

Ottaviani (1987) and Hyde and Subczynski (1984) also reported temperature dependence of the proton coupling constants.

Clearly, a lot more work will be required before one may feel confident that ΔH_{pp}^{G} is "known."

Example 4. Dependence of ΔH_{pp}^{G} on Spin-Label Alignment in an Ordered Fluid. The anisotropy of the proton hyperfine coupling leads in general to a quantity ΔH_{pp}^{G} that depends on the orientation of the label with respect to the magnetic field (Polnaszek and Freed, 1975; Bales *et al.*, 1984). Figure 13 shows results (Bales *et al.*, 1984) derived from ESR spectra of DTBN in the nematic liquid crystal *N*-(*p*-methoxybenzylidene)-*p*-butylaniline (MBBA). Measuring ψ and ΔH_{pp}^{0} and following the procedure in Figure 11 gave ΔH_{pp}^{G}, from which a_e was calculated using equation (3). DTBN is almost spherical and therefore shows only a small alignment (Bales *et al.*, 1984), and yet the change in a_e below the transition temperature of 44 °C is dramatic.

TABLE 8
Calculation of ΔH_{pp}^{G} (gauss) from a Measurement of a_N Using $\Delta H_{pp}^{G} = Da_N + E$ at $T = 295$ K[a]

	D	*E*
TEMPO	−0.0710	2.310
TEMPONE	−0.1232	2.202
TEMPAMINE	−0.1074	3.226
TEMPOL	0.0117	1.220
TEMPYO	−0.0927	2.303
DTBN	−0.1169	2.270

[a] a_N and E in gauss.

6.2. Unknown Hyperfine Coupling Constants

In a sense, most experiments fall into this category—even those involving the spin labels of Table 8—since ΔH_{pp}^{G} varies with different experimental parameters. Thus it makes sense to approach each spectrum as if it were due to a spin label of unknown ΔH_{pp}^{G} and use Table 8 as a consistency check. The procedure is summarized in Figure 12.

We first determine if the unresolved line is approximately a Voight. In most cases this needs to be established only once during an experiment, except for exceptional cases when relatively large long-range couplings are manifest under some experimental conditions. For example, at 202 K in 1:1 pentane:isopentane solvent, the ESR of doxylcyclododecane shows a 2.0 G coupling to a single proton that disappears at high temperature (Eaton *et al.*, 1980). At 432 K, the $M_I = 0$ resonance line is a good Voight but at low temperature it obviously is not, so one would have to make several checks in a variable-temperature experiment. These cases are rare—they seem to occur mostly for doxyl-labeled cyclic compounds (Michon and Rassat, 1971; Marriott *et al.*, 1976; Eaton *et al.*, 1980).

The easiest way to determine if a line is approximately Voight is to measure ψ, use the inverse of equation (14),

$$\eta_A = \frac{0.1292 - 1.936\psi}{0.0120 - 1.384\psi} \tag{17}$$

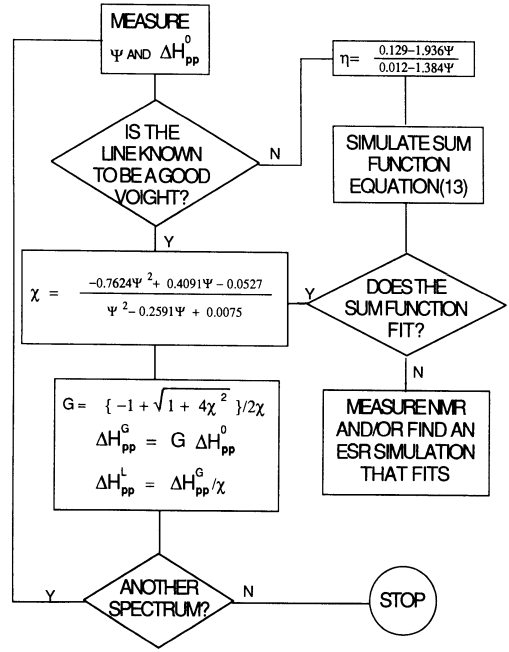

Figure 12. Scheme to correct the linewidth and/or find the Gaussian content of an ESR line if the coupling constants are unknown. The procedure is recommended whenever ψ may be measured.

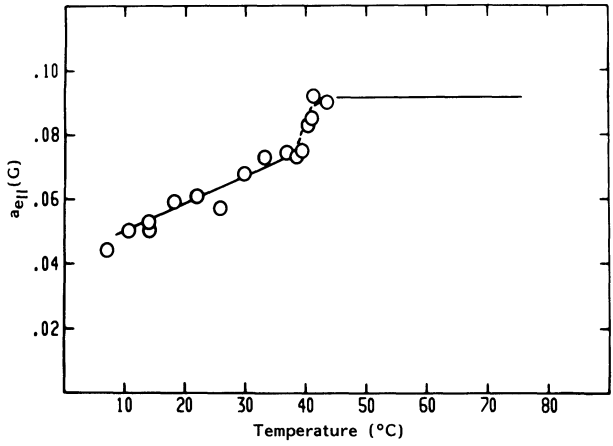

Figure 13. Variation of the effective proton hyperfine coupling constant with spin label DTBN alignment in the nematic liquid crystal MBBA. (From Bales *et al.*, 1984, with premission.)

and simulate the sum function equation (13). If the simulation fits, this means that the line is approximately a Voight and χ may be calculated from equation (10).

Example 5. Figure 14 shows three runs of the spectrum of the $M_I = 0$ line of 5-doxylstearic acid in methanol at 1 °C. The hyperfine pattern of this spin label is unknown. Following the scheme outlined in Figure 12 we measure $\Delta H_{pp}^G = 0.946$ G and $\psi = 0.094$. Equation (17) gives $\eta_A = 0.424$ and the overlaid dotted line is a plot of the sum function equation (13). The experimental spectrum shows a slight asymmetry, but it is clear that it is a good Voight shape. Substituting $\psi = 0.094$ into equation (10) gives $\chi = 2.61$ and equations (7b) and (7c) give $\Delta H_{pp}^L = 0.299$ G and $\Delta H_{pp}^G = 0.783$ G. Checks at other temperatures and in liquid-crystal solvents in which the spin label is partially aligned and for the entire series JN14, $J = 1, 2, \ldots, 7$ (Figure 1) in various solvents show that these type doxyl-labeled n-alkyl chains are good Voights in general.

To get an idea of the random errors involved in the procedure, ten spectra taken with the same sample of 5-doxylstearic acid in methanol were measured and the data treated as above. The results are $\Delta H_{pp}^G = 0.780 \pm 0.012$ G and $\Delta H_{pp}^L = 0.304 \pm 0.019$ G, where the errors are the standard deviations in the ten χ measurements. The reproducibility in ΔH_{pp}^G is excellent but, inevitably at high χ, the random error in ΔH_{pp}^L is somewhat larger—about 6% in this case. In addition to random errors, one worries about the systematic error involved in ΔH_{pp}^L for spin labels of unknown hyperfine pattern. One way to estimate this is to ask what would result if you used the various patterns of Table 5 and known hyperfine patterns to analyze 5-doxylstearate in methanol. Table 9 gives the results. Using eleven different patterns to analyze 5-doxylstearate in methanol gives $\Delta H_{pp}^G = 0.763 \pm 0.020$ G and $\Delta H_{pp}^L = 0.330 \pm 0.032$ G. Note that the Voight gives results more than three standard deviations away from the patterns. Thus the Gaussian and Lorentzian linewidths are uncertain by about 3% and 10% respectively owing to ignorance of the hyperfine pattern. In most cases one is more interested in *relative* values of ΔH_{pp}^L in which case using one fixed pattern, say equation (10), is

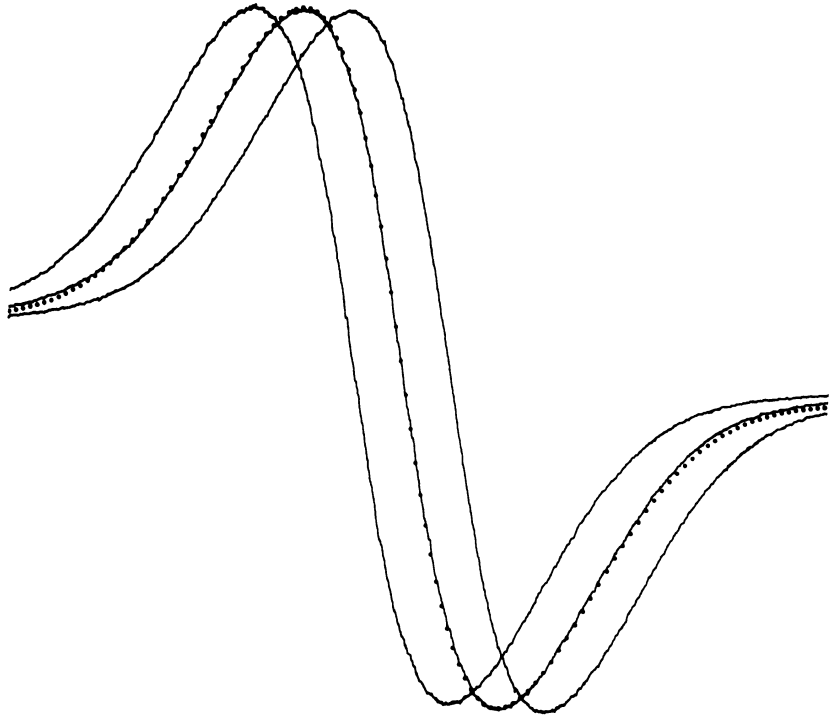

Figure 14. Experimental spectra of the $M_I = 0$ line of 5-doxylstearate in methanol at 1.0 °C. The dots are a sum function with $\eta_A = 0.424$ calculated from equation (17) using the measured $\psi = 0.094$. Despite a slight asymmetry, the experiment line is a good Voight. The linewidth $\Delta H^0_{pp} = 0.95$ G.

expected to give results whose uncertainty is dominated by the reproducibility in the measurement of ψ.

In summary, ΔH^L_{pp} for 5-doxylstearate in methanol at 1.0 °C is uncertain by about 6% due to the reproducibility of the measurements, by about 10% due to ignorance of the hyperfine pattern, and would be in error by 200% if we made no corrections.

It would obviously be better if the hyperfine patterns of all spin labels were known. One would gain the added precision of equations (11), and escape the uneasy feeling that the spin label at hand is the one exception to the behavior of all of the others thus far investigated. This is unlikely, because a line that passes the test of being a good Voight has a Gaussian profile for its inhomogenous component. One has two other sources of assurance available. First, in all cases except DTBN—an oddity that depends on certain numbers of fully equivalent protons—incipient resolution reveals the fact that the results are deviating from the universal results. Second, an internal consistency check is available with nitroxides. Application of the scheme in Figure 12 to two different nitrogen multiplets in the same spectrum ought to give the same ΔH^G_{pp} for the two lines.

TABLE 9
Analysis of 5-Doxylstearic Acid in Methanol Using the Hyperfine Patterns of Table 5 and Known Hyperfine Patterns[a]

Pattern	χ	ΔH_{pp}^{G}	ΔH_{pp}^{L}
1	2.25	0.759	0.337
2	2.85	0.794	0.279
3	2.48	0.774	0.312
4	2.27	0.760	0.335
5	1.86	0.725	0.390
6	2.11	0.748	0.355
7	2.61	0.780	0.304
8	2.03	0.741	0.365
TEMPOL	2.25	0.759	0.337
TEMPAMINE	2.40	0.769	0.321
TEMPO	2.65	0.784	0.296
	Average	0.763 ± 0.020	0.330 ± 0.032
Voight	4.10	0.838	0.204

[a] $\psi = 0.095$ and $\Delta H_{pp}^{0} = 0.946$ are assumed. Linewidths in gauss.

6.3. Additional Broadening Method

Kuznetsov *et al.* (1974) proposed adding paramagnetic species, such as oxygen, to a solution containing nitroxides in order to increase ΔH_{pp}^{L} and thereby decrease the error associated with inhomogeneous broadening. The experimental strategy (Kuznetsov *et al.*, 1974) was to increase ΔH_{pp}^{L} (decrease χ) until no further change in the experimental parameter of interest was observed. In other words, the original aim of the method was to produce a line that was nearly Lorentzian, but from Figure 10 we see that extremes are not necessary. One needs only to reduce χ to $\chi = 2.0$. One might not wish, or be able, to include enough oxygen to reduce χ to the point of being able to ignore the inhomogeneous broadening. Further, signal-to-noise is reduced as the line is broadened.

We suggest that the additional broadening method can be a valuable tool if small amounts of additional paramagnetic species can be tolerated, but we think of the method as a way to increase the precision of our correction procedures rather than eliminating the need for them. Also, spectra may be avoided that fall in the troublesome region between unresolved spectra and spectra with usable resolution.

7. THE RELATIONSHIP OF LINEWIDTH RATIOS TO MEASURED LINE-HEIGHT RATIOS

7.1. Rotational Correlation Times

For any reasonably shaped first-derivative spectrum, the doubly integrated intensity A is given by Chesnut (1977) in the form

$$A = \tfrac{1}{2}[\Delta H^0_{pp}(M_I)]^2 V_{pp}(M_I) F(M_I) \tag{18}$$

where $F(M_I)$ depends only on the line shape. Since A is independent of M_I, forming the ratio of equation (18) with $M_I = 0$ and with $M_I' = \pm 1$ gives

$$\frac{\Delta H^0_{pp}(\pm 1)}{\Delta H^0_{pp}(0)} = \sqrt{\frac{V_{pp}(0)}{V_{pp}(\pm 1)}} \cdot \sqrt{\frac{F(0)}{F(\pm 1)}} \tag{19}$$

If the three lines of the spin-label spectrum possessed the same shape, we would have

$$\frac{\Delta H^0_{pp}(\pm 1)}{\Delta H^0_{pp}(0)} = \sqrt{\frac{V_{pp}(0)}{V_{pp}(\pm 1)}} \tag{20}$$

and, further, if they were not inhomogeneously broadened, we would have

$$\frac{\Delta H^L_{pp}(\pm 1)}{\Delta H^L_{pp}(0)} = \sqrt{\frac{V_{pp}(0)}{V_{pp}(\pm 1)}} \tag{21}$$

This latter ratio is pertinent, because rotational correlation times computed from ESR spectra depend on the coefficients

$$B = \tfrac{1}{2}\Delta H^L_{pp}(0)\left\{\frac{\Delta H^L_{pp}(+1)}{\Delta H^L_{pp}(0)} - \frac{\Delta H^L_{pp}(-1)}{\Delta H^L_{pp}(0)}\right\} \tag{22}$$

and

$$C = \tfrac{1}{2}\Delta H^L_{pp}(0)\left\{\frac{\Delta H^L_{pp}(+1)}{\Delta H^L_{pp}(0)} + \frac{\Delta H^L_{pp}(-1)}{\Delta H^L_{pp}(0)} - 2\right\} \tag{23}$$

(Kivelson, 1972; Goldman *et al.*, 1972). Since relative line heights may be measured with more precision than linewidths, most authors substitute equation (20) into the analogs of equations (22) and (23), where each ΔH^L_{pp} is replaced by ΔH^0_{pp},

$$C_{\text{uncorrected}} = \tfrac{1}{2}\Delta H^0_{pp}(0)\left\{\sqrt{\frac{V_{pp}(0)}{V_{pp}(+1)}} + \sqrt{\frac{V_{pp}(0)}{V_{pp}(-1)}} - 2\right\} \tag{24}$$

$$B_{\text{uncorrected}} = \tfrac{1}{2}\Delta H^0_{pp}(0)\left\{\sqrt{\frac{V_{pp}(0)}{V_{pp}(+1)}} - \sqrt{\frac{V_{pp}(0)}{V_{pp}(-1)}}\right\} \tag{25}$$

But these are in error because the lines are neither Lorentzian nor of the same shape. Errors involved in the use of equation (21) are substantial and are summarized in Table 10. To solve this problem, we seek the relationship between the proper intrinsic linewidth ratios and the line heights of the inhomogeneously broadened lines. To include the line-shape information we specify the shape of the $M_I = 0$ line, χ_0, by any of the schemes in Section 6. Since it is the departure of the pertinent ratios in equations (19)-(21) from unity that are significant, we write

$$\frac{\Delta H^L_{pp}(\pm 1)}{\Delta H^L_{pp}(0)} - 1 = \left(\sqrt{\frac{V_{pp}(0)}{V_{pp}(\pm 1)}} - 1\right) S(\chi_0) \tag{26}$$

TABLE 10
Errors in the Determination of $\Delta H^{L}_{pp}(\pm 1)/\Delta H^{L}_{pp}(0)$ from $\sqrt{V_{pp}(0)/V_{pp}(\pm)}$[a]

$\chi(0)$	$\frac{\Delta H^{L}_{pp}(\pm 1)}{\Delta H^{L}_{pp}(0)}$	No correction equation (21)	Equations (26) and (27)	Equations (26) and (31)
6.0	2	41%	−2%	0%
	3	54	−5	0
	20	73	−32	−3
4.8	2	39	−2	0
	3	52	−5	−1
	20	68	−32	−3
2.8	2	32	−3	−1
	3	43	−7	−2
	20	53	−30	−2
2.0	2	27	−3	−1
	3	35	−7	−2
	20	41	−25	−3
1.6	2	23	−3	−1
	3	29	−7	−2
	16[b]	35	−22	−2
0.8	2	11	−2	0
	3	14	−5	0
	8[b]	16	−10	−3

[a] % Error = 10 × (true value − calculated value)/true value. Errors less than 0.5% are entered as zero.
[b] Corresponds to $\chi(\pm 1) = 0.2$.

and evaluate the correction factor $S(\chi_0)$. The pertinent range of the ratio $\Delta H^{L}_{pp}(-1)/\Delta H^{L}_{pp}(0)$, which is the larger of the two for nitroxides at X-band, is limited by the range of applicability of equations (22) and (23) in fast-motion theories. The simple theories of rotational correlation times are not applicable when the rotational correlation times τ_R are larger than approximately 10^{-9} s (Schreier *et al.*, 1978). Near $\tau_R = 10^{-9}$ s, ΔH^{L}_{pp}, B, and C are all of the order of one gauss (Goldman *et al.*, 1972; Hwang *et al.*, 1975), which means that $\Delta H^{L}_{pp}(-1)/\Delta H^{L}_{pp}(0)$ must be about 2 or less.

It is a simple matter to simulate a series of spectra varying ΔH^{L}_{pp} while maintaining the same hyperfine pattern, measure V_{pp}, and form the ratios in equation (26). This exploits the fact that the three nitrogen lines have the same hyperfine pattern. Interestingly and fortunately, the results are practically independent of which pattern is used or if the Voight is used. For example, the largest discrepancy for the value of $\Delta H^{L}_{pp}(\pm 1)/\Delta H^{L}_{pp}(0)$ using the Voight as opposed to the universal nitroxide is 1%, and the average discrepancy is less than 0.5%.

For the Voight shape in which ΔH^{G}_{pp} is maintained the same in the two lines, $S(\chi_0)$ is accurately given by

$$S(\chi_0) = (1 + 1.78\chi_0 + 1.85\chi_0^2)/(1 + 2.08\chi_0) \tag{27}$$

Errors involved in the use of equations (26) and (27) are given in Table 10. Up to $\Delta H^{L}_{pp}(\pm 1)/\Delta H^{L}_{pp}(0) = 2$, the range relevant to rotational correlation time measurements, the errors are 3% or less, a substantial improvement over no corrections. Even as high

as $\Delta H_{pp}^{L}(\pm 1)/\Delta H_{pp}^{L}(0) = 3$ the error in using equations (26) and (27) is 5-7% while no corrections lead to errors of 14-54%.

Substituting equation (26) into equations (22) and (23) while making use of equation (7b) gives

$$B = Q_0 \cdot S(\chi_0) \cdot B_{\text{uncorrected}} \tag{28}$$

and

$$C = Q_0 \cdot S(\chi_0) \cdot C_{\text{uncorrected}} \tag{29}$$

where

$$Q_0 = (-1 + \sqrt{1 + 4\chi_0^2})/2\chi_0^2 \tag{30}$$

We note that the simplicity of equations (28) and (29) depends on the facts that only the shape of the *central* line is involved and $S(\chi_0)$ in equation (27) is independent of $V_{pp}(0)/V_{pp}(\pm 1)$.

Thus, correcting rotational correlation times in the fast-motion region is a question of determining the shape of the central line, χ_0, calculating the usual, uncorrected coefficients in equations (24) and (25), and using equations (28) and (29). See Figure

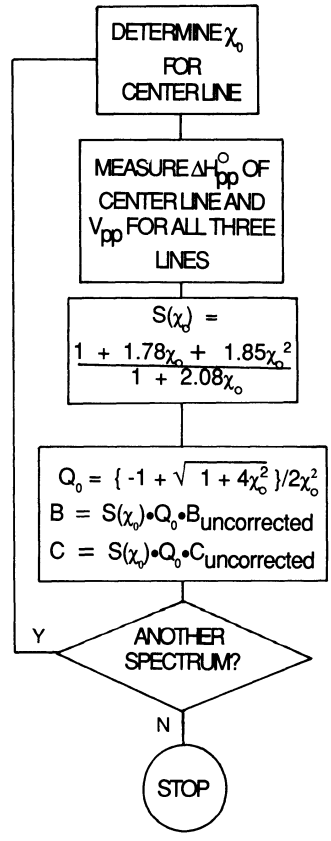
DETERMINE χ_0 FOR CENTER LINE
MEASURE ΔH_{pp}^{o} OF CENTER LINE AND V_{pp} FOR ALL THREE LINES
$S(\chi_0) = \frac{1 + 1.78\chi_0 + 1.85\chi_0^2}{1 + 2.08\chi_0}$
$Q_0 = \{-1 + \sqrt{1 + 4\chi_0^2}\}/2\chi_0^2$
$B = S(\chi_0) \cdot Q_0 \cdot B_{\text{uncorrected}}$
$C = S(\chi_0) \cdot Q_0 \cdot C_{\text{uncorrected}}$
ANOTHER SPECTRUM?
Y
N
STOP

Figure 15. Scheme to correct coefficients B and C used in the computation of rotational correlation times.

15. Equations (28) and (29) permit the correction of previously reported uncorrected rotational correlation times of spin labels of known ΔH^{G}_{pp}, provided linewidth data on the central line are given.

Example 6. Kowert *et al.* (1985) found experimentally and by computer simulation for DTBN and a spin-labeled liquid-crystal analog that

$$C/B = C_{\text{uncorrected}}/B_{\text{uncorrected}}$$

Division of equation (29) by equation (28) gives this result immediately and extends the earlier work (Kowert *et al.*, 1985) to all Voight-shaped lines. These same workers could write ΔH^{L}_{pp} as a linear function of $V_{pp}^{-1/2}$ for a number of computer-synthesized spectra. Equation (26) describes a more universal linearity.

7.2. Linewidth Ratios Over a Broader Range

A slightly more complicated relationship,

$$\Delta H^{L}_{pp}(\pm 1)/\Delta H^{L}_{pp}(0) - 1 = [\sqrt{V_{pp}(0)/V_{pp}(\pm 1)} - 1]S(\chi_0)[V_{pp}(0)/V_{pp}(\pm 1)]^{-0.8\sqrt{\chi_0}} \tag{31}$$

permits accurate intrinsic linewidth determinations from line-height ratios over the entire range $\chi_0 = 0$–6 and to all values of $\Delta H^{L}_{pp}(0)$ conceivably accessible using spin labels. Equation (31) resulted from trial and error, and the last column of Table 10 shows that it is accurate to within 3% over the incredible range, up to either $\Delta H^{L}_{pp}(\pm 1)/\Delta H^{L}_{pp}(0) = 20$ or to a value corresponding to $\chi = 0.2$ for $M_I = \pm 1$ at which point the lines are essentially Lorentzian.

Example 7. Measuring Oxygen Concentrations Using Unresolved Spin-Label Spectra. Equation (31) is probably not worth the extra accuracy for rotational correlation time measurements but could find use in experiments in which the spin label is used to measure oxygen concentrations. Techniques have been developed that use the relative loss of resolution in partially resolved ESR spectra (Hyde and Subczynski, 1984; Swartz, 1987). Here, we suggest a method if one wishes to use unresolved spectra. The experiment would exploit the fact that paramagnetic oxygen broadens the spin-label resonance line due to collisions. Here, the two intrinsic widths of interest are those for the *same* line in the spin-label spectrum at different oxygen concentrations, $[O_2]$. Assuming that the temperature and spin-label concentration are constant, ΔH^{G}_{pp} is the same in the two measurements and an equation similar to (31) is valid where, instead of labeling the value of M_I, we label the value of $[O_2]$. Also, since the broadening is proportional to $[O_2]$, we may write

$$\Delta H^{L}_{pp}([O_2]) - \Delta H^{L}_{pp}([O]) = K_{O_2}[O_2] \tag{32}$$

Rearrangement and the use of equations (7b) and (31) gives

$$[O_2] = K_{O_2}^{-1}\Gamma([O])\Delta H^{0}_{pp}([O])\{\sqrt{V_{pp}([O])/V_{pp}([O_2])} - 1\} \times V_{pp}([O])/V_{pp}([O_2])\}^{-0.8\sqrt{\chi([O])}} \tag{33}$$

where $\Gamma([O]) \equiv Q_0\chi([O])S(\chi([O])$ is evaluated from the resonance line in the absence of oxygen and is fixed during the experiment. The constant K_{O_2} would have to be determined in a control experiment.

8. ACCURATE ESTIMATE OF RELATIVE DOUBLY-INTEGRATED SPECTRAL INTENSITIES

In principle, one simply integrates the first-derivative spectrum twice in order to get the spectral intensity A. In practice, good precision is difficult to obtain and if there are nearby resonances, for example, the split high-field line in a spectrum that shows label partitioning (Bales and Baur, 1970; Hubbell and McConnell, 1969) or adjacent lines in a spin-trap adduct, then the only convenient parameters are V_{pp} and ΔH^0_{pp}. According to equation (18), two lines would have relative areas given by the ratio of $(\Delta H^0_{pp})^2 V_{pp}$ if they were the same shape, but in almost every interesting case they are not. This is a serious matter, because the factor F varies from $F^G = 1.03$ for a Gaussian to $F^L = 3.63$ for a Lorentzian. From the same computer simulations described previously, F may be calculated. The result for the universal shape is well approximated by

$$F_{(\text{universal})} = (1.03\chi^2 + 1.21\chi + 1.71)/(\chi^2 + 0.298\chi + 0.471) \tag{34}$$

Evaluation, using procedures parallel to those discussed following equations (9) and (10), shows that equation (34) is superior to a similar equation derived from the Voight shape. Figure 16 shows results for specific spin labels and the observations about Figure 10 hold here as well. An equation similar to equation (11) is as follows:

$$F_{(\text{nitroxide})}/F_{(\text{universal})} = B_0 + B_1\chi + B_2\chi^2 + B_3\chi^3 \tag{35}$$

which may be used if more precision is justified. Some values of the coefficients of this equation are given in Table 11. We note that application of equation (34) to two different lines in the nitrogen multiplet of the same spectrum is a good internal consistency check.

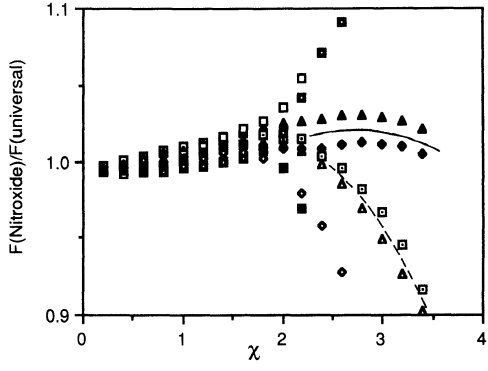

Figure 16. The ratio of the true value of F used in doubly-integrated intensity calculations, equation (18), to the value of F estimated from equation (34). The symbols correspond to the labels and solvents in Figure 10. The solid line is a plot of equation (35) for TEMPO and the dashed line for TEMPAMINE. Plots of equation (35) for the other labels pass through the points with high precision and are not shown.

TABLE 11
Coefficients in Equation (35)

Spin label	B_0	B_1	B_2	B_3	Maximum χ
TEMPO	0.99	0.003	0.009	−0.0025	3.4
TEMPONE	1.01	−0.075	0.105	−0.0358	2.2
TEMPAMINE	1.00	0.0	0.021	−0.0084	3.4
TEMPOL	1.01	−0.055	0.074	−0.0245	2.6
DTBN	0.99	0.010	−0.001	0.0041	2.2
TEMPYO	0.99	0.028	−0.039	0.0170	2.6

Example 8. A Hypothetical Spin-Label Partitioning Experiment. Suppose that TEMPO in a lipid dispersion gives a spectrum with a partially resolved $M_I = -1$ line (Polnaszek *et al.*, 1978 and references cited therein) from which the measurements in Table 12 are made. In this example, we suppose that the line heights of the two high-field lines are equal. Measurement of ψ is impossible, so we check for spin exchange by halving the concentration (see caveat, p. 119) and must be content with assuming that the data in Table 8 are valid. From a_N, ΔH_{pp}^G is calculated in the two fractions using equation (16) and equation (7d) yields the respective values of χ. Equation (34) gives F. See Table 12 for the results of these calculations. Various levels of approximation for the spin concentration ratio $[TEMPO_{water}]/[TEMPO_{lipid}]$ are (1) the line-height ratio which ignores the differences in linewidth and line shape, (2) the ratio of $V_{pp}(\Delta H_{pp}^0)^2$ which ignores the differences in line shape, and (3) the correct ratio of

TABLE 12
Calculation of the Partition Coefficient in the Hypothetical Problem of Example 8[a]

	Measured Quantities		
	ΔH_{pp}^0	V_{pp}	a_N
Water fraction	1.29	1	17.1
Lipid fraction	1.81	1	15.8
	Calculated Quantities		
	ΔH_{pp}^G	χ	F
	Equation (16)	Equation (7d)	Equation (34)
Water fraction	1.10	3.12	1.39
Lipid fraction	1.19	1.16	2.08
	Partition Coefficients		
	Derived from ratio of V_{pp}	Derived from ratio of $V_{pp}(\Delta H_{pp}^0)^2$	Derived from ratio of $V_{pp}(\Delta H_{pp}^0)^2 F$
Water fraction	0.50	0.34	0.25
Lipid fraction	0.50	0.66	0.75

[a] Linewidths and a_N in gauss.

$V_{pp}(\Delta H^0_{pp})^2 F$. These three ratios are 1.0, 0.51, and 0.34 respectively, from which the water:lipid partition coefficients are calculated to be 1:1, 1:2, and 1:3 respectively (see Table 12). Thus, in this example, ignoring the shape differences gives a 50% error, and ignoring both the shape and linewidth differences gives a 200% error in the computed spin concentration ratios. Note that in a typical experiment of this type, there would not normally be sufficient precision in the measurements to make the change in ΔH^G_{pp} from water to lipid important. If we had used $\Delta H^G_{pp} = 1.10$ G in the lipid as well as the water fractions, χ would have been 0.96 giving $F = 2.28$ in the lipid fraction, leading to a spin concentration ratio of 0.31 instead of 0.34, only a 10% change. Further, equation (11) probably would not be justified in this type of experiment.

While the above example dealt with a case in which ψ could not be measured, we recommend that A be determined routinely from the four-point method if possible. In addition to the reasons given in Section 6, in the calculation of A, small errors in the measurements tend to cancel out and one measures F more reproducibly than χ and ΔH^L_{pp}.

9. DETERMINING SPIN-EXCHANGE FREQUENCIES OF SPIN LABELS IN LIQUIDS OF LOW VISCOSITY

As the spin-label concentration C is increased, the ESR linewidth is increased due to spin exchange and dipolar interactions. We consider liquids of low viscosity in which spin exchange dominates the increase in linewidth (Eastman *et al.*, 1969; Keith *et al.*, 1977; Molin *et al.*, 1980). Theoretically and experimentally, at the relatively low concentrations involved in spin-exchange experiments, the spin-exchange frequency is proportional to the concentration,

$$\omega_{HE} = KC \tag{36}$$

where K depends on the relative diffusion coefficient of the two spin labels, the probability of spin exchange upon collision, and the effective distance for the spin-exchange interaction. The subject is well developed and the reader is referred to the literature for details (Freed, 1976; Molin *et al.*, 1980). Our concern is how to get K from measurements of spin-exchange broadening of the ESR lines.

If the spin-label spectrum were not inhomogeneously broadened, it would be a simple matter to determine the spin-exchange frequency ω_{HE} by measuring the difference in the linewidth ΔH^L_{pp} at concentration C and near concentration zero. The existence of hyperfine structure complicates the interpretation of the measurements in three ways: (1) at $\omega_{HE} \ll a_e$, the *initial* rate of broadening, $d(\Delta H^L_{pp})/d(\omega_{HE})$, of each line in the multiplet upon increasing C depends on its degeneracy and is different than the rate of broadening when $\omega_{HE} \gg a_e$, (2) the measured linewidth is not the intrinsic width, and (3) the effective value of ΔH^G_{pp} varies with ω_{HE} so the relationship between the measured linewidth and ΔH^L_{pp} changes.

Freed (1967) discussed spin-exchange broadening in terms of a statistical factor related to the degeneracy of the line in question. To illustrate, consider the stick spectrum of a hypothetical nitroxide spin label in Figure 17 which shows hyperfine

coupling to four equivalent protons with coupling constant a_H, exaggerated relative to the nitrogen hyperfine coupling constant a_N. The lines in one multiplet have normalized intensities of 1/48, 4/48, 6/48, 4/48, 1/48 corresponding to the projections of the total proton angular momentum $M_I^P = -2, -1, 0, +1, +2$. Consider, for example, spin labels that are in the population $M_I = 0$, $M_I^P = -1$ with intensity 4/48. At low spin-exchange frequencies, $\omega_{HE} \ll a_H$, if members of that population undergo spin exchange with other members of the same population no broadening occurs, but if they undergo spin exchange with members of any other population, spin exchange broadens the first-derivative line by $2\omega_{HE}/\gamma\sqrt{3}$. Considering all the possibilities, the line in question would be broadened by $(2\omega_{HE}/\gamma\sqrt{3})(1 - 4/48)$. This is an example of the well-known effect that lines of lower degeneracy broaden faster initially (Currin, 1962; Freed, 1967) because the term that is subtracted is proportional to the degeneracy. The *initial* average rate of broadening may be found by weighting the broadening of each line by its intensity and summing over the lines, the result being

$$(2\omega_{HE}/\gamma\sqrt{3})(1 - 70/768) = (2\omega_{HE}/\gamma\sqrt{3}) \cdot 0.909$$

In general, for a multiplet of N equivalent protons, the same type of argument shows that the average rate of initial broadening is

$$(2\omega_{HE}/\gamma\sqrt{3})\left(1 - \frac{1}{3}\frac{1}{2^{2N}}\frac{(2N)!}{(N!)^2}\right)$$

where one uses the theorem

$$\sum_{n=0}^{N} N!/(N-n)!\,n! = (2N)!/(N!)^2$$

We may write the average initial broadening $(2\omega_{HE}/\gamma\sqrt{3})f$ and find that $f = 0.946$ for $N = 12$ (TEMPONE) and $f = 0.956$ for $N = 18$ (DTBN). For patterns involving inequivalent protons f is more complicated, but for large numbers of protons it is of the order unity, initially.

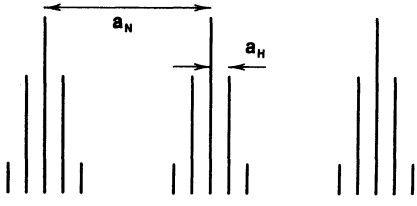

Figure 17. Schematic hyperfine pattern of a spin label with four equivalent protons with a_H exaggerated with respect to a_N. If spin labels in a population associated with one line undergo spin exchange with labels from any other population, broadening occurs, but spin exchanges within a population do not affect the linewidth. The smaller the degeneracy, the more likely spin exchange will broaden the line. In this example, the smallest line broadens with respect to ω_{HE} at a rate of $(1 - 1/48)/(1 - 6/48) = 1.12$ faster than the largest line when $\omega_{HE} \ll a_H$. Near $\omega_{HE} = a_H$, the five lines in each multiplet coalesce into one line which broadens at a rate approximately 2/3 of the initial rate of broadening experienced by the individual lines.

The initial rate of broadening is only valid until $\omega_{HE} \sim a_e$, at which point the intramanifold exchanges tend to collapse the multiplet to a single Lorentzian and intermanifold exchanges continue to broaden the lines. At $\omega_{HE} \gg a_e$ the three Lorentzians broaden with $f = 2/3$. For real nitroxides, the lines are not infinitely sharp at $\omega_{HE} = 0$ and, for spin labels not composed of N equivalent protons, the "line spacing" is complicated so the transition through the so-called intermediate spin-exchange region is complicated (Bales and Willett, 1984). The best we can do is solve the problem numerically (Currin, 1962; Freed, 1967) to evaluate the terms in the following equation,

$$\Delta H_{pp}^{L}(\omega_{HE}) - \Delta H_{pp}^{L}(0) = (2\omega_{HE}/\gamma\sqrt{3}) \cdot f^*(\omega_{HE}) \tag{37}$$

where f^* goes from near $f = 1$ at $\omega_{HE} = 0$ to $f = 2/3$ at $\omega_{HE} \gg a_e$.

Various theoretical techniques have been used to solve the spin-exchange problem, varying widely in sophistication and yielding identical results in the case of nitroxides (Currin, 1962; Freed, 1966; Johnson, 1967; Stillman and Schwartz, 1976). We used Currin's (1962) correlation function approach and solved the equations on a PC (Bales and Willett, 1984). One inputs $\Delta H_{pp}^{L}(0)$, the hyperfine pattern, and ω_{HE}, and out comes the spectrum. One then asks the computer to find ΔH_{pp}, the manifold width with spin exchange, ψ, and V_{pp}.

In an attempt to model the complicated processes of multiplet collapse and line broadening, we suggested (Bales, 1980) a simple scheme to "turn off" the Gaussian component and "turn on" a Lorentzian component exponentially near $\omega_{HE} = a_e$ and, using equation (7), we wrote a transcendental equation in ω_{HE} which we solved to second order giving

$$\omega_{HE}^{(0)} = (3\sqrt{3}\gamma/4)(\Delta H_{pp} - \Delta H_{pp}^{0}) \tag{38a}$$

$$\omega_{HE}^{(1)} = \omega_{HE}^{(0)}[1 + (\Delta H_{pp}^{G})^2/\Delta H_{pp}\Delta H_{pp}^{0}] \tag{38b}$$

$$\omega_{HE}^{(2)} = \omega_{HE}^{(1)} + (\Delta H_{pp}^{G})^2(3\sqrt{3}\alpha/4\Delta H_{pp})\{1 - \exp(-4\omega_{HE}^{(1)}/3\gamma a_e) - (\sqrt{3}\gamma\Delta H_{pp}/4\omega_{HE}^{(1)})[1 - \exp(-\omega_{HE}^{(1)}/2\gamma a_e)]^2\} \tag{38c}$$

Here ΔH_{pp} is the manifold linewidth at concentration C and ΔH_{pp}^{0} at a very low concentration, while ΔH_{pp}^{G} is the Gaussian linewidth in the absence of spin exchange computed from equation (2) or evaluated from a measurement of ψ on a spectrum at low C using equation (10).

Equation (38a) ignores the inhomogeneous broadening and is the approximation most often used. Equations (38) are handy from an experimentalist's point of view because ΔH_{pp}^{L} does not have to be computed first; only measurements of the manifold width and a knowledge of ΔH_{pp}^{G} are involved. They are surprisingly accurate (Bales, 1980) and may be used to correct previously published data for spin labels of known ΔH_{pp}^{G}. The accuracy of equations (38) is demonstrated in Figures 18 and 19, where the true value of ω_{HE} (the input parameter to the computer) is plotted against the various approximations of equations (38) for DTBN and TEMPOL.

The numerical solution of the spin-exchange problem gives an envelope that is a good Voight shape (Bales and Willett, 1984), which is not surprising since both the

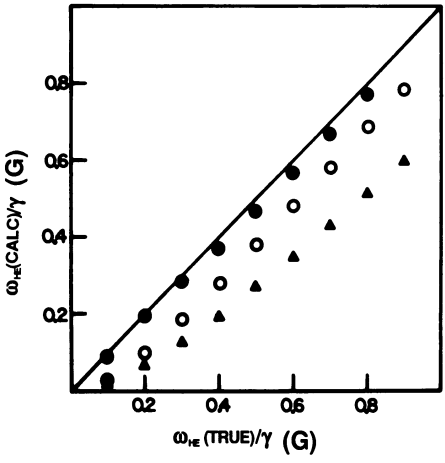

Figure 18. The spin exchange frequency $\omega_{HE}(CALC)/\gamma$ computed from equation (38a) ▲, (38b) ○, and (38c) ● vs. the true $\omega_{HE}(TRUE)/\gamma$ which is the input parameter in the computer-simulated spectra. DTBN, $a_e = a_H = 0.1$ G, $\Delta H^L_{pp} = 0.24$ G. (From Bales, 1980, with permission.)

multiplet collapse and the line broadening decrease χ. Thus, the Lorentzian and Gaussian components may be extracted by the four-point method. Figures 20, 21, and 22 show the results of experiments with DTBN in Mesitylene at $T = 30.00$ °C. In Figure 20, the diamonds show the manifold width, the squares ΔH^L_{pp}, and the triangles ΔH^G_{pp}, vs. the intensity A measured by the methods of Section 8. We are making use of the fact that the intensity is proportional to the concentration. The dotted line shows the result of numerical solution of the spin-exchange problem, with K adjusted to fit the points at large intensity. The Gaussian linewidth collapses as expected, and the Lorentzian linewidth increases more rapidly near the origin than farther out. Combining the four-point method with equation (38c) yields ΔH^L_{pp} vs. ω_{HE}/γ which is effectively a graph of equation (37), the slope of which at higher ω_{HE} is near $4/\gamma 3\sqrt{3}$, as expected (not shown; see Figure 6 in Bales and Willett, 1984). Figure 21 shows why one must be very cautious in correcting inhomogeneous lines if it is not known whether spin

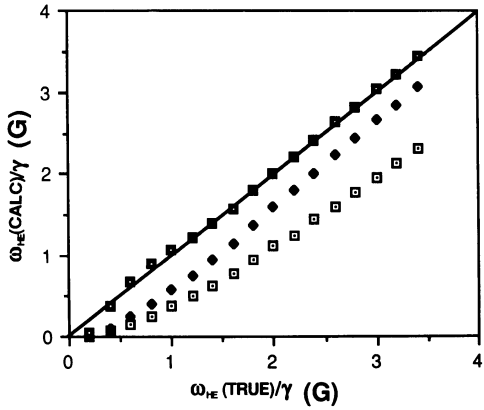

Figure 19. The spin-exchange frequency $\omega_{HE}(CALC)/\gamma$ computed from equation (38a) ⊡, (38b) ◆, and (38c) □ vs. the true $\omega_{HE}(TRUE)/\gamma$ which is the input parameter in the computer-simulated spectra. TEMPOL, $a_e = 0.344$ G, $\Delta H^L_{pp} = 0.74$ G.

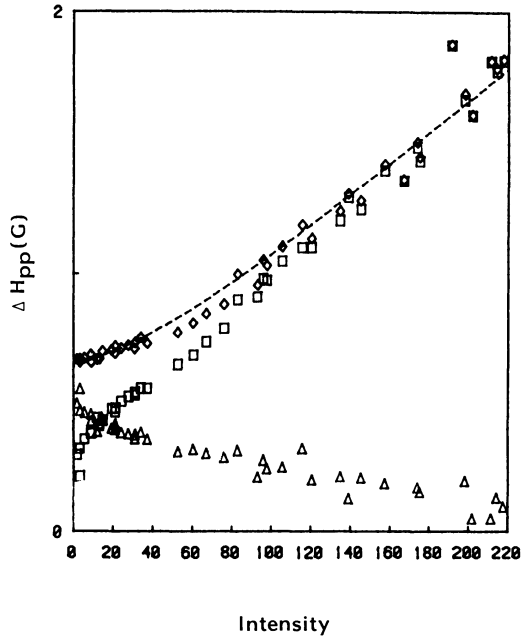

Figure 20. The linewidth of the $M_I = 0$ manifold of DTBN as a function of the doubly integrated EPR spectral intensity. The line is the theoretical prediction for the total linewidth and the experimental points are given by ◇. Deconvolution gives the Lorentzian component linewidths ΔH_{pp}^{L} (□) and Gaussian component linewidths ΔH_{pp}^{G} (△). Mesitylene, $T = 30.00$ °C.

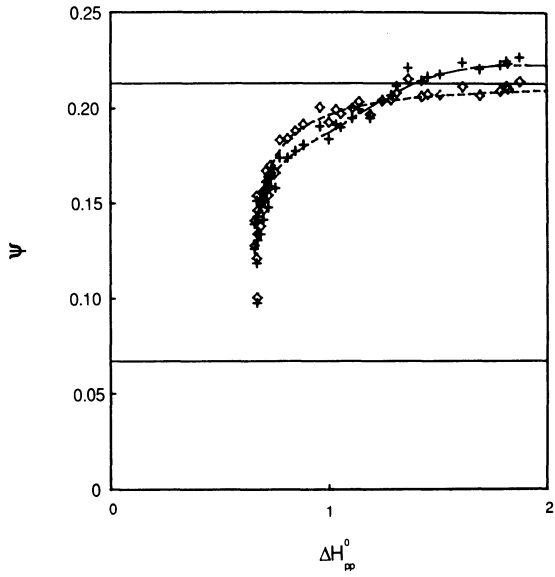

Figure 21. The line-shape parameter ψ of the $M_I = 0$ manifold of DTBN as a function of the overall manifold linewidth. The experimental points are given by + and these points corrected to account for interference from ^{13}C satellites are given by ◇. The horizontal lines correspond to a Gaussian line shape, $\psi^G = 0.067$ and a Lorentzian line shape, $\psi^L = 0.213$, respectively. Mesitylene, $T = 30.00$ °C. (From Bales and Willett, 1984, with permission.)

exchange is affecting the spectra. The shape of the spectrum ψ changes radically with a small change in ΔH^0_{pp}. Testing for spin exchange by increasing the concentration and comparing the linewidths may be insensitive to the presence of spin exchange while the shape is very sensitive. The major shape change in Figure 21 takes place at a concentration near 6×10^{-4} M in this case.

The collapse of the hyperfine structure for DTBN in three solvents is shown in Figure 22 and the solid line is an empirical fit to the theoretical results,

$$a_e(\omega_{HE}) = a_e(0)[1 + \omega_{HE}/7.9a_e(0)\gamma]^{-1}$$

If this is generalized to other nitroxides and equation (37) employed, we obtain

$$\Delta H^G_{pp}(\omega_{HE}) = \Delta H^G_{pp}[1 + \omega_{HE}/7.9a_e(0)\gamma]^{-1} \tag{39}$$

Figure 22 shows that equation (39) works pretty well for DTBN, and King *et al.* (1987) have shown that it works pretty well for 4-(4′,4′-dimethyloxazolidine-*N*-oxyl)valeric acid in water, but more work is needed to establish equation (39) in general.

The rigorous way to measure correct values of K in equation (36) is to measure ψ and ΔH^L_{pp} on a series of spectra taken at various concentrations C while holding all other parameters constant. The scheme of Figure 10 gives ΔH^L_{pp} which can be plotted against C. The slope of the linear part of ΔH^L_{pp} vs. C gives

$$d\Delta H^L_{pp}/dc = d(\Delta H^L_{pp})/d(\omega_{HE}) \cdot K$$

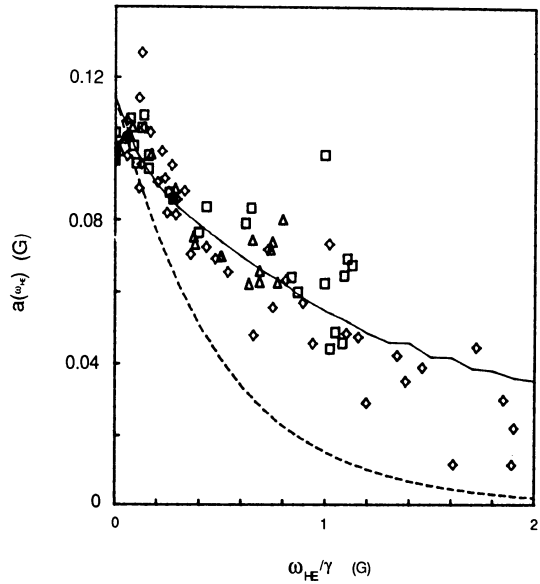

Figure 22. The effective hyperfine coupling constant vs. the spin-exchange frequency for DTBN in mesitylene (△), *trans*-decalin (◇), and *cis*-decalin (□). The theory of Currin (1962) produced the solid line. The scatter of the points indicates the uncertainty which is most severe in the 1.3–2.0 G range due to corrections for ^{13}C satellite lines. The dotted line shows Currin's theory for a single manifold of lines but with ω_{HE}(single) = ω_{HE}(nitroxide)/3. (From Bales and Willett, 1984, with permission.)

using equation (36). Therefore, since $d(\Delta H_{pp}^{L})/d(\omega_{HE}) = 4/3\sqrt{3}\gamma$,

$$K = \frac{3\sqrt{3}\gamma}{4}\frac{d(\Delta H_{pp}^{L})}{dc} \tag{40}$$

This is tedious—the procedure must be carried out at each temperature and/or viscosity of interest. One further problem is that one might need uncomfortably high concentrations to achieve the linear part of the ΔH_{pp}^{L} vs. C curve in some systems—for example, a biological membrane. The attractive feature of equations (38) is that K may be derived from fairly low concentrations of spin label. It should be noted that the slope of the ΔH_{pp}^{L} vs. C curve is different than the slope of the ΔH_{pp}^{0} vs. C curve (Figure 20).

10. DEUTERATED SPIN LABELS

10.1. Gaussian Linewidth of Deuterated Spin Labels

Deuterium substitution is a well-established technique to reduce the problems associated with inhomogeneous broadening in spin-label spectra (Chiarelli and Rassat, 1973; Hwang *et al.*, 1975; Lim *et al.*, 1976; Beth *et al.*, 1980). For perfect perdeuteration, substitution of $a_D = \gamma_D a_H/\gamma_H$ and $I_D = 1$ into equation (2) gives

$$\Delta H_{pp}^{G}\,(\text{perdeuterated}) = \beta\,\Delta H_{pp}^{G} \tag{41}$$

where $\beta \equiv (\gamma_D/\gamma_H)\sqrt{8/3}$ and where we assume that, except for the change in magnetic moment and spin, isotope effects on the coupling constants are negligible. This is probably a very good assumption based on the very small effects of deuteration on a_N (Windle, 1981). Equation (41) further assumes that α is the same for the two patterns. For example, the simple estimate outlined in Section 3 gives $\sqrt{\alpha} = 1.04$ for $N = 8$ equivalent protons and $\sqrt{\alpha} = 1.05$ for $N = 8$ deuterons. Assuming negligible isotope effects on ΔH_{pp}^{L}, it follows that

$$\chi_{(\text{perdeuterated})} = \beta\chi \tag{42}$$

for a given set of experimental parameters. For perfect deuteration, the data in Table 8 may be used by multiplying D and E by $\beta = 0.251$.

After deuteration, is it valid to proceed as if the resonance lines were Lorentzian? Obviously, the answer depends upon which spin label is involved and with what precision one needs to measure the data. In Freed's laboratory, for example, they correct linewidth data for inhomogeneous broadening even in perdeuterated TEMPONE (Freed, 1976). To get an idea of the importance of treating perdeuterated spin labels with the methods of Sections 6-9, we have listed in Table 13 values of ΔH_{pp}^{G} (perdeuterated) for several spin labels in water and a "typical" $\chi_{typical}$ in each case. "Typical" is taken to be a dilute sample in water at $T = 295$ K. The data are taken from Windle (1981). Also given are $Q_{typical}$ from equation (7b), $S_{typical}$ from equation (27), and $F_{typical}$ from equation (34), which give measures of the corrections required for the linewidth equation (7b), the rotational correlation time equations (28) and (29), and the area equation (18). Table 13 makes it clear that, in most cases, one indeed does have to correct for the inhomogeneous broadening in perdeuterated spin labels.

TABLE 13
Gaussian Linewidths and Typical Values of Correction Parameters in Perfectly Perdeuterated Spin Labels for Water at $T = 295$ K[a]

	$\Delta H_{pp}^{L}(0)$[b]	ΔH_{pp}^{G} (perdeuterated)	$\chi_{typical}$	$Q_{typical}$	$S_{typical}$	$F_{typical}$
DTBN	0.180	0.0650	0.361	0.895	1.06	3.22
TEMPO	0.210	0.267	1.27	0.536	1.71	1.99
TEMPONE	0.190	0.0538	0.283	0.931	1.04	3.36
TEMPOL	0.250	0.355	1.42	0.499	1.84	1.89
TEMPYO	0.145	0.204	1.41	0.501	1.83	1.90
TEMPAMINE	0.230	0.353	1.53	0.473	1.93	1.83
Lorentzian				1.000	1.000	3.63

[a] Linewidths in gauss.
[b] Data from Windle (1981).

10.2. Proton Contamination of a Deuterated Spin Label

In the synthesis of a deuterated spin label, there will invariably be some proton contamination. Consider the set j of N_j equivalent protons of hyperfine coupling constant a_j and denote by ξ_j the average fractional deuteration of that set: $\xi_j = 1$ for perfect deuteration and $\xi_j = 0$ for no deuteration. The average second moment due to that set would be proportional to

$$\tfrac{4}{3}\alpha\{\tfrac{1}{2}(\tfrac{1}{2}+1)N_j a_j^2(1-\xi_j) + 1(1+1)N_j a_{Dj}^2 \xi_j\}$$

where a_{Dj} is the deuteron hyperfine coupling constant, α is taken to be the same for the two patterns, and the factors $I(I+1)$ are written explicitly for the two isotopes. The Gaussian linewidth may be calculated from equation (2) by summing over all of the sets j to give

$$\Delta H_{pp}^{G}(\xi_1, \xi_2, \ldots, \xi_K) = \sqrt{\alpha}[\textstyle\sum N_j a_j^2(1 - \xi_j + \xi_j\beta^2)]^{1/2} \tag{43}$$

We may define the average deuteration in the chemical sense,

$$\bar{\xi}_{chem} = \textstyle\sum N_j\xi_j / \sum N_j \tag{44}$$

or in the broadening sense,

$$\bar{\xi}_{inhom} = \textstyle\sum N_j a_j^2 \xi_j / \sum N_j a_j^2 \tag{45}$$

On inserting equation (45) into equation (43) and making use of expression (2), we obtain

$$\Delta H_{pp}^{G}(\bar{\xi}_{inhom}) = \Delta H_{pp}^{G}[(1 - \bar{\xi}_{inhom}) + \beta^2\bar{\xi}_{inhom}]^{1/2} \tag{46}$$

where ΔH_{pp}^{G} is the quantity appropriate for the fully protonated spin label. Perfect deuteration of those nuclei that contribute to hyperfine coupling implies that $\bar{\xi}_{inhom} = 1$ and equation (46) reduces to equation (41).

We may determine $\bar{\xi}_{inhom}$ by measuring or knowing ΔH_{pp}^{G} and measuring $\Delta H_{pp}^{G}(\bar{\xi}_{inhom})$. Equation (46) gives

$$\bar{\xi}_{inhom} = \{1 - [\Delta H_{pp}^{G}(\bar{\xi}_{inhom})/\Delta H_{pp}^{G}]^2\}/(1 - \beta^2) \tag{47}$$

$$\bar{\xi}_{inhom} = \{1 - [\chi^2(\bar{\xi}_{inhom})/\chi^2]\}/(1 - \beta^2) \tag{48}$$

where $\chi(\bar{\xi}_{inhom})$ is measured under identical conditions to those governing χ.

Example 9. Consider the spin label DCH-1 whose hyperfine coupling constants measured by NMR (Michon and Rassat, 1971) and confirmed by ESR (Michon and Rassat, 1971; Marriott *et al.*, 1976) are given in Table 14. Cases 1-5 are hypothetical examples of partially deuterated DCH-1 which illustrate the ideas in this section. In case 1, all $\xi_j = 0$, which means that the spin label is fully protonated so $\Delta H_{pp}^{G} = \sqrt{\alpha}(\sum N_j a_j)^{1/2} = \sqrt{\alpha}\ 1.95$ G. Case 2 is for perfect deuteration, so

$$\Delta H_{pp}^{G}(\text{perdeuterated}) = \sqrt{\alpha\beta}\ 1.95\ \text{G} = \sqrt{\alpha}\ 0.49\ \text{G}$$

TABLE 14
Gaussian Linewidths in Partially Deuterated DCH-1 Example 9[a]

Set J	$a_j(N_j)$	Case 1[b] ξ_j	Case 2[c] ξ_j	Case 3[d] ξ_j	Case 4[e] ξ_j	Case 5[f] ξ_j
1 (4')	−0.12 (6H)	0	1	0	0	1
2 (5')	−0.06 (2H)	0	1	0	0	1
3 (2e)	−0.58 (2H)	0	1	1	0.99	1
4 (2a)	−0.68 (2H)	0	1	1	0.99	1
5 (3e)	+1.01 (2H)	0	1	1	0.99	0.95
6 (3a)	+0.21 (2H)	0	1	1	0.99	1
	$\Delta H_{pp}^{G}/\sqrt{\alpha}$	1.95	0.49	0.57	0.60	0.58
	$\bar{\xi}_{inhom}$	0	1	0.98	0.97	0.97
	$\bar{\xi}_{chem}$	0	1	0.50	0.50	0.99

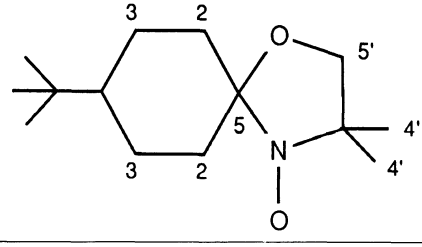

[a] Coupling constants and ΔH_{pp}^{G} in gauss. Data from Michon and Rassat (1971).
[b] Fully protonated.
[c] Fully deuterated.
[d] Deuterated except for the doxy ring.
[e] Doxyl ring protonated and 1% proton contamination elsewhere.
[f] Perfect deuteration everywhere, except for a 5% contamination in the equatorial deuterons at position 3.

by equation (41), or equivalently, equation (46). Case 3 might be motivated by the question: Would it be productive to deuterate the doxyl ring as well as the rest of the label? Assuming perfect deuteration $\xi_j = 1$ for protons other than those at positions 4′ and 5′, equation (43) gives $\Delta H_{pp}^{G}(0, 0, 1, 1, 1, 1) = \sqrt{\alpha}\ 0.57$ G, which is only 0.08 G more than the perfectly deuterated label. More realistically, one would hope to deuterate the rest of the label to 99%, for example, which is case 4. A 1% contamination in the rest of the label increases ΔH_{pp}^{G} by 0.03 G, so deuteration of the doxyl ring to gain 0.08 G is probably marginally profitable. Case 5 assumes perfect deuteration, except at 3e and 95% deuteration there. Chemically, this is only a 1% contamination but gives $\bar{\xi}_{inhom}$ about the same as in cases 3 and 4 which were contaminated chemically by 50%.

Example 10. We recently synthesized CAT-16-d16 deuterated in the piperidine ring except in the 4-position. Measurements in water at room temperature gave

$$\Delta H_{pp}^{0} = 0.753 \pm 0.006\ \text{G} \qquad \text{and} \qquad \psi = 0.122 \pm 0.007$$

Equation (10) gives $\chi = 1.54 \pm 0.20$ and $\Delta H_{pp}^{G}(\xi_{inhom}) = 0.546 \pm 0.033$, the errors being rather large because a dilute ($\sim 10^{-5}$ M) sample was used. Taking $\Delta H_{pp}^{G} = 1.42$ G for protonated CAT-16 (Table 4, using the value for TEMPOL), equation (47) gives

$$\xi_{inhom} = [1 - (0.546/1.42)^2]/[1 - (0.251)^2] = 0.91 \pm 0.03$$

where the error is estimated assuming a 6% error in ΔH_{pp}^{G}. Perfect deuteration of CAT-16 would have given

$$\Delta H_{pp}^{G}(\text{perdeuterated}) = 0.36\ \text{G} \qquad \text{and} \qquad \Delta H_{pp}^{0} = 0.53\ \text{G}$$

11. CONCLUSIONS

When $\chi \leq 2.0$, for all of the spin labels of Table 2 and more than one hundred reasonable, but fictitious, spin labels, correction for inhomogeneous broadening is universal, simple, and accurate. When dealing with a spin label of *unknown* hyperfine structure, the only pertinent consideration for $\chi \leq 2.0$ is whether the line is good Voight, which can be quickly checked by comparing the sum function [equation (13)] of proper η_A [equation (17)] with the experimental spectrum. This comparison uncovers the only exception to the universality of the correction procedures that we have been able to find: the case of having one coupling constant much larger than the others. It would also uncover any other exception that we have not thought of because, if the line is a good Voight, equation (7) applies.

Above $\chi = 2.0$, one requires more detailed information in order to attain high precision in the correction procedures (see Figure 10). Nevertheless, it is important to keep in perspective the errors depicted by Figure 10. Let us consider the worst case, TEMPAMINE at $\chi = 3.4$. Suppose we did *not* know the hyperfine pattern of TEMPAMINE and proceeded to analyze an obviously misshapened spectrum (see Figure 5) with equation (10). From Figure 10 we see that we would make a 31% error,

but if we were to do nothing we would make a 300% error. For specific spin labels (Table 7), precise correction procedures are available all the way up to χ_{incip}.

Correcting inhomogeneously broadened spin-label spectra turned out to be an unusual problem in that many things that could have gone wrong did not (Anti-Murphy's Law). Spin labels happen to have a lot of protons, producing complex spectra, a fact that helps instead of hindering our efforts because the patterns are nearly Gaussian. Only a handful of spin labels give rise to the difficulty of showing a large coupling to a single proton. The simple-to-measure parameter ψ is a monotonic function of χ and is similar for all spin labels to high values of χ. The Dobryakov–Lebedev (1968) relation has an intriguing simplicity that tremendously simplifies the calculations, a simplicity that evolves because we happen to study first-derivative lines in ESR. The precision with which the sum function, given by equation (13), approximates a Voight is a blessing that allows one to quickly determine whether these methods apply. Equations (10) and (34) could be written in such a simple, algebraically invertible, form because one does not have to insist that they fit well at small χ. That one can write such a simple relationship between linewidth and line-height ratios [in equations (26) and (27)] that is universal, was a pleasant and unexpected surprise which carries the bonus of being able to calculate rotational correlation times the old way, tacking on at the end a multiplicative correction factor that happens to be the same for B and C and depends only on the shape of the central line [see equations (28) and (29)]. The fact that equations (38) work (we hope they continue to work; they have not been tested experimentally nearly enough) must be considered lucky, considering the complexity of the problem and the simplicity of the heuristic derivation (Bales, 1980).

Knowledge of inhomogeneous broadening will likely continue to evolve in the context that it has evolved to date—not as a research topic in its own right, but rather as a necessary evil in order to carry out the work of real interest. One hopes that the NMR of doxyl-labeled n-alkyl chains and of PCA is carried out and interpreted so that the results due to those patterns could be added to equation (11). It should be emphasized that careful work in two solvents that yield widely different values of a_N, such as that performed by Windle (1981) and by Ottaviani (1987), is necessary in order to add to the list in Table 7 and verify the insensitivity of the coefficients in equation (11) to solvent polarity.

ACKNOWLEDGMENTS. Support by the Army Research Office, contract DAALO 3-88-K-0006, during the preparation of this chapter is gratefully acknowledged. J. Bales and D. Sack assisted with the curve fitting, C. Stenland wrote the software to analyze the experimental spectra, and Professor F. Harris synthesized the series JN14 and the deuterated CAT-16.

APPENDIX

Spectra were simulated on Apple II computers. Either the full spectrum was simulated and stored on floppy disks to be plotted later on a Serigor digital plotter, or V_{pp}, ΔH^0_{pp}, and ψ were "measured" by simulating only in the pertinent portions of the spectra. A search for the peak maximum was begun at the position predicted by

equation (7) using a resolution of $\Delta H^0_{pp}/2000$. Finding the peak maximum determines V_{pp} and ΔH_{pp}; computing the spectrum at $1.32\Delta H^0_{pp}$ determines V_W and therefore ψ. Computation leading to the results reported here, and much not reported, was, to say the least, time-consuming and was made possible by our primitive version of parallel processing. We would make 24 copies of the program at hand and use the 24 Apples in the student's lab at night, writing the results to disk and reading them to a data base the next morning.

Experimentally, we measure ψ using a program written by Mr. Chris Stenland, presently at the Department of Chemistry, University of Houston, which measures all three lines or just one depending on the operator's choice. The program fits experimental data points in the vicinity of the pertinent portion of the spectrum to a third-order polynomial from which the maximum or spectral intensity is found analytically. Equations (10), (27), and (34) are then computed from which the rest of the results of this chapter may be computed. The program is in BASIC implemented on the IBM 9000 series workstation interfaced with our Bruker ESR spectrometer. Copies of the program are available by sending Mr. Stenland an 8″ floppy disk.

REFERENCES

Ahn, M., 1976, Electron spin relaxation of di-tertiary-butyl nitroxide in supercooled water, *J. Chem. Phys.* **64**:134-138.

Atherton, N. M., and Strach, S. J., 1975, Environment dependence of proton hyperfine coupling in a nitroxide radical, *J. Magn. Reson.* **17**:134-135.

Bales, B. L., and Baur, M. E., 1970, EPR studies of DTBN in a lipid-water system, *Chem. Phys. Lett.* **7**:341-345.

Bales, B. L., 1980, A simple, accurate method of correcting for unresolved hyperfine broadening in the EPR of nitroxide spin probes to determine the intrinsic linewidth and Heisenberg spin exchange frequency, *J. Magn. Reson.* **38**:193-205.

Bales, B. L., 1982, Correction for inhomogeneous line broadening in spin labels. II, *J. Magn. Reson.* **48**:418-430.

Bales, B. L., and Willett, D., 1983, Experimental verification of a method to extract spin exchange frequencies from EPR spectra of nitroxides, *J. Magn. Reson.* **51**:138-144.

Bales, B. L., and Willett, D., 1984, EPR investigation of the intermediate spin exchange regime, *J. Chem. Phys.* **80**:2997-3004.

Bales, B. L., Dolin, R. A., and Schwartz, Robert N., 1984, An effective proton hyperfine tensor for di-tertbutylnitroxide, *Liq. Cryst. Ord. Fluids* **4**:579-596.

Bales, B. L., Schumacher, K. L., and Harris, F. L., 1987a, Correction for inhomogeneous line broadening in spin labels. III. Doxyl-labeled alkyl chains, *J. Magn. Reson.* **72**:364-368.

Bales, B. L., Schumacher, K. L., and Harris, F. L., 1987b, Temperature dependence of the inhomogeneous line broadening in the EPR spectra of doxyl-labeled alkyl chains, *J. Phys. Chem.* **91**:1701-1702.

Barbarin, F., Chevarin, B., Germain, J. P., Fabre, C., and Cabaret, D., 1978a, Resonance Paramagnetique, *Mol. Cryst. Liq. Cryst.* **46**:181-193.

Barbarin, F., Chevarin, B., Germain, J. P., Fabre, C., and Cabaret, C., 1978b, Synthèse d'une sonde nitroxyde deuterée de forme allongée, *Mol. Cryst. Liq. Cryst.* **46**:195-207.

Beth, A. H., Perkins Jr., R. C., Venkataramu, S. D., Pearson, D. E., Park, C. R., Park, J. H., and Dalton, L. R., 1980, Advantages of deuterium modification of nitroxide spin labels for biological EPR studies, *Chem. Phys. Lett.*, **69**:24-28.

Brière, R., Lemaire, H., Rassat, A., Rey, P., and Pousseau, A., 1967, Résonance magnétique nucléaire de radicaux libres nitroxydes piperidiniques, *Bull. Soc. Chim. Fr.*:4479-4484.

Brière, R., Lemaire, H., Rassat, A., and Dunand, J., 1970, Etude de l'interconversion d'un radical libre nitroxyde piperidinique, par RMN à 310 MHz, *Bull. Soc. Chim. Fr.*:4220-4226.

Bullock, A. T., Cameron, G. G., and Smith, P. M., 1975, Electron spin resonance studies of spin-labelled polymers—VIII, *Eur. Poly. J.*, **11**:617-624.

Calder, A., Forrester, A. R., Emsley, J. W., Luckhurst, G. R., and Storey, R. A., 1970, Nitroxide radicals Part VII. Nuclear and electron resonance spectra of some aromatic *t*-butyl nitroxides, *Mol. Phys.* **18**:481-489.

Chesnut, D. B., 1977, On the use of the AW^2 method for integrated line intensities from first derivative presentations, *J. Magn. Reson.* **25**:373-374.

Chiarelli, R., and Rassat, A., 1973, Nitroxydes LVI. Synthèses de radicaux nitroxydes deuteries, *Tetrahedron* **29**:3639-3647.

Currin, J. D., 1962, Theory of exchange relaxation of hyperfine structure in electron spin resonance, *Phys. Rev.* **126**:1995-2001.

Dalton, L. A., Monge, J. L., Dalton, L. R., and Kwiram, A. L., 1974, Molecular and applied modulation effects in electron-electron double resonance. III. Bloch equation analysis for inhomogeneous broadening, *Chem. Phys.* **6**:166-169.

Dobryakov, S. N., and Lebedev, Ya. S., 1969, Analysis of spectral lines whose profile is described by a composition of Gaussian and Lorentz profiles, *Sov. Phys. Dokl.* **13**:873-875.

Dunand, J., 1968, Résonance magnétique nucléaire—Haute résolution du proton dans des radicaux libres nitroxydes à 310 MHz, *C. R. Acad. Sci. Paris* **267**:82-85.

Eastman, M. P., Kooser, R. G., Das, M. R., and Freed, J. H., 1969, Studies of Heisenberg spin exchange in ESR spectra. I. Linewidth and saturation effects, *J. Chem. Phys.* **51**:2690-2709.

Eaton, S. S., Willigen, H. V., Heinig, M. J., and Eaton, G. R., 1980, Endor measurement of long-range hyperfine coupling in a nitroxyl radical, *J. Magn. Res.* **38**:325-330.

Faber, R. J., Markley, F. W., and Weil, J. A., 1967, Hyperfine structure in the solution ESR spectrum of di-*tert*-butyl nitroxide, *J. Chem. Phys.* **46**:1652-1654.

Farach, H. A., and Teilelbaum, H., 1967, Spectroscopic line analysis using a Gaussian and Lorentzian convolution technique, *Can. J. Phys.* **45**:2913-2921.

Fox, K. K., 1976, Isotropic proton hyperfine coupling constants of two cationic nitroxides, *J. Chem. Soc., Faraday Trans.* **2**:975-982.

Freed, J. H., 1966, On Heisenberg spin exchange in liquids, *J. Chem. Phys.* **45**:3452-3453.

Freed, J. H., 1967, Theory of saturation and double resonance effects in electron spin resonance spectra. II. Exchange vs. dipolar mechanisms, *J. Phys. Chem.* **71**:38-51.

Freed, J. H., 1976, Theory of slow tumbling ESR spectra for nitroxides, in *Spin Labeling Theory and Application* (L. J. Berliner, ed.), Chap. 3, Academic Press, New York.

Goldman, S. A., Bruno, G. V., Polnaszek, C. F., and Freed, J. H., 1972, An ESR study of anistropic rotational reorientation and slow tumbling in liquid and frozen media, *J. Chem. Phys.* **56**:716-735.

Hatch, G. F., and Kreilick, R. W., 1972, NMR of some nitroxide radicals: ^{13}C coupling constants, *J. Chem. Phys.* **57**:3696-3699.

Hauser, K. H., Brunner, H., and Jochims, J. C., 1966, Nuclear magnetic resonance of organic free radicals, *Mol. Phys.* **10**:253-260.

Hommel, H., Faccini, L., Legrand, A. P., and Lecourtier, J., 1978, Mobility of spin labeled polyethylene oxide chains grafted on silica. *Eur. Polym. J.* **14**:803-806.

Hubbell, W. L., and McConnell, H. M., 1968, Spin-label studies of the excitable membranes of nerve and muscle, *Proc. Natl. Acad. Sci. USA* **61**:12-16.

Hwang, J. S., Mason, R. P., Hwang, L., and Freed, J. H., 1975, Electron spin resonance studies of anisotropic rotational reorientation and slow tumbling in liquid and frozen media. III. Perdeuterated 2,2,6,-tetramethyl-4-piperidone *N*-oxide and an analysis of fluctuating torques, *J. Phys. Chem.* **79**:489-511.

Hyde, J. S., and Subczynski, W. K., 1984, Simulation of ESR spectra of the oxygen sensitive spin label probe CTPO, *J. Magn. Res.* **56**:125-130.

Janzen, E. G., Coulter, G. A., Oehler, V. M., and Bergsma, J. H., 1982, Solvent effects on the nitrogen and β-hydrogen hyperfine splitting constants of aminoxyl radicals obtained in spin trapping experiments, *Can. J. Chem.* **60**:2725-2733.

Johnson, Jr., C. S., 1967, Theory of line widths and shifts in electron spin resonance arising from spin exchange interactions, *Mol. Phys.* **12**:25-31.

Jolicoeur, C., and Friedman, H. L., 1971, Effects of hydrophobic interactions on dynamics in aqueous solutions studied by EPR, *Ber. Bunsenges. Phys. Chem.* **75**:248-257.

Jones, L. L., and Schwartz, R. N., 1981, An electron paramagnetic resonance study of rotational and translational motion in solution, *Mol. Phys.* **43**:527-555.

Kamlet, J. J., and Taft, R. W., 1979, Linear solvation energy relationships, Part 3. Some reinterpretations of solvent effects based on correlations with solvent and values, *J. Chem. Soc., Perkin Trans. 2* **54**:349-356.

Keith, A. D., Snipes, W., Mehlhorn, R. J., and Gunter, T., 1977, Factors restricting diffusion of water-soluble spin labels, *Biophys. J.* **19**:205-218.

King, M. D., Sachse, J. H., and Marsh, D., 1987, Unconstrained optimization method for interpreting the concentration and temperature dependence of the linewidths of interacting nitroxide spin labels. Application to the measurement of translational diffusion coefficients of spin-labeled phospholipids in membranes, *J. Magn. Reson.* **72**:257-267.

Kirste, B., Kruger, A., and Kurreck, H., 1982, ESR and ENDOR investigations of spin exchange in mixed galvinoxyl/nitroxide biradicals. Syntheses, *J. Am. Chem. Soc.* **104**:3850-3858.

Kivelson, D., 1972, Electron spin relaxation in liquids, in *Electron Spin Relaxation in Liquids*, (L. T. Muus and P. W. Atkins, eds.), Plenum, New York, pp. 213-277.

Knauer, B. R., and Napier, J. J., 1976, The nitrogen hyperfine splitting constant of the nitroxide functional group as a solvent polarity parameter. The relative importance for a solvent polarity parameter of its being a cybotactic probe vs. its being a model process, *J. Am. Chem. Soc.* **98**:4395-4400.

Kopf, P. W., and Kreilick, R. W., 1969, Magnetic resonance studies of some phenoxy and nitroxide biradicals, *J. Am. Chem. Soc.* **91**:6569-6573.

Kotake, Y., Tomita, Y., and Kuwata, K., 1985, Proton hyperfine splitting and slow motion of spin labels in frozen glycerol as detected by ENDOR, *J. Phys. Chem.* **89**:207-209.

Kovarskii, A. L., Wasserman, A. M., and Buchachenko, A. L., 1972, The study of rotational and translational diffusion constants for stable nitroxide radicals in liquids and polymers, *J. Magn. Reson.* **7**:225-237.

Kowert, B. A., Bamoro, J. J., Walters, K. M., Crimi, J. J., and Mendez Jr., S., 1985, Reorientational information from the intensities of nitroxide electron spin resonance spectra, *J. Magn. Reson.* **63**:573-578.

Kreilick, R. W., 1966, NMR spectra of some nitroxide radicals, *J. Chem. Phys.* **45**:1922-1924.

Kreilick, R. W., 1967, NMR studies of a series of aliphatic nitroxide radicals, *J. Chem. Phys.* **46**:4260-4264.

Kuznetsov, A. N., Volkov, A. Y., Livshits, V. A., and Mirzoian, A. T., 1974, A method of studying anisotropic rotation of organic nitroxyl radicals, *Chem. Phys. Lett.* **26**:369-372.

Labsky, J. J., Pilar, J., and Lovy, J., 1980, Magnetic resonance study of 4-amino-2,2,6,6-tetramethylpiperidine-*N*-oxyl and its deuterated derivatives, *J. Magn. Reson.* **37**:515-522.

Lang Jr., J. C., and Freed, J. H., 1972, ESR study of Heisenberg spin exchange in a binary liquid solution near the critical point, *J. Chem. Phys.* **56**:4103-4114.

Lee, P. L., 1977, Width of a Lorentzian convoluted with a Gaussian, *Nucl. Instrum. Methods* **144**:363-365.

Lee, S, and Shetty, A., 1985, Fast orientational-motional correlation time measurements from ESR hyperfine spectra of perdeuterated nitroxides with ^{15}N ($I = 1/2$), *J. Chem. Phys.* **83**:499-505.

Lim, Y. Y., Smith, E. A., and Symons, R. C., 1976, Solvation spectra Part 51.—Di-*t*-butyl nitroxide as a probe for studying water and aqueous solutions, *J. Chem. Soc., Faraday Trans. 1* **72**:2876-2891.

Marriott, T. B., Van, S. P., and Griffith, O. H., 1976, Axial isomer and ESR spectra of the steroid spin label, 3-doxyl-5-cholestane, *J. Magn. Reson.* **24**:41-52.

Michon, P., and Rassat, A., 1971, No. 601.—Nitroxydes XLII: Signe des couplages à longue distance, électro-protons dans des nitroxydes oxazolidiniques. Etude conformationnelle par RMN, *Bull. Soc. Chim. Fr.*:3561-3567.

Michon, P., and Rassat, A., 1974, Nitroxides. LVIII. Structure of steroidal spin labels, *J. Org. Chem.* **39**:2121-2124.

Miller, W. G., 1979, Spin-labeled synthetic polymers, in *Spin Labeling II Theory and Applications* (L. J. Berliner, ed.), Chap. 4, Academic Press, New York.

Molin, Yu. N., Salikhov, K. M., and Zamaraev, K. I., 1980 *Spin exchange principles and applications in chemistry and biology*, Springer-Verlag, Berlin.

More, K. M., Eaton, G. R., and Eaton, S. S., 1984, Determination of T_1 and T_2 by simulation of EPR power saturation curves and saturated spectra. Application to spin-labeled iron porphyrins, *J. Magn. Res.* **60**:54-65.

Morrisett, J. D., 1976, The use of spin labels for studying the structure and function of enzymes, in *Spin Labeling Theory and Applications* (L. J. Berliner, ed.), Chap. 8, Academic Press, New York.

Mossoba, M. M., Makino, K., Riesz, P., and Perkins Jr., R. C., 1984, Long-range proton hyperfine coupling in alicyclic nitroxide radicals by resolution-enhanced electron paramagnetic resonance, *J. Phys. Chem.* **88**:4717-4723.

Mukerjee, P., Ramachandran, C., and Pyter, R. A., 1982, Solvent effects on the visible spectra of nitroxides and relation to nitrogen hyperfine splitting constants. Nonempirical polarity scales for aprotic and hydroxylic solvents, *J. Phys. Chem.* **86**:3189-3197.

Ohzeki, F., Kispert, L. D., Arroyo, D. C., and Steffan, M., 1982, Electron nuclear double resonance study of the spin-label tanol (tempol) oriented in the inclusion compound 2'hydroxy-2,4,4,7,4'-pentamethylflavan, *J. Phys. Chem.* **86**:4011-4016.

Ottaviani, M. F., Baglioni, P., and Martini, G., 1983, Micellar solutions of sulfate surfactants studied by electron spin resonance of nitroxide radicals. 1. Use of neutral and positively charged spin probes, *J. Phys. Chem.* **87**:3146-3153.

Ottaviani, M. F., 1987, Analysis of resolved ESR spectra of neutral nitroxide radicals in ethanol and pyridine: The dynamic behavior in fast motion conditions, *J. Phys. Chem.* **91**:779-784.

Parker, G. W., 1970, Nuclear magnetic resonance line shapes in solids, *Am. J. Phys.* **38**:1432-1439.

Plachy, W., and Kivelson, D., 1967, Spin exchange in solutions of di-tertiary-butyl nitroxide, *J. Chem. Phys.* **47**:3312-3318.

Poggi, G., and Johnson Jr., C. S., 1970, Factors involved in the determination of rotational correlation times for spin labels, *J. Magn. Res.* **3**:436-445.

Polnaszek, C. F., and Freed, J. H., 1975, Electron spin resonance studies of anisotropic ordering, spin relaxation, and slow tumbling in liquid crystalline solvents, *J. Phys. Chem.* **79**:2283-2306.

Polnaszek, C. F., Schreier, S., Butler, K. W., and Smith, I. C. P., 1978, Analysis of the factors determining the EPR spectra of spin probes that partition between aqueous and lipid phases, *J. Am. Chem. Soc.* **100**:8223-8232.

Portis, A. M., 1953, Electronic structure of F centers: Saturation of the electron spin resonance, *Phys. Rev.* **91**:1071-1078.

Reddock, A. H., and Konishi, S., 1979, The solvent effect on di-*tert*-butyl nitroxide. A dipole-dipole model for polar solutes in polar solvents, *J. Chem. Phys.* **70**:2121-2130.

Reif, F., 1965, *Fundamental of Statistical and Thermal Physics*, Chap. 1, McGraw-Hill, New York.

Schreier, S., Polnaszek, C. F., and Smith, I. C. P., 1978, Spin labels in membranes, problems in practice, *Biochim. Biophys. Acta* **515**:375-436.

Stillman, A. M., and Schwartz, R. N., 1976, Heisenberg exchange in inhomogeneously broadened nitroxide EPR spectra, *J. Magn. Reson.* **22**:269–277.

Stoneham, A. M., 1972, Linewidths with Gaussian and Lorentzian broadening, *J. Phys. D* **5**:670–672.

Swartz, H. M., 1987, Use of nitroxides to measure redox metabolism in cells and tissues, *J. Chem. Soc., Faraday Trans. 1* **83**:191–202.

Trousson, P., and Lion, Y., 1985, Fourier transform numerical analysis of the long-range proton hyperfine coupling in nitroxide radicals, *J. Phys. Chem.* **89**:154–158.

Tsay, F. D., Hong, S. D., Moacanin, J., and Gupta, A., 1982, Studies of magnetic resonance phenomena in polymers. I. The effects of free volume and segmental mobility on the motion of nitroxide spin probes and labels in poly(methyl methacrylate), *J. Polym. Sci., Polym. Phys. Ed.* **20**:763–775.

Wertheim, G. K., Butler, M. A., West, K. W., and Buchanan, D. N. E., 1974, Determination of the Gaussian and Lorentzian content of experimental line shapes, *Rev. Sci. Instrum.* **45**:1369–1371.

Whisnant, C. C., Ferguson, S., and Chesnut, D. B., 1974, Hyperfine models for piperidine nitroxides, *J. Phys. Chem.* **78**:1410–1415.

Windle, J. J., 1981, Hyperfine coupling constants for nitroxide spin probes in water and carbon tetrachloride, *J. Magn. Reson.* **45**:432–439.

Zager, S. A., and Freed, J. H., 1982a, Electron-spin relaxation and molecular dynamics in liquids. I. Solvent dependence, *J. Chem. Phys.* **77**:3344–3359.

Zager, S. A., and Freed, J. H., 1982b, Electron-spin relaxation and molecular dynamics in liquids. II. Density dependence, *J. Chem. Phys.* **77**:3360–3375.

Zemansky, M. W., 1930, Absorption and collision broadening of the mercury resonance line, *Phys. Rev.* **36**:219–238.

3

Saturation Transfer Spectroscopy of Spin Labels

Techniques and Interpretation of Spectra

M. A. Hemminga and P. A. de Jager

1. INTRODUCTION

Saturation transfer (ST) ESR is a relatively new ESR technique that is sensitive to very slow motions with rotational correlation times from 10^{-6} to 10^{-3} s, a region where conventional ESR is not sensitive. The ST-ESR technique has been used especially in spin-label studies of biological systems: supramolecular aggregates and gel-like lipid and membrane systems. A large number of papers has appeared since the first introduction of the technique by Hyde and co-workers (Hyde and Dalton, 1972; Hyde and Thomas, 1973), including some excellent review papers about the technique and biological applications (Dalton *et al.*, 1976; Hyde, 1978; Hyde and Dalton, 1979; Hyde and Thomas, 1980; Hemminga, 1983; Dalton, 1985).

The objective of this chapter is to provide a physical insight into the theory and methodology of ST-ESR, which is largely dictated by the experience with the technique in the authors' group. No detailed review will be given of the existing literature and applications of ST-ESR. The reader is then referred to a recent book by Dalton and co-workers (Dalton, 1985) and other of the above-mentioned review articles.

ST-ESR is a method that measures the transfer of saturation throughout a spectrum by reorientational molecular motions. Therefore the shape of ST-ESR spectra is not only sensitive to molecular motion but also depends on the saturation properties of the spin label. A detailed theoretical description of ST-ESR is very complicated. Computer simulation is expensive in computer time and memory and the results are

M. A. Hemminga and P. A. de Jager • Department of Molecular Physics, Agricultural University, 6703 HA Wageningen, The Netherlands.

rather poor. For this reason a number of qualitative methods has been developed in the literature for the analysis of spectra. The theory and basic principles for such an analysis are given in Section 2.

In contrast to conventional ESR, which is generally carried out below saturation and with small field modulation amplitudes, ST-ESR is a highly nonlinear ESR technique. To observe transfer of saturation the experiment is performed under saturating conditions and high field modulation amplitudes are used. Since the microwave field strength and field modulation amplitude vary over the cavity, the resulting ST-ESR spectrum depends strongly on these parameters. Since it is important to be aware of these effects and recognise them in practical situations, these aspects will be treated in Section 3.

In Section 4 some methods will be discussed for a qualitative analysis of ST-ESR spectra in various biological systems. In such an analysis an important question is not only the sensitivity of the ST-ESR spectrum to changes in the rotational correlation time, but also the signal-to-noise ratio in the spectra. Currently available methods will be discussed in the light of this question. Finally, in Section 5 future developments for ST-ESR will be discussed.

2. BASIC PRINCIPLES OF SATURATION TRANSFER ESR

In the analysis of conventional ESR line shapes in terms of motional and orientational parameters, experiments are carried out below saturation and with small values of the field modulation amplitude to avoid distortion of the line shape. In contrast, ST-ESR spectra are recorded under saturation conditions and high modulation amplitudes to observe the response of the spin system on spectral diffusion of saturation by molecular motion.

To obtain a physical insight in the principles of ST-ESR, the ESR theory of nitroxide spin labels is briefly repeated here. For a more elaborate treatment, the reader is referred to a number of general textbooks (Carrington and McLachlan, 1967; Poole, 1967; Poole and Farrach, 1971), books especially devoted to spin labeling (Berliner, 1976, 1979), and recent review papers (Schreier *et al.*, 1978; Marsh, 1981; Hemminga, 1983). This theory will be extended to ST-ESR by introducing the effects of saturation, spectral diffusion, and field modulation.

2.1. The Spin Hamiltonian

The spin Hamiltonian of a nitroxide radical expressed in energy units is given by

$$\mathcal{H} = \mu_B \mathbf{B} \cdot \mathbf{g} \cdot \mathbf{S} + \mathbf{I} \cdot \mathbf{A} \cdot \mathbf{S} \tag{1}$$

The first term describes the interaction of the unpaired electron with a strong externally applied stationary magnetic field **B** (Zeeman interaction). This interaction is anisotropic as indicated by the g-factor tensor **g**. The constant μ_B denotes the Bohr magneton and **S** is the electron spin operator. The second term gives the hyperfine interaction of the unpaired electron with the ^{14}N nucleus (nuclear spin $I = 1$). This interaction also is anisotropic and given by a hyperfine tensor **A**. The nuclear spin operator is **I**.

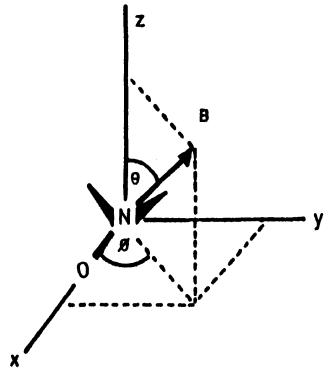

Figure 1. The nitroxide principal axes system $\{x, y, z\}$. The orientation of the magnetic field **B** is given by the polar angles θ, ϕ. (From Hemminga, 1983.)

The success and importance of the spin-label method in studying the structure and dynamics of the labeled system is based on the fact that the **g** and **A** tensors are anisotropic, making the ESR spectra critically dependent on the orientation of the spin label. Therefore it is convenient to define a Cartesian molecule-fixed axes system $\{x, y, z\}$ for nitroxide radicals as depicted in Figure 1. The x axis coincides with the N—O bond and the z axis is along the $2p\pi$ orbital, which is occupied by the unpaired electron. It is generally assumed that this axis system coincides with both the principal-axes system of the **g** and **A** tensors. Thus **g** and **A** are simultaneously diagonal in this system. The diagonal elements (or principal values) are indicated by g_{xx}, A_{xx}, etc. Values for the principal values of the **g** and **A** tensors are given in Table 1.

2.2. ESR Spectra of Immobilized Spin Labels

To illustrate the anisotropic behavior of the **g** and **A** tensors, we apply the magnetic field **B** along the z axis of the spin label and calculate the ESR spectrum. The spin Hamiltonian equation (1) then reduces to

$$\mathcal{H} = \mu_B g_{zz} B S_z + A_{zz} I_z S_z \tag{2}$$

This spin Hamiltonian is readily solved, yielding the energy levels

$$E(M_S, M_I) = \mu_B g_{zz} B M_S + A_{zz} M_I M_S \tag{3}$$

TABLE 1
Approximate Values for the Components of the g and A Tensor of Nitroxide Spin Labels

g_{xx}	g_{yy}	g_{zz}	A_{xx} (mT)	A_{yy} (mT)	A_{zz} (mT)
2.009	2.006	2.002	0.6	0.6	3.2

The electron spin quantum number M_S takes the values $+\frac{1}{2}$ (α spin) and $-\frac{1}{2}$ (β spin), while M_I can take the values 1, 0, and -1. In an ESR experiment an oscillating magnetic field ($2B_1 \cos \omega_0 t$, where B_1 is a circularly polarized rf field component) is applied perpendicular to **B**, inducing transitions between the electron spin states (M_S: $-\frac{1}{2} \leftrightarrow +\frac{1}{2}$) provided that the frequency $\omega_0 = 2\pi\nu_0$ satisfies the resonance condition. This gives

$$\Delta E = h\nu_0 = \mu_B g_{zz} B + A_{zz} M_I \tag{4}$$

where h is Planck's constant. This is the basic principle of magnetic resonance. The resonance condition is usually found by varying the magnetic field, yielding three resonance lines with equal height and separation corresponding to the M_I states of the nitrogen nucleus. The resonance positions and the corresponding ESR spectrum, which is the first derivative of the absorption spectrum, are shown in Figure 2. The center of the ESR spectrum is given by g_{zz}; the splitting is A_{zz}.

A similar analysis can be made for **B** oriented along the x and y axes of the spin label. This is illustrated in Figure 2, which follows experimentally from orientation-dependent ESR studies of nitroxide molecules dissolved in single-crystal hosts. From

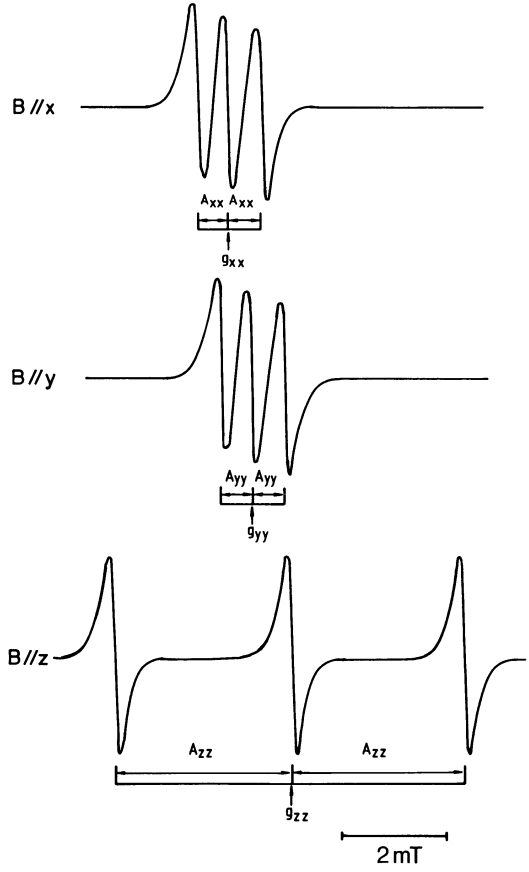

Figure 2. Theoretical ESR spectra of a single nitroxide molecule with the magnetic field **B** directed along the principal axes x, y, and z. For the calculation, the values of the **g** and **A** tensor components from Table 1 have been used. The microwave frequency is 9.5 GHz. (From Hemminga, 1983.)

Figure 2 it is seen that, because the components of the **g** and **A** tensors are different, the ESR spectra depend strongly on the orientation of **B**.

For a quantitative description of the ESR spectra with a general orientation of **B**, a first-order solution of equation (1) yields

$$h\nu_0 = \mu_B g(\theta, \phi)B + A(\theta, \phi)M_I \tag{5}$$

where

$$g(\theta, \phi) = g_{xx} \sin^2 \theta \cos^2 \phi + g_{yy} \sin^2 \theta \sin^2 \phi + g_{zz} \cos^2 \theta \tag{6}$$

and

$$A(\theta, \phi) = (A_{xx}^2 \sin^2 \theta \cos^2 \phi + A_{yy}^2 \sin^2 \theta \sin^2 \phi + A_{zz}^2 \cos^2 \theta)^{1/2} \tag{7}$$

The polar angles θ and ϕ specify the orientation of **B** with respect to the molecule-fixed principal-axes system (Figure 1).

For samples that are not oriented single crystals but consist of a random isotropic distribution of the molecular axes, an ESR powder spectrum is obtained which is a superposition of spectra at all orientations of **B** with respect to the molecule-fixed axes system.

Since ST-ESR is concerned with powder-like spectra, it is important to consider them in more detail. Let us calculate, therefore, the powder spectrum for a rather simple case of a radical ($S = \frac{1}{2}$) with an axially symmetric **g** tensor (i.e., $g_{xx} = g_{yy} = g_\perp$; $g_{zz} = g_\parallel$) and no hyperfine interaction. Equation (5) then yields

$$h\nu_0 = \mu_B(g_\perp \sin^2 \theta + g_\parallel \cos^2 \theta)B$$

and the angular-dependent resonance value $B(\theta)$ is given by

$$B(\theta) = (h\nu_0/\mu_B)(g_\perp \sin^2 \theta + g_\parallel \cos^2 \theta)^{-1} \tag{8}$$

The powder line shape $L(B)$ is given by the proportionality

$$L(B) \sim [dB(\theta)/d\theta]^{-1} \sin \theta$$

which results in

$$L(B) = \{[B(\theta)]^2(g_\parallel - g_\perp) \cos \theta\}^{-1} \tag{9}$$

This function is depicted in Figure 3a. In real situations line broadening mechanisms (e.g., spin–spin relaxation and unresolved proton hyperfine splittings) broaden the line-shape function. If $f(B')$ denotes the line-broadening function, the broadened absorption line shape $A(B)$ is given by the convolution integral

$$A(B) = \int f(B')L(B - B')\, dB' \tag{10}$$

This results in the absorption spectrum in Figure 3b. The ESR spectrum is the first derivative of this spectrum (Figure 3c).

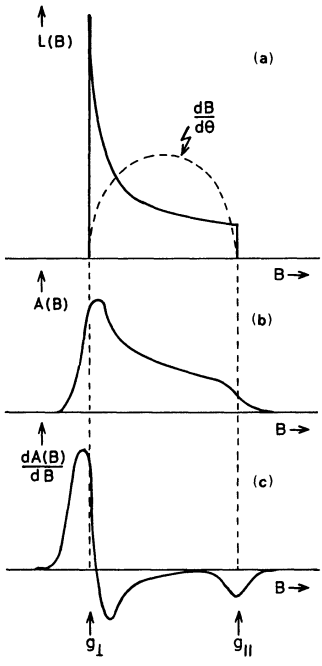

Figure 3. Theoretical line shapes for a random distribution of simple radicals ($S = \frac{1}{2}$) with an axially symmetric **g** tensor and no hyperfine interaction. (a) Unbroadened powder line-shape function $L(B)$ as given by equation (9). The broken line is the function $dB(\theta)/d\theta$ given by equation (33). (b) Broadened absorption spectrum $A(B)$ calculated from equation (10). (c) ESR powder spectrum $dA(B)/dB$. The principal values of the **g** tensor are $g_{\parallel}$ and $g_{\perp}$. (From Hemminga, 1983.)

Without going into complex mathematics we present in Figure 4 the schematic line shape of a powder sample of a radical with $g_{xx} > g_{yy} > g_{zz}$ by joining two line shapes, as in Figure 3a, back to back. Figure 4 actually represents the $M_I = 0$ part of the ESR powder spectrum for a nitroxide radical. We can apply the same principle to the $M_I = \pm 1$ parts, as is illustrated in Figure 5. This demonstrates that the powder spectrum of a nitroxide radical is a sum of three line shapes as given in Figure 4. Although this simple principle does not quantitatively predict ESR powder line shapes, the main features can be well understood qualitatively.

2.3. The Bloch Equations

Let us assume a simple system, consisting of an ensemble of electron spins. Relaxation effects can be introduced by a set of differential equations that describe the macroscopic magnetization **M** of the electron spins in the presence of an external magnetic field **B** and a circularly polarized rf magnetic field $\mathbf{B}_1 = B_1(\mathbf{i}\cos\omega t - \mathbf{j}\sin\omega t)$, which rotates in the same sense as the precessing spins:

$$d\mathbf{M}/dt = \gamma(\mathbf{M} \times \mathbf{B}) + \gamma(\mathbf{M} \times \mathbf{B}_1) - (M_x\mathbf{i} + M_y\mathbf{j})/T_2 - (M_z - M_0)\mathbf{k}/T_1 \qquad (11)$$

where **i**, **j**, and **k** are unit vectors along the x, y, and z axes; M_x, M_y, and M_z are the components of **M**, and ω is the angular frequency. The equilibrium value of M_z is M_0. The constant γ is the gyromagnetic ratio of the electron spin; T_1 indicates the spin-lattice relaxation time. Line-broadening processes of the spin system are characterized by a

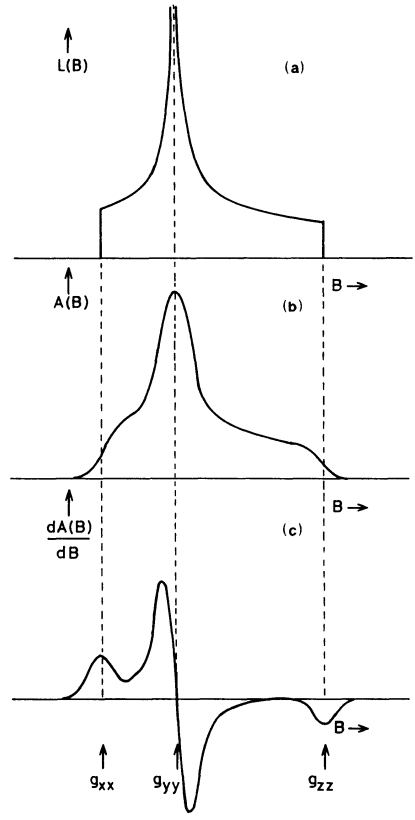

Figure 4. Schematic line shapes of a random distribution of simple radicals ($S = \frac{1}{2}$) with **g** tensor components $g_{xx} > g_{yy} > g_{zz}$ and no hyperfine interaction. (a) Unbroadened absorption powder spectrum $L(B)$; (b) Broadened absorption powder spectrum $A(B)$. (c) ESR powder spectrum $dA(B)/dB$. (From Hemminga, 1983.)

relaxation time T_2, the spin-spin relaxation time. For nitroxide radicals T_1 is of the order of 10^{-6}-10^{-5} s, while T_2 is of the order of 10^{-8} s (Huisjen and Hyde, 1974; Percival and Hyde, 1976). The equations for the time derivative of the components of **M** are called the Bloch equations.

Equation (11) can be solved under steady-state conditions, yielding the absorption line shape $A(B)$ of the electron spins,

$$A(B) \sim \frac{B_1}{1 + (B - B_0)^2\gamma^2T_2^2 + B_1^2\gamma^2T_1T_2} \tag{12}$$

The first-derivative ESR line shape $A' = dA/dB$ is then

$$A'(B) \sim \frac{(B - B_0)\gamma T_2 B_1}{[1 + (B - B_0)^2\gamma^2T_2^2 + B_1^2\gamma^2T_1T_2]^2} \tag{13}$$

B_0 is the center of the absorption line.

Both line shapes are depicted in Figure 6. The dispersion line shape can be found as well, but will not be considered here.

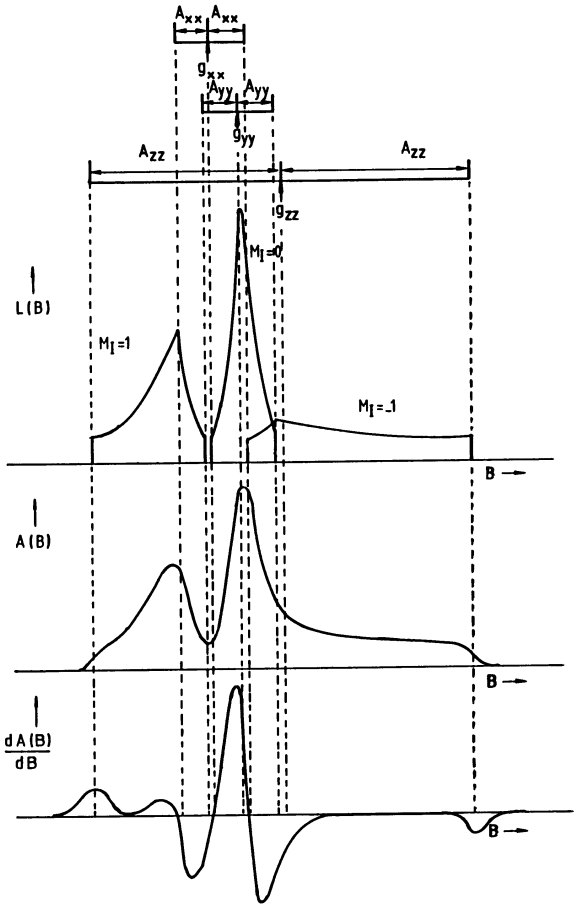

Figure 5. Schematic line shape of randomly oriented nitroxide spin labels at 9.5 GHz. For the calculation the values of the **g** and **A** tensor components from Table 1 have been used. (From Hemminga, 1983.)

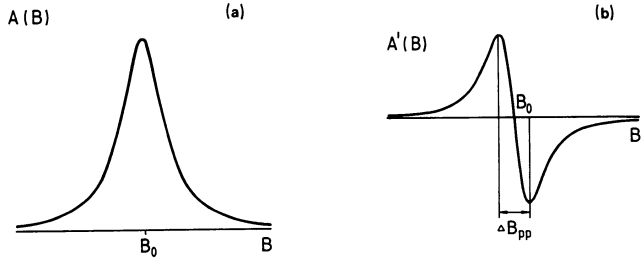

Figure 6. (a) Characteristic absorption line shape $[A(B)]$ and (b) first-derivative ESR line shape $(A' = dA/dB)$ of electron spins in the presence of an external magnetic field **B** and a circularly polarized rf magnetic field $\mathbf{B}_1$, below saturation, $B_1 \ll (\gamma^2 T_1 T_2)^{-1/2}$ (see text).

From equations (12) and (13) it follows that the line shapes depend on the value of B_1 and the relaxation times T_1 and T_2. Below saturation (i.e., $B_1^2\gamma^2 T_1 T_2 \ll 1$), the amplitude of the absorption line shape is proportional to B_1, while at high values of B_1 saturation occurs and the amplitude reduces to zero with B_1^{-1}. For the ESR line shape $A'(B)$, the saturation effects can be expressed by calculating the peak-to-peak line width ΔB_{pp} from equation (13):

$$\Delta B_{pp}^2 = \frac{4}{3}\frac{1}{\gamma^2 T_2^2}(1 + B_1^2\gamma^2 T_1 T_2) \tag{14}$$

which shows that, with increasing values of B_1, the width of the line shape increases. Another parameter that characterizes the ESR line shape is its maximum height A'_{max} which, from equation (13), is found to be

$$A'_{max} \sim B_1(1 + B_1^2\gamma^2 T_1 T_2)^{-3/2} \tag{15}$$

A plot of A'_{max} against B_1 is shown in Figure 7. Below saturation A'_{max} increases linearly with B_1. For high values of B_1, A'_{max} is proportional to B_1^{-2}.

The saturation behavior of the spin system is accurately characterized by a value of B_1 given by $B_1 = (B_1)_{1/2}$ for which A'_{max} is half the value of a linear extrapolation (see Figure 7). It can be derived from equation (15) that

$$(B_1)_{1/2} = \left(\frac{2^{2/3} - 1}{\gamma^2 T_1 T_2}\right)^{1/2} \tag{16}$$

It will be seen in Section 3.4 that equations (14) and (16) are useful to calibrate the microwave field strength of an ESR spectrometer for ST-ESR studies.

For a more complex spin system such as a nitroxide radical, the Bloch equations cannot be well applied. Then, a more powerful and appropriate way to describe spin relaxation is the density matrix theory.

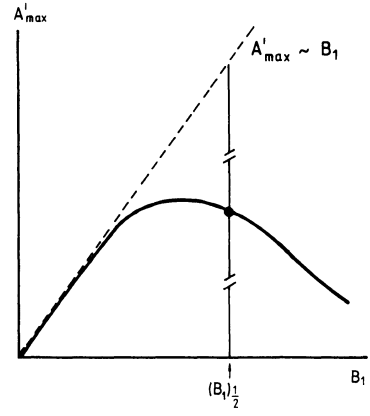

Figure 7. Saturation curve of the ESR signal of the spin system of Figure 6. $(B_1)_{1/2}$ is the value of B_1 for which A'_{max} is half the value of a linear extrapolation of the first part of the curve.

2.4. Qualitative Explanation of ST-ESR

Since the ESR spectra of spin labels are dependent upon the molecular orientation, reorientation by molecular motion will affect the spectra. Molecular motion can be physically characterized by a rotational correlation time τ_c. For isotropic motion of a sphere with radius r in a medium with viscosity η, τ_c is given by the Stokes-Einstein relation

$$\tau_c = 4\pi\eta r^3/3kT \tag{17}$$

where k is the Boltzmann constant and T the absolute temperature. If the motion is very fast, i.e., $\tau_c < 10^{-11}$ s, the ESR spectrum will consist of three sharp lines of equal height and positions given by the averages of the components of the **g** and **A** tensors. As the motion becomes progressively slower, there is a differential broadening of the lines in the spectrum, while the line positions remain constant. This is called the fast motional region. For values of $\tau_c > 3 \times 10^{-9}$ s a distortion of the line positions and line shape is observed. This region is the slow motional region. In the very slow motional region ($\tau_c > 10^{-6}$ s) the rigid powder spectrum is reached for conventional ESR. In this region, however, ST-ESR results in spectra still sensitive to molecular motion, the final limit of τ_c being approximately 10^{-3} s. The various ranges of isotropic molecular motion and the resulting ESR and ST-ESR spectra are shown in Figure 8.

The principle of ST-ESR, i.e., the effects of saturation and very slow, molecular motion on ESR powder line shapes, can be qualitatively explained by considering a rigid powder line shape of randomly oriented nitroxide spin labels (cf. Figure 5) (Hemminga, 1979). Each point of the line shape represents a number of spin labels with a specific orientation in the powder. Suppose we set a stationary magnetic field at a value B and apply a strong microwave rf field to the sample. Then a hole will be burned in the line shape at field position B. This arises from those spin labels that have an orientation (θ, ϕ) satisfying the resonance condition, equation (5). The width of the hole is determined by the line-shape function $f(B')$ of equation (10). This is illustrated in Figure 9 where, for simplicity, the microwave field is assumed to be strong

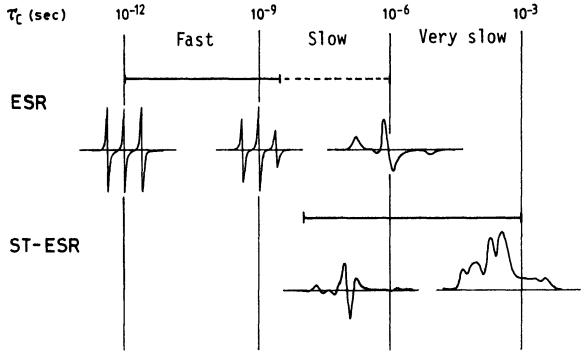

Figure 8. Survey of various motional regions and characteristic ESR and ST-ESR spectra for isotropic motion. The isotropic rotational correlation time is τ_c. The ST-ESR spectra shown are the second harmonic quadrature spectra. (From Hemminga, 1983.)

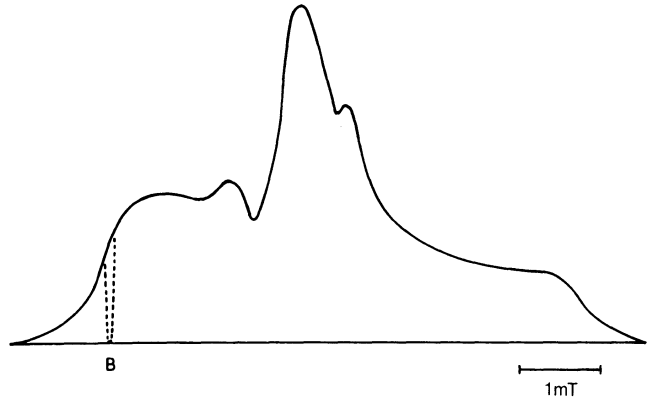

Figure 9. Schematic drawing of the absorption line shape of randomly oriented nitroxide spin labels. The dashed line indicates a hole that is burned in the line shape at B by strong resonant microwave radiation. (From Hemminga, 1979.)

enough for complete saturation. After switching-off the microwave field, the hole will exponentially fill up at a rate T_1^{-1} and the powder spectrum will return to its original shape.

Suppose now that after switching-off the microwave field the spin labels make a coherent rotational motion with a rate fast as compared to the lifetime of the hole, T_1. The hole will then move in the line shape to a field value B', belonging to the new orientation of the spin labels. In the case of a random rotational diffusion with rotational correlation time $\tau_c < T_1$, the hole at B will broaden and eventually fill up as the spectral diffusion of holes (i.e., transfer of saturation) proceeds. The shorter τ_c, the faster the hole at B fills up. This is very similar to the effect of T_1 on the hole-burning process, except that a broadening of the hole also appears. The effect of motion on the holes is illustrated in Figure 10. These theoretical aspects on a hole in an absorption line shape have been confirmed experimentally by Dzuba *et al.* (1984).

In conventional ESR and ST-ESR, field modulation in combination with phase-sensitive detection is used to observe the signals under continuous microwave radiation. If we denote the absorption signal by $A(B)$ and define the instantaneous external magnetic field as

$$B(t) = B + \tfrac{1}{2}B_m \cos \omega_m t \tag{18}$$

where B_m is the peak-to-peak modulation amplitude and ω_m is the modulation frequency, the absorption signal $A(B)$ becomes time-dependent. For low microwave field strength ($B_1 \lesssim 1\ \mu$T, i.e., in the absence of saturation) and neglecting fast passage effects, the time-dependent response of the system can be written as a Taylor expansion (Hemminga, 1983; Hemminga *et al.*, 1984a):

$$A(B, t) = A(B) + (\tfrac{1}{2}B_m \cos \omega_m t)A'(B) + \tfrac{1}{2}(\tfrac{1}{2}B_m \cos \omega_m t)^2 A''(B) + \cdots \tag{19}$$

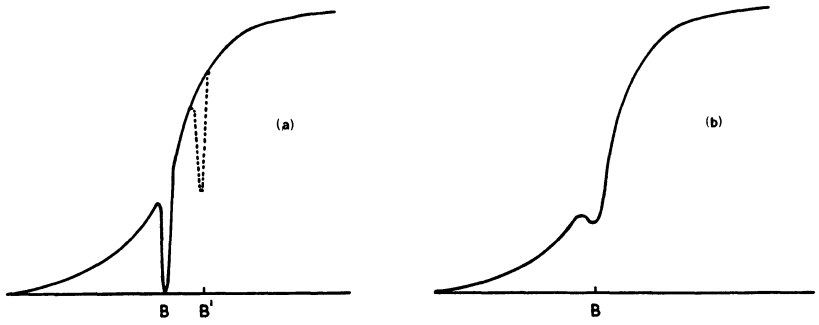

Figure 10. Schematic drawing of the effect of rotational motion on hole burning. (a) A hole is burned in the absorption line shape at B with a strong pulse of resonant microwave radiation. The hole shifts to B' when all nitroxide spin labels make a similar coherent very slow rotational motion. (b) Random rotational diffusion broadens the hole at B after a pulse of resonant microwave radiation because holes of individual nitroxide spin labels shift randomly around B. (From Hemminga, 1979.)

which can be shown to be an expansion of harmonics of the modulation frequency:

$$A(B, t) = \sum_{n=0}^{\infty} a_n \cos n\omega_m t \tag{20}$$

where the coefficients a_n depend on B_m, A, and the derivatives of A ($A' = dA/dB$, $A'' = d^2A/dB^2$, etc.).

When the reference frequency of the phase-sensitive detector is set at ω_r, in general two independent signals can be detected, one which oscillates with $\cos \omega_r t$ (the in-phase signal), and one which oscillates with $\sin \omega_r t$ (the quadrature or 90° phase shifted signal). For conventional ESR at low microwave field strength, the first harmonic ($\omega_r = \omega_m$) in-phase signal is detected. This signal is proportional to $B_m A'(B)$ provided B_m is small [see equation (19)]. Alternatively, the second harmonic ($\omega_r = 2\omega_m$) in-phase signal is approximately proportional to $B_m^2 A''(B)$. From equation (20) it is clear that no quadrature signals are present.

Under saturation conditions at high microwave field strength (typically $B_1 \cong 25\ \mu T$) holes are burned in the absorption line shape between $B \pm \frac{1}{2}B_m$ (see Figure 11). Assume now that the field modulation is switched on at time t_0. After time $t_1 = \pi\omega_m^{-1}$, the magnetic field $B(t)$ will meet holes in the line shape which have been burned previously and are not completely filled up. This is especially the case if $t_1 \cong T_1 \cong \tau_c$, or

$$\omega_m^{-1} \cong T_1 \cong \tau_c \tag{21}$$

This means that the spin system is unable to follow the field modulation. In a first approximation this nonlinear response can be represented by phase lags Φ_n in the signal $A(B, t)$ in equation (20) (Hemminga, 1983; Hemminga *et al.*, 1984a):

$$A(B, t) = \sum_{n=0}^{\infty} a_n \cos(n\omega_m t - \Phi_n) \tag{22}$$

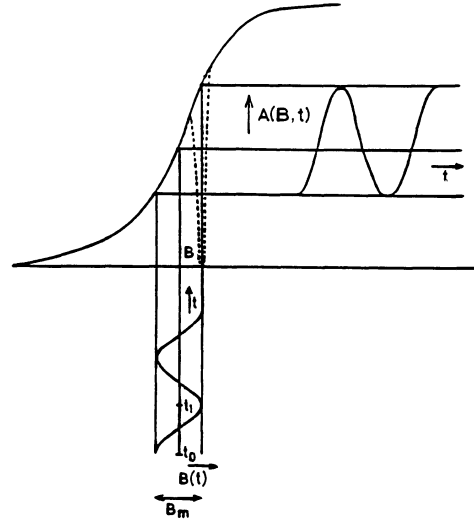

Figure 11. Effect of magnetic field modulation on the absorption line shape of randomly oriented nitroxide spin labels. $B(t)$ is the field modulation at B [see equation (19)] and B_m is the peak-to-peak modulation amplitude. $A(B, t)$ is the response of the spin system to field modulation. The broken line indicates a hole burned at $B + \frac{1}{2}B_m$ at time t_1. (From Hemminga, 1979.)

which can be separated into in-phase and quadrature signals:

$$A(B, t) = \sum_{n=0}^{\infty} a_n \cos \Phi_n \cos n\omega_m t \quad \text{(in-phase)}$$

$$+ \sum_{n=0}^{\infty} a_n \sin \Phi_n \sin n\omega_m t \quad \text{(quadrature)} \tag{23}$$

This shows that hole-burning effects in combination with field modulation generate quadrature signals. Furthermore, the quadrature as well as the in-phase signals depend upon the field modulation parameters (ω_m, B_m) and the hole-burning parameters (T_1, B_1). At low values of the microwave field strength, the quadrature signals vanish.

2.5. Spectral Displays of ST-ESR

The attractive point of the simple approach introduced in the previous section is that it clearly demonstrates the origin of in-phase $I_n(B)$ and quadrature $Q_n(B)$ spectra. It predicts that both types of spectra are affected by saturation effects through the phase lags Φ_n. However, the experimental line shapes are not well given by this theory, because the rate of spectral diffusion depends upon the position in the line shape, so that both a_n and Φ_n are a function of B. The exact dependence is not important here, but can be calculated from the density matrix theory by solving the stochastic Liouville equation (Dalton, 1985).

Equation (22) can be generalized, however, to the following equation which is true for any ST-ESR experiment:

$$A(B, t) = \sum_{n=0}^{\infty} M_n(B) \cos[n\omega_m t - \Phi_n(B)] \tag{24}$$

TABLE 2
Spectral Displays at the *n*th Harmonic in ST-ESR Spectroscopy

Symbol	Description
$I_n(B)$	Pure in-phase spectrum
$I'_n(B)$	Phase-shifted in-phase spectrum
$Q_n(B)$	Pure quadrature spectrum
$Q'_n(B)$	Phase-shifted quadrature spectrum
$M_n(B)$	Magnitude spectrum
$\Phi_n(B)$	Magnetization hysteresis spectrum
P_n	Phase plot of $Q_n(B)$ against $I_n(B)$

Here $M_n(B)$ is called the nth harmonic magnitude spectrum (Hemminga and de Jager, 1981) and $\Phi_n(B)$ the nth harmonic magnetization hysteresis spectrum (Vistnes, 1983). In analogy with equation (23), we can write

$$A(B, t) = \sum_{n=0}^{\infty} [I_n(B) \cos n\omega_m t + Q_n(B) \sin n\omega_m t] \tag{25}$$

where the nth harmonic in-phase $I_n(B)$ and quadrature $Q_n(B)$ spectra are given by

$$I_n(B) = M_n(B) \cos \Phi_n(B) \tag{26}$$

and

$$Q_n(B) = M_n(B) \sin \Phi_n(B) \tag{27}$$

A survey of several spectral displays is given in Table 2. It will be clear that, although quite a number of spectral displays of a ST-ESR experiment can be obtained at the nth harmonic, these displays are not independent.

Most commercial phase-sensitive detectors are able to measure two unique signals simultaneously in quadrature, so that experimentally one determines $I_n(B)$ and $Q_n(B)$. The magnitude and magnetization hysteresis spectra can then be calculated following the mathematical properties of a vector (see Figure 12):

$$M_n(B) = [I_n^2(B) + Q_n^2(B)]^{1/2} \tag{28}$$

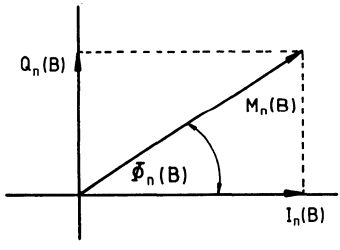

Figure 12. Vector diagram representing the relation between the various spectral displays $I_n(B)$: pure in-phase spectrum, $Q_n(B)$: pure quadrature spectrum, $M_n(B)$: magnitude spectrum, $\Phi_n(B)$: magnetization hysteresis spectrum.

and

$$\Phi_m(B) = \arctan[Q_n(B)/I_n(B)] \tag{29}$$

Another way of displaying a ST-ESR spectrum is by constructing a phase plot P_n of $Q_n(B)$ against $I_n(B)$. The P_n plot gives the locus of all end points of the vector M_n in Figure 12 as a function of B.

One unknown parameter in a ST-ESR experiment is the phase setting of the phase-sensitive detector. In general, a simultaneous set of experimental quadrature spectra $I'_n(B)$ and $Q'_n(B)$ is obtained from a dual phase-sensitive detector. This can be written as a linear combinatoin of the "pure" in-phase $I_n(B)$ and quadrature $Q_n(B)$ signals (Watanabe *et al.*, 1982) (also see Table 2):

$$I'_n(B) = I_n(B)\cos(\phi - \phi_0) + Q_n(B)\sin(\phi - \phi_0) \tag{30}$$

$$Q'_n(B) = -I_n(B)\sin(\phi - \phi_0) + Q_n(B)\cos(\phi - \phi_0) \tag{31}$$

where ϕ is the phase of the detector and ϕ_0 the phase setting for "pure" I_n and Q_n signals.

For values of ϕ close to ϕ_0, equation (31) can be approximated by

$$Q'_n(B) \cong -I_n(B)(\phi - \phi_0) + Q_n(B) \tag{32}$$

At a low microwave field strength, $Q_n(B)$ is small relative to $I_n(B)$, so that ϕ_0 can be obtained with high precision by minimizing $|Q'_n(B)|$ (Thomas *et al.*, 1976), or by plottting $Q'_n(B)$ (or a part of the spectrum that contains the largest amplitude) as a fuction of ϕ (null interpolation) (De Jager and Hemminga, 1978). The I_n and Q_n signals are then recorded at the desired value of the rf field without changing the phase of the detector, i.e., at $\phi = \phi_0$. These methods are called "self-null" methods, because the sample is used for calibration and observation. An alternative method has been suggested by Shimoyama and Watari (1986). In this method the phase angle is determined in an indirect way, giving less accurate values.

It can be seen that the shape of the magnitude spectrum $M_n(B)$ and magnetization hysteresis spectrum $\Phi_n(B)$ is insensitive to the phase setting ϕ of the phase-sensitive detector. The same is true for the phase plot P_n. These spectral displays may therefore be attractive in cases where phase setting is a problem.

An example of second-harmonic ST-ESR displays of nitroxide spin-labeled hemoglobin is given in Figure 13. The I_2 and Q_2 displays are measured using a dual phase-sensitive detector after setting the correct phase at low microwave field strength using the null interpolation method (see inset). The M_2 and Φ_2 displays are derived from the I_2 and Q_2 displays using equations (28) and (29), respectively, after performing a baseline correction. The P_2 plot is found by plotting Q_2 against I_2 for all values of the magnetic field B. Because of its shape, the P_2 plot is loosely called: "spin label's signature." We note that it contains all the available information about the ESR experiment in a single display.

2.6. Analysis of ST-ESR Spectra

From the previous discussion it is clear that, in general, many spectral displays at several harmonics of the modulation frequency can be used to monitor the transfer of

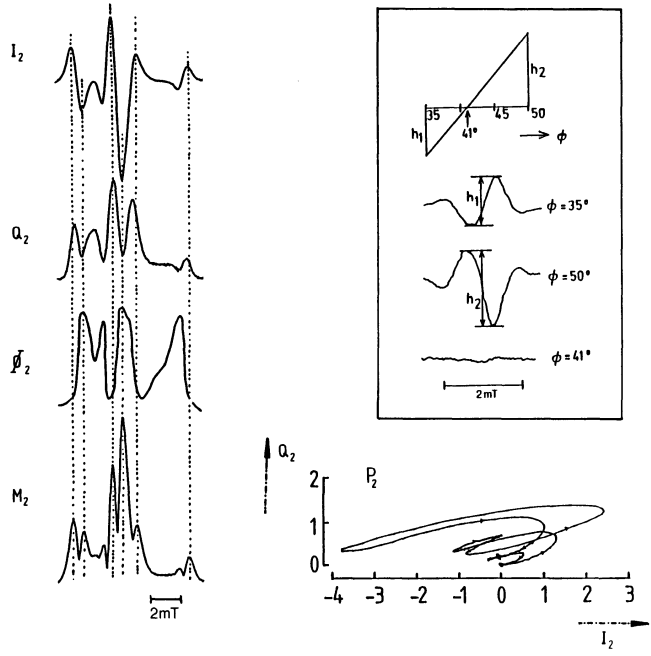

Figure 13. Survey of second-harmonic spectral displays of a ST-ESR experiment. I_2: in-phase spectrum; Q_2: quadrature spectrum; M_2: magnitude spectrum: Φ_2: magnetization hysteresis spectrum; P_2: phase plot. Spectra were obtained from maleimide spin-labeled hemoglobin for $\tau_c = 1.0 \times 10^{-4}$ s. The modulation frequency ν_m is 100 kHz. Inset: Null interpolation of the maximum top-top heights h_1 and h_2 of Q_2' displays at low microwave field strength, giving $\phi_0 = 41°$ for the phase setting of pure I_2 and Q_2 displays. (From de Jager and Hemminga, 1978.)

saturation due to molecular motion in a ST-ESR experiment. Using equation (21), it can be estimated that maximal effects of saturation transfer are expected at $\tau_c \cong 10^{-6}$-10^{-5} s, which is in the very slow motional region. The question now arises: which spectral display is the most sensitive to changes of τ_c, has the best signal-to-noise ratio, and is least sensitive to experimental parameters? This question cannot be easily answered, even with the help of elaborate computer simulations. However, using a number of simple theoretical arguments some important conclusions can be drawn.

Let us consider again the simple radical discussed in Section 2.2. The rate of transfer of saturation in the absorption line shape, which we define as $dB(\theta)/d\theta$, can be calculated from the resonance equation (8) (Hemminga, 1983):

$$dB(\theta)/d\theta = (h\nu_0/\mu_B)(g_\parallel - g_\perp) \sin 2\theta (g_\perp \sin^2\theta + g_\parallel \cos^2\theta)^{-2} \qquad (33)$$

This function, which is indicated by the broken line in Figure 3a, is zero at the extreme "turning" points determined by $g_\parallel$ and $g_\perp$ and has a maximum at a field value determined approximately by $\frac{1}{2}(g_\parallel + g_\perp)$. Therefore saturation transfer leaves the turning points unaffected and has maximal effect between the turning points.

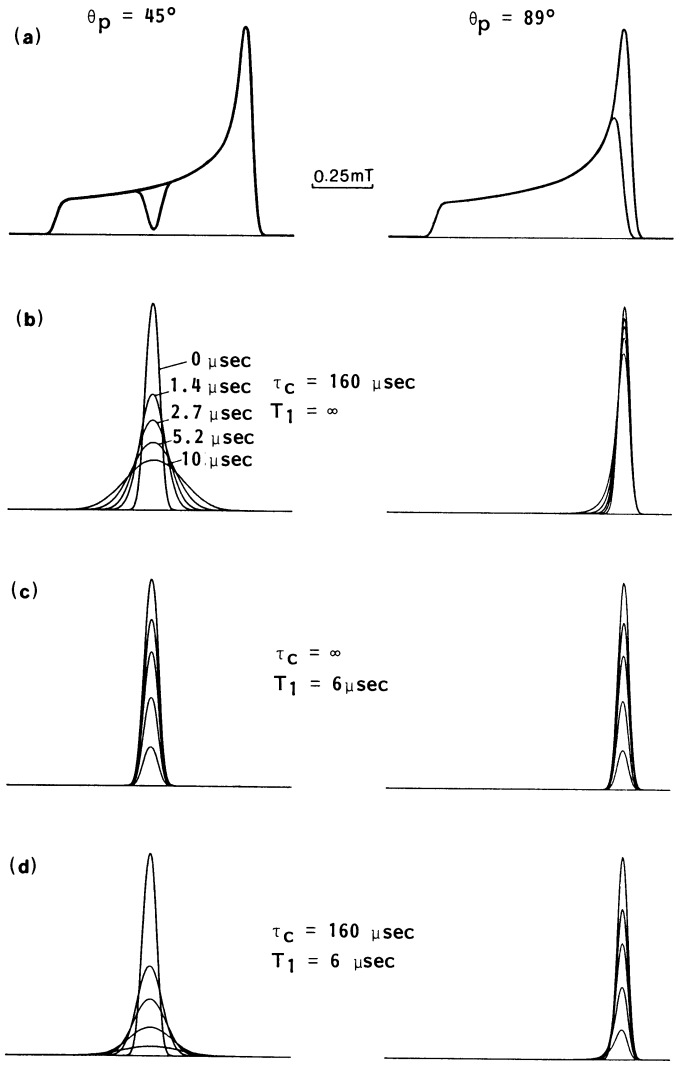

Figure 14. Computer simulation of hole-burning effect. (a) Effect of hole burning on an ESR powder line shape of a radical ($S = \frac{1}{2}$) with an axially symmetric **g** tensor and no hyperfine interaction. Holes are burned at $\theta_p = 45°$ (in the center of the line shape) and at $\theta_p = 89°$ (the right edge). (b-d) Time evolution of the hole at $\theta_p = 45$ and 89° for the indicated values of τ_c and T_1. Parameters for the calculation: g-tensor values: $g_\parallel = 2.009$, $g_\perp = 2.004$; microwave frequency: 9 GHz; width of the hole: 50 μT; Gaussian line broadening with $T_2 = 20\ \mu$T; $T_2 = \infty$; number of angular steps: 180. (From Hemminga and Schilthuis, unpublished results.)

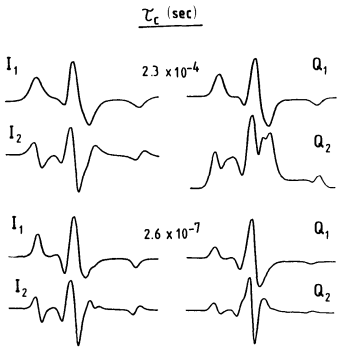

Figure 15. Sensitivity of first- (I_1 and Q_1) and second-harmonic (I_2 and Q_2) ST-ESR spectra of maleimide spin-labeled hemoglobin to molecular motion. The modulation frequency ν_m is 50 kHz. (Adapted from Thomas *et al.*, 1976.)

The separate and combined effects of saturation transfer and spin-lattice relaxation are illustrated in Figure 14 for a simulation of the hole-burning experiment, using an algorithm described by McCalley *et al.* (1972). It can be seen that the hole does not broaden at the turning points, because spectral diffusion is absent. In the center of the line shape, saturation transfer is maximal, giving a maximal broadening effect. The same arguments can be applied to all three individual M_I parts of the nitroxide powder line shape (cf. Figure 5), as has been discussed by Thomas *et al.* (1976).

The first harmonic spectra (I_1 and Q_1) of immobilized nitroxide spin labels have almost no spectral intensity between the turning points. These displays are therefore not suitable to monitor very slow molecular motions (see Figure 15). However, the second-harmonic quadrature spectrum (Q_2) has appreciable intensity between the turning points in the completely immobilized case ($\tau_c \cong 10^{-3}$ s). An increase in motion will reduce the spectral intensity at these positions. Therefore a Q_2 spectrum can be well characterized by three independent line-shape parameters (L''/L, C'/C, and H''/H), introduced by Thomas *et al.* (1976), relating the intensity between the turning points to the intensity at the turning points for the three M_I parts (low-field, central, and high-field) of the spectrum. The sensitivity of the Q_2 display to very slow isotropic molecular motion of spin-labeled hemoglobin is illustrated in Figure 15. A more detailed discussion of the sensitivity of the Q_2 display and other displays to molecular motion will be given in Section 4.

3. MEASUREMENT OF SATURATION TRANSFER ESR SPECTRA

In this section we will deal with the experimental and instrumental aspects of ST-ESR. In many cases, this is an extension of conventional ESR, which has been well treated by Poole (1967). Here, we will therefore use Poole's work as a basis and only mention those aspects that are new for ST-ESR.

3.1. The Resonant Cavity

In most biological ESR studies the sample holder is a resonant microwave cavity. This is a copper box with dimensions comparable to the wavelength of the microwaves.

At resonance, the microwaves set up standing wave patterns by reflecting from the cavity walls. In each particular cavity size and shape, a number of different standing wave configurations, or modes, are obtained. A typical TE_{102} mode for a commonly used rectangular cavity is shown in Figure 16. The cavity is coupled to a wave guide that is connected to a microwave source, generally a klystron, and a microwave detector. A resonant cavity is the microwave analog of an rf tuned L-C circuit. Such a device is characterized by a quality factor Q, giving the efficiency in which energy is stored:

$$Q = \omega_0 \frac{\text{energy stored}}{\text{energy lost per second}} \tag{34}$$

where ω_0 is the resonance frequency of the tuned circuit. For a resonant cavity containing a sample, there are four important contributions to the Q-factor, which combine as the sum of reciprocals:

$$\frac{1}{Q_L} = \frac{1}{Q_u} + \frac{1}{Q_\varepsilon} + \frac{1}{Q_r} + \frac{1}{Q_\chi} \tag{35}$$

In this equation Q_L is the loaded or measured Q, Q_u is the unloaded Q (loss is attributable only to the resistance of the walls of the empty cavity), Q_ε is due to dielectric losses, Q_r (the radiation quality factor) is the effect of energy lost through the cavity coupling hole to the wave guide, and Q_χ is the effect of power loss due to resonance absorption from electron spins in the sample. In equation (35) we have neglected effects from conductivity and susceptibility of the sample.

For simplicity, we will consider a critically coupled cavity, i.e., one that is perfectly matched to the wave guide, so that maximum power is transferred between wave guide

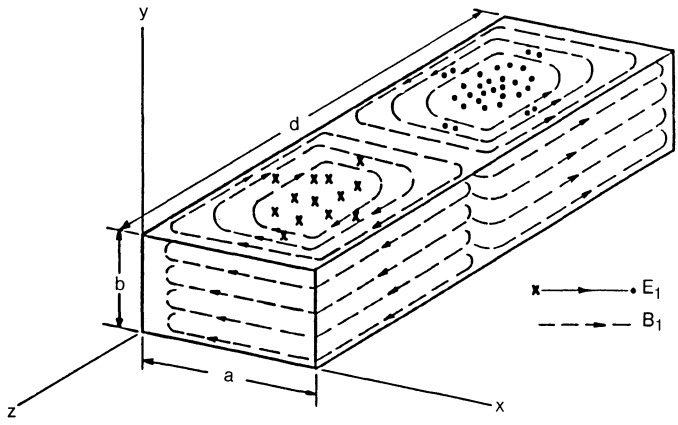

Figure 16. Schematic drawing of the electric (E_1) and magnetic (B_1) field lines in a rectangular cavity in the TE_{102} mode. The dimensions of the cavity are given by *a*, *b*, and *d*. The symbols *x*, *y*, and *z* define the coordinate system. (From Poole, 1967.)

and cavity and backward. Then Q_r equals the Q effects from all features internal to the cavity, so that

$$\frac{0.5}{Q_L} = \frac{1}{Q_u} + \frac{1}{Q_\varepsilon} + \frac{1}{Q_\chi} \tag{36}$$

Rectangular cavities have values for Q_u of about 7000, while cylindrical resonators give even higher values.

3.2. Effects of Sample on Cavity Properties

The quantity Q_ε in equations (35) and (36) results from the power loss attributable to the imaginary component of the dielectric constant ε of the sample:

$$\varepsilon = \varepsilon' + i\varepsilon'' \tag{37}$$

For a cylindrical sample positioned parallel to the x axis of a rectangular cavity (see Figure 17), Q_ε is given by (Dalal *et al.*, 1981)

$$1/Q_\varepsilon \sim r^4\varepsilon'' \tag{38}$$

where r is the inner radius of the tube. For samples with a high ε'' (i.e., an aqueous solution of nitroxide spin labels) power loss of microwave energy can be minimized by reducing r. This can be accomplished by using small capillaries. The same is true for "flat cell" sample holders placed in the cavity where the E field is minimal.

The amplitude of an ESR spectrum depends on the amount of power that is absorbed by the spins in the sample. In turn, this depends upon the value of the microwave magnetic field B_1 at the sample (Mailer *et al.*, 1977). For a rectangular cavity in the TE_{102} mode, the value of B_1 along the x axis at $y = \frac{1}{2}b$, $z = \frac{1}{2}d$ (see Figure 17) is given by

$$B_1(x) \sim \sin \pi x/a \tag{39}$$

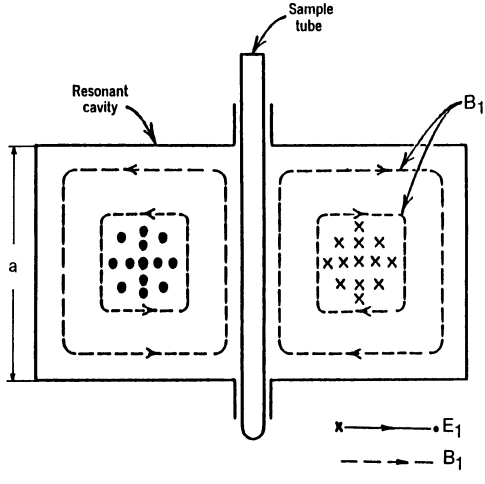

Figure 17. Schematic drawing of a cylindrical sample extending through a rectangular TE_{102} mode cavity along the x axis. The sample is positioned at $y = \frac{1}{2}b$ and $z = \frac{1}{2}d$ (see Figure 16). (From Poole, 1967.)

This function is shown in Figure 18a. Thus we have to deal with a distribution of B_1 over the sample. In ESR spectroscopy it is conventional to use the mean-square value of the magnetic field $\langle B_1^2 \rangle_s$, given by

$$\langle B_1^2 \rangle_s = \frac{1}{V_s} \int B_1^2 \, dV \tag{40}$$

where V_s is the sample volume. If the sample has a magnetic susceptibility χ'', the amount of power absorbed by the sample below saturation is proportional to

$$\chi'' V_s \langle B_1^2 \rangle_s \tag{41}$$

It follows then that Q_χ can be written as

$$1/Q_\chi = \chi'' \eta \tag{42}$$

where η is the geometric filling factor given by the relation

$$\eta = \frac{\int B_1^2 \, dV_s}{\int B_1^2 \, dV_c} = \frac{\langle B_1^2 \rangle_s V_s}{\langle B_1^2 \rangle_c V_c} = K \frac{V_s}{V_c} \tag{43}$$

Here, V_c is the cavity volume and K a constant. From equation (43) it can be seen that η gives the way in which the microwave field strength is distributed over the sample and the cavity. For a point sample located in the center of the cavity (i.e., $x = \frac{1}{2}a$, $y = \frac{1}{2}b$, and $z = \frac{1}{2}d$), $K = 2$. A cylindrical sample inserted along the x axis of a rectangular cavity, as shown in Figure 17, gives $K = 1$. This is true only if the sample does not disturb the distribution of microwaves in the cavity. The quantity $\langle B_1^2 \rangle_c$ can be expressed as

$$\langle B_1^2 \rangle_c = \mu_0 Q_L P_i / 2 V_c \omega_0 \tag{44}$$

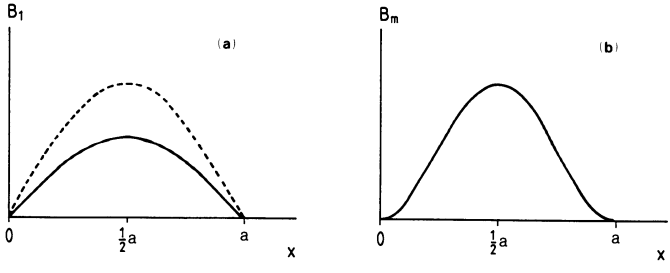

Figure 18. Schematic drawing of the variation of (a) B_1 and (b) B_m along the cylindrical sample of Figure 17. The dotted line shows the increase of B_1 within the sample due to the sucking-in or lens effect.

where μ_0 is the magnetic permeability of free space and P_i is the incident microwave power. From equations (43) and (44) we obtain

$$\langle B_1^2 \rangle_s = \mu_0 \eta Q_L P_i / 2 V_s \omega_0 \tag{45}$$

The real part, ε', of the dielectric constant in equation (37) causes a shift in the resonant frequency of the cavity and a concentration of the electric and magnetic fields inside the dielectric. This has been called the "sucking-in" or "lens" effect (Poole, 1967, p. 306; Dalal *et al.*, 1981; Hemminga *et al.*, 1984b). This concentration effect causes an increase in the value of B_1 at the sample, as is illustrated in Figure 18a. For solvents with large values of ε', this can partially compensate the decrease in B_1 at the same sample resulting from large values of ε''. Theoretical expressions for the lens effect have been derived by Stoodley (1963).

If we define L as the enhancement of $\langle B_1^2 \rangle_s$ due to the lens effect, i.e., $L \geq 1$, then equation (45) can be modified to

$$\langle B_1^2 \rangle_s = \frac{\mu_0 \eta Q_L P_i}{2 V_s \omega_0} L \tag{46}$$

Then it follows from equation (42) that

$$1/Q_\chi = \chi'' \eta L \tag{47}$$

The filling factor η may be a useful parameter in conventional ESR. However, ST-ESR is a nonlinear ESR technique in which saturation of the sample plays a role. Because of the B_1 distribution, some spins feel more saturation effects than others; this gives rise to a superposition of different ST-ESR spectra each belonging to a particular value of B_1. For this reason, in ST-ESR spectroscopy special attention should be paid to the calibration and distribution of B_1. The same is true for B_m (see Section 3.4).

3.3. Phase-Sensitive Detection

In ESR spectrometers the signal $A(B, t)$ from the microwave detector is amplified by the preamplifier. The nth harmonic in-phase and quadrature ST-ESR signals I_n and Q_n [see equations (26) and (27)] can then be detected with an analog or digital phase-sensitive detector (PSD). Analog phase-sensitive detection is the conventional way of signal detection in ESR spectroscopy. It is based on the principle that the input signal $A(B, t)$ is multiplied electronically by a reference signal $R(t) \sim \cos(\omega_r t)$, with $\omega_r = n\omega_m$, for detection of the in-phase signal I_n. This can be represented mathematically as

$$I_n \sim \int_0^{2\pi/\omega_m} A(B, t) R(t)\, dt \tag{48}$$

where I_n is the DC output voltage of the PSD. A 90° phase-shifted reference signal, i.e., $R(t) \sim \sin(\omega_r t)$, yields the quadrature signal Q_n. A dual PSD has the possibility of detecting both signals simultaneously, where the relative phase of 90° is very accurately determined. A block diagram of a dual PSD is shown in Figure 19.

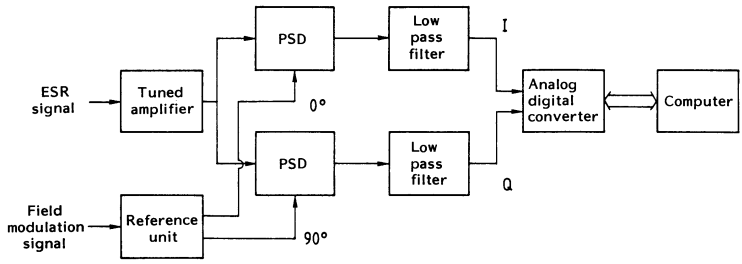

Figure 19. Block diagram of a dual phase-sensitive detector in ST-ESR, interfaced with a computer. The in-phase signal is I; the quadrature signal is Q (see text).

The advantage of using field modulation in combination with a PSD is that it improves the signal-to-noise (S/N) ratio by shifting the ESR signals to a low-noise part of the frequency spectrum. At the output of the PSD a low-pass filter (i.e., a R-C circuit) is employed to improve the S/N ratio by reducing the bandwidth. The amplitude of the noise is proportional to the square root of the bandwidth. The bandwidth must not be reduced to such a small level that spectral information is lost. Even at moderate values of the bandwidth, some distortion of the spectral line shapes is unavoidable. However, by using digital filtering techniques that have more favorable properties (Savitzky and Golay, 1964; Vancamp and Heiss, 1981; Marchand and Marmet, 1983) such problems can be overcome. The output of the PSD is then digitized using an ADC (analog-to-digital converter) interfaced with a computer (see Figure 19). The bandwidth of the low-pass filter should have a higher value than that of the digital noise filter, because its only purpose is to eliminate the aliasing of noise.

The reference unit of the PSD converts the sine-wave signal of the field modulation unit into a square-wave signal. Because this signal can be written as a Fourier series

$$R(t) \sim \sin \omega_r t + \tfrac{1}{3} \sin 3\omega_r t + \tfrac{1}{5} \sin 5\omega_r t + \cdots \tag{49}$$

the PSD also monitors signals and noise with frequency components at odd harmonics of the reference frequency, but with decreasing sensitivity given by the coefficients in equation (49). This can be eliminated by filtering the input signal of the PSD using a tuned amplifier that passes only signals at frequency ω_r. Another possibility is to use frequency translation schemes by which the signal is shifted to an intermediate frequency.

The output of the microwave crystal detector contains the signal $A(B, t)$ and noise, but also some spurious signals from the spectrometer: the AFC signal and higher harmonics (e.g., 70 and 140 kHz on a Varian ESR spectrometer) and harmonics of the switching mode power supplies of the klystron and oscilloscope. The detection frequency should not be chosen too close to one of these frequencies.

Generally, the signal $A(B, t)$ contains weak quadrature components Q_n in the presence of intense in-phase components I_n. Increase of the AC gain at the input of the PSD can then not be used to amplify the Q_n signals, because then the intense I_n signals lead to a nonlinear response of the PSD, and hence a distortion of the signals.

This can be avoided by using a DC amplifier at the output of the PSD (De Jager and Hemminga, 1978). For detection of second-harmonic signals a notch filter can be used at the input of the PSD, to eliminate the intense first-harmonic signals (De Jager and Hemminga, 1978).

Digital phase-sensitive detection has not yet received much attention in ESR spectroscopy. However, it may be expected that modern ESR spectrometers will have this feature available. Especially for ST-ESR spectroscopy this can be an interesting accessory, as will be discussed below (Sasaki *et al.*, 1980; Watanabe *et al.*, 1980; Vistnes *et al.*, 1984).

For digital phase-sensitive detection the signal $A(B, t)$ is taken from the output of the microwave detector and, after amplification, fed into an ADC interfaced with a computer. This signal is digitized at one particular value of the magnetic field B, synchronously with the field modulation. The signal is averaged until a sufficient high S/N ratio is obtained. The averaged signal is Fourier transformed, yielding directly the amplitudes of the cosine and sine components at the first, second, etc., harmonics of the modulation frequency, i.e., $I_n(B)$ and $Q_n(B)$. The magnetic field B is stepped through the whole spectrum. The advantage of a digital PSD is that the entire signal $A(B, t)$ is recorded. Therefore all relevant spectra I_n and Q_n, for $n = 1, 2, \cdots$, can be obtained in one single experiment. Furthermore, digital filtering techniques with favorable properties can be employed also for noise reduction.

The magnetic-field modulation is generated by two modulation coils in a Helmholtz configuration embedded in the cavity walls. The current through the coils is supplied by the modulation unit, an audio amplifier. Ideally, the magnetic-field modulation should be a pure sine wave with a high phase stability relative to the reference signal of the PSD. The presence of higher harmonics in the field modulation and changes of the phase will lead to a distortion of the I_n and Q_n spectra.

Losses in the modulation coils increase at higher modulation frequencies. This provides an upper limit for the modulation frequency, which is about 400 kHz for a B_m value of 0.5 mT. Since B_m is proportional to the current through the modulation coils, independent of ω_m, it can be determined easily by measuring the voltage drop over a small resistor in series with these coils (De Jager and Bremer, 1982).

3.4. Calibration Procedures

In contrast to conventional ESR spectroscopy, ST-ESR gives rise to spectra that depend strongly upon the microwave field strength and setting of the modulation amplitude. For this reason quantitative knowledge of the values of the microwave field (B_1) and modulation field (B_m) is necessary, taking into account the inhomogenities of these fields in the cavity.

For a TE_{102} mode cavity, the variation of B_1 along the x axis at $y = \frac{1}{2}b$, $z = \frac{1}{2}d$ is given by equation (39) (see Figure 18a). The dependence of B_m is approximately (Mailer *et al.*, 1977)

$$B_m(x) \sim \sin^2 \pi x/a \tag{50}$$

Figure 18b illustrates the variation of B_m for a cylindrical sample in this cavity. Only

for point samples can B_1 and B_m be considered as constant. For other sample types the ST-ESR line shape is sensitive to the sample shape and position in the cavity, as has been described in a number of papers (Beth *et al.*, 1979; Kusumi *et al.*, 1980; Fajer and Marsh, 1982; Delmelle, 1983; Vistnes and Dalton, 1983; Hemminga *et al.*, 1984a).

Calibration of B_1. Calibration of the microwave field intensity B_1 within the sample is one of the most difficult experimental problems in ST-ESR spectroscopy. As has been discussed in Section 3.2, this arises because the sample, sample holder, and other glassware in the cavity strongly influence the properties of the cavity. This is reflected by a change in cavity Q-factor and the lens effect, as given by equation (46). Therefore the relation between B_1 and P_i is in general unknown.

For radicals in aqueous solutions, a method has been developed for the determination of B_1 that relates the properties of a degassed aqueous sample of 0.9 mM PADS (peroxylamine disulfonate, or Fremy's salt), in 50 mM K_2CO_3 solution (Kooser *et al.*, 1969), with the sample of interest (Thomas *et al.*, 1976). A commonly used method involves measuring the amplitude of the conventional ESR spectrum of the PADS sample as a function of the square root of the microwave power (saturation curve). For the PADS sample at room temperature $T_1 = T_2 = 4.1 \times 10^{-7}$ s (Kooser *et al.*, 1969), so that from equation (16) it follows that $(B_1)_{1/2} = 10.62\ \mu$T. Using this value, the microwave field intensity can be found from the proportionality in equation (46):

$$(B_1)_{av} = (B_1)_{1/2}(P_i/P_{1/2})^{1/2} \tag{51}$$

where $(B_1)_{av}$ is the sample-averaged rotating component of the rf field in μT at the incident microwave power P_i. Quantity $P_{1/2}$ is determined from a plot of the conventional ESR signal height against $(P_i)^{1/2}$. Another procedure is to determine the line broadening of the PADS sample as a function of P_i [see equation (14)] (Kooser *et al.*, 1969).

It is clear that this method is applicable only for samples that have the same dimensions and dielectric properties as the PADS reference sample. For example, for spin-labeled molecules dissolved in glycerol–water mixtures, as is used for reference spectra for ST-ESR spectroscopy, the method fails, since such samples have quite different dielectric properties, as compared to aqueous solutions (Hemminga *et al.*, 1984b).

An alternative method is to use a point reference sample and locate that within the sample of interest in the center of the cavity, where B_1 is maximal. This procedure yields $B_1(0)$, where (0) denotes the center of the cavity. As a reference sample, a small drop of DPPH (1,1-diphenyl-2-picrylhydrazyl) embedded in epoxy resin and mounted on a glass fiber has been used. The value of $B_1(0)$ can then be determined from the conventional ESR signal amplitude of the reference sample, provided the absolute value of the B_1 field in the cavity with necessary glassware is determined separately, e.g., using the perturbing sphere method (Hemminga *et al.*, 1984b). Quantity $B_1(0)$ is related to $(B_1)_{av}$ by the following approximate relation for line samples in a TE_{102} mode cavity: $(B_1)_{av} \cong 0.85\ B_1(0)$ (Kooser *et al.*, 1969).

The principle of the perturbing sphere method is that a small metallic sphere placed in the cavity induces a shift in the cavity resonance frequency. If r is the radius of the sphere, ω_0 is the resonance frequency without the sphere, and ω the perturbed

resonance frequency, then the value of B_1 for a perfectly matched cavity at the position of the sphere is given by (Ginzton, 1957; Kooser *et al.*, 1969)

$$B_1^2 = \frac{\omega^2 - \omega_0^2}{\omega_0^2} \frac{1}{2\pi r^3} \frac{\mu_0 Q_L}{2\omega_0} P_i \tag{52}$$

Calibration of B_m. The modulation amplitude B_m can be determined with point samples of compounds that have ESR signals with a very small natural linewidth, placed in the center of the cavity [e.g., a small crystal of TCNQ (tetracyanoquinodimethane) having a natural linewidth of 13 mT]. For such samples, the peak-to-peak distance of the over-modulated first-harmonic conventional ESR signal equals B_m for modulation frequencies around 100 kHz. Once calibrated for a particular cavity, B_m is known for all further experiments, since the value of B_m is insensitive to the filling of the cavity. This value of B_m is referred to as $B_m(0)$, indicating the value of B_m in the center of the cavity (Hemminga *et al.*, 1984c).

3.5. Standard Conditions for ST-ESR Spectroscopy

The shape of the I_n and Q_n spectra in ST-ESR spectroscopy is determined by a large number of experimental parameters. Especially, the value and distribution of B_1 and B_m affect the spectral shapes, since the experiments are carried out under nonlinear conditions (high values of B_1 and B_m). Therefore, a standard experimental procedure is very important to facilitate intercomparison of experimental spectra from different sources and comparison of experimental with computer simulated spectra (Hemminga *et al.*, 1984a; Squier and Thomas, 1986).

A standardized protocol has been proposed for samples contained in glass capillaries, which is particularly useful for temperature-dependent studies of biological samples. In this protocol, special attention is paid to the effects of the distribution of the microwave and modulation fields and to the microwave-field concentrating and dissipating effects (Hemminga *et al.*, 1984c).

The recommended standard conditions for nitroxide spin-labeled molecules in capillaries contained in 4 mm quartz ESR tubes are presented in Table 3. A distinction is made between samples with a low spin-label concentration ($\leq 30\ \mu M$) and a high

TABLE 3
Recommended Standard Conditions for the Measurement of Q_2 Spectra of Samples Contained in Capillaries (From Hemminga *et al.*, 1984c)

Sample conditions		Microwave part			Modulation part		Detection part	
Spin-label concentration (μM)	Sample length (mm)	ν_0 (GHz)	$B_1(0)$ (μT)	Phase	ν_m (kHz)	$B_m(0)$ (mT)	ν_r (kHz)	Phase
≥ 30	5	≈ 9.5	25	Absorption	50	0.5	100	Quadrature
≤ 30	>20	≈ 9.5	25	Absorption	50	1.0	100	Quadrature

spin-label concentration ($\geq 30\ \mu M$). If the spin-label concentration is high, the sample length is kept small (≤ 5 mm). This actually approximates a "point" sample. If such a sample is placed in the center of the cavity, the distribution of the B_1 and B_m field over the sample can be neglected. Furthermore, both parameters are maximal in the cavity center. This experimental situation approaches the optimum and is the best starting point for an analysis of the experimental I_n and Q_n spectra and comparisons of experimental and computer-simulated spectra.

Low spin-label concentrations make it necessary to use line samples. The length of these samples is taken longer than 20 mm so that they fully extend through a rectangular TE_{102} mode cavity (Figure 17). The vertical position and length of the sample are then not critical. In this case, the distribution of B_1 and B_m along the capillary axis is important and contributes to the shape of the I_n and Q_n spectra. This generally results in a loss of spectral detail. It should be noted that in this case spectra obtained from different types of cavities do not give the same results.

For low spin-label concentrations a line sample is a compromise between point samples and samples contained in flat quartz cells. The standard conditions may also be used for flat cells. Flat cells have the advantage that they yield relatively high signal-to-noise ratios. For small 5-mm flat quartz cells the shape of the ST-ESR spectra is similar to that obtained for line samples with the same sample length, if a correction is made for the Q and lens effects. An advantage of using capillaries instead of flat cells is that capillaries are easy to handle, are disposable, and can be used easily in temperature-dependent studies.

The shape of I_n and Q_n spectra is affected by the relaxation times T_1 and T_2, which in turn depend on the temperature. The value of T_1 is affected by the oxygen concentration as well (Popp and Hyde, 1981). For ideal ST-ESR experiments, T_1 and T_2 should be constant. Therefore it is necessary to check these parameters: (a) T_1 can be checked in a saturation study performed at a point in the spectrum that is minimally affected by saturation transfer, the best point being the low-field peak; (b) T_2 can be checked from the width of the low-field peak in a conventional (I_1) ESR spectrum (Hemminga *et al.*, 1984c). When the relaxation times are not constant in a series of ST-ESR experiments, great care should be taken not to misinterpret the spectra.

The incident microwave power is not given in Table 3, because a constant value of the microwave power does not guarantee constant B_1 values [see equation (46)]. Instead, the value of B_1 in the center of the sample/cavity is defined [$B_1(0)$]. The value of $B_1(0)$ at a given level of microwave power depends strongly on the dielectric properties of the sample and glassware in the cavity (see Section 3.2). The lens effect of the material in the cavity results in a concentration of the B_1 field within this material. The dielectric loss reduces the B_1 field. A procedure that adjusts $B_1(0)$ to the desired value should take into account both effects. The best way is to use reference point samples that are placed *within* the sample, exactly in the center of the cavity (see Section 3.4). If this is not possible, an approach may be to construct empirical calibrations for samples of a given dielectric composition and size. Alternatively, a PADS reference sample may be used, giving the sample-averaged value of B_1 [see equation (51)].

The importance of measuring B_1 *within* the sample has already been stressed by Singer and Kommandeur (1961). They measured an enhancement of the ESR signal of a small solid sample by a factor of 2, when it was moved from 1 mm above a drop of water in the cavity to inside the water drop.

The dielectric constant of the sample depends on the sample composition and temperature (Hemminga *et al.*, 1984b; Mohanty and Rifkind, 1984). The same therefore applies to the dielectric loss and lens effect. For this reason it is necessary to set $B_1(0)$ to the desired value before each ST-ESR spectrum is recorded.

In Table 3 a value of 25 μT is taken for $B_1(0)$. This value was suggested originally by Thomas *et al.* (1976) and has been successfully applied in a large number of ST-ESR experiments on spin-labeled systems.

For samples that cannot be accommodated in capillaries, but require flat cells or stacks of glass plates, as is encountered for samples with low spin-label concentration or in studies on oriented membranes (see Section 4.2.1), the same standard conditions as given in Table 3 can be employed. Depending on the particular type of experiment, a procedure for the determination of $B_1(0)$ should be developed. It should be noted that the shape of the I_n and Q_n spectra will be affected by the shape of the sample through the distribution of the B_1 and B_m field.

The modulation frequency of the ESR spectrometer in Table 3 is 50 kHz, the value most commonly used. For the modulation amplitude the value in the center is taken $[B_m(0)]$, as for the B_1 field. In the case of low spin-label concentrations ($\leq$30 μM), the modulation amplitude is increased from 0.5 to 1.0 mT, as compared to the situation with high spin-label concentrations ($\geq$30 μM). This modulation amplitude is necessary for a better signal-to-noise ratio in the ST-ESR spectrum. A high value of the modulation amplitude may be a disadvantage, since spectral detail is lost. However, line samples are used in this instance, for which this is already partly the case.

Among the possible spectral displays, the Q_2 display in the X-band region ($\nu_0 \cong$ 9.5 GHz) has been chosen as the standard, in agreement with the proposal of Thomas *et al.* (1976). The reason is that this Q_2 display has good sensitivity to molecular motion and has already been used routinely in ST-ESR spectroscopy.

It is also possible to measure dispersion spectra instead of absorption spectra. Measurement of dispersion spectra is difficult, because of the high noise level in the spectra arising from the frequency modulation noise of the microwave source. Although several techniques have been applied to reduce this noise (Mailer *et al.*, 1980, 1981; Hyde *et al.*, 1982; Anderson and Mailer, 1982; Fajer and Marsh, 1983b; Sehr *et al.*, 1983), dispersion ST-ESR spectroscopy has not received much attention in applications to biological systems and will not be further discussed here.

ST-ESR in the Q-band region ($\nu_0 \cong$ 35 GHz) has been carried out in a few cases (Johnson and Hyde, 1981; Johnson *et al.*, 1982a, 1982b). This results in an approximately fourfold increase in resolution in the central part of the spectrum. This microwave frequency has not become popular in spin-label research of biological systems, mainly because of difficult technical problems, e.g., small microwave cavity, severe dielectric loss problems. An advantage of using 35 GHz ST-ESR is that the sensitivity to rotational correlation times is extended to 10^{-2} s.

4. ANALYSIS OF SATURATION TRANSFER ESR SPECTRA

ST-ESR has been carried out on quite a number of biological systems. Very slow molecular motion is encountered in supramolecular aggregates, such as myosin, actin, viruses, and proteins (i.e., hemoglobin) in high-viscosity media. The hemoglobin system

has been used especially for development of calibration procedures and fundamental studies of ST-ESR effects. Also for membrane proteins in lipid systems, such as ATP-ase, cytochrome oxidase, and rhodopsin, ST-ESR has been employed. Not in all cases is molecular motion isotropic. Anisotropic motion has been particularly well studied in lipid and membrane systems in the gel phase.

For an excellent recent review of the biological applications of ST-ESR, the reader is referred to the book by Dalton (1985). Here we will in particular discuss the way in which dynamical information can be obtained from ST-ESR spectra.

4.1. Isotropic Motion

4.1.1. Analysis of Spectral Displays

The basic principle for the analysis of ST-ESR spectra of isotropic reorienting molecules has already been given in Section 2.6. Here we will consider in more detail the effect of the rotational correlation time on the various spectral displays in ST-ESR spectroscopy. As argued in the previous section, we will confine ourselves to absorption ST-ESR spectroscopy in the X-band region.

Let us consider the effect of very slow molecular motion on the second-harmonic in-phase (I_2) and quadrature (Q_2) spectra of isotropically reorienting nitroxide molecules. This is illustrated in Figure 20 for maleimide spin-labeled hemoglobin in glycerol-water mixtures. Since the spin label is rigidly attached to the protein, the rotational correlation time τ_c can be found from the Stokes-Einstein relation, equation (17), where r is 2.9 nm for hemoglobin. Clearly the I_2 and Q_2 spectra are sensitive to molecular motion in the region from $\tau_c \approx 10^{-7}$ to 10^{-4} s.

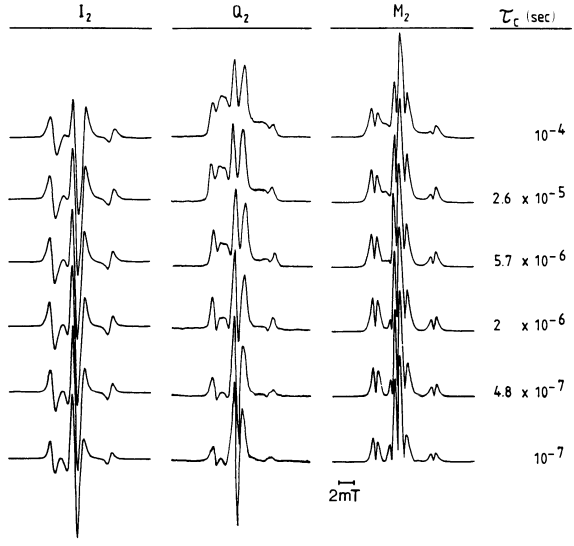

Figure 20. Second-harmonic ST-ESR I_2, Q_2, and M_2 displays of maleimide spin-labeled hemoglobin at various values of the rotational correlation times τ_c. (From Hemminga *et al.*, 1984a.)

The Q_2 spectra of Figure 20 have been used as reference spectra for isotropic motion, by calculating the spectral parameters L''/L, C'/C, and H''/H for the low-field, center, and high-field parts of the spectra. Such reference curves are shown in Figure 21. In the reverse manner, values of τ_c may be determined from the spectral parameters of the Q_2 spectra. This procedure, which was first introduced by Thomas *et al.* (1976), is now generally accepted as the empirical way to obtain the rotational correlation time from Q_2 spectra. This method yields three independent values for τ_c, that should be almost equal for pure isotropic motion.

Although the experimental spectra in Figure 20 have been verified by computer simulations, it has not been possible to use theoretical calculations as a tool for determining τ_c. For single values of B_1 and B_m, calculations are already very complex and require large amounts of computer time (Coffey *et al.*, 1976; Perkins *et al.*, 1976; Galloway and Dalton, 1978a, 1978b; Robinson *et al.*, 1978; Robinson, 1983). Up to now distributions of B_1 and B_m have not been taken into account in simulations.

A similar approach, as employed for the analysis of the Q_2 displays, has been used for I_2 and M_2 displays, by selecting the most sensitive spectral parameters (Hemminga *et al.*, 1984a). This is illustrated in Figure 21. The I_2, Q_2, and M_2 displays are almost equally good in determining τ_c in the range from 10^{-7} to 10^{-4} s. Since the I_2 display has a much better signal-to-noise ratio than the Q_2 display and shows less sensitivity to missetting of the phase ϕ_0 of the PSD, it may be a better choice in low signal-to-noise cases. Also, the M_2 display has a high signal-to-noise ratio and has the additional advantage of being independent of the phase setting ϕ_0 [see equation (28)].

The shape of the phase plot (P_2) is sensitive to τ_c and has been used for determination of τ_c (see Figure 22) (Hemminga *et al.*, 1984a). The P_2 plot contains a number of characteristic loops that cross each other. The smaller loops arise from the low- and high-field parts of the I_2 and Q_2 display; the large loop comes from the central part. The shape of the loops is independent of the phase setting ϕ of the PSD. For the analysis of the P_2 plot a rectangle is constructed, which fits around the plot, as is indicated in the inset of Figure 23. The area of the rectangle is minimized by rotating it around the plot. The ratio of the sides A/B of the final rectangle defines uniquely the P_2 plot. Figure 23 shows the variation of the ratio A/B with τ_c. Such an algorithm is easily implemented in a computer program, allowing an automatic determination of τ_c.

Also, magnetization hysteresis (Φ_2) displays have been used for the determination of τ_c (Vistnes, 1983). Characteristic Φ_2 displays are shown in Figure 24. These can be parameterized as well.

Although the M_2 and Φ_2 displays are advantageous from the standpoint of being independent of the phase setting ϕ of the PSD, they have some disadvantages. In the M_2 display, sharp dips are visible at magnetic field positions where $I_2(B) = 0$. The intensity of these dips is sensitive to τ_c and has therefore been used for analysis of the M_2 displays. However, the dips are easily distorted by the digitizing process and response time of the low-pass filter of the PSD. The Φ_2 display shows strong noise components at the same positions. In practical situations, these effects should be taken into account.

The line shape of various displays of ST-ESR (Q_2, I_2, M_2, Φ_2, P_2) does not only depend on τ_c, but also on a large number of instrumental parameters, as discussed in Section 3. Therefore, a comparison of experimental and reference spectra must be

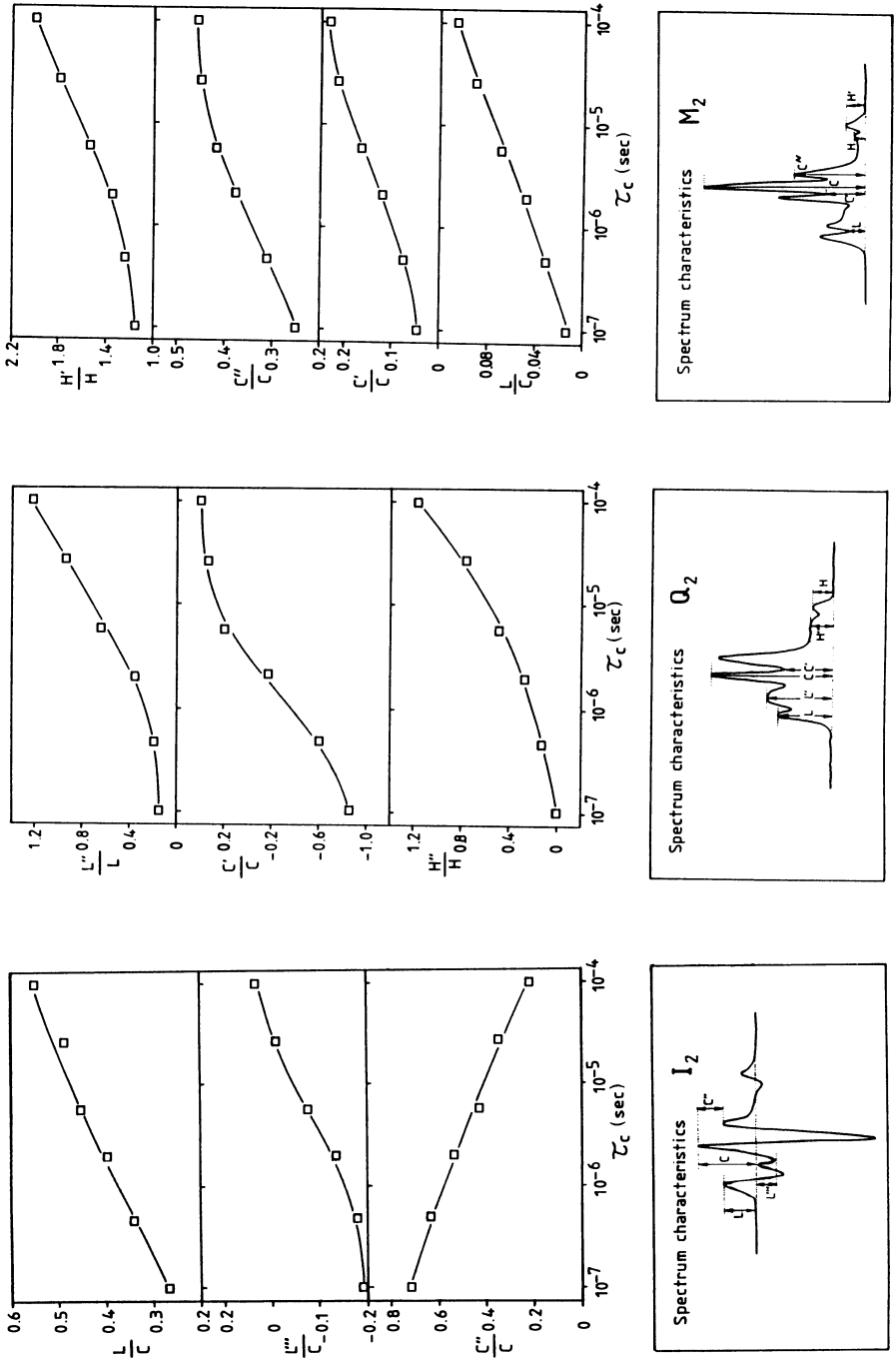

Figure 21. Spectral characteristics of the I_2, Q_2, and M_2 displays of Figure 20 as a function of τ_c. (From Hemminga *et al.*, 1984a.)

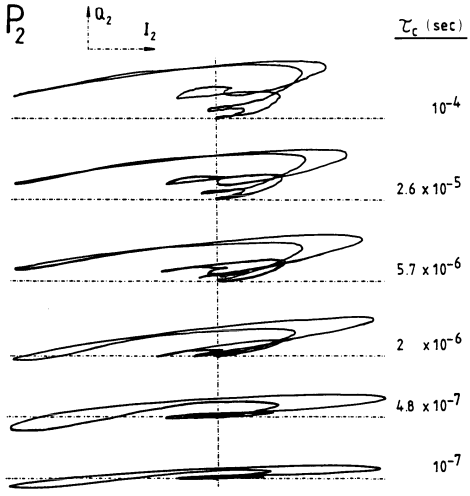

Figure 22. Second-harmonic phase plot (P_2) ST-ESR displays at various values of the rotational correlation time τ_c, derived from the I_2 and Q_2 displays of Figure 20. (From Hemminga *et al.* 1984a.)

carried out under strictly defined experimental conditions for reliable and reproducible results. In general one should not use published reference spectra, but prepare sets for one's own use. A standard procedure has been discussed in Section 3.5. Detailed methods for preparing reference samples have been described (Sehr *et al.*, 1983; Hemminga *et al.*, 1984a).

In addition to the instrumental parameters, molecular parameters affect the ST-ESR displays. These are the magnetic parameters of the spin label (**g** and **A** tensor), and

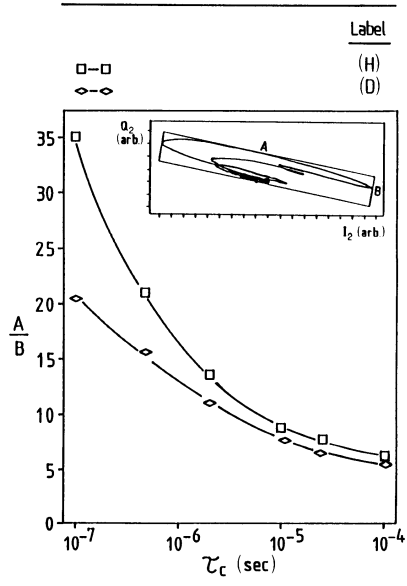

Figure 23. Spectral characteristic (A/B) of the P_2 display of Figure 22 as a function of τ_c. (H): protonated maleimide spin-labeled hemoglobin; (D): deuterated maleimide spin-labeled hemoglobin. The inset shows the definition of the characteristic A and B parameters that uniquely define the P_2 display. (From Hemminga *et al.*, 1984a.)

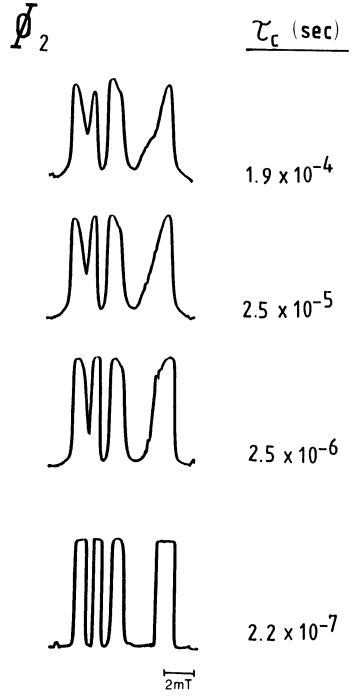

Figure 24. Second-harmonic magnetization hysteresis Φ_2 displays of maleimide spin-labeled hemoglobin at various values of the rotational correlation time τ_c. (Adapted from Vistnes, 1983.)

the relaxation times T_1 and T_2. For example, the polarity of the medium influences the **g** and **A** tensor as well as the value of T_1. The spectrometrist should take into account these effects and use standard conditions for the experiments.

The integral of the Q_2 display varies with the rotational correlation time and this spectral parameter has been used for a τ_c determination (Evans, 1981). The integral method can be used also to analyze overlapping spectra characterized by different rotational correlation times. An extension of this method has been described by Horváth and Marsh (1983), which is also applicable for analysis of multicomponent spectra with anisotropic motion. A refinement of the integral method for suppression of the interference from rapidly tumbling spin labels has been described by Squier and Thomas (1986). A simplification of Q_2 spectra has also been obtained by selectively suppressing components with a small value of τ_c ($\approx 10^{-7}$ s) by the use of paramagnetic broadening agents, such as $K_3Fe(CN)_6$ (Schwartz *et al.*, 1982). These methods may be useful, since overlapping spectra of slowly and rapidly tumbling spin labels are frequently encountered in biological applications.

4.1.2. Effect of Field Modulation Frequency

The effect of modulation frequency $\nu_m = \omega_m/2\pi$ on the Q_2 display is shown in Figure 25 (Hemminga *et al.*, 1984a). It is seen that at 100 kHz, the Q_2 display is more sensitive to variation of τ_c than at lower modulation frequencies. The sensitivity of the

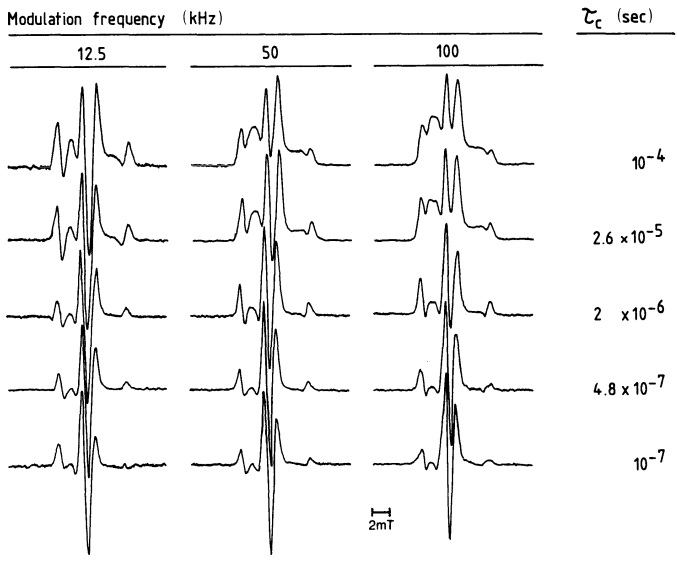

Figure 25. The effect of modulation frequency (ν_m) on the Q_2 displays of maleimide spin-labeled hemoglobin at various values of τ_c. (From Hemminga *et al.*, 1984a.)

Q_2 display to τ_c and ν_m is illustrated more quantitatively in Figure 26. In all cases the variation of the spectral parameters on τ_c becomes less when ν_m decreases.

Application of modulation frequencies above 100 kHz is experimentally limited, especially for the range of modulation amplitudes required for ST-ESR spectroscopy ($\approx$1 mT). By using computer simulations it has been found that an increasing sensitivity for τ_c may be obtained at modulation frequencies above 100 kHz (Hemminga *et al.*, 1984a). This is illustrated in Figure 27. At higher values of ν_m, spectral intensity between the turning points increases, giving an increase in the scale of the spectral parameters. From the simulations it follows also that the line shape of the Q_2 display at 12.5 kHz is the limiting shape for low values of ν_m, since the line shapes at 1 and 12.5 kHz are almost identical.

By varying ν_m, it is possible to resolve overlapping Q_2 spectra characterized by different τ_c values. It is seen from Figures 25 and 26 that such a separation is possible, if the τ_c values are very different. Because the Q_2 display of a fast component ($\tau_c = 10^{-7}$ s) is almost insensitive to ν_m, a mixed line shape can be resolved by varying ν_m and subsequent spectral subtraction.

4.1.3. Isotope Enrichment of Spin Labels

The effect of isotopically enriched spin labels (^{2}H and/or ^{15}N) has been investigated by a number of groups (Dalton *et al.*, 1976; Beth *et al.*, 1981; Johnson *et al.*, 1982b; Hemminga *et al.*, 1984a). Deuteration of maleimide spin-labeled hemoglobin results in spectral displays with a better resolution and a somewhat higher signal-to-noise ratio, because the inhomogeneous broadening is reduced. However, it does not result

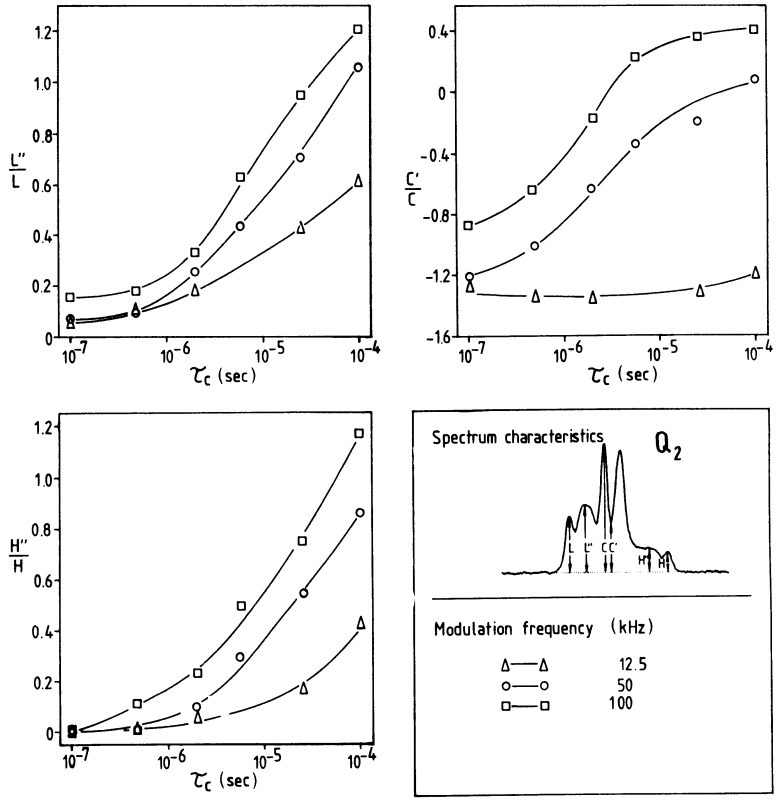

Figure 26. Effect of the modulation frequency (ν_m) on the spectral characteristics of the Q_2 displays of Figure 25 as a function of τ_c. (From Hemminga *et al.*, 1984a.)

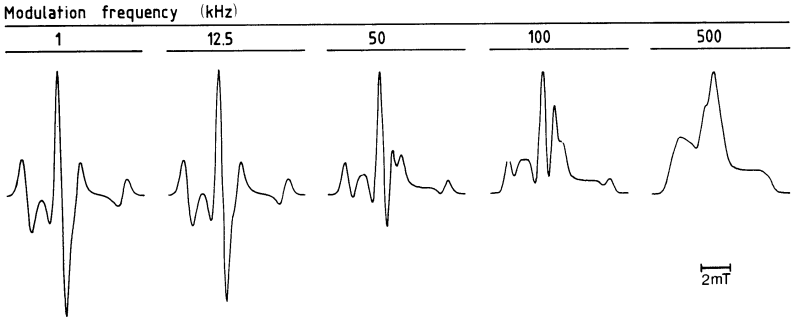

Figure 27. Computer-simulated Q_2 displays for various values of the modulation frequency ν_m. The computer program used has been described by Perkins *et al.* (1976). Input parameters: **g** tensor components: 2.00241, 2.00741; **A** tensor components: 3.5 mT, 0.7 mT; $T_1 = 6.6 \times 10^{-6}$ s; $T_2 = 2.0 \times 10^{-7}$ s; T_2(inhom) $= 5.7 \times 10^{-8}$ s; $B_m = 0.5$ mT, $B_1 = 80\ \mu$T; $\tau_c = 2.5 \times 10^{-5}$ s. (From Hemminga *et al.*, 1984a.)

in an increased sensitivity to τ_c, as is illustrated in Figure 23. This arises because of the presence of strong line-broadening effects due to saturation and overmodulation. ^{15}N substitution can be interesting in cases where computer simulations are carried out. Because the number of quantum levels of this radical is less, the computer time for the calculations is reduced.

4.2. Anisotropic Motion

4.2.1. ST-ESR Spectra of Oriented Spin Labels

In this section we will consider a two-dimensional system consisting of perfectly oriented spin labels that can only reorient about one axis. This situation is approached experimentally for the cholestane spin label in macroscopically oriented lipid multibilayers (Hemminga and Berendsen, 1972; Smith and Butler, 1976; Hemminga, 1977). The long molecular axis of the cholestane spin label coincides with the principal y axis, which is parallel to the bilayer normal.

For $\theta = 90°$, where θ is the angle between the magnetic field **B** and bilayer normal, ESR and ST-ESR spectra reflect the two-dimensional anisotropic motion, the cholestane spin label characterized by a rotational correlation time $\tau_\parallel$. If $\tau_\parallel$ is small, the x and z components of the **g** and **A** tensors average, yielding a "two-dimensional" liquid ESR spectrum, with hyperfine splitting $\frac{1}{2}(A_{xx} + A_{zz})$. In the rigid limit case a broad "two-dimensional" powder ESR spectrum is obtained. The ESR spectrum for $\theta = 0°$ is essentially unaffected by the correlation time $\tau_\parallel$, showing a sharp single-crystal-like ESR spectrum with hyperfine splitting given by A_{yy}.

The powder spectrum of the two-dimensional system is calculated by first considering the anisotropy of the **g** tensor. Then the hyperfine interaction shall be taken into account. For $\theta = 90°$, equation (5) yields

$$h\nu_0 = \mu_B(g_{xx} \cos^2 \phi + g_{zz} \sin^2 \phi)B(\phi) \tag{53}$$

The powder line shape is in this case given by the relation $L(B) \sim (dB/d\phi)^{-1}$, which results in

$$L(B) \sim 1/B(\phi)\{[B_x - B(\phi)][B(\phi) - B_z]\}^{1/2} \tag{54}$$

This function has two infinite values at $B_x = h\nu_0/\mu_B g_{xx}$ and $B_z = h\nu_0/\mu_B g_{zz}$, in contrast to the three-dimensional case, where only one infinite value is found (see Figure 3). The function $L(B)$ is shown in Figure 28a. In practice, the broadened absorption spectrum is obtained (Figure 28b), resulting in the first-derivative ESR spectrum shown in Figure 28c. The powder spectrum of a nitroxide spin label with the hyperfine interaction taken into account follows from adding together three envelopes of Figure 28c belonging to $M_I = 1$, 0, and -1, as illustrated in Figure 29 (Hemminga, 1977).

It is possible to observe very slow rotational motions of the cholestane spin label about its long axis (i.e., $\tau_\parallel$ in the region 10^{-7} to 10^{-3} s) directly with ST-ESR spectroscopy of a macroscopically oriented lipid system at $\theta = 90°$ (Delmelle *et al.*, 1980; Koole *et al.*, 1981). Saturation transfer effects in these spectra can be interpreted in a way similar to that in Section 2.6. In a powder spectrum of a two-dimensional system, as shown

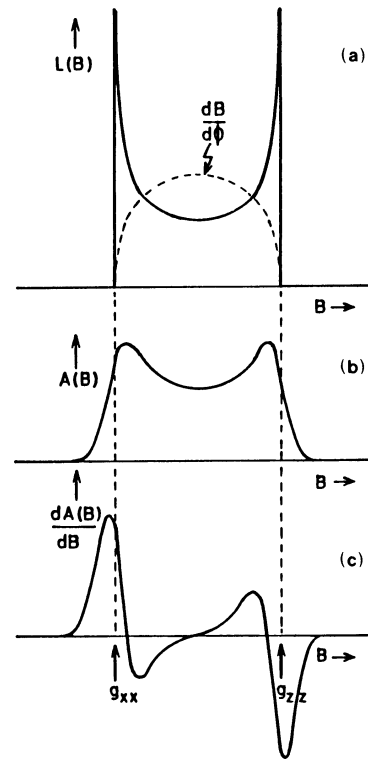

Figure 28. Theoretical line shapes of the two-dimensional powder spectrum of a simple radical with a **g** tensor and no hyperfine interaction. (a) Unbroadened powder line-shape function $L(B)$ as given by equation (54). The broken line is the function $dB(\phi)/d\phi = [L(B)]^{-1}$. (b) Broadened absorption spectrum $A(B)$. (c) Two-dimensional ESR powder spectrum $dA(B)/dB$. The principal values of the **g** tensor are g_{xx}, g_{yy}, and g_{zz}. It is assumed that g_{yy} coincides with the director so that the two-dimensional powder spectrum is determined only by g_{xx} and g_{zz}. (From Hemminga, 1983.)

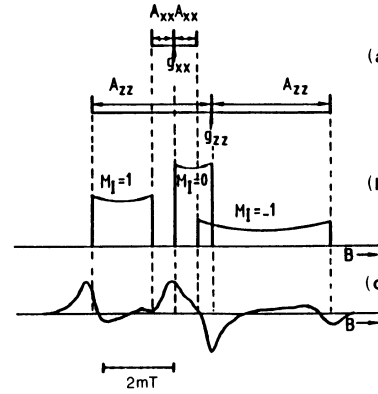

Figure 29. Analysis of the two-dimensional ESR powder spectrum of the cholestane spin label perfectly oriented in a macroscopically oriented dipalmitoyl phosphatidylcholine multibilayer with 25 mol% cholesterol. (a) Resonance field values for the x and z directions. A_x, A_z and g_x, g_z are the x and z components of the **g** and **A** tensors. (b) Schematic line shape of the absorption spectrum. (c) Experimental $\theta = 90°$ ESR spectrum. (From Hemminga, 1977.)

in Figure 29, saturation transfer is affected by the angle ϕ only. Therefore the rate of saturation transfer is determined by $dB/d\phi$. This function, which follows directly from the inverse of the line-shape function $L(B)$, is depicted in Figure 28a by a broken line. Again, saturation transfer leaves the turning points unaffected, while the maximal effect occurs between the turning points.

A similar analysis for the whole Q_2 spectrum is presented in Figure 30. It is not allowed to obtain the rotational correlation time $\tau_\parallel$ from the reference curves obtained for isotropic motion, because the molecular distribution function is different and only the x and z components of the **g** and **A** tensors affect the spectrum. In addition the motion is non-Brownian, as the spin-labeled lipid and the solvent lipid molecules have approximately the same size. A qualitative analysis of the spectra results in an estimate of $\tau_\parallel$ given by (Koole *et al.*, 1981)

$$\tau_\parallel \cong 10^{(2C'/C-6)} \tag{55}$$

where C'/C is defined in Figure 30a. The result of the analysis of the spectra at various temperatures is shown in Figure 30b. The best way to obtain reliable values of $\tau_\parallel$ is

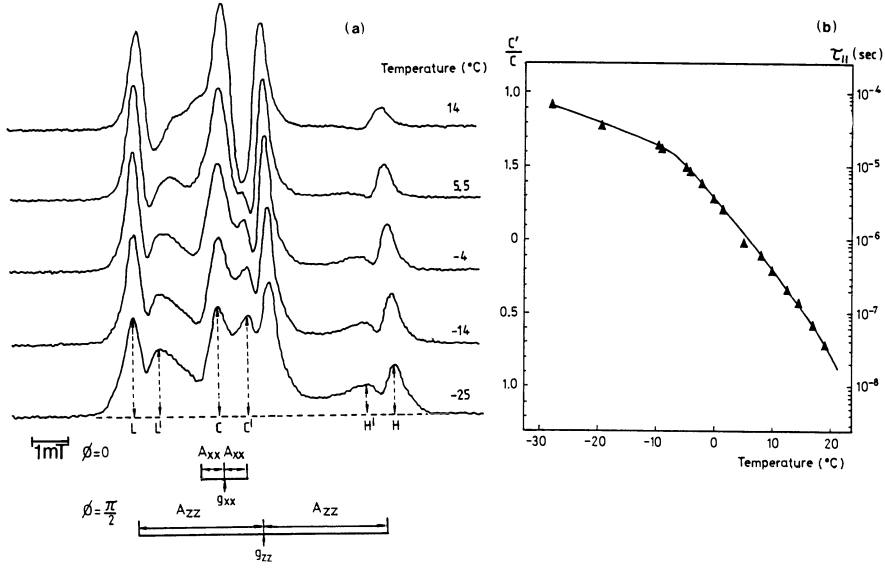

Figure 30. (a) Temperature dependence of the two-dimensional second-harmonic quadrature (Q_2) ST-ESR spectra of cholestane spin label in a macroscopically oriented multibilayer system of dimyristoyl phosphatidylcholine with 9 mol% cholesterol. The angle θ between the director and magnetic field direction is 90°. The parameters L', C', and H' are defined as the heights of the maxima between the turning points. At high temperatures maximum C' changes into a minimum at the same place. L, C, and H are heights at positions near the turning points. ϕ gives the angle between the x axis and the direction of the magnetic field in the x-z plane of the cholestane spin label. (b) Plot of the ratio C'/C as a function of temperature. $\tau_\parallel$ is the rotational correlation time calculated from equation (55). (Adapted from Koole *et al.*, 1981.)

from computer simulation of the Q_2 spectra. However, such an analysis has not yet been successfully carried out.

The Q_2 spectra of the cholestane spin label in macroscopically oriented multibilayers also show a marked angular dependence, as is illustrated in Figure 31a. The Q_2 spectrum at $\theta = 0°$ is insensitive to the anisotropic motion described by $\tau_{\|}$. This provides an interesting situation, since in the same system saturation effects in ST-ESR spectroscopy can be studied that are unaffected by spectral diffusion.

The I_2 and Q_2 spectra obtained at $\theta = 0°$ exhibit characteristic changes upon different incident microwave power levels (P_i) and modulation frequencies (ν_m) (Koole and Hemminga, 1985). The observed changes reflect the nonlinear response of the spin system, which is governed by ν_m, T_1, and B_1. Such spectra can be simulated using a computer program for isotropic reorientation (Perkins *et al.*, 1976), by assuming that the **g** and **A** tensors are isotropic, with values g_{yy} and A_{yy}. This has enabled the determination of the T_1 values of the cholestane spin label at various temperatures, as shown in Figure 32. Such information may be valuable in a more quantitative approach of the analysis of ST-ESR spectra using computer simulations.

The Q_2 spectra of the cholestane spin label in randomly oriented bilayers (membrane dispersions) are simply the addition of the angular-dependent spectra of oriented multibilayers for θ between 0 and 90° (see Figure 31b). However, retrieving information on spin-label motion from such spectra is less straightforward than the analysis of the oriented-bilayer spectra (Koole *et al.*, 1981).

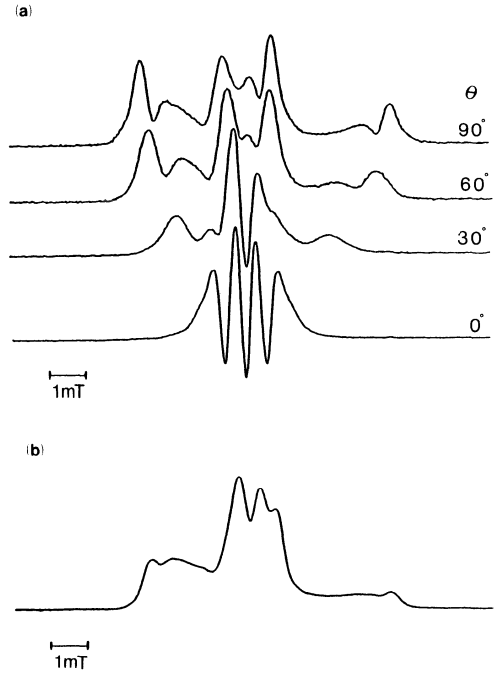

Figure 31. (a) Angular dependence of the Q_2 spectra of the cholestane spin label in macroscopically oriented multibilayers of DMPC with 9 mol% cholesterol at a temperature of −18 °C. The angle θ between the director and the magnetic-field direction is indicated on the spectra. (b) Q_2 spectrum of the cholestane spin label in an unoriented bilayer dispersion. (From Koole *et al.*, 1981.)

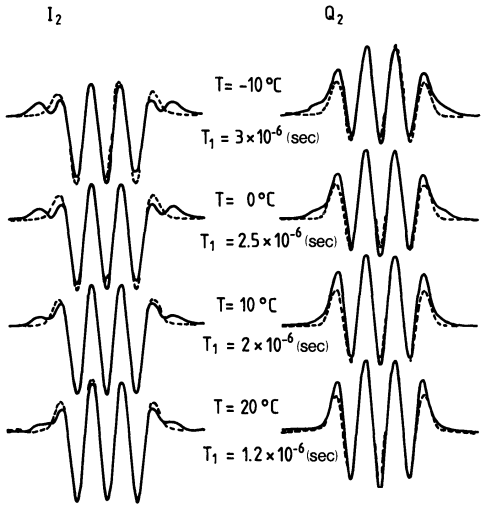

Figure 32. Experimental (——) and calculated (- - - -) I_2 and Q_2 spectra of the cholestane spin label in macroscopically oriented multibilayers of dimyristoyl phosphatidylcholine with 33 mol% cholesterol at $\theta = 0°$. For the computer simulations the program of Perkins *et al.* (1976) has been used. The T_1 values at various temperatures have been deduced from the best computer fits. (From Koole and Hemminga, 1985.)

4.2.2. ST-ESR Spectra of Unoriented Spin Labels

For spin-labeled molecules that perform an anisotropic motion, a method has been suggested that relates the spectral parameters L''/L, C'/C, and H''/H from the experimental Q_2 spectra with those of the isotropic reference spectra determined for maleimide spin-labeled hemoglobin (Gaffney, 1979; Robinson and Dalton, 1980; Johnson *et al.*, 1982a; Beth *et al.*, 1983). In general, this analysis yields three different values for the correlation time τ_c, which is assumed to be diagnostic for anisotropic motion. However, in using this analysis, it is not possible to obtain information about effects of molecular ordering in the system.

This approach has been followed for the analysis of Q_2 spectra of spin-labeled fatty acids of membrane systems in the gel phase. For these spin labels the three correlation times have been interpreted in terms of an anisotropic motion of the molecule about its long molecular axis (Marsh, 1980; Fajer and Marsh, 1983a). Figure 33a gives the Q_2 spectra of such a spin label in an unoriented lipid dispersion in the gel phase. By comparison with the Q_2 spectra for isotropic motion (see Figure 20), the anisotropic motion clearly affects the central part of the spectra and thus the ratio C'/C. Since the long molecular axis approximately coincides with the nitroxide z axis, anisotropic motion modulates the **g** and **A** tensors in the x-y plane, leaving the z components unaffected (see Figure 5). Therefore, this motion gives rise to saturation transfer in the central part of the spectrum and thus only affects C'/C. Motion of the long axis itself will cause saturation transfer throughout the whole spectrum. Therefore C'/C yields a value for $\tau_\parallel$, the correlation time for the motion about the long axis, while L''/L and H''/H give $\tau_\perp$, the correlation time for the long axis itself. In this way it is possible to interpret changes in the shape of Q_2 spectra in terms of $\tau_\parallel$ and $\tau_\perp$. The temperature dependence of C'/C and H''/H of the Q_2 spectra is shown in Figure 33b. For gel-phase lipids, the value of $\tau_\perp$ turns out to be approximately 10^{-4} s, while $\tau_\parallel$ is two orders of magnitude smaller.

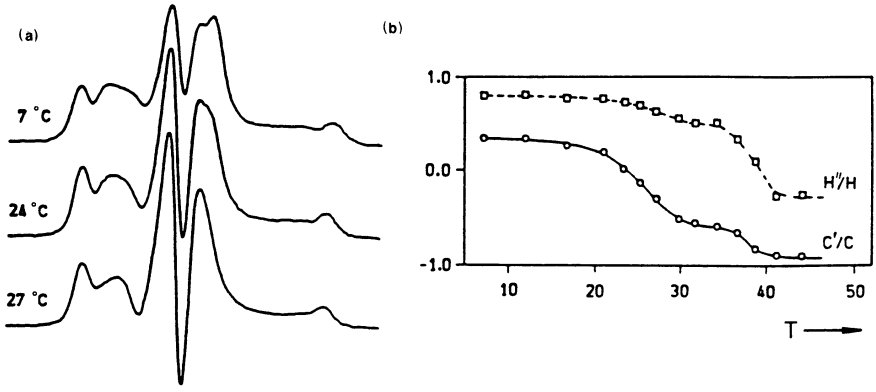

Figure 33. (a) Q_2 spectra of a phospholipid spin label in a random dispersion of dipalmitoyl phosphatidylcholine. (b) Temperature (in °C) profile of the ratios C'/C and H''/H. (From Marsh, 1980.)

In the case of spin-labeled proteins, differences in the three correlation times reflect the nonspherical character of the protein, provided the spin label is tightly bound to the protein surface. This situation is generally difficult to discriminate from one where the spin label performs an internal motion on the protein (Hemminga, 1987). The latter case has been examined for maleimide spin-labeled coat proteins of a spherical virus particle (Krüse and Hemminga, 1981; Vriend *et al.*, 1984; Hemminga and Faber, 1986). The Q_2 spectra of the spin-labeled virus in glycerol-water mixtures are shown in Figure 34. Again, especially in the central region the Q_2 spectra deviate from those for isotropic motion.

For such a system the motion of the spin label is described by the correlation times of the local, anisotropic spin-label motion superimposed on the overall isotropic motion of the virus particle. The correlation time τ_R for the overall rotational motion is given by the Stokes-Einstein relation [equation (17)]. The local motion is described by two correlation times $\tau_\parallel$ and $\tau_\perp$: $\tau_\parallel$ represents the rotational motion about the long molecular axis of the maleimide spin label, which approximately coincides with the nitroxide z axis (Vriend *et al.*, 1984), while $\tau_\perp$ represents the rotational motion of this axis with respect to the virus particle.

In analogy with the analysis of Q_2 spectra of fatty acid spin labels (Marsh, 1980; Fajer and Marsh, 1983a), the ratio C'/C of the Q_2 spectra of the spin-labeled virus gives a good approximation for $\tau_\parallel$, provided $\tau_\parallel$ is short with respect to the other correlation times:

$$\tau(C'/C) \cong \tau_\parallel \qquad \text{if} \quad \tau_\parallel \ll \tau_\perp, \tau_R \tag{56}$$

The correlation times $\tau_\perp$ and τ_R will affect the whole Q_2 spectrum. The ratio L''/L is used to monitor these correlation times. Also here the fastest motion determines the ratio L''/L, so that the following relations are found:

$$\tau(L''/L) \cong \tau_R \qquad \text{if} \quad \tau_R \ll \tau_\perp \tag{57}$$

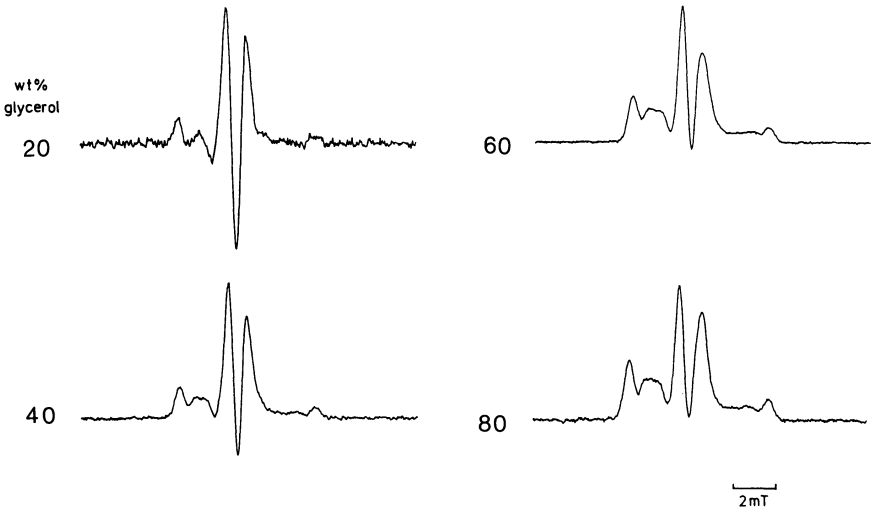

Figure 34. Q_2 spectra of maleimide spin-labeled cowpea chlorotic mottle virus in various glycerol-water systems. (From Hemminga and Faber, 1986.)

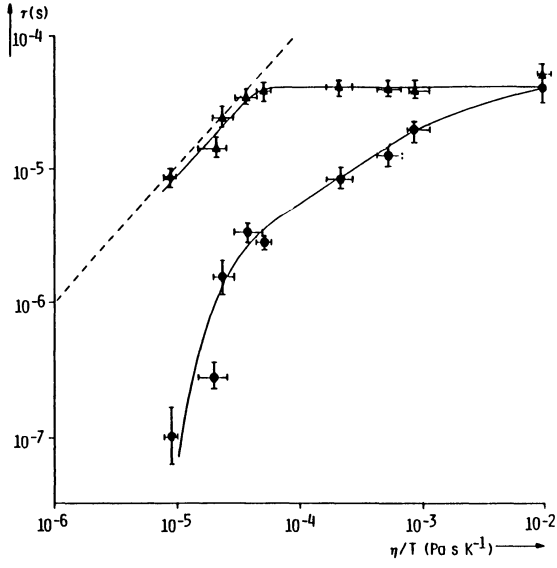

Figure 35. Variation of the rotational correlation time τ with η/T for maleimide spin-labeled cowpea chlorotic mottle virus in glycerol-water mixtures, deduced from the ratios C'/C (●) and L''/L (▲) of the Q_2 spectra in Figure 34. The dotted line gives the Stokes-Einstein relation [equation (17)] for the virus particle. (From Hemminga and Faber, 1986.)

and

$$\tau(L''/L) \cong \tau_\perp \qquad \text{if} \quad \tau_\perp \ll \tau_R \tag{58}$$

The result of such an analysis of spin-labeled virus in glycerol-water mixtures with different viscosities is shown in Figure 35. For low values of η/T ($<5 \times 10^{-5}$ Pa s K^{-1}), $\tau(L''/L)$ obeys the Stokes-Einstein relation, in agreement with equation (57). For high values of η/T the local anisotropic motion determines L''/L, as given by equation (58). This is independent of the macroscopic viscosity. Hence this method allows the approximate determination of τ_R and $\tau_\perp$, giving a value of 2×10^{-5} s for $\tau_\perp$. The correlation time $\tau_\parallel$ for the motion about the long molecular axis of the spin label, which is given by $\tau(C'/C)$, is found to be fast for low values of η/T ($\tau_\parallel \cong 10^{-7}$ s) and to increase at higher values of η/T. Finally, it should be noted that a ST-ESR spectrum of anisotropic motion is not a simple superposition of ST-ESR spectra of isotropic motion. Therefore the discussed qualitative methods are only approximate methods.

5. FUTURE DEVELOPMENTS

In evaluating the prospects of ST-ESR it is important to stress that, for most applications to biological systems, the basic question is not spectral resolution but spectral sensitivity to molecular motion. Information about molecular motion is not only contained in the quadrature (Q_n) displays, but also in the in-phase (I_n) displays. Both displays provide complementary information about the saturation transfer ESR properties of the system at the nth harmonic.

From an experimental point of view, a dual phase-sensitive detector provides this information at one particular harmonic, usually the second harmonic ($n = 2$). For most experimental situations this is sufficient. The advantage of a dual phase-sensitive detector coupled to a computer is that the spectroscopist acquires the complete information in a single ESR experiment. Afterward, spectral manipulations can be carried out, such as base-line correction, phase correction, calculation of new spectral displays, spectral integration, and automatic line-shape analysis. In the near future routine ESR spectrometers will have these facilities available for ST-ESR. A digital phase-sensitive detector can even provide spectral information at several harmonics, i.e., $n = 1, 2, 3, \cdots$, in a single experiment. The spectral analysis can then be extended to correlations between different harmonics.

The analysis of ST-ESR spectral displays is currently based on empirical methods. This approach has been shown to be useful in a large variety of experimental situations. To date, computer simulation has been of limited use to extract motional information from the spectra. This arises because the calculations are enormous and the ST-ESR spectra depend on a large number of experimental and spin-label parameters. Fast and cheap microcomputers with array-processing capabilities will become available within the next few years. This will give an impetus to new developments in the numerical approaches for ST-ESR, allowing novel ways to analyze ST-ESR spectra.

ST-ESR spectroscopy is a stationary technique that is based on the observation of the response of the spin system on field modulation and spectral diffusion by rotational motions. From an analysis of the ST-ESR line shape, the parameters for the molecular motion are indirectly determined. A more direct way to observe molecular motion comes from time-resolved saturation transfer ESR techniques, as is illustrated in Figure 14. Such experiments have been carried out recently (Dzuba *et al.*, 1984; Fajer *et al.*, 1986) using pulsed ESR equipment. These experiments show that the molecular motion of spin-labeled molecules can be determined quantitatively in the microsecond range. Notwithstanding the high investments in money and effort to carry out time-resolved ESR, it may be expected that these types of experiments will contribute to new applications of saturation transfer spectroscopy.

REFERENCES

Anderson, J. R., and Mailer, C., 1982, Balanced cavity scheme for saturation transfer dispersion electron paramagnetic resonance, *Rev. Sci. Instrum.* **53**:1727-1729.

Berliner, L. J. (ed.), 1976, *Spin Labeling: Theory and Applications*, Vol. 1, Academic Press, New York.

Berliner, L. J. (ed.), 1979, *Spin Labeling: Theory and Applications*, Vol. 2, Academic Press, New York.

Beth, A. H., Wilder, R., Wilkerson, L. S., Perkins, R. C., Meriwether, B. P., Dalton, L. R., Park, C. R., and Park, J. H., 1979, EPR and saturation transfer EPR studies on glyceraldehyde 3-phosphate dehydrogenase, *J. Chem. Phys.* **71**:2074-2082.

Beth, A. H., Venkataramu, S. D., Balasubramanian, K., Dalton, L. R., Robinson, B. H., Pearson, D. E., Park, C. R., and Park, J. H., 1981, ^{15}N and ^{2}H-substituted maleimide spin labels: improved sensitivity and resolution for biological EPR studies, *Proc. Natl. Acad. Sci. U.S.A.* **78**:967-971.

Beth, A. H., Balasubramanian, K., Robinson, B. H., Dalton, L. R., Venkataramu, S. D., and Park, J. H., 1983, Sensitivity of V_2' saturation transfer electron paramagnetic resonance signals to anisotropic rotational diffusion with [^{15}N]nitroxide spin-labels. Effects of noncoincident magnetic and diffusion tensor principal axes, *J. Phys. Chem.* **87**:359-367.

Carrington, A., and McLachlan, A. D., 1967, *Introduction to Magnetic Resonance*, Harper and Row, New York.

Coffey, P., Robinson, B. H., and Dalton, L. R., 1976, Rapid computer simulation of ESR spectra. II. Saturation transfer spectroscopy of axially symmetric ^{14}N-nitroxide spin labels, *Mol. Phys.* **31**:1703-1715.

Dalal, D. P., Eaton, S. S., and Eaton, G. R., 1981, The effects of lossy solvents on quantitative EPR studies, *J. Magn. Reson.* **44**:415-428.

Dalton, L. R. (ed.), 1985, *EPR and Advanced EPR Studies of Biological Systems*, CRC Press, Boca Raton, Florida.

Dalton, L. R., Robinson, B. H., Dalton, L. A., and Coffey, P., 1976, Saturation transfer spectroscopy, *Adv. Magn. Reson.* **8**:149-259.

De Jager, P. A., and Hemminga, M. A., 1978, Extension of EPR spectrometers for the measurement of saturation transfer spectra, *J. Magn. Reson.* **31**:491-496.

De Jager, P. A., and Bremer, H. J. L., 1982, Fast determination of the field modulation amplitude of a saturation transfer electron paramagnetic resonance spectrometer at various field modulation frequencies, *Rev. Sci. Instrum.* **53**:1102-1104.

Delmelle, M., 1983, Saturation transfer electron paramagnetic resonance. Influence of some experimental parameters on the spectra, *J. Magn. Reson.* **51**:245-251.

Delmelle, M., Butler, K. W., and Smith, I. C. P., 1980, Saturation transfer electron spin resonance spectroscopy as a probe of anisotropic motion in model membrane systems, *Biochemistry* **19**:698-704.

Dzuba, S. A., Maryasov, A. G., Salikhov, K. M., and Tsvetkov, Yu. D., 1984, Superslow rotations of nitroxide radicals studied by pulse EPR spectroscopy, *J. Magn. Reson.* **58**:95-117.

Evans, C. A., 1981, Use of the integral of saturation transfer electron paramagnetic resonance spectra to determine molecular rotational correlation times. Slowly tumbling spin labels in the presence of rapidly tumbling spin labels, *J. Magn. Reson.* **44**:109-116.

Fajer, P., and Marsh, D., 1982, Microwave and modulation field inhomogeneities and the effect of cavity Q in saturation transfer ESR spectra. Dependence on sample size, *J. Magn. Reson.* **49**:212-224.

Fajer, P., and Marsh, D., 1983a, Sensitivity of saturation transfer ESR spectra to anisotropic rotation. Application to membrane systems, *J. Magn. Reson.* **51**:446-459.

Fajer, P., and Marsh, D., 1983b, Analysis of dispersion-mode saturation transfer ESR spectra. Application to model membranes, *J. Magn. Reson.* **55**:205-215.

Fajer, P., Thomas, D. D., Feix, J. B., and Hyde, J. S., 1986, Measurement of rotational molecular motion by time-resolved saturation transfer electron paramagnetic resonance, *Biophys. J.* **50**:1195-1202.

Gaffney, B. J., 1979, Spin label-thiourea adducts. A model for saturation transfer ESR studies of slow anisotropic rotation, *J. Phys. Chem.* **83**:3345-3349.

Galloway, N. B., and Dalton, L. R., 1978a, Approximate methods for the fast computation of EPR and ST-EPR spectra. I. A perturbation approach, *Chem. Phys.* **10**:445-459.

Galloway, N. B., and Dalton, L. R., 1978b, Approximate methods for the fast computation of EPR and ST-EPR spectra. III. Extension of the perturbation approximation to conditions of overmodulation, *Chem. Phys.* **32**:189-200.

Ginzton, E. L., 1957, *Microwave Measurements*, McGraw-Hill, New York.

Hemminga, M. A., 1977, Analysis of the ESR spectra of the cholestane spin label in oriented multibilayers of lecithin and cholesterol in the gel state, *J. Magn. Reson.* **25**:25-45.

Hemminga, M. A., 1979, Qualitative explanation of saturation transfer ESR effects using the concept of hole-burning, *J. Magn. Reson.* **33**:215-218.

Hemminga, M. A., 1983, Interpretation of ESR and saturation transfer ESR spectra of spin labeled lipids and membranes, *Chem. Phys. Lipids* **32**:323-383.

Hemminga, M. A., 1987, Electron spin resonance and saturation transfer electron spin resonance of virus and membrane systems, *J. Chem. Soc., Faraday Trans. 1*, **83**:203-209.

Hemminga, M. A., and Berendsen, H. J. C., 1972, Magnetic resonance in ordered lecithin-cholesterol multilayers, *J. Magn. Reson.* **8**:133-143.

Hemminga, M. A., and de Jager, P. A., 1981, Magnitude saturation transfer electron paramagnetic resonance spectroscopy: a new ST-EPR technique insensitive to the null-phase setting, *J. Magn. Reson.* **43**:324-327.

Hemminga, M. A., and Faber, A. J., 1986, Analysis of anisotropic spin label motion in saturation transfer ESR spectra of spin-labeled cowpea chlorotic mottle virus, *J. Magn. Reson.* **66**:1-8.

Hemminga, M. A., Reinders, J. H., and de Jager, P. A., 1984a, The effect of modulation frequency and rotational correlation time on various spectral displays in saturation transfer ESR spectroscopy. The use of in-phase, quadrature, magnitude and phase-plot displays, *J. Magn. Reson.* **58**:428-441.

Hemminga, M. A., Leermakers, F. A. M., and de Jager, P. A., 1984b, Quantitative measurement of B_1 in ESR and saturation transfer ESR spectroscopy, *J. Magn. Reson.* **59**:137-140.

Hemminga, M. A., de Jager, P. A., Marsh, D., and Fajer, P., 1984c, Standard conditions for the measurement of saturation-transfer ESR spectra, *J. Magn. Reson.* **59**:160-163.

Horváth, L. I., and Marsh, D., 1983, Analysis of multicomponent saturation transfer EPR spectra, using the integral method. Application to membrane systems, *J. Magn. Reson.* **54**:363-373.

Huisjen, M., and Hyde, J. S., 1974, A pulsed EPR spectrometer, *Rev. Sci. Instrum.* **45**:669-675.

Hyde, J. S., 1978, Saturation transfer spectroscopy, *Meth. Enzymol. Enzyme Struct.* **49**:480-511.

Hyde, J. S., and Dalton, L. R., 1972, Very slowly tumbling spin labels: adiabatic rapid passage, *Chem. Phys. Lett.* **16**:568-572.

Hyde, J. S., and Thomas, D. D., 1973, New EPR methods for the study of very slow motion: Application to spin-labeled hemoglobin, *Ann. N.Y. Acad. Sci.* **222**:680-692.

Hyde, J. S., and Dalton, L. R., 1979, Saturation-transfer spectroscopy, in *Spin Labeling: Theory and Applications*, Vol. 2 (L. J. Berliner, ed.), pp. 1-70, Academic Press, New York.

Hyde, J. S., and Thomas, D. D., 1980, Saturation transfer spectroscopy, *Ann. Rev. Phys. Chem.* **31**:293-317.

Hyde, J. S., Froncisz, W., and Kusumi, A., 1982, Dispersion electron spin resonance with the loop-gap resonator, *Rev. Sci. Instrum.* **53**:1934-1937.

Johnson, M. E., and Hyde, J. S., 1981, 35-GHz (*Q*-band) saturation transfer electron paramagnetic resonance studies of rotational diffusion, *Biochemistry* **20**:2875-2880.

Johnson, M. E., Lee, L., and Fung, L. W.-M., 1982a, Models for slow anisotropic rotational diffusion in saturation transfer electron paramagnetic resonance at 9 and 35 GHz, *Biochemistry* **21**:4459-4467.

Johnson, M. E., Thiyagarajan, P., Bates, B., and Currie, B. L., 1982b, A comparison of resolution-enhancement methods in saturation-transfer EPR. ^{15}N Isotopically substituted spin labels and 35 GHz high-frequency operation, *Biophys. J.* **37**:553-557.

Koole, P., and Hemminga, M. A., 1985, Analysis of the saturation properties of the in-phase and quadrature second harmonic ESR spectra of the cholestane spin label in oriented lipid multibilayers in the gel state, *J. Magn. Reson.* **61**:1-10.

Koole, P., Dijkema, C., Casteleijn, G., and Hemminga, M. A., 1981, A spin label saturation transfer ESR study of very slow anisotropic motion in oriented multibilayers of lecithin and cholesterol in the gel phase, *Chem. Phys. Lett.* **79**:360-365.

Kooser, R. G., Volland, W. V., and Freed, J., 1969, ESR relaxation studies on orbitally degenerate free radicals. I. Benzene anion and tropenyl, *J. Chem. Phys.* **50**:5243-5257.

Krüse, J., and Hemminga, M. A., 1981, Electron paramagnetic resonance spectroscopy of spin-labelled cowpea chlorotic mottle virus, *Eur. J. Biochem.* **113**:575-579.

Kusumi, A., Sakaki, T., Yoshizawa, T., and Ohnishi, S., 1980, Protein-lipid interaction in rhodopsin recombinant membranes as studied by protein rotational mobility and lipid alkyl chain flexibility measurements, *J. Biochem.* **88**:1103-1111.

Mailer, C., Sarna, T., Swartz, H. M., and Hyde, J. S., 1977, Quantitative studies of free radicals in biology: Corrections to ESR saturation data, *J. Magn. Reson.* **25**:205-210.

Mailer, C., Thomann, H., Robinson, B. H., and Dalton, L. R., 1980, Crossed TM_{110} bimodal cavity for measurement of dispersion electron paramagnetic resonance and saturation transfer electron paramagnetic resonance signals for biological materials, *Rev. Sci. Instrum.* **51**:1714-1721.

Mailer, C., Dammers, A. J., and Hemminga, M. A., 1981, ST-EPR dispersion study of spin labeled oriented lipid multibilayers, *Biophys. J.* **33**, 140a.

Marchand, P., and Marmet, L., 1983, Binomial smoothing filter: a way to avoid some pitfalls of least-square polynomial smoothing, *Rev. Sci. Instrum.* **54**:1034-1041.

Marsh, D., 1980, Molecular motion in phospholipid bilayers in the gel phase: long axis rotation, *Biochemistry* **19**:1632-1637.

Marsh, D., 1981, Spin label: electron spin resonance, in *Membrane Spectroscopy* (E. Grell, ed.), pp. 51-142, Springer-Verlag, Berlin.

McCalley, R. C., Shimshick, E. J., and McConnell, H. M., 1972, The effect of slow rotational motion on paramagnetic resonance spectra, *Chem. Phys. Lett.* **13**:115-119.

Mohanty, J. G., and Rifkind, J. M., 1984, The effect of temperature on ESR signal intensities in aqueous solutions, *J. Magn. Reson.* **57**:178-184.

Percival, P. W., and Hyde, J. S., 1976, Saturation-recovery measurements of the spin-lattice relaxation times of some nitroxides in solution, *J. Magn. Reson.* **23**:249-257.

Perkins, R. C., Jr., Lionel, T., Robinson, B. H., Dalton, L. A., and Dalton, L. R., 1976, Saturation transfer spectroscopy: Signals sensitive to very slow molecular reorientation, *Chem. Phys.* **16**:393-404.

Poole, C. P., Jr., 1967, *Electron Spin Resonance: A Comprehensive Treatise on Experimental Techniques*, Wiley-Interscience, New York.

Poole, C. P., and Farach, H. A., 1971, *Relaxation in Magnetic Resonance*, Academic Press, New York.

Popp, C. A., and Hyde, J. S., 1981, Effects of oxygen on EPR spectra of nitroxide spin-label probes of model membranes, *J. Magn. Reson.* **43**:249-258.

Robinson, B. H., 1983, Effects of overmodulation on saturation transfer EPR signals, *J. Chem. Phys.* **78**:2268-2273.

Robinson, B. H., and Dalton, L. R., 1980, Anisotropic rotational diffusion studied by passage saturation transfer electron paramagnetic resonance, *J. Chem. Phys.* **72**:1312-1324.

Robinson, B. H., Beth, A. H., Crooke, P. S., and Dalton, L. R., 1978, Approximate methods for the fast computation of EPR and ST-EPR spectra. II. Gaussian preconvolution followed by Runge-Kutta solution of the master supermatrix equation, *Chem. Phys.* **30**:461-468.

Sasaki, T., Kanaoka, Y., Watanabe, T., and Fujiwara, S., 1980, A digitized EPR system and its application to saturation transfer electron paramagnetic resonance spectroscopy, *J. Magn. Reson.* **38**:385-390.

Savitzky, A., and Golay, J. E., 1964, Smoothing and differentiation of data by simplified least square procedures, *Anal. Chem.* **36**:1627-1639.

Schreier, S., Polnaszek, C. F., and Smith, I. C. P., 1978, Spin labels in membranes. Problems in practice, *Biochim. Biophys. Acta* **515**:375-436.

Schwartz, D., Pirrwitz, J., Rein, H., and Ruckpaul, K., 1982, Selective removal of spectral components in complex ST-EPR spectra of spin-labeled cytochrome P-450, *J. Magn. Reson.* **47**:375-382.

Sehr, P. A., Mailer, C., and Deveaux, P. F., 1983, Saturation transfer dispersion electron paramagnetic resonance using a balanced cavity: dynamical calibration and biological applications, *J. Magn. Reson.* **52**:23-34.

Shimoyama, Y., and Watari, H., 1986, Analysis of saturation transfer electron paramagnetic resonance spectra in terms of amplitude and phase, *J. Chem. Phys.* **84**:3688-3693.

Singer, L. S., and Kommandeur, J., 1961, Electron spin resonance in complexes of aromatic hydrocarbons with iodine, *J. Chem. Phys.* **34**:133-140.

Smith, I. C. P., and Butler, K. W., 1976, Oriented lipid systems as model membranes, in: *Spin Labeling: Theory and Applications*, Vol. 1 (L. J. Berliner, ed.), pp. 411-452, Academic Press, New York.

Squier, T. C., and Thomas, D. D., 1986, Methodology for increased precision in saturation transfer electron paramagnetic resonance studies of rotational dynamics, *Biophys. J.* **49**:921-935.

Stoodley, L. G., 1963, The sensitivity of microwave electron spin resonance spectrometers for use with aqueous solutions, *J. Electron. Contr.* **14**:531-546.

Thomas, D. D., Dalton, L. R., and Hyde, J. S., 1976, Rotational diffusion studied by passage saturation transfer electron paramagnetic resonance, *J. Chem. Phys.* **65**:3006-3024.

Vancamp, H. L., and Heiss, A. H., 1981, Computer applications in electron paramagnetic resonance, *Magn. Res. Rev.* **7**:1-40.

Vistnes, A. I., 1983, Magnetization hysteresis electron paramagnetic resonance. A new null phase insensitive saturation transfer EPR technique with high sensitivity to slow motion, *Biophys. J.* **43**:31-37.

Vistnes, A. I., and Dalton, L. R., 1983, Experimental methods to determine the microwave field strength in electron spin resonance, *J. Magn. Reson.* **54**:78-88.

Vistnes, A. I., Wormald, D. I., Isachsen, S., and Schmalbein, D., 1984, An efficient digital phase-sensitive detector for use in electron-spin-resonance spectroscopy, *Rev. Sci. Instrum.* **55**:527-532.

Vriend, G., Schilthuis, J. G., Verduin, B. J. M., and Hemminga, M. A., 1984, Saturation transfer ESR spectroscopy on maleimide spin-labeled cowpea chlorotic mottle virus, *J. Magn. Reson.* **58**:421–427.

Watanabe, T., Sasaki, T., Sawatari, K., and Fujiwara, S., 1980, A new detection system of saturation transfer electron paramagnetic resonance spectroscopy by a Fourier transformation technique, *Appl. Spectrosc.* **34**:456–460.

Watanabe, T., Sasaki, T., and Fujiwara, S., 1982, Phase dependence of saturation transfer EPR signals and estimated rotational correlation times, *Appl. Spectrosc.* **36**:174–178.

4

Nitrogen-15 and Deuterium Substituted Spin Labels for Studies of Very Slow Rotational Motion

Albert H. Beth and Bruce H. Robinson

1. INTRODUCTION

Since its introduction (Ohnishi and McConnell, 1965; Stone *et al.*, 1965), the spin-labeling technique has enjoyed great success in applications involving quantitation of molecular motion in biological systems. Early studies were largely devoted to characterizations of the nanosecond rotational motions of small soluble proteins and lipid components in membrane bilayers using linear[1] electron paramagnetic resonance (EPR) spectroscopy. However, development of continuous wave saturation transfer electron paramagnetic resonance (cw-ST-EPR) spectroscopy (Hyde and Dalton, 1972; Hyde and Thomas, 1973; Thomas *et al.*, 1976) and time domain techniques including saturation recovery EPR (SR-EPR; Huisjen and Hyde, 1974; Hyde, 1979; Freed, 1979; Fajer *et al.*, 1986) has provided access to a new motional window which is important for studies of dynamics and interactions of membrane proteins and interactions of soluble proteins to form supramolecular structures. While linear EPR spectroscopy provides sensitivity to rotational motions in the 10 ps to 1 μs correlation time range

[1] The terms linear and saturation refer to the microwave power level employed to collect EPR data. Linear spectra are obtained using a power level in the range where signal amplitude increases linearly with the square root of the power setting (in mW). Saturating conditions refers to power levels where the signals do not increase linearly with the square root of power (i.e., partial saturation of the spin energy levels).

Albert H. Beth • Department of Molecular Physiology and Biophysics, Vanderbilt University, Nashville, Tennessee 37232. **Bruce H. Robinson** • Department of Chemistry, University of Washington, Seattle, Washington 98195.

using nitroxide spin labels (McCalley *et al.*, 1972), cw-ST-EPR provides high sensitivity in the 1 μs to 1 ms correlation time range (Thomas *et al.*, 1976) and SR-EPR at least in the 1 to 15 μs range (Fajer *et al.*, 1986). The range of rotational times spanned by cw-ST-EPR, generally referred to as the very slow motional region, is characteristic of proteins embedded in lipid bilayers and of single proteins or protein-protein complexes of combined molecular weight $\geq$300 kDa in aqueous media.

A motivation for developing cw-ST-EPR and SR-EPR spectroscopies for biological samples (low concentrations of spin label in aqueous media) was provided by recognition of their potential for characterizing protein-protein and protein-lipid interactions through observation of changes in rotational diffusion. Mathematical models (Saffman and Delbruck, 1975; Broersma, 1960; Tirado and de la Torre, 1979, 1980) point to the exquisite sensitivity of the rotational correlation time on the solvated radius of a protein, and hence on the size, shape, and number of proteins which are interacting to form a stable complex. One area where ST-EPR has, and promises to continue to yield, important insight is in observing protein-protein and protein-lipid interactions in cell membranes and reconstituted vesicle systems. Characterizations of the sizes and stabilities of protein complexes in membranes, in conjunction with studies of protein topology and lateral mobility, can provide unique data for elucidating relationships between structure, motion, and function. Citing but a few examples: it is possible to probe how interactions of transmembrane proteins on one side of a bilayer are coupled to motion of the protein on the other side thereby establishing potential mechanisms of transmembrane signaling; how binding of hormones or other effectors to cell surface receptors regulate interactions between intrinsic and peripheral membrane proteins; how the physical state and composition of membrane lipids influences protein motion, interactions, and function; and how genetic and site directed mutations in protein sequences affect normal interactions. Such measurements are of fundamental importance for understanding the roles of protein-protein and protein-lipid interactions in determining cellular structural properties and in transducing extracellular signals through cell membranes. However, analyses of experimental data from spin-labeling studies on these types of systems routinely requires characterization and quantitation of anisotropic rotational diffusion.

Clearly, many biological macromolecules other than the aforementioned membrane proteins exhibit motions which fall in the very slow rotational motion region and are thus amenable to study by ST-EPR spectroscopies with appropriately designed spin-labeling reagents. A number of reviews have appeared which provide an overview of the systems which have been studied by cw-ST-EPR, the approaches employed for collection of spectral data and their analyses, and development of theory for simulation of line shapes in the very slow motional time range (Hyde and Thomas, 1973, 1980; Hyde, 1978; Hyde and Dalton, 1979; Marsh, 1981; Devaux, 1982; Thomas, 1982, 1985, 1986; Fajer and Marsh, 1983; Fung and Johnson, 1984; Robinson *et al.*, 1985). Since applications of cw-ST-EPR have been comprehensively covered, they will not be repeated here. Instead, the general theme of Sections 2-4 will be to provide definitions of quantities and an overview of concepts useful for quantitation of very slow rotational motions. Sections 5-9 will examine the dependence of cw-ST-EPR signals on rotational correlation times, on microwave and modulation frequencies, and on motional models relevant to studies of protein complexes and membrane proteins; and, more specifically, on the contributions of nitrogen-15 and deuterium substituted spin-labeling reagents

to the cw-ST-EPR methodology for quantitating large-scale, very slow, anisotropic rotational diffusion of spin-labeled proteins. Section 10 will outline potential advantages of nitrogen-15, deuterium substituted spin labels for time domain ST-EPR studies of very slow rotational dynamics of proteins. Finally, Section 11 will provide an overview of the data and discussions presented.

The emphasis throughout will be on data obtainable with nitrogen-15 spin labels. However, results will be compared and contrasted with those obtainable using conventional nitrogen-14 spin labels whenever possible. It is our intention to provide sufficient experimental and theoretical data so that investigators can predict the magnitude of spectral change for a given change in rotational dynamics of a spin-labeled protein for relevant motional models, and can then select the optimum set of machine parameters for quantitating the motion. The data presented will enable evaluation of how nitrogen-15, deuterium substituted spin labels can be employed to enhance data analysis for a range of experimental problems, and, in particular, in cases where the rotational diffusion is complicated by anisotropic environments and/or molecular asymmetry.

The use of nitrogen-15 nitroxide spin labels dates from the early synthetic work of Brière *et al.* (1965) while incorporation of deuterium into the nitroxide ring system dates from the work of Chiarelli and Rassat (1973). Accounts of many of the early papers employing these singly isotopically substituted spin labels can be found in the chapter by Gaffney (1976). The use of doubly substituted spin labels containing both nitrogen-15 and deuterium for covalent modification of proteins dates from the work of Beth *et al.* (1981a, 1981b) and Johnson *et al.* (1982b). These studies with the doubly substituted spin labels provided impetus for further development of labeling reagents and spectral characterizations relevant to biological spin-labeling studies, particularly in the area of studies of very slow rotational motions.

Before beginning discussions of spin labeling, it should be emphasized that transient optical anisotropy techniques also provide convenient access to the very slow motional time window. Since these techniques have been reviewed in a number of recent articles, extensive discussions will be omitted in this chapter. However, the interested reader is directed to a review of ST-EPR and transient optical anisotropy by Thomas (1986) which compares the complementary motional information obtainable from these two techniques.

2. OVERVIEW OF ROTATIONAL DIFFUSION MODELS

Before addressing the sensitivity of ST-EPR for studies of rotational diffusion of spin-labeled proteins and biomolecular assemblies, areas of potential applications will be outlined in terms of relevant motional models. The primary use of ST-EPR spectroscopy to date has been to observe the microsecond to millisecond rotational motions of a nitroxide spin label rigidly held within the local structure of a protein. For globular proteins in solution, rotational diffusion of the entire protein molecule or protein complex is observed while for more flexible, asymmetric proteins, segmental motions of a large portion of the protein to which the spin label is attached may be observed. For practical reasons, the diffusion models which have received the most experimental and theoretical attention have been the Brownian rotational diffusion of a spherical or cylindrical protein, tumbling as a rigid body, to which a single nitroxide is rigidly and

uniquely attached such that the motion of the spin label accurately reflects the rotational motion of the entire protein. Using these models as a starting point, three limiting cases for rotational diffusion will be discussed following a brief mathematical definition of rotational correlation times and their relationship to the size and shape of a macromolecule.

2.1. Definition of Rotational Correlation Times

The definition of a correlation time comes from the characteristic time associated with a particular function which is being driven by a specified stochastic process. The correlation time represents the time that that function is no longer correlated with itself, i.e., the memory has been lost due to the stochastic nature of the motional process. We begin by considering the definition of a motional process in terms of a motional operator, Γ_Ω. The diffusion process for a distribution of spins, $P(\Omega, t)$, satisfies the time-dependent, partial differential Smoluchowski equation:

$$\dot{P}(\Omega, t) = -\Gamma_\Omega P(\Omega, t) \tag{1}$$

The solution to this equation is easily obtained, if only in a formal manner, as

$$P(\Omega, t) = \exp(-t\Gamma_\Omega)P(\Omega, 0) \tag{2}$$

That is, if the initial distribution at time zero ($t = 0$) is specified, then since Γ_Ω is time independent, the distribution at any time later (t) can be calculated according to the above prescription. The exponential form containing Γ_Ω is often referred to as an evolution operator, since it will evolve the distribution from time zero up to time t in a probabilistic fashion. At equilibrium, the distribution $P_0(\Omega)$ must satisfy the condition that it will not change under evolution. Therefore, it must be true that the equilibrium can be found by requiring that $\Gamma_\Omega P_0(\Omega) = 0$. It is now a simple matter to consider the conditional probability, $W(\Omega, t\,|\,\Omega', 0)$, which defines the probability of being at orientation Ω at time t, given that one started at orientation Ω' at time zero as

$$W(\Omega, t\,|\,\Omega', 0) = \exp(-t\Gamma_\Omega)\delta(\Omega - \Omega') \tag{3}$$

where $\delta(\Omega - \Omega')$ is the Dirac "delta function," which places unit probability at the single orientation of Ω' at time zero.

Now that the diffusion process has been characterized, one decides on a suitable function for examining the particular evolution. For rotational reorientation, the functions of interest are generally the spherical harmonics, $Y^l_m(\Omega)$, or the more general Wigner matrix elements, $D^l_{m,n}(\Omega)$, the latter often being more convenient for considering generalized tensorial rotations. The correlation function for a given function, $D^l_{m,n}(\Omega)$, is the average overlap of the function at time t with the form that it had at time zero:

$$\rho(t) = \langle D^l_{m,n}(\Omega(t))\,|\,D^l_{m,n}(\Omega(0))\rangle \tag{4}$$

where the function of time, $\rho(t)$, is in the form of an autocorrelation function. Here the averaging is over all orientation variables Ω and the problem is to determine how the orientation variables change in time. The above definitions of the conditional probability provide an opportunity to be more explicit about the nature of the averaging. In particular, we define $\rho(t)$ using the conditional probability:

$$\rho(t) = \int_{\Omega} \int_{\Omega'} P_0(\Omega') D^{l*}_{m,n}(\Omega) W(\Omega, t|\Omega', 0) D^{l}_{m,n}(\Omega')\, d\Omega\, d\Omega' \tag{5}$$

The above double integral can be done explicitly, in principle, for any given motional process and any function D. The quantity $P_0(\Omega')$ is included to insure that the initial orientations are weighted according to their equilibrium values. One may convert this integral into one over a single orientation variable, using the above definition of $W(\Omega, t|\Omega', 0)$ and the property of the delta function, by integrating over Ω':

$$\rho(t) = \int_{\Omega} D^{l*}_{m,n}(\Omega) \exp(-t\Gamma_{\Omega}) D^{l}_{m,n}(\Omega) P_0(\Omega)\, d\Omega \tag{6}$$

It is often convenient to use the adjoint operator for Γ_{Ω} (denoted Γ_{Ω^+}) in which case the correlation function can be computed as

$$\rho(t) = \int_{\Omega} P_0(\Omega) D^{l*}_{m,n}(\Omega) \exp(-t\Gamma_{\Omega^+}) D^{l}_{m,n}(\Omega)\, d\Omega \tag{7}$$

In addition to an autocorrelation function for a given orientation function, cross-correlation functions can also be defined where the two functions in the above integral are different. An interesting example of a cross correlation occurs in the case of anisotropic rigid-body Brownian motion: when the spin tensor axes and the principal axes of diffusion are not coincident, there is cross correlation between the motion of the major elements [as given by $Y^2_0(\Omega)$] and the minor elements [from $Y^2_2(\Omega)$].

The correlation function should have the property that $\rho(0) = 1$ and that $\rho(\infty) = 0$. When considering auto and cross correlations of the Wigner matrix elements, as well as the spherical harmonics, these conditions are automatically satisfied, for nonzero l values, and so for this reason also they are ideal functions to consider. With these restrictions on $\rho(t)$, a correlation time τ can be computed as

$$\tau = \int_{t=0}^{\infty} \rho(t)\, dt \tag{8}$$

As an example, if the correlation function is a simple exponential decay, then the correlation time is just the characteristic decay time. For the case of isotropic Brownian rotational diffusion

$$\Gamma_{\Omega} = -D_r \nabla^2_{\Omega} \tag{9}$$

where D_r is the Stokes-Einstein rotational diffusion coefficient for a sphere in a viscous medium, and ∇_Ω^2 is the angular Laplacian operator. With this operator, the cross-correlation functions are zero and only the autocorrelation functions are nonvanishing (Favro, 1965):

$$\rho(t) = \int_\Omega P_0(\Omega) D^{l*}_{m,n}(\Omega) \exp(-tD_r\nabla_\Omega^2) D^l_{m,n}(\Omega)\, d\Omega \tag{10}$$

which, upon integration, yields

$$\rho(t) = \exp[-tD_r l(l+1)] \tag{11}$$

Generally, one is interested in the rotation of the second-rank tensor elements (e.g., $\cos^2\theta$) in which case $l = 2$ and

$$\tau_r = 1/6D_r \tag{12}$$

which is the well-known relation between the rotational correlation time (τ_r) and the rotational diffusion coefficient (D_r) for isotropic Brownian rotational diffusion. This formalism allows one to consider more general forms for complicated motional processes and to consider a large set of characteristic rotational times. In Sections 2.3 and 2.4 below, the case of anisotropic rigid-body motion will be outlined and the resultant set of characteristic times produced by such motion defined.

2.2. Isotropic Rotational Diffusion

A spherical protein in an isotropic environment will give rise to isotropic rotational diffusion characterized by a single correlation time, τ_r, which is related to the diffusion operator as defined in the previous section. Quantity τ_r can be further related to molecular dimensions by the Stokes-Einstein relationship:

$$\tau_r = 4\pi\eta r^3/3kT \tag{13}$$

The important point is that τ_r is proportional to the third power of the solvated radius (r) while it is linearly related to the solvent viscosity (η), and is inversely proportional to the absolute temperature (T). For a spherical protein, the orientation of the spin label with respect to the molecular structure will not affect the shape of the cw-ST-EPR spectrum, since motion occurs about all axes with equal probability and at equal rates.

2.3. Anisotropic Rotational Diffusion in an Isotropic Medium

The rotational diffusion of a cylindrical protein in an isotropic environment can be characterized by two unique rotational correlation times, $\tau_\parallel$ and $\tau_\perp$, about the major and minor axes of the protein, respectively. The connection between rotational correlation times and hydrodynamics begins with the definition of the rotational friction factors Ξ_{ii}, where Ξ is a 3×3 matrix containing the friction factors. The work of Tirado and de la Torre (1979) summarizes the relation of Ξ to the viscosity, η, for the physical

model of a right circular cylinder of length $2a$ and radius b. In this case, there are two unique elements of the diagonal friction tensor denoted $\Xi_{\|}$ and $\Xi_{\perp}$. The rotational friction factor for rotation about the unique axis, $\Xi_{\|}$, is given by

$$\Xi_{\|} = 8\pi\eta ab^2[0.96(1 + \delta_{\|})] \tag{14}$$

and the rotational friction factor for rotation about the axis perpendicular to the unique axis, $\Xi_{\perp}$, is given by

$$\Xi_{\perp} = 8\pi\eta a^3/\{3[\ln(a/b) + \delta_{\perp}]\} \tag{15}$$

Values of $\delta_{\|}$ and $\delta_{\perp}$ have been calculated by Torado and de la Torre (1980) for a variety of ratios b/a. The tabulated data can be well represented by the least-squares optimized functional forms

$$\delta_{\|} = 0.688(b/a) - 0.202(b/a)^2 \tag{16}$$

and

$$\delta_{\perp} = -0.661 + 0.891(b/a) \tag{17}$$

Alternative expressions are given by Broersma (1960), Perrin (1934), and Koening (1975) for rotations of an ellipsoid of revolution. The recent review of Schurr and Schmitz (1986) indicated that the results of Tirado and de la Torre are strongly favored over others when compared with experimentally determined quantities measured on TMV and short DNA fragments.

Now that the friction factors have been defined in terms of the physical dimensions of a macromolecule, a relationship between the friction factors and the Stokes-Einstein diffusion coefficients, D, can be defined as

$$D = kT\Xi^{-1} \tag{18}$$

The diffusion coefficients are simply related to the inverse of the friction factors as a 3×3 matrix. The motional operator for rigid-body anisotropic rotational diffusion has been elegantly developed by Favro (1965), and recently reviewed by Schneider and Freed (1989). Using this definition, the Schmolowski equation may be written as

$$\Gamma_{\Omega} = \nabla_{\Omega} \cdot D \cdot \nabla_{\Omega} \tag{19}$$

where the definition of the rotational gradient operator has been reviewed elsewhere (Robinson *et al.*, 1985, Schneider and Freed, 1989). The spherical harmonics $Y^l_m(\Omega)$ [or the Wigner rotational matrix elements $D^l_{m,n}(\Omega)$] are eigenfunctions of this operator for the case where

$$D = \begin{vmatrix} D_{\perp} & 0 & 0 \\ 0 & D_{\perp} & 0 \\ 0 & 0 & D_{\|} \end{vmatrix} \tag{20}$$

The important results can be summarized for the axial diffusion case where $D_{\perp} = kT/\Xi_{\perp}$ and $D_{\|} = kT/\Xi_{\|}$. In the reference frame of the macromolecule (*not* the reference frame of the spin label) the eigenvalues satisfy

$$\Gamma_{\Omega} D^l_{m,n} = \lambda^l_m D^l_{m,n} \tag{21}$$

$$\lambda^l_m = l(l+1)D_{\perp} + m^2(D_{\|} - D_{\perp}) \tag{22}$$

Using these rules, all of the auto- and cross-correlation functions associated with the rigid-body motion of an axially symmetric macromolecule can be determined.

From the friction factors, one may define a correlation time, for the autocorrelation of the $Y_0^2(\theta, \phi)$ [or $D_{0,0}^2(\Omega)$], which is associated with the $\Xi_\perp$ friction factor corresponding to rotation about the axes perpendicular to the unique axis. There is another correlation time, $\tau_\parallel$, which is the correlation time associated with the autocorrelation of the $Y_2^2(\theta, \phi)$ [or $D_{2,0}^2(\Omega)$]:

$$\tau_\parallel = (\lambda_2^2)^{-1} = \Xi_\parallel / 4kT/(1 + \Xi_\parallel / 2\Xi_\perp) \tag{23}$$

$$\tau_\perp = (\lambda_0^2)^{-1} = \Xi_\perp / 6kT \tag{24}$$

Unlike spherical molecules, it is necessary to specify the orientation of the magnetic tensors of the spin label relative to the unique axis of rotation for the case of a cylinder, since rotational diffusion does not occur at equal rates about orthogonal molecular axes. The geometrical arrangement between these tensor systems defined in Figure 1 will be referred to in subsequent discussions.

In the more general case where the spin-label Z axis (assumed coincident with the nitroxide nitrogen p_z orbital) is tilted by some angle Θ_t away from the principal or unique rotational axis, the effective correlation times will be a mix of times, $\tau_\parallel$ and $\tau_\perp$, given above. The more general considerations begin with setting $\tau_2^2 = \tau_\parallel$ and $\tau_0^2 = \tau_\perp$.

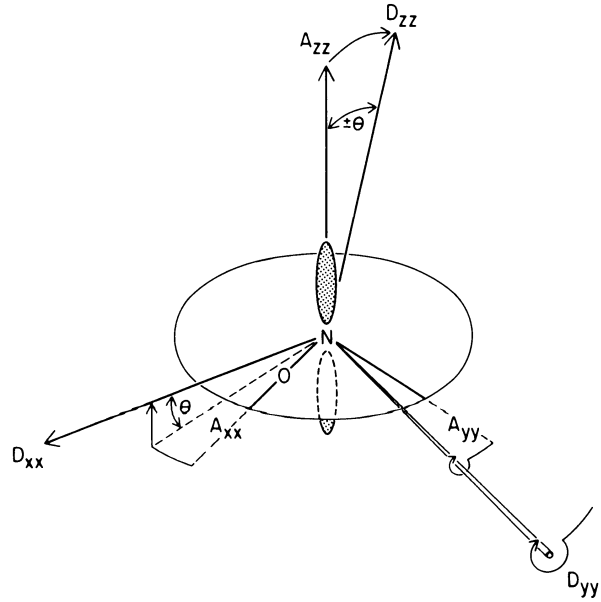

Figure 1. Geometrical relationship between magnetic and diffusion tensor principal-axis systems for a nitroxide spin label. The magnetic tensors (A and G) are assumed coincident and to exhibit principal elements A_{xx}, g_{xx}; A_{yy}, g_{yy}; and A_{zz}, g_{zz} in the molecular coordinate system as indicated. The diffusion tensor, characterized by principal elements D_{xx}, D_{yy}, and D_{zz}, is assumed coincident with the inertial tensor for the macromolecule. The two coordinate systems are related by Θ_{yy} which is generated by a rotation about D_{yy} and A_{yy}. (From Robinson and Dalton, 1980.)

Then one may define another correlation time, τ_1^2, as the correlation time associated with the autocorrelation of the $Y_1^2(\theta, \phi)$ spherical harmonic [or $D_{1,0}^2(\Omega)$]. This correlation time is

$$\tau_1^2 = (\lambda_1^2)^{-1} = \Xi_\parallel / kT / (1 + 5\Xi_\parallel / \Xi_\perp) \tag{25}$$

With these definitions, the correlation time for the spin label can be written in terms of the three correlation times for the molecule and the reduced Wigner rotational matrix elements $d^l_{m,n}(\Theta_t)$ (Wigner, 1959), where Θ_t is the angle between the nitroxide Z axis and the major diffusion axis. Specifically, we define a correlation time τ^l_m as the correlation time associated with the autocorrelation of $Y^l_m(\Theta, \phi)$ in the frame of the spin label,

$$\tau^l_m = \sum_{m'=-1}^{+1} |d^l_{m',m}(\Theta_t)|^2 (\lambda^l_{m'})^{-1} \tag{26}$$

From this form it is easy to see that the effective correlation times seen by the spin label are simple linear combinations of the correlation times determined in the frame of the molecule. It is these effective times that will govern the motional sensitivity of the ST-EPR spectrum. Normally, it is the $l = 2$, $m = 0$ component which is of interest and corresponds to autocorrelation of $\cos^2(\Theta)$ or to averaging of the major-minor axes. For the case $l = 2$, $m = 2$, the correlation time computed corresponds to minor-element averaging. If the angle $\Theta_t = 0$, then

$$\tau^l_m = (\lambda^l_m)^{-1} \tag{27}$$

However, when the spin label and diffusion tensor axes are not coincident, then there are cross couplings or mixing of motional processes.

2.4. Uniaxial Rotational Diffusion in an Anisotropic Medium

Rotational diffusion of a cylindrical protein in an anisotropic environment which permits rotation about the cylinder axis only has been examined in the work of Saffman and Delbrück (1975). This is the simplest model appropriate for modeling the rotational diffusion of a transmembrane protein about the membrane normal axis. In this case, the rotational correlation time can be related to the cross-sectional radius of the protein in the plane of the membrane in the form

$$\tau_\parallel = \pi \eta' r^2 h / kT \tag{28}$$

where η' is the effective viscosity of the bilayer, r is the solvated radius of the protein in the plane of the membrane, h is the height or thickness of the bilayer abutting the protein, and T is the absolute temperature. As in the case of a cylinder in an isotropic medium, it is necessary to define the orientation of the magnetic tensors of the spin label with respect to the membrane normal axis for interpretation of ST-EPR data.

The above equations predict that for the molecular shapes and environments considered, the rotational correlation time will be a sensitive indicator of the effective size of a spin-labeled protein. Therefore, if this protein interacts with other proteins or lipids to form a stable complex, diagnostic alterations in the rotational correlation times should result which depend on the shape and size of the complex in accordance with the hydrodynamic expressions given. The equations provided in Sections 2.1–2.4 enable relationships between rotational correlation times obtained from cw-ST-EPR studies and the hydrodynamic shape and size of the protein under investigation to be established.

It should be noted that the expressions for rotational correlation times do not depend explicitly upon the molecular weight of the protein or its complexes. The percent increase in size of a protein upon binding to another protein will depend critically upon the nature of the interactions between them. This can range from two rigid spheres or cylinders interacting at limited contact points thereby resulting in a complex with dimensions which approximate the sum of the dimensions of the interacting species, to an intimate intertwining of the primary structures of the two proteins resulting in a significantly smaller percent increase in effective size. For asymmetric proteins, the shape and size of the complex between two proteins will depend critically upon the geometry of the interaction. Specifically, if two rod-like proteins are interacting end-to-end, the resulting complex will exhibit substantially different hydrodynamic properties than if they are interacting side-to-side; cw-ST-EPR spectroscopy can provide evidence for the geometry of such interactions through rigorous analysis of experimental line shapes.

In order for such analyses to be successful, the dependence of cw-ST-EPR line shapes on correlation times for systems other than those exhibiting spherical symmetry must be characterized and quantitated. Nitrogen-15 spin labels have made a significant contribution toward characterizing spectral sensitivity (Beth *et al.*, 1981a, 1981b; Gaffney *et al.*, 1981; Johnson *et al.*, 1982b) by enabling direct comparisons between experimental and computer-generated spectra (Beth *et al.*, 1983). The following discussions will be devoted to defining the dependence of cw-ST-EPR spectra from nitrogen-15 spin labels on correlation times for the three motional models discussed above. Line-shape dependence on rotational correlation times, microwave observer frequency, and Zeeman field modulation frequency will be the central focus. Discussions will assume familiarity with cw-ST-EPR spectroscopy and the practical aspects of collecting experimental data. For those readers who have not had experience with the technique, several fundamental papers and chapters will provide valuable background information (Thomas *et al.*, 1976; Hyde and Dalton, 1979; Robinson *et al.*, 1985; Squier and Thomas, 1986).

3. SENSITIVITY OF cw-ST-EPR SIGNALS TO ROTATIONAL MOTION

3.1. Choice of Signal

Cw-ST-EPR spectra are sensitive to motion which is characterized by correlation times on the order of the intrinsic (motion-independent) spin-lattice relaxation time (T_{1e}). This sensitivity is provided by spectrometers which observe only the transverse

components of the magnetization. Under linear conditions, the transverse components are sensitive only to relaxation through spin–spin dephasing, or T_{2e} processes, and motional processes which compete with the field-dependent anisotropy (that is, they have correlation times on the order of the field anisotropy, and faster than the intrinsic, motion-independent T_{2e}). However, cw-ST-EPR derives sensitivity from motions which affect the longitudinal component of the magnetization, the effect being transferred to the transverse components by increasing the intensity of the microwave observer field and thereby strongly coupling the transverse components to the longitudinal components. In this way the transverse components of the magnetization depend on T_{1e} and on motional processes on the order of T_{1e} (Hyde and Dalton, 1972; Hyde and Thomas, 1973; Thomas *et al.*, 1976).

Modern spectrometers provide a choice of observable signals based on the detection system. By adjusting the phase of the microwave reference biasing the detector, one can select signals which are in-phase with the reference (dispersion signals) or 90° out-of-phase with the reference (absorption signals). There is also Zeeman (or DC) magnetic field modulation. Lock-in analyzing amplifiers allow one to detect signals at selected harmonics of the Zeeman modulation which are also either in-phase or out-of-phase (also called phase quadrature) with respect to the driving modulation. Therefore, there is a choice of absorption or dispersion with respect to the microwave and a choice of harmonic and phase with respect to the Zeeman modulation.

The connection between the choice of cw-ST-EPR signal and the motion is that one chooses a signal which is very small when the microwave power is low but increases as the microwave power is increased, thereby providing a display which is visually more sensitive to motion. There are two such signals in common use. The first is the dispersion signal at the first harmonic of the Zeeman modulation and quadrature to it, denoted U_1'[2] (Thomas *et al.*, 1976). The second signal, and by far the more popular one to date, is the absorption signal at the second harmonic of the Zeeman modulation and quadrature to it commonly denoted V_2' (Thomas *et al.*, 1976). Though our discussions will focus on the V_2' signal, it should be noted that development of "loop-gap" resonators (Froncisz and Hyde, 1982; Hyde *et al.*, 1982) permits acquisition of the U_1' signal with signal-to-noise comparable, or in certain instances superior, to that of the V_2' signal (Thomas *et al.*, 1983). It is anticipated that many future studies of protein dynamics will take advantage of being able to acquire and analyze both of these cw-ST-EPR signals. Though results from the U_1' signal will not be discussed explicitly in this chapter, we note that computer modeling work to date has indicated that its sensitivity to motion and diffusional anisotropy is qualitatively similar to that of V_2' (Robinson and Dalton, 1980).

3.2. Sensitivity to Motion

The phenomenon of cw-ST-EPR sensitivity to motion can be understood in mathematical form by analyzing characteristics of the absorption component. For

[2] The designation of signals follows the convention U_n, U_n', V_n, and V_n' for the in-phase dispersion detected at the nth harmonic of the driving Zeeman field modulation, the out-of-phase dispersion detected at the nth harmonic, the in-phase absorption detected at the nth harmonic, and the out-of-phase absorption detected at the nth harmonic, respectively. Saturation transfer refers to acquisition of the signals using a partially saturating microwave observer power.

discussion purposes, it is assumed that the Zeeman modulation is not inherently responsible for sensitivity to motion but is a convenient basis for a detection scheme. We begin with an orientation-dependent Hamiltonian $H(\Omega)$, and a motional process which moves the molecules from one orientation to another, Γ_Ω. The stochastic Liouville equation defines how the spin response is coupled to the coherent Hamiltonian and the motional process:

$$\dot{\chi} = -\iota[H(\Omega), \chi] - \Gamma_\Omega(\chi - \chi_0) \tag{29}$$

In the above expression, Γ_Ω is the motional operator which depends on the angles $\Omega = \{\theta, \phi\}$ (Figure 3 below); the orientation-dependent part of the Hamiltonian also depends on these angles.

We begin by considering a single nitroxide manifold such that the Hamiltonian contains only the secular transitions. Balasubramanian and Dalton (1979) showed that a simplified Hamiltonian, which took into account the pseudosecular transitions by the change they manifested in the eigenstates, served as a suitable approximation for the full Hamiltonian for motion in the very slow (ST-EPR) motional regime. This is a first-order correction to the secular equations but does not correctly predict the relaxation phenomenon in this correlation time range. Therefore, we can use either a purely secular Hamiltonian or the one modified to include the effects on the eigenvalues by the pseudosecular components.

The equations for the three components of the macroscopic magnetization can then be written as

$$\dot{M}_x = -\Delta(\Omega)M_y - (1/T_{2e} + \Gamma_\Omega)M_x \tag{30}$$

$$\dot{M}_y = \Delta(\Omega)M_x - (1/T_{2e} + \Gamma_\Omega)M_y - H_1 M_z + Q \tag{31}$$

$$\dot{M}_z = H_1 M_y - (1/T_{1e} + \Gamma_\Omega)M_z \tag{32}$$

where $\Delta(\Omega)$ is defined by

$$\Delta(\Omega) = g_{\text{eff}}\beta H_0 - \omega_0 - m_i A_{\text{eff}}\gamma_e \tag{33}$$

where γ_e $(=\bar{g}\beta)$ and β are in units of rad gauss^{-1}. At resonance, $\Delta(\Omega) = 0$ and the field value $H_0 = H_{\text{res}}$. Therefore

$$H_{\text{res}} = \bar{g}[(\omega_0/\gamma_e) - m_i A_{\text{eff}}]/g_{\text{eff}} \tag{34}$$

The value of H_{res} can be calculated using equation (34) to define the center of the Lorentzian for polar angles $\Omega = \{\theta, \phi\}$, where g_{eff} and A_{eff} are functions of Ω:

$$g_{\text{eff}} = g_{xx}\sin^2\theta\cos^2\phi + g_{yy}\sin^2\theta\sin^2\phi + g_{zz}\cos^2\theta \tag{35}$$

$$A_{\text{eff}} = [A_{xx}^2\sin^2\theta\cos^2\phi + A_{yy}^2\sin^2\theta\sin^2\phi + A_{zz}^2\cos^2\theta]^{1/2} \tag{36}$$

The quantity $\Delta(\Omega)$ determines the orientation-dependent resonance position and is the difference between the energy eigenvalue for the spin and the energy provided by the microwave (or rf source). The term Q is the inhomogeneous term due to the interaction of the spin system at equilibrium with the driving microwaves (i.e., it represents the tilt away from equilibrium when the spectrometer is on).

Neglecting the Zeeman modulation and keeping only secular terms in the Hamiltonian (modified or not) leads to the above equations. The M_z component is the deviation in the z component from equilibrium, not the total z component of the magnetization. The absorption component is M_y, and the dispersion component is M_x. At equilibrium, the time rate of change of all three components is zero. Therefore, M_y can be solved from equations (30)-(32). While Γ_Ω is really an operator in Ω, the effect of Γ_Ω can be neglected in comparison to $1/T_{2e}$, thereby simplifying the dependence of the absorption signal on the motional process. Then, formally, M_y is given by

$$M_y = [\Delta^2(\Omega) + (1/T_{2e})^2 + H_1^2/T_{2e}(1/T_{1e} + \Gamma_\Omega)^{-1}]^{-1} Q/T_{2e} \tag{37}$$

This result is straightforward to interpret. First, consider the no-motion or powder-pattern limit. In this case $\Gamma_\Omega = 0$. Here M_y is a Lorentzian centered about the point where $\Delta(\Omega) = 0$. The linewidth L is

$$L = 1/T_{2e}[(1 + H_1^2 T_{1e} T_{2e})]^{1/2} \tag{38}$$

This linewidth is related to T_{2e} in the normal way and contains the saturation effect if $H_1 > [(1/T_{2e}T_{1e})]^{1/2}$. The powder-pattern result may also be obtained by setting H_1 (the amplitude of the microwaves) to a small value regardless of the motion, assuming that the motional process does not affect the linear EPR response. This demonstrates the need for strong, saturating microwave power to couple the relaxation effects (embodied in Γ_Ω) coming from the z component to the y component of the magnetization.

The actual signal for a powder or disordered or semiordered sample, regardless of the motion, is the average over all orientations. If $P_0(\Omega)$ is assumed to be the orientation distribution of spins, then the absorption signal S is

$$S(H_0) = \int M_y(H_0, \Omega) P_0(\Omega)\, d\Omega \tag{39}$$

Since the Zeeman modulation has been neglected, the ST-EPR signals cannot be directly computed. The traditional approximation of relating the linear cw-EPR signal to the derivative of S, i.e., dS/dH_0, does not apply to the ST-EPR signals. Therefore, without the explicit inclusion of Zeeman modulation, there is no way to get the actual line shape. However, it can be determined where the signal above (M_y or S) is sensitive to motion. To do this, the eigenfunctions of the motional operator Γ_Ω, $|l, m, n\rangle$, which are the Wigner rotational matrix elements $[D^l_{m,n}(\Omega)]$, are employed:

$$\Gamma_\Omega |l, m, n\rangle = g_{l,m,n} |l, m, n\rangle \tag{40}$$

For the case of isotropic motion, $g_{l,m,n}$ depends only on the l index. Further, considering only Brownian motion, $g_l = l(l+1)D_r$, where D_r is the Stokes-Einstein rotational diffusion coefficient, and the correlation time (as the autocorrelation of the second-rank spherical harmonic) is $\tau_r = 1/6D_r$.

Expanding M_y in terms of the functions $|l, m, n\rangle$ allows one to express the dependence of the signal S directly on the correlation time τ_r. Let $M^l_{m,n} = \langle l, m, n | M_y \rangle$. Then from equation (31)

$$M^l_{m,n} = \langle l, m, n | [\Delta^2(\Omega) + (1/T_{2e})^2 + H_1^2/T_{2e}(1/T_{1e} + \Gamma_\Omega)^{-1}]^{-1} Q/T_{2e} \rangle \tag{41}$$

The signal, assuming $P_0(\Omega)$ to be uniform, is proportional to $M^0_{0,0}$, which itself is coupled to all the other components of M_y by the resonance condition, $\Delta(\Omega) = 0$. The qualitative dependence of S on τ_r is the quantity of interest, so $dS/d\tau_r$ is estimated. If $P_0(\Omega)$ is uniform, then with no approximations it can be shown that

$$\tau_r \, \delta S/\delta\tau_r = (H_1^2/T_{2e}) \sum_{l,m,n} [g_l/(1/T_{1e} + g_l)^2] |M^l_{m,n}|^2 \tag{42}$$

This expression shows that the sensitivity to motion is the total contribution due to the many components of M. The sensitivity of each component is maximized when $g_l = 1/T_{1e}$. Like the true ST-EPR signals, $dS/d\tau_r$ has the property of going to zero under linear conditions. An approximate idea of the sensitivity of S with respect to the resonance condition, as a function of field, can be obtained by assuming that the $M^l_{m,n}$ components can be calculated in the absence of the motional contribution (again set $\Gamma_\Omega = 0$ to estimate the components of M). The dependencies of $|M^l_{m,n}|^2$ as a function of field are shown in Figure 2 for different values of l. The most important one, and the one that is largest for microsecond motions, is the $l = 2$ component (the $l = 0$ component does not contribute). In this case, the initial effects are maximal between the extrema and the magic angle. For moderate levels of H_1 and narrow lines, the values of $M^l_{m,n}$ can be approximated by assuming that the integral is that of a Lorentzian which maximizes at $\Delta(\Omega) = 0$. This gives the resonance condition and shows that

$$M^l_{m,n}(H_{res}) \simeq D^l_{m,n}(\Omega) \tag{43}$$

where the relation between H_{res} and Ω is specified by equation (34). We now have a relation between motional sensitivity and the orientation of the spin label in the external magnetic field. Computations of M_l for different motional rates have demonstrated that the qualitative nature of each component is correct regardless of the motional rate (Sugano, 1987). One can see that as the motion becomes slower, the higher l components become more important, and begin to contribute motional sensitivity in the middle of the spectrum (or in the middle of each nuclear manifold in the case of a nitroxide spin label). Finally, at the slowest motion, sensitivity becomes more uniformly distributed. We note that there is no sensitivity to motion for the individual manifolds at the turning points (i.e., where $dH_{res}/d\Omega \to 0$).

The absorption signal gives the sensitivity for various field settings. As previously noted, due to the resonance condition [$\Delta(\Omega) = 0$], the dependence of the sensitivity on orientation Ω as well as H_{res} is defined. The dependence of signal sensitivity on orientation for a fixed value of τ_r can be defined by considering the quantity

$$d(dS/d\tau_r)/d\Omega \tag{44}$$

This quantity provides information on the orientation-dependent sensitivity of the motionally dependent part of the ST-EPR signal. The angle Ω can be either θ or ϕ,

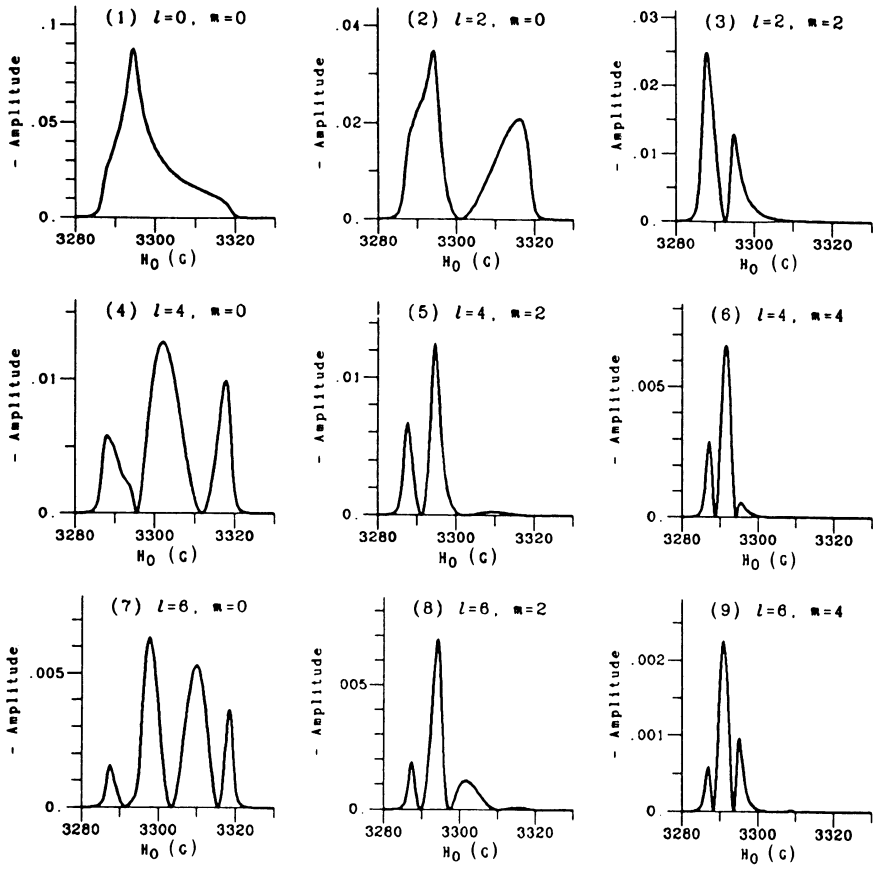

Figure 2. Contributions of relaxation components to a single manifold characterized by g-only anisotropy. The amplitudes are $|M^{l}_{m,n}(\Omega)|^2$, where the quantities M are defined in equation (41) with $H_1 = 0$, and $n = 0$. For the computations, $g_{xx} = 2.020$, $g_{yy} = 2.015$, and $g_{zz} = 2.000$ which results in X, Y, and Z turning points at 3286 G, 3295 G, and 3319 G, respectively. The amplitudes provide a model of where motional sensitivity occurs for a given manifold.

for the case when the other is fixed. The dependence of this motionally sensitive term on spin orientation or field position is now explored. Since S does not directly depend on Ω, except through the resonance condition, the above quantity can be estimated using the chain rule

$$\frac{d(dS/d\tau_r)}{d\Omega} = \frac{\delta\, dS/d\tau_r}{\delta H_0}\frac{\delta H_{res}}{\delta\Omega} \tag{45}$$

The first quantity on the right can be calculated using equation (42). The second quantity, $dH_{res}/d\Omega$, the change in field with respect to change in angle, can be found using equation (34). While this second term is only a part of the overall field-dependent sensitivity, it is an important part as discussed by Thomas *et al.* (1976). Figures 3 and

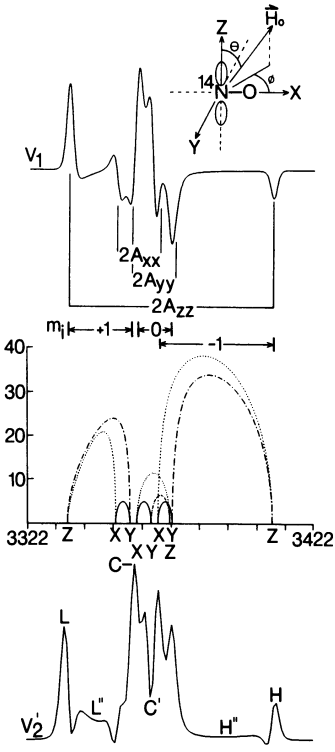

Figure 3. Relationship between line-shape features in V_1 and V_2' displays and regions of predicted motional sensitivity of V_2' for nitrogen-14 spin labels. Top: The computed V_1 spectrum shows the field values spanned by the m_i = +1, 0, and −1 nuclear manifolds and spectral structurings arising from orientation of the X, Y, and Z nitroxide axes parallel to the external magnetic field, H_0. Middle: Plots of absolute value of change in resonance condition (H_{res}) versus field position for rotations about the three nitroxide principal axes. (· · · · ·) $|[\delta H_{res}(m_i)/\delta\theta]_{\phi=0}|$; (· - · - ·) $|[\delta H_{res}(m_i)/\delta\theta]_{\phi=90}|$; and (——) $|[\delta H_{res}(m_i)/\delta\phi]_{\theta=90}|$ for m_i = +1, 0, and −1. Values on the ordinate are gauss rad^{-1}. Bottom: The computed V_2' line shape showing how observable features are related to spectral turning points and to regions of maximum change in resonance condition with respect to field value. Field positions where spectral amplitudes for computing motionally sensitive ratio parameters are defined in the V_2' display. Simulation parameters were: A_{xx} = 7.4 G; A_{yy} = 7.4 G; A_{zz} = 35.9 G; g_{xx} = 2.0091; g_{yy} = 2.0061; g_{zz} = 2.0022; ν_0 = 9.45 GHz; h_1 = 0.01 and 0.20 G; T_{2e} = 100 ns and 40 ns; T_{1e} = 15 μs and 25 μs; τ_r = ∞ and 20 μs; ν_m = 100 kHz and 50 kHz; h_m = 0.5 G and 5.0 G (effective) for the V_1 and V_2' displays, respectively. Each was post-broadened with a Gaussian function of 0.9 G half-width to simulate the interaction of the unpaired electron with nearby deuterons on the nitroxide ring system.

4, middle, show plots of $dH_{res}/d\Omega$ versus field position for nitrogen-14 and nitrogen-15 spin labels characterized by nonaxial tensors. An important observation to be made about $dH_{res}/d\Omega$ is that this term shows that motional sensitivity is, to first order, simply proportional to the width of the magnetic anisotropy (in gauss or hertz) being modulated by the motion: manifolds which extend over a wider set of field values are proportionally more sensitive to the effects of motion in the ST-EPR regime. The second term can be estimated: at slow motions this term becomes nearly constant. Therefore, at the slowest motional rates (near the millisecond correlation time, in practice), $dH_{res}/d\Omega$ is a good indicator of regions of motional sensitivity. However, in the fast motional regions (on the order of microseconds) the summation form for $dS/d\tau_r$ is a better indicator of motional and orientational sensitivity. Throughout the very slow motional region, all the sensitivity is in the interior with no sensitivity at the turning points. These arguments are based on the assumption that the motion is slow enough that it does not affect the linear EPR spectrum (i.e., there is no motional narrowing).

The plots of $dH_{res}/d\Omega$ versus field in Figures 3 and 4 allow prediction of regions of motional sensitivity for nitrogen-14 and nitrogen-15 spin labels. Moreover, they allow some direct comparisons of relative sensitivities to motions about the three principal nitroxide axes. Both nitrogen isotope spin labels are predicted to provide high sensitivity to motions which rotate the nitroxide Z axis into the X, Y plane (major-minor element averaging) at X-band microwave frequency. Sensitivity to these motions is greatest for both labels in the center of the low- and high-field extrema

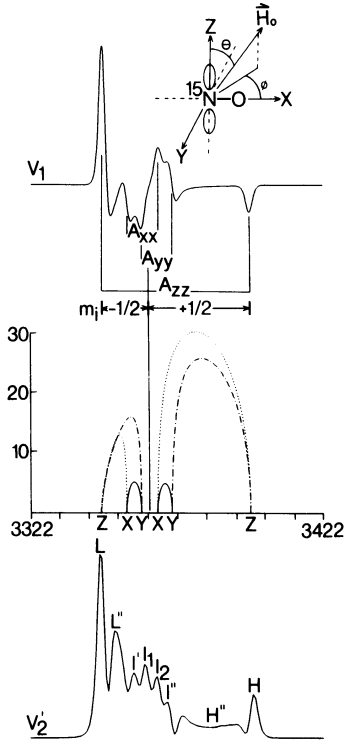

Figure 4. Relationship between line-shape features in V_1 and V_2' displays and regions of predicted motional sensitivity of V_2' for nitrogen-15 spin labels. Top: The computed V_1 spectrum shows the field values spanned by the $m_i = -\frac{1}{2}$ and $+\frac{1}{2}$ nuclear manifolds and spectral structurings arising from orientation of the X, Y, and Z nitroxide axes parallel to the external magnetic field, H_0. Middle: Plots of absolute value of change in resonance condition (H_{res}) versus field position for rotations about the three nitroxide principal axes. (· · · ·) $|[\delta H_{res}(m_i)/\delta\theta]_{\phi=0}|$; (· - · - ·) $|[\delta H_{res}(m_i)/\delta\theta]_{\phi=90}|$; and (——) $|[\delta H_{res}(m_i)/\delta\phi]_{\theta=90}|$ for $m_i = -\frac{1}{2}$ and $+\frac{1}{2}$. Values on the ordinate are gauss rad^{-1}. Bottom: The computed V_2' line shape showing how observable features are related to spectral turning points and to regions of maximum change in resonance condition with respect to field value. Field positions where spectral amplitudes for computing motionally sensitive ratio parameters are defined in the V_2' display. Simulation parameters were: $A_{xx} = 10.6$ G; $A_{yy} = 10.4$ G; $A_{zz} = 50.15$ G; $g_{xx} = 2.0091$; $g_{yy} = 2.0061$; $g_{zz} = 2.0022$; $\nu_0 = 9.45$ GHz; $h_1 = 0.01$ and 0.20 G; $T_{2e} = 100$ ns and 40 ns; $T_{1e} = 15\ \mu$s and 25 μs; $\tau_r = \infty$ and 20 μs; $\nu_m = 100$ kHz and 50 kHz; $h_m = 0.5$ G and 5.0 G (effective) for the V_1 and V_2' displays, respectively. Each was post-broadened with a Gaussian function of 0.9 G half-width to simulate interaction of the unpaired electron with nearby deuterons on the nitroxide ring system.

regions, labeled L'' and H''. The major-minor element anisotropy of the individual nuclear manifolds decreases in the order: $m_i = -1$ (nitrogen-14) > $m_i = +\frac{1}{2}$ (nitrogen-15) > $m_i = +1$ (nitrogen-14) > $m_i = -\frac{1}{2}$ (nitrogen-15), which is the approximate order of sensitivity to motion determined in a number of experimental studies.

The minor element anisotropy (X-Y nitroxide axes) is very nearly the same for all three nuclear manifolds of nitrogen-14 spin labels at X-band (Figure 3, middle). Likewise, the minor element anisotropies of the two nuclear manifolds of nitrogen-15 spin labels are approximately equal (Figure 4, middle). A point which may not have previously been appreciated, however, is that the minor element anisotropies from both nitrogen isotope spin labels are very nearly the same (compare solid curves in Figures 3 and 4, middle). Thus, both isotopes should provide approximately the same true sensitivity to motional processes that lead to minor element averaging which, in both cases, should be much lower than sensitivity to major-minor element averaging at X-band. Further discussions and data relevant to this point will be provided in Sections 6 and 9.

3.3. The Case of Isotropic Motion and Anisotropic Magnetic Tensors

The work of Thomas *et al.* (1976) on maleimide spin-labeled hemoglobin demonstrated that the U_1' and V_2' ST-EPR signals obtained from nitrogen-14 spin labels changed in characteristic ways as the rotational correlation time for hemoglobin was

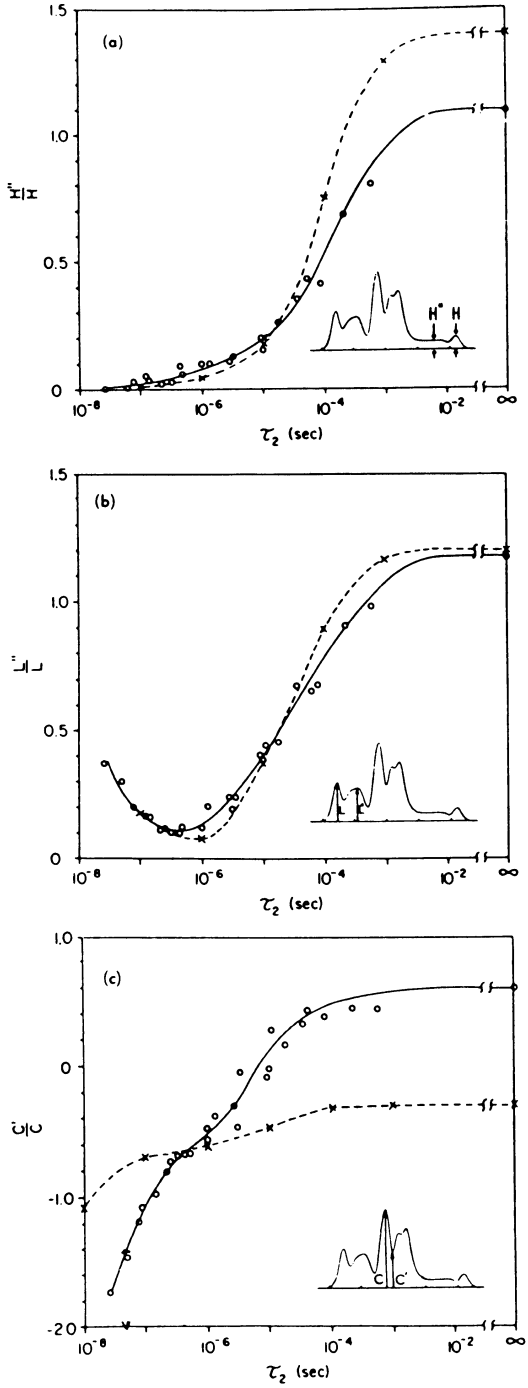

Figure 5. Dependence of V_2' ratio parameters on τ_r for nitrogen-14 spin labels. Open circles are experimentally measured ratios from maleimide spin-labeled hemoglobin in glycerol/buffer solutions. × denotes a ratio measured from computer-generated spectra using axial A and G tensors. (From Thomas *et al.*, 1976.)

altered in the range of 0.1 μs to 1 ms (Figure 5). This seminal paper also defined three ratios of spectral intensities, namely L''/L, C'/C, and H''/H (Figure 5), from the V_2' signal as a function of τ_r. These ratio parameter plots have been employed almost universally to analyze ST-EPR spectra from nitrogen-14 spin-labeled proteins for determination of rotational correlation times. Spectral amplitudes at the field positions labeled L'', C', and H'' were shown to be very sensitive indicators of the rotational rate in agreement with the predicted regions of motional sensitivity (Figure 3, center). These positions approximate the field values at which the change in resonance condition with respect to field value is maximum for each of the three nuclear manifolds [i.e., where $\delta H_{res}(m_i)/\delta\theta$ reaches its maximum value; the variable θ specifies the orientation of the nitroxide Z axis relative to the external magnetic field]. In contrast, spectral amplitudes at field positions where $\delta H_{res}(m_i)/\delta\theta$ go to zero are insensitive to motion and thus serve as convenient internal markers for changes manifested at L'', C', and H''. The motionally insensitive positions, designated L, C, and H, are defined in Figure 5. The peak labeled L arises from the +1 nuclear manifold of that subpopulation of nitrogen-14 spin labels in the ensemble which are instantaneously oriented parallel to the external magnetic field. The peak labeled C arises from the superposition of lines from the +1 and 0 nuclear manifolds of spin labels oriented perpendicular to the external field. The peak labeled H arises from the −1 nuclear manifold of spin labels oriented parallel to the external field. In the 1 μs to 1 ms correlation time range, the linear EPR spectrum is not sensitive to motion and, hence, line positions do not change significantly as a function of rotational times. Alignment of the linear, V_1 EPR spectrum and the V_2' ST-EPR spectrum aids in visualizing how peaks in the two signals are related as shown in Figure 3.

3.4. Effects of Anisotropic Motion and Anisotropic Tensors

The above discussions and experimental results provide bases for understanding the effects of different types of motion on ST-EPR spectra. We now consider two cases: first, the case of axial A and G tensors with anisotropic motion; second, the more general case of fully anisotropic A and G tensors and anisotropic motion.

3.4.1. Axial Tensors and Anisotropic Motion

In this case, there is only a single orientation-dependent component in the field-dependent Hamiltonian, namely $D^2_{0,0}(\Omega)$, which is $\frac{1}{2}(1 - 3\cos^2\theta)$. The pseudosecular terms do not contribute terms which mix with this component because they are rigorously orthogonal but have the same eigenspectrum. Therefore, it is not possible to obtain any additional information on the anisotropic nature of the motion through these terms. The true character of anisotropic motion in this system is any motional process which changes the single angle θ. Since anisotropic motion produces motion about different axes, there will be different effective rates which compete to rotate about θ. The result is that there is a single effective rate of motion and one cannot learn anything about the anisotropic nature of the motion with a simple axial tensor system. This is true for each individual nuclear manifold even though they are of different widths. Each will appear to be controlled by isotropic motion of the same apparent rate.

Nitroxide spin labels typically exhibit nearly axial A tensors. However, the G tensor is nonaxial and therefore, as the operating frequency of the spectrometer is increased, experimental spectra appear increasingly nonaxial. From a practical standpoint, nitrogen-15 and nitrogen-14 spin labels will exhibit sufficient G anisotropy at X-band to provide sensitivity to anisotropic motion. At lower frequencies (L- and S-band for example), sensitivity to anisotropic motion will be minimal. Further discussions of these points will be provided in section 7.

3.4.2. Both Nonaxial Tensors and Anisotropic Rigid Body Motion

In the case where there exists both nonaxial tensors and anisotropic rigid-body motion, it is possible, in theory, to interpret cw-ST-EPR spectra, obtained at X-band or higher microwave frequencies, in terms of the correct motional model. The terms previously defined as $dH_{res}/d\Omega$ allow one to get an idea of the effects of the relation of orientation to resonance position, without considering the complication of the types of motion (which can then be done in the $d^2S/d\tau_r\, dH_{res}$ terms). Now that $\Delta(\Omega)$ contains terms that depend on both θ and ϕ, $dH_{res}/d\phi = 0$ is no longer true as was the case above, but depends on both θ and ϕ. Furthermore $dH_{res}/d\theta$ is a function of ϕ as well. Therefore, we consider $dH_{res}/d\phi$ and $dH_{res}/d\theta$. It is seen that the terms which depend on θ mix the Z turning point of each manifold with either the X or Y turning points (or in the middle for an intermediate value of ϕ). The X and Y turning points are related by rotations corresponding to changes in ϕ. For both nitrogen-15 and nitrogen-14 spin labels, the sensitivity to motion is maximal in the region between the turning points being modulated by the motion. Regions of predicted motional sensitivity for rotational motions about orthogonal spin-label axes are defined in the plots of $dH_{res}/d\Omega$ versus H_{res} in Figures 3 and 4.

3.5. Geometric Considerations for Analyzing Anisotropic Motion

Anisotropic motion results in a large number of degrees of freedom to the problem. For isotropic Brownian rotational motion, there is only the rotational correlation time to be determined. For generalized, rigid-body Brownian rotational motion, there are six adjustable parameters: the correlation times about each of the three (potentially) unique macromolecular axes and the three Euler angles which define the geometrical relationship between the diffusion tensor and the spin tensor. Clearly, there are too many parameters to consider generally. Therefore, we consider only a single tilt angle (Θ_{yy}, Figure 1) and assume an axial diffusion tensor. This covers the case of motion of prolate or oblate ellipsoids and cylindrical proteins or other macromolecules with the spin label tilted by a single angle (the angle between the Z axis of the spin label and the principal axis of the diffusion tensor).

First, let us consider the case of aligned diffusion and spin tensors ($\Theta_{yy} = 0°$). In this case the rotation about $D_{\|}$ defines the rate at which the X and Y nitroxide axes will interconvert, and thus this rotational component dominates the dynamic response of the minor elements. The motion about the other two axes ($D_{\perp}$) dominates the motional interconversion from the Z axis to the X or Y axis.

Next, if the spin tensor and the diffusion tensor are orthogonal ($\Theta_{yy} = 90°$), rotation about $D_{\|}$ defines the rate at which the Y and Z nitroxide axes will interconvert. Motion

about the other two macromolecular axes ($D_\perp$) leads to interconversion of the nitroxide X-Y and X-Z axes. Thus, the minor elements are dominated by $D_\perp$ motion while the major-to-minor element averaging is a composite of $D_\parallel$ and $D_\perp$ motions. A similar situation exists when the nitroxide is tilted by 90° about X ($\Theta_{xx} = 90°$), except now $D_\parallel$ motion leads to interconversion of the nitroxide X and Z axes.

Finally, if the spin tensor is tilted from the diffusion tensor by some intermediate angle ($0° < \Theta_{yy} < 90°$), averaging of spectral positions is less easily visualized in terms of $D_\parallel$ and $D_\perp$ rotations than for the previous examples. Both pure minor element and major-minor element interconversions will depend on $D_\parallel$ and $D_\perp$, the magnitude of the dependence being determined by the geometrical relationship between the spin and diffusion tensors. An interesting case occurs when $\Theta_{yy} = 54.7°$. At this geometry, sensitivity to the anisotropy of the diffusion process is minimal. Line shapes will appear to be governed by an isotropic rotational correlation time intermediate between the true values of $\tau_\parallel$ and $\tau_\perp$ (Robinson and Dalton, 1980; Beth *et al.*, 1983). In progressing away from the magic angle toward 0° and 90°, the line shapes will become increasingly sensitive to the anisotropy of the motion with maximum sensitivity at the two extremes. More in-depth discussions of sensitivity of the V_2' signal to anisotropic motions will be provided in Sections 6 and 7.

4. ANALYSIS OF cw-ST-EPR DATA

The first step in carrying out a study of very slow rotational motion by cw-ST-EPR spectroscopy is to define conditions for spin labeling such that the probe location in the protein (or macromolecular) structure is unique and the motion of the probe accurately monitors the motion of the entire protein or segment of protein of interest. If these criteria are not met, then subsequent discussions of sensitivity to motion and methods of data analysis will not be strictly valid, particularly for anisotropic diffusion models. Moreover, data analyses will undoubtedly be severely complicated and information gained from the studies will be limited to a speculative, qualitative nature. Methods for achieving labeling specificity and motional coupling will vary widely according to the properties of the system under investigation. However, it should be stressed that time and effort spent in this phase of a study will be amply rewarded by the quality and scope of information obtained. The next step in the study involves extracting accurate rotational dynamics information from the ST-EPR spectrum. The difficulty encountered in this process depends critically upon the size and shape of the spin-labeled protein. Several approaches to the data analysis problem have been pursued which will be elaborated upon in the following sections.

4.1. Isotropic Model Systems

Numerous spin-labeling studies on globular proteins in solution using conventional nitrogen-14 spin labels have shown that the ratio parameter plots shown in Figure 5 can be employed to accurately determine the rotational correlation time of spin-labeled proteins provided that they exhibit isotropic rotational diffusion. The procedure normally followed is to record the V_2' spectrum of the spin-labeled protein and then measure the three ratio parameters L''/L, C'/C, and H''/H. These values are then

compared with the ratio parameter plots shown in Figure 5 to obtain predicted correlation times from each of the three parameters (Thomas *et al.*, 1976). If the experiments have been carried out with properly calibrated microwave power level, modulation amplitude, and modulation phase setting (Thomas *et al.*, 1976; Fajer and Marsh, 1982; Beth *et al.*, 1983; Vistnes and Dalton, 1983; Hemminga *et al.*, 1984a, 1984b; Squier and Thomas, 1986), then very similar times will be obtained from each of the ratio parameters which accurately describe the motion of the protein. For spin-labeled systems characterized by spherical symmetry, the use of nitrogen-14 spin labels and the model system analysis approach is normally sufficient for obtaining the desired motional information.

A difficulty arises, however, when it is desired to determine the rotational correlation times for an anisotropically diffusing protein by the isotropic model system plots. For such systems, each of the three ratio parameters may, depending on labeling geometry and specificity, indicate different rotational correlation times. The origin of this apparent discrepancy can be understood qualitatively by observing that each of the three ratio parameters and, more specifically, the spectral amplitudes at positions L'', C', and H'', are differentially sensitive to rotational motions which interconvert the nitroxide X, Y, and Z molecular axes (Figure 3). Thus, the problem confronting the experimentalist attempting to quantitate the rotational diffusion of a highly asymmetric protein in solution or a membrane protein in the asymmetric environment of the lipid bilayer is how to analyze the data (i.e., extract true rotational correlation times from the ST-EPR line shape) in terms of a physically relevant motional model. Two different approaches to this problem have been pursued.

4.2. Anisotropic Model Systems

Anisotropic model systems have been investigated experimentally in order to determine how the V_2' line shape is altered in response to changes in rotational diffusion about the nitroxide Y or Z axes (Gaffney, 1979; Delmelle *et al.*, 1980; Johnson *et al.*, 1982a; Fajer and Marsh, 1983). The model systems investigated were either cholestane or doxyl fatty acid spin labels incorporated into model lipid bilayers or thiourea crystals, where orientational parameters are reasonably well known. The data obtained from these studies have been valuable for demonstrating which regions of the spectrum provide sensitivity to motions about different spin-label axes. In theory, it would be possible to construct ratio parameter versus correlation time plots for a model system exhibiting the same motional processes as the system under investigation, thereby allowing quantitation of the motional rates by simple comparison of experimentally measured ratio parameters with the model system plots. The limitation of this approach is in identifying a model system which exhibits the same type of rotational diffusion (Brownian versus jump, for example), the same diffusional anisotropy, and the same orientational properties between the magnetic and rotational diffusion tensors as the system being investigated. Clearly, the dimensionality of the data analysis problem increases from a single experimental unknown, τ_r, in the case of isotropic Brownian rotational diffusion to a minimum of three experimental unknowns ($\tau_\parallel$, $\tau_\perp$, and Θ_t) for axial Brownian rotational diffusion. The paucity of protein model systems exhibiting well-characterized axial anisotropic rotational diffusion has severely limited the applicability of this approach to analysis of ST-EPR data. Therefore, the primary use of

anisotropic model system spectra to date has been to provide a qualitative assessment of the geometrical relationship between the magnetic tensors and the diffusion tensor for anisotropically diffusing systems (Johnson *et al.*, 1982a; Fung and Johnson, 1984; Thiyagarajan and Johnson, 1987). There remain many opportunities for future work in this area with current progress limited by the virtual lack of appropriately characterized anisotropically diffusing protein model systems.

4.3. Anisotropic Motional Modeling by Computer Simulations

The second approach which has been employed for data analyses involves the use of computational algorithms for modeling the effects of rotational diffusion and spin-label binding geometry on the ST-EPR spectrum (Thomas and McConnell, 1974; Robinson *et al.*, 1974; Thomas *et al.*, 1976; Perkins, 1976; Coffey *et al.*, 1976; Robinson and Dalton, 1979, 1980, 1981; Galloway and Dalton, 1979; Beth *et al.*, 1981a, 1981b, 1983; Thomas, 1986). The potential power and flexibility of this avenue for spectral interpretation was realized in the early work of Thomas and McConnell (1974), Robinson *et al.* (1974), and Thomas *et al.* (1976). Limited access to high-speed computational facilities has historically hampered explicit inclusion of many of the anisotropic and time-dependent magnetic interactions necessary for quantitative computations of ST-EPR spectra. Robinson and Dalton (1980) were able to decrease the computational requirements necessary for modeling the effects of rotational diffusion on ST-EPR spectra by taking advantage of the reduction in the number of nitrogen hyperfine lines exhibited by spin-$\frac{1}{2}$, nitrogen-15 nitroxides relative to common spin-1, nitrogen-14 nitroxides. This simplification allowed inclusion of terms in the spin Hamiltonian for anisotropic A and G tensors as well as time-dependent Zeeman field modulation and microwave saturation effects necessary for quantitative simulation of ST-EPR spectra while maintaining reasonable computation times on universally available one MIPS class computer systems.

During this time, it was demonstrated experimentally that nitrogen-15 spin labels provided sensitivity to the same range of very slow rotational correlation times as observed previously with nitrogen-14 spin labels (Beth *et al.*, 1981a; Gaffney, 1981; Johnson *et al.*, 1982b). Moreover, Beth *et al.* (1980, 1981a) showed that replacement of hydrogens on the nitroxide ring system with deuterium resulted in significant resolution enhancement of spectral structurings throughout the very slow tumbling region. This improved resolution enables accurate determination of elements of the nitrogen hyperfine (A) and electron-Zeeman (G) tensors (Figure 4, upper) which are required as input for computer modeling of effects of rotational diffusion on ST-EPR spectra and provides resolution of important spectral structurings which are diagnostic of motional processes.

By virtue of the theoretical simplifications afforded by nitrogen-15 and the resolution enhancements afforded by deuterium replacement, Beth *et al.* (1983) were able to carry out direct computer simulations of isotropic model system V_2' ST-EPR spectra in the very slow motional region. Results indicated (see Figure 7 below) that it is possible to accurately model the effects of isotropic rotational diffusion on experimental spectra throughout this correlation time range with nitrogen-15 spin labels. These simulations were carried out on 1 MIPS class computers (VAX 11/780 or equivalent) with CPU time requirements of less than 10 hours per complete spectral simulation.

Advances in the production of relatively low-cost computers and high-speed work stations with CPU performance equivalent or superior to the VAX 11/780 in recent years have enabled investigators to pursue quantitation of ST-EPR spectra by direct simulation approaches without relying on availability of CPU time from mainframe or supercomputer facilities.

The importance of developing computer-simulation approaches lies in their flexibility for predicting line shapes for a wide variety of motional models. In the following sections, data from experimental measurements and from computer simulations will be presented which provide a definition of the sensitivity of ST-EPR signals to various motional models and how this sensitivity can be optimized by judicious selection of microwave and modulation frequencies. Initial discussions will be devoted to V_2' signals from nitrogen-15 spin labels. These will be followed by experimental results and computations of V_2' spectra with conventional nitrogen-14 spin labels. The focus of the discussions will be on the motional information contained in the ST-EPR spectrum, how specific motions affect spectral shapes, and what set of experimentally accessible instrument parameters will provide the optimum sensitivity for a desired measurement.

4.4. Overview of Theory for Computation of ST-EPR Spectra

A detailed derivation of the equations which have been employed for computation of ST-EPR spectra has been provided in previous work (Robinson and Dalton, 1980; Robinson *et al.*, 1985). However, it will be useful for subsequent discussions to outline the magnetic interactions and rotational diffusion operators which have been included in the derivation of the equations. First, nonaxial electron-Zeeman (G tensor) and nitrogen hyperfine (A tensor) interactions have been retained. Though this results in a significant increase in complexity (i.e., size of the problem for computer solution) of the resulting equations, it is necessary for direct comparisons between experiment and theory since these interactions, particularly the G tensor for nitroxides, are normally characterized by nonaxial tensors in experimental systems. Coincidence of these tensor systems has been assumed. A nonaxial rotational diffusion tensor, which is assumed diagonal in the inertial frame of the macromolecule to which the label is attached with principal elements τ_x, τ_y, and τ_z, is included allowing computations on anisotropically diffusing systems to be carried out. Finally, the theory has been generalized for nonalignment of magnetic and diffusion tensors allowing characterization of effects of various labeling geometries for anisotropically diffusing proteins. Algorithms for both nitrogen-15 and nitrogen-14 spin labels have been developed.

5. STUDIES OF ISOTROPIC MOTION WITH NITROGEN-15 SPIN LABELS

5.1. V_1 EPR Signals as a Function of τ_r

It will be instructive to briefly examine the characteristics of the V_1 EPR signal from nitrogen-15 nitroxide spin labels before turning to the V_2' signal. The spin-$\frac{1}{2}$ nitrogen-15 atom results in hyperfine splitting of the V_1 signal into two lines (or manifolds) whose rigid limit widths are determined primarily by the principal elements of the electron-Zeeman (G) and nitrogen hyperfine (A) tensors (Figure 4). The V_1 line shapes shown

in Figures 4 (upper) and 6 (lower) illustrate that it is possible to measure all of the principal values for the A and G tensors directly from the experimental spectrum when nitrogen-15, deuterium-substituted spin labels are employed [see Beth *et al.* (1981a) for an extensive discussion of this point]. This is a significant advantage over nitrogen-14, hydrogen-containing spin labels where it is virtually impossible to uniquely determine values for A_{xx}, A_{yy}, g_{xx}, and g_{yy} at X-band, even if computer-simulation approaches are employed, since minor-element splittings are not resolved.

Previous work has indicated that the G-tensor elements for nitrogen-15 and nitrogen-14 spin labels are the same, within experimental limits of resolution, and that the A-tensor elements are increased by a factor of γ_N(nitrogen-15)/γ_N(nitrogen-14) or approximately 1.4 (Beth *et al.*, 1981a; Gaffney, 1981). Thus, typical principal values of G and A for 2,2,6,6-tetramethylpiperidine analogue spin labels in aqueous media (G_{xx} = 2.0090, G_{yy} = 2.0060, G_{zz} = 2.0022; A_{xx} = 11.0 G, A_{yy} = 10.8 G, A_{zz} = 50.5 G) give rise to $-\frac{1}{2}$ and $+\frac{1}{2}$ nuclear manifolds of approximate widths 13.5 gauss and 31.3 gauss, respectively. These compare with 16.7 gauss, 11.4 gauss, and 39.6 gauss for

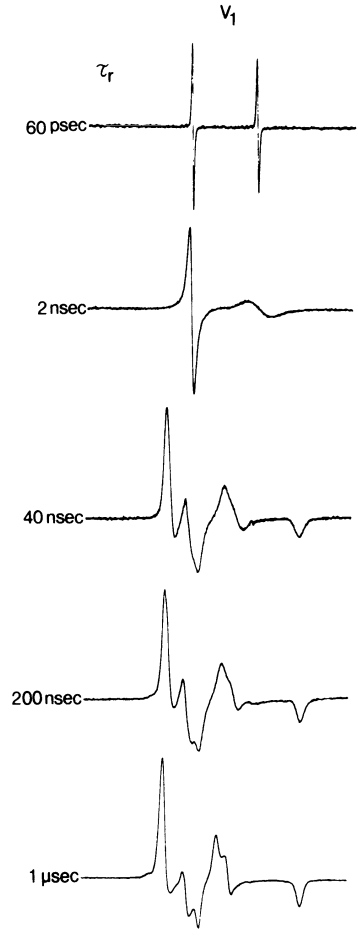

Figure 6. Dependence of the V_1 line shape on τ_r for nitrogen-15 spin labels. The experimental displays shown were collected from [^{15}N, $^{2}H_{17}$]maleimide spin label in: buffer at room temperature; 70% glycerol at 21 °C; bound to bovine serum albumin in buffer at 21 °C; bound to glyceraldehyde-3-phosphate dehydrogenase in buffer at 2 °C; and bound to glyceraldehyde-3-phosphate dehydrogenase in 50% glycerol at 2 °C. Scans are 100 gauss in width and are normalized to the same amplitude for display.

the $m_i = +1, 0$, and -1 nuclear manifolds of nitrogen-14 spin labels characterized by comparable tensor values.

Rotational motion modulates the nitrogen-15 spin label's magnetic anisotropies leading to correlation-time-dependent changes in the V_1 signal in proceeding from the fast motion to the rigid lattice limit as shown in Figure 6. Previous work has provided discussions of: the sensitivity of nitrogen-15 spin labels to motions in this correlation time range (Beth *et al.*, 1981a; Gaffney, 1981); the increased signal-to-noise ratio provided by the reduction in the number of hyperfine lines relative to nitrogen-14 spin labels (Beth *et al.*, 1981a; Gaffney, 1981); and the resolution enhancement provided by deuteration of the nitroxide ring system (Beth *et al.*, 1980, 1981a, 1984; Johnson *et al.*, 1982b).

Important characteristics of nitrogen-15 spin labels for biological cw-ST-EPR studies of very slow rotational diffusion of proteins are that:

1. The two nuclear manifolds are resolved on the field axis allowing direct determination of elements of the A and G tensors (Beth *et al.*, 1981a).
2. Characteristic structurings from all six spectral turning points are resolved for labels in aqueous environments at X-band microwave frequency (Beth *et al.*, 1981a; Johnson *et al.*, 1982b).
3. The sensitivity of V_2' to very slow motion is roughly equivalent to nitrogen-14 spin labels (Beth *et al.*, 1981a; Gaffney, 1981).
4. The reduction in the number of resonance lines from three to two simplifies the equations for computation of V_2' spectra such that time-dependent and anisotropic magnetic interactions and relevant motional models can be included while maintaining acceptable computation times (Robinson and Dalton, 1980; Beth *et al.*, 1983).

5.2. Dependence of the V_2' Signal on τ_r

The experimental data presented in Figure 7 illustrate the changes in the V_2' line shape which result from altering the isotropic rotational correlation time of a protein labeled with a nitrogen-15 nitroxide spin label. The regions of the spectrum labeled L'' and H'' are very sensitive to the rate at which rotational motion is sweeping the nitroxide Z axis into the X-Y plane. Figure 4 defines these positions as the mean field values at which $(\delta H_{res}/\delta\theta)_{\phi=0}$ and $(\delta H_{res}/\delta\theta)_{\phi=90}$ are maximum for the $-\frac{1}{2}$ and $+\frac{1}{2}$ nuclear manifolds, respectively (i.e., the positions where changes in orientation of the nitroxide result in the maximum change in resonance condition and, hence, transfer of saturation to other orientational spin packets). The peaks labeled L and H correspond to the field positions at which $(\delta H_{res}/\delta\theta)_{\phi}$ goes to zero for the $-\frac{1}{2}$ and $+\frac{1}{2}$ manifolds, respectively. Spectral amplitudes at positions L and H are very insensitive to the motional rate and can serve as internal references for the motionally sensitive positions as described originally for nitrogen-14 spin labels (Thomas *et al.*, 1976). Plots of the ratio parameters L''/L and H''/H (Figure 8) indicate that each provides high sensitivity to the correlation time for isotropic rotational diffusion throughout the very slow motional region (Beth *et al.*, 1981a; Gaffney, 1981; Johnson *et al.*, 1982b).

With nitrogen-15 spin labels, there is no direct counterpart to the C'/C ratio parameter previously defined for nitrogen-14 spin labels. Figure 3 indicates that the C' parameter from nitrogen-14 labels should provide sensitivity to motions which

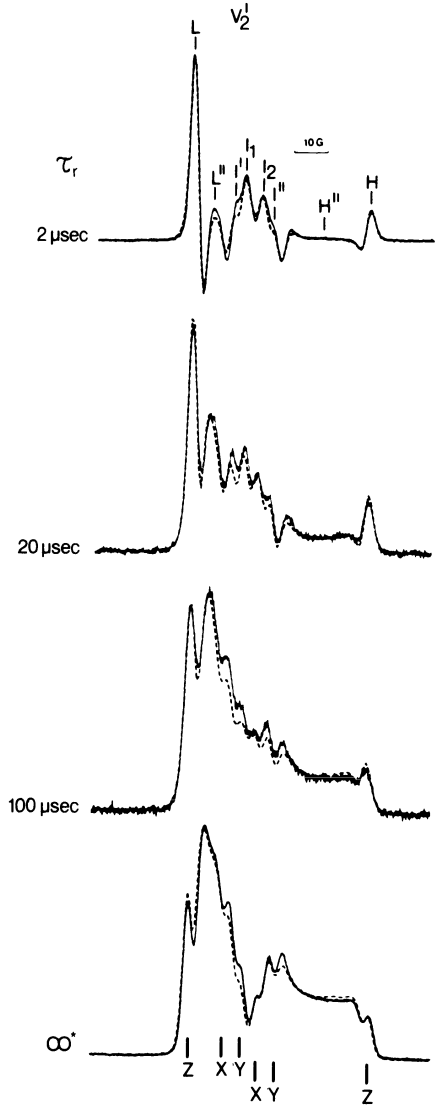

Figure 7. Dependence of the V_2' line shape on τ_r with nitrogen-15 spin labels. Experimental spectra (solid lines) were obtained from [^{15}N, $^{2}H_{17}$]maleimide spin-labeled glyceraldehyde-3-phosphate dehydrogenase ($r_h = 41$ Å) in: 53% glycerol; 78% glycerol; 89% glycerol; and ammonium sulfate precipitated form from top to bottom. Rotational correlation times were determined from the hydrated radius of the protein and measured solvent viscosities using equation (13). Computed spectra (dashed lines) are overlaid on the expeimental results. Experimental spectra are 100 gauss in width and are normalized to the same total amplitude. (From Beth *et al.*, 1983.)

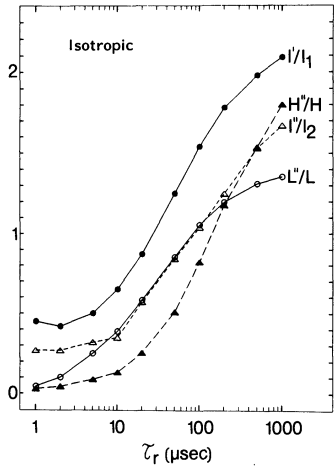

Figure 8. Dependence of ratio parameters on τ_r with nitrogen-15 spin labels. The data shown are from the spectra shown in Figure 7 plus additional computed spectra at the rotational correlation times indicated by the data points. (Adapted from Beth *et al.*, 1983.)

interconvert X-Z nitroxide axes with lesser sensitivity to motions which interconvert X-Y axes. Rotational motions which interconvert the X-Y axis of nitrogen-15 spin labels will give rise to spectral diffusion in the regions labeled I' and I''. These positions correspond to the field values where $(\delta H_{res}/\delta\phi)_{\theta=90}$ are maximum for the $-\frac{1}{2}$ and $+\frac{1}{2}$ nuclear manifolds, respectively (Figure 4, center). Positions labeled I_1 and I_2 correspond to field values where $(\delta H_{res}/\delta\phi)_{\theta=90}$ go to zero. Thus, the ratio parameters I'/I_1 and I''/I_2 provide sensitivity to the correlation time for X-Y averaging, though sensitivity to X-Z ($-\frac{1}{2}$ manifold) and Y-Z ($+\frac{1}{2}$ manifold) motions is manifested in these regions as well. Dependence of these ratio parameters on rotational correlation time is defined in Figure 8.

As with nitrogen-14 spin labels, V_2' spectra from spin-labeled proteins characterized by spherical symmetry can be analyzed by comparison of the experimentally measured ratios with standard plots (Figure 8). The sensitivity to motion, as expressed by change in value of ratio parameters versus change in rotational correlation time, is not significantly different for the two nitrogen isotope spin labels, and therefore either will serve as a reliable reporter group for studies of isotropic rotational diffusion. The advantage of the nitrogen-15 and deuterium-substituted spin labels over nitrogen-14 counterparts for studies of spherical proteins lies in their threefold increase in signal-to-noise ratio throughout the very slow motional region (Beth *et al.*, 1981a). This increase may be unimportant for studies of soluble proteins or protein complexes where it is possible to isolate and solubilize large quantities of protein. However, as demonstrated by the experimental V_2' spectra in Figure 9, the increased signal-to-noise can be advantageous in cases where intrinsic or peripheral membrane proteins are being investigated and concentrations available for observation are limited by the number of proteins or receptors present in a packed membrane suspension [for comparisons of the relative signal-to-noise observed from nitrogen-15, deuterium-substituted, nitrogen-14, deuterium substituted, and nitrogen-14, hydrogen-containing spin labels in the very slow motional time range, see Beth *et al.* (1981a, 1981b)].

The experimental data presented in Figure 9 illustrate that the region of the nitrogen-14 V_2' spectrum which provides the highest signal-to-noise is the central (C'/C)

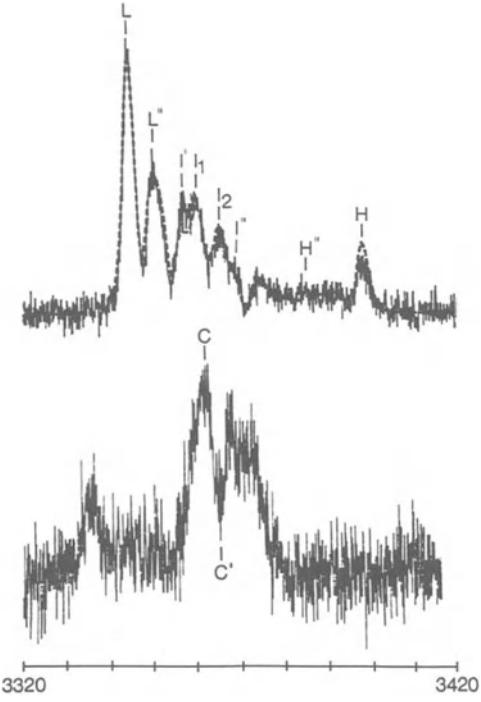

Figure 9. Signal-to-noise advantage of nitrogen-15, deuterium spin labels for studies of very slow rotational motions. The experimental V_2' spectra were obtained from 2 μmolar glyceraldehyde-3-phosphate dehydrogenase bound to the cytoplasmic domain of the anion channel in erythrocyte ghost membranes. In the upper display, the dehydrogenase was labeled with [^{15}N, $^{2}H_{17}$]maleimide spin label and in the lower display with conventional [^{14}N, ^{1}H]maleimide spin label. Instrument settings were the same for both scans. However, the upper spectrum was obtained after 1 hour of signal averaging while the lower display required 2 hours to provide the signal-to-noise ratios presented. The rotational correlation time for the bound enzyme is 20 μs from the computer simulation shown as the superimposed dashed line in the upper display. (Adapted from Beth *et al.*, 1981b.)

region which is dominated by the $m_i = 0$ nuclear manifold. Sensitivity to very slow motions is much less for this manifold than it is for the other two, due to its relatively narrow width (Figure 3, middle). The parameter C'/C exhibits its greatest sensitivity to motion in the 0.1 to 10 μs correlation time range with almost no sensitivity to motions characterized by correlation times longer than 50–100 μs (Figure 5, lower). Thus, for investigations of very slow protein motions ($10\,\mu s < \tau_r < 1$ ms), the extrema regions of the nitrogen-14 spectrum will have to be analyzed in order to obtain reliable information. The signal-to-noise advantage of the nitrogen-15, deuterium-substituted spin labels for these applications will greatly exceed a factor of three as illustrated in Figure 9. Theoretical calculations of ^{15}N, DMSL can be correlated with the biochemical experiments presented by J. Park and W. Trommer in this volume in Chapter 11 (see pages 549–561).

6. EFFECTS OF ANISOTROPIC ROTATIONAL DIFFUSION ON V_2' SPECTRA

Cw-ST-EPR studies of very slow rotational diffusion of asymmetric proteins and membrane bound proteins using the V_2' signal have often yielded line shapes which differ perceptibly from V_2' reference spectra obtained from isotropically diffusing proteins (for representative examples see Thomas and Hidalgo, 1978; Sakaki *et al.*, 1982; Fung and Johnson, 1983; Willingham and Gaffney, 1983; Beth *et al.*, 1986;

Thiyagarajan and Johnson, 1987). In many of these examples, a significant factor in determining the observed line shapes is anisotropic rotational diffusion. However, to date, the nature and frequency of the motions giving rise to these line shapes have remained largely undefined. The first step in unraveling the motional information contained in the V_2' signal is to define sensitivity to rotational motions about different nitroxide axes and then to relate this information to the binding geometry between the spin label and the protein to which it is attached. In this section, results will be provided which define how V_2' spectral shapes from nitrogen-15 spin labels depend on rotational correlation times about the nitroxide X, Y, and Z axes. In Section 9 below, line shapes from nitrogen-14 labels undergoing anisotropic rotational diffusion will be presented.

6.1. Sensitivity of V_2' to Uniaxial Rotation

The first model to be considered is the rotation of a cylindrical protein about its long axis. The V_2' line shape in this case will be determined in large part by the rotational correlation time, $\tau_\parallel$, and the geometrical arrangement between the magnetic and diffusion tensors (Θ_{yy} in Figure 1; Robinson and Dalton, 1980; Beth *et al.*, 1983). Consideration of two limiting geometries will provide insight into sensitivity to specific rotational motions. First, if the nitroxide Z axis is aligned with the cylinder axis ($\Theta_{yy} = 0$), rotational diffusion will result in interconversion of the X and Y nitroxide axes which will lead to spectral diffusion in the I' and I'' regions of the nitrogen-15 V_2' spectrum (solid lines in Figure 4, middle) and no spectral diffusion in the L'' and H'' regions of the spectrum (dashed lines in Figure 4, middle). Thus, the I' and I'' regions vary with changes in $\tau_\parallel$ with minimal sensitivity to the motion in the L'' and H'' regions of the spectrum. This sensitivity is illustrated by the computed spectra in Figure 10, left panel, and by the ratio parameter plots in Figure 10, right panel. At X-band (and lower microwave frequencies), coincidence of the magnetic and diffusion tensors will result in the least sensitivity to the motional process, since only the X to Y interconversion (nitroxide axes) is modulated by the motion. The X-Y anisotropy is on the order of 5 gauss for the $\pm\frac{1}{2}$ manifolds resulting in considerably less efficient saturation transfer due to rotation as compared with the X-Z and Y-Z interconversions (Figure 4, middle).

For the second model, the nitroxide X axis is aligned with the cylinder axis ($\Theta_{yy} = 90°$). With this labeling geometry, rotational diffusion will lead to interconversion of the Y and Z nitroxide axes which results in maximum spectral diffusion in the L'' and H'' regions of the spectrum (dot-dash lines in Figure 4, middle). Thus, the extrema regions exhibit the greatest sensitivity to $\tau_\parallel$ as shown by the computed spectra in Figure 11, left panel, and by the ratio parameter plots in Figure 11, right panel. This labeling geometry, or the complementary one where the Y nitroxide axis is aligned with the cylinder axis ($\Theta_{xx} = 90°$, Figure 12), will provide the highest sensitivity to $\tau_\parallel$ for uniaxial diffusion at X-band microwave frequency.

These two examples illustrate how the plots shown in Figure 4, middle, predict which regions of the V_2' spectrum will provide the greatest sensitivity to rotational motions about different nitroxide axes. Experimental variation of the rotational correlation time by adjusting temperature or protein aggregation state can provide insight into labeling geometry if one of the three nitroxide axes is aligned with the diffusion axis. If one of these labeling geometries is observed, the ratio parameter plots in Figure 10

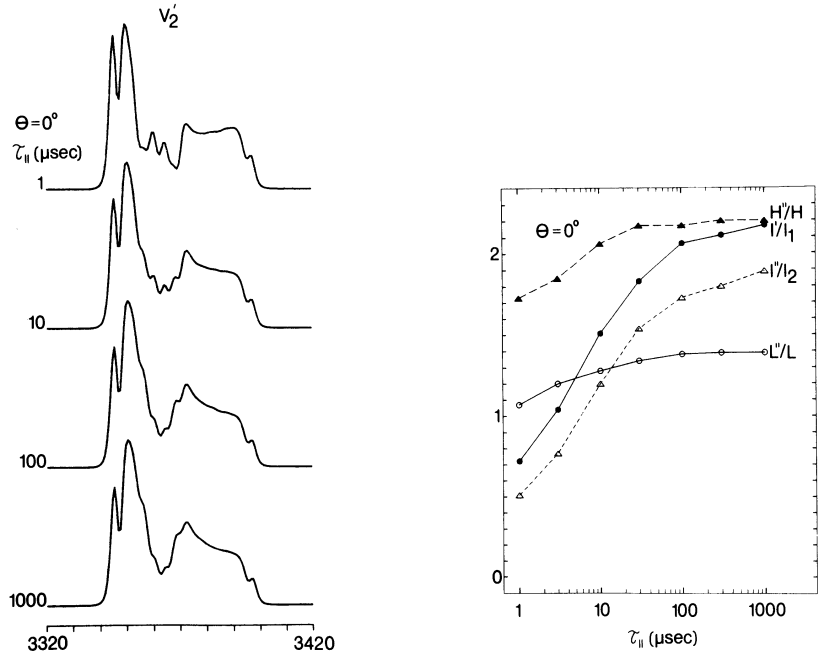

Figure 10. V_2' line shape (left) and ratio parameter (right) dependence on $\tau_\parallel$ for a uniaxial model with aligned magnetic and diffusion tensors. The graphical data was taken from the computed line shapes shown plus additional computations carried out at the indicated values of $\tau_\parallel$. Input parameters for the computations included: A_{xx} = 10.62 G; A_{yy} = 10.38 G; A_{zz} = 50.15 G; g_{xx} = 2.0091; g_{yy} = 2.0061; g_{zz} = 2.0022; h_1 = 0.2 G; ν_m = 50 kHz; h_m = 5.0 G (effective); T_{1e} = 25 μs; T_{2e} = 40 ns; ν_0 = 9.45 GHz; $\tau_\perp$ = 0.1 s; and Θ_{yy} = 0°. Each spectrum was post-broadened with a Gaussian function of 0.9 G half-width to simulate broadening by deuteriums on the nitroxide ring system.

or 11 can be employed to provide an accurate determination of $\tau_\parallel$. However, in spin-labeling applications, it is more likely (from probability considerations) that some intermediate orientation of the spin label relative to the rotation axis will be obtained. In this case, $\tau_\parallel$ can be equated with τ_2^2 defined in equation (26). In any case, it is highly desirable to determine labeling geometry by an independent approach. One such approach is to experimentally orient the spin-labeled protein in the magnetic field and then observe the orientational dependence of the V_1 spectrum. If orientational dependence is observed, then the orientation of the spin label relative to the director axis of the system can be determined by straightforward analysis of the linear EPR spectrum, where the interpretation is not obscured by rotational dynamics. The method of choice for achieving orientation will depend on the physical properties of the system under investigation. For transmembrane proteins, a promising approach is to orient the membrane bilayer containing the protein on glass surfaces. Sakaki *et al.* (1982) employed this approach to observe orientational properties of spin-labeled band-3 protein in phospholipid bilayers. Other systems may lend themselves to flow orientation or to orientation in an electrical field followed by fixation with glutaraldehyde or other

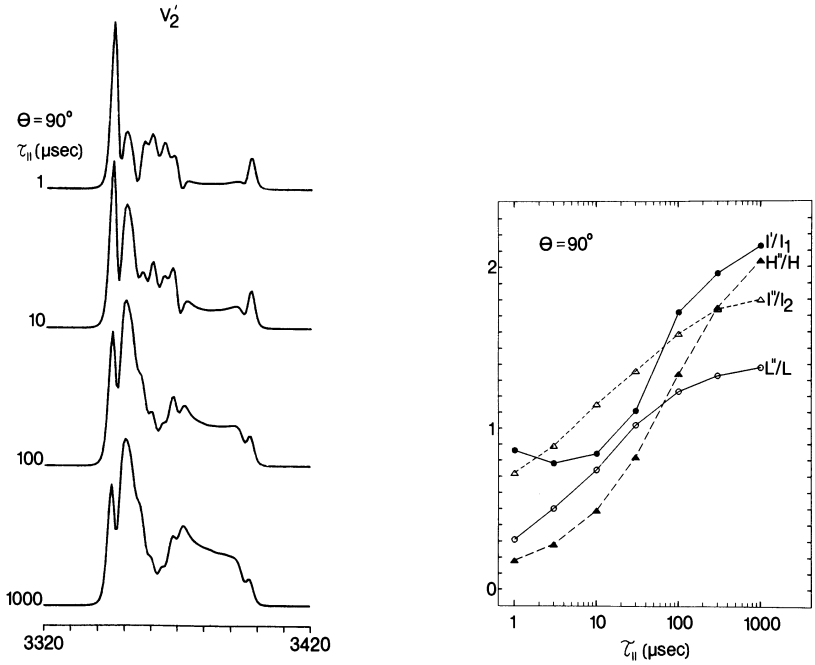

Figure 11. V_2' line shape (left) and ratio parameter (right) dependence on $\tau_\parallel$ for a uniaxial model with orthogonal magnetic and diffusion tensors. The graphical data was taken from the computed line shapes shown plus additional computations carried out at the indicated values of $\tau_\parallel$. Input parameters for the computations included: A_{xx} = 10.62 G; A_{yy} = 10.38 G; A_{zz} = 50.15 G; g_{xx} = 2.0091; g_{yy} = 2.0061; g_{zz} = 2.0022; h_1 = 0.2 G; ν_m = 50 kHz; h_m = 5.0 G (effective); T_{1e} = 25 μs; T_{2e} = 40 ns; ν_0 = 9.45 GHz; $\tau_\perp$ = 0.1 s; and Θ_{yy} = 90°. Each spectrum was post-broadened with a Gaussian function of 0.9 G half-width to simulate broadening by deuteriums on the nitroxide ring system.

crosslinking reagents. Regardless of whether the ratio parameter plots shown in Figures 10 and 11 or a computational approach is to be employed to analyze data from a system characterized by uniaxial rotational diffusion, determination of the labeling geometry (and orientational uniqueness) is essential if it is desired to determine true rotational correlation times. This is a point which has not received sufficient emphasis in many previous spin-labeling studies, but one that will undoubtedly become more important as applications of the approach evolve in sophistication of labeling and in the quest for quantitative analysis of data.

6.2. Effects of Labeling Geometry

The V_2' spectra shown in Figure 12 illustrate the variations in line shape which result from selected labeling geometries for a uniaxial rotational diffusion model (Beth *et al.*, 1983). The motional model chosen for discussion is characterized by an axial rotational correlation time ($\tau_\parallel$) of 10 μs and therefore is a reasonable model for

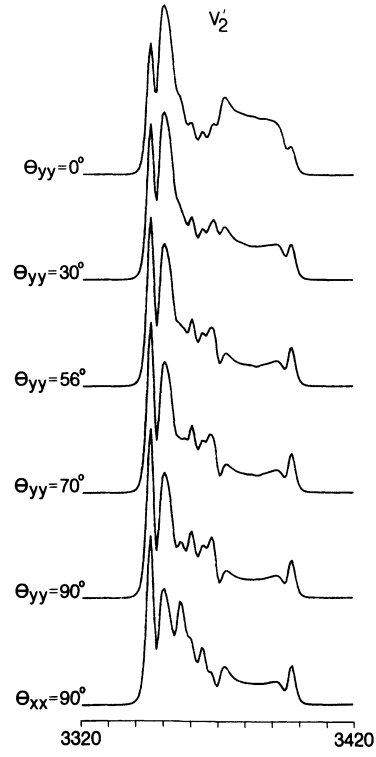

Figure 12. V_2' line-shape dependence on labeling geometry for a uniaxial rotational diffusion model. The computed line shapes are for a constant diffusion model characterized by $\tau_{\parallel} = 10\ \mu s$ and $\tau_{\perp} = 0.1$ s. The first five spectra were obtained by rotating the magnetic tensors by angle Θ_{yy} relative to the $\tau_{\parallel}$ axis. The lower spectrum was obtained by rotating the magnetic tensors by angle Θ_{xx} (i.e., about the A_{xx} and D_{xx} axes in Figure 1) relative to the $\tau_{\parallel}$ axis. All other input parameters in the computations were the same as in Figure 11.

rotational diffusion of an intrinsic membrane protein about its membrane normal axis. The spectra show the evolution in V_2' line shape from pure X-Y nitroxide axis averaging by the motion in the upper display to pure Y-Z or X-Z averaging in the lower two displays, respectively. It is apparent that as the nitroxide Z axis is tilted away from the axis of rotation of the cylinder, the wings (L'' and H'' regions) of the spectrum become increasingly sensitive to the motion. At Θ_t equal to 90°, the L'' and H'' regions of the spectrum are composite functions of one very slow ($\tau_{\perp} = 0.1$ s) and one 10 μs motional process. Consequently, the spectral amplitudes in these regions are intermediate between the case where both motional rates are fast and both are slow. At labeling geometries near 55°, the line shapes show minimal evidence for the anisotropic nature of the rotational diffusion with line shapes approximating those from an isotropic model at an intermediate rotational correlation time. An important point to appreciate is how changes in labeling geometry alter the "apparent" motional times predicted when the isotropic model system ratio parameters (Figure 8) are employed for data analysis.

A number of conclusions can be drawn from the data presented in Figures 10-12. First, if a uniaxial rotational diffusion process dominates motion, the isotropic model system curves will always predict a longer rotational correlation time than the true $\tau_{\parallel}$, the error being greatest at $\Theta_t = 0°$ and least at $\Theta_t = 90°$. Next, changes in labeling geometry, such as might result from a conformational change in the labeled protein

due to interaction with other factors present, can mimic a change in rotational dynamics if line shapes are analyzed solely by isotropic model system ratio parameters. Finally, preliminary analysis of the V_2' line shape by comparison of ratio parameters L''/L, I'/I_1, I''/I_2, and H''/H from the system under investigation with the isotropic model system plots can provide a clue to labeling geometry and the anisotropic nature of the motion. Whenever experimentally feasible, labeling geometry and uniqueness should be established by independent approaches before final data analysis. However, it should be pointed out that the presence of multiple, very slow motional populations can mimic line shapes characteristic of anisotropic diffusion. Methods of potential use for characterizing multiple, very slow motional populations will be elaborated upon in Section 8.

6.3. Sensitivity of V_2' to Anisotropic Rotational Diffusion of Axially Symmetric Ellipsoids in an Isotropic Medium

The shape of the experimental V_2' spectrum for an axially symmetric ellipsoid will be determined primarily by the two rotational correlation times $\tau_\parallel$ and $\tau_\perp$ and by the orientation, Θ_t, of the nitroxide Z axis with respect to the symmetry axis of the macromolecule or macromolecular assembly. This number of experimental observables precludes an exhaustive survey of possible line shapes for all unique permutations. However, it is instructive to examine the sensitivity to $\tau_\parallel$ and $\tau_\perp$ motions for one labeling geometry in order to illustrate the inherent sensitivity to changes in motional rates. Figure 13 shows a 3×3 array of computed V_2' spectra where $\tau_\parallel$ and $\tau_\perp$ are varied from 2 to 200 μs in each column and row of the array, respectively. The labeling geometry presented assumes coincidence of the magnetic and diffusion tensors such that $\tau_\parallel$ rotation modulates X-Y (nitroxide axes) magnetic anisotropy and $\tau_\perp$ rotations modulate X-Z and Y-Z anisotropies.

The trends in spectral ratios discussed in the previous section on uniaxial rotational diffusion also hold true for axial models in isotropic environments. However, the magnitude of change in these parameters for a given change in $\tau_\parallel$ now critically depends on the value of $\tau_\perp$. This point is most clearly illustrated by comparing the three spectra in each column of Figure 13. When $\tau_\perp$ is held constant at 2 μs and $\tau_\parallel$ is increased from 2 to 200 μs (column 1), the parameters I'/I_1 and I''/I_2 show very little sensitivity. However, when $\tau_\perp$ is held constant at 200 μs and $\tau_\parallel$ is increased from 2 to 200 μs (column 3), I'/I_1 and I''/I_2 are very sensitive to $\tau_\parallel$. This differential sensitivity to $\tau_\parallel$ can be explained qualitatively on the basis of inherent lack of sensitivity to one slow motional process (relative) in the presence of two orthogonal faster ones.

Given the complex way in which the ratio parameters depend upon both rotational correlation times and the labeling geometry, it is difficult to construct enough ratio parameter versus correlation time plots (i.e., two-parameter families of curves) to be of general utility. The best approach for analyzing data from this type of system is direct computer simulation following determination of the relationship between the magnetic and diffusion tensors by independent approaches. Quantitative analysis of V_2' spectra from such systems is very demanding, even when employing nitrogen-15 spin labels and computational approaches. However, when important questions concerning biological function necessitate in-depth analysis of such systems, analyses may be possible under favorable circumstances.

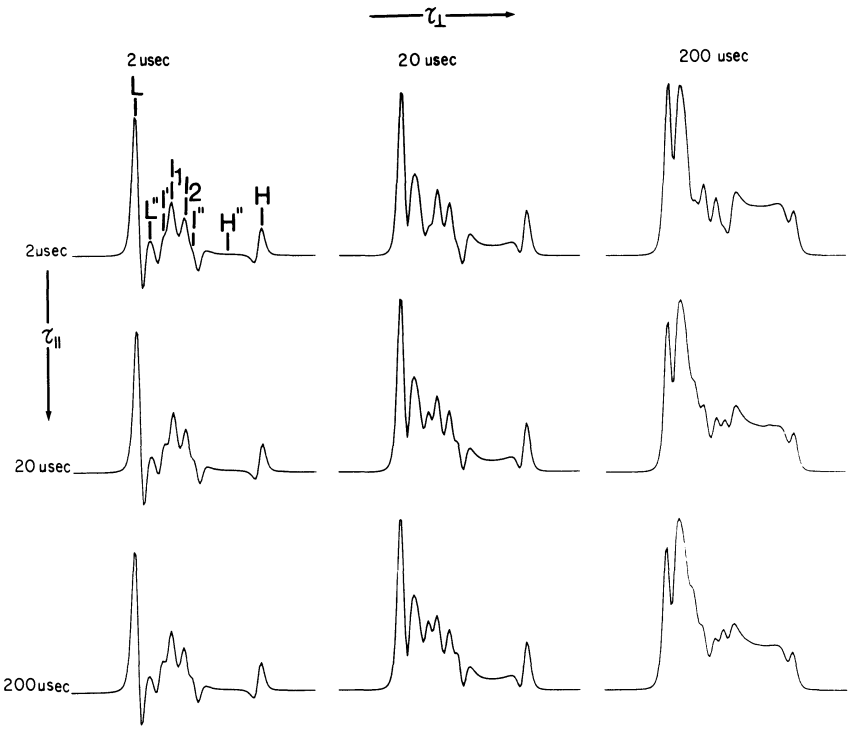

Figure 13. V_2' line shapes for anisotropic rotational diffusion models. Rotational correlation times $\tau_\parallel$ and $\tau_\perp$ are increased from 2 to 200 μs along the columns and rows of the 3 × 3 array of computed spectra, respectively. In each display, the magnetic and diffusion tensors are coincident. Simulation parameters included: $A_{xx} = 11.30$ G; $A_{yy} = 11.00$ G; $A_{zz} = 49.75$ G; $g_{xx} = 2.0088$; $g_{yy} = 2.0060$; $g_{zz} = 2.0022$; $h_1 = 0.2$ G; $T_{1e} = 25$ μs; $T_{2e} = 40$ ns; $\nu_m = 50$ kHz; $h_m = 5.0$ G (effective); $\nu_0 = 9.45$ GHz; and a Gaussian post-broadening of 0.9 G in each. (Aadapted from Beth *et al.*, 1983.)

6.4. Relationship Between Effective Correlation Times and Anisotropic Motion

Most experimental studies utilizing cw-ST-EPR to date have analyzed data by comparison of ratio parameters with the same parameters from isotropic model system curves, such as those shown in Figures 5 and 8 for nitrogen-14 and nitrogen-15 spin labels, respectively. When the systems being studied were diffusing anisotropically, rotational mobility was generally reported in terms of rotational correlation times τ_r obtained from the model system plots. This practice has often led to different values for τ_r being predicted by the different ratio parameters analyzed. It is important to define how these effective rotational correlation times relate to the true correlation times for an anisotropically diffusing macromolecule. Alternatively stated, it is desirable to be able to estimate the true rotational correlation times from the effective correlation times obtained from different regions of the V_2' spectrum for cases where labeling geometry is unique and definable. Nitrogen-15 spin labels should be particularly useful

for such applications, since regions of the V_2' spectrum dependent on rotations about the nitroxide X, Y, and Z axes are more clearly resolved than with nitrogen-14 labels (see Figures 3 and 4).

A workable solution to the problem begins with the generalized equations for rotational correlation times of an axially symmetric protein presented in Section 2.3. For ST-EPR, the total relaxation operator is given as $\Gamma_\Omega + 1/T_{1e}$. The total relaxation makes clear that the molecular motion is not observable in ST-EPR spectra if it is too slow as compared to $1/T_{1e}$. Inclusion of this term leads to modified equations for the eigenvalues of the relaxation operator:

$$(\Gamma_\Omega + R_{1e})D^l_{m,n}(\Omega) = \lambda'^l_m D^l_{m,n}(\Omega) \tag{46}$$

where $R_{1e} = 1/T_{1e}$ and λ'^l_m is related to λ^l_m given in equation (22),

$$\lambda'^l_m = \lambda^l_m + R_{1e} \tag{47}$$

and is further related to the principal elements of the diffusion tensor,

$$\lambda'^l_m = l(l+1)D_\perp + m^2(D_\parallel - D_\perp) + R_{1e} \tag{48}$$

With these definitions, an effective correlation time can be defined as

$$\tau^l_{m\,\mathrm{eff}} = \sum_{m'} |d^l_{m',m}(\Theta_t)|^2(\lambda'^l_{m'})^{-1} \tag{49}$$

For the case of isotropic motion, the value for τ_{eff} reduces to

$$\tau^l_{m\,\mathrm{eff}} = [Dl(l+1) + R_{1e}]^{-1} = (\tau_r^{-1} + R_{1e})^{-1} \tag{50}$$

The quantity τ_r can represent the apparent motional rate for the isotropically moving molecules, and one should be able to compare τ_{eff} values from ST-EPR spectra obtained for a variety of motional processes. Rather than directly compare this quantity, it is more reasonable to define

$$(\tau^l_{m\,\mathrm{eff}})^{-1} = (\tau'^l_m)^{-1} + R_{1e} \tag{51}$$

One can also compare τ'^l_m due to different motional processes. From the above definition of τ'^l_m, when the motion is isotropic, then

$$\tau'^l_m = \tau_r \tag{52}$$

Therefore, in a qualitative way, it should be possible to compare values of τ'^l_m for isotropic motion with τ'^l_m for any type of anisotropic motion by requiring that

$$[(\tau'^l_m)^{-1} + R_{1e}]^{-1} = \Sigma_{m'}|d^l_{m',m}(\Theta_t)|^2(\lambda'^l_{m'})^{-1} \tag{53}$$

for all motional processes. Thus, for any given motional process, this expression can be rearranged to compute $\tau_m'^I$.

This formalism provides a framework for comparing effective correlation times from anisotropic motional processes with those of isotropic motion. A similar approach has been employed to interpret linear EPR spectra (Robinson *et al.*, 1980, 1985) where the total motional operator is $\Gamma_\Omega + 1/T_{2e}$ instead of $\Gamma_\Omega + 1/T_{1e}$ as it is for ST-EPR. A variation on this method of comparison was suggested by the tabulated data of Robinson and Dalton (1980) and in the application of Sakaki *et al.* (1982). Let us begin by assuming that H''/H is diagnostic for $\tau_0'^2$ and I''/I_2 is diagnostic for $\tau_2'^2$. For nitrogen-15 spin labels, L''/L and I'/I_1, respectively, would also be valid parameters for estimating the two correlation times. There are fundamentally three parameters that must be known in order to estimate the two motional rates of an axial, anisotropically diffusing protein: (1) the effective mobility of the protein, (2) the axial-to-equatorial ratio of the protein (or the shape factor), and (3) the tilt angle of the spin-label Z axis relative to the principal diffusion axis. If the tilt angle can be determined, then the shape factor and effective mobility can be calculated. For uniaxial diffusion, for example, if the tilt angle can be determined, then the shape factor and effective mobility can be estimated uniquely.

Consideration of the uniaxial diffusion model in Figure 11 illustrates the utility of the approach. For the uniaxial model presented, $\tau_\parallel = 1/6D_\parallel$ and $\tau_\perp \simeq \infty$. From Figure 11 (right panel), the ratio parameters H''/H and I''/I_2 can be determined as a function of $\tau_\parallel$. The values for the ratio parameters can then be compared with the isotropic model ratio parameters in Figure 8 to yield values for τ_r. Next, using the formula for $\tau_m'^I$ above, values for $\tau_0'^2$ and $\tau_2'^2$ can be computed. As shown in Table 1, the computed values correspond closely to the predicted values from the isotropic model system curves throughout the very slow motional range for $\tau_\parallel$ for both the wings and the center region.

Measurement of H''/H and I''/I_2 from the V_2' spectra shown in Figure 12 permits determination of τ_r values as a function of tilt angle for a single uniaxial diffusion model. These values are compared with the computed values for $\tau_0'^2$ and $\tau_2'^2$ in Table 2. Again, agreement between the values determined from the isotropic model system and the calculated ones is encouraging. For this particular model of uniaxial motion, it is difficult to obtain meaningful ratio parameters in the center of the spectrum when

TABLE 1
Comparison[a] of $\tau_\parallel$, $\tau_0'^2$, $\tau_2'^2$, and τ_r Values for the Data in Figure 11

$\tau_\parallel$ [b]	$\tau_0'^2$ [c]	$\tau_r(H''/H)$ [d]	$\tau_2'^2$ [c]	$\tau_r(I''/I_2)$ [d]
1	13	15	29	30
10	31	40	94	120
100	212	175	648	500
1000	2000	>1000	6052	≫1000

[a] All values for correlation times in μs.
[b] Values for $\tau_\parallel$ are the actual values used in the computations.
[c] Values for $\tau_0'^2$ and $\tau_2'^2$ were computed using equation (53).
[d] Values for $\tau_r(H''/H)$ and $\tau_r(I''/I_2)$ were determined from the isotropic model plots shown in Figure 8.

TABLE 2
Dependence[a] of $\tau_0'^2$, $\tau_2'^2$, and τ_r Values on Θ_{yy} for the Uniaxial Diffusion Model in Figure 12

Θ_{yy} [b]	$\tau_0'^2$ [c]	$\tau_r(H''/H)$ [d]	$\tau_2'^2$ [c]	$\tau_r(I''/I_2)$ [d]
0	∞	>1000	15	170
30	110	120	22	165
56	37	50	47	110
70	32	30	71	110
90	32	30	94	120

[a] All values for correlation times in μs.
[b] Values for Θ_{yy}, the tilt of the nitroxide Z axis from the uniaxial diffusion axis, are in degrees.
[c] Values for $\tau_0'^2$ and $\tau_2'^2$ were computed using equation (53).
[d] Values for $\tau_r(H''/H)$ and $\tau_r(I''/I_2)$ were determined from the isotropic model plots shown in Figure 8.

the intensity in the wings is so large. However, one can use these effective numbers to compute first-order estimates of the motional rates and tilt angle. The next step then is to use estimated parameters to simulate the entire line shape. Certainly, there is sensitivity in the simulations to more than the simple formulas indicate. For example, the spectra for $\Theta_{yy} = 90°$ and $\Theta_{xx} = 90°$ (Figure 12, bottom) are quite different (in accordance with predicted motional sensitivity for these two models in Figure 4, center) and hence show a dependence on the direction of the tilt angle as well as the magnitude.

The data in Figure 13 for axial anisotropic rotational diffusion can also be understood in terms of the effective correlation times, $\tau_0'^2$ and $\tau_2'^2$. The data shown in Table 3 allow comparison of true values for $\tau_\parallel$ and $\tau_\perp$ and the computed effective correlation times. As described in the previous section, when $\tau_\perp$ is fast (left columns of Figure 13 and Table 3), there is very little sensitivity to $\tau_\parallel$. When $\tau_\perp$ is slow (right columns of Figure 13 and Table 3), there is high sensitivity to $\tau_\parallel$ reflected in the center of the spectrum and in the computed values for $\tau_2'^2$. Sensitivity to $\tau_\perp$ is seen in $\tau_0'^2$ independent of $\tau_\parallel$. However, there is sensitivity to $\tau_\perp$ in I''/I_2, and thus the method provides only an estimate of the true rotational correlation times.

TABLE 3
Dependence[a] of $\tau_0'^2$ and $\tau_2'^2$ on $\tau_\parallel$ and $\tau_\perp$ for the Axial Anisotropic Diffusion Models in Figure 13

		$\tau_\perp$		
		2	20	200
$\tau_\parallel$	2	2/2[b]	20/3	200/3
	20	2/5	20/20	200/30
	200	2/6	20/50	200/200

[a] All values for correlation times in μs.
[b] Values for $\tau_0'^2$ and $\tau_2'^2$ were computed using equation (53) and are given as $\tau_0'^2/\tau_2'^2$.

7. OPTIMIZATION OF SENSITIVITY OF V_2' TO MOTION

Discussions to this point have centered on V_2' line shapes collected experimentally or calculated using what have become "standard" instrument parameters. These are X-band (~9.4 GHz) microwave frequency, a microwave observer field of 0.20 to 0.25 gauss in the rotating frame, 50 kHz reference Zeeman field modulation with detection of the second-harmonic signal at 100 kHz, and a Zeeman field modulation amplitude of 5 gauss (peak-to-peak). These instrument settings are essentially the same as those defined originally by Thomas *et al.* (1976) which were the result of an extensive survey for defining a balance between sensitivity of ST-EPR signals to rotational diffusion, obtaining acceptable signal-to-noise, and engineering considerations for developing commercial hardware for making the measurements. The microwave power level is chosen to provide partial saturation of the nitroxide spin energy levels. Variations in the power level in the 0.20 to 0.25 gauss range result in significant changes in line shape for the V_2' signal (Thomas *et al.*, 1976) but such variations do not normally provide useful changes in sensitivity to motion. Likewise, the modulation amplitude can be chosen to provide adequate signal-to-noise and resolution of spectral features (Thomas *et al.*, 1976; Robinson, 1983). However, the standard value of 5 gauss has proven to be a very good compromise between signal-to-noise and resolution even in the case of the narrow linewidths afforded by deuterium-substituted spin labels. The other parameters listed, however, can be selected to substantially alter the sensitivity of the V_2' signal to the motional rate and to the anisotropy of the motion. Commercial EPR spectrometers are now available which operate at microwave frequencies of ~1 GHz (L-band), ~3 GHz (S-band), 9.0–9.5 GHz (X-band), 22–24 GHz (K-band), and ~35 GHz (Q-band). Likewise, detection of either the first or second harmonic signal at selected modulation amplitudes at reference Zeeman field modulation frequencies in the 1 kHz to 200 kHz range is possible using commercially available equipment.

In the following sections the effects of these experimental variables on the line shape and motional sensitivity of the V_2' spectrum from nitrogen-15 spin labels are considered. These data can serve as a guide for selecting the set of instrument parameters which provide the highest sensitivity to the type and frequency of motion of a spin-labeled protein or other biomolecule.

7.1. Altering Sensitivity to Motion by Selection of ν_0

The magnitude of the G-tensor anisotropy is a linear function of the operational frequency ν_0 of the EPR spectrometer while the A-tensor anisotropy is frequency independent. Unlike the A tensor, the G tensor for a nitroxide spin label is distinctively nonaxial. A compilation of principal elements measured from a variety of spin labels (Gaffney, 1976) indicates that reasonable average values would be $g_{xx} \sim 2.0090$, $g_{yy} \sim 2.0060$, and $g_{zz} \sim 2.0022$, values which agree closely with ones determined experimentally from nitrogen-15 spin-labeled proteins (Beth *et al.*, 1983). At 3 GHz, the G-tensor anisotropy is only 3.6 gauss as compared with an A-tensor anisotropy of approximately 40 gauss for nitrogen-15 spin labels, calculated as $A_{zz} - [A_{xx}$ or $A_{yy}]$. Therefore, the line shape is dominated by the pseudoaxial A tensor at low microwave frequencies with minimal nonaxial character in the spectrum. This is demonstrated by the computed V_1 spectrum in Figure 14, upper panel. Sensitivity to rotational motion

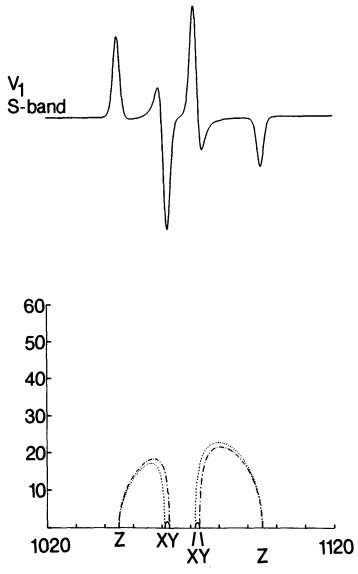

Figure 14. Relationship between line-shape features in the V_1 display and regions of predicted motional sensitivity of V_2' for nitrogen-15 spin labels at S-band. Upper: Computed V_1 spectrum. Lower: Plots of absolute value of change in resonance condition (H_{res}) versus field position for rotations about the three nitroxide principal axes. (· · · ·) $|[\delta H_{res}(m_i)/\delta\theta]_{\phi=0}|$; (· - · - ·) $|[\delta H_{res}(m_i)/\delta\theta]_{\phi=90}|$; and (——) $|[\delta H_{res}(m_i)/\delta\phi]_{\theta=90}|$ for $m_i = -\frac{1}{2}$ and $+\frac{1}{2}$. Values on the ordinate are gauss rad^{-1}. Simulation parameters were: A_{xx} = 10.6 G; A_{yy} = 10.4 G; A_{zz} = 50.15 G; g_{xx} = 2.0091; g_{yy} = 2.0061; g_{zz} = 2.0022; ν_0 = 3.00 GHz; h_1 = 0.01 G; T_{2e} = 100 ns; T_{1e} = 15 μs; $\tau_r = \infty$; ν_m = 100 kHz; h_m = 0.5 G. The V_1 spectrum was post-broadened with a Gaussian function of 0.9 G half-width.

is confined to the extrema (L'' and H'') regions of the V_2' spectrum (Figure 14, lower panel; Figure 15) and therefore dominated by the rate at which rotational motion is

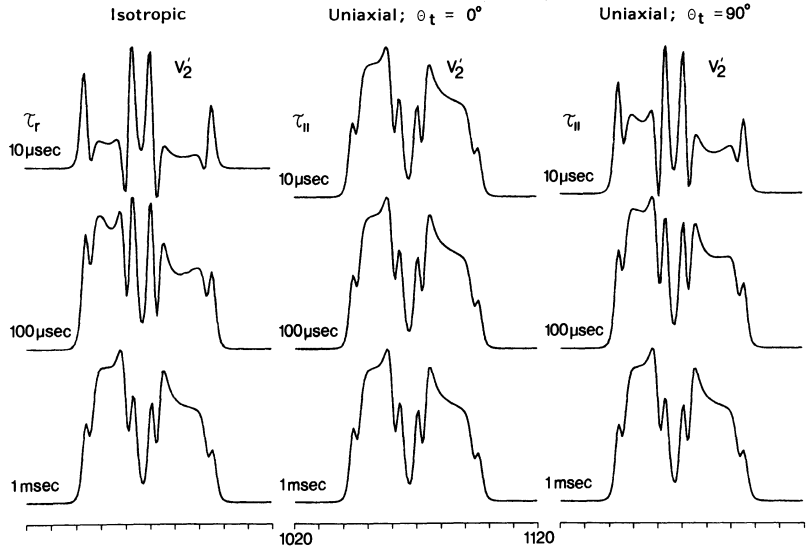

Figure 15. Dependence of S-band V_2' line shapes on rotational correlation times. Computations were carried out for the rotational correlation times and labeling geometries indicated. Additional parameters included: A_{xx} = 10.6 G; A_{yy} = 10.4 G; A_{zz} = 50.15 G; g_{xx} = 2.0091; g_{yy} = 2.0061; g_{zz} = 2.0022; ν_0 = 3.00 GHz; h_1 = 0.2 G; T_{2e} = 40 ns; T_{1e} = 25 μs; ν_m = 50 kHz; and h_m = 5.0 G (effective). Each spectrum was post-broadened with a Gaussian function of 0.9 G half-width.

sweeping the nitroxide Z axis into the $X-Y$ plane. There is very little sensitivity to the rate of $X-Y$ nitroxide axis interconversion at microwave frequencies in the 1 to 3 GHz range (Figure 15, center column). For a uniaxial rotational diffusion model, the V_2' spectrum will provide sensitivity to $\tau_\parallel$ only if the nitroxide Z axis is tilted from the diffusion axis with maximum sensitivity at $\Theta_t = 90°$.

Since experimental studies of the V_2' signal at S-band have not been reported, it is difficult to establish signal-to-noise relative to more common X- and Q-band measurements. However, the large volumes which can be accommodated in S-band resonators should overcome reductions in signal-to-noise due to the lower observation frequency. For sparingly soluble or cell membrane samples, S-band may provide very competitive signal-to-noise ratio due to its favorable filling factor.

At X-band (~9.4 GHz), the G-tensor anisotropy is increased to 12 gauss and the V_1 spectrum is distinctively nonaxial in appearance (Figure 4, upper panel). The greatest sensitivity to motion is still in the extrema regions and hence determined by the rate at which molecular rotation is sweeping the nitroxide Z axis into the $X-Y$ plane. However, the $X-Y$ anisotropy is now on the order of 5 gauss for both the $m_i = \pm\frac{1}{2}$ nuclear manifolds and there is appreciable sensitivity to motions which interconvert these spin-label axes (Figure 4, center, Figure 10). It is thus possible to obtain insight into the anisotropy of the rotational diffusion from analysis of the X-band V_2' spectrum.

Using nitrogen-15 and deuterium-substituted spin labels, it is possible to make X-band V_2' measurements in the 1 to 5 μM concentration range with acceptable signal-to-noise for data analysis in 1 to 2 hours of signal averaging time (Figure 9; Beth *et al.*, 1981b). This signal-to-noise permits measurements to be made on a number of membrane proteins in their natural membranes.

At K-band (22 GHz), the G-tensor anisotropy is 27 gauss and the V_1 spectrum reflects the nonaxial magnetic interactions (Figure 16, upper panel). The X turning point is positioned downfield from the Z turning point, which is positioned midway

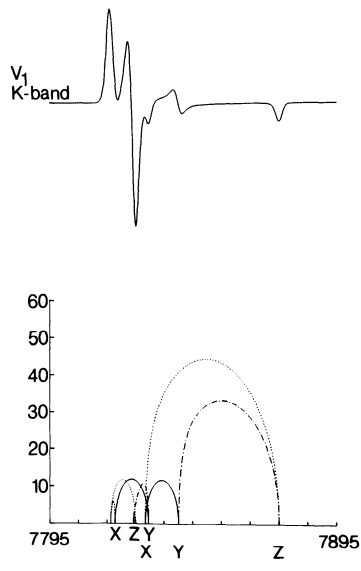

Figure 16. Relationship between line-shape features in the V_1 display and regions of predicted motional sensitivity of V_2' for nitrogen-15 spin labels at K-band. Upper: Computed V_1 spectrum. Lower: Plots of absolute value of change in resonance condition (H_{res}) versus field position for rotations about the three nitroxide principal axes. (· · · ·) $|[\delta H_{res}(m_i)/\delta\theta]_{\phi=0}|$; (· - · - ·) $|[\delta H_{res}(m_i)/\delta\theta]_{\phi=90}|$; and (——) $|[\delta H_{res}(m_i)/\delta\phi]_{\theta=90}|$ for $m_i = -\frac{1}{2}$ and $+\frac{1}{2}$. Values on the ordinate are gauss rad^{-1}. Simulation parameters were: $A_{xx} = 10.6$ G; $A_{yy} = 10.4$ G; $A_{zz} = 50.15$ G; $g_{xx} = 2.0091$; $g_{yy} = 2.0061$; $g_{zz} = 2.0022$; $\nu_0 = 22.0$ GHz; $h_1 = 0.01$ G; $T_{2e} = 100$ ns; $T_{1e} = 15$ μs; $\tau_r = \infty$; $\nu_m = 100$ kHz; $h_m = 0.5$ G. The V_1 spectrum was post-broadened with a Gaussian function of 0.9 G half-width.

between X and Y in the $m_i = -\frac{1}{2}$ nuclear manifold. The X-Y anisotropy is increased to approximately 12 gauss and hence the region of the V_2' spectrum in the vicinity of the Z turning point for this manifold is very sensitive to motions which interconvert nitroxide X and Y axes. There is no directly observable counterpart to the L'' and L regions of the X-band spectrum at this frequency. However, the H'' and H regions are preserved and provide high sensitivity to motions which interconvert the nitroxide X-Z and Y-Z axes (Figure 17, left). Sensitivity of K-band V_2' spectra to rotational motion which interconverts the nitroxide X and Y axes has been investigated in the modeling work of Beth *et al.* (1983) as shown in Figure 17, right. Spectral intensity at the position designated I', which is measured from the spectrum at the field position of the Z turning point of the $m_i = -\frac{1}{2}$ manifold, is a very sensitive monitor of $\tau_\parallel$ ($\Theta_t = 0°$) for the uniaxial diffusion model presented. Though K-band measurements hold the potential for providing substantial insight into anisotropic rotational diffusion, particularly with nitrogen-15 spin labels, experimental V_2' signals at this microwave frequency have not been reported. This is largely due to the paucity of EPR spectrometers in research laboratories at the present time which operate at this microwave frequency.

Since experimental measurements of the V_2' signal at K-band are currently lacking, it is difficult to estimate how signal-to-noise at this frequency will compare with spectrometers operating at X-band. However, it is anticipated that problems of small sample size for aqueous samples experienced at Q-band will be somewhat less severe at K-band.

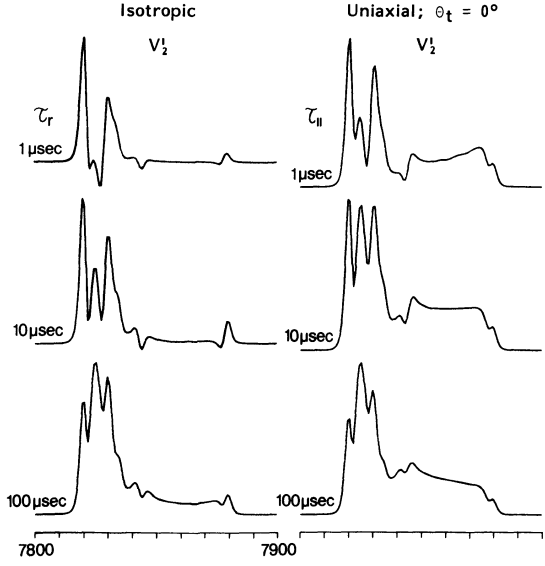

Figure 17. Dependence of K-band V_2' line shapes on rotational correlation times. Computations were carried out for the rotational correlation times and labeling geometries indicated. Additional parameters included: $A_{xx} = 10.6$ G; $A_{yy} = 10.4$ G; $A_{zz} = 50.15$ G; $g_{xx} = 2.0091$; $g_{yy} = 2.0061$; $g_{zz} = 2.0022$; $\nu_0 = 22.0$ GHz; $h_1 = 0.2$ G; $T_{2e} = 40$ ns; $T_{1e} = 25$ μs; $\nu_m = 50$ kHz; and $h_m = 5.0$ G (effective). Each spectrum was post-broadened with a Gaussian function of 0.9 G half-width. (Adapted from Beth *et al.*, 1983.)

To date, Q-band has been the primary alternative to X-band for EPR and ST-EPR investigations of spin-labeled biomolecules (Johnson and Hyde, 1981; Johnson *et al.*, 1982a, 1982b; Fung and Johnson, 1983; Thiyagarajan and Johnson, 1987). At Q-band, the G-tensor anisotropy is approximately 42 gauss and is thus roughly equivalent to the A-tensor anisotropy for nitrogen-15 spin labels. The X and Y turning points are positioned downfield from the Z turning point in the $m_i = -\frac{1}{2}$ nuclear manifold and the X-Y anisotropy is on the order of 18 gauss (Figure 18, upper). Johnson *et al.* (1982b) have examined the spectral behavior of both the V_2' and U_1' ST-EPR signals with nitrogen-15 spin labels as a function of isotropic rotational correlation time. As shown in Figure 19, spectral amplitudes at field positions labeled A', B', and E' in the V_2' signals were very sensitive monitors of the rotational correlation time. The parameter A' provides sensitivity to the rate at which molecular motion is sweeping the nitroxide X axis into the Y-Z plane while the spectral amplitude at field position A is the X turning point for the $m_i = -\frac{1}{2}$ nuclear manifold. Therefore, the ratio parameter A'/A should provide high sensitivity to Y- and Z-axial rotational diffusion processes. The parameter E' provides sensitivity to motions which rotate the nitroxide Z axis into the X-Y plane while the spectral amplitude at E corresponds to the Z turning point for the $m_i = +\frac{1}{2}$ nuclear manifold. Thus, the ratio parameter E'/E, which corresponds to H''/H in the scheme of Thomas *et al.* (1976), provides sensitivity to X- and Y-axial motion. The parameters B' and B are measured at field positions which contain motional information from rotations about all three nitroxide axes.

It should be noted that while Q-band provides high sensitivity to motion, particularly motion which interconverts nitroxide X and Y axes, the experimental signal-to-noise of the V_2' signal using commercially available resonators is reduced by approximately an order of magnitude relative to X-band (Johnson *et al.*, 1982b). This may not be a severe limitation for studies of highly soluble proteins which can be isolated in large quantity. However, it becomes a critical consideration for membrane proteins,

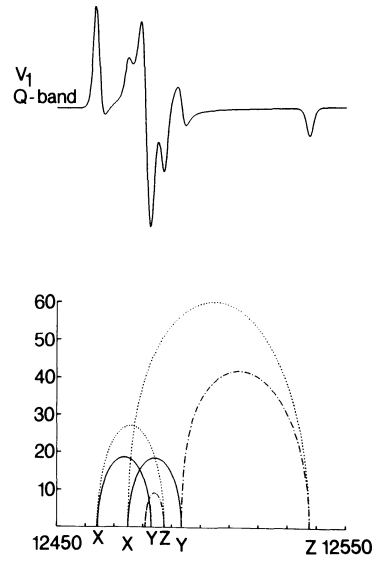

Figure 18. Relationship between line-shape features in the V_1 display and regions of predicted motional sensitivity of V_2' for nitrogen-15 spin labels at Q-band. Upper: Computed V_1 spectrum. Lower: Plots of absolute value of change in resonance condition (H_{res}) versus field position for rotations about the three nitroxide principal axes. (· · · · ·) $|[\delta H_{res}(m_i)/\delta\theta]_{\phi=0}|$; (· - · - ·) $|[\delta H_{res}(m_i)/\delta\theta]_{\phi=90}|$; and (——) $|[\delta H_{res}(m_i)/\delta\phi]_{\theta=90}|$ for $m_i = -\frac{1}{2}$ and $+\frac{1}{2}$. Values on the ordinate are gauss rad^{-1}. Simulation parameters were: $A_{xx} = 10.6$ G; $A_{yy} = 10.4$ G; $A_{zz} = 50.15$ G; $g_{xx} = 2.0091$; $g_{yy} = 2.0061$; $g_{zz} = 2.0022$; $\nu_0 = 35.0$ GHz; $h_1 = 0.01$ G; $T_{2e} = 100$ ns; $T_{1e} = 15\ \mu$s; $\tau_r = \infty$; $\nu_m = 100$ kHz; $h_m = 0.5$ G. The V_1 spectrum was post-broadened with a Gaussian function of 0.9 G half-width.

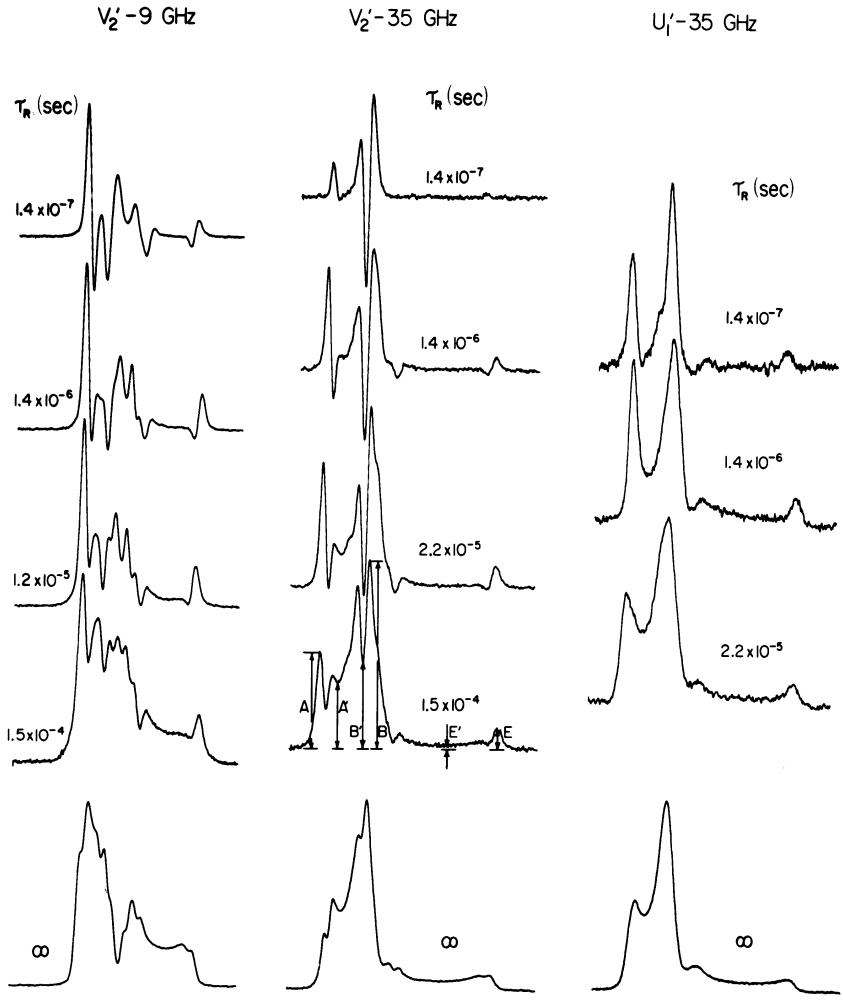

Figure 19. Dependence of nitrogen-15 V_2' and U_1' Q-band spectra on τ_r. The experimental spectra shown were obtained from [^{15}N, ^{2}H]maleimide spin-labeled hemoglobin in glycerol/buffer solutions of different viscosities. Field positions where motionally sensitive ratio parameters A'/A, B'/B, and E'/E are measured from the V_2' spectrum are defined in the 150 μs spectrum in the center column. (From Johnson *et al.*, 1982b.)

particularly when it is desired to investigate their dynamics in natural cell membranes where their concentrations are often very low. Another consideration for analyzing Q-band experimental data is that computer simulations of V_2' spectra are very CPU intensive, even when using nitrogen-15 spin labels. Convergence requires coupling over much higher N and L indices (of the Wigner matrix elements; Robinson and Dalton, 1980) than is required at X- or even K-band. Computation of V_2' signals at Q-band will likely require access to a supercomputer in order to obtain convergence of computed

data in a resonable time period. Moreover, the sensitivity to motion, particularly the E'/E parameter, is reduced relative to H''/H at X-band because the anisotropy is larger. This points out the approximate nature of employing $\delta H_{res}/\delta\Omega$, as shown in Figure 18, bottom, as the sole indicator of motional sensitivity. Equation (43) shows that one needs to consider that as the anisotropy increases, the sensitivity of the extrema regions can become less and that the spectral sensitivity is eventually compromised by fields as high or higher than Q-band.

7.2. Altering Sensitivity to Motion by Selection of ν_m

Early work by Hyde and Dalton (1972) demonstrated that the U_1' ST-EPR signal was very sensitive to the Zeeman field modulation frequency, $\nu_m = \omega_m/2\pi$, employed to collect the data. Hyde and Thomas (1973) subsequently examined the V_2' signal at reference modulation frequencies of 5 and 50 kHz. For both ST-EPR signals, it was observed that the experimental line shape gave the appearance of faster apparent motion as the reference modulation frequency was lowered from 100 kHz to 1 kHz. Thomas *et al.* (1976) indicated that the optimum sensitivity to rotational motion was provided when the product of modulation frequency and rotational correlation time was approximately equal to unity (i.e., when $\omega_m\tau_r \sim 1$). Hemminga *et al.* (1984c) have explored the effect of modulation frequency on various ST-EPR spectral displays. Dalton and Trommer were able to take advantage of the modulation frequency dependence of the V_2' signal to optimize sensitivity to changes in rotational diffusion of lactate dehydrogenase resulting from binding of substrates (summarized in Robinson *et al.*, 1985). However, ST-EPR studies to date have been carried out almost exclusively at a standard reference modulation frequency of 50 kHz with detection of the second-harmonic absorption signal at 100 kHz. This is the result of a number of factors, but perhaps the most critical one is that many commercial spectrometers were designed to detect the second-harmonic signal only at the 50 kHz setting. If it was desired to explore the variable motional sensitivity resulting from modulation at a different frequency, it was necessary to modify the existing signal channel or to replace it with a lock-in amplifier system.

Commercial EPR spectrometers are now available which provide a number of reference modulation frequencies in the 1 kHz to 100 kHz range. Thus, it is important to define how ST-EPR signals depend on the reference modulation frequency and how this dependence can be employed to optimize characterization of the rotational diffusion of spin-labeled proteins. Behavior of the V_2' signal from nitrogen-15 spin-labeled proteins have been examined at a number of reference modulation frequencies in the 1 kHz to 100 kHz range (Beth *et al.*, 1987). The experimental and calculated data presented in Figure 20 illustrate that, as the modulation frequency is lowered in this range, the line shapes evolve monotonically to an apparent faster rotational correlation time by comparison with reference spectra collected at the standard 50 kHz setting (Figure 7). The sensitivity of the V_2' signal from nitrogen-15 spin labels as a function of reference modulation frequency is summarized in the ratio parameter plots shown in Figure 21.

The experimentalist has the option of choosing the modulation frequency which provides the greatest sensitivity to motion in the correlation time range expected for the system under study. Clearly, the 100 kHz ratio parameters provide the highest

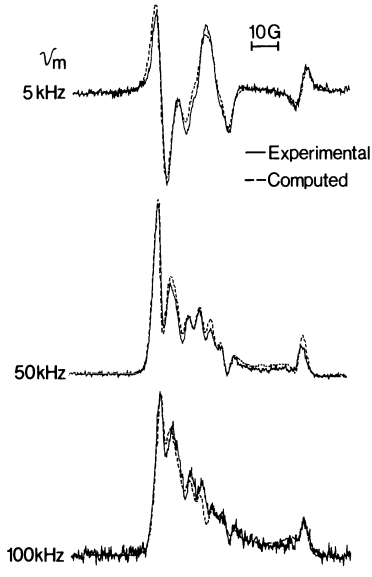

Figure 20. Dependence of nitrogen-15 V_2' signals on ν_m. Experimental spectra (solid lines) were obtained from [^{15}N,$^{2}H_{17}$]maleimide spin-labeled glyceraldehyde-3-phosphate dehydrogenase at reference Zeeman modulation frequencies of 5, 50, and 100 kHz. The rotational correlation time for the protein from molecular dimensions and measured solvent viscosity is 20 μs. The superimposed dashed lines were computed using input parameters: A_{xx} = 10.62 G; A_{yy} = 10.38 G; A_{zz} = 50.15 G; g_{xx} = 2.0091; g_{yy} = 2.0061; g_{zz} = 2.0022; h_1 = 0.2 G; ν_0 = 9.45 GHz; T_{1e} = 50 μs, 25 μs, and 15 μs; T_{2e} = 60 ns, 40 ns, and 40 ns for the upper, middle, and lower spectra, respectively. Each computed spectrum was post-broadened with a Gaussian function of 0.9 G half-width.

sensitivity to isotropic rotational correlation time throughout the very slow motional region. At higher modulation frequencies, the low-field region of the V_2' signal (L''/L region) coalesces into a single peak such that measurement of L''/L becomes more difficult. At very high modulation frequencies, the V_2' line shape closely resembles U_1' with significant loss of spectral structurings. The desirability of recording spectra at modulation frequencies other than 50 kHz will depend on the nature of the study being conducted. In those cases where macromolecular associations are being studied and the complex is characterized by a rotational correlation time only slightly longer than that of the unassociated species, then optimization of sensitivity by selection of modulation frequency may be very important. The family of ratio parameter curves provided in Figure 21 will serve as a guide in selecting the optimum modulation frequency.

8. ANALYSIS OF OVERLAPPING MOTIONAL SPECIES

In spin-labeling applications, experimental spectra are often obtained which are indicative of the presence of two or more motional species. The approach of choice for analyzing composite spectra from cw-EPR and cw-ST-EPR studies depends upon the characteristic rotational correlation times of the individual components. Methods for analyzing systems exhibiting one fast (ns) component in the presence of a very slow ($\geq\mu$s) component are considered first, and then methods which potentially may be useful for analyzing two very slow components will be outlined.

8.1. One Fast and One Slow Motional Component

In this case, both the V_1 and V_2' spectrum will exhibit a motionally narrowed component which normally is visually distinct from the slow motion signal, provided

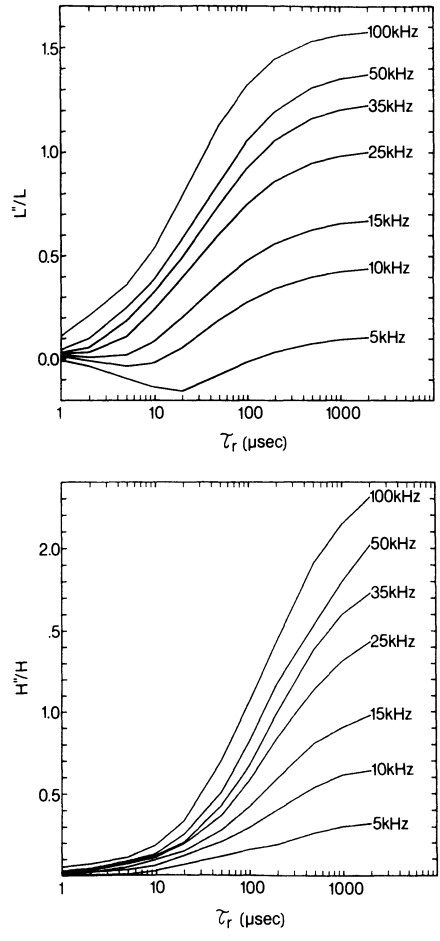

Figure 21. Dependence of L''/L and H''/H on τ_r for different ν_m values. Ratios shown were obtained from computed V_2' spectra as shown in Figure 20. All input parameters for the computations were the same, except that T_{1e} and T_{2e} were scaled to the modulation frequency (Robinson, 1983) using a value of 15 μs for the intrinsic T_{1e}.

that the correlation time for the fast component is shorter than about 5 ns. If the objective of the study is to observe and analyze the slow component without interference from the fast component, then a number of different approaches can be pursued. First, Graceffa and Seidel (1980) have shown that treatment of a protein with $K_3Fe(CN)_6$ can result in selective reduction of partially immobilized spin labels bound to surface or exposed residues under favorable conditions. However, Thomas and Cooke (1980) found that such treatment can also result in unwanted reduction of the strongly immobilized component. Next, the partially immobilized component can be suppressed by numerically taking the first integral of the V_2' spectrum before data analysis (Evans, 1981; Horváth and Marsh, 1983; Squier and Thomas, 1986) or by recording and analyzing the U_1' signal in place of V_2' provided that available hardware capabilities permit acquisition of this signal (Thomas *et al.*, 1983). Finally, the contribution of the partially immobilized component can be digitally subtracted from the composite (Jost *et al.*, 1971; Fung and Johnson, 1983; Robinson *et al.*, 1985; Beth *et al.*, 1986). Of the

approaches listed, digital subtraction is probably the most straightforward and universally applicable, since most modern EPR spectrometers have the capability to record signals digitally using attached microcomputer systems. The most difficult aspect of the subtraction procedure is obtaining a digital record of the partially immobilized component free of the immobilized one for use in the subtraction procedure. However, this can normally be accomplished by varying the labeling procedure through including known inhibitors and/or substrates. The use of deuterium-substituted spin labels, be they nitrogen-15 or nitrogen-14, will facilitate visual resolution of different spectral components due to the decreased linewidths (Beth *et al.*, 1980, 1984) thereby enabling more reliable estimation of the end point in the subtraction procedure. The only caveat for use of deuterium-substituted labels for improved end-point determination in spectral subtractions is that decreased linewidths are *not* observed if the motional times are on the order of 5 to 10 ns (Beth *et al.*, 1980). In this range of correlation times, the homogeneous broadening by the motion overwhelms the inhomogeneous proton or deuteron broadening, resulting in indistinguishable line shapes from the hydrogen- and deuterium-containing spin labels.

8.2. Two or More Slow Motional Components

In the case where all motional components present are characterized by rotational correlation times longer than about 0.1 μs, there will normally be no obvious visual resolution of motional species in the cw V_1, V_2', or U_1' displays. Thus, even if the line shape for one of the motional species present is known, it is still not possible to subtract it from the composite at the correct stoichiometry to obtain the line shape for the second slow-motion species, since there is no way of knowing the end point in the subtraction without additional, independent data.

Two different spin-labeling approaches show potential applicability for analyzing composite very slow motion systems. First, measurement in the time domain such as saturation recovery EPR (SR-EPR; Fajer *et al.*, 1986) on spin-labeled proteins has indicated that rotational correlation times in the 1 to 15 μs window can be quantitated. Since signals are collected in the time domain, sensitivity to motions which decay with different characteristic times may be observable directly, thereby allowing resolution. Sensitivity of saturation recovery measurements with nitrogen-15 spin labels will be covered in Section 10 below. The second method which has been explored involves analysis of cw V_2' data collected on the system under investigation at Zeeman field modulation frequencies in the 1 to 100 kHz range by a least-squares fitting procedure (Beth *et al.*, 1987).

The experimental and computed data presented in Figures 20 and 21 show that, for a constant motional rate, spectral amplitudes at motionally sensitive positions of V_2' (Figure 4) decrease monotonically as the reference modulation frequency is lowered. The rate at which the parameters increase with increasing motional frequency is proportional to the modulation frequency. Thus, if two motional components characterized by rotational correlation times τ_a and τ_b are present in a sample, then they will contribute a different fractional percent of signal intensity to the composite at the different modulation frequencies. Coffey *et al.* (1976) and Hemminga *et al.* (1984c) pointed out that, by varying the modulation frequency, it should be possible to increase or decrease the contribution of one motional component to the composite spectrum

thereby potentially allowing separation of overlapping species. The applicability of such an approach for spin-labeling studies has been explored with encouraging results (Beth *et al.*, 1987). One multiple modulation frequency approach for analyzing multicomponent systems can be formally defined as follows.

Two isotropic motional species characterized by rotational correlation times τ_a and τ_b (τ_a and $\tau_b \geq 1\ \mu s$) will give rise to a composite V_2' spectrum, where the motionally sensitive ratio parameters L''/L and H''/H are determined by contributions from each component spectrum weighted according to its mole fraction, f_a or f_b, present. The composite ratio parameters are given at each modulation frequency in terms of spectral amplitudes of the components and their mole fractions as

$$\left(\frac{L''}{L}\right)_{\omega_m}^{\text{comp}} = \left(\frac{fL''_{\tau a} + (1-f)L''_{\tau b}}{fL_{\tau a} + (1-f)L_{\tau b}}\right)_{\omega_m} \tag{54}$$

and

$$\left(\frac{H''}{H}\right)_{\omega_m}^{\text{comp}} = \left(\frac{fH''_{\tau a} + (1-f)H''_{\tau b}}{fH_{\tau a} + (1-f)H_{\tau b}}\right)_{\omega_m} \tag{55}$$

where the mole fractions have been expressed as $f_a = f$ and $f_b = (1-f)$ for contributions from motional species a and b, respectively. The problem to be solved is to determine the three independent variables, τ_a, τ_b, and f (i.e., the rotational correlation times for the two species and their relative abundance) from the ratio parameters experimentally measured at each of the separate modulation frequencies.

Analysis of two (or more) motional components by this method begins with establishing a basis set of model isotropic motion spectra at rotational correlation times which span the possible values for the components expressed in the composite. An iterative least-squares fitting procedure is then employed to compute theoretical values of the composite ratio parameters for all unique permutations of τ_a, τ_b, and f according to the above expressions. The theoretical values are compared with actual experimental observations by difference to provide a set of residuals,

$$R(L''/L)_{\omega_m} = (L''/L)_{\omega_m}^{\text{exp}} - (L''/L)_{\omega_m}^{\text{comp}} \tag{56}$$

$$R(H''/H)_{\omega_m} = (H''/H)_{\omega_m}^{\text{exp}} - (H''/H)_{\omega_m}^{\text{comp}} \tag{57}$$

which are employed to compute the sum of residuals squared,

$$\sum R^2 = \sum_{\omega_m} R(L''/L)_{\omega_m}^2 + R(H''/H)_{\omega_m}^2 \tag{58}$$

The best fit of the experimental data is taken as those values of the independent variables which provide the minimum $\sum R^2$. Figure 22 shows the results of analyses of two theoretical two-component systems using this iterative least-squares approach (Beth *et al.*, 1987, 1989).

It is significant that the method predicts a unique fit of the data with no local minima. It would be straightforward to consider other approaches to fitting the data set obtained as a function of modulation frequency including the use of other ratio parameters, other microwave frequencies, and other motionally sensitive signals such

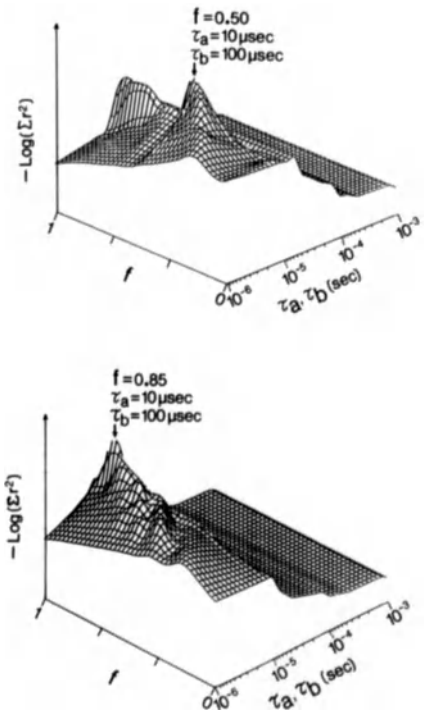

Figure 22. Surface plots of $\sum R^2$ versus τ_a, τ_b, and f. Computed V_2' spectra for isotropic motional models characterized by rotational correlation times of 10 and 100 μs were added digitally at mole fractions of 0.5 (upper) and 0.85 (lower) of the 10 μs component. The resulting composite V_2' signals at 5, 10, 15, 25, 50, and 100 kHz reference modulation frequencies were plotted and the ratio parameters $(L''/L)_{\omega_m}$ and $(H''/H)_{\omega_m}$ determined graphically from each. An iterative procedure was employed to compute theoretical ratios according to equations (54) and (55) and, from these, a value for $\sum R^2$ was computed according to equation (58). The plots show the $-\log(\sum R^2)$ versus unique combinations of f, τ_a, and τ_b. Thus, minima in $\sum R^2$ are displayed as peaks in the surface plots. The basis set of spectra used to obtain theoretical ratio parameters was computed as described in Figures 20 and 21.

as U_1'. Moreover, the method should provide reliable analyses regardless of whether nitrogen-14 or nitrogen-15 labels are employed. However, it should be noted that the absolute amplitudes of the basis spectra at positions L, L'', H'', and H are required for computation of composite ratios with equations (54) and (55). If experimental spectra are to be employed for generation of the basis spectra, they will have to be collected under very standardized machine settings at known concentrations in order to provide accurate results. Since rotational correlation times of model systems are normally altered by changing buffer composition and/or temperature (Thomas *et al.*, 1976), careful calibrations will need to be performed. Alternatively, the basis spectra can be computed (Figure 7) in which case the data set will be internally consistent. Given the large number of spectra which must be computed to uniformly span the correlation time range from 1 μs to 1 ms, nitrogen-15 spin labels provide a significant advantage over their nitrogen-14 counterparts due to the factor-of-eight reduction in CPU time required to carry out the corresponding computations (Robinson and Dalton, 1980).

It is possible to linearize the problem to be solved by transforming from true mole fractions to parameters which depend only upon f_a, f_b, and the amplitude of one of the turning points in the V_2' spectrum. Specifically, by modifying equations (54) and (55) appropriately, the composite ratio parameters can be written as

$$(L''/L)^{\text{comp}}_{\omega_m} = \chi_a(L''/L)_{\omega_m,a} + \chi_b(L''/L)_{\omega_m,b} \tag{59}$$

$$(H''/L)_{\omega_m}^{comp} = \chi_a(H''/L)_{\omega_m,a} + \chi_b(H''/L)_{\omega_m,b} \tag{60}$$

where

$$\chi_a = [f_a L_a/(f_a L_a + f_b L_b)] \tag{61}$$

and

$$\chi_b = [f_b L_b/(f_a L_a + f_b L_b)] \tag{62}$$

Like the true mole fractions, $\chi_a + \chi_b = 1$, and the problem becomes fitting the experimental ratio parameters $(L''/L)_{\omega m}$ and $(H''/L)_{\omega m}$ with the best values for τ_a, τ_b, and χ. The potential advantages of the linearization over the previous formalism are: (1) experimentally determined ratio parameters can be employed which are concentration

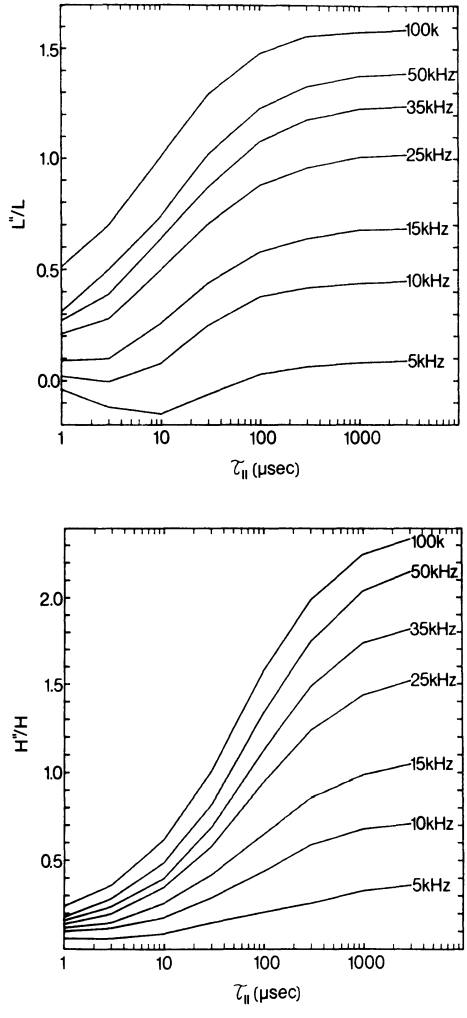

Figure 23. Dependence of ratio parameters on $\tau_\parallel$ for a uniaxial rotational diffusion model as a function of ν_m. The ratios shown were measured from computed spectra for a diffusion model characterized by $\tau_\perp$ = 0.1 s and the indicated values for $\tau_\parallel$. The nitroxide principal-axis system was tilted by $\Theta_{yy} = 90°$ from the $\tau_\parallel$ axis. All other simulation parameters were the same as listed in Figure 20.

independent and (2) the optimization of χ can now be solved analytically by linear least-squares methods. It will still be necessary to have absolute amplitudes for L as a function of τ_r in order to transform the quantities χ thus determined back into true mole fractions using equations (61) and (62). Again, these values can be obtained from computed model spectra or from carefully collected experimental model spectra.

The data presented provide impetus for further investigations of experimental applications of these formalisms. Other variations of these general themes may also be applicable.

It may be possible to extend these formalisms to analysis of overlapping spectra from anisotropically diffusing systems. The plots shown in Figure 23 illustrate how the ratio parameters for a uniaxial diffusion model ($\Theta_t = 90°$) vary with $\tau_\parallel$ for modulation frequencies in the 5 kHz to 100 kHz range. Given this sensitivity, composite V_2' signals collected at a number of modulation frequencies should allow unique fitting of the data by a similar approach. In the case of anisotropic diffusion, it will be necessary to compute the basis spectra, since suitable protein model systems do not exist and therefore nitrogen-15 spin labels will greatly facilitate the studies. Many of the characteristics of this approach remain to be established through experimental studies. Certainly there are many opportunities for studies in this area and also in the area of correlation of results with analyses from time-domain techniques, such as saturation recovery.

9. COMPUTER MODELING OF NITROGEN-14 V_2' SIGNALS

Since the majority of spin-labeling studies of very slow protein motion by ST-EPR spectroscopy have recorded the V_2' signal using nitrogen-14 spin labels, it is appropriate to outline prospects for quantitative analyses of these data. We have carried out simulations of V_2' spectra obtained from proteins labeled with nitrogen-14 spin labels. The calculations have been done at the same level as those previously reported for nitrogen-15 spin labels (Beth *et al.*, 1983; Robinson *et al.*, 1985). In the case of nitrogen-14 one has three secular terms, three pseudosecular terms, and a saturation term associated with each (Robinson *et al.*, 1985). Thus, the size of the computational problem for nitrogen-14 spin labels at this level is twice that of the nitrogen-15 problem, and hence the computation time is 8 times longer using matrix inversion algorithms (Robinson and Dalton, 1979, 1980).

9.1. Isotropic Motion Simulations

Figure 24 shows overlays of experimental and computed V_2' signals obtained from a spin-labeled protein undergoing isotropic rotational diffusion in the range of correlation times from 1 to 100 μs. The nitrogen-14 spin label employed for the measurements shown contained deuterium in place of hydrogen on the nitroxide ring system, thereby providing high resolution of spectral features (Beth *et al.*, 1980). Simulation of experimental results is very good in every region of the spectrum except the high- and low-field extrema, with deviations in these regions being very apparent at the faster correlation times.

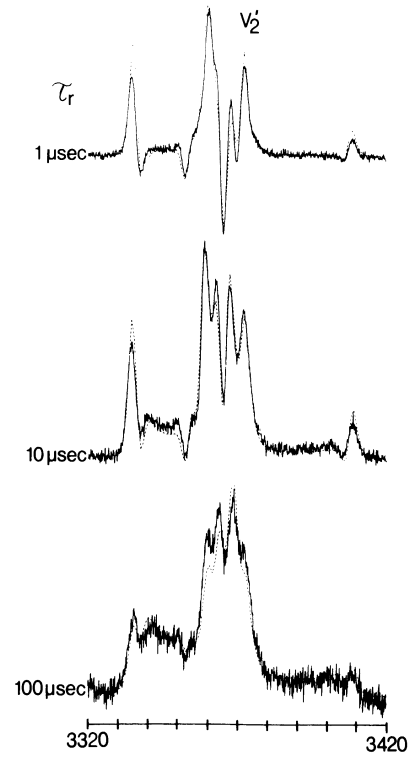

Figure 24. Dependence of experimental and computed V_2' line shapes on τ_r with nitrogen-14 spin labels. Experimental spectra (solid lines) were obtained from [^{14}N, $^{2}H_{17}$]maleimide spin-labeled glyceraldehyde-3-phosphate dehydrogenase (r_h = 41 Å) in 50% glycerol, 75% glycerol, and 89% glycerol from top to bottom. Rotational correlation times were determined from the hydrated radius of the protein and measured solvent viscosities using equation (13). Computed spectra (dashed lines) are overlaid on the experimental results. Experimental spectra are 100 gauss in width and are normalized to the same total amplitude. Simulation parameters included: A_{xx} = 7.65, 7.40, 7.70 G; A_{yy} = 7.65, 7.40, 7.60 G; A_{zz} = 35.95, 35.90, 35.90 G; g_{xx} = 2.0089, 2.0092, 2.0089; g_{yy} = 2.0058, 2.0061, 2.0060; T_{1e} = 25 μs; T_{2e} = 40 ns; h_1 = 0.2 G; ν_0 = 9.45 GHz; ν_m = 50 kHz; h_m = 5.0 G (effective); and the indicated rotational correlation times for the upper, middle, and lower spectra, respectively. Each computed spectrum was post-broadened with a Gaussian function of 0.9 G half-width.

Since the computations shown in Figure 24 are analogous to the calculations with nitrogen-15 spin labels shown in Figure 7, one might expect to have the same excellent agreement between theory and experiment for the nitrogen-14 spin label. The question is then: why does the simulation disagree with the experimental data in this one feature when using nitrogen-14? From the nature of the discrepancy, it appears that one could bring the experimental and computed results into agreement by incorporating an orientation-dependent linewidth which was wider at the Z turning points than at X and Y. The incorporation of such a feature is done routinely by Freed and co-workers (Polnaszek and Freed, 1975) in the simulation of linear EPR spectra for nitrogen-14 spin labels.

An additional, differential broadening of about 1 gauss at the Z turning points relative to X and Y for the three nuclear manifolds will account for the observed discrepancy. One possible explanation for the disagreement could be found in the inherent difference between nitrogen-14 and nitrogen-15. Since the gyromagnetic ratio is larger for nitrogen-15 than nitrogen-14, it seems reasonable that the dipolar and scalar terms are being treated correctly. However, nitrogen-14 has a quadrupole moment resulting in a term in the spin Hamiltonian of the form $I \cdot D_q \cdot I$, where the quadrupole tensor, D_q, is orientation-dependent. The magnitude of the quadrupolar coupling constant is around 2.8 MHz (Kevan and Kispert, 1976), which would result in a broadening of approximately 1 gauss at the unpaired electron. This term could explain the observed discrepancy if the orientation of the quadrupolar tensor to the dipolar

tensor were near 90°; this issue bears further investigation. Whatever the explanation for the observed anisotropic broadening, the computations indicate that, though the CPU times required are excessive (about 60 hours of VAX 11/780 time per computation), the agreement between experiment and theory is encouraging and the level of confidence in the computations is sufficient to warrant examination of a few selected anisotropic models.

9.2. Anisotropic Motion Simulations

The two anisotropic motional models shown in Figure 25 (center two spectra) serve to illustrate a number of important points, particularly those related to sensitivity of the central manifold of nitrogen-14 spin labels to minor-element (X, Y nitroxide axes) motional averaging. These spectra correspond to the same motional model. The difference between the two, indicated by Θ_t, is that the label is attached differently in the two cases, but the motion is the same. Comparison of the upper two spectra indicates that the C'/C ratio is determined in large part by the rate at which molecular motion is interconverting the nitroxide X and Z axes. This is in agreement with the predicted sensitivity of this manifold to orthogonal rotational motions shown in Figure 3, center. There is sensitivity to minor-element averaging in the C'/C region as illustrated by comparing the lower two spectra in Figure 25. This sensitivity is largely manifested in the low-field half of the central manifold in accordance with the predicted area of motional sensitivity. The motion in the center of the second spectrum appears faster than that of the third; yet the third one represents rapid minor tensor element averaging, while the second does not. Thus, it is not valid to assign changes in C'/C relative to changes in L''/L and/or H''/H to minor-element motions without further data on anisotropy of motion and spin-label binding geometry. Both nitrogen-14 and nitrogen-15

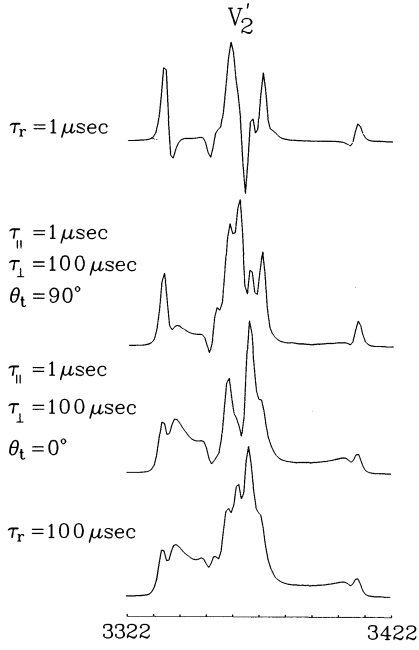

Figure 25. Dependence of nitrogen-14 V_2' line shapes on motional model. Isotropic models at 1 (upper) and 100 μs (lower) are reproduced from Figure 24. The center two spectra are computed for an anisotropic model with $\tau_{\|} = 1\ \mu$s and $\tau_{\perp} = 100\ \mu$s. In the second display the magnetic tensors are tilted by 90° ($\Theta_{yy} = 90°$) relative to the diffusion tensor. In the third spectrum, the magnetic and diffusion tensors are coincident. Simulation parameters for the two isotropic models are given in Figure 24. Parameters for the two anisotropic models are the same as for the isotropic model spectrum at 1 μs.

V_2' spectra contain a wealth of dynamics information which is manifested in line-shape changes throughout the span of the spectrum. However, in both cases, extraction of rotational correlation times for systems other than those characterized by spherical symmetry requires information on spin-label binding geometry before line-shape analysis can proceed by anisotropic model system analysis or by computer simulation. The interested reader is referred to an earlier computational paper by Robinson and Dalton (1981) where V_2' signals from a number of motional models were considered for nitrogen-14 spin labels. Though a number of approximations in the theory were employed in this work, the line shapes are in excellent agreement with those computed using the full matrix inversion approach presented in Figure 24. Particular attention should be given to the effects of deuteration of spin labels on resolution of spectral structurings indicative of the anisotropy of motion and spin-label binding geometry. If nitrogen-14 spin labels are to be employed in a study of anisotropic motion, the narrow linewidths afforded by deuterium-substituted probes will pay substantial dividends in motional information exhibited in the experimental spectra.

9.3. Signal-to-Noise Ratio and Motional Sensitivity of Nitrogen-15 versus Nitrogen-14 Spin Labels

For nitrogen-14 labels, the signal intensity is spread over three nuclear manifolds covering approximately 70 gauss, as opposed to two manifolds for nitrogen-15 which cover approximately 50 gauss. With nitrogen-14 labels, the three nuclear manifolds are severely overlapping in the center of the spectrum (Figure 3). Superficially, this might lead to the conclusion that the nitrogen-14 V_2' signal provides much lower signal-to-noise than nitrogen-15. However, Beth *et al.* (1981a) showed that the narrow central region of the V_2' spectrum using nitrogen-14, hydrogen spin labels (which is dominated by the $m_i = 0$ nuclear manifold) is actually down in signal-to-noise by about a factor of three relative to the low-field manifold of V_2' from nitrogen-15, deuterium-substituted labels throughout the very slow motional range. Therefore, the C'/C ratio parameter (Thomas *et al.*, 1976) provides a reasonable signal-to-noise ratio relative to nitrogen-15 labels. The C'/C ratio parameter has also been shown to change over a wide range of values (Figure 5, lower) as a function of τ_r in the very slow motional range. As shown in Figure 3, this region of the nitrogen-14 spectrum arises from regions of overlap from the three nuclear manifolds. Hence, it is very likely that small changes in values for the A and G tensor elements will result in significant alterations in the experimentally determined value for C'/C. A systematic examination and quantitation of the dependence of this parameter on tensor values has not been published to date. It should be noted that changes in tensor values should be characterized before data analyses based solely upon C'/C are considered reliable.

Investigations have often relied more heavily upon motional sensitivity in the extrema regions of the V_2' spectrum as exhibited by the L''/L and H''/H ratio parameters (Figure 3). If this practice is followed, then the nitrogen-15, deuterium-substituted labels provide a significant signal-to-noise advantage (Figure 9) with little, if any, loss of sensitivity to very slow motions (compare Figures 5 and 8). The computerized simulations of ^{14}N, DMSL are related to the biochemical investigations detailed in Chapter 11 by J. Park and W. Trommer (see pages 549–559) and the choice of isotopic spin labels for specific experimental conditions (see pages 563–564).

10. SATURATION RECOVERY EPR STUDIES WITH NITROGEN-15 SPIN LABELS

Recently, there has been increasing interest in applying time-domain techniques to examine the response of spin-labeled systems to different motional processes. Freed, Schwartz, and co-workers have developed methods to observe spin echoes from nitroxide radicals, and have thereby measured motionally-dependent spin–spin dephasing times (T_{2e}) which depend on the type of motion and the characteristic motional rates (Stillman *et al.*, 1980; Stillman and Schwartz, 1981; Schwartz *et al.*, 1986). Hyde and co-workers have developed approaches for performing time-domain ELDOR and, as a model system, have measured the recovery rates of nitroxide spin labels in paraffin oil (Hyde *et al.*, 1984). Fajer *et al.* (1986) have measured the spin–lattice relaxation times of spin-labeled hemoglobin and have estimated the rotational rates from the saturation-recovery relaxation data. We have performed similar saturation-recovery experiments on nitrogen-15 spin-labeled glyceraldehyde-3-phosphate dehydrogenase using a recently developed computer-controlled SR-/ST-EPR spectrometer (Mailer *et al.*, 1985; Robinson *et al.*, 1987). In the following sections, results from these early studies will be presented in the framework of the theory employed to extract motional information from nitrogen-15 spin-labeled macromolecules.

SR-EPR is an important technique for spin labeling for two reasons. First, it can be employed to unambiguously determine T_{1e} (i.e., the motion-independent spin–lattice relaxation time) needed for computations of cw-ST-EPR spectra. Second, it is possible that SR-EPR will ultimately be more sensitive than cw-ST-EPR for characterizing very slow rotational diffusion of spin-labeled proteins and other macromolecules. At present, it is clear that motional information can, in principle, be extracted from the SR-EPR data for spins at a given orientation relative to the external magnetic field. The potential then exists for monitoring motion of a select subpopulation (from among a randomly distributed population) and eventually mapping out the entire motional profile. This approach may ultimately be preferred over cw-ST-EPR for defining the anisotropic nature of the motion and for resolving overlapping slow motional species.

The following sections provide a review of the SR-EPR experiment and of the results of theoretical analyses to explain the dependence of the recovery rates on motional processes as well as the intrinsic spin–lattice relaxation time, T_{1e}. In addition to a complete treatment of the simulation problem starting with the Stochastic Liouville Equation (SLE), some approximate, insightful, formulas for calculating the relaxation rate and the associated amplitude of each component will be reviewed. The theory applies to both nitrogen-14, hydrogen-containing spin labels and nitrogen-15, deuterium-substituted spin labels. However, discussions will focus on the nitrogen-15, deuterium-substituted spin labels, since the use of nitrogen-15 simplifies the theory significantly and deuteration removes the complication of extra relaxation introduced by protons (Stillman and Schwartz, 1979, 1981).

10.1. Overview of the Experiment

The SR-EPR experiment is a simple time-domain experiment. Let us consider the cw-EPR experiment designed to detect $\langle S_x \rangle$ or M_x (the dispersion signal) or $\langle S_y \rangle$ or M_y (the absorption signal), which are stationary in the rotating frame of the observer.

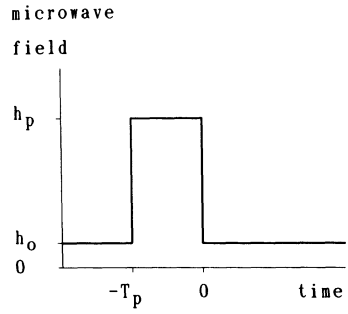

Figure 26. Diagram of pump and observer fields. In the saturation recovery experiment, the system comes to equilibrium with the observer field of low amplitude, h_0, prior to the pump period, which begins at time $-T_p$. The pump field is turned on by raising the amplitude to h_p for a time T_p. At time 0, the microwave field level is then reduced back to the observer level h_0, and the recovery signal is detected at time t from this point.

Signal intensity is observed as a function of field position for nitroxide spin labels as detailed in equations (34)-(36). The SR-EPR experiment requires one to first set the field frequency condition so that spins at a particular orientation with respect to the external field are on resonance with a weak observing field, h_0, to which the spins are responding linearly. Initially, the spin system is at equilibrium with the observing field (Figure 26). At a time $-T_p$, the intensity of the microwave field is increased to a higher, partially saturating level, h_p, and stays on for time T_p. At time zero, the microwave field is returned to its low observer level, h_0, and the time-dependent response is recorded. During the observation period (i.e., from time zero) the system is returning to equilibrium with the weak observing field. As shown in Figure 27, the observation period includes an initial FID decaying with time constant T_{2e} followed by a longitudinal recovery back to equilibrium with time constant T_{1e}. The case of a single line with no motion has been discussed extensively (Hyde, 1979).

10.2. Spectrometer Variables

There are many possibilities for varying spectrometer settings to alter the shape and information content of the recovery curves. As noted above, there is a choice of

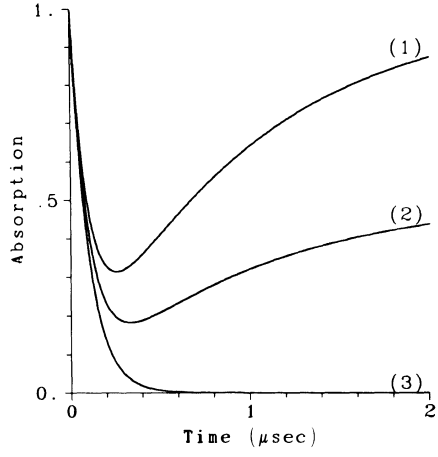

Figure 27. Representative theoretical saturation-recovery absorption signals at three observer levels. The following parameters have been employed in the computations: $H_0 = 3300$ G; $H_{res} = 3300$ G; $T_{1e} = 1.0\ \mu$s; $T_{2e} = 0.1\ \mu$s; $\phi = 85°$; $h_p = 1.0$ G; $T_p = 1.0$ s; and $h_0 = 0.01$, 0.005, and 0.0 G for curves (1), (2) and (3), respectively. Each curve [except (3)] is a biexponential decay with decay constants $1/T_{1e}$ and $1/T_{2e}$. The former (true recovery) component has a negative amplitude proportional to the observer field strength h_0, while the latter (free-induction decay) component is independent of h_0. Curve (3) is a pure free-induction decay signal and expressed as a single exponential curve with decay constant $1/T_{2e}$.

field position, pump time (T_p), and pump field strength (h_p). There are also various other possibilities: one may arbitrarily adjust the relative phase of the pump and the observer, and one may decide on a dispersion or absorption mode of detection for the observer. If time-domain, or pulsed, ELDOR are included, the field setting for the pump can be different from the field setting for the observer. There is obviously a variety of spectrometer settings that will affect the presentation of the SR-EPR data. Such a range of choices of spectrometer variables merits close examination in order to capitalize on the flexibility offered by the experiment for extracting motional information.

10.3. Strategies for Extraction of Motional Information

Fajer *et al.* (1986) and Robinson *et al.* (1987) have shown that one method for obtaining direct motional information is to employ a short pulse, long pulse procedure. By using this approach, the biexponential (or multiexponential) nature of the recovery curves can be seen if the pump pulse is "short," while with a long pump pulse the recovery curves can appear to be nearly single exponential. This has suggested that a variation of the T_p parameter will be a basis for obtaining meaningful motional information. The method of pulsed ELDOR (Hyde *et al.*, 1984) has shown that some of the exponential components of the recovery invert the sign, thereby suggesting a method for extracting information. Accordingly, Freed has suggested that a combination of pulsed ELDOR and SR-EPR might prove to be a valuable way to obtain motional information (Freed, 1974). Dispersion-mode detection SR-EPR also shows promise in that some components change sign as a function of field position, and hence one has the possibility of extracting the motional rates in this fashion. Robinson and co-workers (Robinson *et al.*, 1987; Sugano, 1987) have suggested that all approaches can be considered systematically by applying Principal Components and Target Factor Analysis to a set of data with different spectrometer settings, and treating that data set in a single data matrix.

10.4. Theory of Saturation Recovery

When considering the effects of motion, the spin response is best considered using the stochastic Liouville equation (SLE) approach. If the spectral diffusion is much faster or much slower than the spin–lattice relaxation rate, then, as has been analyzed previously (Hyde, 1979; Sugano *et al.*, 1987), and for sufficiently low observer power, a single exponential recovery signal at the natural T_{1e} is observed. In cases where spectral diffusion being driven by rotational diffusion is competing with the spin–lattice relaxation, the recovery signal is not, in general, a single exponential. To see how this comes about the general spin response problem, under SR conditions, is considered. The most general consideration begins with the SLE

$$\dot{\chi} = -\iota[H, \chi] - \Gamma_\Omega(\chi - \chi_0) - \Gamma_R(\chi - \chi_0) \tag{63}$$

The Hamiltonian contains the coherent interactions of the electron with the DC Zeeman field of the magnet and the microwave field, as well as the full tensorial interaction with the nitrogen nucleus; the deuterons are neglected in this treatment. Specifically,

$$H = H \cdot G \cdot S + I \cdot A \cdot S \tag{64}$$

The treatment which has generally been followed has been to retain all terms from the Hamiltonian which are stationary in a frame precessing with the electron. The nonsecular terms are treated indirectly in Γ_R. Retaining the terms as described in equations (30)–(36), the SLE is converted into a classical master equation by averaging over the spin variables. The spin variables of interest are $\langle S_+ \rangle$ and $\langle S_z \rangle$. Since $S_+ = S_x + iS_y$, the quantity $\langle S_+ \rangle$ contains the expectation value of both the x and y components of the magnetization (the dispersion and absorption components) which are time-independent in this rotating frame, and are the observed quantities.

Next, the real and imaginary parts of the complex quantities are separated and a set of real differential equations constructed which are of the form

$$\chi + A\chi = B \tag{65}$$

where χ, A, and B are defined as

$$\chi = \begin{vmatrix} \langle S_x \rangle \\ \langle S_y \rangle \\ \langle S_z \rangle \end{vmatrix}, \qquad B = \begin{vmatrix} 0 \\ q \\ 0 \end{vmatrix}, \qquad A = \begin{vmatrix} 1/T_{2e} + \Gamma_\Omega & \Delta(\Omega) & d \\ -\Delta(\Omega) & 1/T_{2e} + \Gamma_\Omega & -d \\ d & -d & 1/T_{1e} + \Gamma_\Omega \end{vmatrix} \tag{66}$$

The matrix A contains the relaxation components, the motional operator Γ_Ω, and the orientation-dependent resonance conditions for the spins. The quantity B is a vector containing the inhomogenous term q, which arises from the interaction of the spin system with the spectrometer's fields, and brings the system to an equilibrium state at infinite time. Quantity χ is a vector containing the elements of the density matrix, which are related to the various averages of the spin system, and some of which are proportional to the observables of the experiment: $\langle S_x \rangle$ and $\langle S_z \rangle$ are just two of the components of the vector χ. The quantity d is equal to $\gamma_e h$, where h is either h_0 during the observing period or h_p during the pumping period (Figure 26).

The evolution of the spin system under the conditions of the SR experiment has been considered in detail (Freed, 1979; Sugano, 1987). Therefore, details will be omitted in pointing out some of the important results. From the above expression, the case of the spin system relaxing during the observing period is

$$\chi(t) = \chi(\infty) + e^{-At}[\chi(0) - \chi(\infty)] \tag{67}$$

where $\chi(\infty)$ is the time-independent equilibrium (and cw) result; $\chi(0)$ is generated by the pump, during the time T_p, prior to observation. Therefore, it is required that the pump induce some deviation from equilibrium. A general observation about the transient part of the response is that the relaxation rates depend only on the relaxation in the observer time period (i.e., the eigenvalues of the A matrix during the observer period). Therefore, those components which relax the z component of the magnetization, in the limit of small observer amplitude, are not coupled to the transverse components; nor can the recovery *rates* depend in any way on how the pumping was performed. In fact, they are independent of *any* spectrometer setting.

The A matrix is separated into two parts during the observing period where h_0, or equivalently d, is very small. One part describes the evolution of the transverse components (or x and y components of the magnetization) which relax at rates $1/T_{2e}$

and motion which contributes to that (which is neglected), and the other contains the evolution of the diagonal (or z components) which relaxes at a rate determined by $1/T_{1e}$ as well as by the motion, which must compete with $1/T_{1e}$ as shown in equation (37). These two components are coupled only by the observer field, h_0. This is a very important point; there is no other coupling. Since $\langle S_y \rangle$ is detected, the only way to see the effect of $\langle S_z \rangle$ (and hence T_{1e} and motional processes on the order of T_{1e}) is through a coupling of $\langle S_z \rangle$ to $\langle S_y \rangle$. If $h_0 = 0$, one will not see any relaxation of the order of T_{1e}, due to the relaxation of $\langle S_z \rangle$ in $\langle S_x \rangle$. This may be further illustrated by diagonalizing the A matrix:

$$e^{-At} = P e^{-\Lambda t} P^{-1} \tag{68}$$

The A matrix can be written as a complex, but symmetric, form. This simplifies the diagonalization somewhat in that the inverse of P is the transpose of P. The Λ matrix, which is diagonal, contains the eigenvalues of A which are the recovery rates seen in the SR experiment. In the limit of low observer power, these rates are divided into two classes: one class is associated with T_{2e} for the transverse components and the other class is associated with T_{1e} for the z components of the magnetization. The diagonalizing matrix P can be visualized as composed of four separate matrices:

$$P = \begin{vmatrix} P_{0xy} & b \\ b' & P_{0z} \end{vmatrix} \tag{69}$$

where the P_{0xy} and P_{0z} matrices separately diagonalize the two major parts of the A matrix. The b and b' parts are now proportional to h_0. It is these two parts which couple the deviation of the z components from equilibrium, which is generated by the pump, to the observer, $\langle S_y \rangle$. Therefore, with low observer power, it is correct to assume that the slow components have amplitudes proportional to the observer amplitude. This is true regardless of the motional process.

Terms that contribute to the SR signal are those terms that relax through the z component of the magnetization and have a $1/T_{1e}$ intrinsic relaxation rate. In practice, these terms have amplitudes which are proportional to h_0. The FID terms may extend into the region of the recovery and compete with the true SR components. However, such terms are independent of the observer amplitude and can be removed by phase techniques (Hyde, 1979; Sugano, 1987). If the observer amplitude is zero, which is nearly the case, then it is rigorously correct that $\langle S_z \rangle$ relaxes completely uncoupled from the other terms. Therefore, $\langle S_z \rangle$ obeys the equation

$$\langle \dot{S}_z \rangle = -(1/T_{1e} + \Gamma_\Omega)\langle S_z \rangle \tag{70}$$

This component of the magnetization is then the major term contributing to the SR signal.

10.5. Pseudosecular Terms

There are terms in the Hamiltonian which contain the I_+ or I_- operators, as well as I_z, which are stationary in the rotating frame of the electron. When these terms are

retained, the observables are coupled to additional terms of the density matrix called pseudosecular terms. Since nitrogen-15 is a spin-$\frac{1}{2}$ nucleus, there are only nine independent terms in the full density matrix. Of those nine, four are associated with the transverse components: $\langle S_+\rangle$, $\langle S_+I_z\rangle$, $\langle S_+I_+\rangle$, and $\langle S_+I_-\rangle$. Additionally, there are five other terms to be considered: $\langle S_z\rangle$, $\langle S_zI_+\rangle$, $\langle I_+\rangle$, $\langle S_zI_z\rangle$, and $\langle I_z\rangle$. These last four components are coupled to the observables only by the microwave amplitude, and these components relax at a rate on the order of $1/T_{1e}$. None of these terms contains a $1/T_{2e}$ relaxation rate term. The $\langle S_z\rangle$ component relaxes independently of these elements. These last four terms, while not directly coupled to $\langle S_z\rangle$, are terms which contribute to the SR signal. These terms contribute relaxation components to $\langle S_y\rangle$ with amplitudes proportional to h_0, and cannot be removed by pump phase procedures, and relax with rates on the order of $1/T_{1e}$ not $1/T_{2e}$.

10.6. Isotropic Brownian Motion—Secular Terms Only

Let us consider the case of isotropic Brownian rotational diffusion and retain only the secular terms in the Hamiltonian. The effect of removing such terms in the simulation of cw spectra is that the intensities of the lines as a function of field (or orientation) within each manifold are no longer reproduced quantitatively. In terms of SR, this precludes using the manifold hopping process as a means of relaxation. Mathematically, the simulations of the SR recovery curves will be missing some relaxation rates due to these processes. These effects will be considered in the next section.

Now the problem is to solve for the transverse components as functions of time and under the conditions of the recovery experiment. How one solves the problem is a matter of choice. However, there is some insight to be gained in expanding the problem in terms of the eigenfunctions of the motional process. The general SR signal is

$$\text{Signal} = \sum_l a_l \exp(-r_l t) \tag{71}$$

where r_l are the recovery rates and a_l the associated amplitudes of each component. The set of recovery rates is infinite, but in practice it is dominated by a rather small set. First, components with T_{2e} in them are neglected in the total recovery signal. These terms arise from the FID and have associated amplitudes which are independent of observer power and are not part of the true SR-EPR signal. For all classes of motion considered, the FID components can be removed by a 180° phase shift on the pump (Hyde, 1979; Sugano *et al.*, 1987). Using this technique, the a_l associated with FID components switch sign while the a_l from true recovery components remain unaffected. Therefore, adding these two components removes components relaxing at rate T_{2e} (or FID components). This reduces enormously the complexity of the problem. While the amplitudes are not yet known, the rates of the components of the SR signal can be written as

$$r_l = \lambda'^{l}_{m} = 1/T_{1e} + f(l)D \tag{72}$$

The recovery rates are simply related to the eigenvalues of the motional process; the $\lambda'^{l}_{m,n}$ are defined in equation (26). For isotropic Brownian motion, $f(l) = l(l+1)$ for even values of l.

It is important to note that this set of recovery terms is independent of the magnetic resonance parameters and depends only on the motional process itself. The amplitudes (a_l) are dependent on the magnetic resonance parameters (i.e., the A and G tensors and other terms in the coherent part of the spin Hamiltonian).

10.7. Results of Calculations of SR Curves for Isotropic Motion

Equation (67) was solved numerically to obtain the rates of relaxation of the individual recovery components and the associated amplitudes. The value of $\chi(0)$ was determined numerically by solving for the evolution of the system under the pump, where $d = \gamma_e h_p$ in equation (66), for time T_p. The eigenvalues of A are the rates r_l during recovery (including the FID, which were recognized as relaxing with rate $1/T_{2e}$ or faster and eliminated). Numerical calculations with small, but finite h_0 verified that the recovery rates, being the eigenvalues of the A matrix, were the motional relaxation rates plus $1/T_{1e}$. The dependence of the amplitudes (a_l) on the other spectral parameters is now examined for a single manifold. Figure 28 (left and right) shows the relative amplitudes of the various components as a function of the pump time, T_p, for different values of l, at three different field positions. Position (1) is at the magic angle, and (2) and (3) move progressively toward the z turning point. The pump power used in Figure 28 (left) is rather modest and for Figure 28 (right) is quite large (as a practical matter). These results demonstrate that the higher components (with faster relaxation rates) have smaller amplitudes and contribute progressively less to the signal. Furthermore, the relative amplitudes can be varied by choosing different field positions. It is noteworthy that even for very long pump times it is quite difficult to remove some of the higher components.

Figure 29 demonstrates the control over amplitudes that is possible as the pump power is continuously varied to extremely high levels. It should be noted that some components can be maximized (or removed) by careful choice of pump power levels; and the signs of some of the components can even be inverted by sufficiently high power levels.

10.8. Results of Calculations of SR Curves for Nonaxial Tensors

The motion is isotropic Brownian rotational diffusion and the Hamiltonian now includes minor elements [after the manner of equations (35) and (36)] in the tensors. Figure 30 shows the dependence of the amplitudes on the field position for a single manifold. We note that the $l = 2$ components have a single node, and the $l = 2$, $m = 0$ component vanishes at the magic angle; in general, we note that each component has $\frac{1}{2}$ nodes, regardless of m.

10.9. Effects of Pseudosecular Terms

The presence of pseudosecular terms, i.e., those terms containing the $S_z I_\pm$ operators, provides a mechanism for coupling different nuclear manifolds. In terms of the master

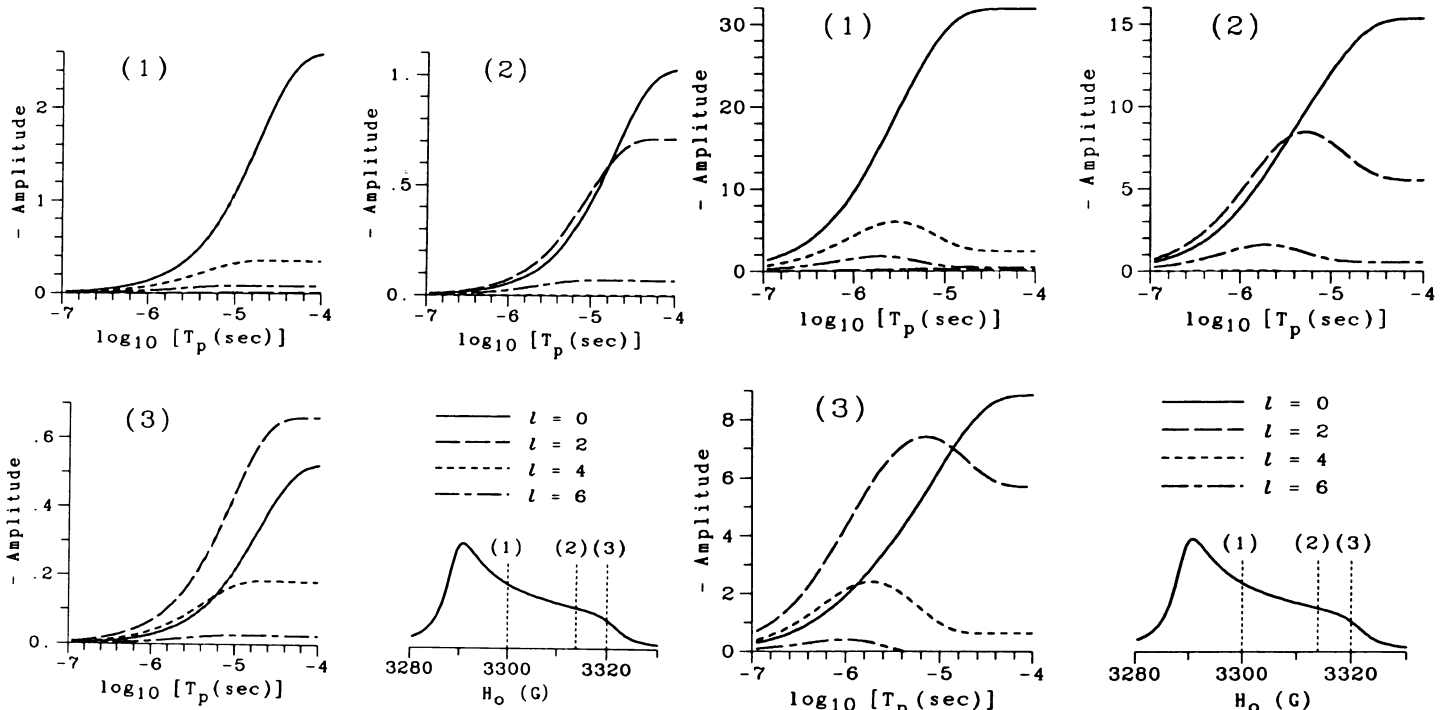

Figure 28. Amplitudes of the first four exponential components of the SR absorption signal for an axial G-tensor system under isotropic Brownian rotational diffusion as functions of pump duration time, T_p, at three different field positions for moderate (left) and high (right) pump powers. The following parameters have been employed in the computations: $H_{res} = 3300$ gauss; $h_p = 0.1$ gauss (left), and $h_p = 1.0$ gauss (right); $g_\perp = 2.0200$; $g_\parallel = 2.0000$; $T_{2e} = 0.02\ \mu$s; $T_{1e} = 20\ \mu$s; and $\tau_r = 20\ \mu$s. Position (1) is at the magic angle, where the $l = 2$ component vanishes. At (2), the $l = 4$ component vanishes. At (3), the $l = 4$ component has a significant amplitude. The cw absorption spectrum is plotted (lower right of each panel) along with the three field positions. Note that the amplitudes in the right panel are much higher than those in the left. Also, the amplitudes for $l \geq 2$ are no longer simple increasing functions of the pump duration times. As a result, the $l = 0$ component is dominant in the long pulse limit at high power.

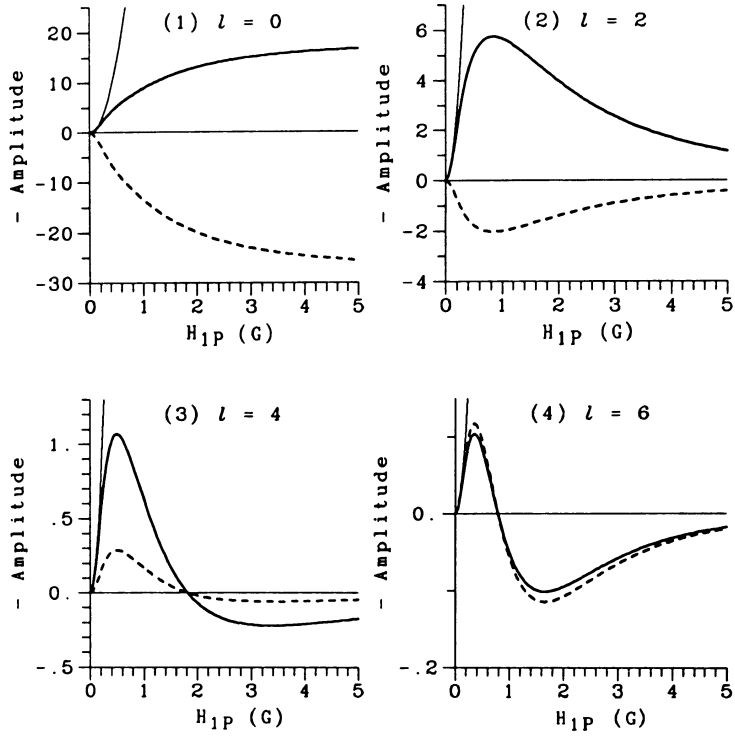

Figure 29. Dispersive and absorptive amplitudes of the first four exponential components of SR signals for an axial G-tensor system under isotropic Brownian rotational diffusion as functions of pump microwave field strength, h_p. The dotted lines are the dispersive components and the solid lines are the absorptive components. The following parameters have been employed in the computations: $H_{res} = 3300$ gauss; $h_0 = 0.001$ gauss; $g_\perp = 2.0200$; $g_\parallel = 2.0000$; $T_{2e} = 0.02\ \mu$s; $T_{1e} = 20\ \mu$s; $T_p = 1$ s; and $\tau_r = 20\ \mu$s. The light solid line in each display is the extrapolation to the low pump power response (proportional to h_p^2).

equation, the components of $\langle S_x \rangle$, $\langle S_y \rangle$, and $\langle S_z \rangle$ are now coupled to additional expectation values: $\langle S_z I_z \rangle$, $\langle S_z I_+ \rangle$, $\langle I_+ \rangle$, and $\langle I_z \rangle$; none of these expectation values is directly observed (although they are in principle observable quantities). Nonetheless, their effects are felt on $\langle S_+ \rangle$ and indirectly detected in that fashion. At this level the simple Bloch structure becomes much more complicated and difficult to understand; but it is possible to gain some understanding of the effects via simulations. The contribution to the SR signal of these, pseudosecular, terms can be determined simply by comparing calculations with and without the terms.

Inclusion of these additional terms leads to coupling of an additional six components; this means that there are an additional six relaxation rates at each l value. The eigenvalues due to these extra terms are clearly more complicated than the simple secular terms. The results of calculations have shown that only two terms from among the six at each l value have real nonvanishing contributions to the SR signal. Figure 31 shows the values of these rates (after removing the $1/T_{1e}$ contribution) as a function

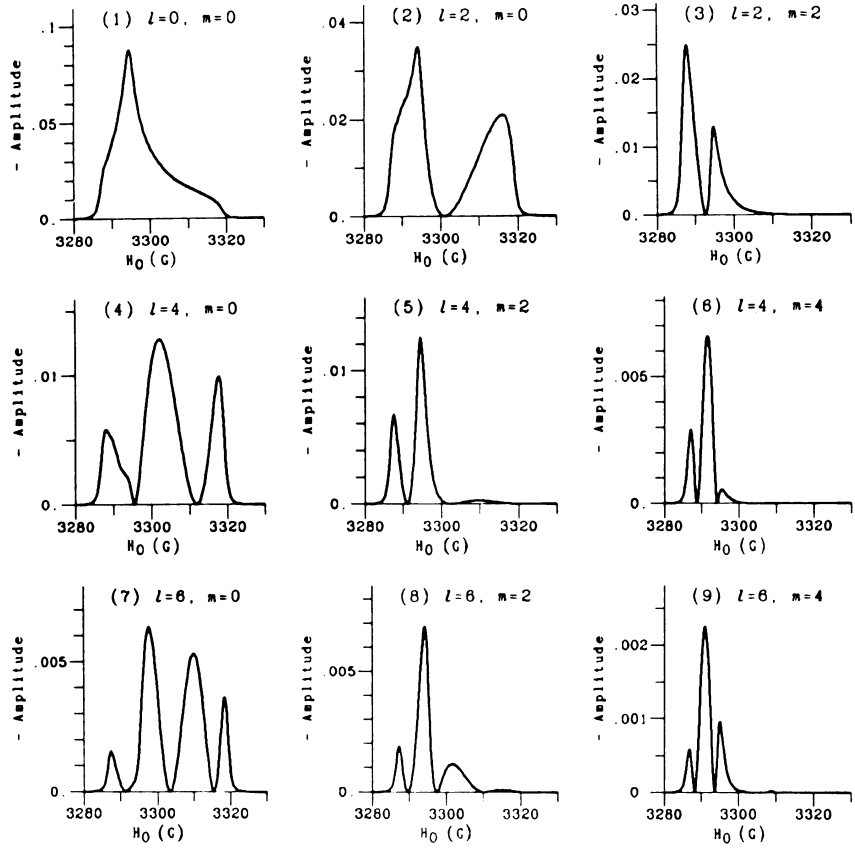

Figure 30. Amplitudes of the first nine exponential components of the SR signal for a nonaxial G-tensor system under anisotropic Brownian rotational diffusion as functions of field position, H_0. The following parameters have been employed in the computations: $H_{res} = 3300$ gauss; $h_p = 0.1$ gauss; $h_0 = 0.001$ gauss; $g_{xx} = 2.0200$; $g_{yy} = 2.0150$; $g_{zz} = 2.0000$; $T_{2e} = 0.05\ \mu$s; $T_{1e} = 20\ \mu$s; $T_p = 1$ s; $\tau_\perp = 50\ \mu$s; and $\tau_\parallel = 40\ \mu$s. The unique axis of the diffusion tensor has been assumed coincident with the Z axis of the G tensor. Calculations were performed at $l_{max} = 8$ and $m_{max} = 8$ with modification.

of $1/\tau_r$, for isotropic Brownian rotation. The trend continues for higher l values: for each relaxation component contributed by the secular terms, there are two contributed by the pseudosecular terms. These two components are faster than the associated secular term (but not a lot faster) and they interlace between neighboring secular terms. Therefore, analysis of SR data is complicated by the presence of these terms. There is no simple analytical form for these rates and they depend on the magnitudes of the A-tensor elements. It has been demonstrated that at least one of them can be related to T_{1n} predicted by the electron-nuclear dipolar fast-motion theory (Hyde *et al.*, 1984; Sugano, 1987). Figure 32 shows the amplitudes of each of the components as a function of field (for the nitrogen-15 case). The amplitude of one of the two pseudosecular components at each l value is nearly equal in amplitude to that of the secular component

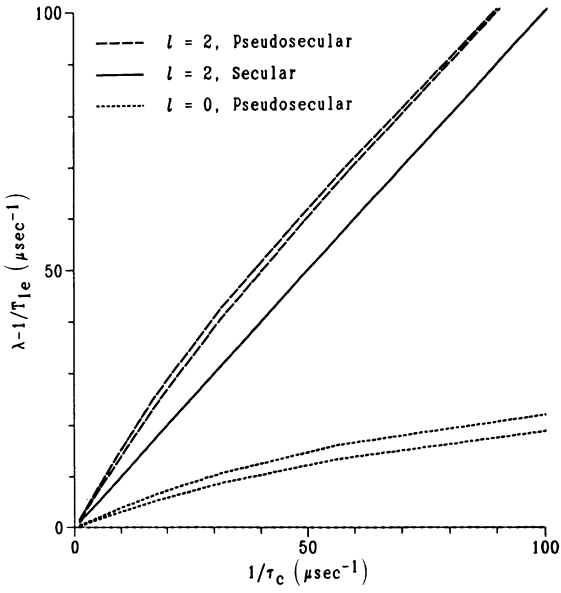

Figure 31. Eigenvalues as functions of $1/\tau_c$ in the very slow motional region. The following parameters have been employed in the computations: $H_{res} = 3300$ gauss; $H_0 = 3292.6$ gauss; $T_{1e} = 34.14\ \mu s$; $T_{2e} = 0.05\ \mu s$; $g_{xx} = g_{yy} = 2.0075$; $g_{zz} = 2.0027$; $A_{xx} = A_{yy} = 6$ gauss; and $A_{zz} = 32$ gauss.

and the second pseudosecular term can be neglected. Therefore, for each secular term there is one pseudosecular term which relaxes slightly faster (by a term on the order of $1/T_{1n}$) and is of comparable amplitude.

One can distinguish between relaxation components that arise from the secular terms and those that arise from the pseudosecular terms by simulating the pulsed ELDOR experiment where the observer is on one manifold and the pump is on the other. In all cases, at all motional rates, all pseudosecular components switch the sign of the amplitudes, while the relaxation components arising from secular terms have amplitudes whose signs remain the same.

10.10. Pseudosecular Terms Using Nitrogen-14

The effects of pseudosecular terms are much more extensive in the case of nitrogen-14 spin labels. In addition to all of the components seen in nitrogen-15 systems, one must contend with another set of components of the form $\langle S_z(I^2 - 3I_z^2)\rangle$, $\langle I^2 - 3I_z^2\rangle$. These terms contribute to the total relaxation. Not only does the problem double in size, causing an order-of-magnitude increase in computation time, but the analysis of SR data is complicated since there are additional relaxation terms. From Redfield theory, it appears that these terms will contribute, at least, another relaxation which will be on the order of $3/T_{1n}$ versus $1/T_{1n}$ for nitrogen-15. Therefore, analysis of nitrogen-14 will be all the more complicated, and compromised by additional terms with similar eigenvalues.

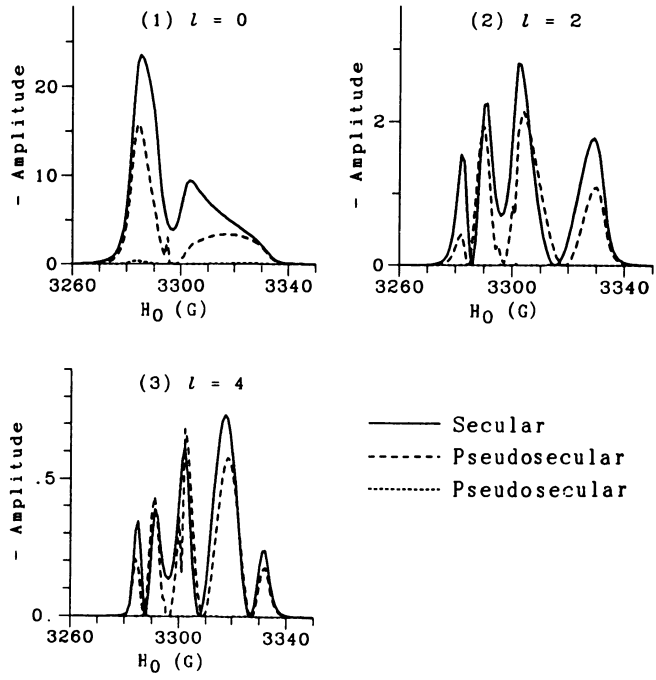

Figure 32. Absorptive amplitudes of the first three secular components and corresponding pseudosecular components of the SR signal for a nitrogen-15 spin label under isotropic Brownian rotational diffusion as functions of field position, H_0. The following parameters have been employed in the computations: $H_{res} = 3300$ gauss; $T_p = 1$ s; $T_{1e} = 20\ \mu$s; $T_{2e} = 0.02\ \mu$s; $\tau_r = 20\ \mu$s; $g_{xx} = g_{yy} = 2.0090$; $g_{zz} = 2.0020$; $A_{xx} = A_{yy} = 11$ gauss; and $A_{zz} = 50$ gauss. For each l, there are one secular and two pseudosecular components, but the second pseudosecular component is negligibly small.

10.11. Population Analysis: An Estimate of Amplitudes

In the course of developing the sensitivity of ST-EPR spectra to motion, it was convenient to define the lth component of M_y as $M^l_{m,n}$, given in equation (41). Furthermore, the absolute squares of the quantities $M^l_{m,n}$ are the amplitudes (shown in Figure 2) of the contributions to ST-EPR spectral sensitivity of the lth component. The amplitudes, a_l, of the lth component to the SR-EPR recovery curves are shown in Figure 30. Comparison of these two figures shows that they are nearly identical. Population analysis can be used to show that it is reasonable to expect these two quantities are nearly equal; then, to a good approximation, this provides a simple basis for understanding the magnitudes of a_l:

$$a_l \simeq |M^l_{m,n}|^2 \tag{73}$$

Following is a summary of the complete mathematical treatment (Sugano, 1987) which demonstrates the relationship given in equation (73).

We begin by considering the motional process. The diagonal components of the density matrix correspond to populations of different states. Equation (66) shows that such components evolve according to t as

$$\langle \dot{S}_z \rangle = -(1/T_{1e} + \Gamma_\Omega)\langle S_z \rangle + h_0 \langle S_y \rangle \tag{74}$$

If the coupling to the $\langle S_y \rangle$ component through the observer amplitude h_0 is neglected, then $\langle S_z \rangle$ satisfies the equation

$$\langle S_z(t) \rangle = \sum_{l,m,n} \langle S_z(0) \rangle^l_{m,n} \exp(-\lambda'^l_{m,n} t) D^l_{m,n}(\Omega) \tag{75}$$

This is the relaxation to the Boltzman level from a deviation due to the presence of $\langle S_z(0) \rangle$ (the result of the pump) which is the initial condition. The contribution to the SR response of the absorption signal $\langle S_y \rangle$ (neglecting the FID terms) is given by

$$\langle S_y(t) \rangle = \int_\Omega \langle S_y(\Omega) \rangle \langle S_z(t) \rangle \, d\Omega \tag{76}$$

where $\langle S_y(\Omega) \rangle$ is the absorption component under observer conditions, but $\langle S_z(0) \rangle$ is the deviation from equilibrium due to the pump at the beginning of the observing period. By substituting in the definition of $\langle S_z(0) \rangle$ given above one has

$$\langle S_y(t) \rangle = \sum_{l,m} \langle S_z(0) \rangle^l_{m,n} \exp(-\lambda'^l_{m,n} t) \int_\Omega \langle S_y(\Omega) \rangle D^l_{m,n}(\Omega) \, d\Omega \tag{77}$$

Therefore, the observed relaxation rates are the eigenfunctions of the motional operator plus the intrinsic relaxation rate $1/T_{1e}$, as stated before. However, this form provides a means of estimating the amplitudes of each of the relaxation components,

$$\langle S_y(t) \rangle = \sum_{l,m} a_{l,m} \exp(-\lambda'^l_{m,n} t) \tag{78}$$

and therefore the coefficients are approximated by

$$a_{l,m} = \langle S_z(0) \rangle^l_{m,n} \int_\Omega \langle S_y(\Omega) \rangle D^l_{m,n}(\Omega) \, d\Omega \tag{79}$$

The product form of $a_{l,m}$ clearly illustrates that the pump produces the deviation $\langle S_z(0) \rangle$ and the detection system produces the other term in the integral.

The components of $\langle S_z(0) \rangle$ are found as

$$\langle S_z(0) \rangle^l_{m,n} = \int_\Omega \langle S_z(\Omega, 0) \rangle D^l_{m,n} \, d\Omega \tag{80}$$

where $S_z(\Omega, 0)$ is the z component of the magnetization after evolving under the influence of the pump for finite time, T_p. If the pump time is very long, then the cw (or simple Lorentzian form) for the S_z and S_y components of the magnetization can be used. In this case, there is a very simple expression for the amplitudes as a function of field given by

$$S_z(\Omega, 0) = \frac{dp^2\, T_1/T_2}{\Delta^2(\Omega) + (1/T_{2e} + \Gamma_\Omega)^2 + dp^2\, T_{1e}/T_{2e}} \tag{81}$$

and the S_y component is

$$S_y(\Omega) = \frac{d_0/T_2}{\Delta^2(\Omega) + (1/T_{2e} + \Gamma_\Omega)^2 + d_0^2 T_{1e}/T_{2e}} \tag{82}$$

The above expression can be further simplified by assuming that Γ_Ω is small compared to $1/T_{2e}$ and that d_0 is small. This gives a very simple expression with which to test a very complicated process.

A theoretical analysis of SR-EPR data has shown that the important information on the nature of the motion is easily interpreted on the basis of the relaxation contributed from the secular terms. Interpretation of such information is obscured by relaxation components from the pseudosecular terms. Use of nitrogen-15 simplifies the complication of these additional terms, and provides a simplified approach to interpretation of the individual recovery components.

Preliminary results on spin-labeled glyceraldehyde-3-phosphate dehydrogenase with nitrogen-15 labels have made it possible to measure the intrinsic T_{1e}, which is about 15 microseconds (Robinson *et al.*, 1987). Studies on nitrogen-14 spin-labeled hemoglobin indicate sensitivity to multiple relaxation rates (Fajer *et al.*, 1986). Studies of mixed nitrogen-15 and nitrogen-14 spin-label systems have provided direct measurements of exchange rates (Yin *et al.*, 1987).

SR may provide more detailed insight into the nature of the motion, since one can probe the relaxation rates of subpopulations from the cw spectrum. A complete reconstruction of the anisotropic nature of the motion is possible: a combination of SR and pulsed ELDOR may prove to be very valuable to identify motionally driven pseudosecular terms. The contribution of secular terms depends very simply on the motional process and gives a direct measurement of the second and (in principle) higher-order correlation terms. It is now a matter of signal-to-noise and experimental design to obtain meaningful SR-EPR data on a variety of biologically important problems; nitrogen-15 and deuterium substitution will help greatly in these studies.

11. CONCLUSIONS

Nitrogen-15 and deuterium-substituted spin labels have provided three important advantages for biological spin-labeling studies of very slow rotational motion. First, the nitrogen-15 substitution decreases the number of nuclear spin states from three to two, thereby simplifying the theory for line-shape computations in the very slow motional regime. This simplification has enabled direct comparisons between experimental and computed cw-ST-EPR spectra on 1 MIPS class computer systems and has also provided simplifications for analysis of saturation-recovery curves for obtaining

dynamics information. Second, the deuterium substitution provides increased resolution of spectral features through a decrease in inhomogeneous broadening, resulting in diagnostic features being observed in experimental cw-ST-EPR spectra that were otherwise obscured and lost. In addition, deuteration leads to a simplification of the analysis of SR-EPR data. Third, the combination of the above changes in magnetic interactions of the spin-label moiety results in a useful increase in signal-to-noise of experimental data, allowing studies to be carried out on smaller amounts of biological material with shorter data acquisition times.

The decision of whether isotopically substituted spin labels are sufficiently advantageous to warrant the time and expense of preparation will depend upon the type of information being sought and the characteristics of the system. The experimental and theoretical data provided in the preceding sections permit evaluation of the line shapes expected from nitrogen-15 spin labels for a wide range of diffusional models and spectrometer settings and demonstrate how these line shapes will be altered by characteristic changes in rotational correlation times. The time factor will vary widely depending on the difficulty of preparing the corresponding nitrogen-14, hydrogen-substituted spin label. The expense factor again will largely be determined by how many synthetic transformations are required to get from an appropriate nitroxide spin-label intermediate to the desired final product. However, in many instances, this will be a minor expense in comparison to the total cost of carrying out a spin-label study. Commercial availability[3] of a number of nitrogen-15 and deuterium-substituted nitroxide spin-label intermediates, as well as nitrogen-14, deuterium-substituted intermediates, enables investigators to pursue experiments involving these materials without the necessity of carrying out multistep organic syntheses with expensive nitroxide precursors. Our experience with these commercial intermediates has been that they are of high isotopic purity and are generally readily available. Synthetic strategies for preparing many commonly employed spin-labeling reagents, which can be adapted to include isotopically substituted intermediates, are summarized in chapters by Gaffney (1976), Morrisett (1976), and Keana (1979).

Generally, the choice of which isotope spin label to employ may change during the course of a study. Initial experiments will almost always be carried out with conventional nitrogen-14, hydrogen-containing spin labels. As data are obtained, more sophisticated questions concerning subtleties of dynamics exhibited by the system may arise which require in-depth analysis of the line shapes. It is at this point that nitrogen-15, deuterium-substituted labels will be most advantageous. If data analyses require computation of line shapes for motional models presented in this chapter, then the algorithm described can be employed. The version of the program which has been developed runs on VAX computer systems under the VMS operating system. We have made copies of this program available to investigators pursuing studies with nitrogen-15 spin labels in the past with relatively few problems in installing the software.

ACKNOWLEDGMENTS. This work was supported by Public Health Service grants R01 HL-34737 and P01 CA-43720 (A.H.B.) and The National Science Foundation

[3] Merck, Sharpe, and Dohme/isotopes, Pointe Claire-Dorval, Quebec, Canada, supplies a number of nitrogen-15, deuterium and nitrogen-14, deuterium-substituted spin-label intermediates. A complete listing can be found in their stable isotope catalog.

PCM 82-16762 and DMB 87-06175 (B.H.R.). The authors wish to thank Drs. D. D. Thomas and M. E. Johnson for supplying copies of figures from their work and L. R. Dalton for encouraging the use of isotopically substituted labels.

REFERENCES

Balasubramanian, K., and Dalton, L. R., 1979, Computer simulation of EPR and ST-EPR spectra of nitroxide spin labels in the rigid lattice limit, *J. Magn. Reson.* **33**:245-260.

Beth, A. H., Perkins, R. C., Venkataramu, S. D., Pearson, D. E., Park, C. R., Park, J. H., and Dalton, L. R., 1980, Advantages of deuterium modification of nitroxide spin labels for biological EPR studies, *Chem. Phys. Lett.* **69**:24-28.

Beth, A. H., Venkataramu, S. D., Balasubramanian, K., Dalton, L. R., Robinson, B. H., Pearson, D. E., Park, C. R., and Park, J. H., 1981a, ^{15}N- and ^{2}H-substituted maleimide spin labels: Improved sensitivity and resolution for biological EPR studies, *Proc. Natl. Acad. Sci. U.S.A.* **78**:967-971.

Beth, A. H., Balasubramanian, K., Wilder, R. T., Venkataramu, S. D., Robinson, B. H., Dalton, L. R., Pearson, D. E., and Park, J. H., 1981b, Structural and motional changes in glyceraldehyde-3-phosphate dehydrogenase upon binding to the band-3 protein of the erythrocyte membrane examined with [^{15}N, ^{2}H]maleimide spin label and electron paramagnetic resonance, *Proc. Natl. Acad. Sci. U.S.A.* **78**:4955-4959.

Beth, A. H., Balasubramanian, K., Robinson, B. H., Dalton, L. R., Venkataramu, S. D., and Park, J. H., 1983, Sensitivity of V_2' saturation transfer electron paramagnetic resonance signals to anisotropic rotational diffusion with [^{15}N]nitroxide spin-labels. Effects of noncoincident magnetic and diffusion tensor principal axes, *J. Phys. Chem.* **87**:359-367.

Beth, A. H., Robinson, B. H., Cobb, C. E., Dalton, L. R., Trommer, W. E., Birktoft, J. J., and Park, J. H., 1984, Interactions and spatial arrangement of spin-labeled NAD^+ bound to glyceraldehyde-3-phosphate dehydrogenase. Comparison of EPR and X-ray modeling data, *J. Biol. Chem.* **259**:9717-9728.

Beth, A. H., Conturo, T. E., Venkataramu, S. D., and Staros, J. V., 1986, Dynamics and interactions of the anion channel in intact human erythrocytes: An electron paramagnetic resonance spectroscopic study employing a new membrane-impermeant bifunctional spin-label, *Biochemistry* **25**:3824-3832.

Beth, A. H., Robinson, B. H., Cobb, C. E., and Conturo, T. E., 1987, Extracting rotational correlation times from cw-STEPR spectra for systems with two motional components: Variable Zeeman modulation frequency experiments, *Biophys. J.* **51**: 75a (abstract).

Beth, A. H., Conturo, T. E., Auteri, F., and Robinson, B. H., 1989, Sensitivity of saturation transfer EPR signals to Zeeman field modulation frequency: Application to analysis of overlapping spectra, in preparation.

Brière, R., Dupeyre, R. M., Lemaire, H., Norat, C., Rassat, A., and Rey, P., 1965, Nitroxydes XVII: Biradicaux stables du type nitroxyde, *Bull. Soc. Chim. Fr.*: 3290-3297.

Broersma, S., 1960, Rotational diffusion constant of a cylindrical particle, *J. Chem. Phys.* **32**:1626-1631.

Chiarelli, R., and Rassat, A., 1973, Synthèses de radicaux nitroxydes deuteries, *Tetrahedron* **29**:3639-3647.

Coffey, P., Robinson, B. H., and Dalton, L. R., 1976, Rapid computer simulation of ESR spectra. II. Saturation transfer spectroscopy of axially symmetric ^{14}N-nitroxide spin labels, *Mol. Phys.* **31**:1703-1715.

Delmelle, M., Butler, K. W., and Smith, I. C. P., 1980, Saturation transfer electron spin resonance spectroscopy as a probe of anisotropic motion in model membrane systems, *Biochemistry* **19**:698-704.

Devaux, P. F., 1982, Lipid-protein interactions: Saturation transfer electron paramagnetic resonance of spin labeled rhodopsin, in *Methods in Enzymology* (L. Packer, ed.), **81**, pp. 703-709, Academic Press, New York.

Evans, C. A., 1981, Use of integral of saturation transfer electron paramagnetic spectra to determine molecular rotational correlation times. Slowly tumbling spin labels in the presence of rapidly tumbling spin labels, *J. Magn. Reson.* **44**:109-116.

Fajer, P., and Marsh, D., 1982, Microwave and modulation field inhomogeneities and the effect of cavity Q in saturation transfer ESR spectra. Dependence on sample size, *J. Magn. Reson.* **49**:212-224.

Fajer, P., and Marsh, D., 1983, Sensitivity of saturation transfer ESR spectra to anisotropic rotation. Application to membrane systems, *J. Magn. Reson.* **51**:446-459.

Fajer, P., Thomas, D. D., Feix, J. B., and Hyde, J. S., 1986, Measurement of rotational molecular motion by time-resolved saturation transfer electron paramagnetic resonance, *Biophys. J.* **50**:1195-1202.

Favro, L. D., 1965, Rotational brownian motion, in *Fluctuation Phenomena in Solids* (R. E. Burgess, ed.), pp. 79-101, Academic Press, New York.

Freed, J. H., 1979, Theory of saturation recovery in liquids and related media, in *Time Domain Electron Spin Resonance* (L. Kevan and R. N. Schwartz, eds.), pp. 31-66, Wiley, New York.

Froncisz, W., and Hyde, J. S., 1982, The loop-gap resonator: A new microwave circuit ESR sample structure. *J. Magn. Reson.* **47**:515-521.

Fung, L. W.-M., and Johnson, M. E., 1983, Multiple motions of the spectrin-actin complex in the saturation transfer EPR time domain, *J. Magn. Reson.* **51**:233-244.

Fung, L. W.-M., and Johnson, M. E., 1984, Recent developments in spin label EPR methodology for biomembrane studies, in *Current Topics in Bioenergetics* (C. P. Lee, ed.), **13**, pp. 107-157, Academic Press, New York.

Gaffney, B. J., 1976, The chemistry of spin labels, in *Spin Labeling. Theory and Applications* (L. J. Berliner, ed.), pp. 183-238, Academic Press, New York.

Gaffney, B. J., 1979, Spin label-thiourea adducts. A model for saturation transfer EPR studies of slow anisotropic motion, *J. Phys. Chem.* **83**:3345-3349.

Gaffney, B. J., Elbrecht, C. H., and Scibilla, J. P. A., 1981, Enhanced sensitivity to slow motions using ^{15}N-nitroxide spin labels, *J. Magn. Reson.* **44**:436-446.

Galloway, N. B., and Dalton, L. R., 1979, Approximate methods for the fast computation of EPR and ST-EPR spectra. IV. A perturbation approach with back substitution of the diagonal density matrix elements, *Chem. Phys.* **41**:61-66.

Graceffa, P., and Seidel, J. C., 1980, A reaction involving protein SH groups, bound spin labels, and $K_3Fe(CN)_6$, *Biochemistry* **19**:33-39.

Hemminga, M. A., De Jager, P. A., Marsh, D., and Fajer, P., 1984a, Standard conditions for the measurement of saturation-transfer ESR spectra, *J. Magn. Reson.* **59**:160-163.

Hemminga, M. A., Leermakers, F. A. M., and De Jager, P. A., 1984b, Quantitative measurement of B_1 in ESR and saturation-transfer ESR spectroscopy, *J. Magn. Reson.* **59**:137-140.

Hemminga, M. A., Reinders, J. H., and De Jager, P. A., 1984c, The effect of modulation frequency and rotational correlation time on various spectral displays in saturation-transfer ESR spectroscopy. The use of in-phase, quadrature, magnitude, and phase-plot displays, *J. Magn. Reson.* **58**:428-441.

Horváth, L. I., and Marsh, D., 1983, Analysis of multicomponent saturation transfer EPR spectra using the integral method: Application to membrane systems, *J. Magn. Reson.* **54**:363-373.

Huisjen, M., and Hyde, J. S., 1974, A pulsed EPR spectrometer, *Rev. Sci. Instrum.* **45**:669-675.

Hyde, J. S., 1978, Saturation-transfer spectroscopy, in *Methods in Enzymology* (C. H. W. Hirs and S. N. Timasheff, eds.), Vol. 49G, pp. 480-511, Academic Press, New York.

Hyde, J. S., 1979, Saturation recovery methodology, in *Time Domain Electron Spin Resonance* (L. Kevan and R. N. Schwartz, eds.), pp. 1-30, Wiley, New York.

Hyde, J. S., and Dalton, L. R., 1972, Very slow tumbling spin labels: Adiabatic rapid passage, *Chem. Phys. Lett.* **16**: 568-572.

Hyde, J. S., and Thomas, D. D., 1973, New EPR methods for the study of very slow motion: Application to spin-labeled hemoglobin, *Ann. N.Y. Acad. Sci.* **222**:680-692.

Hyde, J. S., and Dalton, L. R., 1979, Saturation-transfer spectroscopy, in *Spin Labeling II: Theory and Applications* (L. J. Berliner, ed.), pp. 1-70, Academic Press, New York.

Hyde, J. S., and Thomas, D. D., 1980, Saturation-transfer spectroscopy, *Ann. Rev. Phys. Chem.* **31**:293-317.

Hyde, J. S., Froncisz, W., and Kusumi, A., 1982, Dispersion ESR with the loop-gap resonator, *Rev. Sci. Instrum.* **53**:1934-1937.

Hyde, J. S., Froncisz, W., and Mottley, C., 1984, Pulsed ELDOR measurement of nitrogen T_1 in spin labels, *Chem. Phys. Lett.* **110**:621-625.

Johnson, M. E., and Hyde, J. S., 1981, 35-GHz (Q-band) saturation transfer electron paramagnetic resonance studies of rotational diffusion, *Biochemistry* **20**:2875-2880.

Johnson, M. E., Lee, L., and Fung, L. W.-M., 1982a, Models for slow anisotropic rotational diffusion in saturation transfer electron paramagnetic resonance at 9 and 35 GHz, *Biochemistry* **21**:4459-4467.

Johnson, M. E., Thiyagarajan, P., Bates, B., and Currie, B. L., 1982b, A comparison of resolution-enhancement methods in saturation-transfer EPR. ^{15}N isotopically substituted spin labels and 35 GHz high-frequency operation, *Biophys. J.* **37**:553-557.

Jost, P. C., Waggoner, A. S., and Griffith, O. H., 1971, Spin labeling and membrane structure, in *Structure and Function of Biological Membranes* (L. Rothfield, ed.), pp. 84-144, Academic Press, New York.

Keana, J. F. W., 1979, New aspects of nitroxide chemistry, in *Spin Labeling II. Theory and Applications* (L. J. Berliner, ed.), pp. 115-172, Academic Press, New York.

Kevan, L., and Kispert, L. D., 1976, *Electron Spin Double Resonance Spectroscopy*, Wiley, New York.

Koening, S., 1975, Brownian motion of an ellipsoid. A correction to Perrin's result, *Biopolymers* **14**:2421-2423.

Mailer, C., Danielson, J. D. S., and Robinson, B. H., 1985, Computer controlled pulse electron paramagnetic resonance spectrometer, *Rev. Sci. Instrum.* **56**:1917-1925.

Marsh, D., 1981, Electron spin resonance: Spin labels, in *Membrane Spectroscopy* (E. Grell, ed.), pp. 51-142, Springer-Verlag, Berlin/Heidelberg.

McCalley, R. C., Shimshick, E. J., and McConnell, H. M., 1972, The effect of slow rotational motion on paramagnetic resonance spectra, *Chem. Phys. Lett.* **13**:115-119.

Morrisett, J. D., 1976, The use of spin labels for studying the structure and function of enzymes, in *Spin Labeling. Theory and Applications* (L. J. Berliner, ed.), pp. 273-338, Academic Press, New York.

Ohnishi, S., and McConnell, H. M., 1965, Interaction of the radical ion of chloropromazine with deoxyribonucleic acid, *J. Am. Chem. Soc.* **87**:2293.

Perkins, R. C., Lionel, T., Robinson, B. H., Dalton, L. A., and Dalton, L. R., 1976, Saturation transfer spectroscopy: Signals sensitive to very slow molecular reorientation, *Chem. Phys.* **16**:393-404.

Perrin, F., 1934, Brownian motion of an ellipsoid. Dielectric absorption for ellipsoidal molecules, *J. de Physique et le Radium* **5**:497-511.

Polnaszek, C. F., and Freed, J. H., 1975, Electron spin resonance studies of anisotropic ordering, spin relaxation, and slow tumbling in liquid crystalline solvents, *J. Phys. Chem.* **79**:2283-2306.

Robinson, B. H., 1983, Effects of overmodulation on saturation transfer EPR signals, *J. Chem. Phys.* **78**:2268-2273.

Robinson, B. H., and Dalton, L. R., 1979, EPR and saturation-transfer EPR spectra at high microwave field intensities, *Chem. Phys.* **36**:207-237.

Robinson, B. H., and Dalton, L. R., 1980, Anisotropic rotational diffusion studied by passage saturation transfer electron paramagnetic resonance, *J. Chem. Phys.* **72**:1312-1324.

Robinson, B. H., and Dalton, L. R., 1981, Approximate methods for the fast computation of EPR and ST-EPR spectra. V. Application of the perturbation approach to the problem of anisotropic motion, *Chem. Phys.* **54**:253-259.

Robinson, B. H., Dalton, L. R., Dalton, L. A., and Keith, A. D., 1974, Fast computer calculation of ESR and nonlinear spin response spectra form the fast motion to the rigid lattice limits, *Chem. Phys. Lett.* **29**:56-64.

Robinson, B. H., Forgacs, G., Dalton, L. R., and Frisch, H. L., 1980, A simple model for internal motion of DNA based upon EPR studies in the slow motion region, *J. Chem. Phys.* **73**:4688-4692.

Robinson, B. H., Thomann, H., Beth, A. H., Fajer, P., and Dalton, L. R., 1985, in *EPR and Advanced EPR Studies of Biological Systems* (L. R. Dalton, ed.), pp. 1-314, CRC Press, Boca Raton, Florida.

Robinson, B. H., Sugano, T., Mailer, C., and Beth, A. H., 1987, Rotational motion of biomolecular model systems studied by saturation recovery EPR, *Biophys. J.* **51**:75a (abstract).

Saffman, P. G., and Delbrück, M., 1975, Brownian motion in biological membranes, *Proc. Nat. Acad. Sci. U.S.A.* **72**:3111-3113.

Sakaki, T., Tsuji, A., Chang, C.-H., and Ohnishi, S., 1982, Rotational mobility of an erythrocyte membrane integral protein band 3 in dimyristoylphosphatidylcholine reconstituted vesicles and effect of binding of cytoskeletal peripheral proteins, *Biochemistry* **21**:2366-2372.

Schneider, D. J., and Freed, J. H., 1989, Spin relaxation and motional dynamics, in *Lasers, Molecules, and Methods: Advances in Chemical Physics* (J. O. Hirshfelder, R. E. Wyatt, and R. D. Coalson, eds.), pp. 387-527, Wiley & Sons, New York.

Schurr, J. M., and Schmitz, K. S., 1986, Dynamic light scattering studies of biopolymers: Effects of charge, shape, and flexibility, *Ann. Rev. Phys. Chem.* **37**:271-305.

Schwartz, L. J., Millhauser, G. L., and Freed, J. H., 1986, Two-dimensional electron spin echoes: Magnetization transfer and molecular dynamics, *Chem. Phys. Lett.* **127**:60-66.

Squier, T. C., and Thomas, D. D., 1986, Methodology for increased precision in saturation transfer electron paramagnetic resonance studies of rotational dynamics, *Biophys. J.* **49**:921-935.

Stillman, A. E., and Schwartz, R. N., 1979, Theory of electron spin echoes in nonviscous and viscous liquids, in *Time Domain Electron Spin Resonance* (L. Kevan and R. N. Schwartz, eds.), pp. 153-193, Wiley, New York.

Stillman, A. E., and Schwartz, R. N., 1981, Study of dynamical processes in liquids by electron spin echo spectroscopy, *J. Phys. Chem.* **85**:3031-3040.

Stillman, A. E., Schwartz, L. J., and Freed, J. H., 1980, Direct determination of rotational correlation time by electron-spin echoes, *J. Chem. Phys.* **73**:3502-3503.

Stone, T. J., Buckman, T., Nordio, R. L., and McConnell, H. M., 1965, Spin labeled biomolecules, *Proc. Nat. Acad. Sci. U.S.A.* **54**:1010-1017.

Sugano, T., 1987, A study of very slow rotational diffusion by SR-EPR, Ph.D. Thesis, University of Washington.

Sugano, T., Mailer, C., and Robinson, B. H., 1987, Direct detection of very slow two-jump processes by saturation recovery electron paramagnetic resonance spectroscopy, *J. Chem. Phys.* **87**:2478-2488.

Thiyagarajan, P., and Johnson, M. E., 1987, Saturation-transfer electron paramagnetic resonance detection of anisotropic motion by sickle hemoglobin molecules in the polymer state, *Biochemistry* **26**:1903-1909.

Thomas, D. D., 1982, Saturation transfer EPR studies of rotational dynamics in membranes, in *Membranes and Transport* (A. Martonosi, ed.), pp. 135-139, Plenum Press, New York.

Thomas, D. D., 1985, Saturation transfer EPR studies of microsecond rotational motions in biological membranes, in *The Enzymes of Biological Membranes* (A. Martonosi, ed.), pp. 287-312, Plenum Press, New York.

Thomas, D. D., 1986, Rotational diffusion of membrane proteins, in *Techniques for the Analysis of Membrane Proteins* (C. I. Ragan and R. J. Cherry, eds.), pp. 379-431, Chapman and Hall, London.

Thomas, D. D., and Hidalgo, C., 1978, Rotational motion of the sarcoplasmic reticulum Ca^{2+}-ATPase, *Proc. Natl. Acad. Sci. U.S.A.* **75**:5488-5492.

Thomas, D. D., and Cooke, R., 1980, Orientation of spin labeled myosin heads in glycerinated muscle fibers, *Biophys. J.* **32**:891-906.

Thomas, D. D., and McConnell, H. M., 1974, Calculation of paramagnetic resonance spectra sensitive to very slow rotational motion, *Chem. Phys. Lett.* **25**:470-475.

Thomas, D. D., Dalton, L. R., and Hyde, J. S., 1976, Rotational diffusion studied by passage saturation transfer electron paramagnetic resonance, *J. Chem. Phys.* **65**:3006-3024.

Thomas, D. D., Wendt, C. H., Froncisz, W., and Hyde, J. S., 1983, Saturation transfer EPR spectroscopy on spin-labeled muscle fibers using a loop-gap resonator, *Biophys. J.* **43**:131-135.

Tirado, M. M., and de la Torre, J. G., 1979, Translational friction coefficients of rigid, symmetric top macromolecules. Application to circular cylinders, *J. Chem. Phys.* **71**:2581-2587.

Tirado, M. M., and de la Torre, J. G., 1980, Rotational dynamics of rigid, symmetric top macromolecules. Application to circular cylinders, *J. Chem. Phys.* **73**:1986-1993.

Vistnes, A. I., and Dalton, L. R., 1983, Experimental methods to determine the microwave field strength in electron spin resonance, *J. Magn. Reson.* **54**:78-88.

Watts, A., and Marsh, D., 1981, Saturation transfer ESR studies of molecular motion in phosphatidylglycerol bilayers in the gel phase, *Biochim. Biophys. Acta* **642**:231-241.

Willingham, G. L., and Gaffney, B. J., 1983, Reactions of spin-label cross-linking reagents with red blood cell proteins, *Biochemistry* **22**:892-898.

Wigner, E. P., 1959, in *Group Theory and its Application to the Quantum Mechanics of Atomic Spectra*, Academic Press, New York. In particular, the quantities $D^l_{m,n}(\Omega)$ are defined (p. 153) and written in terms of specific formulas (p. 167). Also, $D^l_{m,n}(\Omega) = e^{im\phi} d^l_{m,n}(\Theta_t) e^{imr}$ where $d^l_{m,n}(\Theta_t)$ depends only on Θ_t (p. 156).

Yin, J.-J., Pasenkiewicz-Gierula, M., and Hyde, J. S., 1987, Lateral diffusion of lipids in membranes by pulse saturation recovery electron spin resonance, *Proc. Natl. Acad. Sci. U.S.A.* **84**:964-968.

5

Experimental Methods in Spin-Label Spectral Analysis

Derek Marsh

1. INTRODUCTION

This chapter is concerned with the use of nitroxide ESR spectra to study the dynamics of spin-labeled molecules. The rotational motion and orientational molecular order can be determined from the dynamic and static effects of the hyperfine and g-value anisotropies, respectively, of the free radical. The translational motion and molecular collisions can be determined from the spin–spin interactions which occur between radicals when the spin-label concentration is increased.

The spectral anisotropy is described by the spin Hamiltonian for the unpaired electron spin **S** of an isolated nitroxide:

$$\mathcal{H} = \beta \mathbf{H} \cdot \mathbf{g} \cdot \mathbf{S} + \mathbf{I} \cdot \mathbf{A} \cdot \mathbf{S} \tag{1}$$

where β is the the Bohr magneton, I is the ^{14}N nuclear spin, and **H** is the laboratory magnetic field vector. The g value and hyperfine interaction A are both tensor quantities, having the principal elements $(g_{xx}, g_{yy}, g_{zz}) = (2.0088, 2.0058, 2.0021)$ and $(A_{xx}, A_{yy}, A_{zz}) = (5.9, 5.4, 32.9)$G, as determined from single-crystal measurements (Jost *et al.*, 1971). The x and z principal axes lie along the N—O bond and along the free radical 2p-π orbital of the nitroxide, respectively.

The Zeeman and hyperfine interactions therefore allow the determination of molecular orientation from the angular anisotropy of the spectrum with respect to the magnetic field orientation. Molecular motion, which is rapid compared with the anisotropy [$A_{zz} - A_{xx} \sim 70$ MHz; $(g_{xx} - g_{zz})\beta H \sim 30$ MHz], gives rise to motional averaging of the anisotropy, and the degree of averaging is determined by the angular

Derek Marsh • Department of Spectroscopy, Max Planck Institute for Biophysical Chemistry, D-3400 Göttingen, Federal Republic of Germany.

amplitude of the molecular rotation. The transverse relaxation time, which is related to the Lorentzian line broadening, is determined by the rate of modulation of the anisotropies by the molecular motion, and hence can be used to measure the rotational correlation times. This method is applicable in the correlation time range 10^{-11} s $\lesssim \tau_R \lesssim 10^{-8}$ s. In the motional narrowing region (10^{-11} s $\lesssim \tau_R \lesssim 10^{-9}$ s), the spectra may be analyzed using Redfield theory (Redfield, 1965), but in the slow motional regime (10^{-9} s $\lesssim \tau_R \lesssim 10^{-8}$ s) the full stochastic Liouville equation (Freed, 1976) must be used. The effects of rotational modulation of the spectral anisotropy on the spin-lattice relaxation time is used in saturation transfer ESR spectroscopy to extend the range of motional sensitivity to correlation times in the range 10^{-7} s $\lesssim \tau_R \lesssim 10^{-3}$ s. Saturation transfer spectroscopy is much more susceptible to experimental artefacts than is conventional ESR spectroscopy, and for the most part empirical methods of spectral analysis have been used. Simulations using either the stochastic Liouville equation or the diffusion-coupled Bloch equations have been used to validate the empirical methods.

The magnetic interactions between radicals, the magnetic dipole-dipole interaction, and Heisenberg spin exchange are described by the following contribution to the spin Hamiltonian:

$$\mathcal{H}_{12} = J\mathbf{S}_1 \cdot \mathbf{S}_2 + (g^2\beta^2/r^3)[\mathbf{S}_1 \cdot \mathbf{S}_2 - 3(\mathbf{S}_1 \cdot \mathbf{r})(\mathbf{S}_2 \cdot \mathbf{r})/r^2] \tag{2}$$

where J is the exchange constant and $\mathbf{r}$ is the vector joining the two spins. The first term on the right is the exchange interaction, which is of extremely short range and therefore can be used for counting molecular collisions and hence studying translational motion. The second term is the dipole-dipole interaction, which is of considerably longer range and depends on both intermolecular separation and orientation of the interspin vector. In principle, the latter can therefore be used both for determining intermolecular distances (Marsh and Smith, 1973) and for studying translational diffusion.

2. INHOMOGENEOUS BROADENING

Dynamic effects in spin-label ESR spectra, induced for example by molecular rotation or spin exchange, are normally characterized by an increase in the Lorentzian linewidth, from which the relevant motional correlation times may be obtained. For motionally narrowed spectra with no residual hyperfine or g-value anisotropy (or oriented samples), the line broadening can be determined from the peak-to-peak linewidth in the first-derivative ESR spectra. The analysis is complicated, however, by the presence of unresolved proton hyperfine structure, which gives rise to inhomogeneous (non-Lorentzian) broadening. For equivalent protons the unresolved hyperfine pattern consists of equally spaced Lorentzian lines whose intensities are given by the binomial distribution. In practice it is found that the inhomogeneous broadening, from all sources, can be approximated well by a Gaussian distribution of Lorentzian lines.

For a given ^{14}N hyperfine component, the total peak-to-peak, first-derivative linewidth ΔH_{pp}^{tot} is related to the peak-to-peak Gaussian (ΔH_{pp}^{G}) and Lorentzian (ΔH_{pp}^{L}) linewidths by the following equation (Dobryakov and Lebedev, 1969):

$$(\Delta H_{pp}^{G}/\Delta H_{pp}^{tot})^2 + \Delta H_{pp}^{L}/\Delta H_{pp}^{tot} = 1 \tag{3}$$

This relation has been obtained by numerical integration of the Voigt line shape, and can be used to extract the Lorentzian linewidth from the measured peak-to-peak linewidth, if the Gaussian broadening is known. For hyperfine multiplets of N_j equivalent nuclei of spin I_j, the Gaussian linewidth is given by

$$(\Delta H_{pp}^{G})^2 = (4\alpha/3) \sum N_j I_j (I_j + 1) a_j^2 \tag{4}$$

where a_j is the proton hyperfine coupling constant of the jth multiplet, and α is the factor relating the square of the width of the multiplet to the square of the width of a Gaussian line of equivalent second moment. By simulation it is found that, within the range of likely proton hyperfine splittings for nitroxide spin labels, the effective Gaussian broadening is not sensitively dependent on the detailed multiplet pattern and can be expressed simply in terms of an effective hyperfine coupling, a_e, for $n = \sum N_j$ equivalent protons (Bales, 1980):

$$\Delta H_{pp}^{G} = (n\alpha)^{1/2} a_e \tag{5}$$

where $\alpha \simeq 1.06$ is obtained from the simulations. Some representative values of n, a_e, and ΔH_{pp}^{G} are given in Table 1. It will be noted that if all protons are equivalent, a_e is given by the true hyperfine coupling constant a_H, and the value of α is accurately determined. It should also be remembered that the proton hyperfine coupling will depend on solvent polarity, as does the nitrogen hyperfine coupling.

In many cases the proton hyperfine couplings may not be known accurately, or may be subject to exchange narrowing. Bales (1982) has devised a simple empirical method for separating the Gaussian and Lorentzian contributions to the total linewidth,

TABLE 1
Values for the Effective Proton/Deuteron Hyperfine Coupling a_e (n Equivalent Protons/Deuterons) and the Gaussian Inhomogeneous Linewidth ΔH_{pp}^{G} in Equation (5) for Various Nitroxide Spin Labels [A Value of $\alpha = 1.06$ is Assumed in Equation (5)]

Spin label[a]	n	a_e (G)	ΔH_{pp}^{G} (G)	Reference[b]
DTBN	18	0.10–0.11	0.44–0.48	1
MBATPO	10	0.41	1.33	2
PD-tempone	12	0.02	0.07	2
3N14	10[c]	0.34	1.1	1
4-VASL	10[c]	0.23	0.76	3
16-PCSL	10[c]	0.22	0.73	3

[a] DTBN, di-*tert*-butyl nitroxide.
MBATPO, *N*-(*p*-methoxybenzylidene)-4-amino-2,2,6,6-tetramethylpiperidino-1-oxyl.
PD-tempone, [$^2H_{16}$]-2,2,6,6-tetramethyl-piperidone *N*-oxide.
3N14, 3-(4,4-dimethyloxazolidine-*N*-oxyl) tetradecane.
4-VASL, 4-(4,4-dimethyloxazolidine-*N*-oxyl) valeric acid.
16-PCSL, 1-acyl-2-[16-(4,4-dimethyloxazolidine-*N*-oxyl)-stearoyl]-*sn*-glycero-3-phosphocholine.
[b] References: 1. Bales (1982); 2. Bales (1980); 3. King *et al.* (1987).
[c] Inequivalent protons; a value of $n = 10$ is assumed arbitrarily.

which is based on measurements of the relative intensity in the wings of the spectrum, as indicated in Figure 1. The diagnostic region is taken to be at a magnetic field which is $\pm 1.32\Delta H_{pp}$ distant from the resonance field. At this point, the amplitude in the wings, V', relative to the peak-to-peak amplitude, V_{pp}, differs considerably between the Gaussian and Lorentzian line shapes. The diagnostic ratio, defined by

$$\Psi = V'/(2V_{pp}) \tag{6}$$

is $\Psi^G = 0.067$ for a pure Gaussian line, and for a pure Lorentzian line $\Psi^L = 0.213$. By simulating a 19-proton multiplet, with differing values of the hyperfine coupling, the following empirical calibration of the ratio of the Gaussian to Lorentzian linewidths in terms of the diagnostic ratio Ψ was obtained (Bales, 1982):

$$\Delta H_{pp}^G/\Delta H_{pp}^L = 16.02 - 236.6\Psi + 1263\Psi^2 - 2373\Psi^3 \tag{7}$$

This calibration is valid in the range $\Delta H_{pp}^G/\Delta H_{pp}^L = 0$ to 2.04, the latter limit corresponding to the point at which the multiplet hyperfine structure no longer remains unresolved. Combination of equation (7) with equation (3) then allows both Gaussian and Lorentzian linewidths to be determined separately.

The method has also been extended to include estimation of the double integrated intensities of inhomogeneously broadened lines. The double integrated intensity of the first-derivative line is given by

$$A_{int} = \tfrac{1}{2}(\Delta H_{pp}^{tot})^2 V_{pp} F \tag{8}$$

where F is a factor which depends only on the line shape and has the values $F = 1.03$ and 3.63 for Gaussian and Lorentzian lines, respectively. For intermediate cases, the calibration obtained from the simulations is (Bales, 1982)

$$F = 0.7883 + 1.319\Psi + 56.65\Psi^2 \tag{9}$$

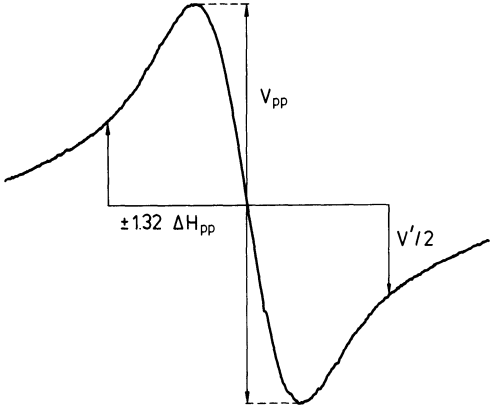

Figure 1. Single manifold ($m_I = 0$) ^{14}N hyperfine line, illustrating the position in the wings of the spectrum ($\pm 1.32\ \Delta H_{pp}$) at which the diagnostic amplitude V' for the Gaussian-Lorentzian deconvolution is defined according to Bales (1982).

For lines with a high proportion of Lorentzian character, this method could well be preferable to numerical integration.

3. FAST ROTATIONAL MOTION

Nitroxide spin labels undergoing rapid rotational motion in an isotropic medium have their spectral anisotropy completely averaged and give rise to a three-line spectrum. The homogeneous (Lorentzian) line broadening, given by the spin-spin relaxation time T_2, depends on the rate of motion and can be used to determine the rotational correlation times. In the fast motional (or motional narrowing) regime the relaxation times may be determined by time-dependent perturbation theory. The relaxation is induced by modulation of the angular anisotropy of the hyperfine and Zeeman interactions by the molecular rotation. The modulation of the magnetic anisotropies is expressed in terms of the autocorrelation function (Redfield, 1965):

$$G(\tau) = \langle \mathcal{H}_1^*(t)\mathcal{H}_1(t+\tau)\rangle \tag{10}$$

where $\mathcal{H}_1(t)$ is the time-dependent (i.e., angular-dependent) part of the spin Hamiltonian. The frequency dependence of the relaxation times is then given directly in terms of the spectral densities $J(\omega)$, which are Fourier transforms of the autocorrelation functions:

$$J(\omega) = \int_{-\infty}^{\infty} G(\tau)\, e^{i\omega\tau}\, d\tau \tag{11}$$

where ω is the angular frequency.

Assuming a Brownian rotational diffusion model, the probability density p of the time-dependent molecular orientation $\Omega \equiv (\phi, \theta, \psi)$ is given by the solution of the rotational diffusion equation:

$$\frac{\partial p}{\partial t} = D_{R\perp}\left[\frac{1}{\sin\theta}\frac{\partial}{\partial\theta}\left(\sin\theta\frac{\partial}{\partial\theta}\right) + \frac{1}{\sin^2\theta}\frac{\partial^2}{\partial\phi^2} - \frac{2\cos\theta}{\sin^2\theta}\frac{\partial^2}{\partial\phi\,\partial\psi} + \left(\cot^2\theta + \frac{D_{R\parallel}}{D_{R\perp}}\right)\frac{\partial^2}{\partial\psi^2}\right]p \tag{12}$$

where $D_{R\parallel}$ and $D_{R\perp}$ are the rotational diffusion coefficients about the molecular symmetry axis and perpendicular to it, respectively. The correlation function then has an exponential τ dependence of the form (see, e.g., Freed, 1964)

$$G_L(\tau) \sim \sum_{K=-L}^{+L} g_{LK} \exp(-\tau/\tau_{LK}) \tag{13}$$

The rotational correlation times τ_{LK} are given by the eigenvalues of the diffusion equation (12):

$$1/\tau_{L,K} = D_{R\perp}L(L+1) + (D_{R\parallel} - D_{R\perp})K^2 \tag{14}$$

where, for modulation of the hyperfine and Zeeman interactions (second-order spherical harmonics), we require the $L = 2$ terms.

For isotropic rotational diffusion, $D_{R\parallel} = D_{R\perp} = D_R$, and the rotational correlation time is given by

$$\tau_R = \tau_{20} = 1/6D_R \tag{15}$$

For anisotropic rotational diffusion, two independent rotational correlation times, $\tau_{20}^{-1} = 6D_{R\perp}$ and $\tau_{2\pm2}^{-1} = 2D_{R\perp} + 4D_{R\parallel}$, are required to describe the ESR line broadening. The rotational diffusion coefficients are the principal motional parameters, but corresponding effective rotational correlation times can be defined if desired. These are given by

$$\tau_{R\perp} = 1/6D_{R\perp} = \tau_{20} \tag{16}$$

and

$$\tau_{R\parallel} = 1/6D_{R\parallel} = 2\tau_{20}\tau_{22}/(3\tau_{20} - \tau_{22}) \tag{17}$$

Since the Hamiltonian $\mathcal{H}_1(t)$ in the correlation function $G(\tau)$ includes both Zeeman and hyperfine anisotropies, the transverse relaxation rate will involve all possible quadratic cross-products between these two terms. The Lorentzian linewidth therefore has the following dependence on the ^{14}N nuclear spin quantum number:

$$\Delta H_{pp}^{L}(m_I) = A + Bm_I + Cm_I^2 \tag{18}$$

where $m_I = -1, 0, +1$ for the high-field, central, and low-field lines, respectively. The A term contributes a constant broadening to all three lines and cannot be easily distinguished from other homogeneous broadening mechanisms. The B term gives a differential broadening of all three lines, and the C term gives a symmetrical broadening about the central line. Thus B and C may be determined separately from the different Lorentzian linewidths, which are measured according to the methods outlined in the preceding section.

For *isotropic* rotation, the following expressions are obtained for the linewidth coefficients B and C (Fraenkel, 1967; Schreier *et al.*, 1978):

$$B = 1.81 \times 10^6\, H(\Delta g\, \Delta A + 3\delta g \delta A) j(0) \tag{19}$$

$$C = 1.81 \times 10^6 [(\Delta A)^2 + 3(\delta A)^2][j(0) - \tfrac{3}{8} j(\omega_A)] \tag{20}$$

where B, C, and the magnetic field H are in gauss, and the hyperfine anisotropies (also in gauss) are given by

$$\Delta A = A_{zz} - \tfrac{1}{2}(A_{xx} + A_{yy}) \tag{21}$$

$$\delta A = \tfrac{1}{2}(A_{xx} - A_{yy}) \tag{22}$$

with exactly similar expressions for the g-value anisotropies, Δg and δg. The reduced spectral densities, for isotropic liquids and exponential correlation functions, are given by

$$j(\omega) = \tau_R/(1 + \omega^2\tau_R^2) \tag{23}$$

The frequency $\omega_A = \frac{1}{2}a_0 \approx 10^9\ s^{-1}$ corresponds to the hyperfine or nuclear spin-flip frequency in radian s^{-1}. Making the approximation $j(\omega_A) \approx \tau_R$, which requires $\tau_R \lesssim 10^{-9}$ s, it is found that $|C/B| \sim 1$ for *isotropic rotation*, and using the tensor elements from Jost *et al.* (1971) the rotational correlation time is given by (Schreier *et al.*, 1978)

$$\tau_B^{iso}\,(s) = -1.22 \times 10^{-9} B\,(G) \tag{24}$$

or

$$\tau_C^{iso}\,(s) = 1.19 \times 10^{-9} C\,(G) \tag{25}$$

where equation (24) has been calculated for H = 3300 G.

For *anisotropic* rotation which is axially symmetric about the nitroxide z axis, and with the same approximations as for equations (24) and (25), the correlation times can be calculated from the following equations (Polnaszek, 1983; Goldman *et al.*, 1972):

$$\tau_0 = = \frac{1.11 \times 10^{-7}}{H\,\Delta A} \cdot \frac{5(\delta A)B - 8(\delta g)H\,C}{\Delta g\,\delta A - \delta g\,\Delta A} \tag{26}$$

and

$$\tau_{22} = \frac{3.69 \times 10^{-8}}{H\,\delta A} \cdot \frac{8\,\Delta g\,H\,C - 5\,\Delta A\,B}{\Delta g\,\delta A - \delta g\,\Delta A} \tag{27}$$

where again B, C, H, ΔA, and δA are all in gauss, and the correlation times τ_0 and τ_{22} (in seconds) are given by equation (14) above. The same expressions [equations (26) and (27)] hold for axially symmetric rotation about the x and y axes if the indices in equations (21) and (22) and the corresponding expressions for the g-value anisotropy are permuted cyclically.

The numerical expressions for the correlation times corresponding to axial anisotropic rotation [equations (26) and (27) and cyclic permutations] may be written in the form

$$\tau_0 = c_1(C + c_2B) \tag{28}$$

and

$$\tau_{22} = b_1(B + b_2C) \tag{29}$$

Values for the numerical constants c_1, c_2, b_1, and b_2, corresponding to correlation times in seconds and linewidth coefficients in gauss, are given in Table 2. Since B is negative and C is positive, the requirement that the correlation times be positive leads to limits on the possible relative values of the linewidth coefficients. The ranges of values for the ratio $|C/B|$ which are compatible with the various different anisotropic rotations are given in Table 2. The $|C/B|$ ratio increases with increasing rotational anisotropy ($D_{R\parallel}/D_{R\perp}$) for y-axis rotation, and for x-axis rotation it decreases (Goldman *et al.*, 1972).

TABLE 2
Numerical Constants Relating Linewidth Coefficients to Correlation Times; and Range of Validity of the Ratio $|C/B|$, for Axial Rotation: $\tau_{20} = c_1 (C + c_2 B)$, $\tau_{22} = b_1(B + b_2 C)$ (Adapted from Polnaszek, 1983)

Rotation axis	$\lvert C/B \rvert$	c_1 ($s\,G^{-1}$)	c_2	b_1 ($s\,G^{-1}$)	b_2	Tensors[a]
Isotropic	≈1	1.19×10^{-9}	0	-1.22×10^{-9}	0	(1)
z axis	<1.01	1.16×10^{-9}	−0.0316	-0.437×10^{-9}	0.988	(1)
	<0.89	1.28×10^{-9}	−0.0115	-0.335×10^{-9}	1.130	(2)
y axis	0.8-8.8	4.95×10^{-9}	0.775	-1.38×10^{-9}	0.113	(1)
x axis	0.5-1.5	-2.85×10^{-9}	1.447	1.28×10^{-9}	1.912	(2)

[a] Spin Hamiltonian tensors are taken for the following labels: (1) Doxyl propane (Jost *et al.*, 1971); (2) TEMPONE (Snipes *et al.*, 1974). With the exception of z-axis rotation, the values are not very sensitive to the choice of single-crystal tensor values.

4. SLOW ROTATIONAL MOTION

For rotational correlation times longer than $\sim 10^{-9}$ s, motional narrowing theory breaks down and the more exact stochastic Liouville treatment must be applied. The line positions are no longer determined solely by the amplitude of motion, but depend also on the rate of motion, i.e., on the rotational correlation time. The line broadening ceases to be simple Lorentzian, and the spectral line shapes must be simulated. This approach is discussed in Section 5, but in the present section a rather more restricted and empirical method of analysis is described.

For spectra corresponding to nitroxides whose motion is close to the rigid limit on the time scale of conventional ESR spectroscopy, rotational correlation time calibrations exist based on the decrease in separation and increase in linewidth of the outer hyperfine extrema, relative to the rigid limit values (cf. Figure 2). The outer extrema in the slow motion spectra correspond to those nitroxides with their z axes oriented along the magnetic field direction. Molecular rotation causes these nitroxides to exchange with those of different orientation, in other parts of the spectrum. By analogy with the case of two-site exchange in magnetic resonance, it is to be expected that the outer hyperfine maxima will first broaden and then shift closer together, as the rate of spin-label motion increases from the rigid limit. In the slow exchange region, it is

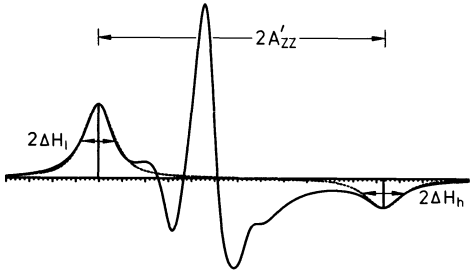

Figure 2. Schematic slow-motion ESR spectrum indicating the method of defining the linewidths, ΔH_l and ΔH_h, and hyperfine splitting, A'_{zz}, used in the correlation time calibration. The linewidth parameters ΔH_m are the half-width at half-height (Marsh, 1986).

unimportant whether the exchange is with one or with many states (Davoust and Devaux, 1982), therefore the results obtained for a two-site model with the exchange-coupled Bloch equations may be used as a starting point.

The increase in Lorentzian linewidth (at half-maximum in angular frequency units) is given simply by $1/\tau_1$, the reciprocal of the exchange lifetime (McConnell, 1958). Thus in this simple model the rotational correlation time is given by

$$\tau_R \approx [\hbar/(g\beta\Delta H_m^R)](\Delta H_m/\Delta H_m^R - 1)^{-1} \tag{30}$$

where ΔH_m^R is the rigid limit value of ΔH_m, the Lorentzian line half-width at half-height of the outer extrema, with $m = 1$ or h for the low-field or high-field extrema, respectively (see Figure 2). In the two-site exchange model the peak separation is decreased by a factor $(1 - 8\tau_1^{-2}\delta\omega^{-2})^{1/2} \simeq (1 - 4\tau_1^{-2}\delta\omega^{-2})$, where $\delta\omega$ is in angular frequency units (Gutowsky and Holm, 1956). Within this model, the rotational correlation time can therefore be approximated by the change in splitting of the outer extrema according to

$$\tau_R \approx [\hbar/(g\beta A_{zz}^R)](1 - A'_{zz}/A_{zz}^R)^{-1/2} \tag{31}$$

where A_{zz}^R is the rigid limit value of the outer hyperfine splitting A'_{zz}, defined for the slow-motion spectrum in Figure 2.

Slow-motion simulations have been performed for isotropic motion using the stochastic Liouville equation (Freed, 1976). Empirical correlation time calibrations have been deduced from the simulations, using the following generalized analogues of equations (30) and (31):

$$\tau_R = a'_m(\Delta H_m/\Delta H_m^R - 1)^{b'_m} \tag{32}$$

$$\tau_R = a(1 - A'_{zz}/A_{zz}^R)^b \tag{33}$$

The calibration constants a'_m, b'_m of equation (32) and a, b of equation (33) are given in Tables 3 and 4, respectively, for various diffusion models and various values of the effective intrinsic peak-to-peak derivative Lorentzian linewidth, $\delta = (2/\sqrt{3})\Delta H_m^R$.

TABLE 3
Parameters for Fitting the Correlation Time Calibration: $\tau_R = a'_m(\Delta H_m/\Delta H_m^R - 1)^{b'_m}$ (Freed, 1976)

Diffusion model	δ (G)	m	a'_m (10^{-8} s)	b'_m
Free diffusion	3.0	l	1.29	−1.033
	3.0	h	1.96	−1.062
	1.0	l	5.32	−1.076
	1.0	h	7.97	−1.125
Brownian diffusion	3.0	l	1.15	−0.943
	3.0	h	2.12	−0.778
	1.0	l	5.45	−0.999
	1.0	h	9.95	−1.014

TABLE 4
Parameters for Fitting the Correlation Time Calibration: $\tau_R = a(1 - A'_{zz}/A^R_{zz})^b$ (Freed, 1976; Polnaszek *et al.*, 1981)

Diffusion model	δ (G)	a (10^{-9} s)	b
Isotropic rotation			
Brownian diffusion	0.3	0.257	−1.78
	3.0	0.54	−1.36
	5.0	0.852	−1.16
	8.0	1.09	−1.05
Free diffusion	0.3	0.699	−1.20
	3.0	1.10	−1.01
Strong jump	0.3	2.46	−0.589
	3.0	2.55	−0.615
y-axis rotation			
Brownian diffusion	—	0.2596	−1.396
Fluctuating torques	—	0.2616	−1.301

In the simple two-site exchange model, the calibration constants from equation (30) are $b'_m = -1$, with $a'_m = 2.9 \times 10^{-8}$ s and 6.57×10^{-8} s for $\delta = 3.0$ G and $\delta = 1.0$ G, respectively. These are in reasonable agreement with the values of Table 3, supporting the concept of lifetime broadening. The two-site exchange values of the calibration constants for the splitting are given from equation (31) by $b = -1/2$ and $a = 1.78 \times 10^{-9}$ s (for $A^R_{zz} = 32$ G). These are similar to the values in Table 4 for strong jump diffusion, for which the exchange analogy is most likely to hold.

The successful application of the calibration method depends on the correct choice of the rigid limit parameters, especially A^R_{zz} since this is also sensitive to the polarity of the environment. The rigid limit linewidths are found from simulation to be related to the peak-to-peak Lorentzian linewidth by (Freed, 1976)

$$2\Delta H^R_l = 1.59\delta \tag{34}$$

$$2\Delta H^R_h = 1.81\delta \tag{35}$$

which are quite close to the predicted value of $\Delta H^R_m = (\sqrt{3}/2)\delta$. Various experimental studies suggest that $\delta \approx 3.0$ G for doxyl nitroxides, and therefore in the absence of more detailed experimental values it is suitable to take $\Delta H^R_l = 2.39$ G, $\Delta H^R_h = 2.72$ G, corresponding to $\delta = 3.0$ G.

The above calibrations were based on simulations for slow *isotropic* motion. However, since they are based on the outer extrema of the spectra, they reflect essentially only the motion of the nitroxide z axis. For rapid axial rotation about the z axis, the formalism is unchanged and the calibrations give the correlation time for the slow rotation of the z axis, i.e., $\tau_R = \tau_{R\perp} = 1/6D_{R\perp}$. For preferentially more rapid rotation about the x or y axis, with relatively small anisotropy ($D_{R\parallel} \lesssim 3D_{R\perp}$), the calibrations approximately yield the compound correlation time $\tau_R = 1/6\sqrt{(D_{R\parallel}D_{R\perp})}$ (Freed, 1976).

For anisotropic rotation about the nitroxide y axis, and very much slower motion perpendicular to this axis, correlation time calibrations have been given by Polnaszek *et al.* (1981). In the slow-motion regime (2×10^{-9} s $\lesssim \tau_{R\|} \lesssim 7.5 \times 10^{-8}$ s), the spectra resemble the rigid limit spectra and the calibration in terms of the outer hyperfine splitting [equation (33)] may be used with the calibration constants for y-axis rotation given in Table 4. Values are given for both Brownian diffusion and including the effects of time-dependent fluctuations in the order parameter, such as are found for the cholestane spin label in gel-phase lipid bilayers.

5. ANISOTROPIC ROTATION: LIPIDS/MEMBRANES

A topic of wide interest concerns the analysis of the motion of spin-labeled lipid chains in membranes. The rotational motion has very anisotropic components and the chains are strongly ordered in an orienting potential. Such spectra have been subjected to an extremely detailed analysis based on measurements with oriented samples and simulations using the stochastic Liouville equation which incorporate a comprehensive motional model (Lange *et al.*, 1985). Representative spectra of dimyristoyl phosphatidylcholine spin labeled on the C-6 position of the *sn*-2 chain, in oriented bilayers of dimyristoyl phosphatidylcholine in the fluid L_α phase, are given in Figure 3. The angular anisotropy of the spectra is clear. However, if the spectra were wholly in the motional narrowing regime, the spectrum at each magnetic field orientation should consist of just three, essentially Lorentzian, lines with hyperfine splittings determined by the amplitude of motion and linewidths by the rate of motion. This is clearly not the case for the spectrum with the 45° magnetic field orientation in Figure 3. Since the bilayers have been found to be well-ordered, these spectra provide unambiguous experimental evidence for motional components of the spin-labeled lipid chains in the slow regime of conventional ESR spectroscopy. The spectra therefore cannot be analyzed by the standard order-parameter formalism of motional narrowing theory, except in a rather empirical manner.

A full analysis of the angular dependence and the temperature dependence of the spectra has allowed discrimination of the different motional modes and determination of their rates. The basis of the simulation method is the stochastic Liouville equation (Kubo, 1969; Freed, 1976)

$$\frac{\partial \rho(\Omega, t)}{\partial t} = -i[\mathcal{H}(\Omega), \rho(\Omega, t)] - \Gamma_\Omega \rho(\Omega, t) \tag{36}$$

where the time dependence is contained solely within the elements, $\rho(\Omega, t)$, of the density matrix. Here $\mathcal{H}(\Omega)$ is the spin Hamiltonian operator, which depends on the orientation and conformation of the molecule, specified by the Euler angles Ω; Γ_Ω is the time-independent Markov operator for the various motional processes, where for rotational diffusion for instance the diffusion equation (12) can be written as

$$\partial p(\Omega, t)/\partial t = -\Gamma_\Omega p(\Omega, t)$$

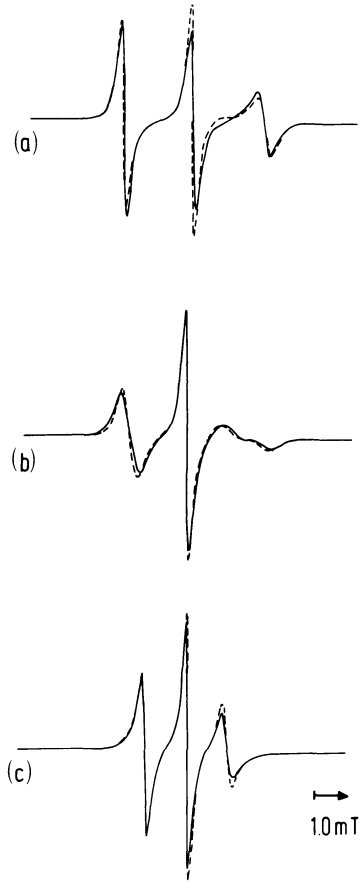

Figure 3. Experimental (——) and simulated (- - - -) ESR spectra of spin-labeled dimyristoyl phosphatidylcholine in oriented bilayers of dimyristoyl phosphatidylcholine in the fluid phase at 40 °C. The spin label was on the C-6 position of the *sn*-2 chain. Spectra as a function of the magnetic field orientation relative to the bilayer normal: (a) $\theta = 0°$, (b) $\theta = 45°$, (c) $\theta = 90°$ (Lange *et al.*, 1985).

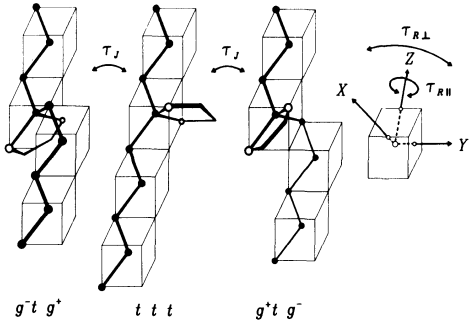

Figure 4. Conformations of the spin-labeled phospholipid chain in its all-*trans* state (*ttt*) and with a single kink (g^+tg^- or g^-tg^+) at the point of attachment of the spin-label ring. The *X*, *Y*, *Z* molecular axes specify the diffusion tensor of the chain. The motional modes incorporated in the simulation model are represented by the arrows. They refer to chain rotation ($\tau_{R\parallel}$), chain fluctuation ($\tau_{R\perp}$), and *trans-gauche* isomerization (τ_J) (Lange *et al.*, 1985).

The Markov operator includes both long-axis and segmental motions, which are indicated schematically in Figure 4. The long-axis motion is the anisotropic rotational diffusion of the lipid molecule as a whole, within an orienting potential. The segmental chain motion consists of *trans-gauche* isomerization, which is represented by a jump process. The dynamics of the system are characterized by three correlation times: $\tau_{R\|}$ ($=1/6D_{R\|}$) and $\tau_{R\perp}$ ($=1/6D_{R\perp}$) for rotation about the diffusion tensor axis and rotation of this axis, respectively, and τ_J for *trans-gauche* isomerization. The order of the chain segments is described in terms of the chain conformations and the chain orientations. Generally, there are four different conformational states corresponding to 0°, 60°, 90°, and 120° orientations of a particular chain segment, relative to a putative preceding all-*trans* chain (Meraldi and Schlitter, 1981; Moser *et al.*, 1989). Particular examples would be, for instance, the all-*trans* configuration for the 0° orientation, an isolated *gauche* conformation for the 60° orientation, a g^+g^+ combination for the 90° orientation, and a $g^+g^+tg^+$ combination for the 120° orientation.

The orientational distribution of the phospholipid molecules is described in the mean field approximation, using an orienting potential from the molecular theories of liquid crystals (Cotter, 1977). For axially symmetric ordering the normalized distribution function

$$f(\beta) = N_1 \exp(A \cos^2 \beta) \tag{37}$$

depends on a single parameter A, characterizing the orientation of the molecules with respect to the local director. The orientational order parameter, S_{ZZ}, is related to the coefficient A by a mean value integral

$$S_{ZZ} = \tfrac{1}{2} N_1 \int_0^{\pi} (3 \cos^2 \beta - 1) \exp(A \cos^2 \beta) \sin \beta \, d\beta \tag{38}$$

where β is the orientation of the diffusion axis relative to the director, and the normalization factor is given by

$$1/N_1 = \int_0^{\pi} \exp(A \cos^2 \beta) \sin \beta \, d\beta \tag{39}$$

The molecular order of the phospholipid molecules is thus specified by the orientational order parameter S_{ZZ} plus the populations of the different allowed chain conformations, e.g., p_t and p_g for the *trans* and isolated *gauche* conformations, respectively. If required, the net effect of the different conformational populations can be summarized in terms of the diagonal elements, $S_{Z'Z'}$ and $S_{X'X'} - S_{Y'Y'}$, of a segmental order-parameter matrix (Moser *et al.*, 1989).

The parameters obtained from a consistent simulation of the angular dependence and temperature dependence of the ESR spectra of dimyristoyl phosphatidylcholine spin-labeled on the 6-C atom of the *sn*-2 chain in oriented bilayers of dimyristoyl phosphatidylcholine are given in Table 5. Representative simulations have already been given in Figure 3. It is found that below the chain melting transition of the phospholipid bilayer ($T < 23$ °C) all correlation times lie in the slow motional regime, $\tau > 10^{-9}$ s, as expected for the gel phase. However, although the *trans-gauche* isomerization rate is

TABLE 5

Motional Parameters Obtained by Simulation of the ESR Spectra of Dimyristoyl Phosphatidylcholine Spin-Labeled on the 6-C Atom of the *sn*-2 Chain in Oriented Dimyristoyl Phosphatidylcholine Bilayers (Lange *et al.*, 1985)

Temp.	Distribution[a]		Order parameter[b]	*Trans* population[c]	Correlation times[d]		
T(°C)	δ_{min}	δ_{max}	S_{ZZ}	p_t	$\tau_{R\perp}$(ns)	$\tau_{R\parallel}$(ns)	τ_j(ns)
50	0	0	0.47	0.51	13	1.4	≤0.2
47	0	0	0.50	0.51	15	1.7	≤0.2
44	0	0	0.51	0.51	19	1.9	≤0.2
40	0	0	0.53	0.51	23	2.3	≤0.2
37	0	0	0.55	0.52	29	2.8	≤0.2
34	0	0	0.55	0.52	35	3.7	≤0.2
30	0	0	0.57	0.53	44	4.4	≤0.2
27	0	0	0.60	0.54	56	5.4	≤0.2
25	0	0	0.61	0.53	61	6.6	≤0.2
22	0	25	0.79	0.45	≥100	≥100	3.7
20	0	25	0.81	0.44	≥100	≥100	3.8
18	0	25	0.83	0.44	≥100	≥100	4.3
16	0	25	0.84	0.44	≥100	≥100	4.5
14	0	25	0.85	0.44	≥100	≥100	4.8
10	28	28	0.86	0.44	≥100	≥100	7.5
8	28	28	0.86	0.45	≥100	≥100	8.0
6	28	28	0.86	0.44	≥100	≥100	8.4
4	28	28	0.86	0.44	≥100	≥100	8.9
2	28	28	0.86	0.45	≥100	≥100	9.5

[a] The uncertainty in fixed tilt angles ($\delta_{min} = \delta_{max}$) is ≤5°.
[b] See equation (38).
[c] Population of the *trans* conformation of the 6th chain segment.
[d] $\tau_{R\perp}$ refers to reorientation of the chain axis, and $\tau_{R\parallel}$ to rotation about it. τ_j is the average lifetime of a conformation at the 6th chain segment.

fast in the fluid bilayer phase ($T > 23$ °C), the correlation times $\tau_{R\parallel}$ and $\tau_{R\perp}$ for the long-axis motion still lie in the slow-motion regime. This is the reason for the complex spectral line shape at the 45° orientation in Figure 3b, which can be very adequately accounted for by the simulations based on the stochastic Liouville equation, with slow motion of the chain long axis.

The chain order is characterized in Table 5 by the order parameter of the long axis, S_{ZZ}, and the *trans* population, p_t. It is found that only *trans* and isolated *gauche* conformations were required to account fully for the spectra of the label at the 6-position ($p_t + 2p_g = 1$). In this region of the chain, the other possible conformations must be suppressed to achieve good chain packing. Comparison with the results of similar simulations of the ^{2}H NMR spectra from dimyristoyl phosphatidylcholine deuterium-labeled at the same chain position have indicated that the order parameter of the chain long axis is accurately recorded by the spin-label spectra, while the segmental order is considerably lower as a result of local conformational distortions induced by the nitroxide ring (Lange *et al.*, 1985). On the whole, the correlation times indicated by the two methods are rather similar.

The static order of the chains is characterized by a fixed molecular tilt δ, which can be determined only with oriented samples. This is found to be zero in the fluid phase, has a single value of 28° in the gel ($L_{\beta'}$) phase, and has a continuous distribution of values from 0 to 25° in the intermediate ($P_{\beta'}$) rippled phase (see Table 5). These results are in agreement with the findings of X-ray diffraction for the $L_{\beta'}$ and $P_{\beta'}$ phases.

In summary, the ESR spectra of chain-labeled lipids contain contributions from slow modes of molecular reorientation, even in the fluid phase, and therefore slow-motion theory (the stochastic Liouville equation) is required for their analysis. Methods of analysis using motional narrowing theory, such as the conventional order-parameter measurement, can only be considered as empirical, and will be biased toward the faster motional components, i.e., *trans-gauche* isomerism. A fuller description of the theoretical model can be found in Lange *et al.* (1985) and Moser *et al.* (1989), and an alternative approach which includes description of isotropic and nematic liquid crystalline systems can be found in Freed (1976).

6. SPIN–SPIN INTERACTIONS AND LATERAL DIFFUSION

In principle, both the Heisenberg spin exchange and the magnetic dipole-dipole interactions [cf. the spin Hamiltonian in equation (2)] contribute to the concentration-dependent spin-spin interactions between nitroxide spin labels. As will be seen below, for spin labels undergoing rapid translational diffusion, both interactions increase linearly with the spin-label concentration, but while the exchange frequency is directly proportional to the translational diffusion coefficient, the dipole-dipole interaction is inversely proportional to the diffusion coefficient. For small spin-labeled molecules in nonviscous media (e.g., aqueous systems) the dipole-dipole interactions may therefore be neglected, and the translational diffusion coefficient can be readily determined directly from the exchange interactions (see, e.g., King and Marsh, 1986; King *et al.*, 1987).

The translational diffusion of spin-labeled lipid molecules in bilayers and in membranes is considerably slower than in aqueous solution, and in general both the spin exchange and dipole-dipole interactions will be appreciable. At high spin-label concentrations the spin exchange and dipole-dipole interactions may be distinguished, since the former gives rise to exchange narrowing at high concentrations while the latter gives rise to a progressive Lorentzian broadening throughout the entire concentration range (see below). At low concentrations the two interactions can only be distinguished from their inverse dependence on the diffusion coefficient (via the temperature dependence of the spin-spin broadening), since, as will be seen below, both interactions give rise to a pure Lorentzian broadening in this concentration regime. An alternative method, based on the relaxation enhancement induced by spin-spin interactions, as monitored by electron-electron double resonance (ELDOR), eliminates all but the pseudosecular ($S_1^{\pm}S_2^{\mp}$) dipole-dipole interactions and may also be employed at low spin-label concentrations (Popp and Hyde, 1982; Feix *et al.*, 1984).

In the following we concentrate on the more conventional methods involving the ESR line broadening and line shapes, and particularly on measurements at low concentrations, since then any perturbing effects of the nitroxide group will be minimized. The emphasis will be on lateral diffusion of lipid molecules in membranes, using spin

labels with the nitroxide group close to the terminal methyl group of the fatty acid chain. For the latter label position there is a high degree of motional averaging of the spectral angular anisotropies, and the linewidth of the $m_I = 0$ manifold can be measured directly. As mentioned previously, the method is also directly applicable to the three-dimensional diffusion of small spin-labeled molecules in aqueous systems, without the complication of dipolar interactions.

6.1. Spin–Spin Exchange

The Heisenberg exchange interaction $J\mathbf{S}_1 \cdot \mathbf{S}_2$ [cf. equation (2)] couples the individual $S = 1/2$ spin states to a triplet and a singlet state which are split in energy by an amount J. Within a given two-electron state there is rapid exchange of the individual electron spin orientations, with a frequency which is again dependent on the exchange constant, J/h (for a simple derivation see, e.g., Marsh, 1986). The effects of this spin exchange on the nitroxide ESR spectrum can be determined from the exchange-coupled Bloch equations. The steady-state equations for the out-of-phase (real) and in-phase (imaginary) electron spin magnetizations, u_m and v_m, associated with the nitrogen nuclear spin quantum number m, are given by (Sackmann and Träuble, 1972; Devaux *et al.*, 1973)

$$(T_{2,m}^{-1} + 3\nu_{ex})u_m - \nu_{ex} \sum_{m'=-1}^{+1} u_{m'} + (\omega_m - \omega)v_m = 0 \tag{40}$$

$$(T_{2,m}^{-1} + 3\nu_{ex})v_m - \nu_{ex} \sum_{m'=-1}^{+1} v_{m'} - (\omega_m - \omega)u_m = -\gamma H_1 M_m^0 \tag{41}$$

where ω_m is the angular resonance frequency of the $m_I = m$ hyperfine line, M_m^0 is the value of the static magnetization in the direction of the applied magnetic field, H_1 is the microwave magnetic field, and γ is the gyromagnetic ratio of the electron; $T_{2,m}$ is the transverse relaxation time and is related to the peak-to-peak, first-derivative linewidth by $\Delta\omega_{pp} = (2/\sqrt{3})T_2^{-1}$. Here ν_{ex} is the rate of spin exchange between any two hyperfine manifolds. For $I(^{14}N) = 1$ this corresponds to a net spin transfer rate for a given hyperfine line of $\tau_{ex}^{-1} = 2\nu_{ex}$ (Devaux *et al.*, 1973). Representative first-derivative ESR spectra simulated according to equations (40) and (41), and ignoring inhomogeneous broadening, are given in Figure 5 for a nitroxide with isotropic ^{14}N hyperfine splitting.

For slow rates of exchange ($\nu_{ex} \lesssim 10^{-7}\,s \ll |\omega_0 - \omega_{\pm 1}|$) the exchange interaction gives rise to a Lorentzian broadening of the individual hyperfine lines, which in analogy to the classical two-site exchange situation [see Marsh (1986) for a review] is given by

$$T_{2,m}^{-1}(\nu_{ex}) = T_{2,m}^{-1}(0) + \tau_{ex}^{-1} \tag{42}$$

For slightly faster exchange rates ($\nu_{ex} \lesssim 5 \times 10^{-7}\,s < |\omega_0 - \omega_{\pm 1}|$), the lines begin to move toward each other, exhibiting incipient exchange narrowing. For the simplified situation in which the intrinsic linewidth may be neglected [$T_{2,m}^{-1}(0) = 0$] the two-site exchange model yields the following for the hyperfine line separation in the presence of exchange (Gutowsky and Holm, 1956):

$$(\omega_0 - \omega_{\pm 1})_{ex} = (\omega_0 - \omega_{\pm 1})[1 - 8\tau_{ex}^{-2}(\omega_0 - \omega_{\pm 1})^{-2}]^{1/2} \tag{43}$$

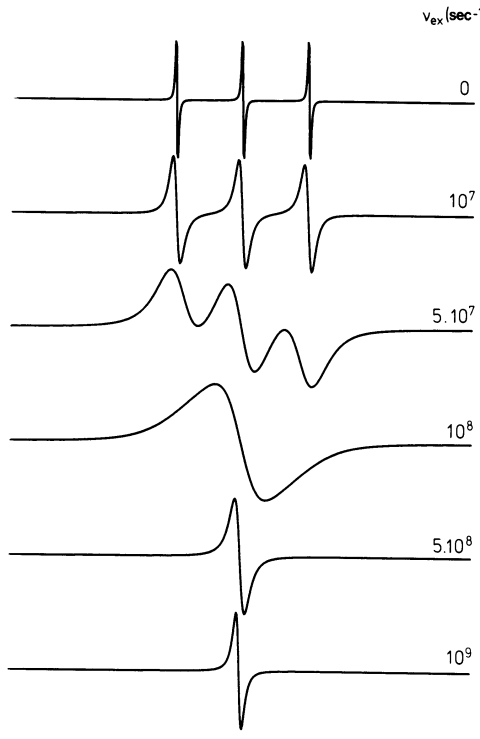

Figure 5. Simulated first-derivative ESR spectra of nitroxide free radicals with various values of the spin-spin exchange frequency, ν_{ex}. Intrinsic Lorentzian linewidth $\Delta H_{pp} = 0.35$ G and the hyperfine splitting constant $A = 14.4$ G. Spectra are plotted with constant line height (Sachse and Marsh, 1986).

In the fast exchange limit ($\tau_{ex}^{-1} \gtrsim 10^{-9}\,\text{s} \gg |\omega_0 - \omega_{\pm 1}|$) the hyperfine lines collapse to a single Lorentzian line with additional broadening determined by the exchange frequency (see, e.g., Johnson, 1967):

$$T_{2,m}^{-1}(\nu_{ex}) = T_{2,m}^{-1}(0) + \tfrac{1}{8}(\omega_0 - \omega_{\pm 1})^2 \tau_{ex} \tag{44}$$

The collapse of the isotropic hyperfine multiplet is a unique feature of the exchange interaction and can be used to distinguish it from the magnetic dipole-dipole interaction. By simulation, even incipient exchange narrowing can be detected unambiguously (Galla and Sackmann, 1975; Sachse *et al.*, 1987). However, this method cannot be applied at low spin-label concentrations, nor can simple simulations such as those in Figure 5 be used, since they ignore the inhomogeneous broadening (which is removed by exchange-narrowing at higher spin-label concentrations).

The exchange frequency τ_{ex}^{-1} is related to the frequency of collisions τ_{coll}^{-1} between spin labels by

$$\tau_{ex}^{-1} = \left(\frac{2I}{2I+1}\right) p_{ex} \tau_{coll}^{-1} \tag{45}$$

where I is the ^{14}N nuclear spin quantum number and p_{ex} is the probability of spin exchange on collision. The factor $2I/(2I+1)$ arises, because only spin exchanges

between radicals with different nuclear spin orientations give rise to a shift in resonance position and hence an observable effect on the ESR spectrum. The exchange probability is determined by the exchange constant $J/\hbar$ and the mean lifetime of the collision pair τ_P (Johnson, 1967; see also Marsh, 1986):

$$p_{ex} = \frac{1}{2}\left(\frac{(J/\hbar)^2\tau_P^2}{1+(J/\hbar)^2\tau_P^2}\right) \tag{46}$$

For nitroxide free radicals the exchange constant is $(J/\hbar) \approx 6 \times 10^{10}\,s^{-1}$ (Plachy and Kivelson, 1967). Hence $p_{ex} = \frac{1}{2}$ for collision pair lifetimes of $\tau_P \gg 2 \times 10^{-11}$ s, which is certainly the case for lateral diffusion of lipid molecules in membranes.

As an illustration of the effects of spin-spin interactions in the low-concentration regime, the Gaussian and Lorentzian contributions to the peak-to-peak first-derivative linewidth of spin-labeled phosphatidylcholine (16-PCSL) in fluid-phase dimyristoyl phosphatidylcholine bilayers are given in Figure 6. The linewidth deconvolution was performed for the $m_I = 0$ central hyperfine manifold, using the methods described in Section 2. In the concentration range $c \lesssim 3$ mol% the ^{14}N hyperfine line broadening is in the slow-exchange regime, as evidenced by the linear concentration dependence of the Lorentzian linewidth (cf. below), but the Gaussian broadening from the unresolved proton hyperfine structure within the ^{14}N manifold exhibits exchange narrowing. The collapse of the Gaussian broadening is practically complete at a concentration of approximately $c \approx 3$ mol%. From the discussion of Figure 5, it is to be expected that this occurs when the exchange frequency is comparable to the unresolved proton hyperfine splitting, namely $\tau_{ex}^{-1} \sim \Delta H_p^G(0)$, where $\Delta H_p^G(0)$ is the Gaussian linewidth in the absence of exchange. This is found to be in approximate agreement with the exchange frequencies determined from the concentration dependence of the exchange contribution to the Lorentzian broadening (Sachse *et al.*, 1987).

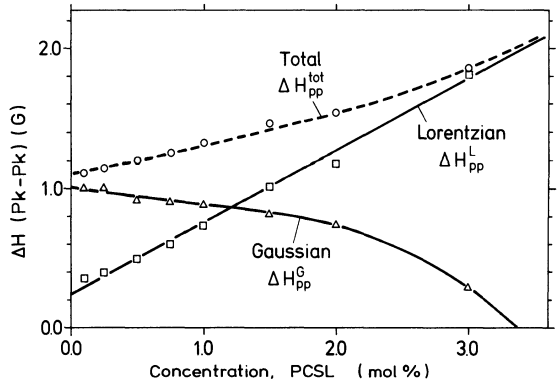

Figure 6. Concentration dependence of the total (ΔH_{pp}^{tot}), Gaussian (ΔH_{pp}^{G}), and Lorentzian (ΔH_{pp}^{L}) peak-to-peak linewidths of the central ($m_I = 0$) hyperfine line of phosphatidylcholine spin-labeled on the 16-C atom of the *sn*-2 chain (16-PCSL) in dimyristoyl phosphatidylcholine bilayers at 53 °C (Sachse *et al.*, 1987).

The concentration dependence of the exchange narrowing of the Gaussian linewidth can be approximated, at least semiquantitatively, using equation (43). If the Gaussian broadening is represented by the coupling of n equivalent protons with effective hyperfine coupling constant $a_{\text{eff}}^{\text{H}}$, the Gaussian linewidth is given by $\Delta H_{\text{pp}}^{\text{G}} \propto \sqrt{n a_{\text{eff}}^{\text{H}}}$. Equation (43) can then be rewritten as $(\Delta H_{\text{pp}}^{\text{G}})^2 = \Delta H_{\text{pp}}^{\text{G}}(0)^2 - (8/\gamma^2)\tau_{\text{ex}}^{-2}$, where γ is required for the conversion to magnetic field units. Experimentally it is found that the square of the Gaussian linewidth is approximately linearly related to the square of the spin-label concentration (Sachse *et al.*, 1987), and this affords an order-of-magnitude estimate for the diffusion coefficient.

6.2. Translational Diffusion and Bimolecular Collision Rate

The concentration dependence of the collision frequency appearing in equation (45) is determined by the diffusive motions of the lipid molecules. The two-dimensional translational diffusion equation is written as

$$\frac{\partial P}{\partial t} = D_{\text{T}} \nabla^2 P$$

$$= D_{\text{T}} \left[\frac{\partial^2}{\partial r^2} + \frac{1}{r} \frac{\partial}{\partial r} \right] P \tag{47}$$

where $P(r, t)$ is the probability that a given molecule is situated at distance r from the origin at time t and D_{T} is the translational diffusion coefficient. The solution of equation (47) for the initial boundary condition $P(r, 0) = \delta(r)$ is given by

$$P(r, t) = (4\pi D_{\text{T}} t)^{-1} \exp(-r^2/4D_{\text{T}}t) \tag{48}$$

Either equation (48) or a two-dimensional random walk model may be used to determine the mean-square displacement $\langle r^2 \rangle$ in time t'. This is given by the Einstein relation

$$\langle r^2 \rangle = 4 D_{\text{T}} t' \tag{49}$$

If a lattice model is used for the diffusion process, the diffusion coefficient is then given by

$$D_{\text{T}} = \tfrac{1}{4} \nu_j \lambda^2 \tag{50}$$

where λ is the lattice spacing (or mean free path) and ν_j is the hopping frequency between adjacent lattice sites. For bimolecular diffusive encounters, the origin of coordinates ($r = 0$) is not a fixed position but is defined by the position of another identical molecule. Then D_{T} must be replaced by $2D_{\text{T}}$ in equations (48)–(50).

The frequency of collision is directly related to the lateral diffusion coefficient, via the lattice model. If a given lipid exchanges with one of its six nearest neighbors, it encounters three new nearest neighbors and the collision frequency is given by (Devaux *et al.*, 1973)

$$\tau_{\text{coll}}^{-1} = 3 \nu_j c \tag{51}$$

where c is the mole fraction of spin label. Combining equations (50) and (51), including the substitution of $2D_T$ for bimolecular collisions, the diffusion coefficient is

$$D_T = \left(\frac{\lambda^2}{24}\right)\left(\frac{\tau_{coll}^{-1}}{c}\right) \tag{52}$$

Combined with equation (45), this allows evaluation of the diffusion coefficient from the concentration dependence of the measured exchange frequency, i.e., from the exchange contribution to the Lorentzian line broadening. Before this may be done, however, allowance must be made for the dipolar contribution to the exchange broadening.

6.3. Dipolar Spin–Spin Broadening

The contribution to the transverse relaxation from magnetic dipole-dipole interactions can be evaluated using motional narrowing theory as described previously for nuclear spin relaxation (Abragam, 1961; Berner and Kivelson, 1979). Motional narrowing theory is applicable in the dynamic limit:

$$\tau_D / T_{2,m} \ll 1 \tag{53}$$

where τ_D is a characteristic relaxation time for translational diffusion defined by

$$\tau_D = 2r_c^2 / D_T \tag{54}$$

and $2r_c$ is the distance of closest approach of the two spin dipoles.

The treatment here follows that of Berner and Kivelson (1979). For two like spins S (i.e., having the same nitrogen nuclear magnetic quantum number, $m_I = m$) the transverse relaxation time is given by (see Abragam, 1961)

$$\frac{1}{T_{2,m}(\mathrm{dd})} = \gamma^4\hbar^2 S(S+1)[\tfrac{3}{8}J^{(2)}(2\omega_m) + \tfrac{15}{4}J^{(1)}(\omega_m) + \tfrac{3}{8}J^{(0)}(0)] \tag{55}$$

where $J^{(i)}$ are the spectral densities appropriate to translational diffusion. For two unlike spins (i.e., with different nuclear magnetic quantum numbers, m and m') the transverse relaxation time of the spin with nuclear quantum number m is given by (see Abragam, 1961)

$$\frac{1}{T'_{2,m}(\mathrm{dd})} = \gamma^4\hbar^2 S(S+1)[\tfrac{1}{6}J^{(0)}(0) + \tfrac{1}{24}J^{(0)}(\omega_m - \omega_{m'}) + \tfrac{3}{4}J^{(1)}(\omega_m) + \tfrac{3}{2}J^{(1)}(\omega_{m'}) + \tfrac{3}{8}J^{(2)}(\omega_m + \omega_{m'})] \tag{56}$$

If it is assumed that

$$\omega_m^2 \tau_D^2 \gg 1 \tag{57}$$

i.e., that $\tau_D \gg 2 \times 10^{-11}$ s, then all spectral density terms at frequencies ω_m and $(\omega_m + \omega_{m'})$ can be neglected. If it is further assumed that

$$a^2\tau_D^2 \ll 1 \tag{58}$$

i.e., that $\tau_D \ll 3 \times 10^{-9}$ s, where a is the hyperfine splitting constant: $\omega_m - \omega_{m'} \approx a$, then the spectral density at frequencies $(\omega_m - \omega_{m'})$ may be set equal to those at zero frequency. The spectral density at zero frequency can be obtained from solution of the three-dimensional analogue of the translational diffusion equation given in equation (47). Including the substitution of $2D_T$ for bimolecular processes, this is given in Abragam (1961) as

$$J^{(0)}(0) = \frac{48 \times 10^{-3}\pi}{15^2} \frac{N_{AV}c_m}{D_T r_c} \tag{59}$$

where N_{AV} is Avogadro's number and c_m is the molar concentration of spin label. The three-dimensional rather than the two-dimensional diffusion equation is used here to allow for the effect of the angular motion of the lipid chains, which does not contribute to the exchange frequency but gives rise to an additional averaging of the dipolar interaction.

The probability of collisions between spins of like nuclear magnetic quantum number is $(2I + 1)^{-1}$ and that between unlike spins is $2I(2I + 1)^{-1}$. Here I is the nitrogen nuclear spin. Thus the net transverse relaxation time is given by

$$\frac{1}{T_2^{dd}} = \frac{(2I + 1)^{-1}}{T_{2,m}(dd)} + \frac{2I(2I + 1)^{-1}}{T'_{2,m}(dd)} \tag{60}$$

Hence from equations (55), (56), and (59), the transverse relaxation time due to dipole-dipole interaction between spins with $S = \frac{1}{2}$ is given by

$$\frac{1}{T_2^{dd}} = \frac{\gamma^4\hbar^2\pi N_{AV}(10^{-3})}{150(2I + 1)} \frac{(9 + 10I)}{D_T r_c} c_m \tag{61}$$

This equation allows an independent estimate of the diffusion coefficient from the magnetic dipole-dipole contribution to the Lorentzian line broadening. To do this the dipolar and exchange contributions to the concentration-dependent Lorentzian broadening must be resolved.

6.4. Separation of Exchange and Dipole–Dipole Interactions

The temperature dependence of the linear concentration dependence of the Lorentzian broadening, $d(\Delta H_{pp}^{L})/dc$, deduced from plots such as those of Figure 6, is given in Figure 7, and is clearly biphasic. At lower temperatures the concentration dependence of the broadening decreases with increasing temperature, indicating that the dipolar broadening, which is inversely proportional to the translational diffusion coefficient [cf. equation (61)], is dominating over the exchange broadening. At higher temperatures

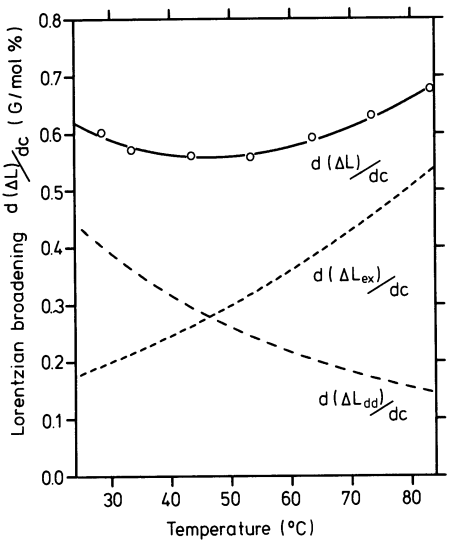

Figure 7. Temperature dependence of the gradient with respect to concentration of the Lorentzian linewidth, $d(\Delta H^{L}_{pp})/dc = d(\Delta L)/dc$, of the 16-PCSL phosphatidylcholine spin label in dimyristoyl phosphatidylcholine bilayers. The full curve represents the nonlinear least-squares optimized fit of equation (64) to the experimental points, and the dashed lines are the exchange, $d[\Delta H^{L}_{pp}(ex)]/dc = d(\Delta L_{ex})/dc$, and dipole-dipole, $d[\Delta H^{L}_{pp}(dd)]/dc = d(\Delta L_{dd})/dc$, contributions represented by the first and second terms in equation (64), respectively (Sachse *et al.*, 1987).

the gradient of the broadening increases with increasing temperature, as expected when the exchange interaction dominates [cf. equations (42) and (45)]. Since the diffusion coefficient is given by the Einstein relation $D_T = kT/f$, where the friction coefficient f is proportional to the effective membrane viscosity, its temperature dependence is expected to be of the form

$$D_T = D_{T,0} T \exp(-E_a/RT) \tag{62}$$

where E_a is the activation energy associated with the effective membrane viscosity. The concentration-dependent gradient of the total Lorentzian line broadening is the sum of the exchange and dipolar contributions:

$$d(\Delta H^{L}_{pp})/dc = d[\Delta H^{L}_{pp}(ex)]/dc + d[\Delta H^{L}_{pp}(dd)]/dc \tag{63}$$

Therefore its temperature dependence will have the following form:

$$d(\Delta H^{L}_{pp})/dc = AT \exp(-E_a/RT) + BT^{-1} \exp(+E_a/RT) \tag{64}$$

where A and B are temperature-independent constants representing the exchange and dipolar contributions, respectively. From equations (42), (45), and (52), the exchange contribution is given by

$$A = \left(\frac{I}{2I+1}\right)\left(\frac{96}{\sqrt{3}\gamma\lambda^2}\right) D_{T,0} \tag{65}$$

where an additional factor of 2 has been introduced in the numerator to allow for collisions with labels at C-16 position in the other half of the bilayer. From equation (61), the dipolar contribution is

$$B = \frac{\gamma^3 \hbar^2 \pi N_{AV}}{75(2I+1)} \frac{(9+10I)}{\sqrt{3} r_c} (M_1 \bar{v}_1) \ {}^1D_{T,0}^{-1} \tag{66}$$

where M_1 and $\bar{v}_1$ are the lipid molecular weight and partial specific volume, respectively, which are needed in the conversion of the molar concentration c_m to the mole fraction c. [An additional factor of 2 has not been introduced into this equation, because equation (61) is already based on a three-dimensional model.]

The exchange and dipolar contributions to the Lorentzian line broadening can be separated by fitting the temperature dependence in Figure 7 to the expression given in equation (64), using a numerical procedure. With the fits given in Figure 7, the diffusion coefficients obtained from the combined concentration and temperature dependences of the exchange and dipolar Lorentzian broadening are given by

$$D_T = 0.973 \times 10^{-7} \times T \exp(-3310/RT) \qquad \text{and}$$

$$D_T = 2.10 \times 10^{-7} \times T \exp(-3310/RT) \qquad \text{cm}^2 \text{ s}^{-1}$$

respectively, where a value of $\lambda = 8$ Å has been assumed for the mean jump length, and $r_c \sim \lambda = 8$ Å for the critical contact distance. It is found that the diffusion coefficients lie in the region of 10^{-7} cm^2 s^{-1}, and that those deduced from the dipolar interaction are approximately twice as large as those deduced from the exchange interaction. In view of the quite different diffusion models used in the two cases, the agreement can be considered to be very satisfactory, and gives support for the method used to separate the dipolar and exchange contributions to the Lorentzian broadening. Since the exchange interaction is essentially a contact interaction, it gives a direct measure of the molecular collision rate and therefore is likely to be more reliable and is also generally applicable to situations with faster diffusion, for which the dipolar interaction is completely averaged.

In conclusion, translational diffusion rates may be measured from the spin-spin broadening at low spin-label concentrations, but correction must be made for the inhomogeneous broadening and, for slower diffusion, allowance must also be made for the dipolar broadening.

7. LIPID–PROTEIN INTERACTIONS

As mentioned in the Introduction, conventional nitroxide ESR is sensitive to motions faster than the ^{14}N hyperfine anisotropy, i.e., to rotational correlation times shorter than about 10^{-8} s. If the lipid exchange at the surface of integral proteins in membranes is appreciably slower than this, the spin-labeled lipids at the protein interface will be distinguishable from those in the bulk lipid regions, provided that there is a difference in lipid molecular mobility between these two states. This unique motional sensitivity of spin-label ESR spectra was exploited by Jost *et al.* (1973a), who were the

first to resolve the ESR spectra from the so-called boundary layer of lipids interacting with the protein, in this case cytochrome oxidase in progressively delipidated preparations.

Lipid spin-label ESR spectra in membranes or reconstituted lipid-protein systems can therefore be interpreted in terms of two components in slow exchange on the nanosecond time scale. One component is characteristic of the lipid mobility in fluid, protein-free bilayers, and the other corresponds to lipids whose mobility is restricted by direct interaction with the intramembranous hydrophobic surface of the integral proteins. The two-component nature of the spectra has allowed direct study of the stoichiometry and specificity of the interaction in a wide variety of different lipid-protein systems (see Marsh, 1985, for a review). The two lipid populations are coupled by exchange on and off the intramembranous surface of the protein, and it is found that the rate of this exchange lies within the range of motional sensitivity of nitroxide ESR spectroscopy, which therefore may be used to characterize the dynamics as well as the thermodynamics of the lipid-protein interaction.

Evidence for the two-component nature of the ESR spectra comes from: (1) spectral subtraction and addition, (2) spectra of spin labels with different orientations of the nitroxide group and hence quite different spectral line shapes, (3) measurements at different microwave frequencies, (4) the selectivity between different phospholipids and the variation of this selectivity with pH and salt concentration, and (5) spectral simulation using two-site exchange models. All of these aspects of the spectroscopy and the lipid-protein interaction are discussed below (see also, Marsh, 1983, 1985).

7.1. Spectral Subtraction/Addition

An example of spectral subtraction and addition is given in Figure 8 for a lipid-protein recombinant of the proteolipid apoprotein from nerve myelin with the synthetic lipid, dimyristoyl phosphatidylcholine (DMPC). Choice of a lipid probe spin-labeled close to the terminal methyl end of the chain (in the C-14 position of the *sn*-2 chain) ensures that a narrow, motionally averaged spectrum is obtained in fluid lipid bilayers (see Figure 8c, full line). In order to allow for the broadening effects of exchange on the spectral line shapes, spectra from spin labels in the lipid alone and in the delipidated protein, which best fit the apparent fluid and restricted components in the recombinant spectrum, are chosen for the subtraction. For the fluid component (Figure 8c, full line), this corresponds to a spectrum from DMPC alone recorded at a temperature lower than that at which the recombinant spectrum (Figure 8a, full line) was recorded, and for the protein alone (Figure 8b, full line) corresponds to a higher temperature than that for the recombinant. Essentially consistent values for the relative proportions of the fluid and motionally restricted components are obtained from spectral addition (Figure 8a, dotted line) and from the two complementary methods of spectral subtraction (Figures 8b and 8c, dotted lines). These relative proportions are determined from the double integrals of the first-derivative line shapes for the composite and single-component spectra. The most convenient method is to normalize all the original spectra to the same double integral.

An iterative protocol for choosing the single components and the subtraction endpoints is described in Marsh and Watts (1982). Briefly, the steps are as follows. (1) A fluid spectrum is chosen which corresponds most closely to the apparent fluid

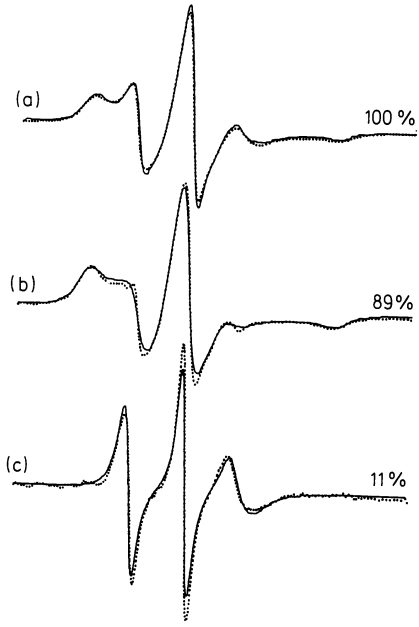

Figure 8. Spectral subtraction and addition with the 14-PASL phosphatidic acid spin label in a lipid-protein complex. Full lines represent original ESR spectra: (a) myelin proteolipid apoprotein/dimyristoyl phosphatidylcholine recombinant of lipid/protein ratio 12:1 mole/mole at 30 °C; (b) proteolipid apoprotein alone at 32 °C; (c) dimyristoyl phosphatidylcholine alone at 25 °C. Dotted lines are summed spectra and difference spectra: (a) 11% lipid-alone spectrum plus 89% protein-alone spectrum; (b) recombinant spectrum minus 11% lipid-alone spectrum; (c) recombinant spectrum minus 89% protein-alone spectrum. Percents refer to the relative double integrated intensity of the total recombinant spectrum. Microwave frequency, 9 GHz; total scan width, 100 gauss (Brophy *et al.*, 1984).

component in the composite spectrum (usually the pure lipid spectrum recorded at a slightly lower temperature). (2) The fluid component is subtracted to yield a motionally restricted endpoint which corresponds most closely to one of a series of motionally restricted spectra either from delipidated protein or gel phase lipids. (3) The fluid endpoint obtained by subtracting the selected motionally restricted spectrum is optimized by comparing with the library of fluid spectra at considerably expanded vertical gain. (4) The cycle is repeated to optimize the single-component spectra selected in (2) and (3). Criteria for valid subtraction endpoints have also been discussed in some detail by Jost and Griffith (1978), the most important being a well-behaved first integral with no negative excursions below the baseline.

Subtractions/additions of the type illustrated in Figure 8 require knowledge of the two single components, which are best found by empirically matching trial spectra, using the protocols given above. Alternatively, the method may be extended to perform pairwise intersubtractions between composite spectra containing different proportions of the two components (Brotherus *et al.*, 1980; Knowles *et al.*, 1981). Let S^A and S^B refer to two such spectra composed of fluid and motionally restricted components s_f and s_b, respectively. Then assuming that the spectra are all normalized to the same double-integrated intensity, the relative compositions of the two spectra are

$$S^A = \alpha^A s_b + (1 - \alpha^A) s_f \tag{67}$$

$$S^B = \alpha^B s_b + (1 - \alpha^B) s_f \tag{68}$$

where α^A and $(1 - \alpha^A)$ are the fractions of the total integrated intensity in the motionally restricted and fluid components, respectively, for spectrum A, and similarly with change

of suffix for spectrum B. Taking spectrum A to be that with the greater proportion of motionally restricted component, it is clear that subtraction of a fraction $f^A = (1 - \alpha^A)/(1 - \alpha^B)$ of spectrum B from spectrum A is required to obtain a motionally restricted subtraction endpoint, and similarly subtraction of a fraction $f^B = \alpha^B/\alpha^A$ of spectrum A from spectrum B is required to give a fluid endpoint. Hence the fractions of motionally restricted component, α^A and α^B, in the two spectra can be obtained from the complementary intersubtractions. The method will work strictly, only if the exchange rates and any longer-range perturbations in the two spectra are comparable. This is often the case for variations in selectivity with salt and pH titration, or with different lipids, at a fixed lipid/protein ratio. Intersubtraction is in general less successful with samples of different lipid/protein ratios, exactly for the above-mentioned reasons.

In general, two-component spectra from lipid-protein systems have been observed with phospholipids and fatty acids spin-labeled close to the terminal methyl group of the chain. Because the nitroxide z axis is parallel to the long axis of the chain, a high degree of segmental motion is required to reduce the spectral anisotropy in the fluid component before it is possible to resolve this from the motionally restricted component. Other spin-labeled lipids, notably the steroids cholestane or androstanol (Jost *et al.*, 1973b; Marsh and Barrantes, 1978) and the azethoxy chain labels (Lee *et al.*, 1979), have their nitroxide z axes perpendicular (or more nearly perpendicular) to the long axis of the lipid molecule. The result is not only rather different spectral line shapes, but also a different motional sensitivity. In these cases, the spin labels are primarily sensitive to rotation about the long axis of the molecule (see Polnaszek *et al.*, 1981, for quantitative simulations). The fact that motionally restricted components are also seen with these labels, when the long-axis rotation rate is sufficiently rapid to average the spectral anisotropy in the fluid lipid component, is further evidence for the existence of two motionally distinct lipid spin-label populations in lipid-protein systems.

7.2. Measurements at 35 GHz

Spin-label spectra are normally recorded at a microwave frequency of 9 GHz (see, e.g., Figure 8). At the resonance field (*ca* 3200 gauss) corresponding to this frequency, the effects on the spectra of the g-tensor anisotropy are considerably less than those of the hyperfine anisotropy [cf. equation (1)]. At 35 GHz (resonance field about 12,500 gauss) the two become comparable. This has a large effect not only on the relative line positions in the spectra, but also on the differential line broadenings. Comparison of the spectra from lipid-protein systems recorded at the two microwave frequencies therefore provides a rather critical test of the two-component nature of the spectra.

The spectra from myelin proteolipid protein/dimyristoyl phosphatidylcholine recombinants of various lipid/protein ratios, recorded at 9 and 35 GHz, are given in Figure 9. For the pure lipid samples (bottom line in Figure 9), the effect of microwave frequency on the line positions is slight because nearly all spectral anisotropy is averaged at the C-14 label position, but the increased differential broadening of the central and high-field lines is very clear at the higher frequency. In the protein-containing samples, a second component, the relative proportion of which increases with increasing protein content, can be seen in the outer wings at low and high field for the spectra recorded at either frequency. At low field the second component is better separated from the

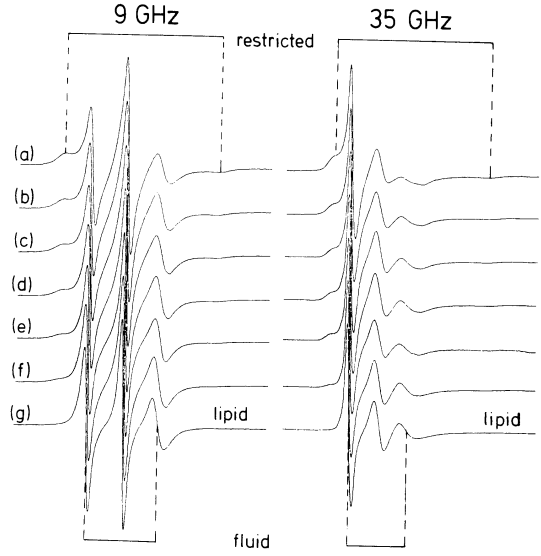

Figure 9. ESR spectra of the 14-PASL phosphatidic acid spin label in myelin proteolipid apoprotein/dimyristoyl phosphatidylcholine recombinants of various lipid/protein ratios recorded at microwave frequencies of 9 GHz (left-hand side) and 35 GHz (right-hand side), $T = 30\,°C$. Lipid/protein ratios of the various samples are: (a) 23:1 mole/mole and gradually increasing from (b) to (f), and (g) lipid alone. The spectra of the fluid and motionally restricted lipid components are indicated by the lower and upper pairs of dashed lines, respectively, for the two spectral series. Total scan width is 100 gauss for the 9 GHz spectra and 120 gauss for the 35 GHz spectra (Horvath *et al.*, 1989).

fluid component at 9 GHz, while the second component is shifted much further to high field of the fluid component at 35 GHz than at 9 GHz. In addition, at high protein contents, one of the $m_I = 0$ lines can be seen superimposed on the high-field line of the fluid component at 35 GHz. At 9 GHz, all $m_I = 0$ lines of the second component are unresolved from the fluid component in the central region of the spectrum. These effects are exactly what would be expected from the difference in g-value anisotropies between the fluid and motionally restricted components.

These data at two microwave frequencies leave little doubt that the spin-label ESR spectra from the lipid-protein recombinants consist of two components in slow exchange. Similar results have also been observed with Na^+, K^+-ATPase membranes (Epperlein, D., Esmann, M., and Marsh, D., unpublished). In cases of possible ambiguity, measurement at a higher microwave frequency can therefore be of considerable help in substantiating the two-component nature of the spectra from lipid-protein systems. In general, detection of the motionally restricted component may be more difficult at 35 GHz, because of the higher intensity of the low-field line in the fluid component and also the greater broadening of the high-field lines in the motionally restricted component. The latter effect, on the other hand, can be of considerable assistance in investigating the dynamic properties of the motionally restricted component (Hyde and Rao, 1980)—see also Section 4.

7.3. Analysis of Lipid–Protein Association

By varying the lipid-to-protein ratio in the recombinant, it is possible to check whether the number of lipids motionally restricted bears a fixed relation to the total amount of protein. In the absence of protein aggregation, such a fixed stoichiometry

would be expected if the motionally restricted ESR component really represents those lipids forming the first shell around the protein. Brotherus *et al.* (1981) have modeled the lipid-protein association as an exchange equilibrium between labeled and unlabeled lipids, L^* and L, respectively, competing for sites at the intramembranous surface of the protein:

$$B_iL + L^* \rightleftharpoons B_iL^* + L \tag{69}$$

Here it is assumed that there are m classes of different association sites, B_i $(i = 1, \ldots, m)$ each of which can accommodate n_i lipid molecules. The relative association constant of a labeled lipid with a given site is then

$$K_i' = \frac{L_{b_i}^* L_f}{L_{b_i} L_f^*} \left(\frac{\gamma_{b_i}^* \gamma_f}{\gamma_{b_i} \gamma_f^*} \right) \tag{70}$$

where $L_{b_i}^*$ and L_{b_i} are the moles of labeled and unlabeled lipid, respectively, associated with sites B_i, and $\gamma_{b_i}^*$ and γ_{b_i} are the corresponding activity coefficients (defined in terms of mole fractions); L_f^* and L_f, and γ_f^* and γ_f, are defined similarly for the free (nonassociated) lipid populations. The standard state for the unlabeled lipid in the bilayer is the pure bilayer of unlabeled lipids, and that for the labeled lipids is chosen such that the activity becomes equal to the mole fraction as the latter tends to zero. Here the activity coefficients will be assumed to be unity, which should be the case for low concentrations of protein and labeled lipids, in the absence of specific protein-protein or lipid-lipid interactions. (Variations in activity coefficients for specific lipid-protein interactions will be dealt with later below.) A new effective association constant may then be defined solely in terms of moles of lipid:

$$K_i = K_i' \left(\frac{\gamma_{b_i} \gamma_f^*}{\gamma_{b_i}^* \gamma_f} \right) = \frac{L_{b_i}^* L_f}{L_{b_i} L_f^*} \tag{71}$$

The conservation of the total number of labeled and unlabeled lipids, and of the protein association sites, leads to the following respective equations:

$$L_f^* + \sum_{i=1}^{m} L_{b_i}^* = L_t^* \tag{72}$$

$$L_f + \sum_{i=1}^{m} L_{b_i} = L_t \tag{73}$$

$$L_{b_i} + L_{b_i}^* = n_i P \tag{74}$$

where L_t^* and L_t are the total numbers of moles of labeled and unlabeled lipids, respectively, and P is the total number of moles of protein. Combination of equations (71) and (72)-(74) leads to the following expression for the equilibrium association of lipids with the protein (Brotherus *et al.*, 1981):

$$\sum_{i=1}^{m} \frac{n_i K_i (n_f^*/n_b^*)}{[1 + K_i (n_f^*/n_b^*)](1 + n_f^*/n_b^*)^{-1} n_t^* + n_t - N_t} = 1 \tag{75}$$

where $N_1 = \sum_{i=1}^{m} n_i$ is the total number of first-shell association sites on the protein, $n_t^* = L_t^*/P$ and $n_t = L_t/P$ are the total numbers of labeled and unlabeled lipids per protein, and n_f^*/n_b^* is the ratio of labeled lipids free in the bilayer to those associated in first-shell sites on the protein, i.e., n_f^*/n_b^* is the ratio of fluid to motionally restricted component intensities obtained by ESR spectroscopy.

Equation (75) contains no restrictions, other than that all sites on the protein be occupied, and can be applied quite generally to the competition between different lipid species for sites on the protein. The approximation normally applicable in spin-label ESR experiments is that the concentration of labeled lipids relative to unlabeled lipids is very low:

$$[1 + K_i(n_f^*/n_b^*)](1 + n_f^*/n_b^*)^{-1} n_t^* \ll n_t - N_1$$

The equilibrium association equation can then be written as

$$(n_f^*/n_b^*) = n_t/(N_1 K_r^{av}) - 1/K_r^{av} \tag{76}$$

where the average relative association constant for all N_1 sites is defined by

$$K_r^{av} = \sum_{i=1}^{m} n_i K_i / N_1 \tag{77}$$

The spin-label ESR experiment therefore allows determination of the total number of first-shell sites on the protein (i.e., the stoichiometry of the lipid/protein interaction), and the average association constant of the labeled lipids relative to the unlabeled lipids, K_r^{av}.

Equation (76) has been applied to the analysis of ESR data from several reconstituted lipid-protein systems, including cytochrome oxidase (Knowles *et al.*, 1979; Brotherus *et al.*, 1981), myelin-proteolipid protein (Brophy *et al.*, 1984), Na^+, K^+-ATPase (Brotherus *et al.*, 1981), Ca^{2+}-ATPase (Silvius *et al.*, 1984), and the acetylcholine receptor (Ellena *et al.*, 1983). It is found that, for complexes with reasonably high lipid-to-protein ratios ($n_t \gtrsim 2N_1$) at which protein-protein contacts are expected not to be appreciable, the lipid-protein titration data can be described adequately by equation (76). In all reconstitutions with unlabeled phosphatidylcholine investigated so far, it is found that the relative association constant for spin-labeled phosphatidylcholine is unity, $K_r^{av}(PC^*/PC) = 1$, indicating no selectivity for the spin-labeled lipid over that of the unlabeled lipid. Apparently the presence of the nitroxide spin-label group does not affect the energetics of the lipid-protein interaction appreciably. A list of the lipid/protein stoichiometries obtained in this way can be found in Marsh (1985).

The finding that the lipid-protein titration data can be described by a fixed number of sites N_1 on the intramembranous surface of the protein, independent of the total number of lipids in the complex, validates the model for the lipid-protein association, and indicates that (at least operationally) the motionally restricted lipid component observed by ESR spectroscopy may be identified with the first shell of lipid molecules interacting directly with the intramembranous hydrophobic surface of the protein. To obtain a more precise structural assignment of the first shell of motionally restricted lipids, it is necessary to make a comparison with the protein structures. This has been

done in the review by Marsh (1985). It is found that not only does the number of motionally restricted lipids correlate with the protein molecular weight, but also there is a very good correspondence with estimates of the number of lipids which can be accommodated around the intramembranous perimeter of the protein, based on presently available structural data. This suggests that, overall, the motionally restricted lipids correspond geometrically, as well as operationally, to the first shell of lipids surrounding the protein in the membrane. However, the structural information used for the comparisons is mostly of rather low resolution and it cannot be excluded that the motionally restricted lipids are accommodated within pockets on the surface of the protein, rather than covering the entire intramembranous surface.

A similar method of analysis may be used to investigate the selectivity of interaction of the various lipid classes with integral membrane proteins. Spin labels are used which have the same chain composition (including the spin-label group) and differ only in their polar headgroups. For lipid-protein recombinants of the same lipid/protein ratio, preferential associations of the different lipids with the protein will be manifest by differences in the proportion of motionally restricted spin-labeled lipid in the two-component ESR spectra. Such selective associations are found in the interaction of certain lipids with some, but not all, integral membrane proteins. An example is given by the pH titration of the interaction of spin-labeled stearic acid with the myelin proteolipid protein in Figure 11, below. The deprotonated form of the fatty acid displays a clear selectivity, in terms of the fraction of motionally restricted lipid, over that of the protonated fatty acid. The selectivity can be quantitated in terms of the relative association constants K_r^{av} and numbers of first-shell lipids N_1 using equation (76). Titrations of the lipid/protein ratio in recombinants with myelin proteolipid protein (Brophy *et al.*, 1984), cytochrome oxidase (Knowles *et al.*, 1981), Na^+, K^+-ATPase (Brotherus *et al.*, 1981), acetylcholine receptor (Ellena *et al.*, 1983), and Ca^{2+}-ATPase (Silvius *et al.*, 1984) have demonstrated that the lipid selectivity arises from differences in the average association constants, rather than in the total number of association sites. Thus, even in systems for which the lipid/protein ratio cannot be varied, the average association constants for each lipid L may be determined relative to a particular lipid, e.g., phosphatidylcholine, PC. From equation (76), the ratio of association constants is given by

$$(n_f^*/n_b^*)^{PC}/(n_f^*/n_b^*)^{L} = K_r^{av}(L)/K_r^{av}(PC) = K^{av}(L)/K^{av}(PC) \tag{78}$$

where the second equality indicates that the association constants can be referred to any desired standard state. The values for the relative association constants can be related to the effective free energy of association arising from the selectivity via the relation

$$\Delta G_L - \Delta G_{PC} = -RT \ln[K_r^{av}(L)/K_r^{av}(PC)] \tag{79}$$

The order of selectivity of different lipid species, in terms of their relative association constants, is listed for a variety of membrane proteins by Marsh (1985).

Whether the average association constants defined in equation (77) in fact correspond to a general increase in selectivity for all N_1 sites, or to a higher specificity for fewer sites, n_i, can be tested by increasing the concentration of the specific lipid

(Brotherus *et al.*, 1981). If there are just a few specific sites, these will rapidly become saturated as the concentration of the specific lipid is increased, while if all sites are equivalent in specificity, the fraction of protein-associated lipid will decrease only rather slowly with increasing concentration of the specific lipid. Quantitatively the lipid-protein association must then be analyzed using the full equation (75), rather than the approximation for low label concentrations [equation (76)]. For the interaction of cardiolipin with cytochrome oxidase it was found that the specificity was approximately equal for all $N_1 = 50$ sites on the protein, with a relative association constant for cardiolipin with respect to phosphatidylcholine of $K_r(\mathrm{CL}) = 5.4$, as opposed to a value of $K_r(\mathrm{CL}) = 221$ which would be obtained if, for instance, there were just one highly specific site and the other 49 sites exhibited no preferential interaction (Powell *et al.*, 1985). It remains to be seen whether this is the case for the specific interaction with other proteins.

Electrostatic contributions to the selectivity for negatively charged lipids can be studied via the dependence of the fraction of motionally restricted lipid on ionic strength. A screening of the electrostatic interaction between the protein and lipid arises because the activity coefficients γ_j of the charged species are reduced by the counterion cloud. Hence, according to equation (71), the average relative lipid association constant in the presence of salt is related to the corresponding value K_r^0 in the absence of salt by

$$K_r = K_r^0(\gamma_L^* \gamma_P / \gamma_{LP}^*) \tag{80}$$

where γ_L^* is the activity coefficient of the charged spin-labeled lipid, and γ_{LP}^* and γ_P are the activity coefficients for the lipid-protein complex and for the protein, respectively. The ionic strength dependence can then be described, at least semiquantitatively, using the standard Debye-Hückel expressions for the activities of the charged species, j:

$$\ln \gamma_j = \frac{-Z_j^2 e^2}{8\pi\varepsilon_0 \varepsilon kT} \cdot \frac{\kappa}{1 + \kappa a_j} \tag{81}$$

where Z_j is the charge on species j, a_j is the effective interaction distance of species j with counterions, and the inverse Debye screening length is $\kappa = (2000 N_A e^2 I / \varepsilon_0 \varepsilon kT)^{1/2}$, I being the ionic strength of the assumed 1:1 electrolyte. Hence the ratio of relative association constants in the presence and absence of salt is given by

$$\ln(K_r / K_r^0) = \frac{-e^2 \kappa}{8\pi\varepsilon_0 \varepsilon kT} \left(\frac{Z_{L^*}^2}{1 + \kappa a_{L^*}} + \frac{Z_P^2}{1 + \kappa a_P} - \frac{(Z_P + Z_{L^*})^2}{1 + \kappa a_{L^*P}} \right) \tag{82}$$

where L*, P and L*P represent the lipid spin label, the protein, and the lipid-protein complex, respectively. Results for the salt dependence of interaction of negatively charged phospholipids with the Na^+, K^+-ATPase (Esmann and Marsh, 1985), and with the myelin proteolipid protein (Horvath *et al.*, 1988a), conform reasonably well with a screening of the type indicated by equations (80)-(82).

7.4. Two-Site Exchange Simulations

The exchange rate for lipids at the protein interface may be estimated by simulation of the lipid spin-label ESR spectra, using the exchange-coupled Bloch equations (see, e.g., Davoust and Devaux, 1982; Marsh, 1986). The simulations also provide a check on the validity of the spectral subtraction and addition methods of analysis described previously. If M_b and M_f are the spin magnetizations associated with the motionally restricted and fluid spin-label populations, respectively, then the change of magnetization due to exchange between these two sites is described by the equations

$$\frac{dM_b}{dt} = -\tau_b^{-1}M_b + \tau_f^{-1}M_f \tag{83}$$

and

$$\frac{dM_f}{dt} = \tau_b^{-1}M_b - \tau_f^{-1}M_f \tag{84}$$

where τ_b^{-1} and τ_f^{-1} are the probabilities per unit time of transfer from the motionally restricted component to the fluid component and vice versa, respectively. These equations assume rapid mixing of the fluid pool by lateral diffusion, such that all fluid lipids encounter the lipid–protein interface within the lifetime τ_b. At exchange equilibrium $dM_b/dt = dM_f/dt = 0$, and therefore equations (83) and (84) yield the following relationship between the on- and off-rate constants:

$$\tau_b^{-1}/\tau_f^{-1} = M_f^0/M_b^0 = (1-f)/f \tag{85}$$

where M_f^0 and M_b^0 are the steady-state magnetizations associated with the fluid and motionally restricted components, respectively, and $f = n_b^*/(n_b^* + n_f^*)$ is the fraction of motionally restricted lipid. Equations (83) and (84) are then incorporated into the Bloch equations for the response of the spin system to the microwave magnetic field H_1 of angular frequency ω. The equations are written in terms of the complex magnetizations $\hat{M}_m = u_m + iv_m$, where m = f or m = b, corresponding to the fluid and motionally restricted components, respectively. The steady-state equations for the out-of-phase (real) and in-phase (imaginary) electron spin magnetizations, u_m and v_m, associated with the two components, m = f and b, are then analogous to those given for the case of Heisenberg spin exchange in equations (40) and (41), above (see, e.g., McConnell, 1958):

$$(T_{2,m}^{-1} + \tau_m^{-1})u_m - \tau_{m'}^{-1}u_{m'} + (\omega_m - \omega)v_m = 0 \tag{86}$$

and

$$(T_{2,m}^{-1} + \tau_m^{-1})v_m - \tau_{m'}^{-1}v_{m'} - (\omega_m - \omega)u_m = -\gamma H_1 M_m^0 \tag{87}$$

where m = b and m' = f, and vice versa, giving four coupled equations. Quantity $T_{2,m}$ is the transverse relaxation time which is related to the peak-to-peak, first-derivative linewidth by $\Delta\omega_{pp} = (2/\sqrt{3})T_2^{-1}$, and γ is the gyromagnetic ratio of the electron. The out-of-phase part of the magnetization, $v = v_b + v_f$, then gives the intensity of the resonance absorption.

To simulate the entire line shape, a summation must be made over all angular orientations θ of the spin-label director axes relative to the magnetic field direction (Davoust and Devaux, 1982). Spectra corresponding to transitions between sites with resonance frequencies $\omega_f(\theta)$ and $\omega_b(\theta')$ are added with a weighting factor $p(\theta)\, d\theta = \sin\theta \cdot d\theta$. Since the nuclear spin orientation is preserved during exchange, the line shapes corresponding to the $m_I = +1, 0, -1$ nuclear manifolds are calculated separately. Some model must also be assumed for the reorientation of the spin-label director axes ($\theta \rightarrow \theta'$) on exchange. Two different models have been put forward by Davoust and Devaux (1982). In model I, it is assumed that the unique director orientation in the fluid component is preserved on exchange. This corresponds to the nitroxide axes being aligned along the membrane normal in the motionally restricted component (i.e., a right cylindrical protein). In model II, exchange takes place with labels having all possible orientations in the motionally restricted component, corresponding to random reorientation of the chain segments on collision with an invaginated protein surface. In the slow exchange regime there is very little difference between the two models, since the principal effect is a lifetime broadening (see later) which is essentially independent of the position of the line with which exchange takes place. In this regime, which applies to essentially all lipid-protein systems, model I is therefore to be preferred because of the considerable savings in time required for the computation.

Simulations performed according to model I are given in Figure 10 for various values of the exchange frequency. The relative intensities of the two components are equal and the spectral parameters are chosen to correspond to typical experimental spectra. Initially, as the exchange frequency is increased, the lines of the two spectral components first broaden, while remaining at their original positions in the absence of exchange (Figures 10a and 10b). This corresponds to the slow-exchange limit $[\tau_b^{-1}, \tau_f^{-1} \ll (\omega_b - \omega_f)]$. Then, as the rate of exchange increases further, the lines come together (Figure 10d), and finally merge to yield a sharp spectrum whose anisotropy is the mean of that of the two exchanging components (Figure 10f). The latter corresponds to the fast-exchange limit $[\tau_b^{-1}, \tau_f^{-1} \gg (\omega_b - \omega_f)]$.

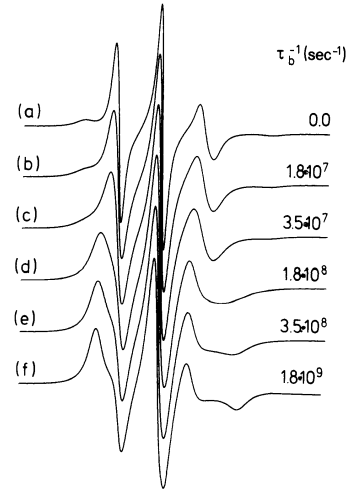

Figure 10. Effect of exchange rate on the simulated line shapes of two-component, anisotropic ESR spectra. The spectral parameters of the two components are those appropriate to the fluid and motionally restricted components for lipid-protein complexes. The spectral intensities of the two components are equal ($f = 0.5$), and the exchange rate τ_b^{-1} ($= \tau_f^{-1}$) is varied from 0 to $1.8 \times 10^9\ s^{-1}$. It is assumed that the orientation of the spin probes is preserved during exchange (Horváth *et al.*, 1988b).

The essential two-component nature of the ESR spectra from lipid-protein complexes suggests that these lie in the slow-exchange regime, and this is borne out by close comparison with experiment (East *et al.*, 1985; Horváth *et al.*, 1988a, 1988b; Ryba *et al.*, 1987). For slow exchange $[\tau_b^{-1}, \tau_f^{-1} \ll (\omega_b - \omega_f)]$, the out-of-phase component of the magnetization, which corresponds to the resonance absorption, is given by

$$v(\omega) = \frac{f(T_{2,b}^{-1} + \tau_b^{-1})}{(T_{2,b}^{-1} + \tau_b^{-1})^2 + (\omega_b - \omega)^2} + \frac{(1-f)(T_{2,f}^{-1} + \tau_f^{-1})}{(T_{2,f}^{-1} + \tau_f^{-1})^2 + (\omega_f - \omega)^2} \tag{88}$$

Clearly, in this regime the slow-exchange line shape is a weighted sum of two Lorentzians whose linewidths are increased due to lifetime broadening. The amount of the increase in linewidth is given by the reciprocal of the exchange lifetime, i.e.,

$$T_2^{-1} = T_{2,f}^{-1} + \tau_f^{-1} \tag{89}$$

with a similar expression for the motionally restricted component. Equation (88) indicates why the simulations in the slow-exchange regime are relatively insensitive to the model used for the exchange. The lifetime broadening is principally seen in the fluid component, since this has the narrowest lines, and is not dependent on the positions of the lines with which it is exchanging, provided that these are sufficiently far removed to fulfil the slow-exchange condition.

The applicability of equation (89) to the line broadening of the fluid component in slow-exchange simulations has been tested over a range of exchange rates corresponding to the experimental spectra from myelin proteolipid/dimyristoyl phosphatidylcholine recombinants (Horváth *et al.*, 1988b). Because the anisotropy in the fluid component is low, the line shapes of the individual hyperfine lines approximate reasonably closely to those of single, first-derivative ESR lines (cf. Figures 10a, b). Even so, some allowance must be made for the residual anisotropy and other sources of inhomogeneous broadening. This inhomogeneous broadening can be modeled as a Gaussian distribution of Lorentzian lines, as was done in Section 2, above. Making the approximation in equation (3), Section 2, that the inhomogeneous broadening is considerably greater than the Lorentzian broadening ($\Delta H_{pp}^{G} \gg \Delta H_{pp}^{L}$), and substituting from equation (89) for the Lorentzian linewidth, the total peak-to-peak experimental linewidth is given by

$$\Delta H_{pp}^{tot} = (\hbar/\sqrt{3}g\beta)\tau_f^{-1} + \Delta H_{pp}^{G} + H_{pp}^{L}(0) \tag{90}$$

where g is the nitroxide g-value, $\Delta H_{pp}^{L}(0)$ is the Lorentzian linewidth in the absence of exchange, and other symbols have their usual meaning. Therefore, according to equation (90), the linewidths of the fluid component should have an approximately linear dependence on the on-rate constant τ_f^{-1} with a gradient of 3.3×10^4 G s. A linear dependence is found from simulations, over the range of on-rate constants $\tau_f^{-1} = 0$ to 4×10^7 s^{-1}, with gradients of 2.9×10^4 and 2.0×10^4 G s for the low-field and high-field lines, respectively. The value from the simulations for the low-field line, which best approximates a single first-derivative line shape, is in reasonable agreement with the prediction from equation (90). The latter therefore provides a quick method for estimating exchange rates from the linewidth of the low-field fluid component, particularly if the gradient obtained from simulation is used.

Exchange rates are, of course, much better determined by a combination of spectral simulation with optimization. Typical simulations for myelin proteolipid/dimyristoyl phosphatidylcholine protein-lipid recombinants are given in Figure 11. The samples all have the same lipid/protein ratio, but the relative proportions of the fluid and motionally restricted components are varied by pH titration of the selectivity of the spin-labelled fatty acid for the protein. The simulations were performed with the same single-component spectra, corresponding to the protein-alone and the lipid-alone, for all the recombinant spectra. Only the fraction of motionally restricted component f and the exchange rate τ_b^{-1} were varied in the simulations, using a search routine based on the method of steepest descents to minimize the root-mean-square (rms) differences between experimental and simulated spectra. Typically, rms errors for the best fit obtained in this way are $\lesssim 0.8\%$, and the uncertainty in the value of f is $\lesssim 3\%$ and that in τ_b^{-1} is $\lesssim 20\%$ (Horváth *et al.*, 1988b). The optimization method gives an objective means of assessing the goodness-of-fit, and hence allows a systematic study of variations in motionally restricted fractions and exchange rates.

It is of considerable technical interest to compare values obtained for the fraction of motionally restricted lipid, f, by simulation with those obtained from spectral

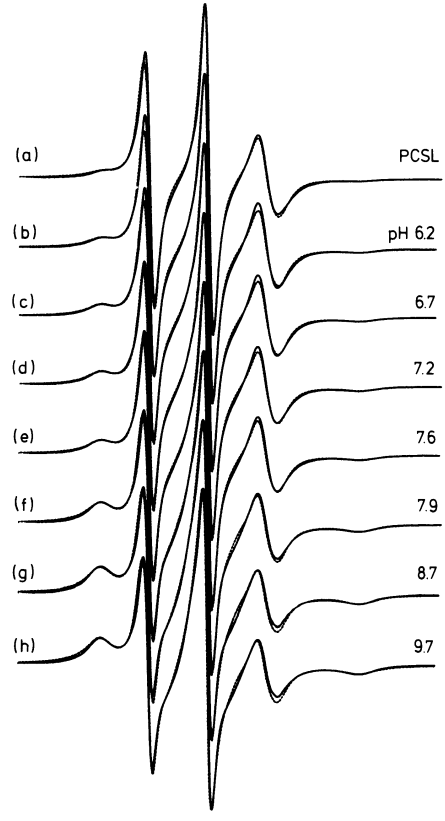

Figure 11. Simulated spectra of the 14-SASL stearic acid spin label in myelin proteolipid apoprotein/dimyristoyl phosphatidylcholine recombinants of lipid/protein ratio 37:1 mole/mole as a function of pH, $T = 30\,°C$. The full lines are the experimental spectra and the dashed lines are spectra simulated with the exchange-coupled Bloch equations using a two-component model. (a) 14-PCSL phosphatidylcholine spin label at pH 7.4; (c)-(h) 14-SASL spin label at the indicated pH values: pH 6.2-pH 9.7. Scan width = 100 gauss. Exchange rates used in the simulations are given in Table 6 (Horváth *et al.*, 1988a).

TABLE 6
On- and Off-Rate Constants, τ_f^{-1} and τ_b^{-1}, Respectively, for Lipid Exchange of the 14-SASL Stearic Acid and 14-PCSL Phosphatidylcholine Spin Labels at the Lipid–Protein Interface in Myelin Proteolipid Protein/Dimyristoyl Phosphatidylcholine Recombinants, as a Function of pH in 10 mM Sodium Phosphate Buffer[a]

pH	$\tau_f^{-1}(s^{-1})$	$\tau_b^{-1}(s^{-1})$
6.1	6.1×10^6	5.9×10^6
6.5	5.5×10^6	4.3×10^6
7.0	5.4×10^6	3.8×10^6
7.4	5.3×10^6	3.5×10^6
7.9	5.7×10^6	2.3×10^6
8.6	6.5×10^6	2.1×10^6
9.6	6.1×10^6	2.0×10^6
14-PCSL pH 7.4	7.9×10^6	1.2×10^7

[a] All samples have the same lipid/protein ratio. Data are obtained from spectral simulations (see Figure 11) using a two-component exchange model as described in the text (Horváth *et al.*, 1988a).

subtraction/addition, as described above. In the latter case, any effects of exchange are allowed for empirically by choosing individual components recorded at temperatures slightly different from that for the recombinant (see Figure 8, above). In general, a rather good agreement is obtained between the values of f obtained from the two methods (Horváth *et al.*, 1988b). Significant differences are found only at low values of f, and for these the deviations are maximally 30%. It thus appears that the subtraction strategy of empirically matching the two spectral components in the composite spectrum is quite successful in allowing for the effects of exchange.

It is found for both myelin proteolipid protein (Horváth *et al.*, 1988b) and rhodopsin (Ryba *et al.*, 1987) recombinants with dimyristoyl phosphatidylcholine, that the off-rate constant τ_b^{-1} for exchange of any given spin label is essentially independent of the lipid/protein ratio. This is to be expected if the number of second-shell lipids is not limiting and there is rapid equilibration by lateral diffusion within the pool of fluid, exchangeable lipids. The effective on-rate τ_f^{-1} for any one lipid in the fluid pool then decreases with increasing lipid–protein ratio, being determined by the condition for material balance given by equation (85). Correspondingly, if the lipid/protein ratio is maintained constant and the selectivity is varied, e.g., by pH or salt titration, one would expect the on-rate constant to remain fixed (i.e., diffusion-controlled), and the selectivity to be reflected by differences in the off-rate constant. This is found to be the case for the exchange rates given in Table 6, which are determined from the simulations of the spectra as a function of pH in Figure 11. The on-rate constants are independent of pH, and essentially equal to the value for phosphatidylcholine, while the off-rate constants titrate with pH and are quite different from the value for phosphatidylcholine. Further evidence that the on-rates are diffusion-controlled has been provided by measurements of the collision rate between diffusible ^{14}N-nitroxide-labeled lipids and ^{15}N-nitroxide-labeled chains covalently linked to rhodopsin (Davoust *et al.*, 1983). The

collision rates with the protein surface were found to be the same as those with other lipids in fluid bilayers.

Quantitatively, the effects of selectivity on the exchange rates can be described in terms of the equilibrium association equation (76), combined with the condition for material balance, equation (85). The ratio of exchange rate constants is then given by

$$\tau_b^{-1}/\tau_f^{-1} = n_t/(N_1 K_r^{av}) - 1/K_r^{av} \tag{91}$$

At a fixed lipid/protein ratio and a given temperature, the on-rate τ_f^{-1} is approximately the same for all lipids, independent of the degree of selectivity, because it is diffusion-controlled (cf. Table 6). Therefore for different lipid spin labels, say L and PC, the ratio of off-rate constants is given from equation (91) by

$$\tau_b^{-1}(\mathrm{PC})/\tau_b^{-1}(\mathrm{L}) = K_r^{av}(\mathrm{L})/K_r^{av}(\mathrm{PC}) \tag{92}$$

This relation has been found to hold reasonably well for a range of spin labels with differing selectivities in lipid–protein recombinants with the myelin proteolipid protein (Horváth *et al.*, 1988a, 1988b).

8. SATURATION TRANSFER ESR

Saturation transfer methods will be dealt with in greater detail in another chapter. Here only a brief summary of selected aspects will be given. The first concerns experimental settings which are necessary to obtain standardized spectra before the subsequent experimental methods of spectral analysis may be applied. The three particular methods of spectral interpretation reviewed here are: an empirical method of treating anisotropic motion, an integral method for dealing with multicomponent spectra, and the analysis of dispersion spectra by difference spectroscopy. These specialized methods should be considered in the broader context of saturation transfer spectroscopy detailed in Chapter 3.

8.1. Power and Modulation Calibration and the Effects of Sample Shape, Size, and Dielectric Absorption

The extent of saturation depends on the microwave H_1 field, i.e., on the microwave power P. It is therefore necessary to maintain a defined and constant microwave power at the sample, in order to be able to make comparisons between different systems. An effective microwave magnetic field at the sample of $H_1^{eff} = 0.25$ gauss has normally been used for experimental correlation time calibration spectra and in most spectral simulations. The effective H_1 at the sample is given by (Fajer and Marsh, 1982)

$$\langle H_1^2 \rangle_s \propto \eta(V_c/V_s)PQ \tag{93}$$

where V_c and V_s are the volumes of the cavity and sample, respectively, and Q is the cavity Q-factor. Therefore H_1 depends strongly on sample shape, size, composition, and position in the cavity. This is because of different cavity filling factors η,

inhomogeneity of the H_1 field throughout the cavity, and dielectric loss and microwave lens effects within the sample. In addition to the microwave magnetic field, the modulation amplitude of the static magnetic field must also be maintained constant, since this affects the passage conditions in the experiment, and hence the degree of saturation throughout the spectrum. A value of $H_m = 5$ gauss is normally used experimentally, although for computational simplicity simulations have frequently been calculated at low modulation amplitudes. The modulation amplitude at the sample also depends on sample position, and hence on sample size, because the modulation field is normally not homogeneous.

The microwave field at the center of the cavity can be calibrated using the saturation broadening of the conventional ESR spectrum from an aqueous point sample of peroxylamine disulfonate. The peak-to-peak linewidth is given by (Kooser *et al.*, 1969)

$$(\Delta H_{pp})^2 = \tfrac{4}{3}\gamma^2/T_2^2 + \tfrac{4}{3}H_1^2(T_1/T_2) \tag{94}$$

where, for peroxylamine disulfonate at room temperature, $T_1 \simeq T_2$ (Kooser *et al.*, 1969). The modulation amplitude can be determined directly from the additional modulation broadening in the conventional ESR spectrum, again from a point sample of peroxylamine disulfonate. The peak-to-peak modulation amplitude is given by the increase in peak-to-peak linewidth relative to the spectrum recorded at low modulation amplitude. The cavity Q must be measured to correct for changes in microwave field due to differences in dielectric loss in the sample, according to equation (93). This can be most conveniently done by measuring the frequency separation $\Delta\omega$ of the points of half-power in the klystron mode, using a digital frequency meter, in which case

$$Q = \omega_0/\Delta\omega \tag{95}$$

where ω_0 is the resonant frequency of the cavity (see, e.g., Poole, 1967).

The effects of H_1 inhomogeneities, filling factor, and dielectric loss are illustrated in Figure 12 (left-hand side). These have been mapped out using a point (2 mm length) sample of aqueous peroxylamine disulfonate, positioned at various points along the axis of a TE_{102} rectangular 9 GHz cavity. The influence of the inhomogeneity in the modulation field H_m and its profile are also included in Figure 12. The H_1 field varies with sample position, owing to the inherent microwave magnetic field profile of the TE_{102} resonant mode (see Poole, 1967; Fajer and Marsh, 1982), coupled with the changes in cavity Q. This means that the effective filling factor depends not only on sample size, but also on position in the cavity. The cavity Q varies because the dielectric loss of an aqueous sample depends on the profile of the microwave electric field in the TE_{102} mode. The profile of the magnetic field modulation depends, of course, on the modulation coil geometry and can be made more homogeneous by using larger coils. A Helmholtz arrangement is normally employed to improve the homogeneity in the orthogonal direction.

The effects of these inhomogeneities and dielectric loss on the saturation transfer spectra are illustrated on the right-hand side of Figure 12. The two upper spectra are recorded with the same microwave power and the same modulation amplitude, corresponding to the standard values of $H_1 = 0.25$ G and $H_m = 5$ G at the center of the cavity. Point samples are used and differ only by 5 mm in their position in the cavity.

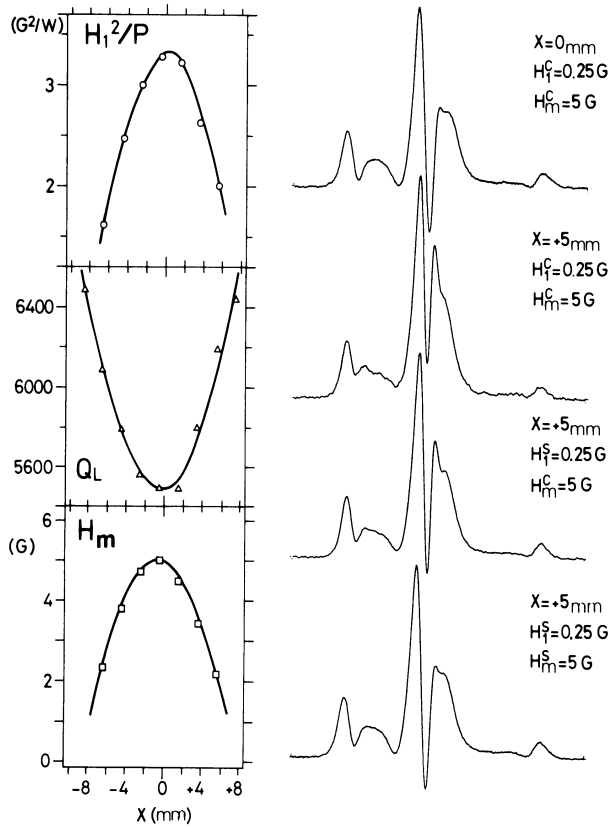

Figure 12. *Left-hand side*: variation of H_1 microwave field (upper), cavity Q (middle), and modulation amplitude H_m (lower), with the vertical position of a 10^{-4} M peroxylamine disulfonate point sample (2 mm height), in a TE_{102} rectangular 9 GHz cavity. The sample was contained in a 1-mm-diameter glass capillary within a 4-mm-diameter quartz tube, in a standard, double-wall quartz dewar. *Right-hand side*: variation of the second-harmonic, 90°-out-of-phase, absorption saturation transfer ESR spectra of a 2-mm point sample of hydrated distearoyl phosphatidylcholine +50 mol% cholesterol, with sample position. Upper spectrum: sample positioned at the cavity center; second spectrum: sample positioned 5 mm above the cavity center; third spectrum: sample positioned 5 mm above the cavity center, but with compensation for change in H_1; fourth spectrum: sample positioned 5 mm above the cavity center, but with compensation for change in both H_1 and H_m (Marsh, 1982; Fajer and Marsh, 1982).

The resulting spectra are quite different, but the effects of the inhomogeneities can be allowed for by adjusting the microwave field and modulation amplitude to the standard values at the sample itself (compare the uppermost and lowermost spectra on the right-hand side of Figure 12). It is clear from these results that the saturation transfer ESR spectra will be sensitive both to sample size and position in the cavity. Samples larger than effectively point samples will experience inhomogeneous microwave and modulation fields along their length, and although this can be corrected for to some

extent by taking average values, it is better whenever possible to use point samples carefully centered in the cavity, especially when comparison is to be made with spectral simulations. If signal-to-noise considerations dictate that larger samples must be used, an average H_1 field can be calculated from the filling factor, as described in Fajer and Marsh (1982). However, it is difficult to make a similar correction for the modulation field inhomogeneities, because the passage conditions in the saturation transfer experiment are not exactly defined. A recommended standard protocol for recording saturation transfer ESR spectra has been discussed by Hemminga *et al.* (1984).

8.2. Anisotropic Rotation

Effective correlation times are frequently calculated from line-height ratios in the low-field, central, and high-field diagnostic regions of the saturation transfer ESR spectra (Thomas *et al.*, 1976). The calculations are based on calibrations from isotropically rotating systems, usually spin-labeled haemoglobin in glycerol–water mixtures. Large discrepancies in the rotational correlation times obtained from the three diagnostic regions in the spectra, using calibrations based on isotropic motional models, may therefore be a useful indicator for anisotropic rotation (Marsh, 1980). Preferential rotation about the nitroxide z axis will give rise to motional averaging of the g-value anisotropy, which at 9 GHz affects only the central region of the spectrum, i.e., the C'/C line-height ratio, without greatly affecting the low-field (L''/L) and high-field (H''/H) line-height ratios. This effect of anisotropic rotation was demonstrated for spin-labeled phospholipids by the motional changes taking place at the pretransition in gel-phase lipid bilayers, and was corroborated by the conventional ESR spectra of spin-labeled steroids which are optimally sensitive to rotation about the long molecular axis (Marsh, 1980; Polnaszek *et al.*, 1981). The effective correlation time for long-axis rotation can then be approximated by the C'/C ratio and that for off-axis rotation by the L''/L and H''/H line-height ratios. The method has been validated, at least in principle, by theoretical simulations for axial rotation (Robinson and Dalton, 1980, 1981), and extended in its application both to higher microwave frequencies and to ^{15}N-nitroxide spin labels (Johnson *et al.*, 1982; Beth *et al.*, 1983).

Although, in principle, spectral simulation is the most satisfactory method of analyzing the effects of anisotropic rotational motion, the theoretical calculations are technically rather complex and often involve approximations to keep computing time within reasonable limits. For this reason, it is useful to pursue the empirical method in rather more detail. This has been done by Fajer and Marsh (1983a), using the principles put forward by Thomas *et al.* (1976) in devising the original line-height ratio method. The rate of change of resonant field position with molecular rotation, $\partial H_r/\partial\theta_i$, is taken as an indicator of the extent of saturation transfer induced by molecular rotation, and used to define the spectral regions most sensitive to a particular mode of molecular rotation, θ_i. The values of $\partial H_r/\partial\theta_i$ must be summed, with appropriate axial degeneracies, over all molecular orientations which contribute to a particular resonance field position, H_r.

The simplest motion to analyze is anisotropic rotation about the nitroxide z axis. Such a motion could correspond, for example, to a phospholipid or fatty acid spin label aligned with the chain axis along the normal to the surface of the membrane.

The resonance field is given by

$$H_r = (h\nu - Am_I)/g\beta \tag{96}$$

where ν is the microwave frequency and m_I is the ^{14}N nuclear spin quantum number. The hyperfine and g values depend on the magnetic field orientation and are obtained by diagonalization of the spin Hamiltonian given in equation (1):

$$g = (g_{xx}^2 \cos^2\phi \sin^2\theta + g_{yy}^2 \sin^2\phi \sin^2\theta + g_{zz}^2 \cos^2\theta)^{1/2} \tag{97}$$

$$A = (A_{xx}^2 \cos^2\phi \sin^2\theta + A_{yy}^2 \sin^2\phi \sin^2\theta + A_{zz}^2 \cos^2\theta)^{1/2} \tag{98}$$

where θ and ϕ are the polar coordinates of the magnetic field direction relative to the nitroxide axes. Aggregate values of $\partial H_r/\partial\theta$ and $\partial H_r/\partial\phi$ calculated from equations (97) and (98), and summed with a $\sin\theta$ weighting factor to allow for the axial spatial degeneracy, are grouped according to magnetic field position in Figure 13. The values for $\sum \partial H_r/\partial\phi$ correspond to rotation about the nitroxide z axis, while those for $\sum \partial H_r/\partial\theta$ do not correspond to rotation about a unique axis, but about an axis in the x–y plane whose direction depends on the angle ϕ.

The sensitivity to off-axial rotation is more pronounced in the low- and high-field regions of the spectrum (Figure 13a). The spectral regions sensitive to this mode span almost the entire field range, corresponding to nitroxide orientations between $\theta = 0°$,

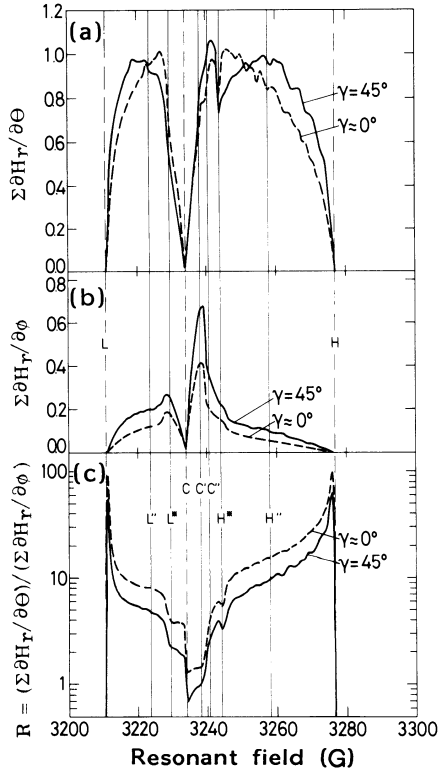

Figure 13. Spectral sensitivity to slow molecular rotation, with off-axial rotations restricted within a cone of angle γ. The nitroxide z axis is assumed to lie along the long molecular axis. (a) Off-axial rotation, $\sum \partial H_r/\partial\theta$. (b) Axial rotation, $\sum \partial H_r/\partial\phi$. (c) Off-axial/axial discrimination, $R = (\sum \partial H_r/\partial\theta)/(\sum \partial H_r/\partial\phi)$. The broken lines are for a cone of angle $\gamma \sim 0°$, and the full lines are for $\gamma = 45°$. Nitroxide tensor values: $A_{xx} = 6.13$ G, $A_{yy} = 5.65$ G, $A_{zz} = 32.5$ G, $g_{xx} = 2.0128$, $g_{yy} = 2.0098$, and $g_{zz} = 2.0068$. Microwave frequency: 9.1127 GHz (Fajer and Marsh, 1983a).

$\phi = 0°$ and $\theta = 90°$, $\phi = 90°$. Off-axial motion modulates the large anisotropy between the (x, y) elements and the z element of the hyperfine tensor, which dominates the extremes of the spectrum. The smaller g-value anisotropy enhances the hyperfine anisotropy in the high-field ($m_I = -1$) region of the spectrum and partially compensates it in the low-field ($m_I = +1$) region. However, this effect is offset by the greater spectral span in the high-field region, giving rise to an approximately equal sensitivity in both regions. In the central ($m_I = 0$) region of the spectrum the sensitivity is determined by the g-value anisotropy, and the nonaxiality of the g tensor gives rise to discrimination between axial and off-axial rotations (compare Figures 13a and b). The resonant fields of the $m_I = 0$ manifold extend over a range of only 10 gauss, which enhances the effect of the relatively small anisotropy of the Zeeman interaction. Axial rotation also modulates the anisotropy of the minor, x and y, elements of the hyperfine tensor, but this effect is small—A_{xx} and A_{yy} differ by only 0.5 gauss. This explains why the central region is more sensitive to axial rotation than are the regions immediately to low and high field of the center (see Figure 13b).

In searching for spectral characteristics diagnostic of particular anisotropic motions, the ratio of the sensitivities, $R = (\sum \partial H_r/\partial\theta)/(\sum \partial H_r/\partial\phi)$, is more useful than the absolute sensitivities themselves for detecting regions of high discrimination between axial and off-axial motion. It is also important in defining diagnostic line-height ratios to choose regions of the spectrum over which the preferential sensitivity R is nearly constant. In Figure 13c, it is seen that the plateau region for which the sensitivity ratio is lowest, $R \approx 1.4$, occurs for the $m_I = 0$ manifold in the central region of the spectrum. The preferential sensitivity in this region (C') is therefore approximately equally weighted to axial and off-axial motion. However, correlation time calibrations indicate that the C' region is sensitive only to faster motions, $\tau_R < 3 \times 10^{-5}$ s. Therefore, if the off-axial motions are slower than this, the central region can be taken as diagnostic of axial motion. Approximate plateau regions of R are also found to low and high field (L'' and H'', respectively), corresponding to nitroxide orientations in the range $\theta = 45°$ to $\theta = 60°$ for the $m_I = +1$ and $m_I = -1$ manifolds. These regions show strong discrimination for off-axial motion, and in addition correspond to the principal maxima of $\sum \partial H_r/\partial\theta$. Plateau regions with intermediate levels of discrimination (L^* and H^*) are also indicated in Figure 13.

Calculations have also been made to investigate the effects of tilt and slow wobble of the nitroxide z axis, relative to a macromolecule- or membrane-fixed axis, e.g., the membrane normal. The results for slow wobble within a cone of angle $\gamma = 45°$ are given by the full lines in Figure 13. The effects are similar to those for the previous case; the major change is to increase sensitivity to axial motion throughout the spectrum. This is an interesting result, since the two approaches differ in that the first assumes only small displacements in the ϕ direction, rather than the continuous slow rotation assumed for the second case.

More important is the consideration of a possible fast wobble of limited amplitude relative to the slow rotation axis, such as might arise from segmental motion of the probe relative to the point of attachment to a macromolecule. This will reduce the sensitivity to slow motion in the regions of the spectrum affected by the fast motion, and also cause partial averaging of the nitroxide tensors, which may shift the positions of the diagnostic regions for anisotropic motion. This effect has been simulated by Fajer and Marsh (1983a), and has led to a more stringent definition of the diagnostic

regions as those parts of the plateau regions in R which are insensitive to the fast oscillation. These are precisely the regions indicated in Figure 13, and are defined in terms of magnetic field position and equivalent orientation of the nitroxide group in Table 7. The definition of diagnostic regions obtained by a similar analysis for preferential rotation about the nitroxide y axis is also given in Table 7. Such data would apply to the cholestane or androstanol spin labels, for instance, in membranes. Correlation time calibrations for all diagnostic regions, derived from spin-labeled haemoglobin, can be found in Fajer and Marsh (1983a).

8.3. Integral Method: Multicomponent Spectra

The normal line-height ratio method cannot be readily applied to multicomponent spectra, since it is not strictly additive and becomes inapplicable in the presence of sharp spectral components. In these cases the integral of the usual second-harmonic, 90°-out-of-phase, absorption saturation transfer spectrum affords several advantages (Evans, 1981), especially when combined with difference spectroscopy of the conventional spectra (Horvath and Marsh, 1983). The first integral of the saturation transfer spectrum increases with decreasing rate of molecular rotation, as indicated by the spectra for spin-labeled haemoglobin in Figure 14. Correlation time calibrations can be established for the spectral integrals, using spin-labeled haemoglobin, if the first integral of the saturation transfer spectrum is normalized to the double integral of the conventional spectrum, and both are normalized to a fixed gain and modulation amplitude. This has been done for the integrals in Figure 14, and a complete calibration curve can be found in Horvath and Marsh (1983).

Linear additivity of the normalized saturation transfer integrals for different motional components has been demonstrated using mixtures of fluid- and gel-phase

TABLE 7
Angular Orientations (θ, ϕ) Specifying the Diagnostic Regions in Saturation Transfer ESR, Appropriate to z-Axis Rotation (L'', C', and H'') and y-axis rotation (L^y, C^y and H^y). The Off-Axial/Axial Discrimination, $R = (\sum \partial H_r/\partial\theta)/(\sum \partial H_r/\partial\phi)$, is Also Indicated (Fajer and Marsh, 1983a)[a]

Region	θ (deg)	ϕ (deg)	H_r (gauss)	R
L''	60	90	3227.5	8-10
C'	75	65	3245.4	1.0-1.4
H''	60	90	3267.1	11-20
L^y	24	65	3237.2	2
C^y	10	75	3245.6	0.1
H^y	10	75	3251.8	0.1-0.2

[a] Resonant field positions, H_r, are given for $\nu = 9.11275$ GHz, and tensors for spin-labeled haemoglobin ($A_{xx} = 8.37$ G, $A_{yy} = 8.18$ G, $A_{zz} = 37$ G; $g_{xx} = 2.0088$, $g_{yy} = 2.0060$, $g_{zz} = 2.0022$).

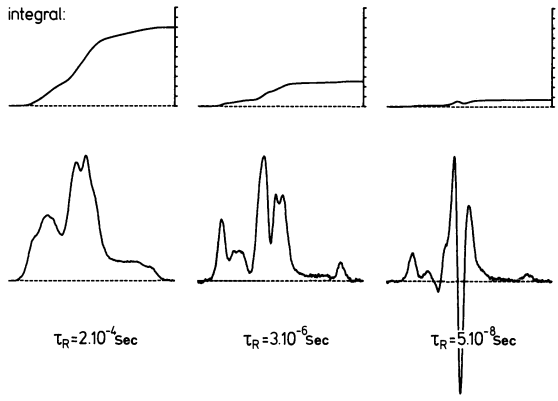

Figure 14. *Lower row*: second-harmonic, 90°-out-of-phase, absorption saturation transfer ESR spectra of spin-labeled haemoglobin in glycerol-water mixtures of different viscosities. The corresponding rotational correlation times are indicated under the spectra. *Upper row*: first integral of the saturation transfer ESR spectra in the lower row. The ordinate is normalized to the integrated intensity of spin-labeled haemoglobin with an effective rotational correlation time of $\tau_R = 2 \times 10^{-2}$ s as full scale (Horvath and Marsh, 1983).

phospholipid liposomes. Thus in a saturation transfer spectrum consisting of components a and b, the normalized integral of the total spectrum is given by

$$I_{tot} = (1 - f)I_a + fI_b \tag{99}$$

where I_a and I_b are the normalized saturation transfer integrals of components a and b alone, and f is the fraction of component b in the mixture. The latter can be obtained by spectral subtraction and double integration of the conventional two-component spectrum as described for lipid-protein systems in Section 7. If both components lie in the slow motional regime for conventional ESR spectroscopy, it may be necessary to raise the temperature or make some other manipulation in order to obtain the spectral resolution necessary for subtraction.

If the intrinsic saturation transfer integral of one component (say b) is known, then that of the other (and hence its correlation time) may be determined:

$$I_a = (I_{tot} - fI_b)/(1 - f) \tag{100}$$

This latter expression is particularly useful for correcting the saturation transfer integrals for a slow-motion component in the presence of a faster component, since the latter have relatively low integrals. For correlation times $\tau_R < 10^{-8}$ s, the saturation transfer integrals are practically zero, and for the range $\tau_R = 5 \times 10^{-8}$-$10^{-6}$ s, the normalized integral is small and almost constant, increasing only from 0.001 to 0.002 over this range. Thus it is not crucial to know the value of I_b very accurately to make the correction in equation (100).

A variation on the integral method is to measure the absolute line heights, rather than line-height ratios, in the diagnostic regions of the saturation transfer spectrum.

This gives a higher sensitivity to changes in correlation times, since it combines the line-shape changes, which are the basis of the line-height ratio method, with the intensity changes associated with the integral. Methods of normalizing the line heights and correlation time calibrations are given by Squier and Thomas (1986).

8.4. Dispersion Spectra: Difference Spectroscopy

The 90°-out-of-phase, first-harmonic, dispersion spectrum (U_1') is the second of the generally recommended saturation transfer spectral displays. It has been much less studied in biological systems than the second-harmonic, 90°-out-of-phase, absorption spectra (V_2'), partly because of problems with klystron FM noise. With the advent of loop-gap resonators (Hyde *et al.*, 1982), the latter is no longer a serious problem, but there still remains the necessity of introducing a convention for the spectral interpretation. Since the dispersion spectra are not characterized by the well-defined peaks and troughs found in the second-harmonic absorption spectra, it is difficult to construct correlation time calibrations in terms of line-height ratios as was done for the latter. This problem is particularly acute in the central region of the dispersion spectra, where the decrease in out-of-phase intensity with increasing rotational motion manifests itself as a narrowing of the central peak, rather than the development of a well-defined negative dip. In this case it is difficult even to measure line heights characteristic of a given field position, because of the steep changes of slope in this region.

A method of analysis is, however, possible based on the similarity of the first-harmonic, out-of-phase, dispersion spectra (U_1') to the in-phase, zeroth-harmonic absorption spectra (V_0). In the absence of saturation transfer, these two line shapes are identical (Weger, 1960), thus motional effects can be detected by constructing a difference spectrum between the integrated conventional ESR spectrum and the dispersion saturation transfer spectrum. The method is illustrated in Figure 15, for spin-labeled haemoglobin. The U_1' dispersion spectrum is subtracted from the V_0 spectrum, the endpoint being defined by the criterion that the intensity in the low- and high-field

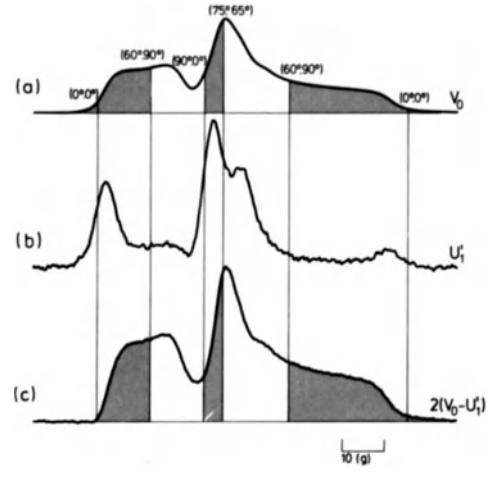

Figure 15. ESR spectra of spin-labeled haemoglobin rotating isotropically in a 20 mol% glycerol-water mixture at −22 °C, with correlation time 2×10^{-7} s. (a) Integrated first-derivative absorption, in-phase (V_0). (b) Dispersion, first-harmonic, 90°-out-of-phase (U_1'). (c) Difference spectrum, $2(V_0 - U_1')$; note the twofold greater vertical gain. Spectra (a) and (b) were normalized to the same integrated area (Fajer and Marsh, 1983b).

wings of the difference spectrum should not become negative. Saturation transfer arising from molecular motion then results in positive intensity in the difference spectrum. If the difference spectrum is normalized to the V_0 spectrum, quite general correlation time calibrations can be constructed based on spin-labeled haemoglobin. Either line heights or areas can be used for the calibration. The area method does not require such good signal-to-noise ratios and sectional integrals may also be defined as indicated in Figure 15, corresponding to the diagnostic regions for anisotropic motion. Correlation time calibration curves may be found in Fajer and Marsh (1983b).

REFERENCES

Abragam, A., 1961, *The Principles of Nuclear Magnetism*, Oxford University Press, London.

Bales, B.L., 1980, A simple, accurate method of correcting for unresolved hyperfine broadening in the EPR of nitroxide spin probes to determine the intrinsic linewidth and Heisenberg spin exchange frequency, *J. Magn. Reson.* **38**:193.

Bales, B. L., 1982, Correction for inhomogeneous line broadening in spin labels, II, *J. Magn. Reson.* **48**:418.

Bales, B. L., and Willett, D., 1984, EPR investigation of the intermediate spin exchange regime, *J. Chem. Phys.* **80**:2997.

Berner, B., and Kivelson, D., 1979, The electron spin resonance linewidth method for measuring diffusion. A critique, *J. Chem. Phys.* **83**:1406.

Beth, A. H., Balasubramanian, K., Robinson, B. H., Dalton, L. R., Venkataramu, S. D., and Park, J. H., 1983, Sensitivity of V_2' saturation transfer electron paramagnetic resonance signals to anisotropic rotational diffusion with [^{15}N]nitroxide spin labels. Effects of noncoincident magnetic and diffusion tensor principal axes, *J. Phys. Chem.* **87**:359.

Brophy, P. J., Horvath, L. I., and Marsh, D., 1984, Stoichiometry and specificity of lipid-protein interaction with myelin proteolipid protein studied by spin label electron spin resonance, *Biochemistry* **23**:860.

Brotherus, J. R., Jost, P. C., Griffith, O. H., Keana, J. F. W., and Hokin, L. E., 1980, Charge selectivity at the lipid-protein interface of membranous Na,K-ATPase, *Proc. Natl. Acad. Sci. U.S.A.* **77**:272.

Brotherus, J. R., Griffith, O. H., Brotherus, M. O., Jost, P. C., Silvius, J. R., and Hokin, L. E., 1981, Lipid-protein multiple binding equilibria in membranes, *Biochemistry* **20**:5261.

Cotter, M. A., 1977, Hard spherocylinders in an anisotropic mean field: a simple model for a nematic liquid crystal, *J. Chem. Phys.* **66**:1098.

Davoust, J., and Devaux, P. F., 1982, Simulation of electron spin resonance spectra of spin-labeled fatty acids covalently attached to the boundary of an intrinsic membrane protein. A chemical exchange model, *J. Magn. Reson.* **48**:475.

Davoust, J., Seigneuret, M., Hervé, P., and Devaux, P. F., 1983, Collisions between nitrogen-14 and nitrogen-15 spin labels. 2. Investigations on the specificity of the lipid environment of rhodopsin, *Biochemistry* **22**:3146.

Devaux, P. F., Scandella, C. J., and McConnell, H. M., 1973, Spin-spin interactions between spin-labelled phospholipids incorporated into membranes, *J. Magn. Reson.* **9**:474.

Dobryakov, S. N., and Lebedev, Ya S., 1969, Analysis of spectral lines whose profile is described by a composition of Gaussian and Lorentzian profiles, *Sov. Phys. Dokl.* **13**:873.

East, J. M., Melville, D., and Lee, A. G., 1985, Exchange rates and numbers of annular lipids for the calcium and magnesium ion dependent adenosinetriphosphatase, *Biochemistry* **24**:2615.

Ellena, J. F., Blazing, M. A., and McNamee, M. G., 1983, Lipid-protein interactions in reconstituted membranes containing acetylcholine receptor, *Biochemistry* **22**:5523.

Esmann, M., and Marsh, D., 1985, Spin-label studies on the origin of the specificity of lipid-protein interactions in Na^+, K^+-ATPase membranes from *Squalus acanthias*, *Biochemistry* **24**:3572.

Evans, C. A., 1981, Use of integral saturation transfer electron paramagnetic spectra to determine molecular rotational correlation times. Slowly tumbling spin labels in the presence of rapidly tumbling spin labels, *J. Magn. Reson.* **44**:109.

Fajer, P., and Marsh, D., 1982, Microwave and modulation field inhomogeneities and the effect of cavity Q in saturation transfer ESR spectra. Dependence on sample size, *J. Magn. Reson.* **49**:212.

Fajer, P., and Marsh, D., 1983a, Sensitivity of saturation transfer ESR spectra to anisotropic rotation. Application to membrane systems, *J. Magn. Reson.* **51**:446.

Fajer, P., and Marsh, D., 1983b, Analysis of dispersion mode saturation transfer ESR spectra. Application to model membranes, *J. Magn. Reson.* **55**:205.

Feix, J. B., Popp, C. A., Venkataramu, S. D., Beth, A. H., Park, J. H., and Hyde, J. S., 1984, An electron-electron double-resonance study of interactions between [N^{14}]- and [N^{15}]stearic acid spin label pairs: lateral diffusion and vertical fluctuations in dimyristoylphosphatidylcholine, *Biochemistry* **23**:2293.

Fraenkel, G. K., 1967, Linewidths and frequency shifts in electron spin resonance spectra, *J. Phys. Chem.* **71**:139.

Freed, J. H., 1964, Anisotropic rotational diffusion and electron spin resonance linewidths, *J. Chem. Phys.* **41**:2077.

Freed, J. H., 1976, Theory of slow tumbling ESR spectra for nitroxides, in *Spin Labeling. Theory and Applications.* Volume I (L. J. Berliner, ed.), pp. 53-132, Academic Press, New York,.

Goldman, S. A., Bruno, G. V., Polnaszek, C. F., and Freed, J. H., 1972, An ESR study of anisotropic rotational reorientation and slow tumbling in liquid and frozen media, *J. Chem. Phys.* **56**:716.

Gutowsky, H. S., and Holm, C. H., 1956, Rate processes and nuclear magnetic resonance spectra. II. Hindered internal rotation of amides, *J. Chem. Phys.* **25**:1228.

Hemminga, M. A., de Jager, P. A., Marsh, D., and Fajer, P., 1984, Standard conditions for the measurement of saturation-transfer ESR spectra, *J. Magn. Reson.* **59**:160.

Horváth, L. I., and Marsh, D., 1983, Analysis of multicomponent saturation transfer ESR spectra using the integral method, *J. Magn. Reson.* **54**:363.

Horváth, L. I., Brophy, P. J., and Marsh, D., 1989, Analysis of lipid-protein interactions in myelin proteolipid protein/dimyristoyl phosphatidylcholine recombinants by spin label electron spin resonance at 9 GHz and 35 GHz microwave frequencies, to appear.

Horváth, L. I., Brophy. P. J., and Marsh, D., 1988a, Influence of lipid headgroup on the specificity and exchange dynamics of lipid-protein interactions. A spin-label study of myelin proteolipid apoprotein/phospholipid complexes, *Biochemistry* **27**:5296.

Horváth, L. I., Brophy, P. J., and Marsh, D., 1988b, Exchange rates at the lipid-protein interface of myelin proteolipid protein studied by spin label electron spin resonance, *Biochemistry*, **27**:46.

Hyde, J. S., and Rao, K. V. S., 1980, Determination of the rotational correlation time and the rigid limit hyperfine coupling from the dependence of spin-label EPR spectra on microwave frequency, *J. Magn. Reson.* **38**:313.

Hyde, J. S., Froncisz, W., and Kusumi, A., 1982, Dispersion electron spin resonance with the loop-gap resonator, *Rev. Sci. Instrum.* **53**:1934.

Johnson, C. S., Jr., 1967, Theory of line widths and shifts in electron spin resonance arising from spin exchange interactions, *Mol. Phys.* **12**:25.

Johnson, M. E., Lee, L., and Fung, L. W. M., 1982, Models for slow anisotropic rotational diffusion in saturation transfer electron paramagnetic resonance at 9 and 35 GHz, *Biochemistry* **21**:4459.

Jost, P. C., and Griffith, O. H., 1978, The spin-labeling technique, *Methods Enzymol.* **XLIX**:369.

Jost, P. C., Libertini, L. J., Hebert, V. C., and Griffith, O. H., 1971, Lipid spin labels in lecithin multilayers. A study of motion along fatty acid chains, *J. Mol. Biol.* **59**:77.

Jost, P. C., Griffith, O. H., Capaldi, R. A., and Vanderkooi, G. A., 1973a, Evidence for boundary lipid in membranes, *Proc. Natl. Acad. Sci. U.S.A.* **70**: 4756.

Jost, P. C., Capaldi, R. A., Vanderkooi, G., and Griffith, O. H., 1973b, Lipid-protein and lipid-lipid interactions in cytochrome oxidase model membranes, *J. Supramol. Struct.* **1**:269.

King, M. D., and Marsh, D., 1986, Translational diffusion of lipid monomers determined by spin label electron spin resonance, *Biochim. Biophys. Acta* **863**:341.

King, M. D., Sachse, J.-H., and Marsh, D., 1987, Unconstrained optimization method for interpreting the concentration and temperature dependence of the linewidths of interacting nitroxide spin labels. Application to the measurement of translational diffusion coefficients of spin-labelled phospholipids in membranes, *J. Mag. Reson.*, **72**:257.

Knowles, P. F., Watts, A., and Marsh, D., 1979, Lipid immobilization in dimyristoyl phosphatidylcholine-substituted cytochrome oxidase, *Biochemistry* **18**:4480.

Knowles, P. F., Watts, A., and Marsh, D., 1981, Spin label studies of headgroup specificity in the interaction of phospholipids with yeast cytochrome oxidase, *Biochemistry* **20**:5888.

Kooser, R. G., Volland, W. V., and Freed, J. H., 1969, ESR relaxation studies on orbitally degenerate free radicals. I. Benzene anion and tropenyl, *J. Chem. Phys.* **50**:5243.

Kubo, R., 1969, A stochastic theory of lineshape, in *Stochastic Processes in Chemical Physics, Advances in Chemical Physics*, Vol. 16 (K. E. Shuler, ed.), pp. 101-127, Wiley, New York.

Lange, A., Marsh, D., Wassmer, K.-H., Meier, P., and Kothe, G., 1985, Electron spin resonance study of phospholipid membranes employing a comprehensive line-shape model, *Biochemistry* **24**:4383.

Lee, T. D., Birrell, G. B., Bjorkman, P. J., and Keana, J. F., 1979, Azethoxy nitroxide spin labels. ESR studies involving thiourea crystals, model membrane systems and chromatophores, and chemical reduction with ascorbate and dithiothreitol, *Biochim. Biophys. Acta* **550**:369.

Marsh, D., 1980, Molecular motion in phospholipid bilayers in the gel phase: long axis rotation, *Biochemistry* **19**:1632.

Marsh, D., 1982, Electron spin resonance: spin label probes, in *Techniques in Lipid and Membrane Biochemistry*, Vol. B4/II (J. C. Metcalfe and T. E. Hesketh, eds.), pp. B426/1-B426/44, Elsevier, Ireland.

Marsh, D., 1983, Spin label answers to lipid-protein interactions, *Trends Biochem. Sci.* **8**:330.

Marsh, D., 1985, ESR spin label studies of lipid-protein interactions, in *Progress in Protein-Lipid Interactions*, Vol. 1 (A. Watts and J. J. H. H. M. de Pont, eds.), pp. 143-172, Elsevier, Amsterdam-New York-Oxford.

Marsh, D., 1986, Spin label ESR spectroscopy and molecular mobility in biological systems, in *Supramolecular Structure and Function* (G. Pifat-Mrzljak, ed.), pp. 48-62, Springer-Verlag, Berlin-Heidelberg.

Marsh, D., and Barrantes, F. J., 1978, Immobilized lipid in acetylcholine receptor-rich membranes from *Torpedo marmorata*, *Proc. Natl. Acad. Sci. U.S.A.* **645**:97.

Marsh, D., and Smith, I. C. P., 1973, An interacting spin label study of the fluidizing and condensing effects of cholesterol on lecithin bilayers, *Biochim. Biophys. Acta* **298**:133.

Marsh, D., and Watts, A., 1982, Diffusible spin labels used to study lipid-protein interactions with rhodopsin and bacteriorhodopsin, *Methods Enzymol.* **88**:762.

McConnell, H. M., 1958, Reaction rates by nuclear magnetic resonance, *J. Chem. Phys.* **28**:430.

Meraldi, J.-P., and Schlitter, J., 1981, A statistical mechanical treatment of fatty acyl chain order in phospholipid bilayers and correlation with experimental data. B. Dipalmitoyl-3-*sn*-phosphatidylcholine, *Biochim. Biophys. Acta* **645**:193.

Moser, M., Marsh, D., Wassmer, K.-H., Meier, P., and Kothe, G., 1989, Chain configuration and flexibility gradient in phospholipid membranes: Comparison between spin-label ESR and deuteron NMR, and identification of new conformations, *Biophys. J.*

Plachy, W., and Kivelson, D., 1967, Spin exchange in solutions of di-tertiary-butyl nitroxide, *J. Chem. Phys.* **47**:3312.

Polnaszek, C. F., 1984, in *Spin Labelling in Pharmacology* (J. L. Holtzmann, ed.), Academic Press, New York.

Polnaszek, C. F., Marsh, D., and Smith, I. C. P., 1981, Simulation of the EPR spectra of the cholestane spin probe under conditions of slow axial rotation. Application to gel phase dipalmitoyl phosphatidylcholine, *J. Magn. Reson.* **43**:54.

Poole, C. P., Jr., 1967, *Electron Spin Resonance. A Comprehensive Treatise on Experimental Techniques*, Wiley-Interscience, New York.

Popp, C. A., and Hyde, J. S., 1982, Electron-electron double resonance and saturation recovery studies of nitroxide electron and nuclear spin-lattice relaxation times and Heisenberg exchange rates: lateral diffusion in dimyristoyl phosphatidylcholine, *Proc. Natl. Acad. Sci. U.S.A.* **79**:2559.

Powell, G. L., Knowles, P. F., and Marsh, D., 1985, Association of spin-labelled cardiolipin with dimyristoyl phosphatidylcholine-substituted bovine heart cytochrome *c* oxidase. A generalized specificity increase rather than highly specific binding sites, *Biochim. Biophys. Acta* **816**:191.

Redfield, A. G., 1965, The theory of relaxation processes, *Adv. Magn. Reson.* **1**:1.

Robinson, B. H., and Dalton, L. R., 1980, Anisotropic rotational diffusion studied by passage saturation transfer electron paramagnetic resonance, *J. Chem. Phys.* **72**:1312.

Robinson, B. H., and Dalton, L. R., 1981, Approximate methods for the fast computation of EPR and ST-EPR spectra. V. Application of the perturbation approach to the problem of anisotropic motion, *Chem. Phys.* **54**:253.

Ryba, N. J. P., Horvath, L. I., Watts, A., and Marsh, D., 1987, Molecular exchange at the lipid-rhodopsin interface: Spin-label ESR studies of rhodopsin-dimyristoylphosphatidylcholine recombinants, *Biochemistry*, **26**:3234.

Sachse, J.-H., and Marsh, D., 1986, Line intensities in spin-exchanged nitroxide ESR spectra, *J. Magn. Reson.* **68**:540.

Sachse, J.-H., King, M. D., and Marsh, D., 1987, ESR determination of lipid translational diffusion coefficients at low spin label concentrations in biological membranes, using exchange broadening, exchange narrowing and dipole-dipole interactions, *J. Magn. Reson.* **71**:385.

Sackmann, E., and Träuble, H., 1972, Studies of the crystalline-liquid crystalline phase transition of lipid model membranes. II. Analysis of electron spin resonance spectra of steroid labels incorporated into lipid membranes, *J. Am. Chem. Soc.* **94**:4492.

Schreier, S., Polnaszek, C. F., and Smith, I. C. P., 1978, Spin labels in membranes. Problems in practice, *Biochim. Biophys. Acta* **515**:375.

Silvius, J. R., McMillen, D. A., Saley, N. D., Jost, P. C., and Griffith, O. H., 1984, Competition between cholesterol and phosphatidylcholine for the hydrophobic surface of sarcoplasmic reticulum Ca^{2+}-ATPase, *Biochemistry* **23**:538.

Snipes, W., Cupp, J., Cohn, G., and Keith, A. D., 1974, Electron spin resonance analysis of the nitroxide spin label 2,2,6,6-tetramethylpiperidone-N-oxyl (Tempone) in single crystals of the reduced Tempone matrix, *Biophys. J.* **14**:20.

Squier, T. C., and Thomas, D. D., 1986, Methodology for increased precision in saturation transfer electron paramagnetic resonance studies of rotational dynamics, *Biophys. J.* **49**:921.

Thomas, D. D., Dalton, L. R., and Hyde, J. S., 1976, Rotational diffusion studied by passage saturation transfer electron paramagnetic resonance, *J. Chem. Phys.* **65**:3006.

Weger, M., 1960, Passage effects in paramagnetic resonance experiments., *Bell Syst. Tech. J.* **39**:1013.

6

Electron–Electron Double Resonance

James S. Hyde and Jim B. Feix

1. INTRODUCTION

1.1. Definitions and Background

ELDOR (electron-electron double resonance) is an acronym for that branch of double electron spin resonance in which two microwave frequencies participate. One of these, called the "pump" microwave source, irradiates a portion of the ESR spectrum. The effect of this irradiation on another portion of the spectrum is monitored by an observe microwave source. The effect derives from a transfer of saturation between spins that contribute to the signal intensity at the pumped spectral fragment and spins at the observed spectral fragment. By "saturation transfer" it is meant that the population difference at the observe location is no longer at the Boltzman population difference. Only the z component of magnetization, in the vocabulary of the Bloch equations, is affected by saturation transfer. However, this z component is not monitored directly, but rather indirectly by the observe microwave power, which itself induces a phase coherence along x or y in the rotating frame, thereby giving rise to an observable signal. The ELDOR effect is measured by the ELDOR reduction factor R given by

$$R = \frac{(\text{signal with pump off}) - (\text{signal with pump on})}{(\text{signal with pump off})} \tag{1}$$

The theory of ELDOR was developed by Hyde *et al.* (1968b) and Freed (1979a). Since only the z components of magnetization are involved, detailed balancing of populations of the various energy levels in the problem lead to a set of equations that can be solved using linear algebra. It was shown that the plot of R^{-1} versus (pump power)$^{-1}$ is linear with an intercept that depends only on the ratio: (saturation-transfer

James S. Hyde and Jim B. Feix • National Biomedical ESR Center, Department of Radiology, Medical College of Wisconsin, Milwaukee, Wisconsin 53226.

rate)/(electron spin-lattice relaxation rate). The quantity in the denominator is designated W_e. One has $T_{1e}^{-1} = 2W_e$, where T_{1e} is the electron spin-lattice relaxation time. The ELDOR reduction is a measure of how competitive saturation transfer is with respect to spin-lattice relaxation. This time T_{1e} may be said to be the "clock" by which saturation-transfer processes are measured.

In order to obtain absolute knowledge of saturation-transfer values, one must determine T_{1e}. Of course it can be estimated by continuous wave (cw) saturation techniques, but the time-domain method of saturation recovery is preferable (Hyde, 1979). In the section of this article on spin-label relaximetry, typical values of T_{1e} are given for nitroxide radical spin labels. These values over the full range of conditions vary from 0.3 to 10 microseconds, which establishes the relevant time scale.

There are three saturation-transfer mechanisms that are effective in this range of times: Heisenberg exchange (HE), nitrogen nuclear relaxation, and very slow rotational diffusion. The first is intermolecular and depends on concentration; the other two are intramolecular. Heisenberg exchange and nitrogen nuclear relaxation in spin labels were invoked in the first ELDOR paper to explain the experimental results (Hyde *et al.*, 1968b).

Heisenberg exchange frequencies depend on bimolecular collisions. Bimolecular collision frequencies are typically 10^5 Hz at 10^{-5} M in fluids, and in hard-sphere collision theory do not depend on molecular dimensions. These numbers match well with the spin-lattice relaxation rate of spin labels. Since Heisenberg exchange seems in the present context to lie in the strong exchange limit—i.e., every collision gives an observable event—one cannot expect to learn much about the details of a collision at a molecular level. But a great deal can be learned about translational diffusion in complex biological systems.

The nitrogen nuclear relaxation probability W_n is greatly enhanced by the fact that an unpaired electron spin is present. The nitrogen nuclear precession frequency in a rapidly tumbling spin label is about 22 MHz, corresponding to a hyperfine field of 68 kG. This huge field is modulated by rotational diffusion of the spin label resulting in a powerful nuclear relaxation mechanism. The value of W_n can even exceed that of W_e. Mostly in our experience nitrogen nuclear relaxation is an unpleasant mechanism that tends to inhibit or complicate our ability to measure the other saturation-transfer mechanisms in which we are mainly interested.

Rotational diffusion of spin-labeled macromolecules at correlation times of the order of 10^{-5} s is too slow to affect the ESR spectrum very much, but is sufficiently fast on the time scale of T_{1e} that saturation transfer can occur. This ELDOR mechanism was studied rather extensively both theoretically and experimentally (Smigel *et al.*, 1974; Hyde *et al.*, 1975). It affects several different ESR displays and, in retrospect, the primary contribution of the ELDOR studies was to build the foundation for the other displays [i.e., second-harmonic out-of-phase absorption (Hyde and Thomas, 1973) or first-harmonic out-of-phase dispersion (Hyde and Dalton, 1972)], which turned out to have better signal-to-noise ratios (SNR). In principle, ELDOR in the very slow tumbling domain can yield increased information because of the additional "dimension." Namely, saturation transfer can be monitored as a function of both observe setting and pump setting. It is suggested here that the advent of the loop-gap resonator (see the Apparatus section) has resulted in sufficiently large improvement in the SNR that this particular ELDOR strategy should be reevaluated.

Most published ELDOR studies have used cw techniques. Recently the short-pulse saturation-recovery technique has been introduced (Fajer *et al.*, 1986; Yin *et al.*, 1987a; Yin and Hyde 1987a, 1987b). A saturating pulse is delivered in a time short compared with saturation transfer, and saturation transfer away from the pump location is observed at this same pump location by a weak microwave field. A multiexponential saturation recovery signal is obtained that contains the same information as cw ELDOR. Of course the short-pulse ELDOR technique also exists, where these same transverse relaxation processes are observed at different spectral locations. There has been one short-pulse ELDOR publication (Hyde *et al.*, 1984), but much work remains to be done; cw saturation, cw ELDOR, saturation recovery, and pulse ELDOR are closely related techniques.

1.2. Historical Overview

The year 1976 provides a convenient dividing line: this was the publication year of the book by Kevan and Kispert on electron spin double resonance, including ELDOR. Publications prior to that time will not be reviewed in detail here, but we will examine more recent developments in considerable depth. The reader is urged to consult that text as background to the present article.

Hyde *et al.* (1968b) (HCF) remains the key citation. In HCF, the main elements of the technique and theory were developed. The theory and experiment were further developed in the paper of Eastman *et al.* (1970), and in the paper on frequency-swept ELDOR by Hyde *et al.* (1968a). A study of these three papers would also provide the reader with desirable background.

In 1976, in a paper that has become increasingly important in the author's own work, Stetter *et al.* proposed the ^{14}N-^{15}N ELDOR technique. These authors extended the Freed analysis to include the situation depicted in Figure 1. The system on which they were working was a mixture of ^{14}N substituted and ^{15}N substituted tanone in various mineral oils. It was reasonable to assume that all values of W_e were the same, as predicted by the spin-rotational mechanism (see the Relaximetry section), but that values of W_n were different because of the electron nuclear dipolar (END) mechanism, which depends on the nuclear spin and magnetogyric ratio.

The Heisenberg exchange rate can be expressed as a rate constant times a concentration. In general, there are four Heisenberg exchange rates in the ^{14}N-^{15}N system: $K(^{14}N\text{-}^{14}N)[^{14}N]$, $K(^{15}N\text{-}^{15}N)[^{15}N]$, $K(^{14}N\text{-}^{15}N)[^{14}N]$, and $K(^{14}N\text{-}^{15}N)[^{15}N]$. Here $K(^{14}N\text{-}^{14}N)$ is the rate for collisions between the ^{14}N labeled species. Similarly $K(^{15}N\text{-}^{15}N)$ refers to collisions between ^{15}N labeled molecules and $K(^{14}N\text{-}^{15}N)$ is the rate for

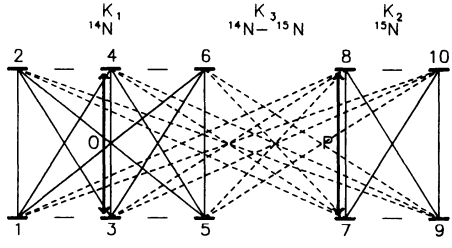

Figure 1. Energy-level diagram for the ^{14}N-^{15}N system. Horizontal lines indicate nuclear spin-lattice relaxation times. Vertical lines represent electron spin-lattice relaxation rates and diagonal lines represent Heisenberg exchange. Induced transitions by the pump and observed microwave field are indicated by heavy vertical lines. This figure is appropriate for cw ELDOR.

collisions between ^{15}N and ^{14}N labeled molecules. However, in the work of Stetter *et al.* (1976) only one rate constant was needed since the ^{14}N and ^{15}N tags were on the identical molecules—i.e., tanone. Heisenberg exchange frequencies then depend on $K \times$ the concentration of one or the other of the two components of the system. They obtained for W_n', $W_n \ll K[^{14}N], K[^{15}N]$,

$$R_\infty^{\pm 1/2,0} = K[^{14}N]/(6W_e + K[^{14}N]) \tag{2}$$

$$R_\infty^{0,\pm 1/2} = K[^{15}N]/(4W_e + K[^{15}N]) \tag{3}$$

and for W_n', $W_n \gg K[^{14}N], K[^{15}N]$,

$$R_\infty^{\pm 1/2,0} = K[^{14}N](2 + 3W_n/W_e)/6W_e(2 + W_n/W_e) \tag{4}$$

$$R_\infty^{0,\pm 1/2} = K[^{15}N](2 + 2W_n'/W_e)/4W_e(2 + W_n'/W_e) \tag{5}$$

These are useful equations to study. The first superscript on R denotes the observe line and the second the pump line. If our goal is to measure K, we note that W_n does not enter at low values of W_n and that it cancels at high values. Only when W_n is comparable to W_e is there a complication. Thus to a considerable degree the problem of measuring K in the presence of nuclear relaxation has been eased by the combined use of ^{14}N and ^{15}N.

We emphasize again that in the analysis of Stetter *et al.*, Heisenberg exchange between ^{15}N species is the same as when observing ^{14}N species that exchange with ^{15}N species, and vice versa (except for a spin-dependent factor to account for the fact that there can be no exchange between identical species). Theirs is a valid approach when the exchanging species are chemically identical as was the case in their work, but is not correct if ^{15}N is on one type of spin label and ^{14}N on another. The introduction of three Heisenberg exchange rate constants $K(1)$, $K(2)$, and $K(3)$ is required in the general case. See Figure 1. We will return to this point, which is an important one.

Popp and Hyde made the first serious biological study using ELDOR (1982). They measured lateral diffusion of lipids in lipid bilayers. Actually, of course, they measured bimolecular collision rates. The diffusion constants were then calculated using the theoretical model of Sackman and Träuble (1972a, 1972b; Träuble and Sackman, 1972). Agreement between their data, which was a measurement of self-diffusion, was in gratifying agreement with NMR field-gradient and fluorescence photobleaching experiments, which measure bulk diffusion against a concentration gradient.

However, the nuclear relaxation rate W_n was so fast that it caused a significant experimental problem. Popp and Hyde concluded that the use of the ^{14}N-^{15}N method would be appropriate in future studies.

Feix *et al.* (1984) did just that. With ^{14}N and ^{15}N substituted moieties at the C16 position near the terminal methyl groups of stearic acid spin labels, they obtained data in good agreement with Popp and Hyde. But something new became possible. One nitroxide moiety could be placed at one position and a second at another position, and the bimolecular collision rate measured. The term "vertical fluctuation" was coined to describe these excursions of the terminal methyl group toward the polar head group

regions. Encounters between labels at C16 and C5 were surprisingly fast—of the order of 1/3 of the bimolecular collision frequency when the labels were each at the same position.

However it became apparent that the theoretical analysis of Stetter *et al.* (1976) needed further development. Vertical fluctuations are a distinct phenomena requiring the introduction of additional Heisenberg exchange frequencies. As indicated above, in a general analysis three exchange rate constants are required: between ^{14}N species, between ^{15}N species, and between ^{14}N and ^{15}N species. Thus in Figure 1, three Heisenberg exchange rate constants have been introduced. Also W_e will be different if the labels are at different positions. This general analysis has now been completed by Yin and Hyde (1987b) and is summarized here. The equations of Stetter follow as a special case, as do equations for a number of other restricted conditions of practical significance.

Yin and Hyde (Yin *et al.*, 1987a; Yin and Hyde, 1987a, 1987b) developed an alternative theoretical approach to that of Freed. Namely, they directly wrote down the differential rate equations coupling the populations of the various levels. Using linear algebra, the time response to any perturbation was obtainable. If all rate-of-change values were set to zero, cw ELDOR results were obtained. The matrices that are eventually required in Freed's theory to calculate ELDOR response are identical to those obtained from the rate equations. Figure 2 shows the energy-level diagram for pulse experiments. It differs from Figure 1 only in that the pump power is off during reception. The nature of the pump pulse determines the initial conditions for the transient solutions.

It could immediately be recognized that short excitation pulses give rise to superimposed exponentials in both the saturation-recovery and pulse-ELDOR responses. The time constants were identical, but the signs of the various exponential terms were not. Pulse ELDOR and saturation recovery became complementary. One method monitors the disappearance of saturation from a pump spectral position because of saturation transfer, and the other measures the appearance of saturation at an observe location that is well separated from the pump location.

It is now apparent that a very wide range of questions concerning transport can be addressed with a ^{14}N label on one bimolecule and a ^{15}N on another. Collision frequencies of any two species that can be labeled can be measured. Both cw and pulse techniques are appropriate. The theory is reasonably in place, and the apparatus has become much more sensitive since the introduction of the loop-gap resonator (see the Applications section).

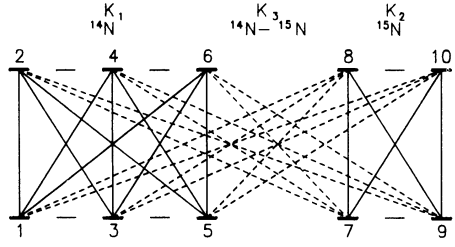

Figure 2. Energy-level diagram for pulse ^{14}N-^{15}N ELDOR. No pump power is present, but it is implied that some sort of initial excitation gives rise to initial values for populations of the levels that differ from equilibrium populations.

2. RATE EQUATIONS

Freed in a long series of papers has developed a general theory of fluid phase ESR reviewed in Freed (1972, 1979a). With coupled Bloch equations in a density matrix formulation as a basis, line shapes, cw saturation effects, saturation recovery signals, spin echo signals, and ELDOR signals were predicted within a uniform theoretical structure over a wide range of rotational correlation times.

In ELDOR an alternative, simpler and completely rigorous theoretical structure is possible. It has been apparent since the earliest days of magnetic resonance that the z components of magnetization in a complex system can be calculated by setting up rate equations for populations of energy levels. One simply connects the levels by every possible relaxation path and every excitation probability. Transient development of z components and stationary equilibrium values under steady-state conditions can be obtained. If the z component were observed directly in magnetic resonance, no further consideration of x or y components would be necessary. The key points are that the ELDOR reduction factor R in stationary ELDOR is the fractional change in the z component at the observe spectral position because of the presence of the pump, and that the transient ELDOR signal is the difference between the instantaneous z component and the equilibrium z component. The x and y components of magnetization do not enter into the analysis of ELDOR. The results by Freed for ELDOR are identical to those obtained from rate equations.

The advantage of the rate-equation approach to ELDOR is that a variety of complex situations involving both ^{14}N and ^{15}N substituted spin labels in different environments with physical and perhaps chemical exchange can be modeled.

In order to illustrate the basic ideas behind the rate equation method, we consider Figure 3. A very simple situation is assumed. A first spin species of concentration N_I and spin-lattice relaxation rate W_{e1} interacts at a Heisenberg exchange rate constant K_x with a second spin species of concentration N_{II} and spin-lattice relaxation rate W_{e2}. Each species is assumed to have a simple one-line spectrum.

$$\frac{d(n_1 - n_2)}{dt} = -2W_{e1}[(n_1 - n_2) - (N_1 - N_2)] + 2K_x(n_2n_3 - n_1n_4) \tag{6}$$

$$\frac{d(n_3 - n_4)}{dt} = -2W_{e2}[(n_3 - n_4) - (N_3 - N_4)] - 2K_x(n_2n_3 - n_1n_4) \tag{7}$$

where $n_j, j = 1, \ldots, 4$ are the instantaneous populations per unit volume of the four levels and $N_j, j = 1, \ldots, 4$ are the equilibrium Boltzmann populations per unit volume. The bimolecular collision rate W_x of species n_a with species n_b is given by $K_x n_b$. Since

$$n_2n_3 - n_1n_4 = (N_{II}/2)(n_2 - n_1) + (N_I/2)(n_3 - n_4) \tag{8}$$

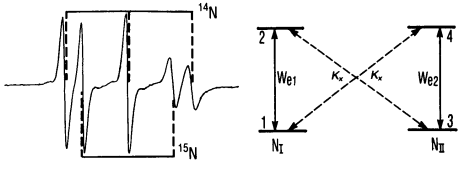

Figure 3. ^{14}NC16 (0.5 mol%) and ^{15}NC16 (0.25 mol%) stearic acid spin labels in DMPC at 37 °C. Because of very fast nuclear relaxation, hyperfine lines of each isotope are assumed to be strongly coupled, resulting in a simplified energy-level diagram.

and $n_1 + n_2 = N_1$; $n_3 + n_4 = N_{11}$, equations (6) and (7) are *linear* differential equations. The observable signals are

$$i_1 = (n_1 - n_2) - (N_1 - N_2) \qquad \text{and} \qquad i_{11} = (n_3 - n_4) - (N_3 - N_4) \tag{9}$$

After some rearrangement, equations (6) and (7) become

$$\frac{di_1}{dt} = -2W_{e1}i_1 - N_{11}K_x i_1 + N_1 K_x i_{11} \tag{10}$$

$$\frac{di_{11}}{dt} = -2W_{e2}i_{11} + N_{11}K_x i_1 - N_1 K_x i_{11} \tag{11}$$

The solutions to equations (10) and (11) are

$$i_1 = I_1 e^{-(A-B)t} + I_2 e^{-(A+B)t} \tag{12}$$

$$i_{11} = I_1 \frac{N_{11}K_x}{-(A-B) + 2W_{e2} + N_1 K_x} e^{-(A-B)t} + I_2 \frac{N_{11}K_x}{-(A+B) + 2W_{e2} + N_1 K_x} e^{-(A+B)t} \tag{13}$$

where

$$A = W_{e1} + W_{e2} + \tfrac{1}{2}K_x(N_1 + N_{11}) \tag{14}$$

$$B = [(W_{e1} - W_{e2})^2 - K_x(N_1 - N_2)(W_{e1} - W_{e2}) + \tfrac{1}{4}K_x^2(N_1 + N_2)^2]^{1/2} \tag{15}$$

and I_1, I_2 are constants to be defined by initial conditions. Quite generally a double exponential is observed. The coefficients are determined by initial conditions after the saturating pulse. If transition I is saturated, i_1 is the saturation-recovery signal and i_{11} is the pulse ELDOR signal. If the two spin species have the same spin-lattice relaxation probability W_e, considerable simplification occurs. Equations (12) and (13) become

$$i_1 = I_1 \exp(-2W_e t) + I_2 \exp\{-[2W_e + K_x(N_1 + N_{11})]t\} \tag{16}$$

$$i_{11} = I_1 \frac{N_{11}}{N_1} \exp(-2W_e t) - I_2 \exp\{-[2W_e + K_x(N_1 + N_{11})]t\} \tag{17}$$

For a short pulse, $n_1 = n_2$, $n_3 = N_3$, and $n_4 = N_4$ immediately after the pulse. Spin system I is fully saturated and spin system II is not yet affected. Differentiating equation (16) and evaluating both it and equation (6) for these initial conditions yields

$$i_1 = I_1 \exp(-2W_e t) + \frac{N_{11}}{N_1} \exp\{-[2W_e + K_x(N_1 + N_{11})]t\} \tag{18}$$

$$i_{11} = I_1 \frac{N_{11}}{N_1} \exp(-2W_e t) - \exp\{-[2W_e + K_x(N_1 + N_{11})]t\} \tag{19}$$

For a short pulse, the second terms in equations (18) and (19) are the same in magnitude. Saturation recovery and ELDOR are both effective from the point of view of sensitivity in measuring Heisenberg exchange. However, the difference in sign in equation (19) is notable. It may be easier to separate double exponentials of opposite sign than of the same sign. Both techniques yield the spin-lattice relaxation probability W_e without contamination from HE at sufficiently long times; the fast initial decay contains HE information.

For a long pulse, spin system II approaches steady state and $d(n_3 - n_4)/dt$ approaches 0 during the pulse. Equation (7) than yields as an initial condition

$$(n_3 - n_4)_{t=0} = \frac{2W_e(N_3 - N_4)}{2W_e + K_x N_I} \tag{20}$$

For cw ELDOR, one sets the time derivatives in equations (10) and (11) to zero. If interval i_I is pumped, one adds to equation (10) the term $(n_1 - n_2)K_p$ where K_p is the transition probability. Equation (9) enables one to obtain

$$-2W_{e1}i_I - N_{II}K_x i_I - 2K_p i_I + N_I K_x i_{II} - 2K_p(N_1 - N_2) = 0 \tag{21}$$

$$-2W_{e2}i_{II} + N_{II}K_x i_I - N_I K_x i_{II} = 0 \tag{22}$$

We have two simultaneous inhomogeneous algebraic equations in two unknowns. Solving for the cw ELDOR signal i_{II} is straightforward. A quite complex equation is obtained. However, if the pump power is allowed to approach infinity, considerable simplification occurs:

$$i_{II} = -(N_1 - N_2)\frac{N_{II}K_x}{2W_{e2} + N_I K_x} \tag{23}$$

We see in this example that the rate-equation approach provides a unified theoretical approach to cw ELDOR, pulse ELDOR, and saturation recovery.

For a ^{14}N containing nitroxide (see Figure 4), Yin *et al.* (1987a) obtain the following time-dependent solution:

$$i_{1,2} = I_1 \exp(-2W_e t) + \tfrac{3}{2}\exp[-(2W_e + W_n + NK_x)t] + \tfrac{1}{2}\exp[-(2W_e + 3W_n + NK_x)t] \tag{24}$$

$$i_{3,4} = I_1 \exp(-2W_e t) - \exp[-(2W_e + 3W_n + NK_x)t] \tag{25}$$

$$i_{5,6} = I_1 \exp(-2W_e t) - \tfrac{3}{2}\exp[-(2W_e + W_n + NK_x)t] + \tfrac{1}{2}\exp[-(2W_e + 3W_n + NK_x)t] \tag{26}$$

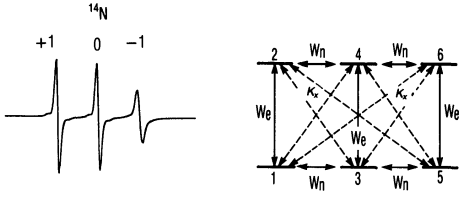

Figure 4. ^{14}NC16 (0.4 mol%) stearic acid spin label in DOPC at 54 °C. This is the normal energy-level diagram for a nitroxide radical spin label.

(If interval 5, 6 is pumped, the signs of the terms with $\frac{3}{2}$ as coefficient change.)

Here $i_{1,2}$ is the saturation-recovery signal and is a triple exponential. A double exponential ELDOR signal is observed at the center line, $i_{3,4}$, and a triple exponential ELDOR signal occurs at $i_{5,6}$.

For short pulse pumping of interval 3, 4,

$$i_{1,2} = i_{5,6} = I_1 \exp(-2W_e t) - \exp[-(2W_e + 3W_n + NK_x)t] \tag{27}$$

$$i_{3,4} = I_1 \exp(-2W_e t) + 2\exp[-(2W_e + 3W_n + NK_x)t] \tag{28}$$

Double exponentials are observed for both saturation recovery, $i_{3,4}$, and ELDOR, $i_{1,2}$, and $i_{5,6}$.

The ^{14}N-^{15}N spin-label pair method is an important one, and Yin and Hyde (1987b) have analyzed it theoretically. They point out as mentioned above that there are three Heisenberg exchange rate constants, between ^{14}N species K_1, between ^{15}N species K_2, and between ^{14}N and ^{15}N species K_3. There are two concentrations, N_I and N_{II}, and therefore four Heisenberg exchange frequencies: K_1N_I, K_2N_{II}, K_3N_I, and K_3N_{II}. Their formulation includes this complication and carries distinct electron and nitrogen nuclear relaxation rates for the two spin species. This problem was sufficiently complex that matrix algebra methods were employed. The approach, however, logically parallels that of equations (6)-(23) above. As in that case, within the same theoretical approach, pulse and cw ELDOR and saturation-recovery experiments were analyzed.

Five superimposed exponentials were predicted for the most general ^{14}N-^{15}N spin-label pair problem. The time constants obtained by Yin and Hyde (1987b) are

$$\lambda_1 = -(2W_{e1} + 3W_{n1} + K_1N_I + K_3N_{II}) \tag{29}$$

$$\lambda_2 = -(2W_{e1} + W_{n1} + K_1N_I + K_3N_{II}) \tag{30}$$

$$\lambda_3 = -(2W_{e2} + 2W_{n2} + K_3N_I + K_2N_{II}) \tag{31}$$

$$\lambda_4 = -(A + B) \tag{32}$$

$$\lambda_5 = -(A - B) \tag{33}$$

where

$$A = \tfrac{1}{2}(2W_{e1} + 2W_{e2} + K_3N_I + K_3N_{II}) \tag{34}$$

$$B = \tfrac{1}{2}[4(W_{e1} - W_{e2})^2 - 4(W_{e1} - W_{e2})(N_I - N_{II})K_3 + (K_3N_I + K_3N_{II})^2]^{1/2} \tag{35}$$

It might be thought that this theoretical approach is not practical. One should not be too sanguine about deconvoluting a multiexponential signal with five time constants. However, there is a great deal of experimental control, and the authors are optimistic. We note the following points.

1. Heisenberg exchange is intermolecular and the other relaxation rates are intramolecular. Independent variation of N_I and N_{II} is straightforward.
2. The number of exponentials is known; this is of great assistance in curve fitting.
3. The system can be examined with one spin species at a time.
4. The time constants (but not the prefactors) are independent of the length of the saturating pulse.
5. Yin and Hyde (1987a) show that introduction of molecular oxygen adds to each time constant a fixed term that is determined by the bimolecular collision rate of oxygen with the spin label. This is another useful control.

3. SPIN-LABEL RELAXIMETRY

We consider here the three relaxation terms that affect the ELDOR response: T_{1e}, T_{1n}, and Heisenberg exchange.

Pulse saturation-recovery measurements of the electron spin-lattice relaxation time of nitroxide spin labels have been reported in a number of publications from the authors' laboratory. However, the data have not been collected in a single paper and no review has been written. Since T_{1e} is the "clock" on which all else depends when doing ELDOR, it is felt to be desirable to bring a portion of these data together here.

For low molecular weight nitroxides, T_{1e} data using pulse techniques were reported by Percival and Hyde (1976). The solvent was *sec*-butyl benzene. In work-in-progress, Subczynski and Hyde have made measurements on small nitroxides in water, glycerol-water, and light paraffin oil. See Table 1 for representative data near room temperature.

Percival and Hyde observed an intermolecular contribution to T_{1e} that arose from dipole-dipole interactions. Similar data were reported more recently by Yin *et al.* (1987a). The values reported in Table 1 were obtained at sufficiently low concentrations of spin labels that only intramolecular contributions were significant. Values of T_{1e} did not change when the ^{15}N isotope was used and were nearly independent of the nuclear quantum number. It is concluded that for small nitroxides (mw ~ 300) in solvents of about 1 cP viscosity, T_{1e} is about 0.5 μs.

TABLE 1
T_{1e} for Small Nitroxides

Nitroxide	Solvent	Temperature	T_{1e}
Tanol	SBB	31	0.38[a]
Tempone	SBB	22	0.47[a]
DTBN	Paraffin oil	20	0.24[b]
Tempo	Paraffin oil	20	0.51[b]
Tempone	Paraffin oil	20	0.61[b]
Tempone	Water	20	0.64[b]
DTBN	DMSO	20	0.41[b]
Tempone	DMSO	20	0.77[b]

[a] Percival and Hyde, 1976. [b] Subczynski and Hyde.

Spin-lattice relaxation times of lipid-type spin labels have been measured in the course of various transport studies in lipid bilayers (Subczynski and Hyde; Kusumi *et al.*, 1982). Some of the values reported at temperatures above the main phase-transition temperature are given in Table 2. Care was taken to remove oxygen. Because of the high partition coefficient of oxygen into hydrocarbons, it will decrease the measured T_{1e} values substantially. It is concluded that for medium-size nitroxides in lipids or viscous hydrocarbons, T_{1e} is typically about 3 μs.

For water-soluble proteins that have been spin labeled, namely, maleimide-labeled bovine serum albumin (BSA) and hemoglobin, the value of T_{1e} increases to about 6 μs. When the protein is frozen, T_{1e} increases further to about 15 μs. No saturation-recovery data on membrane-bound spin-labeled proteins are available, but times longer than 10 μs in fluid membranes would seem unlikely.

Probably the mechanism of spin-lattice relaxation of nitroxides is spin rotation.

$$W_e = \sum_i \frac{(g_i - g_e)^2}{18} \frac{1}{\tau_R} \tag{36}$$

Here g_i are the principle values of the anisotropic Zeeman interaction, g_e is 2.00232, and τ_R is the rotational correlation time. Favoring the spin-rotation mechanism is approximate order-of-magnitude agreement between calculated and observed times, and the absence of an M_I dependence.

However, the predicted linear dependence on macroscopic viscosity is not consistent with the data. The absence of any dependence of T_{1e} on M_I is a great convenience in solving the rate equations. If a different relaxation time had to be assigned to each hyperfine line, the situation could well be too complex to handle. The nitrogen nuclear relaxation time has been estimated by Popp and Hyde (1982) using an equation that is based on Kivelson's theory of relaxation (Kivelson, 1960; Hyde *et al.*, 1968b)

$$W_n = \frac{4\pi^2}{10}\left\{\left[\frac{6^{1/2}}{4}(A_z - A_0)\right]^2 + 2[\tfrac{1}{4}(A_x - A_y)]^2\right\}\left(\frac{\tau_R}{1 + \omega_n^2\tau_R^2}\right) \tag{37}$$

TABLE 2
T_{1e} Data for Lipid-Type Labels

Nitroxide	Lipid or Solvent	Temperature	T_{1e} (μs)
16-SASL	DMPC	37	1.7[a]
ASL	DMPC	37	2.4[b]
CSL	DMPC	37	3.3[b]
5-SASL	DMPC	37	5[b]
16-SASL	Paraffin oil	20	3.1[c]
ASL	Paraffin oil	20	3.8[c]
CSL	Paraffin oil	20	4.9[c]
9-SASL	Paraffin oil	20	4.8[c]

[a] Popp and Hyde, 1982. [b] Kusumi *et al.*, 1982. [c] Subczynski and Hyde.

in which A_0 is the isotropic hyperfine constant and ω_n the nuclear Larmor frequency. Agreement between calculated and measured values of W_n was fair in the lipid system studied by Popp and Hyde (1982). The motion must have been highly anisotropic and no attempt was made to include such effects in the calculation of W_n. It is notable that the value of W_n can be greater than the value of W_e, a fact that may surprise some investigators. See, for example, the pulse ELDOR experiment of Hyde *et al.* (1984).

In principle, ELDOR measurements of W_n can be useful in obtaining information on the motional model. Primarily, however, nuclear relaxation is an impediment to the measurement of other more interesting relaxation processes, particularly Heisenberg exchange.

Numerous workers have contributed to the theory and experiment of liquid-phase Heisenberg exchange. These studies have been discussed in a coherent fashion in the monograph by Molin *et al.* (1980). The reader is urged to consult the text.

It seems over a very wide range of conditions that Heisenberg exchange between spin labels is a strong exchange event:

$$\omega_A = 8\pi R D_A [A] p \tag{38}$$

where ω_A is the bimolecular collision frequency and p is the probability that an observable event occurs when a collision does in fact occur. Strong exchange implies that $p = 1$. R is an interaction distance of the order of 4 Å. [See footnote 22 of Hyde *et al.*, 1968b for commentary on the numerical factor in equation (40).]

For Heisenberg exchange between unlike particles,

$$\omega_A = 4\pi R(D_A + D_B)[B] p \tag{39}$$

This is the classical Smoluchowski equation that predicts the exchange frequency that an observed A species will experience with B species. Note that [A] does not appear.

In equations (38) and (39), ω_A is determined by the product of the diffusion constant and the concentration. There is no possibility of separating these factors except by an independent experiment. Nevertheless, the bimolecular collision frequency is itself a molecular event of great interest. The opportunity created by ELDOR to measure the bimolecular collision frequency is one of the primary rationales for the technique.

Dipole-dipole interactions between spin labels in solution should always be taken into account in ELDOR. Of course since they are intermolecular, they can in general be analyzed by varying the concentration. However, there is one term in the dipolar Hamiltonian, the so-called pseudosecular term $(S_1^{\pm} S_2^{\mp})$, that is nearly indistinguishable from Heisenberg exchange (Freed, 1972).

In fact, there seems to be no direct way to distinguish pseudosecular dipolar relaxation from Heisenberg exchange. An indirect way is to measure the contribution of the nonsecular dipole-dipole term to W_e. Then, if the motional model is known, the pseudosecular term can be calculated. Both Popp and Hyde (1982) and Feix *et al.* (1984) discuss the pseudosecular term. Actually, it probably is not so important: calculation suggests that it is not dominant (Eastman *et al.*, 1970) and even if it is significant, the net effect is to alter the interaction distance R, itself an uncertain

quantity. Primarily in ELDOR it is the relative change in bimolecular collision rates rather than the absolute magnitudes that is of interest.

4. APPARATUS

It is the thesis of this section that the loop-gap resonator (LGR) introduced by Froncisz and Hyde (1982) makes ELDOR a very much easier and better technique than is the case when a bimodal cavity is employed. The key citation is the paper of Hyde *et al.* (1985).

Various ELDOR sweeps are possible: (i) setting of the two microwave frequencies and sweeping the magnetic field, so-called field-swept ELDOR; (ii) setting the observe microwave frequency and the magnetic field, and sweeping the pump microwave frequency, which is frequency-swept ELDOR; (iii) setting the pump microwave frequency and magnetic field and sweeping the observe microwave frequency; and (iv)-(vi) setting any one of the three variable and sweeping the other two. Of these, field-swept ELDOR is much easier. It is the only sweep method now employed in the authors' laboratory. As Eastman *et al.* (1970) and Hyde *et al.* (1968a) point out, the frequency-sweep ELDOR display has certain theoretical advantages and remains an interesting option.

The primary defect in the bimodal cavity approach to ELDOR is the very unsatisfactory filling factor, particularly for aqueous samples.

Figure 5 shows the bimodal cavity that has been used in one variant or another by the senior author for many years. A TE_{103} rectangular cavity mode has been crossed with a TE_{102} cavity mode. Two half-wavelengths are in common or shared, and one half-wavelength belongs only to one mode. The invention of this type of cavity made

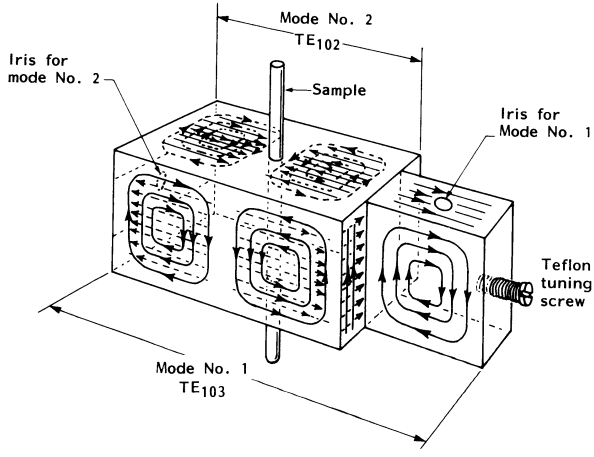

Figure 5. Bimodal cavity used previously for ELDOR (Hyde *et al.*, 1968b). Lines of magnetic flux are shown (solid line, Mode No. 1; dashed lines, Mode No. 2). Isolation screws, not shown, are used to eliminate spurious coupling between modes. Spurious coupling primarily arises from imperfections in the quartz Dewar insert (also not shown) into which the sample is placed.

ELDOR practical, since it became easy to tune one mode in frequency without affecting the resonant frequency of the other modes. The "Teflon tuning screw" of Figure 5 was used for this purpose.

It is customary when using this cavity in careful quantitative work for the TE_{102} mode to serve as pump, since the microwave field is uniform along the sample. The cavity is at an angle of about 60° with respect to the magnetic field, which decreases the efficiency of the pump. A more serious problem is that the observe mode is $\frac{5}{2}$ times bigger than the usual rectangular TE_{102} cavity, immediately decreasing the filling factor for observation by this ratio. For aqueous samples, the pump and observe modes are sometimes interchanged because of heating of the sample due to poor pump efficiency. But then serious loss of signal intensity occurs because the 60° angle. A further problem for aqueous samples is that the nodal planes of the two modes where the electric fields are zero may not coincide. Indeed for the TE_{103} mode, this nodal surface is not even planar. Flat cells have not been possible, and even capillaries are difficult to position. To summarize: the bimodal cavity of Figure 5 was a breakthrough in that it made ELDOR feasible, but the price that was paid in the filling factor was high. It is for this reason that the ELDOR sensitivity has always been poor.

The introduction of the LGR has changed matters. The Q of the LGR is typically 10 times lower than for a cavity resonator and the filling factor η is typically 100 times higher, giving a favorable ηQ product.

The full width at half height of a matched resonator is ν/Q_L MHz, where Q_L is the loaded Q. This is typically 3 MHz for a cavity resonator and 30 MHz for a LGR. The key idea of the paper by Hyde *et al.* (1985) was to introduce both the pump and observe frequencies into the same resonator mode. For ^{14}N ELDOR, the frequency difference is 44 MHz and for ^{14}N-^{15}N ELDOR a frequency difference of 25 MHz has often been used. The mode is sufficiently broad that both of these frequencies can be supported, although obviously some compromise is necessary. We have preferred to put the observe frequency on-resonance in order to achieve the best possible signal intensity. The pump power that is reflected from the resonator because it is mismatched off-resonance is trapped by a microwave filter before it can reach the detector crystal. See Figure 1 of Hyde *et al.* (1985) for details.

The LGR was found to have the following advantages for ELDOR.

1. An improvement in sensitivity expressed on a molarity basis by 20 times. Experiments on spin-labeled plasma membranes of cells became feasible.
2. Sharply reduced pump power for a given pump field. ELDOR becomes feasible on difficult-to-saturate samples.
3. Reduced microphonics and improved system stability. Bimodal cavities were difficult to maintain in balance; the LGR with its low Q is more stable.
4. Dispersion ELDOR becomes feasible. Because of the low Q, there is reduced demodulation of microwave phase noise and the dispersion mode can be observed with good sensitivity.

There remain situations where the features of a bimodal cavity are helpful, and it is interesting to consider whether or not useful bimodal loop-gap resonators can be built for ELDOR. The rationale for such a development effort include the following points.

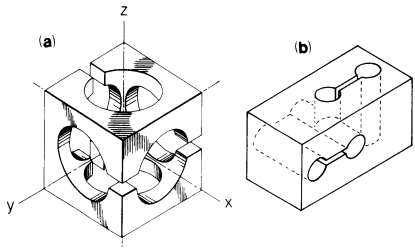

Figure 6. (a) Bimodal loop-gap resonator formed from crossed 1-loop-1-gap resonators. (b) Bimodal loop-gap resonator formed from crossed 2-loop-1-gap resonators.

1. For frequency-swept ELDOR, one would like some sort of a tracking bimodal resonator so that the ratio (incident pump power)/(pump field at the sample) remains constant.
2. An important control in ELDOR is to pump and observe between $M_I = +1$ and $M_I = -1$ of ^{14}N, which is 88 MHz. This separation is too great for the LGR approach of Hyde *et al.* (1985).
3. For ELDOR in the context of saturation transfer of very slowly diffusing macromolecules, the separation of the pump and observing frequencies can also be quite large.

We have built on a microwave test bench the bimodal loop-gap resonators of Figure 6. We have also built the two-mode resonator of Figure 7. (Here the two modes are not orthogonal.) It is possible that these structures will be found useful in frequency-swept ELDOR or in field-swept ELDOR where the pump and observe frequencies are far apart.

A rather complicated automatic electromechanical frequency tracking system with feedback was employed by Hyde *et al.* (1968a) to keep the pump resonant frequency and the pump microwave frequency aligned. Because of the low Q of the LGR, it would appear that a much simpler open-loop tracking system could be employed.

This section on apparatus is concluded with a discussion of pulse ELDOR. Nechtschein and Hyde initiated this branch of the field in 1970. More recently Hyde *et al.* (1984) demonstrated the short-pulse ELDOR technique to measure values of T_{1n} that were shorter than T_{1e}. They used a bimodal cavity similar to that of Figure 5 in their work.

As mentioned previously Yin and Hyde (Yin *et al.*, 1987a; Yin and Hyde, 1987b) have developed the theoretical basis for pulse ELDOR by directly solving the coupled differential equations for the z component of magnetization. Freed (1974, 1979b) has also developed some pulse ELDOR theory in the course of his work on saturation-recovery theory.

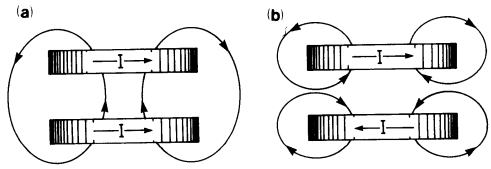

Figure 7. Multimode loop-gap resonator. Mode (a) is the fundamental mode; mode (b) is at a higher frequency. The frequencies are split by the mutual inductance.

There is an intrinsic problem in pulse ELDOR. The short pump pulse is the key idea—one wants to observe directly the arrival of saturation because of some saturation-transfer mechanism followed by saturation recovery. The problem is that a short pulse intrinsically has a spectral width. If τ is the pulse width in seconds, the spectral width in Hz is $(2\pi\tau)^{-1}$, which corresponds to $(\gamma\tau)^{-1}$ G. Here γ is the magnetogyric ratio (1.76×10^7). For $\tau = 10^{-8}$ s, this width becomes about 6 G. This width is simply that calculated from the Heisenberg uncertainty principle for a short pulse. One can calculate the spectral width in another way: the value of H_1 that is required for a 180° pulse (inversion recovery) is 10^{-8} s. $H_1 = \pi(\gamma\tau)^{-1}$ G or about 20 G. With the LGR it is possible to deliver 20 G 10 ns pulses, which would tend to saturate the observe signal as well. When using a cavity resonator, the high Q of the resonator tends to round off the pulse and 10^{-8} s pulses are not possible. The spectral width is of course narrower.

Pulse ELDOR would appear to be an important subject for future development. But the constraints imposed by the pulse width, the pulse height, and the separation of the pump and observe frequencies must be recognized.

5. APPLICATIONS

5.1. Lateral Diffusion in Membranes

As mentioned previously, Popp and Hyde (1982) carried out the first application of ELDOR to the study of lateral diffusion in a model biological membrane. They examined the transfer of saturation between the low-field ($M_I = +1$) and center ($M_I = 0$) lines of ^{14}NC16 in dimyristoylphosphatidylcholine (DMPC) bilayers. Their approach to separating the exchange (intermolecular) and END (intramolecular) contributions to the ELDOR reduction was to manipulate spin-label concentration. They utilized a very low concentration (*ca* 0.075 mol%), at which they reasoned that the exchange contributions would be negligible, and a higher concentration (0.25–0.5 mol%) which would contain information on bimolecular collisions.

From the ELDOR reduction at low spin-label concentration, a value for W_n/W_e was calculated assuming saturation transfer due to the END mechanism only. The value of W_e was determined independently by saturation recovery and the Heisenberg exchange probability W_x was calculated from ELDOR data at a higher spin-label concentration using the previously determined value of W_n to separate reduction due to END interactions. Quantity W_x, in turn, was utilized to calculate D from the model of Sackmann and Träuble (1972a, 1972b), Träuble and Sackmann (1972).

The study was successful in obtaining values for D in good agreement with generally accepted rates of lipid diffusion in model lipid bilayer, i.e., on the order of 5×10^{-8} cm^2 s^{-1}. Values for D were obtained from 37–57 °C, however at 27 °C the contribution from END relaxation was so overwhelming that exchange data could not be obtained.

In addition to demonstrating the viability of ELDOR as an approach to the study of lateral diffusion in membranes, the paper by Popp and Hyde established valuable information regarding nuclear relaxation of stearic acid spin labels in membranes. At all temperatures studied, the relative probability of nuclear relaxation (W_n) was greater than W_e. The W_n/W_e ratio was 13.8 at 27 °C, which illustrates the dominance of nuclear

relaxation as a saturation-transfer mechanism. The occurrence of very fast nuclear relaxation indicates that the hyperfine lines of stearic acid spin labels are strongly coupled in membranes at physiological temperatures, and allows for considerable simplification in the interpretation of results using $^{14}N:^{15}N$ spin-label pairs (see Section 5.2).

Although the work by Popp and Hyde was successful in obtaining lateral diffusion constants by ELDOR and saturation-recovery methods, it also set forth certain limitations to this approach when using ^{14}N spin labels alone. In particular, due to the large intramolecular (END) contribution, information on bimolecular collisions cannot be obtained when the rotational correlation time of the nitroxide is longer than 5×10^{-10} s. This encompasses the majority of systems in which the spin label is attached to a biological macromolecule. To circumvent the limitations imposed by nuclear relaxation, Popp and Hyde suggested the use of systems containing both ^{14}N and ^{15}N spin-label populations, namely $^{14}N:^{15}N$ spin-label pairs.

5.2. Studies Utilizing $^{14}N:^{15}N$ Spin-Label Pairs

5.2.1. General Methodology

The utilization of $^{14}N:^{15}N$ spin-label pairs for ELDOR studies in biological systems was introduced by Feix *et al.* (1984), who examined interactions among various isomers of doxyl stearic acid spin labels. The strategy in such "dual-label" ELDOR experiments is to pump one isotopic spin system and observe transfer of saturation to the other isotopic spin system. Although intramolecular (END) relaxation continues to couple the nuclear manifolds for each isotopic species, it cannot couple the ^{14}N and ^{15}N systems (however, see Section 2 for the possible influence of nuclear relaxation on the observed ELDOR reduction). Only intermolecular mechanisms, namely, Heisenberg exchange (with possible contributions from pseudosecular dipolar interactions, discussed in Section 3), facilitate saturation transfer between the pumped and observed species. Thus one can observe directly the effects of bimolecular collisions between spin labels.

An example of field swept, cw ELDOR between $^{14}N:^{15}N$ spin-label pairs is shown in Figure 8. When the magnetic field is swept through the observed resonance condition for the $M_I = 0$ transition, transfer of saturation occurs from the simultaneously pumped $M_I = -\frac{1}{2}$ transition. This results in a decrease in signal intensity of the observed $M_I = 0$ transition. Similarly, an ELDOR reduction is also observed in the $M_I = +\frac{1}{2}$ transitions as the magnetic field simultaneously sweeps the observing field through $M_I = +\frac{1}{2}$ and the pumping field through $M_I = 0$. No transition is coincidentally saturated when the $M_I = +1, -\frac{1}{2}$, or -1 lines are induced by the observing (rf) field, no transfer of saturation occurs, and no ELDOR reduction is seen. The low-field ^{14}N line is routinely used for normalization.

Normalization to some unaffected line is critical as a control for changes in temperature or tuning of the instrument. Changes in the amplitude of the line used for normalization should be small (i.e., less than 5%) throughout the course of the experiment, and large changes in this line height may be a warning signal (e.g., for loss of isolation).

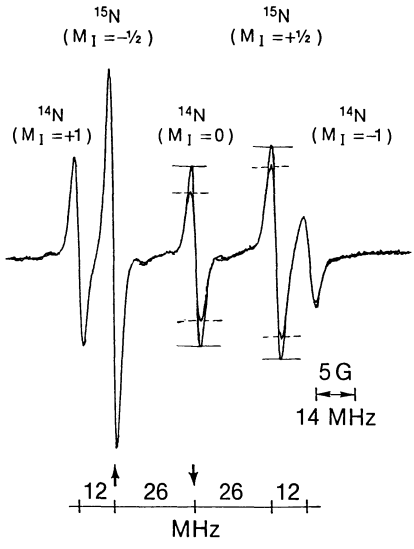

Figure 8. Demonstration of the ELDOR effect for [^{14}NC16:^{15}NC16] (0.25:0.25 mol%) in multibilayer liposomes of DMPC equilibrated with 0.1 M borate buffer, pH 9.5. Temperature was 47 °C. Superimposed spectra were recorded with pump field off and at 400 mW incident power. Horizontal lines indicate the reduction in peak-to-peak amplitude due to transfer of saturation. Arrows define frequency separation between pumping and observing fields, (↑) indicating position of pump field when observer field (↓) is centered on the ^{14}N ($M_I = 0$) resonance (pump-observe frequency difference is 26 MHz). Field calibration in megahertz is given. (From Feix *et al.*, 1984.)

The cw ELDOR reduction R is defined as

$$R = 1 - \frac{i_{II}(\text{pump on})}{i_{II}(\text{pump off})} \tag{40}$$

where i_{II} is the signal intensity of the observed transition. From equations (21) and (22) it can be shown (Yin *et al.*, 1987b) that

$$R^{-1} = \frac{2W_{e1}W_{e2} + W_{e1}N_IK_x + W_{e2}N_{II}K_x}{W_s \times N_IK_x} + \frac{2W_{e2} + N_IK_x}{N_IK_x} \tag{41}$$

A plot of R^{-1} vs. the inverse of the pumping power (P^{-1}, which is proportional to W_s^{-1}) is therefore linear with an intercept (extrapolated to infinite pumping power)

$$R_\infty^{-1} = \frac{(2W_{e2} + N_IK_x)}{N_IK_x} \tag{42}$$

A plot of R^{-1} vs. P^{-1} for various ^{14}N:^{15}N spin-label pairs is shown in Figure 9.

Equation (42) shows that the pertinent spin-lattice relaxation time is that of the observed species (W_{e2}), and that R_∞^{-1} is dependent on the concentration of the pumped species (N_I) but not that of the observed species. This has been verified experimentally (Yin *et al.*, 1987b). We also note that for ^{14}N:^{15}N spin-label pairs, where the ELDOR reduction is due to Heisenberg exchange only, $N_IK_x/2W_{e2}$ is the b'' appearing in the early theory and N_IK_x is the Heisenberg exchange frequency W_x.

The frequency difference ($\Delta\nu = \nu_{\text{pump}} - \nu_{\text{observe}}$) in Figure 8 is 26 MHz. Similar results may be obtained if the pumping and observing fields are reversed ($\Delta\nu = -26$ MHz), except that the ELDOR reductions occurs in the (^{15}N) $M_I = -\frac{1}{2}$ and (^{14}N) $M_I = 0$ lines due to respective saturation transfer from $M_I = 0$ and $M_I = +\frac{1}{2}$ resonances. Although in principle any two lines may be chosen as pumped and observed, this choice is generally governed by considerations of spectral resolution.

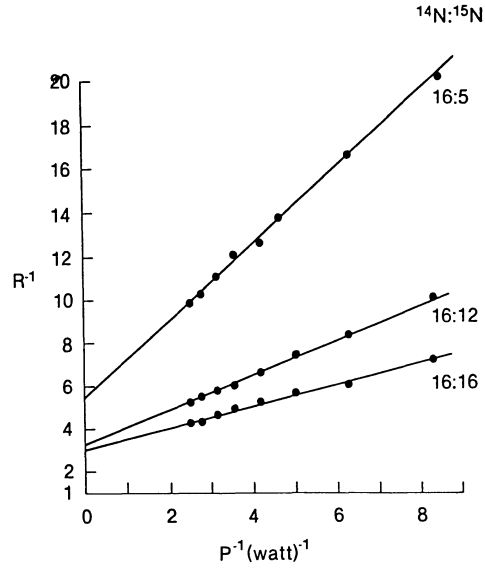

Figure 9. Determination of R_∞^{-1}. Plot of $1/R$ [see equation (40)] vs. the inverse of the measured pump power for 0.25:0.25 mol% [^{14}NC16:^{15}NC16], [^{14}NC16:^{15}NC12], and [^{14}NC16:^{14}NC5] in DMPC at 47 °C, pH 9.5. Each point represents the average of three scans. (From Feix *et al.*, 1984.)

5.2.2. Spectral Resolution

One of the foremost requirements for ELDOR utilizing ^{14}N:^{15}N spin-label pairs is the presence of spectral resolution. That is, one must find regions in the combined ^{14}N:^{15}N spectrum that allow one exclusively to pump one isotopic spin system and exclusively observe the other isotopic spin system. An example of this consideration is provided in Figure 10.

The top two spectra in each column of Figure 10 show superpositions of the spectra from three ^{15}N stearic acid spin labels with that of ^{14}NC16 in DMPC at 47 °C. For all three ^{14}N:^{15}N pairs in Figure 10, the ^{14}N $M_I = 0$ line and at least some part of the low-field ^{15}N ($M_I = -\frac{1}{2}$) manifold are resolved. Thus ELDOR studies of these pairs could be achieved by pumping the ^{15}N spin system in a part of the low-field region not overlapped by ^{14}N spin intensity, and observing reduction in the amplitude of the ^{14}N center line (Feix *et al.*, 1984). The low-field ($M_I = +1$) ^{14}N line amplitude was utilized for normalization.

Superposition spectra such as those shown in Figure 10 have proven quite helpful in deciding what frequency separation (pump-observe) is appropriate for a given ^{14}N:^{15}N spin-label pair. However, the resolution criterion to be met is that control spectra containing either the ^{14}N or ^{15}N spin label alone should give no observable ELDOR effects under the conditions of the dual-label experiment.

Similar resolution to that shown in Figure 10 was obtained when the three ^{15}N-Doxyl stearate positional isomers (C5, C12, and C16) were paired with ^{14}NC12. However, the resolution in the low-field region of the spectrum becomes less well-defined as rotational motion slows and lines broaden. Indeed, for the 12:12 and 12:16 pairs the separation of pumping and observing microwave field was decreased to 24 MHz (from the usual 26-28 MHz) to avoid saturating the low-field ^{14}N line.

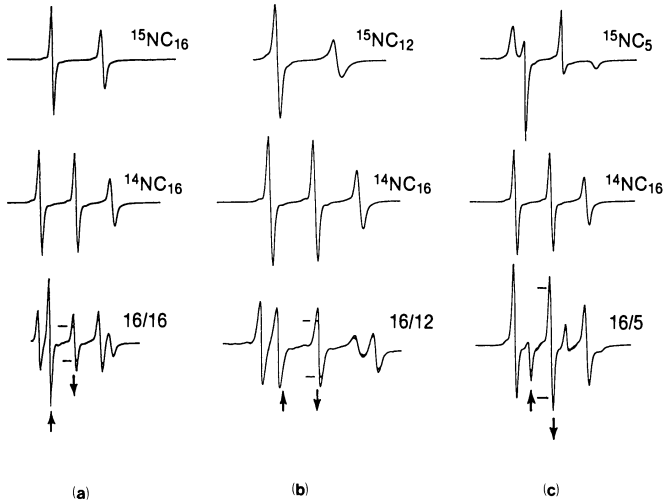

Figure 10. Spectra of (a) ^{15}NC16, (b) ^{15}NC12, and (c) ^{15}NC5 (each at 0.25 mol%) paired with 0.25 mol% ^{14}NC16 in DMPC liposomes equilibrated with 0.1 M sodium borate, pH 9.5. All spectra were recorded at 47 °C. Arrows indicated the relative position of the pump power (↑) and observer (↓) fields employed in ELDOR experiments. Spectra are aligned for comparison. Bottom row shows superimposed spectra taken with the pump field off and at 400 mW incident power, demonstrating the ELDOR effect. Horizontal lines denote reductions in the peak-to-peak amplitude of the $M_I = 0$ transition in the spectra obtained at 400 mW pump power. (From Feix *et al.*, 1984.)

The problem of spectral overlap has precluded studies to date with ^{14}NC5. The moderately immobilized spectrum of this spin label has spectral intensity throughout both low- and high-field wings, and thus overlaps the ^{15}N spectrum regardless of the motional properties of the latter probe (e.g., Figure 11). Similar considerations have prevented studies with the androstane and cholestane spin labels below the lipid gel

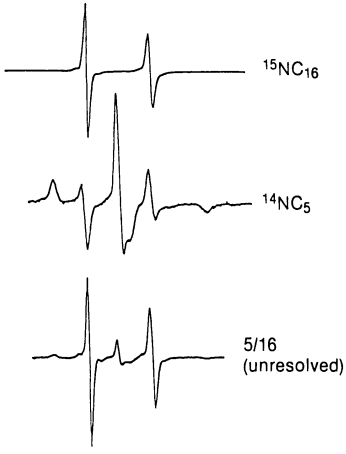

Figure 11. Superposition spectra demonstrating lack of spectral resolution for [^{14}NC5:^{15}NC16] (0.25:0.25 mol%) in DMPC (47 °C, pH 9.5). Both components of the ^{15}N spectrum overlap with the $T_\perp$ features of ^{14}NC5. (From Feix *et al.*, 1984.)

to liquid crystalline phase transition where the spectra of the stearic acid probes are markedly broadened.

Thus, in general, spectral resolution is achieved whenever the motion of the ^{14}N spin label is fast (rotational correlation time 10^{-9} s or less). If the ^{14}N spin-label motion is in the intermediate range (10^{-9}-10^{-8} s) resolution is best with ^{15}N probes whose motion approaches the rigid limit (for which the low-field $T_\perp$ turning point is well-resolved), and less good when the ^{15}N motion is in the intermediate-fast range. Resolution is not achieved when the ^{14}N spin-label motion is in the slow to very slow range (correlation times greater than 5×10^{-7} s). In spite of the above restrictions, spectral resolution is achieved for a wide variety of spin-label pairs and can usually be attained by judicious choice of which member of the pairs is labeled with ^{15}N.

The considerations in this section concerning spectral overlap apply to cw ELDOR. Yin *et al.* (1988) have proposed a general solution to the overlap problem using time-resolved techniques. Overlap cannot affect the time constants obtained in a saturation-recovery experiment; only the prefactors are altered. As we have seen, the time constants contain the same information that is present in the cw ELDOR experiment. These authors used ^{14}N and ^{15}N tagged cholestane spin labels present simultaneously in multilamellar liposomal dispersions of DMPC and obtained values of the diffusion constant of cholestane (and presumably of cholesterol) of $D = 1.7 \times 10^{-8}$ cm^2 s^{-1} at 27 °C and 2.7×10^{-8} cm^2 s^{-1} at 37 °C.

5.2.3. Interactions of ^{14}N:^{15}N Spin-Label Pairs

ELDOR reductions (extrapolated to infinite pumping power) for the spectrally resolved ^{14}N:^{15}N stearic acid spin-label pairs are given in Table 3. The magnitude of the reduction for the various pairs parallels their proximity along the stearic acid alkyl chain (i.e., 16:16 = 12:12 > 16:12 = 12:16 ≫ 12:5 > 16:5), supporting the reliability of these methods in assessing intermolecular (probe-probe) interactions. No interaction is observed between these stearic acid spin labels and a nitroxide moiety attached to the head-group region of phosphatidylcholine.

Based on the interaction frequency of the 16:16 pair, Feix *et al.* (1984) calculated lateral diffusion constants that were in good agreement with those obtained by a variety of biophysical methods (Table 4). Agreement with Popp and Hyde (1982) was quite

TABLE 3
ELDOR Reductions for Stearic Acid Spin-Label Pairs, in Dimyristoylphosphatidylcholine[a]

	^{14}NC12	^{14}NC16
^{15}NC5	26.2%	18.4%
^{15}NC12	32.2%	30.8%
^{15}NC16	30.9%	32.7%

[a] ELDOR reductions (R_∞ values) for the respective ^{14}N:^{15}N pairs at 0.25:0.25 mol% in DMPC at 47 °C. Data from Feix *et al.*, 1984.

TABLE 4
Lipid Lateral Diffusion Constants

Membrane: Temperature	Method	D ($\times 10^8$ cm^2 s^{-1})
DMPC: 38 °C	FRAP	~9-11[a]
DMPC: 30 °C	FRAP	7.6[b]
DMPC: 26 °C	FRAP	4[a]
egg PC: 37 °C	FRAP	8[c]
egg PC: 37 °C	FRAP	~9-11[a]
POPC: 38 °C	FRAP	6-7[d]
DMPC: 35 °C	Pulse gradient NMR	5[e]
egg PC: 35 °C	Pulse gradient NMR	5[f]
POPC: 35 °C	Pulse gradient NMR	6[f]
DPPC: 52 °C	ESR spin-exchange	1.0[g]
DPC: 25 °C	ESR spin-exchange	1.8[h]
egg PC: 25 °C	ESR spin-exchange	7[i]
DMPC: 37 °C	ELDOR	4.6[j]
egg PC: 37 °C	ELDOR	4.4[j]
POPC: 37 °C	ELDOR	4.8[j]
murine RBC: 23 °C	FRAP	1.4[k]
human RBC: 37 °C	FRAP	2.1[l]
human RBC: 25 °C	FRAP	0.8[l]
human RBC: 37 °C	ELDOR	2.3[m]
platelets (fresh/stored): 37 °C	ELDOR	1.0/2.6[n]

[a] Derzko and Jacobson, 1975.
[b] Chang *et al.*, 1981.
[c] Wu *et al.*, 1977.
[d] Vaz *et al.*, 1985.
[e] Kuo and Wade, 1979.
[f] Lindblom *et al.*, 1981.
[g] Träuble and Sackmann, 1972.
[h] Devaux and McConnell, 1972.
[i] Devaux *et al.*, 1973.
[j] Feix *et al.*, 1987b.
[k] Koppel *et al.*, 1981.
[l] Bloom and Webb, 1983.
[m] Hyde *et al.*, 1985.
[n] Lai *et al.*, 1986.

good, and Feix *et al.* reported a value for D at 27 °C that was not accessible using ^{14}N spin labels alone. This clearly demonstrated the advantage of the dual-label approach in eliminating interference from intramolecular saturation-transfer methods. The 16:16 interaction frequency shows the relatively weak temperature dependence previously noted for lateral diffusion of lipid-analogue probes (Derzko and Jacobson, 1975; Wu *et al.*, 1977; Vaz *et al.*, 1985), further supporting the use of the 16:16 pair to determine lateral diffusion rates.

The observation of strong interaction for the 16:5 pair was of particular interest. This implied that the nitroxide moiety at C16, near the terminal methyl group of stearic acid, made rapid excursions to the region of the bilayer near the membrane surface occupied by the C5 spin label. Such "vertical fluctuations" require considerable flexibility on the part of the deeper probe. The ability of alkyl chains in lipid bilayers to undergo *cis-trans* isomerizations, particularly near the center of the bilayer, has long been known (Hubbell and McConnell, 1971; Seelig and Seelig, 1974; Schindler and Seelig, 1975; Yellin and Levin, 1977). However, the extent of such motion by stearic acid spin labels may not have been fully appreciated. Interaction of the 16:5 pair

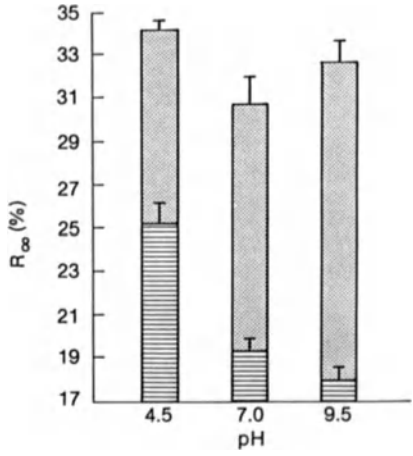

Figure 12. Variation in the ELDOR reduction (R_∞) as a function of pH for the 16:16 (dotted area) and 16:5 (lined area) spin-label pairs. All spin labels were at 0.25 mol%. Temperature was 47 °C. R_∞ values were obtained from intercepts of R^{-1} vs. P^{-1} plots (see Figure 9). Error bars indicate the magnitude of the standard deviation for the linear regression analysis.

displays a strong temperature dependence relative to that displayed by the 16:16 pair (Feix *et al.*, 1984), suggesting that observation of vertical fluctuations may provide a new means to examine the rotational mobility of stearic acid spin labels.

There is also a strong pH dependence for the 16:5 interaction that is not seen with the 16:16 pair (Figure 12). The enhancement of the 16:5 interaction at low pH is presumably due to protonation of stearic acid carboxyl moieties, allowing the C5 nitroxide to sink deeper into the membrane bilayer (Sanson *et al.*, 1976). The pH effects are far more pronounced in model lipid bilayers, where two-component spectra for the C5 spin label are readily demonstrated (Figure 13), than in biological membranes. For biological membranes, the buffering capacity of surface protein and carbohydrate

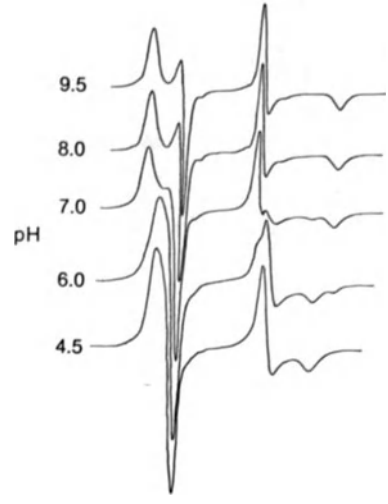

Figure 13. Variation of the ESR spectrum of ^{15}NC5 with pH. Samples containing 0.25 mol% ^{15}NC5 in DMPC were equilibrated with: (top to bottom) 0.1 M sodium borate, pH 9.5; 0.1 M sodium phosphate, pH 8.0; 0.1 M sodium phosphate, pH 7.0; 0.1 M sodium phosphate, pH 6.0; 0.1 M sodium acetate, pH 4.5. Conventional, first-harmonic absorption X-band spectra were recorded at 57 °C.

along with the structural effects of the extracellular matrix apparently dampen the influence of pH on the localization of stearic acid spin labels. Studies in model membranes are routinely conducted at pH 9.5, to ensure that the stearic acid carboxyl groups are in the ionized state.

5.2.4. Effects of Membrane Composition

The effects of specific changes in membrane lipid composition on lateral diffusion and vertical fluctuations of stearic acid spin labels have been examined using the dual-label ELDOR methodology. In particular, the effects of alkyl chain length and unsaturation and the influence of cholesterol have been studied. The 16:16 spin-label pair was used to measure lateral diffusion rates, while the 16:5 pair was utilized to report on vertical fluctuations.

Feix *et al.* (1987) examined the influence of host lipid alkyl chain length and unsaturation on lateral diffusion and vertical fluctuations. They studied the 16:16 and 16:5 interactions in model membranes composed of series of saturated phospholipids with varying alkyl chain length: dimyristoylphosphatidylcholine (DMPC), 14:0, 14:0; dipalmitoylphosphatidylcholine (DPPC), 16:0, 16:0; and distearoylphosphatidylcholine (DSPC), 18:0, 18:0. They also studied an α-saturated, β-unsaturated lipid, 1-palmitoyl-2-oleoylphosphatidylcholine (POPC), 16:0, 18:1; as well as egg yolk phosphatidylcholine (EYPC).

Lateral diffusion rates were found to be quite similar in the three saturated host lipids when compared at temperatures similarly removed from the main phase transition (i.e., corresponding temperatures on a reduced temperature scale). The 16:16 interaction was also similar in POPC, egg PC, and DMPC when compared under conditions where the rotational mobility of 16-doxylstearate was similar (with all systems at 37 °C). However, the value of D for the C16 spin label in POPC at the corresponding reduced temperature was less than half that observed in the saturated systems.

Vertical fluctuations were likewise only slightly affected by alkyl chain length in DMPC, DPPC, and DSPC, but were significantly reduced in EYPC and POPC (Feix *et al.*, 1987). At 37 °C, W_x for the 16:5 spin-label pair in the unsaturated systems was decreased relative to DMPC by approximately 30%. The decrease in 16:5 interaction in EYPC and POPC relative to DMPC was particularly striking in that it was observed under conditions where the conventional EPR parameters (i.e., rotational correlation time for C16, order parameter for C5) for the three systems are not different. This clearly demonstrates that dual-label ELDOR can provide information on spin-label motion beyond that given by conventional EPR.

Yin *et al.* (1987b) have examined the effects of cholesterol on lateral diffusion and vertical fluctuation. They again based estimates of D on W_x for the 16:16 pair, and W_x for the 16:5 spin-label pair was used as a monitor of vertical fluctuations.

Cholesterol was found to enhance 16:16 interaction, particularly in the 0–30 mol% range, in both DMPC and egg PC. Above 30 mol%, cholesterol diminished or had little effect on the 16:16 interaction. The effects of cholesterol were more pronounced in DMPC than in EYPC.

Cholesterol significantly diminished interaction of the 16:5 spin-label pair. Again, cholesterol effects were most prominent in the 0–30 mol% range, and the influence of cholesterol was again much stronger in DMPC than in EYPC.

The effects of cholesterol on the 16:5 interaction were particularly apparent when W_x for 16:5 was normalized to the 16:16 exchange frequency (Figure 14). This normalization procedure, introduced by Feix *et al.* (1987), takes into account the fact that the spin-label carrier molecules must come together for probe-probe interaction to occur—regardless of the relative positions of the nitroxide moieties along the alkyl chain. Such an approach provides a means to compare vertical fluctuation rates in systems where lateral diffusion constants differ. Figure 14 clearly indicates that the addition of cholesterol increasingly dampens the rate of vertical fluctuations in the 0–30 mol% range, above which additional cholesterol has little impact.

The concentration profile for cholesterol effects was suggestive of lateral phase separation. The data appear to support the presence of immiscible fluid phases below 30 mol% cholesterol, and a single phase at higher cholesterol content. This is in good agreement with cholesterol-phospholipid phase diagrams previously proposed by McConnell and co-workers (Reubenstein *et al.*, 1979; Recktenwald and McConnell, 1981), and by Presti and Chan (1982).

In summary (Table 5), neither lateral diffusion nor vertical fluctuations appear to be strongly influenced by lipid alkyl chain length. The presence of a *cis* double bond in the phospholipid sn-2 alkyl chain selectively diminished the 16:5 interaction, and seems to act as a barrier to vertical fluctuation of the C16 spin label. Cholesterol affects both lateral diffusion and vertical fluctuation of stearic acid spin labels. The enhancement of 16:16 interaction at cholesterol concentrations of 0–30 mol% may be due to lateral phase separation, enriching the effective probe concentration in a cholesterol-poor phase. Cholesterol markedly inhibits 16:5 interaction, most likely via steric

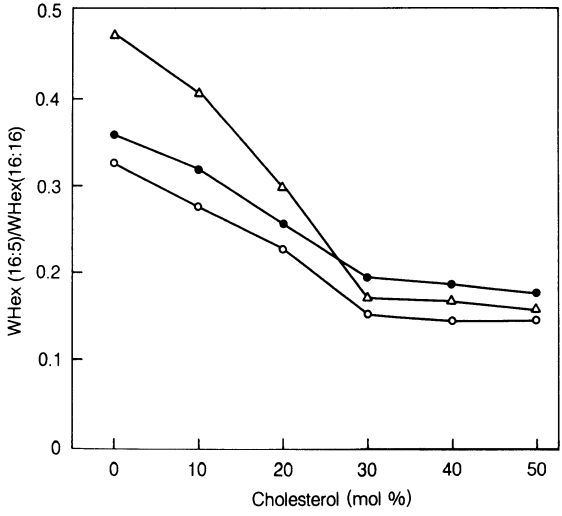

Figure 14. Relative probability of vertical fluctuation as a function of mole fraction of cholesterol. Shown are the Heisenberg exchange rates for the ^{14}NC16:^{15}NC5 pairs normalized to the ^{14}NC16:^{15}NC16 exchange frequency in (△) DMPC at 37 °C, (●) egg PC at 37 °C, (○) egg PC at 27 °C. The mole fraction of the pumped species was 0.5% for both spin-label pairs. (From Yin *et al.*, 1987b.)

TABLE 5
Exchange Frequencies as a Function of Host Lipid Composition[a]

	W_x16:5 (MHz)	W_x16:16 (HMz)
DMPC; 37 °C	0.162	0.396
DPPC; 55 °C	0.162	0.410
DSPC; 68 °C	0.153	0.432
POPC; 37 °C	0.116	0.414
egg PC; 37 °C	0.114	0.380
DMPC/chol (1:1); 37 °C	0.073	0.469
egg PC/chol (1:1); 37 °C	0.098	0.538

[a] All samples contained 0.5 mol% ^{14}N:0.5 mol% ^{15}N spin label and were equilibrated in 0.1 M sodium borate, pH 9.5. Data from Feix *et al.*, 1987 and Yin *et al.*, 1987b.

hindrance of C16 vertical fluctuation. The concentration profiles of cholesterol effects on vertical fluctuations are also suggestive of lateral phase separation.

5.3. ELDOR in Cells

Utilization of the loop-gap resonator (Section 4) has made possible ELDOR experiments on cells and native biological membranes. Such studies were previously precluded by inadequate signal intensity. Hyde *et al.* (1985) demonstrated the ability to perform ELDOR experiments on cells by examining interaction of the ^{14}NC16:^{15}NC16 spin-label pair in membranes of intact red blood cells (RBCs).

Interaction of the 16:16 spin-label pair in the membrane of intact RBCs was much weaker than in model membrane systems. Based on the 16:16 interaction in RBC at 37 °C, one can calculate using the Träuble and Sackmann model that $D = 2.3 \times 10^{-8}$ cm^2 s^{-1}—about half that observed in DMPC, egg PC, and POPC at the same temperature.

Lai *et al.* (1986) have used ^{14}N:^{15}N ELDOR to study lateral diffusion in the plasma membrane of intact platelets. Again based on the 16:16 interaction frequency, they calculated $D = 1.0 \times 10^{-8}$ cm^2 s^{-1} for fresh platelets at 37 °C. Lai *et al.* found that the 16:16 interaction was 2.6 times greater in platelets that had been stored under blood bank conditions for 72 hours. This was particularly interesting in light of the fact that rotational correlation times for ^{14}NC16 in fresh and stored platelets were not greatly different. This again illustrates that dual-label ELDOR is capable of delineating differences not observable by conventional EPR.

Platelets represented the practical limitation for ELDOR studies using the bimodal cavity. The 20-fold increase in SNR with the loop-gap resonator allowed these cells to be studied quite comfortably. As was noted by Hyde *et al.* (1985), the primary experimental limitation for ELDOR studies of lipid diffusion in cells is the amount of plasma membrane in the sample. Since the surface area/volume ratio decreases approximately as (cell radius)$^{-1}$, it should be possible to study cells with a 20-fold greater radius (20^3 greater volume) than platelets. While other technical difficulties (such as spin-label reduction in an oxygen-depleted atmosphere) must be considered for each given system, it would seem that the great majority of cell types are amenable to study by ELDOR.

5.4. Comparison with Spin-Exchange Line Broadening

The utilization of line broadening to determine D for lipid-analog spin labels has been well established for some time (Sackmann and Träuble, 1972a, 1972b; Träuble and Sackmann, 1972; Scandella *et al.*, 1972; Devaux and McConnell, 1972; Devaux *et al.*, 1973). Recently, the use of $^{14}N:^{15}N$ pairs in exchange-broadening experiments has been introduced (Seigneuret *et al.*, 1981; Davoust *et al.*, 1983a, 1983b). Here we wish to denote some of the fundamental differences between exchange broadening and the ELDOR approach.

Because exchange broadening is based on the first-derivative absorption EPR linewidth (governed by the transverse relaxation time, T_2) it is sensitive to collision frequencies comparable to T_2. For nitroxide spin labels, T_2 is generally on the order of 10^{-7} s, and exchange broadening has been reported to be sensitive to collision rates in the 0.1–10 MHz range (Davoust *et al.*, 1983a). On the other hand, sensitivity of the ELDOR method is based on the time scale of T_{1e} and is therefore in the 10^{-6} s range. Thus ELDOR is sensitive to collision frequencies as low as 0.01 MHz (i.e., within an order of magnitude for the particular T_1).

The contribution of dipolar effects in the exchange-broadening experiment will always be a concern. Although exchange contributions clearly dominate in the fast-motional regime (Devaux *et al.*, 1973; Davoust *et al.*, 1983a), dipolar effects are not eliminated.

Spin-label concentrations differ greatly in exchange-broadening and ELDOR experiments. For example, to measure lateral diffusion of lipid spin labels by exchange-broadening methods, spin-label concentrations in the range 2–10 mol% are required (Scandella *et al.*, 1972; Devaux *et al.*, 1973; Davoust *et al.*, 1983). ELDOR studies generally employ spin-label concentrations of 0.25–0.5 mol%. This is a direct result of the greater sensitivity of the ELDOR method (discussed above).

While spin-exchange linewidth enhancement is a viable and valuable EPR method for the study of probe–probe interactions, the ELDOR approach does provide a number of fundamental advantages. Utilization of the loop-gap resonator (which eliminates the need for a bimodal cavity) increases the accessibility of ELDOR instrumentation, and use of the loop-gap resonator along with employment of $^{14}N:^{15}N$ spin-label pairs have greatly expanded the range of applications amenable to study using ELDOR methodology.

5.5. Further Application of $^{14}N:^{15}N$ Methodology

There is a rich variety of biological studies still to be examined by application of the $^{14}N:^{15}N$ spin-label pair methodology. A few examples are listed below.

5.5.1. Lateral Phase Separation

Dual-label ELDOR is extremely well suited for the study of lipid lateral phase separations. Since the ELDOR method is sensitive to probe–probe interactions, rather than displacement over large (i.e., micron) distances, it is capable of detecting rapid lateral diffusion within regions of lateral phase separation. In this way one could observe the collision frequency of probes that partition into a "fluid-like" region in

the presence of more "gel-like" domains. Comparison with the diffusion coefficient in the absence of phase separation would allow determination of the effective mole fraction of the spin label in the fluid region, directly providing information on the size of the fluid domain. Another type of experiment would employ ^{14}N and ^{15}N probes, which putatively segregate into the different regions of a phase-separated system. The absence of or decrease in their interaction would then indicate the occurrence of a phase separation. Model systems amenable to such studies would include mixtures of saturated phospholipids having different alkyl chain lengths, mixtures of phospholipids having different head groups (e.g., choline/serine) which undergo phase separations in the presence of divalent cations, and cholesterol-phospholipid systems.

5.5.2. Phospholipid Spin Labels

Studies to date have primarily employed fatty acid spin labels due to their ready commercial and synthetic availability. There is no doubt that these studies would benefit from the employment of phospholipids spin labeled on one alkyl chain. The degree to which such phospholipid spin labels exhibit vertical fluctuations is in itself an interesting question. Phospholipid labels would also provide more reliable results in studies concerning lateral phase separation (discussed above). By nature, spin-labeling studies examine the motional properties of the probe molecules and use the results to make inferences regarding the system under study. Studies that employ stearic acid spin labels are valid in this respect (i.e., we have examined the degree to which various systems allow vertical fluctuations, not the degree to which phospholipids in these systems undergo such motion). However, utilization of phospholipid spin labels to infer motional properties of membrane phospholipids is clearly a step forward from the use of stearic acid spin labels.

5.5.3. Lipid–Protein Interactions

The dual-label ELDOR methodology lends itself well to the study of lipid-protein interactions. In such studies, spin labels of one isotope would be covalently bound to the protein surface and collisions observed with lipid-analog spin labels of the other isotope. Dual-label studies of this type which examined spin-exchange induced line broadening have already been reported (Seigneuret *et al.*, 1981; Davoust *et al.*, 1983b). ELDOR has distinct sensitivity advantages when compared with exchange broadening (see Section 5.4) and therefore should facilitate such studies.

5.5.4. Protein–Protein Interactions

Perhaps the most interesting, and almost certainly the most difficult, class of studies to which the ^{14}N:^{15}N ELDOR methodology might be applied is that of protein-protein interactions in model and biological membranes. Such studies could involve the labeling of only one type of protein with both ^{14}N and ^{15}N labels, or the ^{14}N and ^{15}N labels could be bound to different protein species. Such experiments could provide direct evidence for interaction of integral membrane protein components, and might prove extremely valuable in the investigation of cytoskeletal control mechanisms. The principle obstacle to such studies is the ability to label membrane protein components selectively

in situ. One approach to solving this problem is the use of monovalent antibody (Fab′) fragments carrying a single, covalently bound spin label. The nitroxide moiety of such spin-labeled Fab′ fragments is located at the end of the molecule distal from the antigen–antibody combining site (~80 Å), and is therefore accessible for collision with other spin probes. Binding characteristics of the native antibody are retained, conveying biological specificity on the immediate spin label. The preparation of spin-labeled monoclonal Fab′ directed at platelet membrane glycoproteins has been described (Kunicki *et al.*, 1986).

5.5.5. Ligand–Receptor Binding

A final class of studies yet to be explored involves the interaction of water-soluble spin probes with spin labels located at the membrane surface. Membrane-surface charge and composition, the precise localization of the membrane-associated spin label, and the charge, size, and hydrophobicity of the soluble probe are all variables that could be readily manipulated. Such studies model the interaction of soluble ligands with membrane receptors. Indeed, the interaction of a probe in three-dimensional space with a receptor confined to a two-dimensional surface is an intriguing problem in biophysics.

6. Future Opportunities

It is apparent that pulse techniques will be used increasingly in future years. The above-listed experiments may be addressed equally well with short-pulse saturation recovery and pulse ELDOR methods as with cw ELDOR, and indeed the former have certain advantages. The saturation recovery experiment has less stringent resolution requirements than ELDOR, requiring only a single position in the spectrum to be resolved. In cw experiments, the effects of a multiplicity of relaxation paths are overlapped and cannot be disentangled. The same processes in pulse experiments give rise to superimposed exponentials that can be deconvoluted using modern curve-fitting strategies. The advantages of cw ELDOR are (at present) a better SNR and more accessible instrumentation.

The theory of ELDOR shows that short-pulse saturation recovery and short-pulse ELDOR experiments contain identical information. However, the signs of the superimposed exponentials are not the same. It becomes apparent that both measurements would be useful, since the computer fits to both saturation-recovery and pulse ELDOR signals would require that the same time constants be used. At this writing, the authors have some confidence that triple exponentials can be deconvoluted reliably in a wide range of practical situations. However, the limitations for four and five superimposed exponentials remain unknown.

It is noted that apparatus could be built that would simultaneously acquire the pulse ELDOR and saturation-recovery signals.

This article has emphasized heavily the use of ^{14}N:^{15}N pairs. The range of questions, in which it is asked how often one labeled species encounters another, is large.

We have commented to a lesser extent on the use of ELDOR to study slow rotational diffusion. The authors and their colleagues, particularly L. R. Dalton, B.

Robinson, and D. D. Thomas, have been attempting for a number of years to develop strategies for studying anisotropic rotational motion of proteins on membranes. Success has been elusive. Possibly the short-pulse ELDOR and saturation-recovery techniques can eventually yield the additional information content that is required.

The step from two interacting spin systems (^{14}N and ^{15}N) to three interacting spin systems (^{14}N, ^{15}N, and X) need not be as complex and forbidding as one might think, particularly if X is molecular oxygen. One can easily introduce oxygen using the TPX gas-exchange method of Popp and Hyde (1981). For example, bimolecular collisions of O_2 with a ^{14}N labeled species might differ from those with a ^{15}N labeled species. And even as a trivial experimental control method, introduction of oxygen in a complicated multiexponential relaxation problem will change only the effective values of W_e (Yin and Hyde, 1987a) and not W_n and W_x.

ACKNOWLEDGMENT. Preparation of this article was assisted by grants GM22923 and RR01008.

REFERENCES

Bloom, J. A., and Webb, W. W., 1983, Lateral diffusibility in the intact erythrocyte membrane, *Biophys. J.* **42**:295-305.

Chang, C.-H., Takeuchi, H., Ito, T., Machida, K., and Ohnishi, S.-I., 1981, Lateral mobility of erythrocyte membrane proteins studied by the fluorescence photobleaching recovery technique, *J. Biochem.* **90**:997-1004.

Davoust, J., Seigneuret, M., Herve, P., and Devaux, P. F., 1983a, Collisions between nitrogen-14 and nitrogen-15 spin-labels. 1. Lipid-lipid interactions in model membranes, *Biochemistry* **22**:3137-3145.

Davoust, J., Seigneuret, M., Herve, P., and Devaux, P. F., 1983b, Collisions between nitrogen-14 and nitrogen-15 spin-labels. 2. Investigations on the specificity of the lipid environment of rhodopson, *Biochemistry* **22**:3146-3151.

Derzko, Z., and Jacobson, K., 1980, Comparative lateral diffusion of fluorescent lipid analogues in phospholipid multibilayers, *Biochemistry* **19**:6050-6057.

Devaux, P., and McConnell, H. M., 1972, Lateral diffusion in spin-labeled phosphatidylcholine multilayers, *J. Am. Chem. Soc.* **94**:4475-4481.

Devaux, P., Scandella, C. J., and McConnell, H. M., 1973, Spin-spin interactions between spin-labeled phospholipids incorporated into membranes, *J. Magn. Reson.* **9**:474-485.

Eastman, M. P., Bruno, G. V., and Freed, J. H., 1970, ESR studies of Heisenberg spin exchange. III. An ELDOR study, *J. Chem. Phys.* **52**:321-327.

Fajer, P., Thomas, D. D., Feix, J. B., and Hyde, J. S., 1986, Measurement of rotational molecular motion by time domain EPR, *Biophys. J.* **50**:1195-1202.

Feix, J. B., Popp, C. A., Venkataramu, D., Beth, A. H., Park, J. H., and Hyde, J. S., 1984, An electron-electron double resonance study of interactions between ^{14}N and ^{15}N stearic acid spin-label pairs: Lateral diffusion and vertical fluctuations in dimyristoylphosphatidylcholine, *Biochemistry* **23**:2293-2299.

Feix, J. B., Yin, J.-J., and Hyde, J. S., 1987, Interactions of ^{14}N:^{15}N stearic acid spin-label pairs: Effects of host lipid alkyl chain length and unsaturation, *Biochemistry* **26**:3850-3855.

Freed, J. H., 1972, in *Electron Spin Relaxation in Liquids* (L. T. Muus and P. W. Atkins, eds.), pp. 165-212, Plenum Press, New York.

Freed, J. H., 1974, Theory of saturation and double resonance in electron spin resonance spectra. VI. Saturation recovery, *J. Phys. Chem.* **78**:1155-1167.

Freed, J. H., 1979a, in *Multiple Electron Resonance Spectroscopy* (M. M. Dorio and J. H. Freed, eds.), pp. 73–142, Plenum Press, New York.

Freed, J. H., 1979b, Theory of ESR saturation recovery in liquids and related media, in *Time Domain Electron Spin Resonance* (L. Kevan and R. N. Schwartz, eds.), pp. 31–66, Wiley, New York.

Froncisz, W., and Hyde, J. S., 1982, The loop-gap resonator: A new microwave lumped circuit ESR sample structure, *J. Magn. Reson.* **47**:515–521.

Hubbell, W., and McConnell, H. M., 1971, Molecular motion in spin-labeled phospholipids and membranes, *J. Am. Chem. Soc.* **93**:314–326.

Hyde, J. S., 1979, Saturation-recovery methodology, in *Time Domain Electron Spin Resonance* (L. Kevan and R. N. Schwartz, eds.), pp. 1–30, Wiley, New York.

Hyde, J. S., and Dalton, L., 1972, Very slowly tumbling spin-labels: Adiabatic rapid-passage, *Chem. Phys. Lett.* **16**:568–572.

Hyde, J. S., and Thomas, D. D., 1973, New EPR methods for the study of very slow motion: application to spin-labeled hemoglobin, *Ann. N.Y. Acad. Sci.* **222**:680–691.

Hyde, J. S., Kispert, L. D., Sneed, R. C., and Chien, J. C. W., 1968a, Frequency swept electron-electron double resonance: Separation of overlapping spectra in irradiated malonic acid, *J. Chem. Phys.* **48**:3824–3825.

Hyde, J. S., Chien, J. C. W., and Freed, J. H., 1968b, Electron-electron double resonance of free radicals in solution, *J. Chem. Phys.* **48**:4211–4226.

Hyde, J. S., Smigel, S. D., Dalton, L. R., and Dalton, L. A., 1975, Molecular and applied modulation effects in electron-electron double resonance IV: Stationary ELDOR of very slowly tumbling spin labels, *J. Chem. Phys.* **62**:1655–1667.

Hyde, J. S., Froncisz, W., and Mottley, C., 1984, Pulsed ELDOR measurement of nitrogen T_1 in spin labels, *Chem. Phys. Lett.* **110**:621–625.

Hyde, J. S., Yin, J.-J., Froncisz, W., and Feix, J. B., 1985, Electron-electron double resonance (ELDOR) with a loop-gap resonator, *J. Magn. Reson.* **63**:142–150.

Kevan, L., and Kispert, L. D., 1976, *Electron Spin Double Resonance Spectroscopy*, Wiley, New York.

Kivelson, D., 1960, Theory of ESR linewidths of free radicals, *J. Chem. Phys.* **33**:1094–1106.

Koppel, D. E., Sheetz, M. P., and Schindler, M., 1981, Matrix control of protein diffusion in biological membranes, *Proc. Natl. Acad. Sci. U.S.A.* **78**:3576–3580.

Kunicki, T. J., Nugent, D. J., Piotrowicz, R. S., and Lai, C.-S. 1986, Covalent attachment of sulfhydryl-specific, electron spin resonance spin-labels to Fab′ fragments of murine monoclonal antibodies that recognize human platelet membrane glycoproteins. Development of membrane protein specific spin probes, *Biochemistry* **25**:4979–4983.

Kuo, A.-L., and Wade, C. G., 1979, Lipid lateral diffusion by pulsed nuclear magnetic resonance, *Biochemistry* **18**:2300–2308.

Kusumi, A., Subczynski, W. K., and Hyde, J. S., 1982, Oxygen transport parameter in membranes as deduced by saturation recovery measurements of spin-lattice relaxation times of spin labels, *Proc. Natl. Acad. Sci. U.S.A.* **79**:1854–1858.

Lai, C.-S., Wirt, M. D., Yin, J.-J., Froncisz, W., Feix, J. B., Kunicki, T. J., and Hyde, J. S., 1986, Lateral diffusion of lipid probes in the surface membrane of human platelets.—An electron-electron double resonance (ELDOR) study, *Biophys. J.* **50**:503–506.

Lindblom, G., Johansson, L. B. A., and Arvidson, G., 1981, Effect of cholesterol in membranes. Pulsed nuclear magnetic resonance measurements of lipid lateral diffusion, *Biochemistry* **20**:2204–2207.

Molin, Yu. N., Salikhov, K. M., and Zamaraev, K. I., 1980, *Spin Exchange*, Springer-Verlag, Berlin.

Nechtschein, M., and Hyde, J. S., 1970, Pulsed electron-electron double resonance in an $S = 1/2$, $I = 1/2$ system, *Phys. Rev. Lett.* **24**:672–674.

Percival, P. W., and Hyde, J. S., 1976, Saturation recovery measurements of the spin-lattice relaxation times of some nitroxides in solution, *J. Magn. Reson.* **23**:249–257.

Popp, C. A., and Hyde, J. S., 1981, Effects of oxygen on ESR spectra of nitroxide spin-label probes of model membranes, *J. Magn. Reson.* **43**:249-258.

Popp, C. A., and Hyde, J. S., 1982, Electron-electron double resonance and saturation recovery studies of nitroxide electron and nuclear spin-lattice relaxation times and Heisenberg exchange rates: Lateral diffusion in dimyristoyl phosphatidylcholine, *Proc. Natl. Acad. Sci. U.S.A.* **79**:2559-2563.

Presti, F. T., and Chan, S. I., 1982, Cholesterol-phospholipid interaction in membranes. 1. Cholestane spin-label studies of phase behavior of cholesterol-phospholipid liposomes, *Biochemistry* **21**:3821-3830.

Recktenwald, D. J., and McConnell, H. M., 1981, Phase equilibria in binary mixtures of phosphatidylcholine and cholesterol, *Biochemistry* **20**:4505-4510.

Reubenstein, J. L. R., Smith, B. A., and McConnell, H. M., 1979, Lateral diffusion in binary mixtures of cholesterol and phosphatidylcholines, *Proc. Natl. Acad. Sci. U.S.A.* **76**:15-18.

Sackmann, E., and Träuble, H., 1972a, Studies of the crystalline-liquid crystalline phase transition of lipid model membranes. I. Use of spin labels and optical probes as indicators of the phase transition, *J. Am. Chem. Soc.* **94**:4482-4491.

Sackmann, E., and Träuble, H., 1972b, Studies of the crystalline-liquid crystalline phase transition of lipid model membranes. II. Analysis of electron spin resonance spectra of steroid labels incorporated into lipid membranes, *J. Am. Chem. Soc.* **94**:4492-4498.

Sanson, A., Ptak, M., Rigand, J. L., and Gary-Bobo, C. M., 1976, An ESR study of the anchoring of spin-labeled stearic acid in lecithin multilayers, *Chem. Phys. Lipids* **17**:435-444.

Scandella, C. D., Devaux, P., and McConnell, H. M., 1972, Rapid lateral diffusion of phospholipids in rabbit sarcoplasmic reticulum, *Proc. Natl. Acad. Sci. U.S.A.* **69**:2056-2060.

Schindler, H., and Seelig, J., 1975, Deuterium order parameters in relation to thermodynamic properties of a phospholipid bilayer. A statistical mechanical interpretation, *Biochemistry* **14**:2283-2287.

Seelig, A., and Seelig, J., 1974, The dynamic structure of fatty acyl chains in a phospholipid bilayer measured by deuterium magnetic resonance, *Biochemistry* **13**:4839-4845.

Seigneuret, M., Davoust, J., Herve, P., and Devaux, P. F., 1981, Lipid-lipid and lipid-protein collision rates in membranes. Determination by evaluation of spin-spin interactions between ^{15}N and ^{14}N spin labels, *Biochimie* **63**:867-870.

Smigel, M., Dalton, L. R., Hyde, J. S., and Dalton, L. A., 1974, Investigation of very slowly tumbling spin labels by nonlinear spin response techniques: Theory and experiment for stationary electron-electron double resonance, *Proc. Natl. Acad. Sci. U.S.A.* **71**:1925-1929.

Stetter, E., Vieth, E.-H., and Hausser, K. H., 1976, ELDOR studies of nitroxide radicals: Discrimination between rotational and translational correlation times in liquids, *J. Magn. Reson.* **23**:493-504.

Subczynski, W. K., and Hyde, J. S., private communication.

Träuble, H., and Sackmann, E., 1972, Studies of the crystalline-liquid crystalline phase transition of lipid model membranes. III. Structure of a steroid-lecithin system below and above the lipid-phase transition, *J. Am. Chem. Soc.* **94**:4499-4510.

Vaz, W. L. C., Clegg, R. M., and Hallmann, D., 1985, Translational diffusion in lipids in liquid crystalline phase phosphatidylcholine multibilayers. A comparison of experiment with theory, *Biochemistry* **24**:781-786.

Wu, E.-S., Jacobson, K., and Papahadjopoulos, D., 1977, Lateral diffusion in phospholipid multibilayers measured by fluorescence recovery after photobleaching, *Biochemistry* **16**:3936-3941.

Yellin, N., and Levin, I. W., 1977, Hydrocarbon chain trans-gauche isomerization in phospholipid bilayer gel assemblies, *Biochemistry* **16**:642-647.

Yin, J.-J., and Hyde, J. S., 1987a, Spin-label saturation-recovery electron spin resonance measurements of oxygen transport in membranes, *Z. Phys. Chem. (Frankfurt Am. Main)* **153**:541-549, S.57-65.

Yin, J.-J., and Hyde, J. S., 1987b, Application of rate equations to ELDOR and saturation recovery experiments on $^{14}N:^{15}N$ spin label pairs, *J. Magn. Reson.* **74**:82–93.

Yin, J.-J., Pasenkiewicz-Gierula, M., and Hyde, J. S., 1987a, Lateral diffusion of lipids in membranes by pulse saturation recovery electron spin resonance, *Proc. Natl. Acad. Sci. U.S.A.* **84**:964–968.

Yin, J.-J., Feix, J. B., and Hyde, J. S., 1987b, The effects of cholesterol on lateral diffusion and vertical fluctuation in lipid bilayers. An electron–electron double resonance study, *Biophys. J.* **52**:1031–1038.

Yin, J.-J., Feix, J. B., and Hyde, J. S., 1988, Solution of the nitroxide spin-label spectral overlap problem using pulse electron spin resonance, *Biophys. J.* **53**:525–531.

7

Resolved Electron–Electron Spin–Spin Splittings in EPR Spectra

Gareth R. Eaton and Sandra S. Eaton

Interactions between unpaired electrons may be examined via a variety of physical techniques. Of particular interest in biological systems are the interactions observable by electron paramagnetic resonance (EPR) between various pairs or clusters of paramagnetic transition metals and/or organic free radicals. These paramagnetic centers may be natural components of the biological system or they may be species added as probes or labels. Interactions between these centers may affect the EPR spectra enough to invalidate the interpretations that would be valid in the absence of interaction. For example, if a paramagnetic metal is present, a spin-labeled biomolecule may yield an EPR spectrum that is not validly interpreted in terms of changes in the motion of the label. If, however, the effect of the metal on the nitroxyl EPR spectrum were understood in detail, additional information could be obtained from the EPR spectrum. An assessment was made several years ago of the effect of the dipolar interaction between a metal and a nitroxyl radical on the EPR line shape of the nitroxyl in a rigid matrix (Leigh, 1970). This approach has been used by many investigators to obtain metrical information on spin-labeled biomolecules. Others have studied the metal-organic radical interactions in vitamin B_{12}-dependent enzyme reactions also seeking metrical information (Pilbrow, 1982). Examples are considered in Section 10.

There is promise of achieving considerable insight into the metric and dynamic features of complicated systems, such as enzymes and membranes, by theoretical analysis and experimental calibration of the impact of interaction between unpaired electrons on EPR spectra and relaxation properties. Substantial confusion can result, however, if proper attention is not given to relevant features of the interaction regime. For example, one must consider relative motion of the two species, whether this motion is correlated or not, the nature of the interaction pathway, environmental effects such

Gareth R. Eaton • University of Denver, Denver, Colorado 80208. **Sandra S. Eaton** • University of Colorado at Denver, Denver, Colorado 80204.

as specific solvation, and potential nonstatistical effects such as specific ion pair or acid/base interactions. Consideration must also be given to relative values of the various characteristic times of the system, such as tumbling or collisional times, electron spin relaxation times, nuclear spin relaxation times, reciprocal of the microwave frequency, and modulation frequency. In some cases the electron-electron interaction can be observed in the line shape of the normal continuous wave (cw) EPR spectrum, and in other cases the interaction is observed only via a nonlinear technique (such as cw saturation studies) or time-domain (pulsed) EPR.

1. THE SCOPE OF ELECTRON SPIN–SPIN INTERACTIONS

Every EPR experiment involves electron-electron spin-spin interactions such as collisions in fluid solution or spin diffusion in solids. Frequently, these interactions are ignored. This chapter outlines the type of information that can be obtained from the subset of spin-spin interactions that yield additional lines in the EPR spectra.

In the general case for two nonequivalent unpaired spins, $g_1 \neq g_2$, the electrons couple differently to all nuclei in the system, and their relaxation times (T_1 and T_2) are different. Spins 1 and 2 could be on two dissimilar metal species, a metal and a free radical, or two dissimilar radicals. The types of electron-electron interaction studies that are of direct biological interest include the following cases:

1. Two paramagnetic centers fixed spatially relative to one another.
   a. Held close to one another with opportunity for through-bond interaction via a small number of bonds.
   b. Held close to one another spatially, but with no short through-bond pathway for interaction.
   c. Spatially fixed relative to one another but at larger distances.
2. Two paramagnetic centers not fixed spatially.
   a. Undergoing random collisional or proximity encounters due to diffusion in solution.
   b. Same, but with one of the paramagnetic centers attached to a surface.
   c. Undergoing nonrandom collisional or proximity encounters due to electrostatic or Lewis acid-Lewis base attractions between centers 1 and 2 or the environments of the centers.
   d. Same, but with one center attached to a surface.
   e. Similar, except in rigid (frozen) solution so that no translational motion is occurring.

Although spin-spin interaction is involved in both cases, the relative magnitudes of the characteristic times for the systems are different. In the first case, the motion of the two centers will in general be correlated and the lifetime of the spin-spin interaction will be long relative to other characteristic times of the molecule. In the second case the motion of the two centers will be correlated only during a brief encounter. The length of the encounter may be long or short relative to the molecular tumbling time, dependent on the size of the molecule, the solvent viscosity, and the temperature.

Case (2) was discussed by Hyde *et al.* (1979) and reflects the literature through late 1986. This review considers only case (1).

2. THE NATURE OF ELECTRON SPIN–SPIN INTERACTIONS

2.1. Dipolar Interaction

The general expression for the interaction energy between two point dipoles is given by the equation

$$W_{\text{dipolar}} = \frac{1}{r^3}\left[\boldsymbol{\mu}_1 \cdot \boldsymbol{\mu}_2 - \frac{3}{r^2}(\boldsymbol{\mu}_1 \cdot \mathbf{r})(\boldsymbol{\mu}_2 \cdot \mathbf{r})\right] \tag{1}$$

In this chapter scalars are represented by letters, vectors are represented by boldface letters, and matrices are represented by boldface sans serif letters. The Hamiltonian used to describe this interaction is determined by the g values and the relative orientations of the principal axes of the g matrices for the two interacting spins.

2.1.1. Isotropic g Values

The simplest case is for two spins with isotropic g values. Under these conditions the Hamiltonian becomes

$$\mathcal{H}_{\text{dipolar}} = D(2S_{1z}S_{2z} - S_{1x}S_{2x} - S_{1y}S_{2y}) = D(3S_{1z}S_{2z} - \mathbf{S}_1 \cdot \mathbf{S}_2) \tag{2}$$

where $D = -g_1 g_2 \beta^2 / r^3$, g_1 and g_2 are the isotropic g values for the two spins, β is the electron Bohr magneton, and r is the distance between the two spins. When the magnetic field makes an angle θ with the interspin vector $\mathbf{r}$, the dipolar interaction is given by the equation

$$\text{dipolar splitting} = g_1 g_2 \beta^2 (1 - 3\cos^2\theta)/r^3 \tag{3}$$

The dipolar splitting vanishes for $\theta = 54.7°$, which is called the "magic angle." It should be emphasized that this simple expression is valid only for isotropic g values.

2.1.2. Anisotropic g Values with Axes Aligned and the Interspin Vector Along the z Axis

Since the expressions for the dipolar interaction in the fully general case become quite complex, it is useful to examine a special case to see some of the changes that occur as a result of g anisotropy. If the two paramagnetic ions have anisotropic g values, but the principal axes of the g matrices are coincident for the two centers and the interspin vector is along the z axis, the Hamiltonian for the dipolar interaction is given by

$$\mathcal{H}_{\text{dipolar}} = -\frac{\beta^2}{r^3}(2g_{1z}g_{2z}S_{1z}S_{2z} - g_{1x}g_{2x}S_{1x}S_{2x} - g_{1y}g_{2y}S_{1y}S_{2y}) \tag{4}$$

Discussions of the dipolar interaction for this case are given in Abragam and Bleaney (1970, pp. 492–495) and Owen and Harris (1972). When the g values are isotropic, the sum of the diagonal elements in the matrix that describes the dipolar interaction is zero (i.e., the trace of the matrix is zero) and the interaction has axial symmetry with respect to the interspin vector. However, when the g values are anisotropic, the trace of the interaction matrix may be nonzero. One way to display the effects of g anisotropy on the dipolar interaction is to divide the Hamiltonian into three components; an isotropic part, an anisotropic part with axial symmetry, and an anisotropic part with rhombic symmetry, as given in the equation

$$\mathcal{H}_{\text{dipolar}} = -J_{\text{d}}\mathbf{S}_1 \cdot \mathbf{S}_2 + D_{\text{d}}(3S_{1z}S_{2z} - \mathbf{S}_1 \cdot \mathbf{S}_2) + E_{\text{d}}(S_{1x}S_{2x} - S_{1y}S_{2y}) \tag{5}$$

where

$$J_{\text{d}} = -(\beta^2/3r^3)(g_{1x}g_{2x} + g_{1y}g_{2y} - 2g_{1z}g_{2z})$$

$$D_{\text{d}} = (-\beta^2/3r^3)[2g_{1z}g_{2z} + 0.5(g_{1x}g_{2x} + g_{1y}g_{2y})]$$

$$E_{\text{d}} = (\beta^2/2r^3)(g_{1x}g_{2x} - g_{1y}g_{2y})$$

This form of the Hamiltonian emphasizes the analogy between the dipolar interaction of two paramagnetic centers and the zero-field splitting for a paramagnetic center with $S > \frac{1}{2}$. (Elimination of the term in J_{d} and replacement of subscripts 2 by 1 gives the zero-field splitting Hamiltonian; see Section 5.) For comparison with the exchange interaction discussed below [see equation (10)], the Hamiltonian for the dipolar interaction can also be expressed in the form

$$\mathcal{H}_{\text{dipolar}} = -J_{\text{d}}\mathbf{S}_1 \cdot \mathbf{S}_2 + \mathbf{S}_1 \cdot \mathbf{D} \cdot \mathbf{S}_2 \tag{6}$$

where the relationship between D and E and the components of traceless matrix $\mathbf{D}$ is given by

$$D = D_{zz} - 0.5(D_{xx} + D_{yy})$$

and

$$E = 0.5(D_{xx} - D_{yy})$$

The interaction matrix would have off-diagonal elements if expressed in other axis systems such as crystal axes or laboratory axes, but would remain symmetrical about the diagonal.

2.1.3. General Description of Dipolar Interaction

In the fully general case, the principal axes of the two g matrices are not aligned and the interspin vector can take any orientation with respect to the axes of the g matrices. Under these conditions the dipolar interaction has isotropic, anisotropic, and antisymmetric contributions and the elements of the dipolar interaction matrix are functions of the angles that describe the relative orientations as well as the g values. The description of this case is given in Boas *et al.* (1978).

Coffman and Buettner (1979b) have examined the "magic angle" effect for the case of anisotropic g values and shown that there is not a unique "magic angle." There is, however, a combination of angles, i.e., a point on the sphere, for which the dipolar splitting along the three principal axes goes to zero. The axis system is defined by the principal axes for the ion in the absence of interaction. They refer to that orientation as the "trimagic" angle. Sample calculations were shown as single-crystal spectra for particular orientations of the molecule in the magnetic field. These spectra might give the impression that the effects of dipolar interaction on the spectra could be negligible, even for short interspin distances, if the interspin vector were oriented at the "trimagic" angle. That is not the case as indicated by the following discussion. If the interspin distance is large, the dipolar interaction is small and does not contribute significantly to the anisotropy of the spectra. In this limit the turning points in the frozen solution spectra are determined by the g and A anisotropy and modified by the dipolar interaction. Under these conditions dipolar interaction at the "trimagic" angle would have negligible impact on the spectra. As the interspin distance is decreased (the dipolar interaction increases) the anisotropy of the dipolar interaction becomes comparable to the g and/or A anisotropy and the turning points in the powder spectra are functions of the value of r, even if the interspin vector is at the "trimagic" angle. At short interspin distances, the anisotropy of the dipolar interaction is the major contribution to the powder spectrum and determines the turning points. In this limit, the orientation of the interspin vector determines the magnitude of the nuclear hyperfine splitting along the principal axes of the dipolar interaction.

The importance of the "trimagic" angle can be summarized as follows. Spin–spin splitting along a set of principal axes can go to zero for a particular orientation of the interspin vector relative to those axes. If anisotropic splitting is not observed, the lower limit on the value of r is less than would be obtained if it was assumed that the interspin vector was along one of the principal axes. An accurate estimate of the lower limit can be obtained only by simulation of the powder spectrum. An example of the application of these principles is given in the discussion of the spin–spin splitting in the spectra of xanthine oxidase and related enzymes (Section 10.2).

2.2. Exchange Interaction

The exchange interaction is most simply illustrated for the case of two spin-$\frac{1}{2}$ species. Although in this chapter we apply the concepts specifically to electrons, the principles are general, and apply to any collection of spin-$\frac{1}{2}$ species, whether electrons, protons, fluorines, or muons. The energy level diagram for the two-electron case is familiar to everyone as the hydrogen molecule problem. At large distances there is essentially no interaction. As the electrons approach each other two energy levels are possible—the spin paired (antiparallel) (singlet) bonding level, and the spin unpaired (parallel) (triplet) antibonding level. The energy separation between the singlet and triplet levels is the exchange energy, J.

This simple heuristic model remains a valid basis for thinking about exchange even as we add some complications, such as anisotropic effects. The key fact to keep in mind is that exchange is due to overlap of orbitals. Some authors have chosen to make a distinction between exchange interaction due to direct overlap of orbitals and superexchange interaction due to interaction via orbitals of intervening atoms. We do

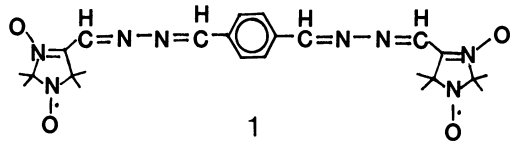

1

not find this distinction useful, since superexchange may also be regarded as overlap of delocalized orbitals. We will therefore use the term exchange to include what some authors describe as superexchange.

2.2.1. Isotropic Exchange

Most of the work on exchange interactions has focused on the isotropic contribution that is expressed in the equation

$$\mathcal{H}_{ex} = -J\mathbf{S}_1 \cdot \mathbf{S}_2 \tag{7}$$

Various authors use different coefficients in equation (7): $\pm J$ or $\pm 2J$. In this review all values of J will be reported using the form of the Hamiltonian with $-J$.

Kreilick and co-workers (Mao and Kreilick, 1976; McNally and Kreilick, 1981) have interpreted exchange in solid dinitroxyls and in copper(II) Tutton salts in terms of an exponential dependence of J on the interspin distance. Coffman and Buettner (1979a) proposed that the maximum absolute value of the exchange coupling constant for a distance r between two paramagnetic centers could be described by the limit function given by

$$J = 1.35 \times 10^7 \exp(-1.80r)\ \text{cm}^{-1} \tag{8}$$

The function was based on experimental data, primarily for values of r less than 8 Å. It was noted that there was need for more data for systems with interspin distances greater than 6 Å.

The following examples are given to show that this function does not adequately describe the long-range exchange interaction in systems with delocalized pathways for spin-spin interaction. Other exceptions to equation (8) have been cited (Francesconi *et al.*, 1981). The EPR spectra of dinitroxyls **1** and **2** were weakly temperature-dependent, which indicated that the exchange interaction was through the bonding pathway rather than due to close encounters of the two paramagnetic centers that arose from conformational flexibility. The values of J for **1** and **2** were $1.2 \times 10^{-2}\ \text{cm}^{-1}$ (Grigor'ev *et al.*, 1982) and $5.2 \times 10^{-4}\ \text{cm}^{-1}$ (Kokorin *et al.*, 1981), respectively. CPK molecular models indicate r values of about 17 Å for **1** and 20-22 Å for **2**. For these distances the limiting function gives $J = 7 \times 10^{-7}$ and $3 \times 10^{-9}\ \text{cm}^{-1}$, respectively. In the spin-labeled vanadyl complexes **3** and **4** the values of J were $0.17\ \text{cm}^{-1}$ (Sawant *et al.*, 1982) and $0.048\ \text{cm}^{-1}$ (More *et al.*, 1982b), respectively. CPK molecular models indicate $r = 12$-14 Å. At these distances the limit function gives $J = 5.6 \times 10^{-3}$ to $1.5 \times 10^{-4}\ \text{cm}^{-1}$, respectively.

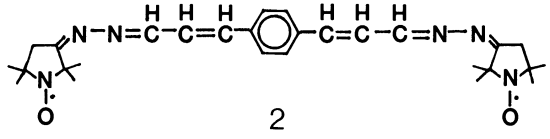

2

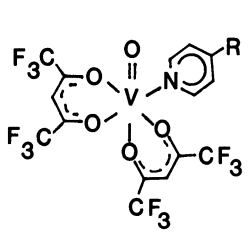

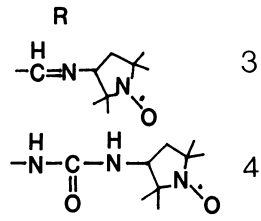

3

4

When spin-labeled Cu(II), Ag(II), and vanadyl porphyrins were studied in doped single crystals, several conformations of the molecules were observed (Damoder *et al.*, 1983a, 1983b, 1983c). There was no correlation between the values of J and r for different conformations of the same molecule. In examining the values of J it is therefore important to consider the nature of the bonds between the two paramagnetic centers and the conformation of the molecule, rather than simply looking at r. Studies of the factors that influence the value of J are discussed in Section 11.

About a decade ago it was firmly believed by many researchers that exchange would be significant over only a few angstroms. Since this continues to affect thinking in the field, it is worth examining the origin of this idea. Early ideas about exchange were formed by bulk magnetic susceptibility measurements. In these measurements, the exchange energy must be of roughly the order of kT to have a measureable effect on the force measurements. Exchange of the order of multiple cm^{-1} does involve rather short distances in the compounds known so far. Most of the current research in exchange interactions continues to use force methods, and hence is concerned with exchange energies large relative to those that are the primary concern of this chapter.

With respect to EPR studies of biological systems, exchange energies too small to be measured by force methods can dominate EPR spectra. Exchange is significant so long as it alters the spectrum, and the spectrum can be altered by exchange energies of the order of EPR linewidths. The recognition of exchange, and the utility of the spectral features caused by exchange, are central topics of this chapter.

2.2.2. Anisotropic Exchange

In systems with spin-orbit coupling, contributions from excited states are mixed into the ground-state wave function. This mixing results in deviations of the g values away from 2.0023 and causes an anisotropic contribution to the exchange interaction. This interaction has also been called "pseudodipolar exchange." The contribution to the Hamiltonian has the same form as the dipolar interaction, i.e., $\mathbf{S}_1 \cdot \mathbf{D}_{ex} \cdot \mathbf{S}_2$ where $\mathbf{D}_{ex}$ is a symmetric, traceless matrix. Moriya (1960) argued that the magnitude of the anisotropic exchange term was of the order of $(\Delta g)^2 J'$, where J' is the exchange coupling constant between the ground-state orbital on one center and the excited-state orbital on the second center. It is important to recognize that J' does not equal J, the interaction between the two ground-state orbitals. A detailed discussion of anisotropic exchange and values for metal dimers is given by Owen and Harris (1972).

The Florence group has examined anisotropic exchange in a series of copper dimers (Bencini *et al.*, 1984, 1985a, 1985b, 1985c, 1986). In all of the cases studied J was many cm^{-1}. The largest component of the anisotropic exchange matrix was found to be perpendicular to the interspin vector rather than parallel to the vector as expected

for dipolar interaction. In dihydroxy and dialkoxy bridged Cu(II) dimers, the anisotropic exchange decreased rapidly as a function of r for values of r between 2.8 and 3.4 Å (Bencini *et al.*, 1985b). The anisotropic exchange interaction was larger than the dipolar interaction for Cu(II) dimers with hydroxy and alkoxy bridges, comparable to the dipolar interaction in a complex with a diatomic bridge through two nitrogens of a triazole ring (Bencini *et al.*, 1985c), and much smaller than the dipolar interaction in oxalato and oxamato bridged dimers (Bencini *et al.*, 1984).

The smaller g anisotropy for vanadyl than for Cu(II) reflects the smaller spin-orbit coupling for vanadyl than for Cu(II). Ozarowski and Reinen (1986) found that for a pair of closely related dihydroxy-bridged vanadyl and Cu(II) dimers the anisotropic exchange interaction was much larger than the dipolar interaction for the Cu(II) dimer and comparable to the dipolar interaction for the vanadyl dimer. The relative importance of the anisotropic exchange interaction for the two metals is consistent with the relative magnitudes of the spin-orbit coupling.

These results suggest that anisotropic exchange interactions are most important when the bonding pathway between two paramagnetic centers is relatively short. However, general criteria have not been established to predict when anisotropic exchange will make significant contributions to spin-spin interaction. In favorable cases it may make significant contributions at longer spin-spin distances than heretofore expected.

2.2.3. Antisymmetric Exchange

Spin-orbit coupling can also cause an antisymmetric exchange contribution in systems that do not have a center of inversion (Moriya, 1960; Owen and Harris, 1972; Bencini and Gatteschi, 1982). Relatively little information is available concerning antisymmetric exchange and its effects are difficult to distinguish from those arising from the antisymmetric dipolar terms in systems with anisotropic g values. Although the general principles have been explicated, no unambiguous examples have been presented.

2.3. Hamiltonian for Spin–Spin Interaction

The discussion above indicates that both exchange and dipolar contributions to the spin-spin interaction can be described by the Hamiltonian

$$\mathcal{H} = \mathbf{S}_1 \cdot \mathbf{I} \cdot \mathbf{S}_2 \tag{9}$$

The interaction matrix $\mathbf{I}$ can be divided into three components—an isotropic term with coupling constant J, an antisymmetric term with interaction vector $\mathbf{d}$, and an anisotropic matrix with elements D_{ij} as indicated in expression (10).

$$\mathbf{I} = \begin{matrix} -J & 0 & 0 \\ 0 & -J & 0 \\ 0 & 0 & -J \end{matrix} + \begin{matrix} 0 & d_z & -d_y \\ -d_z & 0 & d_x \\ d_y & -d_x & 0 \end{matrix} + \begin{matrix} D_{xx} & D_{xy} & D_{xz} \\ D_{yx} & D_{yy} & D_{yz} \\ D_{zx} & D_{zy} & D_{zz} \end{matrix} \tag{10}$$

The contributions to the three terms can be summarized as follows:

J (scalar)—isotropic exchange (Section 2.2.1) + isotropic dipolar contribution that arises from g anisotropy (Section 2.1)

d (vector)—antisymmetric exchange (Section 2.2.3) + antisymmetric dipolar contribution that arises from g anisotropy (Section 2.1)

D (matrix)—anisotropic exchange (Section 2.2.2) + major portion of the dipolar interaction (Section 2.1)

The values of J, **d**, and **D** can, in principle, be obtained from the EPR spectra. In single-crystal studies of well-resolved spectra it should be possible to obtain all of the matrix elements. Studies of frozen solution spectra may yield only the dominant matrix elements. In either case, the assessment of the relative importance of the exchange and dipolar contributions to the matrix elements may require additional information, such as the geometry of the interaction. This ambiguity in the analysis of spin-spin interaction data has been discussed (Buettner and Coffman, 1977; Coffman and Buettner, 1979a).

Under certain circumstances it is reasonable to assume that particular terms dominate the spin-spin interaction, thereby simplifying the interpretation of the components of the interaction matrix.

If molecules are tumbling rapidly in fluid solution, the molecular motion averages out the antisymmetric and anisotropic contributions to the spin-spin splitting and the problem reduces to an analysis of the isotropic term, J. An estimate of the dipolar contribution to J due to g anisotropy can be obtained from equation (5) to ascertain its importance for a particular system. For example, for a spin-labeled copper complex the dipolar contribution to J is $J_d = 2.7 \times 10^{-4}\ \text{cm}^{-1}$ when $r = 8$ Å and $J_d = 0.8 \times 10^{-4}\ \text{cm}^{-1}$ when $r = 12$ Å. These values indicate that for many systems the isotropic contribution from the dipolar interaction is not likely to be a major factor. If the value of J in fluid solution is monitored as a function of temperature, extrapolation of J to the freezing point of the solvent gives an estimate of the value of J in frozen solution (More *et al.*, 1984). This can be a useful starting point for selection of the value of J in simulation of frozen solution spectra.

In rigid lattice spectra both exchange and dipolar contributions must be considered. Experimental data available to date suggest that rigid lattice EPR spectra can be divided into two categories, depending upon the value of J and the importance of spin-orbit coupling. When the value of J is less than the EPR quantum (about 0.3 cm^{-1} at X-band), and too small to be determined by magnetic susceptibility techniques, it is probable that anisotropic exchange has negligible impact on the EPR spectra. Anisotropic exchange is also likely to be negligible in systems with small spin-orbit coupling, which includes most organic radicals. In this limit r can be obtained from the anisotropic component of the interaction. The dipolar contribution to J can then be estimated using equation (5). When J is larger than the EPR quantum, the possibility of anisotropic exchange should be considered for systems with significant spin-orbit coupling. Estimates of plausible values of r may be required to put limits on the maximum dipolar contribution. Experimental uncertainty may prevent a clear identification of the various contributions, but upper and lower bounds may be possible. Unfortunately, relatively

few spin-orbit coupling values are well known, but the few values available at least serve as a guide to the potential importance of these effects. Some values are given in Abragam and Bleaney (1970, pp. 284, 347, 378, 391, 399, 474).

2.4. Computational Approaches

The basic physics of electron-electron spin-spin splitting in fluid solution EPR spectra is the same as for the familiar AB splittings due to nuclear-nuclear splittings in NMR. However, there are fundamental features of EPR spectra that require that a calculation be done differently than in NMR. (1) In NMR spectra the sweep width, for example 20 ppm, is typically a small fraction of the total magnetic field and so the separations between energy levels for the interacting spins can be assumed to be constant across the spectrum. In EPR spectra the sweep width for an experimental spectrum is often a significant fraction of the total magnetic field and therefore the energy separation $(g_1 - g_2)\beta H$ varies across the spectrum. As a result, the interaction matrix has to be reevaluated at the appropriate magnetic field for each transition. (2) In AB splittings calculated for NMR spectra, a single relaxation time or linewidth is usually used for all transitions. EPR linewidths are usually very different for metal ions and organic radicals and therefore calculations of spectra due to interaction of inequivalent spins usually require that different linewidths be associated with different transitions.

In many systems of interest there are nuclear spins that interact with the electron spin. For example, in the spectrum of a nitroxyl spin-labeled copper porphyrin it is necessary to consider the copper nuclear spin ($I = \frac{3}{2}$), the nuclear spins ($I = 1$) of the four porphyrin nitrogens that are coordinated to the copper, and the nitroxyl nitrogen nuclear spin as well as the two electron spins. The proton couplings usually are not resolved although, in principle, they could also be included in the calculation.

Most work on interacting spin systems has been conducted either in low-viscosity fluid solutions or in essentially rigid matrices such as frozen solution or very slowly tumbling biomolecules. Still to be explored are intermediate tumbling regimes, liquid crystals, and phase boundaries, including membrane surfaces.

From the perspective of the types of computations that are involved in interpreting EPR spectra, there are three distinct regimes to consider, distinguished by the rate of molecular motion involved:

1. Motional narrowing region (rapid isotropic tumbling).
2. Intermediate tumbling, anisotropic averaging.
3. Rigid lattice (doped single crystals and frozen solution or "powder" spectra).

Calculations of EPR spectra involving electron-electron spin-spin interaction have been done for regimes (1) and (3).

Many approaches to computer simulation of spectra appear in the literature. Selecting a calculation that will provide insight into the spectrum without requiring impractical computing time is still an art form. The compromises that must be made are changing rapidly as more powerful computational tools become available. The

biggest question confronting the experimenter is whether to use a perturbation calculation or a matrix diagonalization. The first step toward that decision is an analysis of which terms must be included in the Hamiltonian. Perturbation calculations work well if the axis system and basis set can be selected such that all of the off-diagonal matrix elements are small (Boas *et al.*, 1978). Thus, treatment of systems with nuclear hyperfine splitting by numerous nuclei can be treated readily with a perturbation calculation. Diagonalization of these large matrices would not be practical, and it would be especially time-consuming to repeat the diagonalizations as many times as needed to simulate powder EPR spectra. However, systems with large off-diagonal matrix elements, such as for large zero-field splittings, are not well suited for perturbation calculations. Perturbation calculations have been used widely for $S = \frac{1}{2}$, $S = \frac{1}{2}$ interactions and for systems with small zero-field splittings. Diagonalization methods have been used primarily for systems with no nuclear hyperfine coupling. Coffman has recently reported a study of a three-spin system by diagonalization (Coffman and Pezeshk, 1985).

In field-swept EPR spectra, the energy matrix changes continuously across the spectrum. Diagonalization for each value of the magnetic field is not yet practical. Several approaches to the problem have been developed. The most common procedure is to diagonalize at several values of the magnetic field and interpolate. In response to this problem, Belford developed the "frequency shift perturbation" method (Belford *et al.*, 1974; Scullane *et al.*, 1982). In this approach the Hamiltonian is divided into field-dependent and field-independent components. A perturbation treatment of the impact of the field-dependent portion of the Hamiltonian on the separation between a pair of energy levels is used to find the resonant fields at constant spectrometer operating frequency. Equations have been published to carry this treatment to fourth order (Belford *et al.*, 1974). A major advantage of this method is that it can handle systems with large zero-field splittings. In addition, simulation of a powder spectrum that the energy matrix be diagonalized only once for each orientation of the molecule in the magnetic field. Examples of spectra that have been analyzed by this technique are discussed in Sections 4–8.

In principle, diagonalization is preferable, but most diagonalization calculations that are practical today omit nuclear hyperfine couplings from the calculation. If nuclear–electron coupling causes either resolved splitting or observable broadening of the EPR lines, the "better" diagonalization calculation (but without hyperfine coupling) may provide less insight than a perturbation calculation that includes hyperfine coupling.

3. ANALOGIES BETWEEN NUCLEAR–NUCLEAR, ELECTRON–NUCLEAR, AND ELECTRON–ELECTRON SPIN–SPIN INTERACTIONS AND LONG-RANGE ELECTRON TRANSFER

Although the importance of weak exchange (J less than the EPR quantum) in EPR has been slow to be accepted, the analogous features in NMR are well-known. The spin-spin splitting that forms a basis for characterization of compounds by

high-resolution NMR spectroscopy of samples in the rapid tumbling limit is due to exchange interaction. Also well-known is the fact that the coupling constants (as the exchange energy is called in NMR) are dependent on solvent, temperature, and molecular conformation. Very long range proton-proton coupling (for example, a 0.4 Hz coupling through nine bonds) is well-documented (Harris, 1983). In some cases the exchange path is hard to identify, and there is debate, especially in fluorine NMR, about the extent to which coupling is "through space," i.e., that the orbital overlap is not along the path that we connect by lines in a localized bond picture of a molecule (Mallory *et al.*, 1985). However, even in this case, the discussion still concerns orbital overlap. The issue is which orbitals.

Since the electron magnetic moment is 658 times the proton magnetic moment, it is not surprising that electron-nuclear couplings are both larger than nuclear-nuclear couplings and occur over larger distances. The coupling between nuclear spins and electron spins is the basis of paramagnetic NMR (La Mar *et al.*, 1973). In a study of aliphatic chains attached to phenoxy radicals, proton hyperfine coupling constants of 0.02 to 0.05 G were observed through nine bonds (Kreilick, 1973). Since 1 G is approximately 2.8 MHz, these couplings correspond to about 50 to 140 kHz, which is much larger than observed for proton-proton couplings through nine bonds. Part of the increase in this case is due to the delocalization of the unpaired electron spin into the phenyl ring orbitals. Dixon (1972) noted the correlation between proton-proton coupling constants in aliphatic groups and proton-electron coupling constants in aliphatic radicals and emphasized the analogy between the orbital overlap mechanisms that determine these interactions.

This line of thinking leads logically to the major importance of isotropic electron-electron couplings in EPR. The effects of electron-electron spin-spin splitting on fluid solution EPR spectra were first analyzed for nitroxyl diradicals (Brière *et al.*, 1965; Glarum and Marshall, 1967). It was noted that as the value of J increased, the spectra changed from three-line patterns to complex multiplets to five-line patterns. The values of J were found to depend on the bonds between the two nitroxyls, solvent, and temperature. Shortly thereafter electron-electron spin-spin splitting was observed (Dunhill and Symons, 1968) and analyzed (James and Luckhurst, 1970) for vanadyl tartrate dimers in fluid solution. In 1972 Lowe *et al.* proposed that the doublet splitting of the Mo(V) EPR signal in xanthine oxidase in frozen solution was due to spin-spin interaction with a paramagnetic iron-sulfur cluster (Lowe *et al.*, 1972). In 1975 Schepler *et al.* invoked isotropic exchange between Co(II) and an organic radical to explain the "doublet" in the frozen solution EPR spectrum obtained for a vitamin B_{12}-dependent enzyme reaction (Schepler, 1975). In 1977 the first example of resolved splitting in fluid solution between nonequivalent unpaired electrons was reported for a spin-labeled copper complex (Boymel *et al.*, 1977).

The unifying principle for nuclear-nuclear, electron-nuclear, and electron-electron interaction is that the magnitude of the coupling is determined by the extent of orbital overlap, whether through space or through bonds. Orbital overlap also determines rates of long-range electron transfer. Recent studies have demonstrated electron transfer over distances of 12-20 Å (Mayo *et al.*, 1986) and about 25 Å (Peterson-Kennedy *et al.*, 1986). The nature of the spacer between the electron donor and acceptor sites influences the rate of electron transfer (Calcaterra *et al.*, 1983; Isied and Vassilian, 1984; Heitele and Michel-Beyerle, 1985). These several seemingly different areas of

study could be enriched by examination of the analogies between the factors that influence the various manifestations of long-range interaction.

4. SPIN-$\frac{1}{2}$–SPIN-$\frac{1}{2}$ INTERACTION

Most of the general principles of spin-spin interactions can best be illustrated by reference to the spin-$\frac{1}{2}$-spin-$\frac{1}{2}$ case. This is also the case that is easiest to observe experimentally. Thus, in this section substantial detail is given for the $\frac{1}{2}$–$\frac{1}{2}$ problem. In Sections 5–8 other spin systems are presented in less detail.

4.1. Spin–Spin Splitting

4.1.1. Fluid Solution

In this discussion of fluid solution spectra it is assumed that molecular tumbling is sufficiently fast to average anisotropic spin-spin interactions. Thus only the isotropic interaction can be observed. The estimates in Section 2.3 indicated that for most systems it is reasonable to assume that the isotropic contribution to the spin-spin interaction that arises from dipolar interaction between two spins with anisotropic g values is negligible and that the isotropic interaction can be attributed to isotropic exchange.

The following paragraphs outline a perturbation treatment of the spin-spin interaction for a copper(II) complex ($S = \frac{1}{2}$, $I = \frac{3}{2}$) without coordinated nitrogens interacting with a radical without nuclear spin. Details of the derivation and the additional terms that are required to include the spins of a nitroxyl nitrogen and of nitrogens coordinated to the copper are given by Eaton *et al.* (1978). Treatment of this many spins by diagonalization would be a formidable task. However, perturbation methods work well since the basis functions can be selected to make the exchange interaction terms block-diagonal.

The Hamiltonian for the system includes terms for the Zeeman interactions for copper and radical, the coupling between the copper nuclear spin and the copper unpaired electron, and the electron-electron spin-spin interaction with exchange coupling constant J, in Hz. If the magnetic field defines the z direction, then the Hamiltonian can be expressed in the form

$$H_{\text{fluid}} = g_1\beta H S_{1z} + g_2\beta H S_{2z} + hJ S_{1z}S_{2z} + \tfrac{1}{2}hJ(S_{1+}S_{2-} + S_{1-}S_{2+}) + hA_0 S_{1z}I_z + \tfrac{1}{2}hA_0(S_{1+}I_- + S_{1-}I_+) \tag{11}$$

where h is Planck's constant, I refers to the copper nuclear spin, g_1 and g_2 are the copper and nitroxyl g values, and A_0 is the isotropic coupling to the copper nuclear spin, in Hz.

The first five terms in the Hamiltonian can be treated exactly and the last is treated as a perturbation. Since electron spin transitions occur between energy levels that have the same copper nuclear spin, the secular determinant can be factored into four 4×4

blocks as shown in equation (12).

	$\lvert\alpha\alpha m_1\rangle$	$\lvert\alpha\beta m_1\rangle$	$\lvert\beta\alpha m_1\rangle$	$\lvert\beta\beta m_1\rangle$
$\langle\alpha\alpha m_1\rvert$	$\frac{1}{2}\beta H(g_1+g_2)$ $+\frac{1}{2}m_1hA_0$ $+\frac{1}{4}hJ-W$	0	0	0
$\langle\alpha\beta m_1\rvert$	0	$\frac{1}{2}\beta H(g_1-g_2)$ $+\frac{1}{2}m_1hA_0$ $-\frac{1}{4}hJ-W$	$\frac{1}{2}hJ$	0
$\langle\beta\alpha m_1\rvert$	0	$\frac{1}{2}hJ$	$-\frac{1}{2}\beta H(g_1-g_2)$ $-\frac{1}{2}m_1hA_0$ $-\frac{1}{4}hJ-W$	0
$\langle\beta\beta m_1\rvert$	0	0	0	$-\frac{1}{2}\beta H(g_1+g_2)$ $-\frac{1}{2}m_1hA_0$ $+\frac{1}{4}hJ-W$

(12)

Each block has a different, constant, value of the copper nuclear spin, m_1; α is used to represent the $+\frac{1}{2}$ spin for an electron, β is used to represent the $-\frac{1}{2}$ spin for an electron, and $\alpha\beta$ represents the basis function with the $+\frac{1}{2}$ electron spin state for copper (electron 1) and the $-\frac{1}{2}$ spin state for the radical (electron 2). Since the only off-diagonal elements occur as 2×2 blocks, analytical expressions for the energy levels can be obtained by use of the quadratic equation. The resulting equations for the energy levels, wave functions, transition energies, and transition probabilities at constant field are given by Eaton *et al.* (1978). The results are analogous to NMR AB splitting patterns. The relative intensities of the "inner" and "outer" lines are dependent on the ratio $J/2C$, where $C = 0.5*[((\beta H/h)(g_1-g_2)+A_0m_1)^2+J^2]^{1/2}$. The expressions can be manipulated to obtain the corresponding equations for constant frequency experiments. The final term in equation (11) is treated as a perturbation to second order. These results have been generalized to treat any metal nuclear spin (Sawant *et al.*, 1982). Since the exchange interaction is included in the zeroth terms, the solution is reliable for a wide range of values of J. The major limitation is that the denominator of the second-order corrections cannot become small and thus the perturbation treatment fails at low field and for J approximately equal to the observing field.

A sketch of the resulting energy level diagram for a particular value of the copper nuclear spin is shown in Figure 1. The diagram is drawn for antiferromagnetic interaction (singlet lower in energy than triplet) and J comparable to the energy separation between the copper and nitroxyl levels. That energy separation is due to the difference between g_1 and g_2 and the effect of the copper nuclear hyperfine splitting [energy separation equals $(g_1-g_2)\beta H + m_1hA_0$]. In this limit it is convenient to view the transitions as "copper" (lines 1 and 2) or "nitroxyl" (lines 3 and 4) although there is some mixing of the wave functions. The intensities of the "outer" lines (1 and 4) are less than the intensities of the "inner" lines (2 and 3). If notation is used that corresponds to the nature of the transitions in the limit of strong interaction, then the "outer" lines are singlet-triplet transitions or "forbidden" lines and the "inner" lines are triplet-triplet transitions or "allowed" lines. As the value of J increases the "inner" lines move together and the "outer" lines move away from the center of the spectrum and lose

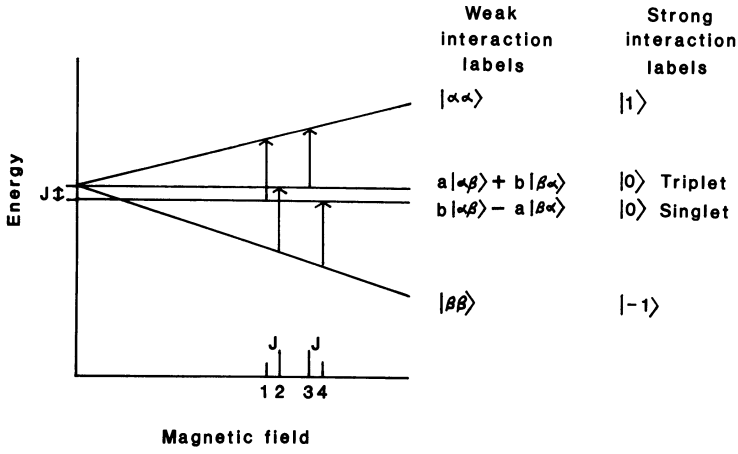

Figure 1. Sketch of the energy level diagram for two interacting $S = \frac{1}{2}$ centers in fluid solution for the case of antiferromagnetic interaction and J comparable to the energy separation due to g-value differences or nuclear hyperfine splitting. The diagram is drawn for $g_1 > g_2$. The coefficients a and b are determined by the ratio $J/2C$ (see text). The diagram is drawn for $a > b$. The assignments of the four lines in the spectrum are (1) "outer" line for electron 1, (2) "inner" line for electron 1, (3) "inner" line for electron 2, and (4) "outer" line for electron 2.

intensity. The separation between the nitroxyl "inner" line and the nitroxyl "outer" line is equal to J. The separation between the copper "inner" and "outer" lines is also equal to J. Thus, the value of J can be measured directly from the spectrum if the "outer" lines are observed. If the "outer" lines are not observed, but the positions of the "inner" lines for electrons 1 and 2 (transitions 2 and 3) do not coincide and the g values in the absence of interaction are known, the value of J can be estimated by simulation of the spectra. Since the peak positions are not dependent on the sign of J, the sign of J is not determined by analysis of the fluid solution spectra.

It is important to keep in mind that there is an AB pattern for each nuclear spin state of the copper. The energy separation between the copper and nitroxyl lines in the absence of interaction is different for each copper nuclear spin state. Thus each AB pattern has a different ratio of J to the energy separation and different relative intensities of the "inner" and "outer" lines. If additional nuclear spins are present such as a nitroxyl nitrogen nuclear spin or nitrogens coordinated to the copper, there is an AB pattern for every combination of nuclear spin states.

To illustrate the number of lines in a fluid solution EPR spectrum, consider a nitroxyl spin-labeled copper complex. Without the electron-electron exchange, the Cu(II) would have two four-line patterns due to electron nuclear coupling to the spin-$\frac{3}{2}$ Cu-63 and Cu-65 (8 lines). The nitroxyl radical would have a three-line pattern due to the spin-1 N-14. The copper-nitroxyl exchange interaction results in a four-line AB pattern or "doublet of doublets" for each of the 24 combinations of a copper nuclear spin state and a nitroxyl nuclear spin state (total of 96 lines). If the copper were coordinated to two nitrogens, there would be a total of 480 lines in the spectrum. Depending on the ratio of J to the nuclear hyperfine A_0 and to the g-value difference, the observed spectrum can take on many different splitting patterns. Indeed, it is

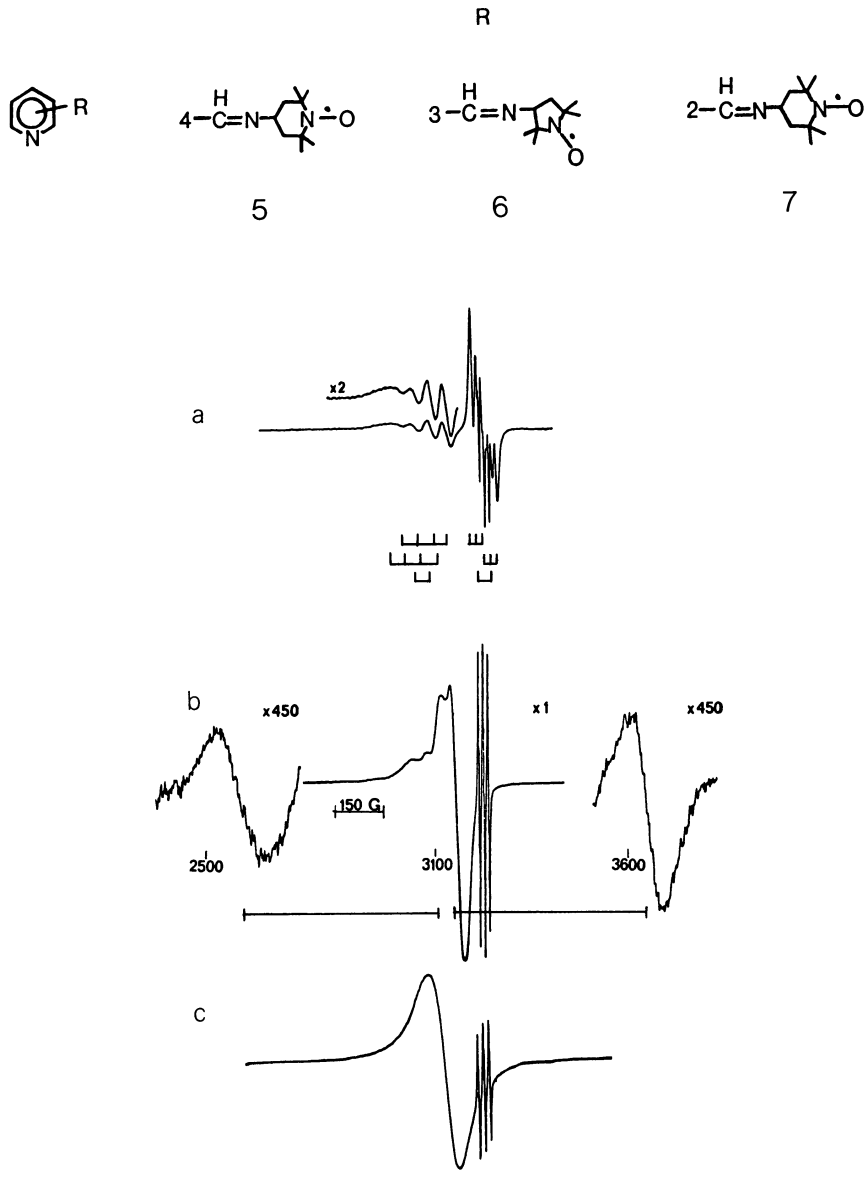

Figure 2. X-band EPR spectra of nitroxyl spin-labeled pyridines **5**–**7** coordinated to Cu(II) bis(hexafluoroacetylacetonate) in fluid solution at room temperature. (a) The value of J is comparable to the copper nuclear hyperfine splitting. The spectrum can be analyzed as a doublet of quartets for the copper lines and a doublet of triplets for the nitroxyl lines. (b) The value of J is about 10 times the copper nuclear hyperfine splitting. The "outer" lines were substantially weaker than the inner lines, but were observed at high gain and modulation amplitudes. (c) The value of J is much greater than the separation between the copper and nitroxyl energy levels and an averaged signal is observed.

important to recognize that a value of J less than the linewidth can give rise to merely a broadening of the lines.

Figure 2 shows spectra for spin-labeled pyridines **5**–**7** coordinated to copper(II) bis(hexafluoroacetylacetonate) that exemplify the effect of increasing spin–spin interaction on the EPR spectra. In Figure 2a the value of J is about the same as the copper nuclear hyperfine splitting. This magnitude of spin–spin interaction is small relative to the separation between the copper and nitroxyl energy levels, and so the lines in the spectrum can readily be identified as "copper" or "nitroxyl" transitions. The spectrum can be viewed as a doublet of quartets for the copper lines and a doublet of triplets for the nitroxyl lines. The intensities of the two nitroxyl triplets are significantly different as expected for an AB pattern. The value of J for the spectrum in Figure 2b is about 10 times the value of J for the spectrum in Figure 2a. The value of J for the spectrum in Figure 2b is sufficiently large that the intensities of the "outer" lines are greatly reduced compared to the intensities of the "inner" lines. For the AB patterns that arise from nitroxyl interaction with the highest-field copper-hyperfine line, J is large enough to make the "copper" and "nitroxyl" "inner" lines coincide. However, J is not large enough to cause the "copper" and "nitroxyl" "inner" lines to coincide for the AB patterns involving the lowest-field copper-hyperfine line. In Figure 2c the value of J is large enough that the "outer" lines are not observed and the "inner" lines are collapsed to a signal at the average g value. Although the copper hyperfine splitting is not resolved, simulation of the spectrum confirms that the hyperfine splitting is one-half that observed in the absence of spin–spin interaction.

The positions of the "outer" lines are more sensitive to changes in the value of J than the positions of the "inner" lines. Thus the value of J can be obtained more accurately if the "outer" lines are observed than if only the "inner" lines are examined. The contribution to the energy level separation from $(g_1 - g_2)$ is proportional to magnetic field strength. Since J is independent of field, the ratio of J to the energy separation decreases at higher field and the intensity of the "outer" lines increases. In complexes with relatively large values of J, detection of the "outer" lines is easier at Q-band (35 GHz) than at X-band (9.5 GHz) (Eaton *et al.*, 1980).

Values of J can thus be obtained in a straightforward fashion from fluid solution EPR spectra with resolved spin–spin splitting. Studies as a function of solvent, temperature, and compound provide valuable information concerning the dependence of the exchange interaction on the bonding pathway and on conformation. Such studies have provided much of the data upon which the discussion in Sections 9 and 11 is based.

4.1.2. Single Crystals

When spin–spin interaction is studied in a rigid medium, both isotropic and anisotropic contributions to the spin–spin interaction must be included in the analysis of the spectra. The Hamiltonian for the system can be described as

$$\mathcal{H} = \mathcal{H}_1 + \mathcal{H}_2 + \mathcal{H}_{\text{int}} \tag{13}$$

where $\mathcal{H}_1$ is the Hamiltonian for paramagnetic center 1 in the absence of spin–spin interaction, $\mathcal{H}_2$ is the Hamiltonian for paramagnetic center 2 in the absence of interaction, and $\mathcal{H}_{\text{int}}$ is the Hamiltonian for the electron–electron spin–spin interaction as described in Section 2. In general $\mathcal{H}_1$ and $\mathcal{H}_2$ include the Zeeman interactions with

anisotropic g values as well as anisotropic nuclear hyperfine interaction. In the rigid lattice spectra (either single crystals or powders), the axes of quantization for the two paramagnetic centers generally do not coincide. This causes off-diagonal elements in the energy matrix that are proportional to J in addition to those in the 2×2 blocks along the diagonal that were found in the fluid solution calculations. The magnitude of these terms increases with increasing g anisotropy. Since these matrix elments are treated as perturbations, perturbation calculations become unreliable if these terms become too large. Thus, perturbation calculations have a more limited applicability in rigid lattice calculations than in fluid solution calculations.

When a sample is doped into a diamagnetic single crystal, the EPR spectra can be studied as a function of the orientation of the crystal in the magnetic field. Data are typically collected in three orthogonal planes at angular increments of 10 to 15°. To analyze the spectra it is necessary to simulate the spin-spin splitting and/or the full spectrum as a function of orientation. Although both the data collection and the data analysis are much more time-consuming than the studies in fluid solution, the information available from single-crystal studies is also much greater. If the spectra are well resolved, it is possible to fully define the anisotropic interaction matrices (g, A, and spin-spin interaction) and the relative orientations of the axes for these interactions. By definition, the isotropic term is independent of orientation so its contribution to the spin-spin interaction can be separated readily from the orientation-dependent terms. The signs of the dipolar interaction terms along the three principal axes are known. Therefore, the sign of J is defined by whether it reinforces or cancels the dipolar terms.

Single-crystal data have been obtained for spin-labeled copper(II), silver(II), and vanadyl porphyrins doped into a zinc porphyrin host (Damoder *et al.*, 1983a, 1983b, 1983c). Analysis of the spectra indicated the presence of multiple conformations of the molecules. Although the data provide interesting insights into the variations in spin-spin interaction for the same molecule in different conformations, they also raise questions concerning the impact of the host lattice on single-crystal EPR studies. Interaction with the host lattice may force conformations of the molecules that are not present under other conditions.

4.1.3. Powders and Frozen Solutions

In a powder or frozen solution sample there is a random distribution of molecular orientations with respect to the magnetic field. Thus the spectra of these samples are the superposition of all possible single-crystal spectra. In principle these spectra contain the same information as the single-crystal spectra, but due to the overlap of the spectra it is usually not possible to unambiguously extract all of the information. The Hamiltonian is the same as discussed in Section 4.1.2. Simulation of the spectra requires summation of spectra for a distribution of orientations of the molecule in the magnetic field.

In many systems it is possible to obtain estimates of the anisotropic g and A values for the two paramagnetic centers in the absence of interaction. In small molecule studies, this frequently can be accomplished by synthesis of analogous compounds in which one paramagnetic center is replaced by a diamagnetic analog. In biological systems this sometimes can be done by controlled redox reactions such that only one

of the centers is in its paramagnetic form, or by examination of samples in which only one of the paramagnetic centers is present for some other reason. If reasonable estimates of these parameters are known, the unknowns for the analysis of the spectrum due to spin-spin interaction are the relative orientations of the g (and A) matrices for the two centers, the orientation of the interspin vector relative to the g (and A) matrix for one center, and the elements of the spin-spin interaction matrix. Under these conditions reasonable estimates for most (or all) of the unknown parameters generally can be obtained from well-resolved spectra at a single EPR frequency (Eaton *et al.*, 1983a). Spectra at additional frequencies are useful to confirm the analysis of the spectra. If the g and A values are not known, an unambiguous analysis of a spectrum obtained at a single frequency is unlikely. Even if spectra are obtained at several frequencies a complete determination of all of the unknowns is difficult. However, in many cases it is possible to obtain values of some of the unknowns and to put limits on possible values of the spin-spin interaction parameters.

The amount of information that can be obtained from the frozen solution spectra is strongly dependent on the resolution of features in the spectra. To define the anisotropy of the spin-spin interaction, and thereby estimate the relative importance of dipolar and exchange contributions, it is necessary to define the orientation dependence of the splitting. If the exchange interaction is of the same magnitude as the dipolar interaction and the spectra are well resolved, it is possible to determine the sign of J from the frozen solution spectra. If J is large relative to the g-value difference and the nuclear hyperfine splittings, the appearance of the spectra is independent of J and the value of J cannot be determined from the splitting of the signals. Most of the examples discussed in Section 10 are based on frozen solution data.

4.2. Half-Field Transitions

In general, the interaction between two unpaired electrons has both isotropic and anisotropic contributions, as discussed in Section 2. One challenge in interpreting the spectra in a rigid lattice is to separate the effects of these two terms. Exchange causes mixing of the spin functions for the two electrons. To first approximation the effect of exchange is to cause an energy separation between the singlet and triplet $m_s = 0$ energy levels. The anisotropic interaction (dipolar and anisotropic exchange) shifts the energy of the triplet $m_s = \pm 1$ levels relative to the triplet $m_s = 0$ level. The resulting energy level diagram is similar to that in Figure 1 (for fluid solution) except that the three triplet energy levels are not degenerate at zero magnetic field. This mixing of the wave functions by the anisotropic interaction also causes the transition probability of the normally "forbidden" transition between the $m_s = -1$ and $m_s = 1$ levels to be nonzero. Since this transition is a two-spin transition it occurs at half the magnetic field for transitions 1-4 (Figure 1) and is called the "half-field" transition. (The NMR analog, at constant magnetic field, is called a double quantum transition.) If anisotropic exchange is negligible and if $r > 5.0$ Å, the resonant field for the half-field transition is independent of the values of J and r. However, the ratio of the intensity of the half-field transition to the intensity of the allowed transitions is a function of r and independent of the value of J. Therefore the determination of the relative intensity of the half-field transition provides a method to separate the isotropic and anisotropic contributions to the spin-spin interaction (Eaton *et al.*, 1983b).

The relative intensity of the half-field transition can be determined by taking the ratio of the double integral of the half-field signal to the double integral of the allowed transitions as indicated in equation (14). The use of ratios of intensities for two portions of the spectrum of one sample eliminates the need for many of the correction factors that would otherwise be required for accurate intensity determinations (see Section 12). Since temperature changes have the same effect on the numerator and denominator of equation (14), the relative intensity is independent of temperature.

$$\text{Relative intensity} = \frac{\text{Intensity of half-field signal}}{\text{Total intensity of allowed transitions 1-4}} \tag{14}$$

For many years the half-field transition has been recognized as a characteristic of spin-spin interaction. Some people have gone so far as to say that the observation of a half-field signal "proved" the existence of a triplet. There is a serious error in this logic. Triplet molecules have half-field transitions, but the half-field transition is diagnostic of anisotropic spin-spin interactions in general, not just of molecular triplets. Dipolar interaction can be intermolecular as well as intramolecular. This means, for example, that one can observe half-field transitions in frozen solutions of monoradicals as has been demonstrated for a nitroxyl radical (Eaton *et al.*, 1983b).

When the spin-spin interaction is intramolecular, both the numerator and denominator of equation (14) are proportional to the concentration of the solution, so the ratio is independent of concentration. The number of molecules with short intermolecular interspin distances is dependent on the square of the concentration. Thus, the intensity of the half-field transition due to intermolecular interaction is dependent on the square of the concentration. The intensity of the allowed transitions (Figure 1, transitions 1 to 4) is still proportional to concentration. Therefore, the relative intensity of the half-field transition due to intermolecular interaction is proportional to concentration. The same conclusion can be obtained by using a shell model of the solute distribution and integrating the effect of spin-spin interaction over a distribution of values of r.

Since the intermolecular contribution is concentration-dependent and the intramolecular contribution is concentration-independent, the intramolecular component can be obtained by plotting the relative intensity of the half-field transition as a function of the concentration and extrapolating to infinite dilution. For molecules with short interspin distances in dilute solution, the contribution of the intermolecular interactions to the relative intensity of the half-field transition is negligible. For molecules with longer interspin distances, it is always necessary to extrapolate to infinite dilution to separate the inter- and intramolecular spin-spin interactions. The relative intensity of the half-field transition extrapolates to zero at infinite dilution for a monoradical. The relative intensity of the half-field transition extrapolates to a finite value characteristic of the interspin distance r for an intramolecular interaction. For large interspin distances, where the intensity of the half-field transition becomes small relative to the noise level, the intermolecular interactions become increasingly important contributors to the half-field intensity. Thus, extrapolation to infinite dilution becomes most important just as it becomes most difficult.

Two characteristics of the half-field transition make signal detection easier than might be expected on the basis of its relative intensity.

(1) The variation of the resonant field for the half-field transition as a function of the orientation of the molecule in the magnetic field is less than for the allowed transitions, so the total intensity of the half-field signal is spread over a relatively narrow range of magnetic fields. Large nuclear hyperfine splitting of the half-field transition spreads the intensity over a wider range of magnetic fields than for signals without nuclear hyperfine splitting and makes detection more difficult. Thus, for example, the ease of detection of the half-field signal for the same interspin distance decreases in the order organic diradical > copper dimer > vanadyl dimer.

(2) The microwave power saturation behavior of the half-field signal is markedly different from that of the allowed transitions. Since the half-field transitions have small transition probabilities, it is harder to perturb the relative populations of the energy levels involved in a transition than would be expected for an allowed transition. Therefore, it is possible to use much higher microwave powers for the forbidden transitions than for the allowed transitions.

Calculations for S-, X-, and Q-band indicate that the relative intensity of the half-field transition can be expressed as

$$\text{Relative intensity} = \frac{A(9.1)^2}{r^6 \nu^2} \tag{15}$$

where ν is the spectrometer operating frequency.

Perturbation calculations for $S_1 = \frac{1}{2}$, $S_2 = \frac{1}{2}$ systems with g values near 2 showed that the coefficient A in equation (15) was equal to 19.5 ± 0.5 (Eaton *et al.*, 1983b). Coffman and Pezeshk (1986) used matrix diagonalization and found $A = 19.5 + 10.9\Delta g$ where $\Delta g = |g_{max} - g_{min}|$ for organic radicals and copper complexes. They concluded that the anisotropic exchange contribution to the anisotropic interaction was negligible for interspin distances greater than 4-6 Å.

Equation (15) indicates an inverse square dependence on the spectrometer operating frequency. Thus it can be expected that at lower operating frequencies the relative intensity of the half-field transition will increase. There is some inherent loss of spectrometer sensitivity at lower frequencies, but the decrease in sensitivity is less than the increase in relative intensity of the half-field transition. In addition, use of the new loop-gap resonator structures provides a sensitivity at S-band almost as high as that obtained with standard cavities at X-band. Thus, it can be anticipated that as lower frequency spectrometers become more readily available, they will be useful in studies of the relative intensity of the half-field transition. The limiting feature will be the overlap of the hyperfine structure of the allowed transitions with the half-field transitions.

When r is less than about 4.5 Å, the splitting of the half-field transition is dominated by the anisotropy of the dipolar interaction. At larger values of r, the splitting of the half-field transition is dominated by nuclear hyperfine interactions. The transition probability for the half-field transition is minimum when the magnetic field is along the principal axes of the dipole tensor and maximum when the magnetic field is 45° away from the interspin vector. Thus, the molecules for which the magnetic field is away from the principal axes of the dipole tensor dominate the spectra, and it is the hyperfine interactions for these molecules that dominate the hyperfine pattern of the half-field transition in powder spectra.

For the allowed transitions, when J is small relative to the separation between the energy levels for the two interacting electrons, the nuclear hyperfine splitting is equal to that observed in the absence of interaction. When J is large relative to the energy separation, the nuclear hyperfine splitting is one-half of that observed in the absence of interaction. For intermediate values of J, the apparent values of the nuclear hyperfine splittings are intermediate between the values for the two extremes. In contrast to this behavior, the hyperfine splittings of the half-field transition are half the values for the noninteracting spin centers, regardless of the strength of the interaction. Because the splitting of the half-field signal (for $r > 4.5$ Å) is independent of the values of r and J, but the intensities depend on orientation, it is possible to obtain information concerning the orientation of the interspin vector relative to the hyperfine axes from the splitting of the half-field signal without complications from the values of r and J. The same orientation information is present in the allowed transitions, but to obtain that information by simulation of the allowed transitions it is necessary to vary the values of both r and J as well as the orientation parameters in seeking a fit to the experimental data (Eaton *et al.*, 1983b).

4.3. Geometrical Information

4.3.1. Distance Measurements

In most studies of spin–spin interaction, one goal is to determine the distance r between the two paramagnetic centers. Three methods have been used widely to obtain values of r.

(1) The position of the low-field edge of the half-field signal in a powder spectrum is given by (Thomson, 1968)

$$H_{\min}(\text{half-field}) = \frac{1}{2g\beta}[(h\nu)^2 - 4(\tfrac{1}{3}D^2 + E^2)]^{1/2} \tag{16}$$

where ν is the spectrometer operating frequency while D and E are the parameters that describe the anisotropic spin–spin interaction [see Section 2.1, equation (6)]. If it is assumed that E is negligible, then the shift between the low-field edge of the half-field signal [equation (16)] and that calculated from $h\nu/(2g\beta)$ is a measure of D. If it is assumed that D is due only to dipolar interaction with no contribution from anisotropic exchange, the value of D can be substituted into equation (17) or (18) to calculate a value of r:

$$D = 3g^2\beta^2/2r^3 \tag{17}$$

where D is in ergs and r is in cm;

$$D = 3g\beta/2r^3 = 1.39 \times 10^4(g/r^3) \tag{18}$$

for D in gauss and r in angstroms.

When r is greater than about 5 Å, the shift in the half-field signal away from $h\nu/(2g\beta)$ is negligibly small so the use of this method is limited to short interspin distances.

(2) The separation $2D$ between the low-field and high-field turning points in the $g \sim 2$ region of frozen glass or powder EPR spectra has been used to obtain r from equation (17) or (18) (Luckhurst, 1976). This method is limited to samples in which J is large relative to the energy separations between the levels for the two interacting spins or samples in which J is negligibly small. It also does not give accurate results when the dipolar interaction is of the same magnitude as the nuclear hyperfine splitting and the interspin vector does not coincide with a principal axis of the nuclear hyperfine interaction (Eaton and Eaton, 1982).

(3) Leigh (1970) proposed a method to obtain the distance between a rapidly relaxing paramagnetic center and a slowly relaxing radical. This technique does not apply to cases in which there is resolved electron-electron spin-spin splitting. A discussion of this method and examples of its applications are given in Eaton and Eaton (1987).

Three less widely used methods have been proposed for the determination of r, primarily in dinitroxyls. Russian workers have used peak height ratios in frozen glass spectra and changes in the second moments of frozen glass spectra to determine values of r in the range of 12 to 22 Å (Kokorin *et al.*, 1972; Kokorin and Formazyuk, 1981; Kulikov *et al.*, 1972). Michon *et al.* (1978) have used the temperature dependence of linewidths to estimate values of r. However, when J is of the same order of magnitude as the dipolar coupling, the splittings of the EPR transitions have contributions from both the exchange and dipolar terms. These methods use only the total splittings and do not provide a means to separate the two contributions to the electron-electron interaction.

A recent review states that metal-nitroxyl interactions depend on distance as r^{-6} and that nitroxyl-nitroxyl interactions depend on r^{-3} (Berliner, 1980). Lest this review confuse the novice, note that the $2D$ splitting in frozen solution spectra (including spectra of dinotroxyls) varies as r^{-3} but that the Leigh calculation of the effect of metal relaxation on nitroxyl EPR linewidth and the expression for the intensity of the half-field transition depends on distance as r^{-6}. The fundamental principle relevant to this matter is that observables that are due to second-order perturbations, such as intensity of forbidden transitions or changes in nitroxyl relaxation time, depend on r^{-6} because they involve products of r^{-3} terms. Consequently, the half-field transition intensities for metal-nitroxyl and for nitroxyl-nitroxyl interactions both depend on r^{-6}. Simple dipolar splittings calculated with equation (17) (a first-order expression), whether for nitroxyl-nitroxyl or metal-nitroxyl interaction, depend on r^{-3}.

As increasingly powerful computers become available for routine use, spectral simulation becomes feasible as a method of extracting distance information from rigid lattice EPR spectra if the spectra are sufficiently well resolved. Several examples of this approach are given in Section 10. The relative intensity of the half-field transition is a more reliable means of distance determination than is the shape of the $g = 2$ region. This method has been calibrated by comparison of values of r calculated from the intensity of the half-field transitions with values of r obtained by X-ray crystallography or from molecular models (Eaton *et al.*, 1983b). There are two major advantages to this method. (1) It separates the isotropic and anisotropic contributions even when the

two are of the same magnitude. (2) Simulation of the spectra is not required. Thus this approach can be used even when the spin-spin splittings are not resolved.

The use of dinitroxyl "strain gauges" proposed by Ferruti *et al.* (1970) was quickly discredited owing to a possible ambiguity of interpretation of the $g = 2$ spectrum (Luckhurst and Pedulli, 1970). Under sufficiently immobilized conditions the technique proposed by Ferruti *et al.* (1970) could be very accurate if the half-field signal were monitored.

The main caution that must be kept in mind when using the intensity of the half-field transition to measure interspin distances is the strong r-dependence. A small fraction of species with shorter distance will dominate the observation. For example, if there are two conformers differing in distance by small amounts, and with equal population, the apparent distances will be:

Distance 1 (Å)	Distance 2 (Å)	Apparent distance (Å)
4	10	4.5
6	8	6.6
6	Infinite	6.7
8	10	8.6

Even more dramatic is the case of, say, 10% at a distance of 5 Å and 90% at a distance of 10 Å. The apparent distance will be 7.2 Å.

To use any of the equations discussed in this section to determine the value of r from the EPR spectra of a two-spin system, it is necessary to assume that the anisotropic exchange is negligible. The extent to which this assumption is valid depends on both the magnitude of J and on the anisotropy of the g values as discussed in Section 2.3.

4.3.2. Angular Measurements

In addition to finding the distance between two paramagnetic centers, it is desirable to find the relative orientations of the magnetic axes for the two centers and the orientation of the interspin vectors relative to these axes. This information can be obtained by simulation of the spectra if there is sufficient g and/or A anisotropy to provide an internal definition of an axis system and if the spectra are well-resolved. An example for copper-copper dimers is given in the following section (4.3.3). Several additional examples of systems for which it has been possible to obtain orientation information are included in Section 10.

4.3.3. Example for Copper–copper Diporphyrins

EPR spectra were studied in frozen solution for six cofacial copper-copper diporphyrins with different organic linkages between the two porphyrins (Eaton *et al.*, 1985). The spectra in Figure 3 for one of these dimers, **8**, present an almost ideal case for comparison of methods for obtaining values of r. The copper-copper dipolar splitting

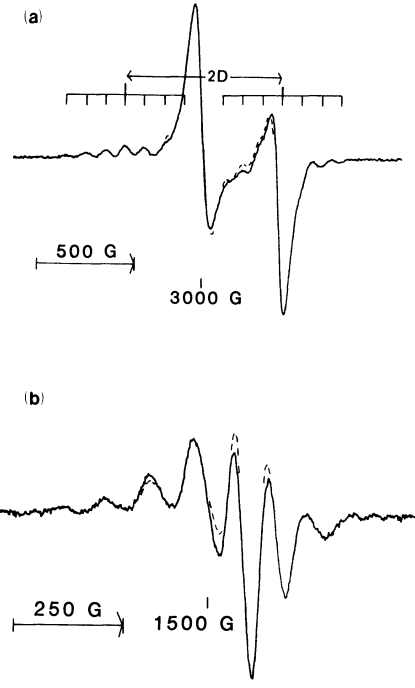

Figure 3. X-band EPR spectra of copper-copper porphyrin dimer **8** in frozen solution. (a) Allowed transitions 1-4 (Figure 1). (b) Half-field transition. The dashed lines in the figure indicate regions in which the simulated curve does not overlay the experimental line.

of both the copper parallel and perpendicular lines was well resolved. The value of $2D$ read from the splitting of the copper parallel lines (800 G) corresponds to $r = 4.2$ Å. Simulation of the spectrum in Figure 3a was obtained with $r = 4.15$ Å, $|J| > 0.5$ cm^{-1}, and ε (the angle between the interspin vector and the normal to the porphyrin plane) = 15°. The relative intensity of the half-field transitions corresponded to $r = 4.04$ Å. The hyperfine splitting by the two copper nuclear spins was well resolved in the half-field transition. The computer simulated half-field transition (Figure 3b) was

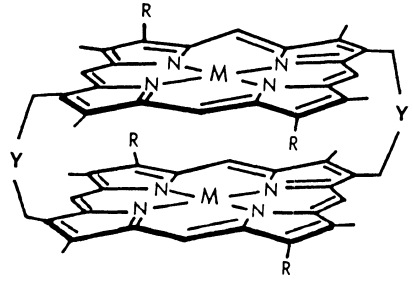

R= pentyl Y= H NC O

M= Cu

8

obtained with $\varepsilon = 15°$. Thus, there was good agreement between three methods of obtaining the value of r.

For some of the other copper-copper porphyrin dimers the allowed transitions were not well enough resolved to obtain a value of $2D$. The relative intensity of the half-field transitions, however, provided a measure of the copper-copper distance, and the line shape of the half-field transition provided, via computer simulation, the angle (ε) between the interspin vector and the normal to the porphyrin planes. The values of r and ε were used to calculate the distance between the parallel porphyrin planes. The interplanar separation was approximately constant at 3.9 Å. The exception to this observation was an anthracene pillared porphyrin for which the interplanar spacing was 4.5 Å.

The analysis of the EPR spectra showed that these attempts to vary the distance between the porphyrin planes by varying the length of spacer arms did not cause changes in the interplanar distances, except for a very rigid spacer. Instead there were changes in ε that reflect the slippage of one porphyrin plane relative to another such that the distance between the two copper ions varied while maintaining a nearly constant interplanar separation. This information could not have been obtained if only the values of r were measured. It was crucial to the understanding of the system to obtain the angular information as well as the distance information.

5. SPIN 1–SPIN $\frac{1}{2}$

Two factors that have not been discussed for the $S = \frac{1}{2}$ case must be considered in analyzing spin-spin interaction with an $S > \frac{1}{2}$ center.

The interaction between the two unpaired electrons of the $S = 1$ center results in zero-field splitting of the energy levels for that center. This requires inclusion of a term in the Hamiltonian, $\mathbf{S}_1 \cdot \mathbf{D}_1 \cdot \mathbf{S}_1$, where $\mathbf{D}_1$ is the zero-field splitting for the $S = 1$ center independent of the interaction with the second paramagentic center ($S = \frac{1}{2}$). This term can also be written as $D(3S_{1z}^2 - S_1^2) + E(S_{1x}^2 - S_{1y}^2)$. If the zero-field splitting is larger than the EPR quantum (about 0.3 cm^{-1} at X-band), EPR spectra are not observed for the $S = 1$ center. In this case information concerning the spin-spin interaction can be obtained only from changes in the EPR spectrum of the $S = \frac{1}{2}$ center, or, if the interaction is sufficiently strong, from magnetic susceptibility measurements. If the zero-field splitting is larger than about 0.02 to 0.03 cm^{-1}, diagonalization methods must be used to obtain the energy levels for the pair of interacting spins.

Rapid electron spin relaxation can cause collapse of electron spin-spin splitting, analogous to the familiar process of spin decoupling in NMR spectroscopy. Modulation of zero-field splitting or large g anisotropy provides a mechanism for electron spin relaxation, so the rate of electron spin relaxation typically is faster for centers with $S > \frac{1}{2}$ than for centers with $S = \frac{1}{2}$ and small to moderate g anisotropy. Therefore, the collapse of spin-spin splitting due to rapid electron spin relaxation is more likely to be a factor for an $S = \frac{1}{2}$ center interacting with an $S > \frac{1}{2}$ center than for an $S = \frac{1}{2}$ center interacting with a second $S = \frac{1}{2}$ center.

There are only a few examples in the EPR literature of splitting of the spectrum of an $S = \frac{1}{2}$ signal due to interaction with an $S = 1$ center. When Ni(II) was coordinated to spin-labeled xanthates, broadened and shifted nitroxyl signals were observed in

frozen solution at −180 °C (Smith *et al.*, 1984). In a spin-labeled EDTA complex of Ni(II), the linewidth of the nitroxyl signal in frozen solution was about 100 G (More *et al.*, 1986a). Since the shape of the signal did not change between 10 K and 90 K, the broad line must be due to unresolved splitting rather than partial collapse of the splitting due to rapid electron spin relaxation.

It is likely that in some Ni(II) complexes the electron spin relaxation rate is sufficiently fast that spectra at or near liquid helium temperatures may be required to observe resolved electron spin-spin splitting.

6. SPIN $\frac{3}{2}$–SPIN $\frac{1}{2}$

When there is an odd number (greater than 1) of unpaired electrons on a center (i.e., $S = \frac{3}{2}, \frac{5}{2}, \frac{7}{2}$), zero-field splitting makes the energy levels pairwise degenerate in the absence of an applied magnetic field. These pairs are known as Kramers's doublets. The energy separations between the pairs are dependent on the magnitude of the zero-field splitting. For example, for $S = \frac{3}{2}$, the $m_s = \pm\frac{1}{2}$ levels are degenerate and the $m_s = \pm\frac{3}{2}$ energy levels are degenerate. When a magnetic field is applied, the Zeeman interaction causes the energy levels within a pair to diverge. Since the separation between the $\pm\frac{1}{2}$ energy levels depends on the Zeeman interaction and not on the magnitude of the zero-field splitting, the transition between these two energy levels can be observed in the EPR spectra, independent of the magnitude of the zero-field splitting. Thus, unlike the situation for $S = 1$, the effects of spin-spin interaction can be monitored for both paramagnetic centers, even if the zero-field splitting is large.

Several examples have been obtained recently of resolved spin-spin splitting between Cr(III) ($S = \frac{3}{2}$) and nitroxyl radicals ($S = \frac{1}{2}$) (More *et al.*, 1986a, 1986b). In fluid solution the Cr(III) electron spin relaxation rate in a tetraphenylporphyrin complex was fast enough to collapse small splittings (J less than about 0.02 cm^{-1}) into broadened lines. For stronger spin-spin interaction resolved splitting was observed in fluid solution. In frozen solution resolved splittings were observed for values of J ranging from about 0.005 cm^{-1} to 0.27 cm^{-1} (More *et al.*, 1986b).

Studies of homonuclear and heteronuclear metal-metal dimers have shown that for spin-spin interaction that is large enough to measure by magnetic susceptibility, the magnitude of the electron-electron exchange interaction decreased as the number of unpaired electrons on the metal increased (Spiro *et al.*, 1981; O'Connor *et al.*, 1979). If the geometry of a metal-nitroxyl interaction is held constant and the electron-electron spin-spin interaction involves a single half-filled orbital on the metal, the value of the exchange coupling constant J is expected to be proportional to $1/n$ where n is the number of unpaired electrons on the metal (Hay *et al.*, 1975). The value of n cannot be varied experimentally without altering other properties of the metal that may also contribute to changes in the value of J. However, comparison of complexes with similar bonding pathways between the metal and a nitroxyl radical, but with different numbers of unpaired electrons on the metal, permits examination of the extent to which J is dependent on $1/n$.

Values of J were determined for a series of spin-labeled pyridines coordinated to Cr(III) tetraphenylporphyrin chloride (More *et al.*, 1986b). The zero-field splitting parameter D was 0.16 cm^{-1} in these complexes. The dependence of the value of J on

the position of attachment of the spin label to the pyridine confirmed that the dominant pathway for spin-spin interaction between the metal and the nitroxyl was by π-delocalization of the spin density on the metal into the pyridine orbitals. Earlier studies of the same spin-labeled pyridines bound to vanadyl bis(β-diketonates) had also shown that π-delocalization was dominant (More *et al.*, 1982b). The values of J for the chromium complexes were $\frac{1}{2}$ to $\frac{2}{3}$ of the values observed for the vanadyl complexes of the same ligands. If the only difference between the two series of complexes was the number of unpaired electrons on the metal, a factor of $\frac{1}{3}$ would have been expected. The lower oxidation state of the chromium(III) than of the vanadyl ion (+4) may cause a greater spin-delocalization of the chromium unpaired electrons than of the vanadyl electrons. Although this difference, and perhaps small differences in the geometries of the complex, are significant and cause some uncertainty in the factor by which J changes when the number of unpaired electrons is varied, it is important to show that patterns in the value of J for one metal are transferable to another metal ion, provided the mechanism of spin-delocalization remains constant.

7. SPIN $\frac{5}{2}$–SPIN $\frac{1}{2}$

The two common examples of $S = \frac{5}{2}$ are Mn(II) and high-spin Fe(III). Zero-field splittings for Mn(II) in some environments are small enough to be treated by perturbation techniques, but zero-field splittings for Fe(III) are frequently greater than the EPR quantum and have to be treated by diagonalization. These two cases are discussed in the following two sections.

7.1. Mn(II) Interacting With $S = \frac{1}{2}$

Mn(II) is of substantial interest because of its widespread occurrence in biological systems. Since Mn has a nuclear spin of $I = \frac{5}{2}$ in addition to the electron spin $S = \frac{5}{2}$, there are 36 energy levels for Mn(II) in the absence of interaction with a second paramagnetic center. Even if there were no nuclear spin on the $S = \frac{1}{2}$ center, the spin-spin interaction problem would be a 72×72 matrix. This is a formidable problem to treat by diagonalization. Fortunately Mn(II) commonly has relatively small zero-field splittings so the resulting off-diagonal terms are small enough to treat by perturbation methods. Analogous to the $S = \frac{1}{2}$ case, the major terms from the exchange interaction occur in 2×2 blocks along the diagonal of the energy matrix, which can be solved analytically. Thus, for at least some cases it is possible to analyze spectra without diagonalization of the full matrix.

7.1.1. Fluid Solution

For small molecules that are tumbling rapidly in fluid solution the problem is simpler than in frozen solution. The tumbling averages out the dipolar interaction so the spin-spin splitting is due to the exchange term. The zero-field splitting also is averaged out by the tumbling. Under these conditions the Mn(II) EPR spectrum appears to be a six-line pattern due to splitting by the nuclear spin. Each of these six lines is actually five nearly-degenerate transitions between different electron spin energy levels

($m_s = -\frac{5}{2}$ to $-\frac{3}{2}$, $-\frac{3}{2}$ to $-\frac{1}{2}$, $-\frac{1}{2}$ to $\frac{1}{2}$, $\frac{1}{2}$ to $\frac{3}{2}$, and $\frac{3}{2}$ to $\frac{5}{2}$). Since Mn(II) has g values close to 2, there is little g-value difference between Mn(II) and organic radical centers. However, the large nuclear hyperfine splitting causes substantial splittings between some of the Mn(II) energy levels and the energy levels for an organic radical.

In the limit of weak spin-spin interaction between Mn(II) and a nitroxyl radical, for each combination of a manganese nuclear spin state (there are six of these) and a nitroxyl nuclear spin state (there are three of these), each of the five lines of the manganese spectrum is split into a doublet, and the nitroxyl line is split into six equally spaced lines. There are 6×3 of these subspectra for a total of 288 lines. The ratio of the total intensity of the Mn(II) lines to the total intensity of the nitroxyl lines is 11.67 as in the absence of spin-spin interaction. For some of the manganese nuclear spin states the energy separation from the nitroxyl energy levels is so small that even a value of J of 0.001 cm^{-1} is sufficient to cause large mixing of the energy levels (More *et al.*, 1984b).

When J is large relative to the separations between the manganese and nitroxyl energy levels, it is convenient to describe the spectrum in terms of the total spin for the two paramagnetic centers. The calculated spectrum is a superposition of $S = 2$ (four closely-spaced lines) and $S = 3$ (six closely-spaced lines) contributions. The total intensity of the $S = 3$ transitions is 2.7 times the intensity of the $S = 2$ transitions. Transitions between the two spin states have negligible intensity. The nuclear hyperfine splittings for the $S = 2$ and $S = 3$ spectra are $\frac{7}{6}$ and $\frac{5}{6}$, respectively, of the nuclear hyperfine splitting in the absence of spin-spin interaction. Thus the strong exchange spectrum consists of two six-line patterns with different nuclear coupling constants and different intensities. For typical Mn(II) g values near 2.00 and A values near 0.0100 cm^{-1}, a J value of about 0.02 cm^{-1} is large enough to give a strong exchange spectrum (More *et al.*, 1984b).

The correlation between transitions in the weak and strong exchange limits is as follows. Within each weak exchange nitroxyl sextet, the line that is originally closest to the manganese lines moves toward the manganese lines as J increases and becomes one of the six $S = 3$ transitions in the strong interaction limit. The other five nitroxyl lines move away from the manganese lines and rapidly lose intensity as J increases. From each of the five manganese doublets the component that is closer to the nitroxyl lines moves toward the nitroxyl lines, and these become the other five lines for the $S = 3$ state. Four of the components of the five manganese doublets that are further from the nitroxyl lines become the four lines of the $S = 2$ state and the fifth line loses intensity in the strong interaction limit.

Examples of Mn(II)-nitroxyl spin-spin interaction in fluid solution have been obtained for spin-labeled pyridines bound to Mn(II) bis(hexafluoroacetylacetonate) (More *et al.*, 1984b). Due to the large number of transitions in the spectra it is not surprising that the spectra are not well-resolved. Some broadening of the nitroxyl signals may be due to the rate of relaxation of the Mn(II) electron spin. However, the spectra clearly show that the relaxation rate is not sufficiently fast to fully collapse the spin-spin interaction.

For two Mn(II) complexes of spin-labeled pyridines the values of J were sufficiently large to cause averaging of the Mn(II) and nitroxyl transitions (More *et al.*, 1984b). In these cases only the $S = 3$ transitions were observed. The linewidths of the $S = 2$ transitions were apparently too great to permit detection in the presence of the $S = 3$

transitions. The Mn(II) nuclear hyperfine splitting of the $S = 3$ transitions was $\frac{5}{6}$ of the hyperfine splitting observed in the absence of spin-spin interaction, as predicted. This small change in the splitting indicates that a strong-exchange spectrum could easily be mistaken for a noninteracting spectrum if the nuclear hyperfine splitting were not measured carefully.

7.1.2. Frozen Solution

In frozen solution the five Mn transitions ($m_s = -\frac{5}{2}$ to $-\frac{3}{2}$, $-\frac{3}{2}$ to $-\frac{1}{2}$, $-\frac{1}{2}$ to $\frac{1}{2}$, $\frac{1}{2}$ to $\frac{3}{2}$, and $\frac{3}{2}$ to $\frac{5}{2}$) occur at different magnetic fields, determined by the zero-field splitting. Each of these is split into six lines by the nuclear hyperfine interaction. Thus, spectra often appear as five groups of six lines each. The $-\frac{1}{2}$ to $\frac{1}{2}$ transitions are frequently sharper than the other lines in the spectrum and occur close to $g = 2$.

To analyze the Mn(II)-radical interactions, the zero-field splitting and anisotropic spin-spin interaction must be included, in addition to the terms that were included in fluid solution. The derivation of the equations for a perturbation treatment has been published (More *et al.*, 1985). Analogous to the situation in fluid solution, there are many lines in the spectrum for a single orientation of the molecule in the magnetic field. In addition, the lines are orientation-dependent due to the zero-field splitting and the anisotropic spin-spin interaction. In the limit of weak spin-spin interaction there are characteristic signals for the $S = \frac{1}{2}$ center. However, as the strength of the interaction increases, the intensity for that signal is spread over a wider range of magnetic fields. The intensity of the $S = \frac{1}{2}$ signal is only 1/11.67 times the intensity of the $S = \frac{5}{2}$ signal. In addition, the Mn(II) $m_s = -\frac{1}{2}$ to $\frac{1}{2}$ transitions are close to $g = 2$ in frozen solution, so some transitions are extensively averaged even for relatively weak spin-spin interaction.

The fluid solution spectra for the Mn(II) bis(hexafluoroacetylacetonate) complexes of spin-labeled pyridines **9** and **10** indicated that the exchange interaction was less than 0.0002 cm^{-1} (More *et al.*, 1985). The frozen solution spectra of the nitroxyl and Mn $m_s = -\frac{1}{2}$ to $+\frac{1}{2}$ lines are shown in Figure 4. The dotted lines show simulated spectra obtained for dipolar interaction with $r = 9.7$ Å (Figure 4a) and 9.0 Å (Figure 4b). Well-resolved splitting of a nitroxyl signal due to interaction with Mn(II) has also been observed for a spin-labeled EDTA complex with r about 8.5 Å and $J = 0.004$ cm^{-1} (More *et al.*, 1986a). In other cases the spectra were broad and did not show resolved features for the nitroxyl transitions (More *et al.*, 1985). These spectra probably reflect more extensive mixing of the transitions and are more difficult to interpret.

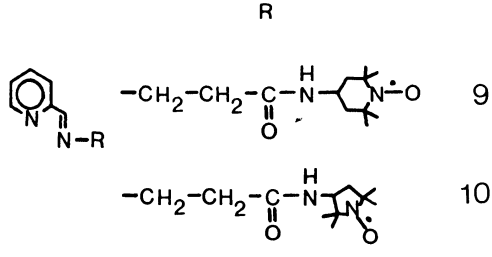

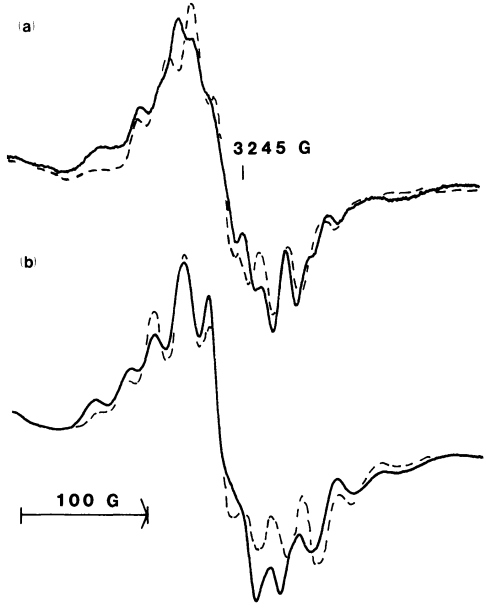

Figure 4. 400 G scans of the X-band (9.105 GHz) EPR spectra of spin-labeled pyridines **9** (a) and **10** (b) coordinated to Mn(II) bis(hexafluoroacetylacetonate) in toluene:acetone solution at −180 °C. These scans show the nitroxyl lines and the manganese $m_s = -\frac{1}{2}$ to $\frac{1}{2}$ transitions. The solid lines are the experimental curves. The dashed lines show the calculated spectra obtained for dipolar interaction between the paramagnetic centers. The simulations are discussed by More *et al.* (1985). (From More *et al.*, 1985.)

The observation of resolved splittings in the frozen solution spectra indicates that for these complexes at about −180 °C the manganese electron spin relaxation rate is not sufficiently fast to collapse the spin-spin splitting. This suggests that Mn(II) relaxation rates may be slower than assumed by some authors. The implications of this observation with respect to the use of Leigh's model (1970) for determining spin-spin distances between Mn(II) and radicals have been discussed (More *et al.*, 1985).

7.2. High-Spin Fe(III) Interacting with $S = \frac{1}{2}$

Zero-field splittings for high-spin Fe(III) typically are much larger than the EPR quantum which makes perturbation calculations unreliable. Fortunately, only about 2% of iron has a nuclear spin, so nuclear hyperfine splitting can be neglected. If nuclear hyperfine splitting of the $S = \frac{1}{2}$ center can be neglected, the energy matrix is 12×12 and diagonalization is a practical method for analyzing the EPR spectra.

Electron spin relaxation rates for iron(III) are relatively fast. One indication of this fact is the widespread use of paramagnetic NMR to study iron(III) complexes. Since the electron spin relaxation rate is dependent both on temperature and zero-field splitting, the ability to observe resolved spin-spin splitting due to interaction with iron(III) is strongly dependent on the environment of the iron(III) and on temperature.

In high-spin iron(III) complexes of spin-labeled porphyrins, the electron spin relaxation rate at room temperature in fluid solution is sufficiently fast to collapse small electron-electron spin-spin splittings. Stronger interaction causes broadening and shifting of the nitroxyl signals (Fielding *et al.*, 1987).

In an Fe(III) complex of a spin-labeled EDTA,, splitting of both the iron and nitroxyl signals was well-resolved at −180 °C (More *et al.*, 1986a). The spectra were

simulated with $r = 7.5$ Å and $|J| = 0.013$ cm^{-1}. However, in fluid solution the iron(III) electron spin relaxation was sufficiently fast to collapse the electron spin-spin splitting and a typical three-line nitroxyl signal was observed.

In high-spin iron(III) complexes of spin-labeled porphyrin **11**, resolved spin-spin splitting of the iron and nitroxyl signals was observed at 7 K (Figure 5e) (Fielding *et al.*, 1986b). The spectra include signals due to several species designated 1, 2, and 3. Species 1 has an electron-nitroxyl coupling constant J of about 0.04 cm^{-1}. The weak signals labeled 2 are due to small amounts of high-spin Fe(III) and nitroxyl impurities and/or a small amount of a conformation with very weak iron-nitroxyl interaction. The signals labeled 3 are due to one or more conformations with substantially stronger iron-nitroxyl interaction than was observed for 1. As the temperature was raised, the iron signal broadened due to the increasing rate of relaxation of the iron(III) unpaired electrons and the splitting of the nitroxyl signal for species 1 collapsed. The temperature at which the splitting was collapsed increased as the axial ligand was varied (Br < Cl < F). That dependence was consistent with the expectation that complexes with larger zero-field splitting had faster rates of electron spin relaxation at constant temperature. These spectra provide the opportunity to analyze the line shape of the nitroxyl signal as the iron relaxation rate changes. The spectra in Figure 5 are the typical first derivatives of the EPR spectra. These spectra emphasize sharp lines and minimize the importance of broader components of the spectra. The changes in the line shape of the nitroxyl signal can be seen more clearly in the first integrals of the spectra as shown in Figure 6 (Fielding *et al.*, 1986b).

The zero-field splitting for Fe(TPP)Br is 12.5 cm^{-1} (Behere *et al.*, 1981) so at 7 K almost all of the molecules have $m_s = \pm\frac{1}{2}$. The spectrum in Figure 5e was simulated as an $S = \frac{1}{2}, \frac{1}{2}$ interaction (Fielding *et al.*, 1986b). Due to the large g anisotropy, a frequency shift perturbation calculation was used. The doublet splitting of the iron $g = 6$ signal showed little anisotropy of the spin-spin interaction in the x-y (porphyrin) plane. The small anisotropy could indicate that the dominant contribution to the spin-spin interaction was exchange or that the nitroxyl was located close to the iron z axis. The iron $g = 2$ signal was obscured by the more intense nitroxyl signal. The nitroxyl signal was a broad doublet. If the splitting were predominantly dipolar, additional splitting would be expected due to the anisotropy of the interaction. The low-field component of the nitroxyl signal was more intense than the high-field component, as expected for an "inner" line of an AB pattern in which the exchange contribution is greater than the dipolar contribution. The relative intensities of the two

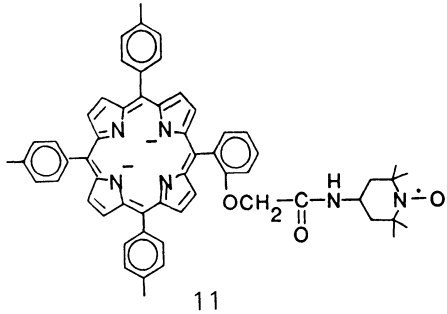

11

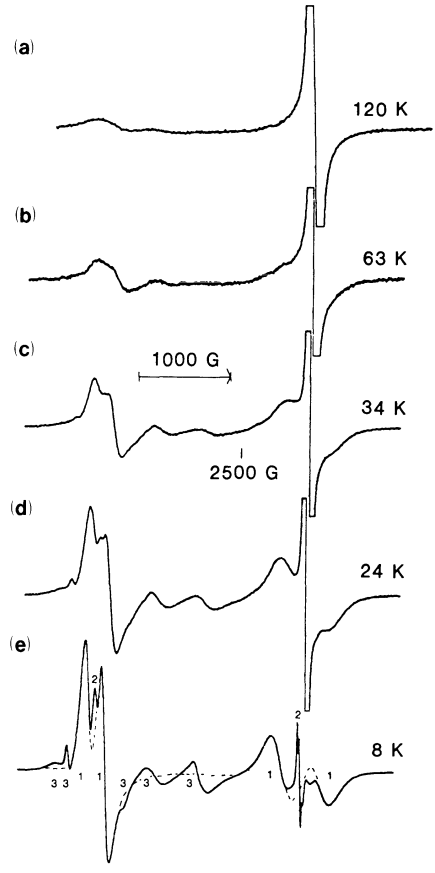

Figure 5. 4000 G scans of the X-band (9.1 GHz) EPR spectra of a 1 mM solution of Fe(**11**)Br as a function of temperature. The dotted line in part e indicates regions in which the simulated spectrum for component 1 does not overlay the experimental spectrum. (From Fielding *et al.*, 1986b.)

components of the nitroxyl signal could not be reproduced with $r < 7$ Å. The simulated spectrum shown in Figure 5e was obtained with an interspin distance $r = 8$ Å, $J = -0.034\ \text{cm}^{-1}$, and a 25° angle between the iron z axis and the interspin vector. Comparable agreement with the experimental data could be obtained for smaller angles between the iron z axis and the interspin vector, including $r = 8$ Å, $J = 0.045\ \text{cm}^{-1}$, and the interspin vector along the z axis. Larger angles between the interspin vector and the iron z axis caused additional splitting of the iron $g = 6$ signal, so these could be excluded (Fielding *et al.*, 1986b).

8. SPIN $\frac{7}{2}$–SPIN $\frac{1}{2}$

Gd(III) ($S = \frac{7}{2}$) gives a broad EPR signal with g approximately equal to 2.0 that can be observed in fluid and frozen solution. The electron spin relaxation rates for Gd(III) in fluid solution have been estimated to be between 10^9 and $10^{10}\ \text{s}^{-1}$ (Dwek *et al.*, 1975; Hyde and Sarna, 1978) which is much slower than for other +3 lanthanides.

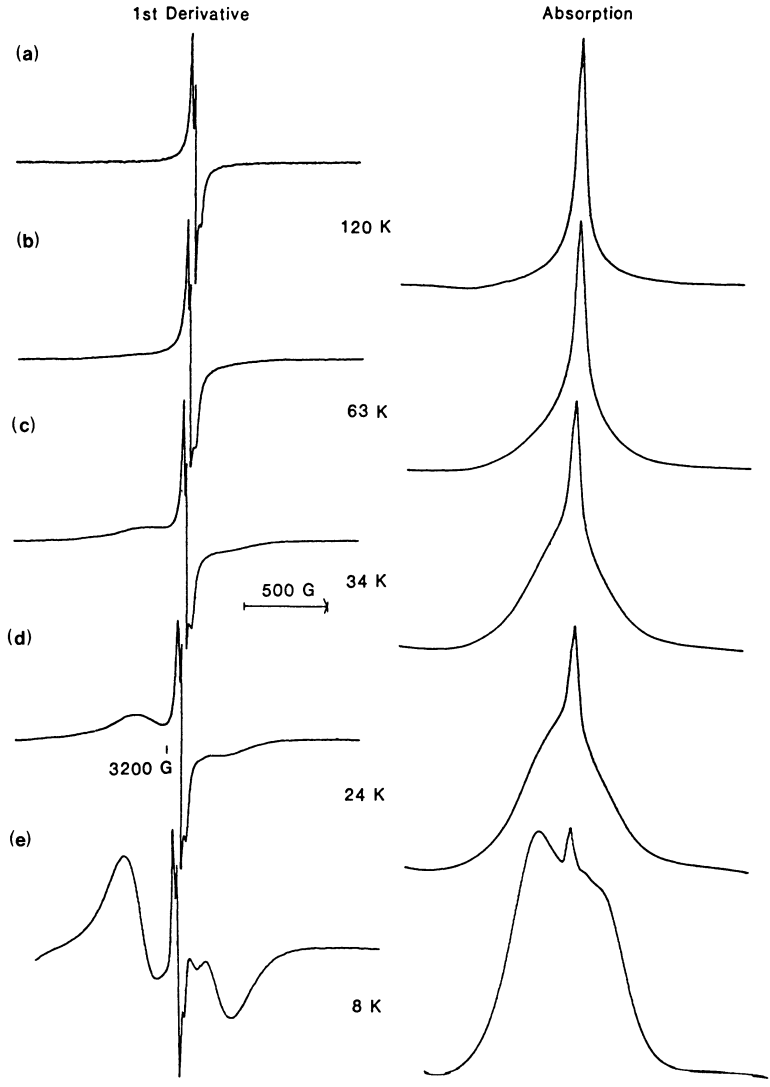

Figure 6. 2000 G scans of the nitroxyl regions of the spectra shown in Figure 5. The first derivative and absorption presentations of the spectra are compared. (From Fielding *et al.*, 1986b.)

These rates suggest that it may be possible to observe splitting due to spin-spin interaction with Gd(III) in some complexes at room temperature and that resolved splitting certainly would not be collapsed by electron spin relaxation at lower temperatures.

When a spin-labeled EDTA was coordinated to Gd(III) the nitroxyl signals at room temperature were about 60 G wide, which suggests substantial spin-spin interaction (More *et al.*, 1986a). In frozen solution the spin-spin interaction was sufficiently

strong that there were no signals that could be clearly identified as coordinated nitroxyl signals. Since the nitroxyl signal is superimposed on the broad gadolinium signal, some of the gadolinium energy levels are nearly degenerate with the nitroxyl energy levels. In such a case, even a relatively weak spin-spin interaction is sufficiently strong to cause substantial mixing of the wave functions and major changes in the nitroxyl EPR spectrum.

It is frequently assumed that since the unpaired electrons are in f orbitals, interaction with lanthanide ions is dipolar rather than exchange. However, nitrogen nuclear hyperfine splitting has been reported in the EPR spectrum of Gd(III) myoglobin (Srivastava, 1980). We observed that there was a correlation between the magnitude of the nitrogen nuclear hyperfine coupling in metalloporphyrins and the magnitude of the exchange interaction between the metal and a spin label attached to the periphery of the porphyrin (More *et al.*, 1981b). These two observations suggest that exchange interaction may be more significant for Gd(III) than had been thought previously.

9. CHEMICAL PROPERTIES REVEALED VIA SPIN–SPIN INTERACTIONS

Since electron-electron spin-spin interaction provides distinctive EPR spectra and since the coupling constants are sensitive to changes in molecular geometry and coordination, the EPR spectra of spin-coupled systems can provide chemical information that would be difficult to obtain by other techniques. Some examples are given below for small molecules. Examples are given in section 10 for biological systems.

9.1. Kinetics of Ligand Exchange for Cu(II)

Much of the study of ligand exchange kinetics for Cu(II) has been done in aqueous solution. These studies show rapid ligand exchange. When there is strong exchange interaction between Cu(II) and one spin-labeled ligand, the copper nuclear hyperfine splitting is one-half that observed in the absence of spin-spin interaction. If two spin-labeled ligands are coordinated, the nuclear hyperfine splitting is reduced to one-third of the noninteracting value. If a solution initially contains a mixture of CuL_2 and CuL'_2 (where L is a spin-labeled ligand and L′ is a structurally analogous diamagnetic ligand), the rate of ligand exchange can be monitored by following the rate of formation of CuLL′ (Eaton and Eaton, 1979). For spin-labeled salicylaldimines in toluene solution the process is associative, and the second-order rate constant is about $20\ M^{-1}\ min^{-1}$.

9.2. Coordination Equilibria

Some multidentate ligands offer the possibility of several modes of coordination. Eckberg *et al.* (1977a, 1977b) examined a series of quadridentate ligands in which there was a possibility of binding via an acetyl oxygen, an amide oxygen, or an amide nitrogen. Infrared data in the solid state indicated coordination of the acetyl oxygen. In analogous complexes with a spin label bound to the amide nitrogen, two isomers with substantially different magnitudes of copper-nitroxyl spin-spin interaction were observed in the fluid solution EPR spectra (DuBois *et al.*, 1979a, 1979b; Eaton *et al.*,

1980). The relative populations were dependent on solvent and temperature. The isomer with the smaller value of J was assigned to the species with the acetyl oxygen bound. The stronger spin-spin interaction for the second isomer indicated coordination of the amide oxygen.

When a spin-labeled pyridine is in a solution with a metal ion, there is the possibility of coordination via the nitroxyl oxygen or the pyridine nitrogen and the possibility of formation of a dimer in which the pyridine nitrogen is bound to one metal ion and the nitroxyl oxygen of the same ligand is bound to a second metal ion. When the metal ion has $S = \frac{1}{2}$, these modes of coordination have dramatically different effects on the EPR spectra. When the nitroxyl oxygen is coordinated to either Cu(II) or vanadyl ion, the spin-spin interaction is so strong that no EPR signal has been detected for either the nitroxyl or metal spin. When the pyridine nitrogen is coordinated, the copper-nitroxyl interaction causes characteristic splitting of the EPR spectra (Boymel *et al.*, 1980a, 1980b). In the spin-labeled pyridine bridged dimer, the strong interaction between one metal and the coordinated nitroxyl causes those spins not to be observed and the spectrum of the second metal is that expected in the absence of spin-spin interaction. If the initial complex is not coordinatively saturated, there is also the possibility of binding a second mole of pyridine at high pyridine concentrations. The visible spectra of the copper bis(hexafluoroacetylacetonate) adducts are also different when one or two nitrogens are coordinated than when the nitroxyl oxygen is coordinated. However, analysis of the equilibria based on the visible spectral data would be difficult because the molar extinction coefficients for the various species are unknowns, as are the equilibrium constants. Examination of the integrated intensity of the EPR spectra, the line shape of the EPR signal (by subtraction or simulation), and the visible spectra as a function of the concentration of spin-labeled ligand added to the solution, permitted analysis of a system with four independent equilibrium constants (Boymel *et al.*, 1980a, 1980b). The first binding constant for the pyridine nitrogen was several orders of magnitude larger than the second pyridine binding constant, the nitroxyl oxygen binding constant, or the equilibrium constant for formation of a dimer.

9.3. Weak Orbital Overlaps

One of the important questions in areas as diverse as electron transport, fluorescent energy transfer, and NMR coupling constants is the significance of weak orbital overlaps that are sometimes called "through-space" interactions. These are not interactions through the normal bonding pathways. Rather, these are interactions due to spatial proximity of orbitals on atoms that are not bonded to each other. When such orbital overlaps permit spin-spin interaction between two paramagnetic centers, the result is stronger exchange coupling than would have been expected through the bonding pathway.

EPR spectra of copper(II) complexes of spin-labeled porphyrins **12** and **13** have been examined in a variety of solvents (More *et al.*, 1981a). The values of J for the *trans* isomer were 0.0003 to 0.0005 cm^{-1}. The values of J for the *cis* isomer were 0.0005 to 0.0010 cm^{-1} in solvents that coordinated to the copper (such as pyridine or tetrahydrofuran), but increased to about 0.055 cm^{-1} in chloroform solution. ^1H NMR spectra of porphyrins analogous to **12** and **13**, but with *t*-butyl groups in place of the nitroxyls, indicated that the amide substituent was beside the porphyrin plane in the *trans* isomer

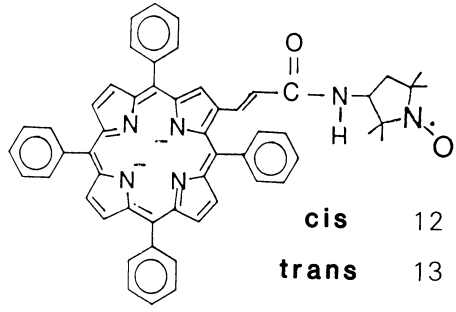

cis 12

trans 13

and above the porphyrin plane in the *cis* isomer. It was therefore proposed that in the absence of a coordinating solvent there was weak orbital overlap between the amide oxygen in the *cis* isomer and the copper or the porphyrin π-orbitals.

A series of copper(II) tetraphenylporphyrins were studied in which a spin label was attached to one phenyl ring. The values of J in fluid solution were several orders of magnitude larger when the substituent was attached to the *ortho* position of the phenyl ring, than when the substituent was attached to the *meta* or *para* positions (More *et al.*, 1981c). The values of J were strongly solvent-dependent for the *ortho* isomers, but not for the *meta* or *para* isomers. These results indicate that there was a pathway for spin-spin interaction that was accessible only to the *ortho* isomers, presumably involving direct interaction of side-chain orbitals with metalloporphyrin orbitals.

In fluid solution the value of J for spin-labeled silver porphyrin **14** was substantially greater (about 0.1 cm^{-1}) in noncoordinating solvents than in coordinating solvents (about 0.01 cm^{-1}) (More *et al.*, 1984a). EPR spectra in frozen solution indicated that the increase in J was accompanied by about a 2 Å decrease in the silver-nitroxyl distance. Thus the increase in the value of J was due to conformational change that increased the interaction between the side-chain orbitals and the metalloporphyrin orbitals. Two or more conformations with substantially different values of J have also been observed in the frozen solution EPR spectra of low spin iron(III) complexes of *ortho* spin-labeled porphyrins (Fielding *et al.*, 1986a). The presence of these conformations and the importance of weak orbital overlap with the *ortho* substituents would be difficult to detect by other techniques.

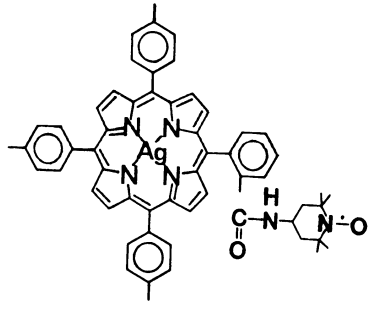

14

10. SPIN–SPIN INTERACTIONS IN BIOLOGICAL SYSTEMS

A number of studies have been reported in which the analysis of resolved electron spin-spin splitting has been used to obtain structural information concerning biological systems. Several examples are discussed in this section.

10.1. Cobalt(II)–Radical Interaction

Vitamin B_{12} (5′-deoxyadenosyl cobalamin) is a coenzyme for a class of enzymes including ribonucleotide reductase, glycerol dehydrase, ethanolamine ammonia lyase, and diol dehydrase (Schepler *et al.*, 1975). During the catalytic process a characteristic "doublet" EPR spectrum is observed. For several enzyme-substrate combinations it was shown that the magnitude of the doublet splitting was the same at two microwave frequencies, which indicated that the splitting was due to spin-spin interaction rather than the presence of two signals with slightly different g values. Schepler *et al.* (1975) proposed that the doublet splitting was due to exchange interaction between low spin Co(II) (B_{12r}) and a substrate radical. They pointed out the analogy with AB splitting in NMR spectra and obtained simulated spectra that matched the relative intensities of the two peaks of the doublet. The values of J obtained by analysis of five spectra from the literature ranged from 0.0073 to 0.0107 cm^{-1}. They argued that the dipolar splitting was less than the linewidths of the signals.

Schepler *et al.* (1975) proposed that the small dipolar interaction might be due to a dynamic process that averaged away the dipolar contribution. Boas *et al.* (1978) made the important point that it is not valid to consider the effect of a dynamic process on one component of the Hamiltonian without also considering the impact on other terms. For example, if the dynamic process were motional averaging of anisotropic interactions, there would be some effect on the anisotropic g and A values as well as the anisotropic dipolar interaction. If the dynamic process were rapid relaxation of the cobalt electron spin, both the dipolar and exchange contributions to the spin-spin interaction would be averaged and there would be broadening of the cobalt lines in the spectra.

Buettner and Coffman (1977) noted that at 35 GHz the "doublet" signal for the reaction involving ribonucleotide reductase and coenzyme B_{12} showed three components. The additional splitting of the signal indicated an anisotropic component in the spin-spin interaction as expected for the dipolar contribution. Matrix diagonalization was used to analyze the spectra. To avoid large matrices, the cobalt nuclear spin was not included in the calculations. The simulated spectra were in good agreement with the experimental data for $r = 9.9$ Å, $|J| = 0.00756$ cm^{-1}, and a 34° angle between the Co(II) z axis and the interspin vector. This value of J is about 30% smaller than the value obtained by Schepler *et al.* for the same system. The difference is due to the inclusion of the dipolar contribution to the splitting.

Boas *et al.* (1978) used second-order perturbation calculations to analyze the "doublet" spectra. The calculations included the cobalt nuclear hyperfine splitting. Their analysis of the spectrum from the ribonucleotide reductase and coenzyme B_{12} system gave $J = -0.0085$ cm^{-1}, $r \geq 10$ Å, and the interspin vector oriented along the Co(II) z axis. The results for J and r are in good agreement with the values obtained by Buettner and Coffman by diagonalization. It is not clear whether the discrepancy in the angle between the interspin vector and the Co(II) z axis reflects inadequacies

in the perturbation treatment or the absence of the nuclear hyperfine terms in the diagonalization analysis. These particular spectra are not very sensitive to the orientation of the interspin vector due to the small contribution from the dipolar term, so this parameter is subject to greater uncertainty than the values of r and J. The overall agreement between the results obtained by the two methods indicates that, at least for the case of weak spin-spin interaction, the two approaches are comparable.

One important conclusion from the analysis of the spectra is that there is a substantial distance between the Co(II) and the organic radical. There is general agreement that one step in the catalytic process is homolytic cleavage of a cobalt-carbon bond to form Co(II) and an organic radical. The initial radical must move away from the Co(II) to produce the species that gives the "doublet" spectrum (Boas *et al.*, 1978; Pilbrow, 1982).

When ribonucleotide reductase, coenzyme B_{12}, dihydrolipoate, and dGTP are mixed and frozen rapidly, an EPR spectrum is observed that differs from that of the "doublet" spectrum. The interpretation of this "rapid intermediate" spectrum has been controversial (Blakeley *et al.*, 1979; Pilbrow, 1982). It appears to be due to strong spin-spin interaction between Co(II) and an organic radical, although a satisfactory simulation of the spectrum has not been obtained. The appearance of a strong half-field transition indicates a shorter interspin distance than observed for the "doublet" species. EPR spectra that have been attributed to strong exchange interaction between Co(II) and an organic radical have also been observed in samples prepared by photolysis of coenzyme B_{12} (Ghanekar *et al.*, 1981; Pezeshk and Coffman, 1985). Simulations have not been reported for these spectra. These spectra may be due to the initial species that is formed by cleavage of the cobalt-carbon bond, prior to the migration that forms the "doublet" species.

10.2. Mo(V) Interaction with Fe/S Cluster

Xanthine oxidases and xanthine dehydrogenases are redox-active proteins that contain molybdenum and two Fe/S clusters. These enzymes can be isolated in several forms in which the molybdenum is in the +5 oxidation state ($S = \frac{1}{2}$). The EPR spectrum of the Mo(V) has three distinct g values (for example, one form has $g = 1.978$, 1.971, and 1.965) and linewidths less than 5.0 G (Lowe and Bray, 1978). When Fe/S cluster I is the oxidation state with $S = \frac{1}{2}$, each of the lines in the Mo(V) signal is split into a doublet (Lowe *et al.*, 1972; Lowe and Bray, 1978). The following evidence indicated that the splitting was due to spin-spin interaction with the Fe/S cluster. (1) The splitting was observed only when the Fe/S cluster was in the oxidation state with $S = \frac{1}{2}$. (2) Although the EPR signal for the Fe/S cluster did not show splitting, the line was broader when the molybdenum had $S = \frac{1}{2}$ than when the molybdenum was diamagnetic. (3) The splitting was observed below about 40 K. At higher temperatures the electron spin relaxation rate for the Fe/S cluster was fast enough to collapse the spin-spin splitting.

Xanthine oxidase and xanthine dehydrogenase obtained from milk, turkey, and *v. alcalescens* were studied at 9 and/or 35 GHz (Lowe and Bray, 1978). In samples prepared by several methods, the magnitude of the splittings ranged from 7 to 24 G. In all cases, the splitting was about the same along the three axes of the Mo(V) signal—the anisotropy was about 10% of the total splitting. The nearly isotropic

interaction indicated a dominant exchange contribution. The similarity in the splittings indicated that the interaction pathway was conserved in a variety of states of the enzyme. The magnitude of the splitting did not correlate with the enzymatic activity, which indicated that, in this system, the pathway for spin-spin interaction was not the same as the pathway for electron transfer. Lowe and Bray (1978) noted that if the largest anisotropy observed (4.0 G) were assumed to be equal to the largest component of the dipolar interaction, the interspin distance would be 20-25 Å. This estimate assumes that the interspin vector lies along a principal axis for Mo(V). The calculated distance would be smaller for other orientations of the interspin vector. The possibility of a "magic angle" orientation for the interspin vector was considered to be unlikely, since the anisotropy of the interaction was small for a variety of preparations.

Coffman and Buettner (1979b) discussed the dipolar contribution to the spin-spin splitting in the xanthine oxidase spectra. They pointed out that if the interspin vector were located at the "trimagic" angle (see discussion in Section 2.1) with respect to the Mo(V) g axes, the dipolar interaction would be small along the principal axes of the Mo(V) spectrum. Sample calculations were shown for single-crystal spectra with the magnetic field along a principal axis. They proposed that r could be as short as a normal bond and still give no splitting along the principal axes. To counter the argument that a unique orientation was unlikely, they showed that the dipolar interaction remained quite small for a cone of angles near the "trimagic" angle. On the basis of the limit function for the dependence of J on interspin distance (Coffman and Buettner, 1979a), they argued that exchange interaction of the magnitude observed in the xanthine oxidase spectra was inconsistent with r greater than about 14 Å. (See Section 2.2.1 for discussion of this limit law.) They concluded that the interspin distance was between 8 and 14 Å. The problem with this discussion is that it does not consider the effect of the dipolar interaction on the full powder spectrum. When r is short, the turning points in the spectra are determined by the dipolar interaction, not by the principal axes of the Mo(V), and the full powder spectrum would bear no resemblance to the spectrum of Mo(V). A distance as short as 8 Å is inconsistent with the powder spectrum.

George (1984) showed that the spectrum of Mo(V) in aldehyde oxidase showed splitting that was similar to that obtained for a similarly prepared sample of xanthine oxidase. In this case resolved splitting of the spectrum for the Fe/S cluster was also observed. The spectra indicated substantial similarity of the metal sites in the two enzymes. Perturbation calculations were used to simulate the powder spectra at 9 and 35 GHz. It was found that $r > 15$ Å fit the data for both aldehyde oxidase and xanthine oxidase. A simulated spectrum showed that if r were as short as the 8 Å previously suggested, the dipolar interaction dominated the spectrum and was clearly inconsistent with the experimental data. These spectra are examples of significant exchange interaction over a relatively long distance.

10.3. Iron–Nitroxyl Interaction

10.3.1. Spin-Labeled Cytochrome P-450

Cytochrome P-450 contains a heme iron center that binds a variety of ligands. Several groups have used spin-labeled ligands to examine spin-spin interaction with

the heme. These studies provide a useful "case history" of increasing sophistication in interpretation of metal-nitroxyl interactions.

In 1972 Reichman *et al.* used changes in visible spectra to show that the spin-labeled isocyanide, **15**, bound to the heme of cytochrome P-450. They used EPR spectra of the nitroxyl to study molecular motion without mention of iron-nitroxyl interaction.

In 1974 Ruf and Nastainczyk noted that, although visible spectra indicated that **15** bound to cytochrome P-450, no EPR signal was observed for the bound spin label. They proposed that the nitroxyl signal was severely broadened by interaction with the iron(III). Their results suggest that the spectrum studied by Reichman *et al.* (1972) was not due to spin label bound to the heme iron and point out the importance of doing quantitative EPR spectroscopy on spin-labeled systems (see Section 12). They also noted that the interaction with the nitroxyl caused the appearance of new signals at $g = 2.09$ and 2.18 in the frozen solution EPR spectra of the low-spin iron.

In 1979 Pirrwitz *et al.* (1979a, 1979b) reported that coordination of **15** to cytochrome P-450 resulted in loss of the nitroxyl EPR signal and the appearance of new iron signals at $g = 2.19$, 2.08, and 1.97. They attributed the changes in the spectra to dipolar interaction between the iron and nitroxyl. On the basis of molecular models they estimated an interspin distance of 6 Å. Their spectra for cytochrome P-450 and cytochrome P-450 + **15** are shown in Figure 7. One complication in examining these spectra is that some of the P-450 and some of the nitroxyl is not coordinated, so there are strong signals from these species superimposed on the spectrum of the complex.

In 1986 it was noted that the signals in the spectra of cytochrome P-450 + **15** are approximately at the average of the g values for P-450 (2.44, 2.24, and 1.92) and nitroxyl (2.00) and can therefore be assigned to strong exchange ($J > 0.4\ \text{cm}^{-1}$) between the two paramagnetic centers (Fielding *et al.*, 1986b). Interaction of this magnitude is consistent with coordination of the isocyanide to the heme iron. Due to the large value of J and the large g anisotropy, the simulated spectrum in Figure 7 was obtained with a frequency shift perturbation calculation. The input parameters were: iron $g = 1.90$, 2.27, 2.48, nitroxyl $g = 2.00$, $r = 7.0$ Å, $J = -0.40\ \text{cm}^{-1}$, an angle of 40° between the interspin vector and the iron z axis, and an angle of 65° between the iron y axis and the projection of the interspin vector on the iron x-y plane. Due to extensive overlap of the spectrum of the spin-labeled complex with the signals from unlabeled cytochrome P-450, there is substantial uncertainty in these parameters. However, the simulated spectrum indicates that the experimental spectrum is consistent with coordination of the isocyanide to the heme iron. Similar agreement cannot be obtained with exclusively dipolar interaction.

In 1979 Pirrwitz *et al.* (1979a) also reported EPR spectra for spin-labeled amine, **16**, bound to cytochrome P-450 (Figure 8) and noted that the changes in the heme

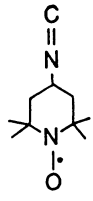

15

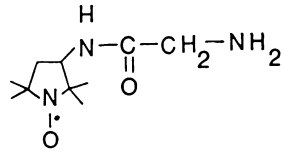

16

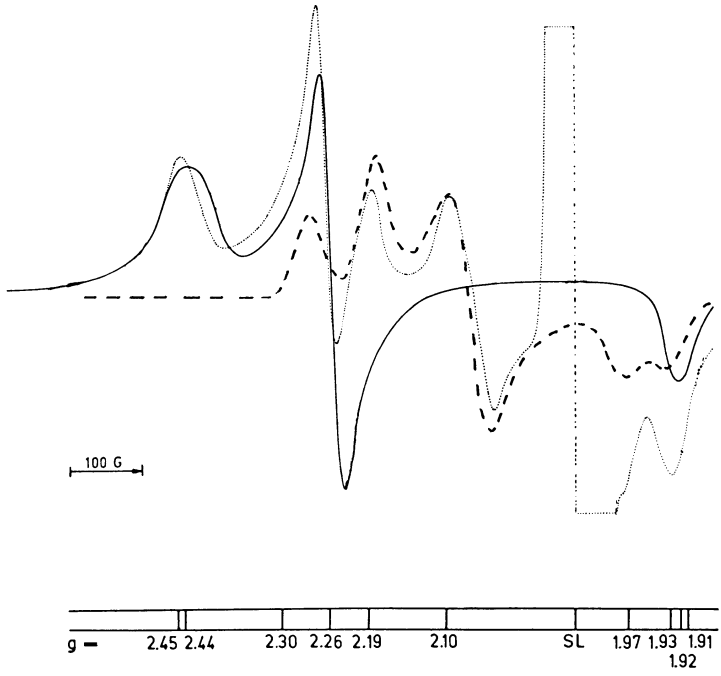

Figure 7. X-band EPR spectra of the heme iron center in solubilized P-450 in frozen solution at −190 °C: (——) without substrate, (· · ·) with spin-labeled isocyanide **15**, (- - -) simulated spectrum. (Experimental data taken from Pirrwitz *et al.*, 1979b.)

spectrum due to coordination of the spin-labeled ligand were smaller than for the complex of **15**. The iron signals for the complex with **16** appear to be superimposed on the signals for iron that is not coordinated to the spin-labeled ligand. They noted new signals at $g = 2.101$ and 2.047. The spectra also had a partially resolved peak at about $g = 1.90$. These features are the nitroxyl lines for the complex (Fielding *et al.*, 1986a). Since the iron spectrum has turning points to both lower and higher field of the nitroxyl, exchange interaction between the iron and nitroxyl causes "nitroxyl inner" lines at both low and high field of $g = 2$. For sufficiently large values of J, the anisotropy of the iron signal would cause anisotropy of the "nitroxyl" lines. For the magnitude of spin-spin interaction in this spectrum, if all of the interaction were exchange, the anisotropy would be too small to account for the splitting of the signals at $g = 2.047$ and 2.101. That splitting could only be reproduced in the simulated spectra by introducing a substantial dipolar contribution to the interaction. If only dipolar interaction was included in the simulations, the relative intensities of the peaks did not agree with the experimental data. The simulated spectrum shown in Figure 8 was obtained by a perturbation calculation with $r = 7.0$ Å, $J = -0.03$ cm^{-1}, and a 25° angle between the iron z axis and the interspin vector. The calculated nitroxyl spectrum was sensitive to the value of r, but was not strongly dependent on the orientation of the interspin vector relative to the iron axes. The calculations confirmed that the iron signals in the complex would not be resolved from the signals for iron that was not interacting with the

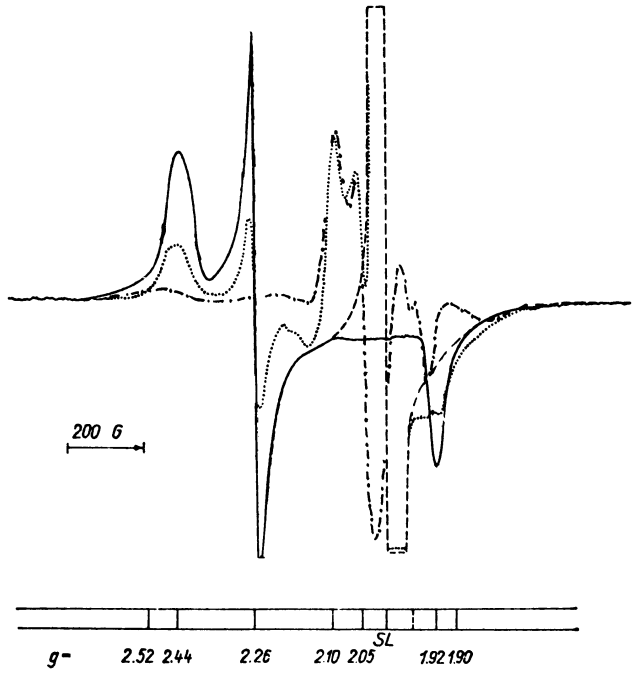

Figure 8. X-band EPR spectra of the heme iron center in solubilized P-450 in frozen solution at −190 °C: (——) without substrate, (· · · ·) with spin-labeled amine **16**, (- - -) signal from noninteracting spin label, (- · - · -) simulated spectrum. (Experimental data taken from Pirrwitz *et al.*, 1979a.)

nitroxyl. Without resolution of these signals the orientation of the interspin vector could not be defined accurately.

Griffin *et al.* (1974, 1975) reported that the spin-labeled metyrapone analog, **17**, coordinated to cytochrome P-450. In solution at room temperature they observed that the intensity of the nitroxyl EPR spectrum was reduced, due to interaction with the iron(III). The iron-nitroxyl distance was estimated to be 6.7 to 8.8 Å on the basis of Leigh's model (1970) of the effect of a rapidly relaxing metal on the nitroxyl line shape. They also noted that, in frozen solution, the EPR spectra showed splittings of the iron signals. Mock *et al.* (1982) analyzed the splittings of iron signals in the frozen solution EPR spectra of **17** bound to cytochrome P-450. The spectra indicated dipolar interaction with $r = 5.7$ Å. The interspin vector was 80° away from the normal to the porphyrin plane. The absence of a large exchange contribution to the spin-spin interaction in this complex is consistent with studies on small molecules. The iron unpaired electron is in the $d_{xz,yz}$ pair which has the appropriate symmetry to interact with the p-orbital on the pyridine nitrogen. The symmetry of this interaction is analogous to that for pyridine coordinated to vanadyl bis(hexafluoroacetylacetonate), $VO(hfac)_2$. Therefore the exchange interaction is expected to be similar if the same ligand is coordinated to $VO(hfac)_2$ or to the heme in cytochrome P-450. The values of J for spin-labeled pyridines bound to $VO(hfac)_2$ were smaller when the spin-labeled substituent was on

the 3-position of the pyridine than on the 4-position, so weaker exchange interaction would be expected for the complex of **17** than for **18** (Sawant *et al.*, 1982). Since the value of J for the complex of **18** with $VO(hfac)_2$ was 0.0007 cm^{-1}, the value of J for the **17** coordinated to $VO(hfac)_2$ would be expected to be less than 0.0007 cm^{-1}. By analogy, the value of J is expected to be small for the complex of **17** with cytochrome P-450, which is consistent with the experimental results.

These studies provide three examples of spin-spin interaction between spin labels and the heme in cytochrome P-450. Exchange was large relative to the energy separations for **15**, comparable to the dipolar interaction for **16**, and much smaller than the dipolar interaction for **17**. These examples serve to illustrate the importance of molecular structure in determining the magnitude of exchange interactions and the need to consider both exchange and dipolar interaction in biological systems.

10.3.2. Spin-Labeled Aconitase

Bovine heart aconitase is an iron-sulfur protein. As isolated, the iron-sulfur cluster has $S = \frac{1}{2}$. There is also a reactive sulfhydryl group. A series of spin-labeling experiments was performed to obtain information concerning the spatial relationship between the iron-sulfur cluster and the reactive sulfhydryl (Dreyer *et al.*, 1983). Aconitase was spin-labeled with three different nitroxyl radicals (two maleimides and one bromoacyl). EPR spectra of each of these products at 13 K exhibited a half-field transition. The relative intensity of the half-field transition yielded distances of 10.5, 11, and 13 Å between the three spin labels and the center of the FeS cluster. The shape of the half-field transition (Figure 9) is dependent on the angle (A_1) between the interspin vector and the z axis of the nitroxyl hyperfine interaction. Simulation of the line shape was used to obtain that angle. The g values for the Fe/S cluster EPR signal were so nearly isotropic that the nitroxyl anisotropy dominated the shape of the half-field transition and information could not be obtained concerning the orientation of the interspin vector relative to the axes of the Fe/S cluster. The combined distance and orientation information for the three labels indicates that the reactive sulfhydryl group is about 12 Å from the center of the Fe/S cluster.

10.4. Nitroxyl–Nitroxyl Interaction

Glyceraldehyde-3-phosphate dehydrogenase is a tetrameric enzyme with one active site and one NAD^+ binding site per subunit (Beth *et al.*, 1984). Since an X-ray crystal structure had been obtained for the enzyme from lobster muscle, it was possible to compare EPR results with predictions based on computer modeling of coenzyme binding. When the NAD coenzyme was spin-labeled at the 6- or 8- position of the

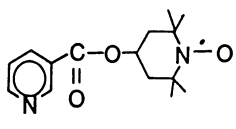

17

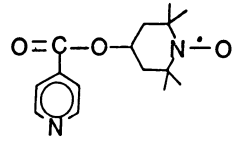

18

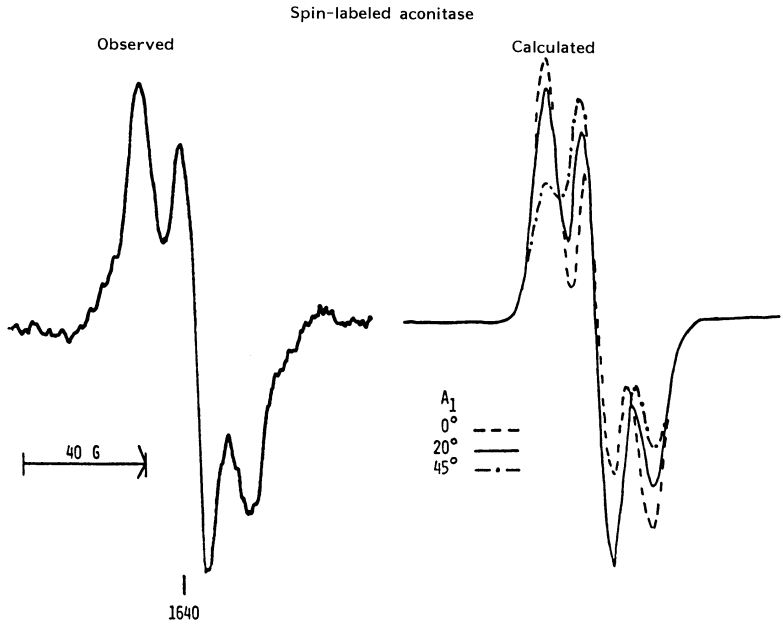

Figure 9. X-band EPR spectra of the half-field transition for spin-labeled aconitase at 13 K. The three curves for calculated spectra demonstrate the sensitivity of the line shape to the angle (A_1) between the interspin vector and the z axis of the nitroxyl g and A matrices. The calculated spectrum for $A_1 = 20°$ is in good agreement with the experimental line shape. (Experimental data taken from Dreyer *et al.*, 1983.)

adenine ring, the binding affinities and catalytic constants for glyceraldehyde-3-phosphate dehydrogenase from rabbit muscle were similar to values for the native coenzyme, which suggested that the spin label did not perturb the binding geometry. To decrease the linewidths of the EPR spectra due to unresolved hyperfine splitting, deuterated spin labels were used. To assist in the assignment of the lines in the spectra, samples were prepared with both ^{14}N and ^{15}N spin labels. When four moles of spin-labeled NAD^+ were bound to the enzyme, the EPR spectra showed pairwise spin–spin interaction between nitroxyl radicals and no interaction between the two pairs. The crystal structure indicated two symmetry-related pairs of binding sites. The distance between nitroxyls in a pair obtained from the EPR spectra (12.8 Å) fell within the range predicted by calculations based on the crystal structure data (11–13 Å). The well-resolved nitrogen hyperfine splitting provided a molecular axis definition. Computer simulation of the spin–spin splitting in the powder spectrum was used to determine the relative orientations of the axes for the two spin labels and the orientation of the interspin vector. The agreement with the experimental data was good for *anti–anti* conformations of the adenine and ribose and poor for the *anti–syn* conformations. Thus, the analysis of the spin–spin interaction provided a detailed picture of the conformations of the coordinated coenzymes. The simulated spectra were obtained by a perturbation calculation. The electron spin–spin interaction was dipolar. There was no short through-bond pathway for spin–spin interaction, so there was negligible contribution from exchange.

Since the EPR spectra due to spin-spin interaction are strongly dependent on the interspin distance and the relative orientations of the two spin labels, changes in the enzyme conformation would have significant impacts on the spectra. Comparison of the EPR spectra for spin-labeled NAD^+ bound to glyceraldehyde-3-phosphate dehydrogenase in the soluble form and precipitated with ammonium sulfate indicated that the coenzyme was bound similarly in the two forms.

11. EXCHANGE INTERACTION THROUGH MULTIATOM LINKAGES

Since there is no simple relation between distance and the magnitude of the exchange interaction, and since exchange has been observed to dominate EPR spectra at very large distances, there is need for a way to guess whether in any particular case it is safe to neglect exchange in order to attempt to use a dipolar relationship to estimate interspin distance. Substantial progress has been made in the past ten years in molecular orbital calculations of the exchange interaction in metal dimers with one or two atom bridges (Kahn, 1985a, 1985b). However, the understanding of longer-range interaction is still predominantly at a phenomenological level.

Parmon (1977) summarized studies of the value of J in nitroxyl biradicals with various bridges between the two rings. When an O was replaced by NH, the value of J decreased by a factor of 1.12. When Si was replaced by the following atoms, the value of J decreased by factors of 4.5 (C), 1.1 (S), 1.2 (P). The factor by which exchange was attenuated by the introduction of a particular functional group in the bond pathway for interaction was called the exchange coefficient and denoted as γ. The values of γ for a series of dinitroxyls with delocalized linkages between the two nitroxyl rings are shown in Table 1.

Exchange may be via σ- or π-bond pathways (or both). The attenuation coefficient γ for an atom or grouping of atoms depends upon the relative importance of σ and

TABLE 1
Effect of Additional Atoms on the Value of J for Dinitroxyls

Added atoms	Reduction factor, γ	Reference
CH=CH	1.7	Parmon *et al.*, 1977
$(CH=CH)_2$	3.2	Parmon *et al.*, 1977
$(CH=CH)_3$	5.6	Parmon *et al.*, 1977
C≡C	2.2-2.4	Kokorin *et al.*, 1980
p-C_6H_4	5.5-6.4	Parmon *et al.*, 1977, Kokorin *et al.*, 1980, Kokorin *et al.*, 1981
2,5-thiophene	3.1-3.7	Parmon *et al.*, 1977, Kokorin *et al.*, 1981
3,4-thiophene	0.7	Kokorin *et al.*, 1981
−N=	1.3	Kokorin *et al.*, 1981
Hg	24	Kokorin *et al.*, 1980

π pathways for the particular case. For example, introduction of a urea linkage caused a small increase in the exchange interaction relative to that for an amide linkage for a case in which π interaction dominated, even though the urea linkage is one atom longer than the amide linkage (More *et al.*, 1982b). However, in a system where σ interaction dominated, exchange through a urea linkage was smaller by factors of 2 to 40 than for an amide linkage (More *et al.*, 1983).

The effect of an additional CH_2 group on the magnitude of exchange is strongly dependent on the nature of the linkages. Many years ago McConnell estimated that a CH_2 group would attenuate exchange by about a factor of ten (McConnell, 1960). In titanium(III) dimers with dicarboxylic acid linkages an additional CH_2 group caused about a factor of 2 decrease in the exchange interaction (Francesconi *et al.*, 1981). In a series of spin-labeled pyridine complexes, it was observed that the effect of a CH_2 group ranged from a factor of 4 decrease in J for a complex with predominantly σ interaction to >100 for a system with extensive π contribution (More *et al.*, 1982b). Observation of spin coupling to the in-plane protons at both ends of the hydrocarbon chain in $[H(CH_2)_nH]^+$ cations indicated a σ-delocalized radical structure (Toriyama *et al.*, 1981). Similar delocalization of σ spin density may occur in other saturated systems. Thus some knowledge of the nature of the orbitals involved in spin delocalization is important to estimate the impact of a CH_2 group on exchange.

Conformational effects also play an important role in determining the magnitude of the exchange interaction. In a system with predominantly σ interaction, the value of J through a C_2 unit was found to increase in the order *cis* isomer < saturated linkage < *trans* isomer (More *et al.*, 1982a). It was proposed that the exchange interaction through the saturated linkage was due to a conformation analogous to the "extended W-plan" that is known to contribute to long-range hyperfine coupling in organic radicals (King, 1976).

Two linkages that are of interest in biological systems are phosphates and hydrogen bonds. Magnetic susceptibility studies of copper dimers with O—H—O bridges between the two metals found $J = -56$ to $-95\ cm^{-1}$ (Bertrand *et al.*, 1980). In an iron dimer with an indirect hydrogen-bonded pathway the exchange interaction was $1.0\ cm^{-1}$ (Klein *et al.*, 1982). A calculational study estimated that the exchange interaction would be as large as $60\ cm^{-1}$ through a hydrogen bond with an O-O distance of 2.84 Å (Nepveu *et al.*, 1986). Magnetic susceptibility studies of copper(II) and chromium(III) dimers have shown values of J through O—P—O linkages between 2.4 and $10.8\ cm^{-1}$ (Scott *et al.*, 1975; Krasicky *et al.*, 1978; Lambert *et al.*, 1978). These results for relatively direct metal-metal interaction pathways suggest that smaller, but still important, long-range exchange interaction through hydrogen bonds or phosphate linkages may be significant in some biological systems.

Metal complexes of spin-labeled pyridines have been used to examine spin-spin interaction for a range of bonding pathways. Results are summarized in Table 2. The following generalization can be obtained from the data. The magnitude of the exchange interaction decreases in the order Schiff base > urea > amide > ester, which parallels the decreasing π contribution to the bonding in the linkage. The value of J also depends on the nitroxyl ring, decreasing in the order pyrroline (unsaturated 5-membered ring nitroxyl) ≥ tetrahydropyridine-1-oxyl (unsaturated 6-membered ring nitroxyl) > pyrrolidine (saturated 5-membered ring nitroxyl) > piperidine (saturated 6-membered ring nitroxyl) (Sawant *et al.*, 1982). The effects of the metal ions can be understood as

TABLE 2
Values of J (cm^{-1})[a] for Spin-Labeled Pyridines

Ligand R[f]	Metal spin	Temp. (°C)	$Cu(hfac)_2$[b] 1/2	Co(II)P[c] 1/2	$VO(tfac)_2$[d] 1/2	CrTPPCl[e] 3/2
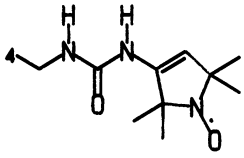		22	<0.0002		0.0002	
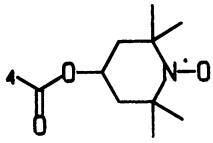		22 −180	<0.0002 0.0006		0.0007	
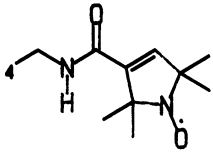		22 −180	0.0002	<0.0015	0.0025	<0.003
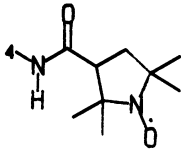		22 −180	0.0004		0.015	~0.01
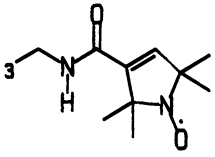		22	0.0015		0.0008	
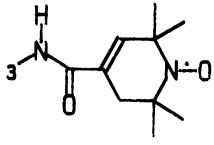		22 −180	0.0031	0.0080	0.0104	~0.005
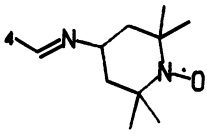		22 −180	0.0043 0.0070	0.0087	0.0112 0.0107	0.0073

TABLE 2
(*Continued*)

Ligand R[f] / Metal spin	Temp. (°C)	$Cu(hfac)_2$[b] 1/2	Co(II)P[c] 1/2	$VO(tfac)_2$[d] 1/2	CrTPPCl[e] 3/2
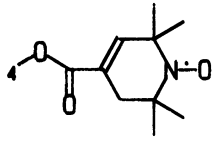	22	0.0046		0.0135	
	−180	0.0052	0.0085		0.0085
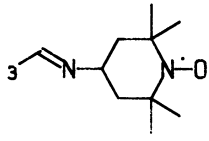	22	0.0063		0.0032	
	−180	0.0080	0.0085	0.0037	<0.003
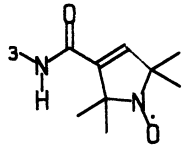	22	0.0077		0.0088	
	−180	0.017	0.016	0.0084	<0.005
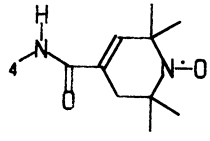	22	0.016		0.038	
	−180	0.017	0.030	~0.037	0.022
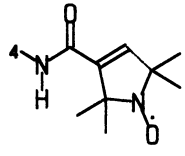	22	0.016		0.041	
	−180		0.027		~0.022
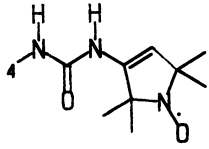	22	0.022		0.048	
	−180		0.043		0.037

(*continued*)

TABLE 2
(*Continued*)

Ligand R[f]	Metal spin	Temp. (°C)	$Cu(hfac)_2$[b] 1/2	Co(II)P[c] 1/2	$VO(tfac)_2$[d] 1/2	CrTPPCl[e] 3/2
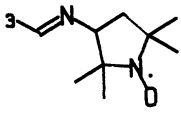		22	0.048		0.040	
		−180	0.040	<0.055	0.035	~0.022
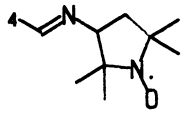		22	0.060		0.17	
		−180	0.05	0.090	0.19	~0.13
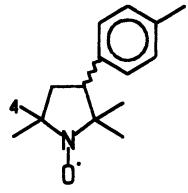		22				
		−180				0.27

[a] Spectra were obtained in toluene, toluene:chloroform, or carbon tetrachloride solution. For most of the complexes the sign of J is not known. For cases in which isomers were observed, an average value of J is given.
[b] Data taken from Boymel *et al.* (1980a, 1980b), Eaton *et al.* (1983a), More *et al.* (1982b, 1984c), and Sawant *et al.* (1982).
[c] P = tetra(*p*-trifluoromethylphenyl)porphyrin. Data taken from Eaton *et al.* (1984).
[d] Data taken from More *et al.* (1982b, 1984c) and Sawant *et al.* (1982).
[e] Data taken from More *et al.* (1986b).
[f] Substituent on pyridine ring.

follows. In $Cu(hfac)_2$ complexes the pyridine is in the basal plane of a square pyramid and the Cu(II) unpaired electron is in the $d_{x^2-y^2}$ orbital which has σ symmetry with respect to the orbitals on the pyridine nitrogen (Sawant *et al.*, 1982). Pyridine binds axially to Co(II) porphyrins and the Co(II) unpaired electron is in the d_{z^2} orbital, which has σ symmetry with respect to the pyridine nitrogen (Eaton *et al.*, 1984). Similar patterns of spin delocalization are thus expected for the Cu(II) and Co(II) complexes. This expectation is affirmed by the similarities in the values of J when the same ligand is coordinated to the two metals (Table 2). The values of J for these complexes are similar for the 3- and 4-isomers of the ligands which is consistent with a substantial σ contribution to the spin delocalization. Pyridine binds *cis* to the V=O in $VO(hfac)_2$ and the vanadyl unpaired electron is in the d_{xy} orbital, which has π symmetry with respect to the orbitals on the pyridine nitrogen (Sawant *et al.*, 1982). Pyridine binds axially to Cr(III) porphyrins, and the Cr(III) unpaired electrons in the d_{xz} and d_{yz} orbitals have π symmetry with respect to the pyridine (More *et al.*, 1986b). The values of J in Table 2 reflect similar patterns of spin delocalization for the VO(IV) and Cr(III) complexes. For both of these metals the values of J are substantially greater for the

4-isomer than for the 3-isomer of the ligand, which is consistent with a substantial π contribution to the spin delocalization. These results indicate that if the unpaired electrons on two metals occupy orbitals of the same symmetry and the bonding is similar, data obtained from one metal can be used to estimate the magnitude of J for another metal. The effect of the metal spin was discussed in Section 6.

When Cu(II), Ag(II), and vanadyl were coordinated to a porphyrin with spin labels attached to a pyrrole carbon, the values of J decreased in the order Ag(II) > Cu(II) > vanadyl (More *et al.*, 1981b). The hyperfine splitting of the metal EPR spectrum due to the coordinated nitrogens decreased in the same order. An ENDOR study of the hyperfine interaction with the pyrrole protons also decreased in that order (Brown and Hoffman, 1980). It was concluded that all three parameters reflect the extent of metal spin delocalization into the porphyrin orbitals.

12. QUANTITATIVE EPR MEASUREMENTS

Except for the cases discussed in the following two paragraphs, spin-spin interaction, either dipolar or exchange, does not cause a change in the integrated intensity of the EPR spectrum. However, the interaction often causes transitions to be spread over a wider range of magnetic fields than was observed in the absence of spin-spin interaction. Although the integrated intensity of the signal is constant, the maximum amplitude is decreased. Such signals can easily be missed if the spectroscopist looks only at the sharpest signals. If the integration of the sharp signals accounts for only a fraction of the expected signal, then effort should be made to look for additional signals. Therefore, double integration is an important check that the selected spectral window encompasses all of the spectrum. Many early papers reported signals without attention to whether the signal corresponded to 1% or 100% of the sample. Some papers reported sharp nitroxyl signals (probably due to noninteracting nitroxyl), failed to see the underlying signals, and erroneously concluded that there was no spin-spin interaction.

If the exchange interaction is comparable to, or greater than, kT, there are substantial differences in the populations of the energy levels. If the lower energy level does not give an EPR signal, strong spin-spin interaction results in loss of intensity of the EPR signal. A typical example is the strong antiferromagnetic coupling between two $S = \frac{1}{2}$ centers that results in a diamagnetic ground state and loss of intensity of the EPR spectrum.

A second exception occurs for interaction of $S = \frac{1}{2}$ centers with $S > \frac{1}{2}$ metals with large zero-field splittings. In the presence of strong spin-spin interaction, mixing of the $S = \frac{1}{2}$ energy levels with the $S > \frac{1}{2}$ levels can cause some transitions to shift beyond the range of accessible magnetic fields.

General discussions of the quantitation of EPR signals can be found in Randolph (1972), Eaton and Eaton (1980), and Goldberg and Bard (1983). The following discussion examines only the question of sweep width and cavity Q.

Lorentzian line shapes approach baseline relatively slowly and therefore wide sweeps are required to obtain accurate integration of the signal. The table on p. 127 of Randolph (1972) points out that, to obtain 95.8% of the integral for a Lorentzian line, it is necessary to use a sweep width that is 120 times the peak-to-peak linewidth

of a signal at the center of the scan. This means that if the maximum spin-spin splitting is 160 G (for example, dipolar interaction of two $S = \frac{1}{2}$ centers separated by 7 Å) and the maximum peak-to-peak first-derivative linewidth is 10 G, a sweep width of 1360 G ($160 + 120 \cdot 10$) is needed to obtain 95.8% of the integral. Additional calculations that illustrate the need for wide sweeps are given in Eaton *et al.* (1979). Integration of such wide sweeps will frequently require subtraction of cavity background signals.

In comparing integrals for a sample with the integral for a standard, it is necessary to recognize the importance of cavity quality factor Q, which is the ratio of the microwave energy stored in the standing wave pattern in the cavity to the power dissipated in the cavity per cycle. The larger Q, the greater the integrated intensity of the EPR signal for a sample. Solvents with high dielectric loss such as water and alcohols reduce the cavity Q proportional to the amount of solvent in the cavity (Dalal *et al.*, 1981). Therefore, it is necessary to either compare integrals for samples obtained in the same solvent and with the same size of sample tube, or to measure cavity Q and correct the integrals for the changes in Q. Also, materials such as the quartz dewars used for variable-temperature work perturb the distribution of microwaves in the cavity. The integrated signal intensity for a spectrum obtained when the dewar is in the cavity is greater than when the dewar is not in the cavity. Thus integrals should be compared for samples obtained with the same dewar (Dalal *et al.*, 1981).

13. SUMMARY AND PROGNOSIS

Electron-electron spin-spin interactions promise to reveal detailed information about biological systems. In favorable cases it is already possible to estimate the distances between unpaired electrons, whether native to the system or added as labels or probes, and to estimate the relative orientations of the axis systems of these spins. In order to reap this rich harvest, however, the researcher must perform very careful, and often quantitative, EPR measurements, and be aware of the many factors that can influence the EPR signal intensity and line shape.

Before any distance estimate is made using a purely dipolar calculation, it is essential to prove that exchange can be neglected. Since it will rarely be true that exchange can be neglected, it is better to eschew simplified methods that assume only dipolar interaction and use full spectral simulations, including both exchange and dipolar interactions.

The main exception to these strictures is that the distance can be estimated from the relative intensity of the half-field and $g = 2$ regions for any case of two spin-$\frac{1}{2}$ species, regardless of the magnitude of the exchange, and without worrying about cavity Q, etc. Clearly, for systems to which it is applicable, this is the method of choice.

All of this chapter has dealt with cases in which the spin-spin interaction results in cw EPR line-shape changes. It has been emphasized that the exchange interactions that cause significant EPR line-shape changes are small relative to those that affect force measurements of magnetic susceptibility, and hence were once thought to be negligible. Another major step in sensitivity to spin-spin interaction is possible. The electron spin relaxation times are more sensitive to spin-spin interactions than is the cw line shape. As nonlinear and time-domain spectroscopy become more common, an ever more subtle view of biological structure and dynamics will become available. Most

applications of time-domain EPR to biological systems have focused on the detail obtainable about electron-nuclear interactions. Extension to electron-electron interactions is just beginning. Relaxation time measurements, largely neglected in many time-domain studies, are the next frontier in biological EPR. Indeed, if recent history is a guide, one might expect that the applications to metrical and dynamical aspects of biological systems will drive the development and accessibility of time-domain EPR.

REFERENCES

Abragam, A., and Bleaney, B., 1970, *Electron Paramagnetic Resonance of Transition Ions*, Clarendon Press, Oxford.

Behere, D. V., Birdy, R., and Mitra, S., 1981, Effect of axial interaction in high-spin iron(III) porphyrins. Paramagnetic anisotropy and zero-field splitting in (tetraphenylporphyrin)iron(III) thiocyanate and iodide, *Inorg. Chem.* **20**:2786–2789.

Belford, R. L., Davis, P. H., Belford, G. G., and Lenhardt, T. M., 1974, Computation of field-swept EPR spectra for systems with large interelectronic interactions, in *Extended Interactions between Metal Ions in Transition Metal Complexes*, pp. 40–50, ACS Symposium Series Number 5, American Chemical Society, Washington, D.C.

Bencini, A., and Gatteschi, D., 1982, The effect of antisymmetric exchange on the EPR spectra of coupled pairs of transition metal ions, *Mol. Phys.* **47**:161–169.

Bencini, A., DiVaira, M., Fabretti, A. C., Gatteschi, D., and Zanchini, C., 1984, Anisotropic exchange in transition-metal dinuclear complexes. 2. Crystal and molecular structure and EPR spectra of a dinuclear copper oxamidato complex, *Inorg. Chem.* **23**:1620–1623.

Bencini, A., Gatteschi, D., Reedijk, J., and Zanchini, C., 1985a, Anisotropic exchange in transition-metal dinuclear complexes. 4. (μ-benzotriazolato-N^1,N^3)bis[[tris(N^1-methylbenzimidazol-2-ylmethyl)amine-$N,N^3,N^{3'},N^{3''}$]copper(II)] trinitrate, *Inorg. Chem.* **24**:207–209.

Bencini, A., Gatteschi, D., Zanchini, C., and Haase, W., 1985b, Anisotropic exchange in transition-metal dinuclear complexes. 7. Bis[μ-2-(diethylamino)ethanolato]dibromodicopper(II), *Inorg. Chem.* **24**:3485–3486.

Bencini, A., Gatteschi, D., Zanchini, C., Haasnoot, J. G., Prins, R., and Reedijk, J., 1985c, EPR spectra of binuclear triazolato- and imidazolato-bridged copper(II) complexes including the four-copper form of bovine erythrocyte superoxide dismutase, *Inorg. Chem.* **24**:2812–2815.

Bencini, A., Gatteschi, D., and Zanchini, C., 1986, Anisotropic exchange in transition-metal dinuclear complexes. 8. Bis(μ-pyridine N-oxide)bis[dichloro(dimethyl sulfoxide)copper(II)], *Inorg. Chem.* **25**:2211–2214.

Berliner, L. J., 1980, Spin labels: historical overview and some future prospects in macromolecular research, in *Molecular Motion in Polymers by ESR* (R. F. Boyer and S. E. Keinath, eds.), Chap. 2, Michigan Molecular Institute Press, New York.

Bertrand, J. A., Fujita, E., and VanDerveer, D. G., 1980, Polynuclear complexes with hydrogen-bonded bridges. 4. Structure and magnetic properties of dinuclear copper(II) complexes of amino alcohols, *Inorg. Chem.* **19**:2022–2028.

Beth, A. H., Robinson, B. H., Cobb, C. E., Dalton, L. R., Trommer, W. E., Birktoft, J. J., and Park, J. H., 1984, Interactions and spatial arrangement of spin-labeled NAD^+ bound glyceraldehyde-3-phosphate dehydrogenase, *J. Biol. Chem.* **259**:9717–9728.

Blakley, R. L., Orme-Johnson, W. H., and Bozdech, J. M., 1979, Mechanism of lactobacillus leichmannii ribonucleotide reductase studied with Coα-[α-(aden-9-yl)]-Coβ-adenosylcobamide (pseudocoenzyme B_{12}) as coenzyme, *Biochemistry* **18**:2335–2339.

Boas, J. F., Hicks, P. R., and Pilbrow, J. R., 1978, Interpretation of electron spin resonance spectra due to some B_{12}-dependent enzyme reactions, *J. Chem. Soc., Faraday Trans. 2* **74**:417–431.

Boymel, P. M., Chang, J. R., DuBois, D. L., Greenslade, D. J., Eaton, G. R., and Eaton, S. S., 1977, Metal-nitroxyl interactions. 2. A resolved weak exchange electron paramagnetic resonance spectrum in solution, *J. Am. Chem. Soc.* **99**:5500-5502.

Boymel, P. M., Eaton, G. R., and Eaton, S. S., 1980a, Metal-nitroxyl interactions. 14. Bis(hexafluoroacetylacetonato)copper(II) adducts of spin-labeled pyridines, *Inorg. Chem.* **19**:727-735.

Boymel, P. M., Braden, G. A., Eaton, G. R., and Eaton, S. S., 1980b, Metal-nitroxyl interactions. 17. Spin-labeled adducts of bis(hexafluoroacetylacetonato)copper(II), *Inorg. Chem.* **19**:735-739.

Brière, P., Dupeyre, R.-M., Lemaire, H., Morat, C., Rassat, A., and Rey, P., 1965, Nitroxydes XVII: biradicaux stable du type nitroxyde, *Bull. Soc. Chim. Fr*:3290-3297.

Brown, T. G., and Hoffman, B. M., 1980, ^{14}N, ^{1}H, and metal ENDOR of single crystal Ag(II) (TPP) and Cu(II) (TPP), *Mol. Phys.* **39**:1073-1109.

Buettner, G. R., and Coffman, R. E., 1977, EPR Determination of the Co(II)-free radical magnetic geometry of the "doublet" species arising in a coenzyme B-12-enzyme reaction, *Biochim. Biophys. Acta* **480**:495-505.

Calcaterra, L. T., Closs, G. L., and Miller, J. R., 1983, Fast intramolecular electron transfer in radical ions over long distances across rigid saturated hydrocarbon spacers, *J. Am. Chem. Soc.* **105**:670-671.

Coffman, R. E., and Buettner, G. R., 1979a, A limit function for long-range ferromagnetic and antiferromagnetic superexchange, *J. Phys. Chem.* **83**:2387-2392.

Coffman, R. E., and Buettner, G. R., 1979b, General magnetic dipolar interaction of spin-spin coupled molecular dimers. Application to the EPR spectrum of xanthine oxidase, *J. Phys. Chem.* **83**:2392-2400.

Coffman, R. E., and Pezeshk, A., 1985, ESR rigid-lattice lineshapes for a three-electronic-spin system. A triradical or 'three-spin label', *J. Magn. Reson.* **65**:62-81.

Coffman, R. E., and Pezeshk, A., 1986, Analytical considerations of Eaton's formula for the interspin distance between unpaired electrons in ESR, *J. Magn. Reson.* **70**:21-33.

Dalal, D. P., Eaton, S. S., and Eaton, G. R., 1981, The effects of lossy solvents on quantitative EPR studies, *J. Magn. Reson.* **44**:415-428.

Damoder, R., More, K. M., Eaton, G. R., and Eaton, S. S., 1983a, Metal-nitroxyl interactions. 30. Single-crystal EPR spectra of two spin-labeled copper porphyrins, *J. Am. Chem. Soc.* **105**:2147-2154.

Damoder, R., More, K. M., Eaton, G. R., and Eaton, S. S., 1983b, Metal-nitroxyl interactions. 31. Single-crystal EPR spectra of a spin-labeled vanadyl porphyrin, *Inorg. Chem.* **22**:2836-2841.

Damoder, R., More, K. M., Eaton, G. R., and Eaton, S. S., 1983c, Metal-nitroxyl interactions. 33. Single-crystal EPR spectra of two spin-labeled silver porphyrins, *Inorg. Chem.* **22**:3738-3744.

Dixon, W. T., 1972, *Theory and Interpretation of Magnetic Resonance Spectra*, pp. 117-120, Plenum Press, New York/London.

Dreyer, J.-L., Beinert, H., Keana, J. F. W., Hankovsky, O. H., Hideg, K., Eaton, S. S., and Eaton, G. R., 1983, A spin-label study of the disposition of the Fe-S cluster with respect to the active center of aconitase, *Biochim. Biophys. Acta* **745**:229-236.

DuBois, D. L., Eaton, G. R., and Eaton, S. S., 1979a, Metal-nitroxyl interactions. 8. Exchange interactions in a spin-labeled copper complex (3-(*N*-(3-2,2,5,5-tetramethylpyrroline-1-oxyl)-amido)-4,9-dimethyl-5,8-diazadodeca-4,8-diene-2,11-dione)copper(II), *J. Am. Chem. Soc.* **101**:2624-2627.

DuBois, D. L., Eaton, G. R., and Eaton, S. S., 1979b, Metal-nitroxyl interactions. 9. Electron-electron coupling in the copper complex (3-(*N*-(2,2,5,5-tetramethylpyrrolin-3-yl-1-oxy)-amido)-4,10-dimethyl-5,9-diazatrideca-4,9-diene-2,12-dione)copper(II), *Inorg. Chem.* **18**:75-79.

Dunhill, R. H., and Symons, M. C. R., 1968, Triplet state E.S.R. spectra of vanadyl tartrate chelates in aqueous solution, *Mol. Phys.* **15**:105-107.

Dwek, R. A., Levy, H. R., Radda, G. K., and Seeley, P. J., 1975, Spin label and lanthanide binding sites on glyceraldehyde-3-phosphate dehydrogenase, *Biochim. Biophys. Acta* **377**:26-33.

Eaton, S. S., and Eaton, G. R., 1979, EPR measurement of the rate of ligand exchange in copper salicylaldimine complexes, *Inorg. Nucl. Chem. Lett.* **15**:29-31.

Eaton, S. S., and Eaton, G. R., 1980, Signal area measurements in EPR, *Bull. Magn. Reson.* **1**:130-138.

Eaton, S. S., and Eaton, G. R., 1982, Measurement of spin-spin distances from the intensity of the EPR half-field transition, *J. Am. Chem. Soc.* **104**:5002-5003.

Eaton, S. S., and Eaton, G. R., 1987, Interaction of spin labels with transition metals, part 2, *Coord. Chem. Rev.*, **83**:29-72.

Eaton, S. S., DuBois, D. L., and Eaton, G. R., 1978, Metal-nitroxyl interactions. 6. Analysis of EPR spectra of spin-labeled copper complexes, *J. Magn. Reson.* **32**:251-263.

Eaton, S. S., Law, M. L., Peterson, J., Eaton, G. R., and Greenslade, D. J., 1979, Metal-nitroxyl interactions. 7. Quantitative aspects of EPR spectra resulting from dipolar interactions, *J. Magn. Reson.* **33**:135-141.

Eaton, S. S., More, K. M., DuBois, D. L., Boymel, P. M., and Eaton, G. R., 1980, Metal-nitroxyl interactions. 15. Comparison of EPR spectra at X band and Q band, *J. Magn. Reson.* **41**:150-157.

Eaton, S. S., More, K. M., Sawant, B. M., Boymel, P. M., and Eaton, G. R., 1983a, Metal-nitroxyl interactions. 29. EPR studies of spin-labeled copper complexes in frozen solution, *J. Magn. Reson.* **52**:435-449.

Eaton, S. S., More, K. M., Sawant, B. M., and Eaton, G. R., 1983b, Use of the EPR half-field transition to determine the interspin distance and the orientation of the interspin vector in systems with two unpaired electrons, *J. Am. Chem. Soc.* **105**:6560-6567.

Eaton, S. S., Boymel, P. M., Sawant, B. M., More, J. K., and Eaton, G. R., 1984, Metal-nitroxyl interactions. 32. Spin-spin splitting in EPR spectra of spin-labeled pyridine adducts of a cobalt(II) porphyrin in frozen solution, *J. Magn. Reson.* **56**:183-199.

Eaton, S. S., Eaton, G. R., and Chang, C. K., 1985, Synthesis and geometry determination of cofacial diporphyrins. EPR spectroscopy of dicopper diporphyrins in frozen solution, *J. Am. Chem. Soc.* **107**:3177-3184.

Eckberg, R. P., Henry, R. A., Cary, L. W., and Nelson, J. H., 1977a, Reactions of copper(II) and nickel(II) β-keto imine complexes, *Inorg. Chem.* **16**:2977-2979.

Eckberg, R. P., Nelson, J. H., Kenney, J. W., and Howells, P. N., 1977b, Reaction of bis(2,4-pentanedionato)nickel(II) with isocyanates and other electrophiles. Electrophilic addition to 2,4-pentanedione catalyzed by $Ni(acac)_2$, *Inorg. Chem.* **16**:3128-3132.

Ferruti, P., Gill, D., Klein, M. P., Wang, H. H., Entine, G., and Calvin, M., 1970, Synthesis of mono-, di-, and polynitroxides. Classification of electron spin resonance spectra of flexible dinitroxides dissolved in liquids and glasses, *J. Am. Chem. Soc.* **92**:3704-3713.

Fielding, L., More, K. M., Eaton, G. R., and Eaton, S. S., 1986a, Metal-nitroxyl interactions. 46. EPR spectra of low-spin iron(III) complexes of spin-labeled tetraphenylporphyrins and their implications for the interpretation of EPR spectra of spin-labeled cytochrome P450, *J. Am. Chem. Soc.* **108**:618-625.

Fielding, L., More, K. M., Eaton, G. R., and Eaton, S. S., 1986b, Metal-nitroxyl interactions. 51. Collapse of the iron-nitroxyl electron-electron spin-spin splitting due to the increase in the electron spin relaxation rate for high-spin iron(III) when temperature is increased, *J. Am. Chem. Soc.* **108**:8194-8196.

Fielding, L., More, K. M., Eaton, G. R., and Eaton, S. S., 1987, Metal-nitroxyl interactions. 50. EPR spectra of high-spin iron(III) in complexes of spin-labeled tetraphenylporphyrins in fluid solution, *Inorg. Chem.* **27**:856-861.

Francesconi, L. C., Corbin, D. R., Clauss, A. W., Hendrickson, D. N., and Stucky, G. D., 1981, Binuclear dicyclopentadienyltitanium(III) complexes: Magnetic exchange interactions propagated by the methylene groups of aliphatic dicarboxylic acid dianions, *Inorg. Chem.* **20**:2059-2069.

George, G. N., 1984, Coupling between Mo(V) and reduced Fe/S 1 centres in aldehyde oxidase and xanthine oxidase, in *Flavins and Flavoproteins* (R. C. Bray, P. C. Engel, and S. G. Mayhew, eds.), pp. 325-330, Walter de Gruyter and Co., Berlin, West Germany.

Ghanekar, V. D., Lin, R. J., Coffman, R. E., and Blakley, R. L., 1981, Detection by electron spin resonance of an exchange-coupled cob(II)alamin . . . free radical pair species generated by anaerobic photolysis of polycrystalline adenosylcobalamin, *Biochem. Biophys. Res. Commun.* **101**:215-221.

Glarum, S. H., and Marshall, J. H., 1967, Spin exchange in nitroxide biradicals, *J. Chem. Phys.* **47**:1374-1378.

Goldberg, I. B., and Bard, A. J., 1983, Electron-spin resonance spectroscopy, in *Treatise on Analytical Chemistry* (J. Elving, ed.), Pt. 1, Vol. 10, pp. 226-289, 2nd edn., Wiley, New York.

Griffin, B. W., Smith, S. M., and Peterson, J. A., 1974, *Pseudomonas putida* cytochrome P-450. Binding of a spin-labeled analog of the inhibitor metyrapone, *Arch. Biochem. Biophys.* **160**:323-332.

Griffin, B. W., Peterson, J. A., Werringloer, J., and Estabrook, R. W., 1975, Chemistry of soluble and membrane-bound cytochrome P-450, *Ann. N.Y. Acad. Sci.* **244**:107-131.

Grigor'ev, I. A., Dikanov, S. A., Shchukin, G. I., Volodarskii, L. B., and Tsvetkov, Yu. D., 1982, Influence of the N-oxide group in biradicals of the imidazoline series on the intramolecular spin exchange over systems of conjugated bonds, *Zh. Strukt. Khim.* **23**(6):59-65; pp. 870-875 in transl.

Harris, R. K., 1983, *Nuclear Magnetic Resonance Spectroscopy*, p. 226, Pitman, London.

Hay, P. J., Thibeault, J. C., and Hoffmann, R., 1975, Orbital interactions in metal dimer complexes, *J. Am. Chem. Soc.* **97**:4884-4899.

Heitele, H., and Michel-Beyerle, H., 1985, Electron transfer through aromatic spacers in bridged electron-donor-acceptor molecules, *J. Am. Chem. Soc.* **107**:8286-8288.

Hyde, J. S., and Sarna, T., 1978, Magnetic interactions between nitroxide free radicals and lanthanides or Cu(II) in liquids, *J. Chem. Phys.* **68**:4439-4447.

Hyde, J. S., Swartz, H. M., and Antholine, W. E., 1979, The spin-probe-spin-label method, in *Spin Labeling II* (L. J. Berliner, ed.), pp. 71-113, Academic Press, New York.

Isied, S. S., and Vassilian, A., 1984, Electron transfer across polypeptides. 3. Oligoproline bridging ligands, *J. Am. Chem. Soc.* **106**:1732-1736.

James, P. G., and Luckhurst, G. R., 1970, The electron resonance spectra of exchange coupled vanadyl ions, *Mol. Phys.* **18**:141-144.

Kahn, O., 1985a, Orbital mechanism of the exchange interaction, in *Magneto-Structural Correlations in Exchange Coupled Systems* (R. D. Willett, D. Gatteschi, and O. Kahn, eds.), pp. 37-56, Reidel, Dordrecht.

Kahn, O., 1985b, Dinuclear complexes with predictable magnetic properties, *Angew. Chem., Int. Ed. Engl.* **24**:834-850.

King, F. W., 1976, Long-range proton hyperfine coupling, *Chem. Rev.* **76**:157-186.

Klein, C. L., O'Connor, C. J., Majeste, R. J., and Trefonas, L. M., 1982, Magnetic properties and molecular structure of complexes of substituted pyrazine ligands coordinated to iron(II) and copper(II). Low dimensional antiferromagnetic interactions in diaquabis(pyrazinecarboxylato)iron(II), *J. Chem. Soc., Dalton Trans.*:2419-2423.

Kokorin, A. I., and Formazyuk, 1981, New method of measuring distances between spin label and paramagnetic metal ions in macromolecules, *Molek. Biol.* **15**:930-938; pp. 722-728 in transl.

Kokorin, A. I., Zamarayev, K. I., Grigoryan, G. L., Ivanov, V. P., Rozantsev, E. G., 1972, Measurement of the distances between the paramagnetic centres in solid solutions of nitroxide radicals, biradicals, and spin-labeled proteins, *Biofizika* **17**:34-41; pp. 31-39 in transl.

Kokorin, A. I., Pavlikov, V. V., and Shapiro, A. B., 1980, Electron spin exchange in rigid nitroxide radicals of the acetylene series, *Dokl. Akad. Nauk SSSR* **253**:147–149; pp. 525–527 in transl.

Kokorin, A. I., Novozhilova, G. A., and Shapiro, A. B., 1981, Spin exchange in nitroxide biradicals with polyeneazomethine and polyeneazine bridges, *Izv. Akad. Nauk SSSR, Ser. Khim.*:286–290; pp. 215–219 in transl.

Krasicky, P. D., Scott, S. C., Silsbee, R. H., and Ritter, A. L., 1978, ESR of exchange coupled pairs in the dimer di-μ-diphenylphosphinatoacetylacetonatochromium(III) (DPACr), *J. Phys. Chem. Solids* **39**:991–998.

Kreilick, R. W., 1973, NMR studies of organic radicals, in *NMR of Paramagnetic Molecules* (G. N. La Mar, W. DeW. Horrocks, Jr., and R. H. Holm, eds.), pp. 595–641, Academic Press, New York.

Kulikov, A. V., Likhtenshtein, G. I., Rozantsev, E. G., Suskina, V. I., and Shapiro, A. B., 1972, Possibility of determining the distances between the functional groups of protein by the method of paramagnetic labels, *Biofizika* **17**:42–48; pp. 40–47 in transl.

La Mar, G. N., Horrocks, W. DeW., Jr., and Holm, R. H., 1973, *NMR of Paramagnetic Molecules*, Academic Press, New York.

Lambert, S. L., Felthouse, T. R., and Hendrickson, D. N., 1978, Magnetic properties of a phosphate-bridged copper(II) dimer, *Inorg. Chim. Acta* **29**:L223–L224.

Leigh, J. S., 1970, ESR rigid-lattice line shape in a system of two interacting spins, *J. Chem. Phys.* **52**:2608–2612.

Lowe, D. J., and Bray, R. C., 1978, Magnetic coupling of the molybdenum and iron–sulfur centres in xanthine oxidase and xanthine dehydrogenases, *Biochem. J.* **169**:471–479.

Lowe, D. J., Lynden-Bell, R. M., Bray, R. C., 1972, Spin–spin interaction between molybdenum and one of the iron–sulfur systems of xanthine oxidase and its relevance to the enzymic mechanism, *Biochem. J.* **130**:239–249.

Luckhurst, G. R., and Pedulli, G. F., 1970, Interpretation of biradical electron resonance spectra, *J. Am. Chem. Soc.* **92**:4738–4739.

Luckhurst, G. R., 1976, Biradicals as spin probes, in *Spin Labeling: Theory and Applications* (L. J. Berliner, ed.), Volume 1, pp. 133–181, particularly Figure 4 and equation 49, Academic Press, New York.

Mallory, F. B., Mallory, C. W., and Ricker, W. M., 1985, Nuclear spin–spin coupling via non-bonded interactions. 4. F–F and H–F coupling in substituted benzo[*c*]phenanthrenes, *J. Org. Chem.* **50**:457–461.

Mao, C. R., and Kreilick, R. W., 1976, Exchange and dipolar interactions in solid organic radicals—nitroxide, verdazyl, and hydrazyl, *Mol. Phys.* **31**:1447–1455.

Mayo, S. L., Ellis, W. R., Jr., Crutchley, R. J., and Gray, H. B., 1986, Long-range electron transfer in heme proteins, *Science* **233**:948–952.

McConnell, H. M., 1960, Theory of singlet-triplet splittings in large biradicals, *J. Chem. Phys.* **33**:115–121.

McNally, J. M., and Kreilick, R. W., 1981, Measurement of nuclear and electron spin relaxation times by magic angle spin locking experiments: Electron spin relaxation in copper Tutton salt, *Chem. Phys. Lett.* **79**:534–540.

Michon, J., Michon, P., and Rassat, A., 1978, Nitroxydes: utilisation de biradicaux nitroxydes comme sonde de distances, *Nouv. J. Chim.* **2**:619–624.

Mock, D. M., Bruno, G. V., Griffin, B. W., and Peterson, J. A., 1982, Low temperature EPR spectroscopic characterization of the interaction of cytochrome P-450$_{cam}$ with a spin label analog of metyrapone, *J. Biol. Chem.* **257**:5372–5379.

More, K. M., Eaton, S. S., and Eaton, G. R., 1981a, Metal-nitroxyl interactions 19. Spin-labeled derivatives of copper *meso*-tetraphenyl-1-(3-acrylic acid) porphyrin, *Inorg. Chem.* **20**:2641–2647.

More, K. M., Eaton, S. S., and Eaton, G. R., 1981b, Metal-nitroxyl interactions. 20. Electron paramagnetic resonance spectra of spin-labeled vanadyl and silver porphyrins, *J. Am. Chem. Soc.* **103**:1087–1090.

More, K. M., Sawant, B. M., Eaton, G. R., and Eaton, S. S., 1981c, Metal-nitroxyl interactions. 22. Copper-nitroxyl spin-spin interaction as a probe of weak orbital overlaps in derivatives of copper tetraphenylporphyrin, *Inorg. Chem.* **20**:3354-3362.

More, K. M., Eaton, G. R., and Eaton, S. S., 1982a, Metal-nitroxyl interactions 25. Exchange interaction via saturated linkages in spin-labeled porphyrins, *Can. J. Chem.* **60**:1392-1401.

More, J. K., More, K. M., Eaton, G. R., and Eaton, S. S., 1982b, Metal-nitroxyl interactions 26. Impact of an additional atom in the metal-nitroxyl linkage on the magnitude of electron-electron spin-spin coupling constants in spin-labeled pyridine adducts of vanadyl and copper(II) bis(β-diketonates), *Inorg. Chem.* **21**:2455-2460.

More, K. M., Eaton, G. R., and Eaton, S. S., 1983, Metal-nitroxyl interactions 27. Comparison of electron-electron spin-spin coupling constants for urea and amide linkages in spin-labeled copper porphyrins, *Inorg. Chem.* **22**:934-939.

More, K. M., Eaton, G. R., and Eaton, S. S., 1984a, Metal-nitroxyl interactions 41. Comparison of electron-electron spin-spin interactions in spin-labeled silver porphyrins in fluid solution, frozen solution, and on imbiber beads, *Inorg. Chem.* **23**:4084-4087.

More, J. K., More, K. M., Eaton, G. R., and Eaton, S. S., 1984b, Metal-nitroxyl interactions. 39. Electron-electron spin-spin splitting in the EPR spectra of nitroxyl spin-labeled Mn(II) complexes in fluid solution, *J. Am. Chem. Soc.* **106**:5395-5402.

More, K. M., Eaton, G. R., and Eaton, S. S., 1984c, Metal-nitroxyl interactions 40. EPR spectra of spin-labeled copper(II) and vanadyl complexes immobilized on imbiber beads, *J. Magn. Reson.* **59**:497-505.

More, K. M., Eaton, G. R., and Eaton, S. S., 1985, Metal-nitroxyl interactions. 42. Spin-spin interaction in frozen solution EPR spectra of spin-labeled Mn(II) complexes, *J. Magn. Reson.* **63**:151-167.

More, K. M., Eaton, G. R., and Eaton, S. S., 1986a, Metal-nitroxyl interactions 47. EPR spectra of two spin-labeled derivatives of EDTA coordinated to paramagnetic metal ions, *Inorg. Chem.* **25**:2638-2646.

More, K. M., Eaton, G. R., Eaton, S. S., and Hideg, K., 1986b, Metal-nitroxyl interactions. 48. EPR spectra of spin-labeled pyridines coordinated to chromium(III) tetraphenylporphyrin chloride ($S = 3/2$) and comparison of the electron-electron exchange interaction with analogous complexes with metal $S = 1/2$, *Inorg. Chem.* **25**:3865-3869.

Moriya, T., 1960, Anisotropic superexchange interaction and weak ferromagnetism, *Phys. Rev.* **120**:91-98.

Nepveu, F., Gehring, S., and Walz, L., 1986, Exchange interaction via hydrogen bridges in dimeric copper(II) complexes—a theoretical analysis, *Chem. Phys. Lett.* **128**:300-304.

O'Connor, C. J., Freyberg, D. P., and Sinn, E., 1979, Relation between structure and magnetic exchange interactions in the mixed metal complexes bis(hexafluoroacetylacetonato)[*N,N'*-ethylenebis[2-hydroxypropiophenone iminato-*N,O*(2-)]copper(II)]M'(II), Cu((prp)$_2$en)M'(hfa)$_2$, where M' = Cu, Ni, and Mn. Crystal structures of the complexes (M((prp)$_2$en)M'(hfa)$_2$), where M = Cu and Ni and M' = Cu, Co, and Mn, *Inorg. Chem.* **18**:1077-1088.

Owen, J., and Harris, E. A., 1972, Pair spectra and exchange interactions, in *Electron Paramagnetic Resonance* (S. Geschwind, ed.), pp. 427-492, Plenum Press, New York.

Ozarowski, A., and Reinen, D., 1986, Anisotropic exchange interactions in the copper(II) and vanadium(IV) dimers [(L')Cu(μ-OH)$_2$Cu(L')](ClO$_4$)$_2$ and [(L)VO(μ-OH)$_2$VO(L)]Br$_2$ with 1,4,7-triazacyclononane (L) and its *N,N',N''*-trimethyl derivative (L'): a single-crystal EPR study, *Inorg. Chem.* **25**:1704-1708.

Parmon, V. N., Kokorin, A. I., and Zhidomirov, G. M., 1977, Conformational structure of nitroxide biradicals: Use of biradicals as spin probes, *Zh. Strukt. Khim.* **18**:132-177; pp. 104-147 in transl.

Peterson Kennedy, S. E., McGourty, J. L., Kalweit, J. A., and Hoffman, B. M., 1986, Temperature dependence of and ligation effects on long-range electron transfer in complementary [Zn,Fe(III)]hemoglobin hybrids, *J. Am. Chem. Soc.* **108**:1739-1746.

Pezeshk, A., and Coffman, R. E., 1985, A new electron spin resonance spectrum for an exchange and dipole-dipole coupled superoxocobalamin . . . free-radical pair occurring in adenosylcobalamin-containing systems, *J. Chem. Soc., Dalton Trans.*: 891-893.

Pilbrow, J. R., 1982, EPR of B_{12}-dependent enzyme reactions and related systems, in B_{12} (D. Dolphin, ed.), Vol. 1, pp. 431-462, Wiley, New York.

Pirrwitz, J., Lassmann, G., Rein, H., Janig, G.-R., Pecar, S., and Ruckpaul, K., 1979a, Stereochemical properties of the binding site of liver microsomal cytochrome P-450 as studied by substrate analogous spin labels, *Acta. Biol. Med. Germ.* **38**:235-247.

Pirrwitz, J., Rein, H., Lassmann, G., Janig, G. R., Pecar, S., and Ruckpaul, K., 1979b, Spin-labeled isocyanides as stereochemical probes for the active center of cytochrome P-450, *FEBS Lett.* **101**:195-200.

Randolph, M. L., 1972, Quantitative considerations in electron spin resonance studies of biological materials, in *Biological Applications of Electron Spin Resonance* (H. M. Swartz, J. R. Bolton, and D. C. Borg, eds.), pp. 119-153, Wiley, New York.

Reichman, L. M., Annaev, B., and Rozantzev, E. G., 1972, Studies of microsomal cytochrome P-450 with isocyanide spin label, *Biochim. Biophys. Acta* **263**:41-51.

Ruf, H. H., Nastainczyk, W., and Ullrich, H., 1974, Interactions of microsomal cytochrome P-450 with ligand spin labels, in *6th Int. Conf. on Magnetic Resonance in Biological Systems*, abstract C14.

Sawant, B. M., Shroyer, A. L. W., Eaton, G. R., and Eaton, S. S., 1982, Metal-nitroxyl interactions 24. Electron spin delocalization in vanadyl and copper(II) bis(β-diketonates), *Inorg. Chem.* **21**:1093-1101.

Schepler, K. L., Dunham, W. R., Sands, R. H., Fee, J. A., and Abeles, R. H., 1975, A physical explanation of the EPR spectrum observed during catalysis by enzymes utilizing coenzyme B_{12}, *Biochim. Biophys. Acta* **397**:510-518.

Scott, J. C., Garito, A. F., Heeger, A. J., Nannelli, P., and Gillman, H. D., 1975, Magnetic properties of poly(metal phosphinates): the effects of structural disorder on one-dimensional antiferromagnetic chains, *Phys. Rev. B* **12**:356-361.

Scullane, M. I., White, L. K., and Chasteen, N. D., 1982, An efficient approach to computer simulation of EPR spectra of high-spin iron(III) in rhombic ligand fields, *J. Magn. Reson.* **47**:383-397.

Smith, P. H., Eaton, G. R., and Eaton, S. S., 1984, Metal-nitroxyl interactions. 38. Effect of the nickel-nitroxyl linkage on the electron-electron spin-spin interaction in fluid and frozen solution, *J. Am. Chem. Soc.* **106**:1986-1991.

Spiro, C. L., Lambert, S. L., Smith, T. J., Duesler, E. N., Gagne, R. P., and Hendrickson, D. N., 1981, Binuclear complexes of macrocyclic ligands: variation of magnetic exchange interaction in a series of six-coordinate iron(II), cobalt(II), and nickel(II) complexes and the x-ray structure of a binuclear iron(II) macrocyclic ligand complex, *Inorg. Chem.* **20**:1229-1237.

Srivastava, T. S., 1980, Gadolinium(III) myoglobin: interaction of gadolinium(III) mesoporphyrin IX with apomyoglobin, *Curr. Sci.* **49**:429-430.

Thomson, C., 1968, Electron spin resonance studies of the triplet state, *Q. Rev. Chem. Soc.* **22**:45-74.

Toriyama, K., Nunome, K., and Iwasaki, M., 1981, σ-delocalized radical cations $[H(CH_2)_nH]^+$ of primary alkanes: ESR evidence, *J. Phys. Chem.* **85**:2149-2150.

8

Spin-Label Oximetry

James S. Hyde and Witold K. Subczynski

1. INTRODUCTION

Molecular oxygen is paramagnetic and gives strong EPR signals in the gas phase. At sufficiently low pressure the number of observed lines is large indeed (see Figure 1 obtained at 180 micron pressure). Tinkham and Strandberg (1955a, 1955b) developed the theory for the spectrum of molecular oxygen and were able to assign 120 lines observed at X-band. As the pressure increases, the linewidths increase greatly. Even at atmospheric pressure, intense EPR signals can be detected from molecular oxygen (Figure 2). However, to the authors' best knowledge no EPR spectra have been reported from oxygen dissolved in fluids near room temperature. Apparently lines are so broadened as to be undetectable. Thus there seems to be no possibility for the *direct* detection of oxygen in biological systems using magnetic resonance techniques. However, an indirect method does exist and is the subject of this chapter. Bimolecular collisions of oxygen with free radicals (and we consider particularly spin labels) alter the resonance characteristics of the radical. As will become apparent, it is a remarkable fact that effects can be detected at dissolved oxygen concentrations as low as 10^{-7} M in a measurement that requires only a few seconds. This method has been called "spin-label oximetry." The National Biomedical ESR Center has been active in the development of the field. A rigorous foundation has been laid down, and it is believed that the method can be applied with confidence to a wide range of biological systems.

The concentration of oxygen in air-saturated water at 37 °C is 6.8 mg liter^{-1} (2.1×10^{-4} M). Thus the dynamic range of spin-label oximetry as applied to the biological systems is a factor of 2.1×10^3.

The method of spin-label oximetry to measure oxygen transport has a close analogy with methods that depend on quenching of fluorescence by oxygen. See Lakowicz (1982) for an overview.

James S. Hyde • National Biomedical ESR Center, Department of Radiology, Medical College of Wisconsin, Milwaukee, Wisconsin 53226 **Witold K. Subczynski** • Department of Biophysics, Institute of Molecular Biology, Jagiellonian University, Krakow, Poland.

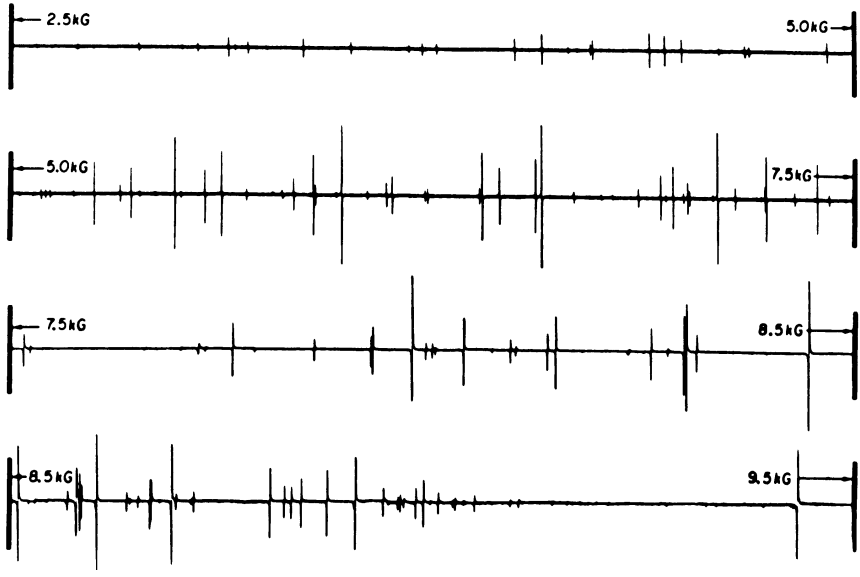

Figure 1. EPR spectrum of molecular oxygen at 180 micron Hg pressure. The microwave frequency was 9.265 GHz.

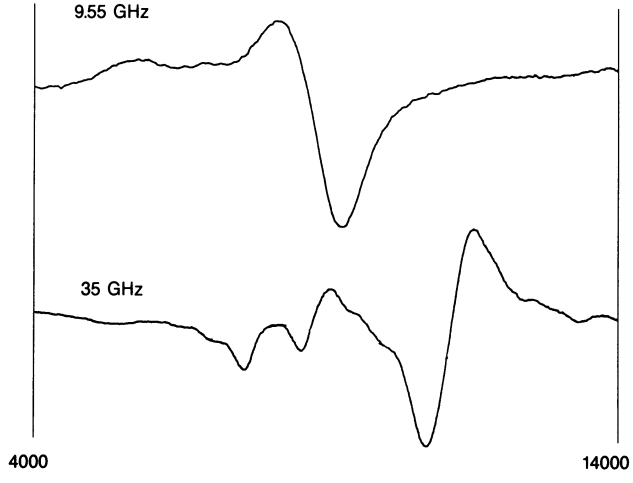

Figure 2. EPR spectrum of molecular oxygen in air.

We review briefly the early history of spin-label oximetry. In 1960 independent reports of the effect of oxygen on EPR spectra of organic free radicals by Deguchi and by Hausser appeared. Edelstein *et al.* (1964) attributed the effect without discussion to liquid-phase Heisenberg exchange between oxygen and free radical, referring to the theoretical paper of Pake and Tuttle (1959), which discusses Heisenberg exchange between free radicals in solution. Povich (1975a, 1975b) seems first to have pointed out that the effect could be useful in studying oxygen transport in various systems using spin labels, and Backer *et al.* (1977) emphasized applications of spin-label oximetry to biological systems. The first rigorous spin-label oximetric study seems to be that of Windrem and Plachy (1980) who were concerned with oxygen transport in membranes.

These citations are relevant to the effects of oxygen on linewidth. Very early, Ingalls and Pearson (1961) suggested that the effect of oxygen on the cw saturation characteristics of a free radical could be used for analytical purposes. Our group at the National Biomedical ESR Center is largely responsible for development and applications of T_1 sensitive methods of spin-label oximetry (Popp and Hyde, 1981; Subczynski and Hyde, 1981).

2. PHYSICS

2.1. Bimolecular Collisions

The Smoluchowski equation forms the basis of spin-label oximetry:

$$\omega = 4\pi R\{D(\mathrm{SL}) + D(O_2)\}[\mathrm{O_2}] \tag{1}$$

This equation expresses the frequency of collisions of molecular oxygen with a given spin label. The concentration of spin labels does not appear in the equation. The Smoluchowski equation was originally derived from Fick's second law in an isotropic continuum. It is a "hard sphere" or billiard ball theory. When molecules approach to an interaction distance R, a collision is said to occur.

In order to measure ω, an experimental observable is needed. One then introduces the factor $p(x)$ in equation (1), so that the equation assumes the form

$$\omega = 4\pi Rp(x)\{D(\mathrm{SL}) + D(\mathrm{O_2})\}[\mathrm{O_2}] \tag{2}$$

Here $p(x)$ is the probability that an observable event occurs if a collision does in fact occur. Each observable, x, can be expected generally to have its own p. An impressive body of literature has accumulated to support the assumption that for Heisenberg exchange between spin labels and molecular oxygen, $p = 1$. It is this fact that is responsible for making the method quantitative.

It is customary to argue that the diffusion constant of oxygen $D(\mathrm{O_2}) \gg D(\mathrm{SL})$, where $D(\mathrm{SL})$ is the diffusion constant of the spin label. This assumption should always be considered critically, but if it can be made, then an experimental observable that depends on ω yields the so-called diffusion-concentration product of oxygen, $D(\mathrm{O_2})[\mathrm{O_2}]$.

If a medium is employed that is homogeneous, such as water, the diffusion constant may be available from the literature. In that case, the method yields $[O_2]$. Or if oxygen is produced or consumed one can obtain $[O_2](t)$.

It should be noted that data on diffusion of oxygen is remarkably sparse. Himmelblau (1964) reviewed the subject and Windrem and Plachy (1980) provide a search of the literature through 1977. We have found no classical data based on Fick's second law for diffusion of oxygen in long-chain hydrocarbons. St.-Denis and Fell (1971) collected all data through 1971 on diffusivity of oxygen in water. The scatter was surprisingly great for such an important and fundamental quantity. At 25 °C, $D[O_2]$ varied from 1.8 to 2.6×10^{-5} cm^2 s^{-1}. Twenty-three papers using eleven different methods were cited.

Sometimes a distinction is made between values of $D(O_2)$ obtained from measurements of diffusion against a concentration gradient (macroscopic diffusion) and measurements from the Smoluchowski equation (self-diffusion). But in our experience agreement is easily forced in homogeneous fluids by making reasonable assumptions for R (4 to 5 Å), and the distinction is not necessary.

Numerous theoretical refinements of the Smoluchowski equation have been developed. Nemzek and Ware (1975) provide key citations in the Introduction to their paper on fluorescence quenching. A complaint in their paper is that experimental tests of various diffusion models have lagged badly behind the theory.

The reader is advised to proceed with caution in application of the Smoluchowski equation in heterogeneous or anisotropic media. Probes may not sample space in a uniform manner, the interaction distance R can be anisotropic (Nemzek and Ware, 1975), and the diffusion constant $D(O_2)$ is of course a tensor. The methods of spin-label oximetry will reliably give the bimolecular collision rate, but inferences on concentration and diffusion separately (i.e., not the product) can only be drawn with confidence in isotropic media.

2.2. Magnetic Interactions

The monograph by Molin *et al.* (1980) is the authoritative theoretical source for Heisenberg exchange in liquids including the situation at hand, namely, inequivalent exchanging species, one of which is presumed to have an exceptionally short spin-lattice relaxation time. See also Pake and Tuttle (1959). The following considerations enter into the theory.

Let J be the exchange integral, τ_c the time two particles are in contact (i.e., the translational correlation time), δ the difference in energy of the spin states of the colliding particles, and T_1 the spin-lattice relaxation time of the fast relaxing species. Various combinations of these four parameters result in different conditions, as described in Tables 1 and 2 of Salikhov *et al.* (1971). However, since T_1 and J are not known, δ varies over an enormous range (Figure 1), and τ_c can only be estimated; detailed experimental verification of the theory remains lacking.

The distinction is not explicitly made by these workers of the possible difference in p between EPR observables that depend on the spin-lattice relaxation time T_1 and those that depend on the transverse relaxation time T_2. Primarily they consider line-broadening (i.e., T_2-type) observables. Saturation is an alternative observable that occurs when there is an exchange of z components of magnetization. If one of the

exchanging species has a short spin-lattice relaxation time, Heisenberg exchange events provide a coupling to the lattice and make effective contributions to spin-lattice relaxation of the slow relaxer. This mechanism was pointed out by Hyde and Sarna (1978) and developed in mathematical detail by Yin and Hyde (1987b). As shown by Salikhov *et al.* (1971), there can exist exchange processes involving loss of phase coherence that do not involve exchange of S_z components. Thus it is theoretically possible that $p(T_1 \text{ observable}) \neq p(T_2 \text{ observable})$.

And, in fact, such is the case. Figure 3 from unpublished work by the authors shows a plot of the ratio of $p(T_1)/p(T_2)$ from saturation-recovery and linewidth data in the presence of oxygen for a wide variety of labels and viscosities. Absolute values of ω [equation (2)] were obtained by both methods, and the ratio plotted.

At high viscosities, dipole-dipole broadening of lines because of interaction between spin labels and oxygen occurs in some but not all solvents. The ratio varies between $\frac{2}{3}$ and 2 over a wide range of conditions where Heisenberg exchange can be expected to be the dominant intermolecular mechanism. These factors seem generally consistent with factors predicted by the theory, but a detailed experimental check of the theory has not yet been carried out.

The main point from Figure 3 is that the statistical factor is indeed about the same for both methods of observation over a wide range of conditions. It can also very easily be shown that it is about 1 using known values of $D(O_2)$ and $[O_2]$ and assuming an interaction distance R of 4–5 Å. For example, Hyde and Subczynski (1984) measured the absolute value of ω [equation (2)] by determining the broadening of EPR lines, assumed $R = 4.5$ Å and $p = 1$, and introduced Hitchman's (1978) data for oxygen concentration. They calculated a value for the diffusion constant of oxygen in water at 37 °C of

$$D(O_2, 37\,°C) = 2.8 \times 10^{-5}\ \text{cm}^2\ \text{s}^{-1}$$

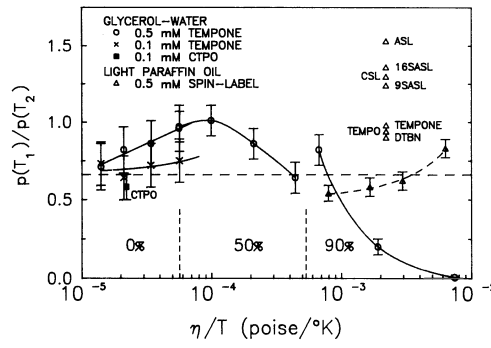

Figure 3. Ratio of probabilities [equation (2)] that an observable event occurs when a collision occurs for saturation recovery [$p(T_1)$] and line broadening [$p(T_2)$]. Spin labels were TEMPONE (**2**), CTPO (**12**), ASL (**9**), CSL (**8**), TEMPO (**1**), DTBN (**3**), 9-SASL (**5**), and 16-SASL (**7**). Open triangles in light paraffin oil; other data points in glycerol-water as indicated. Various combinations of temperature and glycerol-water mixture were used to arrive at the indicated values of η/T. The dotted TEMPONE curve was obtained using the low-field line of perdeutero ^{15}N-TEMPONE; the single TEMPONE point in the right upper portion of the figure was obtained on the central line of a protonated ^{14}N spin label. An unidentified systematic error probably associated with line-shape differences accounts for the failure of this point to coincide with the dotted curve. The dotted horizontal line is drawn at $\frac{2}{3}$, a value for $p(T_1)/p(T_2)$ that was predicted theoretically by Subczynski and Hyde (1981).

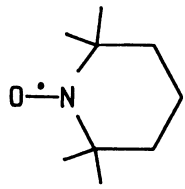

1

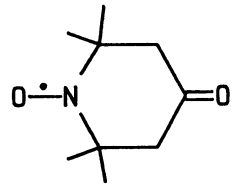

2

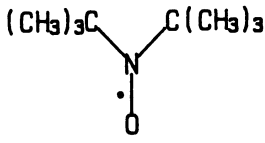

3

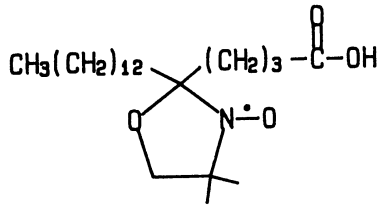

4

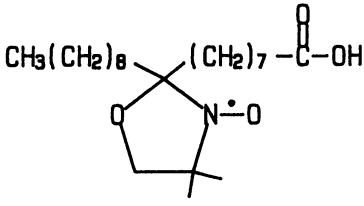

5

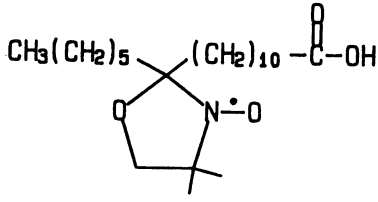

6

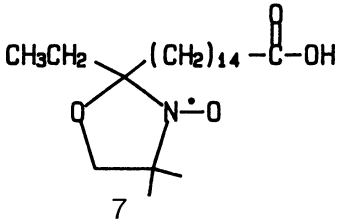

7

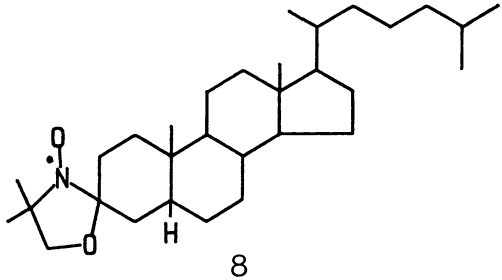

8

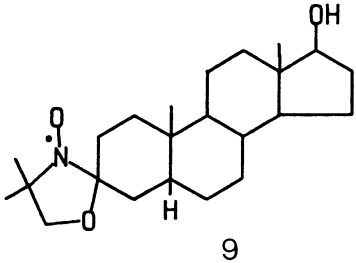

9

10

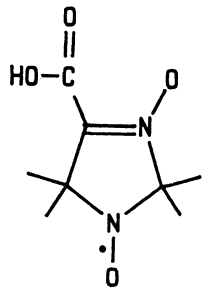

11

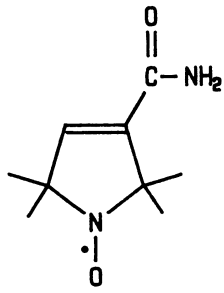

12

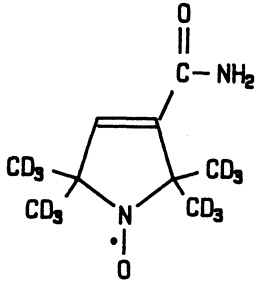

13

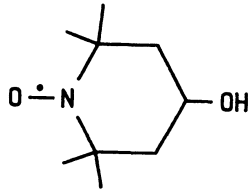

14

St.-Denis and Fell (1971) report

$$D(O_2, 37\,^{\circ}C) = 3.1 \times 10^{-5}\ cm^2\ s^{-1}$$

in very good agreement.

Data such as shown in Figure 3, together with the good agreement between measured and calculated bimolecular collision rates, provide the experimental foundation for spin-label oximetry.

The relative magnitudes of dipole-dipole and Heisenberg exchange interactions between oxygen and spin labels is of some concern. Dipole-dipole interactions are discussed in Vol. II of this series under the heading "The Spin-Probe-Spin-Label Method" (Hyde *et al.*, 1979). Both interactions must be present. Data shown in Figure 3 and the good agreement with calculated values of ω support the notion that Heisenberg exchange is generally dominant. Evidence of dipole-dipole interaction can be obtained if $p(T_1)/p(T_2)$ departs far from 1, or if the dependence of ω is not linear in macroscopic viscosity (Subczynski and Hyde, 1984). Apparently for oxygen, either the translational correlation time τ_c or the oxygen spin-lattice relaxation time $T_1(O_2)$ (or both) is so short that the spectral density terms appearing in the theory for dipolar relaxation are very small. But the exchange integral J is so great that Heisenberg exchange is in the

strong exchange limit (i.e., every collision requires an observable event) in spite of short τ_c and/or $T_1(O_2)$.

2.3. The Absolute T_1 Method

Figure 4 from Yin and Hyde (1987b) shows the energy-level diagram of a nitroxide where Heisenberg exchange rates with the O_2 spin reservoir are given by ω_x. Nitrogen nuclear relaxation rates are given by W_n, electron relaxation rates by W_e, and Heisenberg exchange rate constants for the nitroxide by K_e.

Rate equations for the instantaneous population differences of the three transitions can easily be written. If n_i and N_i are instantaneous and Boltzmann equilibrium population differences, then the rate equations are

$$\begin{aligned}\frac{d}{dt}[(n_1 - n_2) - (N_1 - N_2)] = &-2W_e[(n_1 - n_2) - (N_1 - N_2)] \\ &- W_n[(n_1 - n_3) - (n_2 - n_4)] \\ &+ 2K_e[(n_2n_3 - n_1n_4) + (n_2n_5 - n_1n_6)] \\ &- 2\omega_x[(n_1 - n_2) - (N_1 - N_2)] \end{aligned} \tag{3}$$

$$\begin{aligned}\frac{d}{dt}[(n_3 - n_4) - (N_3 - N_4)] = &-2W_e[(n_3 - n_4) - (N_3 - N_4)] \\ &+ W_n[(n_1 - n_2) - (n_5 - n_6) - 2(n_3 - n_4)] \\ &- 2K_e[(n_2n_3 - n_1n_4) + (n_3n_6 - n_4n_5)] \\ &- 2\omega_x[(n_3 - n_4) - (N_3 - N_4)] \end{aligned} \tag{4}$$

$$\begin{aligned}\frac{d}{dt}[(n_5 - n_6) - (N_5 - N_6)] = &-2W_e[(n_5 - n_6) - (N_5 - N_6)] \\ &- W_n[(n_5 - n_2) - (n_6 - n_4)] \\ &+ 2K_e[(n_3n_6 - n_4n_5) + (n_1n_6 - n_2n_5)] \\ &- 2\omega_x[(n_5 - n_6) - (N_5 - N_6)] \end{aligned}$$

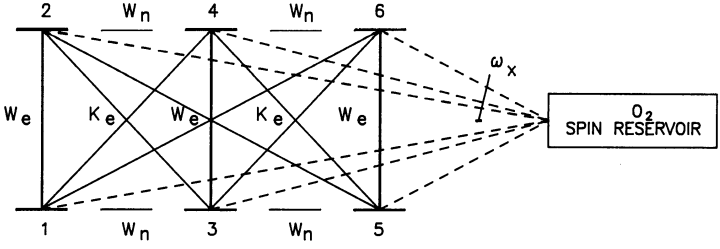

Figure 4. Energy-level diagram of a ^{14}N spin label coupled to a spin reservoir (the O_2 system). It is assumed that the spin-lattice relaxation time of molecular oxygen is so short that the O_2 spin reservoir is always at thermal equilibrium. Thus the reservoir is effectively part of the lattice bath. (From Yin and Hyde, 1987b.)

Since equations of the form

$$(n_2n_3 - n_1n_4) = ([SL]/6)\{(n_2 - n_1) + (n_3 - n_4)\} \tag{6}$$

can be written, these are linear differential equations that can be solved readily. The general solutions are

$$i_{1,2} = I_1 \exp(-t/\tau_1) + I_2 \exp(-t/\tau_2) + I_3 \exp(-t/\tau_3) \tag{7}$$

$$i_{3,4} = I_1 \exp(-t/\tau_1) - 2I_3 \exp(-t/\tau_2) \tag{8}$$

$$i_{5,6} = I_1 \exp(-t/\tau_1) - I_2 \exp(-t/\tau_2) + I_3 \exp(-t/\tau_3) \tag{9}$$

where

$$\tau_1^{-1} = 2W_e + 2\omega_x \tag{10}$$

$$\tau_2^{-1} = 2W_e + 2\omega_x + W_n + K_e[SL] \tag{11}$$

$$\tau_3^{-1} = 2W_e + 2\omega_x + 3W_n + K_e[SL] \tag{12}$$

If a way is found to perturb the populations from equilibrium, say by a saturating microwave pulse irradiating one of the transitions, double [equation (8)] or triple [equations (7) and (9)] exponentials are obtained. The time constants (or eigenvalues) are always the same regardless of how the spin system is prepared; only the prefactors of the exponentials can vary.

If we have an experimental method for determining the time constants, we find that the presence of oxygen shortens each of the time constants by an amount $2\omega_x$. If time constants in the absence of oxygen are known, the difference yields the product $p(T_1)\omega_x$ in absolute units. As noted, $p(T_1)$ is close to unity and ω_x is the bimolecular collision rate.

We have described in a series of papers (Yin and Hyde, 1987a, 1987b; Yin *et al.*, 1987) the technique of saturation recovery to measure indirectly the time evolution of the z component of magnetization, and further methodological details are given in the Methods section of this article. These papers demonstrate that triple exponentials can in fact be reliably deconvoluted. Figure 5 shows the effect of oxygen on the three time constants for 0.0015 mol ratio spin label **7**: lipid in DMPC (dimyristoylphosphatidylcholine) multilamellar dispersions.

2.4. The Absolute T_2 Method

Hyde and Subczynski (1984) were able to simulate the proton "superhyperfine" couplings of the spin-label 3-carbamoyl-2,2,5,5-tetramethyl-3-pyrroline-1-yloxyl (CTPO) **12** in water and in the absence of dissolved oxygen using purely Lorentzian line shapes. When low levels of oxygen were introduced, individual superhyperfine linewidths increased linearly with oxygen concentration. The increase in linewidth in gauss is related by the magnetogyric ratio to the increase in linewidth in cycles per second (hertz), which can in turn be identified with ω in equations (1) and (2). Thus the bimolecular collision frequency is determined absolutely.

Figure 6 (left) shows the effect of temperature on the superhyperfine spectrum of one line of CTPO in the absence of oxygen. The ring proton coupling is temperature

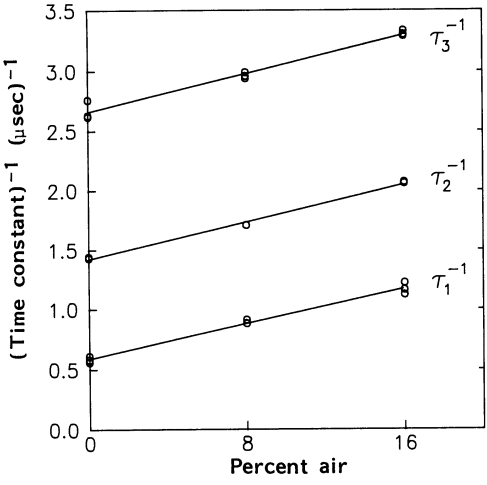

Figure 5. Plots of experimental data at 54 °C (well above the main phase-transition temperature of 23 °C) for 0, 8, and 16% air for a mole ratio of spin label 7 to lipid (DMPC) of 0.0015. It is notable that all three relaxation rates vary linearly with oxygen concentration with the same slope. (From Yin and Hyde, 1987b.)

dependent and is accidentally about 2.5 times that of the methyl protons. In the presence of oxygen, lines are considerably broadened (Figure 6, right). Superimposed and virtually indistinguishable are simulations of all spectra.

In the method illustrated here, the spin-packet width (i.e., the linewidth as determined from a lifetime-limiting event) was known, and the full spectrum could be simulated. It has been pointed out (Hyde and Hyde, 1981) that even in the absence of detailed knowledge of the inhomogeneous character of the line, the distant wings of a motionally narrowed line can be analyzed to obtain the spin-packet linewidth. This method is also absolute, and useful at high oxygen concentrations when using spin labels whose pattern of proton superhyperfine couplings is unknown.

3. EXPERIMENTAL METHODS

The editor has requested that a section of this chapter be devoted to specific experimental details.

3.1. TPX Gas-Exchange Sample Cell

After Deguchi (1960) and Hausser (1960) described the broadening effects of oxygen on EPR spectra, it became customary to remove oxygen from liquid-phase samples more or less routinely using multiple freeze-pump-thaw cycles. Sometimes, the more convenient but less thorough method of bubbling nitrogen gas through the sample was employed.

However, these methods were not suitable for many biological samples since they compromised the sample integrity and worked poorly when the viscosity was high (for example, protein solutions). Windrem and Plachy (1980) suggested an alternative and more appropriate degassing method. They placed the sample in a capillary of polytetrafluoroethylene (teflon) of 1.2 mm ID, 0.05 mm wall thickness, and allowed a gas of dry nitrogen to flow over it. Satisfactory deoxygenation occurred in 8 min at 25 °C. In fact

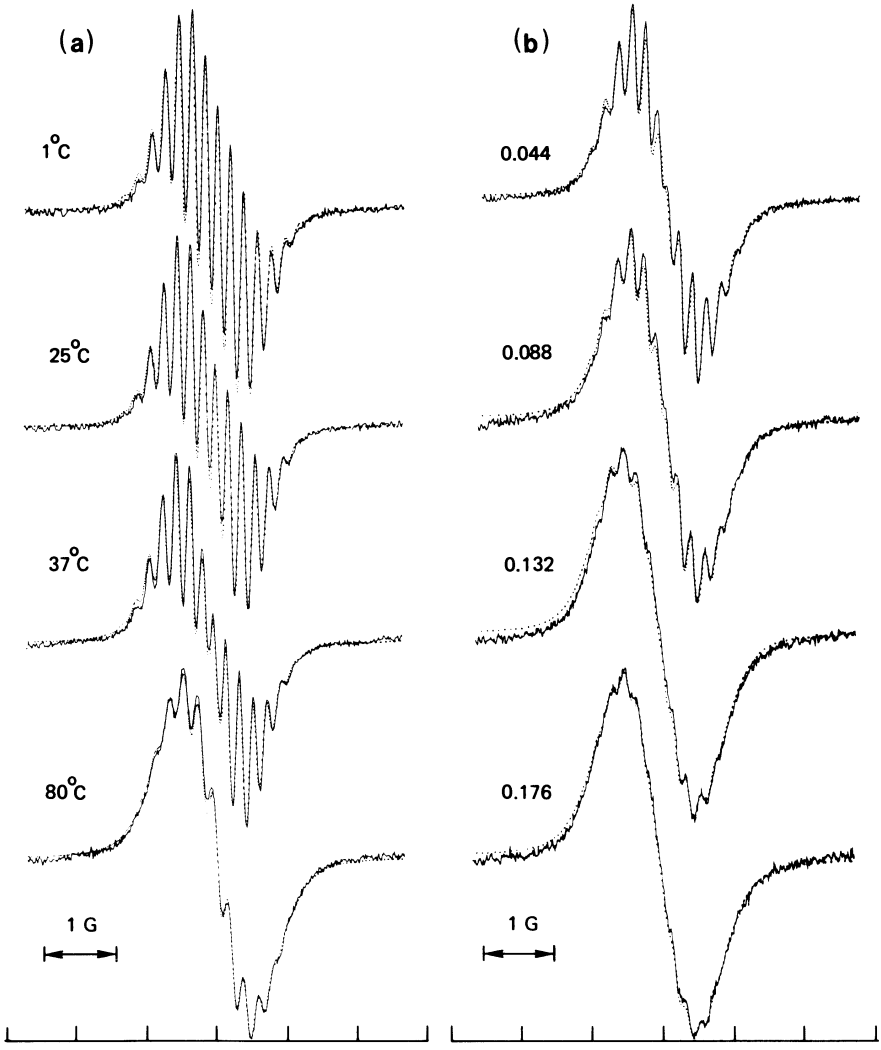

Figure 6. (a) EPR experimental spectra of CTPO in deoxygenated samples as a function of temperature (——). Simulated EPR spectra (· · ·). (b) EPR experimental spectra of CTPO at 37 °C as a function of oxygen concentration (——) ($[O_2]$ = 0.22 mM in water saturated by air at 37 °C). Simulated EPR spectra (· · ·) using the same coupling as for Figure 6a at 37 °C, varying only the linewidth. (All data are from the central $M_I = 0$ nitrogen hyperfine line.) (From Hyde and Subczynski, 1984.)

the capillary could be placed directly in the resonant cavity, and the exchange gas could also be the temperature regulating gas.

In our efforts to develop the methodology of spin-label oximetry, it became apparent that we needed a precise and convenient way to control the oxygen tension. The method of Windrem and Plachy seemed appropriate. The idea was to use a gas

blender, combining various mixtures of nitrogen and oxygen, and to flow the mixture over the plastic sample tube. However, we had trouble implementing this geometry primarily because of lack of structural integrity of the very thin walled teflon tubing. It twisted and curled when the temperature was changed, and degassing was too slow for teflon tubes with thicker walls. Many plastics show permeability to oxygen, and we therefore initiated a search for one with more suitable physical properties.

A methylpentene polymer known as TPX has the most optimum set of physical properties of the plastics considered by us thus far. Primarily, the oxygen permeability is much greater and therefore sample tubes with thicker walls and greater structural integrity can be employed. This material is produced by Mitsui Petrochemical Industries Limited, Tokyo, Japan and much of the physical data reported below on this plastic is abstracted from information supplied by this firm.

TPX is a fairly rigid plastic with good impact strength and heat resistance. It can be used continuously to 175 °C and withstands repeated autoclaving. It melts at 240 °C and becomes brittle at 0 °C. It has generally excellent chemical resistance to water, salts, acids, alkalies, and alcohols, but is affected by prolonged exposure to hydrocarbons, aldehydes, ketones, and ethers. Strong oxidizing agents and organic solvents eventually caused embrittlement. The plastic is attacked by carbon tetrachloride and cyclohexane.

The gas permeability specifications for TPX sheets 45 μm thick in units of ml m^{-2} for 24 h are: CO_2, 1.4×10^5; N_2, 1.0×10^4; O_2, 4.0×10^4; H_2O (vapor phase), 8.4×10^1. The high permeability of CO_2, O_2, and N_2, and the low permeability for H_2O are the key properties that make TPX suitable for the present application.

Microwave dielectric properties have not, to our knowledge, been reported in detail. It can reasonably be assumed that the dielectric constant is about 2.1 based on lower-frequency measurements. The loss angle is low (350 μrad at 1 GHz) and no significant changes in cavity or resonator Q have been noticed at 9.5 GHz. No background EPR signals have been attributed to the plastic. TPX has favorable UV/vis transmission characteristics according to the manufacturer, but this property has not yet been exploited in our own work.

TPX capillaries were machined from 1/4″ diam rod by first drilling an axial hole and then removing the excess material on a lathe with a single cut and without support. Typical dimensions are 0.5 mm ID, 1.0 mm OD, 2 cm long. One end was threaded and could be screwed into the tapped end of a plastic support rod. An angled hole in the rod permitted insertion of a thermocouple into the capillary. After sample insertion, the open end was sealed with Miniseal (Scientific Products). Other diameters and wall thicknesses have been used. The degassing can be as short as 2 min but is typically 10 min. See Figure 7, which illustrates the TPX geometry for a cavity resonator. The same holder is also used for loop-gap resonators.

An alternative geometry is to cut cover slips from 0.125 mm films of TPX and use them in conjunction with quartz tissue cells (i.e., flat cell geometry, X-band, multipurpose TE_{102} rectangular cavity). The cover slips can be sealed to the cell around the edges with paraffin wax.

Gas flow mixtures were measured and adjusted using flowmeters produced by Matheson Gas Products, 7630 series.

We have encountered two problems with the TPX gas-exchange method. (1) There is some loss of water in the sample if the experiment is carried out over several hours.

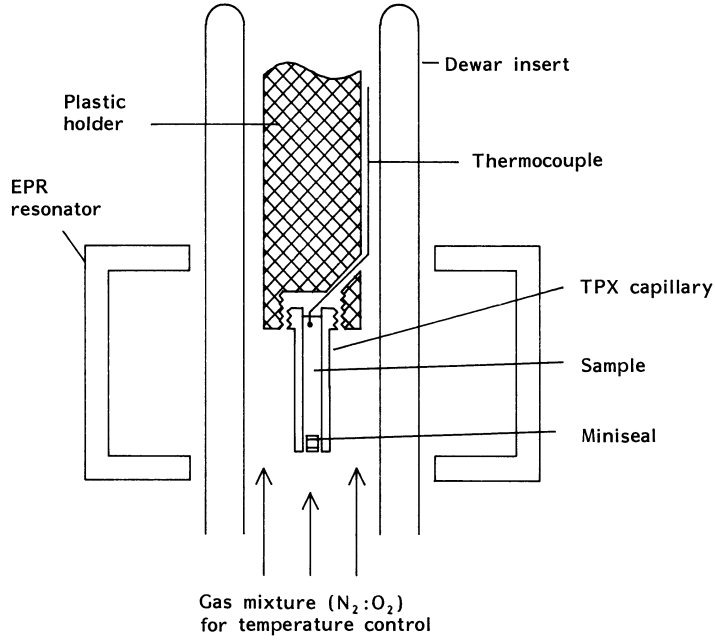

Figure 7. Schematic diagram of a TPX sample cell positioned in an EPR resonator inside a dewar insert.

In principle one could alleviate this problem by saturating the exchange gas with water vapor. (2) The plastic itself can hold quite a lot of oxygen, which complicates the kinetics of oxygen removal.

This last point is considered further. Figure 8a is a calibration curve for oxygen concentration using the technique of cw saturation. The incident microwave power was set at 100 mW in a TE_{102} rectangular cavity at X-band. Quantity ΔI is the difference in signal intensities from CTPO (**12**) in water with and without oxygen and $[O_2]_0$ is the concentration of oxygen in water equilibrated with one atmosphere air at 25 °C. In a subsequent experiment, at time $t = 0$ the mix in the gas blender was suddenly changed from air to nitrogen. The time dependence of the saturated signal was observed directly and the data of Figure 8a used to obtain the time dependence of oxygen concentration (Figure 8b).

The sample tube inner radius was 0.35 mm. The value of $D(O_2)$ in water at 25 °C is 2×10^{-5} cm^2 s^{-1}. Therefore, the characteristic time for diffusion of oxygen in this cylindrical geometry is $t = (r_1 - r_2)^2/6D(O_2) = 10$ s. This time is much slower than that found in Figure 8b. As shown in the figure, the oxygen concentration can be fitted empirically to an equation of exponential form,

$$[O_2](t) = [O_2]_0 \exp\left(-\frac{t}{\tau(\mathrm{TPX})}\right) \tag{13}$$

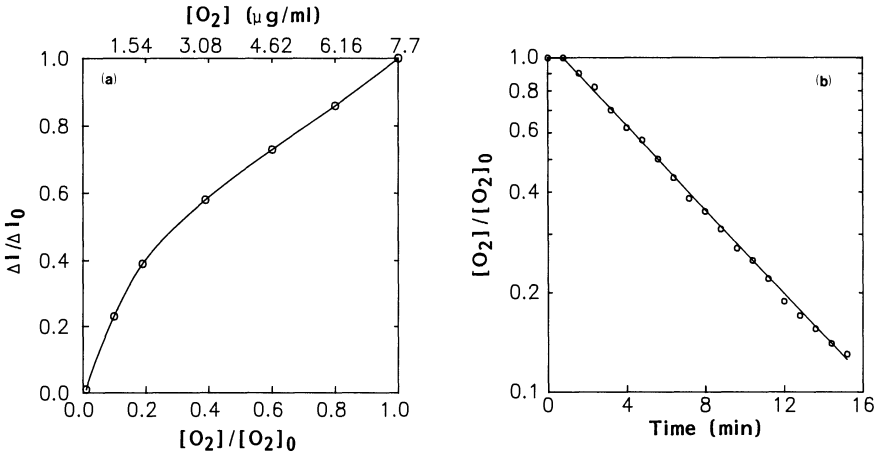

Figure 8. (a) Calibration curve for oxygen concentration using cw saturation. Experiments were performed on 10^{-4} M CTPO (**12**) at 25 °C in water using 1 G field modulation and 100 mW incident microwave power at X-band with a TE_{102} rectangular cavity. ΔI is the difference in signal amplitude with and without oxygen. Subscript zero is for air. (b) Time dependence of the change in oxygen concentration using a TPX capillary of ID 0.7 mm, OD 1.4 mm following a step change in the exchange gas mixture from air to nitrogen. The calibration curve of Figure 8a was used.

The barrier to oxygen transport is the TPX wall, which was 0.35 mm for the experiment of Figure 8b. Because τ(TPX) $\gg$ 10 s, it can be assumed throughout the oxygenation-deoxygenation cycle that $[O_2]$ is uniform across the sample. The temperature dependence of τ(TPX) for this capillary (0.35 mm wall thickness) is shown in Figure 9.

The initial delay in oxygen removal (Figure 8b) is attributed to removal of oxygen from TPX itself. It was found (Subczynski and Hyde, 1983) that the oxygen concentration in TPX is 1.4 times higher than in water for temperatures between 15 and 35 °C.

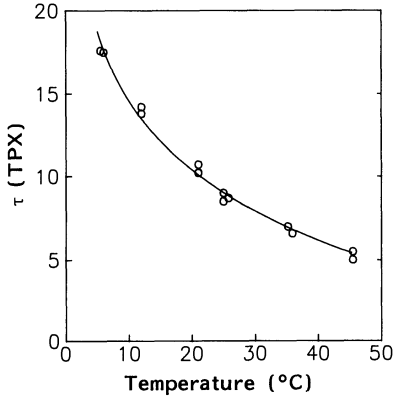

Figure 9. Temperature dependence of τ(TPX); see equation (13).

The importance of the TPX gas exchange sample cell to the development of spin-label oximetry has been very great.

3.2. T_1-Sensitive Methods

As motion slows and the rotational correlation time increases, quantity T_2 becomes shorter and T_1 becomes longer. We have seen that the contributions to T_1^{-1} and T_2^{-1} of Heisenberg exchange are numerically the same within a factor of two. But the percent change in T_1 rapidly becomes much greater than the percent change in T_2. It therefore follows that T_1-sensitive methods become increasingly preferable to T_2-sensitive methods as motion slows.

Well-resolved superhyperfine structure of spin labels is detectable in a rather narrow range of conditions. More typically, even in the fast tumbling domain, superhyperfine couplings are not observed, and the overall linewidth is of the order of 3 G. Bimolecular collision must compete with an effective T_2^*, 2×10^{-8} s, to be easily observable, which requires a high oxygen concentration. As motion slows further, direct effects of oxygen on spectra become unobservable, and T_1-sensitive methods are required. The value of T_1 always falls in the range 10^{-6}–10^{-5} s for spin labels, and effects are therefore readily observable at low oxygen concentrations.

We have developed three T_1-sensitive techniques: (1) The absolute T_1 method using pulse saturation-recovery apparatus, (2) continuous wave (cw) saturation, and (3) rapid passage displays.

If one is to obtain any information about changes in thermal contact of the spin reservoir with the lattice because of the presence of oxygen, saturating microwave power must be employed. Nonuniform microwave field distribution over the sample can create problems in quantitation, and there is a possibility that power delivered to the sample will be sufficiently great that its temperature will rise significantly.

Applications of T_1-sensitive spin-label oximetry include measurement of bimolecular collision frequencies involving spin-labeled proteins, spin labels in lipid bilayers, spin labels in micelles, and spin labels in any homogeneous viscous fluid.

3.2.1. Saturation Recovery

Saturation-recovery EPR spectroscopy permits the measurement in absolute units of the bimolecular collision frequency. The method was reviewed by Hyde (1979) and the recent series of papers by Yin and Hyde (1987a, 1987b; Yin *et al.*, 1987, 1988) provide a technological update. This method is not widespread, but it seems likely that pulse EPR apparatus including saturation-recovery capability will be increasingly available.

Distinction is made between the long-pulse and short-pulse saturation-recovery techniques. It is clear from the work of Yin *et al.* (1987) that multiexponential recovery signals are always expected and that the time constants cannot be affected by the way in which the spin system is prepared. However, a long saturating microwave pulse tends to decrease the amplitudes of the exponentials with shorter time constants compared with the exponential of longest time constant (which is always directly a T_1 measurement).

In a key paper, Kusumi *et al.* (1982) used the long-pulse saturation-recovery technique to study bimolecular collisions of oxygen with a number of spin labels introduced into lipid bilayers. They emphasized the importance of collecting data only in the distant tails of the recovery signals and requiring that these curves be monoexponential. The difference between the relaxation probability with and without oxygen was termed by these workers the "oxygen transport parameter."

Kusumi *et al.* used a saturation-recovery apparatus that employed a bimodal cavity resonator. The equipment itself was in a somewhat primitive form, and in part their use of the long-pulse method was a technical solution to various experimental problems. Yin and Hyde used a loop-gap resonator (see Hyde and Froncisz, 1986 for a review of this class of resonators) and the evolving saturation-recovery spectrometer was at a higher level of development. They emphasized the short-pulse technique, with deconvolution of the multiexponential signals by computer. The distinction between short- and long-pulse saturation recovery now seems somewhat artificial. An experimentalist should vary the length of the saturating pulse and, however the data is acquired and processed, there should be no change in the value of the time constant assigned to T_1. Variation in the length of the saturating pulse is now viewed as an important experimental control.

There are other controls: bimolecular collision rates must be independent of the quantum number of the observed spin-label hyperfine transition and independent of the spin-label concentration. Also, the Heisenberg exchange *rate constant* for exchange between spin labels and oxygen must be independent of the oxygen concentration. Of course the TPX gas-exchange sample cell is central to variation of $[O_2]$. These multiple controls make the method of T_1-sensitive oximetry reliable.

Rather generally, the introduction of 100% air into spin-labeled biological systems renders the effective T_1 somewhat short to measure with optimum reliability. For example, the spin-lattice relaxation time of 16-SASL (7) in DOPC (dioleoylphosphatidylcholine) is 2.3 μs in the absence of oxygen and 0.3 μs in air-saturated samples. Therefore we generally use 25, 33, or 50% air–nitrogen mixtures from the gas blender and extrapolate to 100% air. There are some technical advantages of saturation recovery over cw T_1-sensitive methods. The average microwave power delivered to the sample is reduced, and variations in microwave field intensity over the sample are of no consequence since only prefactors of the multiexponentials and not the time constants are affected.

The thrust of our development of saturation-recovery instrumentation has been to have not only fast acquisition of transient signals, but also fast addition or signal averaging of the acquired signals. Thereby the signal-to-noise ratio in a fixed experimental time interval is optimized. At the present state of the art (1988), the capability to perform experiments on respiring cells exists but is on the sensitivity borderline. Instrumental improvements can reasonably be expected to permit measurement of bimolecular collision rates of oxygen with specific spin-labeled sites in cells.

3.2.2. Continuous Wave Saturation

The technique of cw saturation will be familiar to all EPR spectroscopists. Using the TPX gas-exchange sample cell, it is a trivial matter to carry out cw saturation studies as a function of the amount of oxygen in the exchange gas mixture. An empirical

parameter, $P_{1/2}$, is often used to express cw saturation data. At this power the EPR signal intensity is half as great as it would be in the absence of saturation. Collecting oxygen-sensitive data and parameterizing it is straightforward. Figures 8a and b illustrate one possible method. Here, the incident power was held constant and the signal intensity used as an observable. An alternative approach is to plot $P_{1/2}$ versus oxygen concentration.

The rationale for cw saturation methods, in addition to simplicity and widespread availability, is the same as for saturation recovery, namely, to obtain information on oxygen transport under conditions where the presence of oxygen gives little or no discernible effect on the ordinary unsaturated EPR spectrum.

Subczynski and Hyde (1981) report values of $P_{1/2}$(with oxygen) and $P_{1/2}$(no oxygen) for a variety of spin labels in a number of different lipid bilayers over a range of temperatures. This paper is a good example of the cw saturation method. It was carried out historically in our laboratory at an early stage of our development of saturation-recovery techniques; now, we would prefer the latter, but nevertheless the cw saturation method gave valuable information.

Although oxygen affects both T_1 and T_2, the fact that $T_1 \gg T_2$ in the absence of oxygen means that changes in cw saturation characteristics are almost entirely due to changes in T_1. Values of T_1 in the absence of oxygen (as noted) always fall in the range 10^{-6}–10^{-5} s, are now known for many spin-labeled systems, and also can easily be measured in one of the existing pulse instruments. If a known value of T_1 gives some value of $P_{1/2}$ for a particular system under deoxygenation, one can attempt to predict the effects of oxygen on $P_{1/2}$ quantitatively. This method was used by Subczynski and Hyde (1981).

If cw saturation data are available as a function of oxygen concentration, time-domain spin-label oximetry becomes feasible. By setting the EPR resonance condition at a transition under saturating conditions, one can obtain the time dependence of the relative oxygen concentration. Thus kinetic models can be tested, as shown in Figure 8b.

Continuous wave saturation experiments can be confounded by sample temperature rise from the relatively high average power, and experimental results depend on the choice of field-modulation frequency and amplitude. Continuous wave saturation techniques are easy and sensitive, are very good for qualitative studies, and probably are less good for absolute or quantitative studies of oxygen transport.

3.2.3. Passage Displays

Froncisz *et al.* (1985) introduced an adiabatic rapid passage display into spin-label oximetry. They pointed out that with the loop-gap resonator, one can tune to the dispersion mode and not be sensitive to oscillator phase noise (since the Q is relatively low). The rapid-passage display they used involved tuning to the dispersion under microwave saturating conditions using 100 kHz field modulation. Signal shapes depend on the setting of the reference phase of the lock-in detector, on the degree of saturation, and on the oxygen concentration.

This type of behavior is complex, but yields displays of outstanding sensitivity. These authors developed the method only for spin labels in water, and were able to study cellular respiration to concentrations of oxygen as low as 10^{-7} M.

A procedure was given to set up the equipment to obtain a display that was linear in oxygen concentration over a wide range of conditions. This was convenient in studying the time dependence of cellular respiration.

Primarily, the effect depends on the product $\omega_m T_1$ where ω_m is the field-modulation frequency. The paper provides citations to the relevant papers giving the physical basis of the method.

A number of commercial spectrometers now incorporate second-harmonic detection schemes. It is pointed out that a second-harmonic absorption out-of-phase spin-label oximetric technique can, in principle, be developed following the approach of Froncisz *et al.* (1985). It would then not be essential to employ a loop-gap resonator; the more familiar cavity resonators would suffice. The advantage of this display is that phase noise from the oscillator is less of a problem for absorption than for dispersion.

3.3. T_2 (Linewidth-Sensitive) Methods

Bimolecular collisions of spin labels with oxygen alter the spin-label linewidth. Heisenberg exchange broadens lines according to the Heisenberg uncertainty principle, since the process shortens the spin-state lifetime. If the spin-label line shape were homogeneous and described by a Lorentzian line shape, one could write immediately

$$\Delta H(\text{with oxygen}) = \frac{2}{\gamma\sqrt{3}} + \Delta H(\text{no oxygen}) \tag{14}$$

where ΔH is the linewidth, peak to peak, if the first derivative is expressed in gauss and ω is the bimolecular collision frequency.

In fact, the line shape of a nitroxide is Lorentzian only over a rather narrow range of conditions. If the spin label is tumbling very rapidly, it will often have a Gaussian envelope determined by coupling to twelve equivalent methyl protons. The envelope need not be Gaussian if ring-proton couplings are significant. As rotational motion slows, lines become Lorentzian in shape and equation (14) can be used. But at even slower motion, it begins to fail. The central $M_I = 0$ line of ^{14}N containing spin labels is Lorentzian in shape over the widest range of experimental conditions.

In addition to the fundamental problem of convolution of a Lorentzian line with an experimental spectrum whose underlying structure may be uncertain, there is an experimental problem of measuring the change in linewidth because of bimolecular collisions with oxygen. It is much easier to detect small changes in linewidth indirectly by the resulting changes in signal height. Because of the possibility of chemical reduction of the spin label, however, some sort of internal reference or calibration is needed when line heights are monitored.

We define below several experimental domains and discuss methods that have been developed to solve these problems.

3.3.1. Fast Tumbling; No Resolved Superhyperfine Structure

Subczynski *et al.* (1986) developed the method in considerable detail. They used the spin-label perdeutero ^{15}N Tempone (**2**), which increases the signal intensity relative

to protonated ^{14}N spin label, and also satisfies the criterion of a Lorentzian line shape over a wide range of experimental conditions. They designed an oxygen-sensitive capsule made from TPX and filled with light paraffin oil. This capsule can be placed in a fluid or, in their case, in the peritoneal cavity of a mouse, and used to monitor the oxygen concentration. Because of the extremely favorable partition coefficient of oxygen in hydrocarbons, relative to water, the concentration of oxygen is about 10 times higher at a given oxygen tension. The use of a long-chain hydrocarbon greatly reduced the translational diffusion of the spin label, but affected its rotational diffusion much less. Thus rather high concentrations of spin label could be used without deleterious spin exchange between spin labels. They used a concentration of 2.5×10^{-2} M. Translational diffusion of oxygen is about as facile in light mineral oil as in water.

A speck of solid DPPH was attached to the capsule. Calibration spectra are shown in Figure 10, which defines the *R* parameter. (Note: these are L-band spectra, not X-band.) The *R* parameter was measured as a function of temperature and oxygen tension to obtain the necessary calibration curves.

In another study, Windrem and Plachy (1980) observed that perdeutero di(*t*-butyl) nitroxide (**3**) exhibits a rather Lorentzian line shape over a wide range of conditions, even though it is composed of 37 underlying lines or spin packets from the 18 equivalent deuterons with a Gaussian or binomial distribution. They showed that a simulation that included not only the deuterons but also ^{13}C satellites, using Lorentzian line shapes for the spin packets, fitted quite well the observed experimental Lorentzian line shapes in a range of conditions where the spin-packet width was at least 80% of the overall width. Bimolecular collisions with oxygen change the spin-packet width. Their calibration curves relate observed width changes to spin-packet width changes.

Belkin *et al.* (1987) describe the use of the spin-label PCAOL (**10**) to measure respiration and oxygen evolution in photosynthetic systems. This label readily crosses cell membranes and does not photoreduce. They observed broadening of the overall nitrogen hyperfine lines in both a first- and second-derivative display.

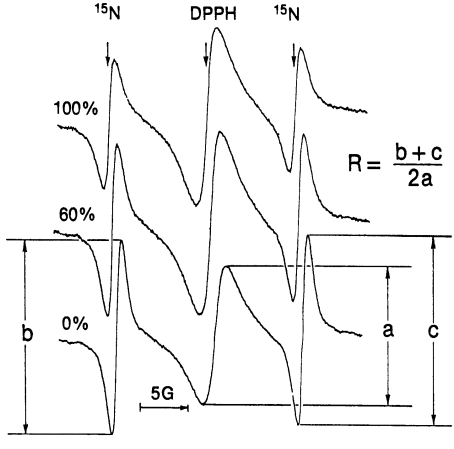

Figure 10. EPR spectra at 37 °C from the oxygen-sensitive capsule at L-band. Spectra were recorded for various air/nitrogen mixtures at 1 atm total pressure: 0, 60, 100% air. The *R* parameter, which relates the height of the ^{15}N hyperfine lines of the spin label to the height of the internal DPPH reference signal, is defined. (From Subczynski *et al.*, 1986.)

3.3.2. Fast Tumbling; Resolved Superhyperfine Structure

Backer *et al.* (1977) first pointed out that the effects of oxygen on the resolution of the proton superhyperfine structure of spin labels could be a useful oximetric methodology. Previous workers had emphasized effects on nitrogen hyperfine lines using labels that exhibited no resolved proton coupling. Since the individual linewidths are about a factor of 10 narrower than the width of the envelope of proton couplings, one could reasonably expect good sensitivity at about 10 times lower oxygen concentration. These workers used spin label **11**.

The spin-label CTPO, structure **12**, was introduced in our laboratories in Krakow and Milwaukee (Sarna *et al.*, 1980; Pajak *et al.*, 1980; Gurbiel *et al.*, 1980; Lai *et al.*, 1982). It has an advantage of partitioning very unfavorably into lipid bilayers, and therefore in a mixed phase system such as a lipid bilayer it samples oxygen in the aqueous phase. Since the diffusion of oxygen in water is known, measurement of the bimolecular collision frequency yields the concentration.

Backer *et al.* (1977) introduced a ratio of line heights (see their Figure 1) as an experimental parameter. In our laboratories the so-called K parameter is used (Figure 11). This parametrization results in an oxygen-sensitive indicator that is independent of spin-label concentration to a good approximation.

Lai *et al.* (1982) considered carefully a number of experimental aspects that can affect the K-parameter calibration curves. These include:

- Spin-label concentration. Spin exchange between labels broadens the superhyperfine linewidths and alters oxygen sensitivity.
- Microwave power. Line broadening because of partial saturation alters oxygen sensitivity.
- Temperature. There are a number of effects including motionally dependent linewidths of the spin label, temperature-dependent proton couplings (Hyde and Subczynski, 1984), and the temperature dependence of the oxygen diffusion constant.
- Field-modulation amplitude, resulting in modulation broadening.
- The selection of nitrogen hyperfine line.
- Choice of field-modulation frequency.

It is very convenient if experimental conditions can be found such that the K parameter is linear in concentration. Of course one wants a high EPR signal-to-noise

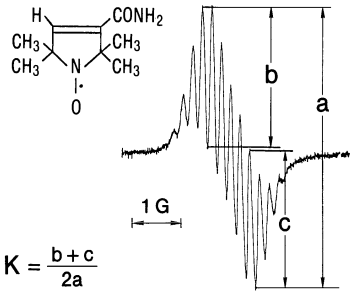

Figure 11. EPR spectrum of the spin-probe CTPO (**12**) (1.1×10^{-4} M) in deoxygenated water at 37 °C. The definition of K, the parameter used in calibration curves to determine $[O_2]$, is indicated.

(S/N) ratio, which favors higher power, higher spin-label concentration, and higher field-modulation amplitude, but the higher these values the lower the sensitivity to oxygen. The compromise values used by Lai *et al.* (1982) for CTPO in water are: 37 °C, 1 mW microwave incident power on an X-band TE_{102} cavity, 0.04G 100 kHz field modulation, central $M_I = 0$ nitrogen hyperfine line, and CTPO concentration of 1.1×10^{-4} M.

The resulting *K*-parameter calibration curves of Lai *et al.* were fairly linear in oxygen concentration.

The sample geometry is of critical importance in careful work. Lai *et al.* used a 1 mm diam capillary in a quartz dewar insert. The resulting microwave field as experienced by the sample was about $2^{1/2}$ higher than if no dewar insert had been used. In an independent study also involving CTPO in water, Sarna and Sealy (1984) obtained a *K*-parameter calibration curve that was surprisingly different from that of Lai *et al.* Tentatively, we attribute the difference to the fact that these latter authors used a flat cell geometry.

In this configuration, the field-modulation amplitude is rather inhomogeneous across the sample. Signals from spins that are close to the field-modulation coils are modulation broadened to a greater extent than signals from spins that are midway between the coils. The overall resolution is lower than if a capillary had been employed. However, the flat cell geometry of Sarna and Sealy (1984) gives better S/N ratio and is more suitable for photochemical experiments. It is concluded that every sample-cell geometry requires its own *K*-parameter calibration curve.

At the 29th Rocky Mountain Conference in August 1987, H. J. Halpern described the use of spin label **13**. This deuterated analog of CTPO has just two resolved superhyperfine lines, which arise from the ring proton. It appears to the authors that this label will have advantages with respect to oxygen sensitivity compared with fully protonated forms.

Almost all protonated spin labels show evidence of resolved superhyperfine structure when dissolved in low-viscosity deoxygenated solvents. For example, superhyperfine structure can be seen from 5-SASL (**4**), 16-SASL (**7**), CSL (**8**), and ASL (**9**) dissolved in chloroform. In our experience, only Tempone (**2**) shows no evidence of proton couplings. Thus it seems apparent that a wide range of experiments can be designed for various systems and problems using various spin labels. For example, Morse and Swartz (1985) used the superhyperfine structure of the spin-label Tempol (**14**) as an indication of intracellular oxygen concentration. This probe readily penetrates across membranes.

3.3.3. Slow Tumbling

Windrem and Plachy (1980) studied the effects of 1 atm O_2 on the spectra of 5-, 12-, and 16-SASL (**4, 6, 8**) in several lipid bilayers above the main phase-transition temperatures. They simply measured the broadening of the central $M_I = 0$ nitrogen hyperfine line and equated the incremental change in width (expressed in frequency units) with the bimolecular collision frequency.

This is a suboptimum approach for the current level of sophistication in simulation of spin-label spectra in membranes. The problem of convoluting Heisenberg exchange with rotational motion has been addressed by Freed (1976) for various motional models.

He considered homo-species exchange, but extension to hetero-species exchange, i.e., O_2 and spin label, should be straightforward.

However, development of line-broadening spin-label oximetric methodology in the slow-tumbling domain has not yet been done. One possible reason is uncertainty concerning the possible role of dipole-dipole interactions between spin label and oxygen, although Figure 3 suggests that it can be neglected, as do the arguments and results of Windrem and Plachy (1980).

The work of Kusumi *et al.* (1982) using T_1 methods shows that above the main phase transition in lipid bilayers the bimolecular collision frequency at 1 atm oxygen is about $10^7\ s^{-1}$. M. Pasenkiewicz-Gierula, of this laboratory, using the Moro and Freed (1981) simulation program, has predicted the effect of a collision frequency of this magnitude on spectra from spin labels undergoing isotropic rotational diffusion with a correlation time of 10^{-9} s (Figure 12). Shown here are simulated second- and first-derivative spectra, pure absorption spectra, and integrated spectra without (solid lines) and with (dotted lines) Heisenberg exchange. It appears very difficult to make oxygen measurements based on linewidth determinations. However, the simulation does suggest that there would be fairly good sensitivity to amplitude measurements with and without oxygen. The TPX gas-exchange technique would permit convenient introduction and removal of oxygen. It is possible that the second-derivative display would be preferable to the first-derivative display.

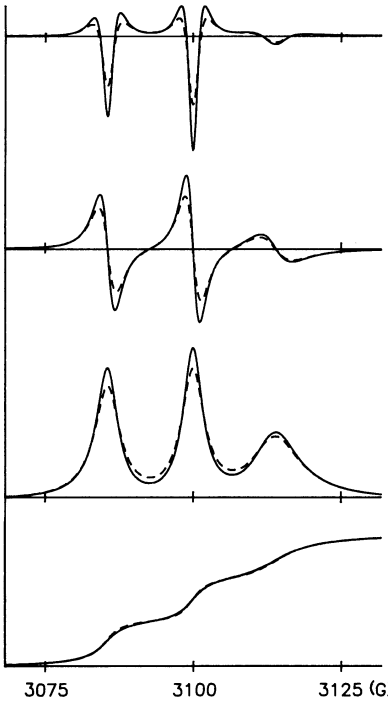

Figure 12. Simulated spectra for isotropic rotational diffusion at a correlation time of 10^{-9} s in second- and first-derivative, absorption, and integral displays. Solid lines: no Heisenberg exchange; dashed lines: exchange frequency of $10^7\ s^{-1}$.

We conclude that this suggested T_2-type methodology for spin-label oximetry for slow-tumbling conditions has promise and should in future years receive further development. We are pessimistic, based on the data of Kusumi *et al.* (1982) (their Figure 4), about the possibility of using this method below the main phase transition of phospholipid bilayers because of the low bimolecular collision frequency.

4. APPLICATIONS

Access to the literature through 1987 of applications of spin-label oximetry is provided.

Cellular respiration studies were first reported by Backer *et al.* (1977). Methodology was developed in some detail by Lai *et al.* (1982) and Froncisz *et al.* (1985). Morse and Swartz (1985) and also Belkin *et al.* (1987) report intracellular probes of cellular respiration. See also Swartz' review (1987). Butler *et al.* (1986) studied the effects of antimalarial drugs on oxygen consumption of parasitized erythrocytes.

Transport of oxygen across lipid bilayers was the central thrust of the pioneering work of Windrem and Plachy (1980). It was studied by Subczynski and Hyde using cw saturation methods (1981) and by Kusumi *et al.* using saturation-recovery methods (1982). Since only the diffusion-concentration product could be determined in these studies, Subczynski and Hyde measured the concentration of oxygen in lipid bilayers as an intermediate step in separating the product into its component factors (Subczynski and Hyde, 1983). In recent studies Subczynski and colleagues have studied oxygen permeability in model and biological membranes.

Spin-label oximetry in the presence of light is a valuable technique in the context of oxy-radical chemistry and photosynthesis. But one must be concerned with the possibility that the label will become part of the chemistry rather than a mere reporter of oxygen concentration. Photosynthetic studies include the paper of Belkin *et al.* (1987) and that of Strzalka *et al.* (1986). Kalyanaraman *et al.* (1987) studied merocyanine 540 (MC540)—mediated photosensitization of model and biological membranes. Ankel *et al.* (1986) studied photosensitized oxygen consumption in a system containing hematoporphyrin incorporated into Chinese hamster ovary (CHO) cells. Reszka and Sealy (1984) studied the oxygen consumption during hematoporphyrin-sensitized photooxidation of dopa (3,4-dihydroxyphenylalanine). A number of spin-label oximetric experiments involving photochemistry of melanin have appeared; *vide infra.*

The technique was used to study the exceptionally slow changes in oxygen concentration during spontaneous lipid peroxidation (Subczynski and Kusumi, 1985).

In principle, spin-label oximetry can be used to monitor oxygen concentration in a wide variety of chemical and biochemical systems. For example, Korytowski *et al.* (1987) studied tyrosinase-catalyzed oxidation of dopa and related catecholamines.

It is apparent that oxygen plays a role in the complex photochemistry of the heterogeneous mammalian polymer melanin. There are a number of studies of this system where spin-label oximetry has been used. In addition to sources previously cited (Sarna *et al.*, 1980; Pajak *et al.*, 1980; Gurbiel *et al.*, 1980; Sarna and Sealy, 1984), attention is called to other work (Pajak *et al.*, 1983; Sarna *et al.*, 1984; Sealy *et al.*, 1984). Melanin exhibits an intense free radical signal that tends to overlap the central $M_I = 0$ peak of ^{14}N nitroxides, and therefore the low-field $M_I = +1$ line has been used.

5. FUTURE OPPORTUNITIES

Three molecular probe techniques exist for the measurement of bimolecular collision frequencies with oxygen at specific labeled sites or in restricted domains such as membranes: phosphorescence quenching, fluorescence quenching, and spin-label oximetry. The match of the bimolecular collision rate with the internal molecular clocks (excited-state lifetime or electron spin-lattice relaxation time) favors phosphorescence quenching and spin-label oximetry, while sensitivity considerations favor the latter. The range of chemically appropriate labels also favors spin labeling over phosphorescence labeling.

Of the various spin-label methods, the T_1 methods are favored for spin-labeled proteins or viscous environments where rotational correlation times are long and lines are relatively broad.

Bimolecular collision frequencies are of fundamental interest in themselves, but separation into component diffusion and concentration factors is conceptually difficult. The latter are bulk properties of matter, while the words "bimolecular collision" imply an event that occurs at a molecular level. In a homogeneous fluid, the separation is possible; in a heterogeneous system that contains labeled sites or enclosed anisotropic domains such as lipid bilayers, the separation seems intrinsically impossible.

T_2-sensitive techniques based on K-parameter measurement are exceptionally convenient for homogeneous fluids or for the extracellular fluid in cell suspensions. In water, the diffusion of oxygen is known, and the concentration is therefore readily determined using, for example, the spin-probe CTPO (**12**). Since the probe samples the fluid uniformly, the experimental parameter is proportional to the integral of the concentration over the sample volume—an important point if there is any reason to believe oxygen gradients are present. The oximetric methodological competition in homogeneous fluids is of course potentiometric, such as the Clark electrode with its very great advantages with respect to availability, cost, and ease of use. Spin-label oximetry advantages with respect to the Clark electrode include smaller sample volume, faster response, the fact that oxygen is not consumed during measurement, good sensitivity, suitability with respect to certain photochemical geometries, the absence of a stirring requirement, and freedom from cross reactivity with H_2O_2. Oxygen is delivered to the Clark electrode by *convection*, while molecular *diffusion* is the transport mechanism that brings molecular oxygen and spin labels into contact.

ACKNOWLEDGMENT. Preparation of this article was assisted by grants GM22923 and RR01008 from the National Institutes of Health.

REFERENCES

Ankel, E., Felix, C. C., and Kalyanaraman, B., 1986, The use of spin-label oximetry in the study of photodynamic inactivation of Chinese hamster ovary cells, *Photochem. Photobiol.* **44**:741–746.

Backer, J. M., Budker, V. G., Eremenko, S. I., and Molin, Yu. N., 1977, Determination of the kinetics of biochemical reactions with oxygen using exchange broadening in the ESR spectra of nitroxide radicals, *Biochim. Biophys. Acta* **460**:152–156.

Belkin, S., Mehlhorn, R. J., and Packer, L., 1987, Determination of dissolved oxygen in photosynthetic systems by nitroxide spin-probe broadening, *Arch. Biochem. Biophys.* **252**: 487-495.

Butler, K. W., Deslauriers, R., and Smith, I. C. P., 1986, Effects of antimalarial drugs on oxygen consumption by erythrocytes infected with *Plasmodium berghei*: An ESR study, *Magn. Reson. Med.* **3**: 312-316.

Deguchi, Y., 1960, Proton hyperfine spectra of diphenyl picryl hydrazyl, *J. Chem. Phys.* **32**:1584-1585.

Edelstein, N., Kwok, A., and Maki, A. H., 1964, Effects of hydrostatic pressure and temperature on spin exchange between free radicals in solution, *J. Chem. Phys.* **41**:3473-3478.

Freed, J. H., 1976, Theory of slow tumbling ESR spectra for nitroxides, in *Spin Labeling Theory and Applications* (L. J. Berliner, ed.), pp. 53-132, Academic Press, New York.

Froncisz, W., Lai, C.-S., and Hyde, J. S., 1985, Spin-label oximetry: kinetic study of cell respiration using a rapid passage T_1 sensitive ESR display, *Proc. Natl. Acad. Sci. U.S.A.* **82**:411-415.

Gurbiel, R., Cieszka, K., Pajak, S., Subczynski, W. K., and Lukiewicz, S., 1980, Detectability of radiation damage to melanoma cells using ESR spectroscopy, *Folia Histochem. Cytochem.* **18**:87-100.

Hausser, K. H., 1960, Über den einfluss des gelösten sauerstoffs auf die linienbreite der electron-spin-resonanz in Lösung," *Naturwissenschaften* **47**:251.

Himmelblau, D. M., 1964, Diffusion of dissolved gases in liquids, *Chem. Rev.* **64**:527-550.

Hitchman, M. L., 1978, *Measurement of Dissolved Oxygen*, Wiley, New York.

Hyde, J. S., 1979, Saturation-recovery methodology, in *Time Domain Electron Spin Resonance* (L. Kevan and R. N. Schwartz, eds.), pp. 1-30, Wiley, New York.

Hyde, J. S., and Froncisz, W., 1986, Loop-gap resonators, in *Electron Spin Resonance* (M. C. R. Symons, ed.), Vol. 10, pp. 175-184, Specialist Periodical Reports, The Royal Society of Chemistry.

Hyde, J. S., and Hyde, D. A., 1981, Determination of T_2 from analysis of wings of symmetrical inhomogeneous lines, *J. Magn. Reson.* **43**:137-140.

Hyde, J. S., and Sarna, T., 1978, Magnetic interactions between nitroxide free radicals and lanthanides or Cu^{2+} in liquids, *J. Chem. Phys.* **68**:4439-4447.

Hyde, J. S., and Subczynski, W. K., 1984, Simulation of ESR spectra of the oxygen-sensitive spin-label probe CTPO, *J. Magn. Reson.* **56**:125-130.

Hyde, J. S., Swartz, H. M., and Antholine, W. E., 1979, The spin-probe—spin-label method, in *Spin Labeling II. Theory and Applications* (L. J. Berliner, ed.), pp. 71-113, Academic Press, New York.

Ingalls, R. B., and Pearson, G. A., 1961, A basis for the determination of dissolved oxygen by electron spin resonance spectroscopy, *Anal. Chim. Acta* **25**:566-569.

Kalyanaraman, B., Feix, J. B., Sieber, F., Thomas, J. P., and Girotti, A. W., 1987, Photodynamic action of Merocyanine 540 on artificial and natural cell membranes: Involvement of singlet molecular oxygen, *Proc. Natl. Acad. Sci. U.S.A.* **84**:2999-3003.

Korytowski, W., Sarna, T., Kalyanaraman, B., and Sealy, R. C., 1987, Tyrosinase-catalyzed oxidation of DOPA and related catechol(amine)s: a kinetic electron spin resonance investigation using spin-stabilization and spin label oximetry, *Biochim. Biophys. Acta* **924**:383-392.

Kusumi, A., Subczynski, W. K., and Hyde, J. S., 1982, Oxygen transport parameter in membranes as deduced by saturation recovery measurements of spin-lattice relaxation times of spin labels, *Proc. Natl. Acad. Sci. U.S.A.* **79**:1854-1858.

Lai, C.-S., Hopwood, L. E., Hyde, J. S., and Lukiewicz, S., 1982, ESR studies of O_2 uptake by Chinese hamster ovary cells during the cell cycle, *Proc. Natl. Acad. Sci. U.S.A.* **79**:1166-1170.

Lakowicz, J. R., 1982, Diffusive transport of oxygen through proteins and membranes quantified by fluorescence quenching, in *Hemoglobin and Oxygen Binding*, Vol. 1 (C. Ho *et al.*, eds.), Elsevier, New York, pp. 443-448.

Molin, Yu. N., Salikhov, K. M., and Zamaraev, K. I., 1980, *Spin Exchange*, Springer-Verlag, Berlin.

Moro, G., and Freed, J. H., 1981, Calculation of ESR spectra and related Fokker-Planck forms by the use of the Lanczos algorithm, *J. Chem. Phys.* **74**:3757-3773.

Morse II, P. D., and Swartz, H. M., 1985, Measurement of intracellular oxygen concentration using the spin label TEMPOL, *Magn. Reson. Med.* **2**:114-127.

Nemzek, T. L., and Ware, W. R., 1975, Kinetics of diffusion-controlled reactions: transient effects in fluorescence quenching, *J. Chem. Phys.* **62**:477-489.

Pajak, S., Hopwood, L. E., Hyde, J. S., Felix, C. C., Sealy, R. C., Kushnaryov, V. M., and Hatchell, M. C., 1983, Melanin endocytosis by cultured mammalian cells: A model for melanin in a cellular environment, *Exp. Cell Res.* **149**:513-526.

Pajak, S., Subczynski, W., Panz, T., and Lukiewicz, S., 1980, Rate of oxygen consumption of hamster melanoma cells as a factor influencing their radio resistance, *Folia Histochem. Cytochem.* **18**:33-40.

Pake, G. E., and Tuttle, T. R., Jr., 1959, Anomalous loss of resolution of paramagnetic resonance hyperfine structure in liquids, *Phys. Rev. Lett.* **3**:423-425.

Popp, C. A., and Hyde, J. S., 1981, Effects of oxygen on EPR spectra of nitroxide spin-label probes of model membranes, *J. Magn. Reson.* **43**:249-258.

Povich, M. J., 1975a, Measurement of dissolved oxygen concentrations and diffusion coefficients by electron spin resonance, *Anal. Chem.* **47**:346-347.

Povich, M. J., 1975b, Electron spin resonance oxygen broadening, *J. Phys. Chem.* **79**:1106-1109.

Reszka, K., and Sealy, R. C., 1984, Photooxidation of 3,4-dihydroxyphenylalanine by hematoporphyrin in aqueous solutions: An electron spin resonance study using 2,2,6,6-tetramethyl-4-piperidone-1-oxyl (TEMPONE), *Photochem. Photobiol.* **39**:293-299.

Salikhov, K. M., Doctorov, A. B., Molin, Yu. N., and Zamaraev, K. I., 1971, Exchange broadening of ESR lines for solutions of free radicals and transition metal complexes, *J. Magn. Reson.* **5**:189-205.

Sarna, T., and Sealy, R. C., 1984, Photoinduced oxygen consumption in melanin systems. Action spectra and quantum yields for eumelanin and synthetic melanin, *Photochem. Photobiol.* **39**:69-74.

Sarna, T., Duleba, A., Korytowski, W., and Swartz, H., 1980, Interaction of melanin with oxygen, *Arch. Biochem. Biophys.* **200**:140-148.

Sarna, T., Menon, I. A., and Sealy, R. C., 1984, Photoinduced oxygen consumption in melanin systems—II. Action spectra and quantum yields for pheomelanins, *Photochem. Photobiol.* **39**:805-809.

Sealy, R. C., Sarna, T., Wanner, E. J., and Reszka, K., 1984, Photosensitization of melanin: An electron spin resonance study of sensitized radical production and oxygen consumption, *Photochem. Photobiol.* **40**:453-459.

St.-Denis, C. E., and Fell, C. J. D., 1971, Diffusivity of oxygen in water, *Can. J. Chem. Eng.* **49**:885.

Strzalka, K., Sarna, T., and Hyde, J. S., 1986, ESR oximetry: Measurement of photosynthetic oxygen evolution by spin-probe technique, *Photobiochem. Photobiophys.* **12**:67-71.

Subczynski, W. K., and Hyde, J. S., 1981, The diffusion-concentration product of oxygen in lipid bilayers using the spin-label T_1 method, *Biochim. Biophys. Acta* **643**:283-291.

Subczynski, W. K., and Hyde, J. S., 1983, Concentration of oxygen in lipid bilayers using a spin-label method, *Biophys. J.* **41**:283-286.

Subczynski, W. K., and Hyde, J. S., 1984, Diffusion of oxygen in water and hydrocarbons using an electron spin resonance spin label technique, *Biophys. J.* **45**:743-748.

Subczynski, W. K., and Kusumi, A., 1985, Detection of oxygen consumption during very early stages of lipid peroxidation by ESR nitroxide spin probe method, *Biochim. Biophys. Acta* **821**:259-263.

Subczynski, W. K., Lukiewicz, S., and Hyde, J. S., 1986, Murine *in-vivo* L-band ESR spin-label oximetry with a loop-gap resonator, *Magn. Reson. Med.* **3**:747-754.

Swartz, H. M., 1987, The use of nitroxides to measure redox metabolism in cells and tissues, *J. Chem. Soc., Faraday Trans. 1,* **83**:191-202.

Tinkham, M., and Strandberg, M. W. P., 1955a, Theory of the fine structure of the molecular oxygen ground state, *Phys. Rev.* **97**:937-951.

Tinkham, M., and Strandberg, M. W. P., 1955b, Interaction of molecular oxygen with a magnetic field, *Phys. Rev.* **97**:951-966.

Windrem, D. A., and Plachy, W. Z., 1980, The diffusion-solubility of oxygen in lipid bilayers, *Biochim. Biophys. Acta* **600**:655-665.

Yin, J.-J., and Hyde, J. S., 1987a, Application of rate equations to ELDOR and saturation recovery experiments on ^{14}N-^{15}N spin-label pairs, *J. Magn. Reson.* **74**:82-93.

Yin, J.-J., and Hyde, J. S., 1987b, Spin-label saturation-recovery electron spin resonance measurements of oxygen transport in membranes, *Z. Phys. Chem.* (*Frankfurt Am Main*) **153**:S, 57-65.

Yin, J.-J., Pasenkiewicz-Gierula, M., and Hyde, J. S., 1987, Lateral diffusion of lipids in membranes by pulse saturation recovery electron spin resonance, *Proc. Natl. Acad. Sci. U.S.A.* **84**:964-968.

Yin, J.-J., Feix, J. B., and Hyde, J. S., 1988, Solution of the nitroxide spin label spectral overlap problem using pulse electron spin resonance, *Biophys. J.* **53**:525-531.

9

Chemistry of Spin-Labeled Amino Acids and Peptides

Some New Mono- and Bifunctionalized Nitroxide Free Radicals

Kálmán Hideg and Olga H. Hankovszky

1. INTRODUCTION

The ESR spectrum of the nitroxide group will be affected by constraint in an oriented electric or magnetic field if the nitroxide moiety combined with a macromolecule is placed in such an environment.

Evaluation of the ESR spectrum of a selectively labeled biological center therefore provides very considerable help in the study of many biochemical and biophysical problems. There is a steadily increasing interest in research on novel nitroxide free radicals containing such reactive functional groups, which make possible coupling to biologically important macromolecules. These investigations using the ESR technique greatly enhance the study of internal properties, such as the relationship between structure and function. There is a number of excellent textbooks and reviews covering the theory and applications of nitroxides as spin labels in the solution of biological problems (Aurich, 1982; Berliner, 1974, 1979, 1983; Buchachenko, 1965; Dugas, 1977; Fehér, 1969; Forrester *et al.*, 1968; Gaffney, 1976; Gaffney and McNamee, 1974; Gnewuch and Sosnovsky, 1986; Griffith and Waggoner, 1969; Jost and Griffith, 1972, 1978; Kalmanson and Grigoryan, 1973; Kamzolova and Postnikova, 1981; Keana, 1978, 1979, 1984; Lichtenshtein, 1974; McConnell and Gaffney-McFarland, 1970; Rozantsev, 1970; Rozantsev and Sholle, 1971a, 1971b; Sinha and Chignell, 1979; Smith, 1972; Zhdanov, 1981). The diverse chemical and physical properties of the reactive centers occurring in the biological systems of interest are the source of the ever-increasing demand for developing novel spin-label reagents.

Kálmán Hideg and Olga H. Hankovszky • Central Laboratory, Chemistry, University of Pécs, H-7643 Pécs, Hungary.

Ever since the introduction of nitroxides as reporter groups, the endeavors were aimed at spin-labeling a given macromolecule in as selective as possible a way, and with minimal perturbance of the biological system itself.

The first nitroxide spin labels were developed by combining the already well-known protein modification reagents with a nitroxide heterocycle, such as **1** (Smith, 1968; Barratt *et al.*, 1972), **2** (Dryer *et al.*, 1983), **3** (Griffith and McConnell, 1966; Smith, 1968; Thomas *et al.*, 1976), **4** (Dryer *et al.*, 1983), **5** (Ogawa and McConnell, 1967; McConnell *et al.*, 1969; Spalholz and Piette, 1972), **6**, **7**, (McConnell *et al.*, 1969), **8** (Hoffman *et al.*, 1970), **9** (Berliner and McConnell, 1966; Berliner and McConnell, 1974), **10** (Berliner and McConnell, 1966; Flohr *et al.*, 1971; Flohr and Kaiser, 1972).

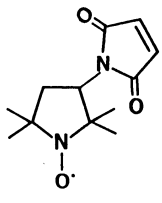

1

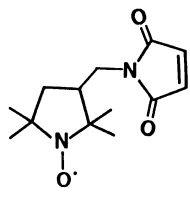

2

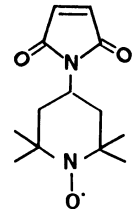

3

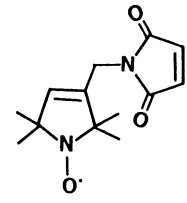

4

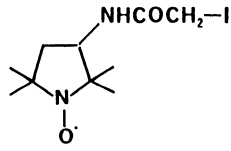

5

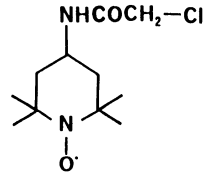

6

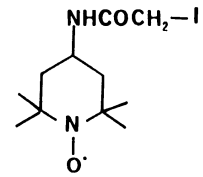

7

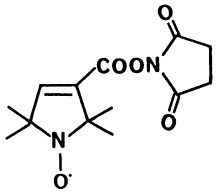

8

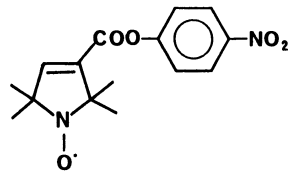

9

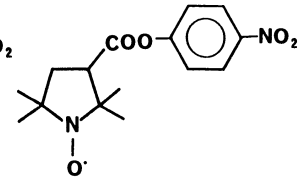

10

Recently, the isotope-labeled iodoacetamido reagent **11** (Prince, 1973) and the maleimido reagent **12** (Venkataramu *et al.*, 1979; Beth *et al.*, 1981a, 1981b) have also been prepared.

Elegant synthetic work was done also in order to obtain minimal perturbance in spin-labeled nitroxide fatty acids and phospholipids (Keana, 1979).

New and promising combined spin-label assays have also been reported, such as spin assay, spin immunoassay. (Stryer, 1965, Hsia, 1968; Leute *et al.*, 1972; Hsia *et al.*, 1973) and spin membrane immunoassay (Hsia and Tan, 1978). A large amount of

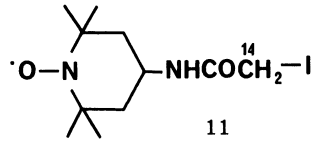

11

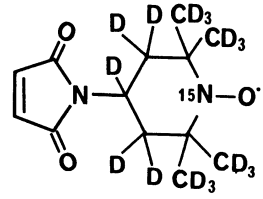

12

interesting work (Konieczny and Sosnovsky, 1981) has been done on phosphor(n)ylated nitroxides.

Relatively less data have been reported concerning the development of new spin-label reagents capable of reacting with minimal perturbance in the course of a systematic stepwise synthesis of amino acids, peptides, and nitroxide-α-amino acids. Methods of synthesis for the preparation of spin-labeled derivatives of some drug molecules, some new nitroxide synthon molecules, cross-linking spin-label reagents, and novel syntheses for spin-labeled fatty acids are summarized in the present review.

2. SPIN LABELING OF AMINO ACIDS AND PEPTIDES

The most important target molecules of spin labeling are probably the proteins. For another pertinent review see Wenzel *et al.* (1983).

In order to develop really promising methods to label a complicated protein molecule, one should design labeling reagents capable of reacting with the different functional groups of an imaginary peptide chain.

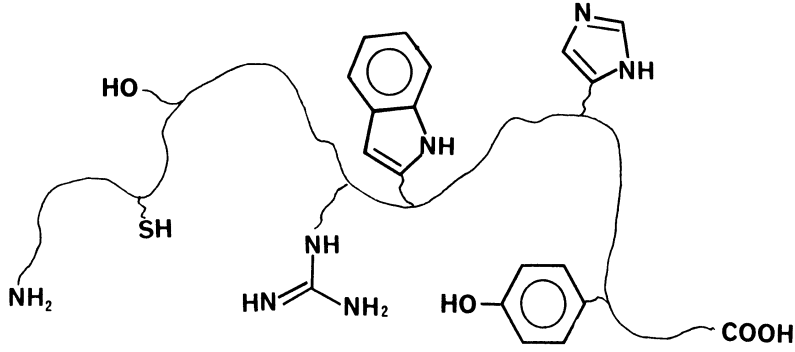

2.1. Reagents for Labeling at the Amino Terminal

2.1.1. Acylation

An acylated glycine ester (**17**) was prepared with a dibromoketone reagent. The reagent (**16**) was obtained by the oxidation of dibrominated triacetoneamine (**15**) (Golding *et al.*, 1975; Alcock *et al.*, 1977) (Scheme 1).

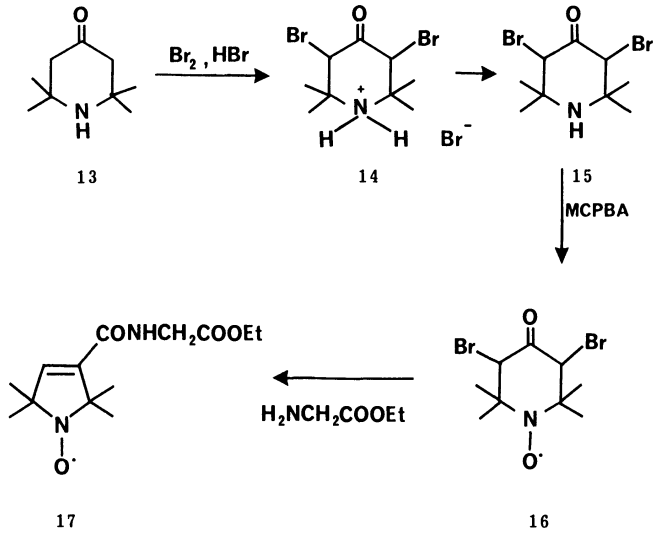
Br2 , HBr
Br
Br
Br

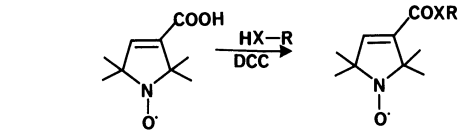

	X	R
9	O	$-NO_2$
18	O	$-NO_2$, NO_2
19	O	Cl Cl Cl Cl Cl
8	O	
20	O	
21	O	
22	S	
23	S	$-CH_2-$
24	O	F F F F F
25		

Scheme 2. References for preparation and/or labeling procedures are as follows: **9**, Berliner *et al.* (1966); Hankovszky *et al.* (1978). **18–20**, **22**, and **23**, Hankovszky *et al.* (1978). **8**, Hoffman *et al.* (1970). **21**, Hideg *et al.* (1978). **24**, **25**, Hideg *et al.* (1980).

Scheme 3.

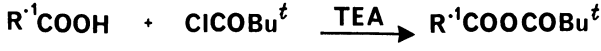

26 27

Scheme 4.

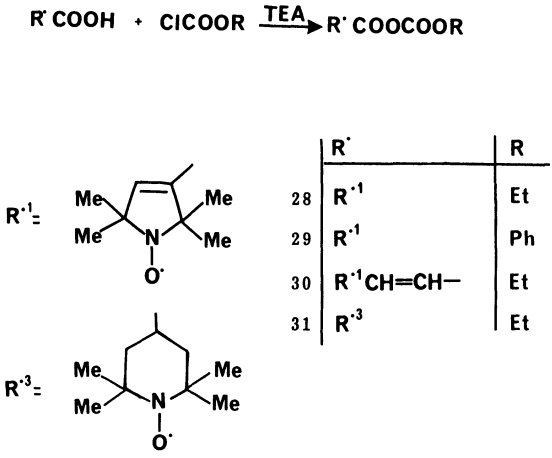

Scheme 5. References for preparation and/or labeling procedures are as follows: **28**, Griffith *et al.* (1967); Hankovszky *et al.* (1978). **29**, Griffith *et al.* (1967). **30**, Hideg *et al.* (1978). **31**, Rauchman and Rosen (1976).

The pyrrolinylcarbonyl azide **32** has been prepared either from an active ester (**8**) or an acyl carbonate (**28**) in aqueous acetone with sodium azide (Hankovszky *et al.*, 1978) (Scheme 6).

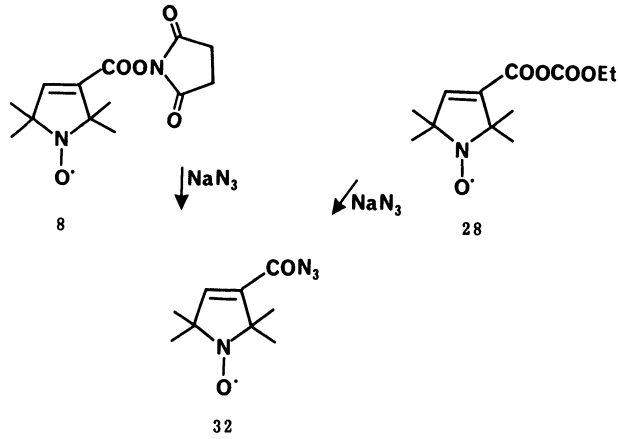

Scheme 6.

This azide is stable for years at 10 °C.

2.1.1d. Acyl Imidazoles. Acyl imidazoles have been prepared from the free acid **26** with carbonyldiimidazole (CDI) (Barratt *et al.*, 1969) or by acylation of imidazole with the acyl carbonate **28** (Hideg *et al.*, 1978) (Scheme 7).

Because of its tendency to undergo hydrolysis, the acyl imidazole **33** is not used frequently for the labeling of biological systems. Like CDI, it is sensitive to moisture.

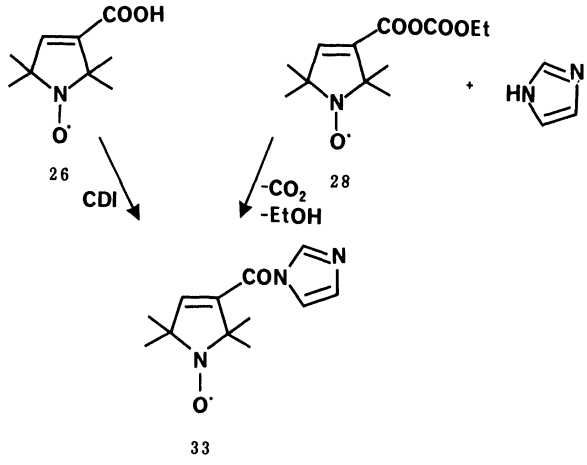

Scheme 7.

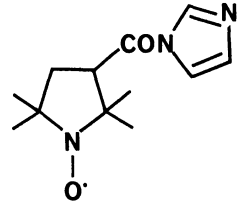

34

The saturated derivative **34** was reported (Adackaparayil and Smith, 1977) to be more stable than the unsaturated one **33**. Recently, the histone H1 from calf thymus (Lawrence *et al.*, 1980) and histone core extracted from chicken erythrocytes (Chan and Piette, 1980) were labeled with compound **34**.

A detailed study (see Scheme 8) revealed that the 1-oxyl-2,2,5,5-tetramethyl-3-pyrroline-3-carbonyl moiety could be introduced into an amino acid by several routes (Hideg *et al.*, 1980).

The coupling of the pyrrolinecarboxylic acid **26** with the amino acid ester **35** in the presence of dicyclohexylcarbodiimide could only be effected if an active hydroxy compound (e.g., 1-hydroxybenzotriazole, *N*-hydroxysuccinimide) had also been added to the reaction mixture. The assumption of the formation of an active ester was supported by the fact that the acylation was readily accomplished with either an active ester (**8**) or mixed anhydrides (**28**, **27**). Alkaline hydrolysis of the esters (**36**) to the free *N*-acylated amino acids involves an increased hazard of racemization of the optically active amino acids. This can be minimized by using a carbonyl azide reagent (**32**) for acylating the free amino acids (**38**).

Direct peptide coupling of compound **37** with amino acid esters in the presence of DCC did give the labeled dipeptides (**39**), but the yields were very low. Higher yields could be attained by adding *N*-hydroxysuccinimide to the reaction mixture or

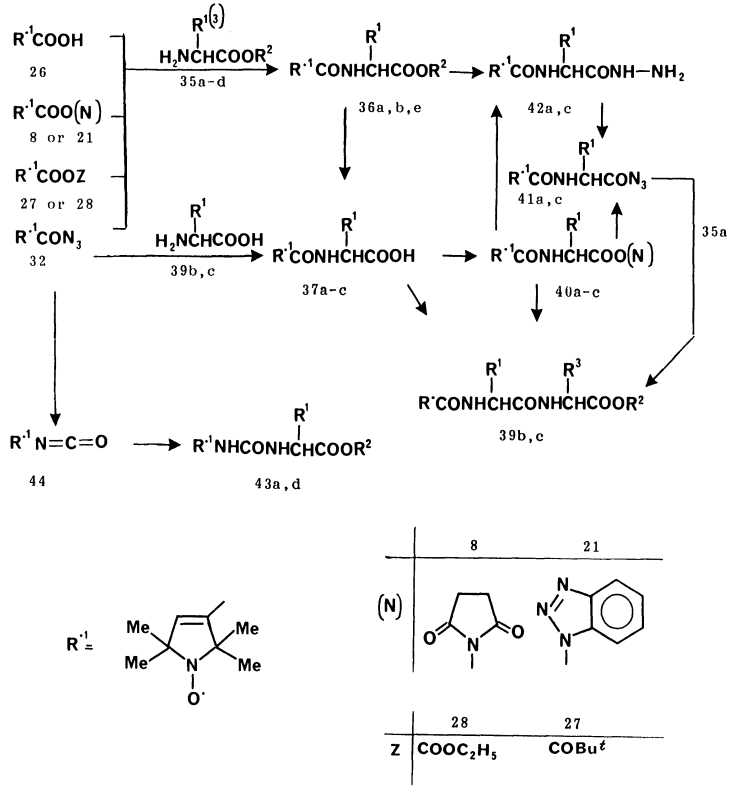

Scheme 8.

by converting the acids with *N*-hydroxysuccinimide into an active ester and then coupling it with the amino acid esters to give the peptides **39** (Scheme 8).

The active ester **40** could readily be converted into the corresponding labeled acyl amino acid azide (**41**) (Hideg *et al.*, 1978) at low temperature (0 °C). The alternative route to compound **41** has also been worked out by reacting **36** or **40** with hydrazine at room temperature; the resulting hydrazides **42** could be then transformed into **41** by treatment with sodium nitrite in dilute hydrochloric acid without destroying the radical moiety. The reaction of **35** with **41** gave a dipeptide **39** (Hideg *et al.*, 1978).

α-Ureido acids **43** (Hideg *et al.*, 1978) can be prepared via the unsaturated isocyanate label **44** obtained by the Curtius reaction of the spin-labeled carbonyl azide **32** (Hideg *et al.*, 1978).

The dipeptide **45** was prepared (Kalk *et al.*, 1975) by coupling the pyrrolinecarboxylic acid (**26**) with Phe-LeuOCH$_3$ in the presence of DCC. Thereafter, the carboxylic acid was liberated by alkaline hydrolysis of the ester.

A tetrapeptide acylated at the amino terminal (**46**) was obtained (Maksimova *et al.*, 1975) from the ester of *N*-hydroxysuccinimide formed with 1-oxyl-2,2,6,6-tetramethyl-4-piperidylacetic acid (**48**) (Scheme 9). This ester (**47**) was prepared by a transacylation reaction from the succinimide ester of trifluoroacetic acid.

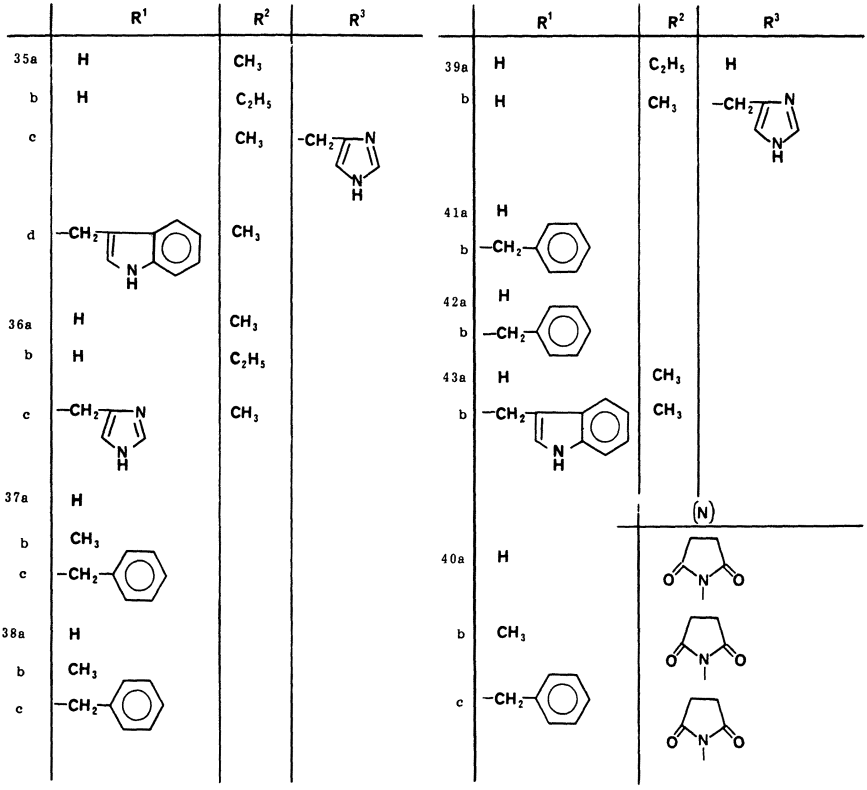

Scheme 8. Continued.

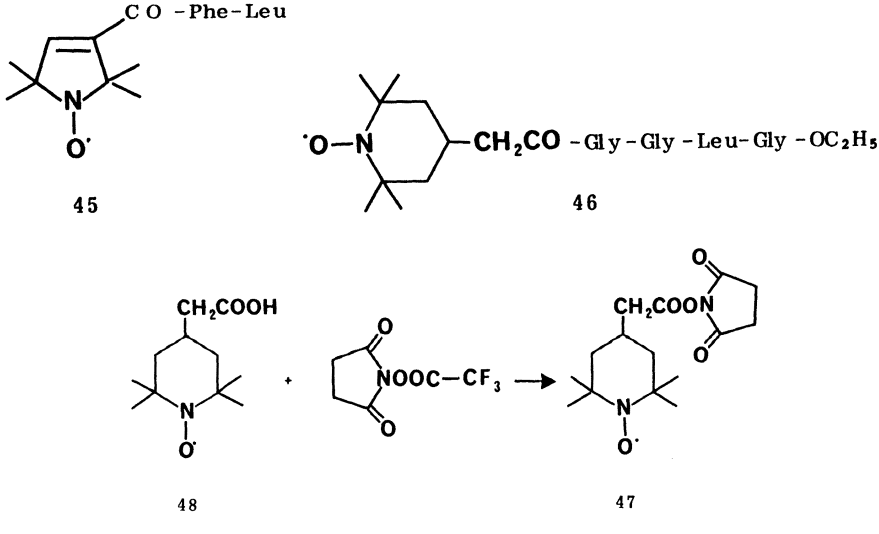

Scheme 9.

2.1.1e. Isocyanates. Because of the stability of the carbonyl azide **32** and the instability of isocyanates, carbonyl azides may serve as ready-to-use precursors of isocyanates.

The saturated isocyanate, 1-oxyl-2,2,5,5-tetramethyl-3-isocyanatopyrrolidine (**49**), was first prepared from 1-oxyl-2,2,5,5-tetramethyl-3-aminopyrrolidine (**50**) and phosgene (Stone *et al.*, 1965) (Scheme 10).

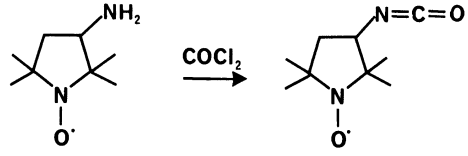

50 49

Scheme 10.

2.1.1f. Isothiocyanates. Synthesis of the more stable isothiocyanates has also been described.

In aqueous sodium hydroxide the reaction of 1-oxyl-2,2,6,6-tetramethyl-4-aminopiperidine (**51**) with thiophosgene gave 4-isothiocyanato-2,2,6,6-tetramethyl-piperidin-1-oxyl (**52**) (Gaffney, 1976).

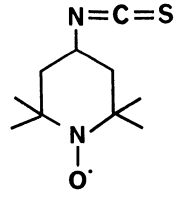

52

The isothiocyanate **52** was applied for labeling at amino terminals. It was also used for synthesis of the spin-labeled analogue of pepstatin (**53**) (Schmidt *et al.*, 1982).

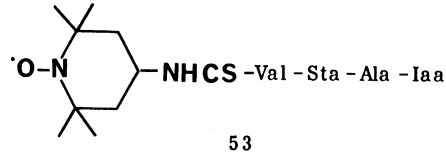

53

Sta = (3S,4S)4-amino-3-hydroxy-6-methylheptanoic acid

Alternative routes (Scheme 11) for the synthesis of **52** and other isothiocyanate derivatives (**56, 57**) (Hankovszky *et al.*, 1981) were also realized by the reaction of

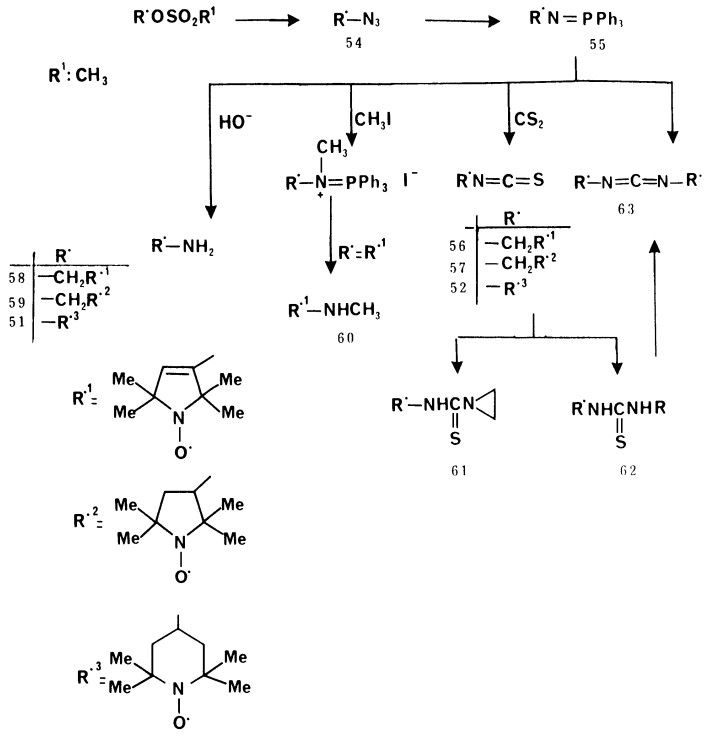

Scheme 11.

phosphinimines (**55**), prepared from the corresponding azides **54** (Hideg *et al.*, 1977; Hankovszky *et al.*, 1981), with carbon disulfide.

The phosphinimines (**55**) also offered an alternative route to obtain amino nitroxides (**58, 59, 51**). The spin-labeled isothiocyanates (**56, 57, 52**) served also as precursors to newer spin-labeled carbodiimides (**63**).

2.1.1g. Carbodiimides. Two spin-labeled carbodiimides have been reported earlier; the spin label **64** has been used for inhibition of membrane-bound ATP-ase, to label the mitochondrial membrane (Azzi *et al.*, 1973); the morpholino derivative **65** has been applied for the labeling of RNA (Kumarev and Knorre, 1970).

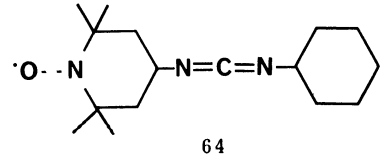

64

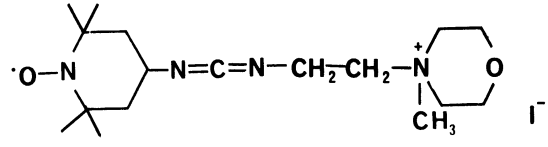

65

2.1.1h. Active Carbonate. An active carbonate (**67**) was synthesized and used for labeling at the amino group in solid phase peptide syntheses (Sparrow, 1976), e.g. of **68** (Scheme 12).

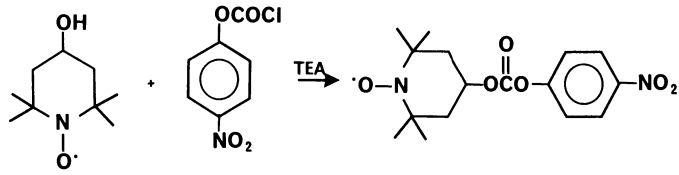

66 67

Scheme 12.

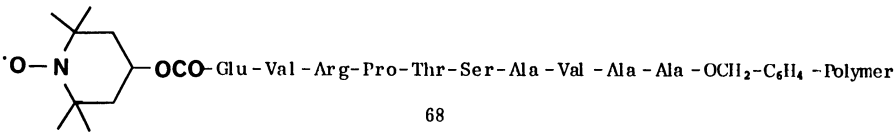

68

2.1.1i. Azidoformate. For spin-labeling at the amino group it is desirable to prepare a spin-labeled group with resemblance to the *t*-butoxycarbonyl azide protecting group (Carpino *et al.*, 1959; Wünsch, 1974).

A piperidinyloxycarbonylimidazole (**69**) was synthesized (Hankovszky *et al.*, 1979) from the *N*-oxyl-4-hydroxypiperidine radical **66** and 1,1'-carbonyldiimidazole (CDI), according to Staab's method (Staab, 1957; Staab and Mannschreck, 1962), described for the synthesis of *N*-*t*-butyloxycarbonyl imidazole (Klee and Brenner, 1961) (Scheme 13). The reagent was highly reactive in the salt form (tosylate) (**70**). With sodium azide it gave 1-oxyl-2,2,6,6-tetramethyl-4-piperidinyloxycarbonyl azide (**71**) instantaneously at room temperature (Scheme 14).

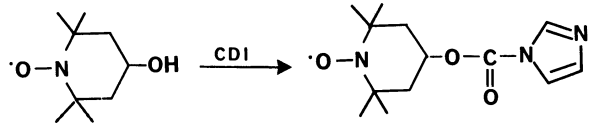

66 69

Scheme 13.

The azide proved to be a convenient reagent also for the preparation of piperidinyloxycarbonylamino acids (**72a-c**). The advantage of the azide reagent was that the labeling of free amino acids and amino acid esters could be carried out equally readily.

2.1.1j. Phosphor(n)ylating Reagents. 1-Oxyl-2,2,6,6-tetramethyl-4-piperidyl-phenyl-phosphono chloride (**73**) and 1-oxyl-2,2,6,6-tetramethyl-4-piperidyl phenyl imidazole-1-phosphonate (**74**) were synthesized and used for the labeling of amino acid esters **75** by Sosnovsky and Konieczny (1976) (Scheme 15).

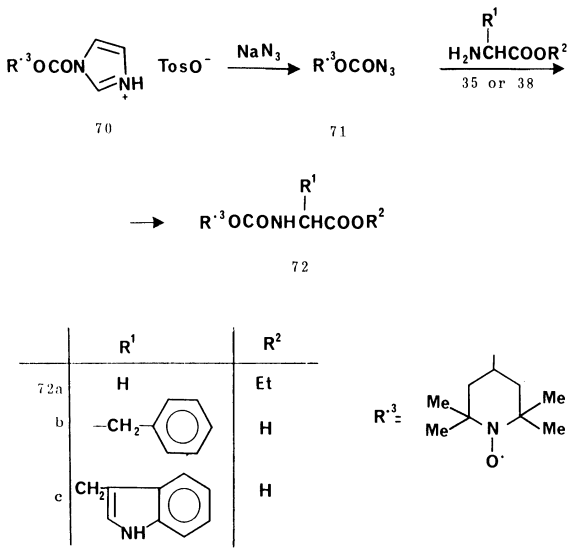

Scheme 14.

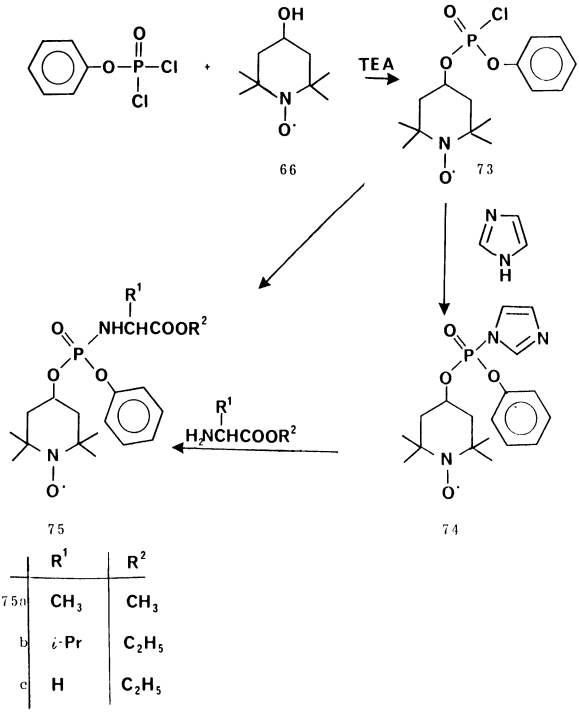

Scheme 15.

The phosphor(n)ylating reagents **76** (Morrisett and Broomfield, 1972), **77** (Hsia *et al.*, 1969), and **78** (Grigoryan *et al.*, 1973) have also been introduced for spin-labeling of enzymes.

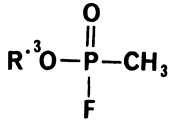

76

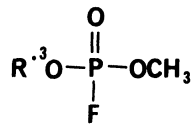

77

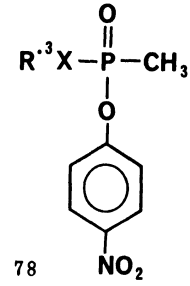

78

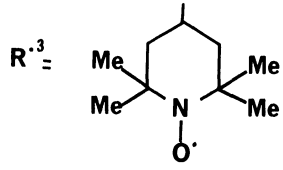

X = O, $-CH_2CH_2O-$

2.2. C-Terminal Spin-Labeled Amino Acids and Peptides

To achieve the amide formation reaction of an amino acid with amino spin-label reagents, first a protecting group has to be attached to the amino terminal. It is advantageous to introduce protective groups that are easy to split off again without destroying the nitroxide label at the carboxyl terminal. Any known peptide-protecting group can be used which fulfils this requirement.

According to Weygand's method (Weygand and Geiger, 1956; Weygand and Freuendorfer, 1970) the amino acid is first transformed into the *N*-trifluoroacetylated derivative (**79a**), which is then used for acylating the amino spin-label reagents. Finally, the trifluoroacetyl group is removed by aqueous ammonia or sodium borohydride (Misharin *et al.*, 1974; Pirrwitz and Damerau, 1976) to obtain, e.g., compound **79b** (Scheme 16).

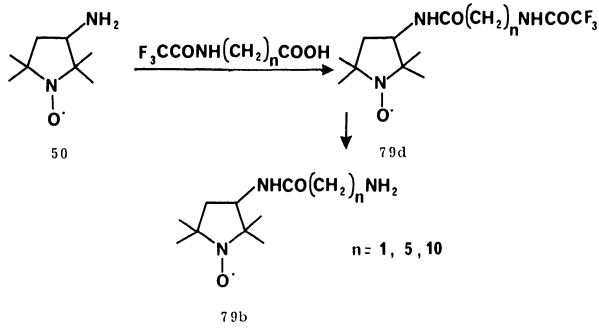

Scheme 16.

In the course of preparation of spin-labeled pepstatin (**80**) the *N*-terminal was protected with trifluoroacetyl group in the tetrapeptide and the spin-labeled product was prepared with NH_2-$R^{\cdot 3}$ in the presence of DCC and hydroxybenzotriazole.

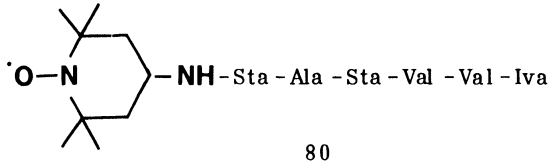

80

The labeled dipeptide Gly-Phe-NH-$R^{\cdot 3}$ (**83**) was synthesized from the benzyloxycarbonyl-protected dipeptide for coupling to the hormone-binding site of neurophysin. Removal of the protecting group by hydrogenation led to the loss of the radical; the piperidine-*N*-oxyl moiety was reduced to the 1-hydroxypiperidyl derivative (**82**) which, however, could readily be reoxidized to the *N*-oxyl compound **83** (Lord and Breslow, 1978, 1979, 1980; Lundt and Breslow, 1976) (Scheme 17).

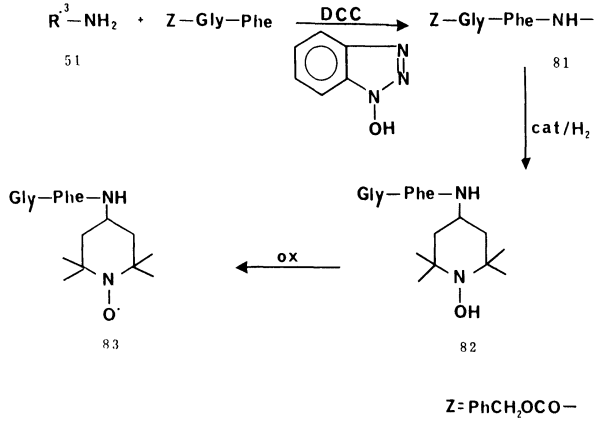

Scheme 17.

In other works the *N*-nitrophenylsulfenyl-(NPS)-protected amino acids were converted into *N*-succinimide esters and allowed to react with $R^{\cdot 2}$-NH_2 (**50**). The free amino C-terminal-labeled amino acids were then obtained by a mild split-off reaction. Deprotecting to give **84** was accomplished with thiocyanate and 2-methylindole in methanol/acetic acid (Fittkau and Damerau, 1980).

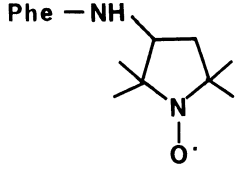

84

Synthesis of C-terminal spin-labeled di- and tripeptides (**85, 86**) have also been described. The amino terminal was protected with an NPS group. For example, the NPS-amino acid *N*-succinimide ester of the NPS peptide carbonyl azide was coupled with the amino radical reagent (Scheme 18). The product **86** proved to be a highly potent competitive inhibitor of leucine aminopeptidase (Fittkau *et al.*, 1979).

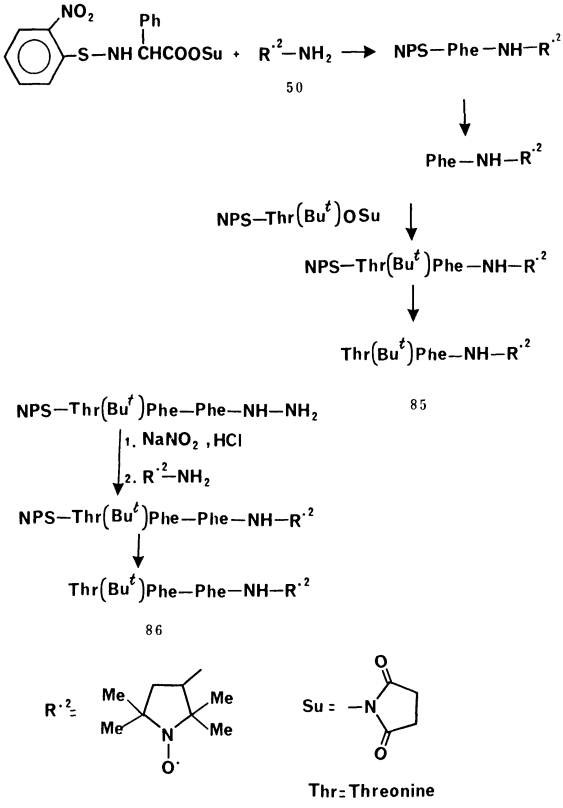

Scheme 18.

2.3. Amino Acids and Peptides Labeled in the Side Chain

Efforts to develop side-chain spin labels are of utmost importance for several reasons:

(1) Side-chain labeled amino acids can be elongated at both the N-terminal and the C-terminal.

(2) The side chains of peptides or proteins very often have an important functional role in the biological activity; therefore, the spin label should be attached in a selective way to the functional group of the side chain of the peptide or protein in question. Consequently, the most wanted spin-label reagents are expected to label at: the ε-amino group of lysine; the cysteine-SH; the hydroxyl group of tyrosine, serine or threonine; the imidazole ring of histidine; the indole NH of tryptophan in a selective way; the guanidine group of arginine.

In recent years a spin-label dinitrobenzene derivate of lysine amide (**87b**) was described (Gerig *et al.*, 1979); it has been prepared from the dinitrofluorobenzene reagent **87a**.

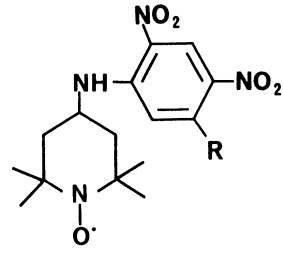

87

	R
87a	—F
b	—NH(CH$_2$)$_4$CHCONH$_2$ NHCOCH$_3$

Similar reagents have also been synthesized in order to couple the radical to the protein by nucleophilic substitution of the reactive fluorine with the amine function (Cazianis *et al.*, 1980; Hsia *et al.*, 1980; Hsia and Kwan, 1981).

The syntheses of the reagents **88**, **89** have been carried out (Hsia, 1968) from commercially available 1,5-difluoro-2,4-dinitrobenzene.

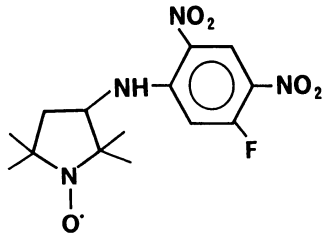

88

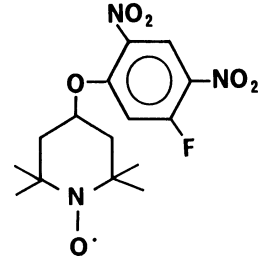

89

Aryl fluorides, however, have the drawback of low specificity. In addition, they can also react with thiol group, imidazole-nitrogen or the phenolic hydroxyl of tyrosine.

A new type of reagent, an imidate (**90**), has recently been introduced (Mehlhorn *et al.*, 1980). It was synthesized from the unsaturated nitrile **91** (Scheme 19). It is interesting to note that the radical does survive treatment with hydrogen chloride.

The imidate spin label was used to study the interactions of cytochrome C with lipids and proteins. The advantages of the reagent are its solubility in water and specificity for lysine.

O-Labeled tyrosine (**92**) was prepared with an allylic type of sulfonate spin label (**93**) (Hankovszky *et al.*, 1980) (Scheme 20).

An unsaturated ketone (**94**) was prepared and used recently to label cysteine (**95**) (Shapiro *et al.*, 1977a, 1977b) (Scheme 21).

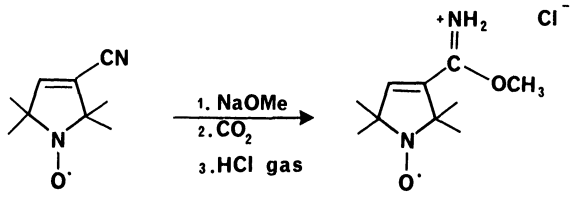

91 90

Scheme 19.

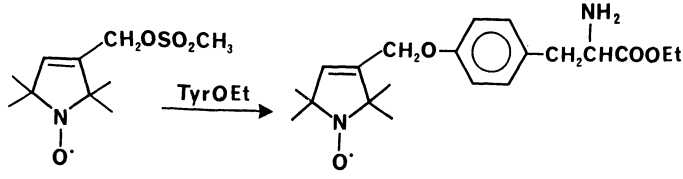

93 92

Scheme 20.

The well-known thiol-specific spin labels: the maleimide (**3**), iodoacetamide (**7**), and *p*-chloromercuribenzoyl derivatives (**96**), have also some drawbacks; they are not reversible labels; further, to achieve complete labeling requires sometimes a long period (several hours). These reagents are not even fully thiol-specific. The iodoacetamides are reactive toward other nucleophiles (such as amines), too. The ability of alkyl

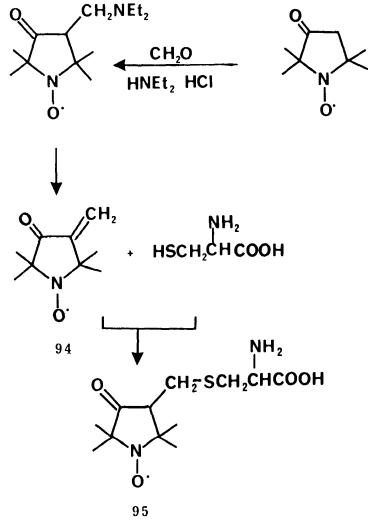

94 95

Scheme 21.

alkane-thiosulfonates (Kenyon and Bruice, 1977) to act as thiol blocking reagents was utilized in the preparation of a new spin label (1-oxyl-2,2,5,5-tetramethyl-3-pyrroline-3-methyl) methane-thiol-sulfonate (**97**) (Berliner *et al.*, 1982). The reactivity of the thiosulfonate reagent is also enhanced by its allylic ester character. Compound **97** meets the requirements of a highly reactive thiol-specific reagent, the sensitivity of which to the thiol site conformation is due to a minimum number of flexible linkages between the nitroxide ring and cysteine side chain (**98**) (Scheme 22).

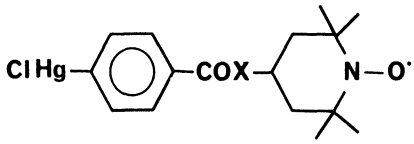

96

X = O, NH

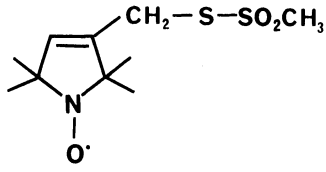

97

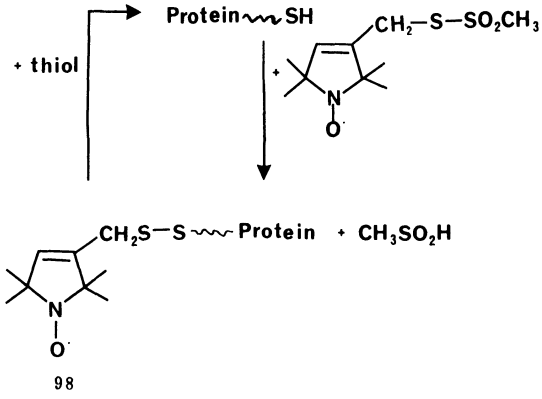

98

Scheme 22.

This label has easy reversibility in the presence of mild reducing agents, such as dithiothreitol. By virtue of the sharp three-line ESR spectrum of the nitroxide released from the protein, it can be used for assaying reactive thiol groups in a protein (Berliner *et al.*, 1982).

An iodoacetamido reagent (**5**) was used to prepare the labeled dipeptide **99**, suitable for studying the neurophysin complex (Lord and Breslow, 1978, 1979, 1980; Lundt and Breslow, 1976).

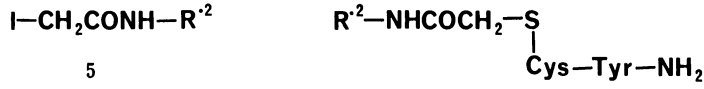

5 99

It was important to find a reagent capable of selectively labeling the guanidino moiety of arginine. Utilizing the results achieved with various 1,2-dioxo compounds, e.g., 1,3-dioxobutane and phenylglyoxals, spin-labeled glyoxals were prepared by the SeO_2 oxidation of aryl methyl ketone spin labels (Hankovszky *et al.*, 1987) (Scheme 23). Arginine-containing polypeptides could be selectively labeled with **100a**.

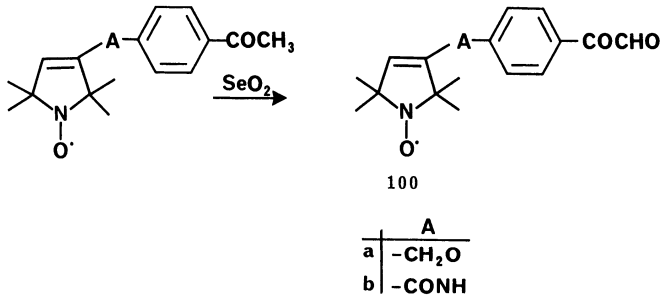

100

	A
a	$-CH_2O$
b	-CONH

Scheme 23.

A series of mono- and bis-labeled bradykinin derivates has been prepared (Reissmann *et al.*, 1976; Filatova *et al.*, 1977) by the reaction of active esters (4-nitrophenyl-*N*-succinimidyl, tri- and pentachlorophenyl) or symmetrical anhydrides of nitroxide acids (**101**, **48**).

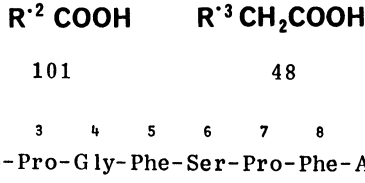

Bradykinin

ESR studies were made on a series of spin-labeled derivatives of bradykinin and its shortened analogues bearing nitroxyl radicals at position 1, 5, 6 or 8. The average 1-4, 1-6, 1-8, and 5-8 distances between the paramagnetic nitroxyl centers were determined by dipole-dipole interaction measurements in frozen (glass) solutions at

−196 °C. The results obtained are indicative of the presence of folded structures in conformational equilibrium.

The 4-nitrophenyl ester proved to be the most suitable reagent for labeling the hydroxyl group of serine or tyrosine.

3. NITROXIDE AMINO ACIDS

The design of stable nitroxide spin labels causing minimal perturbance in the physical and chemical behavior of the biomolecule has been a continuous effort ever since the beginning of their introduction as reporter groups. This target seemed to be approachable by preparating amino acids having nitroxide moiety as a side chain. The results are summarized below.

3.1. Imidazolinyl Nitroxide Amino Acids

Two free radical analogues of histidine (**102, 103**) were synthesized by Weinkam and Jörgensen (1971a, 1971b) on the basis of Ullman's procedure (Ullman *et al.*, 1970, 1972) (Scheme 24).

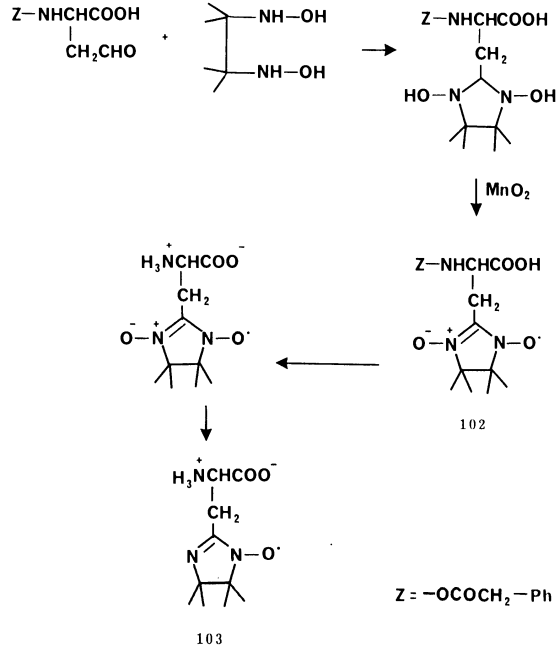

Scheme 24.

These amino acids were used for conformational studies of the carboxyl terminal part of angiotensin II (Weinkam and Jörgensen, 1971b).

3.2. Pyrrolidine Nitroxide Amino Acids

A β-amino acid was prepared by the conjugate addition of ammonia to the unsaturated nitrile **91**; the β-aminonitrile **104** was then hydrolyzed to the amino acid **105** (Rassat and Rey, 1967) (Scheme 25).

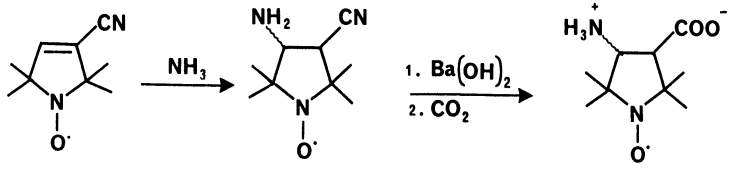

91 104 105

Scheme 25.

3.3. Pyrrolinyl Nitroxide Amino Acids

Three methods were reported recently (Lex *et al.*, 1982) for the synthesis of 2-amino-3-(1-oxyl-2,2,5,5-tetramethyl-3-pyrrolin-3-yl) propionic acid (**106**) and its derivatives according to Scheme 26.

The amino acids are racemates; however, they have only one asymmetric center belonging to the amino acid. This fact makes resolution easier than it would be in the presence of additional asymmetric center(s) in the heterocycle.

The amino acid **106** can be used as a synthon in peptide syntheses, due to its structural resemblance to natural aralkyl amino acids, such as histidine or tryptophan.

3.4. Piperidinyl Nitroxide Amino Acids

The *N*-oxyl-piperidinyl amino acid **119** has been synthesized from **117** in two steps (Rassat and Rey, 1967). The product **119** was used in a proton NMR relaxation study (v. Goldammer *et al.*, 1978) and a series of its complexes with transition metals was also studied (Jahr *et al.*, 1973; Terzian *et al.*, 1976).

The pH dependence of isotopic hyperfine splitting renders this compound suitable for use as a pH indicator in biological systems (Nakaie *et al.*, 1981). It was also employed to label vitamin B_6 (**120**) (Misharin *et al.*, 1975).

The lack of an α-hydrogen in this amino acid makes it unlikely that this compound would be of any great use for peptide reactions. Studies for the preparation of homologues are now in progress, and the next two homologues (**121**, **122**) (Wenzel, unpublished results) seem to be more promising; the same applies to the tetrahydropiperidine-1-oxyl amino acid **123** (Csekö *et al.*, 1985).

It is hoped that in the not too distant future a large selection of nitroxide free radical α-amino acids will be available as synthons to study biologically active peptides with built-in nitroxide α-amino acid unit(s).

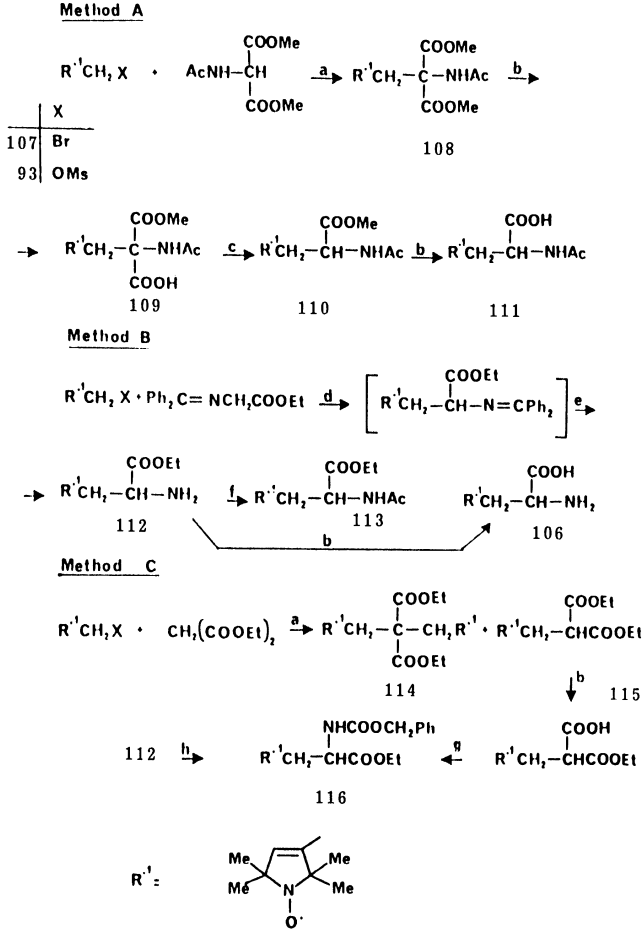

Scheme 26. **a**, sodium ethoxide; **b**, one eq. NaOH; **c**, Δ, $-CO_2$; **d**, tetrabutylammonium hydrogen sulfate (as phase transfer catalyst); **e**, aq. citric acid; **f**, acetylimidazole; **g**, diphenylphosphoryl azide; **h**, benzyloxycarbonyl chloride.

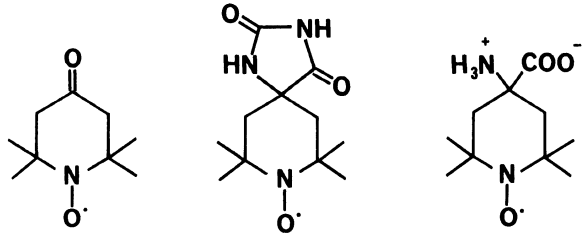

117 118 119

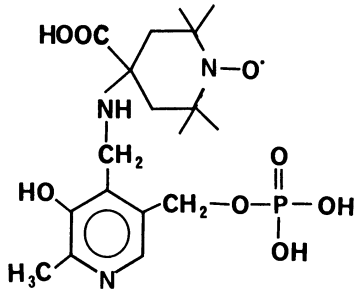

120

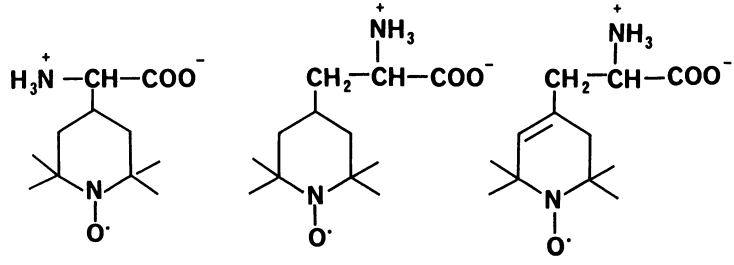

121 122 123

4. NEW MONO- AND BIFUNCTIONALIZED SPIN LABELS

The major incentive in the efforts to synthesize nitroxide molecules with new reactive functional group(s) is their steadily increasing importance in the labeling of biomolecules with either one or two reactive functional groups.

4.1. Reactions with 3-Functionalized-3-Pyrroline-1-Oxyl Derivatives

Syntheses of the most frequently used nitroxide free radicals capable of reacting with amino acids and peptides have led to several new reagents (Scheme 27). The acid **26** and the acyl carbonate **28** proved to be convenient starting materials for the preparation of a versatile nitroxide allylic alcohol (**124**). The saturated alcohol **125** was readily obtained either from the corresponding acid or the sterically hindered unsaturated active esters **19**, **24**, when both the carbon-carbon double bond and the ester function had been attacked by complex metal hydride reagents (e.g., sodium borohydride).

Oxidation of the unsaturated alcohol **124** to the α,β-unsaturated aldehyde **126** has been carried out conveniently by activated MnO_2. The saturated aldehyde **127** was obtained by oxidation of **125** with pyridinium dichromate. Both aldehydes (**126**, **127**) could be prepared via reduction of the corresponding acyl imidazoles (**33**, **34**) with

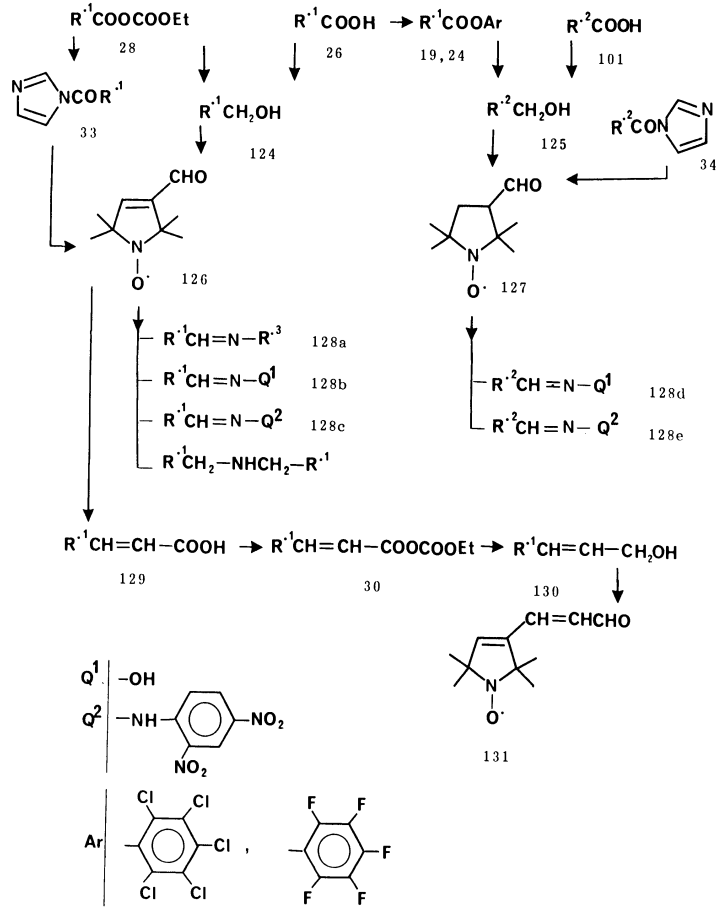

Scheme 27.

diisobutylaluminum hydride (Scheme 27) (Hideg *et al.*, 1980). The aldehydes represent new, convenient spin-label oxo reagents for amines.

Other aldehydes **132**, **133**, **134** (Schlude, 1973, 1975), and **135** (Brière *et al.*, 1979) have also been prepared in different ways.

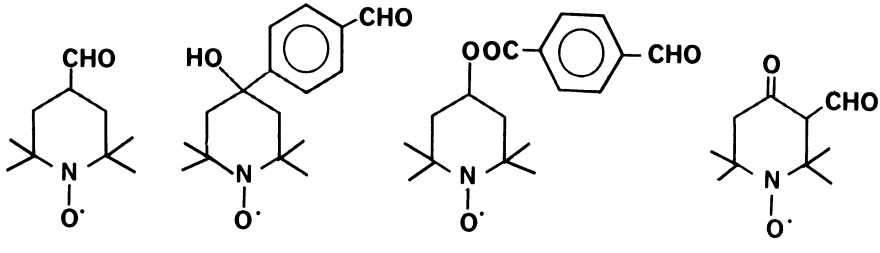

The unsaturated aldehyde **126** was the starting compound in the preparation of various nitroxide polyenes: the diene acid **129** (Hideg *et al.*, 1980; Koch *et al.*, 1979) was formed with malonic acid in a Knoevenagel reaction; from the diene acid (**129**), the diene acyl carbonate (**30**) was obtained by means of ethyl chloroformate; the reduction of **30** gave the diene alcohol **130**, and the latter underwent a convenient allylic oxidation with MnO_2 to yield the diene aldehyde **131** (Scheme 27) (Hideg *et al.*, 1980).

The aldehyde **126** has been used by Crouch *et al.* (1981) for the preparation of a spin-labeled retinal **138** (Scheme 28).

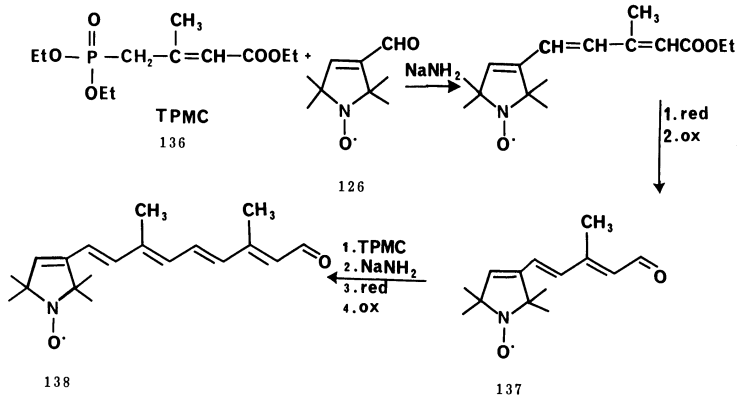

Scheme 28.

Condensation of **126** with triethyl 4-phosphono-3-methylcrotonate (**136**) in the presence of sodium amide gave a triene ester which was reduced to the alcohol, then oxidized to the aldehyde **137**. The same reaction steps, repeated with **136** as before, resulted in **138**.

The allylic alcohol **124**, owing to its enhanced reactivity, has been an extremely useful synthon for preparing new highly reactive and promising alkylating spin labels, such as the sulfonates **93**, **139a-c**, and the halides **107**, **140** (Hankovszky *et al.*, 1980). Compounds **93** and **107** were used for obtaining spin-label-alkylated biologically active phenols (Hankovszky *et al.*, 1980): estrone (**141**), estradiol (**142**), ethynylestradiol (**143**), morphine (**144**), and tyrosine (**145**) (Scheme 29). The allylic reagents were also applied for the synthesis of the benzoate **146**, sulfide **147**, and the thiuronium salt **149** which latter was a source of the free nitroxide radical containing thiol group, **150** (Hankovszky *et al.*, 1980). The allylic reagents were also the starting compounds of a reversible nitroxide thiol spin-label reagent, **97** (Berliner *et al.*, 1982).

The development of novel versatile nitroxide synthons has opened up new opportunities in the synthesis of nitroxide spin labels with two reactive functional groups. The bifunctional labels are capable of becoming rigidly attached to two sites of a macromolecule through simultaneously or subsequently established covalent linkages. A cross-linkage formed by a bifunctional spin label between two reactive centers of a macromolecule can be used for studying the motion of the labeled macromolecule in

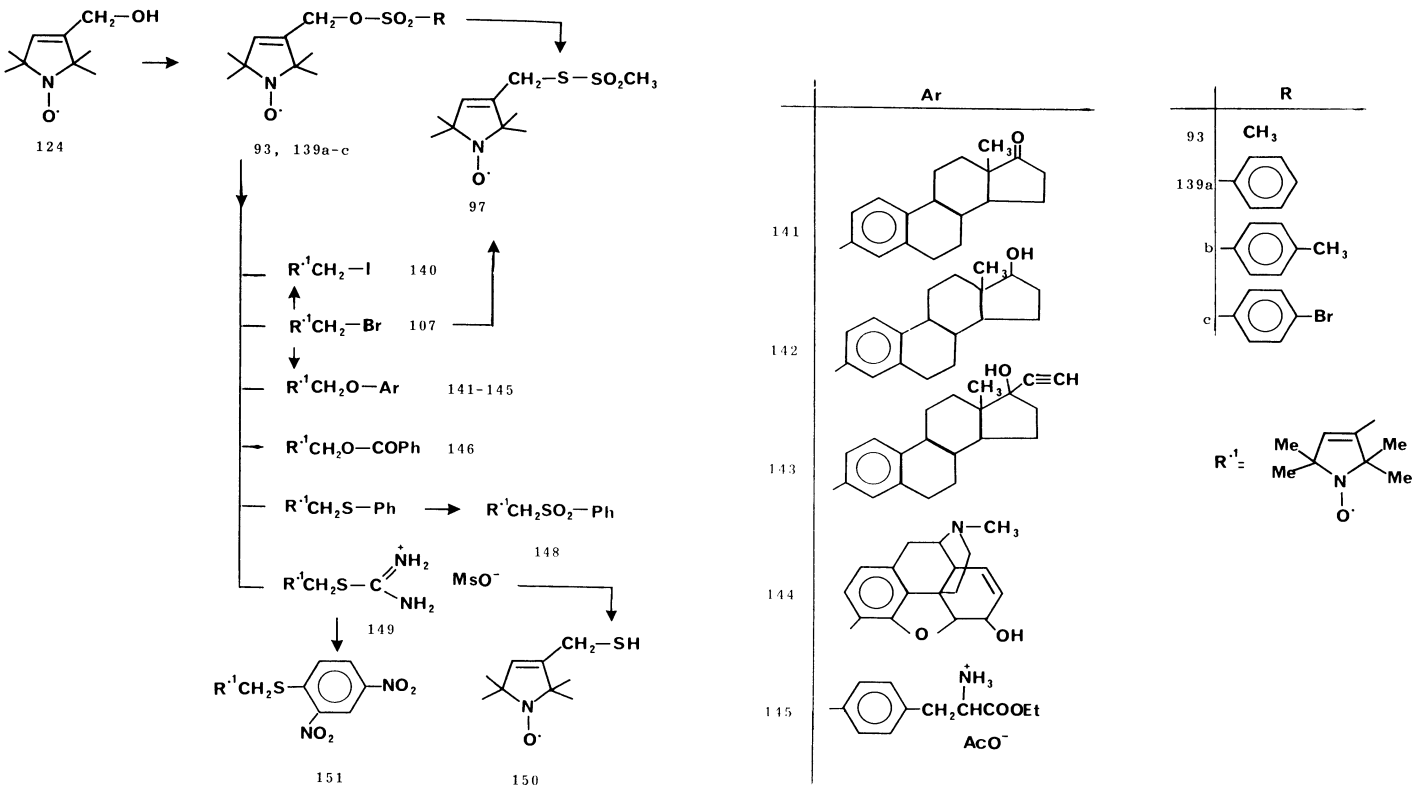
CH2—OH
124
CH2—O—SO2—R
93, 139a-c
CH2—S—SO2CH3
97
R·1CH2—I 140
R·1CH2—Br 107
R·1CH2O—Ar 141-145
R·1CH2O—COPh 146
R·1CH2S—Ph
R·1CH2SO2—Ph
148
R·1CH2S—C(NH2)NH2
MsO⁻
149
CH2—SH
R·1CH2S
NO2
NO2
151
150
Ar
141
142
143
144
145
CH3
OH
HO
C≡CH
N—CH3
O
NH3
CH2CHCOOEt
AcO⁻
R
93
CH3
139a
b
CH3
c
Br
R·1 =
Me
Me
Me
Me
N
O·

Scheme 29.

the correlation time range $10^{-7} < \tau < 10^{-3}$ s by the saturation transfer electron resonance (ST-EPR) method (Cherry, 1979; Hyde and Dalton, 1979).

4.2. Cross-Linking Spin-Label Reagents

4.2.1. 3,4-Bifunctionalized Pyrrolidine-1-Oxyls

Until recently, only a few relevant bifunctional nitroxides have been reported.

A piperidine-oxyl ring fused to a bifunctionalized indole (**152**) has been described (Rozantsev, 1970).

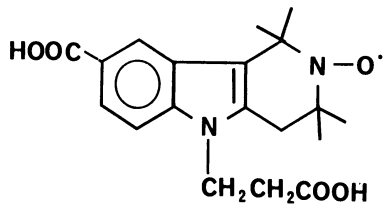

152

A bis-iodoacetamido reagent (**153**) was synthetized by acylation of a diamine (**154**) (Wenzel *et al.*, 1978) obtained from an aminonitrile (**104**) (Scheme 30).

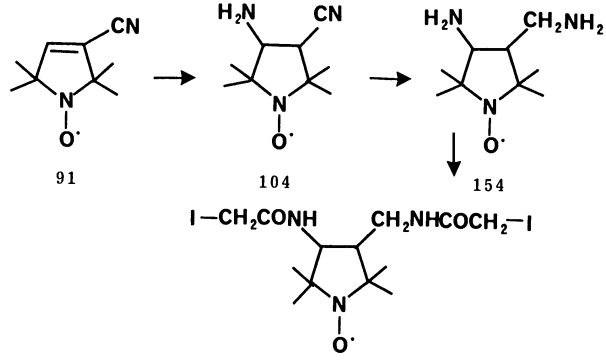

Scheme 30.

Conjugated additions of various nucleophilic reagents to the β-position of the unsaturated nitrile **91** have been carried out in order to obtain homo- or heterobifunctionalized pyrrolidine nitroxide derivatives. With sodium cyanide/ammonium chloride **91** gave the dinitriles **155** (*cis* and *trans*), which were hydrolyzed with $Ba(OH)_2$ to the dicarboxylic acids **156** (Keana *et al.*, 1982) (Scheme 31)..

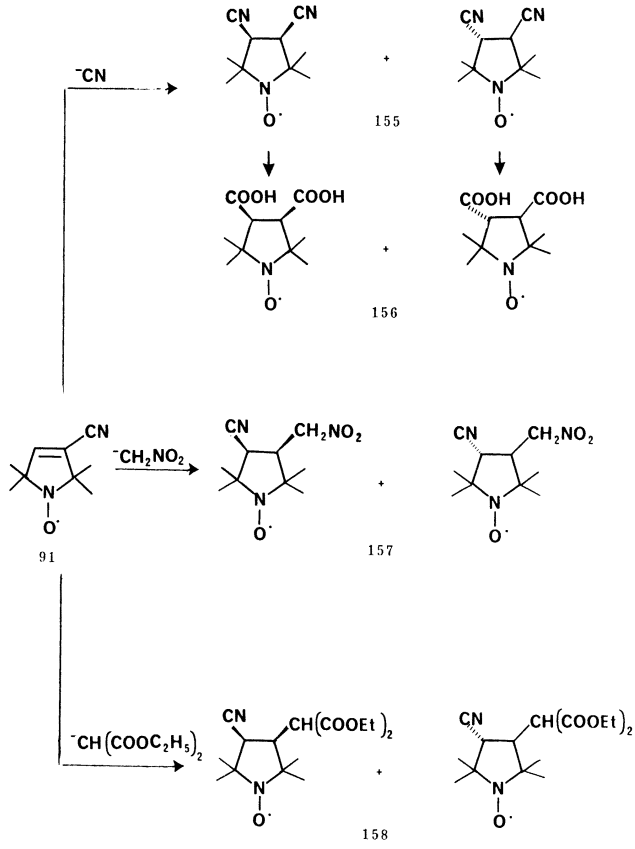

Scheme 31.

The conjugated addition of nitromethane in the presence of a base catalyst gave nitro-, nitrile-functionalized derivatives (**157**) (*cis* and *trans*) (Hankovszky *et al.*, 1982). The reagent with diethylester and nitrile functions (**158**) was obtained with diethyl malonate and a base catalyst. The applied base catalysts were sodium ethoxide, benzyltrimethylammonium hydroxide (Triton B), or tetramethylguanidine (Scheme 31).

Until very recently the use of organometals was not recommended because, according to earlier experiences, the reaction of the nitroxide moiety of 2,2,6,6-tetramethylpiperidine-1-oxyl with BuLi and MeLi led to the corresponding N-H, N-OH, and OBu derivatives (Whitesides and Neuwirth, 1975). Essentially the same type of destruction of nitroxide was described when Grignard reagents were applied (Sholle *et al.*, 1971). Very recently it has been demonstrated in two papers (Hankovszky *et al.*, 1982; Keana *et al.*, 1982) that organometallic reagents can be applied for the synthesis of functionalized nitroxides.

The unsaturated carboxylic acid **26** was converted with an excess of an alkyllithium reagent (methyllithium or *n*-butyllithium) into ketones. However, both the N-OR ketones (**159**) and the N-OH ketones (**160**) were equally formed, *ca* in the same

amounts. The N-OH compounds **160** were readily reoxidized to the **161** nitroxides (Keana *et al.*, 1982) (even by an air oxidation) (Scheme 32).

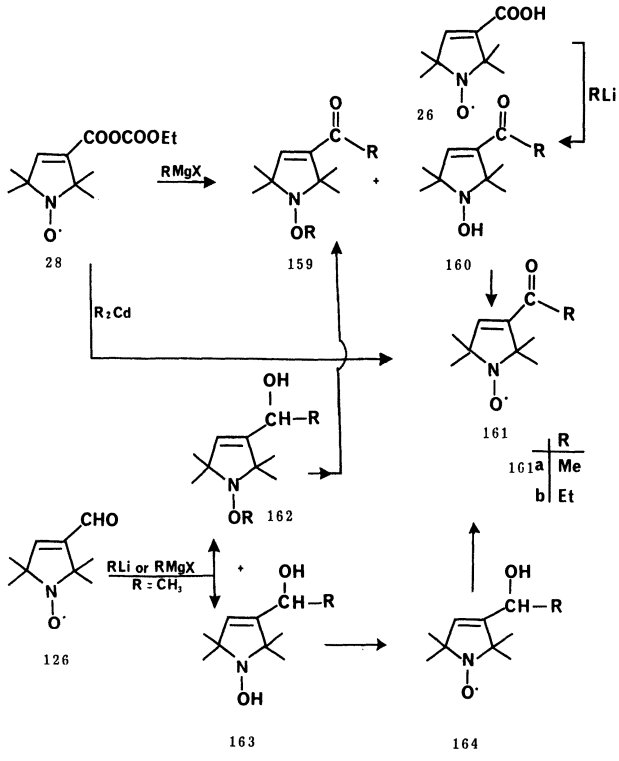

Scheme 32.

Reaction of the alkyllithium reagents with the unsaturated aldehyde **126** gave diamagnetic and paramagnetic secondary alcohols (**162, 163**) (Keana *et al.*, 1982). The *N*-hydroxy derivative **163** underwent spontaneous oxidation to the nitroxide alcohol **164**. The secondary alcohols **162** and **164**, representing an allylic system, are readily oxidizable with activated MnO_2 to give the corresponding ketones, **159, 161.**

The activated carbonate **28** proved to be active enough to react with Grignard reagents (e.g., methylmagnesium iodide or ethylmagnesium iodide) to yield the same ketones (**159, 160, 161**) (Hankovszky *et al.*, 1982) as obtained with the alkyllithium reagents. A change of the organometallic reagents (use of dialkylcadmium instead of an alkylmagnesium halide) gave the same nitroxide ketones, but without the formation of any significant amount of diamagnetic *O*-alkyl ketones (**159**) (Hankovszky *et al.*, 1982) (Scheme 32).

The unsaturated aldehyde **126** in a conjugated addition with ethyl thioglycolate led to a new sulfur heterocycle **165** (Keana *et al.*, 1982) (Scheme 32). Several similar heterocycles were obtained from the stereoisomeric mixture of **165**: acetylation of **165a**

gave an acetate (**165b**); on oxidation with hydrogen peroxide a sulfone (**165c**) was formed, and on alkaline hydrolysis the acid (**165d**) was obtained. The dehydration of **165a** was effected with methanesulfonyl chloride in pyridine; the reaction gave **166** (Keana *et al.*, 1982) (Scheme 33).

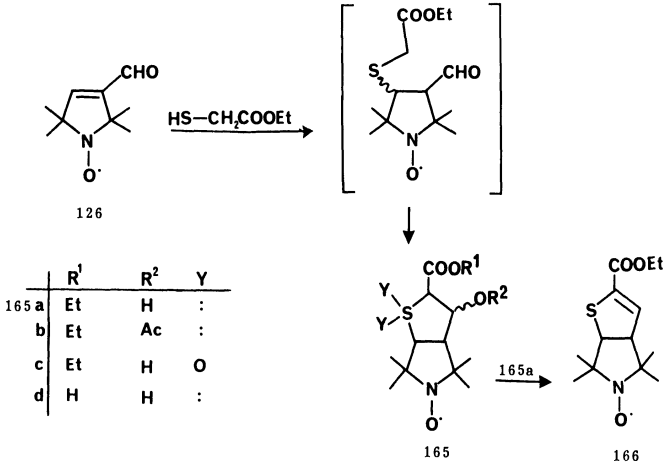

Scheme 33.

The above 1,4-conjugate addition of a sulfur reagent to the nitroxide acceptor may serve as a model for demonstrating that unsaturated carbonyl nitroxide derivatives can be applied to achieve reaction of such spin labels with the sulfhydryl groups of proteins.

On the other analogues obtained by aldol-type condensations, compound **161** ($R = CH_3$) and azidobenzaldehyde gave the product **167**. The reactions of **126** with various methylketones were also performed to yield a series of spin-labeled ketones (**168–173**) (Hankovszky *et al.*, 1982; Keana *et al.*, 1982) (Scheme 34).

These ketones also constitute a potentially versatile series of bifunctional spin labels. Each of them is capable of reacting with protein-SH or $-NH_2$ groups. Compound **168** was used to label hemoglobin in two steps: first by a reaction with the double bond, followed by photolysis generating the nitrene center (Keana *et al.*, 1982).

A second point of attachment was introduced by photolysis of protein adducts of **168**. The reactive phenylnitrene intermediate so generated was capable of forming a covalent bond with an adjacent protein residue, resulting in a substantial reduction of the mobile component in the ESR spectrum.

Bromination of ketone **161** ($R = CH_3$) with $CuBr_2$ gave an α-bromoketone (**174**) in a rather poor yield (Keana *et al.*, 1982). More efficient bromination could be achieved when 2-pyrrolidone hydrotribromide (PHT) 2-pyrrolidone reagent was used, but some dibromo compound (**175**) was also formed; however, the ethyl ketone (**161b**) gave the monobrominated ketone (**176**) selectively (Hankovszky, unpublished data) (Scheme 35).

Compound **161a** was made to react with a single SH group near the Fe-S cluster of aconitase (Dryer *et al.*, 1983).

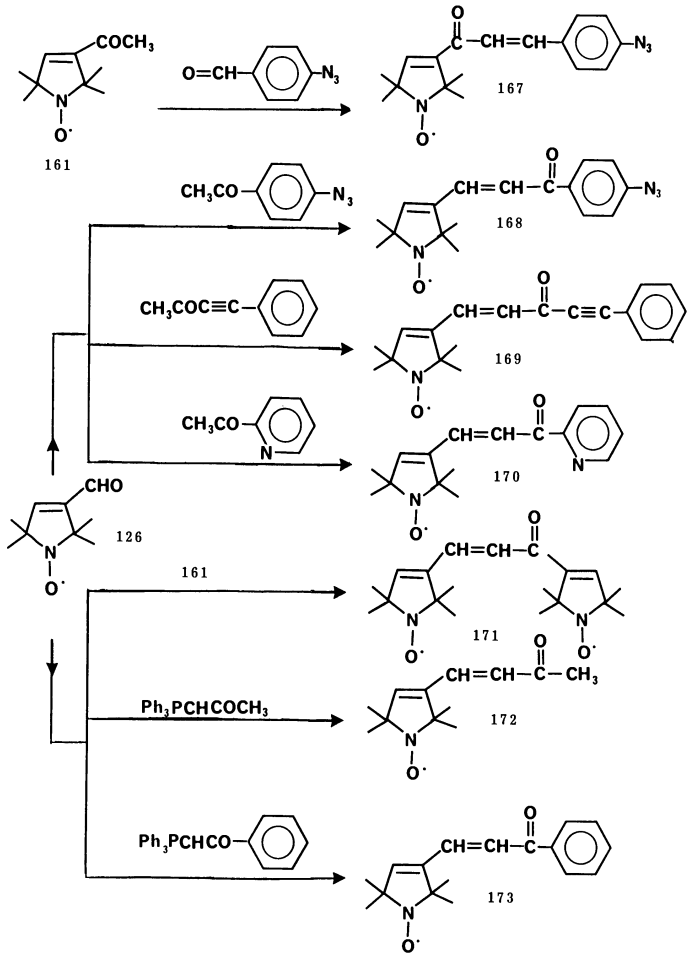

Scheme 34.

Reaction of the unsaturated aldehyde **126** with the enolate of ethyl monomagnesium malonate led to the formation of a conjugate adduct, the δ-oxoester **177** in a moderate yield (Hankovszky *et al.*, 1982) (Scheme 36).

With the above malonate reagent the acyl carbonate **28** or the acyl imidazole **33** gave a β-keto ester (**178**), which proved to be a versatile synthon for the preparation of longer alkyl unsaturated ketones (**161b**, **161c**) on treatment with alkyl halides. The sodium borohydride reduction of **178** gave a dihydro compound (**179**) which, via allylic oxidation with MnO_2, was converted to a β'-hydroxy-α,β-unsaturated ketone (**180**) (Hankovszky *et al.*, 1982) (Scheme 37).

4.2.2. 2,5-Heterobifunctionalized Pyrrolidine-1-Oxyls

An exciting new route has been very recently published for the preparation of various *cis*-mono-, and heterobifunctionalized nitroxides (Keana *et al.*, 1985). The

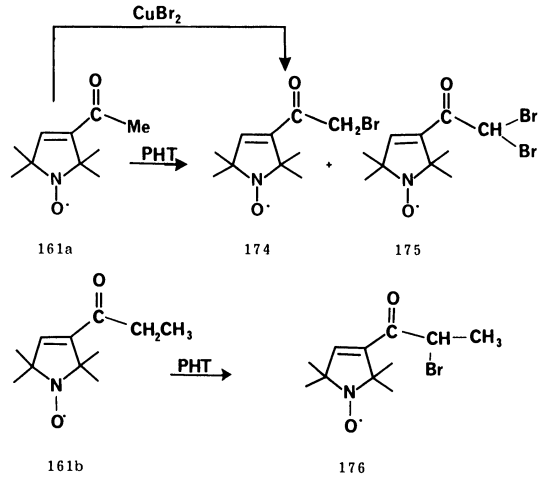

Scheme 35.

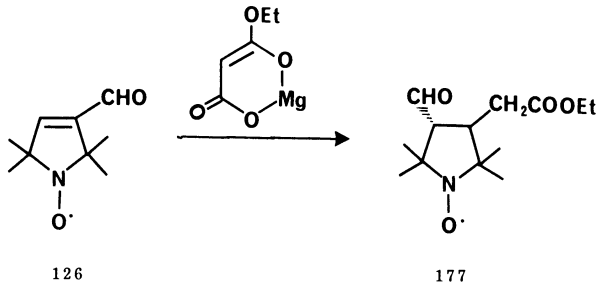

Scheme 36.

synthesis started from dimethylnortropinone nitroxide (**181a**), prepared earlier (Rassat *et al.*, 1976). The nitroxide was reduced to the *N*-hydroxy derivative (**181b**) by catalytic hydrogenation, then protected by reaction either with an acyl chloride (acetyl or pivaloyl) to obtain **181c, d**, or with *tert*-butyldimethylsilyl chloride yielding **181e**. The protected ketone was converted to a bicyclic lactam (**183b**) in a Beckman rearrangement via the oxime-*O*-tosylate (**182**, X = Ts), and finally the lactam ring was cleaved to give the nitroxide amino acid **184** (Scheme 38).

In an alternative reaction the *N*-*O*-protected bicyclic ketone was alkylated with butyllithium to an alcohol (**185**), then dehydrated to alkene (**186**); this was ozonized to a ketoaldehyde from which the unstable *cis*-diol (**187**) was prepared. These new nitroxides may serve as useful synthons when the functional groups are modified, making the compounds suitable for immediate use as bifunctionalized spin labels in biological studies. In a third set of reactions the silylated ketone (**181d**) was converted to the ketal **188**, then to an enol ether (**189**) which, after a few steps (ozonization, $NaBH_4$ reduction and cleavage of the silyl protecting group), gave the 2,5-*cis*-heterobifunctionalized pyrrolidine-1-oxyl (**190**).

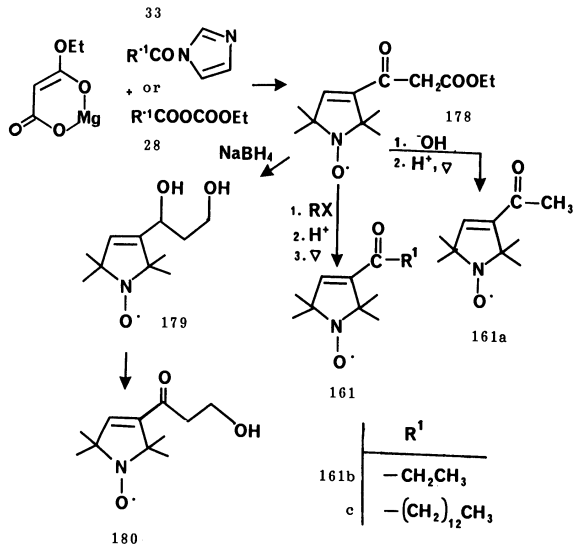

Scheme 37.

4.2.3. 2,5-Homobifunctionalized Pyrrolidine-1-Oxyls

Syntheses of 2,5-homobifunctionalized pyrrolidine-1-oxyls with short or long functionalized arms have been reported (**192–200**) (Tse-Tang *et al.*, 1981; Keana *et al.*, 1983). In these works 2,5-dimethyl-1-pyrroline-1-oxide (**191**) and $XMg(CH_2)_nOTHP$ reagents were used (Scheme 39).

The acids, however, could only be obtained by multistep syntheses. Therefore the procedure in which a nitrone (**191** or **198**) is allowed to react with a Grignard reagent prepared from an ω-halogenoalk-1-ene to get pyrrolidine-1-oxyls with terminal unsaturated bond(s) (**199**) has the advantage that the double bond(s) can be oxidized with KIO_4 in a one-step phase-transfer reaction to aldehyde(s) (**200**) or to carboxyl(s) (**201**). Hydroxy compounds (**202**) are also obtainable by hydroboration of the terminal double bond(s) (Hideg and Lex, 1986b) (Scheme 40).

This reaction has also a practical value in the preparation of 2-monofunctionalized pyrrolidine-1-oxyls.

4.2.4. 2,2-Homobifunctionalized Oxazolidine-3-Oxyls

Bifunctionalized doxyl spin labels with long spacer arms have been prepared and used in cross-linking reactions with components of red blood cells (Gaffney *et al.*, 1983; Willingham and Gaffney, 1983). The syntheses of 2,2-bis(carboxyalkanyl)-oxazolidine-3-oxyls (**203**) start from the corresponding ketone diester (**204**) and an aminoalcohol (**205**). The reaction steps are condensation to oxazolidine, oxidation to the 3-oxyl radical, followed by hydrolysis of the ester groups (Scheme 41).

The diacid (**203a**) was converted to the di-*N*-succinimidyl ester (**206**); in further reactions the spacer arms were extended to get **209** and **210** (Scheme 42).

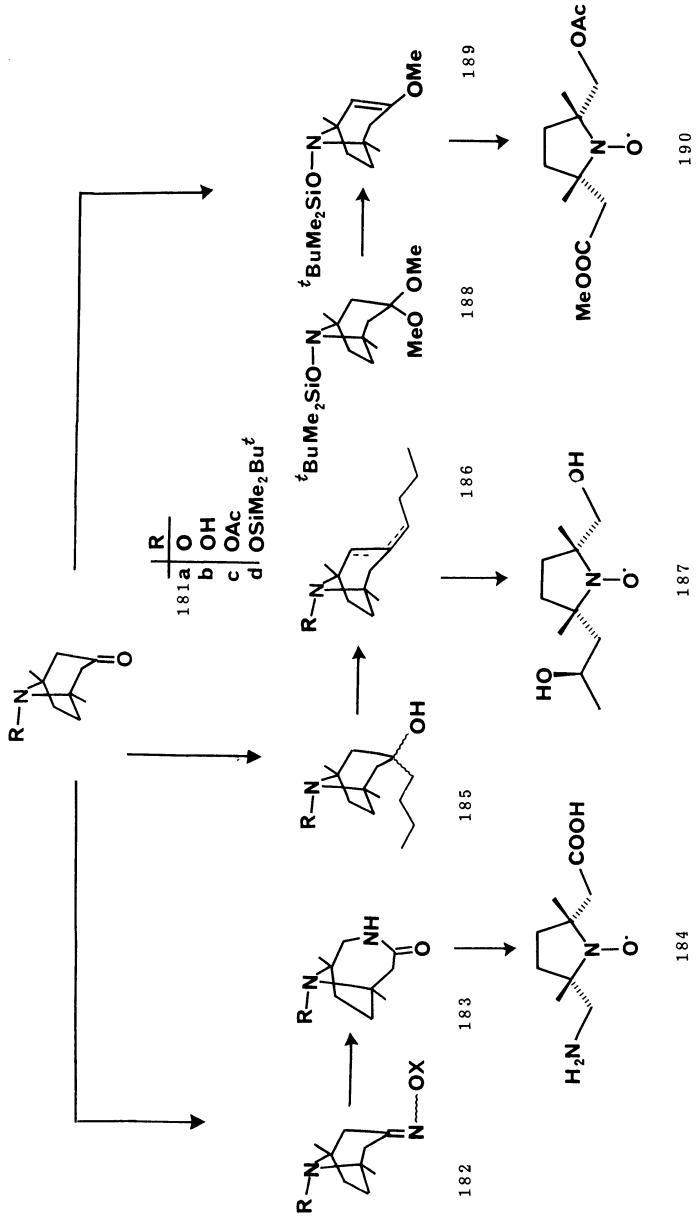
R
181a O
b OH
c OAc
d OSiMe2But
182
183
184
185
186
187
188
189
190
MeO OMe
MeOOC
H2N
HO

Scheme 38.

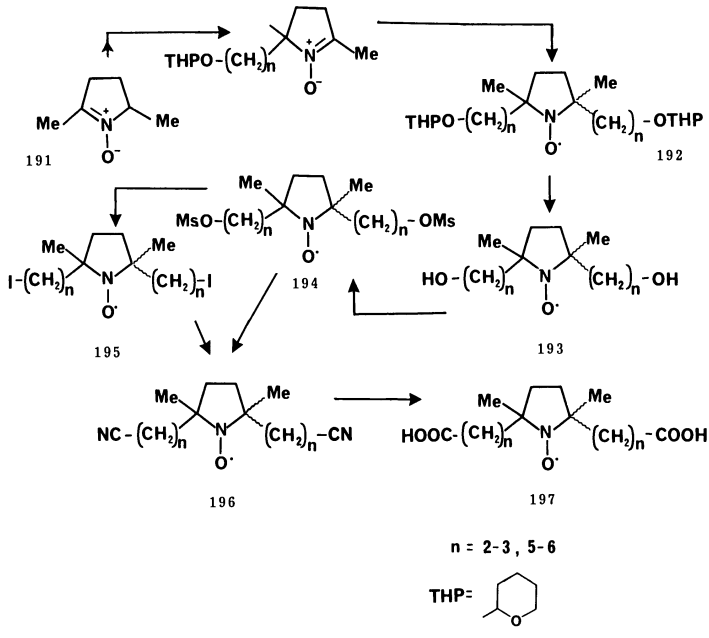

Scheme 39.

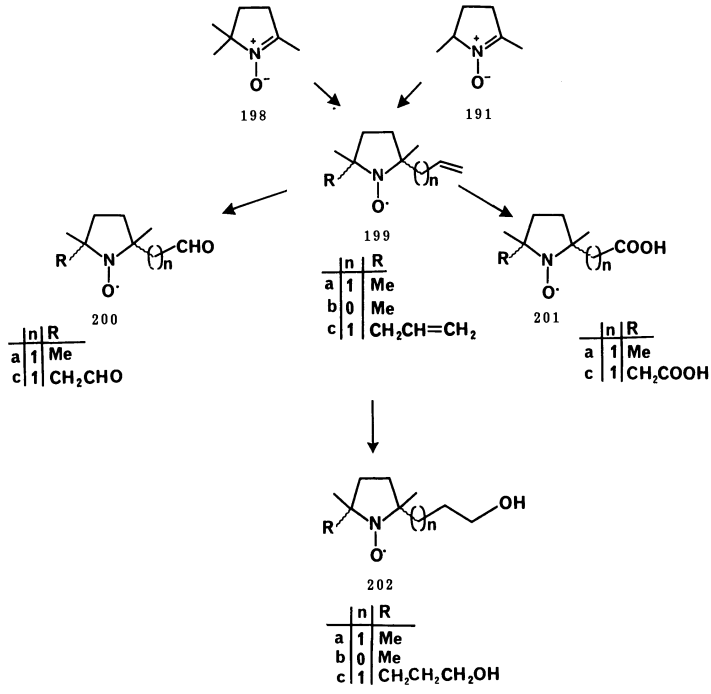

Scheme 40.

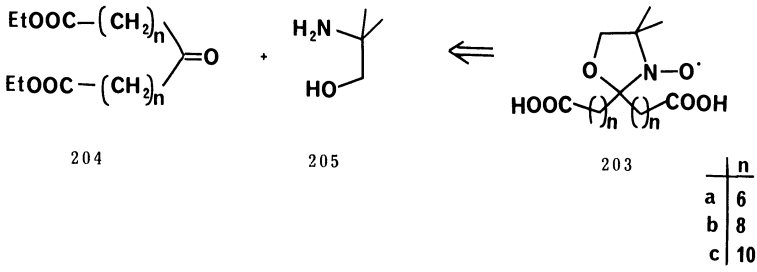

Scheme 41.

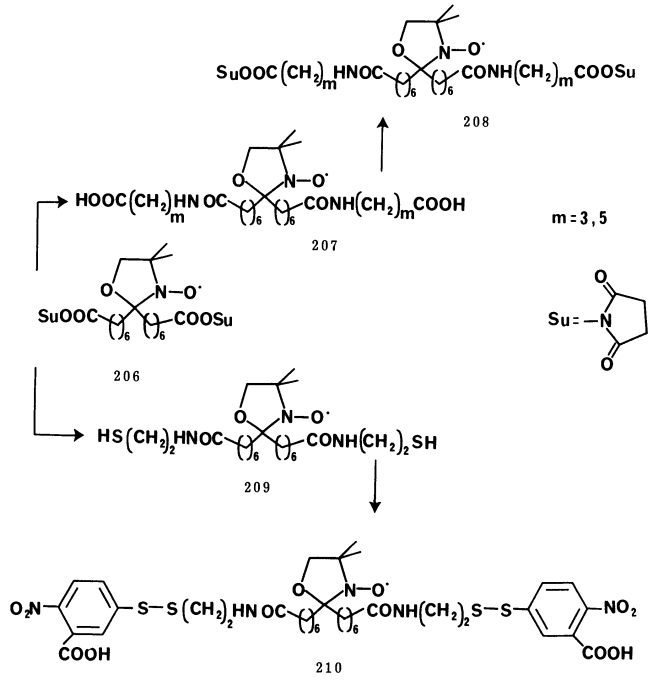

Scheme 42.

4.3. Spin-Labeled Pyrrolidine-1-Oxyl Fatty Acids

Oxazolidine-3-oxyl derivatives (doxyls) have been used for years in biological studies requiring spin-labeled fatty acids, because their synthesis is relatively easy (Keana *et al.*, 1967; Marsh *et al.*, 1982). Another advantage is that the nitroxide principal axes (*A* and *g* tensors) are parallel to the long axis of the molecule (Keana *et al.*, 1976).

However, the doxyl acids **211** also have some drawbacks: the oxazolidine ring easily suffers ring cleavage and the *N*-oxyl part of the molecule is also quite sensitive to reduction (Keana *et al.*, 1976).

Pyrrolidine nitroxides [proxyls (**212**), azethoxyls (**213**)] are more resistant to reduction, but their synthesis is more complicated owing to the laborious multistep formation of the carboxylic groups (Keana *et al.*, 1978), e.g.,

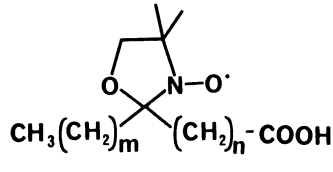

211

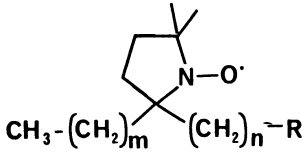

212

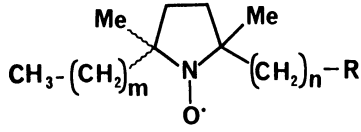

213

$$R = OTHP \longrightarrow OH \rightarrow OSO_2CH_3 \longrightarrow I \longrightarrow CN \rightarrow COOH$$

2,5-Disubstituted pyrrolidine-1-oxyl fatty acids have a further advantage. Their structures are close to the zigzag chains of naturally occurring saturated fatty acids. So they cause relatively less steric perturbance than other isomers do (Lee *et al.*, 1979). However, for a broader approach to solve the problem of causing minimal sterical perturbation to an unlabeled fatty acid within a molecularly highly oriented system, such as membrane bilayers, it is very important to develop synthetic methods which are less elaborate and can be generalized for the synthesis of any pyrrolidine-1-oxyl fatty acid. These were the major objectives of recent reports (Hideg and Lex, 1984, 1986a) on new syntheses generally applicable for the preparation of other isomers, in which two or three atoms of the pyrrolidine ring can be viewed as an integral part of a fatty acid chain, thus probably causing only minimal perturbance. Investigations with all of the isomers will only enable one to determine the effect of the off-axis orientation of the spin-labeled fatty acid isomers on the ESR spectral line shapes.

The synthesis started from such α,β-unsaturated ketones substituted in the β-position (**214a-d**) (Scheme 43), which could be prepared by aldol condensation of Wittig reaction of the suitable starting compounds. The further steps are the following: Michael addition of nitroalkane to the unsaturated ketone to obtain the γ-nitro ketone **215**, utilizing the known route (Bonnett *et al.*, 1959); ring closure to the nitrone **216** was carried out with NH_4Cl and Zn powder; the nitrones (**216a-e**) were alkylated with alkyl Grignard reagents to nitroxides (**217-221**), which could be oxidized with $KMnO_4$ at the olefinic bond to the carboxylic acid derivatives (**222-226**), in a phase-transfer reaction (Scheme 43).

It appears that the scope of these reactions can be extended to any other nitroxide containing terminal unsaturated bond(s).

Outlook. Numerous new reagents have been prepared and applied in the research of biomacromolecules since the introduction of nitroxide free radicals as spin labels.

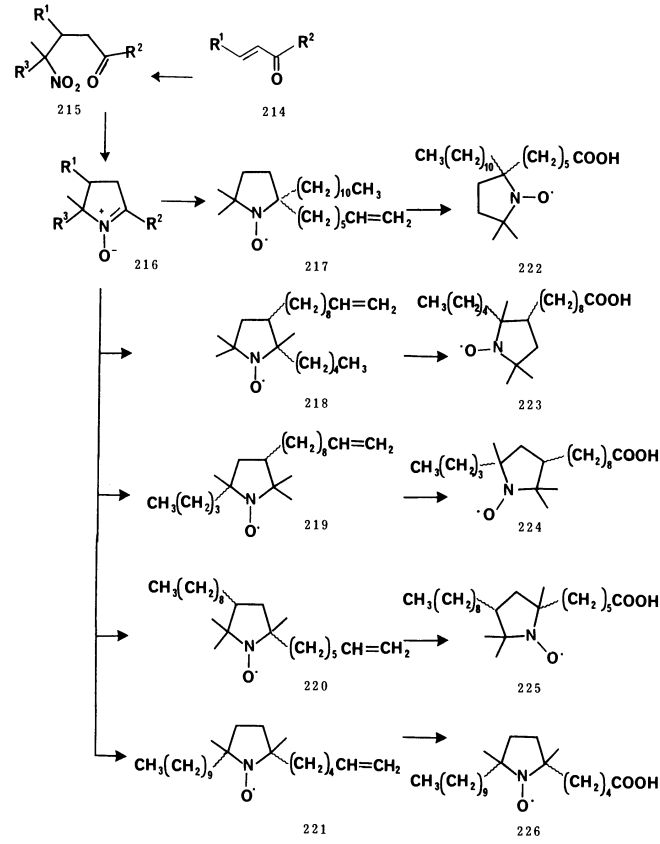

	R^1	R^2	R^3
214-216 a	H	H	Me
b	$CH_2{=}CH(CH_2)_8$	Me	$Me(CH_2)_4$
c	$CH_2{=}CH(CH_2)_8$	Me	Me
d	$CH_3(CH_2)_8$	Me	Me
e	H	Me	H

Scheme 43.

Research in this field will be continued owing to unremitting interest in preparing better selective affinity reagents, which have so little as possible perturbation in the function of biological systems with nonideal reporter molecules.

Other interesting research results, which are, however, beyond the scope of this chapter, have also been published. Examples are quantitative structure-activity relationship (QSAR) analyses of drug molecules having the nitroxide grouping or some of its precursors (e.g., sterically hindered amines). Very recently, in diagnostic medicine, magnetic resonance imaging (MRI) has shown exceptional promise as a useful diagnostic tool for human diseases. It is of utmost importance to further improve MRI diagnostic

sensitivity and its specificity for diseases, by the development of nontoxic paramagnetic pharmaceuticals to be used as contrast enhancing agents. Nitroxide free radicals are among the most promising types of contrast enhancer candidates.

5. EXPERIMENTAL PROCEDURES FOR PREPARATION OF SOME PYRROLINE AND PYRROLIDINE NITROXIDE SPIN LABELS

Preparation of Active Esters

3-(Phenylthiocarbonyl)-1-oxyl-2,2,5,5-tetramethyl-3-pyrroline (**22**) (Hankovszky *et al.*, 1978). (See Scheme 44.) The solution of 1-oxyl-2,2,5,5-tetramethyl-3-pyrroline-3-carboxylic acid (**26**) (1.84 g, 0.01 mol) and of thiophenol (1.10 g, 0.01 mol) in dry ethyl acetate (20 ml) was cooled to 0 °C. Under stirring, a solution of dicyclohexylcarbodiimide (DCC) (2.05 g, 0.01 mol) in ethyl acetate (30 ml) was added dropwise (over about 5 min). The mixture was stirred for a further 2 h at room temperature, filtered, and the filtrate evaporated under vacuum. The residue was crystallized from ether. Yield 2.0 g (72%); mp 133–135 °C.

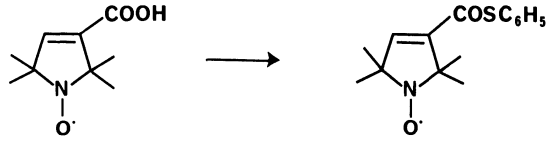

26 22

Scheme 44.

Preparation of Mixed Anhydrides

(Carbonic acid—1-oxyl-2,2,5,5-tetramethyl-3-pyrroline-3-carboxylic acid) anhydride ethyl ester (**28**) (Griffith *et al.*, 1967; Hankovszky *et al.*, 1978). (See Scheme 45.) This mixed anhydride **28** was first described by Griffith *et al.* (1967) from the same starting compounds as below, but without triethylamine. The yield was 59%, mp 65 °C.

To a suspension of **26** (9.2 g, 0.05 mol) in ether (100 ml), triethylamine (5.05 g, 0.05 mol) was added, then the mixture was cooled to 0 °C, and under stirring a solution

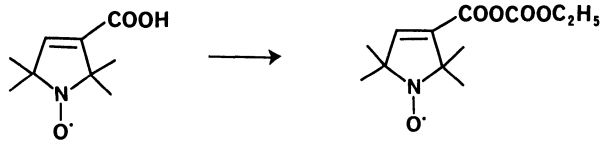

26 28

Scheme 45.

of ethyl chloroformate (5.42 g, 0.05 mol) in ether (50 ml) was added dropwise. After the addition had been completed, stirring was continued for 3 h at room temperature. Triethylamine hydrochloride was filtrated off, the filtrate evaporated, the residue was taken up in hexane (50 ml) and allowed to stand in a refrigerator. The yellow, needle-shaped crystals separated were filtrated. Yield 11.6 g (90%), recrystallized from ether/hexane; mp 63–65 °C.

Preparation of Carboxylic Acid Azide

1-Oxyl-2,2,5,5-tetramethyl-3-pyrroline-3-carbonylazide (**32**) (Hankovszky *et al.*, 1978). (See Scheme 46.) *Method A.* A solution of **28** (10.25 g, 0.04 mol) in acetone-water (2:1, 75 ml) was cooled to 0 °C, solution of sodium azide (3.88 g, 0.06 mol) in water (15 ml) was added, and the mixture was stirred for 30 min. On the evaporation of the acetone in vacuum at 0 °C, the azide (**32**) was separated in yellow crystals. Yield 7.8 g (93%); mp 62–63 °C.

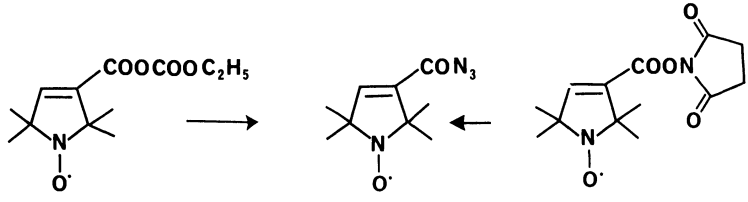

28 32 8

Scheme 46.

Method B. 1-Oxyl-2,2,5,5-tetramethyl-3-pyrroline-3-carboxylic acid *N*-succinimide ester (**8**) (Hoffman *et al.*, 1970) was reacted and processed as above with sodium azide. Reaction time 2 h, yield 88%. The substance is identical with the product obtained in Method A.

Preparation of Acyl Imidazole

N-(1-Oxyl-2,2,5,5-tetramethyl-3-pyrroline-3-carbonyl)imidazole (**33**) (Hideg *et al.*, 1978). (See Scheme 47.) A solution of **28** (2.56 g, 0.01 mol) and imidazole (0.68 g, 0.01 mol) in dry toluene (10 ml) was refluxed for 30 min, then evaporated. The residual

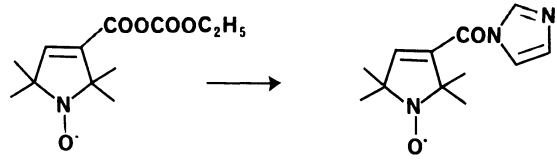

28 33

Scheme 47.

product was recrystallized from ether/hexane; yield 1.5 g (64%), mp 83–86 °C. The **33** was first synthesized from **26** with carbonyldiimidazole (mp 82–85 °C) (Barrett *et al.*, 1969).

Spin-Labeled *N*-Acylamino Acid Esters (36) (Hideg *et al.*, 1978)

General procedures. (See Scheme 48.) *Method A.* A solution of dicyclohexylcarbodiimide (2.06 g, 0.01 mol) in dimethylformamide (10 ml) was added dropwise to a vigorously stirred mixture of **26** (1.84 g, 0.01 mol) triethylamine (1.01 g, 0.01 mol), 1-hydroxybenzotriazole (1.35 g, 0.01 mol), and the amino acid ester (**36**) hydrochloride (0.01 mol) in dimethylformamide (30 ml) at 0 °C. After the addition was complete, the mixture was stirred for a further 3 h at room temperature. The precipitated dicyclohexylurea was filtered off, and the solvent evaporated in vacuo. The residue was dissolved in ethyl acetate. The solution was washed with water, saturated sodium hydrogen carbonate solution, and again water. It was dried with sodium sulfate, then evaporated, and the residue was recrystallized from chloroform/hexane.

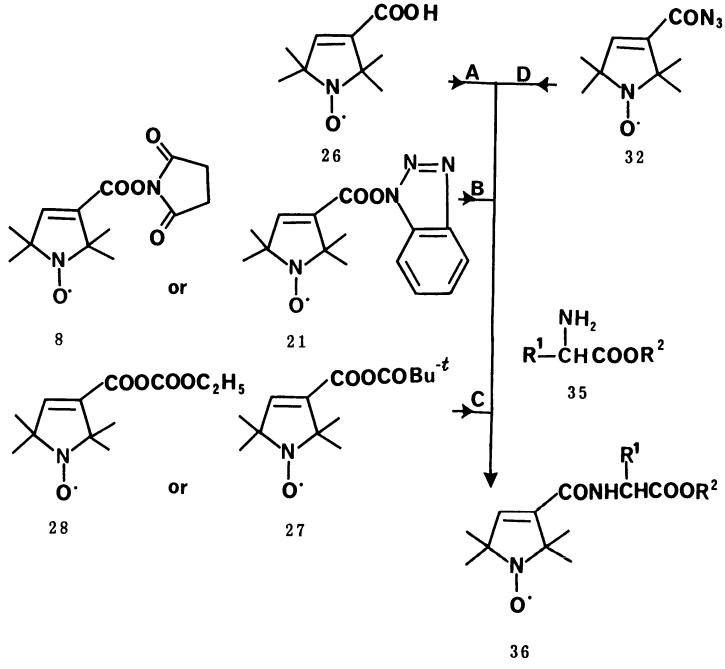

Scheme 48.

Method B. A solution of the *N*-succinimidyl ester (**8**) (0.01 mol) in dimethylformamide (20 ml) was added to a solution of the amino acid ester (**35**) hydrochloride (0.01 mol) and triethylamine (1.01 g, 0.01 mol) in dimethylformamide (20 ml). The

mixture was left to stand overnight, the solvent was then evaporated in vacuo, the residue dissolved in chloroform (40 ml), the solution washed with water, cooled, cautiously shaken with 0.5 normal hydrochloric acid (10 ml), then washed with saturated sodium hydrogen carbonate solution and then water, dried with sodium sulfate, and evaporated. The residue was recrystallized from chloroform/hexane.

Method C. A solution of the mixed anhydride **28** (0.01 mol) in dimethylformamide (10 ml) was added to a solution of the amino acid ester **35** hydrochloride (0.01 mol) and triethylamine (1.01 g, 0.01 mol) in dimethylformamide (20 ml). The mixture was stirred at room temperature for 3 h and then worked up as described in Method B.

Method D. The carbonyl azide (**32**) (2.09 g, 0.01 mol) was added with stirring to a solution of the amino acid ester **35** hydrochloride (0.01 mol) and triethylamine (1.01 g, 0.01 mol) in dimethylformamide (30 ml). The mixture was stirred for 3 h and then worked up as described in Method B.

Spin-Labeled *N*-Acylamino Acids (Hideg *et al.*, 1978)

General Procedures. (See Scheme 49.) *Method E.* To a solution of the spin-labeled *N*-acylamino acid ester **36** (0.01 mol) in methanol (30 ml), a 1 molar aqueous sodium hydroxide solution (20 ml, 0.02 mol) was added and the mixture left to stand for 3 h at room temperature. It was then acidified to pH 4 with a 1 molar hydrochloric acid at 0 °C and extracted with chloroform (40 ml). The extract was washed with water (20 ml), dried with sodium sulfate, and evaporated. The residue was recrystallized from ether.

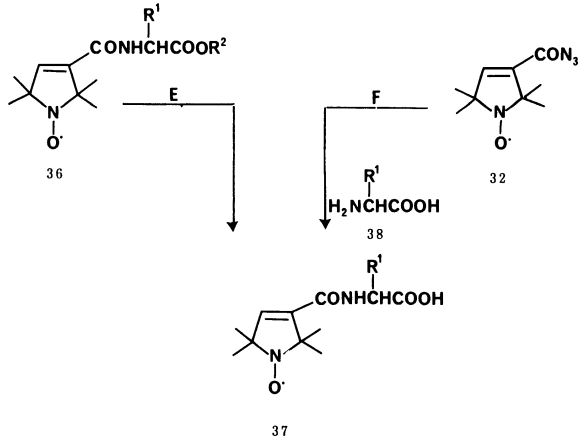

Scheme 49.

Method F. A solution of the carbonyl azide (**32**) (2.09 g, 0.01 mol) in dioxan (20 ml) was added to a stirred suspension of the amino acid (0.01 mol) and magnesium oxide (0.08 g, 0.02 mol) in water (20 ml). The mixture was stirred at room temperature for 24 h, then diluted with water (50 ml), and worked up as described in Method E.

O-Succinimido Derivatives of Spin-Labeled *N*-Acylamino Acids (40) (Hideg *et al.*, 1978)

General Procedure. (See Scheme 50.) *Method G.* A solution of dicyclohexylcarbodiimide (2.06 g, 0.01 mol) in ethyl acetate (15 ml) was added to a stirred suspension of the spin-labeled *N*-acylamino acid **37** (0.01 mol) and *N*-hydroxysuccinimide (1.15 g, 0.01 mol) in ethyl acetate (30 ml) at 0 °C. Stirring was continued for 3 h at room temperature, the dicyclohexylurea was filtered off, and washed with saturated sodium hydrogen carbonate solution and with water. The filtrate was dried with sodium sulfate and evaporated. The residue was recrystallized from chloroform/hexane.

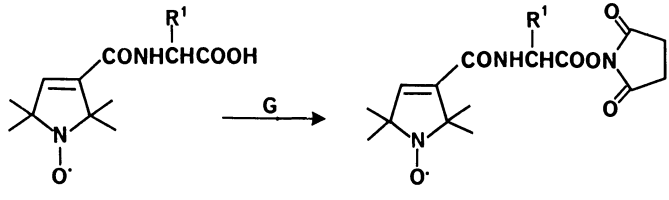

Scheme 50.

Spin-Labeled *N*-Acylamino Acid Hydrazides (42) (Hideg *et al.*, 1978)

General Procedure. (See Scheme 51.) *Method H.* A solution of hydrazine hydrate (2.0 g, 0.04 mol) in water (30 ml) was added to a stirred suspension of the *O*-succinimido derivative **40** (0.01 mol) in ethanol (10 ml). The mixture was stirred at room temperature for 30 min, then saturated with sodium chloride, and extracted with chloroform (60 ml). The extract was dried with sodium sulfate, evaporated to dryness in vacuo, and the residue recrystallized from chloroform/hexane.

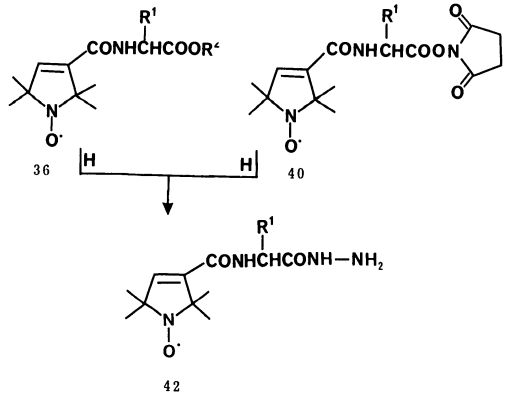

Scheme 51.

The reaction could also be carried out with the spin-labeled *N*-acylamino acid ester **36**; in this case, the reaction time was 24 h.

Spin-Labeled *N*-Acylamino Acid Azides (41) (Hideg *et al.*, 1978)

General Procedures. (See Scheme 52.) *Method I.* 1 molar hydrochloric acid (15 ml) was added to a stirred suspension of the hydrazide **42a** (0.01 mol) in water (20 ml). The mixture was cooled to 0 °C, and a solution of sodium nitrite (1.03 g, 0.015 mol) in water (5 ml) was added, followed by the addition of ether (50 ml). Stirring was continued for 30 min at 0 °C. The organic phase was separated, washed with sodium hydrogen carbonate solution and water, dried with sodium sulfate, and evaporated to dryness in vacuo at 0 °C. In the case of **41a** the solid residue is recrystallized from ether/hexane. Carbonyl azide **41c** is a thick oil which is unstable above 0 °C; at higher temperatures it was decomposed to the isocyanate.

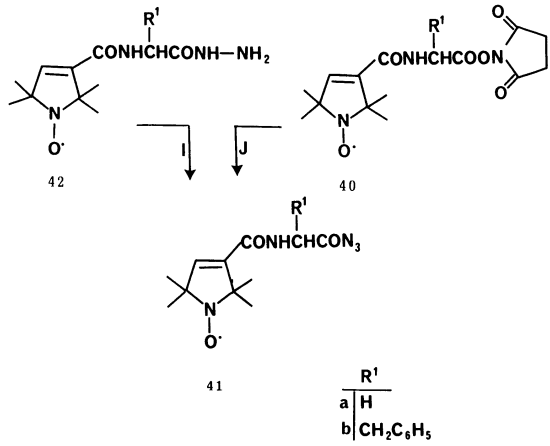

Scheme 52.

Method J. A solution of sodium azide (0.65 g, 0.01 mol) in water (5 ml) was added with stirring to a solution of the *O*-succinimido derivative **40a** (1.69 g, 0.005 mol) in acetone/water (1/1; 20 ml) at 0 °C. The mixture was left to stand at room temperature for 48 h and then extracted with ether. The extract was dried with sodium sulfate, evaporated in vacuo at 0 °C, and the residue recrystallized from ether/hexane.

Spin-Labeled *N*-Acylpeptide Esters (39) (Hideg *et al.*, 1978)

General Procedures. (See Scheme 53.) *Method K.* The *N*-succinimidyl ester **40** (0.338 g, 0.001 mol) was added to a stirred solution of the amino acid ester **35a** or **35b** hydrochloride (0.001 mol) and triethylamine (0.101 g, 0.001 mol) in dimethylformamide (10 ml). The mixture was stirred at room temperature for 3 h and then evaporated in vacuo. The residue was dissolved in chloroform (40 ml), the solution washed with

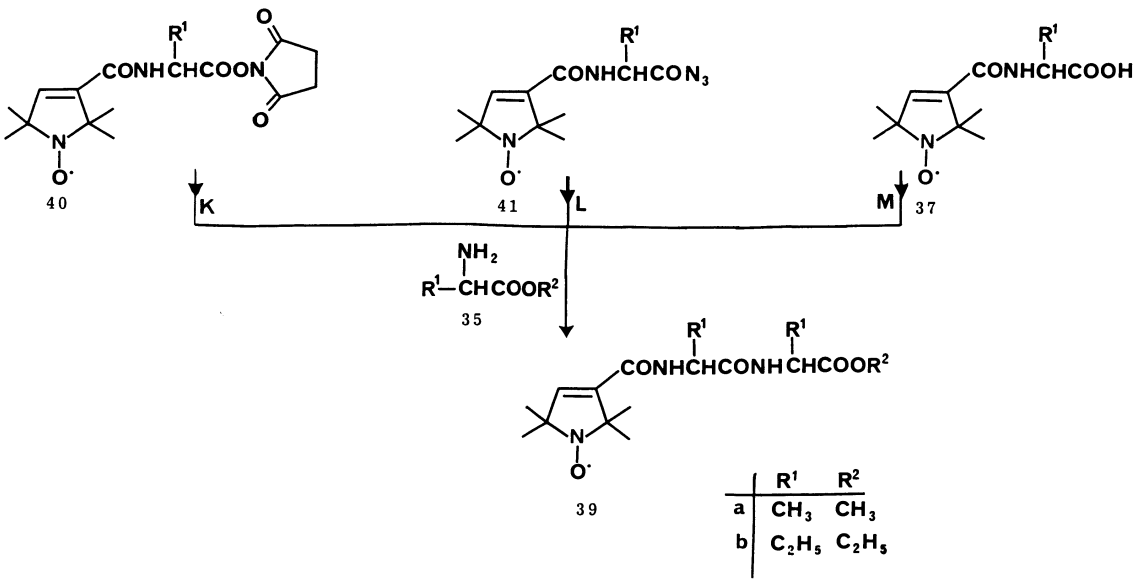
CONHCHCOON
CONHCHCON3
CONHCHCOOH
40
41
37
K
L
M
NH2
R1—CHCOOR2
35
CONHCHCONHCHCOOR2
39
R1 R2
a CH3 CH3
b C2H5 C2H5

Scheme 53.

saturated sodium hydrogen carbonate solution and with water, dried with sodium sulfate, and evaporated in vacuo. The residue was recrystallized from ether.

Method L. The spin-labeled *N*-acylamino acid azide **41** (0.001 mol) was added to a stirred solution of the amino acid ester **35** hydrochloride (0.001 mol) and triethylamine (0.101 g, 0.001 mol) dimethylformamide (10 ml). The mixture was stirred at room temperature for 3 h and was then worked up as described in Method K.

Method M. A solution of DCC (0.206 g, 0.001 mol) in dimethylformamide (10 ml) was added to a vigorously stirred mixture of the spin-labeled *N*-acylamino acid **37** (0.001 mol), the amino acid ester (**35**) hydrochloride (0.001 mol), triethylamine (0.101 g, 0.001 mol), 1-hydroxybenzotriazole (0.135 g, 0.001 mol) in dimethylformamide (20 ml) at 0 °C. Stirring was continued for 3 h at room temperature, the dicyclohexylurea was then filtered off, and the filtrate worked up as described in Method K.

Conversion of Acid Azide into Isocyanate

1-Oxyl-2,2,5,5-tetramethylpyrroline-3-isocyanate (**44**) (Hankovszky *et al.*, 1978). (See Scheme 54.) The solution of the acid azide **32** (2.09 g, 0.01 mol) in cyclohexane (30 ml) was refluxed for 30 min and the solvent was distilled off in vacuo. The residual odorous oil, isocyanate derivative **44** was crystallized on cooling. When thermal decomposition and evaporation were carried out under complete exclusion of moisture, the crystalline substance proved to be fairly pure. Yield is almost quantitative (97%); mp 35–38 °C.

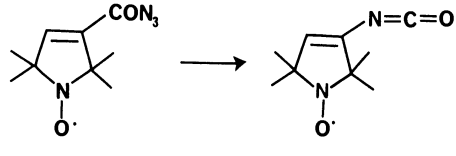

32 44

Scheme 54.

Spin-Labeled α-Ureidocarboxylic Esters (43) (Hideg *et al.*, 1978)

General Procedure. (See Scheme 55.) *Method N.* A solution of **44** (1.81 g, 0.01 mol) in dry ethyl acetate (10 ml) was added to a stirred solution of the amino acid ester

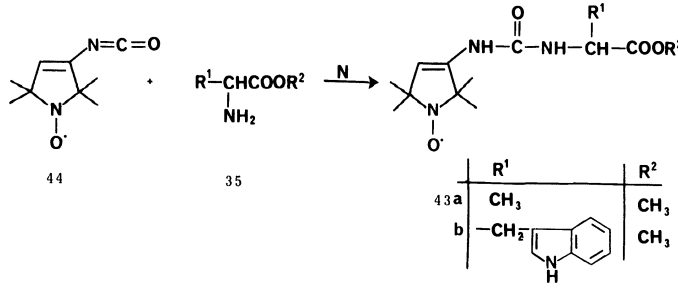

44 35

Scheme 55.

hydrochloride **35** (**a** or **d**) (0.01 mol) and triethylamine (1.01 g, 0.01 mol) in dry ethyl acetate (10 ml) at room temperature. Stirring was continued for 30 min, the mixture was then filtered, the filtrate evaporated to dryness in vacuo, and the residue recrystallized from ether [**43a**; yield: 1.78 g (66%); mp 176–178 °C], [**43d**; yield: 2.56 g (64%); mp 199–200 °C].

Synthesis of Spin-Labeled Azidoformate and Reactions with Amino Acid Derivatives (Hankovszky *et al.*, 1979)

N-(1-Oxyl-2,2,6,6-tetramethyl-4-piperidinyloxycarbonyl)imidazole (**69**). (See Scheme 56.) A solution of 4-hydroxy-2,2,6,6-tetramethylpiperidine-1-oxyl (**66**; 5.16 g, 0.03 mol) in dry ether (20 ml) was added dropwise to a stirred solution of carbonyldiimidazole (4.86 g, 0.03 mol) in dry tetrahydrofuran (30 ml) at room temperature. After the addition was complete, the solution was left for a further 3 h at room temperature, then extracted with water (30 ml) and saturated sodium chloride solution. The organic phase was dried with sodium sulfate and evaporated to dryness. The orange solid obtained was recrystallized from ether/hexane; yield: 6.1 g (76%); mp 62–63 °C.

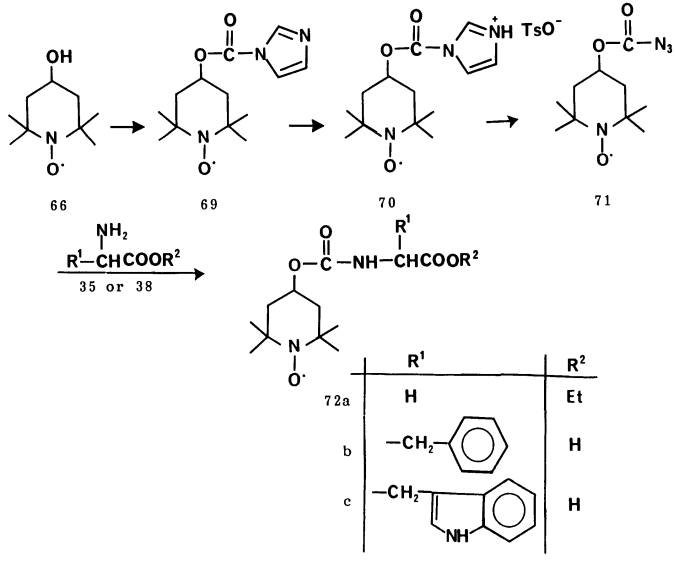

Scheme 56.

N-(1-Oxyl-2,2,6,6-tetramethyl-4-piperidinyloxycarbonyl)imidazolium Tosylate **70**. To a solution of compound **69** (5.32 g, 0.02 mol) in dry acetone (10 ml) was added a solution *p*-toluenesulfonic acid monohydrate (3.80 g, 0.02 mol) in acetone (10 ml). Crystallization was completed by adding ether and the product isolated by suction; yield: 7.9 g (90%); mp 147–149 °C.

1-Oxyl-2,2,6,6-tetramethyl-4-piperidinyloxycarbonyl Azide **71**. The imidazolium salt **70** (4.38 g, 0.01 mol) was added at once to a stirred solution of sodium azide (1.30 g, 0.02 mol) in water (10 ml) at room temperature. The mixture was stirred for 15 min and then extracted with hexane (30 ml). The extract was dried with sodium sulfate and evaporated to a volume of 3 ml and cooled to −20 °C. The product separated as red crystals which were isolated by suction; yield: 2.17 g (92%); mp 47–48 °C.

Ethyl N-(1-oxyl-2,2,6,6-tetramethyl-4-piperidinyloxycarbonyl)aminoacetate **72a**. *Typical Procedure. Method O.* A solution of compound **70** (2.41 g, 0.01 mol) in dimethylformamide (10 ml) was added to a solution of glycine ethyl ester (1.03 g, 0.01 mol) and triethylamine (1.01 g, 0.01 mol) in dimethylformamide (10 ml). The mixture was stirred for 3 h at room temperature, then evaporated to dryness under vacuum. The residue was taken up in ethyl acetate (30 ml) and the solution washed with 1 *N* hydrochloric acid at 0 °C, 5% potassium carbonate solution, and water. It was then dried with sodium sulfate and evaporated under vacuum. The residue crystallized from ether/hexan; yield: 1.0 g (65%); mp 78–79 °C.

N-(1-Oxyl-2,2,6,6-tetramethyl-4-piperidinyloxycarbonyl)amino Acids **72**. *General Procedure. Method P.* A solution of compound **70** (2.41 g, 0.01 mol) in dioxan (20 ml) was added to a stirred suspension of the amino acid (**38**) (0.01 mol), magnesium oxide (0.8 g, 0.02 mol) in water (10 ml). The mixture was stirred for 24 h at 40 °C, then diluted with water (30 ml), and extracted with ethyl acetate. The aqueous phase was acidified with 1 normal hydrochloric acid at 0 °C and extracted with ethyl acetate. The extract was dried with sodium sulfate, and evaporated. The residue was crystallized from ether. [**72b**; yield: 2.90 g (80%); mp 131–132 °C]. [**72c**; yield: 2.90 g (72%); mp 110–112 °C].

(1-Oxyl-2-2-5-5-tetramethyl-3-pyrroline-3-methyl)methanethiolsulfonate (97) (Berliner *et al.*, 1982)

A solution of 1-oxyl-2-2-5-5-tetramethyl-3-bromomethyl-3-pyrroline (**107**) (233.1 mg, 1.0 mmol) in dry ethanol (10 ml) and potassium methanethiolsulfonate (150.0 mg, 1.0 mmol) (see Scheme 57) was refluxed for 3 h, then diluted with saturated sodium chloride and extracted with ether (30 ml). The ether phase was dried over anhydrous magnesium sulfate and evaporated to dryness in vacuo. The residue was a paie-yellow, solid material which was recrystallized from ether/hexane to give 185 mg (70%) pure product; mp 107–108 °C.

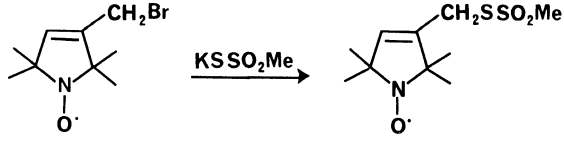

107 97

Scheme 57.

Side-Chain Spin-Labeled α-Amino Acid Ester

Ethyl 2-amino-3-(1-oxyl-2-2-5,5-tetramethyl-3-pyrroline-3-yl)propionate (**112**) (Lex *et al.*, 1982). (See Scheme 58.) A solution of sodium hydroxide (2*N*, 18 ml, 36.0 mmol) was added to a methylene chloride solution (15 ml) of ethyl *N*-(diphenylmethylene)-glycinate (4.0 g, 15.0 mmol), tetrabutylammonium hydrogen sulfate (TBAH) (6.1 g, 18.0 mmol), and **107** (4.2 g, 18.0 mmol) and stirred at room temperature for 2 days. The organic layer was separated, washed with water, dried, and evaporated to dryness to remove the residue quaternary bromide. The residue was taken up in ether and filtered. The filtrate was evaporated to dryness. The aqueous citric acid (10%, 30 ml) was added to the tetrahydrofuran (20 ml) solution of the Schiff's base and stirred overnight. The reaction mixture was diluted with water (30 ml) and extracted with chloroform (2 × 25 ml) to remove the benzophenone. The aqueous phase was basified with 2*N* sodium hydroxide solution to pH 8, extracted with chloroform (3 × 20 ml), dried, and evaporated to dryness to give **112** as a red oil; yield: 2.9 g (75%).

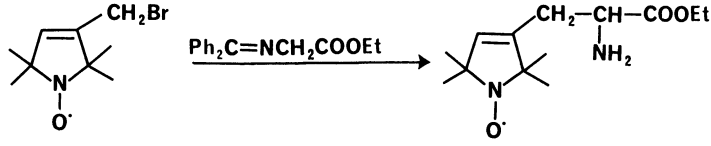

107 112

Scheme 58.

The Tosylate Salt of **112**. A solution of *p*-toluenesulfonic acid monohydrate (0.95 g, 5.0 mmol) was added to the solution of **112** (1.27 g, 5.0 mmol) in dry acetone (10 ml) and diluted with ether until the crystallization started. The crude product was recrystallized from chloroform/ether/hexane to give the pure salt of **112**; yield: 1.8 g (84%); mp 145–146 °C.

1-Oxyl-2,2,5,5-tetramethyl-3-hydroxymethyl-3-pyrroline (124) (Hideg *et al.*, 1980)

Method A. A solution of sodium bis(2-methoxyethoxy)-aluminum hydride (11 ml, ~70%) is added dropwise to a stirred suspension of acid **26** (1.84 g, 0.01 mol) in dry toluene (10 ml). (See Scheme 59.) The solution is refluxed for 2 h. The mixture is then

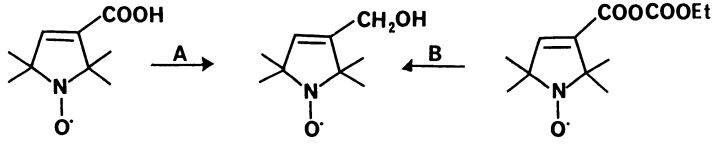

26 124 28

Scheme 59.

added dropwise to a cooled and stirred 5% aqueous solution (100 ml) of sodium hydroxide. The toluene phase is separated and dried with sodium sulfate. The solvent is evaporated to dryness and the yellow solid residue (**124**) is crystallized from ether/hexane; yield: 1.5 g (88%); mp 75–77 °C.

Method B. The acyl carbonate **28** (2.56 g, 0.01 mol) is added to a stirred suspension of sodium borohydride (0.5 g) in ethanol (30 ml) at 0 °C. Stirring is continued for 1 h and the mixture then evaporated to dryness. Water (10 ml) is added to the residue, the mixture is extracted with chloroform (30 ml), and worked up as in Method A to give **124**; yield 94%.

(1-Oxyl-2,2,5,5-tetramethyl-3-pyrroline-3-methyl) Methane Sulfonate (93) (Hankovszky *et al.*, 1980)

Methane sulfonyl chloride (1.55 g, 0.011 mol) was added dropwise to a stirred solution of **124** (1.70 g, 0.01 mol) and triethylamine (1.1 g, 0.011 mol) in dichloromethane (20 ml) at −10 °C (see Scheme 60), and stirring was continued for 3 h at room temperature. The mixture was then extracted with water (10 ml) and with 5% sodium hydrogen carbonate solution (10 ml). The organic phase was dried with sodium sulfate and evaporated to dryness. The residual yellow product was crystallized from chloroform/hexane; yield: 2.9 g (80%); mp 84–85 °C.

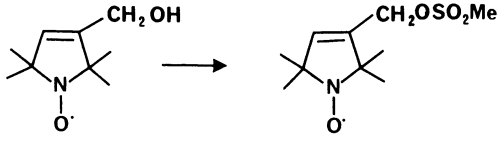

124 93

Scheme 60.

1-Oxyl-2,2,5,5-tetramethyl-3-bromomethyl-3-pyrroline (107) (Hankovszky *et al.*, 1980)

The **93** (2.48 g, 0.01 mol) and lithium bromide (1.73 g, 0.02 mol) were refluxed in dry acetone (20 ml) for 30 min. (See Scheme 61.) The mixture was then diluted with water (20 ml) and extracted with ether (60 ml). The organic phase was dried with sodium sulfate and evaporated to dryness. The bromomethyl compound **107** is a red oil; yield was almost quantitative.

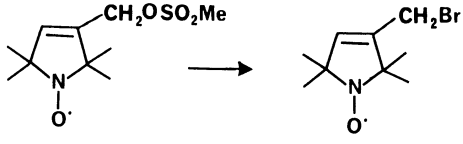

93 107

Scheme 61.

1-Oxyl-2,2,5,5-tetramethyl-3-formyl-3-pyrroline (126) (Hideg *et al.*, 1980)

To a stirred solution of the unsaturated alcohol (3.4 g, 0.02 mol) in tetrachloromethane (60 ml) was added freshly prepared active MnO_2 (30 g). (See Scheme 62.) The mixture was refluxed for 30 min, then filtered, and the filtrate evaporated to dryness. The yellow residue was the practically pure aldehyde; yield: 2.8 g (83%); mp 78–79 °C (ether/hexane).

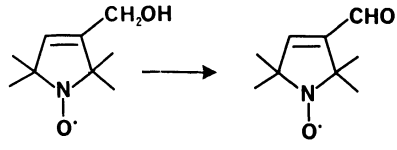

124 126

Scheme 62.

1-Oxyl-2,2,5,5-tetramethyl-3-acetyl-3-pyrroline (161a) (Hankovszky *et al.*, 1982)

To a stirred solution of the Grignard reagent (prepared from magnesium turnings (0.36 g, 0.15 mol) and methyl iodide (2.1 g, 15 mmol) in dry ether (20 ml) a solution of unsaturated aldehyde **126** (1.68 g, 10 mmol) in dry ether (20 ml) was added at 0 °C under nitrogen and stirred for 3 h (see Scheme 63). The reaction was quenched with saturated aqueous NH_4Cl (25 ml). The ether phase was separated, dried, and evaporated to dryness. A mixture of MnO_2 (15 g) and PbO_2 (5 g) was added to the stirred solution of remaining pale yellow oil in carbon tetrachloride (50 ml) and refluxed for 6 h. The filtrate was subjected to column chromatography with carbon tetrachloride/ethyl acetate (10:1); two fractions were separated.

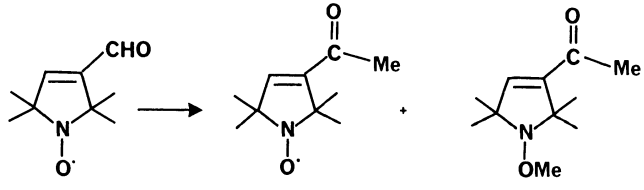

126 161a 159a

Scheme 63.

The first colorless fraction was the *N*-methoxy derivative **159a**, 0.40 g (20%) as a colorless oil. The second yellow fraction was the main product **161a** (from hexane), 1.01 g (55%), mp 71–72 °C.

The ethyl ketone **161b** was prepared in the same way from aldehyde **126** (10 mmol) and ethylmagnesium bromide (15 mmol) to give the *N*-ethoxy derivative **159b**, 0.70 g

(31%) as a colorless oil. The second yellow band was the paramagnetic ethyl ketone **161b**; yield: 0.82 g (41%); mp 65–66 °C.

1-Oxyl-2,2,5,5-tetramethyl-3-bromoacetyl-3-pyrroline (174) and 1-oxyl-2,2,5,5-tetramethyl-3-dibromoacetyl-3-pyrroline (175) (Hankovszky Unpublished Data)

To a stirred solution of **161a** (564 mg, 3.0 mmol) in dry tetrahydrofuran (20 ml), 2-pyrrolidone (0.300 mg, 3.5 mmol) and pyrrolidone hydrotribromide (PHT) (1.73 g, 3.5 mmol) were added (see Scheme 64). The reaction mixture was refluxed for 3 h, then cooled and filtered. The filtrate was evaporated to dryness and dissolved in ether (20 ml). The ether solution was washed with water, dried (Na_2SO_4), and column chromatographed on silica gel with hexane/ethyl acetate (2:1).

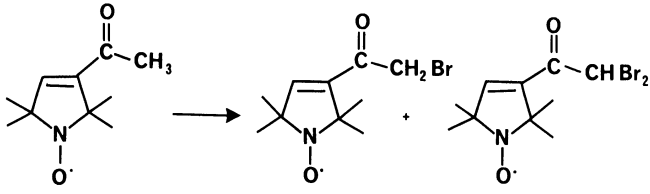

161a 174 175

Scheme 64.

The first yellow band is **175** as the minor product; yield: 153 mg (15%); mp 124–125 °C. The second yellow band is **174** as the major product; yield: 468 mg (60%); mp 64–65 °C.

The 1-oxyl-2,2,5,5-tetramethyl-3-(α-bromopropionyl)-3-pyrroline (**176**) was prepared in the same way from **161b** (588 mg, 3.0 mmol) with 2-pyrrolidone (300 mg, 3.5 mmol) and PHT (1.73 g, 3.5 mmol); yield: 627 mg (76%); mp 98–100 °C.

1-Oxyl-2-allyl-2,5,5-trimethylpyrrolidine (199a) (Hideg and Lex, 1987)

2,5,5-Trimethyl-1-pyrroline-1-oxide (**198**) (12.7 g, 0.1 mol) nitrone was added to a Grignard reagent prepared from magnesium (3.64 g, 0.15 mol) and allyl bromide (18.15 g, 0.15 mol) in ether (100 ml). (See Scheme 65.) The solution was stirred for an

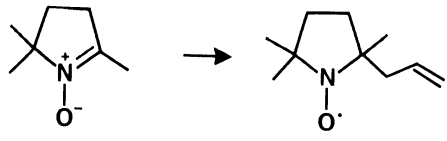

198 199a

Scheme 65.

additional 2 h at room temperature and then treated with saturated aqueous ammonium chloride (5 ml) and water (5 ml). The ether phase was separated and then washed with saturated aqueous sodium chloride. The ether was evaporated, the residue was taken up and stirred in methanol (200 ml) containing concentrated aqueous ammonium hydroxide (5 ml) and copper(II) acetate (0.5 g). Oxygen was bubbling through the reaction mixture until the solution developed a deep blue color. The solvent was evaporated, the residue was taken up in chloroform (50 ml) washed with saturated aqueous sodium hydrogen carbonate, water, then dried and evaporated. The residue was distilled in vacuo to give **202a** as an orange red oil; bp 93-94 °C/13 mm; yield: 13.9 g (83%).

3-(1-Oxyl-2,5,5-trimethyl-2-pyrrolidinyl)ethanal (200a) (Hideg and Lex, 1987)

To the solution of **199a** (1.68 g, 0.01 mol) in dioxane-water (30 ml-10 ml) was added osmium tetroxide (25 mg) and stirred for 5 min (see Scheme 66). (The reaction mixture turned to a brown color.) Potassium periodate (4.6 g, 20.0 mmol) was added in small portions during 30 min, and stirred for an additional 2 h. The color of the reaction mixture was changed back to yellow. The mixture was extracted with ether (3 × 30 ml), the extract was dried and evaporated. The residue yellow oil was chromatographed on silica gel column using hexane-ethyl acetate (2:1) as eluant; yield: 0.66 g (39%).

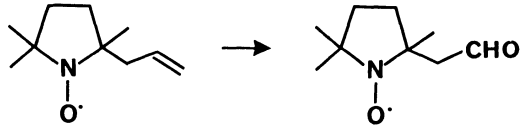

199a 200a

Scheme 66.

(1-Oxyl-2,5,5-trimethyl-2-pyrrolidinyl)acetic Acid (201a) (Hideg and Lex, 1987)

The **199a** (252.4 mg, 15.0 mmol) was added to a suspension of potassium permanganate (7.1 g, 45 mmol) and 18-crown-6 (0.8 g, 3.0 mmol) in benzene (50 ml). (See Scheme 67.) The reaction mixture was stirred for 48 h, filtered, washed with 5% aqueous

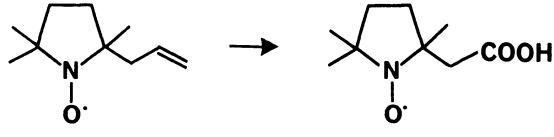

199a 201a

Scheme 67.

sodium hydroxide and water. The combined water washing was acidified with hydrochloric acid, extracted with chloroform, dried, evaporated, and the residue chromatographed on silica gel column with ether–light petroleum–acetic acid (3 : 1 : 0.1) as eluant yielded the acid as a deep yellow oil, 201 mg (72%).

3-(1-Oxyl-2,5,5,-trimethyl-2-pyrrolidinyl)propan-1-ol (202a) (Hideg and Lex, 1987)

To the **202a** (1.68 g, 10.0 mmol) was added dropwise the 0.5 molar tetrahydrofuran solution of the 9-borabicyclo[3.3.1]nonane (40 ml, 20 mmol). (See Scheme 68.) The reaction mixture was stirred for 1 h. The 19% aqueous sodium hydroxide (8 ml, 10 mmol) and (carefully) 30% aqueous hydrogen peroxide (7 ml) were added at 0 °C. The reaction mixture was saturated with potassium carbonate and extracted with ether (3 × 30 ml). The organic extracts were combined, dried, and evaporated. The residue was chromatographed on silica gel column with hexane-ethyl acetate (1 : 2) as eluant to give nitroxide hydroxy compound **202a** as a yellow oil; yield: 0.98 g (47%).

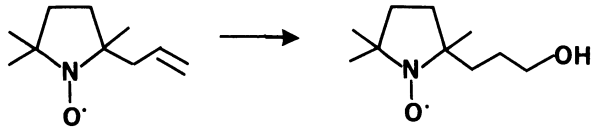

199a 202a

Scheme 68.

ACKNOWLEDGMENT. The work of the authors discussed in this chapter was supported by Grant 301/A/82 from the Hungarian Academy of Sciences.

REFERENCES

Adackaparayil, M., and Smith, J. H., 1977, Preparation and reactivity of a new spin label reagent, *J. Org. Chem.* **42**:1655–1656.

Alcock, N. W., Golding B. T., Ioannou, P. V., and Sawyer, J. F., 1977, Preparation, crystal structure and reaction of a new spin-labeling reagent, *cis*-3,5-dibromo-4-oxo-2,2,6,6-tetramethylpiperidin-1-yloxyl, *Tetrahedron* **33**:2969–2980.

Aurich, H. G., 1982, Nitroxides, in *The Chemistry of Functional Groups, Suppl. F.*: The chemistry of amino, nitroso and nitro compounds and their derivatives, Chap. 14 (S. Patai, ed.), pp. 565–622, Interscience-Wiley, London.

Azzi, A., Bragadin, M. A., Tamburro, A. M., and Santato, M., 1973, Site-directed spin labeling of mitrochondrial membrane, *J. Biol. Chem.* **248**:2520–2526.

Barratt, M. D., Dodd, G. H., and Chapman, D., 1969, A spin label for tyrosine residues, *Biochim. Biophys. Acta* **194**:602–605.

Barratt, M. D., Davies, A. P., and Evans, M. T. A., 1971, Maleimide and isomaleimide pyrrolidine-nitroxide spin labels, *Eur. J. Biochem.* **24**:280–283.

Berliner, L. J., 1974, Applications of spin labeling to structure conformation studies of enzymes, *Prog. Bioorg. Chem.* **3**:1-80.

Berliner, L. J. (ed.), 1976, *Spin Labeling: Theory and Applications*, Vol. I, Academic Press, New York.

Berliner, L. J. (ed.), 1979, *Spin Labeling: Theory and Applications*, Vol. II, Academic Press, New York.

Berliner, L. J., 1983, The spin-label approach to labeling membrane protein sulfhydryl groups. *Ann. N.Y. Acad. Sci.* **414**:153-161.

Berliner, L. J., and McConnell, H. M., 1966, A spin-labeled substrate for α-chymotrypsin, *Proc. Natl. Acad. Sci. U.S.A.* **55**:708-712.

Berliner, L. J., and McConnell, H. M., 1974, Urea denaturation of active-site spin-labeled α-chymotrypsin, *Biochemistry* **11**:2921-2924.

Berliner, L. J., Grünwald, J., Hankovszky, H. O., and Hideg, K., 1982, A novel reversible thiol-specific spin label: Papaine active site labeling and inhibition, *Anal. Biochem.* **119**:450-455.

Beth, A. H., Balasubramanian, K., Wilder, R. T., Venkataramu, S. D., Robinson, B. H., Dalton, L. R., Pearson, D. E., and Park, J. H., 1981a, Structural and motional changes in glycerin-aldehyde-3-phosphate dehydrogenase upon binding to the band-3 protein of the erythrocyte membrane examined with ^{15}N-, ^{2}H-maleimide spin label and electron paramagnetic resonance, *Proc. Natl. Acad. Sci. U.S.A.* **78**:4955-4959.

Beth, A. H., Venketaramu, S. D., Balasubramanian, K., Dalton, L. R., Robinson, B. H., Pearson, D. E., Park, C. R., and Park, J. H., 1981b, ^{15}N- and ^{2}H-substituted maleimide spin labels: Improved sensitivity and resolution for biological EPR studies, *Proc. Natl. Acad. Sci. U.S.A.* **78**:967-971.

Bonnett, R. F. R., Brown, R. F. C., Clark, V. M., Sutherland, I. O., and Todd, A., 1959, Experiments toward the synthesis of Corrins. Part II. The preparation and reactions of Δ^1-pyrroline 1-oxides. *J. Chem. Soc.*: 2094-2102.

Brière, R., Espie, J.-C., Ramasseul, R., Rassat, A., and Rey, P., 1979, Nitroxydes 91: β-Cetoenolates nitroxydes, *Tetrahedron Lett.*: 941-944.

Buchacenko, A. L., 1965, *Stable Radicals*, Consultants Bureau, New York.

Carpino, L. A., Giza, C. A., and Carpino, B. A., 1959, O-Acylhydroxylamines. I. Synthesis of O-benzoylhydroxylamine, *J. Am. Chem. Soc.* **81**:955-957.

Cazianis, C. T., Sotiroudis, T. G., and Evangelopoulos, A. E., 1980, Spin-labelling of phosphorylase *b* using a paramagnetic 1-fluoro-2,4-dinitrobenzene derivative, *Biochim. Biophys. Acta* **621**:117-129.

Chan, D. C. F., and Piette, L. H., 1980, ESR spin label studies of the nucleosome core particle and hystone core, *Biochim. Biophys. Acta* **623**:32-45.

Cherry, R. J., 1979, Rotational and lateral diffusion of membrane proteins, *Biochem. Biophys. Acta* **559**:289-327.

Crouch, R. K., Ebrey, T. G., and Govindjee, R., 1981, A bacteriorhodopsin analogue containing the retinal nitroxide free radical, *J. Am. Chem. Soc.* **103**:7364-7366.

Csekö, J., Hankovszky, H. O., and Hideg, K., 1985, Synthesis of novel highly reactive 1-oxyl-2,2,6,6-tetramethyl-1,2,5,6-tetrahydropyridine derivatives, *Can. J. Chem.* **63**:940-943.

Dreyer, J.-L., Beinert, H., Keana, J. F. W., Hankovszky, H. O., Hideg, K., Eaton, S. S., and Eaton, G., 1983, A spin label study of the disposition of the Fe-S cluster with respect to the active center of aconitase. *Biochim. Biophys. Acta* **745**:229-236.

Dugas, H., 1977, Spin-labelled nucleic acids, *Acc. Chem. Res.* **10**:47-54.

Fehér, G., 1969, *Electron Paramagnetic Resonance with Applications to Selected Problems in Biology*, Gordon and Breach, New York.

Filatova, M. P., Reissmann, Z., Reutova, T. O., Ivanov, V. T., Grigoryan, G. L., Shapiro, A. M., and Rozantsev, E. G., 1977, Conformational states of bradykinin and its analogs in solution. III. EPR spectra of spin-labeled analogs, *Bioorg. Chim.* **3**:1181-1189.

Fittkau, S., and Damerau, W., 1980, Spinmarkierte Oligopeptide als Substratanaloge Inhibitoren der Leucinaminopeptidase, *J. Prakt. Chem.* **322**:1032-1038.

Fittkau, S., Kaemmerer, G., and Damerau, W., 1979, The binding center of leucine aminopeptidase. Investigations with substrate analogs and spin-labeled inhibitors, *Ophthalmic Res.* **11**:381–385.

Flohr, K., and Kaiser, E. T., 1972, Enantiomeric specificity in the chymotrypsin-catalyzed hydrolysis of 3-carboxy-2,2,5,5-tetramethylpyrrolidin-1-oxy-*p*-nitrophenyl ester, *J. Am. Chem. Soc.* **94**:3675–3676.

Flohr, K., Paton, R. M., and Kaiser, E. T., 1971, Enantiomeric specificity in the cyclohexamylase-catalyzed hydrolysis of 3-carboxy-2,2,5,5-tetramethylpyrrolidin-1-oxy *m*-nitrophenyl ester, *J. Chem. Soc.*: 1621–1622.

Forrester, A. R., Hay, J. M., and Thomson, R. H., 1968, Organic Chemistry of Stable Free Radicals, Academic Press, New York.

Gaffney, B. J., 1976, The chemistry of spin labels, in *Spin Labeling: Theory and Applications*, Vol. I (L. J. Berliner, ed.), Chap. 5, pp. 183–272, Academic Press, New York.

Gaffney, B. J., and McNamee, C. M., 1974, Spin label measurements in membranes, *Methods Enzymol.* **32**:161.

Gaffney, B. J., Willingham, G. L., and Schepp, R. S., 1983, Synthesis and membrane interactions of spin-label bifunctional reagents, *Biochemistry* **22**:881–892.

Gerig, J. T., Reinheimer, J. D., and Robinson, R. H., 1979, Modification of human serum albumin with *N*-(2,5-dinitro-4-fluorophenyl)-4-amino-2,2,6,6-tetramethylpiperidinooxy radical, *Biochim. Biophys. Acta* **579**:409–420.

Gnewuch, T., and Sosnovsky, G., 1986, Spin-labeled carbohydrates, *Chem. Rev.* **86**:203–238.

v. Goldammer, E., Kreysch, W., and Wenzel, H., 1978, Proton NMR relaxation studies of several nitroxyl-water systems, *J. Solution Chem.* **7**:197–204.

Golding, B. T., Ioannou, P. V., and O'Brien, M. M., 1975, A short-cut to spin-labelled amides, *Synthesis*: 462–463.

Griffith, H. O., and McConnell, H. M., 1966, A nitroxide-maleimide spin label, *Proc. Natl. Acad. Sci. U.S.A.* **55**:8–11.

Griffith, O. H., and Waggoner, A. S., 1969, Nitroxide free radicals: Spin labels for probing biomolecular structure, *Acc. Chem. Res.* **2**:17–24.

Griffith, O. H., Keana, J. F. W., Noall, D. L., and Ivey, J. L., 1967, Nitroxide mixed carboxylic-carbonic acid anhydrides. A new class of versatile spin labels, *Biochim. Biophys. Acta* **148**:583–585.

Grigoryan, G. D., Rozantsev, E. G., Teplov, N. E., Ivanov, V. P., and Korkmazyan, M. M., 1973, Investigation of α-chymotripsin by the "Spin label method" at Serine-195, *Izv. Akad. Nauk SSSR, Ser. Khim.*: 1654–1656.

Hankovszky, H. O., Hideg, K., and Tigyi, J., 1978, Nitroxides II. 1-Oxyl-2,2,5,5-tetramethylpyrroline-3-carboxylic acid derivatives, *Acta Chim. Acad. Sci. Hung.* **98**:339–348.

Hankovszky, H. O., Hideg, K., Lex, L., and Tigyi, J., 1979, Nitroxyls IV. Synthesis of spin labelled *N*-(4-piperidinyl-oxycarbonyl)imidazoles and 4-piperidinyloxycarbonyl azides and their reaction with amino acid derivatives, *Synthesis*: 530–531.

Hankovszky, H. O., Hideg, K., and Lex, L., 1980, Nitroxyls VII. Synthesis and reactions of highly reactive 1-oxyl-2,2,5,5-tetramethyl-2,5-dihydropyrrole-3-ylmethyl sulfonates, *Synthesis*: 914–916.

Hankovszky, H. O., Hideg, K., and Lex, L., 1981, Nitroxyls VIII. Synthesis of nitroxylphosphinimines; A convenient route to Amine, Isothiocyanate, Aminocarbonylaziridine and Carbodiimide nitroxyls, *Synthesis*: 147–149.

Hankovszky, H. O., Hideg, K., Lex, L., Kulcsár, Gy., and Halász, A. H., 1982, Methods for preparation of heterobifunctional nitroxides: α,β-unsaturated ketones, β-ketoesters, cyanonitro-derivatives. *Can. J. Chem.* **60**:1432–1438.

Hankovszky, H. O., Hideg, K., Goldammer, E. v., Matuszak, E., Kolkenbrock, H., Tschesche, H., and Wenzel, H., 1987, New nitroxide reagents for the selective spin labeling at the guanidino moiety of arginine residues in peptides and proteins, *Biochim. Biophys. Acta* **916**:152–155.

Hideg, K., and Lex, L., 1984, A versatile new method for the synthesis of various pyrrolidin-1-oxyl fatty acids. *J. Chem. Soc., Chem. Commun.*: 1263-1265.

Hideg, K., and Lex, L., 1986a, Synthesis of various new nitroxide free radical fatty acids. *J. Chem. Soc., Perkin Trans. 1*: 1431-1438.

Hideg, K., and Lex, L., 1987, Synthesis of new 2-mono and 2,5-bis-functionalized pyrrolidine-1-oxyl spin labels. *J. Chem. Soc., Perkin Trans. 1*: 1117-1121.

Hideg, K., Hankovszky, H. O., and Tigyi, J., 1977, Nitroxides I. Sulfonic esters of 4-hydroxy-2,2,6,6-tetramethylpiperidine-1-oxyl and their reaction with dinucleophilic reactants, *Acta Chim. Acad. Sci. Hung.* **92**:85-87.

Hideg, K., Lex, L., Hankovszky, H. O., and Tigyi, J., 1978, Nitroxyls III. Synthesis of spin-labelled amino acids and their derivatives. *Synthesis*: 914-917.

Hideg, K., Hankovszky, H. O., Lex, L., and Kulcsár, Gy., 1980, Nitroxyls VI. Synthesis and reactions of 3-hydroxymethyl-2,2,5,5-tetramethyl-2,5-dihydropyrrole-1-oxyl and 3-formyl derivatives, *Synthesis*: 911-914.

Hoffman, B. M., Schofield, P., and Rich, A., 1969, Spin-labeled transfer RNA, *Proc. Nat. Acad. Sci. U.S.A.* **62**:1195-1202.

Hoffman, B. M., Schofield, P., and Rich, A., 1970, Spin labeling studies of aminoacyl transfer ribonucleic acid, *Biochemistry* **9**:2525-2532.

Hsia, J. C., 1968, Development of single and double spin labelling methods and their application to study of antibody active sites, Ph.D. Thesis, University of Hawaii, Honolulu.

Hsia, J. C., and Tan, C. T., 1978, Membrane immunoassay: Principle and application of spin membrane immunoassay, *Ann. N.Y. Acad. Sci.* **308**:139-148.

Hsia, J. C., and Kwan, N. H., 1981, Human serum albumin: Binding specificity and allosteric effects of parinarate and stearate, A dianionic spin label study, *J. Biol. Chem.* **256**:2242-2244.

Hsia, J. C., Kosman, D. J., and Piette, L. H., 1969, Organophosphate spin-label studies of inhibited esterases, α-chymotripsin and cholinesterase, *Biochem. Biophys. Res. Commun.* **36**:75-88.

Hsia, J. C., Wong, L. T. L., and Kalow, W., 1973, Homogenous murine myeloma protein 315 and spin labeled DNP as a model system for spin labeled hapten titration. Technical and spin immunoassay, *J. Immunol. Methods* **3**:17-24.

Hsia, J. C., Er, S. S., Tan, C. T., Estes, T., and Ruoslahti, E., 1980, α-Fetoprotein binding specificity for arachidonate, bilirubin, docosa-hexanoate and palmitate; A spin label study, *J. Biol. Chem.* **255**:4224-4227.

Hyde, J. S., and Dalton, L. R., 1979, Saturation-transfer spectroscopy, in: *Spin Labeling: Theory and Applications*, Vol. II (L. J. Berliner, ed.), Chap. 1, pp. 1-70, Academic Press, New York.

Jahr, D., Rebhan, K. H., Schwarzhans, K. E., and Wildemann, J., 1973, Metal complexes with paramagnetic derivatives of 1-piperidine-oxyl, *Z. Naturforsch.* **28b**:55-62.

Jost, P., and Griffith, O. H., 1972, Electron spin resonance and the spin labeling method, *Methods Pharmacol.* **2**:223-276.

Jost, P. C., and Griffith, O. H., 1978, The spin labeling technique, *Methods Enzymol.* **49**:369-418.

Kalk, A., de Jong, A. S. H., and Barratt, M. D., 1975, The binding of a spin-labelled dipeptide to papain, *FEBS Lett.* **60**:58-61.

Kalmanson, A. E., and Grigoryan, G. L., 1973, Spin labels in E.P.R. investigation of biological systems, in *Experimental Methods in Biophysical Chemistry* (C. Nicolau, ed.), pp. 589-612, Wiley, New York.

Kamzolova, S. G., and Postnikova, G. B., 1981, Spin-labeled nucleic acids, *Q. Rev. Biophys.* **14**:223-288.

Keana, J. F. W., 1978, Newer aspects of the synthesis and chemistry of nitroxide spin labels, *Chem. Rev.* **78**:37-64.

Keana, J. F. W., 1979, New aspects of nitroxide chemistry, in *Spin Labeling: Theory and Applications* (L. J. Berliner, ed.), Chap. 3, pp. 115-172, Academic Press, New York.

Keana, J. F. W., 1984, Synthesis and chemistry of nitroxide spin labels, in *Spin Labeling in Pharmacology* (J. L. Holtzman, ed.), Chap. 1, pp. 1-85, Academic Press, Orlando.

Keana, J. F. W., Keana, S. B., and Beetham, D., 1967, A new versatile ketone spin label, *J. Am. Chem. Soc.* **89**:3055-3056.

Keana, J. F. W., Lee, T. D., and Bernard, E. M., 1976, Side chain substituted 2,2,5,5-tetramethylpyrrolidine-*N*-oxyl (proxyl) nitroxides. A new series of lipid spin labels showing improved properties for the study of biological membranes, *J. Am. Chem. Soc.* **98**:3052-3053.

Keana, J. F. W., Hideg, K., Birrell, B. G., Hankovszky, H. O., Ferguson, G., and Parvez, M., 1982, New mono- and difunctionalized 2,2,5,5-tetramethylpyrrolidine- and Δ^3-pyrroline-1-oxyl nitroxide spin labels, *Can. J. Chem.* **60**:1439-1447.

Keana, J. F. W., Cuomo, J., Lex, L., and Seyedrezai, S. E., 1983a, Azethoxyl nitroxide spin labeled crown ethers and cryptands with the N-O group positioned near the cavity, *J. Org. Chem.* **48**:2647-2654.

Keana, J. F. W., Seyedrezai, S. E., and Gaughan, G., 1983b, Difunctionalized trans-2,5-disubstituted pyrrolidine (azethoxyl) nitroxide spin labels, *J. Org. Chem.* **48**:2644-2647.

Keana, J. F. W., Heo, G. S., and Gaughan, G. T., 1985, Stereospecific synthesis of difunctionalized 2,5-disubstituted cis-2,5-dimethylpyrrolidine (azethoxyl) nitroxides by oxidative cleavage of protected 8-azabicyclo(3.2.1)octane precursors, *J. Org. Chem.* **50**:2346-2351.

Kemp, D. S., Wang, S. W., Busby, G., and Hugel, G., 1970, Microanalysis by successive isotopic dilution. A new assay for racemic content, *J. Am. Chem. Soc.* **92**:1043-1055.

Kenyon, G. L., and Bruice, T. W., 1977, Novel sulfhydryl reagents, *Methods Enzymol.* **47E**:407-430.

Klee, W., and Brenner, M., 1961, *t*-Butyloxycarbonyl-imidazol und *t*-butyl-oxycarbonyl-hydrazin, *Helv. Chim. Acta* **44**:2141-2153.

Koch, T. R., Kuo, L. C., Douglas, E. G., Jaffer, S., and Makinen, M. W., 1979, Synthesis of chromophoric, spin-label enzyme substrates useful for cryoenzymology, *J. Biol. Chem.* **254**:12310-12313.

Konieczny, M., and Sosnovsky, G., 1981, Methods for the preparation of spin labeled phosphorous compounds and applications of some of them to phosphorylative spin labeling, *Synthesis*: 682-699.

Kumarev, V. P., and Knorre, D. G., 1970, Water-soluble carbodiimides with spin label, *Dokl. Akad. Nauk SSSR* **193**:103-105.

Lawrence, J.-J., Berne, L., Ouvrier-Buffer, J. L., and Piette, L. H., 1980, Spin label study of histone H1-DNA interaction. Comparative properties of the central part of the molecule and the amino- and carboxy-amino tails, *Eur. J. Biochem.* **107**:263-269.

Lee, T. D., and Keana, J. F. W., 1978, Nitroxides derived from 3,4-dihydro-2,5-dimethyl-2H-pyrrole 1-oxide. A new series of minimum steric perturbation lipid spin labels. *J. Org. Chem.* **43**:4226-4231.

Lee, T. D., Birrell, G. B., and Keana, J. F. W., 1979, Azetoxyl nitroxide spin labels. ESR studies involving thiourea crystals, model membrane systems and chromatophores, and chemical reduction with ascorbate and dithiothreitol. *Biochim. Biophys. Acta* **550**:369-383.

Leute, R., Ullman, E. F., Goldstein, A., and Herzenberg, L. A., 1972, Spin immunoassay technique for determination of morphine, *Nature (London), New Biol.* **236**:93-94.

Lex, L., Hideg, K., and Hankovszky, H. O., 1982, Nitroxides IX. Synthesis of nitroxide free radical α-amino acids, *Can. J. Chem.* **60**:1448-1451.

Likhtenshtein, G. I., 1974, *Method spinovykh metok v. molekularnoi biologii*, Nauka, Moscow (in Russian); translation: Likhtenshtein, G. I., 1976, *Spin Labeling Methods in Molecular Biology*, Wiley-Interscience, New York.

Lord, S. T., and Breslow, E., 1978, Nuclear magnetic resonance of neurophysin: Evidence for secondary peptid-binding sites, *Biochem. Biophys. Res. Commun.* **80**:63-70.

Lord, S. T., and Breslow, E., 1979, Identification and observation of alkyl proton resonances of the amino-terminal residues of bovine neurophysins. Evidence for conformational differences between neurophysin I., and neurophysin II., *Int. J. Pept. Protein Res.* **13**:71-77.

Lord, S. T., and Breslow, E., 1980, Synthesis of peptide spin-labels that bind to neurophysin and their application to distance measurements within neurophysin complexes, *Biochemistry* **19**:5593-5602.

Lundt, S. L., and Breslow, E., 1976, Electron spin resonance studies of neurophysin and its interaction with spin-labeled peptides, *J. Phys. Chem.* **80**:1123-1126.

Maksimova, L. A., Grigoryan, G. L., and Rozantsev, E. G., 1975, Synthesis of spin labeled peptides, *Izv. Akad. Nauk SSSR, Ser. Khim.*: 945-948.

Marsh, D., 1981, Electron spin-resonance: Spin-labels, in *Membrane Spectroscopy, Molecular Biology, Biochemistry and Biophysics*, Vol. 31 (E. Grell, ed.), pp. 51-141, Springer-Verlag, Berlin, Heidelberg, New York.

Marsh, D., and Watts, A., 1982, Spin labeling and lipid-protein interactions in membranes, in *Lipid-Protein Interactions*, Vol. 2 (P. Jost, and G. H. Griffith, eds.), pp. 53-126, Wiley, New York.

McConnell, H. M., and Gaffney-McFarland, B., 1970, Physics and chemistry of spin labels, *Q. Rev. Biophys.* **3**:91-136.

McConnell, H. M., Deal, W., and Ogata, R. T., 1969, Spin labelled hemoglobin derivatives in solution, polycrystalline suspensions and single crystals, *Biochemistry* **8**:2580-2585.

Mehlhorn, R., Swanson, M., Packer, L., and Smith, P., 1980, An imidoester spin probe to membrane protein interactions: Application to cytochrome C, *Arch. Biochem. Biophys.* **204**:471-476.

Misharin, A. Yu., Vinokurov, L. M., and Polyanovskii, O. L., 1974, New paramagnetic derivative of iodoacetic acid, *Izv. Akad. Nauk SSSR, Ser. Khim.*: 1897-1898.

Misharin, A. Yu., Azhaev, A. V., Timofeev, P. V., and Polyanovskii, O. L., 1975, Interaction of spin-labeled inhibitors with aspartate aminotransferase, *Bioorg. Khim.* **1**:257-266.

Morrisett, J. D., 1976, The use of spin labels for studying the structure and function of enzymes, in *Spin Labelling: Theory and Application*, Vol. I. (L. J. Berliner, ed.), pp. 273-372, Academic Press, New York.

Morrisett, J. D., and Broomfield, C. A., 1972, A comparative study of spin labelled serine enzymes: Acetylcholinesterase, trypsin, α-chymotrypsin, elastase, and subtilisin, *J. Biol. Chem.* **247**:7224-7231.

Nakaie, C. R., Goissis, G., Schreier, S., and Paiva, A. C. M., 1981, pH-dependence of EPR spectra of nitroxides containing ionizable groups, *Brazilian J. Med. Biol. Res.* **14**:173-180.

Ogawa, S., and McConnell, H. M., 1967, A spin label study of hemoglobin conformations in solution, *Proc. Natl. Acad. Sci. U.S.A.* **58**:19-26.

Pirrwitz, J., and Damerau, W., 1976, Synthese spinmarkierter Alkylamine als potentielle Enzym-effektoren, *Z. Chem.* **16**:401-402.

Price, N. C., 1973, Improvement of the spin-labeling technique by the use of a radioactive spin label, *FEBS Lett.* **36**:351-354.

Rassat, A., and Rey, P., 1967, Nitroxides, XXIII. Préparation d'aminoacides radicalaires et de leurs sels complexes. *Bull. Soc. Chim. Fr.*: 815-817.

Rassat, A., and Ronzaud, J., 1976, Nitroxides—LXXI. Synthèse de dérivés nitroxydes du tropane. Etude par RPE et RMN des interactions hyperfines à longue distance dans ces radicaux, *Tetrahedron*: 239-244.

Rauchman, E. J., and Rosen, G. M., 1976, Synthesis of spin labeled probes: Esterification and reduction, *Synth. Commun.* **6**:325-329.

Reissmann, S., Filatova, M. P., Reutova, T. O., Arold, H., and Ivanov, V. T., 1976, Peptide XXV. Synthese von Bradykinin-Analoga und Partialsequenzen mit Tyrosin für Elektronenspin-rezonanz- und Fluoreszenzuntersuchungen, *J. Prakt. Chem.* **318**:429-440.

Rozantsev, E. G., 1970, *Free Nitroxyl Radicals*, Plenum Press, New York. (Translated from Russian by B. J. Hazzard.)

Rozantsev, E. G., and Sholle, V. D., 1971a, Synthesis and reactions of stable nitroxyl radicals, I. Synthesis, *Synthesis*: 190-202.

Rozantsev, E. G., and Sholle, V. D., 1971b, Synthesis and reactions of stable nitroxyl radicals, II. Reactions, *Synthesis*: 401-414.

Schlude, H., 1973, Oxidation of hydroxylamines to nitroxyl radicals with Fremy's salt, *Tetrahedron*: 4007-4011.

Schlude, H., 1975, New phosphonium salts for the Wittig synthesis of aldehydes from ketones. Acetal, triphenyl phosphorane, enol ether, acidic hydrolysis, nitroxyl, *Tetrahedron*: 89-92.

Schmidt, P. G., Bertanowicz, M. S., and Rich, D. H., 1982, Spin-labeled pepstatin binding to pepsin. A study by electron spin resonance and nuclear magnetic resonance, *Biochemistry* **21**:1830-1835.

Shapiro, A. B., Pavlikov, V. V., and Rozantsev, E., 1977a, Stable radicals in diene synthesis, *Dokl. Akad. Nauk SSSR* **232**:398-400.

Shapiro, A. B., Skripnichenko, L. N., Chumakov, V. M., Pavlikov, V. V., and Rozantsev, E. G., 1977b, Interaction of paramagnetic Mannich-bases with cysteine and biopolymer molecules, *Bioorg. Khim.* **3**:707-708.

Sholle, V. D., Golubev, V. A., and Rozantsev, E. G., 1971, Interaction of nitroxyl radicals with Grignard reagents, *Dokl. Akad. Nauk SSSR* **200**:137-139.

Sinha, B. K., and Chignell, C. F., 1979, The synthesis and use of spin-labeled analogs of biotin in the study of avidin, *Methods Enzymol.* **62**:295-308.

Smith, I. C. P., 1968, A study of the conformational properties of bovine pancreatic ribonuclease A by electron paramagnetic resonance, *Biochemistry* **7**:745-757.

Smith, I. C. P., 1972, The spin label method, in *Biological Applications of Electron Spin Resonance Spectroscopy* (J. R. Bolton, D. Borg, and H. Schwartz, eds.), pp. 483-539, Wiley, New York.

Soltys, B. J., and Hsia, J. C., 1978a, Human serum albumin, *J. Biol. Chem.* **253**:3029-3034.

Soltys, B. J., and Hsia, J. C., 1978b, Steroid modulation of human serum albumin binding properties, *J. Biol. Chem.* **253**:4266-4269.

Sosnovsky, G., and Konieczny, M., 1976, Phosphorylative spin-labeling of amino acids and steroids, *Synthesis*: 537-539.

Spallholz, J. E., and Piette, L. H., 1972, Interactions of spin-labelled analogs of 1,10-phenanthroline and iodoacetamides with horse liver alcohol dehydrogenase, *Arch. Biochem. Biophys.* **148**:596-606.

Sparrow, J. T., 1976, An improved polystyrene support for solid phase peptide synthesis, *J. Org. Chem.* **41**:1350-1353.

Staab, H. A., 1977, Reactionsfähige heterocyclische Diamine der Kohlensäure, *Justus Liebigs Ann. Chem.* **609**:75-83.

Staab, H. A., and Mannschreck, A., 1962, Synthese von Carbonsäureestern nach der Imidazolid-methode, *Chem. Ber.* **95**:1284-1297.

Stone, T. J., Buckmann, T., Nordio, R. L., and McConnell, H. M., 1965, Spin labeled biomolecules, *Proc. Natl. Acad. Sci. U.S.A.* **54**:1010-1017.

Stryer, L., and Griffith, H. O., 1965, A spin label hapten, *Proc. Natl. Acad. Sci. U.S.A.* **54**:1785-1791.

Terzian, G., Cormons, A., Asso, M., and Benlian, D., 1976, Complexes de l'acide amino-4 tétraméthyl-2,2,6,6-pipéridine oxyle-1 carboxylique-4 avec Co^{2+} et Mn^{2+} en solution. *J. Chim. Phys.* **73**:146-248.

Thomas, D. P., Dalton, L. R., and Hyde, J. S., 1976, Rotational diffusion studied by passage saturation transfer electron paramagnetic resonance, *J. Chem. Phys.* **65**:3006-3024.

Tse-Tang, M. W., Gaffney, B. J., and Kelly, R. E., 1981, Synthesis of bifunctional spin label molecules and their orientations in membranes, *Heterocycles* **15**:965-974.

Ullman, E. F., Call, L., and Osiecki, J. H., 1970, Stable free radicals. VIII. New imino, amido and carbamoyl nitroxides, *J. Org. Chem.* **35**:3623-3631.

Ullman, E. F., Osiecki, J. H., Boocok, D. G. B., and Darcy, R., 1972, Studies of stable free radicals. X. Nitronyl nitroxide monoradicals and biradicals as possible small molecule spin labels, *J. Am. Chem. Soc.* **94**:7049-7059.

Venkataramu, S. D., Pearson, D. E., Beth, A. H., Perkins, R. C., Park, C. R., and Park, J. H., 1979, Synthesis of perdeuterio-*N*-1-(1-oxyl-2,2,6,6-tetramethyl-4-peperidinyl)maleimide, a highly sensitive spin probe, *J. Labelled Compd.* **18**:371-383.

Weinkam, R. J., and Jörgensen, E. C., 1971a, Free radical analogs of histidine, *J. Am. Chem. Soc.* **93**:7028-7033.

Weinkam, R. J., and Jörgensen, E. C., 1971b, Angiotensin II analogs. VIII. The use of free radicals containing peptides to indicate the conformation of the carboxyl terminal region of angiotensin II., *J. Am. Chem. Soc.* **93**:7033-7038.

Wenzel, H., *et al.*, unpublished results.

Wenzel, H. R., Becker, G., and v. Goldammer, E., 1978, Synthese eines bifunctionellen Spin-labels zur Quervernetzung von Proteinen, *Chem. Ber.* **111**:2453-2454.

Wenzel, H. R., Tschesche, H., and v. Goldammer, E., 1983, Spin-labelled amino acids, peptides and proteins—Synthesis and applications, in *Modern Methods in Protein Chemistry* (H. Tschesche, ed.), pp. 385-408, Walter de Gruyler, Berlin.

Weygand, F., and Geiger, W., 1956, *N*-Trifluoroacetyl-aminosäuren, IV. Mitteil: *N*-Trifluoroacetylierung von Aminosäuren in wasserfreier Trifluoressigsäure, *Chem. Ber.* **89**:647-652.

Weygand, F., and Freuendorfer, E., 1970, *N*-Trifluoracetyl-aminosäuren, XXI. Reduktive Entfernung des *N*-Trifluoracetyl- und *N*-Trichloracetylesters durch Natriumborhydrid mit Anwendungen in der Peptidchemie, *Chem. Ber.* **103**:2437-2449.

Whitesides, G. M., and Newirth, T. L., 1975, Reaction of *n*-butyllithium and 2,2,6,6-tetramethylpiperidine nitroxide, *J. Org. Chem.* **40**:3448-3450.

Willingham, G. L., and Gaffney, B. J., 1983, Reactions of spin-label cross-linking reagents with red blood cell protein, *Biochemistry* **22**:892-898.

Wünsch, E., 1974, Synthese von Peptiden, in *Houben-Weyl, Methoden der Organischen Chemie*, 4th edn. (E. Müller, ed.), Vol. XV/1,2, George Thieme Verlag, Stuttgart.

Zhdanov, R. I., 1981, *Paramagnetnüe modeli biologeckij aktivnükh soedidienii* (*Paramagnetic Models of Biologically Active Compounds*), Nauka, Moscow (Russian).

10

Nitroxide Radical Adducts in Biology: Chemistry, Applications, and Pitfalls

Carolyn Mottley and Ronald P. Mason

1. INTRODUCTION

Spin trapping is a technique in which a reactive free radical reacts with a double bond of a diamagnetic compound, the spin trap, to form a less reactive free radical, the spin adduct. Spin trapping is often necessary when the primary free radical cannot be observed by conventional ESR either because of low concentration or very short radical relaxation times which lead to very broad lines (Janzen, 1980).

Compounds commonly used as spin traps fall into two categories: nitroso compounds and nitrones. In each case the resulting spin adduct is a relatively stable nitroxide free radical. Nitroso compounds have a distinct advantage over nitrones in that the reactive free radical attaches directly to the nitrogen atom and usually gives rise to distinctive hyperfine splittings. The nitroso compounds unfortunately have the disadvantage of being photochemically and thermally unstable (Perkins, 1980).

There are four commonly used spin traps in biological systems. The most common nitroso compound used as a spin trap is 2-methyl-2-nitrosopropane or *tert*-nitrosobutane (tNB).

$$\underset{\text{tNB}}{(CH_3)_3C-N=O} + R\cdot \rightarrow (CH_3)_3C-\underset{\displaystyle R}{\underset{|}{N}}-O\cdot$$

A major disadvantage of tNB is that it decomposes thermally and photochemically to

Carolyn Mottley • Department of Chemistry, Luther College, Decorah, Iowa 52101. **Ronald P. Mason** • Laboratory of Molecular Biophysics, National Institute of Environmental Health Sciences, Research Triangle Park, North Carolina 27709.

give di-*t*-butyl nitroxide, a very stable radical which gives an often observed three-line signal. The other three common spin traps are nitrones:

phenyl-*tert*-butylnitrone (PBN),

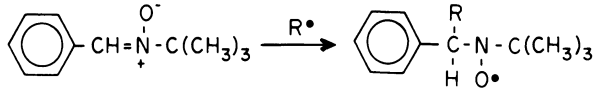

α-4-Pyridyl-1-oxide N-*tert*-butylnitrone (4-POBN),

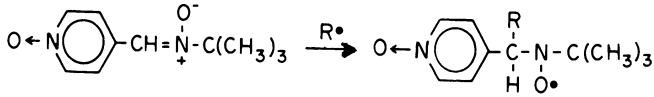

5,5-dimethylpyrroline N-oxide (DMPO),

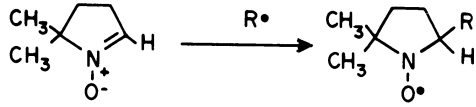

The major disadvantage of the nitrone spin traps is the lack of spectral information obtained about the primary radical. With few exceptions, spin adducts of the nitrone spin traps give six-line ESR spectra with hyperfine splittings from the nitrogen and the β-hydrogen originating from the spin trap itself. This means that structural identification must be done by careful comparison of the magnitude of the hyperfine coupling constants with those of reference nitroxides whose spectra are recorded under exactly the same experimental conditions (Perkins, 1980) or by the use of isotopically labeled compounds.

Perkins (1980), in his excellent review of spin trapping, points out four questions which must be asked when designing a spin-trapping experiment:

1. Will the spin trap participate in reactions other than those with reactive radicals generated in the experiment? Can these alternative reactions yield nitroxides which will appear as spin-adduct imposters?
2. How readily can the spectrum be interpreted and the structure of R· be determined?
3. How fast is the trapping reaction, and how stable are the spin adducts formed?
4. Does the appearance of a spin adduct signify a major reaction pathway, or can it be a minor side reaction?

To these questions perhaps a fifth should be added:

5. Is there isotopically labeled (^{13}C, ^{2}H, ^{17}O, ^{15}N, etc.) material available for proof of structure? If not, is there an independent synthesis for the spin adduct?

These questions must be carefully addressed by anyone undertaking spin trapping experiments.

In addition to the review articles mentioned previously there are several good reviews of spin trapping (Evans, 1979; Finkelstein *et al.*, 1980; Buettner, 1982;

Kalyanaraman, 1982; Mason, 1982, 1984; Rosen and Finkelstein, 1985; Green *et al.*, 1985; Mason and Mottley, 1987), which discuss biological applications.

2. HALOGENATED COMPOUNDS

2.1. Carbon Tetrachloride

Perhaps the best known free radical metabolite of a xenobiotic is the trichloromethyl radical ($\cdot CCl_3$) first proposed by Butler (1961) and confirmed by Poyer *et al.* (1980) using [^{13}C]carbon tetrachloride. The evidence for trichloromethyl radical formation and that of related polyhaloalkyl radicals has been reviewed many times (Mason, 1982, 1984; Kalyanaraman, 1982; Janzen *et al.*, 1985a) so all details will not be repeated here.

In the first spin-trapping publication on CCl_4 metabolism, a free radical was reported in microsomal incubations containing NADPH, CCl_4 or $CBrCl_3$, and PBN (Poyer *et al.*, 1978). The radical was identified as the PBN-trichloromethyl radical adduct based on the similarity of its six-line ESR spectrum to that of the radical produced by UV irradiation of a carbon tetrachloride solution of PBN. Poyer *et al.* (1980) reinvestigated this system using [^{13}C]carbon tetrachloride and observed an extra hyperfine coupling from the ^{13}C nucleus ($I = \frac{1}{2}$) resulting in a 12-line ESR spectrum of PBN/$^{13}\cdot CCl_3$ after relatively long incubation times.

Similar results were obtained when microsomes or isolated hepatocytes were incubated for 10 min with $^{13}CCl_4$, PBN, and NADPH either aerobically or anaerobically, and then extracted into chloroform:methanol (Tomasi *et al.*, 1980, 1984; Albano *et al.*, 1982). The PBN/$\cdot CCl_3$ radical adduct has also been observed in extractions of CCl_4-perfused livers from phenobarbital-treated rats (Connor *et al.*, 1986b) and in a reconstituted system containing purified cytochrome P-450, NADPH-cytochrome P-450 reductase, NADPH, CCl_4, and PBN (Noguchi *et al.*, 1982).

The spin-trapping technique was extended to an *in vivo* system when Lai *et al.* (1979) reported the trapping of $^{12}\cdot CCl_3$ after administering CCl_4 and PBN by stomach tube to a rat. Chloroform–methanol extracts of the liver or liver microsomes, but not of nuclear-plasma membrane or mitochondria, contained the PBN/$\cdot CCl_3$ radical adduct. This first *in vivo* experiment was confirmed by Poyer *et al.* (1980) using $^{13}CCl_4$.

Since carbon tetrachloride is known to induce lipid peroxidation, Kalyanaraman *et al.* (1979a) decided to compare the spin adduct from microsomal incubations containing carbon tetrachloride with that from a lipid peroxidation system of microsomes and lipoxygenase. The ESR spectrum of the PBN-microsomal lipid radical adduct from incubations containing lipoxygenase, PBN, and microsomes is very similar to that of the PBN/$\cdot CCl_3$ radical adduct. The preliminary results of Kalyanaraman *et al.* (1979a) with tNB are much clearer in that the spin adduct produced in microsomal incubations containing carbon tetrachloride has the doublet splitting of a dienyl-type fatty acid free radical (L$\cdot$). Further experiments suggest that the spectrum is a composite of NADPH-dependent (enzymatic) and NADPH-independent (nonenzymatic) reactions (Kalyanaraman, 1982). The nonenzymatic reaction is presumably a pseudo-Diels–Alder or ene reaction between the microsomal lipid and tNB which appears to be promoted by the high lipid and tNB concentrations in the CCl_4-microsome phase. In

the work of Poyer *et al.* (1980) with $^{13}CCl_4$ and microsomes, a six-line ESR spectrum, presumably a PBN-carbon-centered lipid dienyl radical adduct, was observed initially. The 12-line PBN/^{13}·CCl_3 radical adduct did not appear until 36 min after incubation. It was proposed that, with increasing incubation time, the ^{13}·CCl_3 radicals react with PBN to give the 12-line spectrum as a result of the depletion of lipid at the site of ·CCl_3 radical formation.

The $^{13}CCl_4$ invariant spectrum (a^N = 13.8 G, a^H = 2.2 G) has been assigned more recently to the LO· radical adduct of PBN while a second $^{13}CCl_4$-invariant spectrum (a^N = 14.4 G, a^H = 3.25 G), found under conditions of low oxygen tension, has been assigned to the carbon-centered L· radical adduct (McCay *et al.*, 1984). The assignment involving oxygen incorporation into the one radical but not the other should be confirmed with $^{17}O_2$. Using deuterated PBN to increase spectral resolution, Janzen *et al.* (1987) have detected two γ-hydrogen couplings from the carbon-centered L· radical. This result suggests that in this system "L·" is of a primary alkyl type (·CH_2—R) and not the dienyl-type free radical previously thought.

Alterations in liver mitochondria as a consequence of CCl_4 exposure have been reported over many years, but the mechanisms responsible for causing this damage are still largely unknown. Isolated rat liver mitochondria incubated under hypoxic conditions with succinate and ADP were found to reduce $^{13}CCl_4$ to ·CCl_3 as demonstrated by PBN/^{13}·CCl_3 formation (Tomasi *et al.*, 1987). The addition of inhibitors of the respiratory chain such as antimycin A and KCN decreased PBN/·CCl_3 formation by only 30%, while rotenone displayed a greater effect if preincubated for 15 min with mitochondria not supplemented with succinate. These findings suggest that the mitochondrial electron-transport chain is responsible for the reduction of CCl_4.

From the foregoing discussion, it can be seen that the production of the ·CCl_3 radical from CCl_4 metabolism is well-established. Using pulse radiolysis, the ·CCl_3 radical has been shown to react rapidly with oxygen to form the Cl_3COO· peroxyl radical (Packer *et al.*, 1978). Since carbon tetrachloride is metabolized to phosgene (Kubic and Anders, 1980) and carbon dioxide (Paul and Rubinstein, 1963), it is reasonable to assume the Cl_3COO· radical is formed in biological systems, but direct ESR evidence is lacking. A unique ESR signal with distinctly different coupling constants from the PBN/·CCl_3 radical adduct was obtained in effluent perfusate from livers perfused with CCl_4 and PBN (Connor *et al.*, 1986b). This new radical was identified as the PBN/·CO_2^- radical adduct based on comparison of the hyperfine coupling constants with those of the authentic PBN/·CO_2^- radical adduct and on its pK_a of 2.85. That the ·CO_2^- radical arises from CCl_4 was proven by perfusing $^{13}CCl_4$ and observing the 12-line PBN/^{13}·CO_2^- ESR spectrum. Detection of PBN/·CO_2^- radical adduct in the effluent perfusate was decreased 3–4-fold by DIDS, an inhibitor of the plasma membrane anion transport system (LaCagnin *et al.*, 1988). The rate of formation of PBN/·CO_2^- was decreased 2–3-fold following inhibition of cytochrome P-450-dependent monooxygenases by metyrapone and was increased about two-fold by induction of cytochrome P-450 by phenobarbital pretreatment. The toxicity of halocarbons in the perfused liver was assessed by measuring the release of lactate dehydrogenase into the effluent perfusate in livers from phenobarbital-treated rats under conditions identical to those employed to detect radical adducts. A good correlation between the concentration of PBN/·CO_2^- and the time to onset of lactate dehydrogenase release following halocarbon infusion was observed (LaCagnin *et al.*, 1988).

Owing to the absence of any mention of the PBN/$\cdot CO_2^-$ radical adduct in previous *in vivo* literature, Connor *et al.* (1986b) concluded that this species moves quickly into the bloodstream and is eventually excreted in the urine. Indeed in this first report of the detection of an adduct of a free radical metabolite in a body fluid of a living whole animal, the PBN/$\cdot CO_2^-$ radical adduct was observed in rat urine collected two hours after the rat was treated intragastrically with PBN and $^{13}CCl_4$.

The PBN/$\cdot CO_2^-$ adduct had not been observed in the previous ESR studies because those experiments involved organic extraction techniques. Since the PBN/$\cdot CO_2^-$ radical is essentially completely ionized at physiological pH and is therefore charged, it will not be extracted into the organic solvent. This $\cdot CO_2^-$ radical apparently does not come from phosgene, formate, or carbon dioxide and is unlikely to result from dechlorination of the PBN/$\cdot CCl_3$ radical adduct. The most likely source of the PBN/$\cdot CO_2^-$ radical adduct was thought to be the trichloromethyl peroxyl radical, $Cl_3COO\cdot$ (Connor *et al.*, 1986b), but the mechanism for the formation of this radical adduct is unknown. In any case, the $\cdot CO_2^-$ radical would react rapidly with oxygen (Adams and Willson, 1969) to form carbon dioxide, the final product of CCl_4 metabolism, and the superoxide radical anion. Recently, the formation of PBN/$\cdot CO_2^-$ by microsomal incubations under vacuum (Janzen *et al.*, 1988), in concord with the results from hypoxic perfused liver (La Cagnin *et al.*, 1988), has excluded any role for molecular oxygen in the formation of PBN/$\cdot CO_2^-$.

In the broadest sense, spin trapping is the addition of a free radical to any double bond to form a more stable radical (Janzen, 1980). If the radical attacks a carbon–carbon double bond, the resulting carbon-centered free radical can abstract a proton to form a diamagnetic product. Mass spectrometry has been used to detect these products or "spin adducts." The addition of the trichloromethyl radical to one of the oleic acids in phosphatidylcholine in a reconstituted system of human cytochrome P-450, NADPH-cytochrome P-450 reductase, and cytochrome b_5 in phospholipid vesicles was detected by identification of 9- and 10-(trichloromethyl)stearate methyl esters by desorption electron-impact mass spectrometry (Trudell *et al.*, 1982).

Mass spectrometry has also been used to study the trichloromethyl radical attack on saturated fatty acids. Cunningham *et al.* (1985) have detected monochlorostearic acid methyl ester in a system containing trichloromethyl free radicals and the saturated fatty acid ester, methyl stearate. In addition, chloroform production was detected. The mechanism was postulated to be an abstraction of a hydrogen from a fully saturated carbon in the fatty acid by the $\cdot CCl_3$ radical. The resulting fatty acid free radical then abstracts a chlorine acid from CCl_4 forming the chlorinated fatty acid and a $\cdot CCl_3$ radical to propagate the reaction. In the same work it was shown that the $\cdot CCl_3$ radical attacks the unsaturated site of methyl oleate to form chloro-trichloromethyl stearate and chloroform.

2.2. Halothane

Various anesthetics were reported by McCay *et al.* (1980) to form spin adducts when metabolized in microsomal-NADPH incubations. Poyer *et al.* (1981) identified the PBN spin adduct with the carbon-centered free radical metabolite of halothane formed in incubations of microsomes, NADPH, and PBN as either PBN/$\cdot CHClCF_3$ or PBN/$\cdot CHBrCF_3$. This same species was extracted from the liver of rats exposed to

halothane by inhalation (Poyer *et al.*, 1981; Plummer *et al.*, 1982; Fujii *et al.*, 1984). Mass spectrometry was used to identify 9- and 10-$CHClCF_3$ stearate methyl ester as products of the addition of the halothane radical to dioleoyl phosphatidylcholine in a reconstituted system of human cytochrome P-450, NADPH-cytochrome P-450 reductase, and cytochrome b_5 in phospholipid vesicles (Trudell *et al.*, 1981).

2.3. Others

Rat liver microsomes or hepatocytes under hypoxic conditions form the PBN/^{13}·CH_2CH_2Br radical adduct by the cytochrome P-450-catalyzed reduction of the fumigant dibromoethane (Tomasi *et al.*, 1983a). Using rat hepatocytes Tomasi *et al.* (1984) demonstrated the formation of PBN adducts involving free radicals produced from chloroform, 1,1,1-trichloroethane under normoxic as well as hypoxic conditions and from 1,2-dibromoethane, 1,1-dichloroethane, 1,2-dichloroethane, and 1,1,2-trichloroethane under hypoxic conditions only.

In spin-trapping experiments with PBN and trihalomethanes, Tomasi *et al.* (1985) have demonstrated that radicals are formed from chloroform, bromoform, iodoform, and bromodichloromethane by isolated rat hepatocytes, liver microsomes, and *in vivo*. The origin of the chloroform-derived radical was proven using [^{13}C]chloroform. The chloroform-derived radical adduct was assigned a structure of PBN/·$CHCl_2$ since the hyperfine splitting constants (a^N = 14.4 G, a^H = 2.37 G) were significantly different from those of PBN/·CCl_3 (a^N = 14 G, a^H = 1.8 G). Further evidence for this structure lies in the fact that the reduction of deuterated chloroform resulted in a decrease in the ESR signal intensity of only 23% rather than the 2–4-fold isotope effect expected if breaking a C—H bond were involved. Bromoform gave rise to a radical adduct with the same coupling constants as chloroform, again suggesting that a halogen–carbon bond is broken in the formation of the haloform-derived radical.

3. LIPID PEROXIDATION

Many types of free radicals have been postulated to form during lipid peroxidation, including L· (the carbon-centered pentadienyl radical), LOO· (the peroxyl free radical resulting from the addition of oxygen to L·), LO· (the alkoxy free radical), and R· (the carbon-centered primary alkyl radical from the β-scission of LO·).

3.1. Linoleic Acid

Lipid peroxidation has long been thought to involve free radical intermediates (Farmer, 1946; Bolland, 1950; Bateman, 1954; Porter *et al.*, 1980). The initiation step is thought to be hydrogen abstraction from the C-11 position of linoleic acid followed by extensive rearrangement of the double bond system to form 1:3 conjugated forms (Mead, 1976). Egmond *et al.* (1973) used [11,11-$^2H_2$]linoleic acid to show, from the observed isotope effects, that the rate-determining step was hydrogen abstraction from C-11.

The first application of spin trapping to a biological problem involved trapping a carbon-centered linoleic acid free radical formed by soybean lipoxygenase with 2-methyl-2-nitrosopropanol (a more water soluble form of tNB) (De Groot *et al.*, 1973).

Since a proton splitting was observed (a^N = 16.0 G, a^H = 2.0 G) the radical must have had the structure

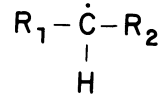

where R_1 and R_2 could not be ascertained. Numerous workers have confirmed this result (Kalyanaraman *et al.*, 1979a; Rosen and Rauckman, 1981a, 1981b; Albano *et al.*, 1982). An identical spectrum was obtained using *cis,cis*-9,12-[11,11,^{2}H]linoleic acid, indicating that the trapped radical is not at C-11 (De Groot *et al.*, 1973; Vliegenthart and Veldink, 1982; Evans *et al.*, 1985).

Since the initial observation, there has been much discussion in the literature about the position of the trapped radical. A detailed discussion of this debate can be found in a review by Mason (1984). A recent paper by Evans *et al.* (1985) reports ESR and ENDOR spectra of the tNB-trapped carbon-centered radicals from the autoxidation of linoleic acid; 11,11-dideuterio-9-*cis*,12-*cis*-linoleic acid; 9,10,12,13-tetradeuterio-9-*cis*,12-*cis*-linoleic acid; and 9,10,11,11,12,13-hexadeuterio-9-*cis*,12-*cis*-linoleic acid. In this work hyperfine couplings were observed and assigned for the protons on carbons 10,11,12,13, and 14 of the linoleic acid in addition to the *t*-butyl protons on the spin trap.

In the linoleic acid species which were deuterated at the C-11 position Evans *et al.* (1985) observed two linoleic acid radical adducts which were separable on HPLC. The first of these was the adduct resulting from the carbon-centered radical at C-9 or C-13 (the usual positions). The second was a new adduct formed from a radical at position C-10 or C-12. Radical production at these positions was explained in terms of hydrogen abstraction from positions C-8 or C-14 with subsequent rearrangement to a radical at position C-10 or C-12. Because of the kinetic isotope effect, hydrogen abstraction at the allylic positions C-8 and C-14 can efficiently compete with deuterium abstraction from the bis-allylic position C-11 in the C-11 deuterated linoleic acid.

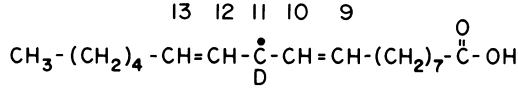

3.2. Methyl Linoleate

An interesting example of carbon-centered pentadienyl free radical formation is in the low temperature ozonation of methyl linoleate in the presence of tNB (Pryor *et al.*, 1981). In this case L· is proposed to form by the decomposition of a methyl linoleate trioxide species. The L· radical can be observed directly in the photolysis of di-*tert*-butyl peroxide and methyl linoleate (Pryor *et al.*, 1981; Bascetta *et al.*, 1982).

3.3. Arachidonic Acid

Prostaglandins are acidic lipids formed from polyunsaturated fatty acids, particularly arachidonic acid. The enzyme prostaglandin synthase which catalyzes the

conversion of arachidonic acid to prostaglandin H_2 contains both cyclooxygenase and hydroperoxidase activities which copurify. The cyclooxygenase component, inhibitable by indomethacin and aspirin, catalyzes the conversion of arachidonic acid to the hydroperoxyendoperoxide, prostaglandin G_2, which is reduced by the hydroperoxidase component to the corresponding alcohol endoperoxide, prostaglandin H_2. Oxidation of xenobiotics occurs during the reduction of prostaglandin G_2 (Eling *et al.*, 1983). Since the mechanism of soybean lipoxygenase is formally similar to that of the prostaglandin fatty acid cyclooxygenase, we tried to spin trap any carbon-centered arachidonic acid free radical formed in the prostaglandin cyclooxygenase-catalyzed conversion of arachidonic acid to prostaglandin G_2 (Mason *et al.*, 1980).

Tritium-labeling studies have shown that the 13-L hydrogen of arachidonic acid is removed in the cyclooxygenation step, because isotopic substitution at this position decreases the rate of prostaglandin formation (Porter, 1980). This is the best evidence for radical formation at C-13. The reaction mechanism for the oxygenation of arachidonic acid by prostaglandin cyclooxygenase involves hydrogen abstraction at C-13 and isomerization of the C-11=C-12 *cis* double bond to a C-12=C-13 *trans* double bond to form a free radical at C-11. The addition of oxygen to this conjugate dienyl radical occurs giving rise to the 11-peroxyl arachidonic acid radical as the first oxygen-containing intermediate in the synthesis of prostaglandin G_2 from arachidonic acid (Nugteren *et al.*, 1966; Hamberg and Samuelsson, 1967).

The ESR spectrum of the spin adduct observed in an incubation mixture containing ram seminal vesicles microsomes (a source of prostaglandin synthase), arachidonic acid, and tNB clearly indicated the nitroxide nitrogen of a carbon-centered radical adduct and the arachidonic acid-derived β-hydrogen (Mason *et al.*, 1980) and was attributed to the trapping of the C-11 and/or C-15 carbon-centered radical. Indomethacin, a classic cyclooxygenase inhibitor, decreased the ESR signal intensity in a concentration-dependent manner. Concomitant with the ESR signal appearance, there was oxygen consumption upon the addition of arachidonic acid to an incubation mixture containing ram seminal vesicle microsomes. This oxygen consumption, which is considered a good index of prostaglandin synthase activity (Egan *et al.*, 1976), was inhibited by indomethacin with a concentration dependence similar to that observed for the arachidonic acid radical adduct.

In order to spectroscopically identify the arachidonic free radical as a particular carbon-centered free radical, specific deuteration is necessary. If arachidonic acid could be specifically labeled with deuterium at C-11 and C-15, a three-line ESR spectrum would presumably be observed because the deuteration would remove the β-hydrogen splitting. Unfortunately, only octadeuterated arachidonic acid, which has all eight vinyl hydrogens of the four double bonds replaced by deuterium, is commercially available. When octadeuterated arachidonic acid was incubated with ram seminal vesicles and tNB, the six-line spectrum collapsed to three lines with the same nitrogen hyperfine coupling (Schreiber *et al.*, 1986a). This demonstrates that tNB does not react with the initial C-13 carbon-centered radical since the resulting adduct would still have a β-hydrogen.

Evidence that the carbon-centered free radical of arachidonic acid is an obligatory intermediate in the formation of prostaglandin G_2 is that tNB is an inhibitor of the bio-oxygenation of arachidonic acid (Mason *et al.*, 1980; Schreiber *et al.*, 1986a). This inhibition implies that the reaction with nitroso compounds is stereospecific and carbon

atom specific as is the reaction with oxygen. Nitrosobenzene (another spin trap) was shown to be a much stronger inhibitor of the bio-oxygenation of arachidonic acid than tNB, which is consistent with the known faster trapping rates of nitrosobenzene for carbon-centered radicals. Proof that the radical is formed by the cyclooxygenase function of the enzyme has recently been provided by Schreiber *et al.* (1986a). In this study the radical was produced in incubations containing tNB, arachidonic acid, and one of four enzyme systems: ram seminal vesicles, which contain both the cyclooxygenase and peroxidase activities of prostaglandin synthase; the purified holoenzyme, which also contains both activities; the apoenzyme reconstituted with hematin, which contains both activities; and the apoenzyme reconstituted with Mn^{2+} protoporphyrin IX, which contains only the cyclooxygenase activity. In order to explain an observed time lag between the metabolic activity of the enzyme (measured by oxygen uptake) and the appearance of ESR signals, it was proposed that the arachidonic acid radical reacts with the tNB spin trap to form an enzyme-arachidonic acid radical adduct complex. The spin adduct is then reduced by the enzyme to the hydroxylamine and the complex dissociates. The arachidonic acid-hydroxylamine adduct is then oxidized by either oxygen or tNB to yield the tNB-arachidonic acid radical adduct which accumulates and is detected by ESR. If the arachidonic acid-hydroxylamine adduct is oxidized by tNB, the one-electron reduction product of the spin trap, the tNB-hydrogen atom adduct, should also be observed. This four-line spectrum is a small component of the total ESR spectrum observed in this work (Schreiber *et al.*, 1986a).

The well-resolved hyperfine spectrum of the enzymatically formed tNB-arachidonic acid radical adduct is indicative of a small molecule rotating freely in solution. In contrast, if the arachidonic acid adduct were bound to the enzyme, the ESR spectrum would be broadened and resemble those of nitroxide-labeled fatty acids bound to enzymes or membranes. The inhibition of oxygen consumption implies that the spin trap reacts with the radical on the surface of the enzyme; however, the ESR spectrum of the tNB-arachidonic acid radical adduct is that of a nitroxide which is free in solution and dissociated from the enzyme. For a variety of reasons, free radicals bound to the enzyme will result in ESR spectra with poor signal-to-noise ratios and have not been detected.

3.4. Lipid Peroxyl and Alkoxy Radicals

The formation of peroxyl and alkoxy free radicals, which serve as chain carriers, in the oxidation of polyunsaturated fatty acids has been the focus of much attention in biological spin trapping for a number of years. It is well known that carbon-centered free radicals react with oxygen to form peroxyl radicals

$$L\cdot + O_2 \rightarrow LOO\cdot$$

which have been implicated in a variety of biological processes such as endogenous (Wittig, 1980) and chemically-induced lipid peroxidation (Bus and Gibson, 1979; Recknagel *et al.*, 1977) and the decomposition of lipid hydroperoxides by hemoproteins (Kalyanaraman *et al.*, 1983; Schreiber *et al.*, 1986b). The formation of prostaglandin H_2 by prostaglandin cyclooxygenase (Porter, 1980) and the formation of fatty acid

hydroperoxides by lipoxygenases (De Groot *et al.*, 1975; Vliegenthart and Veldink, 1982) are also believed to proceed through peroxyl radical intermediates.

The PBN-peroxyl radical adduct is generally not thought to be stable enough to be observed at room temperature (Janzen *et al.*, 1978; Howard and Tait, 1978) though it has been reported in benzene at room temperature (Yamada *et al.*, 1984). Peroxyl radicals are usually derived from carbon-centered free radicals leading to the serious problem of differentiating between PBN adducts of L· and LOO· since PBN-OOR adducts can have hyperfine coupling constants similar to the corresponding carbon-centered radical. For example, the PBN/·CCl_3 adduct with coupling constants a^N = 13.5 G and a_β^H = 1.5 G is indistinguishable from the PBN/·$OOCCl_3$ adduct with coupling constants a^N = 13.5 G and a_β^H = 1.6 G (Symons *et al.*, 1982).

The best solution to this problem is to use isotopic substitution. Howard and Tait (1978) trapped the *tert*-butylperoxyl radical with PBN at low temperatures by photolysis of di-*tert*-butyl ketone in $^{17}O_2$-saturated solvents. The resulting PBN-*tert*-butylperoxyl radical adduct thus formed is characterized by an ^{17}O hyperfine coupling constant of 2.9 G. Above −20 °C, this radical adduct decomposed to the PBN-*tert*-butalkoxy adduct with an ^{17}O coupling constant of 5.05 G.

Yamada *et al.* (1984) were able to trap and distinguish LOO·, LO·, and L· radicals with PBN and methyl-*N*-duryl nitrone (another spin trap) in benzene. The peroxyl radical was generated by an alkoxy radical (from the thermal decomposition of di-*tert*-butylperoxy oxalate) hydrogen abstraction from the hydroperoxide of methyl linoleate. The alkoxy radical adduct was formed by the decomposition of the methyl linoleate hydroperoxide by cobaltous ion. The differences in the coupling constants of the PBN adducts were significant (PBN-OOL, a^N = 13.44 G, a_β^H = 1.63 G; PBN-OL, a^N = 14.22 G, a_β^H = 2.10 G; PBN-L, a^N = 15.03 G, a_β^H = 2.83 G).

The PBN-alkoxy spin adduct has also been reported in the low-temperature ozonation of methyl linoleate (Pryor *et al.*, 1981). The assignment of this species is supported by the trapping of the alkoxy radical with DMPO. The question of whether the PBN-alkoxy adducts could be distinguished from PBN-carbon-centered radical adducts could be answered using [$^{17}O_3$]ozone but the DMPO results make the possibility of multiple PBN adducts a moot question.

The trapping of LOO· by 4-POBN has been reported in the lipoxygenase-catalyzed oxygenation of linoleic acid (Rosen and Rauckman, 1981a, b) and the NADPH-supported hepatic microsomal lipid peroxidation (Rosen and Rauckman, 1981a, b) which is stimulated by CCl_4 (Rosen and Rauckman, 1982) or cocaine-derived nitroxide (Rosen *et al.*, 1982a). The hyperfine coupling constants observed in these experiments (a^N = 15.8 G and a_β^H = 2.6 G) are what one would expect for 4-POBN-carbon-centered radical adducts (Augusto *et al.*, 1982a; Ortiz de Montellano *et al.*, 1983). In fact it has been shown by $^{17}O_2$ experiments that the radicals trapped by Rosen and Rauckman (1981a, b) must be carbon-centered (L·) since no ^{17}O hyperfine coupling is observed (Connor *et al.*, 1986*a*).

4. HEMOPROTEIN–ORGANIC HYDROPEROXIDES

Both hematin and hemoproteins react with organic hydroperoxides making the role of the apoprotein in these reactions unclear. Three different mechanisms, each

predicting peroxyl radical formation in both the presence and absence of oxygen, have been proposed. In the first mechanism, hematin catalyzes the decomposition of hydroperoxides (Rosen and Rauckman, 1980) through the same redox reactions reported for transition metal ions (Pryor, 1973):

$$\text{Hematin}(Fe^{3+}) + \text{ROOH} \rightarrow \text{hematin}(Fe^{2+}) + \text{ROO}\cdot + H^+$$

$$\text{Hematin}(Fe^{2+}) + \text{ROOH} \rightarrow \text{hematin}(Fe^{3+}) + \text{RO}\cdot + OH^-$$

The second reaction is essentially the classical Fenton reaction with hydrogen peroxide replaced by the organic hydroperoxide. Tappel (1961) has proposed an alternative scheme whereby the hydroperoxides are broken down by hematin or cytochrome c in a reaction in which no change in the valency of iron occurs, but which involves instead the homolytic scission of the oxygen-oxygen bond of the hydroperoxide molecule to form the alkoxy radical and hematin-bound hydroxyl radical (Cadenas *et al.*, 1980):

$$\text{Hematin}(Fe^{3+}) + \text{ROOH} \rightarrow \text{hematin}(Fe^{3+})\text{—OH}\cdot + \text{RO}\cdot$$

$$\text{Hematin}(Fe^{3+})\text{—OH}\cdot + \text{ROOH} \rightarrow \text{hematin}(Fe^{3+}) + \text{ROO}\cdot + H_2O$$

Overall the net result of these two mechanisms is the same:

$$2\text{ROOH} \rightarrow \text{RO}\cdot + \text{ROO}\cdot + H_2O$$

The third mechanism is suggested by the report of the oxidation of deuteroferriheme by hydrogen peroxide or peroxobenzoic acids to a species analogous to the compound I of peroxidases and catalase (Jones *et al.*, 1977). If this species oxidizes organic hydroperoxides, as catalase compound I is thought to do (Chance, 1952), then the peroxyl radical will be formed:

$$\text{Catalase compound I} + \text{ROOH} \rightarrow \text{ROO}\cdot + \text{catalase compound II}$$

The *tert*-butylperoxyl and cumylperoxyl radicals have been observed directly in a hematin-hydroperoxide system by ESR (Kalyanaraman *et al.*, 1983) and characterized by their distinctive g values ($g = 2.014$).

Spin-trapping evidence for peroxyl free radical formation is also convincing. The trapping of cumylperoxyl radical by DMPO ($a^N = 14.5$ G, $a_\beta^H = 10.75$ G, $a_\gamma^H = 1.75$ G) in a hematin-cumene hydroperoxide system at pH 3.0 has been reported (Rosen and Rauckman, 1980). This work has been criticized because only a weak spectrum was observed at a pH where nitrones readily undergo acid-catalyzed hydrolysis (Griffin, 1982) and hematin is very insoluble.

In spite of these criticisms, the assignment of this spectrum to the DMPO-cumylperoxyl radical adduct appears sound. The assignment is supported by the direct detection of a peroxyl free radical in this system (Kalyanaraman *et al.*, 1983). In addition, in a hematin-ethyl hydroperoxide system at pH 7.5 the DMPO-ethylperoxyl radical adduct ($a^N = 14.6$ G, $a_\beta^H = 11.0$ G, $a_\gamma^H = 1.25$ G) is observed (Kalyanaraman *et al.*, 1983). Both the DMPO-cumylperoxyl and DMPO-ethylperoxyl radical adducts have spectral parameters very similar to the structurally related DMPO-hydroperoxyl (superoxide) radical adduct ($a^N = 14.3$ G, $a_\beta^H = 11.7$ G, $a_\gamma^H = 1.25$ G) (Harbour *et al.*, 1974; Perez-Reyes *et al.*, 1980) and distinct from the *tert*-butylalkoxy adduct ($a^N = 14.84$ G, $a_\beta^H = 16.03$ G) (Janzen *et al.*, 1982).

DMPO-ethylperoxyl radical adduct formation is totally unaffected by superoxide dismutase (Kalyanaraman *et al.*, 1983), in contrast to the complete inhibition of DMPO-hydroperoxyl(superoxide) radical adduct formation. Spin trapping with DMPO in conjunction with the use of superoxide dismutase can detect and identify the peroxyl radical resulting from the one-electron oxidation of hydroperoxides.

Evidence for alkoxy radical formation in the hematin- or hemoprotein-catalyzed decomposition of hydroperoxides is less direct. The methyl radical formed from the β-scission of the cumylalkoxy radicals

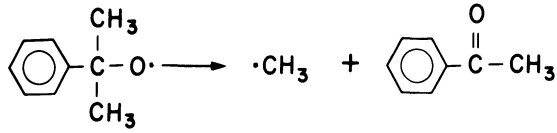

has been spin trapped with tNB in the cumene hydroperoxide-metmyoglobin system (Griffin and Ting, 1978). Acetophenone was also formed, which is consistent with the alkoxyl radical intermediate (Griffin, 1982).

Investigations of the cumene hydroperoxide-metmyoglobin and the cumene hydroperoxide-rat liver microsome systems with the spin-trap nitrosobenzene have led to indirect evidence for the cumylalkoxy radical (Griffin, 1980). A well-resolved ESR spectrum with no evidence of hyperfine coupling from the trapped nuclei was observed. This spectrum is consistent with the trapping of either a tertiary carbon-centered cumyl radical or an oxygen-centered cumyloxy radical. The spectrum was originally assigned to the nitrosobenzene-cumyloxy spin adduct (Griffin, 1981) but was later reassigned to the nitrosobenzene-cumyl radical adduct (Griffin and Ramirez, 1981) formed via the decomposition of the cumyloxy adduct. Terabe and Konaka (1972) were the first to conclude that the ESR spectrum observed with nitrosobenzene as the spin trap in a cumylalkoxy-generating system is the cumyl spin adduct. Nevertheless, this radical adduct can be considered to provide indirect evidence for the formation of the cumylalkoxy radical

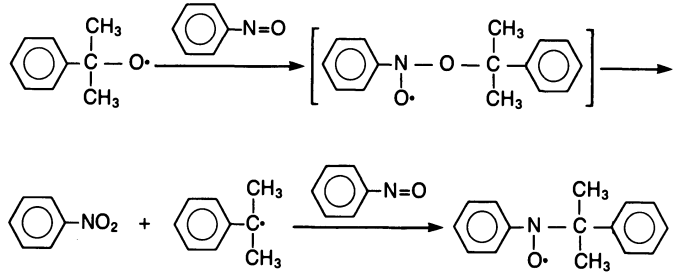

Metyrapone, an inhibitor of cytochrome P-450, decreased the concentration of cumyl radical adduct detected with liver microsomes, cumene hydroperoxide, and nitrosobenzene by a factor of two but had no effect on the concentration detected with metmyoglobin, cumene hydroperoxide, and nitrosobenzene (Griffin, 1980). On the other hand, cyanide inhibited the formation of the cumyl radical adduct by metmyoglobin much more than it inhibited the microsomal system.

The hematin-cumene hydroperoxide system gave rise to a six-line spectrum (a^N = 16 G, a_β^H = 2.8 G) when 4-POBN was used as a spin trap (Rosen *et al.*, 1980). The assignment of this spectrum to the 4-POBN-cumylperoxyl radical adduct was made on chemical, rather than spectroscopic, grounds. The trapping of either methyl or cumyl carbon-centered free radicals [assigned unambiguously using nitroso spin traps in a hemoprotein-cumene hydroperoxide system (Griffin and Ting, 1978; Griffin and Ramirez, 1981)] by 4-POBN will give a six-line spectrum similar to that reported for the cumylperoxyl radical adduct reported by Rosen *et al.* (1980). These possibilities, as well as other carbon-centered and alkoxy radical adducts, many of which may give similar six-line spectra when trapped with 4-POBN, must be excluded before the assignment of the observed 4-POBN adduct to a peroxyl adduct can be made. In addition, the assignment of the spectrum to the 4-POBN-cumylperoxyl radical adduct must be questioned since the peroxyl adduct is probably the most unstable of the possible PBN adducts (Niki *et al.*, 1983), and PBN is a congener of 4-POBN. Similar difficulties with the assignment of PBN adducts have been overcome by the preparation of ^{17}O-enriched peroxyl and alkoxy adducts (Howard and Tait, 1978).

When DMPO is used as a spin trap in the hematin-cumene hydroperoxide system no radical adduct is trapped but instead the DMPO is oxidized to DMPOX, which has a ketone group conjugated to the nitroxide (Floyd and Soong, 1977) giving coupling constants of a^N = 7.1 G and a_γ^H = 4.2 (2H) G.

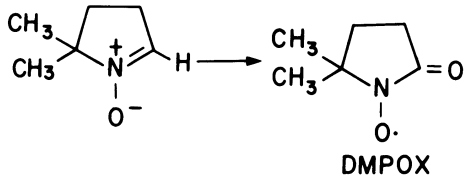

DMPOX

The source of the oxygen in the DMPOX radical is not known but molecular oxygen is required for its formation. If the carcinogen 2-acetylaminofluorene is added, no effect on the DMPOX spectrum is found. On the other hand, if the more active carcinogens 2-nitrosofluorene or *N*-hydroxy-2-acetylaminofluorene are added, the DMPOX signal intensity is decreased indicating a competition for active oxidants in this system. In these experiments, no primary radicals were trapped by DMPO even though they are assumed to be formed. In this system the probability of DMPO being oxidized is much higher than is the probability of trapping a primary radical. This can be explained by the differences in the rates of formation and decay of the trapped species and the rate of oxidation of DMPO and the stability of the product DMPOX (Floyd and Soong, 1977).

DMPO has been used to trap *t*-butyloxy radicals formed in oxyhemoglobin-containing suspensions of erythrocytes in the presence of *t*-butylhydroperoxide (a^N = 14.8 G, a_β^H = 16.0 G) while the oxidized species DMPOX (a^N = 7.2 G, a_γ^H = 4.1 (2H) G) was formed in methemoglobin-containing suspensions of erythrocytes (Thornalley *et al.*, 1983). The carbon monoxyhemoglobin containing system produced both the DMPO/·$OC(CH_3)_3$ adduct and DMPOX, though much more slowly than the hemoglobin system. Free radical production in intact cell systems was slower than that in hemoglobin solutions, indicating that membrane transport of *t*-butyl hydroperoxide may be a rate-determining step since DMPO is rapidly transported into red blood cells.

The *t*-butyloxy radicals are relatively rapidly scavenged by DMPO [rate constant, $4 \times 10^8\ M^{-1}\ s^{-1}$ at 25 °C (Janzen and Evans, 1973)] though 100 mM DMPO reduced the rate of oxyhemoglobin oxidation by only about 30%. This failure of a 1000-fold excess of DMPO over oxyhemoglobin and *t*-butyl hydroperoxide to stop the hemoglobin oxidation suggests that *t*-butyloxy radicals may not be the major oxidants of oxyhemoglobin. Thornalley *et al.* (1983) suggest that the oxyhemoglobin may be oxidized in the free radical forming process.

$$Hb(Fe^{II}\text{-}O_2) + t\text{-}BuOOH \rightarrow Hb(Fe^{III}) + O_2 + t\text{-}BuO\cdot + OH^-$$

Cumene and *t*-butyl hydroperoxide are tumor promoters in skin, and this activity is presumed to be mediated through the activation of these hydroperoxides to free radicals. DMPO/*t*-BuO· and DMPO/R· were detected shortly after the addition of *t*-butylhydroperoxide to the target cell, the murine basel keratinocyte (Taffe *et al.*, 1987). Only DMPO/R· was detected with cumene hydroperoxide. Spin trapping with tNB identified R· as the methyl radical. The radical generating capacity of subcellular fractions of these epidermal cells was limited to the 105,000 × *g* supernatant fraction and was heat labile.

5. SULFUR-CENTERED RADICALS

5.1. Sulfur Dioxide, Bisulfite, Sulfite, and Sulfate

Sulfur dioxide is a major air pollutant, while the ionized forms, bisulfite and sulfite, are found as preservatives in food and wine. Sulfur dioxide is hydrated rapidly to form the weak acid bisulfite

$$SO_2 + H_2O \rightleftarrows HSO_3^- + H^+$$

which dissociates according to the reaction

$$HSO_3^- + H_2O \rightleftarrows H_3^+O + SO_3^{2-}$$

with an equilibrium constant 1.20×10^{-7} M (Petering, 1977). At pH values above 7, the equilibrium lies to the right and sulfite predominates. These reactions are fundamentally responsible for acid rain. The air oxidation of SO_2 to SO_3 forms an acid anhydride of a stronger acid. The sulfur atoms of SO_2, HSO_3^-, and SO_3^{2-} all have a formal oxidation state of +4. The precise species involved in a given reaction is generally unknown, resulting in an ambiguity indicated by the terminology (bi)sulfite. The overall metabolism of (bi)sulfite is known to involve oxidation to sulfate and eventual excretion of the sulfate in the urine. Most of the oxidation probably occurs as a result of the action of the mitochondrial enzyme sulfite oxidase, which oxidizes (bi)sulfite to sulfate in a direct two-electron oxidation (Rajagopalan and Johnson, 1977).

The autoxidation of (bi)sulfite involves the one-electron oxidation of (bi)sulfite to the sulfur trioxide radical anion (Reed *et al.*, 1986). (Bi)sulfite-derived free radicals formed by autoxidation are involved in a number of biologically important reactions:

the oxidation of diphosphopyridine nucleotide (Klebanoff, 1961) and methionine (Yang, 1970), the destruction of tryptophan (Yang, 1973) and β-carotene (Peiser and Yang, 1979), the addition of bisulfite across the double bonds of unsaturated fatty acids (Southerland *et al.*, 1982) and various nucleotides and nucleic acids (Hayatsu, 1976), the peroxidation of fatty acids (Lizada and Yang, 1981) and rat liver homogenate (Inouye *et al.*, 1978), the cleavage of DNA (Hayatsu and Miller, 1972), the inactivation of bacteriophages by damaging their protein coat (Kudo *et al.*, 1978), and the epoxidation of (±)-7,8-dihydroxy-7,8-dihydrobenzo(a)pyrene (Reed *et al.*, 1986).

Since (bi)sulfite autoxidation is not thought to occur *in vivo*, the free radical reactions of (bi)sulfite have a highly speculative role in (bi)sulfite toxicity (Gunnison, 1981). The oxidation of (bi)sulfite by peroxidase enzymes, which yields the same radical produced by autoxidation, raises the possibility of the free radical metabolism of (bi)sulfite *in vivo*.

The direct observation of $\cdot SO_3^-$ radicals (Mottley *et al.*, 1982a) and the spin trapping with DMPO of these same radicals in a horseradish peroxidase/hydrogen peroxide system and in a guinea pig lung microsome system (Mottley *et al.*, 1982b) has been reviewed extensively (Mason, 1984). The details given in that review will not be repeated here, but recent work along the same lines will be described.

The metal-catalyzed autoxidation of the (bi)sulfite anion, which has been studied for decades, is an oxygen-consuming reaction. The exact mechanism for the autoxidation has been a subject of much discussion in the scientific literature. The initiating reaction is a one-electron oxidation yielding the sulfur trioxide radical anion, a predominantly sulfur-centered radical (Chantry *et al.*, 1962), which reacts with molecular oxygen. Superoxide, which has been implicated in the mechanism, initiates (bi)sulfite oxidation (McCord and Fridovich, 1968, 1969), but is not a chain propagator (McCord and Fridovich, 1968; Hayon *et al.*, 1972), implying superoxide is not formed by reactions of the sulfur trioxide anion radical. Huie and Neta (1985) have presented a kinetic argument that the reaction product of $\cdot SO_3^-$ with oxygen is a peroxyl free radical.

$$\cdot SO_3^- + O_2 \rightarrow {}^-O_3SOO\cdot$$

Chemical evidence for the formation of the peroxyl radical during (bi)sulfite autoxidation was obtained using (±)-*trans*-7,8-dihydroxy-7,8-dihydrobenzo(a)pyrene (BP-7,8-diol) as a specific trap (Reed *et al.*, 1986). BP-7,8-diol is stereoselectively epoxidized to form (±)-7*r*,8*t*-dihydroxy-9*t*,10*t*-epoxy-7,8,9,10-tetrahydrobenzo(a)pyrene (*anti*-BPDE) by either peroxyl radicals (Dix and Marnett, 1981, 1983; Dix *et al.*, 1985; Reed *et al.*, 1984) or peracids (Yagi *et al.*, 1975; McCaustland and Engel, 1975; Yagi *et al.*, 1977). The autoxidation of (bi)sulfite resulted in the formation of the $\cdot SO_3^-$ radical, which was spin trapped with DMPO, and in rapid oxygen consumption (Reed *et al.*, 1986). The inclusion of BP-7,8-diol in the autoxidation system did not affect oxygen consumption, but HPLC analysis of organic extracts demonstrated extensive consumption of BP-7,8-diol and the production of BP tetrols with an approximately 6:1 ratio of *anti*- to *syn*-diolepoxides providing positive evidence for the production of the peroxyl radical ${}^-O_3SOO\cdot$. Two modifiers of (bi)sulfite autoxidation, the metal ion chelator diethylenetriaminepentaacetic acid and the phenolic antioxidant butylated hydroxyanisole, were used to prove the role of (bi)sulfite autoxidation in the BP-7,8-diol

consumption. The peracid, peroxomonosulfate, also epoxidized BP-7,8-diol, though much more slowly than did (bi)sulfite.

The next step in the mechanism involves the formation of the sulfate anion radical from the peroxyl radical (Hayon *et al.*, 1972; Neta and Huie, 1985). Definitive proof of the existence of this radical in (bi)sulfite oxidation came through spin trapping with DMPO (Mottley and Mason, 1988). In this work the initiation step was an enzymatic oxidation by horseradish peroxidase and hydrogen peroxide rather than autoxidation, but the rest of the mechanism is the same. The sulfur trioxide anion radical was trapped initially at high concentrations of DMPO (270 mM). That this radical was sulfur-centered was proven using ^{33}S-labeled (bi)sulfite, resulting in ^{33}S hyperfine structure observed in the ESR spectrum ($a^N = 14.7$ G, $a_\beta^H = 16.0$ G, $a_\beta^{^{33}S} = 11.5$ G). In order to trap possible secondary radicals, $\cdot OOSO_3^-$ and $S\dot{O}_4^-$, the concentration of DMPO was decreased so that not all the $\cdot SO_3^-$ radical would be trapped, but would react further. Using a DMPO concentration of 3 mM the ESR spectrum consisted of a superposition of the four-line DMPO/·OH radical adduct ($a^N = a_\beta^H = 15.0$ G), the DMPO/$\cdot SO_3^-$ radical adduct ($a^N = 14.7$ G, $a_\beta^H = 16.0$ G), and the DMPO/$S\dot{O}_4^-$ radical adduct ($a^N = 13.8$ G, $a_\beta^H = 10.1$ G, $a_\gamma^H = 1.34$ G, $a_\gamma^H = 0.8$ G). The assignment of the DMPO/$S\dot{O}_4^-$ radical adduct was made by comparison to literature coupling constants reported by Harbour and Hair (1979) for this radical formed from peroxysulfate. Oxygen was required for the formation of both the hydroxyl and sulfate radical adducts. The DMPO-hydroxyl radical adduct formation is probably the result of the oxidation of the spin trap by the sulfate radical anion forming a DMPO cation radical, which subsequently reacts with hydroxide (Janzen and Coulter, 1984). Adding ethanol or sodium formate, compounds which react with the sulfate radical anion, resulted in a decrease in the DMPO-sulfate radical adduct intensity and the concomitant appearance of the carbon-centered hydroxyethyl radical adduct ($a^N = 15.8$ G, $a_\beta^H = 22.9$ G) or carbon dioxide anion radical adduct ($a^N = 15.8$ G, $a_\beta^H = 19.1$ G), respectively. The $S\dot{O}_2^-$ radical is not trapped by DMPO (Mottley *et al.*, 1982b) or nitroso spin traps contrary to previous reports (Stolze *et al.*, 1988).

5.2. Thiols

Thiol-containing compounds are important in many biochemical and pharmacological reactions: the structural role of disulfide bonds in proteins, the effects and side effects of thiol-containing drugs, and the protective effect of reduced cellular glutathione. In general, the reductive activity of thiols is considered beneficial: cysteine and cysteamine are radioprotectants (Jocelyn, 1972; Bird, 1980), cysteamine and *N*-acetylcysteine are used as antidotes in acetaminophen overdose (Prescott *et al.*, 1976; Gerber *et al.*, 1977) and glutathione is a major cellular defense against reactive species in the body. On the other hand, the ability to reduce reactive species implies a susceptibility to oxidation which may produce potentially toxic sulfur-centered free radicals and other reactive species (Mason, 1984).

5.2.1. Cysteine

The oxidation of cysteine by metal ions has been well studied. Among the stable products are L-cystine, L-cysteine sulfinic acid, and cysteine sulfonic acid (Jocelyn,

1972; Saez *et al.*, 1982). The formation of the cysteinyl radical during autoxidation was proven by Saez *et al.* (1982) when the radical was trapped with DMPO ($a^N = 15.3$ G, $a_\beta^H = 17.2$ G) and the adduct was positively identified using mass spectrometry and NMR. The same DMPO-cysteinyl radical adduct ($a^N = 15.3$ G, $a_\beta^H = 17.0$ G) was formed enzymatically in a system containing horseradish peroxidase, hydrogen peroxide, and cysteine (Harman *et al.*, 1984). Under aerobic conditions no exogenous hydrogen peroxide was necessary, implying that peroxide(s) is generated as a consequence of the cysteine oxidation. The rate constant for trapping the cysteinyl radical with DMPO is 2.1×10^8 M^{-1} s^{-1} (Davies *et al.*, 1987).

Since the addition of molecular oxygen or hydrogen peroxide to the cysteinyl radical eventually leads to cysteine sulfinic and cysteine sulfonic acids (Saez, 1982; Schafer *et al.*, 1978; Gilbert *et al.*, 1975) and since cysteine sulfinic acid is a metabolite of cysteine oxidation found in human urine (Cederblad, 1980), the oxidation of this compound by horseradish peroxidase was investigated using spin trapping with tNB (Harman *et al.*, 1984). In this case the initial ESR spectrum was a three-line signal ($a^N = 12.7$ G) which was assigned to the tNB/$\cdot SO_2CH_2CH(NH_3)COO^-$ radical adduct based on the magnitude of the nitrogen hyperfine splitting constant. After 12 min, this species disappeared and was replaced by a different three-line signal ($a^N = 14.8$ G) previously assigned (Chignell *et al.*, 1980) to the tNB/$\cdot SO_3^-$ radical adduct.

The fragmentation of the cysteine sulfonyl radical should result in equimolar concentrations of sulfur dioxide and the carbon-centered alanine-derived radical (Gilbert *et al.*, 1975).

$$O_2\dot{S}CH_2CH(NH_3)COO^- \rightarrow SO_2 + \cdot CH_2CH(NH_3)COO^-$$

The horseradish peroxidase/hydrogen peroxide system then oxidizes the aqueous sulfur dioxide (sulfite) to the sulfur trioxide anion radical which can be detected by either direct ESR (Mottley *et al.*, 1982a) or by spin trapping (Mottley *et al.*, 1982b). Since the sulfur trioxide radical was trapped as a secondary species coincident with the disappearance of the cysteine sulfonyl adduct signal, the alanine-derived radical was also expected to be present. The tNB-alanine spin adduct signal ($a^N = 16.3$ G, $a_\beta^H = 16.7$ G, $a_\beta^H = 10.9$ G, and $a_\gamma^H = 0.45$ G) was observed with high concentrations of cysteine sulfinic acid, horseradish peroxidase, and hydrogen peroxide. These splitting constants are in agreement with those previously reported for the spectrum obtained by the irradiation of alanine in solution (Moriya *et al.*, 1980).

5.2.2. Glutathione

The ubiquitous thiol glutathione is involved in the protection of cells against reactive endo- and xeno-biotics. This tripeptide detoxifies electrophilic species by forming glutathione conjugates which are then excreted from the cell (Larsson, 1983). The involvement of free radicals in this process has been postulated since the free radical metabolites of many drugs including chlorpromazine (Ohnishi *et al.*, 1969), aminopyrine (Moldeus *et al.*, 1983; Eling *et al.*, 1985), and acetaminophen (Ross *et al.*, 1984) and some toxic chemicals such as 4-hydroxyaminoquinoline-1-oxide (Hozumi *et al.*, 1967), *p*-phenetidine (Ross *et al.*, 1985b, 1985c), and dimethylaniline (Moldeus *et al.*, 1983) all oxidize glutathione to its thiyl free radical.

The oxidation of glutathione by horseradish peroxidase has been shown to form a thiyl free radical using spin-trapping techniques. When DMPO was used as the spin trap in a system containing horseradish peroxidase, hydrogen peroxide, and glutathione a four-line ESR signal was observed ($a^N = 15.4$ G, $a_\beta^H = 16.2$ G) which could be assigned to the DMPO-glutathione thiyl radical adduct (Harman *et al.*, 1986). It was proposed that the glutathione thiyl radical formation in this system follows the classic one-electron oxidation pathway of peroxidase substrates with compound I and II enzyme intermediates. In contrast to the horseradish peroxidase oxidation of glutathione, glutathione peroxidase forms glutathione disulfide without forming a thiyl free radical intermediate. No radical was trapped by DMPO in the glutathione peroxidase system (Harman *et al.*, 1986).

Glutathione plays an important role in the metabolism of arachidonic acid to prostaglandins since it is a cofactor of prostaglandin E isomerase, which converts prostaglandin endoperoxides to PGE (Miyamoto *et al.*, 1974). Glutathione has not been generally recognized as a cofactor for the hydroperoxidase during prostaglandin formation, though oxidation of glutathione during prostaglandin formation from fatty acids has been reported (Nugteren *et al.*, 1966; Yoshimoto *et al.*, 1970). Recent spin-trapping experiments with DMPO prove that glutathione does, in fact, serve as a reducing cofactor for the prostaglandin hydroperoxidase and is oxidized to its thiyl free radical metabolite (Eling *et al.*, 1986). Since glutathione is present in millimolar concentrations in most cells, it may function as an endogenous cofactor for the hydroperoxidase.

Glutathione has been used as a spin trap of sorts by allowing glutathione to be oxidized by primary radicals formed during the oxidation of various xenobiotics. This forms the glutathione thiyl free radical, which can then be trapped with DMPO. This procedure has been used in the peroxidase-catalyzed metabolism of acetaminophen (Ross *et al.*, 1984) and *p*-phenetidine (Ross *et al.*, 1985b, 1985c), and in ram seminal vesicle microsomes or intact mouse epidermal cells (both sources of prostaglandin hydroperoxidase) incubated with phenol (Schreiber *et al.*, 1989). This cellular system provided direct evidence that free radicals metabolite formation by the prostaglandin H synthase occurs in cells.

The glutathione thiyl radical adduct of DMPO has also been detected as a result of the reaction of reduced glutathione with superoxide anion radical generated by the xanthine oxidase-catalyzed oxidation of xanthine (Ross *et al.*, 1985a). The hydroxyl radical, which can be formed through the iron-catalyzed reaction between superoxide anion radical and hydrogen peroxide, was shown not to be involved in the formation of oxidized glutathione on the basis of scavenging experiments.

5.2.3. Other

Lactoperoxidase has been used to initiate the oxidation of several thiol compounds of pharmacological significance (Mottley *et al.*, 1987). ESR and oxygen uptake studies confirm that the thiols cysteine, cysteamine, penicillamine, *N*-acetylcysteine, glutathione, and captopril all produce thiol free radicals (RS·) when incubated with lactoperoxidase and hydrogen peroxide. Penicillamine and cysteine do not require exogenous hydrogen peroxide. The hyperfine splitting constants for the DMPO-thiyl radical adducts were as follows: cysteamine, $a^N = 15.2$ G, $a_\beta^H = 17.0$ G, $a_\gamma^H = 0.72$ G;

N-acetylcysteine, $a^N = 15.1$ G, $a_\beta^H = 16.7$ G, $a_\gamma^H = 0.48$ G; penicillamine, $a^N = 15.3$ G, $a_\beta^H = 20.0$ G; captopril, $a^N = 15.4$ G, $a_\beta^H = 16.0$ G; cysteine, $a^N = 15.1$ G, $a_\beta^H = 17.4$ G; glutathione, $a^N = 15.1$ G, $a_\beta^H = 17.0$ G, $a_\gamma^H = 0.64$ G.

6. PYRIDINYL RADICALS

The reduction of enzymes by NAD(P)H is generally accepted to proceed through a formal hydride transfer, though the formation of an intermediate pyridinyl radical NAD(P)· is a possibility (Kosower, 1976). In exceptional cases, NADH bound to lactate dehydrogenase or glyceraldehyde-3-phosphate dehydrogenase is oxidized to enzyme-bound NAD· by either $\dot{O}_2^-$ or $H\dot{O}_2$ (Chan and Bielski, 1974, 1980).

$$\cdot O_2^-(HO_2\cdot) + \text{E-NADH} \rightarrow \text{E-NAD}\cdot + H_2O_2$$

A chain reaction results when the NAD· reacts with oxygen to form NAD^+ and superoxide.

The destruction of cytochrome P-450 by several 4-alkyl-substituted 1,4-dihydropyridine compounds has been studied by Augusto *et al.* (1982a). In these cases the 4-alkyl group can be transferred to a nitrogen of the heme of the cytochrome P-450. The spin-trap 4-POBN was used to trap the ethyl alkyl group proposed to form via the decomposition of a pyridine cation radical, which closely resembles NAD(P)·.

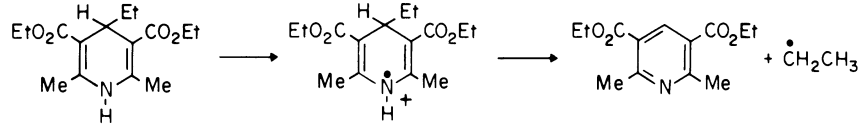

Formation of the resulting radical adduct was found to be dependent on NADPH and microsomes and was inhibited by carbon monoxide. In contrast to most cytochrome P-450-dependent reactions, catalase inhibited the formation of the radical adduct and NADPH could be replaced by hydrogen peroxide. For these dihydropyridine substrates, cytochrome P-450 appears to function as a one-electron oxidant similar to a peroxidase.

7. HYDRAZINES

Phenylhydrazine is typical of a wide range of drugs that react with oxyhemoglobin via a redox mechanism in which the heme-bound oxygen is reduced to superoxide and hydrogen peroxide while both the hemoglobin and drug are oxidized. The superoxide is a chain propagator that oxidizes phenylhydrazine (Misra and Fridovich, 1976):

$$\dot{O}_2^- + H^+ + \text{Ph—NH—NH}_2 \rightarrow H_2O_2 + \text{Ph—}\dot{\text{N}}\text{—NH}_2$$

The superoxide-forming species was proposed to be the phenylhydrazyl radical by Misra and Fridovich (1976),

$$\text{Ph—}\dot{\text{N}}\text{—NH}_2 + O_2 \rightarrow \text{Ph—N=NH} + H^+ + \dot{O}_2^-$$

and the phenyldiazine by Goldberg *et al.* (1976),

$$\text{Ph—N=NH} + O_2 \rightarrow \text{Ph—N=N}\cdot + H^+ + \dot{O}_2^-$$

The phenyldiazenyl radical produced in the latter reaction should decompose to form the phenyl radical which would ultimately form benzene via hydrogen abstraction (Goldberg *et al.*, 1976). The formation of the phenyl radical was conclusively proven by the trapping of the phenyl radical with DMPO in incubations of phenylhydrazine with either oxyhemoglobin or human erythrocytes and the subsequent identification of the spin adduct by mass spectrometry (Hill and Thornalley, 1981).

When phenylhydrazine-4-sulfonic acid was used in place of phenylhydrazine, oxyhemoglobin formed as much DMPO/$\cdot PhSO_3^-$ radical adduct as it did DMPO-phenyl radical adduct from phenylhydrazine. Erythrocytes, on the other hand, produced relatively small amounts of DMPO/$\cdot PhSO_3^-$. This low yield of sulfonated phenyl radical adducts with erythrocytes was interpreted to indicate that the reaction takes place intracellularly, since the charge on the sulfonated derivative would impede transport across the membrane (Hill and Thornalley, 1981). The membrane-soluble spin-trap 4-(*N*-linoleyl-pyridinium chloride)-*N*-*tert*-butyl nitrone trapped four times more phenyl radical adduct than DMPO. Carbon monoxyhemoglobin protected erythrocytes against phenylhydrazine-induced hemolysis and decreased the amount of phenyl radical adduct formed (Hill and Thornalley, 1982a). The rate of oxygen uptake and hemoglobin oxidation in the reaction of phenylhydrazine with oxyhemoglobin were inhibited by spin traps. Spin traps also inhibited hemolysis and lipid peroxidation induced in erythrocytes by phenylhydrazine (Hill and Thornalley, 1983).

When the spin-trap 5-octadecyl-3,3,5-trimethyl-1-pyrroline-*N*-oxide (M_3POC_{18}) was used in these phenylhydrazine-induced hemolysis studies (Hill and Thornalley, 1983) a new spin adduct was observed which had unusually large proton hyperfine coupling constants ($a^N = 16.7$, $a_\beta^H = 18.5$, $a_\beta^H = 24.0$ G). This spectrum was assigned to a radical arising from the rearrangement of a trapped lipid allyl free radical.

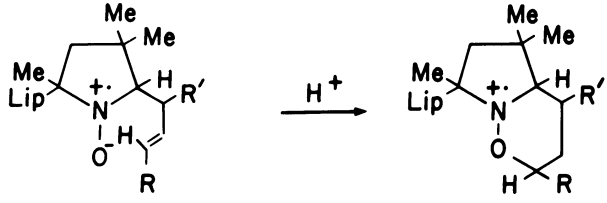

Barker *et al.* (1985) have questioned this assignment on the grounds that the radical proposed by Hill and Thornalley (1983) is an aminium radical cation, not a nitroxyl radical, and is likely to be too unstable to be detected. Instead they propose that the radical observed by Hill and Thornalley is the hydrogen atom adduct of M_3POC_{18}, since it does not have hyperfine constants comparable to legitimate M_3POC_{18}-allyl radical adducts ($a^N = 13.0$ and $a_\beta^H = 5.8$ G) but is similar to the hydrogen atom adduct with two nonequivalent β-hydrogen atoms ($a^N = 15.8$, $a_\beta^H = 17.5$, and $a_\beta^H = 23.3$ G). The larger hyperfine coupling constants reported by Hill and Thornalley are due to a solvent effect.

The hemoglobin-catalyzed phenylhydrazine oxidation is terminated by inactivation of the prosthetic heme group after each heme moiety catalyzes the consumption of six oxygen molecules and six phenylhydrazines and the formation of five benzene molecules. The phenyl radical not converted to benzene is found covalently bound to a nitrogen of protoporphyrin IX after methanol extraction (Augusto *et al.*, 1982b). The

phenyl group was proposed to migrate to a nitrogen of the porphyrin ligand from a catalytically inactive iron-phenylhemoglobin complex during the isolation procedure.

DMPO-benzyl, -ethyl, and -phenyl carbon-centered radical adducts were formed during the oxyhemoglobin-catalyzed reaction of the respective hydrazines (Augusto *et al.*, 1982b). 2-Phenylethylhydrazine forms the 4-POBN-phenylethyl radical adduct when incubated with oxyhemoglobin and 4-POBN (Augusto *et al.*, 1984). The 2-phenylethyl radical produced in this system was shown to induce strand breaks in supercoiled pBR322 plasmid DNA. The reaction of 1-acetyl-2-phenylhydrazine with oxyhemoglobin in the presence of DMPO yields various proportions of the DMPO-phenyl radical adduct, the DMPO-hydroxyl radical adduct, and the oxidized derivative DMPOX depending on the 1-acetyl-2-phenylhydrazine/oxyhemoglobin concentration ratio. In the same system, hydrazine gave a nitroxide which was identified as a reduced dimer of DMPO (Thornalley, 1984). Hydrazine-treated red blood cells, in the presence of DMPO, gave only the DMPO-hydroxyl radical adduct. 1-Acetyl-2- phenylhydrazine-treated red blood cells gave the DMPO-phenyl and DMPO/·OH adducts.

The incubation of phenylhydrazine with horseradish peroxidase and hydrogen peroxide also results in the formation of the phenyl radical which was trapped with DMPO (Sinha, 1983). The inhibition of the DMPO-phenyl radical adduct by nitrogen or by superoxide dismutase implies the involvement of the superoxide anion radical as a chain propagator (Misra and Fridovich, 1976). Prostaglandin synthase and arachidonic acid (or hydrogen peroxide) also formed the DMPO-phenyl radical adduct. The hydrogen peroxide-driven prostaglandin synthase reaction was much less sensitive to superoxide dismutase than the horseradish peroxidase-catalyzed reaction and was also independent of molecular oxygen (Sinha, 1983). Horseradish peroxidase and hydrogen peroxide also oxidize 1,2-dimethylhydrazine to form the tNB-methyl radical adduct in the presence of the spin-trap tNB and the 4-POBN-methyl radical adduct in the presence of 4-POBN (Augusto *et al.*, 1985).

Procarbazine was oxidized by horseradish peroxidase to form both the methyl and the benzylic-type, $R(C_6H_4)CH_2\cdot$, radicals which were trapped with DMPO and tNB (Sinha, 1984). The assignment of the benzylic-type radical adduct is tentative since the splitting constants of the tNB adduct ($a^N = 15.5$, $a_\beta^H = 6.0$ (2H) G) are different from those reported for an unsubstituted tNB-benzylic adduct, $a^N = 16.8$, $a_\beta^H = 10.9$ G (2H) (Sargent and Gardy, 1976). An oxygen-centered adduct with DMPO was also formed in this system ($a^N = 14.0$ G, $a_\beta^H = 12.5$ G, $a_\gamma^H = 1.5$ G) and was assigned to a peroxyl radical formed from the reaction of oxygen with one of the carbon-centered radicals (Sinha, 1984). Procarbazine, in the presence of ram seminal vesicle microsomes (a source of prostaglandin synthase), arachidonic acid, and DMPO produced a carbon-centered adduct ($a^N = 16.1$ G, $a_\beta^H = 23.2$ G) (Sinha, 1984). The use of tNB as the spin trap resulted in the trapping of the benzylic-type radical with splitting constants $a^N = 15.5$ G and $a_\beta^H = 6.0$ (2H) G. Only traces of the methyl adduct were detected, presumably because the methyl radical reacts very rapidly with the microsomal membranes (Sinha, 1984). Since the formation of the radical required oxygen and was inhibited by indomethacin, it was suggested that oxygenation of arachidonic acid to the hydroperoxy-endoperoxide, PGG_2, was required.

The neutrophil myeloperoxidase system has been shown to generate phenyl radicals from phenylhydrazine (Kalyanaraman and Sohnle, 1985). The radicals produced were trapped with DMPO. The radical production was almost completely eliminated by

sodium azide, a myeloperoxidase inhibitor. In addition, supernatant from neutrophils and the myeloperoxidase products, HOCl and chloramines, were able to produce relatively large amounts of the DMPO-phenyl adduct.

In many respects, Cu^{2+} can replace oxyhemoglobin as the radical initiator of phenylhydrazine oxidation, including superoxide formation (Misra and Fridovich, 1976) and phenyl radical formation (Hill and Thornalley, 1981; Augusto *et al.*, 1982b). In the presence of Cu^{2+}, Fe^{2+}, or Fe^{3+}, the antihypertensive drug hydralazine forms a DMPO-nitrogen-centered spin adduct ($a^N = 15.0$ G, $a_\beta^H = 16.7$ G, $a_\beta^N = 2.55$ G) which is completely inhibitable by superoxide dismutase (Sinha and Motten, 1982). The DMPO-hydralazyl radical adduct as well as other adducts were shown to be present by extraction with benzene and mass spectral analysis. The amount of adduct formation by metal ions was decreased by binding the hydralazine to DNA (Sinha and Patterson, 1983). It should be noted that neither the hyperfine coupling constants nor the mass spectrum indicates which of the two hydrazine nitrogens was bound to DMPO in the spin adduct.

Dopamine β-hydroxylase, which catalyzes the hydroxylation of dopamine to form norepinephrine, has been reported to be inhibited by benzylhydrazine. Since inactivation by hydrazines seems to be a general feature of redox-active proteins, a study of the effect of several hydrazines on dopamine β-hydroxylase was carried out. In this study (Fitzpatrick and Villafranca, 1986) phenyl-, phenethyl-, benzyl-, and methylhydrazine were all shown to inactivate the enzyme. The carbon-centered radicals, phenyl, ethylbenzene, benzyl, and methyl, generated from the respective compounds were trapped with 4-POBN. The hydrazines were divided into two classes. Phenylhydrazine, phenethylhydrazine, and methylhydrazine inactivation of the enzyme was slowed in the presence of ascorbate, leading the authors to conclude that the copper at the active site of the enzyme must be oxidized in order for inactivation to occur. Benzylhydrazine inactivation, on the other hand, was increased by fivefold in the presence of ascorbate, implicating the reduced form of the enzyme in the inactivation. In the presence of the tyramine substrate, phenylhydrazine, methylhydrazine, and phenethylhydrazine inactivation either increased or remained the same while benzylhydrazine inactivation decreased. In the presence of both tyramine and ascorbate the rate of inactivation decreased in all cases, demonstrating the involvement of the enzyme in the process. Based on these experiments, Fitzpatrick and Villafranca (1986) propose that the inactivation of dopamine β-hydroxylase by hydrazines involves the generation of a hydrazine cation radical at the active site of the enzyme, followed by homolytic cleavage of the carbon-nitrogen bond to form a carbon-centered radical and diazene. The carbon-centered radical then reacts with the active site of the enzyme rendering it inactive.

Human erythrocytes react with hydralazine to form a different DMPO-nitrogen-centered adduct ($a^N = 15.9$ G, $a_\beta^H = 19.4$ G, $a_\beta^N = 1.7$ G) (Sinha and Motten, 1982), which has the same hyperfine couplings as the DMPO/$\cdot NH_2$ radical adduct (Chignell *et al.*, 1981), implying that $\cdot NH_2$ is produced from hydralazine by red blood cells. The DMPO/$\cdot$H adduct was also detected (Sinha and Motten, 1982). The formation of this spin adduct was attributed to the reduction of DMPO by hydrazine or hydralazine-derived diimide (HN=NH) and not to the trapping of the hydrogen atom.

A variety of hydrazine derivatives have been associated with liver injury, including the drugs iproniazid, pheniprazine, phenelzine, isoniazid, isocarboxazid, and

hydralazine. A common activation mechanism has been proposed (Nelson *et al.*, 1978; Reynolds and Moslen, 1980).

A hydrazine metabolite is first formed that is unsubstituted at one end. Iproniazid is hydrolyzed to the more potent hepatotoxin, isopropylhydrazine. Isoniazid is first acetylated, then hydrolyzed to acetylhydrazine, a more potent hepatotoxin. The drugs pheniprazine, phenelzine, and hydralazine have an unsubstituted end and hence are potent hepatotoxins. If these drugs are acetylated, the other end cannot be hydrolyzed to form a hydrazine metabolite with an unsubstituted end and hence acetylation should be a deactivation step which hinders their oxidation.

Once a hydrazine with an unsubstituted nitrogen is formed, the microsomal cytochrome P-450 monooxygenase forms a reactive species that covalently binds to microsomal protein. Hydroxylation of the hydrazine to form an N-hydroxy intermediate followed by the loss of water would form a monosubstituted diazine which can be air oxidized to form carbon-centered free radicals and superoxide

$$R{-}N{=}N{-}H + O_2 \rightarrow R\cdot + N_2 + O_2^{-}\cdot + H^+$$

or decompose without reaction with oxygen to produce a carbon-centered free radical and the hydrogen atom (Drewer, 1975; Koga *et al.*, 1975).

$$R{-}N{=}N{-}H \rightarrow R\cdot + N_2 + H\cdot$$

The first example of this general mechanism was the activation of iproniazid-derived isopropylhydrazine. Early evidence for the formation of carbon-centered free radicals showed that a tritium- and ^{14}C-labeled metabolite of isopropylhydrazine covalently bound to liver protein without loss of the methine hydrogen at the 2 position (Nelson *et al.*, 1976). Concomitantly, propane retaining the methine hydrogen at position 2 is expired. The isopropyl free radical ($CH_3{-}\dot{C}H{-}CH_3$) was proposed to be the common intermediate that could form propane by hydrogen abstraction or covalently bind via a free radical addition reaction to double bonds (Nelson *et al.*, 1976).

Good evidence for the formation of carbon-centered free radicals during the microsomal oxidation of ethylhydrazine was obtained by spin trapping with PBN (Augusto *et al.*, 1981). The formation of the adduct was dependent on ethylhydrazine, NADPH, and O_2. The same PBN-ethyl adduct was formed by the Cu^{2+}-catalyzed oxidation of ethylhydrazine. The hyperfine coupling constants of the benzene-extracted adduct were compared to the literature values for this solvent. A carbon-centered radical was also trapped with 4-POBN during microsomal oxidation of 1,2-dimethylhydrazine in the presence of NADPH (Augusto *et al.*, 1985). This adduct had hyperfine splittings ($a^N = 16.0$ G, $a_\beta^H = 2.7$ G) very similar to those obtained in the horseradish peroxidase oxidation ($a^N = 16.12$ G, $a_\beta^H = 2.77$ G). This radical was not unambiguously assigned to the methyl radical, however, since it was not trapped by tNB or DMPO.

Cytochrome P-450 oxidizes the monosubstituted hydrazine phenelzine to the phenylethyl radical, which was trapped with 4-POBN (Ortiz de Montellano *et al.*, 1983). The heme of cytochrome P-450 is alkylated by the phenylethyl radical, which can also abstract hydrogen to form ethylbenzene.

Acetylation of isoniazid ultimately leads to the formation of acetylhydrazine. The entire acetyl group becomes covalently bound to protein. The reactive species is proposed to be either the acetyl radical or the acetyl-onium ion (Timbrell *et al.*, 1980).

Contrary to expectation, spin-trapping studies with acetylhydrazine have demonstrated that the PBN spin adduct detected was not the PBN–acetyl radical adduct (Augusto *et al.*, 1981).

Isolated hepatocytes prepared from phenobarbitone-induced rats and treated with either isoniazid or iproniazid in the presence of PBN produced carbon-centered free radical adducts with splitting constants in chloroform of $a^N = 14.4$ G and $a_\beta^H = 2.47$ G for isoniazid and $a^N = 14.9$ G and $a_\beta^H = 2.49$ G for iproniazid (Tomasi *et al.*, 1983b; Albano *et al.*, 1985). These PBN radical adducts of acetyl and isopropyl free radicals, respectively, were assigned on the basis of the equality of the hyperfine coupling constants of the chemically prepared radical adducts (Albano and Tomasi, 1987). The same two radical adducts obtained with isoniazid and iproniazid are also obtained with their respective metabolites, acetyl-hydrazine and isopropyl-hydrazine. The addition of bis-*para*-nitrophenyl phosphate, an inhibitor of the arylamidase enzymes, to isolated hepatocytes decreased free radical formation from isoniazid and iproniazid, but not from their metabolites, confirming the role of arylamidase in the metabolic activation of these compounds (Albano and Tomasi, 1987). In microsomal incubations both cytochrome P-450 inhibitors and destruction of cytochrome P-450 by $CoCl_2$ treatment *in vivo* decreased radical adduct formation. The addition of GSH also decreased the radical trapping, indicating GSH can compete with the spin traps for the free radicals. This effect is not due to the reduction of the nitroxide adducts by GSH, because adding GSH at the end of the incubation had no effect (Albano and Tomasi, 1987).

In the perfused liver, PBN trapped the same radical from hydrazine, acetylhydrazine, and isoniazid (Sinha, 1987). The hyperfine splitting constants of this species in benzene ($a^N = 14.2$ G and $a_\beta^H = 3.2$ G) are the same as those of PBN/·$COCH_3$. Although PBN radical adducts have a narrow, undistinctive range of hyperfine coupling constants, these results can be explained by rapid acetylation and subsequent metabolism of the acetylated hydrazine to the acetyl radical. The liver perfusion of iproniazid formed another species ($a^N = 14.6$ G and $a_\beta^H = 2.7$ G), which was assigned to the PBN/isopropyl radical adduct (Sinha, 1987). In the absence of any hydrazine a third species, present in the fluosal-43 perfusate, was assigned as a lipid-derived radical adduct by Sinha (1987). The marked difference in the hyperfine coupling constants reported for the PBN/·$COCH_3$ and PBN/isopropyl radical adducts by Albano and Tomasi (1987) and Sinha (1987) may be due to the solvent effect of chloroform and benzene, respectively.

The hydrazine drugs isoniazid and iproniazid can also be oxidized to free radicals by either horseradish peroxidase or prostaglandin hydroperoxidase (Sinha, 1983). The oxidation of iproniazid by either peroxidase formed a carbon-centered free radical, which was trapped with DMPO ($a^N = 16.1$ G, $a_\beta^H = 24.4$ G) or tNB ($a^N = 16.6$ G, $a_\beta^H = 2.0$ G). With tNB, the β-hydrogen of the adduct arises from the methine hydrogen at position 2 of the isopropyl radical. With DMPO, an oxygen-centered peroxyl radical adduct ($a^N = 14.7$ G, $a_\beta^H = 11.5$ G, $a_\gamma^H = 1.1$ G) was detected that was oxygen-dependent. This species implies the reaction of oxygen with the isopropyl radical to form the isopropyl peroxyl radical (Sinha, 1983).

Noda *et al.* (1985) claim to have trapped the hydrazyl radical in the microsomal metabolism of hydrazine. An ESR signal was observed in incubations containing liver microsomes, hydrazine, NADPH, and PBN. The PBN-radical adduct was extracted

with benzene and purified using TLC. The appropriate section of the TLC plate was extracted with chloroform and an ESR signal with splitting constants of $a^N = 16.6$ G and $a_\beta^H = 3.1$ G was obtained. The same radical was formed during the copper-catalyzed autoxidation of hydrazine in the presence of PBN. Mass spectrometry was used to identify the radical as the PBN/·$NHNH_2$ radical adduct, although no nitrogen hyperfine coupling ($I = 1$) was discernible in the ESR spectrum. This assignment cannot be correct, since the use of even [$^{15}N_2$]hydrazine gave the identical ESR spectrum while the coupling due to ^{15}N ($I = \frac{1}{2}$) should give a detectable change if a nitrogen-centered species is trapped by PBN (Kalyanaraman *et al.*, 1985).

8. OXYGEN-CENTERED RADICALS

Oxygen-centered radicals, particularly hydroxyl and superoxide radicals, have been postulated in many biochemical reactions and have been implicated in many adverse reactions *in vivo*. The DMPO-hydroxyl, DMPO-superoxide, PBN-hydroxyl, and PBN-superoxide radical adducts were first assigned in 1974 (Harbour *et al.*, 1974) using chemical evidence for their formation. These adducts were only recently shown to be oxygen-centered using [$^{17}O_2$]oxygen (Mottley *et al.*, 1986).

The first report of spin trapping an oxygen-centered radical in a biological system was the trapping of the light-induced superoxide radical anion by chloroplasts (Harbour and Bolton, 1975). Since that first report, the use of spin trapping to detect oxygen-centered radicals in biological systems has mushroomed. This review will center on the problems involved in proving that the DMPO-oxygen-centered radical adducts are not artifactual. No attempt will be made to review the vast literature, since several reviews are already available (Finkelstein *et al.*, 1980; Janzen, 1980; Buettner, 1982; Kalyanaraman, 1982; Rosen and Finkelstein, 1985).

Three of the most used spin traps, DMPO, PBN, and 4-POBN, form identifiable adducts with both superoxide and hydroxyl radicals. DMPO is the most widely used, because its adducts are distinctive and the most stable. The splitting constants for the DMPO-hydroxyl radical adduct are $a^N = a_\beta^H = 15.0$ G while those for the DMPO-superoxide radical adduct are $a^N = 14.2$ G, $a_\beta^H = 11.34$ G, and $a_\gamma^H = 1.25$ G. The problem with attempting to spin trap oxygen-centered radicals is in proving that the radical adducts were formed by trapping the actual radical. Sufficient controls must be run to verify the results.

If superoxide radicals are believed to be trapped, then the signal must be sensitive to superoxide dismutase (Finkelstein *et al.*, 1980). Often a hydroxyl radical adduct signal is superoxide dismutase sensitive, which implies that (1) the hydroxyl radical formation is dependent on superoxide (perhaps through the reduction of ferric ion for the Fenton reaction), or (2) superoxide is trapped first with the resulting superoxide radical adduct decomposing to form the hydroxyl radical adduct (Finkelstein *et al.*, 1979), or (3) the decomposition of the superoxide radical adduct to the hydroxyl radical, which may then be trapped (Finkelstein *et al.*, 1982).

The DMPO/·OH radical adduct is a very common artifact in any study using DMPO. In fact, it is a common impurity in DMPO solutions. The best way to prove the existence of the hydroxyl radical in a system is to do a competition experiment in which the hydroxyl radical abstracts a hydrogen from ethanol, methanol, or another

alcohol and the resulting carbon-centered radical is trapped (Harbour and Bolton, 1978; Finkelstein *et al.*, 1980). Formate, which forms the $\cdot CO_2^-$ radical upon hydroxyl radical attack, can also be used in competition experiments (Harbour and Hair, 1979). Dimethylsulfoxide is also used in competition experiments since the reaction with hydroxyl radical produces methyl radicals which are easily trapped (Saprin and Piette, 1977), although care must be taken since Rosenthal *et al.* (1982) have shown that methyl spin adducts can be formed under conditions that do not involve the hydroxyl radical, such as the chemical reaction of dimethylsulfoxide with hydroxide. A uniquely stable radical adduct of superoxide with the spin-trap 3,5-dibromo-4-nitrosobenzenesulfonate has been reassigned as a DMSO-derived radical adduct of $\cdot SO_3^-$ (Stolze and Mason, 1987).

It is important to remember that not trapping superoxide or hydroxyl radicals does not mean that these radicals are not present and taking part in the reaction. Likewise, the observation of an apparent DMPO/·OH radical adduct does not necessarily mean that the hydroxyl radical is involved. Careful controls are absolutely necessary to rule out artifacts.

The formation of the hydroxyl radical via the NADPH-supported enzymatic reduction of oxygen by the ferredoxin-ferredoxin: $NADP^+$ oxidoreductase was studied using many of the approaches outlined in this review (Morehouse and Mason, 1988). The DMPO/·OH radical adduct formation appeared to be totally due to the trapping of the hydroxyl radical. The effects of transition metal chelators on the DMPO/·OH radical adduct concentration suggest that the reduction of chelated iron by ferredoxin is necessary for the reduction of hydrogen peroxide to the hydroxyl radical via Fenton-type chemistry, and even the low-potential ferredoxin does not reduce hydrogen peroxide directly (Morehouse and Mason, 1988).

Oxygen-derived radicals in ischemic and post-ischemic rat hearts have been investigated by spin trapping with DMPO (Arroyo *et al.*, 1987; Kramer *et al.*, 1987). DMPO/carbon-centered radical adducts were detected in ischemic and DMPO/superoxide and DMPO/hydroxyl radical adducts in post-ischemic rat heart. All radical adducts were inhibited by the addition of superoxide dismutase to the coronary perfusate (Arroyo *et al.*, 1987). The concentration of the DMPO/hydroxyl radical adduct in post-ischemic effluent increased with the duration of ischemia and reached a peak 3 min after initiation of reperfusion (Kramer *et al.*, 1987). It will probably not be possible to determine the origin of the DMPO/hydroxyl radical adduct in complicated biological systems such as the perfused heart, in view of all the possible pathways for DMPO/hydroxyl radical adduct formation other than trapping the hydroxyl radical.

9. ALDEHYDES

9.1. Glyceraldehyde and Other Monosaccharides

The area of autoxidation of monosaccharides is covered very well in a review by Thornalley (1985), so this discussion will include only the spin-trapping studies carried out to prove the involvement of free radicals in the autoxidation. The review by Thornalley (1985) includes discussions of the products, the kinetics, and the mechanism of the autoxidation of monosaccharides.

The autoxidation of monosaccharides has been shown to involve hydroxyl and 1-hydroxylalkyl free radicals by spin trapping these radicals with DMPO (Thornalley and Stern, 1984; Thornalley *et al.*, 1984). At pH 8.6, incubating glyceraldehyde with DMPO gives rise to an ESR spectrum with two components, DMPO/·OH and DMPO/carbon-centered radical adduct. The DMPO/carbon-centered spectrum is characterized by the splitting constants $a^N = 15.8$ G and $a^H_\beta = 22.8$ G. These parameters are similar to the previously assigned DMPO-hydroxyethyl spin adduct (Finkelstein *et al.*, 1980) which has a large β-hydrogen splitting constant. Catalase completely inhibited, while superoxide dismutase stimulated the formation of both spin adducts. This is consistent with radical formation as a result of a reaction with hydrogen peroxide, which is produced by dismutation of the superoxide radical anion formed during the oxidation of the ene-diol form of the monosaccharide. At a pH below 8.2, only the carbon-centered radical was trapped. From radiolysis studies (Steeken and Schulte-Frohlinde, 1973; Von Sonntag, 1980), the major carbon-centered radical formed in the reaction of hydroxyl radicals with glyceraldehyde is that produced by the abstraction of a hydrogen atom from the acetal bond in the aldehyde hydrates.

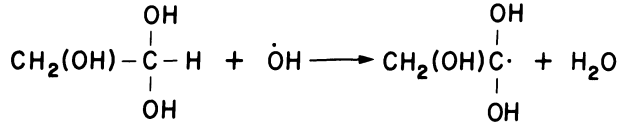

Thus the carbon-centered radical trapped by DMPO is assigned the structure above. The disappearance of the DMPO/·OH adduct below pH 8.2 is explained by the protonation of the ene-diol which leaves a species relatively stable to autoxidation and which scavenges the decreased level of hydroxyl radical by an addition reaction (Thornalley *et al.*, 1984).

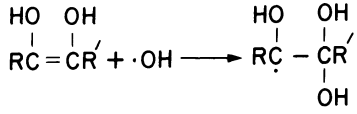

In the same manner, glycolaldehyde and erythrose form similar carbon-centered radicals when they undergo autoxidation (Thornalley *et al.*, 1984; Thornalley and Stern, 1984). Dihydroxyacetone hydrate, which also forms a DMPO-carbon-centered radical adduct, has no acetal C—H group and one of the four β-hydroxy hydrogen atoms is extracted to form the radical (Thornalley *et al.*, 1984).

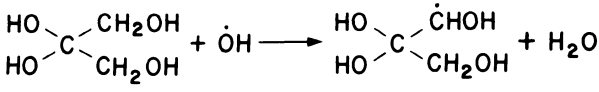

The DMPO-glycolaldehyde radical adduct and the DMPO-dihydroxyacetone radical adduct have splitting constants of $a^N = 15.8$ G and $a^H = 22.8$ G, which are typical of DMPO/carbon-centered radical adducts (Thornalley and Stern, 1984).

9.2. Malonaldehyde and Acetylacetone

Malonaldehyde is a major product of lipid peroxidation and as such is used as a measure of free radical production. Malonaldehyde is metabolized *in vivo* (Siu and Draper, 1982; McGirr *et al.*, 1985) and *in vitro* (Siu and Draper, 1982) by the enzyme aldehyde dehydrogenase. The major product is CO_2 (Siu and Draper, 1982) although a portion is excreted in the urine as N^{α}-acetyl-ε-(2-propenal)lysine (McGirr *et al.*, 1985). Malonaldehyde is also reported to produce singlet oxygen as a result of peroxidase-catalyzed oxidation (Vidigal-Martinelli *et al.*, 1979).

The methyl-substituted malonaldehyde analogue, acetylacetone, undergoes a one-electron oxidation in the presence of horseradish peroxidase and hydrogen peroxide (Mottley *et al.*, 1988). A carbon-centered radical

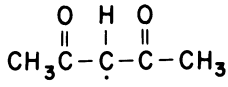

1

was first trapped with tNB (splitting constants $a^N = 14.6$ G and $a^H = 3.4$ G). This radical adduct then disappeared and was replaced by two adducts, one resulting from the trapping of an unknown species and the other resulting from the trapping of the acetyl radical

2

with a splitting constant of $a^N = 8.3$ G. The structure of this adduct was proven using (2, 4-$^{13}C_2$, 99%) acetylacetone and (1,5-$^2H_3$, 99%) acetylacetone. Again with the spin-trap DMPO, no oxygen-centered radical was trapped but the two carbon-centered species were trapped and had splitting constants of $a^N = 15.65$ G and $a^H = 24.4$ G for species 1 and $a^N = 15.3$ G and $a^H = 18.8$ G for the acetyl radical adduct. When the pH was raised, the carbon-centered radical adduct with tNB became stable and the acetyl radical and the unknown species were not trapped. At higher pH values a second carbon-centered adduct formed from trapping the enolate form

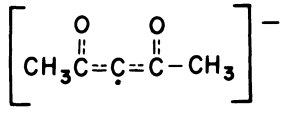

3

[splitting constants $a^N = 15.8$ G and $a^H = 0.29$ (9H) G]. This adduct exhibited hyperfine coupling with the nine equivalent protons of the *t*-butyl group of the spin trap (shown by using deuterated acetylacetone). At pH 9.0 and above this adduct was the predominant species.

Since both malonaldehyde and acetylacetone rapidly consume oxygen in the presence of hydrogen peroxide and horseradish peroxidase, an attempt was made to trap with DMPO the peroxyl radicals which should be formed. To do this the concentration of the spin-trap DMPO was decreased to allow time for the reaction with oxygen before radicals were trapped. In the case of malonaldehyde no new species were trapped. With acetylacetone, a new species which required oxygen appeared and was the most prominent species at a DMPO concentration of 5 mM. This species has hyperfine coupling constants of $a^N = 14.4$ G and $a^H = 3.3$ G. It is obviously lacking the large β-proton hyperfine coupling usually found in DMPO adducts and may be a spin adduct imposter

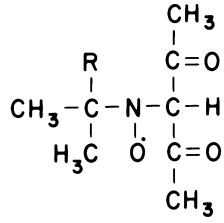

formed by opening of the DMPO ring.

10. LIGNIN MODEL DIMERS

Biochemists have had a major problem elucidating the mechanism by which lignin, one of the major constituents of wood, is degraded. Lignin is a complex polymer which is highly resistant to biodegradation but which is efficiently decomposed by higher basidiomycetous fungi. Spin trapping, using model dimers, has recently been used to show that the mechanism involves an enzymatic one-electron oxidation of lignin which yields free radicals (Hammel *et al.*, 1985, 1986).

The first model compound used was 1-(3,4-dimethoxyphenyl)-2-phenylethane-diol (trivial name: dimethoxyhydrobenzoin (DMHB)] which was shown to give only two products, veratraldehyde and benzaldehyde.

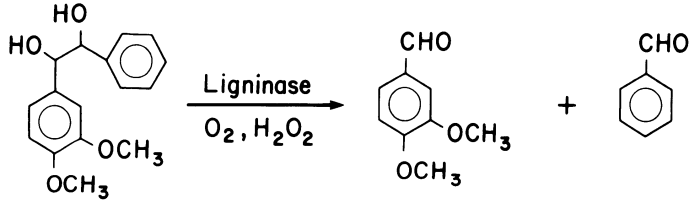

This cleavage takes place both anaerobically (when stoichiometric amounts of hydrogen peroxide are present) and aerobically (in which case oxygen is involved) (Hammel *et al.*, 1985). The spin-trap tNB was used to try to trap carbon-centered radicals while DMPO was used to try to trap oxygen-centered radicals.

Anaerobically and with tNB as the spin trap, a six-line ESR spectrum was obtained from a solution of tNB, DMHB, hydrogen peroxide, and ligninase. The spectrum is characteristic of a carbon-centered adduct with a single β-hydrogen and was assigned, using computer simulation, to two overlapping spectra with $a^N = 15.4$ G and $a_\beta^H = 2.6$ G, and $a^N = 15.6$ G and $a_\beta^H = 2.1$ G (Hammel *et al.*, 1985). When DMHB was 99% ^{13}C labeled at C_β, the ESR spectrum clearly showed two tNB adducts, one containing ^{13}C ($a^N = 15.4$ G, $a_\beta^H = 2.6$ G, $a^{^{13}C} = 4.5$ G) and one containing no ^{13}C ($a^N = 15.6$ G and $a_\beta^H = 2.1$ G). The ^{13}C-containing radical was assigned to the α-hydroxybenzyl radical adduct and the other radical was assigned to the α-hydroxy(dimethoxybenzyl) radical adduct. Two similar radicals were trapped with DMPO ($a^N = 16.0$ G, $a_\beta^H = 22.7$ G, and $a^{^{13}C} = 8.3$ G; $a^N = 16.0$ G and $a_\beta^H = 22.3$ G).

Aerobic experiments with DMPO to trap oxygen-centered species gave an ESR spectrum with hyperfine splitting constants $a^N = 14.5$ G, $a_\beta^H = 11.5$ G, and $a_\gamma^H = 1.3$ G which are characteristic of a DMPO-peroxyl or DMPO-superoxide radical adduct. Even large amounts of superoxide dismutase caused an inhibition of only 45%. Since superoxide dismutase was shown not to inhibit ligninase, it was proposed that both superoxide and peroxyl radicals were trapped during DMHB cleavage. The initial carbon-centered radical reacted with oxygen forming an α-hydroxybenzylperoxyl radical, which would probably decompose to give superoxide and a benzaldehyde radical similar to the breakdown of α-hydroxyalkylperoxyl radicals (Bothe *et al.*, 1978). DMPO was shown to decrease the amount of benzaldehyde product formation, so the α-hydroxybenzyl radical was proposed as the precursor of benzaldehyde.

Three different model dimers to be used in ligninase studies were synthesized:

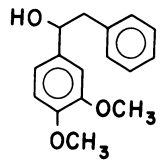

1

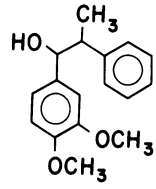

2

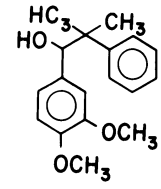

3

(Hammel *et al.*, 1986). In these anaerobic studies the spin trap used was nitrosobenzene, which has a very high rate constant for its reaction with carbon-centered radicals. No radical adducts were observed using **1** as the substrate. When **2** was used, a nitrosobenzene spin adduct with one β-hydrogen ($a^N = 14.0$ G, $a_\beta^H = 5.0$ G, $a_{o,p}^H = 3.4$ G, and $a_m^H = 1.1$ G) was detected. With **3**, an adduct with no β-hydrogen ($a^N = 12.6$ G, $a_{o,p}^H = 2.5$ G, and $a_m^H = 1.0$ G) was detected. The formation of these radicals correlates nicely with the observation of the formation of symmetrical diphenylalkanes from **2** and **3** but not from **1**.

That the carbon-centered radicals are involved in a major pathway of the ligninase reaction was proven by the observation that *meso*- and *dl*-2,3-diphenylbutane accounted for 26% of all liberated phenylethyl groups from species **2** under anaerobic conditions (Hammel *et al.*, 1986). These two isomers occurred in equal concentrations as would be expected for a nonstereoselective radical reaction. In the case of species **3**, it was shown that cumene hydroperoxide is a major cleavage product when the reaction is run aerobically. Peroxyl radicals and the resulting hydroperoxides are expected products resulting from the addition of oxygen to the carbon-centered radicals produced by the cleavage of a carbon-carbon bond.

11. 3-METHYLINDOLE

A nitrogen-centered free radical was spin trapped with PBN ($a^N = 13.6$ G, $a_\beta^H = 2.3$ G, and $a_\beta^N = 3.6$ G) when various indolic compounds were oxidized by superoxide (Kubow *et al.*, 1983) or UV light (Kubow *et al.*, 1984). Only the specific lung toxin 3-methylindole formed a nitrogen-centered radical when incubated in a system containing goat lung microsomes and NADPH. A carbon-centered lipid radical adduct with PBN ($a^N = 14.4$ G and $a_\beta^H = 3.2$ G) formed over time. The carbon-centered radical adduct was also found in goat lung extracts after infusion of 3-methylindole under conditions where 3-methylindole causes pulmonary lesions. Goat liver microsomes also produced the nitrogen-centered 3-methylindole adduct and the carbon-centered lipid adduct (Kubow *et al.*, 1985). No radicals appeared in liver extracts, however. Since the carbon-centered radical adduct formation was inhibited by the addition of GSH and vitamin E to the liver microsomal incubation (Kubow *et al.*, 1985) and to the lung microsomal incubation (Kubow *et al.*, 1984), the absence of an ESR signal in the liver extract was proposed to be due to the higher concentration of GSH and other antioxidant defense systems in the liver. It was proposed that GSH may protect against 3-methylindole damage by reacting directly with the nitrogen-centered free radical and thus preventing its covalent binding to macromolecules and/or the initiation of lipid peroxidation (Kubow *et al.*, 1985). However, NMR and MS data indicate that the conjugation of GSH occurs at the methyl group of 3-methylindole (Nocerini *et al.*, 1985). Nocerini *et al.* (1985) proposed that the initial nitrogen-centered radical species undergoes hydrogen atom abstraction from the methyl group to form the electrophilic imine methide intermediate, which can then alkylate protein, trap water, or trap GSH. The imine methide was proposed to be the toxic intermediate, with the radical merely being an intermediate in its formation.

12. INDOLE ACETIC ACID

The oxidation of indole-3-acetic acid by horseradish peroxidase has been extensively studied and it has been generally accepted from the beginning that a free radical of indole-3-acetic acid was an intermediate in the reaction. Only recently has the structure of the radical intermediate been determined through spin trapping (Mottley and Mason, 1986) along with further information concerning the oxidation mechanism.

Oxidation of indole-3-acetic acid by horseradish peroxidase in the presence of tNB gave rise to an ESR spectrum of a radical adduct with hyperfine coupling constants of $a^N = 17.1$ G and $a_\beta^H = 10.9$ (2H) G, which is consistent with the skatole carbon-centered radical

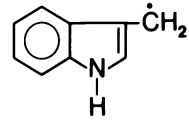

having been trapped (Mottley and Mason, 1986). Unambiguous proof of this structure was provided when indole-3-acetic-2,2-$^2H_2$ acid was used as the substrate. In this case the triplets from the two equivalent protons were replaced by quintets from the two equivalent deuterium atoms ($a^N = 17.1$ G and $a_\beta^{^2H} = 1.6$ G).

When DMPO was used as the spin trap at least three species were observed: the DMPO-superoxide radical adduct ($a^N = 14.4$ G, $a_\beta^H = 11.4$ G, and $a_\gamma^H = 1.3$ G); the DMPO-hydroxyl radical adduct ($a^N = a_\beta^H = 14.8$ G); and a DMPO-carbon-centered radical adduct, presumably the DMPO-skatole radical adduct ($a^N = 16.0$ G and $a_\beta^H = 22.4$ G) (Mottley and Mason, 1986). When the system went anaerobic, the DMPO-skatole radical adduct dominated and the DMPO-superoxide radical adduct disappeared. The DMPO-superoxide radical adduct spectrum was inhibited by superoxide dismutase, but the DMPO-hydroxyl radical adduct signal was not affected. Free hydroxyl radical was apparently not present, since addition of ethanol did not result in a decrease in the DMPO-hydroxyl radical adduct signal and no DMPO-α-hydroxyethyl radical adduct was formed. Carbon monoxide did not inhibit the formation of the superoxide radical as would be expected if the superoxide were formed through compound III of the enzyme. It was therefore proposed that the skatole carbon-centered radical added oxygen to form the peroxyl radical, which then decomposed to form the superoxide radical and 3-methylene-[2*H*]-indole.

13. ETHANOL

Liver microsomes incubated with an NADPH-generating system, ethanol (Albano *et al.*, 1986, 1987, 1988), 2-propanol or 2-butanol (Albano *et al.*, 1987), and 4-POBN form the 4-POBN/α-hydroxyalkyl free radical. The 4-POBN/$\cdot$CHOHCH$_3$ radical adduct was identified by the formation of a species with the same coupling constants ($a^N = 14.97$ and $a_\beta^H = 3.48$) in a hydroxyl radical-generating Fenton system and by ^{13}C-labeling of both carbons (Albano *et al.*, 1986, 1987). Subsequently Reinke *et al.* (1987) detected PBN/$\cdot$CHOHCH$_3$ in a microsomal incubation and proved the electron was localized on the carbon α to the hydroxyl group by using 1-^{13}C-ethanol. The involvement of the hydroxyl radical from microsomal hydrogen peroxide was suggested by stimulation by azide (to inhibit endogenous catalase) and inhibition by added catalase (Albano *et al.*, 1986, 1987, 1988). The iron chelator desferrioxamine inhibited and EDTA-iron increased the 4-POBN/$\cdot$CHOHCH$_3$ radical adduct concentration.

Microsomes washed with desferrioxamine in chelexed incubations still produce the α-hydroxyethyl radical, although at a reduced rate (Albano *et al.*, 1988). Under

these conditions 4-POBN/·$CHOHCH_3$ formation was independent of the hydroxyl radical and inhibited by cytochrome P-450 inhibitors. GSH appears to scavenge the α-hydroxyethyl radical and thereby prevent its trapping by 4-POBN (Albano *et al.*, 1988). Rats fed a high fat, ethanol-containing diet generate a lipid-derived radical adduct in liver and heart *in vivo* (Reinke *et al.*, 1987). Rats fed ethanol in a low fat diet showed significantly less free radical generation. It is not known if the initial radical which initiates lipid peroxidation *in vivo* is the α-hydroxyethyl radical, but in any case this free radical has not been detected *in vivo.*

14. TRYPTOPHAN

A carbon-centered radical has been trapped with tNB in incubations containing tryptophan, hydrogen peroxide, and horseradish peroxidase and in incubations containing tryptophan, arachidonic acid, and prostaglandin synthase (Eling *et al.*, 1988). The three-line ESR spectrum was the result of trapping a radical centered on the carbon in the 3 position of tryptophan.

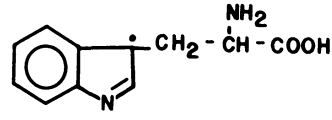

If the radical were formed at any other position in the molecule, a hydrogen splitting would have been observed in the ESR spectrum. The location of the free electron in the radical was definitively proven by using labeled tryptophan (indole-3^{13}C). The resulting spectrum exhibited the expected ^{13}C splitting.

15. NITROBENZYL CHLORIDES

o-Nitrobenzyl chloride, *m*-nitrobenzyl chloride, and *p*-nitrobenzyl chloride were reduced aerobically and anaerobically by NADPH and rat hepatic microsomes (Moreno *et al.*, 1986). Incubations containing *m*-nitrobenzyl chloride resulted in the formation of the corresponding anion radical with splitting constants $a^N = 13.93$ G, $a_o^H = 3.38$ G, $a_p^H = 3.62$ G, $a_m^H = 1.08$ G, $a_{CH_2}^H = 0.57$ G, and $a^{Cl} = 0.62$ G, while incubations containing either *o*- or *p*-nitrobenzyl chloride did not give direct ESR signals.

Aerobic incubations containing liver microsomes, NADPH, DMPO, and either *p*- or *o*-nitrobenzyl chloride gave rise to both the DMPO-superoxide and DMPO-hydroxyl radical adducts. Superoxide dismutase, but not catalase, inhibited the formation of both adducts indicating that the DMPO-hydroxyl radical adduct arose from the DMPO-superoxide radical adduct (Finkelstein *et al.*, 1979). Under anaerobic conditions, the same incubations gave rise to carbon-centered radical adducts with DMPO (*p*-nitrobenzyl chloride: $a^N = 16.0$ G, $a_\beta^H = 21.4$ G, and $a_\gamma^H = 0.7$ G; and *o*-nitrobenzyl chloride: $a^N = 15.8$ G and $a_\beta^H = 22.4$ G). When tNB was used as the spin trap, carbon-centered radical adducts with two equivalent hydrogens were formed (*p*-nitrobenzyl chloride: $a^N = 16.5$ G and $a_\beta^H = 10.6$ (2H) G; *o*-nitrobenzyl chloride: $a^N = 17.1$ G and

a_β^H = 14.4 (2H) G). The carbon-centered adducts of both DMPO and tNB are consistent with the trapping of the respective neutral carbon-centered *p*- and *o*-nitrobenzyl radicals formed from an intramolecular electron transfer within the corresponding nitro anion radicals. The generation of superoxide anion radicals indicates that these nitro anion radicals are formed, but are too unstable to detect.

16. AZIDE AND CYANIDE

The azidyl radical formed as a result of the one-electron oxidation of azide has been detected by spin trapping in chemical (Okhlobystina *et al.*, 1975; Janzen *et al.*, 1980), photochemical (Janzen *et al.*, 1980; Rehorek *et al.*, 1979; Kremers and Singh, 1980; Buettner and Oberley, 1980; Harbour and Issler, 1982), electrochemical (Janzen *et al.*, 1980; Walter *et al.*, 1982), and radiochemical (Kremers and Singh, 1980) oxidizing systems. In these reports the coupling constants were a^N = 15.2 G and $a_\beta^N = a_\beta^H$ = 2.1 G for the PBN-azidyl radical adduct and either $a^N = a_\beta^H$ = 14.5 G and a^N = 3.1 G (Harbour and Issler, 1982) or $a^N = a_\beta^H$ = 14.9 G and a^N = 3.0 G (Buettner and Oberley, 1980) for the DMPO-azidyl radical adduct.

Recently the azidyl radical has been trapped as a result of the oxidation of azide by hydrogen peroxide and catalase, horseradish peroxidase, chloroperoxidase, lactoperoxidase, or myeloperoxidase (Kalyanaraman *et al.*, 1985). In these studies the PBN-azidyl radical adduct was found to have splitting constants of a^N = 15.2 G, a_β^H = 2.3 G, and a_β^N = 2.0 G, with a_β^{15N} = 2.8 G when [$^{15}N_3$]azide was used. The inequivalence of the a^N and a^H values was necessary to simulate the ^{14}N and ^{15}N spectra in a self-consistent manner. With DMPO as the spin trap the azidyl radical adduct was found to have splitting constants of a^N = 14.8 G, a_β^H = 14.2 G, and a_β^N = 3.1 G and an a_β^{15N} splitting of 4.3 G. Since azidyl radicals react very rapidly and selectively with the amino acids cysteine, tyrosine, and tryptophan (Land and Prutz, 1979) as well as the tryptophan in proteins (Prütz *et al.*, 1980), some consideration should be given to possible reactions of the azidyl free radical before azide is used as an inhibitor of catalase or myeloperoxidase.

In the presence of hydrogen peroxide, the cyanyl radical was formed during the oxidation of cyanide by either horseradish peroxidase, lactoperoxidase, chloroperoxidase, NADH peroxidase, or methemoglobin (Moreno *et al.*, 1988). The identity of the PBN/·CN (a^N = 16.0 G, a_β^H = 2.4 G, and a_β^{13C} = 10.7 G) and the DMPO/·CN (a^N = 15.5 G, a_β^H = 18.9 G, and a_β^{13C} = 13.0 G) radical adducts could be demonstrated using ^{13}C-labeled cyanide. The radical adducts of the formamide radical, a hydrolysis product of the cyanyl radical adduct, are distinctly different. The enzymatic conversion of cyanide to cyanyl radical by peroxidases should be considered in addition to its well-known role as a metal ligand (Moreno *et al.*, 1988).

17. STYRENE

The reaction of glutathione with epoxides of chemical carcinogens to form glutathione conjugates is an important mechanism for the inactivation of these reactive metabolites (Oesch, 1973). The formation of glutathione adducts can also be catalyzed

through a free radical mechanism by peroxidases (Stock *et al.*, 1986a, 1986b). When styrene, glutathione, horseradish peroxidase, and hydrogen peroxide were incubated in pH 7.6 buffer in the presence of tNB, a carbon-centered radical was trapped with coupling constants $a^N = 16.0$ G and $a_\beta^H = 3.7$ G. In addition the tNB-hydrogen atom adduct ($a^N = 14.6$ G and $a_\alpha^H = 14.4$ G) was detected (Stock *et al.*, 1986b). The carbon-centered radical was shown to arise from the styrene by using uniformly deuterated [$^2H_{1-8}$]styrene, in which case the hydrogen doublets collapsed into unresolved deuterium triplets. The radical was proven to be localized on the C-7 position of styrene by using specifically labeled [$^2H_7$]styrene. The addition of aminopyrine increased the intensity of the styrene radical adduct through the formation of the aminopyrine cation radical by peroxidase and its subsequent oxidation of glutathione to the thiyl radical (Eling *et al.*, 1985). The addition of phenol had the same effect.

The use of the spin-trap DMPO instead of tNB resulted in the DMPO-glutathione thiyl radical adduct ($a^N = 15.4$ G and $a_\beta^H = 16.2$ G) and a DMPO-carbon-centered radical adduct ($a^N = 16.0$ G and $a_\beta^H = 22.4$ G) which was assigned to the styrene C-7 carbon-centered radical.

In incubations containing prostaglandin H synthase, arachidonic acid as cyclooxygenase substrate, either aminopyrine or phenol as good substrates that facilitate the oxidation of glutathione, styrene, and spin trap, the same glutathione thiyl and styrene radical adducts were observed as above. Formation of these species was inhibited by indomethacin, a cyclooxygenase inhibitor.

The proposed mechanism for the formation of the glutathione-styrene conjugate products goes through a peroxyl radical intermediate:

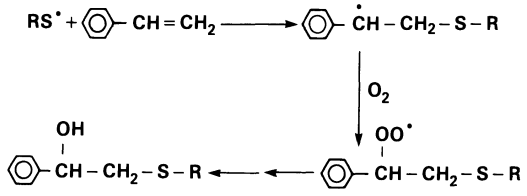

Oxygen consumption was demonstrated using an oxygen electrode and was inhibited by DMPO. The glutathione conjugate formation was also inhibited by DMPO. Under anaerobic conditions the major metabolite lacked the oxygen atom attached to the C-7 position and was identified as *S*-(2-phenyl)ethylglutathione.

18. SPIN TRAPS AS ENZYME INHIBITORS

Since spin-trap concentrations often exceed that of any other constituent of an incubation, it is surprising that the inhibition of enzymes by spin traps has not been a serious problem. Neither DMPO, PBN, nor 4-POBN affects the NADPH-cytochrome c (P-450) reductase activity of rat liver microsomes (Kalyanaraman *et al.*, 1980; Cheeseman *et al.*, 1985). DMPO does not inhibit xanthine oxidase activity as measured by the oxidation of xanthine to uric acid (Finkelstein *et al.*, 1979). At 30 mM, DMPO has no effect on the demethylation of aminopyrine or the hydroxylation of aniline by rat liver microsomes (Cederbaum and Cohen, 1980).

DMPO (Augusto *et al.*, 1982a), PBN, and 4-POBN (Augusto *et al.*, 1982a; Cheeseman *et al.*, 1985) have been shown to interact with microsomal cytochrome P-450. PBN showed a type I binding spectrum indicating interaction with the substrate-binding site of the cytochrome (Cheeseman *et al.*, 1985), while DMPO (Augusto *et al.*, 1982a) and 4-POBN (Cheeseman *et al.*, 1985) showed a type II spectrum resulting from coordination of the N-oxide to the heme iron of the cytochrome. DMPO is a weak inhibitor, PBN inhibits strongly, and 4-POBN inhibits less effectively than PBN. PBN significantly inhibits the cytochrome P-450-catalyzed formation of carbon-centered free radicals from alkylhydrazines (Ortiz de Montellano *et al.*, 1983), 3,5-bis(ethoxycarbonyl)-4-ethyl-2,6-dimethyl-1,4-dihydropyridine (Augusto *et al.*, 1982a), and carbon tetrachloride (Albano *et al.*, 1982). Both PBN and 4-POBN inhibit P-450 mixed function oxidase catalyzed aminopyrine *N*-demethylation, aniline *p*-hydroxylation and ethoxycoumarin *O*-deethylation (Cheeseman *et al.*, 1985). On the other hand, at low concentrations PBN stimulated aniline hydroxylase activity (Cheeseman *et al.*, 1985). This stimulatory effect on aniline hydroxylase activity has been observed for other compounds such as 2,2′-bipyridine, acetone, and various nitrogen heterocycles (Cinti, 1978; Murray and Ryan, 1982) but the mechanism is not known.

Mason *et al.* (1980) found that tNB and nitrosobenzene inhibited the biooxygenation of arachidonic acid by prostaglandin synthase. The enzyme-bound carbon-centered arachidonic acid intermediate was proposed to react with these spin traps, inhibiting oxygen consumption and forming the characteristic adducts. DMPO does not inhibit prostaglandin formation, nor does it form a detectable concentration of the DMPO-carbon-centered arachidonic acid radical adduct (Mottley *et al.*, 1982a). The inhibition of prostaglandin synthase and soybean lipoxygenase (Aoshima *et al.*, 1977) by spin traps appears to depend on the rate of trapping of the carbon-centered radical intermediate.

These effects on enzyme activity must be considered when spin traps are used in the presence of these or other enzymes. Quantitative data should be severely questioned, since one cannot be certain that the spin trap is not affecting the results by either increasing or decreasing the enzyme activity either directly or by reacting with substrate radical metabolites.

19. SPIN TRAPS AS ENZYME SUBSTRATES

Spin adducts are nitroxides, and most nitroxides can be reduced by ascorbate to their corresponding hydroxylamines (Eriksson *et al.*, 1987). Nitroxides are also reduced in microsomal incubations by NADPH-cytochrome c reductase (Stier and Sackman, 1973) or cytochrome P-450 (Rosen and Rauckman, 1977). In general, spin adducts will be reduced at some rate in microsomal incubations containing NADPH, especially under anaerobic conditions.

Nitroso spin traps can also be reduced by mild conditions. The reduction of tNB by the superoxide formed in rat liver microsomal incubations with NADPH results in the formation of *tert*-butyl hydronitroxide (Kalyanaraman *et al.*, 1979b). The enzymatic formation of hydronitroxides via the one-electron reduction of nitroso compounds by flavoproteins has not been reported, but enzymatic nitrosoreduction is known (Becker and Sternson, 1980; Horie *et al.*, 1980) and enzymatic hydronitroxide formation is to

be expected. Phenyl hydronitroxide is formed by the reduction of the spin-trap nitrosobenzene with ascorbate, epinephrine (Mottley *et al.*, 1981), or isoproterenol (Sridhar, 1981). In some cases the ESR spectra of hydronitroxides have been misidentified as spin adducts (Kalyanaraman *et al.*, 1979b; Mottley *et al.*, 1981).

PBN increases endogenous microsomal NADPH oxidation and oxygen consumption as if it were a substrate of cytochrome P-450 (Wolf *et al.*, 1980), but the microsomal oxidation product is unknown.

20. *IN VIVO* SPIN TRAPPING AND SPIN TRAPPING IN CELLS

In using the spin-trapping technique in complex biological systems, such as cells or whole animals, the possible inhibition or stimulation of enzymes as discussed in Section 18 and the possible reduction of the spin adduct as discussed in Section 19 as well as the possible toxicity of the spin trap must be considered. There is little information about toxicity of spin traps in the literature, though this does not seem to be a problem in the *in vivo* work to date.

The mutagenicity of many spin traps has been determined using Salmonella typhimurium histidine (−) mutants in the Ames test (Hampton *et al.*, 1981). This work showed that none of the eighteen spin traps tested were very potent mutagens and the commonly used spin traps (DMPO, PBN, and tNB) are not mutagenic at the levels tested.

20.1. Spin Trapping in Cells

Relatively little work has been done using spin trapping in whole cells and most of that involves the trapping of the oxygen-centered radicals, hydroxyl and superoxide.

Whole cells of *Methanobacterium formicicum* incubated aerobically with formate and DMPO results in an ESR spectrum clearly containing two distinct species, the DMPO/$\cdot CO_2^-$ radical adduct and the DMPO/$\cdot$OH radical adduct (Barber *et al.*, 1983). Competition experiments with ethanol failed to decrease the DMPO/$\cdot$OH radical adduct signal leading to the conclusion that free hydroxyl radicals were not produced. Since the oxidation of the hydroxylamine, OXANOH, to the corresponding nitroxide OXANO, was inhibited by superoxide dismutase, superoxide was shown to be produced (Rosen *et al.*, 1982b), although this assay is not specific for superoxide *per se* (Ross *et al.*, 1984). The DMPO/$\cdot$OH radical adduct was attributed to the formation of the DMPO-superoxide radical adduct, which was then enzymatically reduced to the DMPO-hydroxyl radical adduct. The sensitivity of this adduct to superoxide dismutase was not determined. When 4-POBN was used in the same system as the spin trap, a six-line spectrum with splitting constants of $a^N = 15.8$ G and $a_\beta^H = 3.4$ G was observed and assigned to 4-POBN-lipid peroxyl radical adducts. This latter assignment was based on a model system of lipoxygenase-linoleic acid in which a similar spectrum was reported to be observed only in the presence of oxygen; nevertheless this assignment is in error (Connor *et al.*, 1986a).

Incubation of cultured endothelial cell monolayers with menadione (in DMSO) in the presence of DMPO yields an ESR spectrum consisting of three species: the DMPO/$\cdot CH_3$ radical adduct, the DMPO/hydroxyl radical adduct, and the

DMPO/superoxide radical adduct (Rosen and Freeman, 1984). The apparent DMPO/hydroxyl radical adduct was attributed to the decomposition of DMPO/superoxide radical adduct, since the DMSO present was in excess concentration (40% greater than DMPO) and would have reacted with any free hydroxyl radical produced to form methyl radicals. This is the source of the small amount of methyl radical adduct formed. The DMPO-hydroxyl radical adduct was also not affected by the addition of catalase. DMPO is known to diffuse across cell walls (Rosen *et al.*, 1982b) so the question arises as to whether the superoxide formed is produced intra- or extracellularly. Experiments with succinoylated-cytochrome c reduction by superoxide and with cells maintained in 95% oxygen suggest that superoxide does not diffuse across the plasma membrane but is instead produced both intra- and extracellularly. Intracellularly formed DMPO-superoxide was not detected, but was proposed to be reduced by glutathione peroxidase to the DMPO-hydroxyl radical adduct.

Suspensions of erythrocytes produced *t*-butyloxyl free radicals from *t*-butyl hydroperoxide (Thornalley *et al.*, 1983) as discussed in Section 4 on hydroperoxides. In this case, the formation of the DMPO/$\cdot OC(CH_3)_3$ radical adduct in erythrocytes was slower than that in solutions of free oxyhemoglobin. In the cellular incubation, 60% of the DMPO/$\cdot OC(CH_3)_3$ radical adduct production occurred intracellularly as determined by observing the ESR signal of the supernatant separately. This could be done since the DMPO/$\cdot OC(CH_3)_3$ adduct is transported across the erythrocyte membrane slowly.

The incorporation of the spin-traps DMPO, PBN, 4-POBN, and tNB into cultured fetal mouse liver cells has been studied using UV irradiation of hydrogen peroxide as a source of hydroxyl radicals (Morgan *et al.*, 1985). The results indicate that only DMPO was incorporated into this type of cell. The viability of the cells after treatment with DMPO was at least 90%, so the toxic effects were minimal. The spin-trap tNB caused the cells to detach from the surface of the plate on which they were grown and also produced a marked decrease in viability. PBN, which is not very water soluble, did not produce a cell-dependent signal and so cell uptake of the spin trap could not be demonstrated. A more water-soluble analog of PBN, 4-POBN, produced only an artifactual signal and so was not usable.

In a very good recent paper Samuni *et al.* (1986) discuss the problems of spin-trapping oxygen-derived radicals inside cells and report the study of several cellular test systems with several spin traps. The radicals were generated by radiation which ensured the generation of water-derived radicals both inside and outside the cell in a homogeneous manner. The 4-POBN/$\cdot CH_3$ radical adduct was produced by irradiation of a solution of 4-POBN and DMSO, and was then mixed with red blood cells. The 4-POBN/$\cdot CH_3$ adduct was observed (a^N = 15.9 G and a_β^H = 2.65 G). The cells did not change the half-life of these adducts. The addition of chromium oxalate (a broadening agent which through spin-spin interaction with radicals causes the ESR signal to broaden so much that it is not observable) caused a decrease of about 70% in the ESR signal of the spin adduct. The magnitude of the residual signal was consistent with the volume of the red blood cells. In other words the spin adduct which diffused inside the cell was protected from the broadening agent, indicating the ease with which the spin adduct moves across the membrane. The broadening agent discriminates between the radical inside and outside the cell on the basis of location not on the basis of site of formation and so cannot be used to prove cellular formation of radicals. DMPO-hydroxyl radical adducts and DMPO-hydrogen atom adducts were produced by

irradiation of red blood cells in the presence of DMPO. The red blood cells decreased the DMPO adduct intensity compared to a cell-free system irradiated for the same length of time and, in fact, if the cells were added after irradiation, the DMPO-hydroxyl adduct decayed very rapidly. When chromium oxalate was added to the red blood cell system immediately after irradiation, no ESR signal was detected indicating that the ESR signal is due entirely to adducts outside the cell. When the hydroxyl and hydrogen atom scavenger polyethylene glycol (which cannot enter the cell because of its high molecular weight) was added to the system, only the ESR spectrum of the DMPO-polyethylene glycol ($a^N = 15.6$ G and $a_\beta^H = 22.5$ G) was observed. It was shown that the DMPO reversibly partitions between the cells and the surrounding medium, so the lack of a DMPO-hydroxyl radical adduct inside the cell must be due to the rapid decay of these adducts in cells. This means that in spin-trapping studies in cellular systems in which DMPO-hydroxyl radical adducts are detected, care must be taken to prove that they are formed inside the cell. In order to accurately use spin-trapping techniques within cells, it will be necessary to increase the stability of the spin adducts. The retardation of their currently facile reduction would be especially advantageous.

20.2. Site-Directed Spin Traps

In order to study mechanisms which involve radical intermediates of many physiological processes, it is necessary to localize the spin trap in a well-defined area of a cell, such as the cell membrane. Micelles and vesicles are membrane-mimetic systems which have been devised for studying membrane/solution interfaces. A limited number of spin-trapping studies have been conducted using these systems, though it is an area in which interest should increase in the future.

Bakalik and Thomas (1977) detected the formation of carbon-centered radicals from reactions of hydroxyl radicals in SDS solutions by spin trapping with tNB. Harbour and Bolton (1978) trapped the superoxide radical with DMPO in photolyzed TRITON X-100 micelles containing chlorophyll. Harbour and Hair (1980) used DMPO to trap hydroxyl, $S\dot{O}_4^-$, and carbon-centered radicals in a relatively complex microemulsion system and showed that radicals formed in either the aqueous or oil phase could be trapped. Walter *et al.* (1981, 1982) used the spin-trap α-(4-dodecyloxyphenyl)-*N*-*tert*-butyl nitrone (4-DoPBN) in SDS micelles to trap transient phenyl radicals generated either in the bulk aqueous phase or the hydrophobic region of the micelle. Janzen and Coulter (1984) have shown that of a series of spin traps [PBN, sodium 2-sulfonatophenyl *tert*-butyl nitrone (2-SSPBN), 4-trimethylaminophenyl *tert*-butyl nitrone, 4-*tert*-butylphenyl *tert*-butyl nitrone, and 4-dodecyloxyphenyl *tert*-butyl nitrone (4-DoPBN)] only the pair 2-SSPBN and 4-DoPBN have persistent spin adducts and can be used to trap radicals in the aqueous or hydrocarbon phase respectively, of SDS micelles. Barker *et al.* (1985) have tabulated splitting constants for phenyl, hydrogen atom, hydroxyl, and 2-cyano-2-propyl radical adducts of a series of DMPO-derived spin traps with long alkyl side-chains. The side-chains make these spin traps soluble in the hydrophobic portion of a micelle or similar structure. Because these spin traps are unsymmetrical, they have very different splittings from those observed with DMPO so care must be taken in spectral interpretation when these traps are used. For example the hydrogen-atom adduct of the nonsymmetric traps have two magnetically non-equivalent β-hydrogens.

20.3. *In Vivo* Spin Trapping

Comparatively little spin trapping has been done in living animals. One of the major drawbacks is producing a radical adduct which is stable enough to be detected. Most of the *in vivo* spin trapping has involved the trichloromethyl free radical formed in the metabolism of carbon tetrachloride. The trichloromethyl radical was first trapped with PBN *in vivo* in rats by Lai *et al.* (1979); the structure of the adduct was proven using [^{13}C]carbon tetrachloride by Poyer *et al.* (1980). In these studies the carbon tetrachloride was administered intragastrically and the adducts observed in liver extracts after the animal was sacrificed. The first report of the detection of a spin adduct of a free radical metabolite in a body fluid of a living whole animal was the report of the PBN/$\cdot CO_2^-$ radical adduct in rat urine from an animal treated orally with carbon tetrachloride (Connor *et al.*, 1986b). This radical adduct demonstrated ^{13}C splittings when [^{13}C]carbon tetrachloride was used. $CBrCl_3$ also forms PBN/$\cdot CO_2^-$ *in vivo* (LaCagnin *et al.*, 1988). Carbon-centered radicals from trihalomethanes (Tomasi *et al.*, 1985) and halothane (Poyer *et al.*, 1981; Plummer *et al.*, 1982; Fujii *et al.*, 1984) have also been trapped with PBN and detected in liver extracts of rats after treatment with the halogenated compound.

Knecht and Mason (1988) found the PBN/$^{13}\cdot CCl_3$ radical adduct in the bile of rats treated i.p. with PBN and with the $^{13}CCl_4$ injected directly into the stomach. Either hypoxia or pretreatment with phenobarbital increased the biliary concentration of the PBN/$\cdot CCl_3$ radical adduct and resulted in the formation of the PBN/$\cdot CO_2^-$ radical adduct as well.

In rats dosed with PBN prior to irradiation, PBN/carbon-centered lipid radicals were observed in lipid extracts from the brain, spleen, liver, and heart, but not from the kidney (Lai *et al.*, 1986). These ESR signals were observed in these tissues at the lowest nonlethal dose of radiation tested (2 Gy).

A carbon-centered lipid radical adduct with PBN was observed in hexane extracts of goat lungs after infusion of the whole animal with 3-methylindole and PBN (Kubow *et al.*, 1984). This *in vivo* radical adduct was shown to be inhibited by treatment with cysteine which is the precursor of GSH and to be increased by treatment with diethylmaleate which depletes GSH in many organs. The implication was that GSH found in the lung tissue reacts directly with the nitrogen-centered 3-methylindole radical before it can cause lung damage (see Section 11 for further discussion of this point).

When $(CH_3O)_3PBN$ was administered to animals *in vivo* along with $^{13}CCl_4$ a ^{13}C invariant spectrum assigned to $HO(CH_3O)_3PBN/L\cdot$ was detected in Folch extracts of the liver (McCay *et al.*, 1984). This study is clearly complicated by the *O*-demethylation of the spin trap. The same radical adduct is found in Folch extracts of liver or heart after rats are fed a high fat, ethanol-containing diet (Reinke *et al.*, 1987).

The reaction of oxyhemoglobin with phenylhydrazine and hydrazine-based drugs induces hemolytic anemia. Considerable evidence obtained from *in vitro* ESR experiments implicates free radicals in the events leading to red blood cell hemolysis (see Section 7). Maples *et al.* (1988) detected the formation of a radical adduct in the blood of rats which received an intragastic dose of phenylhydrazine followed by an intraperitoneal injection of DMPO. An immobilized radical adduct was detected when phenylhydrazine was administered in a dosage comparable to that prescribed for currently-employed, hydrazine-based drugs. Hydrazine itself gives a weaker spectrum of the same species. The immobilized radical adduct co-chromatographs with

oxyhemoglobin. The sulfhydryl reagents, iodoacetamide, maleimide, and *N*-ethylmaleimide, all inhibit phenylhydrazine-dependent radical adduct formation when whole rat blood is treated *in vitro* (Maples *et al.*, 1988). This sulfhydryl-dependent radical adduct has been assigned to a DMPO/thiyl oxyhemoglobin radical adduct. This is the first report of a radical adduct formation with a biochemical macromolecule as a consequence of free radical metabolism.

21. SPIN ADDUCT IDENTIFICATION

The spin-trapping technique has been successful in detecting a variety of free radical metabolites that could not have been detected with direct ESR. In general, tNB and DMPO give distinctive ESR spectra for a variety of radical adducts. Even though the spectra of these spin adducts are highly solvent-dependent and the local environment in biological systems is not well defined, the structure of the free radical that adds to tNB or DMPO can often be deduced from the ESR spectrum alone. Unfortunately, the spin adducts of tNB are often highly unstable. Although the adducts formed from PBN and 4-POBN are, in general, more stable than the corresponding tNB adducts, the hyperfine coupling constants are much less dependent on the structure of the trapped radical. In fact, for PBN and 4-POBN spin adducts, the magnitude of the hyperfine coupling constants' solvent dependence is generally greater than the effect of the structure of the actual radical trapped. Recently Li *et al.* (1988) have designed a database for spin adducts and successfully implemented it on an IBM PC/AT. With the advent of personal computers, the arduous job of spin-adduct identification could be greatly minimized.

In many cases the concentration of the spin adduct in the enzymatic incubation is too low to detect directly. Either a slow rate of formation of the free radical of interest or the enzymatic reduction of the spin adduct to its corresponding hydroxylamine can lead to a situation where either no signal or a very weak signal is observed in the incubation. Consequently, many investigators have resorted to organic solvent extraction of the spin adduct from large incubations. Subsequent concentration of the spin adduct leads to a large increase in the signal-to-noise ratio of the ESR signal, because aqueous solutions are limited to less than 100 μl for the active region of the largest ESR flat cell.

This extraction procedure adds at least two complications. First, unless the organic solvent is benzene, the literature values of the spin-adduct magnetic parameters will probably be unavailable. Consequently, several spin adducts have been misassigned (Kalyanaraman *et al.*, 1984). Second, the spin adduct(s) that are stable enough to survive extraction are not necessarily the predominant species in the incubation where the enzymes are active, and unstable spin adducts may be present in steady state. In these cases, a weak ESR signal can usually be observed in the active enzymatic incubations. Under these circumstances it is imperative to reextract the spin adduct into the buffer and compare this spectrum with that of the steady-state spin adduct (Kalyanaraman *et al.*, 1984).

As if to emphasize the inherent difficulties in assigning radical adduct spectra in organic solvents other than benzene, the hyperfine coupling constants of DMPO/·OH were interchanged in the work delineating the pitfalls of extraction (Trudell, 1987).

21.1. Isotope Methods

In some cases, isotopic substitution can be used for adduct identification. There are quite a few examples of this technique scattered throughout this review including: the use of [^{13}C]carbon tetrachloride to distinguish the PBN/·CCl_3 adduct from the PBN/lipid-derived radical adduct (Poyer *et al.*, 1980; Tomasi *et al.*, 1980); the use of [^{33}S]bisulfite to verify the assignment of the DMPO/·SO_3^- adduct (Mottley and Mason, 1988); the use of [^{17}O]oxygen and [^{17}O]water to verify the assignment of the DMPO, PBN, and 4-POBN adducts with hydroxyl and superoxide radicals (Mottley *et al.*, 1986); the use of (2,4-$^{13}C_2$)acetylacetone and (1,5-$^{2}H_3$)acetylacetone to prove the structures of radical adducts formed on the oxidation of these compounds by peroxidase enzymes (Mottley *et al.*, 1988); the use of indole-3-acetic-2,2-$^{2}H_2$ to prove the structure of the tNB adduct formed in the oxidation of this compound by horseradish peroxidase (Mottley and Mason, 1986); the use of [^{15}N] sodium azide in spin-trapping studies with PBN (Kalyanaraman *et al.*, 1985); and the use of [$^{2}H_7$]styrene in spin-trapping studies using tNB (Stock *et al.*, 1986b).

21.2. Isolation and Identification by HPLC, GC, and MS

An effective approach to the ambiguity of the ESR parameters is the isolation and purification of the spin adduct by chromatography and analysis by mass spectrometry. If a molecular ion is observed, the structure of the trapped radical can usually be determined unambiguously. It is important to compare the ESR spectrum of the purified spin adduct with the signal detected in the incubation, because small differences in hyperfine coupling constants of PBN or 4-POBN adducts may imply that a minor species has been isolated. A limited number of mass spectral analyses of spin adducts have been carried out but they include: the isolation from an autoxidation system of the DMPO/phenyl radical adduct using silica-gel chromatography and the unambiguous identification of the adduct with MS (Hill and Thornalley, 1981); the isolation by silica gel chromatography and subsequent identification by MS of the 4-POBN/ethyl radical adduct (Augusto, 1982a) and the 4-POBN/phenylethyl radical adduct (Ortiz de Montellano, 1983); the GC separation and MS identification of the hydroxyl and a number of aryl adducts with PBN and 4-POBN (Abe *et al.*, 1984); and the GC separation and the MS identification of the PBN-methyl and -ethyl adducts (Janzen *et al.*, 1985b).

HPLC has been used for separation and detection of several spin adducts. The tNB adducts formed in the γ-irradiation of aqueous solutions of glycylglycylglycine, glycylglycyl-L-alanine, glycyl-L-alanylglycine, and L-alanylglycylglycine were separated with HPLC and detected with ESR (Moriya *et al.*, 1984). A variety of spin adducts formed in the γ-irradiation of amino acids, dipeptides, and tripeptides in the presence of tNB were separated by HPLC on cation-exchange columns and detected with an ESR spectrometer (Makino *et al.*, 1985). The hydroxyl and superoxide adducts of DMPO were separated on an ODS reverse-phase HPLC column and detected electrochemically (Pritsos *et al.*, 1985). The electrochemical detection was confirmed by ESR. Stronks *et al.* (1984) separated several radical adducts of PBN by HPLC with both UV and electrochemical detection with confirmation by ESR. One advantage of the separation by HPLC (or other chromatographic techniques) is that it allows the separation

of radical adducts which may have very similar, if not identical, ESR spectra and cannot be separately identified in a composite spectrum.

22. SPIN ADDUCT IMPOSTERS

Sullivan (1966) proposed an ene addition reaction between nitrosobenzene and an olefin to explain the formation of a nitroxide radical addition product. Floyd *et al.* (1978) used the same scheme to account for the covalent binding of nitrosofluorene to oleic acid. Mason *et al.* (1980) observed that this reaction could occur with nitrosoalkanes such as *tert*-nitrosobutane. This addition reaction is a convenient method of independently synthesizing tNB-carbon-centered fatty acid spin adducts. Unfortunately, this nonfree radical reaction can lead to artifacts. In microsomal incubations containing carbon tetrachloride, a tNB-lipid radical adduct was observed (Kalyanaraman *et al.*, 1979a). However, further experiments suggest that the spectrum results from both enzymatic and nonenzymatic (ene) reactions with similar rates (Kalyanaraman, 1982). Nitrosobenzene is a known enophile, and the special importance of controls using heat-inactivated enzyme has been emphasized (Perkins, 1980).

It should be noted that the ene reaction forms a hydroxylamine, not a nitroxide product. If the oxidation of the hydroxylamine to a nitroxide is enzymatic, then even the heat-denatured control is inadequate. In fact, the authors know of no control that will differentiate an enzymatic spin-trapping reaction from an ene reaction of a nitroso spin trap with the radical precursor followed by the enzymatic oxidation of the hydroxylamine addition product to a spin-adduct imposter. The possibility of an ene reaction is increased by extraction with organic solvents, because the concentration of the nitroso spin trap is greatly increased, facilitating the ene reaction. The oxidation of the hydroxylamine addition product is also promoted by the higher concentration of oxygen in organic solvents. This type of ene reaction may be involved in the apparently anomalous results with tNB where extraction of the tNB-carbon-centered fatty acid adduct gave signal amplitudes that were independent of incubation time (Albano *et al.*, 1982). Similarly, nucleophilic attack of the radical precursor on a nitrone spin trap (Forrester and Hepburn, 1971) followed by enzymatic oxidation of the hydroxylamine addition product will also form a spin-adduct imposter.

The oxidation of DMPO by the hematin-cumene hydroperoxide system forms DMPOX (5,5-dimethyl-1-oxyl-2-pyrrolidine) (Floyd and Soong, 1977) via decomposition of the DMPO-cumylperoxyl radical adduct (Rosen and Rauckman, 1980). The very stable DMPOX is also observed as a product of metal-ion (Schaich and Borg, 1980) or horseradish peroxidase-hydrogen peroxide oxidation (Mottley and Mason, unpublished). The decomposition of DMPOX forms 4-methyl-4-nitroso-pentanoic acid (Hill and Thornalley, 1982b). During the oxidation of this compound to the corresponding nitro compound by ferricyanide, a nitrogen-centered radical is trapped by DMPO ($a^N = 14.3$ G, $a_\beta^H = 16.2$ G, and $a_\beta^N = 4.2$ G). The decomposition of DMPO by the HRP-H_2O_2 system also forms this unexpected species (Mottley and Mason, unpublished).

Nitroso-spin traps have been shown to be reduced to nitroxides by ascorbic acid (Mottley *et al.*, 1981), by the drug anthralin (Mottley *et al.*, 1981), by ferrous ion (Kalyanaraman *et al.*, 1979b), by sodium borohydride (Kalyanaraman *et al.*, 1979a, 1979b), and by microsomal incubations containing NADPH (Kalyanaraman *et al.*,

1979a, 1979b). Reduction of the spin trap has been mistakenly reported as adduct formation in at least two situations: the proposed hydroxyl radical adduct formation with tNB in a Fenton reaction (Lai and Piette, 1979) and the proposed trapping of the 1,8-dihydroxy-9-anthrone by 2,4,6-tri-*tert*-butyl-nitrosobenzene (Martinmaa *et al.*, 1978).

Nitrone-spin traps have lower reduction potentials than nitroso-spin traps and have been reported to be reduced to nitroxides in biological systems only in the presence of hydrazines. Incubation of hydralazine with red blood cells formed DMPO/·H (Sinha and Motten, 1982). Although hydralazine alone will not reduce DMPO, some stronger reducing agent was proposed, e.g., diimide or hydrazine may be formed from hydralazine in the presence of red blood cells. Hydrazine does reduce DMPO to DMPO/·H. In an investigation of phenylhydrazine-induced hemolysis (Hill and Thornalley, 1983), a lipophilic DMPO analogue, but not DMPO itself, was reduced to its hydrogen atom adduct leading to the mistaken report of a rearranged trapped lipid-derived free radical (Barker *et al.*, 1985).

Impurities in either the spin-trap solution or other constituents in the incubation can occasionally lead to misassigned radical adducts. A DMPO spin adduct with splitting constants $a^N = 14.5$ G and $a_\beta^H = 16.2$ G observed in incubations containing ram seminal vesicle microsomes and arachidonic acid was at first believed to be related to the production of prostaglandins (Smith *et al.*, 1981) but was later shown to be the DMPO/·SO_3^- adduct produced from the oxidation of the bisulfite added as an antioxidant to the arachidonic acid (Mottley *et al.*, 1982b). More recently, the trapping of a radical by DMPO during the oxidation of diethylstilbestrol (DES) by horseradish peroxidase and prostaglandin synthase was reported (Ross *et al.*, 1985d), but has since been shown to be due to an unknown impurity in the DMPO, probably a hydroxylamine derived from DMPO, which behaves as a radical indicator by being oxidized to a nitroxide (D. Ross, private communication).

23. SUMMARY

The spin-trapping technique makes possible the study of many free radical metabolites that cannot be detected directly by ESR, either because they do not have detectable direct ESR spectra for spectroscopic reasons or because they are too reactive to detect in biological systems where the radical production rates are limited. The major problem has been, and continues to be, the unambiguous determination of the spin-adduct structures. In this regard, isotopic substitution, chromatography, and mass spectrometry are valuable aids. Extreme care must be taken to ensure that the proposed adduct is legitimate and is not an impostor. The successful spin trapper must question all adducts until absolute proof of the structure is given, so the successful use of spin trapping demands chemical and biochemical ingenuity. Spin trapping is a powerful tool, but the many opportunities for error must be respected.

REFERENCES

Abe, K., Suezawa, H., Hirota, M., and Ishii, T., 1984, Mass spectrometric determination of spin adducts of hydroxyl and aryl free radicals, *J. Chem. Soc., Perkin Trans. II*:29–34.

Adams, G. E., and Willson, R. L., 1969, Pulse radiolysis studies on the oxidation of organic radicals in aqueous solution, *Trans. Faraday Soc.* **65**:2981-2987.

Albano, E., and Tomasi, A., 1987, Spin trapping of free radical intermediates produced during the metabolism of isoniazid and iproniazid in isolated hepatocytes, *Biochem. Pharmacol.* **36**:2913-2920.

Albano, E., Lott, K. A. K., Slater, T. F., Stier, A., Symons, M. C. R., and Tomasi, A., 1982, Spin-trapping studies on the free-radical products formed by metabolic activation of carbon tetrachloride in rat liver microsomal fractions isolated hepatocytes and *in vivo* in the rat, *Biochem. J.* **204**:593-603.

Albano, E., Tomasi, A., Vannini, V., and Dianzani, M. U., 1985, Detection of free radical intermediates during isoniazid and iproniazid metabolism by isolated rat hepatocytes, *Biochem. Pharmacol.* **34**:381-382.

Albano, E., Tomasi, A., Goria-Gatti, L., Carini, R., Vannini, V., and Dianzani, M. U., 1986, Free radical metabolism of ethanol, in *Free Radicals, Cell Damage and Disease* (C. Rice-Evans, ed.), pp. 117-126, Richelieu Press, London.

Albano, E., Tomasi, A., Goria-Gatti, L., Poli, G., Vannini, V., and Dianzani, M. U., 1987, Free radical metabolism of alcohols by rat liver microsomes, *Free Rad. Res. Commun.* **3**:243-249.

Albano, E., Tomasi, A., Goria-Gatti, L., and Dianzani, M. U., 1988, Spin trapping of free radical species produced during the microsomal metabolism of ethanol, *Chem.-Biol. Interact.*, **65**:223-234.

Aoshima, H., Kajiwara, T., Hatanaka, A., and Hatano, H., 1977, Electron spin resonance studies on the lipoxygenase reaction by spin trapping and spin labelling methods, *J. Biochem.* **82**:1559-1565.

Arroyo, C. M., Kramer, J. H., Dickens, B. F., and Weglicki, W. B., 1987, Identification of free radicals in myocardial ischemia/reperfusion by spin trapping with nitrone DMPO, *FEBS Lett.* **221**:101-104.

Augusto, O., and Ortiz de Montellano, P. R., 1981, Spin-trapping of free radicals formed during microsomal metabolism of ethylhydrazine and acetylhydrazine, *Biochem. Biophys. Res. Commun.* **101**:1324-1330.

Augusto, O., Beilan, H. S., and Ortiz de Montellano, P. R., 1982a, The catalytic mechanism of cytochrome P-450. Spin-trapping evidence for one-electron substrate oxidation, *J. Biol. Chem.* **257**:11288-11295.

Augusto, O., Kunze, K. L., and Ortiz de Montellano, P. R., 1982b, *N*-phenylprotoporphyrin IX formation in the hemoglobin-phenylhydrazine reaction, *J. Biol. Chem.* **257**:6231-6241.

Augusto, O., Faljoni-Alário, A., Leite, L. C. C., and Nóbrega, F. G., 1984, DNA strand scission by the carbon radical derived from 2-phenylethylhydrazine metabolism, *Carcinogenesis* **5**:781-784.

Augusto, O., Du Plessis, L. R., and Weingrill, C. L. V., 1985, Spin-trapping of methyl radical in the oxidative metabolism of 1,2-dimethylhydrazine, *Biochem. Biophys. Res. Commun.* **126**:853-858.

Bakalik, D. P., and Thomas, J. K., 1977, Micellar catalysis of radical reactions. A spin trapping study, *J. Phys. Chem.* **81**:1905-1908.

Barber, M. J., Rosen, G. M., Siegel, L. M., and Rauckman, E. J., 1983, Evidence for formation of superoxide and formate radicals in *Methanobacterium formicicum*, *J. Bacteriol.* **153**:1282-1286.

Barker, P., Beckwith, A. L. J., Cherry, W. R., and Huie, R., 1985, Characterization of spin adducts obtained with hydrophobic nitrone spin traps, *J. Chem. Soc., Perkin Trans. 2*:1147-1150.

Bascetta, E., Gunstone, F. D., Scrimgeour, C. M., and Walton, J. C., 1982, ESR observation of pentadienyl and allyl radicals on hydrogen abstraction from unsaturated lipids, *J. Chem. Soc., Chem. Commun.*:110-112.

Bateman, L., 1954, Olefin oxidation, *Q. Rev.* **8**:147-167.

Becker, A. R., and Sternson, L. A., 1980, Nonenzymatic reduction of nitrosobenzene to phenylhydroxylamine by NAD(P)H, *Bioorg. Chem.* **9**:305-312.

Bird, R. P., 1980, Cysteamine as a protective agent with high-LET radiations, *Radiat. Res.* **82**:290-296.

Bolland, J. L., 1950, Kinetic studies in the chemistry of rubber and related materials. VII. Influence of chemical structure on the α-methylenic reactivity of olefins, *Trans. Faraday Soc.* **46**:358-368.

Bothe, E., Schuchmann, M. N., Schulte-Frohlinde, D., and von Sonntag, C., 1978, $HO_2^{\cdot}$ elimination from α-hydroxyalkylperoxyl radicals in aqueous solution, *Photochem. Photobiol.* **28**:639-644.

Buettner, G. R., 1982, The spin trapping of superoxide and hydroxyl radicals, in *Superoxide Dismutase*, Vol. II (L. W. Oberley, ed.), pp. 63-81, CRC Press, Boca Raton, Florida.

Buettner, G. R., and Oberley, L. W., 1980, The apparent production of superoxide and hydroxyl radicals by hematoporphyrin and light as seen by spin-trapping, *FEBS Lett.* **121**:161-164.

Bus, J. S., and Gibson, J. E., 1979, Lipid peroxidation and its role in toxicology, in *Reviews in Biochemical Toxicology*, Vol. 1 (E. Hodgson, J. R. Bend, and R. M. Philpot, eds.), pp. 125-149, Elsevier/North-Holland, New York.

Butler, T. C., 1961, Reduction of carbon tetrachloride *in vivo* and reduction of carbon tetrachloride and chloroform *in vitro* by tissues and tissue constituents, *J. Pharmacol. Exp. Ther.* **134**:311-319.

Cadenas, E., Boveris, A., and Chance, B., 1980, Low-level chemiluminescence of hydroperoxide-supplemented cytochrome c, *Biochem. J.* **187**:131-140.

Cederbaum, A. I., and Cohen, G., 1980, Inhibition of the microsomal oxidation of ethanol and 1-butanol by the free-radical, spin-trapping agent 5,5-dimethyl-1-pyrroline-1-oxide, *Arch. Biochem. Biophys.* **204**:397-403.

Cederblad, G., 1980, On the occurrence of cysteine sulfinate in human urine, *Biochem. Med.* **24**:103-109.

Chan, P. C., and Bielski, B. H. J., 1974, Enzyme-catalyzed free radical reactions with nicotinamide adenine nucleotides, *J. Biol. Chem.* **249**:1317-1319.

Chan, P. C., and Bielski, B. H. J., 1980, Glyceraldehyde-3-phosphate dehydrogenase-catalyzed chain oxidation of reduced nicotinamide adenine dinucleotide by perhydroxyl radicals, *J. Biol. Chem.* **255**:874-876.

Chance, B., 1952, The spectra of the enzyme-substrate complexes of catalase and peroxidase, *Arch. Biochem. Biophys.* **41**:404-415.

Chantry, G. W., Horsfield, A., Morton, J. R., Rowlands, J. R., and Whiffen, D. H., 1962, The optical and electron resonance spectra of SO_3^-, *Mol. Phys.* **5**:233-239.

Cheeseman, K. H., Albano, E. F., Tomasi, A., Dianzani, M. U., and Slater, T. F., 1985, The effects of the spin traps PBN and 4-POBN on microsomal drug metabolism and hepatocyte viability, *Life Chem. Rep.* **3**:259-264.

Chignell, C. F., Kalyanaraman, B., Mason, R. P., and Sik, R. H., 1980, Spectroscopic studies of cutaneous photosensitizing agents. I. Spin trapping of photolysis products from sulfanilamide, 4-aminobenzoic acid and related compounds, *Photochem. Photobiol.* **32**:563-571.

Chignell, C. F., Kalyanaraman, B., Sik, R. H., and Mason, R. P., 1981, Spectroscopic studies of cutaneous photosensitizing agents. II. Spin trapping of photolysis products from sulfanilamide and 4-aminobenzoic acid using 5,5-dimethyl-1-pyrroline-1-oxide, *Photochem. Photobiol.* **34**:147-156.

Cinti, D. L., 1978, Agents activating the liver microsomal mixed function oxidase system, *Pharm. Ther: A* **2**:727-749.

Connor, H. D., Fischer, V., and Mason, R. P., 1986a, A search for oxygen-centered free radicals in the lipoxygenase/linoleic acid system, *Biochem. Biophys. Res. Commun.* **141**:614-621.

Connor, H. D., Thurman, R. G., Galizi, M. D., and Mason, R. P., 1986b, The formation of a novel free radical metabolite from CCl_4 in the perfused rat liver and *in vivo*, *J. Biol. Chem.* **261**:4542-4548.

Cunningham, M. L., Chang, S. Y., and Sipes, I. G., 1985, Covalent adduct formation and chloroform production after free radical attack on fatty-acids by carbon tetrachloride reactive intermediates, *Toxicology* **37**:297-305.

Davies, M. J., Forni, L. G., and Shuter, S. L., 1987, Electron spin resonance and pulse radiolysis studies on the spin trapping of sulphur-centered radicals, *Chem.-Biol. Interact.* **61**:177-188.

De Groot, J. J. M. C., Garssen, G. J., Vliegenthart, J. F. G., and Boldingh, J., 1973, The detection of linoleic acid radicals in the anaerobic reaction of lipoxygenase, *Biochim. Biophys. Acta* **326**:279-284.

Dix, T. A., and Marnett, L. J., 1981, Free radical epoxidation of 7,8-dihydroxy-7,8-dihydrobenzo[*a*]pyrene by hematin and polyunsaturated fatty acid hydroperoxides, *J. Am. Chem. Soc.* **103**:6744-6746.

Dix, T. A., and Marnett, L. J., 1983, Metabolism of polycyclic aromatic hydrocarbon derivatives to ultimate carcinogens during lipid peroxidation, *Science* **221**:77-79.

Dix, T. A., Fontana, R., Panthani, A., and Marnett, L. J., 1985, Hematin-catalyzed epoxidation of 7,8-dihydroxy-7,8-dihydrobenzo[*a*]pyrene by polyunsaturated fatty acid hydroperoxides, *J. Biol. Chem.* **260**:5358-5365.

Drewer, R. J., 1975, The photochemistry of the hydrazo, azo and azoxy groups, in *The Chemistry of the Hydrazo, Azo and Azoxy Groups* (Saul Patai, ed.), pp. 935-1015, Wiley, New York.

Egan, R. W., Paxton, J., and Kuehl, F. A., Jr., 1976, Mechanism for irreversible self-deactivation of prostaglandin synthetase, *J. Biol. Chem.* **251**:7329-7335.

Egmond, M. R., Veldink, G. A., Vliegenthart, J. F. G., and Boldingh, J., 1973, C-11 H-abstraction from linoleic acid, the rate-limiting step in lipoxygenase catalysis, *Biochem. Biophys. Res. Commun.* **54**:1178-1184.

Eling, T., Boyd, J., Reed, G., Mason, R., and Sivarajah, K., 1983, Xenobiotic metabolism by prostaglandin endoperoxide synthetase, *Drug Metab. Rev.* **14**:1023-1053.

Eling, T. E., Mason, R. P., and Sivarajah, K., 1985, The formation of aminopyrine cation radical by the peroxidase activity of prostaglandin H synthase and subsequent reactions of the radical, *J. Biol. Chem.* **260**:1601-1607.

Eling, T. E., Curtis, J. F., Harman, L. S., and Mason, R. P., 1986, Oxidation of glutathione to its thiyl free radical metabolite by prostaglandin H synthase, *J. Biol. Chem.* **261**:5023-5028.

Eling, T. E., Krauss, R. S., Petry, T. W., Mottley, C., and Mason, R. P., 1988, The formation of a tryptophan carbon-centered free radical catalyzed by prostaglandin hydroperoxidase and horseradish peroxidase, unpublished data.

Eriksson, U. G., Brasch, R. C., and Tozer, T. N., 1987, Nonenzymatic bioreduction in rat liver and kidney of nitroxyl spin labels, potential contrast agents in magnetic resonance imaging, *Drug Metab. Dispos.* **15**:155-160.

Evans, C. A., 1979, Spin trapping, *Aldrichimica Acta* **12**:23-29.

Evans, J. C., Jackson, S. K., Rowlands, C. C., and Barratt, M. D., 1985, ENDOR, triple resonance and ESR studies of spin-trapped radicals in autoxidized linoleic acid and its deuterated derivatives, *Biochim. Biophys. Acta* **835**:421-425.

Farmer, E. H., 1946, Peroxidation in relation to olefinic structure, *Trans. Faraday Soc.* **46**:228-236.

Finkelstein, E., Rosen, G. M., Rauckman, E. J., and Paxton, J., 1979, Spin trapping of superoxide, *Mol. Pharmacol.* **16**:676-685.

Finkelstein, E., Rosen, G. M., and Rauckman, E. J., 1980, Spin trapping of superoxide and hydroxyl radical: practical aspects, *Arch. Biochem. Biophys.* **200**:1-16.

Finkelstein, E., Rosen, G. M., and Rauckman, E. J., 1982, Production of hydroxyl radical by decomposition of superoxide spin-trapped adducts, *Mol. Pharmacol.* **21**:262-265.

Fitzpatrick, P. F., and Villafranca, J. J., 1986, The mechanism of inactivation of dopamine β-hydroxylase by hydrazines, *J. Biol. Chem.* **261**:4510-4518.

Floyd, R. A., and Soong, L. M., 1977, Spin trapping in biological systems. Oxidation of the spin trap 5,5-dimethyl-1-pyrroline-1-oxide by a hydroperoxide-hematin system, *Biochem. Biophys. Res. Commun.* **74**:79-84.

Floyd, R. A., Soong, L. M., Stuart, M. A., and Reigh, D. L., 1978, Free radicals and carcinogenesis: Some properties of the nitroxyl free radicals produced by covalent binding of 2-nitrosofluorene to unsaturated lipids of membranes, *Arch. Biochem. Biophys.* **185**:450-457.

Forrester, A. R., and Hepburn, S. P., 1971, Spin traps. A cautionary note, *J. Chem. Soc.* (*C*):701-703.

Fujii, K., Morio, M., Kikuchi, H., Ishihara, S., Okida, M., and Ficor, F., 1984, *In vivo* spin-trap study on anaerobic dehalogenation of halothane, *Life Sci.* **35**:463-468.

Gerber, J. G., MacDonald, J. S., Harbison, R. D., Villeneuve, J-P., Wood, A. J. J., and Nies, A. S., 1977, Effect of N-acetylcysteine on hepatic covalent binding of paracetamol (acetaminophen), *Lancet*:657-658.

Gilbert, B. C., Laue, H. A. H., Norman, R. O. C., and Sealy, R. C., 1975, Electron spin resonance studies. Part XLVI. Oxidation of thiols and disulphides in aqueous solution: Formation of RS·, RSO·, RSO_2·, $RSSR^{\cdot-}$, and carbon radicals, *J. Chem. Soc. Perkin Trans. 2*:892-900.

Goldberg, B., Stern, A., and Peisach, J., 1976, The mechanism of superoxide anion generation by the interaction of phenylhydrazine with hemoglobin, *J. Biol. Chem.* **251**:3045-3051.

Green, M. J., Hill, H. A. O., and Tew, D. G., 1985, Applications of spin-trapping to biological systems, *Biochem. Soc. Trans.* **13**:600-603.

Griffin, B. W., 1980, Detection of free radical species derived from cumene hydroperoxide in model hemeprotein systems and in rat liver microsomes by spin-trapping techniques, in *Microsomes, Drug Oxidations and Chemical Carcinogenesis*, Vol. 1 (M. J. Coon, A. H. Conney, R. W. Estabrook, H. V. Gelboin, J. R. Gillette, and P. J. O'Brien, eds.), pp. 319-322, Academic Press, New York.

Griffin, B. W., 1982, Use of spin traps to elucidate radical mechanisms of oxidations by hydroperoxides catalyzed by hemoproteins, *Can. J. Chem.* **60**:1463-1473.

Griffin, B. W., and Ramirez, D., 1981, Electron paramagnetic resonance probes of the radical decomposition of cumene hydroperoxide initiated by metmyoglobin, *Bioorg. Chem.* **10**:177-188.

Griffin, B. W., and Ting, P. L., 1978, Spin trapping evidence for free radical oxidants of aminopyrine in the metmyoglobin-cumene hydroperoxide system, *FEBS. Lett.* **89**:196-200.

Gunnison, A. F., 1981, Sulphite toxicity: A critical review of *in vitro* and *in vivo* data, *Food Cosmet. Toxicol.* **19**:667-682.

Hamberg, M., and Samuelsson, B., 1967, On the mechanism of the biosynthesis of prostaglandins E_1 and $F_{1\alpha}$, *J. Biol. Chem.* **242**:5336-5343.

Hammel, K. E., Tien, M., Kalyanaraman, B., and Kirk, T. K., 1985, Mechanism of oxidative $C_\alpha-C_\beta$ cleavage of a lignin model dimer by *Phanerochaete chrysosporium* ligninase, *J. Biol. Chem.* **260**:8348-8353.

Hammel, K. E., Kalyanaraman, B., and Kirk, T. K., 1986, Substrate free radicals are intermediates in ligninase catalysis, *Proc. Natl. Acad. Sci. U.S.A.* **83**:3708-3712.

Hampton, M. J., Floyd, R. A., Janzen, E. G., and Shetty, R. V., 1981, Mutagenicity of free-radical spin-trapping compounds, *Mutat. Res.* **91**:279-283.

Harbour, J. R., and Bolton, J. R., 1975, Superoxide formation in spinach chloroplasts: Electron spin resonance detection by spin trapping, *Biochem. Biophys. Res. Commun.* **64**:803-807.

Harbour, J. R., and Bolton, J. R., 1978, The involvement of the hydroxyl radical in the destructive photooxidation of chlorophylls *in vivo* and *in vitro*, *Photochem. Photobiol.* **28**:231-234.

Harbour, J. R., and Hair, M. L., 1979, Spin trapping of the $\cdot CO_2^-$ radical in aqueous medium, *Can. J. Chem.* **57**:1150-1152.

Harbour, J. R., and Hair, M. L., 1980, Detection of radicals in microemulsions using spin trapping techniques, *J. Phys. Chem.* **84**:1500-1503.

Harbour, J. R., and Issler, S. L., 1982, Involvement of the azide radical in the quenching of singlet oxygen by azide anion in water, *J. Am. Chem. Soc.* **104**:903-905.

Harbour, J. R., Chow, V., and Bolton, J. R., 1974, An electron spin resonance study of the spin adducts of OH and HO_2 radicals with nitrones in the ultraviolet photolysis of aqueous hydrogen peroxide solutions, *Can. J. Chem.* **52**:3549-3553.

Harman, L. S., Mottley, C., and Mason, R. P., 1984, Free radical metabolites of L-cysteine oxidation, *J. Biol. Chem.* **259**:5606-5611.

Harman, L. S., Carver, D. K., Schreiber, J., and Mason, R. P., 1986, One- and two-electron oxidation of reduced glutathione by peroxidases, *J. Biol. Chem.* **261**:1642-1648.

Hayatsu, H., 1976, Bisulfite modification of nucleic acids and their constituents, *Prog. Nucleic Acid Res. Mol. Biol.* **16**:75-124.

Hayatsu, H., and Miller, R. C. Jr., 1972, The cleavage of DNA by the oxygen-dependent reaction of bisulfite, *Biochem. Biophys. Res. Commun.* **46**:120-124.

Hayon, E., Treinin, A., and Wilf, J., 1972, Electronic spectra, photochemistry, and autoxidation mechanism of the sulfite-bisulfite-pyrosulfite systems. The SO_2^-, SO_3^-, SO_4^-, and SO_5^- radicals, *J. Am. Chem. Soc.* **94**:47-57.

Hill, H. A. O., and Thornalley, P. J., 1981, Phenyl radical production during the oxidation of phenylhydrazine and in phenylhydrazine-induced haemolysis, *FEBS Lett.* **125**:235-238.

Hill, H. A. O., and Thornalley, P. J., 1982a, Free radical production during phenylhydrazine-induced hemolysis, *Can. J. Chem.* **60**:1528-1531.

Hill, H. A. O., and Thornalley, P. J., 1982b, The oxidative ring opening of the cyclic nitrone spin trap 5,5-dimethyl-1-pyrroline-1-oxide (DMPO): Free radical involvement, *Inorg. Chim. Acta* **67**:L35-L36.

Hill, H. A. O., and Thornalley, P. J., 1983, The effect of spin traps on phenylhydrazine-induced haemolysis, *Biochim. Biophys. Acta* **762**:44-51.

Horie, S., Watanabe, T., and Ogura, Y., 1980, Studies on the enzymatic reduction of C-nitroso compounds, *J. Biochem.* **88**:847-857.

Howard, J. A., and Tait, J. C., 1978, Electron paramagnetic resonance spectra of the *tert*-butylperoxy and *tert*-butoxy adducts to phenyl *tert*-butyl nitrone and 2-methyl-2-nitrosopropane. Oxygen-17 hyperfine coupling constants, *Can. J. Chem.* **56**:176-178.

Hozumi, M., Inuzuka, S., and Sugimura, T., 1967, Oxidation of sulfhydryl compounds *in vitro* by 4-hydroxyaminoquinoline-1-oxide, a carcinogenic metabolite of 4-nitroquinoline-1-oxide, *Cancer Res.* **27**:1378-1383.

Huie, R. E., and Neta, P., 1985, Oxidation of ascorbate and a tocopherol analogue by the sulfite-derived radicals $\dot{S}O_3^-$ and $\dot{S}O_5^-$, *Chem.-Biol. Interact.* **53**:233-238.

Inouye, B., Ikeda, M., Ishida, T., Ogata, M., Akiyama, J., and Utsumi, K., 1978, Participation of superoxide free radical and Mn^{2+} in sulfite oxidation, *Toxicol. Appl. Pharmacol.* **46**:29-38.

Janzen, E. G., 1980, A critical review of spin trapping in biological systems, in *Free Radicals in Biology*, Vol. IV (W. A. Pryor, ed.), pp. 115-154, Academic Press, New York.

Janzen, E. G., and Coulter, G. A., 1984, Spin trapping in SDS micelles, *J. Am. Chem. Soc.* **106**:1962-1968.

Janzen, E. G., and Evans, C. A., 1973, Rate constants for spin trapping *tert*-butoxy radicals as studied by electron spin resonance, *J. Am. Chem. Soc.* **95**:8205-8206.

Janzen, E. G., Nutter, D. E., Jr., Davis, E. R., Blackburn, B. J., Poyer, J. L., and McCay, P. B., 1978, On spin trapping hydroxyl and hydroperoxyl radicals, *Can. J. Chem.* **56**:2237-2242.

Janzen, E. G., Stronks, H. J., Nutter, D. E., Jr., Davis, E. R., Blount, H. N., Poyer, J. L., and McCay, P. B., 1980, Spin trapping azidyl ($N_3\cdot$), cyanatyl (OCN·), cyanyl (·CN) radicals and chlorine atom (Cl·), *Can. J. Chem.*. **58**:1596-1598.

Janzen, E. G., Coulter, G. A., Oehler, U. M., and Bergsma, J. P., 1982, Solvent effects on the nitrogen and β-hydrogen hyperfine splitting constants of aminoxyl radicals obtained in spin trapping experiments, *Can. J. Chem.* **60**:2725-2733.

Janzen, E. G., Stronks, H. J., Dubose, C. M., Poyer, J. L., and McCay, P. B., 1985a, Chemistry and biology of spin-trapping radicals associated with halocarbon metabolism *in vitro* and *in vivo*, *Environ. Health Perspect.* **64**: 151-170.

Janzen, E. G., Weber, J. R., Haire, D. L., and Fung, D. M., 1985b, Gas chromatography-mass spectroscopy (GC/MS) of single and double spin adducts of PBN and the hydroxylamines of corresponding structure, *Anal. Lett.* **18**:1749-1757.

Janzen, E. G., Towner, R. A., and Haire, D. L., 1987, Detection of free radicals generated from the *in vitro* metabolism of carbon tetrachloride using improved ESR spin trapping techniques, *Free Rad. Res. Commun.* **3**:357-364.

Janzen, E. G., Towner, R. A., and Brauer, M., 1988, Factors influencing the formation of the carbon dioxide radical anion ($\cdot CO_2^-$) spin adduct of PBN in the rat liver metabolism of halocarbons, *Free Rad. Res. Commun.* **4**:359-369.

Jocelyn, P. C., 1972, *Biochemistry of the SH Group*, pp. 323-336, Academic Press, New York.

Jones, P., Mantle, D., Davies, D. M., and Kelly, H. C., 1977, Hydroperoxidase activities of ferrihemes: Heme analogues of peroxidase enzyme intermediates, *Biochemistry* **16**:3974-3978.

Kalyanaraman, B., 1982, Detection of toxic free radicals in biology and medicine, in *Reviews in Biochemical Toxicology*, Vol. 4 (E. Hodgson, J. R. Bend, and R. M. Philpot, eds.), pp. 73-139, Elsevier Biomedical, New York.

Kalyanaraman, B., and Sohnle, P. G., 1985, Generation of free radical intermediates from foreign compounds by neutrophil-derived oxidants, *J. Clin. Invest.* **75**:1618-1622.

Kalyanaraman, B., Mason, R. P., Perez-Reyes, E., Chignell, C. F., Wolf, C. R., and Philpot, R. M., 1979a, Characterization of the free radical formed in aerobic microsomal incubations containing carbon tetrachloride and NADPH, *Biochem. Biophys. Res. Commun.* **89**: 1065-1072.

Kalyanaraman, B., Perez-Reyes, E., and Mason, R. P., 1979b, The reduction of nitroso-spin traps in chemical and biological systems. A Cautionary note, *Tetrahedron Lett.*:4809-4812.

Kalyanaraman, B., Perez-Reyes, E., and Mason, R. P., 1980, Spin-trapping and direct electron spin resonance investigations of the redox metabolism of quinone anticancer drugs, *Biochem. Biophys. Acta* **630**:119-130.

Kalyanaraman, B., Mottley, C., and Mason, R. P., 1983, A direct electron spin resonance and spin-trapping investigation of peroxyl free radical formation by hematin/hydroperoxide systems, *J. Biol. Chem.* **258**:3855-3858.

Kalyanaraman, B., Mottley, C., and Mason, R. P., 1984, On the use of organic extraction in the spin-trapping technique as applied to biological systems, *J. Biochem. Biophys. Methods* **9**:27-31.

Kalyanaraman, B., Janzen, E. G., and Mason, R. P., 1985, Spin trapping of the azidyl radical in azide/catalase/H_2O_2 and various azide/peroxidase/H_2O_2 peroxidizing systems, *J. Biol. Chem.* **260**:4003-4006.

Klebanoff, S. J., 1961, The sulfite-activated oxidation of reduced pyridine nucleotides by peroxidase, *Biochim. Biophys. Acta* **48**:93-103.

Knecht, K. T., and Mason, R. P., 1988, In vivo radical trapping and biliary secretion of radical adducts of carbon tetrachloride-derived free radical metabolites, *Drug. Metabol. Dispos.* **16**: 813-817.

Koga, G., Koga, N., and Anselme, J.-P., 1975, Radical reactions of azo, hydrazo and azoxy compounds, in *The Chemistry of the Hydrazo, Azo and Azoxy Groups* (Saul Patai, ed.), pp. 861-934, Wiley, New York.

Kosower, E. M., 1976, Pyridinyl radicals in biology, in *Free Radicals in Biology*, Vol. II (W. A. Pryor, ed.), pp. 1-53, Academic Press, New York.

Kramer, J. H., Arroyo, C. M., Dickens, B. F., and Weglicki, W. B., 1987, Spin-trapping evidence that graded myocardial ischemia alters post-ischemic superoxide production, *Free Rad. Biol. Med.* **3**:153-159.

Kremers, W., and Singh, A., 1980, Electron spin resonance study of spin-trapped azide radicals in aqueous solutions, *Can. J. Chem.* **58**:1592-1595.

Kubic, V. L., and Anders, M. W., 1980, Metabolism of carbon tetrachloride to phosgene, *Life Sci.* **26**:2151-2155.

Kubow, S., Dubose, C. M., Jr., Janzen, E. G., Carlson, J. R., and Bray, T. M., 1983, The spin-trapping of enzymatically and chemically catalyzed free radicals form indolic compounds, *Biochem. Biophys. Res. Commun.* **114**:168-174.

Kubow, S., Janzen, E. G. and Bray, T. M., 1984, Spin-trapping of free radicals formed during *in vitro* and *in vivo* metabolism of 3-methylindole, *J. Biol. Chem.* **259**:4447-4451.

Kubow, S., Bray, T. M., and Janzen, E. G., 1985, Spin-trapping studies on the effects of vitamin E and glutathione on free radical production induced by 3-methylindole, *Biochem. Pharmacol.* **34**:1117-1119.

Kudo, I., Miura, A., and Hayatsu, H., 1978, Inactivation of bacteriophage λ during the aerobic oxidation of bisulfite, *Environ. Res.* **16**:205-215.

LaCagnin, L. B., Connor, H. D., Mason, R. P., and Thurman, R. G., 1988, The carbon dioxide anion radical adduct in the perfused rat liver: Relationship to halocarbon-induced toxicity, *Mol. Pharmacol.*, **33**:351-357.

Lai, C-S., and Piette, L. W., 1979, Further evidence for OH radical production in Fenton's reagent, *Tetrahedron Lett.*:775-778.

Lai, E. K., McCay, P. B., Noguchi, T., and Fong, K.-L., 1979, *In vivo* spin-trapping of trichloromethyl radicals formed from CCl_4, *Biochem. Pharmacol.* **28**:2231-2235.

Lai, E. K., Crossley, C., Sridhar, R., Misra, H. P., Janzen, E. G., and McCay, P. B., 1986, *In vivo* spin trapping of free radicals generated in brain, spleen, and liver during γ radiation of mice, *Arch. Biochem. Biophys.* **244**:156-160.

Land, E. J., and Prütz, W. A., 1979, Reaction of azide radicals with amino acids and proteins, *Int. J. Radiat. Biol. Relat. Stud. Phys., Chem. Med.* **36**:75-83.

Larsson, A., Orrenius, S., Holmgren, A., and Mannervik, B. (eds.), 1983, *Functions of Glutathione: Biochemical, Physiological, Toxicological and Clinical Aspects*, Raven Press, New York.

Li, A. S. W., Cummings, K. B., Roethling, H. P., Buettner, G. R., and Chignell, C. F., 1988, A spin-trapping database implemented on the IBM PC/AT, *J. Magn. Res.* **79**:140-142.

Lizada, M. C. C., and Yang, S. F., 1981, Sulfite-induced lipid peroxidation, *Lipids* **16**:189-194.

Makino, K., Moriya, F., and Hatano, H., 1985, Separation of free radicals by high-performance liquid chromatography with electron spin resonance detection, *J. Chromatogr.* **332**:71-106.

Maples, K. R., Jordan, S. J., and Mason, R. P., 1988, In vivo rat hemoglobin thiyl free radical formation following phenylhydrazine administration, *Mol. Pharmacol.*, **33**:344-350.

Martinmaa, J., Vanhala, L., and Mustakallio, K. K., 1978, Free radical intermediates produced by autoxidation of 1,8-dihydroxy-9-anthrone (dithranol) in pyridine, *Experientia* **34**:872-873.

Mason, R. P., 1982, Free-radical intermediates in the metabolism of toxic chemicals, in *Free Radicals in Biology*, Vol. V (W. A. Pryor, ed.), pp. 161-222, Academic Press, New York.

Mason, R. P., 1984, Spin trapping free radical metabolites of toxic chemicals, in *Spin Labeling in Pharmacology* (J. L. Holtzman, ed.), pp. 87-129, Academic Press, New York.

Mason, R. P., and Mottley, C., 1987, Spin trapping free radical metabolites of inorganic chemicals, in *Electron Spin Resonance*, Vol. 10B (M. C. R. Symons, senior reporter), pp. 185-197, Royal Society of Chemistry, Alden Press, London.

Mason, R. P., Kalyanaraman, B., Tainer, B. E., and Eling, T. E., 1980, A carbon-centered free radical intermediate in the prostaglandin synthetase oxidation of arachidonic acid, *J. Biol. Chem.* **255**:5019-5022.

McCaustland, D. J., and Engel, J. F., 1975, Metabolites of polycyclic aromatic hydrocarbons. II. Synthesis of 7,8-dihydrobenzo[*a*]pyrene-7,8-diol and 7,8-dihydrobenzo[*a*]pyrene-7,8-epoxide, *Tetrahedron Lett.*:2549-2552.

McCay, P. B., Noguchi, T., Fong, K.-L., Lai, E. K., and Poyer, J. L., 1980, Production of radicals from enzyme systems and the use of spin traps, in *Free Radicals in Biology*, Vol. IV (W. A. Pryor, ed.), pp. 155-186, Academic Press, New York.

McCay, P. B., Lai, E. K., Poyer, J. L., DuBose, C. M., and Janzen, E. G., 1984, Oxygen- and carbon-centered free radical formation during carbon tetrachloride metabolism, *J. Biol. Chem.* **259**:2135-2143.

McCord, J. M., and Fridovich, I., 1968, The reduction of cytochrome c by milk xanthine oxidase, *J. Biol. Chem.* **243**:5753-5760.

McCord, J. M., and Fridovich, I., 1969, The utility of superoxide dismutase in studying free radical reactions. I. Radicals generated by the interaction of sulfite, dimethyl sulfoxide, and oxygen, *J. Biol. Chem.* **244**:6056-6063.

McGirr, L. G., Hadley, M., and Draper, H. H., 1985, Identification of N^{α}-acetyl-ε-(2-propenal)-lysine as a urinary metabolite of malondialdehyde, *J. Biol. Chem.* **260**:15427-15431.

Mead, J. F., 1976, Free radical mechanisms of lipid damage and consequences for cellular membranes, in *Free Radicals in Biology*, Vol. I (W. A. Pryor, ed.), pp. 51-68, Academic Press, New York.

Misra, H. P., and Fridovich, I., 1976, The oxidation of phenylhydrazine: superoxide and mechanism, *Biochemistry* **15**:681-687.

Miyamoto, T., Yamamoto, S., and Hayaishi, O., 1974, Prostaglandin synthetase system—resolution into oxygenase and isomerase components, *Proc. Natl. Acad. Sci. U.S.A.* **71**:3645-3648.

Moldéus, P., O'Brien, P. J., Thor, H., Berggren, M., and Orrenius, S., 1983, Oxidation of glutathione by free radical intermediates formed during peroxidase-catalyzed *N*-demethylation reactions, *FEBS Lett.* **162**:411-415.

Morehouse, K. M., and Mason, R. P., 1988, The transition metal-mediated formation of the hydroxyl free radical during the reduction of molecular oxygen by ferredoxin-ferredoxin:$NADP^+$ oxidoreductase, *J. Biol. Chem.* **263**:1204-1211.

Moreno, S. N. J., Schreiber, J., and Mason, R. P., 1986, Nitrobenzyl radical metabolites from microsomal reduction of nitrobenzyl chlorides, *J. Biol. Chem.* **261**:7811-7815.

Moreno, S. N. J., Stolze, K., Janzen, E. G., and Mason, R. P., 1988, Oxidation of cyanide to the cyanyl radical by peroxidase/H_2O_2 systems as determined by spin trapping, *Arch. Biochem. Biophys.* **265**:267-271.

Morgan, D. D., Mendenhall, C. L., Bobst, A. M., and Rouster, S. D., 1985, Incorporation of the spin trap DMPO into cultured fetal mouse liver cells, *Photochem. Photobiol.* **42**: 93-94.

Moriya, F., Makino, K., Suzuki, N., Rokushika, S., and Hatano, H., 1980, Studies on spin-trapped radicals in γ-irradiated aqueous solutions of glycine and L-alanine by high-performance liquid chromatography and ESR spectroscopy, *J. Phys. Chem.* **84**:3085-3090.

Moriya, F., Iguchi, N., Makino, K., Rokushika, S., and Hatano, H., 1984, Studies on γ-irradiated aqueous solutions of tripeptides composed of glycine and L-alanine by the spin-trap high-performance liquid chromatography-electron spin resonance method, *Can. J. Chem.* **62**:2206-2216.

Mottley, C., and Mason, R. P., 1986, An electron spin resonance study of free radical intermediates in the oxidation of indole acetic acid by horseradish peroxidase, *J. Biol. Chem.* **261**:16860-16864.

Mottley, C., and Mason, R. P., 1988, Sulfate anion free radical formation by the peroxidation of (bi)sulfite and its reaction with hydroxyl radical scavengers, *Arch. Biochem. Biophys.* **267**: 681-689.

Mottley, C., Kalyanaraman, B, and Mason, R. P., 1981, Spin trapping artifacts due to the reduction of nitroso spin traps, *FEBS Lett.* **130**:12-14.

Mottley, C., Trice, T. B., and Mason, R. P., 1982a, Direct detection of the sulfur trioxide radical anion during the horseradish peroxidase-hydrogen peroxide oxidation of sulfite (aqueous sulfur dioxide), *Mol. Pharmacol.* **22**:732-737.

Mottley, C., Mason, R. P., Chignell, C. F., Sivarajah, K., and Eling, T. E., 1982b, The formation of sulfur trioxide radical anion during the prostaglandin hydroperoxidase-catalyzed oxidation of bisulfite (hydrated sulfur dioxide), *J. Biol. Chem.* **257**:5050-5055.

Mottley, C., Connor, H. D., and Mason, R. P., 1986, [^{17}O]oxygen hyperfine structure for the hydroxyl and superoxide radical adducts of the spin traps DMPO, PBN and 4-POBN, *Biochem. Biophys. Res. Commun.* **141**:622-628.

Mottley, C., Toy, K., and Mason, R. P., 1987, Oxidation of thiol drugs and biochemicals by the lactoperoxidase/hydrogen peroxide system, *Mol. Pharmacol.* **31**:417-421.

Mottley, C., Robinson, R. E., and Mason, R. P., 1988, Free radical formation in the oxidation of malondialdehyde and acetylacetone by horseradish peroxidase, unpublished data.

Murray, M., and Ryan, A. J., 1982, Inhibition and enhancement of mixed-function oxidases by nitrogen heterocycles, *Biochem. Pharmacol.* **31**:3002-3005.

Nelson, S. D., Mitchell, J. R., Timbrell, J. A., Snodgrass, W. R. and Corcoran, G. B., III, 1976, Isoniazid and iproniazid: activation of metabolites to toxic intermediates in man and rat, *Science* **193**:901-903.

Nelson, S. D., Mitchell, J. R., Snodgrass, W. R., and Timbrell, J. A., 1978, Hepatotoxicity and metabolism of iproniazid and isopropylhydrazine, *J. Pharmacol. Exp. Ther.* **206**:574-585.

Neta, P., and Huie, R. E., 1985, Free-radical chemistry of sulfite, *Environ. Health Perspect.* **64**:209-217.

Niki, E., Yokoi, S., Tsuchiya, J., and Kamiya, Y., 1983, Spin trapping of peroxy radicals by phenyl-*N*-(*tert*-butyl)nitrone and methyl-*N*-durylnitrone, *J. Am. Chem. Soc.* **105**:1498-1503.

Nocerini, M. R., Yost, G. S., Carlson, J. R., Liberato, D. J., and Breeze, R. G., 1985, Structure of the glutathione adduct of activated 3-methylindole indicates that an imine methide is the electrophilic intermediate, *Drug Metab. Dispos.* **13**:690-694.

Noda, A., Noda, H., Ohno, K., Sendo, T., Misaka, A., Kanazawa, Y., Isobe, R., and Hirata, M., 1985, Spin trapping of a free radical intermediate formed during microsomal metabolism of hydrazine, *Biochem. Biophys. Res. Commun.* **133**:1086-1091.

Noguchi, T., Fong, K.-L., Lai, E. K., Alexander, S. S., King, M. M., Olson, L., Poyer, J. L., and McCay, P. B., 1982, Specificity of a phenobarbital-induced cytochrome P-450 for metabolism of carbon tetrachloride to the trichloromethyl radical, *Biochem. Pharmacol.* **31**:615-624.

Nugteren, D. H., Beerthuis, R. K., and Van Dorp., D. A., 1966, The enzymic conversion of *All-cis* 8,11,14-eicosatrienoic acid into prostaglandin E_1, *Recl. Trav. Chim. Pays-Bas* **85**:405-419.

Oesch, F., 1973, Mammalian epoxide hydrases: Inducible enzymes catalysing the inactivation of carcinogenic and cytotoxic metabolites derived from aromatic and olefinic compounds, *Xenobiotica* **3**:305-340.

Ohnishi, T., Yamazaki, H., Iyanagi, T., Nakamura, T., and Yamazaki, I., 1969, One-electron-transfer reactions in biochemical systems. II. The reaction of free radicals formed in the enzymic oxidation, *Biochim. Biophys. Acta* **172**:357-369.

Okhlobystina, L. V., Tyurikov, V. A., Shapiro, B. I., Syrkin, Ya. K., and Fainzil'berg, A. A., 1975, Investigation of the formation of free radicals in reactions of aliphatic nitro compounds by the method of radical traps. Communication 1. Production of a series of α-nitroalkanes and certain O- and N-containing radicals and their identification in the form of nitroxyl radicals by the ESR method, *Bull. Acad. Sci. USSR, Div. Chem. Sci.* (*Engl. Transl.*) **24**:2323-2329.

Ortiz de Montellano, P. R., Augusto, O., Viola, F., and Kunze, K. L., 1983, Carbon radicals in the metabolism of alkyl hydrazines, *J. Biol. Chem.* **258**:8623-8629.

Packer, J. E., Slater, T. F., and Willson, R. L., 1978, Reactions of the carbon tetrachloride-related peroxy free radical ($CCl_3O_2\cdot$) with amino acids: Pulse radiolysis evidence, *Life Sci.* **23**:2617-2620.

Paul, B. B., and Rubinstein, D., 1963, Metabolism of carbon tetrachloride and chloroform by the rat, *J. Pharmacol. Exp. Ther.* **141**:141-148.

Peiser, G. D., and Yang, S. F., 1979, Sulfite-mediated destruction of β-carotene, *J. Agric. Food Chem.* **27**:446-449.

Perez-Reyes, E., Kalyanaraman, B., and Mason, R. P., 1980, The reductive metabolism of metronidazole and ronidazole by aerobic liver microsomes, *Mol. Pharmacol.* **17**:239-244.

Perkins, M. J., 1980, Spin trapping, *Adv. Phys. Org. Chem.* **17**:1-64.

Petering, D. H., 1977, Sulfur dioxide: A view of its reactions with biomolecules, in *Biochemical Effects of Environmental Pollutants* (S. D. Lee, ed.), pp. 293-306, Ann Arbor Sci. Publ., Ann Arbor, Michigan.

Plummer, J. L., Beckwith, A. L. J., Bastin, F. N., Adams, J. F., Cousins, M. J., and Hall, P., 1982, Free radical formation *in vivo* and hepatotoxicity due to anesthesia with halothane, *Anesthesiology* **57**:160-166.

Porter, N. A., 1980, Prostaglandin endoperoxides, in *Free Radicals in Biology*, Vol. IV (W. A. Pryor, ed.), pp. 261-294, Academic Press, New York.

Porter, N. A., Weber, B. A., Weenen, H., and Khan, J. A., 1980, Autoxidation of polyunsaturated lipids. Factors controlling the stereochemistry of product hydroperoxides, *J. Am. Chem. Soc.* **102**:5597-5601.

Poyer, J. L., Floyd, R. A., McCay, P. B., Janzen, E. G., and Davis, E. R., 1978, Spin-trapping of the trichloromethyl radical produced during enzymic NADPH oxidation in the presence of carbon tetrachloride or bromotrichloromethane, *Biochim. Biophys. Acta* **539**:402-409.

Poyer, J. L., McCay, P. B., Lai, E. K., Janzen, E. G., and Davis, E. R., 1980, Confirmation of assignment of the trichloromethyl radical spin adduct detected by spin trapping during ^{13}C-carbon tetrachloride metabolism *in vitro* and *in vivo*, *Biochem. Biophys. Res. Commun.* **94**:1154-1160.

Poyer, J. L., McCay, P. B., Weddle, C. C., and Downs, P. E., 1981, *In vivo* spin trapping of radicals formed during halothane metabolism, *Biochem. Pharmacol.* **30**:1517-1519.

Prescott, L. F., Sutherland, G. R., Park, J., Smith, I. J., and Proudfoot, A. T., 1976, Cysteamine, Methionine, and penicillamine in the treatment of paracetamol poisoning, *Lancet* **II**:109-113.

Pritsos, C. A., Constantinides, P. P., Tritton, T. R., Heimbrook, D. C., and Sartorelli, A. C., 1985, Use of high performance liquid chromatography to detect hydroxyl and superoxide radicals generated from mitomycin C, *Anal. Biochem.* **150**:294-299.

Prütz, W. A., Butler, J., Land, E. J., and Swallow, A. J., 1980, Direct demonstration of electron transfer between tryptophan and tyrosine in proteins, *Biochem. Biophys. Res. Commun.* **96**:408-414.

Pryor, W. A., 1973, Free radical reactions and their importance in biochemical systems, *Fed. Proc., Fed. Am. Soc. Exp. Biol.* **32**:1862-1869.

Pryor, W. A., Prier, D. G., and Church, D. F., 1981, Radical production from the interaction of ozone and PUFA as demonstrated by electron spin resonance spin-trapping techniques, *Environ. Res.* **24**:42-52.

Rajagopalan, K. V., and Johnson, J. L., 1977, Biological origin and metabolism of SO_2, in *Biochemical Effects of Environmental Pollutants* (S. D. Lee, ed.), pp. 307-314, Ann Arbor Sci. Publ., Ann Arbor, Michigan.

Recknagel, R. O., Glende, E. A., Jr., and Hruszkewycz, A. M., 1977, Chemical mechanisms in carbon tetrachloride toxicity, in *Free Radicals in Biology*, Vol. III (W. A. Pryor, ed.), pp. 97-132, Academic Press, New York.

Reed, G. A., Brooks, E. A., and Eling, T. E., 1984, Phenylbutazone-dependent epoxidation of 7,8-dihydroxy-7,8-dihydrobenzo(*a*)pyrene, *J. Biol. Chem.* **259**:5591-5595.

Reed, G. A., Curtis, J. F., Mottley, C., Eling, T. E., and Mason, R. P., 1986, Epoxidation of (±)-7,8-dihydroxy-7,8-dihydrobenzo(*a*)pyrene during (bi)sulfite autoxidation:activation of a procarcinogen by a cocarcinogen, *Proc. Natl. Acad. Sci. U.S.A.* **83**:7499-7502.

Rehorek, D., Thomas, P., and Hennig, H., 1979, Spin trapping of azide radicals in photolysis of azido cobalt (III) complexes, *Inorg. Chim. Acta* **32**:L1-L2.

Reinke, L. A., Lai, E. K., DuBose, C. M., and McCay, P. B., 1987, Reactive free radical generation *in vivo* in the heart and liver of ethanol-fed rats: Correlation with radical formation *in vitro*, *Proc. Natl. Acad. Sci. U.S.A.* **84**:9223-9227.

Reynolds, E. S., and Moslen, M. T., 1980, Free-radical damage in liver, in *Free Radicals in Biology* (W. A. Pryor, ed.), pp. 49-94, Academic Press, New York.

Rosen, G. M., and Finkelstein, E., 1985, Use of spin traps in biological systems, *Adv. Free Rad. Biol. Med.* **1**:345-375.

Rosen, G. M., and Freeman, B. A., 1984, Detection of superoxide generated by endothelial cells, *Proc. Natl. Acad. Sci. U.S.A.* **81**:7269-7273.

Rosen, G. M., and Rauckman, E. J., 1977, Formation and reduction of a nitroxide radical by liver microsomes, *Biochem. Pharmacol.* **26**:675-678.

Rosen, G. M., and Rauckman, E. J., 1980, Spin trapping of the primary radical involved in the activation of the carcinogen *N*-hydroxy-2-acetylaminofluorene by cumene hydroperoxide-hematin, *Mol. Pharmacol.* **17**:233-238.

Rosen, G. M., and Rauckman, E. J., 1981a, Spin traping of free radicals during hepatic microsomal lipid peroxidation, *Proc. Natl. Acad. Sci. U.S.A.* **78**:7346-7349.

Rosen, G. M., and Rauckman, E. J., 1981b, The spin trapping of biologically generated free radicals, in *Oxygen and Oxy-radicals in Chemistry and Biology* (M. A. J. Rodgers and E. L. Powers, eds.), pp. 97-108, Academic Press, New York.

Rosen, G. M., and Rauckman, E. J., 1982, Carbon tetrachloride-induced lipid peroxidation: A spin trapping study, *Toxicol. Lett.* **10**:337-344.

Rosen, G. M., Rauckman, E. J., and Finkelstein, E., 1980, Spin trapping of radical species involved in the propagation of lipid peroxidation, in *Autoxidation in Food and Biological Systems* (M. G. Simic and M. Karel, eds.), pp. 71-87, Plenum Press, New York.

Rosen, G. M., Kloss, M. W., and Rauckman, E. J., 1982a, Initiation of *in vitro* lipid peroxidation by *N*-hydroxynorcocaine and norcocaine nitroxide, *Mol. Pharmacol.* **22**:529-531.

Rosen, G. M., Finkelstein, E., and Rauckman, E. J., 1982b, A method for the detection of superoxide in biological systems, *Arch. Biochem. Biophys.* **215**:367-378.

Rosenthal, I., Mossoba, M. M., and Riesz, P., 1982, Spin trapping with 2-methyl-2-nitrosopropane: photochemistry of carbonyl-containing compounds. Methyl radical formation from dimethyl sulfoxide, *Can. J. Chem.* **60**:1486-1492.

Ross, D., Albano, E., Nilsson, U., and Moldéus, P., 1984, Thiyl radicals—formation during peroxidase-catalyzed metabolism of acetaminophen in the presence of thiols, *Biochem. Biophys. Res. Commun.* **125**:109-115.

Ross, D., Cotgreave, I., and Moldéus, P., 1985a, The interaction of reduced glutathione with active oxygen species generated by xanthine-oxidase-catalyzed metabolism of xanthine, *Biochim. Biophys. Acta* **841**:278-282.

Ross, D., Larsson, R., Andersson, B., Nilsson, U., Lindquist, T., Lindeke, B., and Moldéus, P., 1985b, The oxidation of *p*-phenetidine by horseradish peroxidase and prostaglandin synthase and the fate of glutathione during such oxidations, *Biochem. Pharmacol.* **34**:343-351.

Ross, D., Norbeck, K., and Moldéus, P., 1985c, The generation and subsequent fate of glutathionyl radicals in biological systems, *J. Biol. Chem.* **260**:15028-15032.

Ross, D., Mehlhorn, R. J., Moldéus, P., and Smith, M. T., 1985d, Metabolism of diethylstilbestrol by horseradish peroxidase and prostaglandin-H synthase, *J. Biol. Chem.* **260**:16210-16214.

Saez, G., Thornalley, P. J., Hill, H. A. O., Hems, R., and Bannister, J. V., 1982, The production of free radicals during the autoxidation of cysteine and their effect on isolated rat hepatocytes, *Biochim. Biophys. Acta* **719**:24-31.

Samuni, A., Carmichael, A. J., Russo, A., Mitchell, J. B., and Riesz, P., 1986, On the spin trapping and ESR detection of oxygen-derived radicals generated inside cells, *Proc. Natl. Acad. Sci. U.S.A.* **83**:7593-7597.

Saprin, A. N., and Piette, L. H., 1977, Spin trapping and its application in the study of lipid peroxidation and free radical production with liver microsomes, *Arch. Biochem. Biophys.* **180**:480-492.

Sargent, F. P., and Gardy, E. M., 1976, Spin trapping of radicals formed during radiolysis of aqueous solutions. Direct electron spin resonance observations, *Can. J. Chem.* **54**:275-279.

Schäfer, K., Bonifačić, M., Bahnemann, D., and Asmus, K.-D., 1978, Addition of oxygen to organic sulfur radicals, *J. Phys. Chem.* **82**:2777-2780.

Schaich, K. M., and Borg, D. C., 1980, EPR studies in autoxidation, in *Autoxidation in Food and Biological Systems* (M. G. Simic and M. Karel, eds.), pp. 45-70, Plenum Press, New York.

Schreiber, J., Eling, T. E., and Mason, R. P., 1986a, The oxidation of arachidonic acid by the cyclooxygenase activity of purified prostaglandin H synthase: Spin trapping of a carbon-centered free radical intermediate, *Arch. Biochem. Biophys.* **249**:126-136.

Schreiber, J., Mason, R. P., and Eling, T. E., 1986b, Carbon-centered free radical intermediates in the hematin- and ram seminal vesicle-catalyzed decomposition of fatty acid hydroperoxides, *Arch. Biochem. Biophys.* **251**:17-24.

Schreiber, J., Foureman, G. L., Hughes, N. F., Mason, R. P., and Eling, T. E., 1989, Detection of GSH thiyl free radical catalyzed by prostaglandin hydroperoxidase present in keratinocytes. Study of cooxidation in a cellular system, *J. Bio. Chem.*, to be published.

Sinha, B. K., 1983, Enzymatic activation of hydrazine derivatives. A spin trapping study. *J. Biol. Chem.* **258**:796-801.

Sinha, B. K., 1984, Metabolic activation of procarbazine: Evidence for carbon-centered free-radical intermediates, *Biochem. Pharmacol.* **33**:2777-2781.

Sinha, B. K., 1987, Activation of hydrazine derivatives to free radicals in the perfused rat liver: a spin trapping study, *Biochim. Biophys. Acta* **924**:261-269.

Sinha, B. K., and Motten, A. G., 1982, Oxidative metabolism of hydralazine. Evidence for nitrogen centered radicals formation, *Biochem. Biophys. Res. Commun.* **105**:1044-1051.

Sinha, B. K., and Patterson, M. A., 1983, Free radical metabolism of hydralazine: Binding and degradation of nucleic acids, *Biochem. Pharmacol.* **32**:3279-3284.

Siu, G. M., and Draper, H. H., 1982, Metabolism of malonaldehyde *in vivo* and *in vitro*, *Lipids* **17**:349-355.

Smith, F. L., Floyd, R. A., and Carpenter, M. P., 1981, Prostaglandin synthetase-dependent spin-trapped free radicals, in *Oxygen and Oxy-radicals in Chemistry and Biology* (M. A. J. Rodgers and E. L. Powers, eds.), pp. 743-745, Academic Press, New York.

Southerland, W. M., Akogyeram, C. O., Toghrol, F., Sloan, L., and Scherrer, R., 1982, Interaction of bisulfite with unsaturated fatty acids, *J. Toxicol. Environ. Health* **10**:479-491.

Sridhar, R., 1981, Accelerated oxygen consumption by catecholamines in the presence of aromatic nitro and nitroso compounds. Implications for neurotoxicity of nitro compounds, in *Oxygen and Oxy-radicals in Chemistry and Biology* (M. A. J. Rodgers and E. L. Powers, eds.), pp. 363-365, Academic Press, New York.

Steeken, S., and Schulte-Frohlinde, D., 1973, Fragmentation of radicals derived from glycolaldehyde and glyceraldehyde in aqueous solution. An EPR study, *Tetrahedron Lett.*:653-654.

Stier, A., and Sackmann, E., 1973, Spin labels as enzyme substrates. Heterogeneous lipid distribution in liver microsomal membranes, *Biochim. Biophys. Acta* **311**:400-408.

Stock, B. H., Bend, J. R., and Eling, T. E., 1986a, The formation of styrene glutathione adducts catalyzed by prostaglandin H synthase, *J. Biol. Chem.*, **261**:5959-5964.

Stock, B. H., Schreiber, J., Guenat, C., Mason, R. P., Bend, J. R., and Eling, T. E., 1986b, Evidence for a free radical mechanism of styrene-glutathione conjugate formation catalyzed by prostaglandin H synthase and horseradish peroxidase, *J. Biol. Chem.* **261**:15915-15922.

Stolze, K., and Mason, R. P., 1987, Spin trapping artifacts in DMSO, *Biochem. Biophys. Res. Commun.* **143**:941-946.

Stolze, K., Duling, D. R., and Mason, R. P., 1988, Spin adducts formed from nitroso spin traps and dithionite, *J. Chem. Soc., Chem. Commun.*:268-270.

Stronks, H. J., Janzen, E. G., and Weber, J. R., 1984, Electrochemical detection of PBN spin adduct aminoxyls (nitroxides) separated by high performance liquid chromatography, *Anal. Lett.* **17**:321-328.

Sullivan, A. B., 1966, Electron spin resonance studies of a stable arylnitroso-olefin adduct free radical, *J. Org. Chem.* **31**:2811-2817.

Symons, M. C. R., Albano, E., Slater, T. F., and Tomasi, A., 1982, Radiolysis of tetrachloromethane, *J. Chem. Soc., Faraday Trans. 1* **78**:2205-2214.

Taffe, B. G., Takahashi, N., Kensler, T. W., and Mason, R. P., 1987, Generation of free radicals from organic hydroperoxide tumor promotors in isolated mouse keratinocytes, *J. Biol. Chem.* **262**:12143-12149.

Tappel, A. L., 1961, Biocatalysts: Lipoxidase and hematin compounds, in *Autoxidation and Autoxidants* Vol. 1 (W. O. Lundberg, ed.), pp. 325-366, Wiley, New York.

Terabe, S., and Konaka, R., 1972, Spin trapping by use of nitroso-compounds. Part IV. Electron spin resonance studies on oxidation with nickel peroxide, *J. Chem. Soc., Perkin Trans. 2*:2163-2172.

Thornalley, P. J., 1984, The haemolytic reactions of 1-acetyl-2-phenylhydrazine and hydrazine: A spin trapping study, *Chem.-Biol. Interact.* **50**:339-349.

Thornalley, P. J., 1985, Monosaccharide autoxidation in health and disease, *Environ. Health Perspect.* **64**:297-307.

Thornalley, P. J., and Stern, A., 1984, The production of free radicals during the autoxidation of monosaccharides by buffer ions, *Carbohydrate Res.* **134**:191-204.

Thornalley, P. J., Trotta, R. J., and Stern, A., 1983, Free radical involvement in the oxidative phenomena induced by *tert*-butyl hydroperoxide in erythrocytes, *Biochim. Biophys. Acta* **759**:16-22.

Thornalley, P., Wolff, S., Crabbe, J., and Stern, A., 1984, The autoxidation of glyceraldehyde and other simple monosaccharides under physiological conditions catalysed by buffer ions, *Biochim. Biophys. Acta* **797**:276-287.

Timbrell, J. A., Mitchell, J. R., Snodgrass, W. R., and Nelson, S. D., 1980, Isoniazid hepatotoxicity: The relationship between covalent binding and metabolism *in vivo*, *J. Pharmacol. Exp. Ther.* **213**:364-369.

Tomasi, A., Albano, E., Lott, K. A. K., and Slater, T. F., 1980, Spin trapping of free radical products of CCl_4 activation using pulse radiolysis and high energy radiation procedures, *FEBS Lett.* **122**:303-306.

Tomasi, A., Albano, E., Dianzani, M. U., Slater, T. F., and Vannini, V., 1983a, Metabolic activation of 1,2-dibromoethane to a free radical intermediate by rat liver microsomes and isolated hepatocytes, *FEBS Lett.* **160**:191-194.

Tomasi, A., Albano, E., Vannini, V., and Dianzani, M. U., 1983b, Spin trapping of a free radical reactive intermediate during isoniazid metabolism in isolated hepatocytes, *IRCS Med. Sci.* **11**:851-852.

Tomasi, A., Albano, E., Bini, A., Botti, B., Slater, T. F., and Vannini, V., 1984, Free radical intermediates under hypoxic conditions in the metabolism of halogenated carcinogens, *Toxicol. Pathol.* **12**:240-246.

Tomasi, A., Albano, E., Biasi, F., Slater, T. F., Vannini, V., and Dianzani, M. U., 1985, Activation of chloroform and related trihalomethanes to free radical intermediates in isolated hepatocytes and in the rat *in vivo* as detected by the ESR-spin trapping technique, *Chem.-Biol. Interact.* **55**:303-316.

Tomasi, A., Albano, E., Banni, S., Botti, B., Corongiu, F., Dessi, M. A., Iannone, A., Vannini, V., and Dianzani, M. U., 1987, Free-radical metabolism of carbon tetrachloride in rat liver mitochondria. A study of the mechanism of activation, *Biochem. J.* **246**:313-317.

Trudell, J. R., 1987, Ethyl acetate extraction of spin-trapped free radicals: A reevaluation, *Free Rad. Biol. Med.* **3**:133-136.

Trudell, J. R., Bösterling, B., and Trevor, A., 1981, 1-Chloro-2,2,2-trifluoroethyl radical: Formation from halothane by human cytochrome P-450 in reconstituted vesicles and binding to phospholipids, *Biochem. Biophys. Res. Commun.* **102**:372-377.

Trudell, J. R., Bösterling, B., and Trevor, A. J., 1982, Reductive metabolism of carbon tetrachloride by human cytochromes P-450 reconstituted in phospholipid vesicles: Mass spectral identification of trichloromethyl radical bound to dioleoyl phosphatidylcholine, *Proc. Natl. Acad. Sci. U.S.A.* **79**:2678-2682.

Vidigal-Martinelli, C., Zinner, K., Kachar, B., Duŕan, N., and Cilento, G., 1979, Emission from singlet oxygen during the peroxidase-catalyzed oxidation of malonaldehyde, *FEBS Lett.* **108**:266-268.

Vliegenthart, J. F. G., and Veldink, G. A., 1982, Lipoxygenases, in *Free Radicals in Biology* Vol. V (W. A. Pryor, ed.), pp. 29-64, Academic Press, New York.

Von Sonntag, C., 1980, Free radical reactions of carbohydrates as studied by radiation techniques, *Adv. Carbohydr. Chem. Biochem.* **37**:7-77.

Walter, T. H., McIntire, G. L., Bancroft, E. E., Davis, E. R., Gierasch, L. M., and Blount, H. N., 1981, Interfacial spin trapping in model membrane systems, *Biochem. Biophys. Res. Commun.* **102**:1350-1357.

Walter, T. H., Bancroft, E. E., McIntire, G. L., Davis, E. R., Gierasch, L. M., Blount, H. N., Stronks, H. J., and Janzen, E. G., 1982, Spin trapping in heterogeneous electron transfer processes, *Can. J. Chem.* **60**:1621-1636.

Weiner, L. M., Woldman, Y. Y., and Lyakhovich, V. V., 1982, Possibility of activating substrates by cytochrome P-450, *Dev. Biochem.* **23**:501-508.

Witting, L. A., 1980, Vitamin E and lipid antioxidants in free-radical-initiated reactions, in *Free Radicals in Biology* Vol. IV (W. A. Pryor, ed.), pp. 295-319, Academic Press, New York.

Wolf, C. R., Harrelson, W. G., Jr., Nastainczyk, W. M., Philpot, R. M., Kalyanaraman, B., and Mason, R. P., 1980, Metabolism of carbon tetrachloride in hepatic microsomes and reconstituted monooxygenase systems and its relationship to lipid peroxidation, *Mol. Pharmacol.* **18**:553-558.

Yagi, H., Hernandez, O., and Jerina, D. M., 1975, Synthesis of (±)-7β,8α-dihydroxy-9β,10β-epoxy-7,8,-9,10-tetrahydrobenzo[*a*]pyrene, a potential metabolite of the carcinogen benzo[*a*]pyrene with stereochemistry related to the antileukemic triptolides, *J. Am. Chem. Soc.* **97**:6881-6883.

Yagi, H., Thakker, D. R., Hernandez, O., Koreeda, M., and Jerina, D. M., 1977, Synthesis and reactions of the highly mutagenic 7,8-diol 9,10-epoxides of the carcinogen benzo[*a*]pyrene, *J. Am. Chem. Soc.* **99**:1604-1611.

Yamada, T., Niki, E., Yokoi, S., Tsuchiya, J., Yamamoto, Y., and Kamiya, Y., 1984, Oxidation of lipids. XI. Spin trapping and identification of peroxy and alkoxy radicals of methyl linoleate, *Chem. Phys. Lipids* **36**:189-196.

Yang, S. F., 1970, Sulfoxide formation from methionine or its sulfide analogs during aerobic oxidation of sulfite, *Biochemistry* **9**:5008-5014.

Yang, S. F., 1973, Destruction of tryptophan during the aerobic oxidation of sulfite ions, *Environ. Res.* **6**:395-402.

Yoshimoto, A., Ito, H., and Tomita, K., 1970, Cofactor requirements of the enzyme synthesizing prostaglandin in bovine seminal vesicles, *J. Biochem.* (*Tokyo*) **68**:487-499.

11

Advantages of ^{15}N and Deuterium Spin Probes for Biomedical Electron Paramagnetic Resonance Investigations

Jane H. Park and Wolfgang E. Trommer

1. INTRODUCTION

^{15}N and deuterium spin labels significantly advanced the application of electron paramagnetic resonance (EPR) in the fields of biomedical science and molecular biology. Problems involving the motional dynamics of enzyme catalysis, protein/protein interactions, and membrane structure, which heretofore could not be addressed with EPR techniques, can now be investigated with highly quantitative approaches. The remarkable improvements afforded by isotopic substitutions of ^{15}N and deuterium are due to three factors: (1) simplification of EPR spectral line shapes by reduction in the number of peaks; (2) increased sensitivity of the spin labels as evidenced by the elevated amplitude of spectral peak heights; and (3) enhanced resolution caused by narrowing of peak widths and elimination of overlaps of peaks. These factors facilitate the accurate interpretation of EPR spectral data, particularly for structure-function studies of large proteins and membranes. The purpose of this review is to examine the extraordinary utility of the isotopically substituted spin labels by evaluation of selected EPR investigations which may have wide applicability for biomedical experimentation. Therefore, we shall not present a detailed review of recent literature, but rather outline the uses of these spin labels for structure-function studies of enzymes and for the interactions of proteins and membranes in normal and pathological states.

Briefly, as a historical note, the first isotopic incorporation of ^{15}N into the nitroxide moiety of spin labels was published by Brière *et al.* (1965) who verified the predicted

Jane H. Park • Department of Molecular Physiology and Biophysics, Vanderbilt University School of Medicine, Nashville, Tennessee 37232. **Wolfgang E. Trommer** • Department of Chemistry, University of Kaiserslautern, Kaiserslautern, Federal Republic of Germany.

simplification of the EPR spectra for spin-$\frac{1}{2}$ ^{15}N by reduction of the number of resonance peaks from three to two. Next, several deuterated spin labels were synthesized by Chiarelli and Rassat (1973) and improved sensitivity was noted. On the basis of these and other studies with isotopically substituted spin labels at low temperatures in organic solvents, a body of theoretical calculations accrued suggesting the potential benefits of ^{15}N and deuterium for biological investigations (Dalton *et al.*, 1974, 1975; Keith *et al.*, 1974; Hwang *et al.*, 1975; Hedrick *et al.*, 1979). In the biochemistry laboratory of Park and associates the theoretical propositions were experimentally realized with the synthesis of both deuterated and doubly substituted, ^{15}N-deuterated maleimide spin labels for studies of protein structure and membrane interactions (Figure 1) (Venkataramu *et al.*, 1981; Beth *et al.*, 1981a, 1981b). Subsequently, a number of isotopically substituted analogs of cofactors, substrates, and lipids were prepared for studies of molecular interactions with proteins and membranes. Thus the EPR field entered a new era of quantitation with a powerful capability for exploration of biological (molecular) problems.

The starting point for these pioneering studies was the chemical syntheses of the deuterium and ^{15}N,deuterium spin labels as carried out by Venkataramu *et al.* (1981). Since the synthetic techniques are so fundamental for the success of an EPR investigation, a separate Appendix at the end of this volume is devoted to the technical aspects of the prerequisite organic chemistry (see pages 615-634). Also of prime importance for biomedical research is (1) the choice of isotope(s) for substitution and (2) structural

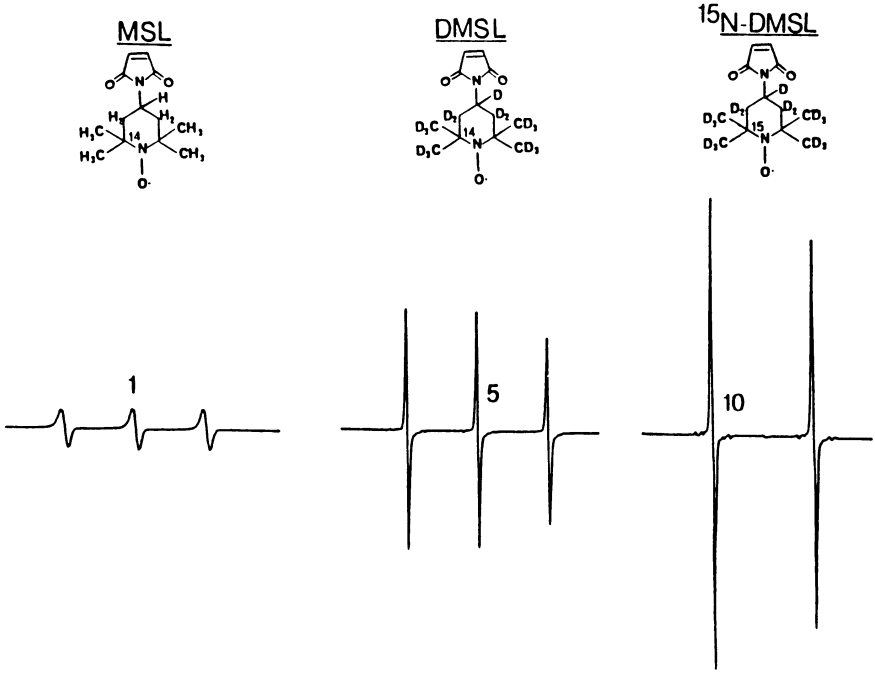

Figure 1. X-band EPR spectra of rapidly tumbling maleimide spin labels MSL, DMSL, and ^{15}N,DMSL at identical instrument settings.

design of the spin-labeled ligand. With regard to the choice of isotopes, in some cases double substitution, ^{15}N and deuterium, is most propitious. On the other hand, certain problems are approached optimally with either ^{15}N or deuterium as a single substitution. In the overall design of the spin-labeled ligand, three characteristics are desirable: (1) specificity of interaction with the designated groups on the protein or membranes; (2) retention of the structural conformation of the spin-labeled material; and (3) in certain cases, preservation of the activity or functions of the biological system. Clearly all ligands, including spin labels, fluorescent probes, coenzyme analogues, etc., introduce some degree of perturbation in a system. The EPR procedures for maximizing sensitivity and resolution while minimizing perturbations will be addressed subsequently in the examples in the text. Finally, for quantitation and accurate interpretation of EPR spectra, appropriate computational programs are often required. Such algorithms have been developed (Balasubramanian and Dalton, 1979; Robinson and Dalton, 1980) and applied to the analyses of complex EPR line shapes from spin-labeled proteins of biological significance (Beth *et al.*, 1981a, 1981b).

The intent of this review is to provide the reader with an EPR format for interesting possibilities and novel approaches to fundamental biomedical problems.

2. MALEIMIDE SPIN LABEL (DMSL OR ^{15}N,DMSL): A COVALENT LIGAND FOR SULFHYDRYL GROUPS OF PROTEINS

2.1. Advantages of Deuterated Maleimide Spin Label (DMSL) for Studies of Proteins

The synthesis and characterization of deuterated maleimide spin label (DMSL) established the utility of isotopically substituted labels for problems of biological importance (Beth *et al.*, 1980; Venkataramu *et al.*, 1981). First, comparison of the freely tumbling DMSL and unsubstituted MSL in solution showed a fivefold increase in peak height of the DMSL (Figure 1). It was established that the improvement in sensitivity was line-shape dependent and that the simple, homogeneous peaks of DMSL were sharper due to a threefold decrease in linewidth.

In order to evaluate the improvements for the protein-bound DMSL, the spin label was covalently attached to the one sulfhydryl (SH) group of bovine serum albumin (BSA), MW = 68,000. Three conditions were prerequisite for the accuracy of EPR measurements: (1) purity of the spin label; (2) homogeneity of the protein and covalent attachment of DMSL to a single amino acid; and (3) stability of the protein with regard to three-dimensional conformation. These conditions were met as evidenced by (1) chemical analyses of MSL and DMSL labels, (2) purification of the BSA and utilization of a protein with only one SH group, and (3) maintenance of the temperature of protein solutions at 2 °C, careful selection of protective buffers, a mild labeling procedure with removal of excess free radical on completion of the covalent binding of MSL or DMSL. Clearly, reliable EPR measurements are dependent upon exacting biochemical procedures. The sensitivity of the EPR spectra of DMSL-BSA complex showed a 1.3- to 1.8-fold increase in peak heights, relative to the MSL-BSA complex, and was dependent on the solvent conditions, either buffer or buffer/50% glycerol, respectively (Figure

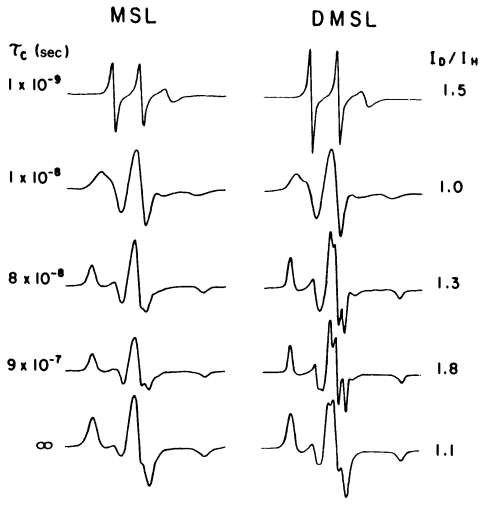

Figure 2. X-band EPR spectra of DMSL and MSL as freely tumbling or covalently bound to bovine serum albumin (BSA). The correlation times (τ_c) correspond to: 1×10^{-9} s, free spin label in 70% glycerol/30% buffer at 23 °C; 1×10^{-8} s, free label in glycerol at 11 °C; 8×10^{-8} s, spin-labeled BSA in buffer at 2 °C; 9×10^{-7} s, spin-labeled BSA in 50% glycerol at 2 °C; ∞, lyophilized-labeled BSA at 2 °C. The ratio I_D/I_H is the height of the DMSL signal compared to HMSL.

2). These spectra also demonstrate typical line-shape changes and broadening of peaks as the correlation time (τ_c) increases (motion decreases). More important was the improved sharpness in the peaks of the DMSL-BSA complex (Figure 3). The line shape was sufficiently resolved so that, for the first time, the EPR spectrum of a spin-labeled protein could be accurately simulated using the computerized curve-fitting program of Balasubramanian and Dalton (1979) (Figure 3, middle spectrum). Curve fitting was greatly facilitated by the fact that all the required parameters of the electron Zeeman (g) and electron-nitrogen nuclear hyperfine (A) tensors were apparent on the experimental EPR spectra and provided the initial estimates for the refinements of the computerized analysis (Beth *et al.*, 1980).

In order to examine slowly tumbling maleimide-albumin complexes in glycerol-buffer mixtures, the more advanced technique of saturation transfer EPR (ST-EPR) was employed because conventional EPR is not sufficiently sensitive for detailed characterization and differentiation of slow motional properties at correlation times (τ_c) $> 1 \times 10^{-7}$ s (Figure 4) (Thomas *et al.*, 1976). The ST-EPR spectra of DMSL-BSA also showed increases of 1.3- to 1.5-fold in sensitivity in the slow motional time range. Moreover, the detailed structurings of the line shape, particularly in the central portion of the DMSL-BSA spectra, were more sharply resolved. These improvements are critical for the computer-assisted analysis of highly immobilized, membrane-bound proteins, as will be discussed.

Deuterium substitution increased the sensitivity and resolution of almost all spectra (Figures 1-4) by narrowing of peak widths. The explanation for this sharpening of resonance lines is that deuterium (spin 1) has only one-seventh the magnetic moment of hydrogen (spin $\frac{1}{2}$). The latter possesses the largest magnetic moment of any of the naturally occurring stable nucleii. Since line broadening results from superhyperfine interactions of the magnetic moments of the nearby hydrogen atoms with the electron spin of nitroxide radical, isotopic substitution will substantially reduce the inhomogeneous line broadening. The above explanation has been verified quantitatively

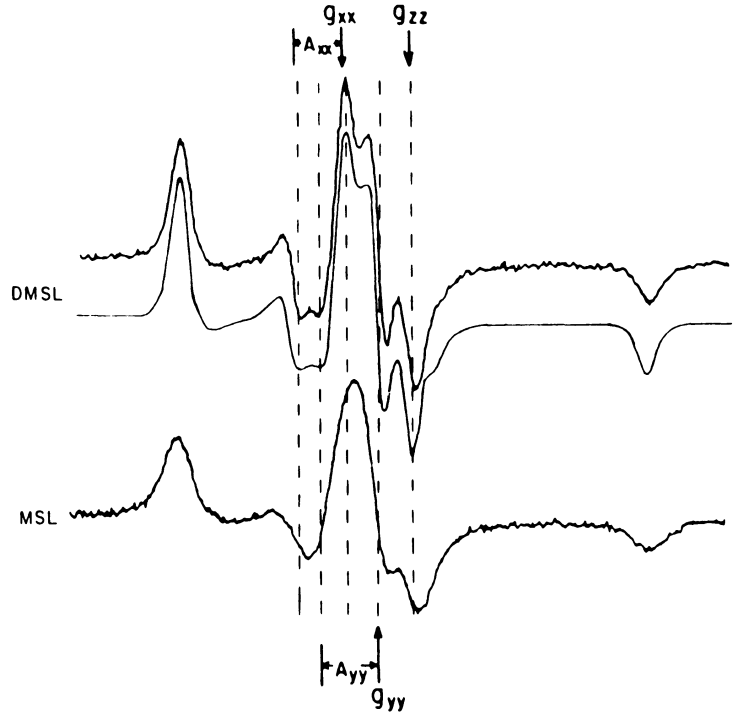

Figure 3. Comparison of rigid lattice line shapes of EPR spectra of DMSL and MSL bound to albumin (BSA) in 80% glycerol/20% buffer at 2 °C. The parameters used to simulate the experimental DMSL spectrum (middle) were: $g_{xx} = 2.0087$, $g_{yy} = 2.0056$, $g_{zz} = 2.0022$, $A_{xx} = 8.0$ G, $A_{yy} = 7.5$ G, $A_{zz} = 35.25$ G, $T_2 = 6 \times 10^{-8}$ s, and $T_1 = 1 \times 10^{-5}$ s.

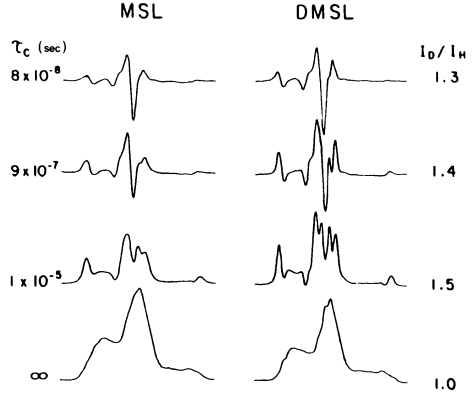

Figure 4. Comparison of ST-EPR spectra of DMSL and MSL bound to bovine serum albumin (BSA). The experimental conditions for the various correlation times (τ_c) are as follows: 8×10^{-8} s, 5 mM phosphate buffer; 9×10^{-7} s, 50% glycerol/50% buffer; 1×10^{-5} s, 80% glycerol/20% buffer; and ∞, lyophilized BSA-spin labeled complex. Each pair of spectra were recorded under identical instrumental conditions and I_D/I_H is the height of the DMSL line shape compared to that of MSL.

by second-harmonic in-phase absorption spectra as well as ENDOR data coupled with computer-generated curves (Beth *et al.*, 1980).

This simple model system (DMSL-BSA) suggested that the benefits afforded in the analysis of a low molecular weight monomer could be extrapolated to more complex proteins with interacting subunits.

2.2. Advantages of Doubly Substituted ^{15}N,Deuterated Maleimide Spin Label (^{15}N,DMSL)

In order to achieve additional gains in sensitivity and improved sharpening of the EPR peaks, the first doubly labeled spin probe was synthesized, namely, ^{15}N,DMSL (Beth *et al.*, 1981a). This spin label showed even greater gains in peak amplitude and resolution than the singly substituted DMSL (Figure 1). The signal height increase of freely tumbling ^{15}N,DMSL was tenfold compared to protonated MSL and twofold compared to DMSL. The latter twofold increase was due to the simplification of the ^{15}N-spectrum from three peaks to two peaks and secondarily to slightly increased deuterium content. This spectral simplification by ^{15}N substitution has proved advantageous in the investigation of a variety of proteins, because the reduction in the number of peaks in turn reduces the complicating overlaps of the broadened peaks of highly immobilized, protein-bound spin labels, as discussed in the following sections.

2.3. Advantages of ^{15}N,Deuterated Maleimide Spin Label (^{15}N,DMSL) for Studies of Soluble and Membrane-Bound Enzymes

2.3.1. Rationale for Selection of Glyceraldehyde-3-Phosphate Dehydrogenase (GAPDH) as the Model Protein for ^{15}N,DMSL Studies

The reasons for selecting glyceraldehyde-3-phosphate dehydrogenase for this investigation are presented here because this rationale may be generally applicable to a variety of EPR studies. First, this protein is an important enzyme as it catalyzes the oxidation of glyceraldehyde-3-phosphate in the presence of the coenzyme NAD^+ and inorganic phosphate and thereby produces 1,3-diphosphoglyceric acid, the initial high-energy phosphate compound in the pathway for glucose utilization (Structure 1).

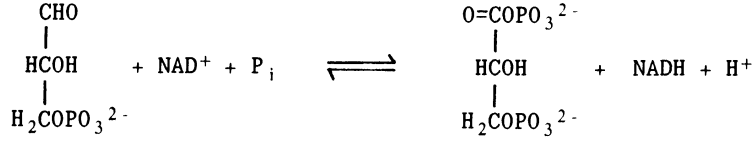

Structure 1.

Second, the enzyme is available in large amounts (1 gram quantities) as the pure, crystalline preparation (Hill *et al.*, 1975). Third, this dehydrogenase has been well-characterized biochemically and is known to be a tetramer with four chemically identical monomers containing a highly reactive cysteine at the active site, amino acid residue 149 (Harris *et al.*, 1963). These four active sites can be specifically labeled with maleimide or maleimide spin label to the exclusion of the 12 other sulfhydryl groups on the tetramer (Harris *et al.*, 1963; Beth *et al.*, 1979). Fourth, the binding of the MSL to the active sites decreases the catalytic activity in direct proportion to the number of bound spin labels. Last, the enzyme is catalytically active either as a soluble enzyme or as a membrane-bound enzyme in the presence of band-3 protein, the transmembrane anion transport protein of erythrocytes (Kant and Steck, 1973; McDaniel *et al.*, 1974; Cabantchik *et al.*, 1978). Since many enzymes are known to be bound to cell membranes or subcellular structures, such as mitochondria, the opportunity to investigate the immobilized glyceraldehyde-3-phosphate dehydrogenase was propitious for evaluation of the utility of the isotopically substituted spin labels to characterize membrane binding. The motional properties of this dehydrogenase were characterized in three very different physical states as the (1) soluble, (2) membrane-bound, and (3) solid crystalline enzyme.

2.3.2. Spin Labeling of GAPDH with MSL, DMSL, and ^{15}N,DMSL

Each of the three maleimide analogs were covalently bound to the SH group of the catalytic site of GAPDH under highly controlled conditions which had been optimized for ^{14}C-iodoacetic acid (IAA) (Harris *et al.*, 1963). Previous work with MSL showed that it was readily feasible to attach one MSL to one active site sulfhydryl group per tetramer and thereby inactivate 25% of the catalytic activity (Beth *et al.*, 1979). Extensive characterization of the spin-labeled enzyme indicated that (1) the active site SH group was specifically labeled, (2) the three-dimensional structure of the enzyme was preserved, and (3) the three unlabelled monomers were fully active with regard to catalytic dehydrogenation. Thus by all criteria the spin probes were monitoring the motion of uniformly labeled, undenatured macromolecules.

2.3.3. Comparison of the Advantages of ^{15}N,DMSL and DMSL Spin Labels for Studies of Soluble Enzymes

Improvements in spectral sensitivity (increase in peak heights) afforded by ^{15}N,DMSL for spin labeling of proteins are shown in Figure 5, upper row. The EPR spectra of GAPDH labeled with ^{15}N,DMSL or DMSL showed 2.9- and 1.5-fold increases in spectral amplitude compared to the parent compound, MSL. Similar gains in sensitivity were noted for hemoglobin and bovine serum albumin, suggesting the general applicability of the isotopically substituted probes (Beth *et al.*, 1981a). Increases were observed in buffer and glycerol solutions with a range of tumbling times from rapid ($\tau_c = 1.7 \times 10^{-7}$ s, in buffer) to very slow ($\tau_c = 1.6 \times 10^{-4}$ s, in 90% glycerol). These τ_c values correspond to the motional frequencies to be expected for soluble enzymes and enzyme complexes in the molecular-weight range from 10^5 to 10^8 or more.

The ST-EPR spectra of the ^{15}N,DMSL- or DMSL-labeled GAPDH also showed similar increases in sensitivity throughout the same correlation time range (Figure 5,

Figure 5. X-band EPR spectra (upper row) and ST-EPR spectra (lower row) of ^{15}N-DMSL, DMSL, and MSL covalently bound to glyceraldehyde-3-phosphate dehydrogenase (GAPDH). The EPR or ST-EPR spectra were acquired under identical conditions. The increased sensitivity of ^{15}N,DMSL (left) and DMSL (middle) is compared to MSL (right) at an assigned intensity of 1.0.

lower row). As in the case of BSA, the exact increase in sensitivity was dependent on the correlation time, but it was generally two- to threefold greater for the ^{15}N,DMSL-enzyme complex as compared to MSL-enzyme and 1.3- to 1.8-fold greater for DMSL-enzyme. Although these increases may seem small, in some cases of limiting amounts of enzyme the increased sensitivity coupled with improved resolution made quantitative analyses possible.

The enhanced resolution (sharpening of peaks) afforded by isotopic substitutions was more important for accurate spectral analysis by computer simulation than the increased sensitivity. As shown in Figure 6a for the normalized experimental spectrum of the ^{15}N,DMSL-enzyme in the rigid-lattice limit ($\tau_c = 2 \times 10^{-6}$ s), the structuring required for precise determination of all the elements of the nitrogen hyperfine (A) and electron Zeeman (g) tensors are clearly visible on the spectrum. This is due to the fact that the two nuclear manifolds of the ^{15}N-spin label, namely, $M_I = +\frac{1}{2}$ and $M_I = -\frac{1}{2}$, are completely separated (lower row). In the case of the DMSL-enzyme spectrum (Figure 6b), there is a more complex superposition of the three nuclear states ($M_I = +1, 0, -1$). The overlapping manifolds in the DMSL spectrum prohibit accurate measurement of at least one of the minor elements, A_{yy}. For the unsubstituted MSL-enzyme spectrum (Figure 5, right), neither the A_{yy} nor A_{xx} positions can be measured accurately. The calculated line shapes for the ^{15}N,DMSL and DMSL spectra (Balasubramanian and Dalton, 1979) are extremely good for both analogs, as seen in the dashed lines superimposed on the experimental spectra (Beth *et al.*, 1981a). However, the DMSL spectrum required much greater refinement and, hence, tenfold more computation time to obtain the desired accuracy than for the ^{15}N,DMSL spectrum.

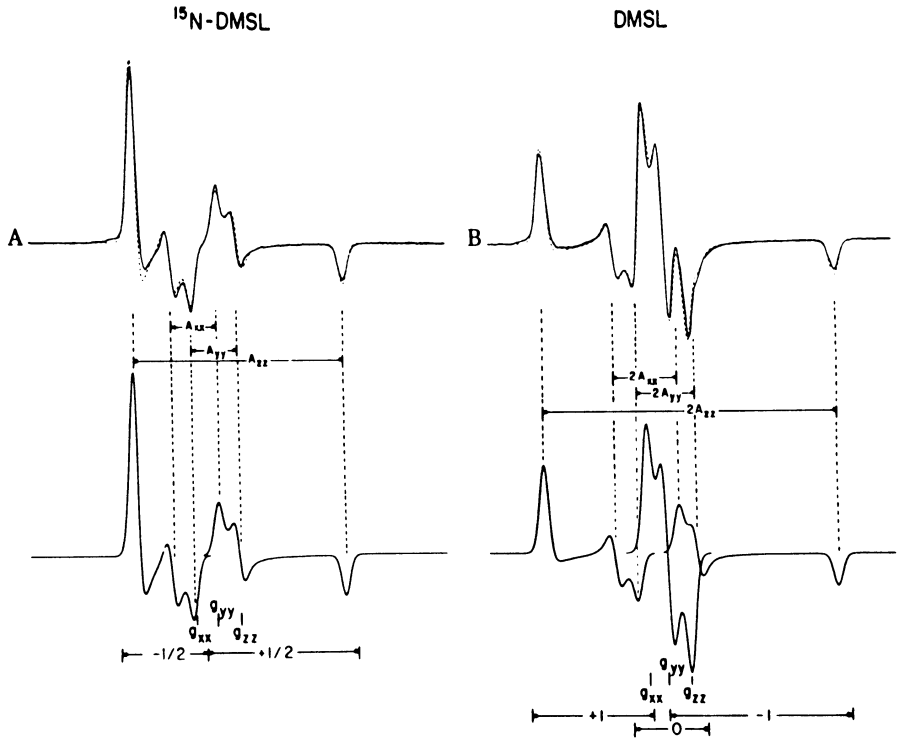

Figure 6. Simulations of normalized EPR spectra of ^{15}N-DMSL and DMSL covalently bound to GAPDH in 50% glycerol/50% buffer at 2 °C. Computer simulated spectra (- - - -) are superimposed on the experimental spectra (——). *A* and *g* tensor values as obtained from the experimental data are indicated as dashed, vertical lines running between the EPR spectra and the displays of the individual manifolds. Exact tensor values were determined using the algorithm of Balasubramanian and Dalton (1979).

This was due to the complexities of overlapping spectral features and the greater number of couplings required in the calculations.

The MSL spectrum could not be satisfactorily simulated employing the tensor values for the DMSL spectrum regardless of the linewidth used. The deuterated nitroxide label may have a slightly different ring conformation and interactions within the catalytic center by virtue of the altered steric effects of deuterium.

As a forerunner for studies on membrane-bound enzymes with slowed and restricted motion, GAPDH was examined in varying concentrations of glycerol by ST-EPR techniques, which have optimal sensitivity for characterization of molecules in the slow correlation time ranges. The ST-EPR spectra of the isotropically diffusing GAPDH labeled with ^{15}N,DMSL showed large spectral modifications throughout the correlation time range from 1×10^{-7} s to 1×10^{-4} s (Figure 7a-d). A simple method for appraising slow motional dynamics of the ^{15}N,DMSL-enzyme complex, as proposed by Robinson and Dalton (1980), is the measurement of the peaks *L*, *L'*, *L''*, *H*, and *H''* (Figure 7). Ratios of L'/L, L''/L, and H''/H are plotted against the correlation time and are

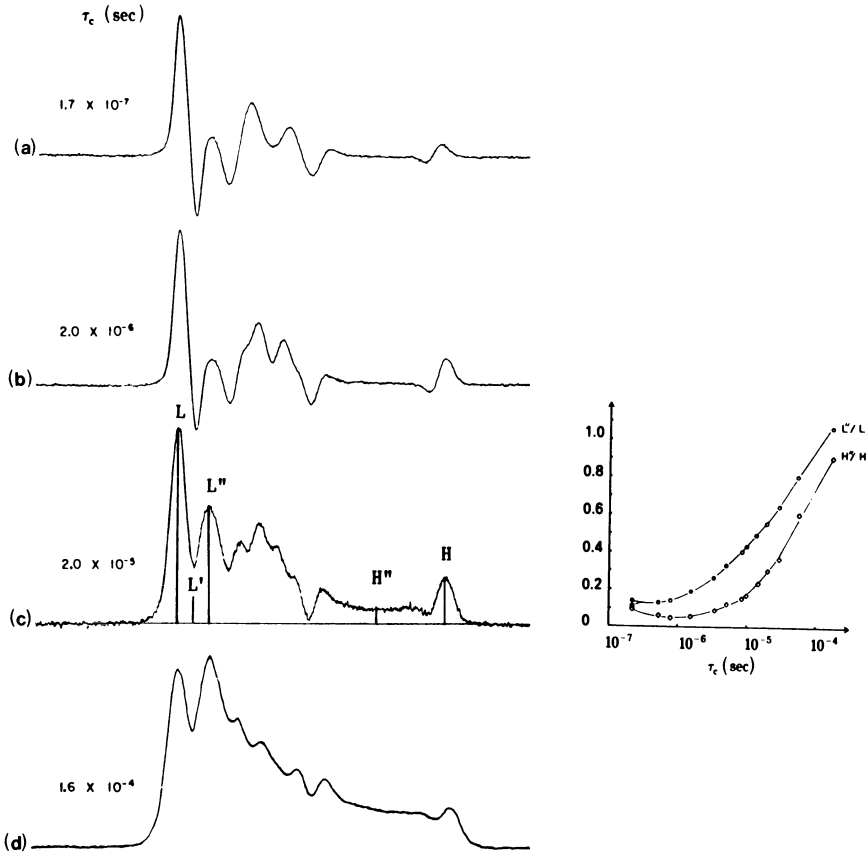

Figure 7. ST-EPR spectra of ^{15}N,DMSL-labeled GAPDH at 2 °C in phosphate buffer containing 0%, 52%, 77%, and 90% glycerol for spectra (a), (b), (c), and (d), respectively. Correlation times (τ_c) vary from 1.7×10^{-7} to 1.6×10^{-4} s as shown on the left side of the spectra. The parameters L, L', L'', H, and H'' are shown on spectrum (c). The plots of the ratio parameters are graphed against the correlation times (τ_c) in the insert.

sensitive to the rate at which the major axis of the nitroxide group along the Z axis is averaged into the minor plane of the X and Y axes (Figure 8a). As the motion is slowed, large changes, L'' and H'', occur relative to L and H. Slow rotational motion (τ_c) of other enzymes can also be analyzed similarly under a given set of conditions using ^{15}N,DMSL-labeled hemoglobin and BSA as standards for model plots of ratio parameters versus isotropic correlation times (Robinson and Dalton, 1980).

Similar analyses of ratios can be performed with ST-EPR spectra of the DMSL-dehydrogenase complex using L''/L, H''/H, and the additional parameter of C'/C in the central portion of the spectrum (see Figure 12, spectrum d, for C and C' positions). The C'/C ratio is an indication of the orientations of the X and Y axes and is a reflection of three nuclear manifolds ($M_I = +1, 0, -1$) instead of two ($M_I = -\frac{1}{2}, +\frac{1}{2}$) (Thomas *et al.*, 1976; Beth *et al.*, 1979, 1980). Since the line shapes of the deuterated

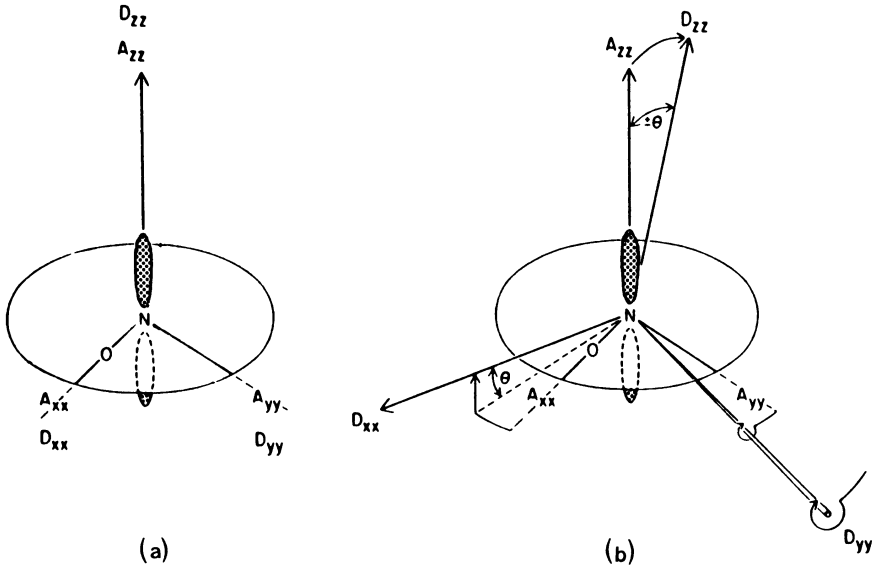

Figure 8. Spatial relationships of the magnetic (A and g) and diffusion (D) tensors of the nitroxide radical. The X axis is along the N—O bond, the Y axis lies in the C-N-C plane, and the Z axis extends along the nitrogen PZ orbital. The unpaired electron is localized mainly in the P_z orbital of nitrogen. The A and g magnetic tensors are assumed to be coincident. On the left (a), the magnetic and diffusion tensors are coincident. For isotropic diffusion models, $D_{xx} = D_{yy} = D_{zz}$ (Section 2.3.3). On the right (b) the coordinate systems A and D are related by the angle Θ arising from the rotation of D_{zz} (Section 2.3.5; $\theta = 90°$).

spin labels are more highly resolved than the protonated counterparts, the accuracy for determination of all peak ratios is improved compared to protonated spin labels. However, the ratios for a DMSL-enzyme complex may not precisely compare with those for the protonated labels (Beth *et al.*, 1981a). Therefore, if this comparative method is used for estimation of correlation times, standard ratio plots should be made using DMSL-labeled hemoglobin and BSA. As pointed out for the determination of correlation times by comparisons with hemoglobin and GAPDH labeled with protonated spin probes (Beth *et al.*, 1979), differences in the conformations and magnetic interactions of proteins in glycerol/water mixtures may also lead to errors in interpretation with deuterated probes. This arises because the value of C'/C is dependent on the extent of overlap of the three nuclear manifolds from ^{14}N in the central portion of the spectrum. Since there are numerous papers dealing with analysis of ST-EPR spectra of ^{14}N spin labels, the reader is referred at this point to the more detailed calculations and explanations in other references (Thomas *et al.*, 1976; Hyde and Dalton, 1979; Robinson and Dalton, 1980, 1981).

The ST-EPR spectra of ^{15}N,DMSL-labeled GAPDH have also been satisfactorily simulated by Beth *et al.* (1981a, 1983) (Figure 9). The spectral resolution and simplification of the doubly substituted probe greatly facilitate the simulations of the large variations in line shapes for isotropic rotation at correlation times from 2×10^{-6} to 2×10^{-4} s as well as in the crystalline state. For simulations of ^{15}N,DMSL spectra, the

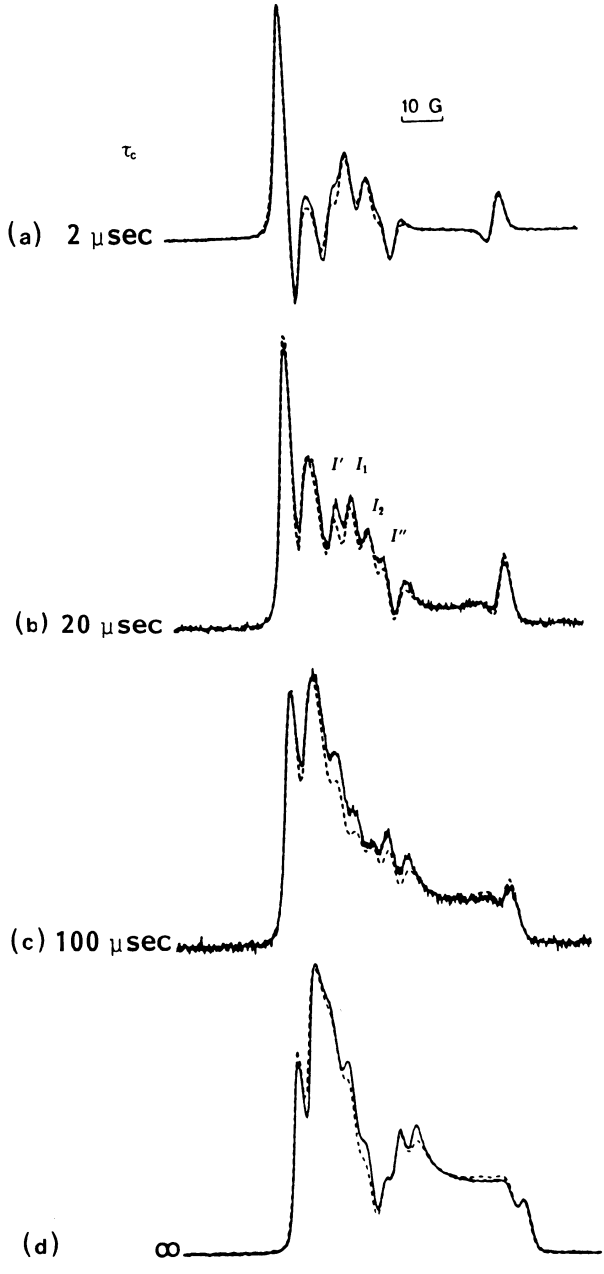

Figure 9. ST-EPR spectra of ^{15}N,DMSL-GAPDH complex in buffer with 53%, 78%, and 89% glycerol and as a crystalline suspension (Spectra a–d). The simulated spectra are superimposed as dashed lines on the experimental data. The additional parameters I', I'', I_1, and I_2 are indicated on spectrum (b).

CPU time is eightfold less than that for a comparable calculation of ^{14}N,DMSL spectra. Although the C'/C ratio is not present in the ^{15}N,DMSL spectra, additional parameters in the central portion of the spectra, I', I'', I, and I_2, have been defined and are in part sensitive to X,Y motion (Figure 9b). For these calculations, $\tau_z = \tau_x = \tau_y = 2.0 \times 10^{-5}$ s.

The algorithms for isotropic rotation of a globular protein have been extended to computations for proteins with asymmetries producing anisotropic rotation. For example, rotation about the major p_z axis of the nitroxide group ($\tau_\parallel$) can be held constant while the minor p_x, p_y axes ($\tau_\perp$) are increased to reproduce motion of a prolate ellipsoid (Figure 10) (Beth *et al.*, 1983). Additionally, the magnetic and diffusion tensors can be changed so that they are no longer coincident, in contrast to GAPDH or BSA (Figure 8b). The ST-EPR calculations of model systems of anisotropic rotation have been very useful in discerning the restricted motional dynamics of membrane-associated proteins (Section 2.3.5). For theoretical discussions, see additional references by Gaffney (1979) and Johnson *et al.* (1982). Detailed calculations for ST-EPR spectra for ^{14}N,DMSL and ^{15}N,DMSL are presented in this volume in Chapter 4 by A. Beth and B. Robinson (see pages 199-207 and 230-233).

2.3.4. Studies of ^{15}N,DMSL-Labeled GAPDH Bound to Red Blood Cell Membranes

Glyceraldehyde-3-phosphate dehydrogenase binds to the transmembrane protein, band-3, which is the anion transport protein in human red blood cells (RBC). The enzyme is positioned on a high-affinity binding site of a 40,000 MW segment of band-3 which extends from the membrane bilayer into the cytoplasm (Kant and Steck, 1973; McDaniel *et al.*, 1974; Strapazon and Steck, 1976; Cabantchik *et al.*, 1978). Such high-affinity binding at a specific site results in a homogeneous preparation of membrane-bound enzyme and greatly facilitates EPR investigations comparing the motional properties of an enzyme in the membrane-associated and soluble states. It is also fortunate that the ^{15}N,DMSL probe does not perturb the molecular structure of the dehydrogenase with regard to stoichiometry or binding affinity to RBC membranes as indicated by Scatchard analyses (Beth *et al.*, 1981b).

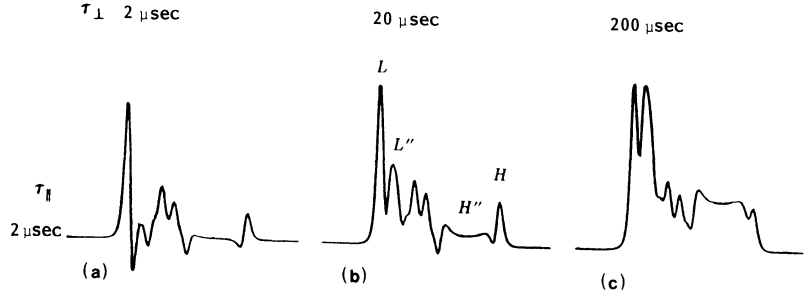

Figure 10. Simulated ST-EPR spectra of ^{15}N,DMSL-GAPDH complex for globular protein (a) and prolate elipsoids (b, c). For all three spectra $\tau_\parallel = 2\ \mu s$; $\tau_\perp = 2\ \mu s$, 20 μs and 200 μs for spectra (a), (b) and (c), respectively. Note that L'' and H'' regions are significantly increased compared to L and H as $\tau_\perp$ increases.

^{15}N,DMSL was selected as the probe of choice for comparison of the EPR and ST-EPR spectra of the soluble and membrane-bound GAPDH. With this high-resolution spin label, it was possible to obtain good spectra with as little as 0.1 mg enzyme per ml. Since packed RBC membranes have a limited number of binding sites and consume considerable volume within the EPR flat cell containing the various components of the reaction mixtures, sensitivity and resolution are of greater importance than in the case of the soluble enzyme (see Figure 4; GAPDH concentration, 7.0 mg per ml). Additionally, for acquisition and calculation of ST-EPR spectra by quantitative simulation, the spectral improvements and simplification afforded by ^{15}N were almost prerequisite for extensive experimentation on the available instrumentation.

The EPR spectra of the soluble and membrane-bound dehydrogenase label with ^{15}N,DMSL are compared in Figure 11. The soluble GAPDH tumbles so rapidly in

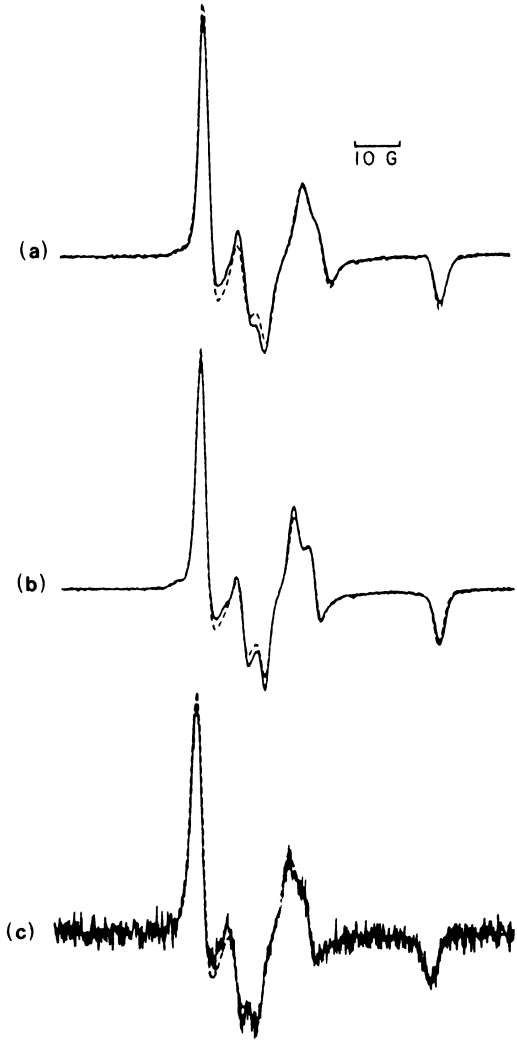

Figure 11. EPR spectra of soluble and membrane-bound GAPDH spin labeled with ^{15}N,DMSL. This figure compares the experimental and simulated EPR spectra of ^{15}N,DMSL-labeled GAPDH (a) in 5 mM phosphate buffer, pH 8.0; (b) in 53% glycerol/5 mM phosphate buffer, pH 8.0; and (c) bound to the cytoplasmic segment of band-3 protein of the RBC membrane. Best-fit computer-simulated line shapes are superimposed as dashed lines on the experimental spectra.

dilute buffer that orientation-dependent nitrogen-hyperfine and electron-Zeeman magnetic interactions are averaged (Figure 11a). Therefore, the A and g tensors were determined for a soluble enzyme in 53% glycerol/buffer, pH 8.0 with a correlation time of 2×10^{-6} s (Figure 11b). These tensor values and a correlation time of 1.6×10^{-7} s were used to simulate spectrum (a) with an excellent fit as indicated by the superimposed, dashed line (Beth *et al.*, 1981b). The simulated spectrum for the membrane-associated GAPDH (Figure 11c) was different from that of the soluble GAPDH as evidenced by a decrease in the A_{zz} splitting from 50.45 to 49.75 G, an increase in A_{xx} from 10.85 to 11.30 G, and an increase in A_{yy} from 10.35 to 11.00 G. Differences were also noted in the g tensor values. The differences in the A and g tensor elements could have resulted from a change in charge distribution within the active center or from an increase in local mobility of the spin label, or both. Either explanation would require a change in the average coordinates of some groups within the active center of the enzyme where spin label was covalently bound. The catalytic activity of GAPDH may be significantly decreased by binding to band-3. Depending upon the pH, the catalytic activity can be inhibited by as much as 90%. The structural changes observed in this study may in part be related to alterations in the catalytic center induced by membrane interactions.

The ST-EPR spectra of the ^{15}N,DMSL-labeled dehydrogenase freely tumbling in buffer or 78% glycerol/buffer and the membrane-bound SL-enzyme are displayed in Figure 12. The large difference between the line shapes of the soluble enzyme in buffer and 78% glycerol (Figures 12a and b) is due to the change in τ_c from 1.6×10^{-7} to 2.0×10^{-5} s. The correlation time of 2.0×10^{-5} s for the membrane-bound enzyme was determined from comparison of L''/L and H''/H ratios obtained from the model system of GADPH in glycerol/buffer solutions at varying viscosities (Figure 7) (Beth *et al.*, 1980, 1981a). Since the calculated τ_c for the RBC membrane is 1.0 s, there is considerable freedom of rotation in the GADPH-band-3 complex. The simulation of the membrane-associated enzyme was best fitted using an isotropic motional model, which was unexpected in view of the overall immobilization of the enzyme indicated in the ST-EPR spectra (Figure 12c).

For comparison, the ST-EPR spectrum of DMSL-labeled dehydrogenase bound to erythrocyte membranes is shown in Figure 12d. With the membrane-bound enzyme, the correlation time (τ_c) as determined by comparisons with C'/C and L''/L ratios of soluble DMSL-GAPDH was 1.6×10^{-5} and 2.0×10^{-5} s, respectively. Additional calculations for K, S, and Q bands are presented in Chapter 4 by A. Beth and B. Robinson (see pages 217-224).

2.3.5. Anisotropic Motion of Membrane-Inserted D-β-Hydroxybutyrate Dehydrogenase

When an enzyme is actually inserted into a lipid bilayer, the rotation may be more restricted as demonstrated in the case of D-β-hydroxybutyrate dehydrogenase (BDH) (McIntyre *et al.*, 1984). This unique dehydrogenase is a lipid-requiring enzyme and was purified from the inner membrane of mitochondria. The tetrameric BDH was reinserted into mitochondrial phospholipid vesicles and then spin-labeled with ^{15}N,DMSL at the essential sulfhydryl group. The ST-EPR spectrum was best simulated using an anisotropic motional model with magnetic and diffusional tensors which did not coincide ($\theta = 90°$). The two motional components had correlation times of $\sim 5 \times$

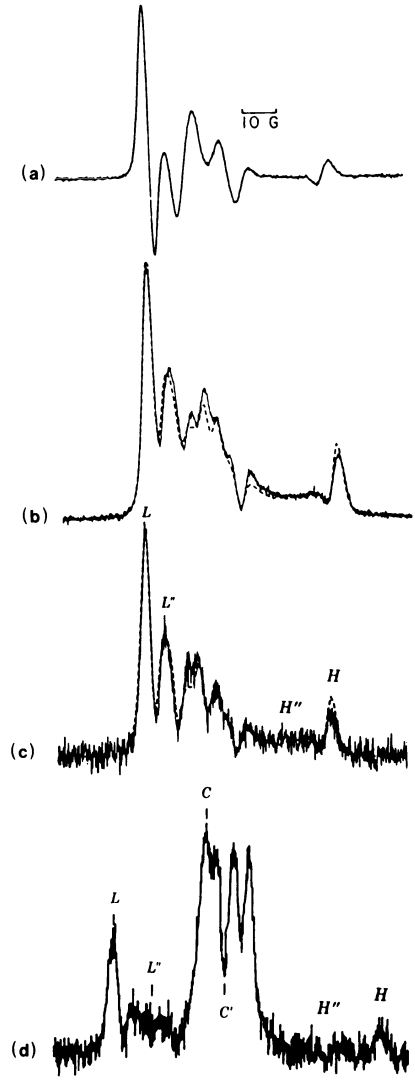

Figure 12. ST-EPR spectra of soluble and membrane-bound GAPDH spin labeled with ^{15}N,DMSL. This figure compares the experimental and calculated ST-EPR spectra from ^{15}N,DMSL-labeled GAPDH, (a) in 5 mM phosphate buffer, pH 8.0; (b), in 78% glycerol/5 mM phosphate buffer; and (c), bound to the cytoplasmic segment of band-3 in the RBC membrane. The normalized ST-EPR spectrum (d) of DMSL-labeled GAPDH bound to band-3 is displayed for comparative purposes. The DMSL spectrum (d) was accumulated over a time period three times greater than that of ^{15}N,DMSL spectrum (c). Parameters *L*, *L''*, *C*, *C'*, *H*, and *H''* are indicated in spectrum (d) and are reflections of the three manifolds of ^{14}N,DMSL.

10^{-8} s ($\tau_{\parallel}$) and $\sim 10^{-6}$ s ($\tau_{\perp}$). The faster $\tau_{\parallel}$ represented rotation about an axis normal to the bilayer, while the slower $\tau_{\perp}$ was indicative of a protein tilting relative to the plane of the bilayer. The latter motion was interpreted as a restoring potential. This investigation was the first quantitative analysis of a membrane-bound enzyme with anisotropic motion and may be representative of a large group of membrane-inserted or transmembrane proteins.

2.4. Future Applications

These studies suggest that DMSL and ^{15}N,DMSL probes may have wide application for studying molecular motion of enzymes, macromolecular enzyme complexes, transport proteins in membranes, and hormone receptors, which may occur in low concentrations and in highly immobilized states. More significant advances in these important areas of motional dynamics will occur, however, with the design and synthesis of new isotopically substituted probes with high site specificity.

3. COENZYME SPIN LABELS: STUDIES ON COENZYME BINDING TO ENZYMES AND CATALYTIC MECHANISMS

3.1. Comparison of Spin-Labeled Maleimide Inhibitors (DMSL and ^{15}N,DMSL) and Coenzyme Analogs (SL-NAD^+) for EPR Studies of Enzymes

The DMSL or ^{15}N,DMSL studies with the glyceraldehyde-3-phosphate dehydrogenase represent an especially favorable EPR model system. The spin label is covalently bound to a single amino acid in the catalytic center of the enzyme, and any unbound, freely tumbling DMSL or ^{15}N,DMSL can be readily removed, leaving the pure MSL-enzyme complex with the probe highly immobilized. By contrast, the experimental conditions for EPR investigations of coenzyme binding are not so conveniently optimized. For example, coenzymes (NAD^+ and NADH) are not covalently bound in the catalytic center. Therefore, the EPR spectrum of the SL-NAD^+-enzyme complex may be complicated by substantial amounts of unbound, freely tumbling SL-NAD^+. Moreover, each of the four NAD^+ molecules bound to a tetrameric dehydrogenase may have a different association constant which introduces additional variables. Clearly, in order to optimize the experimental design for EPR studies, an investigation must be planned against a large background of biochemical data. Under favorable circumstances, EPR technology can address enzymological problems in a unique and often definitive manner.

The crucial starting point for enzymological studies is again the synthesis of the spin labels. The primary synthetic work on the preparation of a wide variety of SL analogs of coenzymes (NAD^+ and NADH) as well as adenine nucleotide cofactors (ATP, ADP, and AMP) was carried out in the laboratory of Trommer and has been reviewed recently (Trommer, 1987). Selected syntheses of isotopically substituted coenzyme analogs and cofactors are detailed in the Appendix. NAD^+ analogs with the spin label on the N^6 or C8 position of the adenine moiety have been the most frequently employed nucleotide probes to date. Both the deuterated and ^{15}N,deuterated analogs have been synthesized for studies on coenzyme binding and catalytic mechanism of various dehydrogenases (Figure 13) (Glöggler *et al.*, 1982a, 1982b; Beth *et al.*, 1984a, 1984b; Philipp *et al.*, 1984).

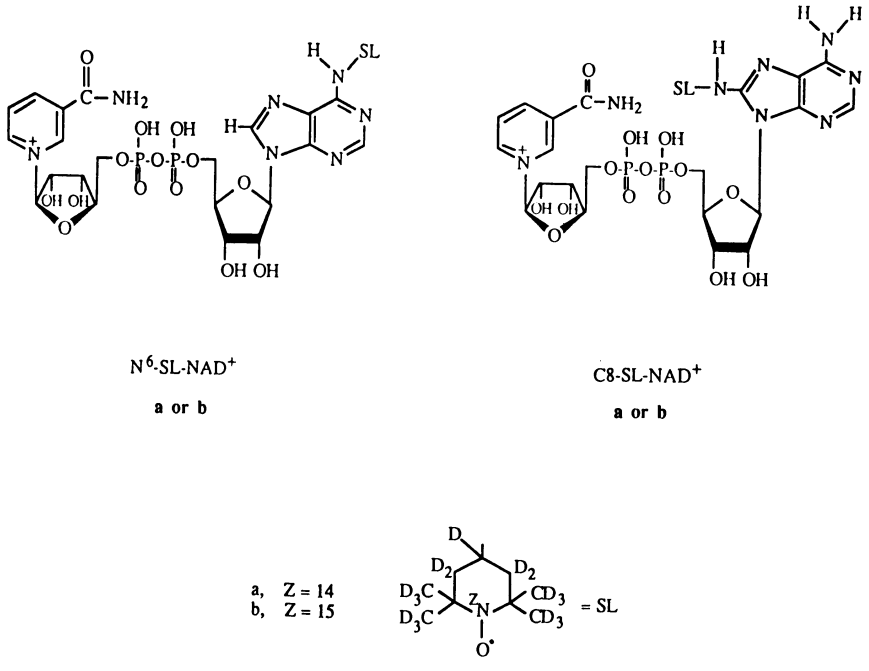

Figure 13. Structural formulas of N^6-(D_{17})SL-NAD^+ and C8-(D_{17})SL-NAD^+. The tetramethylpiperidinoxyl spin label is completely deuterated except for the proton on the secondary amine. The notation "Z" adjacent to the N of the nitroxide group (N—O·) indicates the position of ^{15}N substitution to yield doubly substituted N^6-(^{15}N,D_{17})SL-NAD^+ or C8-(^{15}N,D_{17})SL-NAD^+. Z: a = ^{14}N; b = ^{15}N.

In the case of the SL-coenzymes, the design of the spin label is as important and perhaps more demanding than with an inhibitor such as MSL. First, the SL-NAD^+-enzyme complex must retain its three-dimensional structure. Second, the SL-NAD^+ analog must also participate in the catalytic reaction without significantly altering the binding or catalytic constants. The suitability of SL-NAD^+ analogs for enzyme studies has been verified by Trommer and associates using a number of dehydrogenases, namely, lactic dehydrogenase, glyceraldehyde-3-phosphate dehydrogenase, β-hydroxybutyrate dehydrogenase, and glutamate dehydrogenase (Zantema *et al.*, 1977; Trommer *et al.*, 1979; Trommer and Glöggler, 1979; Deparade *et al.*, 1981; Fritzsche *et al.*, 1984). Additionally, molecular modeling of the crystallographic structure of the SL-coenzyme-enzyme complexes has also demonstrated that the spin label does not interfere with accessibility to the catalytic center of lactic dehydrogenase or glyceraldehyde-3-phosphate dehydrogenase (Trommer and Glöggler, 1979; Birktoft and Park, 1985).

3.2. The Evaluation of Binding of Isotopically Substituted N^6-SL-NAD^+ or C8-SL-NAD^+ Using Lactic Dehydrogenase

Lactic dehydrogenase (LDH) forms a tight ternary complex with native NAD^+ in the presence of the substrate analog, oxalate. The apparent association constant for

NAD^+ is greatly increased in the ternary complex as compared to the binary complex in the absence of oxalate. A similar ternary complex has been shown to form with the protonated N^6-SL-NAD^+ or C8-SL-NAD^+ analog (Trommer *et al.*, 1979; Trommer and Glöggler, 1979) as well as the deuterated N^6-(D_{17})SL-NAD^+ or C8-(D_{17})SL-NAD^+ spin label (Glöggler *et al.*, 1982b). The simple hyperfine EPR spectra of the protonated N^6- and deuterated N^6-(D_{17})SL-NAD^+ bound to LDH are compared in Figure 14. The increase in the signal amplitude of the bound N^6-(D_{17})SL-NAD^+ is approximately 1.4-fold as compared to the N^6-SL-NAD^+. This increased sensitivity is similar to that of DMSL covalently attached to glyceraldehyde-3-phosphate dehydrogenase (1.5-fold). Under these experimental conditions, only about 1% of the N^6-(D_{17})SL-NAD^+ was not bound to the enzyme, as indicated by the freely tumbling component in the spectrum (Figure 14b). Since the signal of the free (D_{17})SL-NAD^+ shows a fourfold enhancement in sensitivity, it is easily identified in contrast to the free signal of N^6-SL-NAD^+ (Figure 14a) which is hardly visible. Clearly, the reduced linewidths and improved resolution of the free deuterated compounds are advantageous in the determination of binding constants and stoichiometries of the enzyme complexes with spin-labeled cofactors (Wenzel and Trommer, 1977). Since coenzyme binding to LDH is so highly specific, nonbinding impurities in SL-NAD^+ preparations can actually be quantitatively assayed by their unbound signal in the presence of this dehydrogenase (Wenzel and Trommer, 1977).

The EPR spectra of the more highly immobilized analogs, C8-(D_{17})SL-NAD^+ and C8-$(^{15}N,D_{17})$SL-NAD^+, and LDH in the rigid-lattice limit have been computer-simulated (Glöggler *et al.*, 1982b; Philipp *et al.*, 1984). The hyperfine spectra were

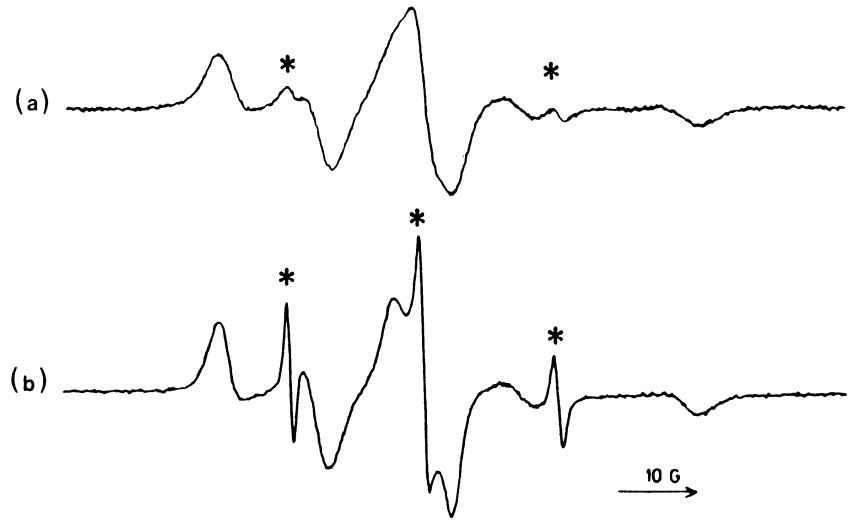

Figure 14. X-band EPR spectra of N^6-SL-NAD^+ and N^6-(D_{17})SL-NAD^+ tightly bound to lactic dehydrogenase in a ternary complex with oxalate. The enzyme-bound N^6-SL-NAD^+ (spectrum a) and bound N^6-(D_{17})SL-NAD^+ (spectrum b) were prepared with one equivalent of coenzyme per tetramer. The unbound, freely tumbling N^6-SL-NAD^+ (a) and unbound N^6-(D_{17})SL-NAD^+ (b) are indicated by asterisks (*).

satisfactorily simulated only after the introduction of Lorentzian broadening, which suggested to the authors either (1) residual motion of the spin label relative to the protein or (2) interaction of the unpaired electron with nearby exchangeable protons on the protein (Philipp *et al.*, 1984). In the case of lactic dehydrogenase, the $^{15}N,D_{17}$ analogs have shown no substantial advantages to date as compared to the D_{17} analogs except for the reduction in CPU time for quantitative simulation of EPR line shapes.

3.3. Glyceraldehyde-3-phosphate Dehydrogenase (GAPDH) and SL-NAD$^+$ Binding with Unusual Electron–Electron Dipolar Interactions (Splitting of Peaks)

Glyceraldehyde-3-phosphate dehydrogenase will be discussed as a model enzyme for detailed consideration of EPR studies on coenzyme binding, conformational changes, and catalytic mechanism. This dehydrogenase has been studied extensively owing to the interesting characteristics of negative cooperativity in coenzyme binding (Chance and Park, 1967; Conway and Koshland, 1968; Glöggler *et al.*, 1982a). As each successive NAD$^+$ combines to one of the four subunits, the binding affinity for the next NAD$^+$ is substantially reduced.

Deparade *et al.* (1981) and Glöggler *et al.* (1982a) examined this negative cooperativity using spin-labeled NAD$^+$ with the nitroxyl moiety on the N^6 or C8 position of the adenine ring. With these two probes, it was demonstrated that the close proximity of the nitroxide moieties of the NAD$^+$ bound on adjacent monomers elicited an electron-electron dipolar interaction as the enzyme became more saturated with coenzyme. This interaction results in the splitting of each hyperfine peak into two new peaks on either side of the original EPR signal. Since the line shapes and positions of the split peaks of dipolar spectra are extremely sensitive to the distances and angles between the two free radicals, the interactions became a valuable tool for enzymological studies. They have been used to investigate the stoichiometry of binding, association constants of SL-NAD$^+$ (K_1-K_4), the order in which the coenzyme binds to four subunits in the tetramer, the positioning and relative distances between spin-labeled analogs, and conformational changes of the enzyme induced by substrate and other active site modifications (Beth *et al.*, 1984b; Wilder, 1985). The following sections (3.3.1-3.3.8) demonstrate the versatility of EPR methodology in attacking this wide range of problems.

3.3.1. Special Advantages of (D_{17})- or ($^{15}N,D_{17}$)SL-NAD$^+$ Analogs for Studies of Coenzyme Binding to GAPDH

The simple hyperfine and complex dipolar spectra of the spin-labeled NAD$^+$ probes bound to GAPDH have been examined using both the (D_{17})- and ($^{15}N,D_{17}$)SL-NAD$^+$ analogs with the nitroxide moiety on the N^6 or C8 position of the adenine ring. The isotopic substitutions provided the same increased sensitivity, high resolution, and spectral simplification as noted with the corresponding DMSL and ^{15}N,DMSL spin labels (Beth *et al.*, 1981a). With this dehydrogenase, N^6-($^{15}N,D_{17}$)SL-NAD$^+$ is the label of choice for computerized spectral simulations and correlative studies with X-ray crystallographic modeling. However, the doubly substituted label has limitations, and for examining the mechanism of enzyme catalysis the perdeuterated analog, C8-(D_{17})SL-NAD$^+$, is the preferred probe. The scope of enzymatic investigations is greatly

expanded by the availability of a variety of spin-labeled analogs (see Appendix, Sections 3.8 and 3.9, SL-NAD^+ analogs).

3.3.2. Advantage of N^6-(D_{17})SL-NAD^+ for Analyses of Hyperfine and Dipolar Spectra of GAPDH–Coenzyme Complexes

The structure of glyceraldehyde-3-phosphate dehydrogenase has been determined by X-ray crystallography at the 2.0 Å level by Moras *et al.* (1975). The enzyme can be represented diagrammatically as a "dimer of dimers" (Figure 15). The unpaired electrons of the nitroxide moieties of two N^6-(D_{17})-SL-NAD^+ bound to adjacent monomers within a single dimer are closely approximated at a distance of 11–13 Å across the *R* axis (Beth *et al.*, 1984b). The modeled nitroxide radicals (↓↓) of two adjacent N^6-(D_{17})SL-NAD^+ in the upper dimer project into the intermonomeric space and produce an electron–electron dipolar interaction with splitting of spectral peaks. Binding of two N^6-(D_{17})SL-NAD^+ on remote subunits related by the *P* and *Q* axes produces no dipolar interaction because the distance between unpaired electrons exceeds 25 Å, and thus a typical hyperfine spectrum is observed.

The special advantage of N^6-(D_{17})SL-NAD^+ or N^6-(^{15}N,D_{17})SL-NAD^+ for studies of dipolar interactions is that the EPR spectra can be readily deconvoluted (Beth *et al.*, 1984b) into the three spectral components which characterize the three different environments of the spin-labeled coenzyme (Figure 16, right-hand column).

Environment 1: Freely Tumbling (top and bottom spectra). The three spectral peaks denoted by asterisks (*) arise from unbound N^6-(D_{17})SL-NAD^+ rapidly tumbling in solution. The freely tumbling component is more prominent in the lower spectrum (b) since the ratio of coenzyme to protein is higher.

Environment 2: Hyperfine (top spectrum). The hyperfine spectral peaks denoted by upward-pointing arrows (↑) represent N^6-(D_{17})SL-NAD^+ bound to GAPDH as one isolated SL-NAD^+ per tetramer or two SL-NAD^+ probes on two distant sites (e.g., 58 Å) related by the nearly exact 2-fold *Q* symmetry axis.

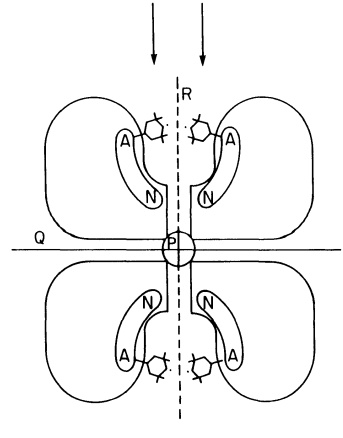

Figure 15. Diagrammatic representation of glyceraldehyde-3-phosphate dehydrogenase as a tetramer with four spin-labeled NAD^+ analogs bound in the catalytic centers. The diagram is derived from the crystallographic structure as determined by Moras *et al.* (1975). The nitroxide groups of the spin labels project into the intermonomeric space. Two nitroxide groups are closely approximated on adjacent monomers across the *R* axis (↓↓), but remotely separated across the *P* and *Q* axes.

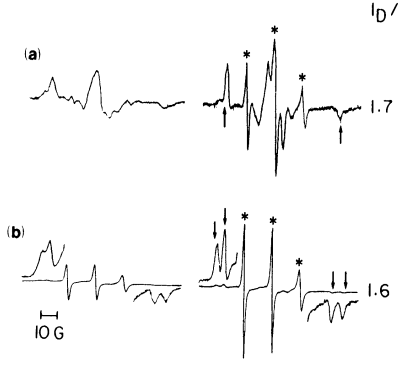

Figure 16. Hyperfine and dipolar EPR spectra of N^6-SL-NAD^+ (left) or N^6-(D_{17})SL-NAD^+ (right) bound to glyceraldehyde-3-phosphate dehydrogenase (GAPDH). The hyperfine (a) and dipolar spectra (b) for the protonated N^6-SL-NAD^+ (left) or deuterated N^6-(D_{17})SL-NAD^+ (right) are compared. The hyperfine spectra (a) were obtained with a low ratio of spin label to enzyme of 0.9 with virtually no dipolar interactions, while the bottom spectra (b) were recorded with a ratio of 3.5. The hyperfine components at the extrema are designated by the upward arrows (↑), the dipolar components by the downward arrows (↓↓), and the freely tumbling, unbound SL-NAD^+ by asterisks (*). In the bottom spectra (b), the low- and high-field extrema are amplified to facilitate viewing of the signal of enzyme-bound spin label. The intensity ratios I_D/I_H are the heights of the N^6-(D_{17})SL-NAD^+ peaks compared to those of N^6-SL-NAD^+ at both high and low extrema.

Environment 3: Dipolar (bottom spectrum). The dipolar components denoted by downward-pointing arrows (↓↓) are produced by interactions of two closely approximated N^6-(D_{17})SL-NAD^+ molecules bound to monomers related by the pseudo-2-fold *R* axis (Moras *et al.*, 1975). The amplified regions of the spectrum show that the extreme high- and low-field peaks (↓↓) have been split and shifted outward relative to the lines of the hyperfine spectrum (↑) because of the electron–electron dipolar interactions between spin labels with a separation of 11–13 Å.

Figure 16 also illustrates the advantages of employing perdeuterated labels. At a low stoichiometry of less than one bound deuterated N^6-(D_{17})SL-NAD^+, the simple hyperfine line shape (↑) showed a 1.7-fold increase in the sensitivity at the low- and high-field turning points (upper right) when compared to protonated N^6-SL-NAD^+ (upper left) (Glöggler *et al.*, 1982a). This is in good agreement with the value of 1.5-fold previously reported for the DMSL probe bound to glyceraldehyde-3-phosphate dehydrogenase. The width of the spectral lines was decreased ($W_D/W_H = 0.52$) when measured as the half width at half height. In the dipolar spectra with 3.5 moles of spin label bound per tetramer (lower right), the deuterated analog again showed a 1.6-fold increase in sensitivity of the dipolar peaks (↓↓) at both high- and low-field extrema (compare spectra b, lower right and left). However, the more important advantage of the deuterated spin probe for enzymological studies is the spectral resolution afforded by narrow linewidths. Dipolar splittings at both extrema are almost completely resolved only with the deuterated label. Additionally, with the deuterated label, overlaps of the bound and free N^6-(D_{17})-NAD^+ peaks (↓↓, *) are minimized particularly in the low-field region of the spectrum. This enhanced resolution greatly facilitates quantitation of the spectral line shapes and accurate characterization of positioning of the bound coenzymes.

As seen in Figure 16, the intensity of the peak heights of the freely tumbling unbound DSL-NAD^+ (*) is increased three- to fourfold compared to the protonated SL-NAD^+, whereas the increase with free DMSL was 5.0 fold (Figure 1). The

reason is that free deuterated labels are broadened to a greater relative extent as a function of increasing molecular size than are the protonated spin labels (Table 1). This can be illustrated by a comparison of (1) tempamine, and tempamine bonded to (2) AMP or (3) NAD^+. The relative molecular weights of the three compounds are 190, 517, and 835, respectively, and the ratios of the signal intensities (I_{DSL} : I_{HSL}) are 5.5, 4.1, and 3.5 (Table 1) (Glöggler *et al.*, 1982a; Wilder, 1985). As a cautionary note, the relative increase in signal intensity of deuterated spin labels is reduced at higher microwave power (compare lines 3 and 4, Table 1). As explained in the next section, the sharp lines of the unbound N^6-(D_{17})SL-NAD^+ are important in the determination of precise binding constants, K_1-K_4, for the four bound coenzymes.

3.3.3. Calculation of Association Constants K_1–K_4 for N^6-(D_{17})SL-NAD^+

In order to quantitate the interactions of the coenzyme and glyceraldehyde-3-phosphate dehydrogenase, a titration was performed at different added stoichiometries ranging from 0.25 to 12.0 equivalents of N^6-(D_{17})SL-NAD^+ per tetramer. Four sample spectra are displayed in Figure 17 to illustrate the determination of binding constants and, in the next section, the order of sequential binding to the monomers. As the added stoichiometry was increased from 0.44 to 5.23 N^6-(D_{17})SL-NAD^+ per tetramer, the number of enzyme-bound probes increased from 0.42 to 3.53 per tetramer. The number of bound N^6-(D_{17})SL-NAD^+ was calculated by subtraction (total spin label – unbound label). The unbound spin label was determined by comparison of the spectral height of the well isolated, unbound peak ($M_I = -1$) with those of freely tumbling N^6-DSL-NAD^+ in standard reference solutions. The experimental values were substituted into the Adair equation for binding to a tetramer (association constants) (Adair, 1925):

$$\frac{[L]_B}{[E]_{tot}} = \frac{[L]K_1 + 2[L]^2K_1K_2 + 3[L]^3K_1K_2K_3 + 4[L]^4K_1K_2K_3K_4}{1 + [L]K_1 + [L]^2K_1K_2 + [L]^3K_1K_2K_3 + [L]^4K_1K_2K_3K_4}$$

where $[L]_B$ is the concentration of bound ligand, [L] is the concentration of free ligand, and $[E]_{tot}$ is the total concentration of enzyme tetramers. Knowing the total protein

TABLE 1
Comparison of Signal Heights and Linewidths of the Central Peak ($M_I = 0$) of Deuterated and Protonated Spin Labels (DSL and HSL)[a]

	Ratio of signal intensity (I)	Linewidth in gauss (peak to peak)		Molecular weight
Spin label	I_{DSL} : I_{HSL}	DSL	HSL	DSL
Tempamine	5.5	0.55	1.65	190
SL-AMP	4.1	0.69	1.70	517
SL-NAD^+	3.5	0.72	1.73	835
SL-NAD^+ (15 mW power)	2.8	0.86	1.80	835

[a] Identical instrument settings were used for the measurements on the first three lines, namely, 2 mW microwave power and 100 kHz field modulation of 0.1 gauss amplitude. The values on the last line were obtained at 15 mW microwave power and 100 kHz field modulation of 0.8 gauss amplitude. The spin labels (50 μM) were dissolved in 5 mM phosphate buffer, pH 8.0.

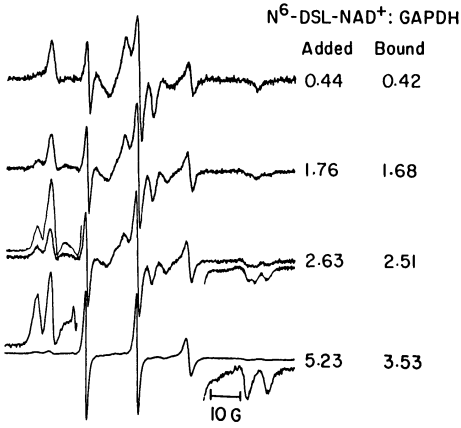

Figure 17. X-band EPR spectra of N^6-(D_{17})SL-NAD^+ bound to glyceraldehyde-3-phosphate dehydrogenase (GAPDH) at four different stoichiometries. The enzyme-N^6-(D_{17})SL-NAD^+ complexes were prepared by addition of the coenzyme to the enzyme at the indicated stoichiometries. The amount of the protein-bound coenzyme was calculated by the simple subtraction procedure described in the text. In the last two spectra, the high- and low-field extrema are amplified to facilitate viewing of the dipolar components.

concentration, the concentration of DSL-NAD^+ bound, and the concentration of free DSL-NAD^+, it is possible to fit a curve through the data points of a plot of free ligand against the stoichiometry of bound DSL-NAD^+ and thereby estimate the association constants K_1, K_2, K_3, and K_4.

The association constants (K_1-K_4) clearly show negative cooperativity as the constants become progressively smaller for the binding of each successive N^6-(D_{17})SL-NAD^+ (Table 2). The close agreement between the association constants determined by EPR and those determined for native NAD^+ by other authors (Table 2) validates the use of this probe in enzymological studies. Henis and Levitzki (1981) determined association constants for the two tight sites by making an indirect measurement in the presence of ADP-ribose. In two other laboratories, direct binding measurements of native NAD^+ at the first two sites were not possible (Conway and Koshland, 1968; De Vijlder and Slater, 1968). By contrast, EPR is an excellent technique for determination of the first two tight binding sites. The reason is that the differential sensitivity and isolated positions of the sharp peaks of unbound N^6-(D_{17})SL-NAD^+ allow accurate measurement of very small concentrations of freely tumbling label in the presence of

TABLE 2
Calculated Association Constants for the Binding of Four N^6-DSL-NAD^+ to Glyceraldehyde-3-phosphate Dehydrogenase and Comparisons to Literature Values[a]

	Thermodynamic association constants for N^6-DSL-NAD^+	Henis and Levitzki (1981)	Conway and Koshland (1968)
K_1	$1.86 \times 10^7\ M^{-1}$	$3.64 \times 10^7\ M^{-1}$	$>10^{11}\ M^{-1}$
K_2	$3.94 \times 10^6\ M^{-1}$	$4.29 \times 10^6\ M^{-1}$	$>10^9\ M^{-1}$
K_3	$1.18 \times 10^6\ M^{-1}$	$1.13 \times 10^6\ M^{-1}$	$2.21 \times 10^6\ M^{-1}$
K_4	$5.94 \times 10^4\ M^{-1}$	$4.60 \times 10^4\ M^{-1}$	$5 \times 10^4\ M^{-1}$

[a] The thermodynamic association constants for N^6-DSL-NAD^+ in the first column were determined as described in the text. The similarity of these association constants and those for native NAD^+ (columns 2 and 3) confirms the utility of N^6-SL-NAD^+ for studies of coenzyme binding.

high concentrations of bound spin label. One part in a thousand can be determined with accuracy.

3.3.4. Calculation of Binding Stoichiometry by Computer-Assisted Spectral Subtraction Using Doubly Substituted N^6-(^{15}N,D_{17})SL-NAD^+

N^6-(^{15}N,D_{17})SL-NAD^+ is bound to the enzyme in the same manner as the deuterated coenzyme (Figure 18) (Beth *et al.*, 1984b). A simple hyperfine line shape indicative of an isolated, tightly bound spin label (↑) was observed with a bound SL-NAD^+ ratio of 1:1 or less. As the bound ratio was raised to 2:1 or 3:1, the line shape developed into a composite spectrum with increasing amounts of dipolar component (↓↓) indicative of the intersubunit electron-electron dipolar interaction between two adjacent spin labels immobilized on the dimer related by the *R* axis. At a bound ratio of 4:1, the spectrum represents a line shape characteristic of only electron-electron dipolar interactions for the bound component. Each dimer gives an identical dipolar spectrum indicating similar positioning of interacting coenzymes. There is no interaction between spin labels related across the *Q* axis. Although association constants were not calculated for this spin label, negative cooperativity was apparent from the titration characteristics.

Figure 18. X-band EPR spectra of doubly substituted N^6-(^{15}N,D_{17})SL-NAD^+ bound to glyceraldehyde-3-phosphate dehydrogenase (GAPDH) at three different stoichiometries. The composite, normalized spectra in the left-hand column represent the N^6-(^{15}N,D_{17})SL-NAD^+ complexed with glyceraldehyde-3-phosphate dehydrogenase at the indicated ratios from 1:1 to 4:1 (SL-NAD^+:tetramer). In the right-hand column, the unbound coenzyme has been removed by computer-assisted subtraction, and only the enzyme-bound SL-NAD^+ spectra are displayed. The N^6-(^{15}N,D_{17})SL-NAD^+ shows a hyperfine line shape at 1:1 ratio (↑) and develops into an almost pure dipolar spectrum at 4:1 ratio (↓↓). Dipolar splitting cannot as yet be resolved in the low-field extremum with (^{15}N,D_{17})SL-NAD^+.

Computer-aided subtraction of the freely tumbling N^6-(^{15}N,D_{17})SL-NAD^+ from each spectrum enabled the visualization of the pure hyperfine spectrum and/or dipolar spectrum at the low and high bound ratios, 1:1 to 2.8. For example, in the composite spectra at intermediate stoichiometries (i.e., 2.5), a double subtraction of the freely tumbling component and then the hyperfine component resulted in a completely deconvoluted spectrum with the residual dipolar component remaining (Figure 19). A double integration of each of the three components yields the area under the three curves which corresponds to the percent concentration of (1) 8% freely tumbling spin probe, (2) 32% SL-NAD^+ bound on remote monomers, and (3) 60% SL-NAD^+ bound on adjacent subunits and interacting across the *R* axis. Using either the sophisticated computerized subtraction method (Beth *et al.*, 1984b) or the simple subtraction procedures (Wilder, 1985), it was possible to determine the order of binding of successive NAD^+ molecules to the four subunits.

3.3.5. Use of N^6-(D_{17})SL-NAD^+ and N^6-(^{15}N,D_{17})SL-NAD^+ for Testing Models of Negative Cooperativity in Coenzyme Binding

The ability to measure dipolar interactions provided a method for choosing between three models of negative cooperativity and sequential binding of NAD^+ to the tetrameric GAPDH.

Model 1. For the ligand-induced sequential model, Conway and Koshland (1968) proposed that the tetrameric apoenzyme consisted of four monomers with equal affinity for the coenzyme (Figure 20). Upon binding of the first SL-NAD^+ molecule, the affinity of the other three monomers is reduced in an identical manner. When one SL-NAD^+ is bound to each tetrameric GAPDH molecule (E_1), a pure hyperfine spectrum results with no dipolar splitting (Figure 19, left-hand column). The second SL-NAD^+ binds to any one of the three unfilled subunits with equal probability, yielding an EPR spectrum with 33% of the total signal split by dipolar interactions across the *R* axis (E_2). Since the two remaining monomers bind with reduced but equal affinity, the spectrum of the enzyme with three bound SL-coenzymes is identical regardless of which three monomers are occupied (E_3). Therefore, the resultant spectrum shows

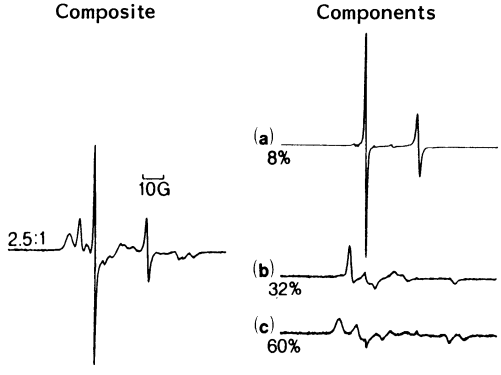

Figure 19. Computer-assisted deconvolution of EPR spectra with 2.5 N^6-(^{15}N,D_{17})SL-NAD^+ bound per tetramer of GAPDH into three components: unbound (a), hyperfine (b), and dipolar (c). The composite spectrum (left) was acquired from an enzyme with a bound stoichiometry of 2.5 spin-labeled NAD^+ per tetramer. The freely tumbling component (a) was obtained by digital computer subtraction from the composite spectrum. The hyperfine component (b) was acquired by a second computer subtraction of the residual spectrum thereby removing the simple hyperfine component and leaving the pure dipolar component (c) with interacting nitroxide spin labels on adjacent monomers.

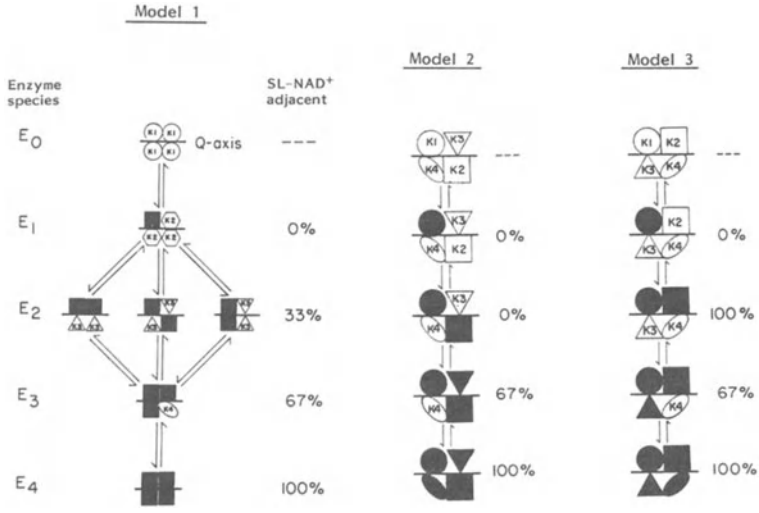

Figure 20. Diagrammatic representation of three models of negative cooperativity in coenzyme binding to tetrameric GAPDH.

Model 1: Ligand-induced sequential model shows the tetrameric apoenzyme with four identical, interacting sites for SL-NAD$^+$ with an affinity constant K_1. In the left-hand column, E_0-E_4 represent the enzyme species with a given number of SL-NAD$^+$ bound to the tetramer. Binding of one molecule of NAD$^+$ to E_1 causes equivalent changes in the affinity constant (K_2) in the remaining subunits. Therefore, the second molecule of SL-NAD$^+$ binds with equal probability to any one of the three unfilled monomers resulting in E_2 with 33% dipolar splitting in the spectrum. In all models, the two monomers for coenzyme binding with dipolar interactions across the *R* axis are shown as sites adjacent to each other in the horizontal plane.

Models 2 and 3: Preexisting asymmetry models cause the coenzyme binding sites to be nonidentical with different association constants K_1-K_4 for SL-NAD$^+$. In Model 2, when the first two SL-NAD$^+$ bind to the apoenzyme the two occupied sites are on remote monomers (E_2). In the idealized case, there is no dipolar interaction (0%), and a pure hyperfine spectrum results. In Model 3, the first two occupied sites with tight binding are on adjacent monomers across the *R* axis, and the resultant spectrum shows 100% dipolar splitting (E_2). The spectra of E_3 and E_4 are identical in all three models.

67% dipolar component. For the enzyme with four bound SL-NAD$^+$, the two pairs of coenzymes on adjacent subunits across the *R* axis produce an EPR spectrum that is 100% dipolar (E_4).

The second and third models for negative cooperativity in ligand binding are the preexisting asymmetry models first proposed by Bernhard and MacQuarrie (1973).

In *Model 2*, the two subunits with the greatest affinity for NAD$^+$ are considered to be remote from each other across the *P* and *Q* axes (Figure 20). The tetramers with two SL-NAD$^+$ bound (E_2) have no dipolar component (0%) in the resultant EPR spectrum, because the distance between the labels is 58 Å. Tetramers with one, three, or four SL-NAD$^+$ bound will produce EPR spectra with 0%, 67%, and 100% dipolar component, respectively, for the reasons outlined above for Model 1.

For *Model 3*, the two monomers with the highest affinity for NAD^+ are assumed to be adjacent to each other, related by the crystallographic *R* axis of symmetry (Figure 20). Thus, the glyceraldehyde-3-phosphate dehydrogenase with two SL-NAD^+ bound (E_2) would give an EPR spectrum with 100% dipolar component. Dehydrogenase tetramers with one, three, or four DSL-NAD^+ bound produce spectra identical to those seen in the other two models. Therefore, the amount of dipolar component for an enzyme with two DSL-NAD^+ bound (E_2) can be used to compare experimental data with theoretical Models 1, 2, and 3 in showing 33%, 0%, and 100% dipolar components, respectively.

Both N^6-(D_{17})SL-NAD^+ and N^6-(^{15}N,D_{17})SL-NAD^+ have been used to determine which model for negative cooperativity in binding best fits the experimental EPR data. In the case of N^6-(D_{17})SL-NAD^+, a series of equations were derived for each of the three models to predict the percent of hyperfine and dipolar components in EPR spectra at any added stoichiometry of coenzyme (Wilder, 1985) (Figure 17). Large differences were noted between the three models at stoichiometries from 0.5 to 2.0 N^6-(D_{17})SL-NAD^+ bound per tetramer of dehydrogenase. Model 1, the ligand-induced sequential model of Conway and Koshland (1968), best fits the experimental data. With Model 2 or Model 3, the preexisting asymmetry models, there is either too little (Model 2) or too much (Model 3) dipolar component at bound stoichiometries below 2.0.

With N^6-(^{15}N,D_{17})SL-NAD^+, the experimental data also indicated that the ligand-induced sequential model is the mathematical model of choice. In this case, the amount of dipolar component in the EPR spectrum at a bound stoichiometry of two N^6-(^{15}N,D_{17})SL-NAD^+ per tetramer was determined by computer-aided spectral subtraction. The experimental value of 40% dipolar component was in good agreement with the 33% predicted by Model 1 and not consistent with the 0% or 100% expected from the preexisting asymmetry models 2 and 3, respectively (Beth *et al.*, 1984b).

Thus a mechanism for negative cooperativity could be supported experimentally by a special application of EPR made possible by the isotopically substituted spin probes.

3.3.6. Computational Simulation of EPR Line Shapes of Hyperfine and Dipolar Spectra of N^6-(D_{17})- and N^6-(^{15}N,D_{17})SL-NAD^+–GAPDH Complexes

The hyperfine and dipolar EPR spectra of both N^6-(D_{17})SL-NAD^+ and N^6-(^{15}N,D_{17})SL-NAD^+ bound to GAPDH have been simulated (Figure 21) (Beth *et al.*, 1984b). Crystalline suspensions of the coenzyme-enzyme complexes were employed, in order to promote immobilization of the probe and to compare accurately the EPR computations with the molecular models constructed on the interactive computer graphics system. Since there are only two distinct types of spectra for GAPDH-coenzyme complexes, hyperfine and dipolar, conditions were selected to maximize homogeneity for each spectral type. For the hyperfine spectra (Figure 21a and c), crystalline samples with 0.5 mol SL-NAD^+ per tetramer were computer-simulated with the program of Balasubramanian and Dalton (1979). The dipolar spectra (Figure 21b and d) of the crystalline suspension with 3.8 equivalents of SL-NAD^+ per tetramer were essentially the same as that for the soluble enzyme, indicating that the relative

Figure 21. Comparisons and simulations of the hyperfine and dipolar spectra of N^6-(^{15}N,D_{17})SL-NAD^+ and N^6-(D_{17})SL-NAD^+. The top spectrum (a) is obtained from a crystalline suspension of GAPDH with 0.5 moles of N^6-(^{15}N,D_{17})SL-NAD^+ bound per tetramer at 2° and the middle spectrum (b) with 3.5 moles of N^6-(^{15}N,D_{17})SL-coenzyme per tetramer. With the highly immobilized spin label, computer simulation was optimized and the dashed lines show good agreement between the calculated (- - -) and experimental (——) lineshapes. Spectra c and d are displays of the N^6-(D_{17})SL-NAD^+ bound to the GAPDH crystalline suspension at the same ratios, 0.5 and 3.5, respectively. Spectrum e is the computer generated spectrum for the anti-syn conformation of two pairs of N^6-(^{15}N,D_{17})SL-NAD^+ probes interacting cross the R-axis. Clearly, this calculated dipolar lineshape does not match that of the experimental data in Spectrum b.

positions of the nitroxide groups are fixed in a static position and not affected by the overall rotation of the protein. The MENO program of Eaton *et al.* (1983) was used for these simulations, which positioned the angles of the two interacting nitroxide groups and assigned the distance between the two unpaired electrons (12.8 Å) (Figure 22). The simulation for the dipolar spectra of the N^6-(^{15}N,D_{17})SL-NAD^+ complex was more accurate than for the N^6-(D_{17})SL-NAD^+. The latter was useful, however, in verifying the *anti-anti* conformation of the NAD^+ molecule.

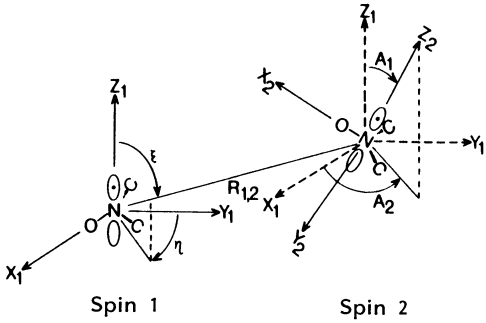

Figure 22. Spatial representation of the angles and distance relating the interacting nitroxide radicals on adjacent monomers across the R-axis. The orientation of the principal axis systems of the electron-Zeeman (g) and nitrogen hyperfine (A) tensors relative to the molecular coordinate system are shown above. The X axis is along the N—O bond, and the Z axis extends along the nitrogen PZ orbital. The Y axis is located such that the C—N—C atoms are in the X, Y plane. The unpaired electron is positioned in the molecular orbital of the N—O bond. With molecular modeling the distance between the interacting nitroxide spin labels, $R_{1,2}$, was ascertained. Likewise, the values for the four angles defining the direction of the interelectron vector $R_{1,2}$ were determined: 1) ξ, the angle between $R_{1,2}$ and Z_1; 2) η, the angle between the projection of $R_{1,2}$ in the X_1, Y_1 plane and the positive Y_1 axis; 3) A_1, the angle between the Z_2 axis of spin 2 and the positive Z_1 axis of spin 1; and 4) A_2, the angle between the projection of Z_2 in the X_1, Y_1 plane and the positive X_1 axis. The MENO program (Eaton *et al.*, 1983) permits the definition of $R_{1,2}$ and angles A_1 and A_2 which were in good agreement with the crystallographic data.

Although these simulations of dipolar spectra are not entirely coincident with the experimental data, no reasonable simulation could have been accomplished without the isotopically substituted probes.

3.3.7. Comparison of EPR Data and Molecular Modeling of the Crystalline GAPDH

The greater analytical strength obtained with the new probes enables a valuable verification by EPR of structural information obtained by molecular modeling. The EPR data were correlated with the molecular models constructed on the interactive computer graphics system using the crystalline structure for the lobster enzyme (Moras *et al.*, 1975). The NAD^+ binding sites are closely related in a wide variety of species, as the pocket for the adenine ring is highly conserved (Olsen *et al.*, 1975). For the molecular modeling, the NAD^+ moieties and the protein structure were left unchanged and the position of the nitroxide ring adjusted to minimize overlap with protein atoms (Beth *et al.*, 1984b). The nitroxide ring projects from the protein backbone into the space between the adjacent subunits across the *R* axis (Figure 23). Only two residues, Phe 34 and Val 98, form close contacts of 3.3 Å and 3.4 Å with the spin label and partially restrain the motion of the nitroxide group. The distance relating the nitroxide radicals of interacting spin-labeled coenzymes was 11-13 Å by molecular modeling, in good agreement with 12.8 Å determined by computer simulation of EPR data.

3.3.8. Characterization of C8-(D_{17})SL-NAD^+ Binding to Glyceraldehyde-3-Phosphate Dehydrogenase

A further demonstration of the utility of the isotopically substituted spin labels is shown here using C8-(D_{17})SL-NAD^+. This analog was added to glyceraldehyde-3-

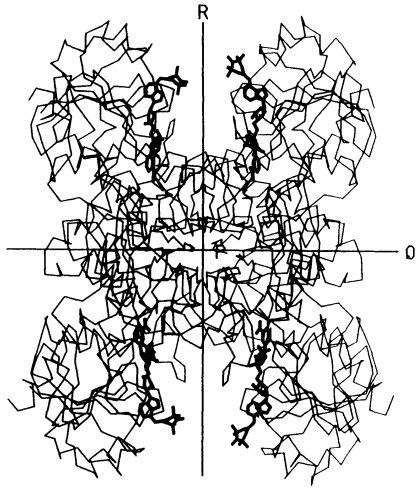

Figure 23. Spatial arrangement of four monomers of crystalline GAPDH with four N^6-SL-NAD^+ bound in the catalytic centers. The α-carbon backbone of the tetramer is viewed along the *P* axis. The four spin labels in the *anti-anti* binding geometry are shown in dark outline projecting into the intermonomeric space as determined by molecular modeling.

phosphate dehydrogenase at stoichiometries from 0.50 to 6.0 mol C8-DSL-NAD^+ per mole of tetramer and the corresponding bound stoichiometries ranged from 0.47 to 3.90 (Figure 24) (Wilder, 1985). At bound stoichiometries of less than one C8-(D_{17})SL-NAD^+ per tetramer, the distance between the extreme low- and high-field peaks in the hyperfine spectra (ΔH) was only 63 gauss. This value was lower than that for N^6-(D_{17})SL-NAD^+ (ΔH = 69 gauss) because of the internal "wobble" of the bound C8-(D_{17})SL-NAD^+. This motion was verified on examination of the ammonium sulfate precipitated enzyme with 0.5 mole of the C8-analog bound per mole of tetramer. The precipitated enzyme at 2 °C was not completely immobilized, because the distance between the extrema was only 66 gauss. However, at −17 °C the ΔH value increased to 70.5 gauss, almost equivalent to the immobilization seen with the N^6 analog at 2 °C.

The dipolar spectra of the soluble enzyme with 3.9 mol C8-(D_{17})SL-NAD^+ bound had a wider ΔH (93.6 gauss) than that of the N^6-(D_{17})SL-NAD^+ (namely, 77.4 gauss).

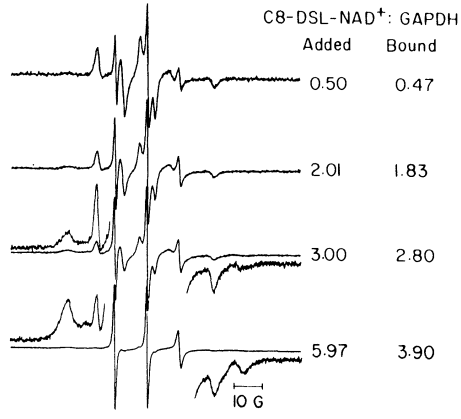

Figure 24. X-band EPR spectra of C8-(D_{17})SL-NAD^+ bound to GAPDH at four different stoichiometries. The C8-(D_{17})SL-NAD^+-enzyme complexes were prepared as in Figure 17. The hyperfine and dipolar line shapes of the C8-(D_{17})SL-NAD^+ complexes are distinctly different from those of N^6-(D_{17})SL-NAD^+ in Figure 17.

The wider ΔH of 93.6 gauss indicated that the nitroxide radicals of the C8 analogs on adjacent monomers were positioned more closely together, 8–9 Å, as confirmed by molecular modeling (Birktoft and Park, 1985). When the positions of the C8 and N^6 analogs are superimposed in a single monomer (Figure 25), it can be seen that the nitroxide spin label of the C8-(D_{17})SL-NAD^+ projects into the intermonomeric cavity without any obstruction, thereby permitting more "wobble" than with the N^6 derivative which is partially restrained by Phe-34 and Val-98. This internal "wobble" dictated against computer simulations of the dipolar spectrum of the C8 spin label.

The binding constants K_1–K_4 for C8-(D_{17})SL-NAD^+ are almost identical to those for the N^6 counterpart. Moreover, when the spectral data for the C8 spin-labeled analog were applied to analyses of the three models for negative cooperativity in NAD^+ binding, the ligand-induced model of Conway and Koshland (1968) showed the best fit with experimental findings. Thus the C8 spin label provided verification for random binding of the second and third SL-NAD^+ to the unfilled monomers of tetrameric GAPDH.

Since the C8-DSL-NAD^+ can participate in the enzymatic reaction with a V_{max} 80% that of native NAD^+, EPR spectroscopy was employed to monitor changes in the interactions between glyceraldehyde-3-phosphate dehydrogenase and C8-DSL-NAD^+ molecules during catalysis (Figure 26). With the addition of substrate, glyceraldehyde-3-phosphate, to the C8-(D_{17})SL-NAD^+-enzyme complex, there was a concomitant increase in the distance between the high- and low-field extrema of the dipolar components, and ΔH went from 93.6 to 96.1 gauss. This indicated that the coenzyme was positioned differently in the ternary complex. Removal of the substrate restored the original dipolar spectrum of the binary coenzyme-enzyme complex with ΔH = 93.6 gauss. Although similar results can be obtained with N^6-(D_{17})SL-NAD^+, the

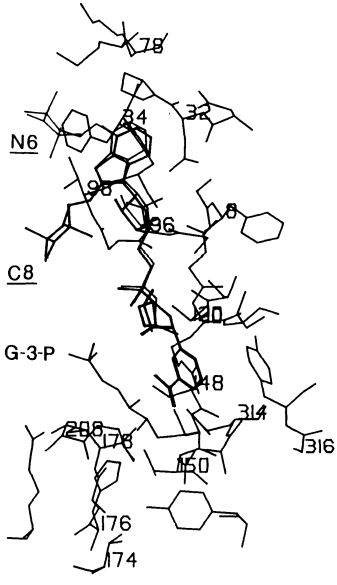

Figure 25. Comparison of the spatial positioning of the N^6-SL-NAD^+ and C8-SL-NAD^+ bound in the catalytic center of a monomer of GAPDH. The protein residues constituting the active center for binding substrate, coenzyme, and phosphate are shown by the lighter lines. The α-carbon backbone of the monomer includes the active site cysteine-149 for the covalent binding of the substrate, glyceraldehyde-3-phosphate (G-3-P). The nicotinamide ring of SL-NAD^+ is displayed in darker lines and is closely approximated to the active site for the catalytic H transfer. The nitroxide spin label on the N^6 position of the adenine ring (N^6) is partially constrained by phenylalanine-34 and valine-98. By contrast, the nitroxide spin label on the C8 carbon of the adenine ring (C8) projects into the intermonomeric space completely unobstructed, thereby permitting more motional mobility.

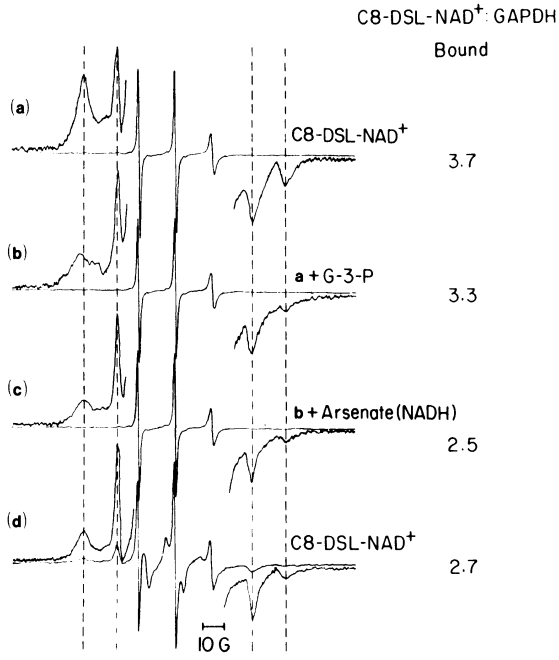

Figure 26. X-band EPR spectra of enzyme-bound C8-(D_{17})SL-NAD^+ in the presence and absence of substrate, glyceraldehyde-3-phosphate. Spectrum (a) represents a binary complex of C8-(D_{17})SL-NAD^+. Spectrum (b) shows the ternary complex formed on addition of substrate, (G-3-P), and formation of SL-NADH. The distance between the extrema (ΔH) increases to 96.8 gauss. When arsenate is added to the ternary complex (spectrum b), the substrate is oxidized, dissociates from the enzyme, and the binary complex of GAPDH-C8-(D_{17})SL-NADH remains (spectrum c). This spectrum shows a ΔH of 93 gauss, identical to that of the binary complex of the GAPDH-C8-(D_{17})SL-NAD^+ at the same stoichiometry (spectrum d). Thus substrate and C8-(D_{17})SL-NAD^+ interact so as to reposition the adenine ring in the active-ternary complex. C8-(D_{17})SL-NADH binds less tightly than C8-(D_{17})SL-NAD^+ in accordance with known coenzyme binding constants.

changes in ΔH are smaller and not as easily discernible. Thus the mobility and proximity of the C8 derivatives make this analog the preferred coenzyme for mechanism studies.

3.4. Interactions of N^6-(D_{17})SL-NAD^+ with GAPDH Bound to Band-3 Protein of Erythrocyte Membranes

As mentioned previously, GAPDH binds to the transmembrane, anion transport protein, Band-3, on the erythrocyte (Section 2.3.4). At physiological pH of 7.0, the catalytic activity of membrane-bound enzyme is substantially inhibited by as much as 70%. Since the inhibition is competitive with NAD^+, it was of interest to examine SL-NAD^+ binding of the membrane-associated dehydrogenase (Beth *et al.*, 1984a; Wilder, 1985). At pH 7.5, the soluble enzyme bound 3.8 mol N^6-(D_{17})SL-NAD^+ per tetramer, and the membrane-associated dehydrogenase only 2.7 mol SL-coenzyme

(Figure 27). When the pH was lowered to 7.0, the coenzyme binding of the soluble enzyme was unchanged, but the membrane-associated enzyme now bound only 2.0 equivalents of SL-NAD^+. Thus the overall inhibition of catalysis by band-3 association may be in part related to inhibition of NAD^+ binding.

Although the above stoichiometries of NAD^+ binding could have been determined by other methodologies, such as ^{14}C-NAD^+, the exact positioning of the coenzyme within the catalytic center was best ascertained by EPR techniques. Since the EPR line shape of the electron-electron dipolar interactions was identical under all the above conditions, it is clear that the positioning of the adenine ring of the coenzyme was not altered and only the binding stoichiometry changed (Figure 27). By contrast, the ^{15}N,DMSL experiments (Section 2.3.4) showed that the conformation of the active site in the area of cysteine-149 was modified when the enzyme was membrane-associated. Thus one can "map" conformational changes in the active center during catalysis or on association with membranes.

3.5. Binding of Deuterated and ^{15}N,Deuterated-SL-NADH Analogs to β-Hydroxybutyrate Dehydrogenase (BDH)

High-resolution N^6-(D_{17})- and C8-(D_{17})SL-NAD^+ or NADH analogs have been employed to study BDH. The NAD^+ analogs formed tight ternary complexes with the enzyme in the presence of sulfite, while binding of spin-labeled NADH was greatly enhanced in the presence of monomethyl malonate. In all these complexes two bound-coenzyme components were observed in the EPR spectrum (Fritzsche *et al.*, 1984). With the exception of the C8-SL-NAD^+-sulfite complex, the two components could not be detected in the spectrum of the enzyme-bound protonated analogs. When the viscosity of the buffer was increased by addition of glycerol, just one highly immobilized coenzyme derivative was observed. Using the doubly substituted spin-label N^6-(^{15}N,D_{17})SL-NADH, it was possible to simulate the complex spectrum and determine from the different tensor elements that the two spectral components did not arise from

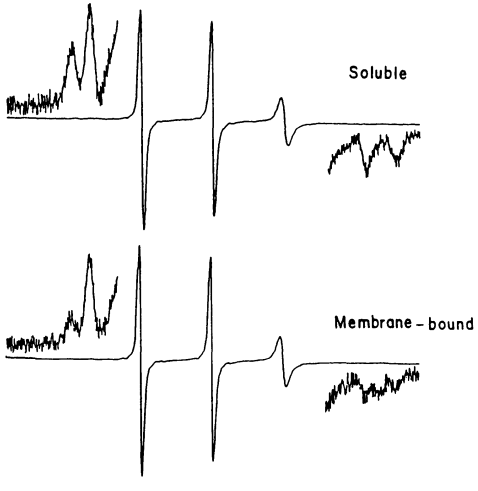

Figure 27. Comparison of EPR spectra of N^6-(D_{17})SL-NAD^+ complexed with soluble and membrane-bound GAPDH. The soluble or membrane-bound GAPDH was incubated with an excess of 15 equivalents of N^6-(D_{17})SL-NAD^+ at pH 7.5. The N^6-(D_{17})SL-NAD^+ complexed with the soluble (top) or membrane-bound enzyme (bottom) is shown in the amplified portions of the high- and low-field extrema. Although SL-NAD^+ was partially displaced by band-3, the spectral line shape of the remaining bound SL-NAD^+ was identical to that of the soluble enzyme at the same bound stoichiometry.

distinct motional environments but rather from environments with different polarities (Philipp *et al.*, 1984).

3.6. Binding of Spin-Labeled Adenine Nucleotides to Dehydrogenases and F_1ATPase

Investigations of the binding of ^{15}N,deuterated-AMP, ADP, and ATP spin-label derivatives (Appendix, Sections 3.1-3.7) to proteins are in the early stages of study. EPR experiments with two enzymes, glyceraldehyde-3-phosphate dehydrogenase and F_1ATPase, will serve to illustrate the EPR effects and significance of adenine nucleotide binding for elucidation of catalytic mechanism and metabolic regulation.

3.6.1. Glyceraldehyde-3-Phosphate Dehydrogenase (GAPDH) Complexes with Adenine Nucleotides and the Regulation of Catalysis

Adenine nucleotide binding (AMP, ADP, ATP, and cyclic-AMP) to glyceraldehyde-3-phosphate dehydrogenase substantially inhibited enzyme activity (Francis *et al.*, 1971). Two types of inhibition were observed: (1) competitive inhibition with NAD^+ or phosphate and (2) irreversible inhibition requiring a long-term incubation of the enzyme and nucleotide. The inhibition data suggested two types of adenine nucleotide binding sites, which have subsequently been verified with spin-label derivatives and EPR techniques. With GAPDH isolated from sturgeon, Glöggler *et al.* (1982a) first observed that C8-SL-AMP bound to a total of eight sites per tetramer as deduced from EPR titrations. Curve-fitting procedures employing nonlinear regression analysis were in accordance with two independent binding sites per monomer (Glöggler *et al.*, 1982a). Using rabbit muscle GAPDH with its tighter binding constants and the more highly resolved N^6-(D_{17})SL-AMP or C8-(^{15}N,D_{17})SL-AMP, detailed analyses of nucleotide interactions with apo-enzyme were possible (Wilder, 1985; Karim, 1986). Both N^6-(D_{17})SL-AMP and C8-(^{15}N,D_{17})SL-AMP showed four tightly bound and three or four loosely bound spin-labeled nucleotides, which were observed as immobilized components in the low- and high-field portions of the EPR spectra.

Interestingly, dipolar interactions were not observed at pH 8.0 where inhibition of catalysis is minimal, but were present at pH 7.2 in the range of strong inhibition (80-90%). Addition of NAD^+ sufficient to occupy only one of the four catalytic centers of the tetramer resulted in the removal of four SL-AMP and retention of three or four equivalents of bound SL-AMP. Thus the first NAD^+ molecule induces conformational changes in all four subunits (Karim, 1986). It is remarkable that the addition of substrate glyceraldehyde-3-phosphate to the enzyme-C8-(^{15}N,D_{17})SL-AMP complex induced conformational changes, which caused the release of 3.6 equivalents of SL-AMP and simultaneously enhanced dipolar interactions between the remaining 2.7 bound SL-AMP. The line shapes of the dipolar spectra of SL-AMP and SL-NAD^+ are not identical, indicating different positionings of the adenine nucleotides and coenzymes (Karim, 1986).

Since adenine nucleotide binding (particularly ATP) to GAPDH in muscle may play a physiological role in the metabolic regulation of the enzyme, the understanding of nucleotide interactions assumes importance for this and many other regulated steps in the glycolytic pathway (Oguchi *et al.*, 1973).

3.6.2. Formation of F_1ATPase Complexes with 2′- and 3′-(^{15}N,D_{13})SL-ATP and/or 2′- and 3′-(^{14}N)SL-ADP (See Appendix, Section 3.6)

F_1ATPases from most species have nine subunits, $\alpha_3\beta_3\gamma\delta\varepsilon$, with six nucleotide binding sites located on the α and β subunits. Three tight sites are filled with ADP, which exchanges slowly and presumably involves structural stabilization of the enzyme. The three loosely binding nucleotide sites are considered to be the catalytic sites and are readily exchangeable. In the F_1ATPase isolated from *Micrococcus leuteus*, there are two tight sites occupied by ADP. The mixture of 2′- and 3′-SL-ATP is hydrolyzed by the enzyme, however, only in the presence of Ca^{2+}. Hydrolysis of ATP itself requires Mg^{2+}, while Ca^{2+} is inhibitory. When a mixture of 2′- and 3′-(^{15}N,D_{13})SL-ATP is added to the enzyme in the absence of Ca^{2+}, primarily loose sites are occupied and no hydrolysis occurs (P. Vogel-Claude, H. J. Schäfer, and W. E. Trommer, unpublished results). Thereafter, a large excess of a mixture of 2′- and 3′-(^{14}N)SL-ADP is added to displace a portion of the tightly bound native ADP. With this second addition, spin–spin interactions are observed between the ^{15}N and ^{14}N labels. More recently, these studies were extended to F_1ATPase from beef heart mitochondria. This enzyme can be totally depleted of intrinsic nucleotides. Specific labeling of noncatalytic sites was achieved by means of a photoaffinity spin-labeled ATP analog (Vogel-Claude *et al.*, 1988). Thus it may be possible to determine short-range distances between the adenine nucleotide binding sites.

3.7. Future Applications

^{15}N and deuterium substitution in the coenzyme analogs, SL-NAD^+ and SL-NADH, provided the spectral simplification, high resolution, and enhanced sensitivity which were prerequisite for most of the studies of ligand binding, conformational changes, and enzyme mechanism. To date, the protonated spin-labeled coenzymes have been shown to be active cofactors for 12 different dehydrogenases, suggesting a promising future for further in-depth analyses of oxidation–reduction reactions with isotopically substituted coenzyme analogs.

The EPR experiments with GAPDH and F_1ATPase using isotopically substituted adenine nucleotide derivatives serve as examples of many possible regulatory and mechanistic studies of enzymes and other functional proteins. With the synthesis of ^{15}N,deuterated-SL-ATP derivatives, the EPR field can be expanded into the area of enzymes involved in energy production, utilization, and regulation. The recent preparation of SL-ATP derivatives which can bind covalently (Trommer, 1987; Vogel-Claude *et al.*, 1988) to the catalytic or allosteric sites of enzymes may be particularly useful in characterizing otherwise very loosely associated adenine nucleotides. Corresponding photoaffinity spin-labeled analogs of NAD^+ have been prepared as well (Trommer, 1987; Wolf *et al.*, 1987).

4. ADVANTAGES OF ^{15}N AND ^{15}N,DEUTERATED STEARIC ACID AND CHOLESTANE SPIN LABELS FOR EVALUATION OF MOTION OF LIPIDS IN MEMBRANES

In order to characterize the motion of membrane lipids with greater accuracy, ^{15}N-5-NS, the stearic acid derivative with a ^{15}N-doxyl group on carbon 5, was

synthesized by a new procedure (see Appendix, Section 4.1) (Venkataramu *et al.*, 1983b). Subsequently, ^{15}N-12-NS and ^{15}N-16-NS were prepared as probes for the deeper levels of the bilayer and ^{15}N-cholestane as a surface monitor (see formulae, page 584). For further enhancement of sensitivity and resolution, (^{15}N,D_{12})-5-NS was prepared with deuterium substituted on the doxyl group bearing the nitroxide radical and on the two adjacent methylene carbons. The totally deuterated (^{15}N,D_{41})-12-NS was made as described in the Appendix, Section 4.2 (Venkataramu *et al.*, 1985). Investigative work with ^{15}N and ^{15}N,deuterated lipid spin labels is still in the preliminary stage. However, the initial experiments presented in the following text and figures clearly indicate the expansion of EPR capabilities using these probes for studies of cell membranes and also for possible clinical applications.

4.1. Improved Spectral Sensitivity of Rapidly Tumbling ^{15}N and ^{15}N,Deuterium Substituted Stearic Acid and Cholestane Analogs

A comparison of the EPR spectra of ^{14}N-5-NS, ^{15}N-5-NS, and (^{15}N,D_{12})-5-NS as freely tumbling entities is shown in Figure 28. The height of the ^{15}N-5-NS low-field peak ($M_I = -\frac{1}{2}$) is 1.6 times greater than that of the ^{14}N-5-NS middle peak ($M_I = 0$) when calculated on the basis of spin concentration as determined by the double integral. Similar increases in sensitivity (1.4- to 1.6-fold) were demonstrated with ^{15}N-12-NS, ^{15}N-16-NS, and ^{15}N-cholestane as compared with their respective ^{14}N counterparts. Since the linewidths of the ^{15}N compounds were not significantly different from those of the corresponding ^{14}N derivatives (<8%), the increase in peak height was due to the reduced number of manifolds from 3 to 2 with the ^{15}N spin labels (Venkataramu *et al.*, 1983b).

The (^{15}N,D_{12})-5-NS showed a 2.5-fold increase in spectral intensity compared to the ^{14}N-5-NS. This gain in sensitivity was due both to spectral simplification and to a decrease in the linewidth of the manifold $M_I = -\frac{1}{2}$ from 1.0 to 0.67 gauss and $M_I = +\frac{1}{2}$ from 1.12 to 0.79 gauss (Venkataramu *et al.*, 1985). The completely deuterated (^{15}N,D_{41})-12-NS showed an even greater fivefold increase in overall spectral intensity compared to ^{14}N-12-NS due to the decreased linewidth of $M_I = -\frac{1}{2}$ to 0.44 gauss and $M_I = +\frac{1}{2}$ to 0.55 gauss (Venkataramu *et al.*, 1985). Since total deuteration of the alkyl chain produced the most significant decreases in linewidth, remote protons on the partially deuterated chain must interact with the nitroxide group to produce inhomogeneous line broadening of the (^{15}N,D_{12})-5-NS spectrum.

4.2. Advantages of ^{15}N and ^{15}N,Deuterated Stearic Acid Spin Labels for Studies on Binding to Proteins

Serum albumin is the physiological carrier of fatty acids in circulating blood. Under normal conditions, albumin binds up to four moles of fatty acid per mole of protein. Stearic acid spin labels bind to bovine serum albumin (BSA) in a manner similar to natural fatty acids, with one very tight site and three progressively looser

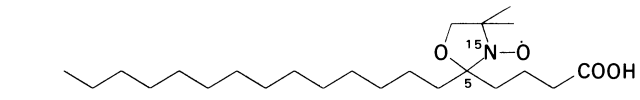

[^{15}N]-5-NS

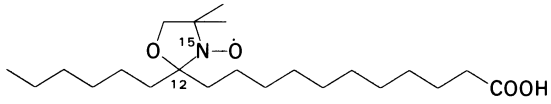

[^{15}N]-12-NS

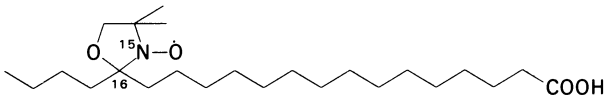

[^{15}N]-16-NS

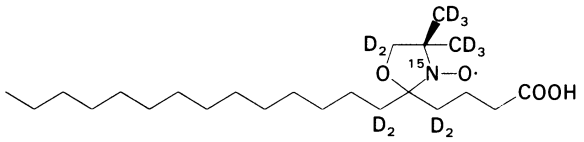

[^{15}N, D_{12}]-5-NS

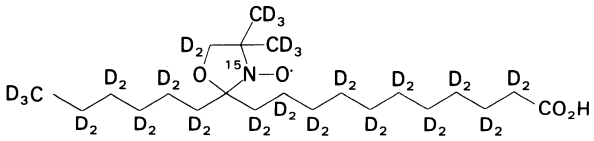

[^{15}N, D_{41}]-12-NS

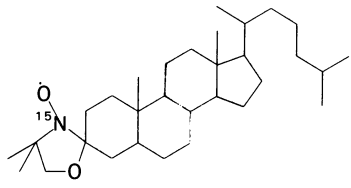

[^{15}N]-Cholestane

sites (Perkins *et al.*, 1982). For examining the effect of ^{15}N and deuterium substitution in the fatty acid derivatives, BSA was spin labeled with ^{14}N-, ^{15}N-, or (^{15}N,D_{12})-5-NS at a low stoichiometry of 0.3 spin label to 1 BSA, to ensure binding primarily at the tight site with minimal unbound, freely tumbling 5-NS (Figure 29). The overall spectral intensity of the tightly bound ^{15}N-5-NS and (^{15}N,D_{12})-5-NS was 1.4- and 1.7-fold greater than the height of the central peak of ^{14}N-5-NS at the same fatty acid:BSA ratio. On comparing the low-field peak ($M_I = -\frac{1}{2}$) for ^{15}N-5-NS and (^{15}N,D_{12})-5-NS with the low-field peak for ^{14}N-5-NS ($M_I = +1$), the ^{15}N analogs showed 3.1- and 3.8-fold increases in intensity, respectively (Venkataramu *et al.*, 1983a).

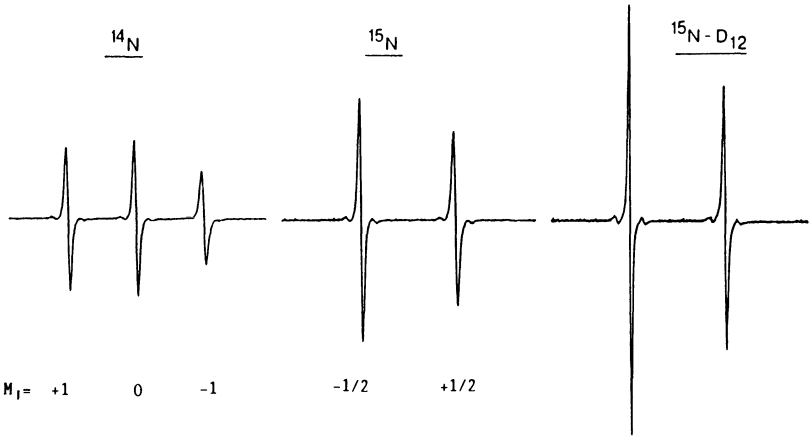

Figure 28. EPR spectra of freely tumbling ^{14}N-, ^{15}N-, and (^{15}N,D_{12})-5-NS. The EPR spectra are 50 gauss scans of 10 μmolar solutions of ^{14}N-, ^{15}N-, and (^{15}N,D_{12})-5-NS spin labels in 5 mmolar sodium phosphate buffer, pH 7.5, at 23 °C. Identical instrument settings were used for all scans, namely, 10 mW microwave power and 100 kHz field modulation of 0.5 gauss amplitude. Values for the improved spectral intensities and linewidths of the ^{15}N spin labels are noted in the text.

The ^{15}N-12-NS or ^{15}N-16-NS complex with BSA displayed improvements in sensitivity and resolution comparable to those of ^{15}N-5-NS. Totally deuterated (^{15}N,D_{41})-12-NS showed a 1.9-fold increase in overall sensitivity as compared to ^{14}N-12-NS. Again, the totally deuterated analog manifested somewhat greater sensitivity than the (^{15}N,D_{12})-5-NS derivative (Park *et al.*, 1988).

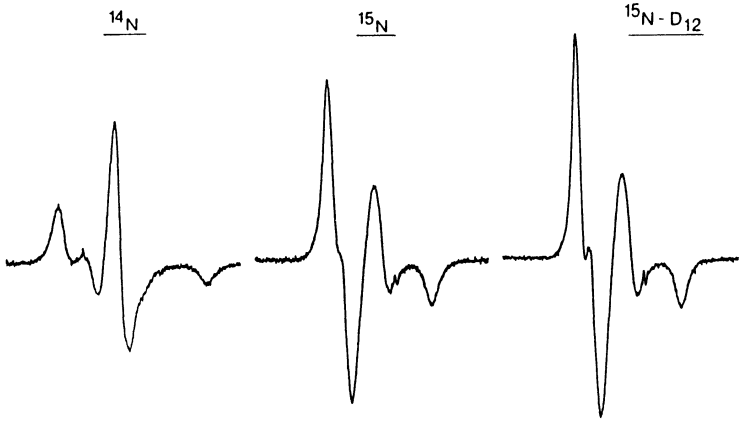

Figure 29. EPR spectra of ^{14}N-, ^{15}N-, and (^{15}N,D_{12})-5-NS bound to bovine serum albumin. The 5-NS spin labels were tightly bound to bovine serum albumin at molar ratios of 0.3 5-NS : 1.0 BSA. The spectra are 100 G displays recorded at 23 °C with identical instrument settings of 10 mW microwave power, and 100 kHz field modulation of 0.5 G amplitude. The enhanced sensitivity and resolution of the ^{15}N spin labels are detailed in the text.

Greater sensitivity and resolution of both EPR and ST-EPR spectra of protein-bound ^{15}N-5-NS could be demonstrated over a wide range of correlation times from 8×10^{-8} to 1×10^{-5} s, obtained in glycerol concentrations from 0 to 70%. At each correlation time, the ^{15}N-5-NS showed a 1.4-fold increase in overall sensitivity compared to ^{14}N-5-NS for both EPR and ST-EPR spectra (Figure 30). This constancy of increase, even for lyophilized samples ($\tau_c = \infty$) was not seen with the DMSL-BSA complex which showed different levels of improvement in sensitivity at the various values of τ_c (Figures 2 and 4). As shown previously (Figures 7 and 9), the values for L, L'', H, and H'' are more accurately measured in the ^{15}N spectra, and consequently the slow motional dynamics are more readily characterized in accordance with the propositions of Robinson and Dalton (1981).

The spectral simplification afforded by ^{15}N substitution was important for computerized simulation of the ^{15}N-5-NS complex with BSA (Figure 31). Although there was some overlap in the $M_I = -\frac{1}{2}$ and $+\frac{1}{2}$ manifolds, all elements of the electron-nuclear hyperfine A tensors and the electron Zeeman g tensors could be determined (Figure 31). Discrepancies in the experimental and simulated line shapes may be due in part to some "wobble" of the bound ^{15}N analog or heterogeneity in binding sites even at the low stoichiometry of 0.3 spin label:1 BSA (Perkins *et al.*, 1982).

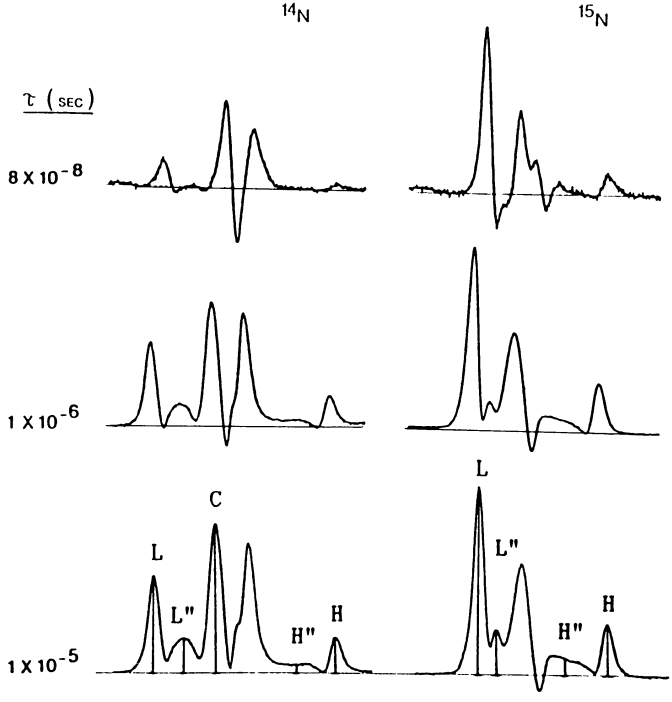

Figure 30. ST-EPR spectra of ^{14}N-5-NS and ^{15}N-5-NS bound to bovine serum albumin. The ST-EPR spectra are 100 G displays recorded at 0 °C with identical instrument settings. The glycerol concentrations were 0, 60, and 70% at τ_c values of 8×10^{-8}, 1×10^{-6}, and 1×10^{-5} s, respectively. ^{15}N-5-NS shows a 1.4-fold increase in overall spectral intensity in all three spectra.

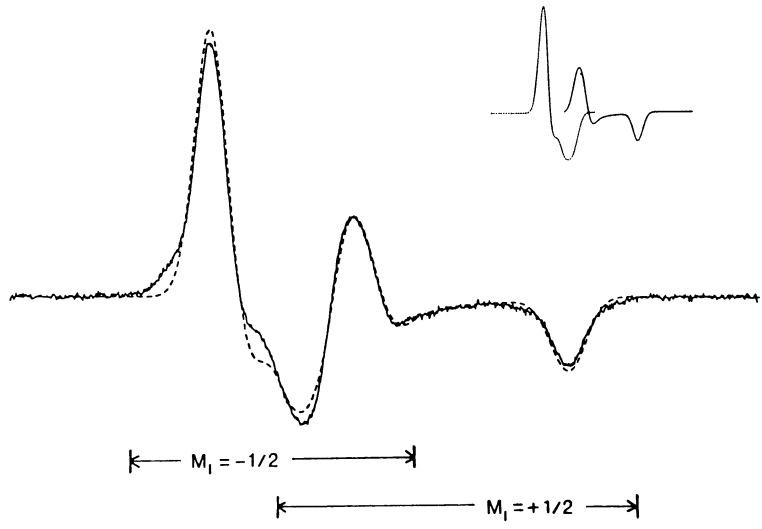

Figure 31. Simulation of rigid-lattice line shape of ^{15}N-5-NS bound to bovine serum albumin. The experimental EPR spectrum of ^{15}N-5-NS bound to albumin in 60% glycerol at 2 °C (——) was obtained as described in Figure 28. The superimposed simulation (- - -) was carried out employing the routine of Balasubramanian and Dalton (1979). The following parameters were used to simulate the experimental spectra: $g_{xx} = 2.0088$, $g_{yy} = 2.0054$, $g_{zz} = 2.0022$, $A_{xx} = 8.0$ G, $A_{yy} = 6.0$ G, $A_{zz} = 46.75$ G, $T_1 = 2\ \mu$s, and $T_2 = 0.2\ \mu$s. A Gaussian post-broadening of 2.3 G was performed to simulate the broadening effects due to unresolved proton couplings. The $M_I = +\frac{1}{2}$ and $M_I = -\frac{1}{2}$ manifolds are indicated above and also shown as separate tracings in the insert.

4.3. Improved Spectral Analysis of Lipid Motion in Erythrocyte (RBC) Membranes with ^{15}N-5-NS and (^{15}N,D_{12})-5-NS

The advantages of the ^{15}N and ^{15}N,deuterium substituted fatty acid spin probes for investigations of RBC membranes have been noted in several preliminary presentations (Venkataramu *et al.*, 1982, 1983a). As an example, the spectra of ^{14}N-, ^{15}N-, and (^{15}N,D_{12})-5-NS inserted into erythrocyte membranes are compared in Figure 32. In this case, there was no increase in overall spectral intensity with the ^{15}N-5-NS probe. Even (^{15}N,D_{12})-5-NS showed only a 1.2-fold increase in intensity as a result of narrowing of the linewidths. However, the marked change in line shape with ^{15}N-5-NS improved the visualization of low- and high-field peaks. Gains of three- to fourfold in the signal height at the low- and high-field extrema were observed. This permits the use of lower concentrations of spin label in biological membranes and thereby minimizes spin–spin interactions and perturbations of the membrane bilayer. Moreover, the spectral simplification and increased resolution of major- and minor-element spectral structurings of ^{15}N-5-NS and (^{15}N,D_{12})-5-NS allow accurate measurement of both the important order parameters, $A_\parallel$ and $A_\perp$, by direct inspection. With conventional ^{14}N lipid spin labels, measurement of $A_\perp$ is complicated by the overlapping of the three manifolds of ^{14}N (spin 1). The order parameter (S) can therefore be more accurately determined with the ^{15}N spin labels, since the correction for overlaps in ^{14}N-5-NS spectra, as calculated by Gaffney (1976), is not necessary.

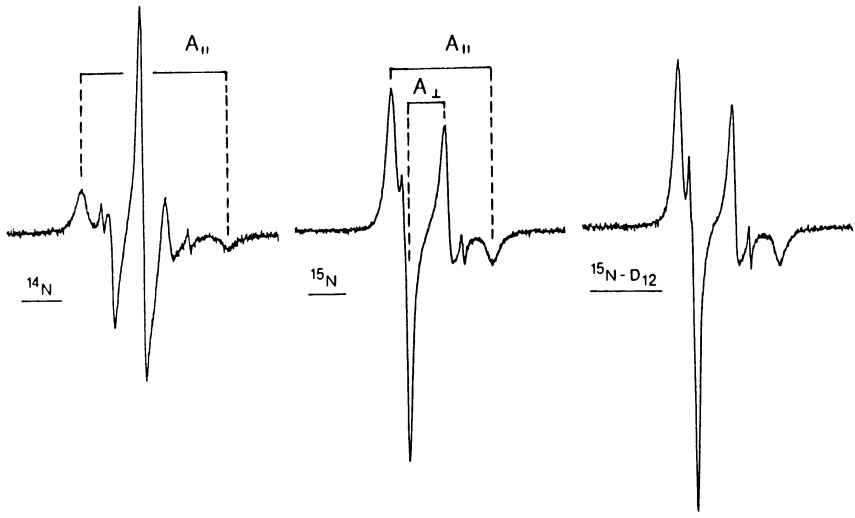

Figure 32. Comparison of EPR spectra of ^{14}N-, ^{15}N-, and (^{15}N,D_{12})-5-NS inserted into red blood cell (RBC) membranes. Washed erythrocytes were spin labeled with the three 5-NS spin probes as described previously (Wilkerson *et al.*, 1978). The 100 G EPR displays were recorded at 37 °C with instrument settings of 10 mW microwave power, and 100 kHz field modulation at 1.0 gauss amplitude. $A_{\parallel}$ and $A_{\perp}$ are indicated on the ^{14}N- and ^{15}N-5-NS spectra as accurately determined by direct inspection.

The EPR spectra of ^{15}N-12-NS and ^{15}N-16-NS inserted in RBC membrane can also be more accurately quantitated than those of the corresponding ^{14}N derivatives with regard to the order parameter (S). Moreover, the spectra of ^{15}N fatty acid analogs are more readily manipulated than their ^{14}N counterparts in subtraction programs for differentiating the immobilized components in the bilayer from the free, rapidly tumbling probe.

4.4. Investigation of Erythrocyte Abnormalities Using ^{15}N-5-NS

Since ^{15}N-5-NS has advantages in the measurement of slow motion parameters using the techniques of ST-EPR (Figure 30), this probe was employed to characterize fatty acid mobility in the RBC membranes of patients with Duchenne muscular dystrophy. It was demonstrated earlier that the ST-EPR spectrum of ^{14}N-5-NS inserted into membranes of erythrocytes from patients with Duchenne muscular dystrophy showed initially a diminished spectral intensity and a relatively featureless line shape in comparison to the corresponding spectra with red cells from normal boys (Figure 33) (Wilkerson *et al.*, 1978). In the course of 24 h, there was a progressive increase in spectral intensity and changes in the ratio of the C'/C parameter with Duchenne RBC but not with normal cells. With isotopically substituted ^{15}N-5-NS, abnormalities in the Duchenne RBCs were more easily quantitated due to sharper peaks (Figure 33) (Park *et al.*, 1988). The increased intensities of the isolated L and L'' parameters were fourfold greater than those obtained with ^{14}N-5-NS. In Duchenne RBC the increase in the L''/L parameter over the 24 h period indicated increasing immobilization of the spin label

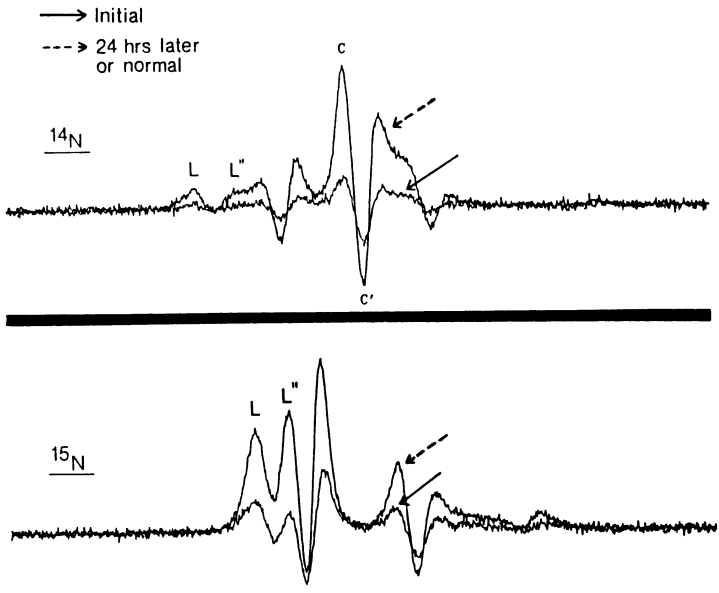

Figure 33. Comparison of ST-EPR spectra of ^{14}N- and ^{15}N-5-NS inserted into erythrocyte membranes of Duchenne patients and normal subjects. The initial ST-EPR spectra of the labeled Duchenne erythrocytes were recorded at 37 °C immediately after the EPR measurements (Figure 32). The 100 G displays were measured at 63 mW microwave power, and 50 kHz field modulation at 5.0 G amplitude. The cells were then shaken slowly for 16–24 h at 37 °C. The late ST-EPR spectra were recorded with the same instrument settings. The peak parameters *L*, *L"*, *C*, and *C'* are indicated on the ST-EPR spectra.

and a substantially slower correlation time. The increase in spectral intensity after 24 h incubation may result from a slow diffusion of spin label from the initial insertion areas of high, focal concentration. This diffusion minimizes Heisenberg spin exchange and increases spectral structuring and intensity. The possibility of oxygen effects has not been completely excluded.

These EPR and ST-EPR line shapes of ^{15}N-5-NS in erythrocyte membranes of Duchenne patients have been seen consistently and demonstrate the improved utility of ^{15}N derivatives for this type of analysis. However, a sufficiently large population of Duchenne patients have not as yet been examined to establish the general clinical utility of examination by EPR for diagnosis and for following the progress of the disease or therapeutic regimes.

4.5. Studies of Collision Frequency and Vertical Fluctuations of ^{14}N and ^{15}N Spin-Labeled Pairs of Fatty Acids in Membranes Using ELDOR Spectroscopy

A combination of ^{14}N and ^{15}N stearic acid spin-label pairs in model membranes was first employed to evaluate collision frequency by using EPR measurements of line broadening which resulted from intermolecular spin–spin interactions (Davoust *et al.*,

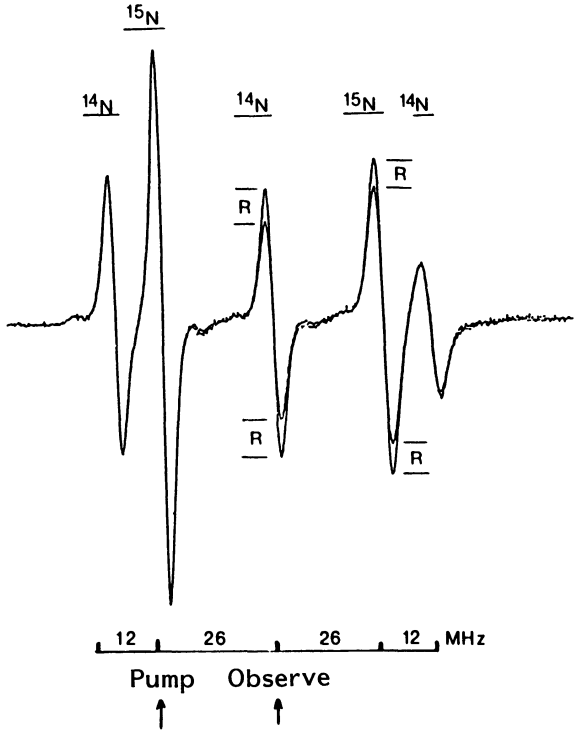

Figure 34. Spectra of the spin-label pair, ^{14}N-16-NS and ^{15}N-16-NS, demonstrating the ELDOR effect. The spin-label pair was inserted in model liposomes of dimyristoylphosphatidylcholine and suspended in borate buffer, pH 9.5, 47 °C. The superimposed ^{14}N and ^{15}N spectra are displayed with the pump field off and at 400 mW power. Horizontal lines indicate reduction in peak height (R) which quantitates ELDOR transfer of saturation. The pump-observed frequency separation of 26 MHz is shown by arrows (↑).

TABLE 3
Percent Reduction (R_∞ Values) of Fatty Acid Spin Label Pairs in DMPC at 47 °C, pH 9.5[a]

Observed	Pumped		
	^{15}N-16-NS	^{15}N-12-NS	^{15}N-5-NS
^{14}N-16-NS	32.7%	30.8%	18.4%
^{14}N-12-NS	30.9%	32.2%	26.2%

[a] Reductions are expressed as maximum percent decrease in the observed peak heights of $M_I = 0$ with pump power on. R_∞ values parallel the spatial separation of the spin labels along the fatty acid alkyl chain, i.e, the interaction of 16:16 = 12:12 > 16:12 = 12:16 ≫ 12:5 > 16:5.

1983a). Subsequently, ELDOR spectroscopy was employed to measure lateral diffusion as well as vertical fluctuations of the alkyl carbon chains of ^{14}N and ^{15}N spin-label pairs inserted into model dimyristoylphosphatidylcholine (DMPC) liposomes (Feix *et al.*, 1984b). This technique essentially rules out intramolecular relaxation processes, and thereby facilitates the characterization of interactions between two types of spin labels. Various pairs of labels were inserted into DMPC, for example: ^{14}N-16-NS and ^{15}N-16-NS; ^{14}N-16-NS and ^{15}N-12-NS; ^{14}N-16-NS and ^{15}N-5-NS. The EPR spectra of ^{14}N spin labels have regions which do not overlap with ^{15}N spectra (Figure 34). Therefore, collisions between ^{14}N and ^{15}N probes were readily detected by the reduction in signal intensity of the ^{14}N ($M_I = 0$) transition as the ^{15}N ($M_I = -\frac{1}{2}$) was pumped with high microwave power using ELDOR methodology (Feix *et al.*, 1984b). Figure 34 shows the experimental field swept, in-phase absorption spectra for equimolar (0.25%) ^{14}N-16-NS and ^{15}N-16-NS in DMPC at 47 °C with $\nu_p - \nu_0 = 26$ MHz with pump off and on. ELDOR reduction is noted by R and the horizontal lines. The decrease in signal intensity is due primarily to Heisenberg spin exchange. R_∞ was determined by extrapolation at a variety of pump powers at 27, 37, and 47 °C.

The percent reduction (R_∞) with various pairs of spin labels (Table 3) demonstrated that interaction with ^{14}N-16-NS was greatest with ^{15}N-16-NS, somewhat less with ^{15}N-12-NS, and decreased only by one-half with ^{15}N-5-NS. Therefore, it was concluded that vertical fluctuations of 16-NS toward the surface of the bilayer were quite pronounced.

These techniques with ^{14}N and ^{15}N spin-label pairs have been extended to include interactions with cholestane and phospholipid spin labels (Feix *et al.*, 1984a). The results indicate that the deeply inserted 16-NS can interact with spin-labeled cholestane at the surface of the bilayer, but not with the spin-labeled head group of phospholipid (dipalmitoylphosphatidylethanolamine) in the aqueous phase. Spin-labeled cholestane and phospholipid do interact, but only slightly. Thus it is possible to measure motional patterns and collision frequency of many lipid components within the hydrophobic membrane and also across the bilayer surface in the aqueous phase. In more recent experiments the composition of the model membrane has been modified (Feix *et al.*, 1987). These ELDOR studies provide a new approach for examining membrane microviscosity.

4.6. Future Applications

The better characterization of the motion of lipids in erythrocyte membranes using ^{15}N and ^{15}N,deuterated lipid spin labels may have important clinical applications. A number of neurological and neuromuscular diseases have been shown to exhibit abnormalities in the RBC as determined by EPR and appropriate spin labels (Butterfield, 1986). With further improvements in spectroscopy, the pathogenesis of disease or the beneficial effects of a therapeutic regime may be studied more easily. RBC are the most available tissue for repeated analyses.

The ELDOR investigations may bring a new experimental dimension to the elucidation of membrane structure-function relationships. The reasons are: (1) that collision rates of a variety of substances, including membrane transport proteins, hormone receptors, and hormones, could be observed if labeled appropriately with ^{14}N and ^{15}N spin probes; and (2) that ELDOR spectroscopy has a high level of

sensitivity. The latter may be a critical factor with transport or receptor proteins which are in very low concentration in biological membranes. The feasibility of ELDOR studies with membrane proteins is supported by early experiments of Davoust *et al.* using the protein, rhodopsin, inserted into reconstituted vesicles (Davoust *et al.*, 1983a).

REFERENCES

Adair, G. S., 1925, The hemoglobin system. VI. The oxygen dissociation curve of hemoglobin, *J. Biol. Chem.* **63**:529-545.

Balasubramanian, K., and Dalton, L. R., 1979, Computer simulation of EPR and ST-EPR spectra of nitroxide spin labels in the rigid lattice limit, *J. Magn. Reson.* **33**:245-260.

Bernhard, S. A., and MacQuarrie, R. A., 1973, Half-site reactivity and the "induced-fit" hypothesis, *J. Mol. Biol.* **74**:73-78.

Beth, A. H., Wilder, R., Wilkerson, L. S., Perkins, R. C., Meriwether, B. P., Dalton, L. R., Park, C. R., and Park, J. H., 1979, EPR and saturation transfer EPR studies on glyceraldehyde 3-phosphate dehydrogenase, *J. Chem. Phys.* **71**:2074-2082.

Beth, A. H., Perkins, R. C., Venkataramu, S. D., Pearson, D. E., Park, C. R., Park, J. H., and Dalton, L. R., 1980, Advantages of deuterium modification of nitroxide spin labels for biological EPR studies, *Chem. Phys. Lett.* **69**:24-28.

Beth, A. H., Venkataramu, S. D., Balasubramanian, K., Robinson, B. H., Dalton, L. R., Pearson, D. E., Park, C. R., and Park, J. H., 1981a, ^{15}N and deuterium substituted maleimide spin labels: Improved sensitivity and resolution for biological studies, *Proc. Natl. Acad. Sci. U.S.A.* **78**:967-971.

Beth, A. H., Balasubramanian, K., Wilder, R. T., Venkataramu, S. D., Robinson, B. H., Dalton, L. R., Pearson, D. E., and Park, J. H., 1981b, Structural and motional changes in glyceraldehyde-3-phosphate dehydrogenase upon binding to band-3 protein of the red blood cell membrane examined with [^{15}N, ^{2}H] maleimide spin label and EPR, *Proc. Natl. Acad. Sci. U.S.A.* **78**:4955-4959.

Beth, A. H., Balasubramanian, K., Robinson, B. H., Dalton, L. R., Venkataramu, S. D., and Park, J. H., 1983, Sensitivity of V_2' saturation transfer electron paramagnetic resonance signals to anisotropic rotational diffusion with ^{15}N-nitroxide spin labels. Effects of noncoincident magnetic and diffusion tensor principal axes, *J. Phys. Chem.* **87**:359-367.

Beth, A. H., Trommer, W., and Park, J. H., 1984a, Interaction of glyceraldehyde-3-phosphate dehydrogenase with band-3 protein of RBC membrane, VIII International Biophysics Congress, Bristol, England, Vol. 8, p. 214.

Beth, A. H., Robinson, B. H., Cobb, C. E., Dalton, L. R., Trommer, W. E., Birktoft, J. J., and Park, J. H., 1984b, Interactions and spatial arrangement of spin-labeled NAD^+ bound to glyceraldehyde-3-phosphate dehydrogenase: Comparison of EPR and x-ray modeling data, *J. Biol. Chem.* **259**:9717-9728.

Birktoft, J. J., and Park, J. H., 1985, The use of molecular graphics and x-ray crystallographic structural data in the interpretation of EPR data obtained from biological molecules, International Magnetic Resonance Conference, Denver, Colorado, Vol. 8, p. 178.

Brière, R., Dupeyre, R., Lemaire, H., Morat, C., Rassat, A., and Rey, P., 1965, Nitroxydes XVII: Biradicaux stables du type nitroxyde, *Bull. Chim. Soc. Fr.*: 3290-3297.

Butterfield, D. A., 1986, Spectroscopic methods in degenerative neurological diseases, *CRC Crit. Rev. Clin. Neurobiol.* **2**:169-240.

Cabantchik, Z. I., Knauf, P. A., and Rothstein, A., 1978, The anion transport system of the red blood cell: The role of membrane protein evaluated by the use of probes, *Biochim. Biophys. Acta* **515**:239-302.

Chance, B., and Park, J. H., 1967, The properties and enzymatic significance of the enzyme-diphosphopyridine nucleotide compound of 3-phosphoglyceraldehyde dehydrogenase, *J. Biol. Chem.* **242**:5093-5105.

Chiarelli, R., and Rassat, A., 1973, Synthèses de radicaux nitroxydes deuteries, *Tetrahedron* **29**:3639-3647.

Conway, A., and Koshland, D. E., 1968, Negative cooperativity in enzyme action. The binding of diphosphopyridine nucleotide to glyceraldehyde 3-phosphate dehydrogenase, *Biochemistry* **1**:4011-4022.

Dalton, L. A., Monge, J. L., Dalton, L. R., and Kwiram, A. L., 1974, Molecular and applied modulation effects in electron-electron double resonance. III. Bloch equation analysis for inhomogeneous broadening, *Chem. Phys.* **6**:166-182.

Dalton, L. R., Coffey, P., Dalton, L. A., Robinson, B. H., and Keith, A. D., 1975, Theory of nonlinear spin response: Rapid passage for very slow molecular reorientation, *Phys. Rev.* **11**:488-498.

Davoust, J., Seigneuret, M., Herve, P., and Devaux, F., 1983a, Collisions between Nitrogen-14 and Nitrogen-15 spin-labels. 1. Lipid-lipid interactions in model membranes, *Biochemistry* **22**:3137-3145.

Davoust, J., Seigneuret, M., Herve, P., and Devaux, F., 1983b, Collisions between Nitrogen-14 and Nitrogen-15 spin-labels. 2. Investigations on the specificity of the lipid environment of rhodopsin, *Biochemistry* **22**:3146-3151.

De Vijlder, J. J. M., and Slater, E. C., 1968, The reaction between NAD^+ and rabbit muscle glyceraldehyde phosphate dehydrogenase, *Biochim. Biophys. Acta* **167**:23-34.

Deparade, M. P., Glöggler, K., and Trommer, W. E., 1981, Isolation and properties of glyceral-dehyde-3-phosphate dehydrogenase from a sturgeon from the Caspian Sea and its interaction with spin labeled NAD^+ derivatives, *Biochim. Biophys. Acta* **659**:422-433.

Eaton, S. S., More, K. M., Sawant, B. M., Boymel, P. M., and Eaton, G. R., 1983, Metal-nitroxyl interactions. 29. EPR studies of spin-labeled copper complexes in frozen solution, *J. Magn. Reson.* **52**:435-449.

Feix, J. B., Venkataramu, S. D., Beth, A. H., Park, C. R., Park, J. H., and Hyde, J. S., 1984a, Electron-electron double resonance investigations on the interactions between ^{14}N and ^{15}N spin-label pairs of cholestane and fatty acids or phospholipids in membrane bilayers, International Conference on Magnetic Resonance in Biological Systems, Goa, India, Vol. 11, p. 73.

Feix, J. B., Popp, C. A., Venkataramu, S. D., Beth, A. H., Park, J. H., and Hyde, J. S., 1984b, An electron-electron double resonance study of interactions between ^{14}N and ^{15}N stearic acid spin-label pairs: Lateral diffusion and vertical fluctuations in dimyristoylphosphatidylcholine, *Biochemistry* **23**:2293-2299.

Feix, J. B., Yin, J. J., and Hyde, J. S., 1987, Interactions of ^{14}N:^{15}N stearic acid spin-label pairs: Effects of host lipid alkyl chain length and unsaturation, *Biochemistry* **26**:3850-3855.

Francis, S. H., Meriwether, B. P., and Park, J. H., 1971, Interaction between adenine nucleotides and 3-phosphoglyceraldehyde dehydrogenase. II. A study of the mechanism of catalysis and metabolic control of the multifunctional enzyme, *J. Biol. Chem.* **246**:5433-5441.

Fritzsche, T. M., McIntyre, J. O., Fleischer, S., and Trommer, W. E., 1984, Complex formation between nucleotides and D-β-hydroxybutyrate dehydrogenase studied by fluorescence and EPR spectroscopy, *Biochim. Biophys. Acta* **791**:173-185.

Gaffney, B. J., 1976, Practical considerations for the calculation of order parameters for fatty acid or phospholipid spin labels in membranes, in *Spin Labeling Theory and Applications* (L. J. Berliner, ed.), Vol. I, pp. 567-571, Academic Press, New York.

Gaffney, B. J., 1979, Spin label-thiourea adducts. A model for saturation transfer EPR studies of slow anisotropic motion, *J. Phys. Chem.* **83**:3345-3349.

Glöggler, K. G., Balasubramanian, K., Beth, A. H., Park, J. H., and Trommer, W. E., 1982a, The role of the nicotinamide moiety for negative cooperativity in glyceraldehyde-3-phosphate dehydrogenase as studied with EPR, *Biochim. Biophys. Acta* **706**:197-202.

Glöggler, K. G., Balasubramanian, K., Beth, A., Fritzsche, T. M., Park, J. H., Pearson, D. E., Trommer, W. E., and Venkataramu, S. D., 1982b, The synthesis of deuterium substituted spin labeled analogues of AMP and NAD^+ and their use in EPR studies of lactate dehydrogenase, *Biochim. Biophys. Acta* **701**:224-228.

Harris, J. I., Meriwether, B. P., and Park, J. H., 1963, Chemical nature of the catalytic sites in glyceraldehyde-3-phosphate dehydrogenase, *Nature (London)* **198**:154-157.

Hedrick, W. R., Mathew, A., Zimbrick, J. D., and Whaley, T. W., 1979, Intracellular viscosity of lymphocytes determined by a ^{15}N spin label probe, *J. Magn. Reson.* **36**:207-214.

Henis, Y. I., and Levitzki, A., 1981, The mechanism of negative cooperativity in rabbit muscle glyceraldehyde-3-phosphate dehydrogenase, *Ann. N.Y. Acad. Sci.* **366**:217-236.

Hill, E. J., Meriwether, B. P., and Park, J. H., 1975, Purification of rabbit muscle glyceraldehyde-3-phosphate dehydrogenase by gel filtration chromatography, *Anal. Biochem.* **63**:175-182.

Hwang, J. S., Mason, R. P., Hwang, L., and Freed, J. H., 1975, Electron spin resonance studies of anisotropic rotational reorientation and slow tumbling in liquid and frozen media. III. Perdeuterated 2,2,6,6-tetramethyl-4-piperidone N-oxide and an analysis of fluctuating torques, *J. Phys. Chem.* **79**:489-511.

Hyde, J. S., and Dalton, L. R., 1979, Saturation-transfer spectroscopy, in *Spin Labeling II. Theory and Applications* (L. Berliner, ed.), pp. 1-70, Academic Press, New York.

Johnson, M. E., Lee, L., and Fung, L.W.-M., 1982, Models for slow anisotropic rotational diffusion in saturation transfer electron paramagnetic resonance at 9 and 35 Ghz, *Biochemistry* **21**:4459-4467.

Kant, J. A., and Steck, T. L., 1973, Specificity in association of glyceraldehyde-3-phosphate dehydrogenase with isolated human erythrocyte membranes, *J. Biol. Chem.* **248**:8457-8464.

Karim, C., 1986, Eine ESR-Bindungsstudie von spinmarkierten Coenzymanaloga und Adenin-Nukleotiden an der Stör- und Kaninchen-Glycerinaldehyd-3-phosphat-Dehydrogenase, Doctoral thesis, University of Kaiserslautern, Kaiserslautern, West Germany.

Keith, A., Horvat, D., and Snipes, W., 1974, Spectral characterization of ^{15}N spin labels, *Chem. Phys. Lipids* **13**:49-62.

McDaniel, C. F., Kirtley, M. E., and Tanner, M. J. A., 1974, Interaction of glyceraldehyde-3-phosphate dehydrogenase with human erythrocyte membranes, *J. Biol. Chem.* **249**:6478-6485.

McIntyre, J. O., Robinson, B. H., and Fleischer, S., 1984, Anisotropic rotational diffusion of D-β-hydroxybutyrate dehydrogenase (BDH) spin-labeled with [^{15}N]-nitroxide and studied by saturation transfer (ST)-EPR, *Biophys. J.* **45**:238a.

Moras, D., Olsen, K. W., Sabesan, M. N., Buehner, M., Ford, G. C., and Rossmann, M. G., 1975, Studies of asymmetry in 3-dimensional structure of lobster D-glyceraldehyde-3-phosphate dehydrogenase, *J. Biol. Chem.* **250**:9137-9162.

Oguchi, M., Meriwether, B. P., and Park, J. H., 1973, Interaction between adenosine triphosphate and glyceraldehyde 3-phosphate dehydrogenase. III. Mechanism of action and metabolic control of the enzyme under simulated *in vivo* conditions, *J. Biol. Chem.* **248**:5562-5570.

Olsen, K. W., Moras, D., Rossmann, M. G., and Harris, J. I., 1975, Sequence variability and structure of D-glyceraldehyde-3-phosphate dehydrogenase, *J. Biol. Chem.* **250**:9313-9321.

Park, J. H., Moore, T. K., Anderson, B., and Park, C. R., 1988, Motional dynamics of fatty acids: Advantages of ^{15}N and deuterium substituted fatty acid spin labels for studies of lipid-protein interactions and motion in membrane bilayers, in *Roots of Modern Biochemistry* (H. Kleinkauf, H. von Dören, and L. Jaenicke, eds.), pp. 637-651, Walter de Gruyter and Co., Berlin and New York.

Perkins, R. C., Abumrad, N., Beth, A. H., Dalton, L. R., Park, J. H., and Park, C. R., 1982, Equilibrium binding of spin labeled fatty acids to bovine serum albumin: Suitability as surrogate ligands, *Biochemistry* **21**:4059-4064.

Philipp, R., McIntyre, J. O., Robinson, B. H., Huth, H., Trommer, W., and Fleischer, S., 1984, The synthesis of ^{15}N- and deuterium-substituted, spin-labeled analogues of NAD^+ and their use in EPR studies of dehydrogenases, *Biochim. Biophys. Acta* **790**:251-258.

Robinson, B. H., and Dalton, L. R., 1980, Anisotropic rotational diffusion studied by passage saturation transfer electron paramagnetic resonance, *J. Chem. Phys.* **72**:1312–1324.

Robinson, B. H., and Dalton, L. R., 1981, Approximate methods for the fast computation of EPR and ST-EPR spectra. V. Application of the perturbation approach to the problem of anisotropic motion, *Chem. Phys.* **54**:253–259.

Strapazon, E., and Steck, T. L., 1976, Binding of rabbit muscle aldolase to Band-3, predominant polypeptide of human erythrocyte membrane, *Biochemistry* **15**:1421–1424.

Thomas, D. D., Dalton, L. R., and Hyde, J. S., 1976, Rotational diffusion studied by passage saturation transfer electron paramagnetic resonance, *J. Chem. Phys.* **65**:3006–3024.

Trommer, W. E., 1987, Spin-labeled pyridine nucleotide derivatives, in *Pyridine Nucleotide Coenzymes: Chemical, Biochemical and Medical Aspects* (D. Dolphin, R. Poulson, and O. Abramovic, eds.), Vol. 2A, pp. 613–640, Wiley, New York.

Trommer, W. E., and Glöggler, K., 1979, Solution conformation of lactate dehydrogenase as studied by saturation transfer ESR spectroscopy, *Biochim. Biophys. Acta* **571**:186–194.

Trommer, W. E., Huth, H., and Wenzel, H. R., 1979, Nature of the substrate inhibition in lactate dehydrogenases as studied by a spin-labeled derivative of NAD, *Biochim. Biophys. Acta* **567**:49–59.

Venkataramu, S. D., Pearson, D. E., Beth, A. H., Perkins, R. C., Park, C. R., and Park, J. H., 1981, Synthesis of perdeuterio-N-(1-oxyl-2,2,6,6-tetramethyl-4-piperidinyl)maleimide, a highly sensitive probe, *J. Labeled Compd. Radiopharm.* **18**:371–383.

Venkataramu, S. D., Pearson, D. E., Park, C. R., and Park, J. H., 1982, Improved EPR analysis of molecular motion by ^{15}N-substitution in stearic acid spin label, EPR Symposium. *Fed. Proc.* **41**:1389.

Venkataramu, S. D., Beth, A. H., Park, C. R., and Park, J. H., 1983a, Advantages of ^{15}N-lipid spin probes for characterizations of biological membranes, *Fed. Proc.* **42**:2409.

Venkataramu, S. D., Pearson, D. E., Beth, A. H., Balasubramanian, K., Park, C. R., and Park, J. H., 1983b, Synthesis of ^{15}N-5-doxylstearic acid for improved EPR characterization of lipid motion in biomembranes, *J. Labeled Compd. Radiopharm.* **20**:433–445.

Venkataramu, S. D., Pearson, D. E., Beth, A. H., Park, C. R., and Park, J. H., 1985, High resolution spin labeled fatty acid: Synthesis and EPR spectral characteristics, *Tetrahedron Lett.* **26**:1403–1406.

Vogel-Claude, P., Schäfer, G., and Trommer, W. E., 1988, Synthesis of a photoaffinity-spin-labeled derivative of ATP and its first application to F_1-ATPase, *FEBS Lett.* **227**:107–109.

Wenzel, H. R., and Trommer, W. E., 1977, 8-Spin-label nicotinamide adenine dinucleotide, synthesis and properties of a new spin-labelled coenzyme, *FEBS Lett.* **78**:184–188.

Wilder, R., 1985, Studies of glyceraldehyde-3-phosphate dehydrogenase: Interactions of the enzyme with NAD^+ and Band-3 of the red blood cell membrane, Doctoral Thesis, Vanderbilt University Medical School, Nashville, TN.

Wilkerson, L. S., Perkins, R. C., Roelofs, R., Swift, L., Dalton, L. R., and Park, J. H., 1978, Erythrocyte membrane abnormalities in duchenne dystrophy monitored by saturation transfer electron paramagnetic resonance spectroscopy, *Proc. Natl. Acad. Sci. U.S.A.* **75**:838–841.

Wolf, A., Fritzsche, T. M., Rudy, B., and Trommer, W. E., 1987, Synthesis of spin-labeled photoaffinity derivatives of NAD^+ and their interaction with lactate dehydrogenase, *FEBS Lett.* **212**:203–207.

Zantema, A., Trommer, W. E., Wenzel, H. R., and Robillard, G. T., 1977, Binding studies of a spin-labelled oxidized coenzyme to bovine-liver glutamate dehydrogenase, *Euro. J. Biochem.* **72**:175–184.

12

Magnetic Resonance Study of the Combining Site Structure of a Monoclonal Anti-Spin-Label Antibody

Jacob Anglister

1. INTRODUCTION

Antibody molecules play a crucial role in the defence of the body against infection. When confronted by almost any foreign molecule, the immune system is capable of producing antibody proteins of high affinity and exquisite specificity. Against each antigen the body produces many types of antibody molecules differing in their amino acid sequences and in their affinities to the antigen.

A diagram of the basic structure of all the IgG immunoglobulins is presented in Figure 1. The antibody molecule consists of two identical polypeptide chains having a molecular weight of 50,000, and called heavy chains, and two identical polypeptide chains having a molecular weight of 25,000, and called light chains. The four chains are held together by both covalent and noncovalent interactions. Each heavy chain forms four structural domains: V_H, C_H1, C_H2 and C_H3, and each light chain forms two structural domains: V_L and C_L. The V_H and V_L domains are variable in their amino acid sequences, while the other domains are constant within a family of antibodies from the same class. The smallest binding fragment of the antibody, Fv, is composed of the two variable domains, each of them about 110 amino acid long. Unfortunately Fv can be obtained only from a very small number of antibodies. All the crystallographic studies and most of the NMR studies of antibody molecules have been carried out with the Fab fragment, which can be easily obtained from most antibodies. The Fab

Jacob Anglister • Department of Polymer Research, Weizmann Institute of Science, Rehovot 76100, Israel.

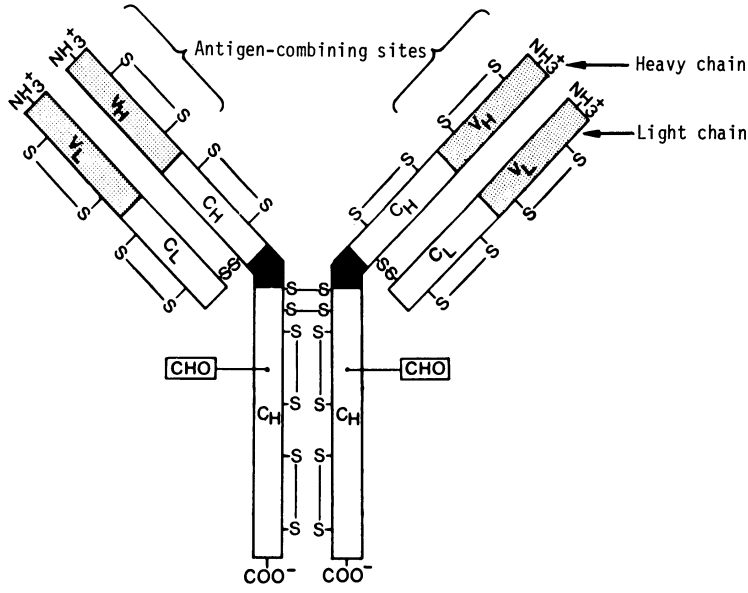

Figure 1. A schematic structure of IgG antibodies.

has a molecular weight of 50,000 daltons, and comprises the whole light chain and a heavy chain fragment that contains the V_H and C_H1 domains.

In the variable domains there are special segments that are very diverse in their amino acid sequences; they are called the hypervariable regions (Wu and Kabat, 1970). There are three hypervariable regions in each of the chains. Crystallographic studies of complexes between antibody molecules and ligands have shown that these segments form the combining site of the antibody molecule (Amzel *et al.*, 1974; Padlan *et al.*, 1976; Amzel and Poljak, 1979). The other parts of the variable domains, that are almost constant in their amino acid sequence, form a typical structure which is called the immunoglobulin fold. This is the basic structural motif in each of the domains in the heavy and light chains and is typical of all antibodies (Amzel and Poljak, 1979).

Nuclear magnetic resonance is a very useful tool in obtaining information on the tertiary structures of small proteins and nucleic acids (Wutrich, 1986). The considerable broadening of the resonances of the individual protons that occurs in the spectrum of large proteins, together with the increasing number of protons, cause total loss of resolution in their NMR spectrum. As a result NMR is being used mostly with proteins having molecular weight less than 15,000 daltons. In order to obtain useful information from the NMR spectrum of larger proteins, simplification of the spectrum is required. Various techniques that can be applied for this purpose have been described in detail by Jardetzky and Roberts (1981).

Dwek and his co-workers used a combination of nuclear magnetic resonance, electron spin resonance, and model building (Dower and Dwek, 1979) for studying the combining site structure of the myeloma antibody MOPC 315, for which dinitrophenol (DNP) was found to be a good ligand. It should be noted that MOPC 315 is one of the rare antibodies that can be digested to give the Fv fragment. In the early

phase of their studies, Dwek and his co-workers linked a nitroxide spin label to the dinitrophenyl ligand and exploited the broadening effect of an odd electron on the NMR spectrum of nuclei close to the paramagnetic center (Dwek *et al.*, 1975). They calculated the difference spectrum between the NMR spectrum of the Fv and the NMR spectrum of the Fv complex with the paramagnetic ligand. The NMR difference spectrum showed only the resonances of the protons within 16 Å of the odd electron. In principle, the broadening effect can yield information about distances since it is inversely proportional to the sixth power of the distances between the magnetic dipoles. However, since resonances of protons that are closer than 13 Å to the unpaired electron practically disappear in the NMR spectrum of the complex, the difference spectrum cannot discriminate between the protons according to the distance from the paramagnetic center. Despite the considerable simplification achieved in the difference spectrum it was still too complicated, and the resonances were not assigned, except those of histidine assigned by pH titration.

About fifteen years ago Kohler and Milstein developed a technique to obtain a homogeneous population of antibodies with any desired specificity (Kohler and Milstein, 1975). In this procedure, the antibodies producing cells (B cells) of immunized mice are hybridized with myeloma B cells that do not produce antibodies. The result of a successful fusion, called hybridoma, secretes the same antibodies that were synthesized by the normal B cells and grows indefinitely like tumor cells. A homogeneous population of antibodies is obtained from cell cultures derived from single cells. The hybridoma technology is now very widely used to obtain large amounts of homogeneous monoclonal antibodies with well-defined specificities.

2. AMINO ACID COMPOSITION OF THE ANTIBODY COMBINING SITE

We have been studying the combining site structure of a monoclonal anti-spin-label antibody ANO2 (Anglister *et al.*, 1984a). The hapten against which the antibody is directed is dinitrobenzene conjugated to tetramethylpiperidinoxy, better known as Tempo. Tempo has an unpaired electron located on the nitrogen atom of the NO group. For the NMR measurements we have used the Fab fragment, which can be easily obtained from most antibodies. The molecular weight of the Fab is 50,000, and it contains about 440 amino acids and more than 2000 nonexchangeable protons. The result is a NMR spectrum with very poor resolution as shown in Figure 2. Like Dwek and his co-workers, we have exploited the effect of the unpaired electron on the relaxation times of the nearby protons in order to obtain difference spectra that show only the contributions of the amino acids in the combining site region.

Three types of difference spectra are calculated from the NMR spectra of the Fab fragment of the antibody and the NMR spectra of its complexes with the spin-label hapten (SL) and with dinitrophenylglycine, which is also a good ligand for the ANO2 antibody; the individual spectra are designated Fab(0), Fab(SL), and Fab(DNP-Gly), respectively. The difference spectra are: (a) Fab(0) − Fab(SL), (b) Fab(DNP-Gly) − Fab(SL), and (c) Fab(0) − Fab(DNP-GLy). In the NMR spectrum of the Fab complex with the spin-labeled hapten, all the resonances of the protons that are within 17 Å of the unpaired electron are considerably broadened. Some of the resonances undergo

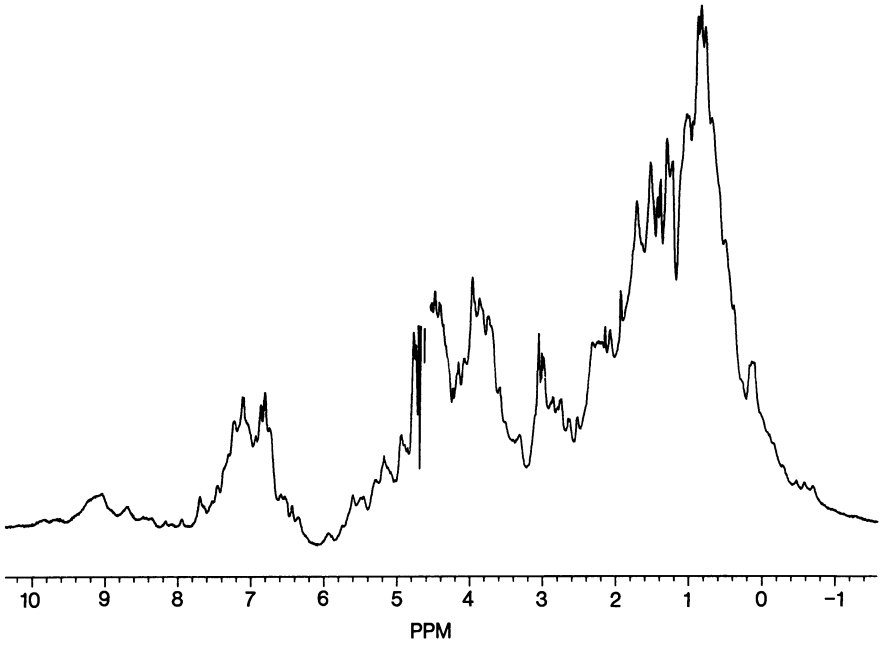

Figure 2. Proton NMR spectrum of an unlabeled Fab fragment of ANO2 measured with a JEOL 500 MHz spectrometer and Fab concentration of 0.3 mM.

changes in chemical shift upon binding of the hapten. These changes are usually accompanied by broadening of the resonances, since the major changes in chemical shift arise from protons that are in the binding site region and, therefore, in the range of the broadening caused by the unpaired electron. We have accumulated evidence that, for most of the resonances, the chemical shift changes that occur upon binding of the spin-label hapten are the same as those occurring upon DNP-Gly binding. Difference spectra of type (b) therefore show only the resonances that are broadened by the spin-labeled hapten and appear as sharp positive peaks upon a base line that may be slightly distorted by broad negative features. Spectrum (c) shows only the resonances that undergo changes in chemical shift upon DNP-Gly binding; this is a complicated combination of sharp positive and negative features. Spectrum (a), given in Figure 3, shows mainly the resonances that are broadened by the unpaired electron,

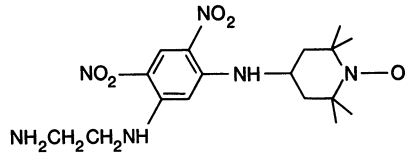

Structure 1.

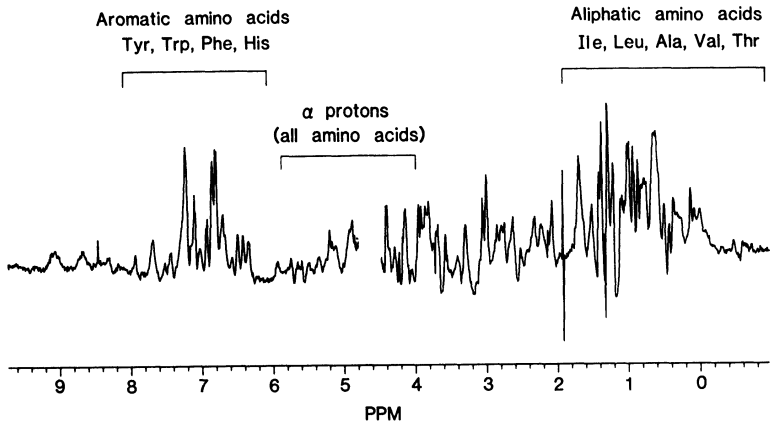

Figure 3. The difference spectrum between the NMR spectrum of the Fab complex with the spin-label hapten and the NMR spectrum of the Fab: Fab(0) – Fab(SL).

but in addition it shows the resonances which undergo changes in chemical shift that are not accompanied by broadening.

Although there is much better resolution in the difference spectrum relative to the Fab spectrum, there are still many overlapping resonances, especially in the region of the aromatic protons. We assume that the difference spectrum represents contributions from about 40–50 amino acids out of 440 amino acids of the Fab. For further simplification of the spectra and in order to assign the resonances to specific types of amino acids, we biosynthetically labeled the antibodies by growing the hybridoma cells on medium containing deuterated amino acids. In order to increase the efficiency of the labeling, the cells were adjusted to grow on the synthetic medium RPMI 1640, supplemented with only 1% of Fetal Calf Serum. Deuterated instead of unlabeled amino acids were added to the medium, and in the same quantities called for by the receipe. The labeling with essential amino acids and with tyrosine was found to be very efficient.

Aromatic amino acids play an important role in the antibody combining site. In a recent crystallographic study of an anti-lysozyme antibody it was found that nine out of 15 side chains of the antibody amino acids that form contacts with the antigen are aromatic while five of them are tyrosine residues (Amit *et al.*, 1986). The difference spectrum obtained for ANO2 is evidence for the high content of aromatic amino acids in the combining site of the anti-spin-label antibody. In order to assess the contributions of the tyrosine residues to the combining site region, we labeled the antibody by growing the hybridoma cell on a culture medium containing perdeuterated tryptophan and phenylalanine and tyrosine deuterated in ring positions 2,6. The aromatic region of the difference spectrum, calculated from the NMR spectra of the labeled Fab, is shown in Figure 4a (Anglister *et al.*, 1984b). This difference spectrum contains only contributions from the protons in ring positions 3,5 of all the tyrosine residues that are in the combining site region, each pair contributing one relatively sharp singlet. From this spectrum we concluded that there are 10 tyrosines in the combining site region of the antibody. The spectrum in Figure 4b is the proton NMR spectrum of Fab 30% occupied

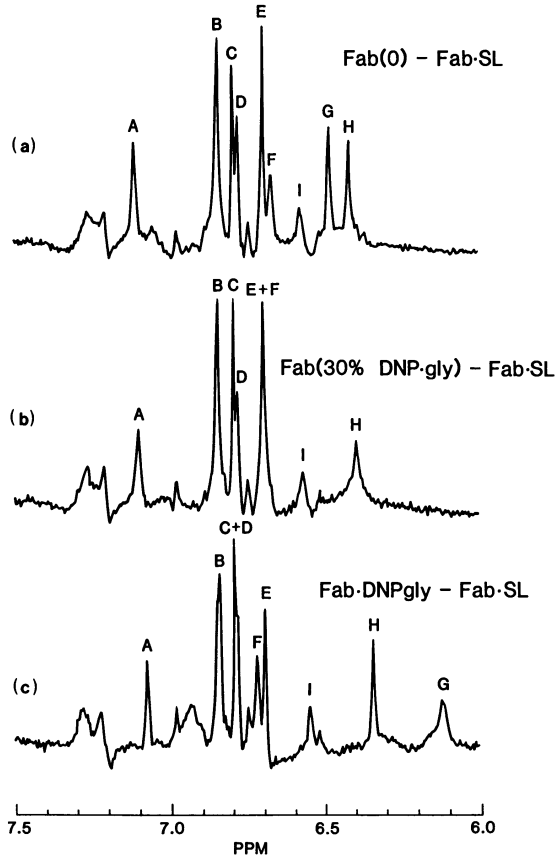

Figure 4. Proton resonance difference spectra for H3,5 Tyr. The spectra are the differences between the proton spectra of Fab solutions of various concentrations of DNP-Gly minus the spectrum of Fab · SL in which the combining site is saturated with the spin-label hapten. The combining site occupations by DNP-Gly are 0%, 30%, and 100% in (a), (b), and (c), respectively. The Fab fragment contains deuterated tryptophan and phenylalanine in addition to the partially deuterated tyrosine. Proton signals A and H are used to estimate the off rate for DNP-Gly.

with DNP-Gly minus the spectrum of the Fab complex with the spin-label hapten. The spectrum in Figure 4c is of Fab fully occupied with DNP-Gly minus Fab with SL. DNP-Gly is also a good hapten for the antibody with slightly lower affinity than the DNP-spin label conjugate. Spectrum (a) shows the resonances from the free Fab, while the lower spectrum shows the resonances from the Fab complex with DNP-Gly. By comparing the three spectra, one can follow the changes in the chemical shift that the different protons undergo upon binding of the DNP to the antibody. Resonances A and H change their chemical shift upon binding of DNP-Gly to the Fab. In spectrum (b) these resonances are broadened relative to their appearance in (a) and (c). By line-shape simulation (Gutowsky *et al.*, 1953; McConnell, 1958) the off rate of DNP-Gly could be determined and was found to be 500 per second.

The spectral region due to the nonaromatic amino acids presents a more complicated problem than the aromatic protons spectrum, since many types of amino acids can give rise to signals in this region. Some of the nonaromatic amino acids may be nonessential, and therefore it will be very difficult to label them biosynthetically. Moreover, excessive deuteration that may be required in order to simplify the spectrum inhibits the growth of the cells and the production of antibodies. We alleviated these problems by calculating double-difference spectra (Frey *et al.*, 1984). In this type of analysis, the normal difference spectra (without hapten minus with hapten) are calculated for Fabs that differ only in the incorporation of one selected deuterated amino acid. The two difference spectra are then subtracted, leaving only the contribution of the selected amino acid in the double-difference spectrum. A large number of resonances in the difference spectrum have been assigned by this technique.

A double-difference spectrum which shows the contribution of lysine is presented in Figure 5. This double difference is calculated from the difference spectra of unlabeled Fab, given in Figure 5a, and that of Fab in which lysine was deuterated. The ε-CH2 of one lysine and the β, γ, δ protons upfield are clearly observed.

By using the double-difference technique we were able to assign all the resonances of the methyl groups of the aliphatic amino acids that appear in the difference spectrum. Figure 6a gives the difference spectrum Fab(DNP-Gly) − Fab(SL) in the spectral region −1.0 to +2.0 ppm. This spectrum reveals all the methyl resonances of all the aliphatic amino acids in the combining site region. These signals are assigned on the basis of double-difference spectra of selectively deuterated Fab fragments, as seen in Figure 6b-f. Some of the double-difference signals due to Thr (Figure 6b), Leu (Figure 6d), and Val (Figure 6c) have particularly large signal-to-noise ratios, probably due to a combination of their narrow intrinsic linewidths and their proximity to the unpaired electron (Anglister *et al.*, 1984b). On the basis of the number of signals and their relative intensities, we can identify five threonines, four or five valines, three or four leucines, two or three isoleucines (with two methyl signals per valine, leucine, and isoleucine), and six or seven alanines.

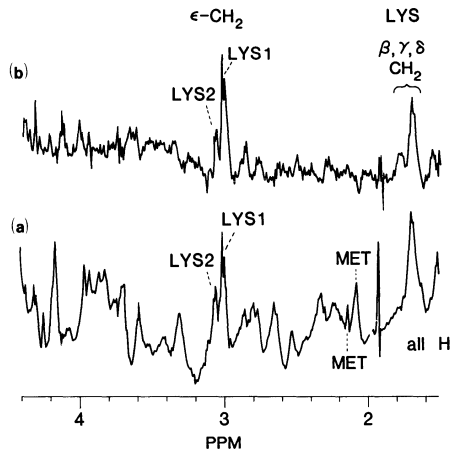

Figure 5. Proton resonances signals of ANO2 in the region 1.5-4.4 ppm showing resonances due to lysine and methionine. (a) Fab(0) − Fab(SL). (b) [Fab(0) − Fab(SL)] − [Fab(0) − Fab(SL)]d(Lys).

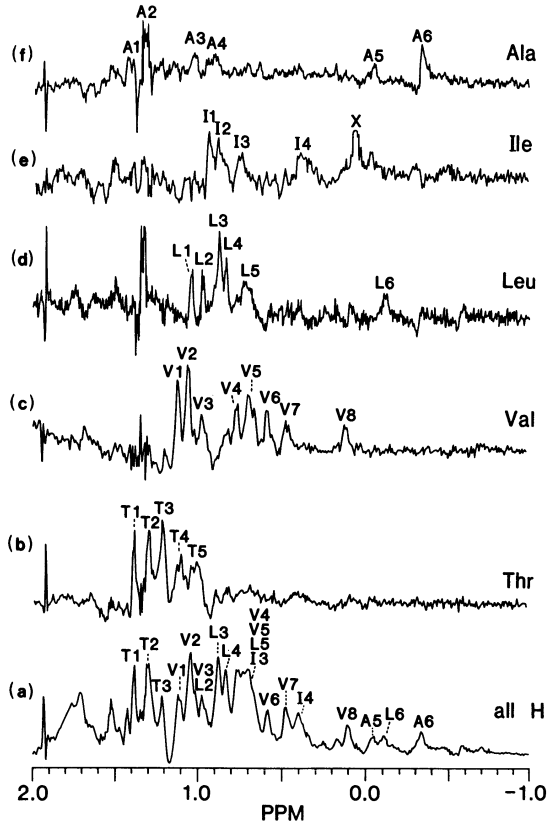

Figure 6. Proton magnetic resonance signals due to aliphatic amino acids in the Fab fragment of the monoclonal anti-spin-label antibody ANO2. (a) Difference spectrum Fab(DNP-Gly) – Fab(SL), giving all aliphatic proton resonance signals in the region −1.0 to +2.0 ppm. (b) Double-difference spectrum for threonine: [Fab(DNP-Gly) – Fab(SL)] – [Fab(DNP-Gly) – Fab(SL)]d(Thr). (c) Valine: [Fab(DNP-Gly) – Fab(SL)]d(Ala, Leu) – [Fab(DNP-Gly) – Fab(SL)]d(Ala, Val, Leu). (d) Leucine: [Fab(DNP-Gly) – Fab(SL)]d(Ala, Val) – [Fab(DNP-Gly) – Fab(SL)]d(Ala, Val, Leu). (e) Isoleucine: [Fab(DNP-Gly) – Fab(SL)] – [Fab(DNP-Gly) – Fab(SL)]d(Ile); Signal X is thought to be contaminant. (f) Alanine: [Fab(DNP-Gly) – Fab(SL)]d(Val, Leu) – [Fab(DNP-Gly) – Fab(SL)]d(Ala, Val, Leu).

3. DISTANCE DETERMINATION

When the resonance lines of the protons that are broadened by the spin label are well resolved, and the broadening can be measured, distances can be determined accurately. Such distances are usually in the range 15-20 Å (Wien *et al.*, 1972). For smaller distances, the broadening is so large that the resonance signals cannot be detected. Campbell *et al.* (1975) suggested a method to measure these shorter distances by varying the fractional occupancy of binding sites for paramagnetic probes. Semiquantitative results were obtained by titrating lysozyme with Gd^{+3}. A detailed analysis of

the broadening effects, which enabled accurate determination of distances smaller than 15 Å, was given by Anglister *et al.* (1984b).

Under conditions of fast hapten chemical exchange between the combining sites in solution of Fab(f), the transverse relaxation time T_2 of an amino acid proton is given by the equation

$$\frac{1}{T_2} = \frac{f}{T_{2M}} + \frac{1-f}{T_{2N}} \tag{1}$$

where f is the fraction of the time the combining site is occupied by the hapten. The transverse nuclear relaxation times T_{2M} and T_{2N} apply to the solutions of Fab(1) and Fab(0), i.e., solutions in which the combining site is always occupied or always empty, respectively. The relaxation rate T_{2M}^{-1} itself is a sum of two terms:

$$\frac{1}{T_{2M}} = \frac{1}{T'_{2M}} + \frac{1}{T_{2N}} \tag{2}$$

where $(T'_{2M})^{-1}$ is the enhancement of the nuclear relaxation rate due to the hapten. The Solomon-Bloembergen dipolar enhancement of the transverse relaxation due to the unpaired electron spin is (Bloembergen, 1957; Solomon, 1955)

$$(T'_{2M})^{-1} = \frac{S(S+1)\gamma_1^2 g^2 \beta^2}{15}\left[4\tau_c + \frac{3\tau_c}{1+\omega_1^2\tau_c^2}\right]\left\langle\frac{1}{r^6}\right\rangle \tag{3}$$

where the broken brackets designate an average over high-frequency intramolecular motions. The correlation time τ_c due to molecular tumbling of Fab fragments has been estimated to be 2×10^{-8} s (Anglister *et al.*, 1984a). The other symbols have their usual meanings; r is the distance between the unpaired electron and the nucleus. The second term in the square brackets is then totally negligible. Insertion of the fundamental constants into equation (3) yields

$$T'_{2M} = \langle (r/30.1)^6 \rangle \tag{4}$$

where r is given in angstroms.

We assume for simplicity that each proton resonance line shape is Lorentzian with intensity $I(\omega)$, given by

$$I(\omega) = \frac{1}{\pi}\frac{T_2}{1+(\omega-\omega_0)^2 T_2^2} \tag{5}$$

Under conditions of fast exchange, at the resonance frequency $(\omega + \omega_0)$, the Lorentzian peak height is

$$I(f, \omega_0) = (1/\pi)(T_{2M}T_{2N})/(f\Delta T_2 + T_{2M}) \tag{6}$$

where $\Delta T_2 = T_{2N} - T_{2M}$. Under conditions of arbitrary exchange rate, the general expression for the peak intensity is

$$I(k, f, \omega_0) = \frac{1}{\pi} \frac{[T_{2M}(1-f) + \Delta T_2(1-f)^2 + kT_{2N}T_{2M}]}{[(1-f) + \Delta T_2 kf + T_{2M}k]} \tag{7}$$

where k is the off rate for hapten dissociation. Equation (7) reduces to equation (6) when k is sufficiently large. In the slow exchange limit, where $k = 0$, we have

$$I(0, f, \omega_0) = (1/\pi)[T_{2M} + \Delta T_2(1-f)] \tag{8}$$

In comparing these theoretical expressions with experimental data, it is convenient to calculate normalized intensities $J(f)$:

$$J(f) = \frac{I(k, 0, \omega_0) - I(k, f, \omega_0)}{I(k, 0, \omega_0) - I(k, 1, \omega_0)} \tag{9}$$

Chemical shifts due to hapten binding are also significant and can sometimes be dominant in affecting difference spectra. Relevant equations allowing for simultaneous effects of chemical shifts and paramagnetic broadening are not given here explicitly; they can be found in the literature (Carrington and McLachlan, 1967).

We have found that when Fab is titrated with spin-label hapten, the change in peak height in the difference spectra is independent of distance if the change in the chemical shift is very large (greater than 100–150 Hz). In such cases the height depends only on the off rate and the transverse relaxation time T_2. By measuring the difference Fab(SL) – Fab(Reduced SL) we could determine the chemical shifts of the tyrosine lines in the complex with the spin-label hapten. Line G of Figure 4a was found to change its chemical shift by 200 Hz. Simulation of the experimental plot of $J(f)$ of line G as a function of the fractional occupancy, as shown in Figure 7b, yields best fit when the off rate of the spin label is taken as $350\ s^{-1}$. As shown in Figure 7a, similar results were obtained for another line (H) of Fab(H2,6 Tyr) in which phenylalanines and tryptophans were perdeuterated as well as the 3,5 phenyl protons of the tyrosine residues. Using the value $350\ s^{-1}$ for the off rate and the linewidths as measured in the difference spectra Fab(0) – Fab(SL) and Fab(DNP-Gly) – Fab(SL), we could simulate the experimental curves of $J(f)$ for the various lines. The distances of the broadened protons from the odd electron are deduced from the best fit. A typical example is given in Figure 8. The distances determined are given in Table 1.

The described technique treats the individual lines separately. This approach is valid when, during the titration, lines do not cross each other. When such complications do occur, a simulation of the whole difference spectrum is required. Such a simulation was carried out recently by Frey *et al.* (1988) and yields more accurate results for the distances between the tyrosine protons and the odd electron, and allows distance determination for overlapping lines. It should be noted that the off rate limits the applicability of the method for the determination of distances larger than 7 Å. With higher off rates, shorter distances can be measured.

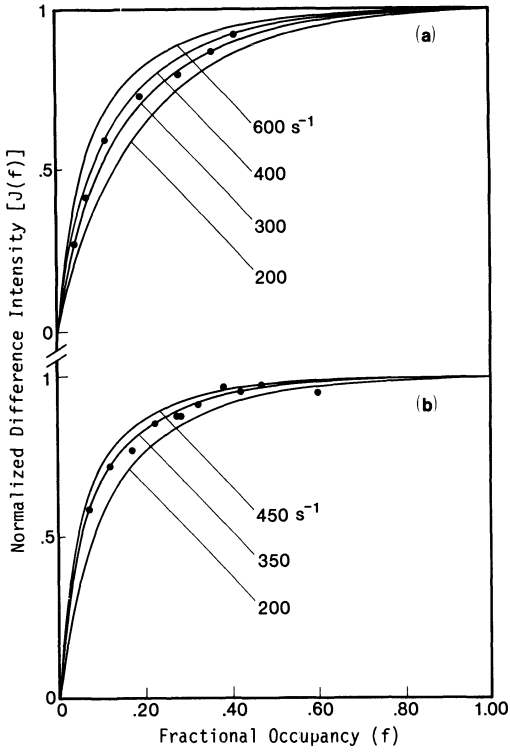

Figure 7. Experimental and theoretical values for the normalized difference spectra peak intensities $J(f)$ for protons signals H (upper part, a) from H 2,6 Tyr and signal G (b) from H 3,5 Tyr. These data are used to calculate the off rate k for the spin-label hapten. Solid lines refer to theoretical calculations using the indicated off rates k. Since calculated values of $J(f)$ are virtually independent of the spin label-proton distance for the large chemical shift that these lines experience upon binding of the hapten, values of r were taken arbitrarily as 7 Å.

4. CONTRIBUTIONS OF HEAVY AND LIGHT CHAINS TO THE COMBINING SITE

Metzger and Mannik (1964) have shown that the light and heavy chains of antibodies can be separated under denaturing conditions and later they can be recombined to reconstitute the native conformation of the antibody. This procedure has been utilized to determine the contributions of the light chain and the heavy chain to the binding (Anglister *et al.*, 1985). Two Fabs were prepared. One had tryptophan, tyrosine, and phenylalanine perdeuterated, and the other had tryptophan and phenylalanine perdeuterated and tyrosine deuterated in phenyl position 2,6 leaving positions 3,5 with hydrogens. The disulfide bond between the chains was reduced and the sulfhydryl groups were alkylated. The chains were separated by ion exchange chromatography under denaturing conditions (8M urea), then recombined, and the native conformation recovered. The light chain, which was fully deuterated in the aromatic region, was recombined with the heavy chain in which all aromatic protons were deuterated except the 3,5 phenyl hydrogen of the tyrosine residues. The difference spectrum of this recombinant Fab is shown in Figure 9b. The heavy chain in which tryptophan, phenylalanine, and tyrosine were deuterated was recombined with the light chain in which tryptophan and phenylalanine were deuterated as well as tyrosine's 2,6 phenyl protons. The difference spectrum obtained for this recombinant Fab is shown in Figure 9c.

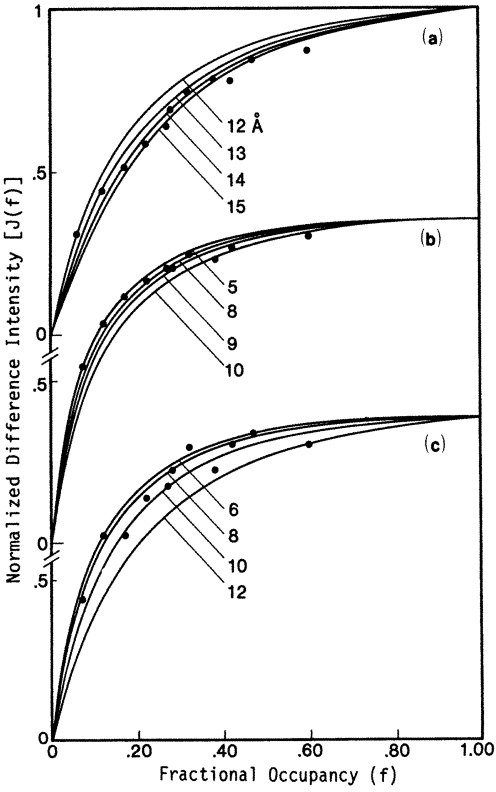

Figure 8. Experimental and theoretical values for the normalized difference spectra peak intensities $J(f)$ for selected proton signals from H 3,5 Tyr. Data are from line A in Figure 4a (a), line B (b), and line F (c). Solid lines are from theoretical calculations for the indicated distances and $k = 350\,s^{-1}$. Linewidths and changes in chemical shift are given in Table 1.

Figure 9a shows the difference spectrum of the native Fab and contains contributions of tyrosine's phenyl 3,5 hydrogens from both chains. Comparison of the spectra shows that the sum of the difference spectra measured for the two recombinant Fabs yields the difference spectrum of the native Fab. From these experiments we concluded that there are ten tyrosines in the combining site region, each chain contributing five tyrosines.

5. DETERMINATION OF SHORT DISTANCES

In principle, short distances between the Fab protons and the hapten can be determined by magnetization transfer experiments using the diamagnetic analog of the spin-label hapten. In order to overcome the problem of the lack of specificity of irradiation in a crowded spectral region, we used recombinant Fab fragments.

On the basis of the observation that the absorption maximum of DNP shifts to the red upon binding to ANO2, we concluded that a Fab tryptophan is involved in the binding (Anglister *et al.*, 1984a). Similiar shifts in the UV absorption spectrum of DNP was observed with other anti DNP antibodies (Little and Eisen, 1967). Since of all the free amino acids only tryptophan was found experimentally to cause such

TABLE 1
Calculated Distances and Relevant Data

	Chemical shift[a] (Hz)	Line width $\Delta\nu_{1/2}$ (Hz)	Distance r (Å)
H 3.5 Tyr			
A	−18.65	7.6	14 ± 1.5
B(2 pairs)	0	8.7[b]	≤9.0[b]
C h	0	5.2	11 ± 2
D	7	7	12 ± 2
E	3	5	13 ± 1.5
F	25	10.5	≤10
G	−200	6.3	?
H	−38.65	7.2	<12
H 2.6 Tyr			
A	?		
B	Overlap		
C	2.5	5	12 ± 1
D	0	8.5	13 ± 1
E	23.5	10	>11
F	7.5	14	12 ± 1
G			"Far"
H	195	13	?

[a] Positive change in chemical shift is toward lower field.
[b] This line may be inhomogeneous because it arises from two pairs of protons. If the width is assumed to be 5 Hz, the calculated distance is 11 Å.

changes, it has been concluded that tryptophan is involved in the binding by a formation of a charge transfer complex with the DNP (Little and Eisen, 1967). In order to assess the role of tryptophan in the binding and assign the interacting tryptophans to a specific chain, we carried out magnetization transfer experiments with two recombined Fab fragments (Anglister *et al.*, 1987).

Figure 10a shows the NMR spectrum of the recombinant Fab A in which phenylalanines and tyrosines were deuterated as well as tryptophan residues of the heavy chain. Figure 10b shows the NMR spectrum of the recombinant Fab B in which phenylalanines and tyrosines were deuterated as well as tryptophan residues of the light chain. Figure 11a is the difference spectrum of the native Fab in which phenylalanine and tyrosine were deuterated. Figure 11b shows the difference spectrum measured with recombinant Fab B and also the contribution of heavy-chain tryptophans to the difference spectrum. Figure 11c shows the difference spectrum measured with recombinant Fab A and gives the contributions of light-chain tryptophans. From the difference spectra we concluded that in the combining site region there is one tryptophan from the light chain and at least two tryptophans from the heavy chain.

The tryptophan proton resonances that appear in the difference spectra between 6.5 and 8 ppm were irradiated in the presence of a large excess of DNP diglycine hapten. Saturation of three resonances of light-chain tryptophan protons, in recombinant A, resulted in magnetization transfer to the aromatic proton at position 6 of the

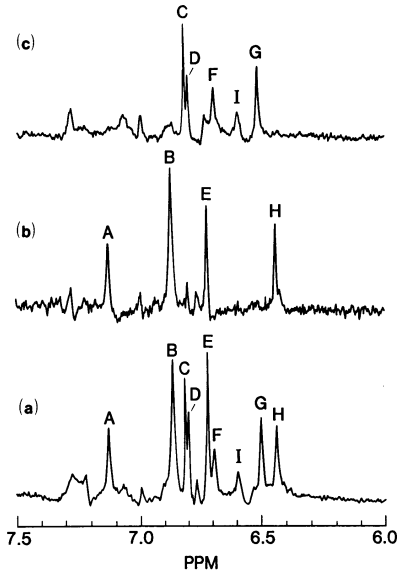

Figure 9. NMR difference spectra for selectively deuterated Fab fragments of a monoclonal anti-spin-label antibody. (a) Signals A–I are each due to pairs of protons in the 3,5 ring positions of tyrosine residues in the combining site region of the ANO2 antibody, except for B which is an overlap of two. Spectra (b) and (c) give the corresponding signals from protons in the heavy chain and light chain, respectively. Note that the spectrum in (a) is, to a good approximation, the sum of the spectra in (b) and (c).

DNP ring and to the methylene protons of the glycine linked to the DNP. Saturation of three resonances of heavy-chain tryptophan protons, in recombinant B, resulted in magnetization transfer to the methylene protons of the glycines linked to the DNP.

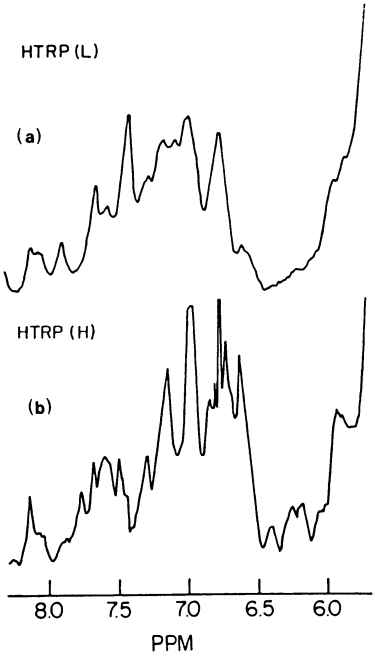

Figure 10. The proton NMR spectrum of two different reconstituted recombinant Fab fragments. (a) The NMR spectrum of recombinant A in which phenylalanines and tyrosines are perdeuterated as well as tryptophan residues of the heavy chain. (b) The NMR spectrum of recombinant B in which phenylalanines and tyrosines are perdeuterated as well as tryptophan residues of the light chain.

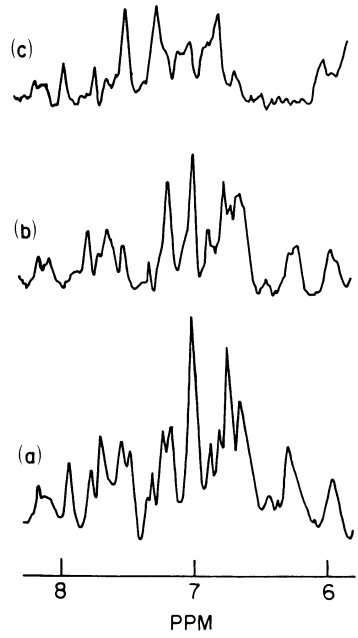

Figure 11. NMR difference spectra, Fab(DNP-DG) – Fab(SL), giving tryptophan proton resonance signals in the combining site region. (a) Tryptophan protons from both chains contribute to the difference spectrum. (b) Reconstituted recombinant Fab B; the difference spectrum shows the contributions of tryptophan protons of the heavy chain. (c) Reconstituted recombinant Fab A; the difference spectrum shows the contributions of tryptophan protons from the light chain.

Irradiation of Fab, in which phenylalanines and tyrosines were deuterated as well as tryptophan residues, at various frequencies in the range of 6.5 to 8.0 ppm, did not result in the transfer observed with the recombinant Fab fragments. We have measured the dependence of the magnetization transfer on the irradiation time. The monotonous increase of the magnetization transfer that was observed excludes the possibility that the transfer is due to spin diffusion. Our estimate is that the tryptophan protons are 3-4 Å away from the protons of the hapten. It should be noted that irradiation of all the samples in the range 6.5 to 8.00 ppm, even when all the aromatic amino acids were perdeuterated, caused transfer of magnetization to the DNP proton whose resonance is at 9.15 ppm. We assume that the resonance of this proton in the complex is very broad and smears between 6.5 and 8.0 ppm. The transfer to 9.15 ppm is actually caused by the irradiation of the extremely broad resonance of the bound hapten proton.

The magnetization transfer experiments with the recombinant Fab prove that there is one tryptophan from the light chain and one tryptophan from the heavy chain which are in contact with the hapten. The tryptophan from the light chain is in more extensive interaction with the DNP ring and is most probably in stacking interaction with the aromatic ring.

The amino acid sequence of the variable domains of the Fab has been obtained by a combination of amino acid and DNA sequencing. A molecular model was constructed from the sequence data by theoretical model building based on the known structures of other antibodies. A single binding site is apparent in the model. The two close trytophans deduced from the magnetic resonance data are identified as tryptophan 91 of the light chain and tryptophan 47 of the heavy chain. The proposed model for the interactions between the Fab tryptophans and the hapten is shown in Figure 12.

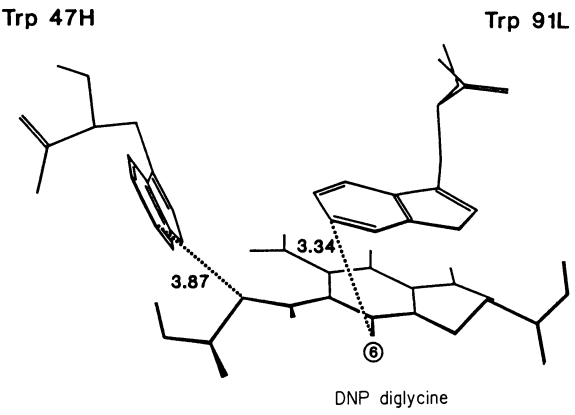

Figure 12. Computer graphics model showing the diamagnetic hapten in relation to Trp 91 of the light chain and Trp 47 of the heavy chain of ANO2. Interatomic distances are indicated by dotted lines.

6. CONCLUSION

The broadening effect of an odd electron on close nuclei together with biosynthetic labeling of the antibody molecule was used for the determination of the amino acid composition of the combining site of the anti-spin-label antibody ANO2. Chain separation and recombination allowed us to specifically label each of the chains and assess the contributions of each of them to the binding. Titration of the Fab with the spin-label hapten and simulation of the difference spectra between the NMR spectrum of the Fab and the spectrum of partially occupied Fab enabled us to determine distances between the unpaired electron and the broadened nuclei. Contact interactions between Fab amino acids and a diamagnetic hapten were identified by magnetization transfer with specifically labeled recombinant Fab. Theoretical model building supported by the NMR yields a model for the combining site. The methods that have been described in this chapter can be used for studies of other antibodies with different specificities after linking a nitroxide group to the hapten.

ACKNOWLEDGMENT. The work described in this chapter was done in the laboratory of Dr. Harden McConnell in collaboration with Dr. Tom Frey.

REFERENCES

Amit, A. G., Mariuzza, R. A., Phillips, S. E. V., and Poljak, R., 1986, Three dimensional structure of an antigen-antibody complex at 2.8 A resolution, *Science* **233**:747-753.

Amzel, L. M., and Poljak, R. J., 1979, Three dimensional structure of immunoglobulins, *Annu. Rev. Biochem.* **48**:961-997.

Amzel, L. M., Poljak, R. J., Saul, F., Varga, J. M., and Richards, F. F., 1974, The three dimensional structure of a combining region—ligand complex of immunoglobulin NEW at 3.5 Å resolution, *Proc. Natl. Acad. Sci. U.S.A.* **71**:1427-1431.

Anglister, J., Frey, T., and McConnell, H. M., 1984a, Magnetic resonance study of a monoclonal anti-spin-label antibody, *Biochemistry* **23**:1138-1142.

Anglister, J., Frey, T., and McConnell, H. M., 1984b, Distances of tyrosine residues from a spin-label hapten in the combining site of a specific monoclonal antibody, *Biochemistry* **23**:5372-5375.

Anglister, J., Frey, T., and McConnell, H. M., 1985, NMR technique for assessing contributions of heavy and light chains to an antibody combining site, *Nature* **315**: 65-67.

Anglister, J., Bond, M., Frey, T., Leahy, D., Levitt, M., McConnell, H. M., Rule, G., Tomasello, J., and Whittaker, M., 1987, Contribution of tryptophan residues to the combining site of a monoclonal anti dinitrophenyl spin-label antibody, *Biochemistry* **26**:6058-6064.

Bloembergen, N., 1957, Proton relaxation times in paramagnetic solutions, *J. Chem Phys.* **27**:572.

Campbell, I. D., Dobson, C. M., and Williams, R. J. P., 1975, Nuclear magnetic resonance studies on the structure of lysozyme in solution, *Proc. R. Soc. London, Ser. A* **345**:41-59.

Carrington, A., and McLachlan, A. D., 1969, *Introduction to Magnetic Resonance*, Harper and Row, New York, 266 pp.

Dower, S., and Dwek, R. A., 1979, An antibody binding site: A combined magnetic resonance and crystallographic approach, in *Biological Applications of Magnetic Resonance* (R. G. Shulman, ed.), pp. 271-303, Academic Press, New York.

Dwek, R. A., Knott, J. C. A., Marsh, D., McLaughlin, A. C., Press, E. M., Price, N. C., and White, A. I., 1975, Structural studies on the combining site of the myeloma protein MOPC 315, *Eur. J. Biochem.* **53**:25-39.

Frey, T., Anglister, J., and McConnell, H. M., 1984, Nonaromatic amino acids in the combining site region of a monoclonal anti-spin-label antibody, *Biochemistry* **23**:6470-6473.

Frey, T., Anglister, J., and McConnell, H. M., 1988, Lineshape analysis of NMR difference spectra of an anti-spin-label antibody, *Biochemistry*, **27**:5161-5165.

Gutowsky, H. S., McCall, D. W., and Slichter, C. P., 1953, Nuclear magnetic resonance of multiplets in liquids, *J. Chem. Phys.* **21**:279-292.

Jardetzky, O., and Roberts, G. C. K., 1981, *NMR in Molecular Biology*, Academic Press, New York, 681 pp.

Kohler, G., and Milstein, C., 1975, Continuous cultures of fused cells secreting antibody of predefined specificity, *Nature* **256**:495-498.

Little, J. R., and Eisen, H. N., 1967, Evidence for tryptophan in the active site of antibodies to polynitrobenzenes, *Biochemistry* **6**:3119-3125.

McConnell, H. M., 1958, Reaction rates by nuclear magnetic resonance, *J. Chem. Phys.* **28**:430-431.

Metzger, H., and Mannik, M. J., 1964, Recombination of antibody polypeptide chains in the presence of antigen, *J. Exp. Med.* **120**:765-782.

Padlan, E. A., Davies, D. R., Rudikoff, S., and Potter, M., 1976, Structural basis for the specificity of phosphorylcholin-binding immunoglobulin, *Immunochemistry* **13**:945-949.

Solomon, I., 1955, Relaxation processes in a system of two systems, *Phys. Rev.* **99**:559-565.

Wien, R. W., Morrisett, J. D., and McConnell, H. M., 1972, Spin-label-induced nuclear relaxation. Distances between bound saccharides, histidine-15, and tryptophan-123 on lysozyme in solution, *Biochemistry* **11**:3707-3716.

Wu, T. T., and Kabat, E. A., 1970, An analysis of the sequences of the variable regions of Bence Jones proteins and myeloma light chains and their implications for antibody complementarity, *J. Exp. Med.* **132**:211-250.

Wutrich, K., *NMR of Proteins and Nucleic Acids*, 1986, Wiley, New York, 292 pp.

APPENDIX

Approaches to the Chemical Synthesis of ^{15}N and Deuterium Substituted Spin Labels

Jane H. Park and Wolfgang E. Trommer

1. INTRODUCTION

With the increasing application of EPR to an expanding field of biomedical problems, the importance of the design and synthesis of spin labels intensifies. The spin label itself can either significantly enhance the productivity of an investigation or constitute the limiting factor. As illustrated in Chapter 11, isotopic substitution of ^{15}N and/or deuterium in the spin probes substantially improves the quality and quantity of information obtained in the areas of enzyme catalysis and membrane characterization. The same design principles apply to $^{14}N,^{1}H$ and $^{15}N,^{2}H$ spin labels; however, the syntheses of isotopically substituted compounds present special problems due to the expense of the isotopes and the stringent requirements for isotopic purity in the product. These problems are addressed in detail in Sections 2–4 below. In Chapter 11 and this Appendix, a circumscribed number of isotopically substituted spin labels have been selected to illustrate the potential for dynamic motional analyses. The scope of the presentation is limited in part by the number of papers available in this relatively new area of isotopic substitution and by the authors' intent to focus on subjects of interest to the biomedical scientist and molecular biologist.

Actually, a large number of spin labels without isotopic substitution have been prepared to address problems ranging from *in vivo* imaging by NMR to the physical chemistry of synthetic polymers. Several excellent articles are available for reviewing

Jane H. Park • Department of Molecular Physiology and Biophysics, Vanderbilt University School of Medicine, Nashville, Tennessee 37232. **Wolfgang E. Trommer** • Department of Chemistry, University of Kaiserslautern, Kaiserslautern, Federal Republic of Germany.

the chemistry, synthesis, and design of nitroxide spin labels (Gaffney, 1976; Keana, 1978, 1979, 1984). Many of the compounds discussed in those papers are candidates for isotopic substitutions which could improve considerably their application to experimental problems.

This Appendix presents an updated report and evaluation of the synthetic procedures for deuterium and ^{15}N labeled spin probes as exemplified by the analogs discussed in Chapter 11. For these syntheses, some of the starting materials are now commercially available, albeit very expensive. These compounds include either singly or doubly substituted, tempone, tempol, tempamine, as well as pyrroline and pyrrolidine analogs. For syntheses of doubly substituted ^{15}N,deuterium spin-labeled analogs, it may be more reasonable to use commercially available starting materials. For the singly substituted, deuterated spin labels, the required $^{14}ND_3$ is not so costly as the $^{15}ND_3$. Therefore, it is more economical to employ $^{14}ND_3$ to synthesize the deuterated tempone, tempol, and tempamine, especially in the case of large-scale syntheses or preparation of a series of related analogs. The reason is that the most difficult step in the reaction sequence for tempone is the initial condensation of $^{14}ND_3$ with deuterated acetone (see Scheme 1), which cannot be scaled down below $\frac{1}{2}$ mol $^{14}ND_3$ without major changes in the conventional laboratory apparatus. This step is somewhat unpredictable, and failures with $^{14}ND_3$ would not incur so great a financial loss as compared with $^{15}ND_3$. Since tempone is the starting material for a wide variety of spin labels, it is best to prepare tempone in large quantities for subsequent conversions to related members. The synthetic procedures for spin-labeled analogs of inhibitors, nucleotides, and fatty acids are described in the subsequent text.

2. SYNTHESIS OF DEUTERATED AND ^{15}N,DEUTERATED MALEIMIDE SPIN LABELS (DMSL AND ^{15}N-DMSL)

Deuterated maleimide spin label (DMSL) was first synthesized by Venkataramu *et al.* (1981) using earlier procedures (Chiarelli and Rassat, 1973; Gaffney, 1976) with modifications for isotopic substitutions (see Scheme 1). It should be emphasized that a high degree of deuterium substitution in the final product, DMSL, is essential for greater sensitivity and resolution in the EPR spectra. For this reason it is critical to exclude moisture by working under an inert gas, e.g., nitrogen. For reasons of economy, in the original synthesis (Scheme 1) (Venkataramu *et al.*, 1981) some protonated solvents and reagents were employed in steps where exchange with protons was deemed marginal. Although deuterated solvents and reagents are expensive, it is preferable to use deuterated materials of highest purity throughout the synthesis for maximum sensitivity and resolution in EPR spectra. The original synthesis of DMSL will be described in detail as a model for techniques to be utilized in these costly procedures. For the preparation of ^{15}N-DMSL, it is likewise essential to procure $^{15}ND_3$ with an isotopic purity greater than 99%. ^{15}N-DMSL was also synthesized by adaptations of the same procedure using $^{15}ND_3$ in place of $^{14}ND_3$ and only deuterated reagents (Venkataramu *et al.*, 1981; Beth *et al.*, 1981). For ^{15}N-DMSL it is also possible to employ the procedure of Bates *et al.* (1983) which has the advantage of fewer reaction steps. However, in our hands, the overall yields of the two procedures are essentially identical.

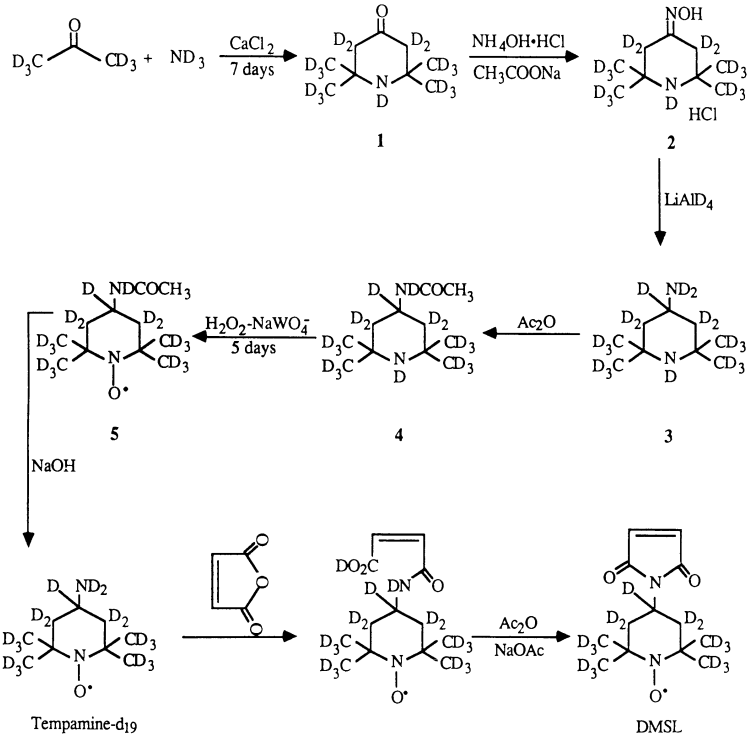

1 2 3 4 5 6 7 8

Scheme 1.

2,2,6,6-Tetramethyl-4-piperidone-d_{17} (**1**). This compound was prepared by modifications of the procedure described by Sosnovsky and Konieczny (1976). In a 1 liter three-necked flask fitted with a gas inlet, an efficient mechanical stirrer, a Y joint carrying a 0–50 °C thermometer, and a dry ice condenser is placed acetone-d_6 (171 g, 2.67 mol) and 4–20 mesh size anhydrous calcium chloride (62 g). With efficient stirring, deuterated ammonia (25.6 g, 1.28 mol) is slowly introduced over a period of 3 days in six equal lots maintaining the temperature of the reaction mixture at 30–35 °C. The reaction mixture is then set aside at room temperature for 4 days, during which time it turns red and becomes thick. Unreacted acetone-d_6 (9.5 g, 0.15 mol) is recovered by distillation, bp 35 °C/100 mm. To the cake, a solution of sodium deuteroxide (30 ml of 50% NaOD diluted with 50 ml D_2O) is added dropwise with vigorous stirring. The liberated oil is extracted with ether (5 × 300 ml) and the combined organic layer is dried (anhydrous $MgSO_4$). After evaporation of the solvent, the residue is distilled in vacuum, collecting the fraction with bp 85–90 °C/15 mm, to give 2,2,6,6-tetramethyl-4-piperidone-d_{17} (**1**) 54.8 g, 35.8%.

Oxime hydrochloride of 2,2,6,6-tetramethyl-4-piperidone-d_{17} (**2**). A solution of the ketone **1** (25.8 g, 0.15 mol) in 25 ml absolute ethanol is cooled in an ice bath and to it is added a solution of hydroxylamine hydrochloride (25.22 g, 0.36 mol) and anhydrous sodium acetate (14.8 g, 0.18 mol) in 50 ml D_2O. After allowing the reaction mixture to

warm to room temperature, it is gently heated on a steam bath for 5 h, diluted with 50 ml absolute ethanol, and allowed to stand overnight. The white crystalline hydrochloride that precipitates is filtered, washed with cold ethanol, and dried at 100 °C/30 mm for 6 h to give the oxime hydrochloride **2**, 32 g (95%), mp 285–290 °C (dec) and is used in the next step without further purification.

2,2,6,6-Tetramethyl-4-aminopiperidine-d_{20} (**3**). To a mechanically stirred suspension of $LiAlD_4$ (10 g, 0.24 mol) in 500 ml anhydrous ether (distilled over $LiAlH_4$), the oxime hydrochloride **2** (30 g, 0.14 mol) is cautiously added in portions from a solid addition flask at such a rate that there is gentle boiling of the solvent. After completion of this addition, the mixture is heated for 10 h and cooled. Excess $LiAlD_4$ is cautiously destroyed (N_2) by successive addition of 10 ml D_2O, 10 ml of 15% NaOD in D_2O, and 30 ml D_2O. The granular precipitate is filtered, pressed on the filter paper, and washed with several portions of anhydrous ether. The organic layer is dried (anhydr. K_2CO_3) and the solvent removed under reduced pressure. Distillation of the residue, bp 58–60 °C/2 mm, furnished 17.8 g (75%) of amine **3**, as a colorless mobile liquid.

2,2,6,6-Tetramethyl-4-acetylaminopiperidine-d_{19} (**4**). Freshly distilled acetic anhydride (21.5 g, 0.23 mol) is added dropwise to a stirred solution of the amine **3** (12 g, 0.068 mol) in 30 ml anhydrous ether at 10 °C. The temperature of the reaction mixture is not permitted to rise above 15 °C. Stirring is continued for 30 min, and the white solid is filtered and dried in a desiccator over KOH pellets to give acetate **4** (14.2 g, 96%), mp 122–124 °C. This material is used in the next step without further purification.

2,2,6,6-Tetramethyl-4-amino-piperidine-1-oxyl-d_{19} (**6**). To a solution of the acetate **4** (12.5 g, 0.058 mol) in 25 ml methanol and 50 ml water is added sodium tungstate (0.9 g), sodium salt of EDTA (0.9 g), and 16 ml of 30% H_2O_2 in 75 ml water. The reaction mixture is allowed to remain in the refrigerator for 6 h and then for 5 days at room temperature in the dark during which time it acquires a red color. The reaction mixture is saturated with K_2CO_3 and then the solution is cautiously extracted with ether (5 × 100 ml). The combined organic layer is dried (K_2CO_3) and the solvent removed in the rotary evaporator to afford radical **5** as an orange yellow solid (14.5 g). Acetate **5** is suspended in 40 ml of 15% NaOD and the contents stirred and boiled for 12 h. The cooled solution is filtered and the aqueous layer is saturated with K_2CO_3 and then the solution is extracted with ether (5 × 100 ml). The combined organic layer is dried (anhydrous $MgSO_4$) and the solvent is rotoevaporated. The residue is distilled in vacuum using a short distillation head to give amino radical **6**, 7.2 g (66%), bp 100–104 °C/4 mm. The product showed a single spot on TLC with $HCCl_3$:MeOH, 9:1 solvent system (R_f = 0.66) identical with an undeuterated sample.

N-(1-oxyl-2,2,6,6-tetramethyl-4-piperidinyl)maleimide-d_{17}(DMSL) (**8**). Amino radical **6** (1.94 g, 10.2 mmol) in 20 ml ether is added to a stirred solution of maleic anhydride (1.0 g, 10.2 mmol) dissolved in 60 ml ether. The precipitated orange solid is filtered, washed with 10 ml of ether to provide maleamic acid **7** (2.70 g, 92%), mp 160–164 °C. The crude acid **7** (2.70 g, 9.40 mmol), anhydrous sodium acetate (0.4 g, 4.87 mmol), and 40 ml of acetic anhydride are heated at 100 °C in an oil bath for 3 h. Excess acetic anhydride is removed under vacuum (bp 40 °C/1 mm) and the residue is dissolved in small amounts of hot benzene. The combined organic extract is passed over a column of silica gel to remove inorganic material. Rotoevaporation of the solvent affords a thick red gum (2.5 g). TLC ($HCCl_3$) showed this to be a mixture of maleimide **8** and isomaleimide. Separation of the required maleimide from the isomer is achieved

by column chromatography on silica gel (75 g, 60–200 mesh size). The column was eluted with hexane–benzene, benzene–chloroform mixtures with increasing amounts of the polar solvent and the separation is monitored by TLC ($HCCl_3$). Maleimide is eluted first and has the R_f value of 0.75. Fractions with this R_f value are pooled together and recrystallized from cyclohexane several times to furnish chemically pure maleimide **8** as an orange yellow solid (1.1 g, 44%). After drying at 80 °C/30 mm for 12 h, the maleimide melted at 107–108 °C, IR (KBr) 1695 cm^{-1}; MS (m/e) 268.

3. SYNTHESIS OF DEUTERATED AND ^{15}N,DEUTERATED ADENINE NUCLEOTIDE DERIVATIVES

A wide variety of protonated spin-labeled analogs of AMP, ADP, ATP, and NAD^+ have been synthesized with the spin-label group covalently attached to: (1) the N^6, C8, or C2 positions of the adenine ring; (2) the 2′ and 3′ positions of the ribose moiety; (3) the terminal phosphate group of AMP, ADP, or ATP; and (4) the amide moiety of the nicotinamide ring of NAD^+ (Weiner, 1969; Trommer *et al.*, 1974; Petrov and Sukhorukov, 1975; Wenzel *et al.*, 1976; Wenzel and Trommer, 1977; Cocco and Blakley, 1979; Streckenbach *et al.*, 1980; Gajewska *et al.*, 1982). With appropriately modified procedures, either the deuterated or ^{15}N,deuterated spin-labeled analogs can be prepared as so indicated by the enzyme or model system under investigation. To date, eleven isotopically substituted adenine nucleotide spin labels have been prepared. Syntheses of these compounds are described with an emphasis on improved or unpublished methodology. Additionally, the methods for important protonated spin labels are outlined, since deuterated or ^{15}N,deuterated analogs can be prepared by employing the appropriate isotopically substituted tempamine in the initial condensation reactions.

3.1. Synthesis of N^6-(D_{17})SL-AMP (10a) or N^6-(^{15}N,D_{17})SL-AMP (10b)

The procedure for synthesizing the isotopically substituted N^6-SL-AMP derivatives (Glöggler *et al.*, 1982; Beth *et al.*, 1984) is essentially that described by Trommer and his collaborators (Trommer *et al.*, 1974; Deparade *et al.*, 1981) except for additional steps to recover unreacted D_{17}- or ^{15}N,D_{17}-tempamine (see Scheme 2). To 1.35 mmol of 6-chloro-9-β-ribofuranosylpurine-5′-monophosphate (barium salt) **9** in 60 ml of water is added 4.05 mmol D_{17}- or ^{15}N,D_{17}-tempamine **6**. The mixture is stirred about 10 h at 50 °C. After cooling, the insoluble material is spun down and the supernatant applied to an anion exchange column (2 × 25 cm, DEAE-Sephadex A-25, acetate form). Transmission is recorded at 276 nm to monitor purines and absorbance at 450 nm with enhanced sensitivity settings for detection of the nitroxy radical. In the first elution with water, tempamine **6** can be recovered from the effluent absorbing at 450 nm. This effluent is saturated with potassium carbonate and extracted with ether several times. After drying over sodium sulfate, the ether is removed by evaporation. For the second elution, a linear gradient of 600 ml water and 600 ml pyridinium acetate buffer (1 M acetic acid, boiled 2 h over a small quantity of chromium(IV) oxide and distilled; 1.5 M pyridine, dried over molecular sieves and freshly distilled) is passed through the column. With this gradient, the 276 nm transmission decreases steadily, and after 350 ml of elution volume the N^6-SL-AMP **10a** or **10b** appears with a sharp minimum in 276 nm

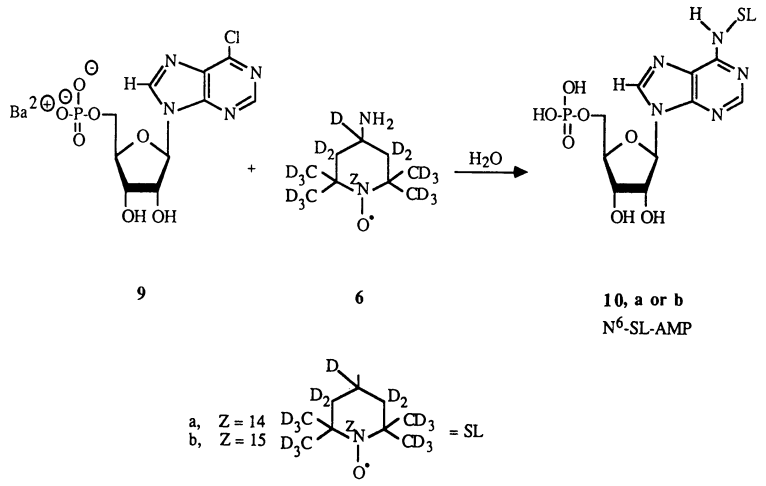

Scheme 2.

transmission and a simultaneous peak at 450 nm. The appropriate fractions are pooled, diluted with water to twice their volume, and lyophilized. The residue is taken up in water and freeze-dried again. The reddish nucleotide in its free-acid form **10a** or **10b** amounts to 73% theoretical yield as based on the adenine nucleotide. As a test of purity, thin-layer chromatography is performed on 0.25 mm precoated silica gel 60 F_{254} plates from Merck, Darmstadt, West Germany. Eluant System 1: 2-propanol/1% aqueous ammonium sulfate (2:1, v:v); Eluant System 2: isobutyric acid/conc. ammonia/water (66:1:33, v:v:v). System 1, $R_f = 0.53$; System 2, $R_f = 0.50$; $\lambda_{max} =$ 267 nm; $\varepsilon = 21{,}500\ M^{-1}\ cm^{-1}$ in 67 mM phosphate buffer, pH 7.2.

3.2. Synthesis of C8-(D_{17})SL-AMP (12a) or C8(^{15}N,D_{17})SL-AMP (12b)

The procedure for isotopically substituted C8-SL-AMP derivative (15, 18) is adapted from that of Wenzel and Trommer (1977) (see Scheme 3). 1 mmol (426 mg) of 8-bromoadenosine 5′-phosphate (free acid) **11** is dissolved in 50 ml water, and the pH is adjusted to 7.0 with 1 M NaOH. After addition of 15 mmol of D_{17}- or ^{15}N,D_{17}-tempamine **6** in 17 ml water (pH 11.0), the solution is refluxed for 13 h. The crude product was purified on a DEAE-Sephadex A-25 column (4 × 40 cm, acetate form). The flow rate is 240 ml per h, and the detection wavelengths are set as described above at 276 nm and 450 nm. The excess, unreacted D_{17}- or ^{15}N,D_{17}-tempamine **6** is eluted with water and recovered as detailed previously. The second elution consists of a linear gradient of 1 liter of water and 1 liter pyridinium acetate buffer (1 M acetic acid, boiled 2 h over a small quantity of chromium(IV) oxide and distilled; 1.5 M pyridine, dried over molecular sieves and freshly distilled). After an elution volume of 1.6 liters, the spin-labeled product **12a** or **12b** appears and is diluted in an equal volume of water before lyophilization. Yield, 60% as based on the nucleotide. $\lambda_{max} = 278$ nm; $\varepsilon =$ $18{,}400\ M^{-1}\ cm^{-1}$ in 67 mM phosphate buffer, pH 7.2. Thin-layer chromatography was

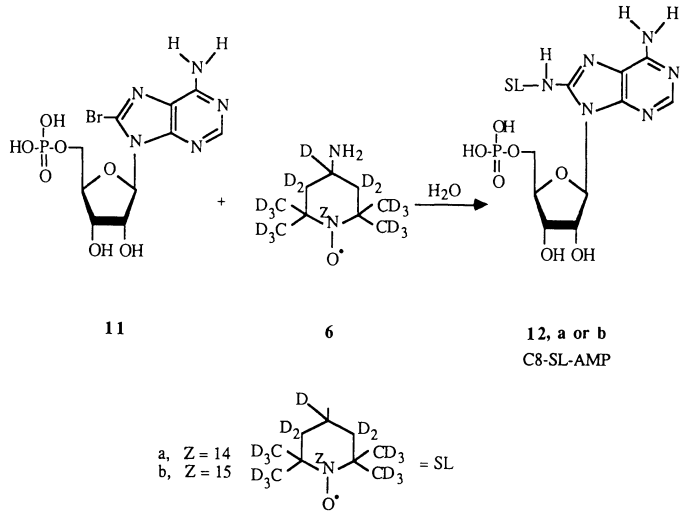

Scheme 3.

performed on precoated silica gel 60 F_{254} plates with the eluants described above for N^6-(D_{17})SL-AMP, **10a**. System 1, R_f = 0.53; System 2, R_f = 0.50.

3.3. Synthesis of N^6-SL-ATP (14)

The N^6-(D_{17})SL-ATP and N^6-(^{15}N,D_{17})SL-ATP analogs have not been prepared as yet. However, for the preparation of the isotopically labeled ATP spin probes, N^6-(D_{17})SL-AMP or N^6-(^{15}N,D_{17})SL-AMP would be employed as starting materials and the preparation carried out as detailed for the protonated probe. For preparation of N^6-SL-ATP **14** according to Glöggler *et al.* (1981), N^6-SL-AMP **10** is converted to its mixed anhydride in pyridine and then treated with dibutylphosphinothioic bromide (Furusawa *et al.*, 1976) (see Scheme 4). First, 0.5 mmol of the N^6-SL-AMP analog **10** is dissolved in 20 ml of dry pyridine together with 0.5 mmol of *N,N'*-dicyclohexyl-morpholino-carboxamidine. Removal of the pyridine by evaporation under reduced pressure is repeated three times to render the mixture anhydrous. Then 1 mmol of dibutylphosphinothioic bromide is added dropwise to the solution, which is stirred 4 h in the dark. Pyridine is then removed, and the residue is dissolved in water containing a small amount of pyridine. The aqueous solution is extracted with ether, and the organic layer is re-extracted with water/pyridine. The combined aqueous phases are concentrated in vacuo. The crude product **13** is purified by anion exchange chromatography on DEAE-Sephadex A-25 (acetate form, 4.5 × 45 cm). After elution with water, a linear gradient of 1 liter each of water and water containing 1 M pyridine (dried over molecular sieves and freshly distilled) and 0.6 M acetic acid (boiled 2 h over a small quantity of chromium(IV) oxide and distilled) is applied. The mixed anhydride is eluted after 1300 to 1400 ml of the gradient as indicated by monitoring at 280 nm (transmission) and 450 nm (absorption). The eluant is diluted with water to about twice its volume and freeze-dried. Repeated lyophilization from water yields about 0.3 mmol

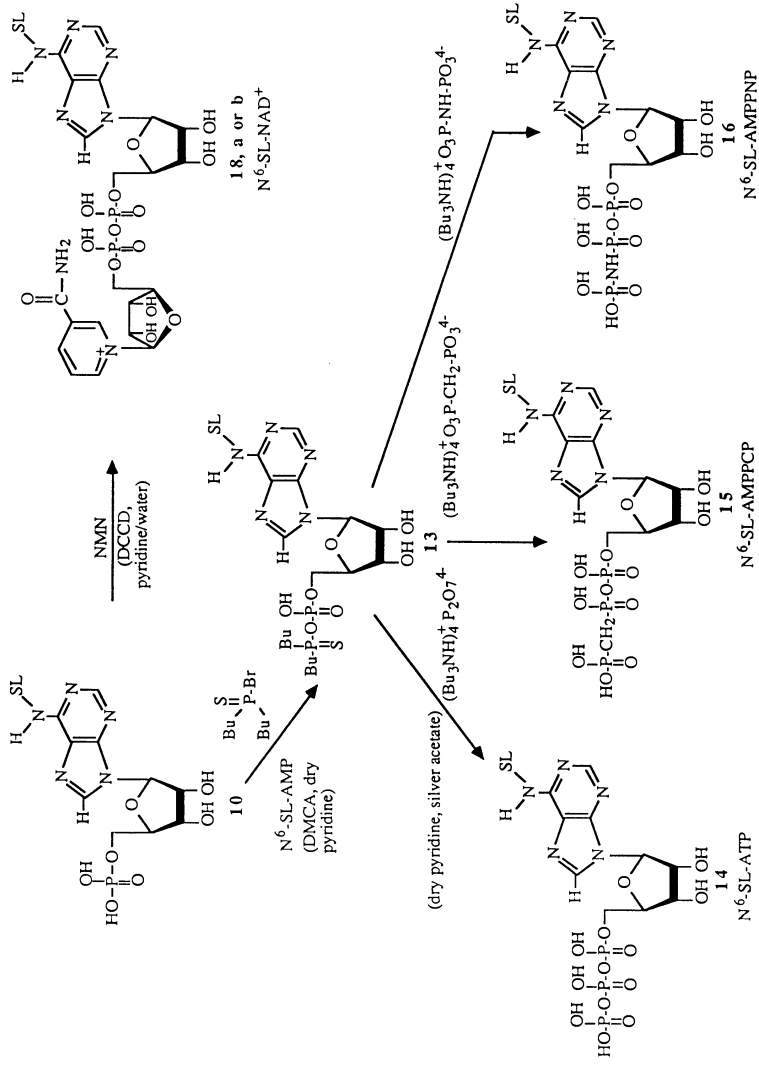

Scheme 4.

of the anhydride **13** (60–65% yield), Some methanol may be required to dissolve the lyophilized compound in water before the excess pyridine is removed. Thin-layer chromatography was performed on silica-gel plates exactly as outlined previously for the preparation of N^6-(D_{17})SL-AMP, **10a**. System 1, $R_f = 0.7$; System 2, $R_f = 0.52$; $\lambda_{max} = 267$ mm; $\varepsilon = 21{,}500\ M^{-1}\ cm^{-1}$.

Tetrakis-(tributylammonium)-diphosphate (1 mmol) is prepared as follows (Glöggler, 1981): 1 mmol (250 mg) of tetrasodium diphosphate in water is passed through a CM-Sephadex C-25 column (pyridinium form). The aqueous eluates are lyophilized, suspended in a trace of water, and then just enough tributylamine is added to dissolve the salt. The solvent is removed in a rotoevaporator leaving the tributylammonium salt as a colorless oil which is utilized for the N^6-SL-ATP preparation on the same day.

For conversion to the final product **14**, 0.2 mmol of the mixed anhydride of N^6-SL-AMP **13** and 1 mmol of tetrakis(tributylammonium) diphosphate is dissolved in 20 ml of dry pyridine (Furusawa *et al.*, 1976). To remove residual traces of water, the mixture is concentrated in vacuo and redissolved repeatedly. It is finally taken up in 3 ml of dry pyridine and, after addition of 0.8 mmol of dry silver acetate, the mixture is stirred at room temperature for 4 h in the dark. The reaction is quenched by addition of 1.5 mmol of potassium cyanide in 4 ml water. After partial evaporation of pyridine, the precipitate is removed by centrifugation or ultrafiltration (filter: Millipore·EA, 1 μm). The supernatant or filtrate, respectively, is diluted with water and purified on DEAE-Sephadex A-25 (3.5 × 40 cm, chloride form). Elution with water is followed by a linear gradient of 1 liter each of 20% methanol/water and 20% methanol/water containing 0.6 M lithium chloride. The spin-labeled nucleotide **14** elutes at 0.5 M lithium chloride. Lyophilization and trituration with anhydrous ethanol yields the N^6-SL-ATP **14**, in 35–40% of theory as based on adenine nucleotide content. Elementary analysis is consistent with $C_{19}H_{29}N_6O_{14}P_3Li_3 \cdot 3H_2O \cdot LiCl$. Thin-layer chromatography was carried out using the same precoated silica-gel 60 F_{254} plates (Merck, Darmstadt, West Germany) and System 2 eluants detailed in the N^6-(D_{17})SL-AMP preparation, **10a**. System 2, $R_f = 0.52$. In order to determine if hydrolysis products, ADP or AMP derivatives, are present in the ATP preparations, the sample is applied to Polygram CEL 300 PEI plates (Macherly and Nagel, Düren, West Germany) and eluted with 0.67 M lithium chloride. The ATP analog has an R_f of 0, while the AMP or ADP derivatives move from the origin, $R_f = 0.10$ for ADP and 0.37 for AMP itself.

3.4. Synthesis of C8-(^{15}N,D_{17})SL-ATP

The protonated C8-SL-ATP analog has been synthesized as described above for the N^6-SL-ATP derivatives using C8-SL-AMP as the starting compound (Glöggler *et al.*, 1981). The yields are the same for both the N^6- and C8-SL-ATP derivatives. Elementary analysis for the protonated derivative is consistent with $C_{19}H_{30}N_7O_{14}P_3Li_3 \cdot 4H_2O \cdot LiCl$. The isotopically substituted C8-(^{15}N,D_{17})SL-ATP has also been prepared using C8-(^{15}N,D_{17})SL-AMP, **12b** as the starting material (I. G. Atchatchloui and W. E. Trommer, unpublished results). Thin-layer chromatography was performed as described for the preceding synthesis of N^6-SL-ATP, **14**. System 2, $R_f = 0.49$. As in the case of N^6-SL-ATP, the C8-SL-ATP analogs do not migrate on Polygram 300 PEI plates.

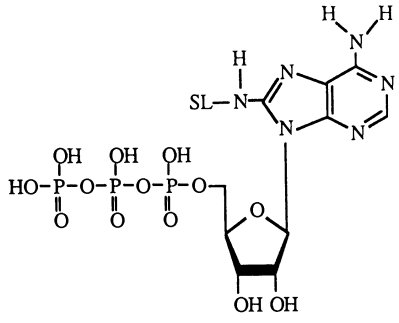

C8-SL-ATP

3.5. Synthesis of N^6- or C8-SL-Analogs of AMPPCP or AMPPNP

A series of SL-ATP analogs, which are not readily cleaved by hydrolytic or phosphorylating enzymes, has been synthesized for motional studies on nucleotide binding and protein conformational changes. These analogs substitute either a carbon or nitrogen atom in place of oxygen in the terminal P—O—P bond of ATP. The selection of the more appropriate analog for a particular enzyme should be initially ascertained with AMPPCP or AMPPNP itself. For example, the Ca^{++} pump-ATPase hydrolyzes AMPPNP rather rapidly and, therefore, AMPPCP is the derivative of choice. The reverse is true for the F_1-ATPase, and AMPPNP is the preferred analog. Although these analogs have not been prepared with isotopic substitutions, the potential usefulness of these compounds for a wide variety of systems validates their inclusion in this Appendix.

N^6-SL-AMPPCP (**15**). The compound is synthesized by the procedure given for N^6-SL-ATP **14** except that methylenediphosphonate (trisodium salt, Sigma Chemical

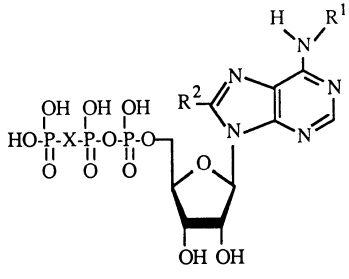

N^6-SL-AMPPCP: X = -CH_2-, R^1 = -SL, R^2 = H (**15**)

C8-SL-AMPPCP: X = -CH_2-, R^2 = -NH-SL, R^1 = H

N^6-SL-AMPPNP: X = -NH-, R^1 = -SL, R^2 = H (**16**)

C8-SL-AMPPNP: X = -NH-, R^2 = -NH-SL, R^1 = H

SL-Analogs of AMPPCP and AMPPNP

Co., St. Louis, Missouri, USA) is used instead of the diphosphate (see Scheme 4) (Glöggler *et al.*, 1981). Yield = 20%. Thin-layer chromatography was executed as described earlier for the synthesis of N^6-(D_{17})SL-AMP, **10a**. System 1, R_f = 0.51; System 2, R_f = 0.55. In contrast to the ATP derivatives, the N^6-SL-AMPPCP has an R_f value of 0.1 on Polygram 300 PEI plates.

C8-SL-AMPPCP. This derivative is prepared according to the methods described above for C8-SL-ATP and N^6-SL-AMPPCP (Glöggler *et al.*, 1981). Yield = 10%. Thin-layer chromatography: System 2, R_f = 0.55. On Polygram 300 PEI plates, R_f = 0.1.

N^6-SL-AMPPNP (**16**). This analog **16** is prepared by substituting tetrasodium imidodiphosphate (Boehringer Mannheim, Mannheim, West Germany) in place of the diphosphate employed in the synthesis of N^6-SL-ATP **14** (see Scheme 4) (Glöggler, 1981).

C8-SL-AMPPNP. This compound is synthesized according to the procedures outlined for C8-SL-ATP and N^6-SL-AMPPNP (Glöggler, 1981).

3.6. Synthesis of a Mixture of 2′- and 3′-($^{15}N,D_{13}$)SL-ATP (17)

The procedure of Streckenbach *et al.* (1980) was modified as follows (Vogel-Claude *et al.*, 1988): 0.3 mmol (50 mg) of ($^{15}N,D_{13}$)2,2,5,5-tetramethyl-1-oxyl-3-pyrroline-3-carboxylic acid and 0.3 mmol (48 mg) of *N,N′*-carbonyldiimidazole are mixed without solvent (see Scheme 5). The solids are subsequently dissolved in about 100 μliters of freshly distilled dimethyl formamide and allowed to stand 1 h at room temperature. Then 0.1 mmol (55 mg) ATP in a minimum amount of water (approximately 100 μliters) is added, and the solution is stirred 3 h at room temperature. After the addition of 0.5 ml of acetone, a yellowish oil forms which is separated by centrifugation at 40,000 × *g* for 10 min. Removal of the residual ATP from this crude product was achieved by reverse phase MPLC (LiChroprep, 6000 theoretical plates and 6 bar pressure; Merck, Darmstadt, West Germany) with 0.1 M aqueous lithium chloride containing 10% 2-propanol. The desired product elutes as a mixture of 2′- and 3′-($^{15}N,D_{13}$)SL-ATP **17** after about twice the volume required for ATP as monitored at 280 nm. It can be

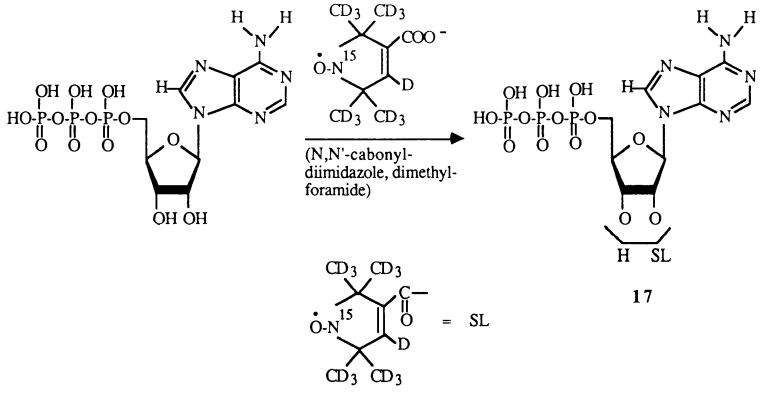

Scheme 5.

desalted by chromatography on Sephadex G-10 with 0.1 M triethylammonium bicarbonate buffer, pH 7.0, as eluant. Fractions exhibiting both a 280 nm absorption and a change in refractive index are collected and lyophilized. Yield = 35% as based on adenine nucleotide. In order to determine whether the 2′- and 3′-($^{15}N,D_{13}$)SL-ATP preparation contains any unlabeled ATP, thin-layer chromatography is performed on Nano-Sil-C_{18}-50 plates (Macherey and Nagel, Düren, West Germany). R_f = 0.6 for the SL-ATP analog and 1.0 for ATP itself. For detection of hydrolysis products, ADP or AMP derivatives, the sample is applied to Polygram CEL 300 PEI plates as described in the preparation of N^6-SL-ATP, **14**.

The 2′ and 3′ esters of the ribose moiety of SL-ATP are in rapid equilibrium in solution. Hence, EPR spectra of corresponding spin-labeled derivatives, particularly when complexed with proteins, may be composed of two components due to these isomers. In order to overcome this ambiguity, 2′- or 3′-deoxy ATP was used to prepare the 3′SL-2′dATP or 2′SL-3′dATP, respectively (Crowder and Cooke, 1987). The deuterated spin label, 3′(D_{13})SL-2′dATP, has recently been synthesized (P. Jacobs and W. E. Trommer, unpublished results). Since the ATP analogs are rapidly hydrolyzed by some of the ATPases of interest to investigators, the more stable 2′ and 3′ mixtures of SL-AMPPCP (Garcia *et al.*, 1987) and also SL-AMPPNP (Claude, 1987) have been synthesized. Thus a variety of ATP spin-labeled analogs can be prepared and designed to match the catalytic specificity of the many ATP requiring systems.

3.7. Synthesis of N^6-SL-ADP and C8-SL-ADP

The two SL-ADP probes can be prepared in a manner analogous to that for SL-ATP **14** by substituting the monophosphate derivative for the tetrakis(tributylammonium) diphosphate (Deparade and Trommer, 1979).

3.8. Synthesis of N^6-(D_{17})SL-NAD^+ (18a) and N^6-($^{15}N,D_{17}$)SL-NAD^+ (18b)

For the synthesis of these compounds, the procedure of Trommer *et al.* (1974) for the corresponding protonated compound was slightly modified to increase the purity of the product (Scheme 4) (Beth *et al.*, 1984; Philipp *et al.*, 1984). To a solution of 0.2 mmol N^6-(D_{17})-SL-AMP **10a** or N^6-($^{15}N,D_{17}$)SL-AMP **10b** and 0.3 mmol (67 mg) nicotinamide mononucleotide (NMN) in 5 ml water, 20 ml pyridine and 2 g *N,N′*-dicyclohexylcarbodiimide are added. The mixture is stirred for 24 h at room temperature, filtered from precipitated dicyclohexylurea, and washed with 1 ml of hot water. The filtrate and the washing solutions are combined and treated again with 2 g of *N,N′*-dicyclohexylcarbodiimide for 24 h. The mixture is filtered and washed as previously described. This treatment is repeated four times. Finally the mixture is poured into 200 ml of water, allowed to stand 1 h at room temperature, and filtered. The filtrate is extracted four times with 100 ml of chloroform each time. The aqueous phase is concentrated under reduced pressure and purified on an anion-exchange column (1.5 × 95 cm, Fractogel TSK-DEAE-650 (S), chloride form). The column is eluted with water until the 276 nm and 450 nm absorption drops to the baseline. Then a linear gradient of 900 ml water and 900 ml of 0.2 lithium chloride is applied. The product **18a** or **18b** is eluted after 690 ml of the gradient.

Various fractions from the anion exchange column are tested for SL-NAD^+ using the enzymatic reaction of alcohol dehydrogenase from yeast (Boehringer Mannheim, Mannheim, West Germany) with 0.5 M ethanol to give N^6-SL-NADH at pH 9.5 in 0.1 M glycine buffer. Fractions are also evaluated on the basis of SL-analog binding to lactic dehydrogenase in the presence of oxalate. The fractions containing the highest quality SL-NAD^+ **17** are pooled and dialyzed in an Amicon cell (Amicon Corp., Lexington, Massachusetts, USA) employing a UM05 or YM05 membrane. The effluent from this cell is checked by UV absorption and enzymatically for SL-NAD^+. The yield of N^6-($^{15}N,D_{17}$)SL-NAD^+ **18b** at this point in the procedure is 20%. For a higher level of purification, the product can be subjected to reverse phase MPLC (LiChroprep, 6000 theoretical plates and 6 bar pressure, Merck, Darmstadt, West Germany) using 0.2 M lithium chloride and 6% 2-propanol as eluant. After this column the preparation **17** is 99% pure as assayed by the enzymatic reaction of alcohol dehydrogenase. The absorbance ratio at 274 nm:340 nm should be 4.3 as measured before (NAD^+) and after (NADH) the reaction with alcohol dehydrogenase. The binding of N^6-SL-NAD^+ to lactic dehydrogenase in the presence of oxalate is examined again at this point.

Those fractions with lower absorbance ratios than 4.3 are submitted to rechromatography on the anion-exchange column. In this case a gradient from 0 to 0.1 M lithium chloride is adequate. Thin-layer chromatography is performed on silica-gel plates using the two eluant systems described for N^6-(D_{17})SL-AMP, **10a**. System 1, $R_f = 0.42$; System 2, $R_f = 0.43$; $\lambda_{max} = 266$; $\varepsilon = 27{,}000\ M^{-1}\ cm^{-1}$.

3.9. Synthesis of C8-(D_{17})SL-NAD^+ and C8-($^{15}N,D_{17}$)SL-NAD^+

The synthesis of the isotopically labeled C8-SL-NAD^+ analogs (Beth *et al.*, 1984; Philipp *et al.*, 1984) has been improved in the following manner: 10 ml pyridine and then 0.5 g *N,N'*-dicyclohexylcarbodiimide are added to a solution of 0.07 mmol C8-($^{15}N,D_{17}$)SL-AMP **12b** and 0.1 mmol nicotinamide mononucleotide (NMN) in 2.5 ml water. The solution is stirred for 24 h at room temperature. The precipitated dicyclohexylurea is removed by suction and washed with pyridine/water (4:1, v:v). The combined filtrates are stirred another 24 h with 0.5 g of the carbodiimide, and the precipitate is filtered and washed again. This procedure is repeated four more times, but the amounts of carbodiimide added during the last two cycles is only 0.2 g. Vigorous stirring is recommended, since there may be formation of two liquid phases. Then the

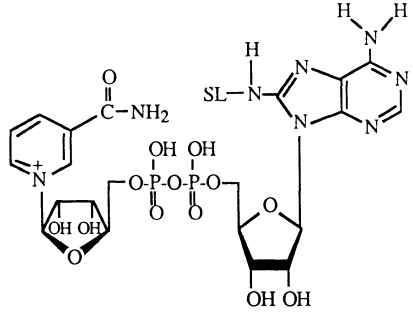

C8-SL-NAD^+

reaction mixture is poured into 70 ml of water, and the purification is executed as described above for the N^6-analog **18**. Yield after anion exchange = 10%. Thin-layer chromatography is used to characterize the derivatives as detailed in the synthesis of N^6-(D_{17})SL-AMP, **10a**. System 1, $R_f = 0.37$; System 2, $R_f = 0.43$; $\lambda_{max} = 274$ nm; $\varepsilon = 22{,}300\ M^{-1}\ cm^{-1}$.

4. SYNTHESIS OF ^{15}N AND ^{15}N,DEUTERATED STEARIC ACID SPIN LABELS

4.1. Synthesis of ^{15}N-5-Doxylstearic Acid Spin Label (26)

^{15}N-2-amino-2-methyl-1-propanol **23** is the key starting material for the synthesis of stearic acid spin labels with a doxyl group at 5, 12, or 16 positions. A simple procedure for this amino alkalol **22** was reported by Venkataramu *et al.* (1983) starting from commercially available ^{15}N-glycine as outlined in Scheme 6. ^{15}N-Glycine is first converted to ^{15}N-glycine ethyl ester hydrochloride **19** by treatment with thionyl chloride and ethanol (Brenner and Huber, 1953). A near quantitative yield of the hydrochloride was achieved by precipitating with anhydrous ether.

Benzylidene derivative of ^{15}N-glycine ethyl ester (**20**). Freshly distilled triethylamine (60 ml, 0.42 mol) is added to a cooled, stirred suspension of ^{15}N-glycine ethyl ester hydrochloride **19** (27.6 g, 0.196 mol), freshly distilled benzaldehyde (21.5 g, 0.202 mol), anhydrous magnesium sulfate (20 g) and 400 ml CH_2Cl_2. After stirring at room temperature for 24 h, the slurry is filtered and the solid washed with several portions of CH_2Cl_2. The solvent is then removed in vacuum at room temperature after which

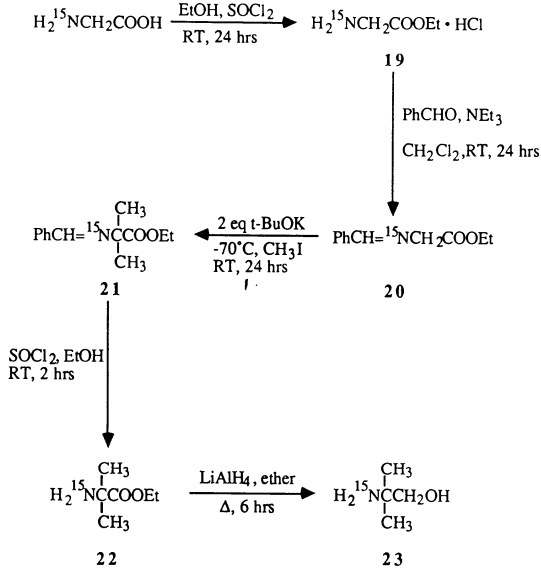

Scheme 6.

the residue is cooled in ice, diluted with 100 ml ice cold water. The oil is extracted with ether (3 × 100 ml) and the combined organic extract washed with brine and dried (anhyd. $MgSO_4$). The solvent is removed in vacuum and finally at the vacuum pump, thereby affording the product **20** as a pale yellow oil (37.1 g, 98.5%). PMR (CCl_4) δ 1.26 (3H, t, $-COOCH_2CH_3$), 4.02-4.24 (2H, q, $COOCH_2CH_3$), 4.24 (2H, s, $-{}^{15}NCH_2$), 7.29-7.42 CCl_4 (3H, m, Ar), 7.62-7.78 (2H, m, Ar), 8.16-8.22 (1H, d, $-CH = {}^{15}N-$). The Schiff base **20** is stored in the refrigerator and on the following day used in the next step without further purification.

Ethyl 2-(benzylidene-^{15}N-amino)propionate (**21**). Schiff base **20** (37.1 g, 0.193 mol) in 100 ml dry THF is added dropwise during 15 min (N_2) to a magnetically stirred suspension of potassium *t*-butoxide (50.3 g, 0.45 mol) in 300 ml dry THF, cooled to −70 °C. After the orange yellow solution is stirred for half an hour, freshly distilled methyl iodide (75.6 g, 0.53 mol) in equal volume of dry THF is added dropwise. The mixture is allowed to attain room temperature and the stirring is continued for 16 h. After removal of THF in vacuum at 35 °C, the resulting slurry is cooled in ice, and 100 ml of ice cold water is added with vigorous stirring. The oily layer is separated and the aqueous layer extracted with ether (3 × 100 ml). The combined organic phase is washed with water, brine, and the organic extract is dried (anhyd. $MgSO_4$). Ether is removed in a rotoevaporator and finally at the pump (0.1 mm) yielding the product **21** as pale yellow oil (40.3 g, 94.8%). PMR (CCl_4) 1.10-1.25 (3H, t, $COOCH_2CH_3$), 1.40-1.44 (6H, d, $2CH_3$), 4.02-4.22 (2H, q, $COOCH_2CH_3$), 7.28-7.40 (3H, m, Ar), 7.62-7.78 (2H, m, Ar), 8.18-8.24 (1H, d, $-CH = {}^{15}N-$). The product **21** is used in the next step without purification.

Ethyl ^{15}N-2-amino-2-methyl propionate (**22**). The benzylidene ester **21** (40.3 g, 0.183 mol) in 200 ml absolute ethanol is cooled to −5 °C. Then thionyl chloride (32.72 g, 0.275 mol) is added in the course of half an hour. After stirring at 0 °C for 1 h and then at room temperature for 2 h, ethanol and thionyl chloride are removed under reduced pressure. The golden yellow oil is extracted with pentane (3 × 100 ml) and the pentane layer washed with ice cold 1 N hydrochloric acid. The combined acid extract is cooled in ice-salt bath and cautiously saturated with solid K_2CO_3. The liberated amine is extracted with ether (4 × 75 ml) and the organic phase dried (K_2CO_3). Removal of the solvent in vacuum at room temperature and distillation of the residual oil at atmospheric pressure gave pure amine **22**, bp 145-148 °C, as a colorless mobile liquid (18.5 g, 77%). The pot residue is dissolved in ether and passed through a short column of silica gel (2 × 6 cm) and eluted with ether to give 0.8 g of additional amine increasing the yield of 80%. PMR (CCl_4) 1.18-1.32 (9H, m, $COOCH_2CH_3$ and $2CH_3$), 1.40 (2H, b, $^{15}NH_2$), 4.00-4.22 (2H, q, $COOCH_2CH_3$).

^{15}N-2-amino-2-methyl-1-propanol (**23**). A solution of the amino ester **22** (19.3 g, 0.146 mol) in 100 ml ether is added to a well-stirred suspension of $LiAlH_4$ (9 g, 0.24 mol) in 300 ml dry ether at such a rate as to maintain a uniform boiling of ether. Stirring is continued at room temperature for 6 h and then the mixture is gently refluxed for 6 h. After cooling on ice, excess $LiAlH_4$ is cautiously destroyed (N_2) by successive addition of 9 ml of water, 9 ml of 15% sodium hydroxide solution, and then 27 ml of water. The ether layer is decanted and washed several times with ether. The combined organic extract is dried (anhyd. K_2CO_3) and the solvent removed in vacuum. The viscous oil is distilled at atmospheric pressure using a short distillation head. The fraction boiling at 162-166 °C is ^{15}N-2-amino-2-methyl-1-propanol **23** (13 g, 76% overall yield from

^{15}N-glycine) PMR (CCl_4) δ 1.02–1.04 (6H, d, $2CH_3$), 2.80 (3H, b, $^{15}NH_2$ and OH), 3.16–3.20 (2H, d, OCH_2).

^{15}N-5-doxylstearic acid (**26**). Keana's general procedure (1979) for the synthesis of "doxyl" substituted spin labels was followed (see Scheme 7). Methyl-5-ketostearate **24** was prepared by the reported procedure (Hubbell and McConnell, 1971). A solution of methyl-5-ketostearate **24** (624 mg, 22 mmol) and amino alkanol **23** (1.8 g, 20 mmole) in 25 ml xylene containing 15 mg *p*-toluenesulfonic acid is stirred and refluxed in a Dean–Stark apparatus containing anhyd. K_2CO_3 for 8 days. The solution is cooled and diluted with an equal volume of ether. The organic phase is washed successively with cold saturated sodium bicarbonate solution (3 × 25 ml), ice-cold water (3 × 25 ml), and brine (2 × 25 ml). After being dried (anhyd. $MgSO_4$), the solvent is removed in a rotoevaporator and finally at the pump (0.1 mm) to afford the oxazolidine **25** as a pale yellow oil (0.8 g).

The crude amine **25** (0.8 g) is dissolved in 100 ml ether and cooled in ice. To this is added dropwise with stirring a solution of *m*-chloroperbenzoic acid (0.5 g) dissolved in 20 ml ether. The stirring is continued at room temperature for 36 h, and the organic phase is washed with cold saturated sodium bicarbonate solution (4 × 242 ml), water (3 × 24 ml), and dried (anhyd. $MgSO_4$). Removal of the solvent in vacuum gave the crude radical as a pale oil (0.6 g). Chromatography on silica gel (40 g, 60–200 mesh size) and elution with hexane–ether mixtures with increasing amounts of the polar solvent furnished the radical ester (0.5 g). This was rechromatographed on silica gel (10 g) and eluted with ether. Approximate 2-ml fractions were collected. Purity of each fraction was assessed by TLC (hexane–benzene, 70:30) employing the corresponding ^{14}N analog for comparison. Homogeneous fractions were pooled and the water removed under reduced pressure to give the pure radical ester **25** (0.37 g) as an orange yellow oil.

The radical ester **25** (0.37 g) is dissolved in 2 ml dioxane and 5 ml of 4% sodium hydroxide solution and let stand at room temperature for 3 h. The solution is cooled in the salt bath and then acidified with conc HCl to pH 2 and diluted with 25 ml ice cold water. The aqueous layer is extracted with ethyl acetate (2 × 25 ml) and the organic

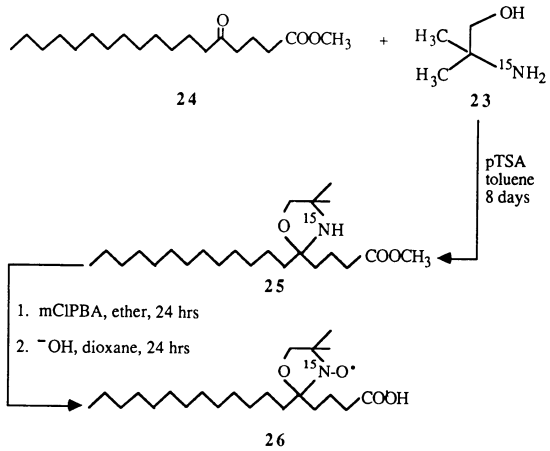

Scheme 7.

phase washed with water (3 × 25 ml) and dried (anhyd. Na_2SO_4). Removal of the solvent in vacuum and then at the pump (0.1 mm) yielded ^{15}N-5-doxyl-stearic acid **26** (220 mg) as a pale yellow solid, mp 48–49 °C. The corresponding ^{14}N analog melts at 47–48 °C.

4.2. Synthesis of ^{15}N-12-Doxylstearic Acid-d_{41} (27)

The synthesis of perdeuterio ^{15}N-12-doxyl-stearic acid **27** has been reported (see Scheme 8), employing essentially the same sequence of reactions outlined in Schemes 6 and 7 (Venkataramu *et al.*, 1985). ^{15}N-2-amino-2-methyl-1-propanol-d_{11}, the crucial starting material, was prepared according to Scheme 6 with modifications using deuterated solvents and reagents throughout. Methyl-12-ketostearate-d_{41} was prepared from commercially available 1,12-dodecanedioic acid-d_{20} by first converting to its ester acid chloride and then interacting with the Grignard reagent prepared from 1-bromohexane-d_{13} (Venkataramu *et al.*, 1983).

The partially deuterated compound ^{15}N-5-doxylstearic acid-d_{12} has been synthesized (Venkataramu *et al.*, 1985). However, this analog displayed only a threefold gain in sensitivity relative to the unsubstituted spin label. Comparison of this value with

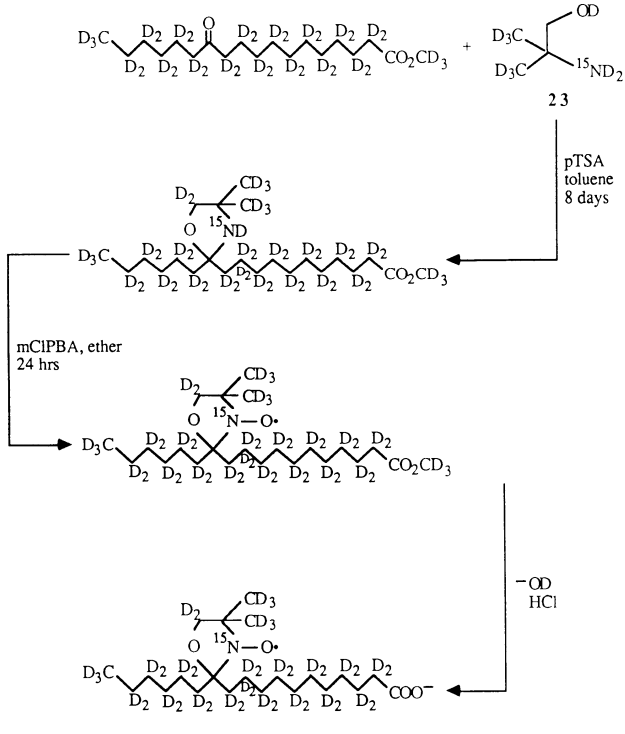

23 27

Scheme 8.

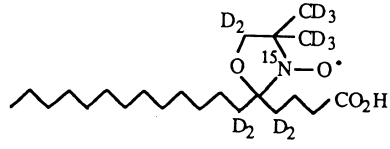

^{15}N-5-NS-d_{12}

the totally deuterated, ^{15}N-12-doxylstearic acid-d_{41}, which showed a 5.5-fold increase in sensitivity, suggested that remote hydrogens in the ^{15}N-5-doxylstearic acid-d_{12} analog were interacting with the nitroxide radical and broadening the linewidth. Although perdeuterated ^{15}N-5-doxylstearic acid-d_{41} would have been useful for comparison of spectral data, the starting materials for this synthesis were not readily available.

5. CONCLUSIONS

On the basis of the extensive body of knowledge concerning the chemical properties and synthesis of spin labels (Gaffney, 1976; Keana, 1978, 1979, 1984), it is clear that a large array of isotopically substituted compounds could be designed. The choice of a specific spin label for synthesis and experimentation is the critical starting point for biophysical EPR investigations. The effort demanded to obtain highly purified isotopically substituted spin probes may be more than compensated for by the resulting improvements in EPR data analysis. Expansion of EPR technology in the biomedical sciences could be greatly accelerated by the availability of new isotopically substituted spin labels for theoretical as well as clinical applications.

ACKNOWLEDGMENTS. The authors wish to thank Drs. S. D. Venkataramu and R. Philipp for their helpful suggestions and detailed critique of this appendix.

REFERENCES

Bates, B. A., Johnson, M. E., and Currie, B. L., 1983, Stable isotope substituted spin labels. 2. An improved synthesis of perdeuterio-^{15}N-(1-oxyl-2,2,6,6-tetramethyl-4-piperidinyl)maleimide, *J. Labelled Compd. Radiopharm.* **20**:33–38.

Beth, A. H., Venkataramu, S. D., Balasubramanian, K., Robinson, B. H., Dalton, L. R., Pearson, D. E., Park, C. R., and Park, J. H., 1981, ^{15}N and deuterium substituted maleimide spin labels: Improved sensitivity and resolution for biological studies, *Proc. Natl. Acad. Sci. U.S.A.* **78**:967–971.

Beth, A. H., Robinson, B. H., Cobb, C. E., Dalton, L. R., Trommer, W. E., Birktoft, J. J., and Park, J. H., 1984, Interactions and spatial arrangement of spin-labeled NAD^+ bound to glyceraldehyde-3-phosphate dehydrogenase: Comparison of EPR and x-ray modeling data, *J. Biol. Chem.* **259**:9717–9728.

Brenner, M., and Huber, W., 1953, Preparation of α-amino acid esters by alcoholysis of the methyl esters, *Helv. Chim. Acta* **36**:1109–1112.

Chiarelli, R., and Rassat, A., 1973, Syntheses de radicaux nitroxydes deuteries, *Tetrahedron* **29**:3639–3647.

Claude, P., 1987, Untersuchungen zur Strukur-Funktionsbeziehung der F_1ATPase mit Hilfe von Spin-Label- und Photoaffinity-Spin-Label-Nucleotiden, Doctoral thesis, University of Kaiserslautern, Kaiserslautern, West Germany.

Cocco, L., and Blakley, R. L., 1979, Synthesis of a spin-labeled analogue of nicotinamide adenine dinucleotide phosphate and its interaction with dihydrofolate reductase, *Biochemistry* **18**:2414-2419.

Crowder, M. S., and Cooke, R., 1987, Orientation of spin-labeled nucleotides bound to myosin in glycerinated muscle fibers, *Biophys. J.* **51**:323-333.

Deparade, M. P., and Trommer, W. E., 1979, The binding of spin-labeled derivatives of NAD^+ and its structural components to pig skeletal muscle lactate dehydrogenase, *Biochim. Biophys. Acta* **568**:177-182.

Deparade, M. P., Glöggler, K., and Trommer, W. E., 1981, Isolation and properties of glyceraldehyde-3-phosphate dehydrogenase from a sturgeon from the Caspian sea and its interaction with spin-labeled NAD^+ derivatives, *Biochim. Biophys. Acta* **659**:422-433.

Furusawa, K., Sekine, M. and Hata, T., 1976, Studies on pyrophosphates. Part III. A new method for the synthesis of nucleotide coenzymes by means of di-n-butylphosphoinothioyl bromide, *J. Chem. Soc., Perkin Trans. 1*: 1711-1718.

Gaffney, B. J., 1976, The chemistry of spin labels, in *Spin Labeling Theory and Applications* (L. J. Berliner, ed.), pp. 183-272, Academic Press, New York.

Gajewska, J., Bierzynski, A., Bolewska, K., Wierzchowski, K. L., Petrov, A. I., and Sukhorukov, B. I., 1982, Fluorescence quenching and spin-label electron spin resonance studies of stacking self-association in aqueous solutions of 2-aminopurine riboside and its 5'-mono- and diphosphate, *Biophys. Chem.* **15**:191-204.

Garcia, C., Coan, C., and Verjovski-Almeida, S., 1987, Binding of spin-labeled ATP and AMP-PCP to SR ATPase: Evidence for two distinct sites, *Biophys. J.* **51**:401A.

Glöggler, K. G., 1981, Synthese und Anwendung spinmarkierter Coenzyme zur Aufkläring der Wirkungsmechanismen von Enzymen, Doctoral thesis, University of Stuttgart, West Germany.

Glöggler, K. G., Fritzsche, T. M., Huth, H., and Trommer, W. E., 1981, Synthesis and preliminary biochemical characterization of spin-labeled derivatives of ATP and its 'non-cleavable' analog, adenosine 5'-β,γ-methylenetriphosphate, *Hoppe-Seyler's Z. Physiol. Chem.* **362**:1561-1565.

Glöggler, K. G., Balasubramanian, K., Beth, A., Fritzsche, T. M., Park, J. H., Pearson, D. E., Trommer, W. E., and Venkataramu, S. D., 1982, The synthesis of deuterium substituted spin labeled analogues of AMP and NAD^+ and their use in EPR studies of lactate dehydrogenase, *Biochim. Biophys. Acta* **701**:224-228.

Hubbell, W. L., and McConnell, B. M., 1971, Molecular motion in spin-labeled phospholipids and membranes, *J. Am. Chem. Soc.* **93**:314-320.

Keana, J. F. W., 1978, New aspects of the synthesis and chemistry of nitroxide spin labels, *Chem. Rev.* **78**:36-64.

Keana, J. F. W., 1979, New aspects of nitroxide chemistry, in *Spin Labeling II; Theory and Applications* (L. J. Berliner, ed.), pp. 115-172, Academic Press, New York.

Keana, J. F. W., 1984, Synthesis and chemistry of nitroxide spin labels, in *Spin Labeling in Pharmacology* (J. L. Holtzman, ed.), pp. 1-85, Academic Press, New York.

Petrov, A. I., and Sukhorukov, B. I., 1975, Spin-labeled nucleosides, nucleoside-5'-mono-, di- and triphosphates, *Biofizika* **20**:965-966.

Philipp, R., McIntyre, J. O., Robinson, B. H., Huth, H., Trommer, W. E., and Fleischer, S., 1984, The synthesis of ^{15}N- and deuterium-substituted, spin-labeled analogues of NAD^+ and their use in EPR studies of dehydrogenases, *Biochim. Biophys. Acta* **790**:251-258.

Sosnovsky, G., and Konieczny, M., 1976, Preparation of triacetoneamine (4-oxo-2,2,6,6-tetramethylpiperidine), an improved method, *Synthesis*: 735-737.

Streckenbach, B., Schwarz, D., and Repke, K. R. H., 1980, Analysis of phosphoryl transfer mechanism and catalytic centre geometries of transport ATPase by means of spin-labeled ATP, *Biochim. Biophys. Acta* **601**:34–46.

Trommer, W. E., Wenzel, H. R., and Pfleiderer, G., 1974, Notiz über Synthese und biochemische Eigenschaften eines Spin-Label-Nicotinamid-Adenin-Dinucleotids, *Liebigs Ann. Chem.*: 1357–1359.

Venkataramu, S. D., Pearson, D. E., Beth, A. H., Perkins, R. C., Park, C. R., and Park, J. H., 1981, Synthesis of perdeuterio-N-(1-oxyl-2,2,6,6-tetramethyl-4-piperidinyl)maleimide, a highly sensitive probe, *J. Labeled Compd. Radiopharm.* **18**:371–383.

Venkataramu, S. D., Pearson, D. E., Beth, A. H., Balasubramanian, K., Park, C. R., and Park, J. H., 1983, Synthesis of ^{15}N-5-doxylstearic acid for improved EPR characterization of lipid motion in biomembranes, *J. Labelled Compd. Radiopharm.* **20**:433–445.

Venkataramu, S. D., Pearson, D. E., Beth, A. H., Park, C. R., and Park, J. H., 1985, High resolution spin labeled fatty acid: Synthesis and EPR spectral characteristics, *Tetrahedron Lett.* **26**:1403–1406.

Vogel-Claude, P., Schäfer, G., and Trommer, W. E., 1988, Synthesis of a photoaffinity-spin-labeled derivative of ATP and its first application to F_1ATPase, *FEBS Lett.* **227**:107–109.

Weiner, H., 1969, Interaction of a spin-labeled analog of nicotinamide-adenine dinucleotide with alcohol dehydrogenase. I. Synthesis, kinetics, and electron paramagnetic resonance studies, *Biochemistry* **8**:526–533.

Wenzel, H. R., Pfleiderer, G., Trommer, W. E., Paschenda, K., and Redhardt, A., 1976, The synthesis of spin-label derivatives of NAD^+ and its structural components and their binding to lactate dehydrogenase, *Biochim. Biophys. Acta* **452**:292–301.

Wenzel, H. R., and Trommer, W. E., 1977, 8-Spin-label nicotinamide adenine dinucleotide, synthesis and properties of a new spin-labelled coenzyme, *FEBS Lett.* **78**:184–188.

Contents of Previous Volumes

VOLUME 1

Chapter 1

NMR of Sodium-23 and Potassium-39 in Biological Systems
Mortimer M. Civan and Mordechai Shporer

Chapter 2

High-Resolution NMR Studies of Histones
C. Crane-Robinson

Chapter 3

PMR Studies of Secondary and Tertiary Structure of Transfer RNA in Solution
Philip H. Bolton and David R. Kearns

Chapter 4

Fluorine Magnetic Resonance in Biochemistry
J. T. Gerig

Chapter 5

ESR of Free Radicals in Enzymatic Systems
Dale E. Edmondson

Chapter 6

Paramagnetic Intermediates in Photosynthetic Systems
Joseph T. Warden

Chapter 7

ESR of Copper in Biological Systems

John F. Boas, John R. Pilbrow, and Thomas D. Smith

Index

VOLUME 2

Chapter 1

Phosphorus NMR of Cells, Tissues, and Organelles

Donald P. Hollis

Chapter 2

EPR of Molybdenum-Containing Enzymes

Robert C. Bray

Chapter 3

ESR of Iron Proteins

Thomas D. Smith and John R. Pilbrow

Chapter 4

Stable Imidazoline Nitroxides

Leonid B. Volodarsky, Igor A. Grigor'ev, and Renad Z. Sagdeev

Chapter 5

The Multinuclear NMR Approach to Peptides: Structures, Conformation, and Dynamics

Roxanne Deslauriers and Ian C. P. Smith

Index

VOLUME 3

Chapter 1

Multiple Irradiation ^{1}H NMR Experiments with Hemoproteins

Regula M. Keller and Kurt Wüthrich

Chapter 2

Vanadyl(IV) EPR Spin Probes: Inorganic and Biochemical Aspects

N. Dennis Chasteen

Chapter 3

ESR Studies of Calcium- and Proton-Induced Photon Separations in Phosphatidylserine-Phosphatidylcholine Mixed Membranes

Shun-ichi Ohnishi and Satoru Tokutomi

Chapter 4

EPR Crystallography of Metalloprotins and Spin-Labeled Enzymes

James C. W. Chien and L. Charles Dickinson

Chapter 5

Electron Spin Echo Spectroscopy and the Study of Metalloproteins

W. B. Mims and J. Peisach

Index

VOLUME 4

Chapter 1

Spin Labeling in Disease

D. Allan Butterfield

Chapter 2

Principles and Applications of ^{113}Cd NMR to Biological Systems

Ian M. Armitage and James D. Otvos

Chapter 3

Photo-CIDNP Studies of Proteins

Robert Kaptein

Chapter 4

Application of Ring Current Calculations to the Proton NMR of Proteins and Transfer RNA

Stephen J. Perkins

Index

VOLUME 5

Chapter 1

CMR as a Probe for Metabolic Pathways *in vivo*
R. L. Baxter, N. E. Mackenzie, and A. I. Scott

Chapter 2

Nitrogen-15 NMR in Biological Systems
Felix Blomberg and Heinz Rüterjans

Chapter 3

Phosphorus-31 Nuclear Magnetic Resonance Investigations of Enzyme Systems
B. D. Nageswara Rao

Chapter 4

NMR Methods Involving Oxygen Isotopes in Biophosphates
Ming-Daw Tsai and Larol Bruzik

Chapter 5

ESR and NMR Studies of Lipid-Protein Interactions in Membranes
Philippe F. Devaux

Index

VOLUME 6

Chapter 1

Two-Dimensional Spectroscopy as a Conformational Probe of Cellular Phosphates
Philip H. Bolton

Chapter 2

Lanthanide Complexes of Peptides and Proteins
Robert E. Lenkinski

Chapter 3

EPR of Mn(II) Complexes with Enzymes and Other Proteins
George H. Reed and George D. Markham

Chapter 4

Biological Applications of Time Domain ESR
Hans Thomann, Larry R. Dalton, and Lauraine A. Dalton

Chapter 5
Techniques, Theory, and Biological Applications of Optically Detected Magnetic Resonance (ODMR)
August H. Maki

Index

VOLUME 7

Chapter 1

NMR Spectroscopy of the Intact Heart
Gabriel A. Elgavish

Chapter 2

NMR Methods for Studying Enzyme Kinetics in Cells and Tissue
K. M. Brindle, I. D. Campbell, and R. J. Simpson

Chapter 3

Endor Spectroscopy in Photobiology and Biochemistry
Klaus Möbius and Wolfgang Lubitz

Chapter 4

NMR Studies of Calcium-Binding Proteins
Hans J. Vogel and Sture Forsén

Index

Index

A tensor, 132, 162–163
  averaged components, 166, 170
  components, 133
  glyceraldehyde-3-phosphate dehydrogenase (GAPDH), 551, 554–557, 561
  maleimide spin label (DMSL), 551, 554–557
  maleimide spin label (^{15}N,DMSL), 554–557, 561
  serum albumin, 586–587
  stearic acid spin label (^{15}N)-SNS, 586–587
  principal axes, 133
A-band microwave region, 158
AB splittings, 348–349, 352–355
Aconitase, 457
  spin-labeled, 382
Active carbonates, 438
Active esters, 430, 432–434, 446, 450, 456, 466–468
Acylated glycine ester, 429–430
Acyl azides, 430, 432, 434, 467–469
Acyl imidazoles, 430, 432, 450–451, 467
Adenine nucleotide spin labels
  formula, 621, 622, 625
  glyceraldehyde-3-phosphate dehydrogenase, 581
  metabolic regulation, 581–582
  C^{8}-(^{15}N,D$_{17}$)SL-AMP, 581
  F_1ATPase binding, 581–582
  N^{6}-(D$_{17}$)SL-AMP, 581
  2′- and 3′-(^{15}N,D$_{13}$)SL-ATP, 582
  2′- and 3′-SL-ADP, 582
  synthesis, 619–627
Adiabatic rapid passage, 415
Albumin, serum
  maleimide spin label (DMSL), 549–553
  stearic acid spin label (^{15}N-5-NS), 583–587
  stearic acid spin label (^{15}N,D-5-NS), 583–585
  sulfhydryl group, 549
Anhydrides, 430–433
Anisotropic motion, 232
  B-hydroxybutyrate dehydrogenase, 561
  lipids, membranes, 265–269
  order parameter, 267
  See also Diffusion, anisotropic rotation
Anisotropic rotational motion, ST-ESR, 166–173
Antibody-ligand interactions, 597–613
Arachidonic acid, 495
Arginine label, 446
ATP spin labels
  C8-(^{15}N,D$_{17}$)SL-ATP, 623–624
  2'- and 3'-(^{15}N,D$_{13}$)SL-ATP, 582, 625–626
Azidoformate, 438–439
α-Bromoketone reagents, 457, 477, 479

Band-3 protein
  glyceraldehyde-3-phosphate dehydrogenase interactions, 553, 559–561, 579–580
  maleimide spin label ^{15}N, DMSL, 559–561
  NAD$^+$ spin label, N^{6}-(D$_{17}$)SL-NAD$^+$, 579–580
B-hydroxybutyrate dehydrogenase
  anisotropic motion, 561
  C8-(D$_{17}$)SL-NAD$^+$, 580
  N^{6}-(D$_{17}$)SL-NAD$^+$, 580–581
  N^{6}-(^{15}N,D$_{17}$)SL-NAD$^+$, 580–581
  ^{15}N, deutrated maleimide spin label, 561–562

Bifunctionalized doxyls, 463
Bilayers: *see* Lipid bilayers
Bimolecular collision, 401, 402, 413
Bloch equations, 136
Boltzmann equilibrium, 406
Bovine serum albumin, 203; *see also* Albumin, serum

Calibration procedures in ST-ESR, 154–156
  calibration
    of B_1, 154–156
    of B_m, 156
  phase setting of phase-sensitive detector, 145–146, 160
Carbodiimides, 437
Carbon tetrachloride trichloromethyl radical, 491
Cavity, 148–150
  calibration of B_1 and B_m, 154–156
  dielectric loss, 150, 157
  distribution of B_1 and B_m, 150–152, 157
  effect of sample on cavity properties, 150–152
  filling factor, 151–152
  lens effect, 152
  perturbing sphere method, 156
  quality factor Q, 149–152, 155
  sucking-in effect, 152
Cellular respiration, 416, 421
Cholestane spin label, 166–170
Cholestane spin label analog, 200
Cholestane spin probes, ^{15}N-doxylcholestane spin label, 583, 591
Cholesterol, 166–170
Chromium (III), nitroxyl interaction, 365–366, 386–388
Clark electrode, 422
Cobalt (II), nitroxyl interaction, 386–388
Collision frequency
  stearic acid spin labels, 589–591
  ^{14}N and ^{15}N spin labeled pairs, 589–591
Computer simulations
  bovine serum albumin, 551, 586–587
  coenzymes SL-NAD$^+$, 574–576
  glyceraldehyde-3-phosphate dehydrogenase (GAPDH), 554–555, 558–562, 574–576
  maleimide spin label (DMSL), 551, 554–555
  maleimide spin label (^{15}N,DMSL), 554–555, 558–562
  spin-labeled stearic acid, 586–587
  ST-ESR spectra, 160, 165, 169–170
Conjugate gradients algorithm (Lanczos), 21–32
Conjugated additions
  to α,β-unsaturated carbonyls, 455, 457, 478
  to α,β-unsaturted nitrile, 448, 454–455
Continuous wave saturation, 414, 415
Coordination equilibria, 373–374
Copper
  copper diporphyrins, 363–364
  nitroxyl interaction, 354–355, 386–388
Correlation times
  anistropic rotation, 216
  effective, 213–214
  glyceraldehyde-3-phosphate dehydrogenase (GAPDH), 556, 558, 559, 562
  rotational, 102–112, 182, 259
  serum albumin, 550–551, 586
  uniaxial rotation, 215–216
  β-hydroxybutyrate dehydrogenase, 561
  τ_c, 140, 142, 147, 148, 159–166
  $\tau_{//}$, 166–168, 170–173
  $\tau_{\perp}$, 170–173
Cross-linking reagents, 454–455, 459
Crystals, glyceraldehyde-3-phosphate dehydrogenase (GAPDH), 575–579
Cyanyl radical, 522–523
Cysteine, 504–505
Cytochrome P-450, 507, 511
  spin-labeled, 378–382
C8-(D_{17})SL-NAD$^+$
  advantages, 565–567
  binding constants K_1–K_4, (GAPDH), 578
  binding stoichiometry (GAPDH), 577
  computer simulation, 566
  crystalline GAPDH, 577–578
  dipolar interactions, 576–579
  dipolar spectra, 577–579
  enzyme mechanism, GAPDH, 578–579
  EPR spectra, 577
  formula, 564
  hyperfine spectra, 577–579
  lactic dehydrogenase, 564–566
  molecular distances, 577–579
  molecular modeling, 577–578
  negative cooperativity, NAD$^+$ binding, 578
  resolution, 565
  sensitivity, 565
  synthesis, 627–628
  β-hydroxybutyrate dehydrogenase, 580
C8-(^{15}N,D_{17})SL-NAD$^+$
  advantages, 565–567
  computer simulation, 566
  dipolar interactions, 576–579
  formula, 564

C8-(^{15}N,D_{17})SL-NAD$^+$ (*Cont.*)
lactic dehydrogenase, 564–566
resolution, 565
sensitivity, 565
spectral simplification, 566
synthesis, 627–628

Deuterated maleimide spin label (DMSL)
A tensors, 551, 554–557
advantages, 548–555
comparison with ^{15}N,DMSL, 553–557
comparison with spin-labeled NAD$^+$, 563
computer simulation, 551, 555
correlation times, 551, 553, 555–557
EPR spectra, 550, 554, 555
g tensors, 551, 554–557
glyceraldehyde-3-phosphate dehydrogenase, 552–555
improved resolution, 548–555
improved sensitivity, 548–555
serum albumin, 549–552
spectral stimulation, 551, 555
ST-EPR spectra, 551, 554, 555
sulfhydryl interactions, 549, 553
synthesis, 616–619
Deuterated spin labels
deuterated maleimide spin label, DMSL, 548–557, 616–619
Gaussian linewidths, 121–125
perdeuterated tempone, 616–618
proton contamination, 122
C8-(D_{17})SL-NAD$^+$, 564–566
C8-(D_{17})SL-AMP, 581
N^6-(D_{17})SL-NAD$^+$, 564–580, 626–627
N^6-(D_{17})SL-AMP, 581
Dielectric loss, 150, 157–158
Diffusion
anistropic rotation, 184, 187, 212, 216, 261
Brownian, 15, 181–183, 259–261
$D_{//}$, $D_{\perp}$, 185, 198
dipolar broadening, 274–277
free, 15
isotropic, 184
jump, 15
lateral, 269–274
rotational Stokes–Einstein, 184, 201
translational, 273
uniaxial, 187, 208–211, 215–216
Diffusion tensor, 6
in anistropic media, 16–18
tilt angle, 6
Dimyristoyl phosphatidylcholine, 168–170
Dipalmitoyl phosphatidylcholine, 167, 171
Dipolar interaction, 341–343, 405–420
distance measurements, 360–361
glyceraldehyde-3-phosphate dehydrogenase, 566–580
spin labeled NAD$^+$, 566–580
C8-(D_{17})SL-NAD$^+$, 576–579
N^6-($D1_7$)SL-NAD$^+$ and N^6-(^{15}N,D_{17})SL-NAD$^+$, 566–576, 579–580
Dipolar splitting, 341
in cytochrome P-450, 378–382
in glyceraldehyde 3-phosphate dehydrogenase (GAPDH), 383–384
used to measure distances, 360–361
Dipole–dipole interaction, 256, 274–277
Director
frame, 5
tilt, 5
Dispersion signal, 189
U'_1,V'_2, 189
Distance measurements, 360–362, 604–607, 609
glyceraldehyde-3-phosphate dehydrogenase (GAPDH), 576–579
C8-(D_{17})SL-NAD$^+$, 577–579
N^6-(^{15}N,D_{17})SL-NAD$^+$, 575–577
DMPC spin label
spectra, 266, 279
table of motional parameters, 267
^{15}N-labeled, ELDOR, 324–330
DMPO
cyanyl radical, 522–523
cumylperoxyl, 499
ethylperoxyl, 499
glutathione, 505–508
hydroxyl, 513
malonaldehyde, 517–518
styrene radical, 523–524
DNP glycine spin-label, 599
Double resonance (ELDOR)
collision frequency, 589–592
vertical fluctuations, 589–592
^{14}N and ^{15}N spin-label fatty acids, 589–592
Doxyl spin labels, 200
DTBN
hyerfine coupline constant in a MBBA liquid crystal, 106
spin exchange, 118–121
5-Doxylstearate, spectra in methanol, 107

ELDOR
apparatus, 317–320

ELDOR (*Cont.*)
in cells, 330
lateral diffusion, 320–321
pulsed, 234, 244, 247, 311
rate equations, 310
Electron–electron interaction: *see* Dipolar interaction
Electron–electron spin-spin splitting, 339–391
diagonalization calculation, 349, 369, 376
Hamiltonian, 346–349
long-range, 394–351, 384–389
perturbation calculation, 349, 351, 366, 376
Electron-spin relaxation, 136–139
ENDOR of nitroxides, proton hyerfine coupling constants, 82–83
Equilibrium probability distribution function, 4, 18
ESR spectrometer, for ST-ESR, 148–158
Exchange interaction, 343–347, 406; *see also* Heisenberg exchange
anisotropic, 345, 347
antisymmetric, 346, 347
attenuation coefficients, 384–385
isotropic, 344, 347
limit function, 344
long-range, 384
strong exchange, 406
table of examples, 386–388

F_1ATPase, 581
Fatty acid spin probes
5-doxylstearic acid (5-NS), 583–591
^{15}N-5-doxylstearic acid (^{15}N-5-NS), 582–591 628–631
^{15}N,D_{12}-5-doxylstearic acid (^{15}N,D_{12}-5-NS), 582–591, 632
^{15}N-12-doxylstearic acid (^{15}N-12-NS), 583–585, 588–591
^{15}N,D_{41}-12-doxylstearic acid (^{15}N,D_{41}-12-NS), 583–631
^{5}N-16-doxylstearic acid (^{15}N-16-NS), 583–585, 588–591
Fentor reaction, 499
Field modulation, 141–143, 153–154
amplitude (B_m), 141, 143, 156, 157–158
frequency, 141, 145, 154, 163–165, 169
Filling factor, 151–152
Frozen solutions, 356–357, 368–369

g-factor tensor, 132, 162–163
averaged components, 166, 170
components, 133
g-factor tensor (*Cont.*)
glyceraldehyde-3-phosphate dehydrogenase, 551, 554–557, 561
maleimide spin label (DMSL), 551–557
maleimide spin label (^{15}N,DMSL), 554–557, 561
principal axes, 133
serum albumin, 586–587
stearic acid spin label (^{15}N-5-NS), 586–587
Gadolinium (III), nitroxyl interaction, 371–373
Gas-exchange sample cell, 408, 414
Gaussian–Lorentzian convolution, 80, 101, 117–121
Glutathione, 505–506
Glyceraldehyde radical, 514–515
Glyceraldehyde-3-phosphate
effects on EPR spectra, 559
substrate, 552–553
Glyceraldehyde-3-phosphate dehydrogenase, 203
A tensors, 554–557, 561
adenine nucleotide spin labels, 581–582
band-3 interactions, 553, 559–561, 579–580
binding soichiometry (SL-NAD$^+$), 571–572
catalysis, 552
computer simulations, 554–555, 558–562, 574–576
correlation times, 555–559, 562
crystal structure, 576–579
deuterated maleimide spin label, 552–561
dipolar interactions, 566–569, 571–580
EPR spectra, 554, 555, 559, 568, 570–572, 575, 577, 579
g tensors, 554–557, 561
membrane-bound, 553, 559–561, 579–580
monomers, 553, 572–574
negative cooperativity, NAD$^+$ binding, 572–574
spin-labeled, 382–384
spin-labeled NAD$^+$, 556–580
ST-EPR spectra, 555–559
sulfhydryl groups, 553–580
tetramers, 553, 572–574
C8-SL-NAD$^+$ binding, 576–579
(D_{17}) and (^{15}N,D_{17})SL-NAD$^+$, 556–580
NAD$^+$ binding constants, 569–571
N^6-SL-NAD$^+$ binding, 576–579
^{15}N, deuterated maleimide spin label, 552–561
^{15}N,^{2}H maleimide spin label, 203, 205, 224, 231
Glycerol-water mixtures, 155, 159, 171–173

Half-field transitions, 357–360, 361–364
concentration dependence, 358
distances, 361–364
frequency dependence, 359
hyperfine splitting, 360
intensity, 358
measurements, 382
Halothene, PBN, 493
Hamiltonian, 132
Heisenberg spin exchange, 115–121, 256, 269–277, 401–405, 419, 420
ELDOR, 310–316
exchange integral, 402, 405
Hematin, 498–499
Hole burning, 140–142
time evolution of hole, 147
Hydrazines, 507–513
Hydroperoxides, 498
DMPO, 499–502
Hydroxyl radical, 513
DMPO adduct, 513
Hyperfine coupling constants
nitroxides, 85–86
solvent dependence, 88
Hyperfine tensor: *see A* tensor

Imidate reagents, 443–444
Interacting spin probes: *see* Dipolar interaction
Iodoacetic acid, ^{14}C-iodoacetic acid, 553
IPG, 597–599
fab fragment, 599–604
Indole acetic acid, 520–521
Inhomogeneous broadening, 77–103, 256–258
Iron (III), nitroxyl interaction, 369–371, 378–382
Isocyanates, 434, 436, 473
Isothiocyanates, 436–437
Isotope-labeled reagents, 428–429
Isotopically substituted spin labels, 547–595
adenine nucleotide spin labels, 581–582
advantages, 547–552
applications, 563, 582, 592, 615–616
deuterated maleimide spin label, DMSL, 552–561
enhanced resolution, 547–549
fatty acid spin labels, 582–592
history, 547–549, 616
increased sensitivity, 547, 549
spectral simplification, 547, 549
syntheses, 615–632
NAD^+ spin labels, 556–580
Isotopically substituted spin labels (*Cont.*)
^{15}N deuterated maleimide spin label, ^{15}N,DMSL, 552–563
Isotropic rotational motion
glyceraldehyde-3-phosphate dehydrogenase (GAPDH), 553–561
lactic dehydrogenase, 564–566
ST-ESR, 140, 159–166

Klystron, 149
$K_3Fe(CN)_6$, 225

Lactoperoxidase, 506–507
Lanczos algorithm, 21–32
computational considerations, 42–52
Gram—Schmidt orthonormalization, 21–23
Lateral diffusion, 269–274
ELDOR, 320–321
stearic acid spin labels, 589–591
^{14}N and ^{15}N spin-labeled pairs, 589–591
Leigh method, 339, 361, 369
Lens effect, 152
Ligand exchange, Cu^{2+}, 373
Lignin degradation, 518–519
Line broadening, 135, 147, 166
Line shape
correcting, 103
four-point method, 91
Gaussian content, 78, 88–93, 103
inhomogeneous broadening, 77–130, 256–258
parameters in ST-ESR, 148, 160–166, 168, 170–173
spin exchange, 115–121
theory, 136–139; *see also* Spectral simulations
Voight shape, 88, 93–100, 105, 111
Linewidth, 407, 409, 416
peak-to-peak line width, 139
Linoleic acid, 494
Liouville equation, 190
density operator, 3
diffusion superoperator, 4, 15
superoperator, 4, 8, 14–15, 20
Tze, 237
Wigner rotation matrix, 5, 8
Lipid bilayers, 414, 419, 421
cholesterol and, 166–170
liposomes, 589–592
molecular motion, 166–171
oriented systems, 166–170
Lipid peroxidation, 494–498

Lipid–protein interactions, 277–290
  activity coefficients, 285
  association equilibria, 281–290
  ELDOR, 333
  serum albumin, 583–587
  ^{15}N-stearic acid spin probes, 583–587
Lipid spin probes, 166–171
Long-range interaction, 349–351
Loop-gap resonator, 189, 319, 414, 415

Magic angle, 341, 343, 378
Magnetic resonance imaging (MRI), 465–466
Magnetic tensors
  anistropic, 197
  axial, 197
Maganese (II), nitroxyl interaction, 366–369
Maleimide spin label, ^{15}N,^{2}H, 203, 224
Malonaldehyde, acetyl radical, 516–518
Membrane fluidity, erythrocytes, 587–589
Membranes
  abnormalities, 591
  Duchenne dystrophy, 588–589
  erythrocytes, 587–588
Microwave
  field strength (B_1), 150–152, 154–158, 169
  power, 152, 155, 169
Model membranes, liposomes, DMPC, 589–591
Modulation
  amplitude: *see* Field modulation
  frequency: *see* Field modulation
Molecular motion: *see* Correlation time
Monofunctionalized labels, 450–451
MOPC, 315
Motional regimes, 140
Multibilayers (see Lipid bilayers)
2-Methyl-2-nitrosopropane, 429
3-Methyl indole, 519–520

NAD$^+$ spin labels
  synthesis, 626–628
  C8-(D_{17})SL-NAD$^+$, 564–566, 576–581
  C8-(^{15}N,D_{17})SL-NAD$^+$, 564–566
  C8-SL-NAD$^+$, 564–566
  N^6-(D_{17})SL-NAD$^+$, 564–580
  N^6-(^{15}N,D_{17})SL-NAD$^+$, 571–580
  N^6-SL-NAD$^+$, 564–566, 567–569
Nickel (II), nitroxyl interaction, 364–365
Nitroxide allylic alcohol, 450–451, 475
Nitroxide amino acids, 448–450, 459, 461
Nitroxide polyenes, 451–452
Nitroxide reduction, 225
NMR, difference spectra, 601–604

N^6-(D_{17})SL-NAD$^+$
  advantages, 565–568
  band-3 protein, 579–580
  binding constants, K_1–K_4, GAPDH, 569–571
  binding stoichiometry (GAPDH), 570
  crystalline GAPDH, 576–578
  dipolar interactions, 567–570
  dipolar spectra, 568, 570
  EPR spectra, 568, 570
  formula, 564
  freely tumbling, 567–569
  hyperfine spectra, 567–570
  lactic dehydrogenase, 564–566
  molecular distances, 575–577
  negative cooperativity, NAD$^+$ binding, 572–574
  resolution, 565
  sensitivity, 565
  spectral simulation, 566, 574–576
  synthesis, 626–627
  β-hydroxybutyrate dehydrogenase, 580–581
N^6-(^{15}N,D_{17})SL-NAD$^+$
  advantages, 565–567
  binding stoichiometry (GAPDH), 571–572
  computer simulation, 566, 574–576
  crystalline GAPDH, 576–578
  dipolar interactions, 567, 571
  dipolar spectra, 567
  EPR spectra, 571
  formula, 564
  freely tumbling, 567
  hyperfine spectra, 567
  lactic dehydrogenase, 564–566
  molecular distances, 575–577
  negative cooperativity, NAD$^+$ binding, 572–574
  resolution, 565
  sensitivity, 565
  spectral simplification, 566
  synthesis, 626–627
^{15}N-5-doxylstearic acid spin label (^{15}N-5-NS)
  A tensors, 586–587
  advantages of ^{15}N substitution, 583–589
  binding to albumin, 583–587
  collision frequency, 589–591
  comparison to (^{15}N,D_{12})-5-NS, 583–585
  computer simulation, 586–587
  Duchenne dystrophy, 588–589
  ELDOR spectroscopy, 589–592
  freely tumbling, 583–585
  g tensors, 586–587
  Heisenberg spin exchange, 591

^{15}N-5-doxylstearic acid spin label (^{15}N-5-NS) (*Cont.*)
improved sensitivity, 583–589
liposomes, 590–591
order parameters, 587–588
parameters, *C, C′, L, L″, H, H″*, 586–589
red blood cells, 587–589
ST-EPR spectra, 586–588–589
synthesis, 628–631
^{15}N-5-doxylstearic acid-D_{12} spin label (^{15}N,D_{12}-5-NS)
advantages of ^{15}N,deuterium, 583–589, 632
applications, 591–592
binding to albumin, 583–587
comparison to (^{15}N)-5-NS, 583–585
freely tumbling, 583–585
improved sensitivity, 583–589
order parameters, 587–588
red blood cells, 587–589
synthesis, 632
^{15}N-12-doxylstearic acid spin label (^{15}N-12-NS)
binding to serum albumin, 585
collision frequency, 590–591
comparison to (^{15}N,D_{41})-12-NS
ELDOR spectroscopy, 589–592
Heisenberg spin exchange, 591
improved sensitivity, 583, 585
liposomes, 590–591
red blood cells, 588
^{15}N-12-doxylstearic acid-d_{41} spin label (^{15}N,D_{41}-12-NS)
advantages of ^{15}N and deuterium, 583, 631–632
applications, 591–592
binding to bovine serum albumin, 585
improved sensitivity, 583
synthesis, 631–632
^{15}N-16-doxylstearic acid spin label (^{15}N-16-NS)
binding to serum albumin, 585
collision frequency, 590–591
ELDOR spectroscopy, 589–592
Heisenberg spin exchange, 591
improved sensitivity, 583, 585
liposomes, 590–591
red blood cells, 588
^{15}N-doxylycholestane spin label
advantages of ^{15}N substitution, 583
collision frequency, 591
ELDOR spectroscopy, 591
^{15}N-spin labels, 181, 201, 204
ELDOR, 321–328
^{15}N-cholestane, 583, 591
^{15}N-spin labels (*Cont.*)
^{15}N-5-doxylstearic acid, 582–591, 628–631
^{15}N-12-doxylstearic acid, 583–585, 588–591
^{15}N-^{14}N pairs, 321–331
^{15}N-16-doxylstearic acid, 583–585, 588–591
^{15}N,deutrated maleimide spin label (^{15}N,DMSL)
A tensors, 554–557, 561
advantages, 552
comparison with DMSL, 553–557
comparison with SL-NAD$^+$, 563
computer simulations, 555, 558–559
correlation times, 553, 555–557
D-β-hydroxybutyrate dehydrogenase, 561–563
EPR spectra, 553–555
future applications, 563
g tensors, 554–557, 561
glyceraldehyde-3-phosphate dehydrogenase, 552–562
improved resolution, 553
improved sensitivity, 553
membrane-bound, 559–563
parameters, *I′, I′, I_1, I_2*, 558–559
parameters, *L, L′, L″, H, H″, C, C′*, 555–557, 561
ST-EPR spectra, 555–559
sulfhydryl interactions, 553
synthesis, 616
^{15}N,deuterated-spin labels
2'- and 3'-(^{15}N,D_{13})SL-ATP, 582
C_8-(^{15}N,D_{17})SL-AMP, 581
C_8-(^{15}N,D_{17})SL-NAD$^+$, 564–566, 627–628
^{15}N,deuterated maleimide spin label (^{15}N,DMSL), 553–563, 616
^{15}N-5-doxylstearic acid-d_{12}, 583–589, 632
^{15}N-12-doxylstearic acid-d_{41}, 583—585, 631–632
N^6-(^{15}N,D_{17})SL-NAD$^+$, 564–578, 626–627

Operator space, 7–10
Optimal basis sets, 2
Orbital overlap, weak, 374–375
Order parameters, 267
^{15}N,deuterated stearic acid spin labeled, ^{15}N,D_{12}-5-NS, 587–588
^{15}N-stearic acid spin labels, ^{15}N-5-NS, 587–588
Oriented samples, ordered bilayers, 166–170
Oxigen concentration, 112
Oximetry, 112
Oxygen (molecular)
ESR spectra in the gas phase, 399, 400
direct measurements, 399

Oxygen (molecular) (*Cont.*)
diffusion in hydrocarbons, 417
diffusion in water, 402–404
partition coefficient, 417
Oxygen transport parameter, 414

PADS (Peroxylamine disulfonate), 155
Paramagnetic broadening
of nitroxides, 108
of nuclei, 604–607, 609
PBN, 490
cyanyl radicals, 522–523
CCl_4, 491
3-methyl indole, 519–520
Peroxides, 498
Peroxyl radicals, 497–498
Perturbing sphere method, 156
Phase plot: *see* Spectral displays of ST-ESR
Phase-sensitive detector, 141–145, 152–154
block diagram, 153
reference signal, 142, 152
Phase setting in ST-ESR spectroscopy, 145–146, 160
Phenylhydrazine, 507–513
Phosphinimines, 437
Phosphor(n)ylating reagents, 438–440
Porphyrins, spin-labeled, 356, 370, 374–375
Protein modification reagents, alkylating maleimide spin label, 551–562
Proton hyperfine coupling constants, ENDOR of nitroxides, 82–83
Pyridines, spin-labeled, 355, 365, 367, 368, 374, 386–388
Pyridinyl radicals, 507
3-Pyrroline-1-oxyls, 450–460
4-POBN, 490
Pyrroline-1-oxyls, 458–463

Q factor of cavity: *see* Cavity
Quadrature ST-ESR spectrum: *see* Spectral displays of ST-ESR
Quantitative EPR, 389–391

Reactions of nitroxide reagents with organometallics, 455–456, 460
Reference samples in ST-ESR, 155, 157. 162
Relaxation, 136–139
T_1, 136–139, 141–143, 147, 155, 163, 165, 169–170
T_2, 136–139, 147, 155, 157, 163, 165
Relaxation rates
electron relaxation, 406
nuclear relaxation, 406
Relaxation times
spin-lattice (longitudinal) T_1, 402, 403, 406, 413, 415
spin-spin (transversal) T_2, 402, 403, 407, 416
T_{1e}, 188–189, 234–240, 247
T_{2e}, 188–189, 235–240, 247
Relaximetry, spin label, 314
Rotational correlation time, 108–112, 182, 259, 263

Sample cells
aqueous cells, 150, 157
sample capillaries, 150–151, 154, 157
line samples, 155, 157
point samples, 151, 155, 157
stacks of glass plates, 158
Saturation, 139, 141–143, 146–148, 155, 157, 166–170
Saturation recovery, 179, 226, 234, 240, 305–309
ELDOR, 305
Saturation recovery measurements, 407, 413, 414
long and short pulse, 413, 414
Saturation transfer (ST-EPR), 179, 197, 201, 291–300
anistropic rotation, 294–297
axial tensors, 197
K-band, 217, 219
L-band, 217
multicomponent spectra, 247–300
Q-band, 217, 221–222
S-band, 217, 218
simulations, ^{14}N spin labels, 230
X-band, 217, 219
Saturation transfer ESR: *see* ST-ESR
Simulated spectra, 407, 409, 420
Single crystals, 355–356
Smoluchowski diffusion, 16, 182, 401–402
Spectra subtraction/addition, 278–280
Spectral displays of ST-ESR
in-phase spectrum (I_n), 143–146, 148, 154, 156–162
magnetization hysteresis spectrum (Φ_n), 144–146, 160–163
magnitude spectrum (M_n), 144–146, 160–163
phase plot (P_n), 144–146, 160–163
quadrature spectrum (Q_n), 144–148, 154, 156–166, 168–172
Spectral function, continued fraction representation, 32–37
Spectral simulations: *see* Computer simulations

Spin exchange, 115–121, 256, 269–277
ELDOR, 331
exchange-coupled Bloch equations, 286–291
See also Heisenberg exchange
Spin Hamiltonian
irreducible spherical tensor operator, 10–14
stochastic Liouville, 190
spin interaction
$\frac{1}{2}$–$\frac{1}{2}$, 351–357
1–$\frac{1}{2}$, 364–365
$\frac{3}{2}$–$\frac{1}{2}$, 365–366
$\frac{5}{2}$–$\frac{1}{2}$, 366–371
$\frac{7}{2}$–$\frac{1}{2}$, 371–373
Spin-labeled
amino acids, 429, 433, 436, 440–444, 447–450, 468–471, 474
cholestane, 166–170
CCMV, 171–173
fatty acids, 170, 463–465
hemoglobin, 148, 159–166
peptides, 430, 434, 438, 440–442, 471–472
retinal, 452
virus, 171–173
Spin probes
cholestane spin label, 166–170
fatty acid spin label, 170
Spin traps, 489–533
characterization, 529–531
as enzyme inhibitors, 524–525
as enzyme substrates, 525
imposters, 531–533
in-vivo, 525–529
isotope methods, 529
site-directed, 527–528
ST-ESR
anisotropic motion, 166–173
analysis of ST-ESR spectra, 145–148
baseline correction, 145
basic principles, 132–148
computer simulation, 160, 165, 169–170
digital filtering, 153
effect of field modulation frequency, 163–165
ESR spectrometer, 148–158
harmonic frequencies in, 142–145
in-phase spectrum (see spectral displays)
integral method, 163
isotope enrichment, 164–165
isotropic motion, 140, 159–166
magnetization hysteresis spectrum (see spectral displays)
magnitude spectrum (see spectral displays)
measurement of ST-ESR spectra, 148–158
ST-ESR (*Cont.*)
oriented spin labels, 166–169
parametrizing spectra, 148, 160–166, 168, 170–173
qualitative explanation, 140–143
reference samples, 155, 157, 162
signal-to-noise ratio, 158, 160
spectral displays, 143–146
standard conditions, 156–158, 162
Stearic acid spin labels
advantages of isotopic substitution, 583–589
binding to bovine serum albumin, 583–587
collision frequency, 589–591
Duchenne muscular dystrophy, 588–589
ELDOR spectroscopy, 589–592
erythrocyte membranes, 587–589
liposomes, 589–591
synthesis, 628–632
^{15}N,deuterium substitution, 583–589
^{15}N-isotopic substitution, 582–591
Stokes–Einstein relation, 140, 171
Styrene radical, 523–524
Sulfhydryl groups
bovine serum albumin, 549
glyceraldehyde-3-phosphate dehydrogenase, 552–561
spin labeling, 549, 553, 580
β-hydroxybutyrate dehydrogenase, 561
Sulfur-centered radicals, 502–506
Superhyperfine coupling, 407, 408, 418, 419
Superoxide radical, 513
Synthesis of spin labels, 615–634
deuterated maleimide spin label (DMSL), 616–619
C8-(D_{17})SL-AMP, 620
C8-(D_{17})SL-NAD$^+$, 627–628
C8-(^{15}N,D_{17}),SL-AMP, 620
C8-(^{15}N,D_{17})SL-ATP, 623
C8-(15N,D17)SL-NAD$^+$, 627–628
C8-SL-ADP, 626
C8-SL-AMPPCP, 624–625
C8-SL-AMPPNP, 624–625
N_6-(D_{17})SL-AMP, 619–620
N^6-(D_{17})SL-NAD$^+$, 626–627
N^6-(^{15}N,D_{17})SL-AMP, 619–620
N^6-(^{15}N,D_{17})SL-NAD$^+$, 626–627
N^6-SL-ADP, 626
N^6-SL-ATP, 621–623
N^6-SL-AMPPCP, 624–625
N^6-SL-AMPPNP, 624–625
N-(1-oxyl-2,2,6,6-tetramethyl-4-piperidinyl) maleimide-d_{17} (DMSL), 616–619

Synthesis of spin labels (*Cont.*)
2,2,6,6-tetramethyl-4-piperidone-d_{17}, 617
2'- and 3'- (^{15}N,D_{13})SL-ATP, 625
^{15}N-2-amino-2-methyl-1-propanol, 629
^{15}N-5-doxylstearic acid, 628–631
^{15}N-12-doxylstearic acid, 628
^{15}N-12-doxylstearic acid-d_{12}, 631–632
^{15}N-12-doxylstearic acid-d_{41}, 631
^{15}N-16-doxylstearic acid, 628
^{15}N,D_{17}-DMSL, 616
^{15}N,D_{17}-maleimide spin label, 616
Tempamine
spectra, 87
TEMPOL, spin exchange, 118–121
Tempone
deuterated, 616–618
Gaussian lineshape, 91–93
isotropic Brownian diffusion, 36–42
2D-ESE spectra, 63–64
^{15}N,deuterated, 616–618
Thiol-specific labels, 444–446, 452, 475
Tryptophan, 521–522
$\tau_{\perp}$, $\tau_{//}$, 184, 186

Unsaturated ketones, 455–460, 478
α,β-Unsaturated aldehydes, 450–452, 456–457

Vanadyl, nitroxyl interaction, 386–388
Vertical fluctuations
ELDOR spectroscopy, 589–591
stearic acid spin labels, 589–591
^{14}N and ^{15}N spin label pairs, 589–591
Very slow motion, 180, 263–264
Virus, 171–173
Vitamin B_{12}, 339, 376
Voight, 88, 93–100, 105, 111

Wigner rotation matrix, 5, 8, 10, 13, 17–19

Xanthine oxidase, 377–378
Xanthine dehydogenase, 377–378

Zero field splitting, 370–371, 389